LBL-7355
c.2

MATERIALS AND MOLECULAR RESEARCH DIVISION

Annual Report 1977

TWO-WEEK LOAN COPY

This is a Library Circulating Copy which may be borrowed for two weeks. For a personal retention copy, call Tech. Info. Division, Ext. 6782

RECEIVED
LAWRENCE
BERKELEY LABORATORY

MAY 18 1978

LIBRARY AND
DOCUMENTS SECTION

Lawrence Berkeley Laboratory
University of California, Berkeley

Prepared for the U.S. Department of Energy under Contract W-7405-ENG-48

LBL-7355
c.2

LEGAL NOTICE

This report was prepared as an account of work sponsored by the United States Government. Neither the United States nor the Department of Energy, nor any of their employees, nor any of their contractors, subcontractors, or their employees, makes any warranty, express or implied, or assumes any legal liability or responsibility for the accuracy, completeness or usefulness of any information, apparatus, product or process disclosed, or represents that its use would not infringe privately owned rights.

LBL-7355 MAY 2 8 1976 c.2

Name Location Date

Lawrence Berkeley Laboratory Library
University of California, Berkeley

LBL-7355
UC-13
TID-4500-R66

MATERIALS AND MOLECULAR RESEARCH DIVISION

Annual Report
1977

Lawrence Berkeley Laboratory
University of California
Berkeley, California

CONTENTS

GENERAL INTRODUCTION 1
David A. Shirley and Rolf H. Muller

I. MATERIALS SCIENCES
A. Metallurgy and Ceramics
1. Structure of Materials

a. Microstructure, Properties and Alloy Design
Gareth Thomas, Principal Investigator

1. Introduction: Fundamentals of Microstructure Property Relations 7
2. Design of Strong, Tough Structural Steels 7
3. Spinodal Alloys 16
4. Duplex Steels 18

b. Ceramic Alloy Program
Gareth Thomas, Principal Investigator

1. Magnetic Ceramics 22
2. Refractory Ceramics-- Silicon Nitride and Sialons 27

c. High Resolution Electron Microscopy
Gareth Thomas, Principal Investigator

1. Direct Observations of Plane Matching By Lattice Imaging Electron Microscopy . . 30
2. High Resolution Analyses of Grain Boundary Reactions 32
3. Lattice Imaging Studies of Spinodal Decomposition 34
4. Determination of Local Composition By Lattice Imaging 35
5. Beam Enhanced Oxidation in the Transmission Electron Microscope 36
6. Research Plans for Calendar Year 1978 38
7. 1977 Publications and Reports 39

d. High Voltage Electron Microscopy
K. H. Westmacott, Principal Investigator

1. Introduction 43
2. Research Plans for Calendar Year 1978 46
3. 1977 Publications and Reports 46

e. Powder Metallurgy
Milton R. Pickus, Principal Investigator

1. Liquid Phase Sintering of Iron Powder Premixed with a Copper-Base Intermetallic Compound 47
2. Investigation of Wear Resistant Materials Based on Intermetallic Compounds of Nickel-Titanium-Silicon Dispersed in Metal Matrices 48
3. The Effect of Magnetically Aligned Powder on the Magnetostriction of Sintered Rare Earth-Iron Laves Phase Compounds 49
4. Research Plans for Calendar Year 1978 50
5. 1977 Publications and Reports 50

2. Mechanical Properties

a. Theoretical Problems in Alloy Design
J. W. Morris, Jr., Principal Investigator

1. Theory of Phase Transformations 51
2. Simulation and Characterization of Polygranular Microstructure 54
3. Mechanical Deformation 57
4. The Influence of Phase Transformation on Mechanical Properties at Cryogenic Temperatures 60
5. The Development of New Structural Alloys for Energy-Related Applications 62
6. Welding Research 67
7. Research Plans for Calendar Year 1978 68
8. 1977 Publications and Reports 68

b. Research in Alloy Design
V. F. Zackay and E. R. Parker, Principal Investigators

1. Fundamental Investigations of Continuous Precipitation in an Fe-Nb Creep-Resistant Alloy 70
2. Modeling of Work Hardening in Transforming Alloy Steels 71
3. Investigation of Microstructure and Mechanical Properties in Transforming Fe-Mn-Cr Alloys 72
4. Fundamental Investigations in Structure-Property Relationships in Eutectoid Steels 73
5. Relationships of Plastic Strain Energy Absorption to Properties in Steels . . . 74
6. Modeling of the Electroslag Refining Process 76
7. Review of Low Alloy Steel Development for Improved Properties 76
8. 1977 Publications and Reports 80

c. Relations Between Dislocations, Point Defects and Properties of Metal
Jack Washburn, Principal Investigator

1. Economic Utilization of Solar Energy 82
2. Ion Implantation in Silicon 85
3. Field Desorption Microscopy 88
4. Environmental Research 88
5. Research Plans for Calendar Year 1978 89
6. 1977 Publications and Reports 89

d. Erosion-Corrosion Behavior of Materials
Alan V. Levy, Principal Investigator

1. Erosion Behavior 91
2. Corrosion Behavior 102
3. Research Plans for Calendar Year 1978 116
4. 1977 Publications and Reports 116

3. Physical Properties

a. Superconductivity Effects -- High Field Superconductivity
Milton R. Pickus, Principal Investigator

1. A New A15 Multifilamentary Superconductor Based on the Niobium-Aluminum-Silicon System 118
2. Kinetic Study of the Formation of the A15 Compound $Nb_3(Al_xGe_{1-x})$ Using an Internal Surface as the Reaction Site 119
3. Improved Formability of Aluminum-Germanium Near Eutectic Compositions Through the Application of Superplasticity Principles 120
4. Preliminary Investigation of Hydrostatic Extrusion of Infiltrated Niobium-Tin Composites 121
5. An Investigation Into the Production of Metastable Nb_3Ge Powder Via the Rotating Electrode Process 122
6. Research Plans for Calendar Year 1978 124
7. 1977 Publications and Reports 124

b. Microstructure and Mechanical Behavior of Ceramics; Glass- and Ceramic-Metal Systems
Joseph A. Pask, Principal Investigator

1. Metastable Phase Relationships in System SiO_2-Al_2O_3 125
2. Microstructure Development and Correlation With 1200°C Stress-Strain Behavior of Sintered Mullite 126
3. Mechanical Properties of Mullite-Alumina Compositions at Room Temperature and 1400°C 129
4. Corrosive Resistance of Mullite-Alumina Compositions 130
5. Elasticity and Internal Friction in Al_2O_3-SiO_2 Compositions at Elevated Temperatures 133
6. Characterization and Strength of Sialon-Type Materials 135
7. High-Temperature Compressive Stress-Strain Behavior of MgO 136
8. Reactions and Diffusion in the Silver-Arsenic Chalcogenide Glass System 137
9. Research Plans for Calendar Year 1978 139
10. 1977 Publications and Reports 139

c. High Temperature Reactions
Alan W. Searcy, Principal Investigator

1. The Kinetics and Thermodynamics of Decomposition of Dolomite to a Metastable Solid Product . . . 141
2. Transport of Gases Through Porous Oxide Barriers . . . 141
3. Characterization of the Gaseous and Solid Products of Aluminum Sulfate Decomposition . . . 142
4. The Influence of Vacuum on the Stability and Surface Area of CaO Powders Formed by Decomposing $CaCO_3$ . . . 142
5. The Influence of CO_2 Partial Pressures and Time on the Structure and Morphology of Calcium Oxide from Calcite Decomposition . . . 143
6. Catalysis of the Hot Pressing of Calcium Oxide by Carbon Dioxide Gas . . . 144
7. Evaluation of Active CaO for Use in Cements . . . 145
8. Thermodynamic Properties of SeS Gas . . . 145
9. Research Plans for Calendar Year 1978 . . . 145
10. 1977 Publications and Reports . . . 146

d. Relation of Microstructure to Properties in Ceramics
Richard M. Fulrath, Principal Investigator

1. Thick Film Conductors . . . 147
2. Phase Equilibria in the $PbO-Al_2O_3$ System . . . 150
3. Kinetics of Solid State Reactions in the $PbO-ZrO_2-TiO_2$ System . . . 151
4. Quantizing the Polarization of Lead Zirconate-Titanate . . . 152
5. Experiments in Liquid Phase Sintering of Si_3N_4 . . . 153
6. Effect of Surface Treatments on Strength of PZT Ceramics . . . 154
7. Research Plans for Calendar Year 1978 . . . 156
8. 1977 Publications and Reports . . . 157

e. Structural and Electrical Properties of Composite Materials
Robert H. Bragg, Principal Investigator

1. Microstructure and Kinetics of Void Growth in Glassy Carbon . . . 158
2. Small Angle X-Ray Scattering from Diffuse Interfaces . . . 162
3. The Texture and Interphase Relationships in Directionally Solidified $Al-CuAl_2$ Eutectic Alloy . . . 164
4. Thermal Expansion of Directionally Solidified $Al-CuAl_2$ Eutectic . . . 166
5. Tensile Properties of Directionally Solidified $Al-CuAl_2$ Eutectic . . . 170
6. Research Plans for Calendar Year 1978 . . . 171
7. 1977 Publications and Reports . . . 172

B. Solid State Physics
1. Experimental Solid State Physics

a. Far Infrared Spectroscopy
Paul L. Richards, Principal Investigator

1. Infrared Surface Spectroscopy . . . 173
2. Far Infrared Photoconductivity of Uniaxially Stressed Germanium . . . 173
3. Far Infrared Bolometer Detectors . . . 175
4. A New Measurement of the Near-Millimeter Spectrum of the Cosmic Background Radiation . . . 175
5. Far Infrared Sky Survey . . . 176
6. New Polarizing Interferometer . . . 176
7. Far Infrared Spectroscopy of Electrons on the Surface of Liquid Helium . . . 177
8. White Mountain Radiometer . . . 177
9. Superconducting Heterodyne Receivers . . . 177
10. Research Plans for Calendar Year 1978 . . . 178
11. 1977 Publications and Reports . . . 178

b. Experimental Solid State Physics and Quantum Electronics
Y. Ron Shen, Principal Investigator

1. Study of Surface Exciton-Polaritons by Optical Mixing . . . 180
2. Multi-Magnon Luminescence in Antiferromagnets . . . 182
3. Sum-Frequency Generation in Na Vapor Via a Resonant Quadrupole Transition . . . 183
4. Third Order Nonlinear Optical Spectroscopy . . . 185
5. Use of Ellipse Rotation Within a Laser Cavity for Pulse Shaping . . . 186
6. Brillouin Scattering Spectrometer . . . 186
7. DC Kerr Effects in Liquid Crystalline Materials . . . 186
8. Transient Behavior of a Nonlinear Optical Fabry-Perot . . . 188
9. Laser Interaction with Molecular Beams . . . 189

10. Theory of Multiphoton Dissociation of Molecules 190
11. Experiments on Multiphoton Dissociation of Molecules 191
12. Research Plans for Calendar Year 1978 191
13. 1977 Publications and Reports 191

c. Excited Quantum Fluids in Solids
Carson D. Jeffries, Principal Investigator

1. Nucleation Phenomena in Electron-Hole Droplet Formation 193
2. Motion of Electron-Hole Droplets in Germanium 194
3. Resonant Scattering of Free Carriers by Electron-Hole Drops 195
4. Properties of the Strain-Confined Electron-Hole Liquid in Ge 196
5. Measurement of Compressibility of the Electron-Hole Liquid in Ge 198
6. Magnetic Properties of Electron-Hole Drops 199
7. Alfvén Wave Resonances in Plasma Spheres 200
8. Research Plans for Calendar Year 1978 201
9. 1977 Publications and Reports 203

d. Superconductivity, Superconducting Devices, and 1/f Noise
John Clarke, Principal Investigator

1. Geophysics with SQUIDs 204
2. Superconducting Thin-Film Gradiometer and Magnetometer 205
3. Microwave-Enhancement of the Superconducting Energy Gap 207
4. Measurement of the Electron-Phonon Relaxation Rate in Aluminum 209
5. Boundary Resistance of SNS Sandwiches and the Measurement of Branch Crossing Times in Lead and Tin 210
6. Research Plans for Calendar Year 1978 211
7. 1977 Publications and Reports 212

2. Theoretical Solid State Physics

a. Theoretical Solid State Physics
Marvin L. Cohen, Principal Investigator

1. Surface States on Clean Germanium and Diamond Crystals 214
2. Reconstruction of Semiconductor Surfaces: The Si (001) Surface 215
3. Surface and Bulk Electronic Properties of Transition Metals 217
4. Electronic Structure of Metal-Ge and Metal-Diamond Interfaces (Schottky Barriers) 217
5. Semiconductor-Semiconductor Interfaces and Superlattices 218
6. Molecular Electronic States and Adsorbates on Solids 219
7. Research Plans for Calendar Year 1978 220
8. 1977 Publications and Reports 220

C. Materials Chemistry
1. Chemical Structure

a. High Pressure Chemistry
George Jura, Principal Investigator

1. Heat Capacity of Aluminum and Heat Diffusivity of Silver Chloride to Pressures of 135 kbars 222
2. Research Plans for Calendar Year 1978 223

b. Low Temperature Properties of Materials
Norman E. Phillips, Principal Investigator

1. Pressure Dependence of the Heat Capacity of Teflon at Low Temperatures 224
2. Heat Capacity of the Spin-Glass CuMn 225
3. Research Plans for Calendar Year 1978 226

c. Electrochemical Processes
Charles W. Tobias, Principal Investigator

1. Fundamental Studies of Transport Phenomena in Electrochemical Reactors 228
2. Research Leading to New Electrolytic Processes 228
3. Research Plans for Calendar Year 1978 229
4. 1977 Publications and Reports 229

2. High Temperature and Surface Chemistry

a. High Temperature Chemistry
Leo Brewer, Principal Investigator

1. Thermodynamics and Phase Diagrams of the Binary Systems of Molybdenum 231
2. High-Temperature Solid-Electrolyte Cell and High-Temperature Gaseous Equilibria Studies of Generalized-Lewis-Acid-Base Interactions in Binary Metallic Alloys 231
3. Matrix Isolation Spectra 232
4. Thermodynamics of Gaseous Metal Clusters 232
5. Research Plans for Calendar Year 1978 232
6. 1977 Publications and Reports 233

b. Nuclear Technology Problems
Donald R. Olander, Principal Investigator

1. Molecular Beam Study of the Kinetics of the Fluorine-Uranium Dioxide Reaction 234
2. A Mechanistic Interpretation of the H_2O/C Reaction 235
3. Particle Cavitation During Hydrogen Reduction of Mixed Oxide Fuel 236
4. In-Pile Homogenization of Mixed-Oxide Fuel 237
5. The Surface Chemistry of Epitaxial Silicon Deposition by Thermal Cracking of Silane 238
6. Retention and Release of Water Vapor by Uranium Dioxide 239
7. Research Plans for Calendar Year 1978 240
8. 1977 Publications and Reports 241

c. Process Technology of Solid State Materials
Lee F. Donaghey, Principal Investigator

1. Thermodynamic Study of the Ternary Liquid Alloy System Ga-In-Sb by Solid State Electrochemistry 242
2. Component Activities in In-Sb Liquid Alloys 242
3. Solid State Electrochemical Studies of Group III-V Alloys Employing A CaF_2 Solid Electrolyte 242
4. Erosion Properties of Reactively Sputtered Titanium Carbonitrides 242
5. Numerical Simulation of Transport Processes in Vertical Cylinder Epitaxy Reactors 244
6. Kinetics of the Chemical Vapor Deposition of GaAs from $Ga(CH_3)_3$ and AsH_3 244
7. Low Pressure Chemical Vapor Deposition of Polysilicon 245
8. 1977 Publications and Reports 245

d. Electrochemical Phase Boundaries
Rolf H. Muller, Principal Investigator

1. Ellipsometry of Electrochemical Interfaces 247
2. Laser Interferometry of Mass-Transfer Boundary Layers 250
3. Research Plans for Calendar Year 1978 250
4. 1977 Publications and Reports 251

e. Solid State and Surface Reaction Studies. Surface Science and Heterogeneous Catalysis
Gabor A. Somorjai, Principal Investigator

1. Surface Structure and Chemisorption by Low-Energy Electron Diffraction 252
2. Electron Spectroscopy Studies of Solid Surfaces and Adsorbates 254
3. Molecular Beam-Surface Interactions 255
4. Studies of Catalyzed Surface Reactions 256
5. Research Plans for Calendar Year 1978 257
6. 1977 Publications and Reports 257

f. Nuclear Magnetic Resonance
Alexander Pines, Principal Investigator

1. Multiple Quantum Spectroscopy 260
2. Multiple Quantum Echoes and Selective Detection 261
3. Distribution of Multiple Quantum Coherence 262
4. NMR Analysis of Whole and Processed Coals 262
5. Synthesis of Isotopically Labeled Liquid Crystals 263
6. Low Temperature Liquid Crystal and Phase Transitions 263
7. Conformation of Aliphatic Chains in Liquid Crystals 264
8. Ferroelectric Phase Transition in Squaric Acid 265
9. Enhancement of the Magnetic Isotope Effect 265
10. Research Plans for Calendar Year 1978 266
11. 1977 Publications and Reports 266

II. CHEMICAL SCIENCES
A. Fundamental Interactions
1. Radiation Sciences

a. Photochemistry of Materials in the Stratosphere
Harold S. Johnston, Principal Investigator

1. The Photochemistry of NO_3 and the Kinetics of the N_2O_5-O_3 System. 271
2. Primary Products in the Photochemistry of Nitrogen Pentoxide 276
3. Nitrous Oxide Ultraviolet Absorption Spectrum at Stratospheric Temperatures 278
4. Kinetic Energy and Wavelength Dependence of the Reaction of Nitric Oxide with Ozone 280
5. The Origin of Nitrous Oxide in Smoke Stacks from High Temperature Combustion 281
6. Interpretation of Observed Trace Species in the Stratosphere 283
7. Research Plans for Calendar Year 1978 288
8. 1977 Publications and Reports 289

b. Radiation Chemistry of Heavy Particles
Michael E. Jayko

1. Introduction 290
2. 1977 Publications and Reports 293

c. Photon-Assisted Surface Reactions on Well-Characterized Surfaces
Gabor A. Somorjai, Principal Investigator

1. Light-Assisted Surface Reactions: Thermodynamically Uphill Catalysis 294
2. Spectral Sensitization of Semiconductor Surfaces by Organic Dyes 294
3. Research Plans for Calendar Year 1978 294
4. 1977 Publications and Reports 294

2. Chemical Physics

a. Energy Transfer and Structural Studies of Molecules on Surfaces
Charles B. Harris, Principal Investigator

1. Introduction 296
2. The Spectroscopy of Molecules Adsorbed on Metal Surfaces 296
3. Energy Transfer Studies in Condensed Phases and Picosecond Laser Spectroscopy 302
4. Coherent Spectroscopy in Excited Triplet States 311
5. Thermal Modulation Spectroscopy 315
6. Remote Satellite Computer Systems Development 320
7. Research Plans for Calendar Year 1978 321
8. 1977 Publications and Reports 322

b. Physical Chemistry with Emphasis on Thermodynamic Properties
Kenneth S. Pitzer, Principal Investigator

1. Effective Potentials Based on Relativistic Wavefunctions 324
2. Potential Curves for Xe_2, Xe_2^+, and Xe_2^* Based on Effective Potentials 325
3. Thermodynamic Properties of Aqueous Solutions of Rare Earth Chlorides, Nitrates and Perchlorates 326
4. Thermodynamics of Electrolytes; Enthalphy and the Effect of Temperature on Activity Coefficients 328
5. Research Plans for Calendar Year 1978 329
6. 1977 Publications and Reports 330

c. Chemical Dynamics Studies
Bruce H. Mahan, Principal Investigator

1. Transport in Gases: An Alternative Treatment 331
2. Laser Induced Fluorescence of Gaseous Ions 331
3. Dynamics of the F^+-H_2 Reaction 331
4. Dynamics of CO_2^+-D_2 Collisions at Low Energies 332
5. Research Plans for Calendar Year 1978 332
6. 1977 Publications and Reports 332

d. Theory of Low Energy Atomic and Molecular Collisions
William H. Miller, Principal Investigator

1. Penning Ionization of H_2 by He 334
2. Unified Treatment of Penning Ionization and Excitation Transfer 334
3. Semiclassical Description of Interference Effects in Rotational State Distributions 336
4. Semiclassical Eigenvalues for Finite Intervals 337
5. Semiclassical Phase Space Distributions 338
6. Research Plans for Calendar Year 1978 339
7. 1977 Publications and Reports 340

e. Photoelectron Spectroscopy
David A. Shirley, Principal Investigator

1. Thermal Diffuse Scattering in Photoemission: A New Effect 341
2. The Band-6 Resonance in Angle-Resolved Photoemission from Cu(110): Direct Determination of Total Valence-Band Dispersion Relations 342
3. Electron Refraction into Vacuum from Angle-Resolved Photoemission 344
4. Evidence for the Itinerant Electron Model of Ferromagnetism and for Surface Photoemission from Angle-Resolved Photoemission Studies of Iron 346
5. Temperature Independence of the Angle-Resolved X-Ray Photoemission Spectra of Gold and Platinum Valence Bands 348
6. Molecular-Orbital Photoemission Enhancement in Adsorbates at Substrate Cooper Minimum Energies 350
7. Direct Observation of Photoelectron Low-Energy Electron Diffraction (PLEED) at High Photon Energies 353
8. D-Orbital Directed Photoemission in MnF_2 356
9. The Relation Between Satellite Peaks in X-Ray Emission and in X-Ray Photoemission Spectra 357
10. Absorption Spectroscopy in the Carbon 1s Shell: Chemical Shifts in Kynar and Exafs in Graphite 359
11. Time-Resolved Fluorescence of XeF* from the VUV Photodissociation $XeF_2 \rightarrow XeF^* + F$ Induced by Synchrotron Radiation 361
12. VUV Studies for $\lambda < 1000$ Å: Time-Resolved Spectroscopy in N_2^+ 362
13. Molecular Orbital Structure of the IV-VI Diatomics from Photoelectron Spectroscopy 364
14. Radiation Damage Studies by X-Ray Photoelectron Spectroscopy. I. Electron-Irradiated $LiNO_3$ and Li_2SO_4 368
15. Radiation Damage Studies by X-Ray Photoelectron Spectroscopy. II. Electron Irradiated Li_2CrO_4 and Li_2WO_4 371
16. Molecular Beam Photoelectron Spectroscopy 373
17. Valence-Band Studies of Liquid Metals 374
18. Research Plans for Calendar Year 1978 376
19. 1977 Publications and Reports 376

f. Crossed Molecular Beams
Yuan T. Lee, Principal Investigator

1. Atomic Oxygen Source Development and a Study of the $O + ICl \rightarrow IO + Cl$ Reaction 379
2. Reactions of $O + C_2H_5I$ and $O + CF_3I$ 381
3. Substitution Reaction of Cl + Bromopropene 382
4. Improved Potentials for Ar-Kr and Ar-Xe 384
5. Proton Affinities of Hydrogen Fluoride and Its Clusters Determined in Molecular Beam-Photoionization Experiments 386
6. Thermochemical Quantities of NH_3 and Its Clusters 388
7. Photoionization Studies of $(C_2H_4)_2$ and $(C_2H_4)_3$ 389
8. Decomposition Channels in Multiphoton Dissociation 392
9. A Phenomenological Model For Multiphoton Dissociation 394
10. Chemiluminescence of $NO + O_3 \rightarrow NO_2^* + O_2$ 396
11. Research Plans for Calendar Year 1978 397
12. 1977 Publications and Reports 398

g. Molecular Electronic Structure Theory
Henry F. Schaefer III, Principal Investigator

1. Energy Separation Between the Open (C_{2v}) and Closed (D_{3h}) Forms of Ozone . . . 400
2. Metal-Carbene Complexes and the Possible Role of Hydroxycarbene in Formaldehyde Laser Photochemistry 401
3. The Fuzzy Interface Between Surface Chemistry, Heterogeneous Catalysis, and Organometallic Chemistry 403
4. Electron Correlation Effects on the Excitation Energies of the Lowest Triplet States of Glyoxal 404

5. Some Features of the Potential Energy Surfaces for the $F^+ + H_2$ Ion-Molecule Reaction 404
6. Research Plans for Calendar Year 1978 406
7. 1977 Publications and Reports 406

3. Atomic Physics

a. Low Energy Atomic Physics
Howard A. Shugart, Principal Investigator

1. Laser Developments 409
2. Thallium Spectroscopy and Neutral Weak Interactions 409
3. Experiments on Stored Ions 410
4. Atomic Absorption Spectroscopy 411
5. Research Plans for Calendar Year 1978 412
6. 1977 Publications and Reports 412

b. Studies on Highly Stripped Heavy Ions
Richard Marrus, Principal Investigator

1. Oscillator Strengths of Low-Lying Transitions of Li-Like and Be-Like Iron (Z=26) 414
2. Quenching of the Metastable State of Hydrogen-Like Argon in an External Electric Field 417
3. Single Photon Decay of Metastable $2S_{1/2}$ State in Hydrogen-Like Atoms 418
4. Theoretical Study of Electric-Field Induced Decays 418
5. Research Plans for Calendar Year 1978 418
6. 1977 Publications and Reports 419

4. Chemical Energy

a. Formation of Oxyacids of Sulfur from SO_2
Robert E. Connick, Principal Investigator

1. The Raman Spectrun of HSO_3^- and $S_2O_5^=$--Isotope Effects 420
2. Chemical Dynamics of Metal Complexes--The Bisiminodiacetate Complex of Nickel Ion 421
3. Research Plans for Calendar Year 1978 422

b. Conversion of Coal to Clean Liquid and Gaseous Fuels
Gabor A. Somorjai and Alexis T. Bell, Principal Investigators

1. Hydrogenation of CO and CO_2 over Iron Foils. Correlations of Rate, Product Distribution and Surface Composition 423
2. Studies of Fischer-Tropsch Synthesis on Supported Ruthenium Catalysts 423
3. Novel Transition-Metal Cluster Catalysts in Hydrogenation, Hydrogenolysis, and Methanation 424
4. Activated Benzenoid Hydrocarbons 426
5. Research Plans for Calendar Year 1978 427
6. 1977 Publications and Reports 428

c. Synthetic and Physical Chemistry
William L. Jolly, Principal Investigator

1. X-Ray Photoelectron Spectroscopy 430
2. Synthetic and Mechanistic Studies 435
3. Research Plans for Calendar Year 1978 438
4. 1977 Publications and Reports 438

d. Electrochemical Systems
John Newman, Principal Investigator

1. Vapor-Liquid Equilibria in Multicomponent Aqueous Solutions of Volatile Electrolytes 439
2. Corrosion of Iron-Based Alloys by Coal Char 439
3. Simultaneous Reactions on a Rotating-Disk Electrode 439
4. A Model for the Anodic Dissolution of Iron in H_2SO_4 441
5. Ring Electrodes 441
6. Mass Transfer in Turbulent and Transitional Flow at Ring Electrodes 442
7. Potential Distributions in Finite Cell Geometries 442
8. Research Plans for Calendar Year 1978 442
9. 1977 Publications and Reports 442

e. Delocalized-Electron Solids and High-Energy Oxidizers
Neil Bartlett, Principal Investigator

1. Graphite and Boron-Nitride Salts 444
2. Salts Derived from $C_5F_5N^+$ and Other Aromatics 446
3. Oxidation of Chlorine by Metal Hexafluorides 447
4. Research Plans for Calendar Year 1978 448
5. 1977 Publications and Reports 449

III. NUCLEAR SCIENCES
A. Low Energy Nuclear Sciences
1. Heavy Element Research

a. Actinide and Lanthanide Chemistry
Norman M. Edelstein, Richard A. Anderson, Neil Bartlett, John G. Conway, Kenneth Raymond, Glenn T. Seaborg, Andrew Streitwieser, Jr., David H. Templeton and Allan Zalkin, Principal Investigators

1. Highly Selective Sequestering Agents for Plutonium and Other Actinides in the 4+ Oxidation State 453
2. Synthetic and Structural Studies of Actinide and Other Compounds 457
3. Physical and Spectroscopic Studies 469
4. Research Plans for Calendar Year 1978 474
5. 1977 Publications and Reports 476

IV. ADVANCES ISOTOPE SEPARATION TECHNOLOGY
1. Laser Concepts

a. Selective Photochemistry
C. Bradley Moore, Principal Investigator

1. Infrared Multiphoton Processes in Formaldehyde 481
2. ICl^* ($A^3\Pi_1$, v') + H_2 Photochemistry 481
3. Appearance Rates of Photochemical Products in Formaldehyde Photodissociation 483
4. Fluorescence Decay Times and Energy Transfer in the $\underset{\sim}{A}\ ^1A_2$ State of Formaldehyde 484
5. Vibrational Relaxation of Matrix-Isolated HCl and DCl 486
6. Optical Parametric Oscillator Development 488
7. Vibrationally Induced Photochemistry 488
8. Research Plans for Calendar Year 1978 489
9. 1977 Publications and Reports. 490

b. Molecular Beam Laser Isotope Separation
Yuan T. Lee and Y. Ron Shen, Principal Investigators

1. Molecular Dimer Dissociation by CO_2 Laser Irradiation 492
2. Dynamics of Infrared Multiphoton Dissociation of Polyatomic Molecules 493
3. Three-Center and Four-Center Elimination in Multiphoton Dissociation of Molecules 495
4. Effect of Hot Band Excitation in Multiphoton Dissociation of Polyatomic Molecules 496
5. Internal Energy Dependence of the CCl_4 Condensation Coefficient Determined from Molecular Beam Surface Scattering Experiments 497
6. Research Plans for Calendar Year 1978 501
7. 1977 Publications and Reports 501

V. ENERGY TECHNOLOGY

a. Development of Electrochemical Synthesis and Energy Conversion
J. W. Evans, R. H. Muller, J. Newman, and C. W. Tobias, Principal Investigators

1. Process Evaluation for the Electrowinning and Refining of Potassium 505
2. Anodic Surface Layers on Battery Materials 505
3. Surface Morphology of Metals in Electro-Deposition 509
4. Analysis and Simulation of Electrochemical Systems 510
5. Current Inefficiencies in Aluminum Reduction Cells 512
6. Research Plans for Calendar Year 1978 513
7. 1977 Publications and Reports 513

VI. FOSSIL ENERGY
Fossil Energy

a. Interfacial Properties of Coal in Relation to Its Direct Utilization
Douglas W. Fuerstenau, Principal Investigator

1. The Interfacial Properties of Coal 517
2. Research Plans for Calendar Year 1978 519
3. 1977 Publications and Reports 519

b. Applied Alloy Design
Victor F. Zackay and Earl R. Parker, Principal Investigators

1. Wear Resistant Alloys for Coal Handling Equipment 520
2. Alloy Development for Sulfidation Resistance and Mechanical Properties at Elevated Temperatures 525
3. Low Alloy Steels for Thick Wall Pressure Vessels 526
4. 1977 Publications and Reports 529

c. Solid State NMR Analysis of Coal
Alexander Pines, Principal Investigator

1. NMR Analysis of Whole and Processed Coals 532
2. High Resolution Deuterium NMR in Solids 532
3. Double Quantum Deuterium NMR 533
4. Research Plans for Calendar Year 1978 534
5. 1977 Publications and Reports 534

VII. SOLAR ENERGY DEVELOPMENT
1. Photovoltaic Energy Conversion

a. Research on CdS-Cu_xS and (CdZn)S-Cu_xS Solar Cell Materials
Jack Washburn, Principal Investigator

1. Growth of (Cd,Zn)S and CdS Thin Films 539
2. Defects in Epitaxial CdS and (Cd,Zn)S Layers 539
3. Theoretical and Experimental Heterojunction Characterization 541
4. Research Plans for Calendar Year 1978 542
5. 1977 Publications and Reports 542

VIII. APPENDICES
A. Materials and Molecular Research Division Staff - 1977 545

B. Surface Science and Catalysis Science Seminars 553

GENERAL INTRODUCTION

David A. Shirley, Division Head
Rolf H. Muller, Assistant to the Division Head

Calendar 1977 was a year of further consolidation and change for the Materials and Molecular Research Division. There were 48 principal investigators in the Division at the end of 1977, as well as 122 postdoctorals and other scientific personnel, 274 graduate students and 63 technical, administrative and clerical support staff for a total of 507. The fiscal 1978 operating budget at this writing is $8,804,000. One hundred and fifty-nine journal articles were published by MMRD members during 1977, and 32 Ph.D. and 20 M.S. degrees were awarded to MMRD students.

During 1977 the Department of Energy came into being, and the Energy Research and Development Administration ceased to exist. The implications of this change for our division are not clear as yet, but MMRD research has continued in a strong and essentially uninterrupted manner. New projects were either started or are planned in the following areas:

- Hot Corrosion of Metal Alloys. Following the identification of this topic as an extremely high priority area for research in Materials Science, MMRD conducted a world-wide search for a new investigator to initiate research in this area. It is expected that an investigator will be added and the project initiated in 1978.

- Ceramics. As part of a long-term program to increase MMRD's strength in ceramics, two positions have been widely advertised, and a number of applicants have been interviewed. It is expected that both positions will be filled during 1978.

- Atomic Resolution Microscopy. In a continuing effort to establish a capability in high resolution electron microscopy, Professor Gareth Thomas and Dr. Ronald Gronsky have developed proposals for an Atomic Resolution Microscopy facility in MMRD.

- Current and Power Inefficiency in Aluminum Reduction Cells. Professor James W. Evans of the Materials Science and Mineral Engineering Department has initiated this project with the Energy Storage Program of DOE.

- Reduction of Energy Losses Through an Understanding of Electrolytic Gas Evolution. This project was initiated by Professor Charles W. Tobias with DOE's Division of Industrial Energy Conservation.

- In-Situ Investigations of Solid-Gas Reactions. This project will be initiated by Professor James W. Evans in fiscal year 1979.

- Plasma Enhanced Deposition of Thin Films. This project will be initiated by Professor Dennis Hess in fiscal year 1979. Professor Hess joined the Chemical Engineering Department in the Fall of 1977.

- Photon-Assisted Surface Reactions, Materials and Mechanisms. Professor Gabor Somorjai of our Division has initiated this project in fiscal year 1978.

- Metal Cluster-Metal Surface Analogy. This project will be initiated in fiscal year 1978 by Professor Earl Muetterties, who will be joining the Berkeley Chemistry Department. Professor Muetterties is a well-known inorganic chemist, with an international reputation in the area of homogeneous catalysis.

- Transition Metal Catalyzed Conversion of CO, NO, H_2 and Organic Molecules to Fuels and Petrochemicals. Professor Robert G. Bergman, a well-known organic chemist, will join Berkeley's Chemistry Department and initiate this project in MMRD in fiscal year 1979.

- Molecular Thermodynamics of Phase Equilibria for Water Hydrocarbon Systems at High Pressures with Special Attention to the System Brine Methane. Professor John M. Prausnitz of Berkeley's Chemical Engineering Department initiated this project in fiscal year 1978.

- Energy Transfer and Structural Studies of Molecules on Surfaces. Professor Charles B. Harris, who has been with the Division for some time, has reprogrammed his research in MMRD to bring his talents to play on the important problem of interactions of molecules on surfaces.

- Dynamics and Chemistry of Highly Excited Molecules. Professor C. B. Moore, who for some years has conducted a laser isotope separation program in the Division has now initiated this program under the auspices of the Basic Energy Sciences Division.

- Molecular Beam Spectroscopy. Professor John S. Winn of the Berkeley Chemistry Department will initiate this program in fiscal year 1979.

- Research on Photovoltaic Solar Energy Converters. Professor Jack Washburn is conducting this program in the Solar Energy Development Division of DOE.

- Coal Liquefaction Alloy Test Program. Mr. Alan Levy began this program in early 1977, under the auspices of the Fossil Energy Development Division of ERDA and now DOE.

MMRD also suffered a number of losses in 1977. Professor Richard M. Fulrath passed away on July 16, 1977. Dick Fulrath had been with the Division since 1962. He served his profession well as an outstanding research scientist and teacher, and he will be sorely missed as a colleague and friend.

Dr. Warren M. Garrison retired July 1, 1977, after some 30 years association with Lawrence Berkeley Laboratory. His work in radiation chemistry was widely known and respected.

Professor Lee Donaghey left the University in 1977 to take a job with Standard Oil of California. We wish him success in his new job.

Professor Earl Parker retired, and, together with Professor Victor Zackay, resigned from MMRD. Professors Parker and Zackay will be long remembered for their services to the Division and for their research in ferrous metallurgy, particularly in connection with the discovery of TRIP steel in 1966, and later work associated with this phenomenon.

MMRD personnel conducted several workshops in 1977:

- Surface Science - organized by G. A. Somorjai, MMRD/LBL, W. L. Clinton, ERDA Division of Physical Research and J. T. Yates, Jr., National Bureau of Standards, held March 16-18, 1977.
- Solid State Sciences Panel and Committee Meeting - organized by D. A. Shirley and hosted by MMRD, March 25-26, 1977.
- Phase Transformation and Stability - organized by J. W. Morris, Jr., and L. Brewer of MMRD/LBL and P. Shewmon, Ohio State University, held April 18-20, 1977.

The above workshops, together with continuing developments in science, evolving research interests of MMRD investigators, and discussions both within the Divisional Council and throughout the Division, have added a focus to the development of the Division's research program. Two themes have emerged which are now being prosecuted actively. The first is surface science and catalysis, a subject which, if interpreted broadly, embraces a fairly large fraction of the Division's research efforts. Because of present scientific interest and technological relevance, this is clearly a growth area for DOE basic research programs. In Materials Sciences, several of MMRD's new programs are clearly surface-science related; e.g., hot corrosion. In Chemical Sciences, the new programs started by Professors Somorjai and Harris are in surface science, while Professors Muetterties and Bergman will be initiating new catalysis programs. Taking these new programs together with our continuing programs in surface science and catalysis, MMRD emerges as a formidable center for surface science and catalysis research on a national scale. A listing of MMRD's strengths in this area is given below:

- Theory of Surfaces (Cohen, Schaefer)
- Surface Structure (Somorjai, Shirley)
- Surface Electronic Structure (Shirley)
- Surface Optical Spectroscopy (Harris)
- Surface Infrared Spectroscopy (Richards)
- Surface-Assisted Photochemistry (Somorjai)
- Solar Photovoltaic Materials (Washburn)
- Molecular Beam Surface Reaction (Olander, Lee/Somorjai)
- Heterogeneous Catalysis (Somorjai, Bell)
- Homogeneous Catalysis (Muetterties, Bergman)
- Electrochemistry (Tobias, Muller, Newman, Evans)
- Hot Corrosion (Whittle)
- Erosion-Corrosion (Levy/Finnie)
- Gas-Ceramic Reactors (Searcy, Evans)
- Alloy Design (Morris, Thomas, Pickus)
- Electron Microscopy (Thomas)
- Atomic Resolution Microscopy (Gronsky)

To help focus attention on this area Professor Somorjai organized a seminar series in MMRD on surface science and catalysis. A list of speakers and topics from October 1976 through December 1977 is given in Appendix B.

The Division has employed Dr. Heinz Heinemann of Mobil Research as a Consultant to assist in developing our program in catalysis and we look forward to further association with Dr. Heinemann. Finally, in MMRD plans for a building addition to Building 62, surface science and catalysis will provide a central theme for a large fraction of the research program in the building addition.

Atomic resolution microscopy is another area in which MMRD can build on present strength to develop a new national capability in materials science. As noted above, plans are under way to develop an atomic resolution microscope facility.

As usual, MMRD scientists received many awards and honors in 1977. A selected few are noted below:

- *John Clarke* received the C. V. Boys prize for experimental physics.
- *Gabor Somorjai* was given the Emmett Award of the American Catalysis Society, and delivered the Baker Lectures at Cornell University in 1977.
- *Gareth Thomas* received the Rosenhain Medal of the Metals Society.
- *Neil Bartlett* was elected a Fellow of the American Academy of Arts and Sciences and

also was elected Corresponding Member of the Akademie der Wissenschaften of Göttingen.

- *Andrew Streitwieser* was also elected to the American Academy of Arts and Sciences.
- *Charles Tobias* was elected to honorary membership in the Electrochemical Society.
- *David Templeton* received an honorary degree from Upsala University during the 500th anniversary festivities of that university.
- *John Clarke* received a Guggenheim Fellowship.
- *Alexander Pines* and *Gabor Somorjai* received Miller Fellowships.
- *Marvin Cohen* served as Chairman of the Division of Solid State Physics, American Physical Society.
- *David Templeton* was elected Vice President of the American Crystallographic Association.
- *William Jolly* was elected Secretary of the Chemistry Section of the American Association for Advancement of Science.
- *Rolf Muller* was elected Secretary of the National Battery Advisory Committee.
- *David Shirley* was appointed to the Chemistry Advisory Committee of the National Science Foundation.

Among the achievements logged by MMRD investigators in 1977 are the following:

- *Gareth Thomas* has designed new Fe/Cr/C quaternary alloys with additions of Mn or Ni that have shown strength and toughness combinations exceeding those of any commercial steel.
- *Milton Pickus* has used infiltration techniques to make new A-15 multifilamentary superconductors based on the Nb-Al-Si systems.
- *John Clarke* has used microwave radiation to produce a large enhancement of the energy gap in superconducting aluminum.
- *Paul Richards* has extended the useful range of Ga:Ge infrared detectors by a factor of two by subjecting them to uniaxial stress.
- *Robert Connick* has found evidence for a new species in HSO_3^- - SO_2 solutions. This new species, $HS_2O_5^-$, together with $SO_2S_2O_5^=$ is responsible for the yellow color of the solutions.
- *Yuan Lee* has developed a high intensity monoenergetic molecular beam source of oxygen atoms. This source should prove important in studying combustion reactions.
- *Henry Schaefer* has shown that the cyclic isomer of ozone lies well above the ground state in energy.
- *David Shirley* and co-workers have confirmed the direct transition model for photoemission in the synchrotron radiation energy range, and have observed thermal diffuse scattering in photoemission.

In summary, as 1978 commences we can be proud of MMRD's recent contributions and optimistic about its future under the auspices of the Department of Energy.

David A. Shirley

I.

Materials Sciences

A. METALLURGY AND CERAMICS

1. STRUCTURE OF MATERIALS

a. Microstructure, Properties and Alloy Design

Gareth Thomas, Principal Investigator

1. INTRODUCTION: FUNDAMENTALS OF MICROSTRUCTURE PROPERTY RELATIONS

The properties of materials are structure-sensitive. Structure is in turn determined by composition, heat treatment and processing. Thus it is necessary to characterize both composition and microstructure at the highest levels of resolution possible in order to design alloys economically with optimum properties. Such characterization requires advanced and sophisticated methods of analysis using microscopic, diffraction and spectrographic techniques. For these electron microscopy is particularly versatile, since we are now routinely synthesizing structure almost at atomic levels of resolution. The interaction between composition, heat treatment and properties also requires a fundamental understanding of phase transformations. Thus there is a constant interchange between our research programs involving fundamental studies of transformation mechanisms, and their manipulation in the design projects. We acknowledge the support of industry (especially Republic Steel, Climax Molybdenum, Daido Steel) in supplying us with alloys to our specifications. The main components of our research programs are outlined in Fig. 1.

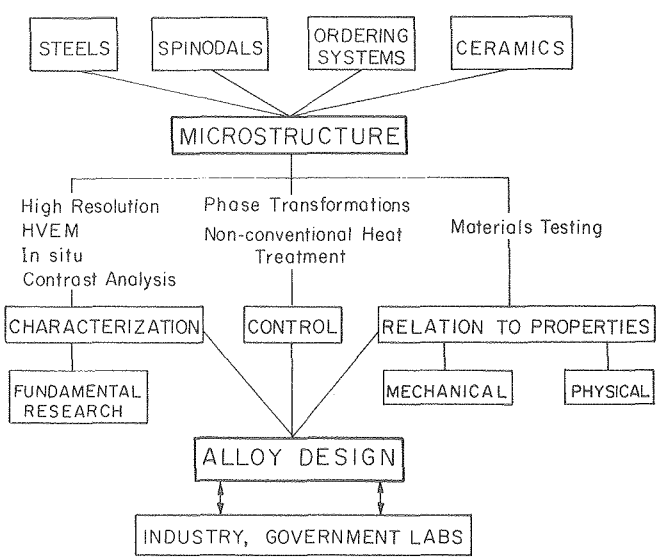

Fig. 1. Summary of research programs. (XBL 761-6298)

2. DESIGN OF STRONG, TOUGH STRUCTURAL STEELS

a. Summary of Current Status

The program has been under way since 1964 and involves a systematic study of the relation between martensitic structures and properties utilizing a series of Fe/C/X experimental steels (X is the substitutional solute). The martensite transformation, if controlled such that the inhomogeneous shear component occurs by slip, not twinning, is the most efficient means of producing dense uniformly dislocated substructure--an essential component for strength and toughness. The main factor controlling this aspect of the transformation is composition, especially percent carbon [affects transformation temperature (M_s) and strength of the austenite], which must be controlled to maintain $M_s > 200°C$. In addition, we have found that stable retained austenite is beneficial to toughness. Thus the microstructure that corresponds to optimum properties is shown in Fig. 1 and the design involves the following principal factors:

1) production of dislocated packet martensite,
2) surrounding of each martensite crystal in the packet by stable retained austenite,
3) hardenability of the steel to avoid upper bainite (or other undesirable transformation products).

The retained austenite has several beneficial aspects: it is itself ductile and therefore enhances toughness, e.g., by crack blunting, and it prevents brittle interlath carbide films from forming due to autotempering during the $\gamma \rightarrow$ martensite transformation.

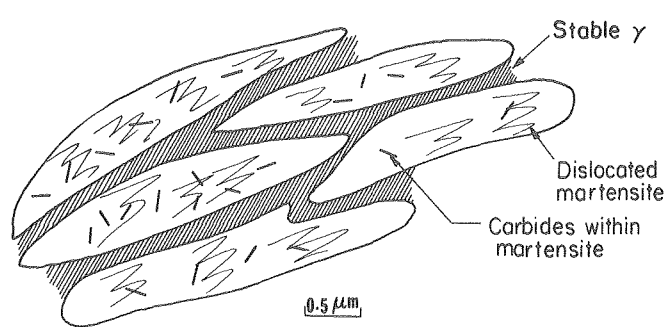

Fig. 1. Schematic illustration of desired microstructure. (XBL 7711-10457)

The current program is aimed at optimizing minimal alloy contents to keep the alloys as economical as possible. New steels based on Fe/Cr/C with Mn or Ni quaternary additions (B.V.N. Rao) show better combinations of strength and toughness than any existing commercial steel (Figs. 2-4). These steels have strong potential for applications in the mining industry. Other properties of commercial interest including fatigue, corrosion behavior and wear resistance are also being investigated (M. Carlson, D. Swain).

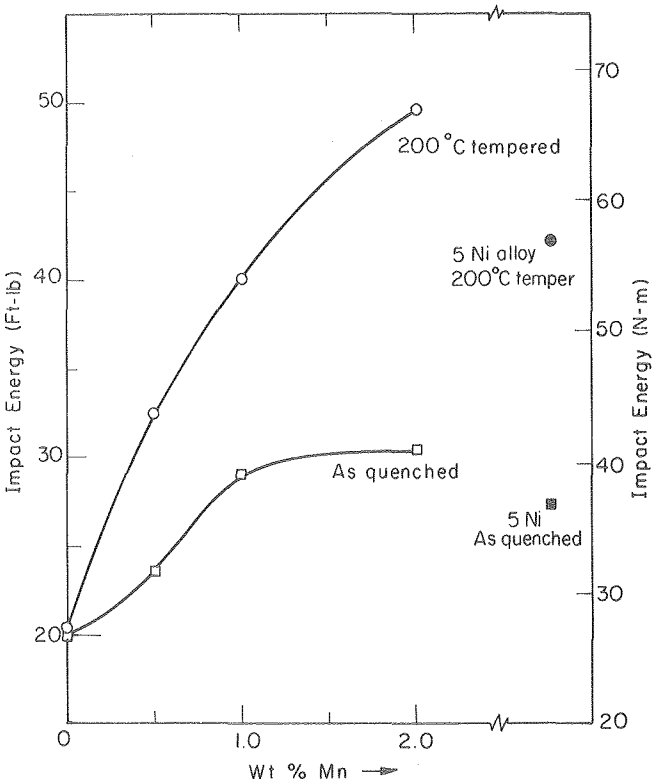

Fig. 2. CVN impact toughness vs. quaternary alloying. (XBL 774-5303)

In order to achieve one of the stated objectives, viz., economy, we have new programs under way to study the influence of substituting air-melting for vacuum-melting on the structure and properties of quaternary Fe/Cr/C/Mn alloys (T. Rabe, B. Steinberg). Since Cr is a strategic alloying element almost totally imported in this country, one of our current research programs is concerned with material substitution, such as replacing some Cr by Mo without altering the desired microstructure and properties.

b. Thermal Stability of Retained Austenite and Tempered Martensite Embrittlement

B. V. N. Rao and G. Thomas

Although our experimental steels are designed to yield superior combinations of properties even

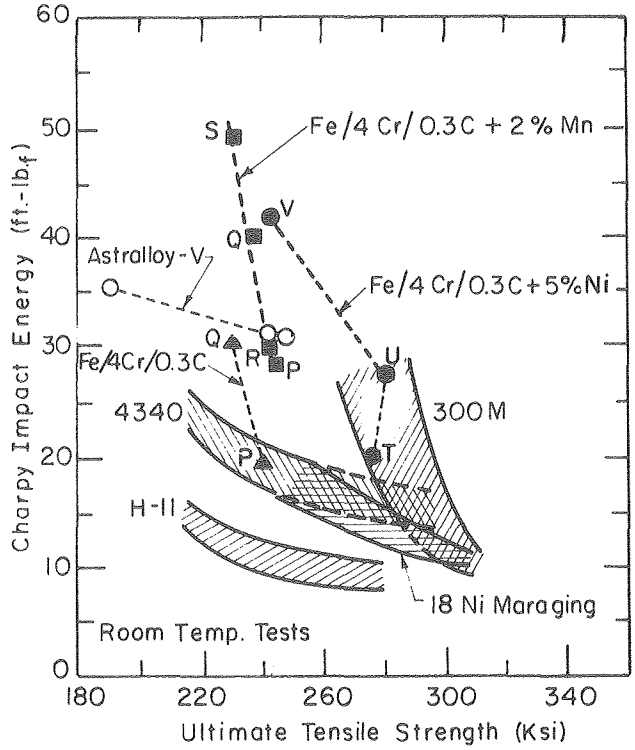

Fig. 3. CVN impact toughness vs tensile strength of the experimental steels in comparison with other commercial steels. (XBL 768-7314A)

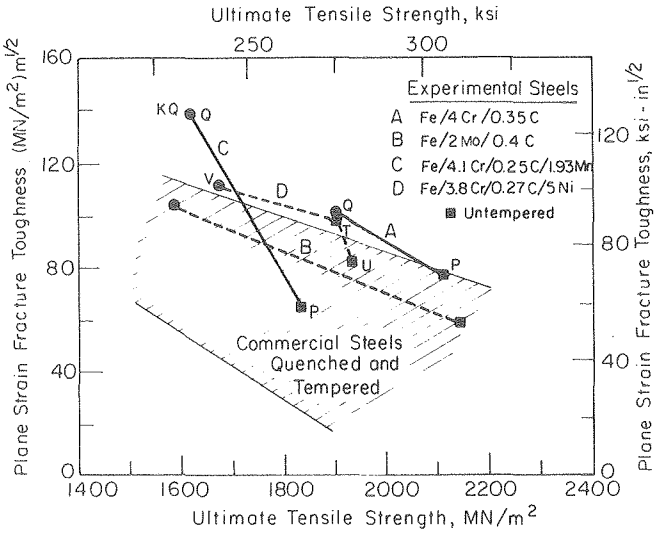

Fig. 4. Plane strain fracture toughness vs tensile strength of the experimental steels in comparison with other commercial steels. (XBL 7710-6803)

in the as-quenched condition, tempering is usually carried out to further improve the plane strain fracture toughness to strength ratio that in turn allows for larger critical flaw sizes. The thermal instability of retained austenite upon tempering

"Fractography of the Evolution of Embrittlement During Tempering of Modified Fe-4Cr-0.3 C Steels"

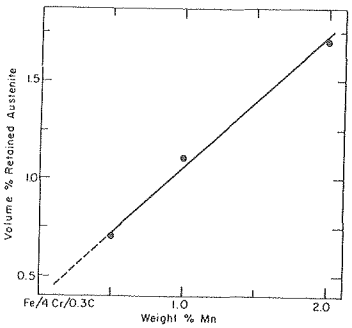

Fig.1

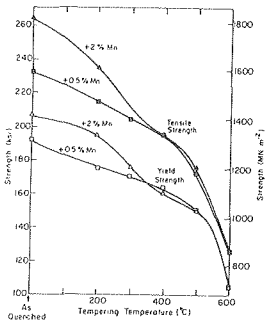

Fig.2

The phenomena of embrittlement during tempering and the accompanying changes in fracture morphology are studied in a series of high purity vacuum melted ultra-high strength Fe-4Cr-03C alloys modified with Mn additions of up to 2 w/o. Mn increases volume fraction of retained austenite (Fig. 1) and lowers temper resistance resulting in identical strength levels for the 0.5% and 2% Mn modified alloys above 300°C tempering (Fig. 2). Mn also lowers the M_S temp and the degree of auto-tempering resulting in poor as-quenched impact toughness (Fig. 4) and the tensile ductility (Fig. 3) which is also reflected in the brittle quasi-cleavage fracture mode shown in Figs. A, which also show secondary cracks resulting from large residual stresses with some tempering in the structure, the fracture mode at 200°C changes to one of dimpled rupture (Figs. B) for both the alloys and is reflected in high charpy impact toughness (Fig. 4) and appreciable tensile ductility (Fig. 3). At higher tempering temperatures, the % Reduction in Area (Fig. 3) shows two minima for the 2% Mn alloy and none for the 0.5% Mn alloy although the impact toughness (Fig. 4) shows a minimum at 300°C for the latter. The 300°C embrittlement in these alloys is associated with the decomposition of retained austenite into stringers of interlath coarse carbides and the fracture mode changes to brittle, transgranular, quasi-cleavage (Figs. C). The fracture surfaces (Figs. C) also reveal parallel ridges indicative of fracture along lath boundaries decorated with brittle particles. The second embrittlement at 500°C observed only in the 2% Mn alloy (Figs. 3 and 4) results in intergranular fracture mode (Fig. D) probably due to segregation effects which weaken the prior austenite grain boundaries. The 0.5% Mn alloy, on the other hand, shows continued improvement in toughness (Figs. 3 and 4) above 300°C tempering as reflected by the transgranular fracture at 500°C (Fig. D) although the fractograph, Fig. D, still shows substantial amounts of quasi-cleavage fracture.

Thus, the present work shows that there are two types of embrittlement: one occuring at a temperature coincidental with the decomposition of retained austenite characterized by transgranular but interlath fracture and the second occurring at a higher temperature but only in certain compositions characterized by intergranular fracture. The severity of the first embrittlement is a function of the amount of initial retained austenite.

The fractographs are taken with an AMR 1000 A Scanning electron microscope with secondary emission at 20kV.

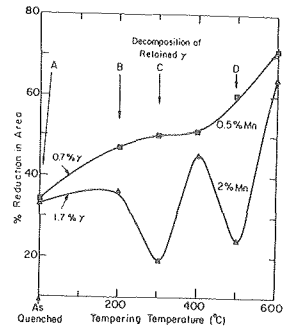

Fig.3

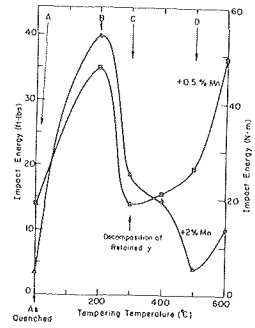

Fig.4

0.5 Mn

2 Mn

Quasi-cleavage fracture with some secondary cracks.

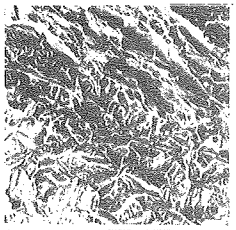

A

As-Quenched

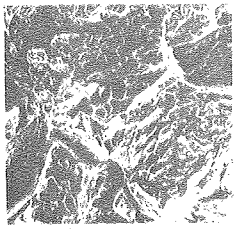

Transgranular quasi-cleavage fracture with secondary cracks.

Ductile dimpled rupture.

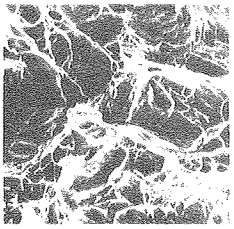

B

200°C Temper

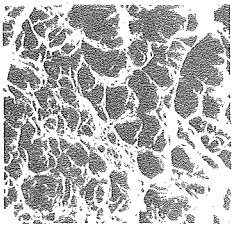

Ductile dimpled rupture. Void nucleation occurs at the MnS particles.

Transgranular quasi-cleavage. Parallel ridges indicate interlath fracture.

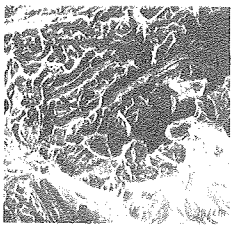

C

300°C Temper

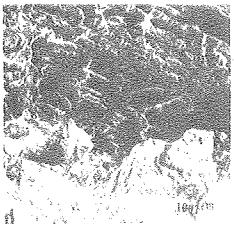

Transgranular quasi-cleavage. Parallel ridges indicate interlath fracture.

Transgranular quasi-cleavage. Some cleave fracture can also be seen.

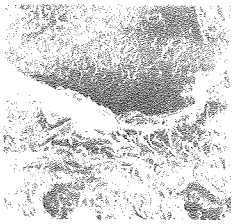

D

500 C Temper

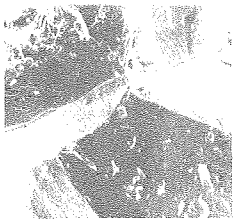

Brittle intergranular fracture. The particles on the surface are residues from the specimen preparation.

Fig. 5. (XBB 776-6137)

Evolution of Microstructure and Embrittlement During Tempering of Modified Ultra-high Strength Fe-4Cr-0.3 C Steels

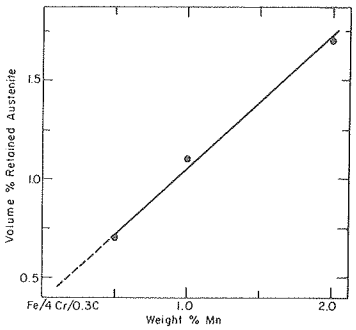

Fig.1

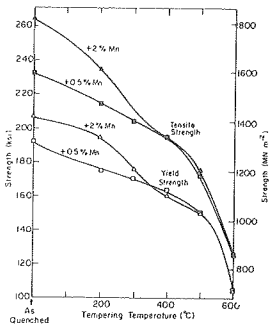

Fig.2

The phenomena of embrittlement during tempering and the accompanying microstructural changes are studied in a series of high purity vacuum melted Ultra-high Strength Fe-4Cr-0.3C alloys modified with Mn additions of up to 2 w/o. Interlath films of retained austenite beneficial to toughness and increasing with w/o Mn addition (Fig. 1) were resolved in the as-quenched structures (Fig. A). However, Mn lowers the Ms temp and the degree of auto-tempering. The as-quenched CVN impact toughness values are, therefore, low (Fig. 4). The loss in yield and tensile strengths with tempering temp is less dramatic till 500°C (Fig. 2) beyond which they drop off sharply. The 0.5% Mn alloy shows more temper resistance than the 2% Mn alloy and above 300°C tempering their strength levels are identical (compare carbide coarsening for the two alloys in B and C). The % Reduction in Area vs. tempering temp. showed two minima for the 2% Mn alloy and none for the 0.5% Mn alloy (Fig. 3) although, the CVN impact toughness (Fig. 4) showed a minimum at 300°C for the latter. At 200°C tempering, the % Reduction in Area is appreciable (Fig. 3) and the CVN energy peaks for both the alloys (Fig. 4), due to untransformed austenite and beneficial carbide morphology (Fig. B). Following embrittlement at 300°C (tempered martensite embrittlement) the retained austenite at lath boundaries in both the alloys transformed to blocky stringers of carbides deleterious to toughness (Fig. C). While the toughness of 0.5% Mn alloy continued to improve above 300°C tempering due to both recovery in the structure as well as breakdown of interlath coarse carbides into finer spheroidal particles (Fig. D), the 2% Mn alloy undergoes a second embrittlement (temper brittleness) at 500°C (Figs. 3 and 4) characterized by intergranular fracture probably due to segregation effects at the prior austenite grain boundaries.

Thus, there are two types of embrittlement: one occurring at a temperature coincidental with the decomposition of retained austenite to a mixture of ferrite and coarse carbides (transgranular fracture) and the second occurring at a higher temp but only in certain compositions (intergranular fracture). The severity of first embrittlement is a function of the amount of initial retained austenite.

The TEM micrographs are taken with Siemens IA and Philips EM 301 microscopes at 25,000 X.

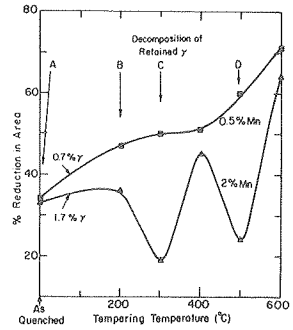

Fig.3

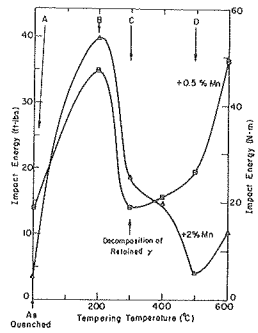

Fig.4

0.5 Mn **2 Mn**

Brightfield (BF) and dark field (DF) revealing continuous interlath films of retained austenite. Very little auto-tempering. Dislocated lath martensite.

A

As-Quenched

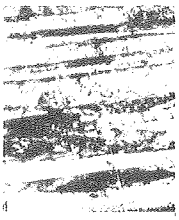

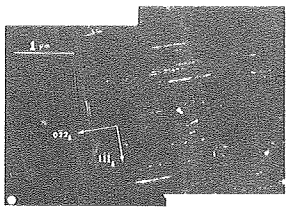

BF and DF showing continuous interlath retained austenite with no auto-tempering or twinning.

BF and DF showing intralath widmanstatten carbide (M_3C) precipitation.

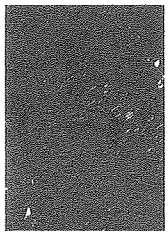

B

200°C Temper

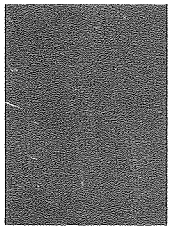

BF and DF revealing intralath widmanstatten $(110)_\alpha$ cementite platelets which are thicker in this alloy compared to 0.5% Mn alloy.

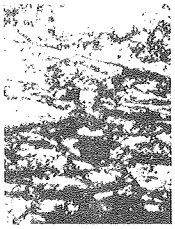

BF and DF showing coarse cementite particles at interlath boundaries resulting from breakdown of existing retained austenite.

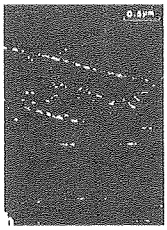

C

300°C Temper

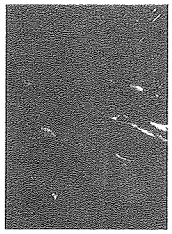

BF and DF showing very coarse interlath cementite from the decomposition of retained austenite. Some intralath cementite platelets can also be seen in DF.

BF and DF showing further breakdown of coarse interlath cementite into fine spheroidal particles.

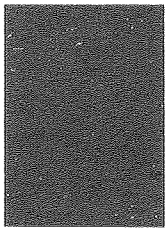

D

500°C Temper

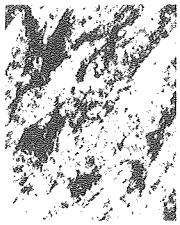

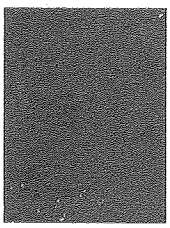

BF and DF showing breakdown of coarse interlath cementite into fine spheroidal particles. Some inter-lath as well as intra-lath M_7C_3 precipitation also seems to be occurring.

Fig. 6. (XBB 776-6136)

poses an important embrittlement problem, viz., tempered martensite embrittlement and this has been investigated as a function of the nature and amount of quaternary alloying to the Fe/Cr/C base steel. It was shown that tempered martensite embrittlement is a fairly general phenomenon and is associated with decomposition of retained austenite into interlath stringers of carbide and ferrite.[1] Figures 5 and 6 illustrate this phenomenon. In the Mn modified steels the amount of retained austenite was observed to increase with wt% Mn. This austenite was found to be stable to transformation below 300°C and at 200°C tempering the stable austenite in these alloys prevented any carbide precipitation at the lath boundaries. Instead tempering gave a fine distribution of carbides within martensite that resulted in the best combinations of strength and toughness (high energy ductile fracture). Following tempering at 300°C, however, as in the base steel, the retained austenite transformed to interlath stringers of coarse carbide and ferrite. These carbides seem to provide easy crack propagation paths as evidenced by parallel ridges on the fracture surface indicative of interlath fracture and the toughness deteriorated. The severity of embrittlement is a function of the original amount of retained austenite and in the 2%Mn modified steel, both slow strain rate as well as high strain rate toughness tests exhibited this embrittlement. Grain refining did not serve to eliminate tempered martensite embrittlement in these alloys. The Ni quaternary alloying is very versatile in this regard as it stabilized austenite to higher temperatures and even after tempering at 400 to 500°C, large amounts of untransformed austenite were found. Consequently, the toughness degradation accompanying tempering of Ni modified steels was much less pronounced and the instability temperature itself is shifted to a higher temperature, viz., 400°C. Figure 7 is a schematic illustrating the important microstructural events accompanying tempered martensite embrittlement[2] for the medium and low C alloy steels (c) and (d) and for high carbon steels wherein plate martensite is observed, (a) and (b). The fracture path following embrittlement in medium C experimental steels was clearly shown to be intergranular, not with respect to prior austenite but with respect to individual martensite crystal (interlath). This conclusion can not be arrived at with high C steels where the morphology of martensite, retianed austenite and consequently those of the decomposition products of austenite are quite different [Fig. 7(a) and (b)].

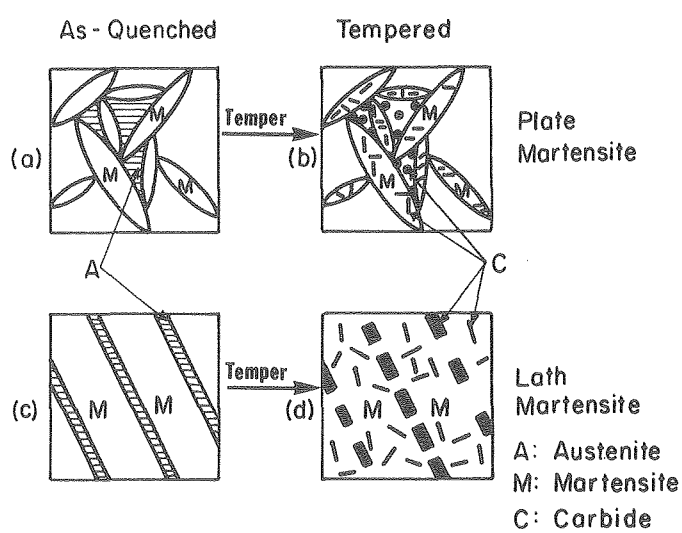

Fig. 7. Schematic illustration of the morphology of retained austenite and martensite in high carbon, high alloy steels (a) and low carbon, low alloy steels (c). Morphology of fracture due to decomposition of retained austenite → carbide on tempering [(b) and (d)] depends on the initial microstructure. (XBL 776-5606)

---

1. G. Thomas, Met. Trans A (in press), LBL-5732.
2. B. V. N. Rao and G. Thomas, Int. J. of Fracture, to appear in December 1977 issue, LBL-6295.

c. Morphology, Crystallography and Formation of Dislocated Lath Martensites in Steels

B. V. N. Rao* and G. Thomas

Background

Although the morphology and crystallography of plate martensites are well understood, the same is not true for the dislocated "lath" martensites occurring in the technologically more important medium and low C steels. A detailed electron diffraction and microscopy examination of dislocated lath martensites has been undertaken partly stimulated by the detection through careful dark-field analysis of small amounts of retained austenite in many lath martensites during an extensive alloy design program on dislocated martensitic steels.[1] Consequently, the unique orientation relationships can be obtained directly by utilizing selected area diffraction analysis of the lath bundles and the surrounding austenite.

Current Progress

The steels used in the present studies are given in Table 1. Binary Fe-Ni alloys were also used to study the effects of interstitial carbon. The results obtained so far are summarized below.

Table 1. Chemistry of the alloys and their M_s temperatures.

Alloy #	Alloy Comp. (wt%), Nominal	M_s (°C)
1)	Fe-12 Ni	300*
2)	Fe-15 Ni	250*
3)	Fe-20 Ni	165*
4)	Fe-4Cr-0.3C	320
5)	Fe-4Cr-5Ni-0.3C	210
6)	Fe-4Cr-2Mn-0.3C	253

*calculated

Morphology and Cell Structure of Martensite. The martensite packet size was found by optical microscopy to increase with austenitizing temperature and prior austenite grain size, although there was no similar variation in the average lath width. Therefore, the aspect ratio of the laths increases with prior austenite grain size (Table 2). A constant aspect ratio with increasing packet size would result in a higher volume dependent strain energy. Transmission electron micrographs taken at 100 kV and 500 kV revealed that the laths are parallel with reasonably straight boundaries and a high dislocation density. Although there were no significant differences in lath morphology or substructure as a function of carbon content, retained austenite could only be detected in carbon containing alloys.

Table 2. Variation of martensite size parameters with austenitizing treatment in Fe/4Cr/0.3C alloy.

Austenitizing temperature (°C)	Prior austenite grain size, μm	Martensite packet size, μm	Martensite lath width μm
870	29	26	0.37
1000	111	31	0.35
1100	202	42	0.39
1200	254	47	0.39

Relative Orientation of Adjacent Laths. Figure 8 is an example of the detailed analysis of parallel "laths" in the packet martensite. The SAD patterns (Fig. 8b) and regions from where the patterns were obtained in the bright field image (Fig. 8a) are identified by 1,2,3, etc. The [110]α crystal direction remains parallel in all the laths in this packet indicating that these laths are separated by [110] rotation boundaries. Using stereographic projection (Fig. 9), it was found that lath 5 is rotated 180° with respect to lath 1 indicating that the shear components are opposite and accommodative. The present observations suggest that the orientations of the laths in a given packet are those that result from minimization of the overall shape deformation and its accommodation over a group of laths. It is also shown that a gradual change in orientation to minimize shape deformation, viz., case II in Fig. 10 is preferred to a twin orientation of the adjacent laths, i.e., case III in Fig. 10, although the tendency for the latter increases with carbon content.

Austenite/Martensite Orientation Relationships. Retained austenite was found in all the carbon containing alloys. Although in most instances the austenite/martensite orientation relationship corresponded to a unique Kurdjumov-Sachs or Nishiyama-Wasserman relation depending on composition, in the Fe/Cr/C ternary alloy, frequently both K-S and N-W orientation relationships were found to alternate within the same packet (see Fig. 11).

Trace Analysis. Habit plane analysis in martensite yielded scatter: both {110}α and {331}α habit planes were observed. Direct habit plane analysis in austenite yielded a single interface plane: {111}α. It is suggested that the austenite-martensite interface may be a ledge boundary and that the macrocopic and microscopic habit planes could be different (see Fig. 12). It is also concluded that the martensite laths are indeed thin platelets and that individual laths and not the packets are the fundamental nucleation events.

*Partially supported by NSF.

1. G. Thomas and B. V. N. Rao, Invited Paper; Proceedings Int. Conf. on Martensitic Transformations, Kiev. USSR, May 1977 (in press), LBL-6242.

d. Fundamental Studies of Austenitizing Treatment on Mechanical Properties of High Strength Structural Steels

M. F. Carlson, R. O. Ritchie and G. Thomas

As part of a continuing program aimed at undertanding the influence of austenitizing treatment on mechanical properties, the fatigue behavior of Fe/Cr/C steels has been investigated as a function of austenitizing temperature. Figure 13 shows the crack growth rate, da/dn as a function of alternating stress intensity, ΔK, for low mean stress values.[1] From this plot it can be seen that for crack growth rates greater than 10^{-5} mm/cycle ($\Delta K > 12M$ Pa $\sqrt{m}$) the growth rate was independent of the austenitizing treatment. As the stress intensity is decreased, the growth rates asymptotically approach a threshold value, ΔK_0 and as the austenitizing temperature is increased, the threshold stress intensity decreases continuously from 41.4 M Pa$\sqrt{m}$ to 3.00 M Pa$\sqrt{m}$ (Fig. 14).

Fig. 8a. B. F. micrograph of parallel laths in a packet martensite (Alloy 1). (XBB 775-4292)

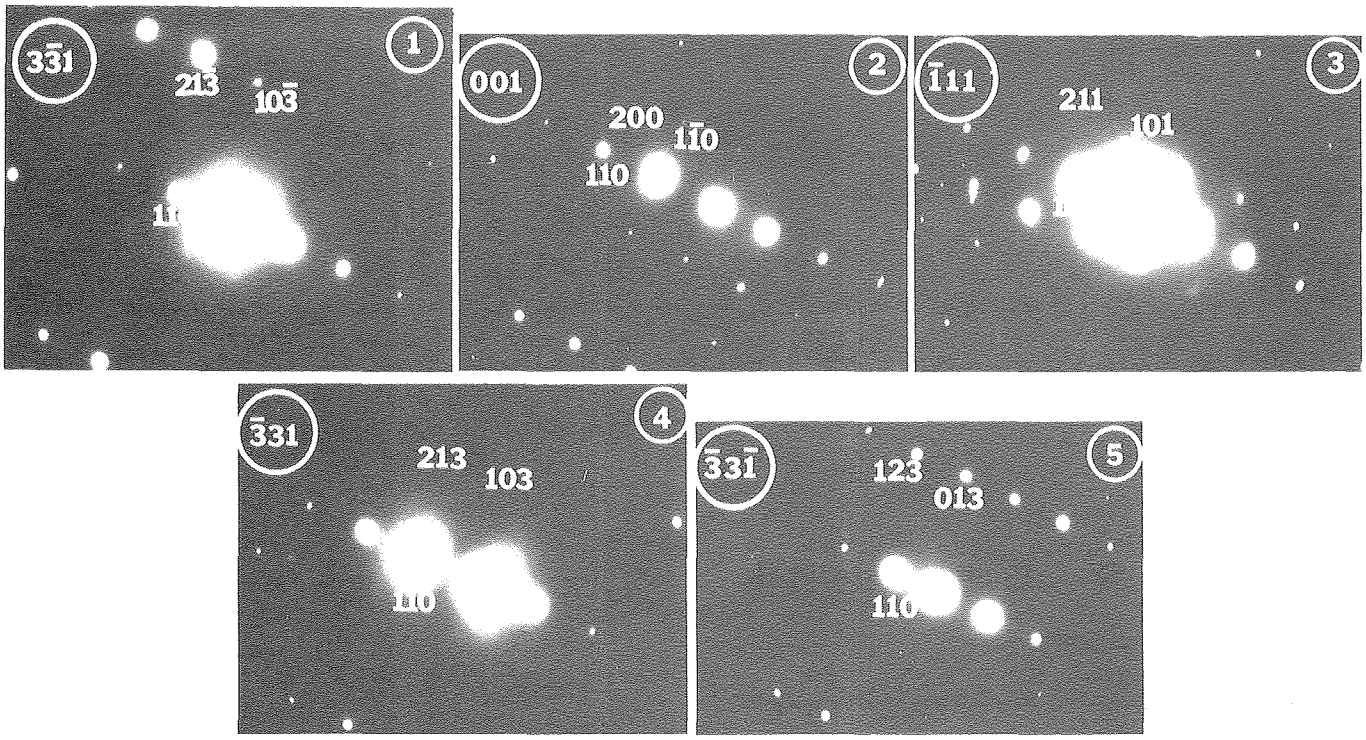

Fig. 8b. Corresponding indexed SAD patterns with the electron zone axes shown in the top left circles. (XBB 775-4293)

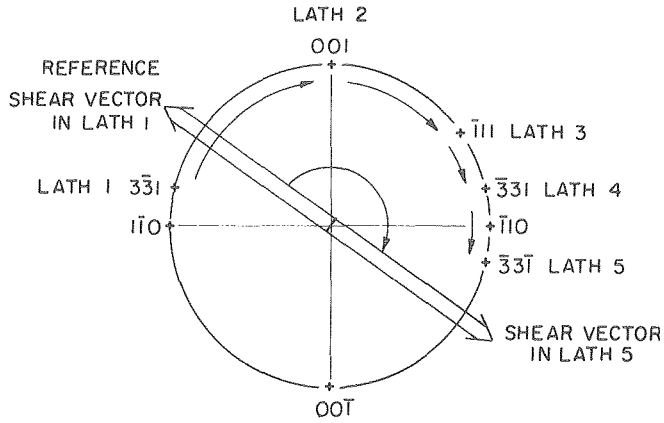

LATH REGION		ROTATION (DEGREES)
FROM	TO	
1	2	76.75
2	3	54.71
3	4	22.01
4	5	26.53
		180 TOTAL

Fig. 9. Stereographic projection illustrating the rotations of adjacent laths. (XBL 7710-6265)

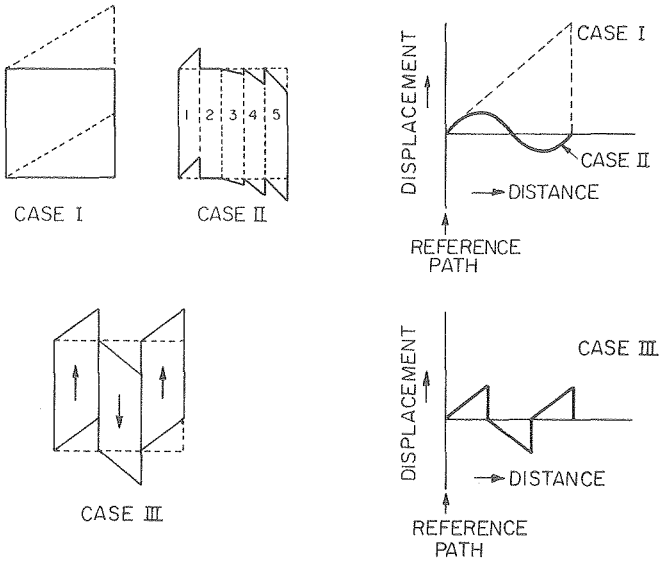

Fig. 10. Schematic representation of shape deformation accompanying lath martensite formation. (XBL 7710-6264)

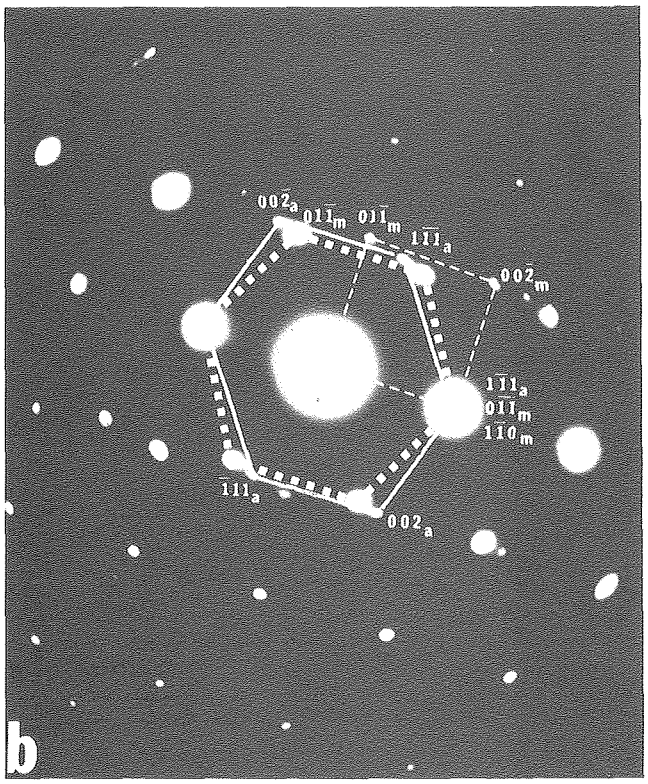

Fig. 11. Indexed SAD pattern illustrating both N-W (between $\langle 100 \rangle_m$ and $\langle 110 \rangle_a$) and K-S (between $\langle 111 \rangle_m$ and $\langle 110 \rangle_a$) orientation relations can alternate within the same martensite packet. (XBB 774-3113)

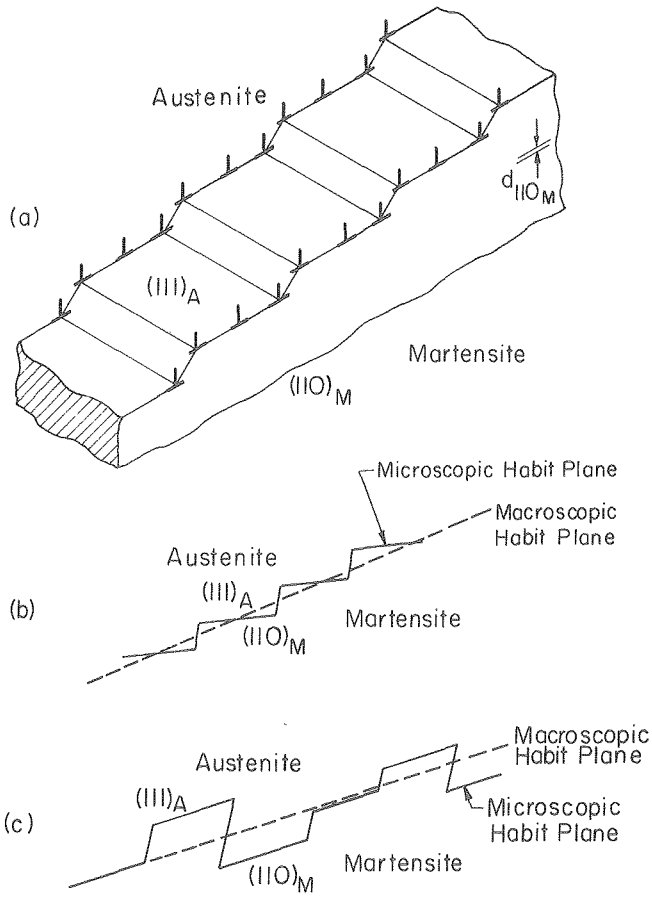

Fig. 12. (a) Suggested ledge model of the γ/α interface. (b) and (c) show different ledge configrations leading to either different macroscopic and microscopic habit planes (b) or a single habit plane (c). (XBL 774-5394)

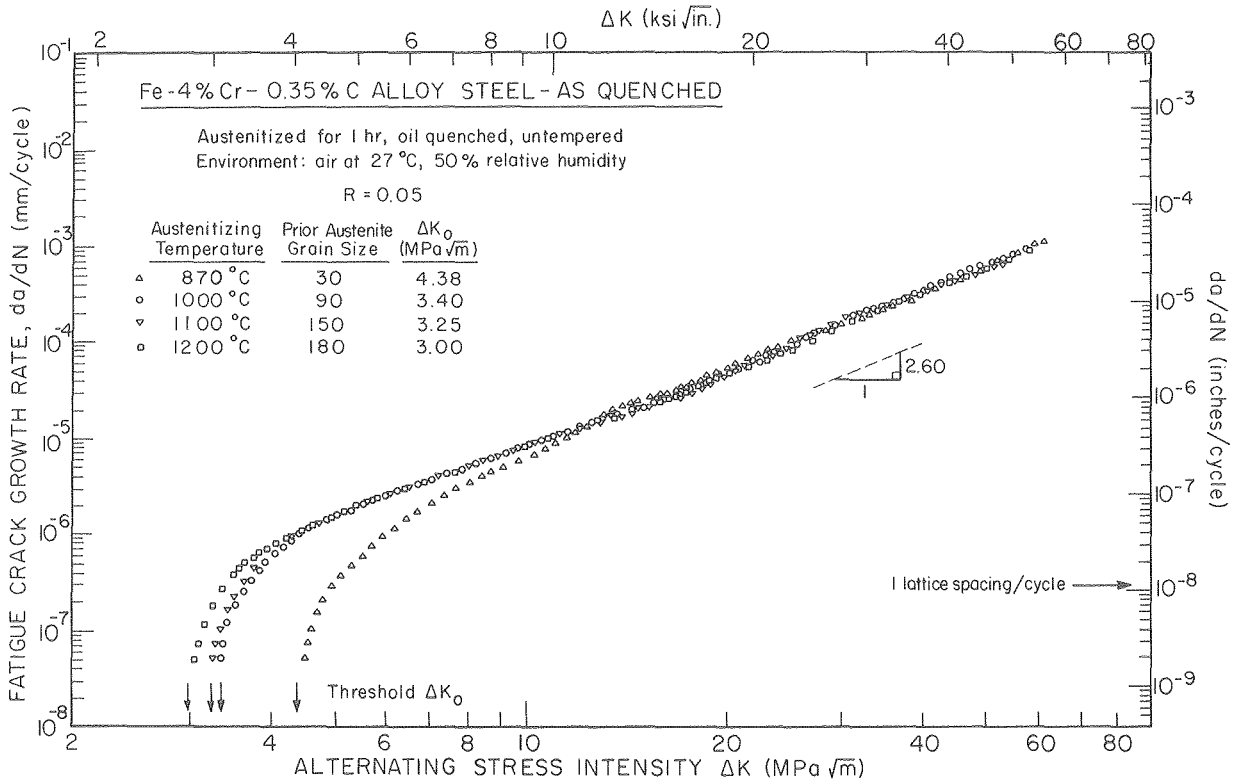

Fig. 13. Effect of prior austenite grain size on fatigue crack growth in Fe-Cr-C high strength steel. (XBL 7612-11028)

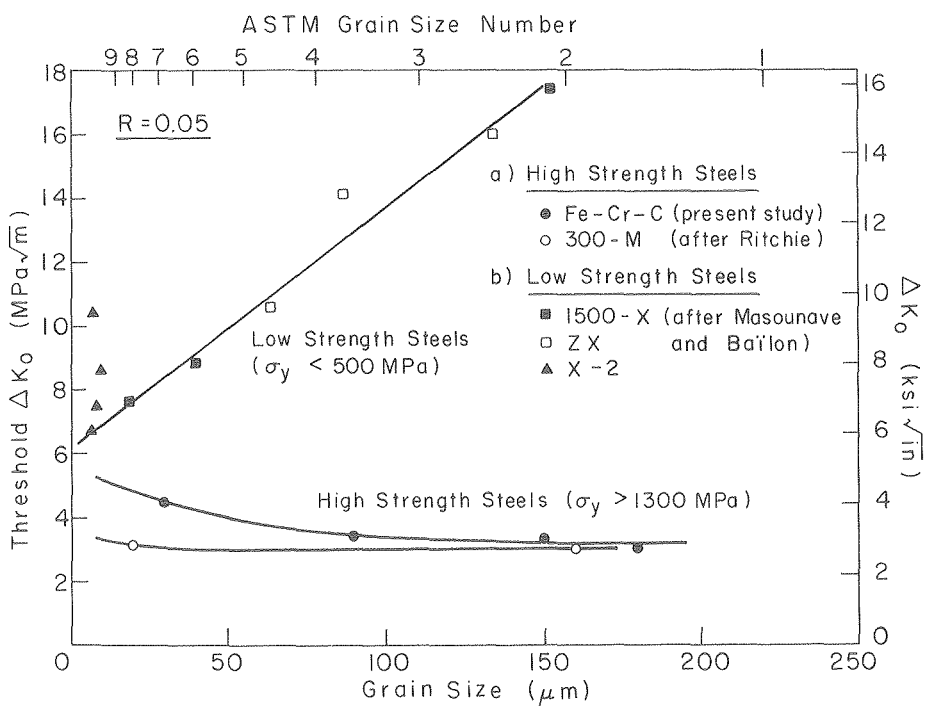

Fig. 14. Variation of threshold ΔK_O with grain size for high and low strength steels. (XBL 7712-6626)

1. M. F. Carlson and R. O. Ritchie, Scripta Met., LBL-6968, December 1977.

3. SPINODAL ALLOYS

a. Heat Treatments for Improved Mechanical Properties of CuNiFe Spinodal Alloys*

K. Kubarych and G. Thomas

Nonconventional heat treatments were designed to produce spinodal microstructures, in two CuNiFe alloys, for the improvement of mechanical properties with a reduction in total aging time. The microstructures were characterized by measuring the Curie temperatures to determine the composition of the NiFe rich phase, and by TEM to measure the spinodal wavelength. Figure 1 shows the variation of yield stress, spinodal wavelength, and Curie temperature as a function of the total time for the alloy 51.5%Cu, 33.5Ni, and 15%Fe. The numbers in Fig. 1 indicate to what position in the aging sequence (Fig. 2) the material was treated, also shown in the figure for comparison is the same alloy isothermally aged.[1] The yield stress is seen to increase with the Curie temperature (i.e., the change in lattice parameter between the decomposing phases, $\Delta a/a$) while the wavelength remains fairly constant.

Since the Curie temperature indicates the composition of the NiFe rich phase, it can be concluded that decomposition has occurred without growth of the spinodal microstructure. This is a consequence of step-aging that allows a large degree of phase separation to occur while maintaining a fine spinodal microstructure. Figure 1 also implies that the yield stress is a function of $\Delta a/a$ and independent of the spinodal wavelength that is consistent with that previously found.[1,2]

*LBL-6905, submitted to Met. Trans.

1. E. P. Butler and G. Thomas, Acta Met. 18, 347 (1970).
2. R. J. Livak and G. Thomas, Acta Met. 19, 497 (1971).

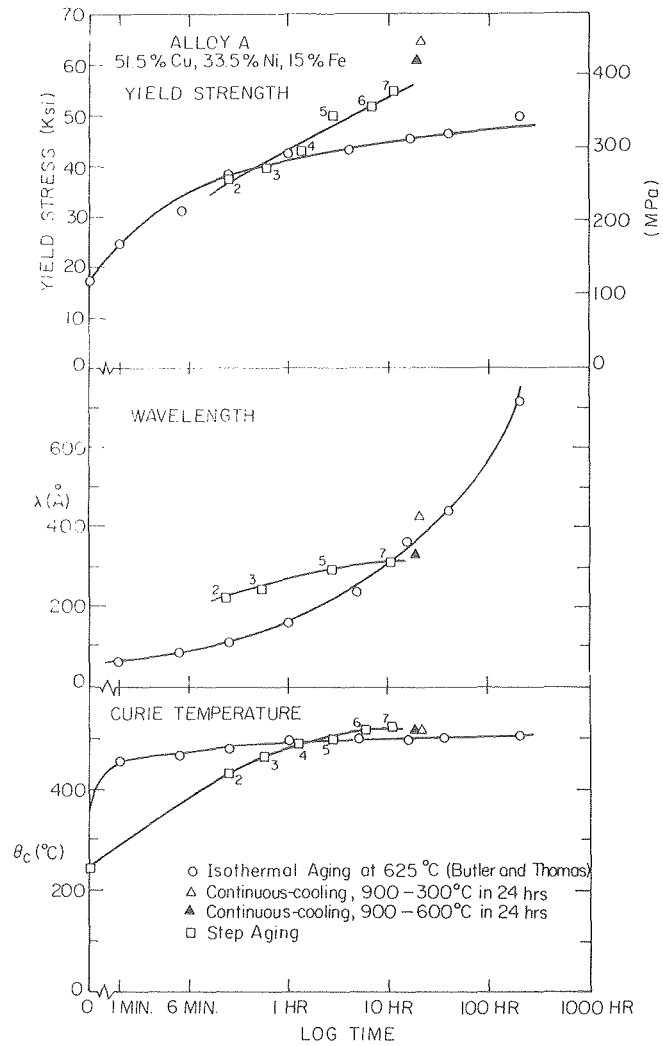

Fig. 1. A summary of the experimental information on alloy A. Plots of yield stress, wavelength, and Curie temperature total-aging time are shown. The numbers refer to the last aging step in the step aging sequence. In each case, the step aging and continuous cooling data are compared with the isothermal data at 625°C taken from Ref. 1. (XBL 776-5661)

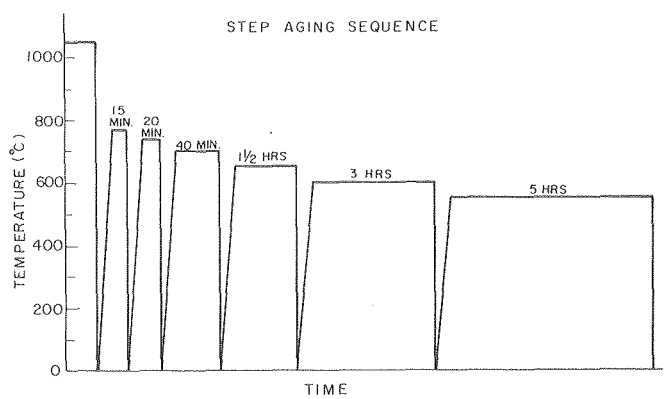

Fig. 2. A schematic representation of the entire aging treatment. (XBL 769-7524)

b. Microstructure and Magnetic Properties of FeCrCo Permanent Magnet Alloys

M. Okada and G. Thomas*

Fe-Cr-Co alloys are known to be potential hard magnets, the energy products of which are comparable to those of Alnico 5. The advantage of these alloys is their good ductility, which enables easier fabrication as compared to Alnico or Ferrite magnets.

These Fe/Cr/Co alloys were designed by extending the miscibility gap in the Fe-Cr system to the Fe-Cr-Co ternary system. The shape of the miscibility gap in the Fe-Cr-Co system is now well established.[1]

The magnetic hardening of the alloys is associated with decomposition within the miscibility gap producing modulated structures, consisting of two phases, an iron-rich phase (α_1) and a chromium-rich phase (α_2). The features of the decomposition are consistent with those expected from spinodal decomposition of the high temperature phase (α) during aging.[2]

The microstructures of an Fe-31 wt% Cr-23 wt%Co permanent magnet alloy after isothermal aging, thermomagnetic treatment and step-aging have been studied in connection with their magnetic properties. The microstructural observation of the alloy is consistent with the results of the reported miscibility gap in the Fe-Cr-Co system. The decomposition process appears to be isotropic, being associated with halo-type diffuse satellites in the diffraction pattern. Continued aging develops a periodically modulated structure along ⟨100⟩ as shown in Fig. 3. Isothermal aging itself produces undesirable microstructures. Aging at 640°C develops the magnetic Cr-rich phase. Aging at 600°C produces a nonmagnetic Cr-rich phase dispersed within the Fe-rich phase. The optimum thermomagnetic treatment of the alloy involves aging at 640°C for 40 min to 1 hr in a magnetic field of 2 KOe. The ferromagnetic phase is then elongated along the direction of the applied magnetic field, independently of crystal orientation. Step-aging produces a beneficial microstructure, viz., the elongated ferromagnetic α_1 phase imbedded in the paramagnetic α_2 phase. The increase in coercivity by step-aging is found to be associated with a change in composition of the two decomposed phases, the morphology of the iron-rich phase remaining unchanged.

---

*In collaboration with Professors M. Homma and H. Kaneko, Department of Materials Science, Faculty of Engineering, Tohoko University, Sendai, Japan 980.

1. H. Kaneko, M. Homma, K. Nakamura, M. Okada and G. Thomas, IEEE Trans. Magnetics Mag. 13, 1325 (1977).
2. M. Okada, M. Homma, H. Kaneko and G. Thomas, 34th Ann. Proc. EMSA, 606, 1976.

c. Microstructure and Magnetic Properties of FeCrCoV Alloys

Y. Belli, M. Okada and G. Thomas

Fe-Cr-Co-V alloys are potential ductile magnets not only because of their good magnetic properties comparable to those of Alnico 5, but they can be easily heat treated to produce optimum properties. The present investigation involves studies of the microstructural changes of an Fe-23%Cr-15%Co-5%V alloy with various heat treatments. The magnetic domain structures of the alloy have also been observed by Lorentz microscopy so as to understand the magnetization reversal process. Three different heat treatments were adopted for the present investigation, viz., 1) isothermal aging; 2) thermomagnetic treatment plus step-aging; and 3) continuous cooling. The microstructure of step-aged alloys with optimum properties (Hc ~ 520 Oe) produces a rod-like Fe-rich phase elongated along the direction of the applied magnetic field, 300Å in diameter and 1200Å in length. Continuous cooling which is an alternative method to produce

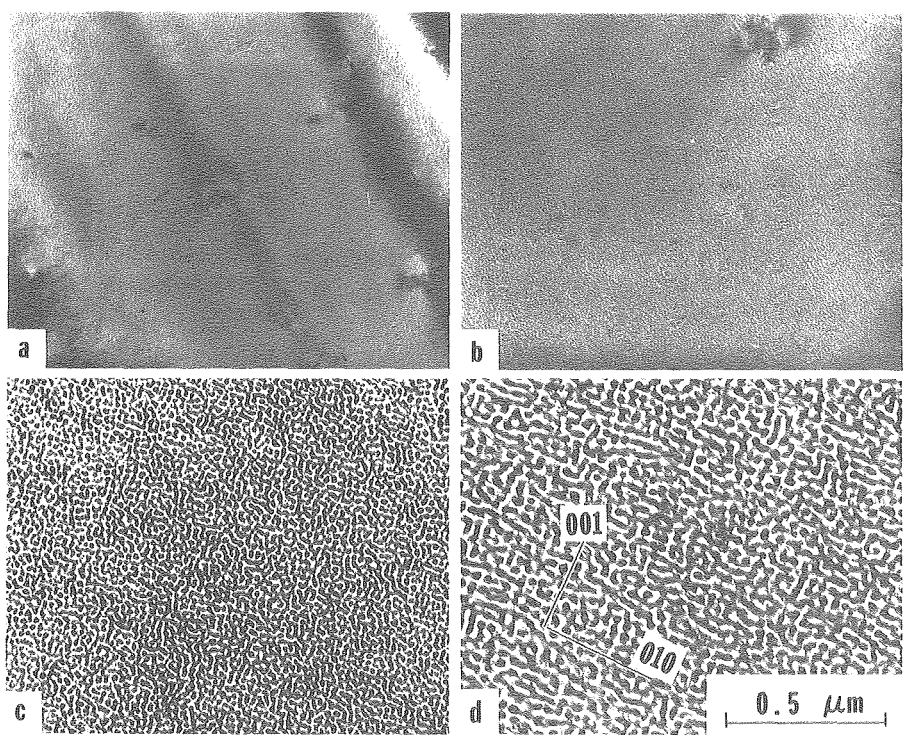

Fig. 3. Bright field micrographs of the alloy at 640° for (a) 3 min., (b) 20 min Hc ~100 Oe, (c) 2 hr Hc ~160 Oe, (d) 20 hr Hc ~125 Oe.
(XBB 773-1699)

optimum properties yields microstructures similar to those after step-aging. Lorentz microscopy revealed domain walls and these lie within the Cr-rich phase and pinned by the Fe-rich phase in the isothermally aged alloy at 650°C as shown in Fig. 4. Magnetic domains of optimally step-aged alloy, 0.5 m in width, are elongated along the direction of the applied magnetic field. These results suggest that the magnetic anisotrophy is introduced parallel to the direction of the applied magnetic field during TMT and step-aging treatments.

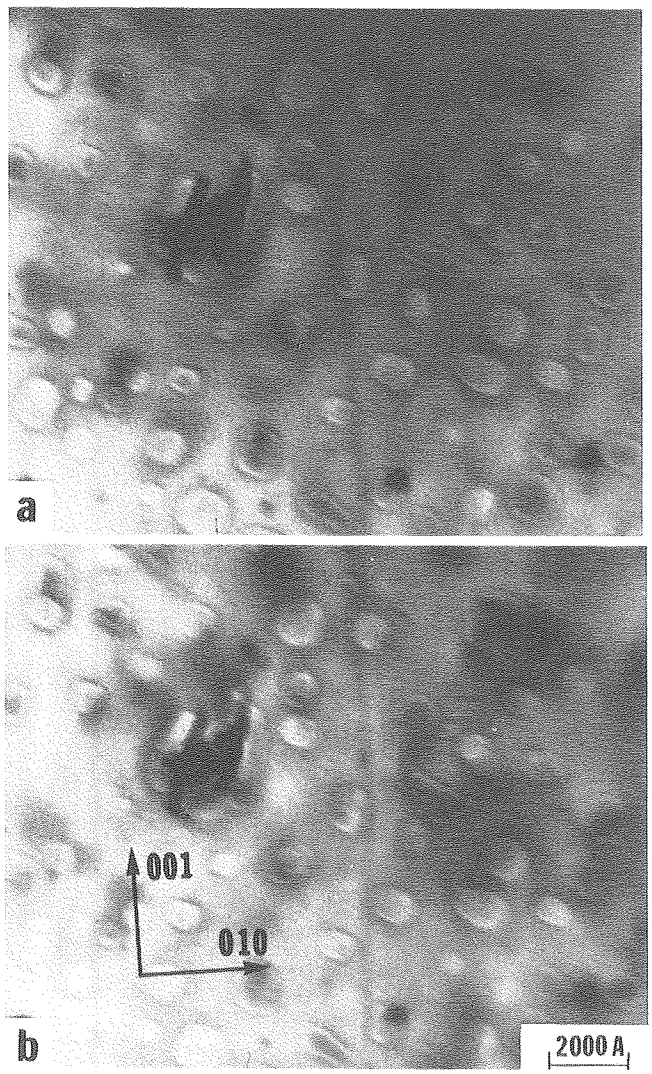

Fig. 4. Fresnel micrographs taken from the alloy aged at 650°C for 50 hr showing the domain wall is pinned by the α_1 particles. (XBB 779-9126A)

4. DUPLEX STEELS

a. Design of Duplex Carbon Steels for Improved Strength: Weight Applications

J. Y. Koo and G. Thomas

A duplex ferrite-martensite (DEM) steel is a two-phase alloy containing a controlled amount of martensite in a ferrite matrix to develop the desired combination of strength, ductility and formability, utilizing the principles of fiber loading concepts. During the past several years, the DFM steels have received increasing emphasis,[1-4] especially in the transportation industries. The strengthening principle of the DEM structure involves the incorporation of inherently strong martensite as a load carrying constituent in a soft ferrite matrix. The latter then supplies the system with the essential element of ductility.

The principles of our alloy design program[5] are as follows:

1) Obtain desirable mixture of (α + martensite) by phase transformation alone;
2) control % C in martensite to ~0.3% (dislocated martensite);
3) large slope in the A_3 line;
4) optimize the properties of the constituent phases.

In the work done so far, the DFM alloy, of composition Fe/2%Si/0.1%C, showed superior tensile properties to a series of Cr and Mn DFM steels, and to some selective commercial HSLA steels including Van 80 (Fig. 1). In Fig. 2 is shown an optical micrograph of the fibrous DFM structures developed in Si containing steels. A magnified view of the individual martensite particles is shown in the composite transmission electron micrograph (Fig. 3). Stress-strain behavior of this new DFM steel includes high work hardening rate, smooth transition from elastic to plastic

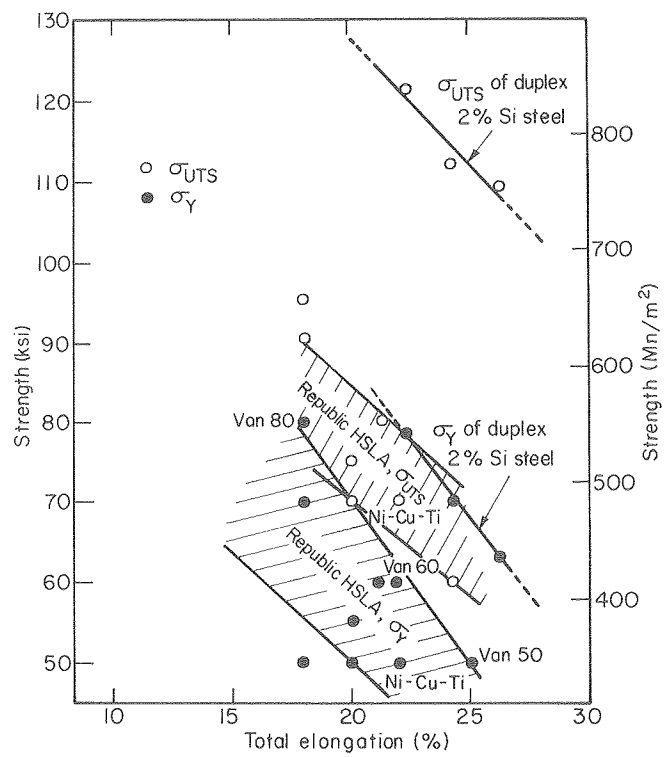

Fig. 1. Tensile properties of the duplex 2%Si steel are compared with those of commercial HSLA steels. (XBL 766-9069A)

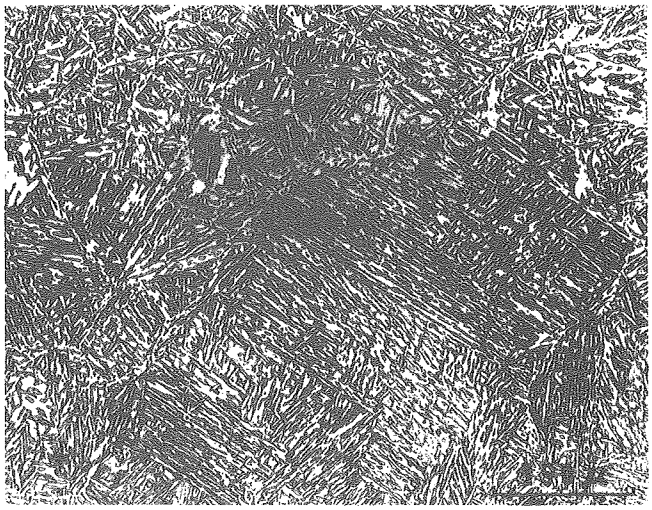

Fig. 2. Optical micrograph of DFM structure developed in alloy 4 (Fe/2%Si/0.1C). (XBB 778-7551)

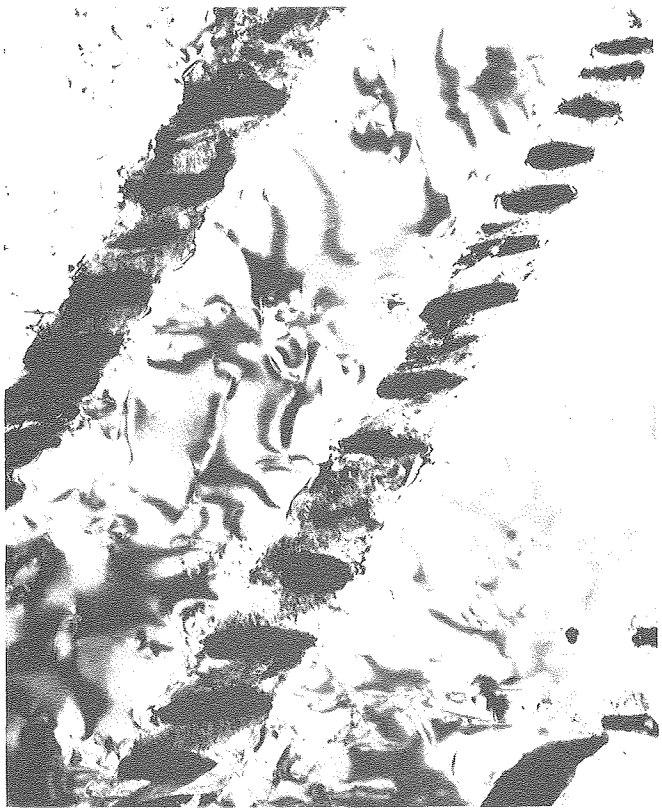

Fig. 3. Transmission electron micrographs showing fibrous DFM structures developed in the 2%Si steel. Two parallel needles are martensite phase surrounded by ferrite with a high density of dislocations. (XBB 778-7555)

deformation, and high ratio of tensile/yield strength and good elongation to necking, as shown in Fig. 4. These characteristics are indicative of excellent formability in combination with high strength. The superior properties found in the 2%Si DFM steel are attributed to the following

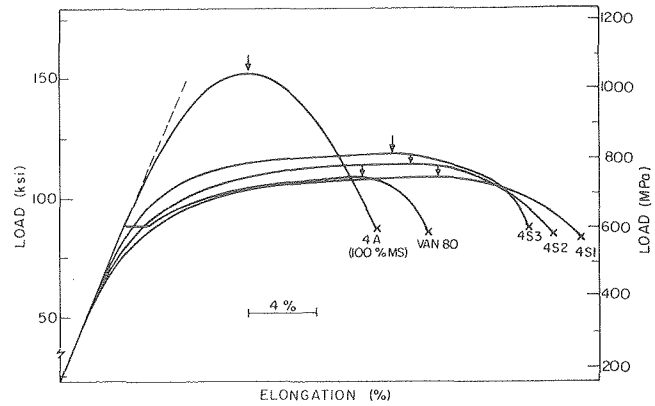

Fig. 4. Load-elongation (engineering stress-engineering strain) curves for the 2% DFM alloy with varying amount of martensite volume fraction (20, 40, and 60%), specimen 4A having 100% martensite, and Van 80. (XBL 777-5865)

features; fine, fibrous and discontinuous distribution of martensite particles in a ferrite matrix, optimized properties of the constituent phases, and maintaining a high degree of coherency at the α/martensite interfaces.

It is found that the impact properties of the various DFM steels (Fe/X/0.1C) are strongly influenced by the connectivity, carbon concentration, and volume fraction of martensite. Yield strength is determined by the flow stress of the ferrite, and is not affected by the strength of martensite while ultimate strength is sensitive to the martensite strength.

High resolution TEM studies have shown that the α/martensite interface is coherent. Lattice imaging enables the carbon composition to be estimated from the fringe spacing-lattice parameter and it is found that, as designed, the martensite composition is 0.3% (See Fig. 5).

---

1. S. Hayami and T. Furukawa, Micro Alloying 75, Symposium on High Strength, Low-Alloy Steels, Washington, D. C., 78, 1975.
2. M. S. Rashid, SAE preprint 760206, Feb. 1976.
3. J. Y. Koo and G. Thomas, Met. Trans. 8A, 525 (1977).
4. R. G. Davies, Ford Research Report #SR-77-29 (1977).
5. J. Y. Koo, (Ph.D. thesis), University of California, Berkeley, LBL-6657, August 1977.

b. Heat Treatment and Characterization of Duplex 1010 and 1020 Steels

M. J. Young* and G. Thomas

This investigation concerning the heat treatment of duplex ferrite-martensite (DFM) 1010 and 1020 steels has been aimed at 1) examining the applicability of the "two-phase mixture rule" developed for composites, and 2) optimizing morphological

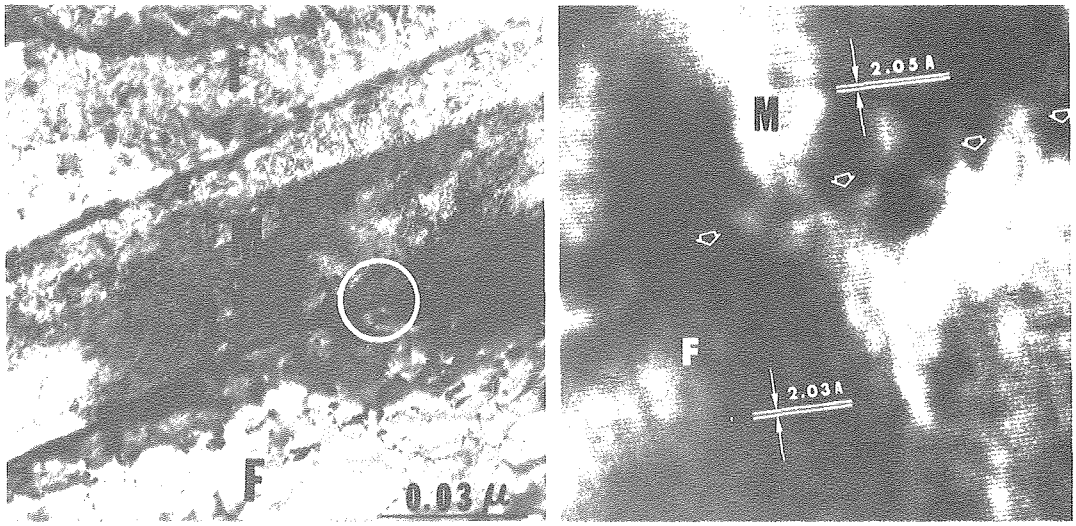

Fig. 5. Conventional bright field (a) and lattice image (b) of a α/martensite interface in the 2%Si DFM steel. The lattice image (b) was taken from the area encircled in (a). Martensite tetragonality creates the larger d_{101} spacing in the martensite region (M). "F"-ferrite. The arrows indicate the interface. (XBB 773-2297)

factors. The rule for two phase mixtures may be used as a fairly good approximation of the mechanical behavior of the duplex system, irrespective of its morphology, composition, and heat treatments (Figs. 6 and 7).

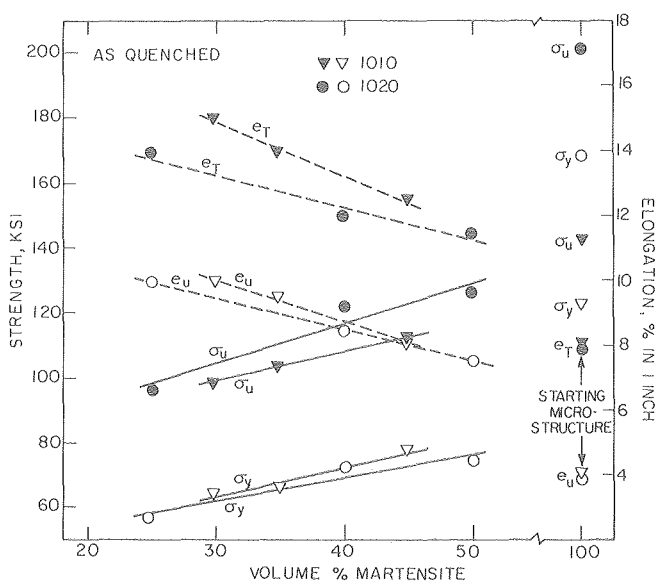

Fig. 6. Strengths and elongation ductility vs martensite fraction for intermediately quenched 1010 and 1020 steels. As-quenched. (XBL 775-5410)

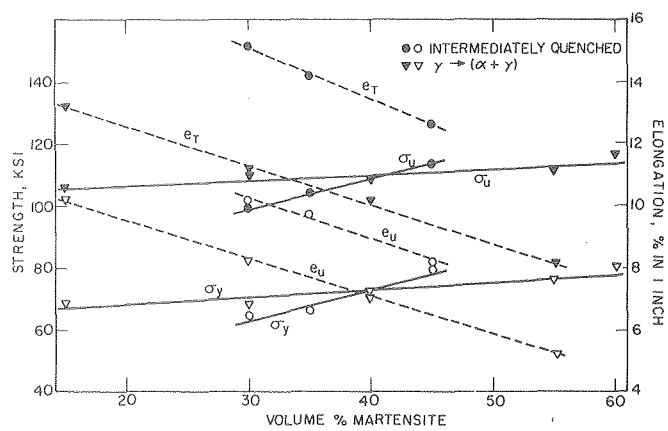

Fig. 7. Strength and elongation ductility vs martensite fraction of intermediately quenched and continuously annealed 1010. Open and closed figures delineate yield and tensile strengths, uniform and total elongations. (XBL 775-5411)

For the 1010 steel, the intermediate quench route enables strength/ductility combinations to be obtained that are superior to those obtained by continuous annealing. This result is explained in terms of the morphological differences between the two microstructures corresponding to each heat treatment.[1]

The property differentials between the duplex 1010 and 1020 at equal volume fractions of martensite are due mainly to the higher carbon content (hence, higher strength) of the 1020 martensite. As the strength of martensite increases, the total elongation is substantially decreased while yield and ultimate strengths, and uniform elongation are not significantly affected. Important metallurgical variables include subgrain formation, retained austenite, transformation twinning and martensite fraction. Of these, the volume fraction of martensite appears to be the most influential in controlling the strength, ductility and impact properties of the duplex systems studied (Figs. 6 and 7).

---

1. M. J. Young, (M. S. thesis), University of California, Berkeley, LBL-6620; also Ref. 1.

b. Ceramic Alloy Program

Gareth Thomas, Principal Investigator

1. MAGNETIC CERAMICS

R. K. Mishra and G. Thomas

The main research areas in ceramics center around processing and microstructure and properties, and their interrelations. In the following we outline our research activities on $LiFe_5O_8$, $NiFe_2O_4$, $BaFe_{12}O_{19}$ and $Ca_3Ga_2Ge_3O_{12}$--all belonging to the ferrite class of ceramic materials. Fundamental studies of phase transformations, defects, material loss characteristics and surface energies, recrystallization and grain growth etc. are some of the topics currently under investigation.

a. Material Loss and Phase Transformation

Lithium ferrite ($LiFe_5O_8$) is a ferrimagnetic material with many attractive properties such as high Curie temperature, low resonance line widths, high electrical resistivity, square hysteresis loop, etc. These properties are, however, strongly dependent on the history of the sample. The samples lose appreciable amounts of lithia and oxygen at elevated temperatures and it is this material loss that has limited the application of lithium ferrite. The same is also true for many other ceramic materials. In the present program, we have studied the characteristics of material loss from the surfaces and have characterized the internal microstructural changes accompanying the mass loss in $LiFe_5O_8$. We have also estimated the surface energies of spinel structure compounds, and correlated them to the material loss characteristics of $LiFe_5O_8$ as well as pore geometries of sintered polycrystalline $NiFe_2O_4$. All these have finally been correlated to the properties of the material.

b. Phase Transformations

The order-disorder transformation at 750°C in lithium ferrite has been studied in detail by our group in the past. At this temperature, material loss is not a very severe limitation. But at temperatures above 1000°C, where these materials are sintered, material loss problems become quite severe. Accompanying the material loss, there is a phase transformation and the processes can be described by the reactions.

$$6LiFe_5O_8 \rightleftharpoons 6LiFeO_2 + 8Fe_3O_4 + 2O_2(g) \quad (1)$$

$$6LiFeO_2 \rightleftharpoons 2Fe_3O_4 + 3Li_2O(g) + \frac{1}{2}O_2(g) \quad (2)$$

Figure 1 schematically shows the progress of this phase transformation as observed by electron microscopy. The precipitation process starts at first at the surface of the samples due to an excess of cations (or deficit of oxygen) according to reaction (1). As the oxygen loss at the surface continues, the oxygen deficiency is gradually transmitted to the interior of the sample, and as a result, precipitation occurs throughout the

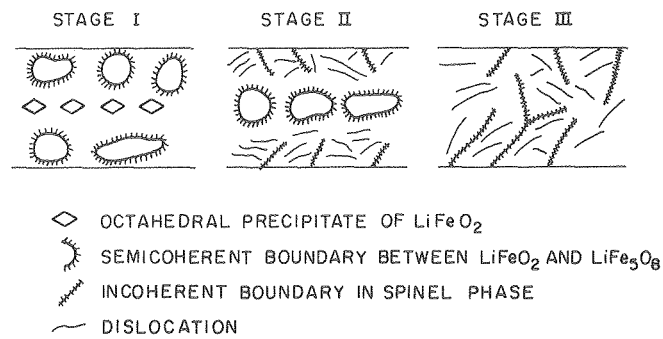

Fig. 1. Sketch to show the position of the $LiFeO_2$ phase and the small angle boundaries inside the $LiFe_5O_8$ crystal as the phase transformation proceeds. The three stages are distinguished by the microstructure-depth relationships as shown. (XBL 765-6875)

sample (Stage I, Fig. 1). However, oxygen deficiency near the surface, is the most severe, and hence at this stage, there is more $LiFeO_2$ present near the surface than in the interior. On the other hand, the loss of lithia gradually causes dissolution of the $LiFeO_2$ phase, again starting near the surface. In Stage II (Fig. 1), the outer layer loses enough lithia so that the $LiFeO_2$ dissolves back leaving behind the interface dislocations introduced during the precipitation process. Ultimately, even at the center of samples that are thin enough, only the spinel phase remains, with the remnants of the interface dislocations and the boundaries (Fig. 1, Stage III). Thus the phase transformations observed during the material loss can be regarded as being due to a competition between oxygen and lithia loss and must be taken into consideration during processing.

The magnetic property changes accompanying the phase transformation have been correlated and the formation of coherent (or semicoherent) precipitates in the matrix improves the squareness of the hysteresis loop and the coercivity of these materials. However, for microstructures corresponding to Stage III, when the material is again a single phase spinel, the hysteresis properties are inferior. This and the poor electrical resistivity (Fig. 2) for these microstructures are due to the material loss and the accompanying reduction of Fe^{+3} to Fe^{+2} state. It may be noted that the electrical resistivity, an asset of the microwave ferrites, is improved for the microstructures corresponding to the best hysteresis properties.

The above results suggest a way to improve permanent magnet characteristics such as coercivity, $(BH)_{max}$, etc. by dispersing nonmagnetic precipitates in the magnetic ceramic matrix. At present, work is in progress to investigate and develop a precipitation hardened magnet by a dispersion of $BaFe_2O_4$ particles in $BaFe_{12}O_{19}$

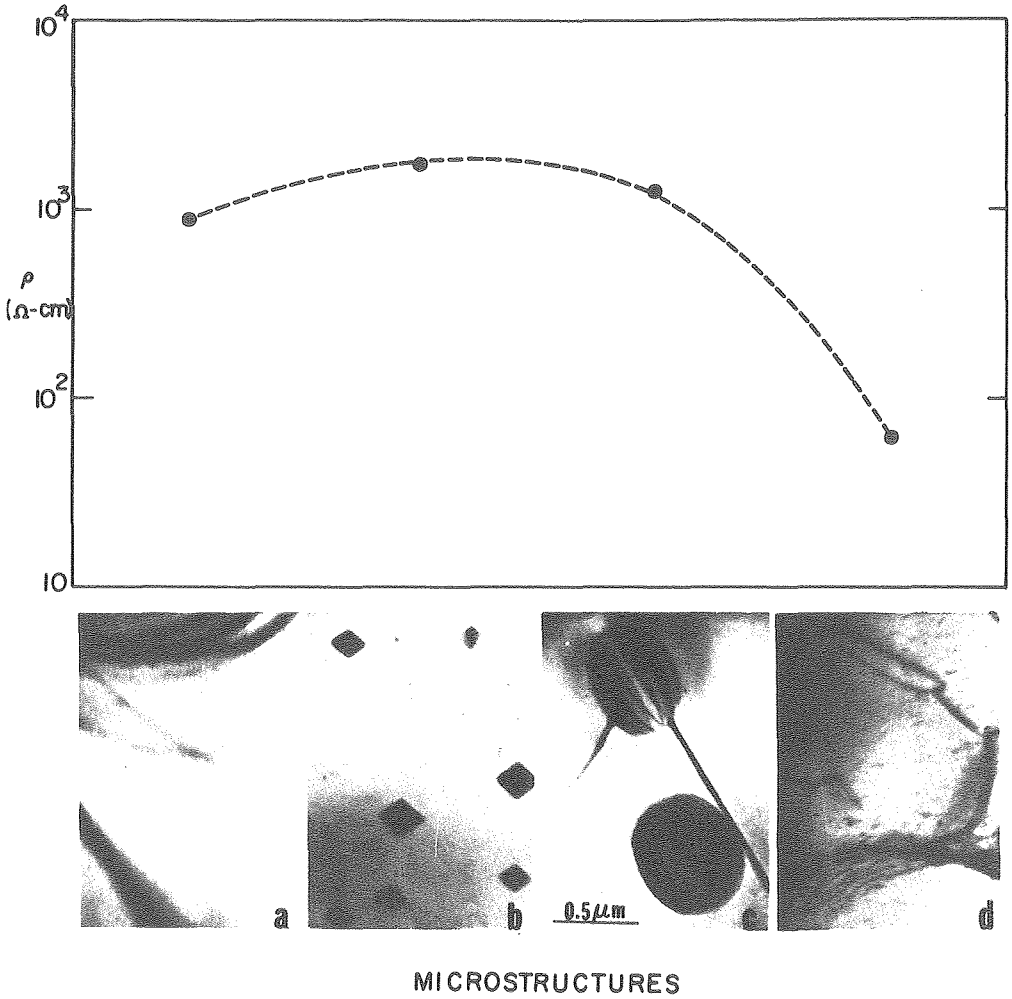

Fig. 2. Variation of DC electrical resistivity of $LiFe_5O_8$ with heat treatment. Typical microstructures of the material are shown beneath the corresponding ρ values. (XBB 760-10725)

permanent magnets through controlled heat treatment.

In addition to the study of the effects of phase transformations on the static or low frequency hysteresis characteristics of soft ferrites, we have started to investigate the effect of microstructure on the dynamic high frequency properties of (CoNiZn) ferrites. By slow cooling these materials from below the Curie temperature, Co^{+2} ions can induce anisotropy. The restoring force on the domain walls is then increased and the magnetic Q parameter as well as the technologically important μQ parameter are increased. It has been observed recently that this effect can be enhanced further by slowly cooling the samples from above the Curie temperature and thus decreasing the domain wall damping. The origin of this effect is believed to be due to oxidation of Fe^{+2} ions along the grain boundaries as well as the grain interiors, and consequent precipitation of Fe_2O_3. Work is under way to identify the Fe_2O_3 phase and study the kinetics and crystallography of this transformation using electron microscopy and diffraction.

c. Material Loss and Surface Energy[1]

As the gaseous species leave the initially flat surface during the heating of a ceramic material at high temperature (such as during processing), the surface becomes spongy. Depending on the initial crystallographic orientation of the surface, different surface topographies as shown in Fig. 3 result in the case of $LiFe_5O_8$ spinel. Analyses shows these topographies to be due to the preferential loss of material from {111} planes. Estimation of the surface energies of spinel structure compounds (Ref. 2), $MgAl_2O_4$, from analyses of the Coulomb interaction and Born-Mayer repulsion contributions yields highly anisotropic values: 4715, 3000 and 615.5 ergs/cm^2, respectively, for {110}, {100} and {111} surfaces.[2] Phenomenological calculations from elastic constants data yield the values of surface energy summarized in Table 1. These calculations are consistent with the observation of octahedral shaped spinel single crystals and the topography of etched surfaces of $MgAl_2O_4$, $LiFe_5O_8$, etc. where {111} planes are preferentially etched as shown in Fig. 4. An important corollary of these calculations is that

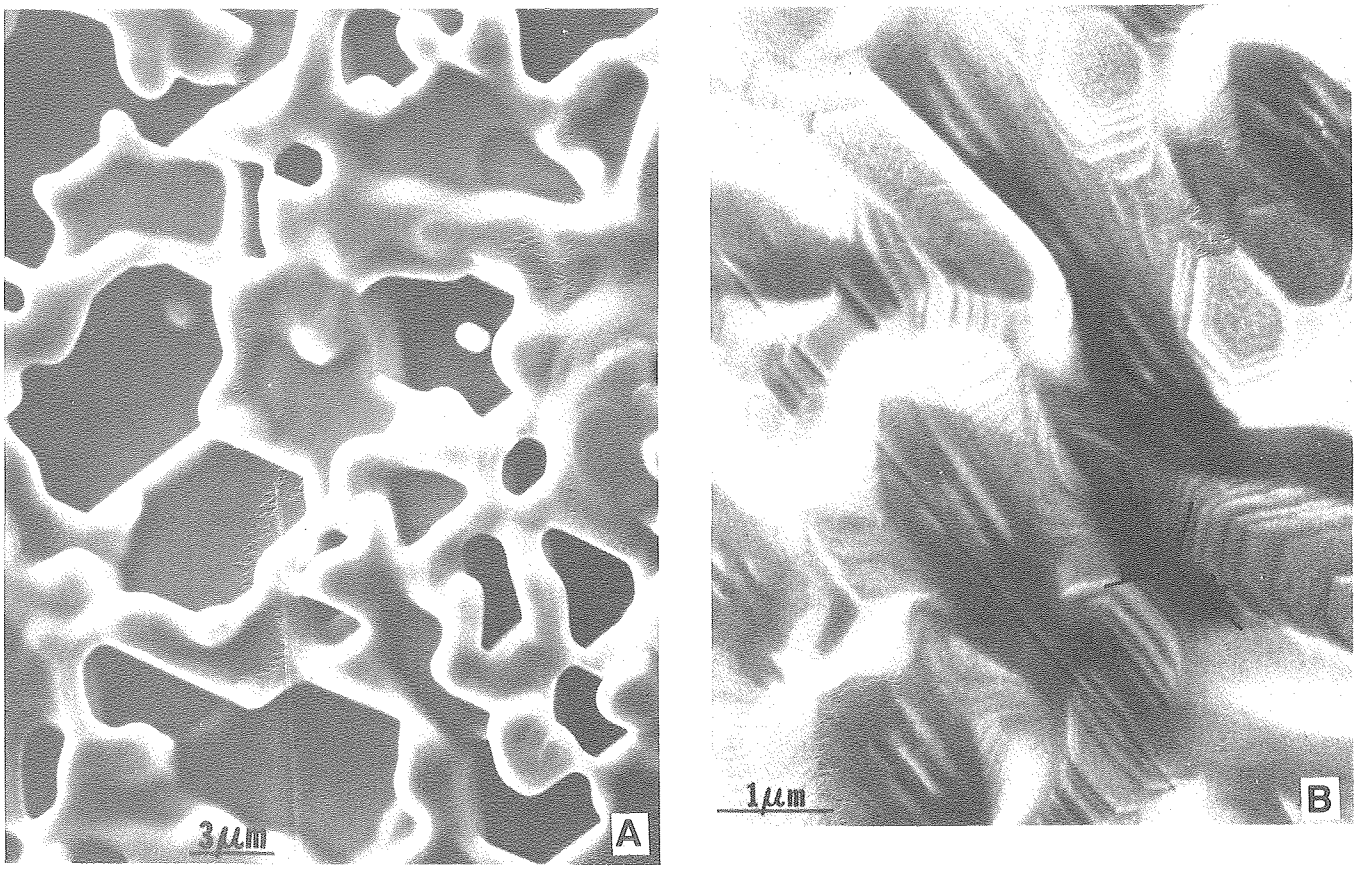

Fig. 3. Scanning electron micrograph of (A) {111} and (B) {110} surface of $LiFe_5O_8$ heated for three hours in vacuum at 1200°C. Note the spongy surface in (A) with flat pore-bottoms and the growth step topography in (B) due to preferential mass loss from {111} surfaces. [(a)XBB 7511-8376; (b)XBB 7511-8377]

Table 1. Surface energy values estimated from elastic constant data.

Material	{111}Surface Ergs/cm^2	{110}Surface Ergs/cm^2	{100}Surface Ergs/cm^2
$LiFe_5O_8$	222	2122	1331
$NiFe_2O_4$	207	1837	1161
Fe_3O_4	223	2164	1451
$MgAl_2O_4$	298	2702	1446

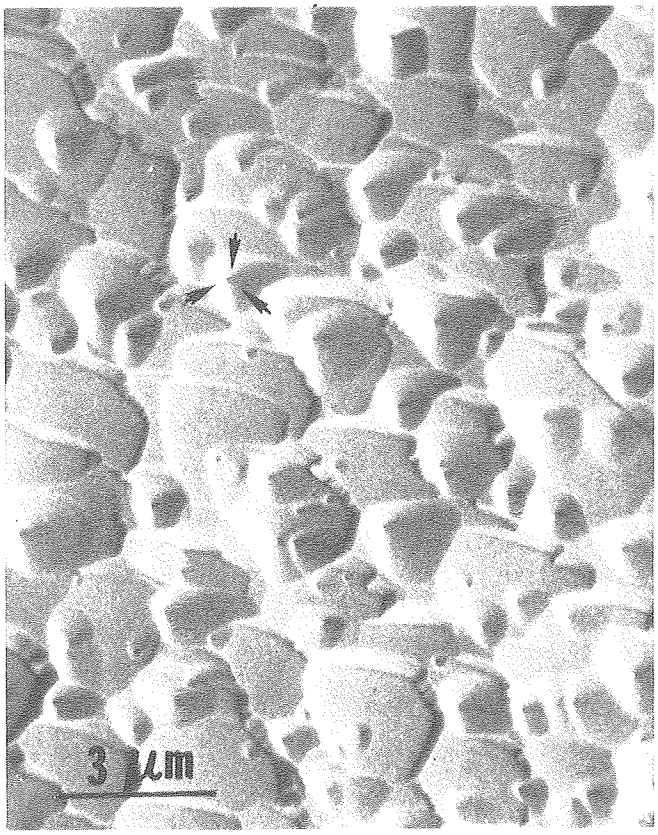

Fig. 4. Scanning electron micrograph of a {111} surface of $LiFe_5O_8$ in H_3PO_4 at 195°C for 15 min. Three other variants $(1\bar{1}\bar{1})$, $(\bar{1}1\bar{1})$ and $(\bar{1}\bar{1}1)$ are exposed (marked by the arrows) due to preferential etching of {111} surfaces. (XBB 760-10727) ⟶

a freshly cleaved unrelaxed surface should have two cation layers of different nature on the two free surfaces in $MgAl_2O_4$. This prediction awaits experimental verification.

The above calculations show that {111} surfaces have the lowest surface energies. This can be used to explain the surface topographies seen in Fig. 3 by assuming that the mass loss occurs from the low energy surfaces by a "surface energy" mechanism rather than an "evaporation" mechanism.[3] In the latter case, in addition to the {111} planes in Fig. 3, several other low index planes should be exposed also. These comments apply not only to $LiFe_5O_8$, but to all spinel structure materials. One other example is given below.

$NiFe_2O_4$, doped with Co and Cu is used as a magnetostrictive transducer material for high power applications in the ultrasonic frequency range. In a systematic study of the relationship between the microstructure and the magnetoacoustic oscillation properties, the effect of one of the commonly neglected features, viz., pores, was studied. It was observed that the changes in the grain size are strongly coupled with the geometry of the pores and hence the processing parameters.[4] The dependence of the magnetomechanical coupling coefficient as shown in Fig. 5 on the grain size is contrary to what one expects, since theoretically, single crystal material should have the highest value of α. The magnetization and hysteresis data also confirm that the dominant microstructural feature that affects the magnetic properties is not the grain size. The only other variable in the microstructure as seen by electron microscopy is the pore shape as shown in Fig. 6. Pore geometry is determined by the material loss mechanisms and is very anisotropic in nature. Thus these results indicate that the processing variables can be tailored to change in pore geometry that in turn would serve as a microstructural variable for controlling the properties.

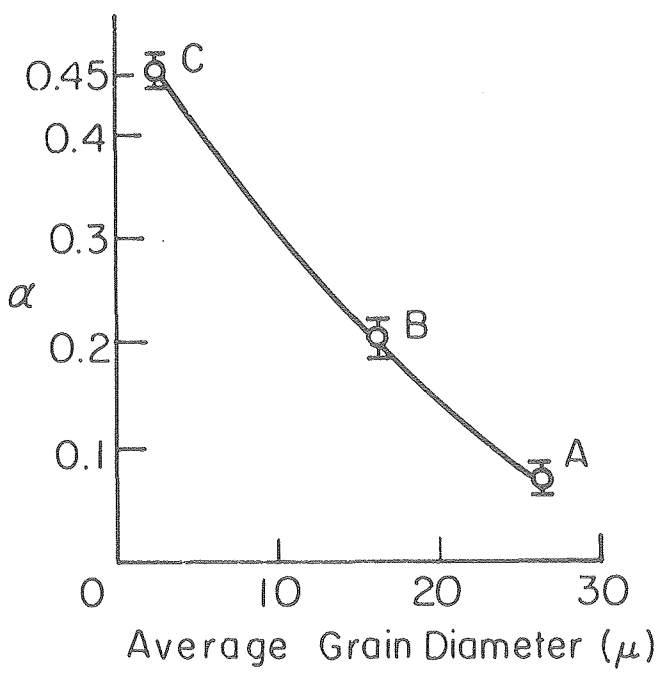

Fig. 5. Plot of magnetomechanical coupling constant (α) vs average grain diameter. (XBL 774-5364)

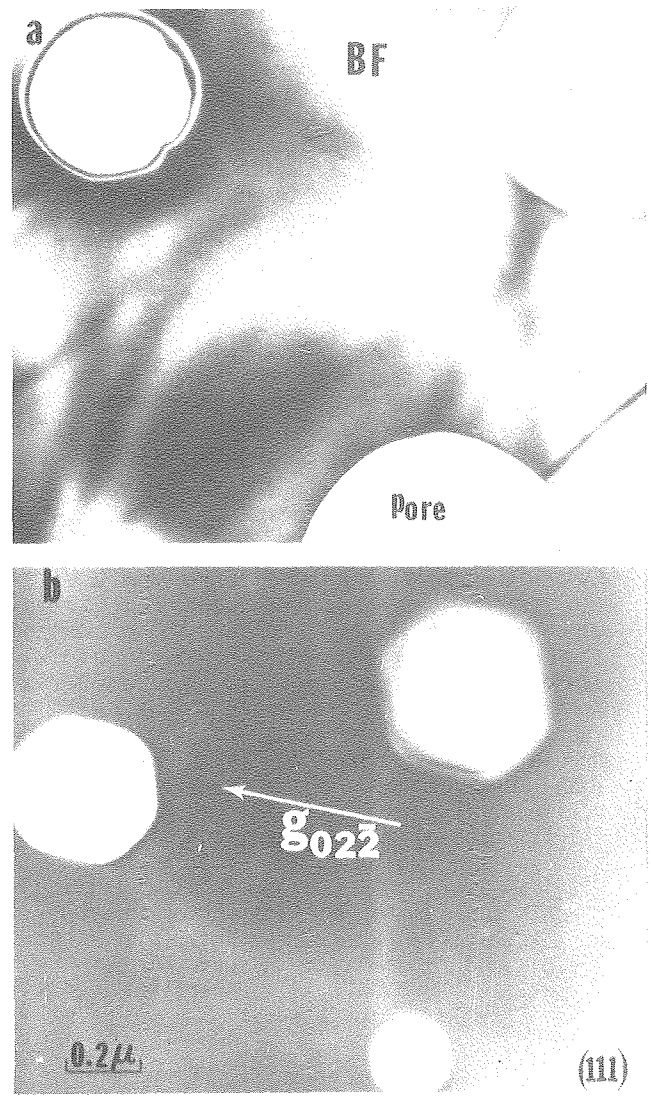

Fig. 6. Transmission electron micrograph showing the geometry of pores in (a) small grain material and (b) large grain material. (XBB 774-3516)

1. R. K. Mishra, (Ph.D. thesis), University of California, Berkeley, LBL-5759.
2. R. K. Mishra and G. Thomas, J. Appl. Phys. 48, 4576, 1977, LBL-6030.
3. R. K. Mishra, O. Van der Biest and G. Thomas, J. Ceramic Society (in press) 1977, LBL-5146.
4. R. K. Mishra and G. Thomas, Intermag. Conf. 1977, Proc. IEEE MAG-13, 1354, 1977, LBL-6095.

d. Magnetic Bubble Materials--Microstructure & Microsegregation in Substrate Garnets

R. K. Mishra and T. Roth

Ferrimagnetic garnets are prime candidates for thin film bubble memory devices. For such applications, single crystal magnetic garnet films are usually grown on nonmagnetic ceramic substrates such as $Gd_3Ga_5O_{12}$. Recently $Ca_3Ga_2Ge_3O_{12}$ (CGGG) has also been demonstrated to be an alternative substrate garnet material. Defects and inhomogeities in the substrate materials are easily replicated in the epifilms and subsequently lead to device degradation. Very little is known about the microstructures of substrate and the epilayer garnets and their role in such occurrences, and the object of this research is to characterize and understand defects-property relations.

Much effort has gone into the study of dislocations in various garnet structure compounds using techniques such as 1) optical birefringence, 2) etch pit and decoration techniques, and 3) x-ray topography, etc. None of these have the resolution to provide information on a microscopic scale. The few attempts by electron microscopy have been hampered by the difficulties in obtaining suitable diffracting conditions for analysis. We have used the special contrast conditions (high order bright field and weak beam methods) to investigate dislocations. Figure 7 shows the contrast from a pair of dislocations in two different diffracting conditions. The computer image profile at X in Fig. 7(a) is shown in (c). From detailed tilting experiments and comparisons with the calculated image profiles, it is concluded that dislocations A & B are mixed in character and have Bergers vectors 1/2[111] and 1/2[$\bar{1}$11], respectively. No evidence of dissociation is seen.

Inhomogeneous regions as in Fig. 8 are very frequently seen in CGGG. These range from 1000 to 5000 Å in size. Detailed stereo microscopic analyses show that the bright patch P has a spherical shape and is surrounded by a cylindrical region Q which from the contrast suggests that it is rich in a heavy element. The inclusions do not give rise to any detectable scattered intensities in the selected area diffraction pattern in any orientation of the matrix and thus are interpreted to have the garnet structure. There is a sharp boundary separating Q from the surrounding matrix and no strain contrast arising due to the inclusion is detected. Contrast analysis lead us to interpret them as voids. It is suggested that such inclusions are due to microsegregation of one of the components in the material. Assuming the activation energies for the formation and migration of a vacancy-atom (V-A) pair to be low, such a pair would form and diffuse through the lattice easily, segregating to form a large cluster. Eventually, when enough V-A pairs have combined, the vacancies dissociate and accumulate to form voids, which the atoms segregate around them. Work is in progress to determine the nature of the segregating atomic species and determine the dependence of the complex chemistries of the systems and the segregation phenomena.

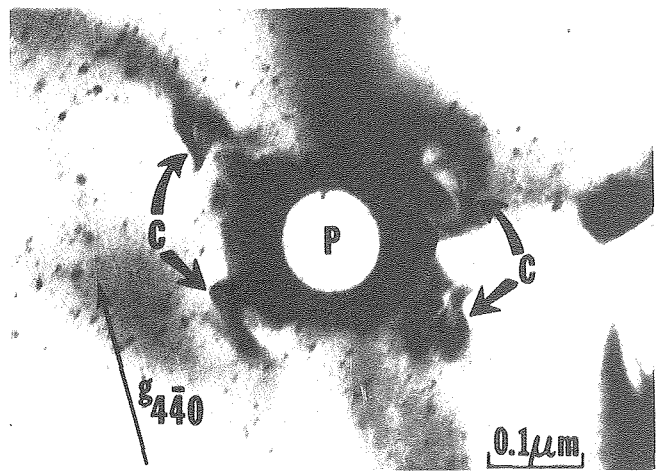

Fig. 8. Bright field image of an inclusion in CGGG consisting of a spherical void (P) surrounded by a cylinderical region (Q) richer is a heavy element. The dislocation images (C) are smeared out due to multibeam interaction dynamical contrast. (XBB 779-6466)

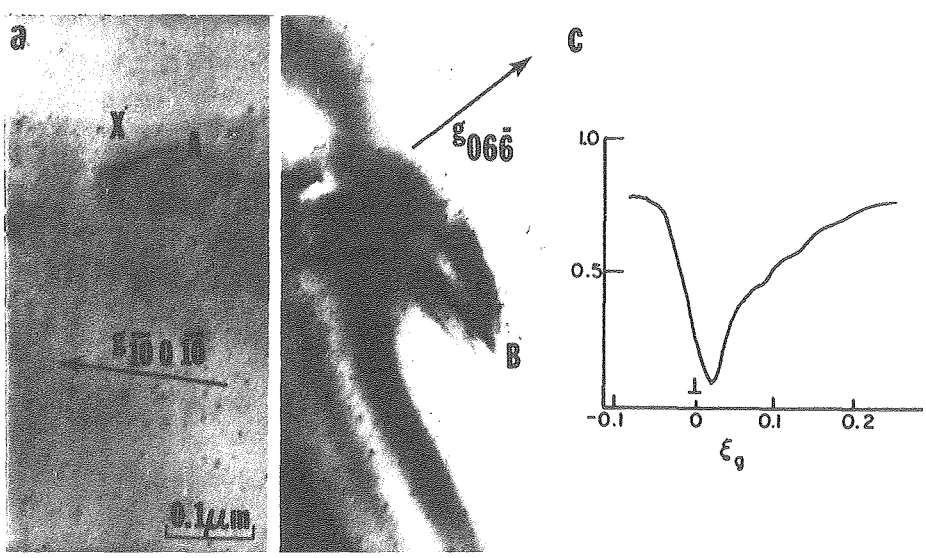

Fig. 7. (a) and (b) one high order bright field images of two isolated dislocations A and B; (c) is the calculated image profile corresponding to point X (center of the foil), and for an undissociated dislocation with b = 1/2[111] in GGG. (XBB 779-9469)

2. REFRACTORY CERAMICS - SILICON NITRIDE AND SIALONS*

a. Intergranular Phases

D. R. Clarke† and G. Thomas

The potential advantages of refractory ceramics for high temperature applications such as turbines, liquid metal containers are well recognized[1] since they have very attractive properties (high modulus: density ratios, high melting points, oxidation resistance, etc). However, due to fabrication difficulties the use of hot-pressing additives such as MgO or Y_2O_3 are needed and the properties at high temperatures are impaired. It has been proposed that the impairment is due to the formation of an intergranular phase, probably glassy as a result of the formation of silicates of crystalline oxy-nitrides. Attempts to prove this directly failed until high resolution TEM was adopted.[2] The problem of resolving intergranular phases and whether they are amorphous or not is not trivial. From an electron microscopy viewpoint therefore, the following features at grain boundaries require characterization: 1) detecting the intergranular phases and their distribution, 2) determining whether these phases are crystalline, and 3) determining their chemical compositions.

From a morphological viewpoint it is essential to choose the proper orientation conditions as sketched in Fig. 1. Under conventional imaging conditions the grain boundary should be viewed edge-on with simultaneous strong Bragg excitation in adjacent grains. The contrast from intergranular phases if present and resolved depend upon whether they are amorphous or crystalline. Amorphous phases (most probably silicates) generally appear in light contrast (low atomic number-mass thickness contrast) as shown in Fig. 2. Dark field imaging of the grains, although difficult, is preferable to enhance grain boundary interphase contrast. However, the failure to detect intergranular phases by this method (good down to about 20 Å or so) does not necessarily mean that no intergranular phase is present. One must then resort to high resolution lattice or structure imaging. This work must be done currently at 100 kV due to the inferior resolution capabilities of our 650 kV microscope, but with the addition of a new 1.5 MeV instrument capable of lattice imaging to 2 Å resolution, solution of these problems will be facilitated greatly.

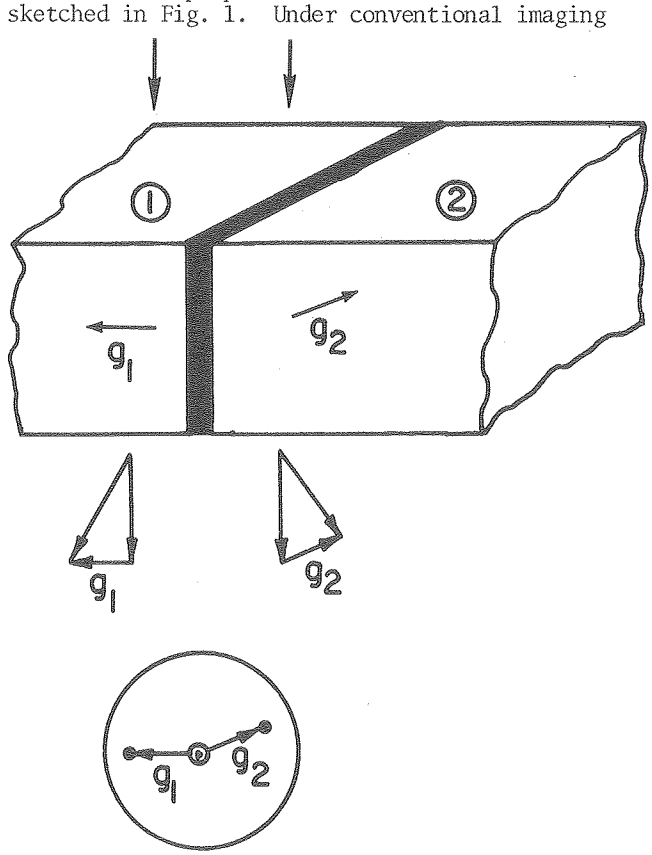

Fig. 1. Contrast conditions to detect intergranular phases; grain boundary must be oriented parallel to incident beam with strong Bragg excitation simultaneously in both grains. Lattice images can be obtained of diffraction planes corresponding to g_1 and g_2. (XBL 778-5991)

The analysis of the state of the intergranular regions, i.e., amorphous or crystalline requires microdiffraction. While the resolution in selected area diffraction for a given spot size is chiefly limited by spherical aberration and scattering angle $\Delta A \sim C a_\alpha^3$ and is greatly improved at high voltages, microbeam analysis using STEM capabilities

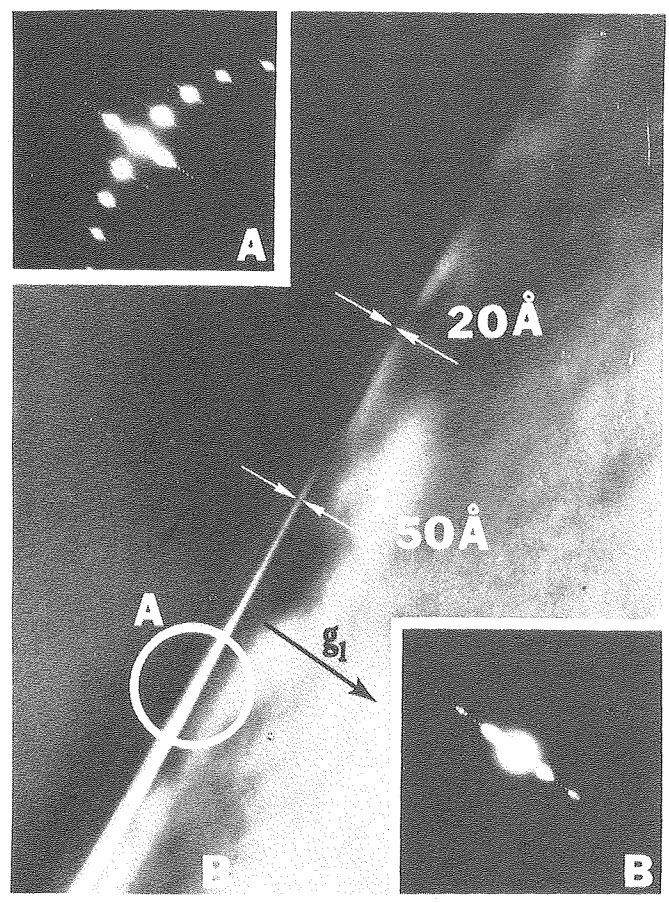

Fig. 2. Bright field image corresponding to Fig. 1 showing intergranular phase and the diffraction conditions. SAD B is from grain B and SAS A is from both the grains at A. Width of the intergranular phase decreases as indicated. (XBB 778-7954)

is essential since we have found the distribution of intergranular phases to be very heterogeneous (concentrated chiefly at triple-points) and these regions are spatially very small. Thus unique identification of the crystallinity or non-crystallinity of the intergranular region is beyond the capability of SAD. Clearly, it will be greatly advantageous for HVEM and STEM to be applied to these problems. Again at the present time at Berkeley we are limited to 100 kV STEM work in collaboration with R. H. Geiss.[3] The results of a detailed study of Y_2O_3 hot pressed Si_3N_4 show the situation to be quite complex as both crystalline and glassy phases exist at the intergranular regions[4] and it required HREM lattice imaging in order to show this [Fig. 3(a)]. STEM work has revealed that these phases act as a sink for impurities as the x-ray microanalysis of Fig. 3(b) shows.[4] This result indicates the possible reason for the high temperature failure due to the lower softening temperatures expected for impure phases compared to solely Y_2O_3-containing phases.

---

*Supported by NSF.

†Now at North American Rockwell, Science Center, Thousand Oaks, CA.

1. See, for example, K. H. Kack, J. Mat. Sci. 11, 1135 (1976).
2. D. R. Clarke and G. Thomas, J. Amer. Ceram. Soc. (1977), (in press).
3. D. R. Clarke and R. H. Geiss, 35th EMSA Proc., Boston, 1977, p. 146.
4. D. R. Clarke and G. Thomas, J. Amer. Ceram. Soc. (1977), (in press).

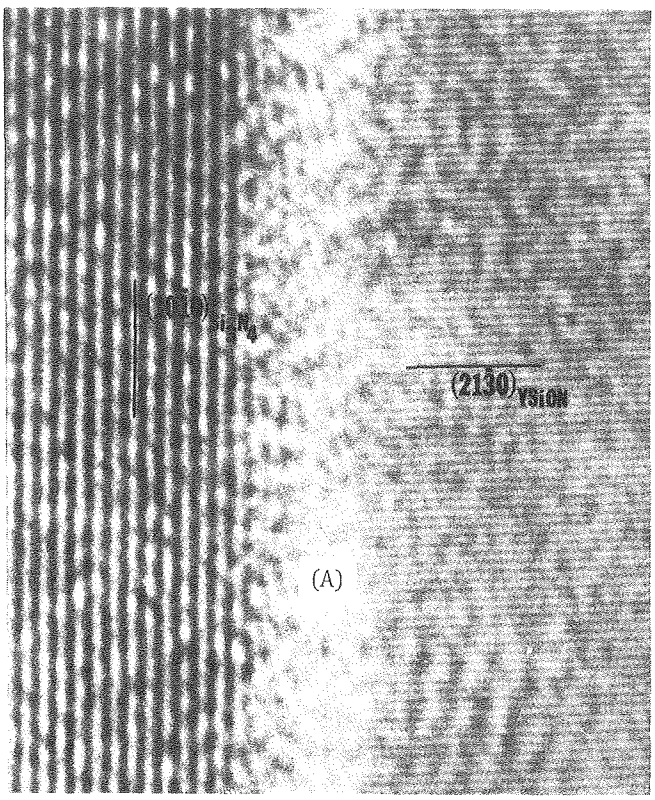

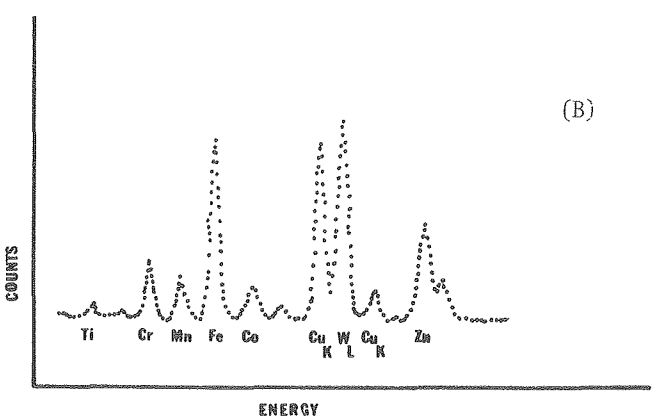

b. Structural Analyses - Sialons

T. M. Shaw and G. Thomas

Jack[1] has shown that Si_3N_4 is easily modified by cation replacement of Si (e.g., MgBe) and anion replacement of N (e.g., O) to form a promising class of ceramic alloys, the Sialons (so named after the original silicon-aluminum-oxygen-nitrogen systems). X-ray analysis has shown that many polytypes can exist in these "alloys" and again electron microscopy is proving to be extremely valuable in sorting out some of the complexities.

Extensive polytypism in which the variable unit cell dimension is determined by composition has been reported in a number of so called sialon ceramics.[2] X-ray analysis suggests that the polytypes are based on the wurtzite structure only with a regular insertion of a cubic stacked layer to accommodate an excess of one atomic species. The periodicity of the cubic stacked layers then determines the composition and unit cell of the polytype. Direct imaging of periodicities in the close packed stacking enables regions of one polytype structure to be identified and disorders and intergrowth between two structures examined.

Fig. 3. (a) A lattice fringe image showing a third phase between two grains of β-Si_3N_4 and YSiON. Note the discontinuity of lattice fringes at the interphase boundary, 100 kV. (b) Microanalysis trace obtained from an oxynitride phase. Note the presence of transition and alkali elements as impurities. [(a)XBB 776-5855; (b)XBL 776-9192]

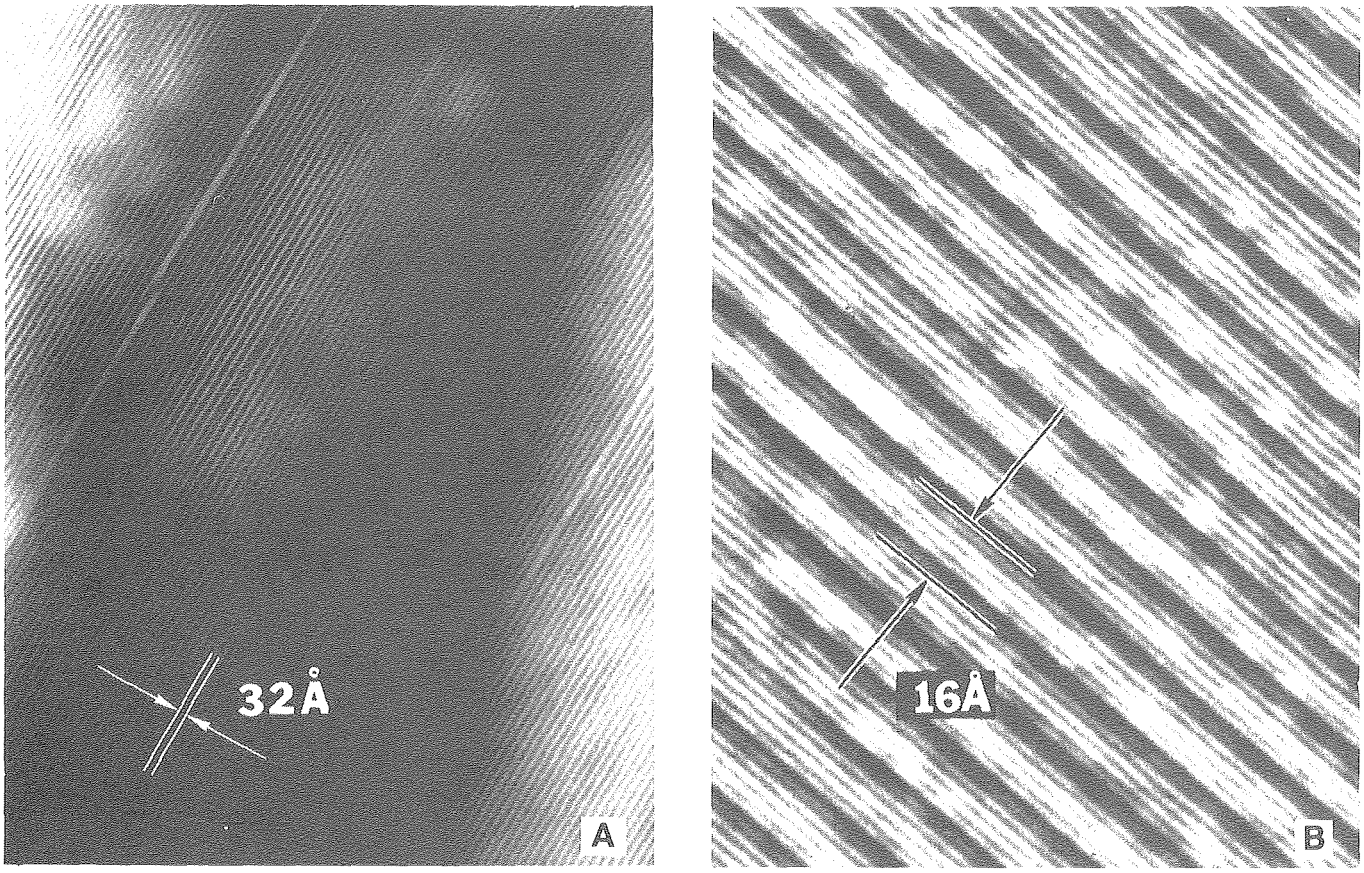

Fig. 4. (a) Lattice fringe image from a polytype of MgSiAlON showing 32 Å fringe periodicity. The irregularities in the fringe spacings are due to disorder in the polytype structure, 650 kV. (b) Lattice fringe image from $Be_9Si_3N_{10}$ with the periodicity corresponding to the close packed planes. Note the change in contrast in every fifth fringe in this 15R polytype, and the deviation from ideal structure at A with 6 fringes in one "block." [(a)XBB 776-7955; (b)XBB 776-7956]

In Fig. 4a a 32 Å periodicity in a grain of Magnesium Sialon polytype structure has been imaged using the Hitachi 650 kV microscope at Berkeley, indicating that a new polytype structure in addition to the 12H detected by x rays[1] exists at this composition.

By directly imaging the close packed planes details of stacking in the close packed direction can be found. In Fig. 4b, the individual close packed layers in a $Be_9Si_3N_{10}$ 15 R polytype have been recorded. The appearance of a darkened fringe every fifth fringe graphically confirms the suggestion by Thompson[2] that a cubic stacked layer of different composition occurs every fifth close packed layer in the 15R structure. Departures from the ideal polytype structure are also directly seen as in the block of 6 planes instead of 5 in Fig. 4b. More details are obviously revealed as the resolution is improved and structure imaging helps indicate the details of the atomic species in localized regions.[3]

---

1. See, for example, K. H. Jack, J. Mat. Sci. 11, 1135 (1976).
2. D. P. Thompson, J. Mat. Sci. 11, 1377 (1976).
3. T. M. Shaw and G. Thomas, Science, (to be published).

c. High Resolution Electron Microscopy

*Gareth Thomas, Principal Investigator**

Introduction. The object of the present program is to identify the localized variations in structure and composition that are responsible for the behavior of alloys. Much of the present understanding of these imperfections has been deduced from conventional transmission electron microscopy evidence, viz., bright field and dark field images as well as selected area diffraction patterns from regions of the specimen that are very much larger than the imperfections of interest. A considerable increase in resolution can be obtained, however, by forming a direct image of the specimen through a recombination of two or more scattered beams. In this way advantage is taken of the simple principle from Fourier optics that a lens produces a (less than perfect) Fourier transform of the object. For the proper orientation and thickness of the specimen, and at a precise value of accelerating voltage, objective lens current and stigmator fields, an image may be formed of the actual diffracting species (i.e., the atoms themselves) comprising a specimen. Because lenses are less than perfect however, high order reflections are eliminated from the image forming process, resulting in an effective truncation of the higher order components of the Fourier transform. The extent to which such an image actually represents the specimen must be judged on the basis of dynamical calculations using electron scattering theory. This, in short, is the status of current applications of high resolution electron microscopy in materials science.

When utilized in the study of close-packed materials such as metals and alloys, the truncation of higher order components during Fourier image formation necessarily becomes rather severe. The applications presented in the following summary articles are examples that have been obtained at the resolution limit of current generation transmission electron microscopes. These lattice images contain one-dimensional detail at the atomic level and reveal not only structural imperfections but also local chemical changes that induced local changes in lattice parameter within the specimen. Clearly as new generation microscopes operating at higher voltages become available, more detailed representations of the structure of metals and alloys will become routinely possible. This work represents a first step towards complete atomic characterization of such materials.

*Ron Gronsky, Staff Scientist

1. DIRECT OBSERVATIONS OF PLANE MATCHING BY LATTICE IMAGING ELECTRON MICROSCOPY*

R. Gronsky† and G. Thomas

The plane matching (PM) model of grain boundary structure was originally proposed by Pumphrey[1] in order to explain certain transmission electron microscopy (TEM) observations of periodic contrast features at grain boundaries. The basic premise of this model is that the matching of a set of close-packed planes across a grain boundary results in a low energy configuration. Since the matching is brought about by a periodic array of defects, it is reponsible for a characteristic structure within the boundary.

Subsequent applications[2] of the PM model to the description of grain boundary structures have met with success. Nevertheless each of these studies has had to rely heavily upon indirect evidence (viz., electron diffraction information) due to the limited spatial resolution of the involved TEM techniques. The purpose of the present research is to demonstrate an exact verification of plane matching conditions at a grain boundary utilizing high resolution electron microscopy. The proof is based upon a direct image of the mismatched atomic planes.

Periodic structural features observed within grain boundaries by TEM are given a simple optical representation in the PM theory.[1]

Idealizing the set of mismatched atomic planes on both sides of a boundary as a pair of optical gratings, the boundary region itself is depicted by their overlap (Fig. 1). Consequently the

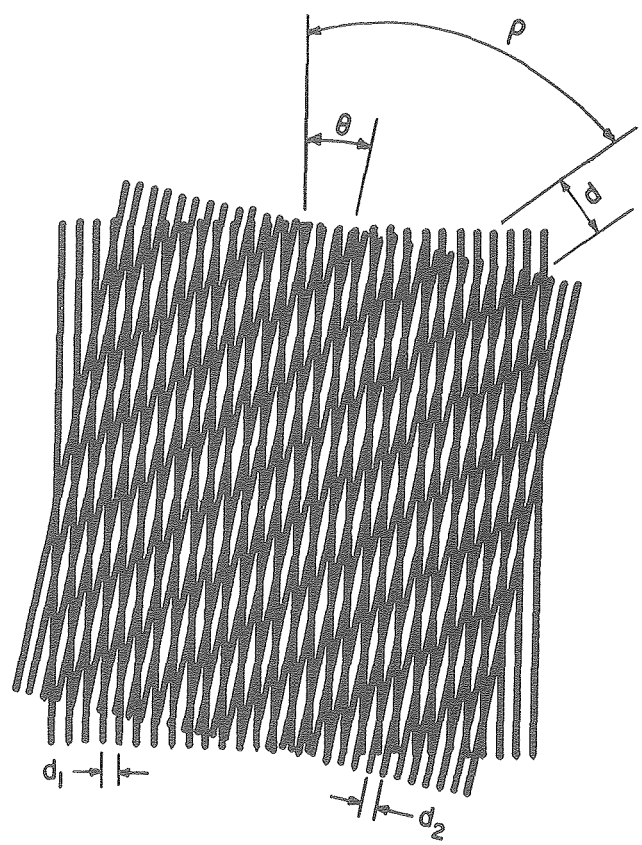

Fig. 1. Optical analogue for the plane matching model. The Moiré pattern of spacing d is produced by overlapping gratings d_1 and d_2 misoriented by θ. The angle between the Moiré bands and the fringes of grating 1 is ρ. (XBL 7611-7802)

observed linear contrast features at the boundary may be visualized as a Moiré effect.

In general the spacings d_1 and d_2 of the two misoriented lattices need not be the same, and as shown in Fig. 1, when rotated by an angle θ the overlapping gratings give rise to a Moiré fringe pattern of characteristic spacing:

$$d = \frac{d_1 d_2}{(d_1^2 + d_2^2 - 2d_1 d_2 \cos\theta)^{1/2}} .$$

Furthermore the rotation angle (ρ) between the Moiré fringes and the fringes of grating 1 may be computed as:

$$\sin\rho = \frac{d_1 \sin\theta}{(d_1^2 + d_2^2 - 2d_1 d_2 \cos\theta)^{1/2}} .$$

In order to test the theory, an Al-9.5 at %Zn alloy was fabricated and aged to encourage grain boundary precipitation. Regions of precipitate/matrix interfaces at grain boundaries (satisfying $d_1 \neq d_2$) were surveyed and imaged in a tilted illumination mode. The objective aperture included only one strongly diffracted beam from each of the regions ot be imaged as well as the transmitted beam.

The lattice image shown in Fig. 2(a) is an example of the type of micrograph used for analysis. Diffraction conditions are shown in Fig. 2(b). The figure includes simultaneous images of the (200) planes from matrix [1], the $(11\bar{2}0)$ planes of the rhombohedrally distorted[3] Zn-rich precipitate (P), and the (200) planes (at much lower visibility) from matrix [2].

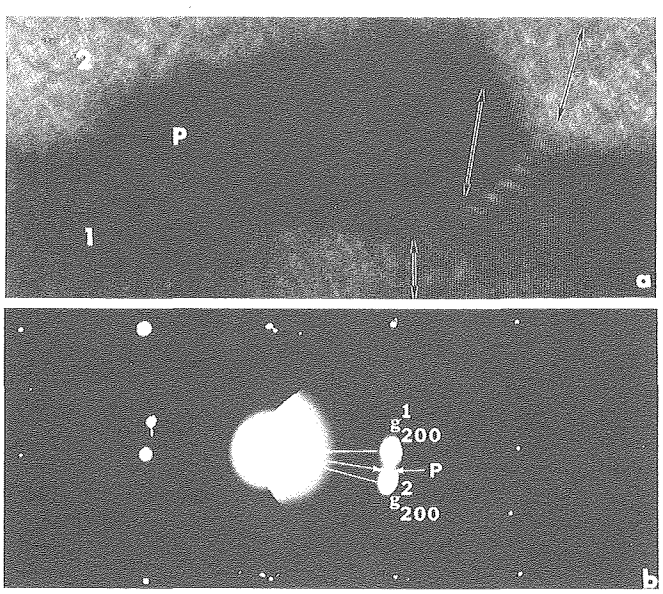

Fig. 2. (a) High resolution image of lattice planes within grains [1] and [2] as well as grain boundary precipitate [P]. (b) Diffraction conditions used in (a). (XBB 767-6532)

Using the highly visible fringes in grain [1] as a magnification standard, their spacing[3] (2.02 Å) By comparison the precipitate fringes were found to be spaced 2.09 ± 0.01Å, indicative of a higher Zn content.

The rotation angle θ between matrix [1] and precipitate (P) fringes was determined from both lattice image and SAD [Fig. 2(b)] measurements to be 9.2 ± 0.1°. Applications of the Moiré formulae given above allowed the measured spacing (d) and rotation angle (ρ) of the boundary structural lines then to be compared with the calculated values (see also Fig. 1), as follows:

d meas. = 12.2 ± 0.5 Å d calc = 12.4 ± 0.2 Å

ρ meas. = 106.5 ± 0.5° ρ calc = 107 ± 1°

The results are in excellent agreement. At this level of resolution, tilting experiments failed to reveal the presence of any other structural lines within the boundary region.

The structural nature of the apparent Moiré fringes is revealed in Fig. 3 that is a high magnification image of the boundary region in Fig. 2(a). Here it is seen that continuity of mismatch is observed within the high density Moiré bands as evidenced by the presence of terminating

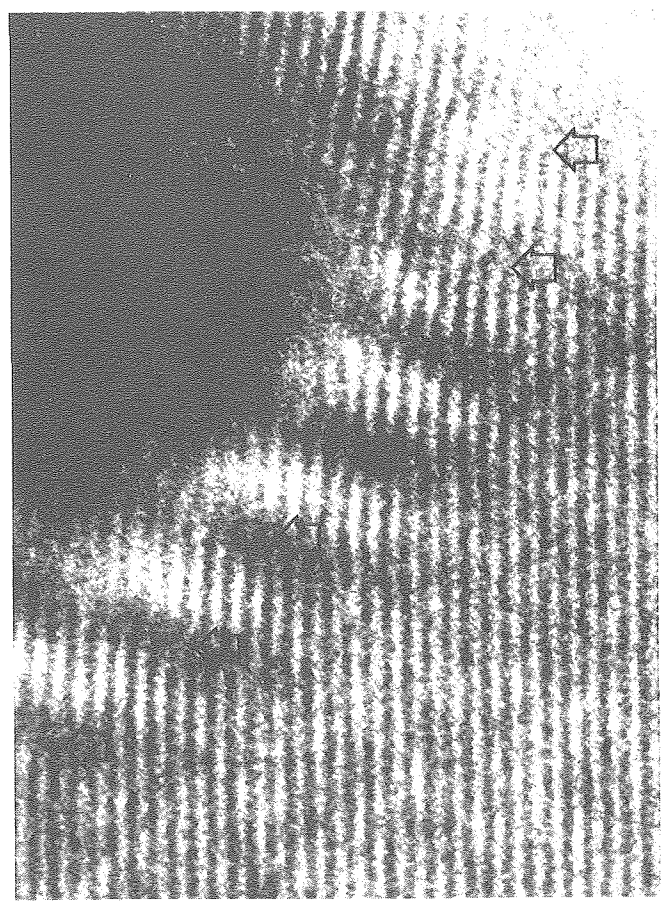

Fig. 3. Enlargement of the interphase boundary in Fig. 2. Open arrows indicate terminating fringes in optically dense regions. (XBB 767-6627)

fringes (arrowed). These terminations furthermore suggest that misorientation dislocations with a Burgers vector equal to the interplanar spacing may be associated with the misfit lines, in exact agreement with the PM theory.[2]

---

*Partially supported by NSF Grant DMR 72-03269 A01

†Published in Scr. Metall. 11, 791 (1977), LBL-6602.

1. P. H. Pumphrey, Scr. Metall. 6, 107 (1972).
2. P. H. Pumphrey, Scr. Metall. 7, 893 (1973).
3. A. V. Dobromyslov, Phys. Met. Metallogr. 33, 63 (1972).

2. HIGH RESOLUTION ANALYSES OF GRAIN BOUNDARY REACTIONS

R. Gronsky*

Because most commercial materials are polycrystals, their properties are largely determined by the presence of segregated species or phase transformation products at grain boundaries. The present study has been directed towards identifying the atomic mechanisms underlying such grain boundary reactions. Experimentation has so far involved well-characterized binary alloys of Al and Zn in order that the research may address questions of a purely fundamental nature. High resolution electron microscopy has been applied throughout the investigation, successfully providing atomic-level detail about the localized structural and compositional variations accompanying grain boundary reactions. These results are summarized below.

Heterogeneous Nucleations. As in the study of spinodal decomposition (article 3), lattice imaging has been used in this research to enable relative measurements of interplanar separation in the vicinity of grain boundary reaction fronts (Fig. 1). This method has revealed the presence of composition profiles (Fig. 2) and/or solute enrichment to within ~8 to 10Å of the boundary plane. It was found during this study that the orientation of the grain boundary plane, rather than specific lattice defects at the boundary (Fig. 3) were most influential in determining active sites for heterogeneous nucleation of the Zn-rich phase. In particular, grain boundaries that were parallel to a family of low index atomic planes in either bordering grain were highly favored as reaction fronts. Boundaries parallel to a {111} matrix trace were furthermore found to enhance reaction kinetics.

Discontinuous Precipitation. The R-phase discontinuous precipitation reaction in the Al-Zn system has caused difficulty in interpretating diffraction evidence for quite some time.[1] The reaction proceeds by the growth of alternating lamellae of the Al-rich matrix phase and the R-phase. These lamellae cluster in colonies and grow until impingement, at which time complex splitting of reflections is seen in diffraction patterns. The origin of these effects are clearly revealed however, by high resolution imaging.

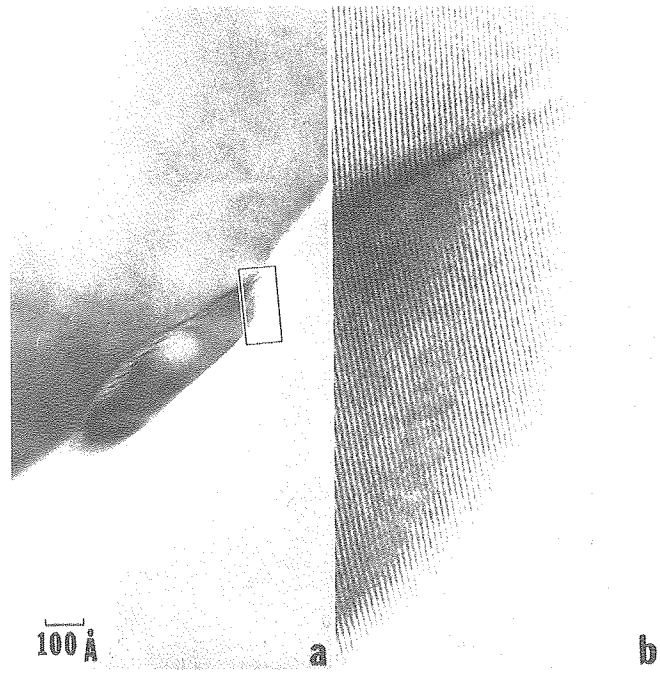

Fig. 1. Lattice image of a grain boundary precipitate in an Al-9.5 at %Zn alloy aged 30 min at 180°C; (a) low magnification and (b) enlargement of the boxed region on which compositional analysis (Fig. 2) was performed. (XBB 7611-10514)

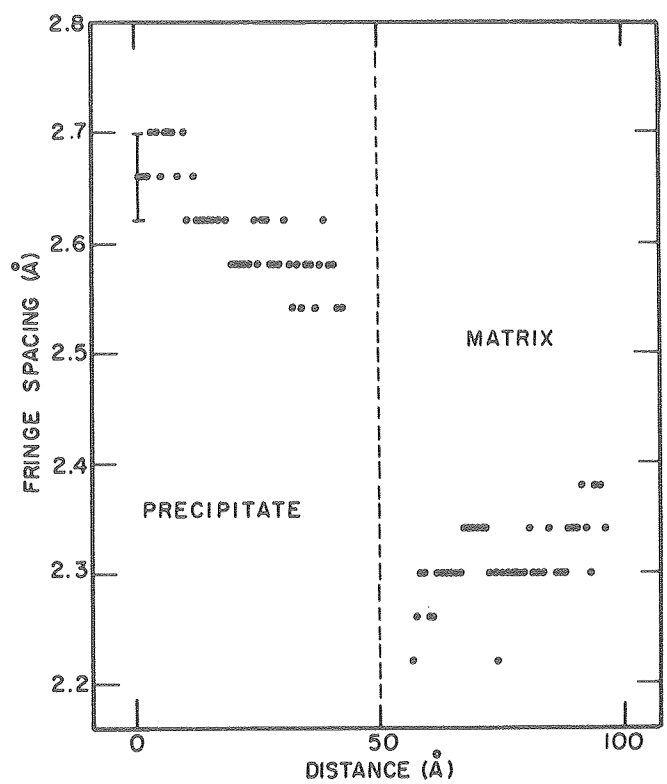

Fig. 2. Plot of fringe spacing vs distance for region of Fig. 1(b) above. Each measurement included 10 fringes (error has shown on first data point). The presence of a composition gradient is clearly revealed. (XBL 7611-7804)

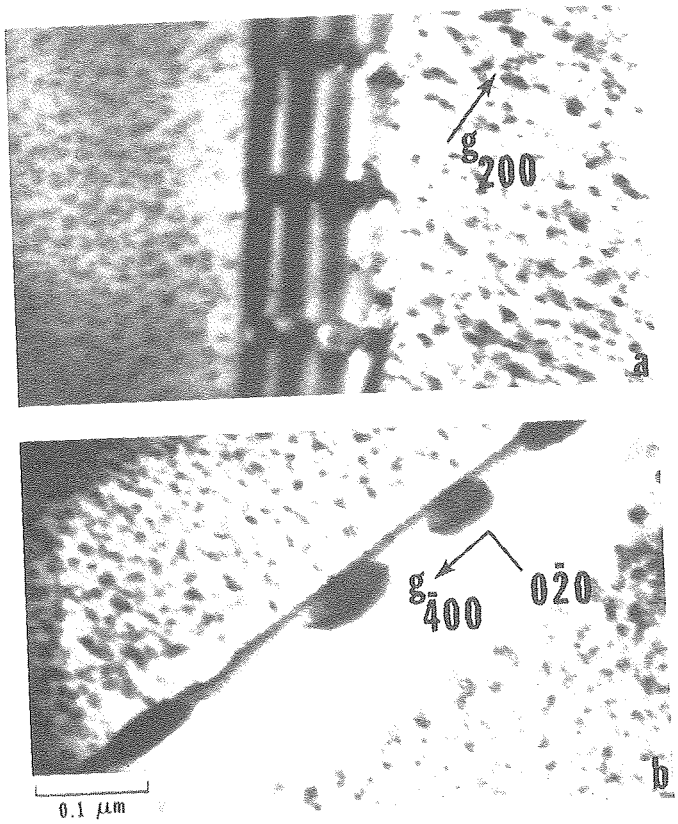

Fig. 3. (a) Aligned equiaxed precipates along the dislocations comprising a pure tilt boundary. (b) Hemispherical cap morphology of grain boundary precipitates that do not appear to be influenced by the dislocation net. Aging conditions identical, orientation of the boundary plane varied. (XBB 7611-10521)

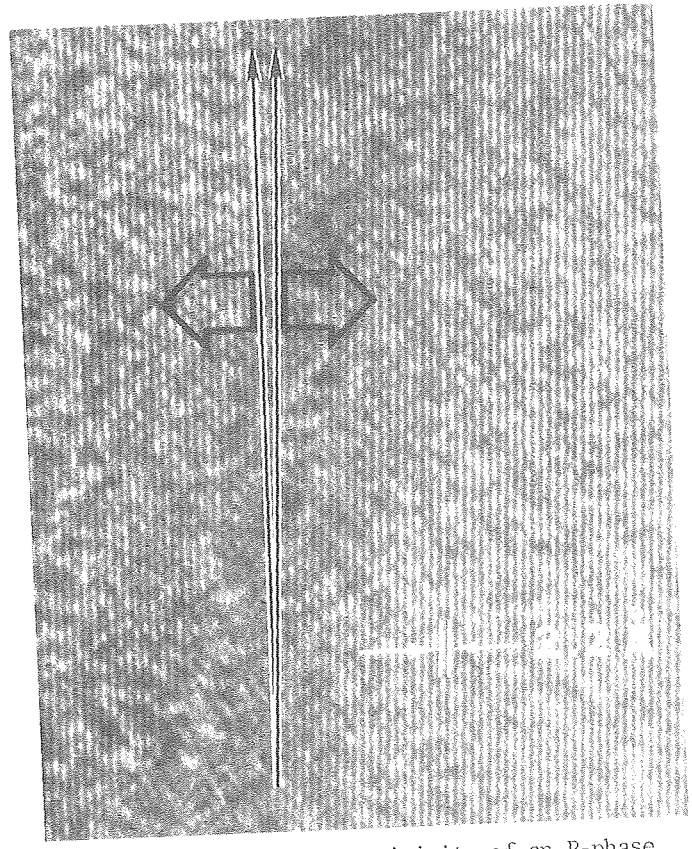

Fig. 4. Lattice image at vicinity of an R-phase lamellar termination. A slight misorientation (~2°) is detected by direct fringe measurement. (XBB 767-6533)

Figure 4 shows the lattice image of an R-phase interlamellar boundary. Direct measurement is possible from the micrograph and indicates that the {111} planes within neighboring lamellae are misoriented by 2.0 ± 0.5°. Images of this sort also show that mismatch strain is accommodated by structural relaxation within the boundary, allowing identification of the defects present at lamellar terminations (Fig. 5) to be accurately made.

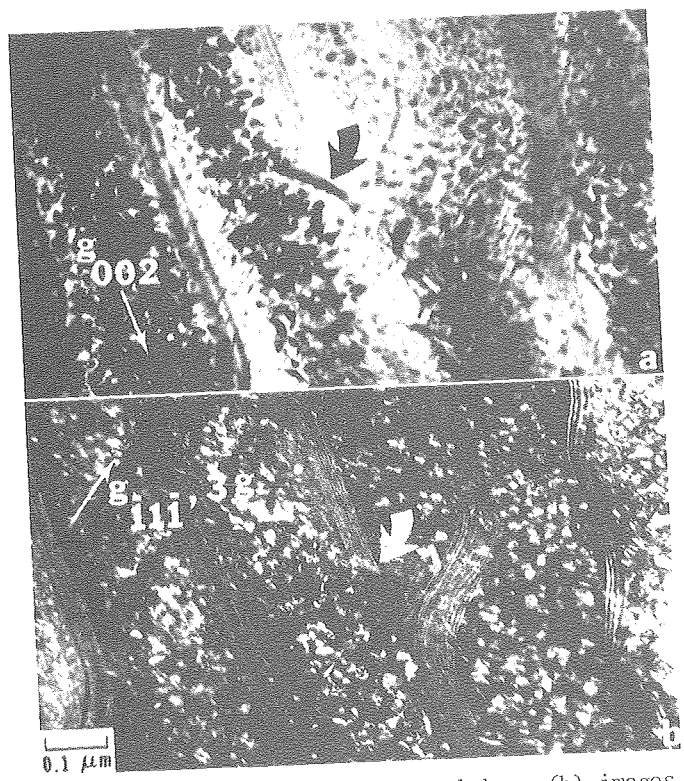

Fig. 5. Bright field (a) and weak beam (b) images of an R-phase lamellar termination indicating that misorientation is abruptly accommodated by a single lattice dislocation (arrowed). (XBB 7611-10517)

---

*Ph.D. thesis, LBL-5784

1. K. N. Melton and J. W. Edington, J. Mat. Sci. 9, 1457 (1974).

3. LATTICE IMAGING STUDIES OF SPINODAL DECOMPOSITION

C. K. Wu, R. Gronsky and G. Thomas

This research is part of a continuing program on the fundamental analysis of phase separation by spinodal decomposition. Although the theory describing this transformation process is essentially complete, there are serious deficiences in the area of experimental characterization. Conventional methods, e.g., x-ray diffraction, resistivity measurements and transmission electron microscopy lack the spatial resolution necessary for a close examination of the decomposition process; therefore, the accuracy of existing theories cannot be tested.

At present, there are two major areas of interest: 1) localized composition amplitude (as well as wavelength) as a function of aging time, and 2) interfacial structure at the latter stages of aging. The only experimental method capable of providing acceptable levels of resolution for these studies is lattice imaging electron microscopy.[1] By monitoring the interplanar separation reflected in the lattice image, composition and structural effects due to atomic lattice modulations can be directly observed. This technique furthermore has the potential for revealing the full range of harmonics present in the modulated lattice. These harmonics are inevitably averaged out and therefore undetected by other techniques.

Figure 1 is an example of a lattice image of a spinodally decomposed Au-53 wt% Ni alloy aged 1 hr at 150°C. The fine fringe structure represents the (200) lattice planes of this material, which are modulated in spacing as shown in Fig. 2. These

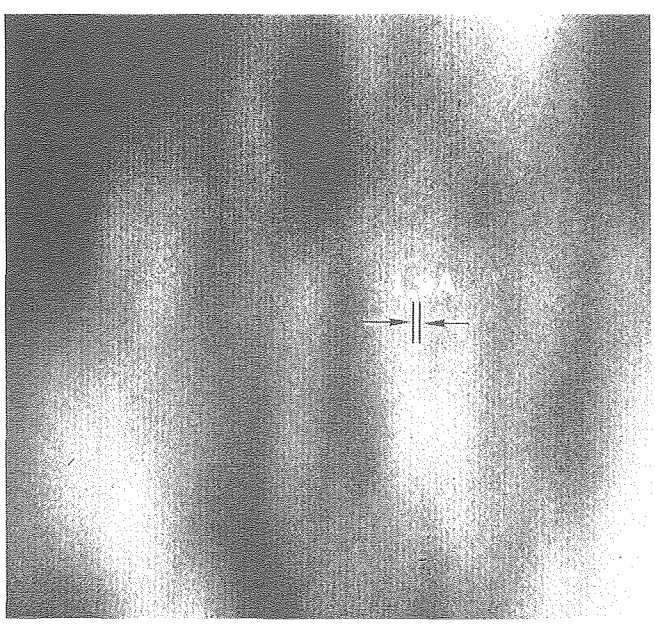

Fig. 1. Lattice image of (200) planes in a Au-53 wt% Ni alloy aged 1 hr at 150°C. The large scale dark/light contrast is typical of a modulated microstructure imaged under two-beam conditions. (XBB 770-10853)

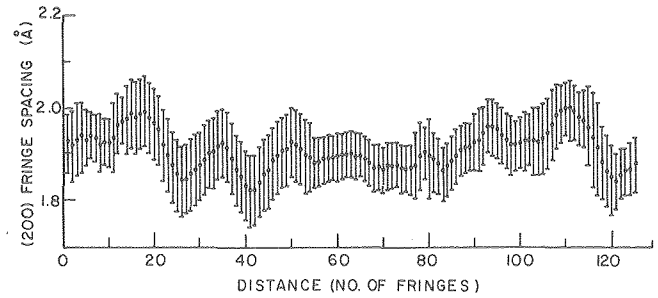

Fig. 2. Smoothed plot of fringe spacing vs. distance along Fig. 1 above, taken from microdensitometer data. The estimated wavelength is 29 ± 5Å, and the estimated lattice parameters are a_0^{Au} = 3.9 ± 0.1 Å, a_0^{Ni} = 3.7 ± 0.1 Å. (XBL 7711-6341)

data indicate directly that the composition wavelength (peak-to-peak) is 29 ± 5Å at a maximum amplitude of $\lesssim$ 10%.

At the later stages of aging, the initially diffuse interphase interfaces sharpen due to composition wave squaring. Lattice imaging also has much to reveal about this microstructure as shown in Fig. 3.

The top low magnification micrograph shows the coarsened microstructure of a commercial Cu-Ni-Cr spinodal alloy after aging 808 hr at 600°C. Three precipitates can be identified in the image. The boxed rectangular area is enlarged to show the fringes in the lower left-hand micrograph. A laser optical diffractometer[1] has also been used to obtain diffraction information from the image. Letters A-F marked in the top micrograph indicate the places where an optical aperture (size ~120Å) was located to produce the corresponding optical diffraction patterns mounted on the lower right of Fig. 3. When the aperture sampled a single phase region (e.g., Cu-rich, as in D or Cu-poor, as in B and F), single diffraction spots were observed as expected. However, the diffraction information from the interfacial regions suggest that three distinct types of interface are present. Their characteristics are:

1) a sharp, discontinuous change in lattice spacing as in A (split diffraction spots);
2) a diffuse, continuous change in lattice spacing as in E (horizontally broadened spots);
3) a modulated change in lattice spacing as in C (satellite diffraction spots). This latter observation is quite unexpected and deserves further investigation. Notably, this level of detail is not possible with other experimental techniques.

---

1. R. Sinclair, R. Gronsky and G. Thomas, Acta Met. 24, 789 (1976).

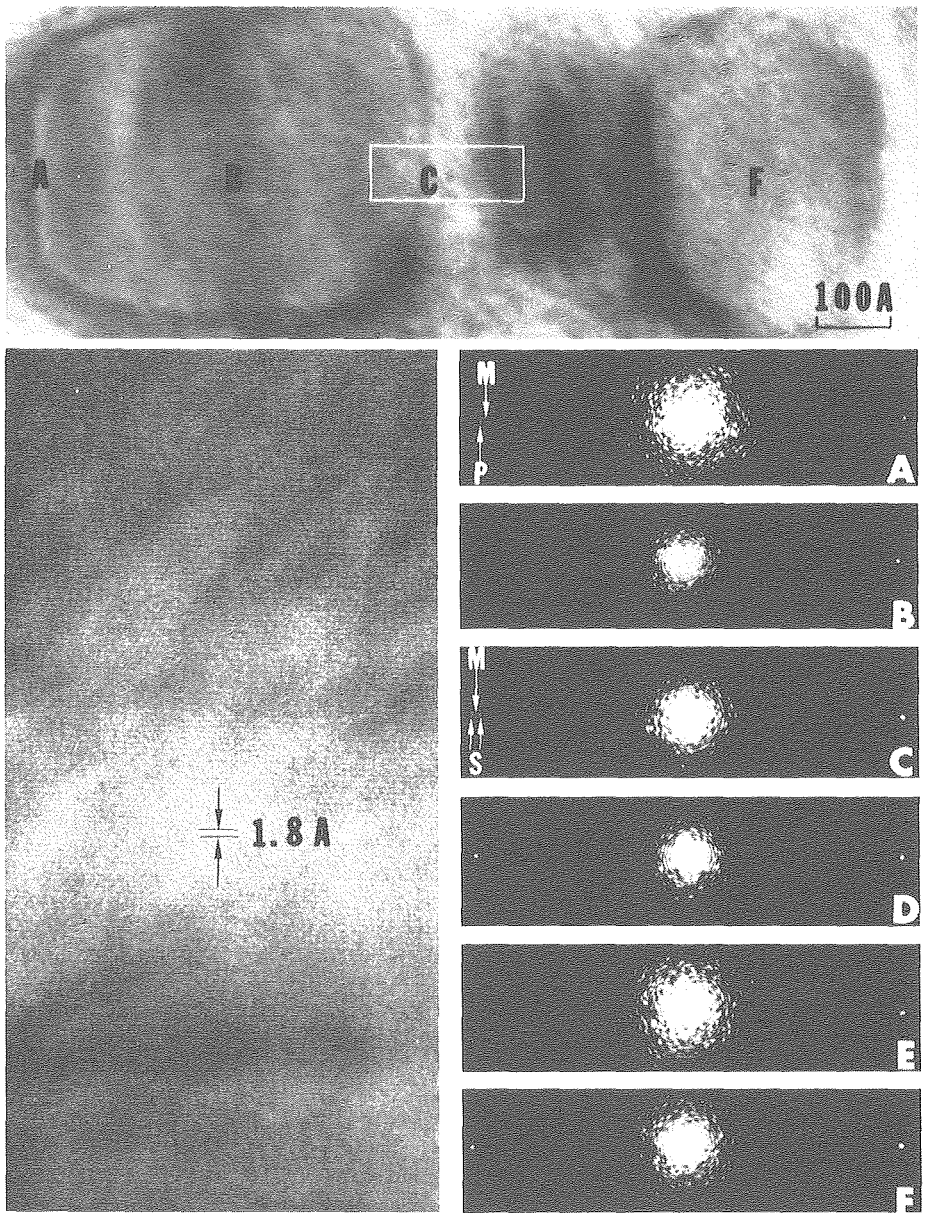

Fig. 3. Lattice image analysis of a commercial Cu-Ni-Cr spinodal alloy after aging 808 hr at 600°C. Three different types of interfaces are revealed (see text for details). (XBB 777-6713)

4. DETERMINATION OF LOCAL COMPOSITION BY LATTICE IMAGING*

R. Sinclair† and G. Thomas

An assessment has been made of the potential for direct lattice imaging to be used for the determination of local chemical composition in alloys by localized lattice parameter measurements. The principle involves correlation of electron microscopy lattice fringe image spacings with composition. This method allows lattice parameters to be measured over highly localized areas. For instance in typical metallurgical studies an accuracy of ± 1% may be achieved over 10 Å, while averaging over 30 Å involves an uncertainty of ± 0.3%. In order to obtain higher precision the resolution of the method must be sacrificed. This situation implies that, in appropriate systems where there is sufficient variation of lattice spacing variation with composition (da/dc), information can be obtained on composition in highly localized areas. Thus in an alloy with da/dc ~ 0.16, composition differences of only ~3% can be detected with a resolution of 20 Å. This should prove to be particularly important for interstitial solid solutions. In addition the results indicate that for many cases the method both has higher resolution and is more precise than currently available, alternative analytical techniques. While the results are very encouraging, the role of electron optical and lattice constraint effects must be examined in more detail to allow general application of the method, especially for the case of multiphase systems involving large interfacial strains.

*LBL-6050, Met. Trans. AIME (in press).

†Now at Department of Materials Science and Engineering, Stanford Univ. Stanford, California 94305; research supported by NSF.

5. BEAM ENHANCED OXIDATION IN THE TRANSMISSION ELECTRON MICROSCOPE*

Ulrich Dahmen†

In spite of the common use of transmission electron microscopy (TEM) for studies of materials, the effect of a conventional 100 kV electron beam on the morphology and diffraction phenomena in thin metal foils has been widely neglected. This study calls attention to the importance of beam enhanced oxidation as a source of serious misinterpretation of electron micrographs. A variety of techniques, with particular emphasis on high resolution, have been used to demonstrate the growth and morphology of oxides on thin foils. Although this study is limited to FeAl, spontaneous or beam enhanced oxidation is observed in a number of systems.[1,2]

Figure 1 shows a high density of small domains that have grown in the limited area exposed to the beam. These domains can be identified as an fcc

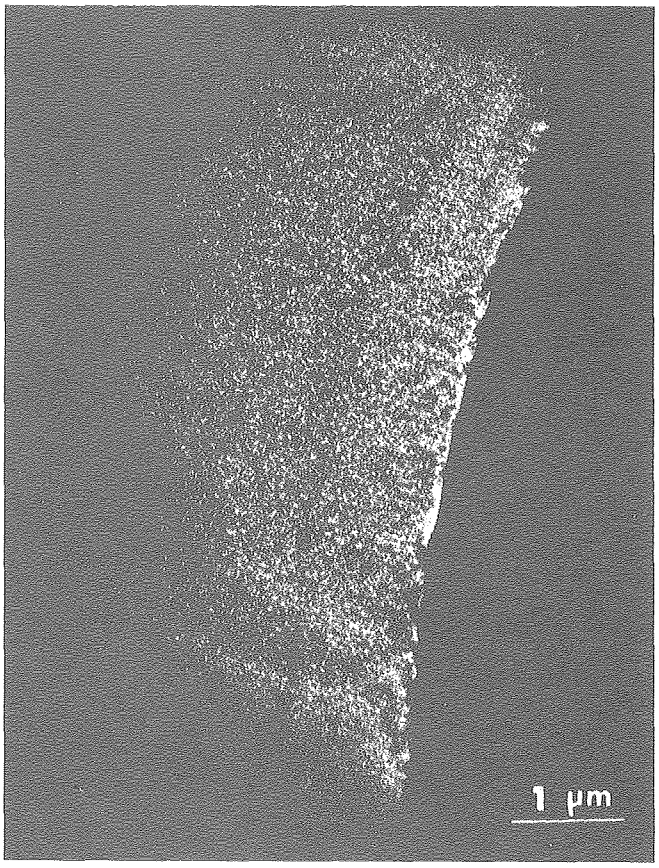

Fig. 1. Dark field image of surface oxides after 60 min beam exposure. Fe-20%Al; foil normal [110]. (XBB 7711-12415)

oxide phase with a lattice parameter of ~ 8.1 Å, in epitaxy with the matrix. The observed orientation relationship is of the Nishiyama-Wassermann type.[3] Oxide growth is most rapid on {110} surfaces for which the N-W relationship allows two orientation variants. Both variants are observed in the latter stages of oxidation while only one is found in the early stages.

Figure 2 is a high resolution dark field micrograph of an advanced stage of oxidation. The large domains are clearly oxides. They are elongated along ⟨110⟩. Among them a high density of small isometric low intensity domains is seen that can be due to either ordering or oxides.

Fig. 2. Same area as in Fig. 1 at high resolution, showing oxide morphology and ordered domains. (XBB 7711-12416)

Figure 3 shows two time sequences of a {110} diffraction pattern at +20°C and -195°C under otherwise identical conditions. Diffuse diffraction spots due to oxidation are very close to, or superimposed on, superlattice reflections caused by DO_3 short range ordering. In both cases, the {111} oxide variant is initially preferred. This cannot be explained by strain energy considerations and is more likely due to the anisotropy of interfacial and surface energies. The reaction has a very small thermal activation energy (about 1 kcal/mole) since the kinetics are relatively insensitive to temperature in the range from +20°C

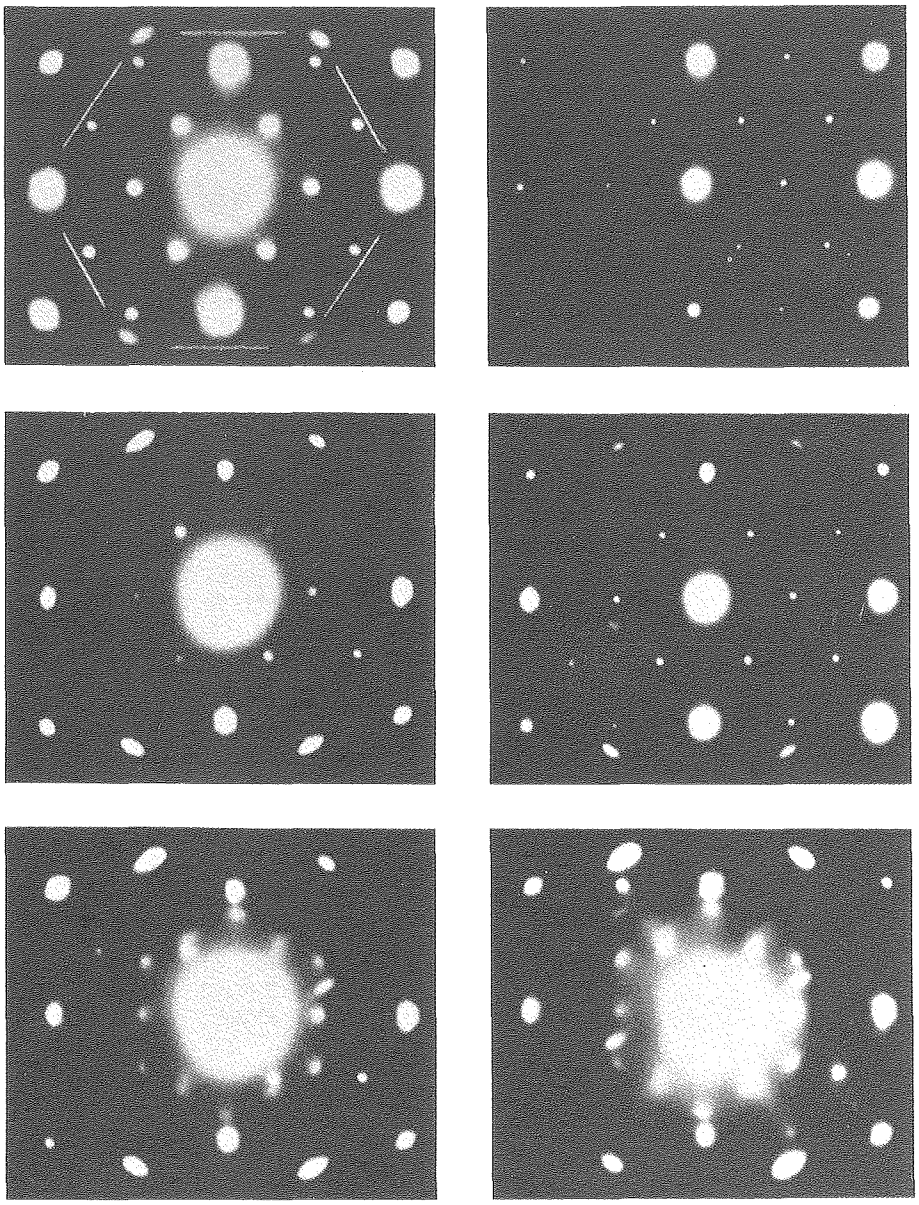

Fig. 3. (Left) T = +20°C; (Right) T = -195°C (110) diffraction pattern of ordered FeAl after 2, 10 and 30 min beam exposure. Note growing intensity of (111) oxide zone (indicated by lines). (XBB 7711-12417)

to -195°C. Because of the closeness of the oxide and superlattice reflections, ordered domains and oxide islands cannot be distinguished by conventional dark field imaging.

Figure 4 shows a high resolution fringe image of the surface oxide. Spacings and directions of the fringes correspond to those of {113} oxide lattice planes. A misorientation of ~2° can be directly observed between adjacent domains. The underlying superlattice has a similar spacing, but does not show any rotational misorientation.

The main contaminant of the microscope vacuum is H_2O vapor. Thus, the mechanism of oxidation is likely to be the cracking of adsorbed H_2O molecules by the electron beam and their reaction with surface atoms.[1,2]

An awareness of these effects is particularly important for the correct interpretation of high resolution electron micrographs. Due to the higher electron flux needed for lattice imaging, surface oxide formation is more likely to occur. However, as shown by this study, surface oxide

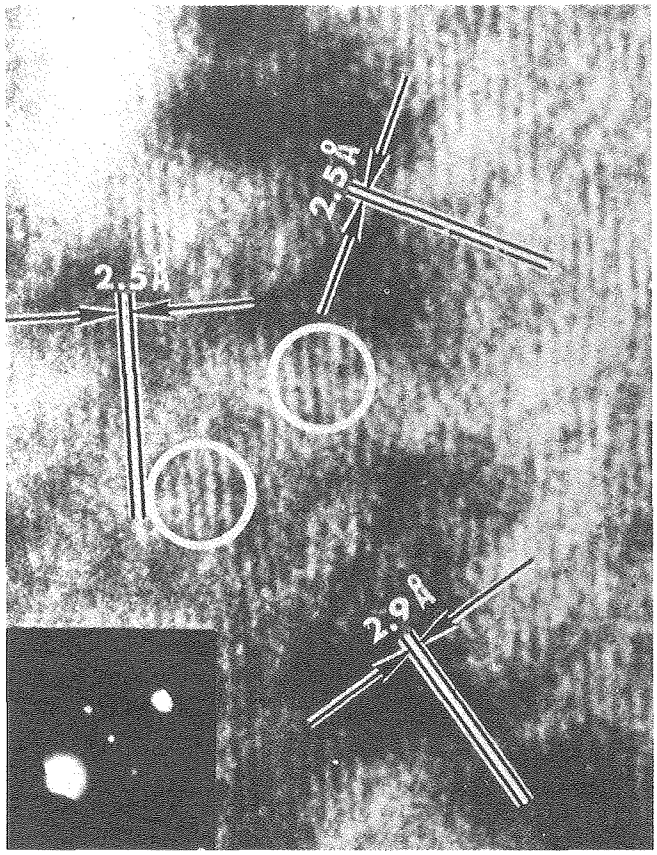

Fig. 4. Phase contrast image resolving (113) oxide planes (2.5Å) and (200) superlattice planes (2.9Å). Small misorientation between oxide islands (encircled areas). (XBB 7711-12418)

effects can also be readily identified with the proper choice of lattice imaging conditions.

---

*Supported by the Fulbright Commision through the German Academic Exchange Service

†Recipient of Electron Microscopy Society of American Student Fellowship Award, 1977.

1. V. Margoninsky, D. Segal and R. E. Kirby, Sur. Sci. 43, 488 (1975).
2. W. Ranke and K. Jacobi, Surf. Sci. 47, 525 (1975).
3. S. H. Chen and U. W. Morris, Met. Trans. 8A, 19 (1977).

6. RESEARCH PLANS FOR CALENDAR YEAR 1978

Gareth Thomas

a. Microstructure, Properties and Alloy Design

Structural Steels. It is clear now that the options available for microstructural control to produce strong, tough structural steels are limited, viz., to start with a homogeneous γ phase that is quenched to form dislocated lath martensitic structure dispersed with fine carbides and decorated with interlath films of stable retained austenite. Our continuing studies are aimed at fully exploiting the retained austenite for improved properties. One of the objectives is to study alloying that promotes stability in austenite without inducing transformation twinning in the matrix martensite. other objectives will be to expand our understanding of the role of alloying on thermal instability temperature of austenite and the coarsening kinetics of cementite in order to defer the onset of tempered martensite embrittlement. Since the experimental steels are designed for adequate hardenability, it will be attempted to obtain the desired microstructure simply by air hardening. Other properties of commercial interest including fatigue, corrosion behavior and especially wear resistance will also be investigated.

On a fundamental basis, a stronger carbide forming element than Cr, for example, Ti will be used in the Fe/Cr/C system in order to isolate the individual roles of prior austenite grain size and undissolved alloy carbides on deformation and fracture properties of martensitic steels.

Duplex Alloys. 1) Optimizing the microstructure and mechanical properties of Fe/Si/C dual phase steels investigating the following: effect of silicon content on tensile and impact properties; shape and distribution of two-phase microstructures and a fundamental understanding of structure-property relations in the systems. 2) Structure and properties quaternary Fe/Si/X/C (X being Mo or V) dual phase steels. The important problems to be investigated are a) the effect of carbide precipitation on the mechanical properties of DFM composites; b) investigation of the possibility of lowering volume-fraction of martensite by substituting secondary strengthening (e.g., carbide precipitation) and comparisons between structures derived from slow and fast quenching.
3) Characterization of dual phase structures in ternary Fe/Al/C and Fe/Mo/C steels. This program aims to establish the structure-property relations in DFM Fe/Al/C and Fe/Mo/C steels in comparison with those in the Fe/Si/C system. 4) The principals of DFM steels should have wider applications than for transportation. However DFM alloy design for thicker section applications requires increased hardenability, e.g., through Boron addition so as to slow down the kinetics of γ decomposition. Thus a series of steels containing boron will be studied to establish appropriate structure-property relations.

Spinodal Alloys. Fe/Cr/Co alloys exhibit good magnetic properties, but the mechanical properties of these alloys have not as yet been studied. It is important to know the mechanical properties of these alloys at various stages of the heat treatments in establishing the fabrication and utilization of these hard magnets. Thus, future work aims to study the relationships between the microstructure and mechanical properties of Fe-28%Cr-15%Co alloy after various heat treatments developed to maximize the magnetic properties of the alloy.

b. Microstructure-Property Relationships in Magnetic Ceramic Materials

The principles of alloy development, as practiced in metallic systems, can also be applied to design ceramic materials. The basis for such applications lies in establishing microstructure-property correlations in candidate ceramic systems. By this time, the effects of structural imperfections and second phases on static magnetic properties in lithium ferrite have been well established by this group. Trends in the microstructure-property correlations suggest that hard magnets with high "maximum energy product" can be designed by dispersing nonmagnetic second phases in the magnetic matrix. Thus the study of phase transformation and the associated high frequency property changes in (NiZnCo) Fe_2O_4, phase transformation and magnetic hardening in $BaFe_{12}O_{19}$ and the segregation of heavy elements in garnets will continue. In addition, work will be initiated to characterize the substrate-epifilm interface structures in magnetic bubble devices, with particular emphasis on defect structure, microsegregation and consequent changes in the film properties. Basic structural studies of the epitaxially grown garnet films will be undertaken to identify the origin of growth induced anisotropy that is central to bubble formation in these films. Plans are underway to develop a joint program with Prof. Hess of the Chemical Engineering Department to plasma spray deposit amorphous bubble films, study their microstructures and properties and gain basic understanding to develop new film growth technology. Finally, the research program will be expanded to include the study of processing, structure, microstructure-mechanical property relationships in mullite in a joint collaborative effort with Professor Pask.

At present, our emphasis is also to study and establish the correlation between microstructure and dynamic microwave properties in some soft spinel ferrites (M. Harmer). We are expanding our program to include garnet ferrites in view of their potential technological application as bubble devices. The present effort is to characterize the substrate bubble film interface that significantly affects the magnetic bubble properties and may ultimately limit the applications (T. Roth). More importantly, the interface studies will benefit other related areas using junction devices such as lasers and solar cells. A new program involves the analysis of grain boundary phases that appear to limit the applications of ZnO as varistors (P. Willimas).

c. High Resolution Studies

Fundamental Studies of Grain Boundaries. The lattice imaging technique has clearly shown superiority in this field and will be further utilized for detailed examinations of grain boundary structure, segregation effects and phase transformation behavior. It is planned to conduct experiments on Al-Zn alloys containing controlled ternary additions during the initial stages of this study, later to incorporate bicrystals of controlled geometry.

Spinodal Decomposition. Research will concentrate on the Au-Ni system for a fundamental understanding of the decomposition mechanism. Analysis of another commercial alloy, Cu-Ni-Sn, will also be initiated to explore its strengthening mechanisms. Both of these systems are characterized by a large strain energy term that strongly influences microstructural development and particle coarsening. The lattice imaging technique offers the potential for direct assessment of this strain component and will be employed to complement recent theoretical work in the field.

Interstitial Ordering in Tantalum. A systematic study of the influence of H and C interstitial ordering in tantalum will be undertaken. Its purpose is to clearify the results of previous studies by providing both microstructural and crystallographic analyses at high resolution. In this way, those problems stemming from the unknown stoichiometry, exceptionally small domain size and occurrences of long period ordering in this system can be readily addressed.

Martensitic Steels*. The initial work on the formation of lath martensite has already resulted in significant new results. The momentum of research activity in this area will be maintained to better understand the mechanism of lath martensite formation. Both high resolution and high voltage microscopy will be employed and the origin of specific orientations of adjacent laths within a given packet will be investigated. Also, the exact role of interstitial carbon in dictating the relative orientations of laths will be examined. Specifically, the hypothesis that some carbon enrichment in austenite is partly responsible for austenite stabilization can be checked by high resolution lattice imaging to measure directly the d-spacing and in addition, characterize the γ/α interface at almost atomic resolution.

---

*Supported by NSF

7. 1977 PUBLICATIONS AND REPORTS

Gareth Thomas and Associates

Journals and Books

a. Microstructure Properties and Alloy Design

1. B. V. N. Rao, R. Miller and G. Thomas, Heat-Treatment, Microstructure and Mechanical Properties of Fe/4Cr/0.4C Steels, Heat Treatment 76, The Metals Society of London, 1 Carlton House Terrace, London, SW1Y 5DB, (1977), p. 75, LBL-3982.

2. G. Thomas, Utilization and Limitations of Phase Transformations and Microstructures in Alloy Design of Strength and Toughness, Proc. on Tenth Battelle Colloquim in Materials Science, Fundamental Aspects of Structural Alloy Design, 1977, Richland, WA, R. Jaffee and B. Wilcox, Eds., Plenum Publishing Corporation, New York, N.Y., (1977), p. 331, LBL-4175.

3. S. Jin, D. Hung, J. W. Morris and G. Thomas, Use of the Reverse Martensitic Transformation and Precipitation to Enhance the Strength and Stability of Austenite, Proc. of the First JIM International Symposium on "New Aspects of Martensitic Transformation", Kobe, May 10-12, 1976, The Japan Institute of Metals, Aoba Aramaki, Sendai 980, Japan, p. 387, LBL-4557.

4. M. Carlson, B. V. N. Rao, R. Ritchie and G. Thomas, Improvements Strength and Toughness of Experimental Fe-Cr-C Steels, 4th International Conference on Strength of Metals and Alloys, August 1976, Nancy, France, 2, 509 (1976), LBL-5111.

5. J. Y. Koo and G. Thomas, Design of Duplex Fe/X/0.1C Steel for Improved Mechanical Properties, Met. Trans. 8A, 525 (1977), LBL-5723.

6. D. R. Clarke and H. Lilholt, Discussion on "On the Bauschinger Effect in Unidirectionally Solidified Eutectic Al-Al_3Ni Crystals" by Lasalmonie and Martine, Scripta Met. 9, 83 (1975).

7. D. H. Huang and G. Thomas, "Metallography of Bainitic Transformations in Silicon Containing Steels", Met. Trans. 8A, 1661 (1977), LBL-4519.

b. Ceramic Alloys

1. R. K. Mishra and G. Thomas, Microstructure and Magnetic Properties of Spinel Ferrites, AIP Conference Proceedings, Magnetism and Magnetic Materials, J. Becker and G. Lander, Eds., (1976), p. 66, LBL-5108.

2. R. K. Mishra and G. Thomas, Lattice Defects in Lithium Ferrite Spinel, Proc. 6th International Materials Symposium, Berkeley, CA, Ceramic Microstructure '76: With Emphasis on Energy Related Applications, R. Fulrath and J. A. Pask, Eds., Westview Press, Boulder, CO, (1977), p. 71, LBL-5700.

3. R. K. Mishra and G. Thomas, Structural Phase Transition in the Spinel $MgAl_2O_4$, Acta. Cryst. A33, 678 (1977), LBL-5702

4. D. R. Clarke, O. Van der Biest and G. Thomas, The Impact of Transmission Electron Microscopy in Ceramics, Proc. 6th International Materials Symposium, Berkeley, CA, Ceramic Microstructure '76: With Emphasis on Energy Related Applications, R. M. Fulrath and J. A. Pask, Eds., Westview Press, Boulder, CO, (1977), p. 29, LBL-5758.

c. High Resolution, High Voltage Electron Microscopy

1. R. Sinclair and G. Thomas, Lattice Image Studies of B19 Ordering in Mg_3Cd, Acta Met. 25, 235 (1977), LBL-5126.

2. R. Sinclair and G. Thomas, Discussion of "An Electron Diffraction Study of Short-Range Order in Ni_4Mo Alloy", Acta Met. 25, No. 3, 231 (1977), LBL-4983.

3. O. Van der Biest and G. Thomas, Absolute Structure Determination Using Electron Microscopy, Acta Cryst. A33, 618 (1977), LBL-5190.

4. J. Cowley, R. Glaeser, R. Sinclair and G. Thomas, Report of the Workshop on High Resolution Electron Microscopy, Proc. Micron 8, xxx (1977), LBL-5722.

5. G. Thomas, Some Applications at Berkeley of High Voltage Transmission Electron Microscopy, Annual Report of 1000 kV Electron Microscopy Research Laboratory, Nagoya University 1976-1977, p. 29, LBL-5762.

6. G. Thomas, High Voltage and High Resolution Electron Microscopy in Materials Science, Journal of Metals, p. 31 (February 1977), LBL-6005.

7. G. Thomas, Applications of High Resolution Electron Microscopy in Materials Science at the University of California, Berkeley, Proc. of U.S.-Japan HVEM Seminar, Honolulu, December 10, 1976 on New Applications and Extensions of the Unique Advantages of HVEM for Physical and Materials Research, T. Imura and R. Fisher, Eds., Lab. of Metal Physics, Nagoya University, Japan, (1977), p. 74, LBL-6037.

8. U. Dahmen and G. Thomas, Specimen-Environment Interactions in Electron Microscopy, Proc. U.S.-Japan HVEM Seminar, Honolulu, December 10, 1976, on New Applications and Extensions of the Unique Advantages of HVEM for Physical and Materials Research, T. Imura and R. Fisher, Eds., Nagoya, Japan, Lab. of Metal Physics, p. 60 (1977), LBL-6038.

9. C. K. Wu, Fringe Spacing Measurement of Lattice Imaging Micrographs, 35th Annual Proceedings, Electron Microscopy Society of America, Boston, MA, 1977, G. W. Bailey, Ed., Claitor's Publishing Division, Baton Rouge, LA, (1977), p. 182, LBL-6072.

10. J. Y. Koo and G. Thomas, Lattice Imaging of Twin, Lath and α/Martensite Boundaries in Duplex Low Carbon Steels, 35th Annual Proceedings Electron Microscopy Society of America, Boston, MA, G. W. Bailey, Ed., Claitor's Publishing Division, Baton Rouge, LA, (1977), p. 118, LBL-6202.

11. D. Clarke and G. Thomas, Lattice Imaging of Grain Boundaries in Ceramics, 35th Annual Proceedings Electron Microscopy Society of America, 1977, Boston, MA, G. W. Bailey, Ed., Claitor's Publishing Division, Baton Rouge, LA, (1977), p. 114, LBL-6204.

12. R. Gronsky and G. Thomas, Lattice Imaging of Grain Boundary Precipitation Reactions, 35th Annual Proceedings Electron Microscopy Society of America, Boston, MA, G. W. Bailey, Ed., Claitor's Publishing Division, Baton Rouge, LA, (1977), p. 116, LBL-6207.

13. D. Clarke and R. H. Geiss, Combined Analytical and High Resolution Microscopy: A Case Study, 35th Annual Proceedings Electron Microscopy Society of America, Boston, MA, G. W. Bailey, Ed., Claitor's Publishing Division, Baton Rouge, LA, (1977), p. 146, LBL-6209.

14. R. Gronsky and G. Thomas, Direct Observations of Plane Matching by Lattice Imaging Electron Microscopy, Scripta Met. 11, 791 (1977), LBL-6602.

15. U. Dahmen, Beam Enhanced Oxidation of Fe-20%Al in a Transmission Electron Microscopy, 35th Annual Proceedings, Electron Microscopy Society of America, Boston, MA, G. W. Bailey, Ed., Claitor's Publishing Division, Baton Rouge, LA, (1977), p.186.

LBL Reports

a. Microstructure Properties and Alloy Design

1. C. K. Wu and G. Thomas, Microstructure and Properties of a Cu-Ni-Cr Spinodal Alloy", Met. Trans. (in press), LBL-6029.

2. R. Sinclair and G. Thomas, Determination of Local Composition by Lattice Imaging, Met. Trans. (in press), LBL-6050.

3. M. Okada, G. Thomas, M. Homma, H. Kaneko, Microstructure and Magnetic Properties of Fe-Cr-Co Alloys, Proceedings of the International Magnetics Conference, June 1977, Los Angeles, Magnetics Society of I.E.E.E. (in press), LBL-6089.

4. G. Thomas and B. V. N. Rao, Morphology, Crystallography and Formation of Dislocated (Lath) Martensites in Steels, Kiev Conference on Martensite, May 1977, Kiev, USSR, (in press), LBL-6242.

5. D. R. Clarke, Cooperative Growth in the Unidirectionally Solidified Copper-Chromium Eutectic, Scripta Met. (in press), LBL-6252.

6. B. V. N. Rao and G. Thomas, Discussion on "Toughness Variations During the Tempering of a Plain Carbon Martensitic Steel", by J. E. King, R. F. Smith and J. F. Knott, Proc. 4th International Conference on Fracture, June 1977, Waterloo, Canada, International Journal of Fracture, (in press), LBL-6295.

7. R. Sinclair and G. Thomas, Structure of Ordered Alloys, International Symposium on Order and Disorder in Solids, Paris, France, July 1977, (in press), LBL-6654.

8. M. Okada, G. Thomas, M. Homma, H. Kaneko and Y. Belli, Microstructure and Magnetic Properties of Fe-Cr-Co-V Alloys, 23rd Conference on Magnetism and Magnetic Materials Proceedings, Minneapolis, MN, 1977, (in press), LBL-6931.

b. Ceramic Alloys

1. D. R. Clarke, The Morphology of the Transformation Interface in Reaction Sintered Silicon Carbide, J. American Ceramic Society (in press), LBL-4167.

2. R. K. Mishra, O. Van der Biest and G. Thomas, Material Loss and High Temperature Phase Transition in Lithium Ferrite, J. American Ceramic Society (in press), LBL-5146.

3. D. R. Clarke and G. Thomas, Grain Boundary Phases in a Hot-Press 5wt%MgO Silicon Fluxed Nitride, J. American Ceramic Society, (in press), LBL-6004.

4. R. K. Mishra and G. Thomas, Surface Energy of Spinel, J. Appl. Phys. (in press), LBL-6030.

5. D. R. Clarke, T. M. Shaw, D. P. Thompson, Direct Observation of the Polytype Periodicities in Be-Si-O-N System, J. Materials Science (in press), LBL-6054.

6. R. K. Mishra and G. Thomas, Microstructure and Magneto-Acoustic Oscillations of (Cu, Co) Nickel Ferrite, Proc. 1977 International Magnetics Conference, June, Los Angeles, Magnetics Society of IEEE (in press), LBL-6095.

7. D. R. Clarke and G. Thomas, Microstructure of Y_2O_3 Hot Pressed Silicon Nitride, J. American Ceramic Society (in press), LBL-6272.

8. D. R. Clarke, The Microstructural Location of the Intergranular Metal Oxide Phase in a Zinc Oxide Varistor, J. Appl. Phys. (in press), LBL-6904.

9. D. R. Clarke and G. Thomas, The Structure of Grain Boundaries in Silicon Nitride Based Alloys, Proc. 14th University Conference on Proceesing of Crystalline Ceramics, North Carolina State University, Raleigh, N.C., November 1977 (in press), LBL-6985.

c. High Resolution, High Voltage Electron Microscopy

1. D. G. Howitt and G. Thomas, Electron Damage in Organic Crystals, J. Rad. Effect (in press), LBL-5426.

2. C. K. Wu, R. Sinclair, G. Thomas, Lattice Imaging of Optical Microanalysis of CuNiCr Spinodal Alloy, Met. Trans. (in press), LBL-6067.

3. S. Bose, U. Dahmen, R. H. Bragg, and G. Thomas, Lattice Image of "LMSC" Glassy Carbon, J. of American Ceramics Society (in press), LBL-6227.

4. G. Thomas, High Voltage Electron Microscopy in Ceramics Research, 5th International Conference on High VOltage Electron Microscopy Proceedings, Kyoto, Japan, August 1977, (in press), LBL-6688.

Theses

1. C. K. Wu, Lattice Imaging and Mechanical Property Studies of a Cu-Ni-Cr Spinodally Decomposed Alloy, (M.S. thesis), LBL-5729.

2. G. Goeser, Tensile Properties and Deformation Induced Transformations in Metastable Austenitic Single Crystals, (M.S. thesis), LBL-5749.

3. R. K. Mishra, Defects, Phase Transformation and Magnetic Properties of Lithium Ferrite, (Ph.D. thesis), LBL-5759.

4. R. Gronsky, Analysis of Grain Boundary Reactions in Aluminum Zinc Alloys Utilizing Lattice Imaging Electron Microscopy, (Ph.D. thesis), LBL-5784.

5. K. Kubarych, The Effect of Treatments on the Mechanical Properties of Cu-Ni-Fe Spinodal Alloys, (M.S. thesis), LBL-5791.

6. F. Dizon, Electron Microscopy Studies of Defects in Boron-Sintered Cubic Silicon Carbide (M.S. thesis), LBL-6269.

7. M. Young, Heat Treatment and Characterization of Duplex 1010 and 1020 Steels, (M.S. thesis),LBL-6620.

8. J. Y. Koo, Design of Duplex Low Carbon Steels for Improved Strength: Weight Applications, (Ph.D. thesis), LBL-6657.

9. T. Shaw, Electron Microscopy Study of Crystallography and Phase Relationships in the Be_3N_2-$BeSiN_2$ System, (M.S. thesis), LBL-6930.

d. High Voltage Electron Microscopy

K. H. Westmacott, Principal Investigator

1. INTRODUCTION

K. H. Westmacott

The advantages afforded by High Voltage Electron Microscopy, especially radiation damage simulation, are being exploited in current research programs. The underlying theme of the research is to understand the behavior of interfaces in an irradiation environment. Past research has provided a great deal of basic information on radiation effects in pure metals. Now similar research on multiphase materials and nonmetallic systems is urgently required to provide the basic background for advanced energy systems designs.

a. Progress Report on New 1.5 MeV High Voltage Electron Microscope Project

During 1977 the future course for High Voltage Electron Microscopy at LBL was set. Negotiations for the new 1.5 MeV HVEM were concluded with the award of a contract to Kratos Inc./AEI Scientific Instruments. The salient features of the new instrument are: 1) a high stability, high voltage Haefley generator and accelerator, 2) facilities for both top and side entry stage operation, and 3) a resolution capability of 3.5 Å point to point with full specimen tilting. Delivery of the instrument is scheduled for summer, 1979.

An ideal location for the new microscope has been found at Building 72 adjacent to MMRD. This is the best available site at LBL since it combines a low magnetic background with quiet ground vibration conditions. Planning for modifying the existing building to provide the microscope laboratory and support facilities and office space is well advanced.

b. Precipitate Behavior in Electron-Irradiated Aluminum-Silicon

Most materials used in nuclear reactor applications are used in conditions where two or more alloy phases are present, and while a great deal is known about the behavior of single phase metals under irradiation, far less is known about precipitate behavior. As part of a program to study changes in precipitate structure during irradiation, binary Al-base alloys are being examined during in-situ irradiation in the HVEM.

Al-Si is a simple eutectic alloy system with a maximum silicon solid solubility of approximately 1.6%Si at the eutectic temperature. When alloys are quenched from the single phase region to room temperature and subsequently aged in the range 150 to 250°C, particles, which have been identified as pure silicon, precipitate from solution. These particles possess a variety of morphologies ranging from platelets on {111} planes to laths and needles that lie along ⟨110⟩ directions. During in-situ irradiation of alloys with compositions in the range 0.5 - 1.0%Si in the HVEM, it became apparent that the strong contrast associated with many of the precipitates arose from the presence of interfacial dislocations around the precipitate periphery. During irradiation the interfacial dislocations absorb point defects and climb away from the precipitate/matrix interface. This behavior is illustrated in Fig. 1. The progressive growth of loops surrounding ⟨110⟩ needles and {111} platelets is seen as a function of irradiation time at a temperature of approximately 150°C. Eventually the loops interact and coalesce with other loops (see Fig. 1d). Identical loop growth rates were measured for loops nucleated in the matrix and for the pre-existing loops around the precipitates. From previous work it was anticipated that the loops were perfect prismatic interstitial loops. This was confirmed by determining the Burgers vector of the loops and performing the standard contrast analysis on the interfacial loops in an as-quenched and aged specimen.

It is surprising that the analysis shows the loops to be interstitial in view of the fact that Si has a larger lattice parameter than Al and precipitation of Si will therefore expand the lattice. Under these circumstances vacancy loops would be expected to form. However, it has been suggested by Beller[1] that precipitation of Si in Al occurs only when accompanied by vacancies in the ratio of one vacancy to four silicon atoms. One way to supply the necessary vacancy concentration is to nucleate an interstitial loop at the precipitate-matrix interface and extract vacancies from the loop by dislocation climb. Thus, the present results support Beller's quasi-stoichiometric model for silicon precipitation. The goal of this research is to introduce a fine distribution of precipitates with associated vacancy loops that will be regenerated as the loops climb away from the interface by vacancy absorption.

c. The Dependence of Radiation Damage Formation on Surface Condition

High voltage electron microscopes have been used extensively to simulate, with electron irradiation, the conditions that exist in the core of nuclear reactors. The ability to concentrate the electron beam into a small area, and observe directly the nucleation and growth of point-defect clusters has been used to good effect in studies of the radiation damage processes in both simple and practical engineering materials. Since the foil specimens used are of the order of 1μ thick, the potential for specimen contamination or changes in chemistry during heating in the microscope is high, and the question of specimen environment is clearly an important one. Preliminary studies of the effect of changing the condition of the specimen surface has confirmed this point.[2] Aluminum-11% magnesium foils were prepared by electropolishing and allowed to oxidize in air either at room temperature or at 200°C. When these specimens were subsequently irradiated at 150°C in the HVEM, secondary defect structures developed that appeared to be similar to those observed in pure Al and other FCC metals (see Fig. 2). During subsequent growth of the loops, however, it became

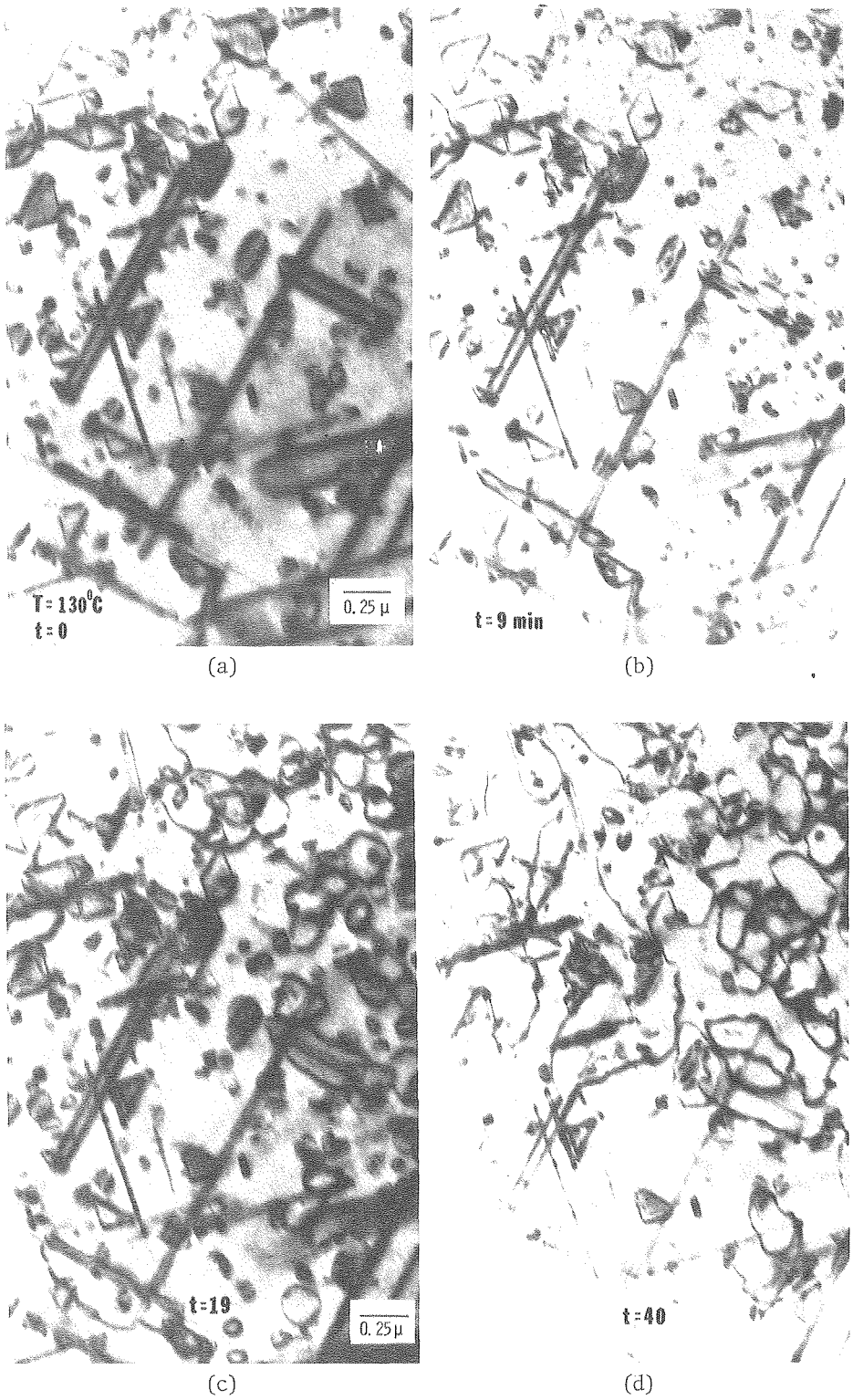

(a) (b) (c) (d)

Fig. 1. Series of micrographs showing the climb of interfacial dislocation loops around precipitate needles and platelets in Al-Si during electron-irradiation at 650 kV in the HVEM. In Fig. 1(d) individual loops have coalesced to form continuous dislocation networks.

[(a)(b) XBB 771-582; (c)(d) XBB 771-583]

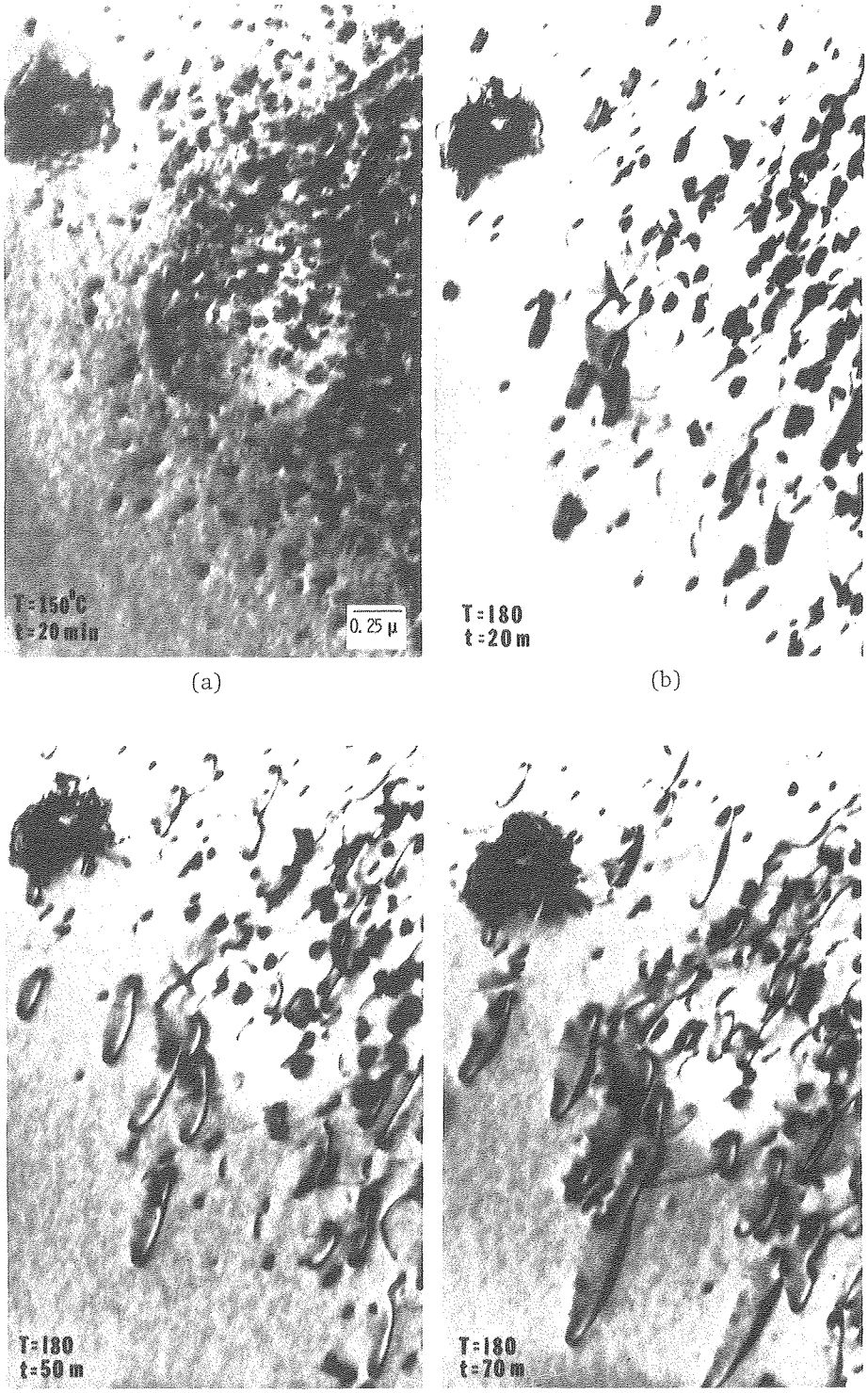

(a) (b)

(c) (d)

Fig. 2. Series of micrographs showing the development of near-surface dislocations in a partially oxidized Al-Mg alloy during in-situ irradiation at 650 kV in the HVEM. The Pilling-Bedworth ratio for MgO is >1 and interstitial loops nucleate in the matrix at the oxide interface to relieve tensile stresses. [(a)(b) XBB 771-577; (c)(d) XBB 771-579]

apparent that the loops had nucleated very close to the foil surfaces since long half loops developed that grew rapidly in a direction parallel to the surface (Fig. 2b-d). The proximity of the loops to the surfaces is suggested by the observed anomolously broad dislocation contrast and was confirmed by stereomicroscopy. Eventually, with continued irradiation and heating, an irregular hexagonal dislocation network developed. The results may be explained in terms of the presence of the oxide films. It is known that surface films of MgO form when Al-Mg alloys are oxidized, and since the lattice parameter of MgO is 3% greater than that of the matrix, the growing films produce tensile stresses in the underlying metal. The preferential formation of interstitial dislocation loops in these regions thus occurs to reduce the stresses.

Several conclusions may be drawn from this preliminary study:

1) the condition of the foil surface can be important in radiation damage experiments, hence environmental control is needed for proper interpretation of experimental results;
2) the formation of near-surface dislocation structure in the presence of an oxide film has interesting implications for void formation in partially oxidized materials;
3) the formation of dislocation loops in a stress field is relevant to the problem of irradiation creep.

Thus, this single example performed without an environmental cell indicates the potential for obtaining greater understanding of interfacial phenomena when closely controlled environmental conditions are maintained in HVEM studies.

---

1. M. Beller, Z. Metallkde 63, 663 (1972).
2. K. H. Westmacott, 35th Ann. Proc. EMSA Boston, Mass., (1977), p. 55.

2. RESEARCH PLANS FOR CALENDAR YEAR 1978

K. H. Westmacott

Studies of structural changes at oxide-metal interfaces during in-situ electron irradiation will be continued. This work may provide new information on the mechanism of the early stages of oxidation as well as the effect of stress fields on dislocation loop and void formation.

A new approach to the solution of the void swelling problem will be investigated using HVEM and heavy-ion simulation techniques. Based on previous work on the important effects of interstitial impurities, the effect of changing the type, concentration and distribution of these impurities will be studied systematically.

A new program to study radiation damage effects in insulators and other nonmetallic systems will be initiated.

3. 1977 PUBLICATIONS AND REPORTS

K. H. Westmacott and Associates

Proceedings

1. K. H. Westmacott and G. Thomas, The Effect of Interstitial Impurities on Vacancy Cluster Formation in FCC Metals, in Proc. U.S.-Japan HVEM Seminar, Honolulu, December 1976, New Applications and Extensions of the Unique Advantages of HVEM for Physical Materials Research, T. Imura and R. Fisher, Eds., Nagoya, Japan, Lab. of Metals, (1977), p. 125, LBL-6039.

2. K. H. Westmacott, Near Surface Formation of Dislocation Loops in Electron-Irradiated Al-Mg, in 35th Annual Proceedings Electron Microscopy Society of America, Boston, MA, 1977, G. W. Bailey, Ed., Claitor's Publishing Division, Baton Rouge, LA, (1977), p. 50, LBL-6203.

Presentations

1. K. H. Westmacott, Recent Electron Irradiation Damage Studies in the Berkeley-High Voltage Electron Microscope, 8th Western Regional Meeting of Electron Microscopists, San Francisco, CA, February 10-12, 1977.

2. K. H. Westmacott, High Resolution and High Voltage Electron Microscopy at the University of California, Berkeley, International Conference on "Metal Science-The Emerging Frontiers," Varanasi, India, November 23-26, 1977.

3. K. H. Westmacott, Interstitial Impurity Effects in Radiation Damage Formation, Bhabha Atomic Research Center, Trombay, India, November 10, 1977.

4. K. H. Westmacott, Neutron Irradiation Damage Simulation Techniques, Indian Institute of Technology, Kanpur, India, November 19, 1977.

e. Powder Metallurgy

Milton R. Pickus, Principal Investigator

1. LIQUID PHASE SINTERING OF IRON POWDER PREMIXED WITH A COPPER-BASE INTERMETALLIC COMPOUND

Meng-Hsiu Chen, John Ling-Fai Wang and Milton R. Pickus

Last year, we reported the development of a low melting (M.P. = 780°C) copper alloy containing manganese and silicon, and its use as infiltrant for sintered iron. X-ray diffraction studies have shown that this alloy is an intermetallic compound with a crystal structure similar to that of Cu_3Si. It has been found that the compound is so brittle that it can be easily reduced to a fine powder. This offers the significant advantage that it can be used as an additive to be blended with iron powder and thus provide a liquid phase during sintering. During the past year, we have carried out studies on iron alloys prepared from such powder blends.

It was found that during heating to the sintering temperature, this compound melts and wets the iron particles so readily that it spreads rapidly over the surfaces, not only of nearest neighbors, but of all the iron particles. This effectively reduces the diffusion distance to the order of one particle radius. During homogenization both silicon and manganese preferentially diffused into the iron particles and left behind a ductile copper alloy to serve as a binder. The alloying with both silicon and manganese greatly increased the hardness of the iron particles, as shown in Table 1.

Table 1. Microhardness before and after sintering.

Material	Hardness (VH - 50 Gram Load)	
	Original	Sintered 1/2 hour, 1175°C
Cu-Mn-Si	678	106
Iron	~64	465

We compared the effect of the addition to unalloyed iron powder of pure copper with that of the Cu-Mn-Si intermetallic compound on the sintered density, tensile strength and transverse rupture strength. The results are shown in Fig. 1. We made similar studies on the effect of additions of the Cu-Mn-Si alloy to both unalloyed iron powder and a prealloyed iron-copper powder. These results are shown in Fig. 2.

This study clearly indicates that additions of the Cu-Mn-Si compound have a strongly beneficial effect, compared with additions of elemental copper, on the mechanical properties of sintered ferrous products. Moreover, the improvement is

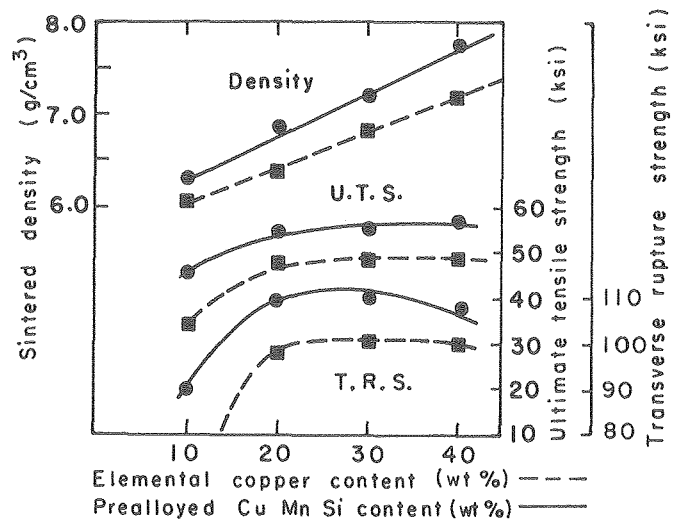

Fig. 1. Influence of elemental copper and Cu-Mn-Si additions on sintered iron compacts.
(XBL 7612-4500)

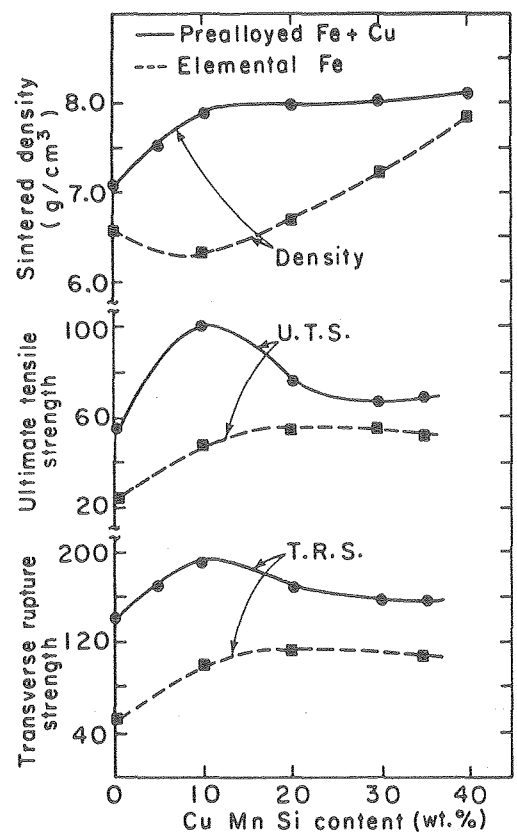

Fig. 2. Influence of Cu-Mn-Si additions on sintered iron and prealloyed iron-copper compacts.
(XBL 7612-4497)

even more dramatic, if iron powder prealloyed with copper is used as a base. In the latter case, densities over 98% of theoretical, and tensile strengths of 100 ksi are readily achieved by simply pressing and sintering.

2. INVESTIGATION OF WEAR RESISTANT MATERIALS BASED ON INTERMETALLIC COMPOUNDS OF NICKEL-TITANIUM-SILICON DISPERSED IN METAL MATRICES

Charles Steinmetz, John Ling-Fai Wang and Milton R. Pickus

Wear is a common mode of material failure, involving complex interactive material mechanisms for which it is difficult to develop analytical models. The study of wear was initially restricted to minimizing friction by lubricants and solving the problems on a case by case basis.

The impetus for further studies in wear control comes from the need for greater conservation in energy and materials, and the need for materials that will withstand the extreme operating conditions of new energy systems. These new energy systems, such as coal liquefaction, require materials to function at high temperatures in corrosive and erosive environments. Materials such as cemented carbides, dispersed oxides, stellites and super-alloys have been tried and tend to wear excessively under these conditions.

The principal objective of this work is to develop a basic materials concept that is adaptable to a wide range of service requirements. After considering many possibilities, the ternary Ni-Ti-Si system was selected as highly promising to provide hard phases with desirable properties to be dispersed in appropriate metallic matrices. This alloy system contains several ternary intermetallic compounds, including the G', V, E, F and G phases, all of which will be investigated and evaluated. The first compound studied was the G' Laves phase with a composition corresponding to Ni_3Ti_2Si. This compound seemed atrractive because preliminary work indicated:

1) it is a hard phase - 1000 vickers hardness;
2) the component elements impart good corrosion resistance;
3) it has good high temperature stability;
4) it interacts with selected matrices to form a broad diffusion layer, thus providing good metallurgical bonding.

The initial composites consisted of G' particles dispersed in an iron matrix. Although the sintering conditions have not yet been optimized, as indicated by the presence of residual porosity, composites based on this concept were tested for wear resistance in comparison with iron and one of the newest and best of the commercial materials designed for similar applications.

The three materials were tested under the same conditions using the pin-on disk friction and wear test machine designed and constructed at MMRD (Fig. 1). The weight loss rate due to wear for each of the three materials is shown in Fig. 2.

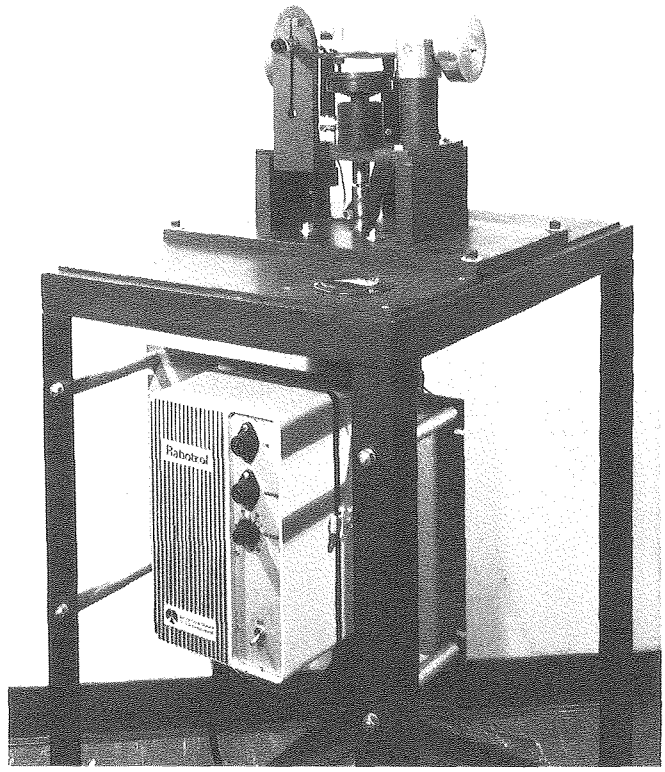

Fig. 1. Front view of pin-on-disk friction and wear test machine. (XBB 779-8894)

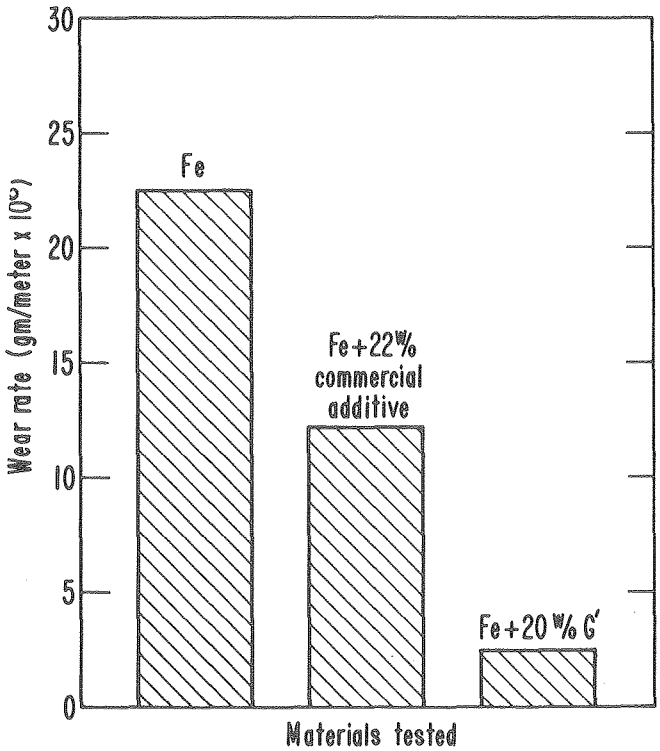

Fig. 2. Comparison of wear rates of sintered iron, iron plus a new commercially available additive, and iron plus G' phase. (XBL 7711-11050)

The superiority of the material based on the Ni-Ti-Si G' phase is evident. Further improvements are anticipated when the sintering conditions are optimized.

3. THE EFFECT OF MAGNETICALLY ALIGNED POWDER ON THE MAGNETOSTRICTION OF SINTERED RARE EARTH-IRON LAVES PHASE COMPOUNDS

Manoochehr Malekzadeh and Milton R. Pickus

Recently, a number of studies have been carried out on the magnetic properties of rare earth-iron Laves phase intermetallic compounds. Of particular interest are the high room temperature magnetostrains of these compounds which make them promising for a variety of technologically important energy conversion applications. Since these materials are brittle intermetallic compounds, they do not lend themselves to conventional fabrication processes such as machining or casting. A powder approach has been developed in this laboratory which makes it possible to obtain these Laves compounds in suitable sizes and shapes. Their magnetostrictive properties were reported last year.

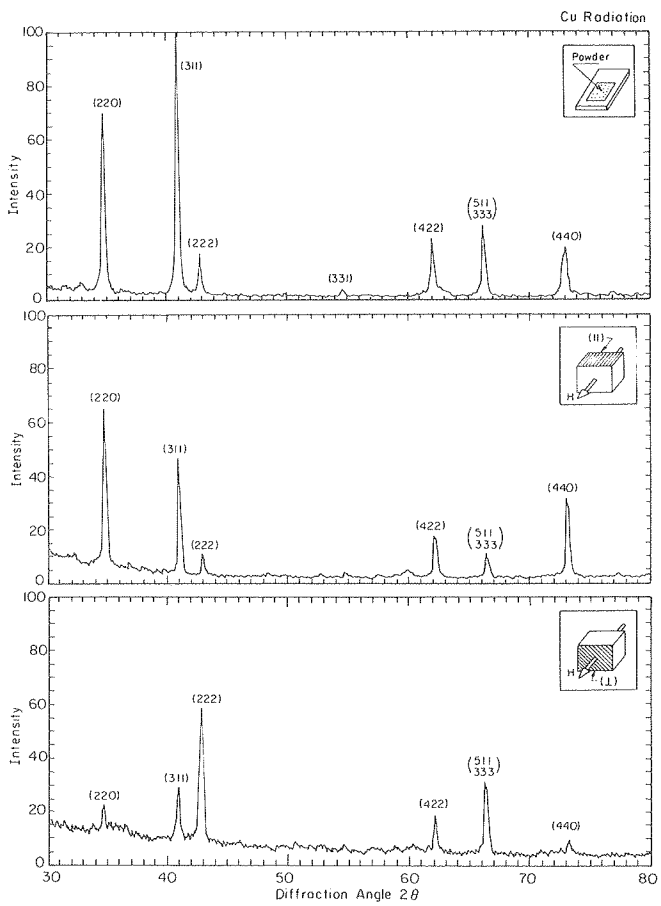

Fig. 1. X-ray diffraction patterns for an almost randomly oriented powder and a magnetically aligned specimen of $Tb_{0.3}Dy_{0.7}Fe_2$ compound. The two lower traces show the effect of alignment on the intensities of reflections from (220) and (222) planes on specimen surfaces parallel and perpendicular to the direction of the applied field. (XBL 799-6122A)

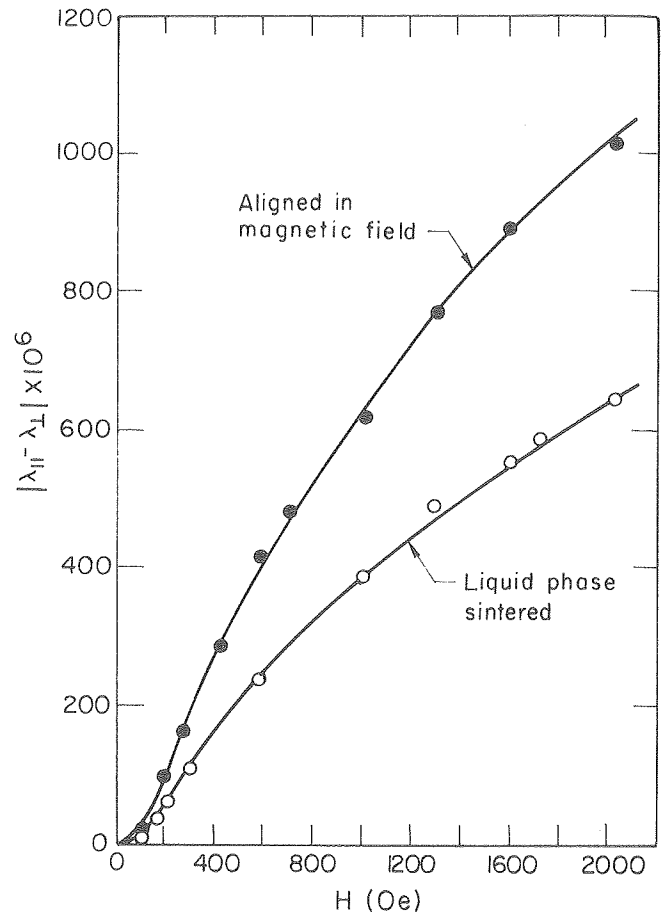

Fig. 2. Room temperature magnetostriction of an aligned and a liquid phase sintered speciment of $Tb_{0.3}Dy_{0.7}Fe_2$. (XBL 799-6101)

In the present study, it is shown that the magnetostrictive properties of these materials--already far superior to other known materials--can be enhanced significantly further by magnetically aligning the powder particles prior to sintering. For this work, the pseudobinary system ($Tb_xDy_{1-x}Fe_2$) with x close to 0.3 was selected because this composition is particularly well suited for a wide range of device applications, since a relatively large magnetostriction is associated with minimal magnetic anisotropy. From spin orientation diagrams, it is known that at room temperature this compound has an axis of easy magnetization along the major cubic symmetry [111] direction. Our powder metallurgical approach can utilize this direction of easy magnetization by aligning the powdered compound in a magnetic field.

A high degree of alignment was achieved when an alternating field of approximately 1000 Oe peak-to-peak at frequencies up to 500 Hz was superimposed on a DC field up to 20 KOe. Figure 1 shows the x-ray diffraction patterns of randomly and magnetically oriented $Tb_{0.3}Dy_{0.7}Fe_2$ compound. The magnetostrains observed (Fig. 2) indicate that the magnetically oriented samples, though as presently prepared contain ~ 20% porosity, are far superior to unaligned high density (< 5% porosity) liquid phase sintered samples, both in regard to the magnitude of the

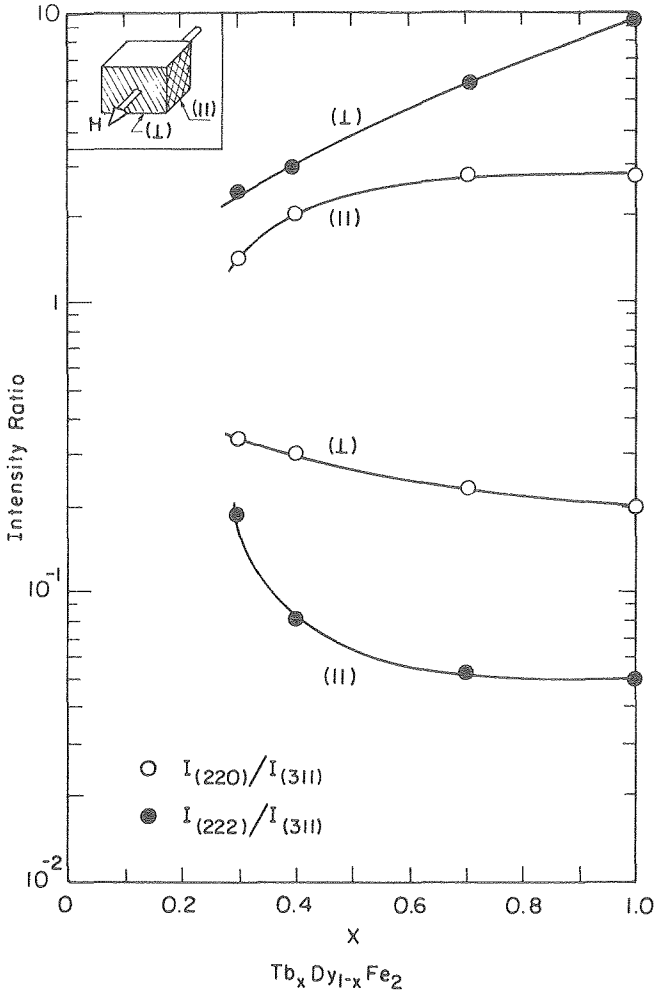

Fig. 3. Change of x-ray reflection intensity ratios, (220)/(311) and (222)/(311), vs. the concentrations of Tb and Dy in magnetically aligned specimens. The ratios are taken on the surfaces of the samples parallel and perpendicular to the direction of the aligning field. (XBL 7710-6203)

strains and the rate of approach to saturation. It has also been found that the degree of alignment improves as the Tb/Dy ratio is increased (due to an increase in magnetic anisotropy) as shown in Fig. 3. Work under way to eliminate the porosity is expected to result in even larger magnetostrains.

4. RESEARCH PLANS FOR CALENDAR YEAR 1978

Milton R. Pickus

New energy systems, such as coal liquefaction, require materials to function at high temperatures, and in corrosive and erosive environments. Materials such as cemented carbides, dispersed oxides, stellites and superalloys have been found to wear excessively under erosive conditions. To address these problems, we have developed a basic materials concept that is adaptable to a wide range of service requirements. The concept is based on the use of the ternary nickel-titanium-silicon system that contains several intermetallic compounds, including the G', V, E, F, and G phases, all of which we plan to investigate and evaluate. In contrast to the presently used materials based on dispersed oxides and carbides, which form limited metallurgical bonds with the matrix, the intermetallic compounds mentioned tend to form wide diffusion bands with the matrix, and thus provide strong bonding, thereby preventing premature failures by pull-outs of the dispersed particles. Moreover, these relatively hard compounds are composed of elements that impart good corrosion resistance and high temperature stability. Preliminary work during the past year on composites composed of the G' phase dispersed in an iron matrix confirms our expectations. Our plans are to optimize the sintering conditions, develop appropriate matrices, and select by a program of testing the best of these ternary intermetallics. In developing matrices, we will investigate the potential of our newly discovered copper-manganese-silicon intermetallic compound. This compound not only makes possible the achievement of full density in sintered ferrous materials by providing a liquid phase at sintering temperatures, but by preferential diffusion both strengthens and improves the corrosion resistance of the iron matrix. We will also investigate the use and potential of non-ferrous matrices, particularly those based on nickel and cobalt. From the standpoint of materials design for low friction and high wear resistance, this is the most basic, comprehensive and versatile program we known of. As we develop materials that appear promising on the basis of our limited wear test facilities, we plan to interface with Alan Levy and his group who are involved in basic studies of erosion mechanisms. In regard to our work on the powder metallurgy of magnetostrictive materials, useful for energy conversion applications, such as early detection of flaws in nuclear reactor systems, we have achieved a position of dominance in this area and we have some interesting ideas for further research we hope to pursue. Also, we will be working in two additional areas to the extent circumstances permit. We have started a program based on polymer coating of niobium particles, which imparts to the niobium powder the fabricating characteristics of a thermoplastic material. This paves the way for converting our infiltration process from a batch process to a continuous process. We are also working on a new approach to the powder metallurgy of iron-carbon alloys. We have already obtained encouraging results in both of these areas.

5. 1977 PUBLICATIONS AND REPORTS

Milton R. Pickus and Associates

LBL Reports

1. Meng-Hsiu Chen, Liquid Phase Sintering of Fe with Cu Base Alloy Powders, (M.E. thesis), LBL-5770, December 1976.

2. Charles R. Steinmetz, Investigation of Wear Resistant Material Using Dispersed Phase Intermetallic Compound of Nickel-Titanium-Silicon in an Iron Matrix, (M.S. thesis), LBL-6983, December 1977.

2. MECHANICAL PROPERTIES

a. Theoretical Problems in Alloy Design

J. W. Morris, Jr., Principal Investigator

Introduction. The research reported here is a multifaceted program of research in physical metallurgy that includes theoretical studies in phase transformations and mechanical properties, basic experimental studies in plastic deformation and in the influence of microstructure, particularly microstructural transformations, on mechanical properties, and applied research in the development of new alloys for advanced energy needs.

Insofar as our research for the Basic Energy Sciences Division of DOE is concerned the research reported below reflects three new areas of interest in addition to a continuation of research activities that have already proven productive. First, we have begun work on the theoretical treatment of elastic effects in solid state phase transformations, including studies of martensite transformation and of precipitation reactions. This subject is one of the major frontiers in the theory of metallurgical phase transformations. Second, we have begun specific research on the influence of strain-induced phase transformations on mechanical properties. This interest is motivated largely by an accumulating body of evidence showing that strain induced transformations at low temperature in austenitic structural steels have effects on strength and toughness that are large enough to affect design decisions but are inconsistent in both magnitude and direction. At the same time there is increasing scientific interest in the mechanism of strain-induced martensitic transformations and in the nature of their mechanical effects. Third, we have begun research in the welding of ferritic cryogenic steels. This new activity was specifically motivated by the recognized engineering need for new welding materials for cryogenic steels. It also addresses what we believe to be a major scientific need for new understanding of welding and joining processes.

Research projects continued from previous years include atomistic studies of precipitation and coarsening in simple systems, the simulation and characterization of polygranular microstructures, plastic deformation, and the design of new alloy steels for cryogenic structures.

1. THEORY OF PHASE TRANSFORMATIONS

a. The Martensite Transformation

S. Chen and A. G. Khachaturyan

Despite major engineering interest and an extensive body of research over several decades, the martensite transformation remains poorly understood. Previous work has, however, shown that it is possible to predict the shape, habit, and crystallographic orientation of individual martensite particles in several systems by treating the martensite particle as a elastic inclusion in the parent matrix and choosing shape, habit and orientation so as to minimize its elastic energy. In the present project the elastic treatment is extended to construct a model of martensite growth in a simple two-dimensional system. The model permits a study of the martensite shape and habit, the autocatalytic process leading to the formation of secondary plates, the criteria establishing a preference for twinned or untwinned plates, and the saturation of the transformation.

In the model an elementary martensite particle is treated as an elastic dipole at a point in a two-dimensional periodic lattice. The particle may grow by inducing like dipoles at adjacent sites, twin by inducing twinning dipoles at adjacent sites, or catalyze an independent transformation by inducing a dipole at a separated point within the lattice. The choice of events is made by computing the consequences for the free energy (chemical plus elastic) of the lattice and requiring that this energy decrease. Quasi-static (or high temperature) transformation is simulated by choosing the most favorable event and recomputing the elastic field for each step of the transformation. Burst (or low temperature) transformation is simulated by permitting a number of favorable events to occur before the elastic field is adjusted for the presence of the new particles. Saturation of the transformation is introduced by assuming a net barrier; a minimum energy decrease per step needed to maintain the process.

The final result of the transformation is found to be sensitive to the kinetic type of the transformation and to the type and distribution of initial particles. Figure 1 shows an example of twinned martensite obtained through a transformation of the low temperature type.

b. The Shape and Orientation of Precipitate Particles

M. Hong and D. E. Wedge

The influence of a precipitate distribution in a metal is often very sensitive to the shape and orientation of the precipitates. The precipitate morphology is, in turn, strongly affected by its elastic distortion relative to the matrix. A general solution for the energy of a coherent inclusion

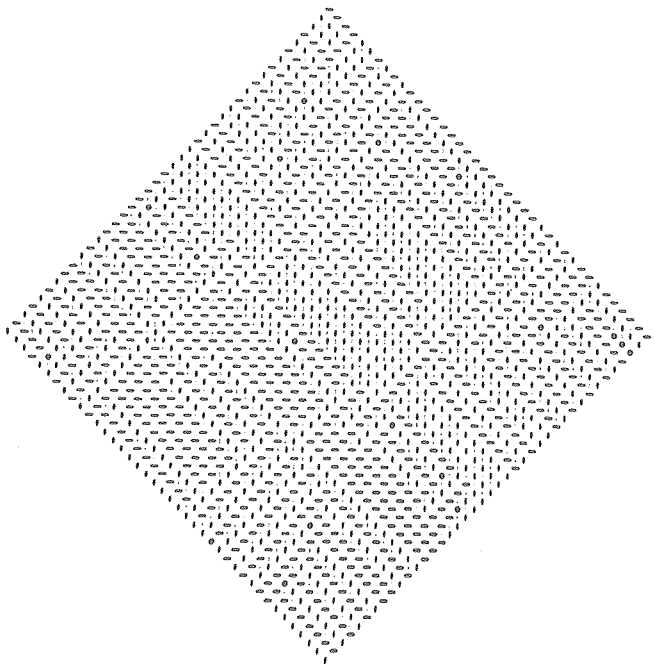

Fig. 1. Twinned martensite. (XBL 7712-10964)

in a matrix of similar elastic constants was obtained some years ago by Khachaturyan. In this project the general solution is specialized to treat precipitation processes of particular metallurgical interest and to permit comparison with experiments.

The elastic energy of an inclusion coherently connected with the matrix and having the same elastic constants may be written:

$$E = 1/2 \iiint \frac{d^3k}{(2\pi)^3} \; B(\vec{n}) \, |\theta(k)|^2 \qquad (1)$$

where $B(\vec{n}) = \lambda_{ij\ell m} \, \varepsilon^{\circ}_{ij} \, \varepsilon^{\circ}_{\ell m} - k_i \sigma^{\circ}_{ij} \, G_{j\ell}(\vec{k}) \, \sigma^{\circ}_{\ell mkm}$, k is the wavevector, $\vec{n} = \vec{k}/|k|$, $\lambda_{ij\ell m}$ is the elasticity tensor, ε°_{ij} is the stress-free-state strain, $\sigma^{\circ}_{ij} = \lambda_{ij\ell m} \, \varepsilon^{\circ}_{\ell m}$, $G_{j\ell}(k)$ is the Fourier transform of the Green's function tensor of the anisotropic elastic problem, $\theta(k)$ is the Fourier component of the inclusion shape function $\tilde{\theta}(r)$ and

$$\theta(r) = \begin{cases} 1 & r \text{ is inside the inclusion} \\ 0 & \text{otherwise} \end{cases}$$

For a GP zone in a matrix of cubic symmetry, $\varepsilon^{\circ}_{ij} = \varepsilon_o \delta_{ij}$ and Eq. (1) can be simplified to:

$$E = \frac{(C_{11}+2C_{12})}{2} \; \varepsilon_o^2 V \left[3 - \frac{C_{11}+C_{12}}{C_{11}} \cdot \frac{1+2\Delta(n_1^2 n_2^2 + n_2^2 n_3^2 + n_3^2 n_1^2)}{1+(1+\frac{C_{12}}{C_{11}})\Delta(n_1^2 n_2^2 + n_2^2 n_3^2 + n_3^2 n_1^2)} + \frac{3\Delta^2 n_1^2 n_2^2 n_3^2}{(1+\frac{2C_{12}}{C_{11}} + \frac{C_{44}}{C_{11}}) 3\Delta^2 n_1^2 n_2^2 n_3^2} \right] \qquad (2)$$

where v is the volume of the inclusion, ε_o = ap-am/am, ap, am are lattice parameters of the precipitate and matrix in the stress-free state, and $\Delta = C_{11} - 2C_{12} - C_{44}/C_{44}$ is the elastic anisotropy parameter. For $\Delta < 0$, the function determined by Eq. (2) takes a minimum value when n is parallel to <100> while for $\Delta > 0$ the function is minimum when n is parallel to <111> .

The method can be applied to the clustering of carbon atoms in an iron-carbon martensite. Those carbon atom clusters have been observed to be thin disks uniformly distributed in supersaturated martensites quenched from the high-temperature austenitic phase. By assuming zero thickness of the disk inclusion, the elastic energy can be written as

$$E = 1/2\lambda_{ij\ell m} \; \varepsilon^{\circ}_{ij} \; \varepsilon^{\circ}_{\ell m} \; V - \frac{(\sigma_1+\sigma_2)^2}{2D(\underset{\sim}{n})} \; V \gamma^2 + An_3^2 + Bn_3^4 + \Delta C n_1^2 n_2^2 n_3^2 + 2\Delta\gamma^2 n_1^2 n_2^2 \qquad (3)$$

where ε°_{ij} is tetragonal, σ_1, σ_2, γ, A, B, C are constants and functions of the elastic constants and ε_{11}, ε_{33}, and

$$D(\underset{\sim}{n}) = C_{11} + \Delta(C_{11}+C_{12}) \; (n_1^2 n_2^2 + n_2^2 n_3^2 + n_3^2 n_1^2) + \Delta^2 \; (C_{11}+2C_{12}+C_{44}) n_1^2 n_2^2 n_3^2 .$$

The orientation of the cluster can be obtained by minimizing the function given by Eq. (3). The calculated result is in good agreement with experimental observations. An improvement of the above calculations has been made to account for the thickness effect of the cluster which gives better agreement with experimental data. An explanation of carbide formation on further tempering is proposed.

The interaction of elastic precipitates is now under study. The results should shed light on the phenomenon of cluster alignment.

c. Spinodal Decomposition and Coarsening

J. W. Morris, Jr. and A. G. Khachaturyan

In spinodal decomposition of a solid solution the solution spontaneously takes on a quasi-periodic modulation in its composition. The early stages of this process were described theoretically by Cahn, who argued that the initial departure from homogeneity in an unstable solution would take the form of sinusoidal compositional fluctuations tending to exhibit a particular dominant wavelength. In the later stages of decomposition it is known experimentally that the initial state will coarsen; the compositional profile becomes somewhat irregular and the dominant wavelength increases with time. This behavior is governed by nonlinear equations which have, to date, defied exact solution. The theory of spinodal decomposition is hence not well developed beyond the initial stages.

To gain insight into the phenomena involved in spinodal coarsening we have been studying a model system consisting of an elastic Ising lattice that undergoes decomposition in one dimension. The governing equations for the evolution of composition in this case, including elastic effects take the form

$$dc_n/dt = F\{c_n, c_{n\pm1}, c_{n\pm2}, \gamma\} \qquad (1)$$

where c_n is the composition of the nth plane along the direction of decomposition and γ is an appropriate combination of elastic constant. These equations can be solved iteratively to follow the development of the composition profile with time.

Initial studies of the behavior of systems governed by this set of equations reveals three types of behavior that have been observed experimentally, but are previously unexplained theoretically.

1) In the early stages of decomposition, systems often show an "inverse" coarsening, in which the dominant wavelength of the composition fluctuation decreases with time. This inverse coarsening is phenomenologically associated with the spread of wave packets that form from an initially random set of fluctuations.

2) After a transient phase the one-dimensional system enters a period of slow coarsening in which

$$\lambda \alpha t^{1/k} \qquad (2)$$

where k is of the order of 10. This coarsening occurs in discrete steps through the disappearance of discrete composition peaks that dissolve in their immediate environment.

3) In the highly asymmetrical case, decomposition of an unstable solution which is very rich in one of its terminal solutions, spinodal decomposition leads to the formation of discrete, sharp precipitate-like particles which resemble GP zones. These form in a continuous fashion from a quasi-periodic, low-amplitude precursor. The initial particle appears in a striking manner from an instability in the precursor wave. It then catalyzes the formation of similar particles in neighboring positions.

Long-term coarsening phenomena are now being studied. A central question concerns whether the value of k in Eq. (2) will decrease to ~ 3, as is experimentally observed, or whether this coarsening behavior necessarily involves two- or three-dimensional coarsening mechanisms. Values of k in this range are observed in the two-dimensional coarsening studies described in the following project.

d. Atomistic Simulation of Precipitation and Coarsening

E. S. Pundarika

Precipitation and coarsening reactions are important metallurgical processes. A thorough understanding of the nature and kinetics of these reactions can only be achieved through theoretical studies at the atomic level. In recent years Monte Carlo simulation models have gained wide acceptance in studying this kind of complex dynamic processes.

We used a computer simulation technique to study the basic processes involved in precipitation and coarsening reactions. In the model, atoms of two types (A and B) are distributed over the available lattice sites and are assumed to interact only with atoms on nearest neighbor sites. Initially we have a random configuration (equilibrium at a very high temperature) and decomposition proceeds after a quench to the reaction temperatures (below the miscibility gap in the phase diagram). By assigning diffusional jump probabilities for the various types of atom exchanges the precipitation and coarsening reactions can be followed with time.

The two important mechanisms of coarsening are: 1) Ostwald ripening or the Lifshitz-Slozov mechanism, where single atoms leave one cluster and join another cluster, which results in the overall growth of big clusters at the expense of small ones, and 2) Binder's mechanism, where atoms that leave a cluster chance to reach the same cluster in some other place, shifting the center of mass of the cluster. This results in the diffusion of clusters which causes collision and coagulation of clusters, leading to coarsening.

Starting from the initial random configuration, four stages can be recognized in the computer simulation of the coarsening reaction. The first stage, a slow initial relaxation stage, leads to the formation of small cluster of about 5 to 15 atoms in size. In the second stage these clusters diffuse and coagulate by Binder's mechanism. In the third stage, which is a transition stage, both Binder's and Lifshitz-Slozov mechanisms gain importance, and finally in the fourth stage the Lifshitz-Slozov mechanism becomes dominant. Figure 2 illustrates two microstructures in a typical coarsening sequence.

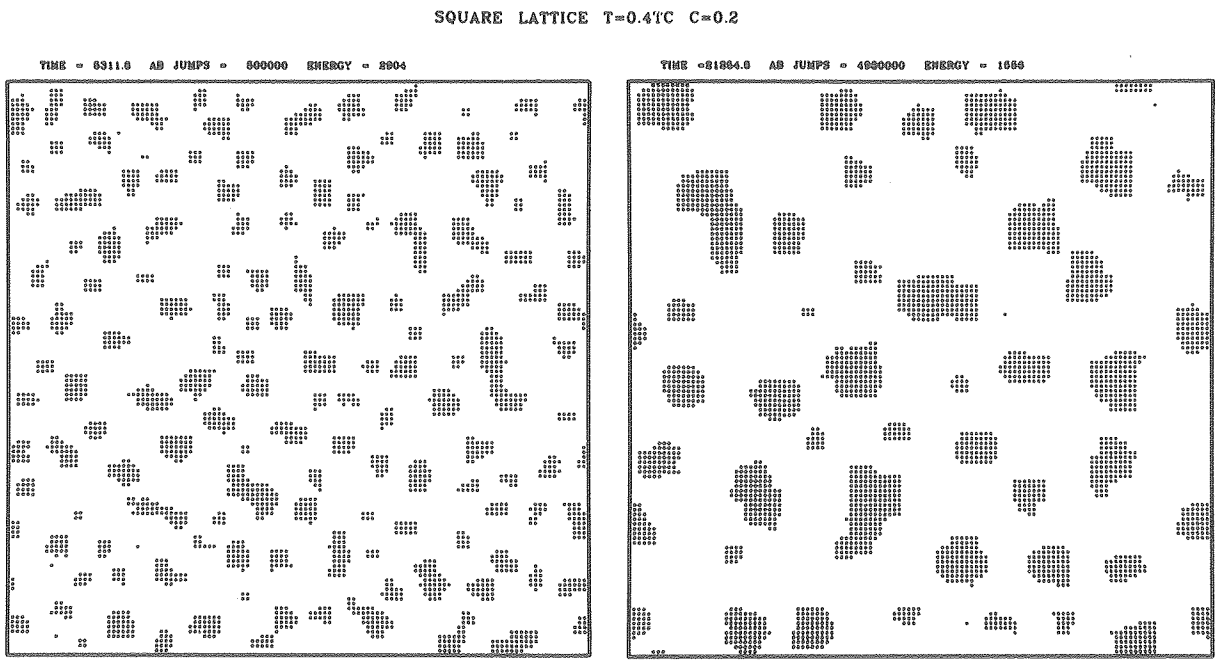

Fig. 2. Microstructures showing the time evolution of a planar lattice with 20% B atoms quenched to a temperature $T = 0.4T_c$. (XBL 7711-10895)

Both mechanisms predict that the energy ε and the average cluster size $\langle \ell \rangle$ vary with time t as $e = t^a$ and $\langle \ell \rangle = t^b$, the values of "a" being 0.2 and 0.33 and of "b" being 0.4 and 0.5 for the Binder's and Lifshitz-Slozov mechanisms, respectively. Thus, following the development of ε and $\langle \ell \rangle$ with time provides a good means of studying the reactions. Figure 3 shows typical $\langle \ell \rangle$ vs. t plots where the slope is seen to gradually increase to the Lifshitz-Slozov value of 0.5. A study at various temperatures indicates that the reaction consists of the four stages at all temperatures, although the relative spans of time for the four stages may change. Comparison of Fig. 3a and b indicates that at lower temperatures the initial relaxation stage is lengthened and the Binder's cluster diffusion stage is shortened. Lower temperatures also yield microstructures with sharply defined surfaces.

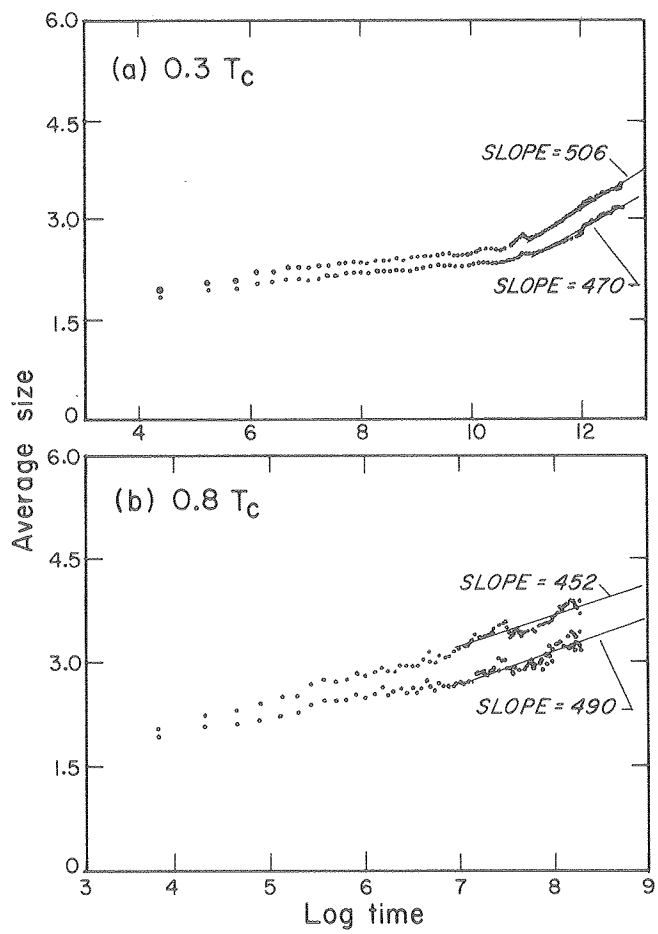

Fig. 3. The evolution of average cluster size $\langle \ell \rangle$ with time for a 14400 atom square lattice with 10% B atoms at (a) $0.3T_c$ and (b) $0.8T_c$. (XBL 7711-10894)

2. Simulation and Characterization of Polygranular Microstructure

a. Three-Dimensional Characterization of the Cellular Microstructure

K. Hanson

A central problem in Physical Metallurgy concerns the manner in which the properties of a material are determined by its history and microstructure. While

average microstructural parameters such as average two-dimensional grain size are easily obtainable and often correlated with observed mechanical properties, it is difficult to parametrize and assess the importance of precise two- and three-dimensional microstructural morphologies. Given the complexity of the microstructures of real materials it is not at all obvious that a useful descriptive parametrization exists.

If we restrict attention to microstructures of the "cellular" type, that is, microstructures obtained through isotropic growth from a distribution of nuclei that form simultaneously, it is possible to construct an efficient code that will completely analyze the microstructure in two and three dimensions. Such a microstructure is completely described by a list of the nucleation sites. Grain corners are points that are equidistant from four adjacent nucleation sites but no closer to any other nucleation site. Grain edges are straight lines that connect corners, and contain points that are equidistant from the three nearest nucleation sites. Grain surfaces are planes equidistant from the two nearest nucleation sites, and are bounded by edges. For the purpose of computer analysis the cellular microstructure is best represented by a graph in which nodes are grain corners and each node is connected to four other nodes by paths representing grain edges. All interesting two- and three-dimensional geometric information can be extracted from this graph.

Although this code is restricted to saturated (i.e., simultaneous) nucleation and isotropic growth, a variety of interesting problems concerning the random and non-random location of nucleation sites can be examined. For example, Fig. 1 is a two-dimensional section of a microstructure created by choosing random nucleation sites. Figure 1b is a two-dimensional section created by nucleating at the corners of a previously randomly nucleated microstructure. Figure 1c is a section of microstructure created by nucleating at the corner sites of microstructure of the type in Fig. 1b, i.e., a double corner transformation of a homogeneously nucleated microstructure. Figure 2a,b, and c show the respective two-dimensional area per cell distributions, while Fig. 3a,b, and c show the respective three-dimensional cell volume distributions. Thus, it can be seen that the microstructures and their distribution functions are strongly dependent on their respective histories that are related to the nature of their originating nucleation sites. In addition to the distribution functions shown in Figs. 2 and 3, angle, edge, surface and various other two- and three-dimensional features are extracted by our computer code. This information will prove useful for determining sensitive parameters relating microstructures to their respective histories.

In the examples shown, nucleation is either homogeneous or occurs at all corner sites of a previous microstructure. Other possible variations include

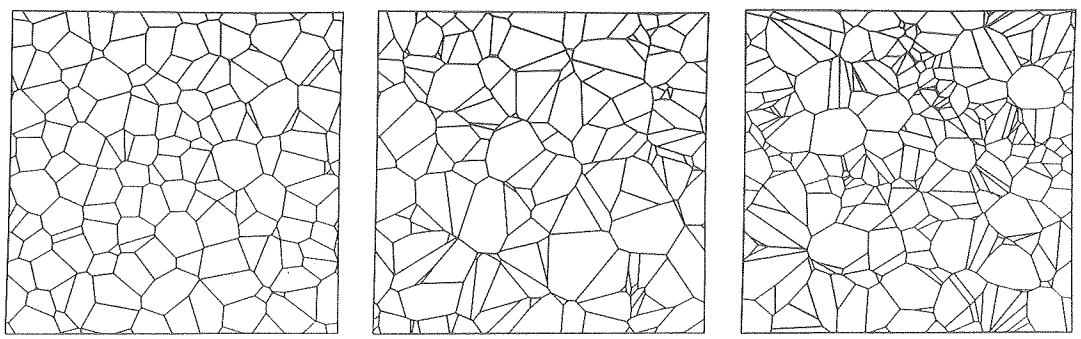

(a) (b) (c)

Fig. 1a,b,c. Microstructures. (XBL 7711-10891)

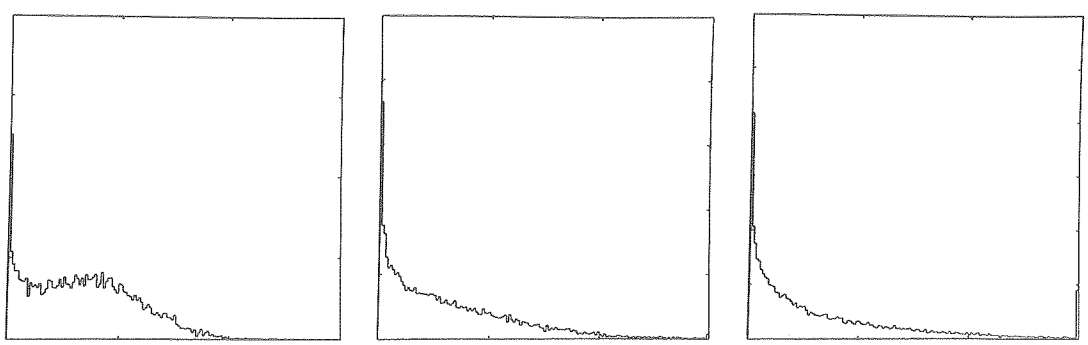

(a) (b) (c)

Fig. 2a,b,c. Area/cell histogram (note last bin contains overflow). (XBL 7711-10891)

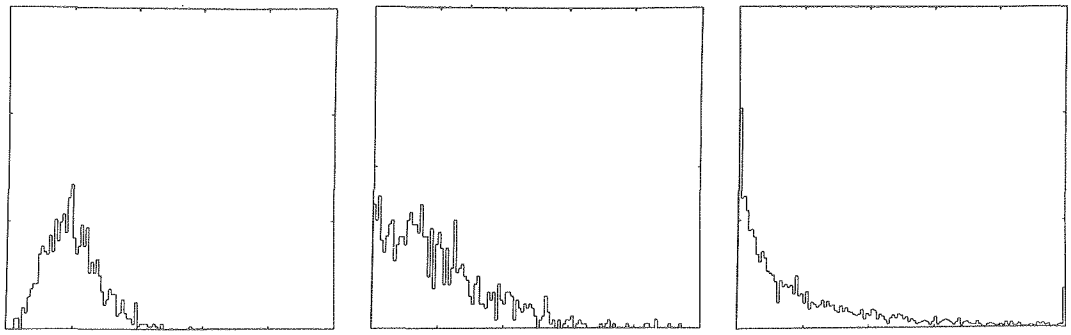

(a) (b) (c)

Fig. 3a,b,c. Vol/cell histogram (note last bin contains overflow). (XBL 7711-10891)

partial nucleation at previous corners of either regular, random or semi-random nucleated microstructures. Also nucleation can be simulated on edges or cell faces in varying densities. It should prove interesting and informative to determine a useful classification system relating microstructures to their histories. A further extension of the code will involve the simulation of various material properties such as diffusion characteristics and mechanical stability.

This computer simulation has the potential for unraveling many of the relationships between the history, material properties, and microstructural features of simple cellular microstructures. Understanding these relationships should provide insight about more complex and realistic microstructures.

b. The Johnson-Mehl Microstructure Generated by a Non-Radial Growth Function

K. Hanson and K. W. Mahin

The previous article describes a versatile computer code for generating microstructures when growth is isotropic and nucleation occurs simultaneously. A separate computer code exists for generating more complex microstructures where nucleation is a function of time and phase, and growth is a function of time, location, direction and phase. The resulting microstructures have curved interfaces that cannot be easily handled by the coding techniques of the previous article. However, we have constructed an alternate code that draws two-dimensional sections of these complex

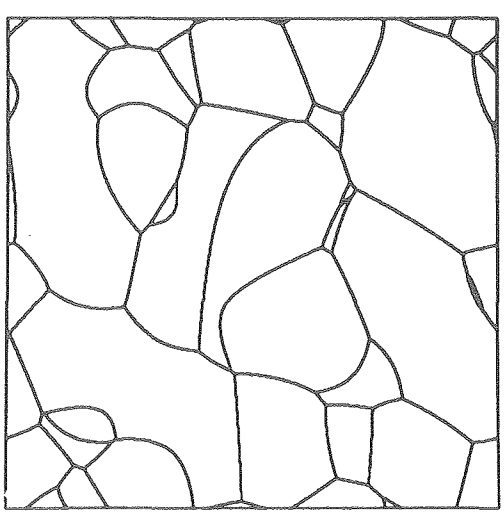

Fig. 4. Microstructure created by prolate spheroidal growth. (XBL 7711-10889)

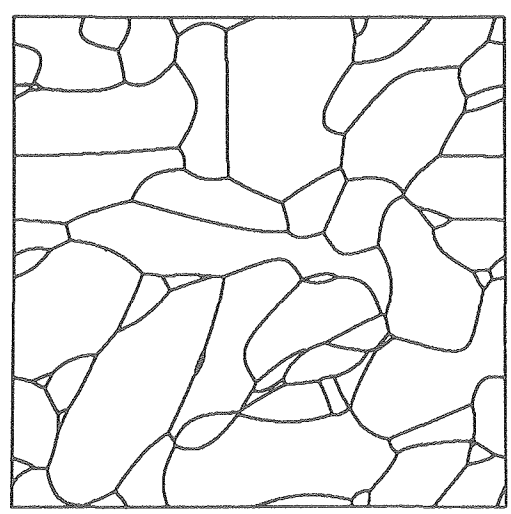

Fig. 5. Microstructure created by oblate spheroidal growth. (XBL 7711-10890)

microstructures on a high resolution grid. The resulting pictures are easily computer analyzed to extract various two-dimensional features (averages and distribution functions). These characteristic features can then be correlated with the microstructures' nucleation and growth parameters.

Figures 4 and 5 are examples of non-radial growth where nucleation occurs simultaneously. Figure 4 was created by growing randomly positioned and oriented prolate spheroids (rod shaped), where the major axis is four times the minor axis. Figure 5 was created by growing randomly positioned and oriented oblate spheroids (plate shaped), where the major axis is three times the minor axis. As anticipated, nonisotropic growth yields many unusual grain shapes.

3. MECHANICAL DEFORMATION

a. A Solution for the Interaction of Dislocations in a Plate with Possible Applications to the Mechanics of Red Blood Cells

F. R. N. Nabarro

My interest has been centered on the mechanical properties of the membrane of the red blood cell, and in particular in the influence of long molecules such as cholesterol, detergents and anaesthetics that may be absorbed in such a way that they extend from the outside of the lipid bilayer to about halfway down the outer of the two layers. Such absorbed molecules will tend to bend the layer. I decided to start with a two-dimensional model in which the absorbed molecules were simulated by edge dislocations with their lines in the mid-plane of an elastic plate, and their Burgers vectors parallel to the plate. The angle of bend is known in this case, but it turned out that the strain field, and consequently the energy of interaction between two such dislocations, was not known. This problem was solved with the collaboration of an undergraduate mathematician, Eric Kostlan. The solution shows some novel mathematical features. The most remarkable physical result is that two such dislocations have a position of stable equilibrium at a separation of about 1·2 plate thickness. It is not known if a similar result applies to peglike molecules. The mathematical problem looks difficult; it would not be surprising if there were indeed an attraction, and stronger than the very weak one found in the two-dimensional model. If it's true that there is a relatively long-range attraction between long molecules absorbed in a lipid layer, it may be possible to explain some quite remarkable observations by the late H. Träuble on the clustering of spin-labeled steroids in lipid layers.

My second problem has been the theory of the crenation of the red blood cell produced by detergents or drugs. The observations are that up to a certain concentration of absorbed molecules nothing happens. Then crenations or spicules form on the surface. Over a very modest range of concentrations these spicules become smaller and more numerous. Up to this point the process may be reversed by removing the foreign chemical. With further increases in concentration a sudden and irreversible change occurs. An essentially mechanical theory has been developed that explains this sequence. The predictions of the theory must, however, be evaluated numerically and compared with observation, a task not rendered easier by apparent contradictions and implausibilities in the experimental evidence.

b. Simulation Studies of Plastic Deformation Through Dislocation Glide*

S. Altintas and K. Hanson

The plastic deformation of a crystal is accomplished usually through the motion of dislocations. The glide of a dislocation is impelled by the applied stress and opposed by microstructural obstacles such as point defects, precipitates and other dislocations.

We consider the planar glide of a dislocation through randomly distributed obstacles. The objective of this work is to calculate the critical resolved shear stress (CRSS) as a function of the strength of the obstacles, and to determine dislocation velocity as a function of temperature, applied stress and strength of the obstacles.

Research progress to date can be summarized under three headings:

1) Dislocation Glide Through Arrays of Unlike Obstacles

In most physically realistic systems the obstacles to dislocation motion are of different type. Their distribution, size and shape are expected to influence the mechanical properties of materials. Even in the simplest case of solution hardening the atoms are arranged above and below the slip plane so as to interact with the moving dislocation differently. Also, in some cases the strengthening mechanisms are superimposed to obtain optimal properties, e.g., solution hardening and precipitation hardening.

Dislocation glide through mixtures of obstacles of different strengths has been studied analytically and by computer simulation. Theoretical considerations have shown that the CRSS is given by the sum of the quadratic mean of the stresses for the individual obstacles, i.e., $\tau^2 = \sum_i x_i \tau_i^2$ where τ_i is a function of the obstacle strength (β_i). This formula applies for a wide range of obstacle strengths (β_i) and fractions (x_i). Figure 1 illustrates the effects of a square spectrum of obstacle strength on the CRSS. We plot the CRSS as a function of the width of the distribution for a given mean strength. Even though the CRSS can be calculated approximately using the average value of the obstacle strength, the deviation is considerable for spectrums of strong and weak obstacles. Computer simulation results of five arrays each containing 1600 obstacles are indicated by data bars in the figure and there is a good agreement with the calculations.

The average segment length and the distribution of forces on the pinned dislocation configuration have been calculated and show good agreement with the simulation data.

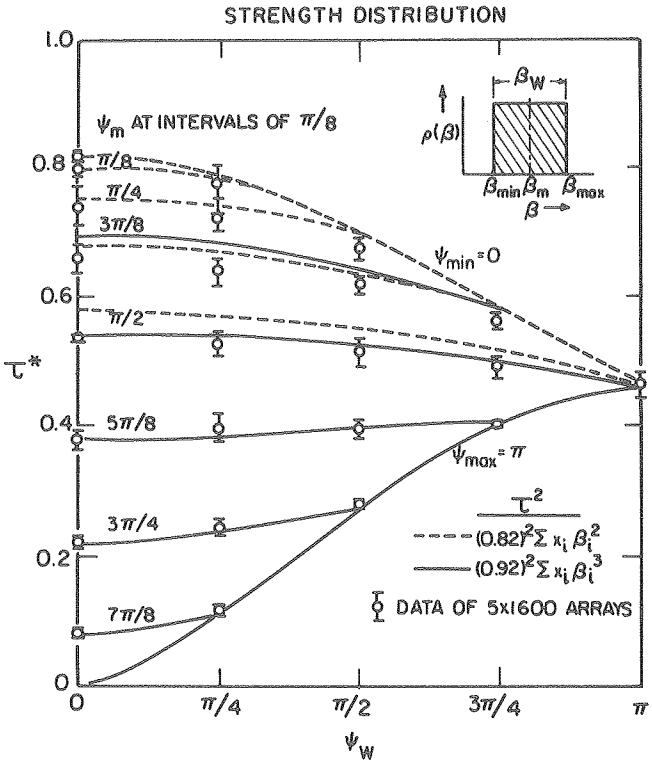

Fig. 1. CRSS as a function of the width of distribution for a square spectrum of obstacle strengths. (XBL 775-5435)

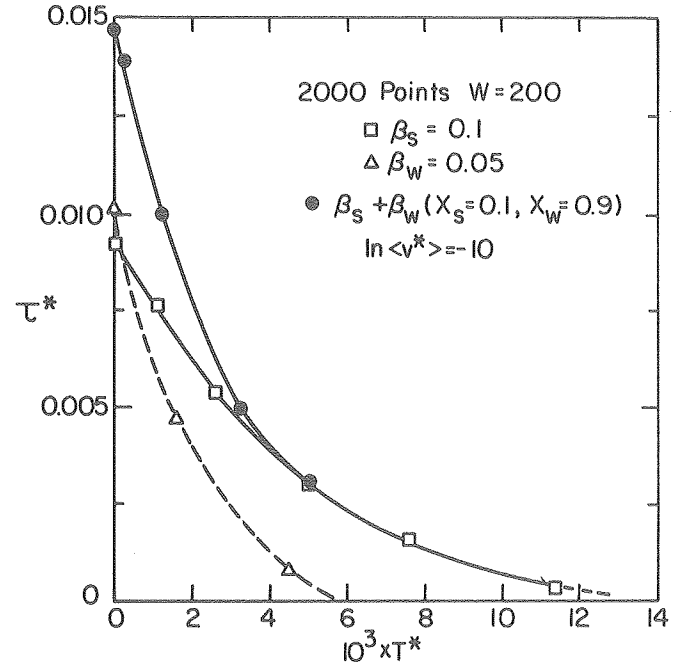

Fig. 2. Stress at a given velocity of glide ($\ln \langle v^* \rangle = -10$) as a function of temperature for arrays containing two kinds of obstacles. (XBL 775-5459)

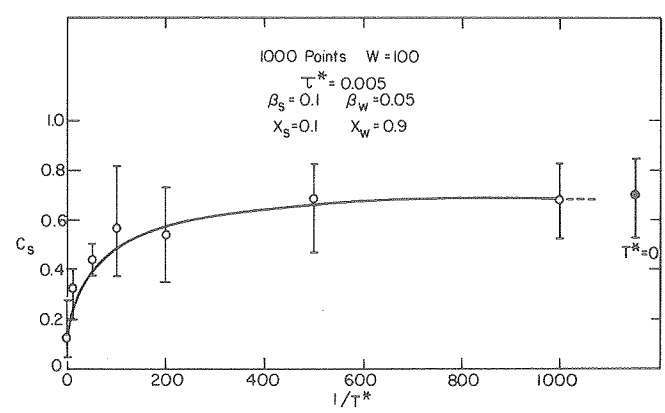

Fig. 3. The fraction of strong obstacles on the dislocation as a function of temperature. (XBL 775-5457)

2) The Effects of Temperature on Dislocation Glide

In crystals containing obstacles whose interaction distance with the dislocation is short compared to their spacing, thermal activation may help to overcome the barriers. Computer simulation and analytic studies indicate that the stress at a given velocity decreases as temperature increases. Figure 2 indicates the effect of temperature on the flow stress for a given velocity for arrays containing two types of obstacles. As is apparent from the figure the contribution of weak obstacles to the stress diminishes at high temperatures. Figure 3 illustrates the effect of temperature on the fraction of strong obstacles on the dislocation. The fraction increases as the temperature decreases, approaching the athermal value.

3) Comparison with Experiment

Even though the results obtained from computer simulation of dislocation motion through point obstacles have been widely used in the literature to explain the strength increase in solution-, irradiation-, and precipitation-hardened materials, very little has been done in direct comparison with experimental data.

Recently, Munjal and Ardell have tried to compare the results obtained from precipitation hardened Ni-Al alloys to computer simulation data and concluded that the experimental data and simulation results obtained by Foreman and Makin were not in complete agreement. However, further considerations regarding more realistic distribution of obstacle strengths brought the agreement closer.

Another study that is of direct interest to computer simulation of plastic deformation is done by Appel et al. The distribution of segment lengths obtained from HVEM in situ deformation of doped MgO single crystal is compared with the computer simulation data in Fig. 4. As shown in the figure the agreement between computer simulation and "real" experiment is excellent.

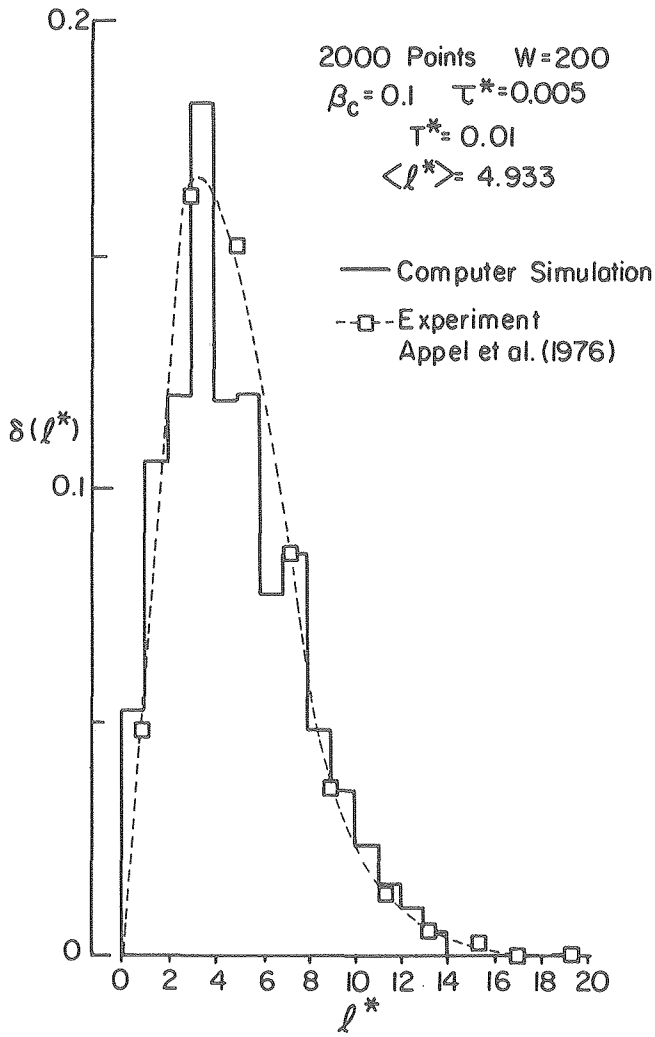

Fig. 4. Comparison of experimental segment length distribution with the computer simulation histogram. (XBL 775-5454)

More recently, studies of solution hardened materials have also shown good agreement with the simulation experiments. However, further work, both experimental and simulation, is necessary to complete the comparison between experiment and theory.

*Supported by the National Science Foundation under Contract No. DMR75-08163.

c. Constitutive Equations for Superplastic Deformation

D. Grivas

Our efforts in the past year have been aimed in the following three directions: 1) to understand the deformation mechanisms involved in the deformation of superplastic alloys over a wide range of strain rates, 2) to study the necessary microstructural characteristics needed to provide a stable two phase microstructure, a basic requirement for superplasticity, and 3) to study the effect of the microstructure on the deformation characteristics of these alloys, in the hope that, through such an understanding, superplasticity may be exploited to its fullest (fastest deformation rates, highest elongations, etc.) while, at the same time, some limitations, such as low tensile strength and creep resistance, may be effectively removed.

It is well accepted that for superplastic materials, a logarithmic plot of the stress vs. the steady-state strain rate reveals three distinct regions of different slope. Each of these regions corresponds to a different rate controlling deformation mechanism. The low stress region in our model is associated with the gliding of dislocations through the grains of the fastest deforming phase. As the stress is increased, and appreciable grain boundary sliding and rotation occurs, stress concentrations at the triple points are created. These stress concentrations cause new slip planes to operate, which transport mass to relieve the stresses, resulting in the second region, whose predominant controlling mechanism is the rate of grain boundary sliding. At the highest stress region, dislocation climb is suggested as the predominant mechanism.

A common feature of most superplastic alloys is a high solubility limit of one element in another at the eutectic or eutectoid temperature, which decreases rapidly with decreasing temperature. This feature, coupled with heterogeneous nuclei, introduced either by mechanical working or by fast quenching from the single phase region, results in a dispersion of precipitates in one of the phases of the multiphase alloy. These precipitates decrease the rate of growth of the grain in which they are dispersed, and, in turn, limit the rate of growth of all grains in the system.

It is usually assumed that for superplastic deformation

$$\dot{e} = \hat{\dot{e}}(\sigma, T, d)$$

where

$\dot{e}$ = steady state strain rate
T = temperature
σ = applied stress
d = microstructure characterization parameter,

such as the mean grain diameter or mean phase diameter. We found that besides the three above parameters σ, T, d the steady-state strain rate depends on the thermal history of the tested specimen. This effect is attributed to the different volume fractions of each phase, resulting from different cooling rates. The thermal history

was also observed to affect the total amount of deformation. In eutectoid systems, the creep resistance and tensile strength can be improved after deformation by bringing the deformed part to the one phase region and then slow cooling to introduce the characteristic plate-like microstructure. This extra thermal treatment can increase the tensile strength by a factor between 8 and 10 at high temperature.

4. THE INFLUENCE OF PHASE TRANSFORMATION ON MECHANICAL PROPERTIES AT CRYOGENIC TEMPERATURES

a. Profile TEM Analysis of Cryogenic Fracture Surfaces in 9Ni Steel*

C. K. Syn

In the course of research into the influence of retained austenite on the cryogenic fracture toughness of grain-refined and tempered 9Ni steel we faced the problem of determining the state of retained austenite (or transformed austenite) in the immediate vicinity of ductile fracture surfaces. The problem was solved by preparing profile specimens (Fig. 1) which permit detailed TEM studies of the deformed microstructures in the first few microns below the fracture surface.

The preparation of the profile specimens requires an elaborate thinning procedure. The fracture surfaces of K_{IC} specimens tested at 77K were electroplated with an iron layer of about 2 mm thickness. The plated specimens were sliced along the direction of crack propagation and at 90° angle to the fracture surface. These slices were chemically and mechanically thinned and ground to thickness of about 40 microns and then spark cut into disks of 3 mm diam such that the boundary (i.e., the fracture surface edge on) between the plated iron layer and fractured materials come to the middle of the disk. The final thinning was frustratingly difficult. Conventional electropolishing techniques such as jet polishing, window technique and other known versions of electropolishing produced either too thick or severely etched foils that could not be thinned beyond a certain initial thickness. Further thinning efforts ably fast edging away of the previously thinned areas rather than a continuous reduction of thickness. Thinning with ion milling led to thin foils with severely etched surfaces. Success was finally achieved by combining the electropolishing and ion milling techniques. Finish thinning by ion milling of thin foils prethinned by electropolishing produced foils of reasonable quality in surface and thickness suitable for the high voltage TEM study.

An example of the microstructure adjacent to the 77K fracture surface in 9 Ni steel is shown in Fig. 1. The upper part is the plated iron layer and the lower part is the microstructure profile from the fracture surface (demarked with white arrows) to about a depth of several microns into the bulk. In this initial observation retained austenite particles were not detected. Microstructural features consisting of lens-shaped particles with high dislocation density were, however, observed. These resemble the retained

Fig. 1. TEM microstructure of fracture surface layer in the grain-refined and tempered 9 Ni steel. The fracture boundary runs from near the top of the left to the middle of the right as demarked by a dotted line. (XBB 7712-12552)

austenite particles in the underformed samples. It, therefore, appears that the retained austenity particles transform during the fracture process to a highly dislocated martensite. More extensive study to confirm this tentative conclusion is in progress.

*Also supported by the Office of Naval Research under Contract #N00014-75-C-0154.

b. Development and Use of Mössbauer Spectroscopy for Phase Analysis of Fracture Surfaces*

B. Fultz

Mössbauer spectroscopy is known to be a useful tool for phase analysis in surfaces. It is specifically applicable to the quantitative analysis of ferrite and austenite phases in iron since these give distinct, characteristic spectra. Mössbauer spectroscopy offers the additional advantage that

the region analyzed is the first 300 Å - 1 μm below the surface (depending on experimental setup) making it particularly attractive as a tool to analyze residual austenite and ferrite (or martensite) in the deformed region immediately below a fracture surface.

We face the problem of determining residual phases near the fracture surface in two current projects: the influence of strain-induced martensite transformation on the cryogenic mechanical properties of austenite (BES/DOE) and the influence of retained austenite on the toughness of ferritic cryogenic steels (ONR) and have hence developed an apparatus for Mössbauer spectroscopy to assist in these projects. The development of the apparatus has progressed to the point where surface measurements of phase concentration is now a routine procedure. The apparatus includes a microcomputer-based data collection and processing system that is sufficient for data collection, storage, and processing including spectral deconvolution.

In research on the influence of retained austenite on the low temperature toughness of ferritic cryogenic steels, the Mössbauer evidence shows that retained austenite in grain refined 9 Ni steel is extensively (though not always completely) transformed to martensite in the deformed region near the ductile fracture surface at 77K. This result is in agreement with recent studies by Schwartz and Kim at Northwestern University, but is at variance with earlier work that suggests that a stable austenite is prerequisite to good toughness. Mössbauer spectroscopy is now being combined with profile TEM studies (reported above) to clarify this matter. Initial results suggest that under certain conditions, which are apparently achieved in 9 Ni steel over a narrow range of tempering temperatures, crack-tip deformation at low temperature transforms the austenite into a ductile, dislocated martensite which does not behave as a source of brittleness.

Mössbauer spectroscopy is also being applied to austenitic alloys to assess the effect of strain induced transformations on toughness. The initial alloy studied is Fe-21Cr-6Ni-9Mn, a proprietary alloy of the Armco Steel Co., which is a major candidate alloy for structural walls for large superconducting magnets. Mechnical property tests at the Boulder Laboratories of the National Bureau of Standards suggest a slight deterioration in fatigue resistance at 4K, which might be associated with austenite instability. Mössbauer analysis of the samples supplied by NBS reveals significant transformation in the fracture surface at both 77 and 4K. The transformation is localized (<10 μm in depth below the fracture surface), and the martensite spectra show hyperfine field effects which, along with other pertinent aspects of the transformation, are now being investigated.

c. Deformation-Induced Martensitic Transformations at Cryogenic Temperature

S. Chen

In the study of the deformation-induced martensitic transformation it is important to determine accurately the temperature associated with the first appearance of martensite under load (M_D). Additional data relating the amount of martensite formed to the temperature and the extent of deformation is needed to clarify the mechanism of deformation-induced martensite and its relation to mechanical properties.

To obtain this data a magnetic device was constructed within a temperature cell in a geometry that allows it to be fit around a tensile specimen inserted in an Instron machine. As magnetic martensite forms in the specimen the input frequency of the magnetic coil is modulated. The difference between the input frequency and the final frequency reveals the amount of martensite produced, assuming the unit has been calibrated by a direct quantitative technique (x-ray diffraction or Mössbauer spectroscopy). Figure 2 shows examples of measurements during tensile tests at -50 and -26°C. The magnetic device may also be attached to a cryogenic

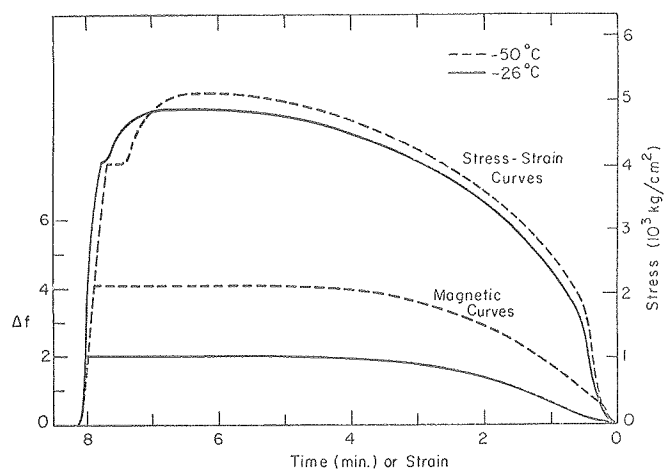

Fig. 2. The stress-strain curve and the martensite transformation curve. (XBL 7712-6585)

dilatometer to study the relation between the martensitic transformation and the magnetic transition in steel.

Current research addresses the influence of Cr and Mn on M_S and M_D temperatures and on features of the deformation-induced transformation in Fe-Ni austenites. The alloys being studied include Fe-Fe-(25-31)Ni-(0-6)Cr - (0-6)Mn. These alloys were chosen in part to test the extrapolation of widely-used "nickel-equivalent" formulae for estimating M_S and M_D to high nickel equivalents. The initial results suggest that these formulae are seriously misleading for high nickel alloys.

*Also supported by the Office of Naval Research under Contract #N00014-75-C-0154.

5. THE DEVELOPMENT OF NEW STRUCTURAL ALLOYS FOR ENERGY-RELATED APPLICATIONS

a. Thermomechanical Processing of Fe-Ni Cryogenic Steel

J. I. Kim

The high cost of nickel coupled with the high nickel content of available cryogenic steels (e.g., 9 Ni steel) has created a need for low nickel alloys having sufficient cryogenic toughness to be suitable for the safe storage and handling of liquified gases. In response to this need 5 Ni (Armco) and 5.5 Ni (Nippon) steels have recently been introduced and low nickel and nickelfree cryogenic steels are under investigation in several laboratories. A significant problem with these alloys is that as the nickel content is lowered an increasingly elaborate thermal treatment seems to be required to establish acceptable cryogenic toughness. The 5 Ni steels are given a three-step heat treatment, and more complex treatments may be needed as the Ni content is made still leaner, involving a trade-off between energy and processing costs and alloy costs in alloy optimization. In the case of low-alloy steels for applications such as Arctic pipelines controlled rolling processes are used to establish low temperature toughness. The present project was begun to explore controlled rolling as an alternative to elaborate heat treatment in processing low nickel alloys for severe cryogenic uses.

The experimental material used in this research to date is commercial 5.5 Ni steel supplied by the Nippon Steel Company. The thermomechanical treatments studied include a three-stage hot rolling followed by a tempering treatment. The three-stage controlled rolling is intended to refine prior austenite grains and to provide a microstructural condition conducive to effective decomposition during tempering. Tempering then decomposes the structure into a mixture of martensite, ferrite and retained austenite (Fig. 1). The desired final structure would consist of a fine distribution of

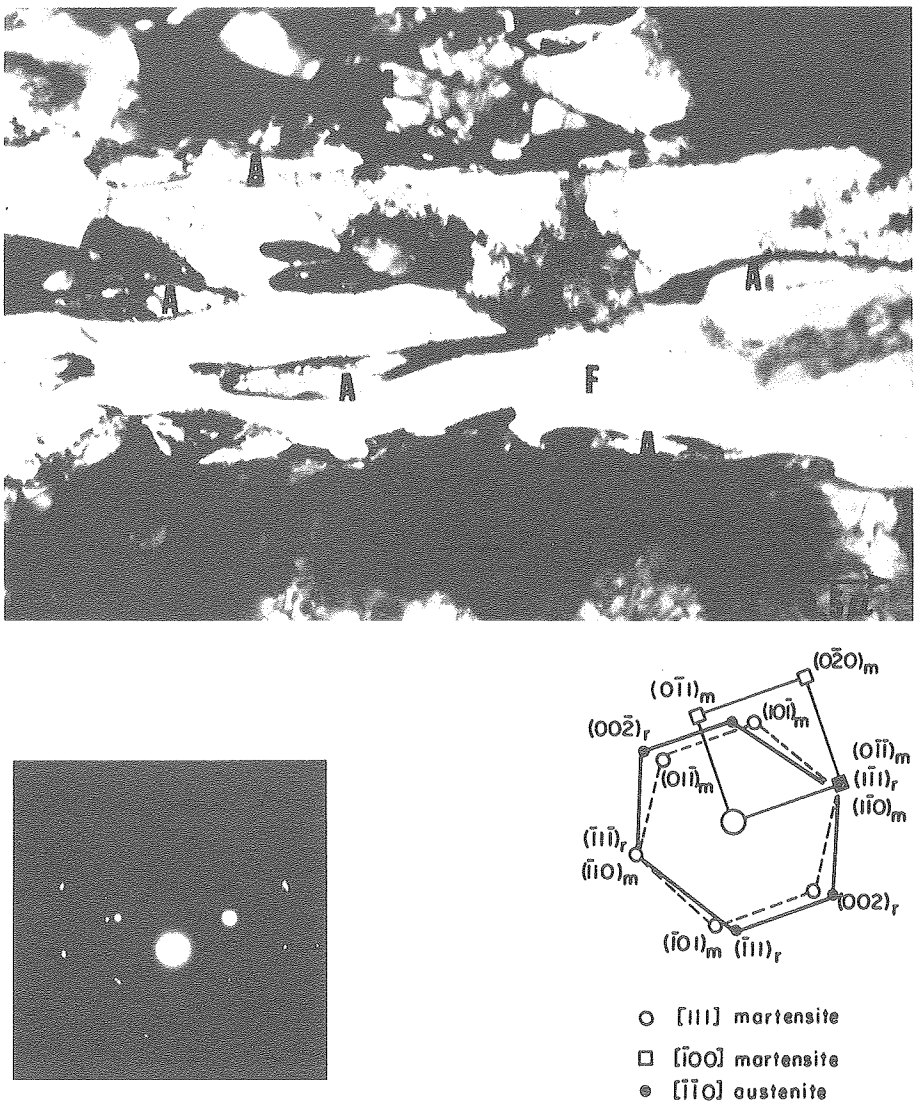

Fig. 1. Transmission electron micrograph of rolled and tempered steel showing a mixture of martensite (M), ferrite (F), and retained austenite (A), and their orientation relationships. (XBB 770-12673)

stable retained austenite interspersed through the interior of tempered martensite grains.

Two difficulties have been encountered in obtaining the desired microstructure through a controlled roll and temper process. First, the decomposition achieved in tempering tends to be concentrated in prior austenite grain boundaries. We have, however, found that grain interiors can be effectively tempered if the rolling conditions are properly chosen. Second, the structure obtained after rolling (with low finishing temperatures) is no longer simply martensite but a mixture of martensite and highly dislocated ferrite containing precipitated carbides (Fig. 2). It has proven difficult to devise a thermal treatment that will introduce a reasonable distribution of retained austenite into this structure while properly tempering the ferrite. While additional research is required to optimize this processing procedure, we have succeeded in obtaining good cryogenic toughness (Fig. 3) while retaining tensile properties equivalent to those of the current heat-treated alloy.

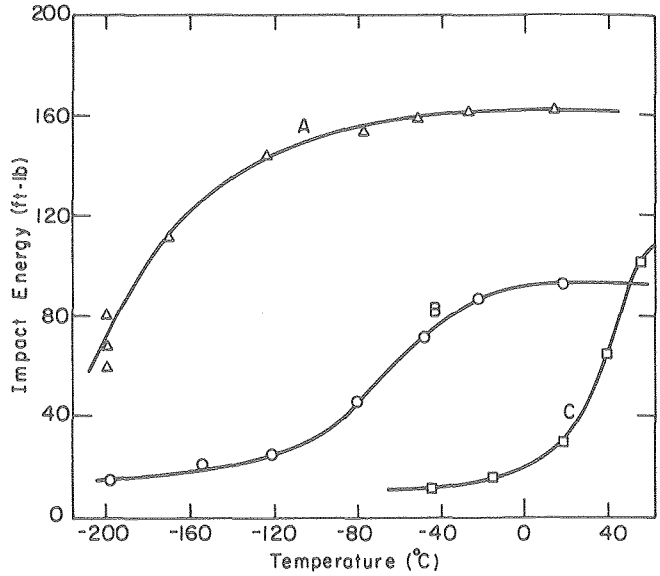

Fig. 3. Charpy transition curves of A) rolled and tempered steel, B) rolled steel and C) solution treated steel before rolling. (XBL 7712-6568)

b. Ferritic Fe-Mn Alloys for Cryogenic Use*

S. K. Hwang

During the past year research to develop nickel-free ferritic cryogenic steel has concentrated on the alloy Fe-12Mn-0.2Ti. Building on prior years' research we focused on two processing techniques to achieve good cryogenic toughness near 77K. The first is a thermomechanical treatment. This process consists of a hot rolling of the austenite at 900°C followed by a tempering at a two-phase temperature, 500°C. The hot working and quenching not only reduces the prior austenite grain size

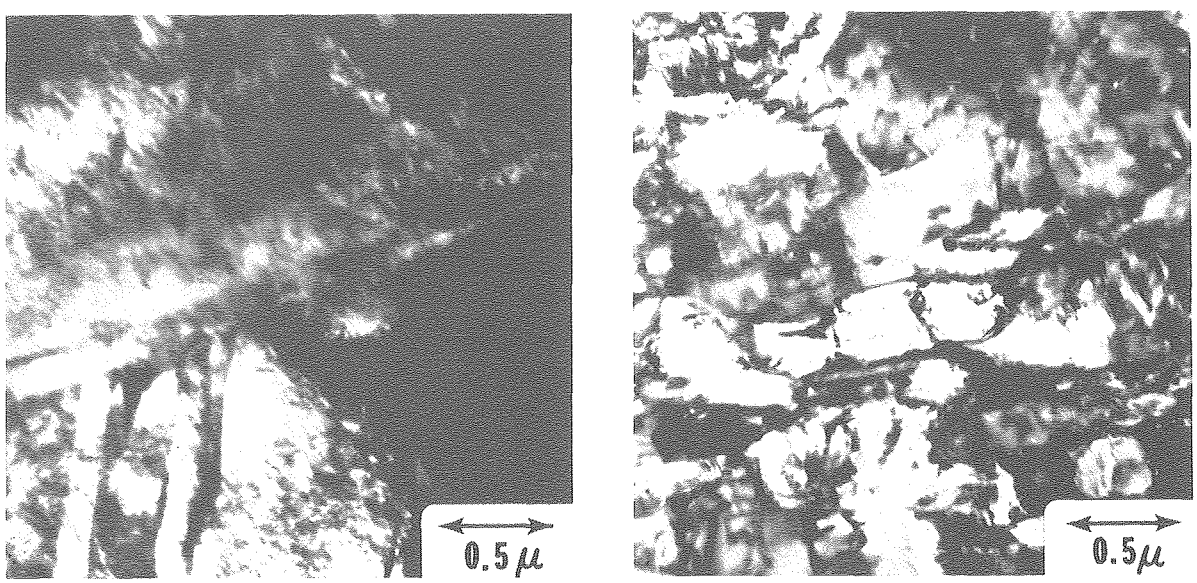

Fig. 2. A) Transmission electron micrograph of rolled steel with a high dislocation density and precipitated carbide. B) Transmission electron micrograph of rolled and tempered steel with subgrains. (XBB 770-12674)

through partial recrystallization but also maintains a residual dislocation density that facilitates the subsequent two-phase tempering. As a result a substantial increase in the Charpy impact energy at 77K, from 8 to 30 joules, is obtained. The improved cryogenic toughness is evident in the fractograph shown in Fig. 4.

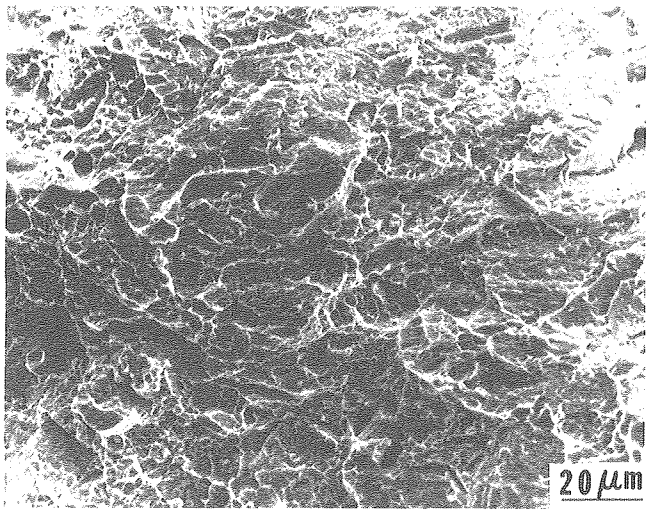

Fig. 4. Fe-12Mn-0.2Ti. SEM fractograph of a Charpy specimen broken at 77K. Hot rolled 50% at 900°C; ice brine quenching tempering 4 hours at 500°C; ice brine quenching. (XBB 770-12550)

A second approach attempted to minimize the characteristic brittle intergranular fracture of this alloy in as-cooled condition. In a practical service environment this phenomenon may present a problem particularly in welded structures. It was learned that a controlled cooling technique could be effective in suppressing intergranular cracking. This technique consists of a slow cooling above M_S temperature and a fast cooling below M_f as illustrated in Fig. 5. The cryogenic impact absorption energy at 77K was substantially improved by this method. The in-situ Auger analyses of the fracture surfaces are shown in Fig. 6. While no segregation was found on the prior austenite grain boundaries of the as-quenched specimen a minute segregation of N was observed in a completely furnace-cooled specimen. The control-cooled specimen showed transgranular ductile fracture. The present findings indicate that more than one cause is involved in the intergranular fracture of this alloy. A quench embrittlement that does not involve significant grain boundary segregation is dominant after fast cooling rates. A thermal embrittlement that does involve some chemical segregation intervenes with extremely slow cooling rates. Controlled cooling at an intermediate rate may avoid both sources of embrittlement, yielding good cryogenic toughness with a ductile fracture mode at 77K.

*Also supported by the NASA-Lewis Research Center under Grant #NGR05-003-562.

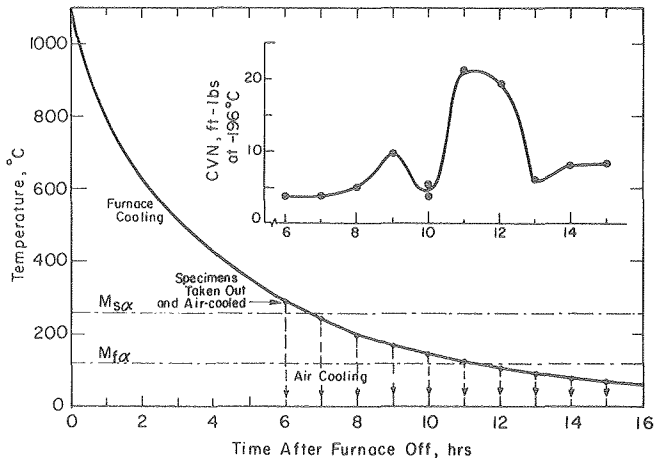

Fig. 5. Fe-12Mn-0.2Ti. Heat treatments and the corresponding Charpy values at 77K of controlled cooling process. (XBL 774-5345)

c. Age-Hardening of Austenitic Fe-Mn-X Alloys

K. M. Chang

Austenitic Fe-Mn alloys have been suggested for both cryogenic applications and uses requiring nonmagnetic alloys at room temperature and above. These alloys characteristically have low strength in the annealed condition. The present research was undertaken to identify useful precipitation-hardening schemes. The occurrence and the structure of intermetallic phases and the morphology and kinetics of their precipitation in austenite depends upon the alloy chemistry including the electron/atom ratio, atomic size, and compressibility. Basic ternary alloys Fe-Mn-X (X = Al, Ti, V, Nb) were studied systematically with regard to their aging response and the microstructure of the precipitation. No homogeneous coherent precipitate [like the γ' (Ni_3Ti) found in Fe-Ni based austenites] was observed; heterogeneous nucleation and continuous growth resulted in very coarsened precipitates that gave only minor increase in hardness and serious reduction in ductility.

To beneficially utilize these precipitates to improve the mechanical properties of Fe-Mn based austenites, efforts were made to alter the precipitation kinetics of the intermetallic compounds. The Fe-Mn-Ti system was chosen for detailed study. The intermetallic precipitates in this alloy were identified as an hexagonal Laves phase of C14 ($MgZn_2$) type with chemical composition $Fe_2(Ti, Mn)$. Aging directly after solution annealing produced a continuous network of precipitate phase along grain boundaries with a low density of individual precipitates dispersed inside the matrix. This microstructure does not strengthen the austenite significantly since the interparticle spacing within the matrix is too large to constitute an effective obstacle to dislocation motion. In addition, the

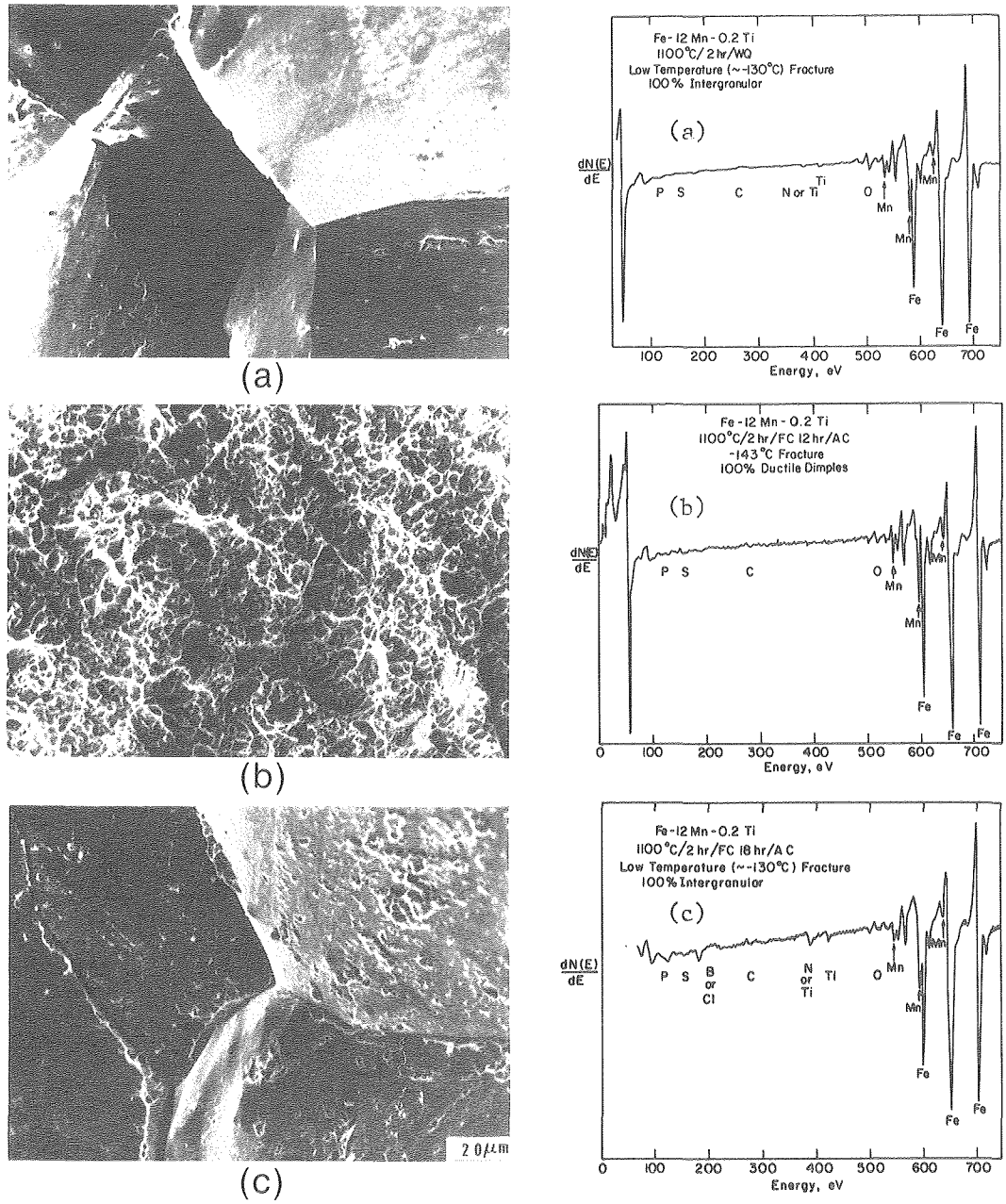

Fig. 6. Fe-12Mn-0.2Ti. SEM fractographs of Charpy specimens broken at 77K and the matching Auger spectra of the fracture surfaces. Heat treatments: a. Furnace cooled 6h/air-cooled; b. Furnace cooled 11 h/air-cooled; c. Furnace cooled 15 h/air-cooled. (XBB 777-6925)

continuous grain boundary precipitation embrittles the alloy and causes intergranular fracture. The reasons for this ineffective precipitation are that the alloy does not have enough beneficial nucleation sites for precipitation within the matrix and that continuous precipitation along grain boundaries dissipates the supersaturation at the early stage of aging. In order to overcome these problems, a 40% reduction by cold rolling was used between the solution annealing and the aging processes to introduce dislocation tangles that might act as effective nucleation sites.

Figure 7 shows the tensile properties of the alloy after different treatments. A good combination of strength and ductility can be achieved by introducing deformation. Intergranular brittle fracture was avoided. The micrography indicated that the dominant precipitate nucleation site was changed from the grain boundary to the matrix inside. The kinetics of precipitation is accelerated by predeformation; very fine precipitates covered the entire structure in one-hour aging. The precipitates were randomly distributed throughout the whole specimen; no continuous grain

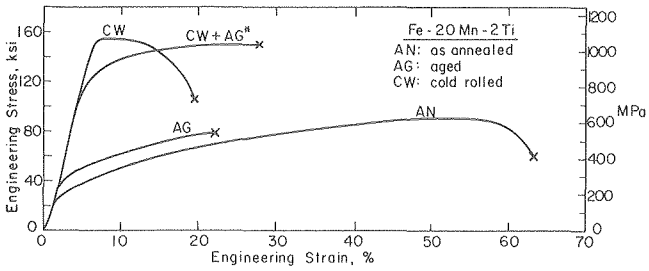

Fig. 7. The stress strain curves of age-hardening Fe-Mn-Ti alloy. (XBL 7712-6553)

boundary precipitate was found. No evidence of overaging was observed even after aging for 96 h, which is believed due to the low diffusivity of the substitutional elements in the austenitic matrix.

d. Use of Double Aging Treatments to Improve the Strength of Austenitic Alloys

A. Ma and D. H. Klahn

It has been known phenomenologically for some time that the strength of ausaged austenitic alloys can be improved by a thermal treatment in which a high temperature aging of the austenite is followed by a second aging at a somewhat lower temperature. The source of this desirable aging effect is, however, unknown. Three explanations suggest themselves: 1) The effect may be kinetic; the higher precipitation kinetics at the more elevated temperature initiate the precipitation process and allow the peak hardness appropriate to the lower temperature to be attained in shorter time. 2) The effect may be associated with a more favorable distribution of precipitate particles due to favorable nucleation behavior at the higher temperature. 3) The low temperature aging may induce a second, independent nucleation process that leads to a much higher effective precipitate density.

Research in this project has concentrated on alloys of composition Fe-(33-36)Ni-Ti-Al which are strengthened by formation of the γ' $Ni_3(Ti,Al)$ precipitate. A variety of aging experiments have shown that, with optimization, a double aging treatment can yield a higher final strength than is attainable through aging at either temperature alone. This evidence suggests that the strength improvement cannot be due to kinetic factors alone, but must involve either a more favorable precipitate distribution or a secondary precipitation process. In earlier work under this project Jin and Huang found persuasive (though indirect) evidence for an independent precipitation process in Fe-(31-33)Ni-Ti alloys aged near 500°C after initial aging near 750°C ($\Delta T \sim 250$°C). The optimal ΔT for maximum strength in stable austenitic alloys, Fe-(34-36)Ni-Ti-Al, is found to be much smaller, in the range $\Delta T \sim 70$ to 100°C. In this case the driving force for secondary precipitation is smaller and no direct evidence for secondary precipitation has been obtained. Resistivity techniques are now being used to test the possibility of a very fine scale secondary precipitation process.

e. High-Strength, Age-Hardenable Austenitic Steels for Generator Retaining Rings

D. Klahn, K. M. Chang, G. Thomas and J. W. Morris, Jr.

The purpose of this project is to design an alloy that can be used for making retaining rings for large electrical generators.

Retaining rings are one-piece hollow cylinders that are shrunk-fit over both ends of a generator rotor and serve to restrain the copper windings from the high centrifugal forces generated during operation. A large retaining ring can be up to 4 ft in diam, 3 ft long, 4 in. thick and weigh up to 3 tons. The retaining ring is the most highly stressed component of the generator system.

An alloy to be used for making retaining rings must have the following room temperature properties:

a) nonmagnetic, to avoid eddy current losses
b) yield stress of ~200 ksi
c) fracture toughness $K_{IC} > 100$ ksi$\sqrt{\text{in.}}$
d) resistant to stress corrosion cracking in hydrogen, which is used to cool the generator.

Currently most retaining rings are made from 18Mn-5Cr austenitic steel. This alloy is inadequate for large retaining ring systems because it is only hardenable to ~170 ksi and is susceptible to stress corrosion cracking in hydrogen.

Our alloy design efforts have concentrated on achieving the desired properties by thermal processing alone. Specifically, two approaches have been taken. First, a novel technique that combines both precipitation hardening and transformation strengthening has been developed. Secondly, age hardening alone has been used to achieve high strength by using a double-aging technique.

A schematic of the thermal processing involved in the first approach is shown in Fig. 8. After annealing, the alloy is first aged to form a fine distribution of γ' precipitates that strengthen the alloy by impairing dislocation motion. This is followed by a liquid nitrogen quench that causes a partial martensitic transformation. The alloy is subsequently heated to above the A_F temperature to cause a retransformation to austenite. A final low temperature anneal serves to lower the M_D temperature and hopefully prevent yielding via mechanically induced transformation. The austenite-martensite-austenite cycle results in an increased dislocation density that strengthens the alloy in an analogous manner to cold working. The sequence of aging first and then transformation strengthening is based on two observations: 1) aging causes the M_S temperature to rise that results in a higher percentage of austenite transforming to martensite than

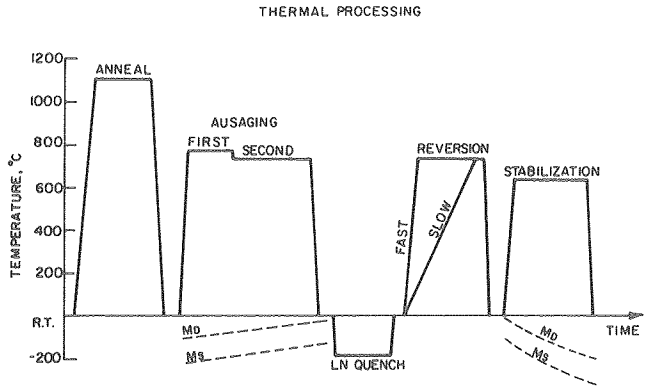

Fig. 8. Schematic of processing sequence used to strengthen Fe-Ni alloys. (XBL 7710-6283)

would result if the sequence were reversed and 2) aging first helps pin the transformation induced substructure and prevents this substructure from annealing during reversion.

The second approach was to obtain the desired properties by precipitation hardening alone. This was achieved by optimizing a double-aging process by utilizing a gradient furnace, shown schematically in Fig. 9. A candidate alloy was inserted in this furnace for a period of time and then hardness readings were taken along its length. Correlating

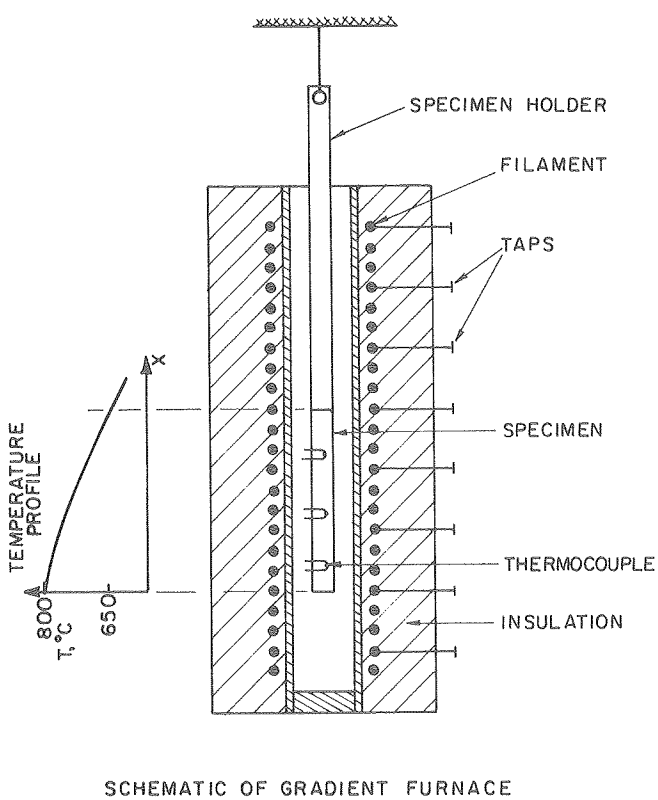

Fig. 9. Schematic of gradient furnace. (XBL 7710-6280)

the position of the maximum hardness with the temperature gradient gave the optimum initial aging conditions. A second specimen was subsequently aged at these conditions in a standard furnace and reinserted in the gradient furnace to determine the optimum second aging conditions.

To date, alloys of Fe-(28-36 at.%)Ni-(3-7 at.%)(Ti,Al,Nb,Ta) have been fabricated, processed and tested. By applying the age hardening plus transformation strengthening approach, yield stresses in excess of 180 ksi have been achieved.

More recent investigations that involve both composition and process modifications have resulted in an austenitic alloy that can be strengthened to a yield stress of >200 ksi with a corresponding fracture toughness K_{IC} of >110 ksi $\sqrt{in.}$, satisfying the strength and toughness goals of the program. Additional testing of notched tensile specimens in a hydrogen environment is being planned.

6. WELDING RESEARCH

a. Establishing a Welding Research Facility at MMRD*

K. W. Mahin

A new research program has been initiated this year in the area of welding metallurgy. The project involves the development of an economical weld wire with good properties to be used in welding Fe-9Ni plate for cryogenic service. Since the project entails not only the design and fabrication of the wire but also the actual welding of test plates using this experimental wire, it has been necessary to establish a welding research facility at MMRD. In order to determine the suitability of the wires for welding Fe-9Ni, it has been necessary to ascertain what are standard welding procedures for this material. While automated gas tungsten arc welding (GTAW) is actively being pursued in Japan, a survey of American firms interested in the development of a new wire indicates that a successful wire for American purposes must be suitable for gas metal arc welding (GMAW). However, associated with this process is a history of defect problems in the weldment, which are assumed to be due to impurities in the shielding atmosphere. In order to study and control this problem, a vacuum chamber has been procured. The chamber will afford control of impurity levels in the atmosphere and provide a good basis for comparing different shielding atmospheres as to their effect on the type and number of defects formed in the weldment. In light of the preference of American industry for GMAW, a semi-automated gas metal arc welding UNH has been purchased. The facility at the present time has the capability to do semi-automated GMAW in a controlled atmosphere with appropriate monitoring devices to record any process fluctuations. The process will be fully automated during the coming year in an attempt to reduce the process variables to a minimum.

The other aspect of the program has entailed the acquisition of Fe-9Ni plates and the development of process procedures for fabricating experimental

wires of varying compositions. 9Ni steel plate has been provided by the Armco Steel Co. The wire production has been carried out at MMRD by modifying existing equipment. The procedure upon which we have decided involves the casting of 5 lb ingots that can be directly hot forged then swaged to 1/8 in. diam rod. At this point, the rod is cold-drawn to its final 1/16 in. diam. Current capability allows for a final wire length of 18 ft.

The welding facility at MMRD is now operational and the welding of the 9 Ni steel plates with the experimental wires using the GMAW process has begun. The work for the coming year will involve the mechanical and chemical testing of the as-welded plates.

*Supported by the LBL Director's Fund under Account #3664-15

7. RESEARCH PLANS FOR CALENDAR YEAR 1978

J. W. Morris, Jr.

1) During 1978 research on the theory of phase transformations will emphasize elastic theories of martensitic transformations and precipitation processes and theory of coarsening of spinodal decomposition and precipitation reactions.

2) Research on the characterization of polygranular microstructures will study transformations nucleated at grain boundaries. The existing codes will also be used to create well-known microstructures for studies of processes sensitive to grain structure, such as grain boundary diffusion and grain size and structure effects on fracture.

3) Theoretical studies of plastic deformation will concentrate on the influence of dislocation-dislocation interactions on the characteristics of deformation through dislocation glide in simple systems.

4) Experimental research on plastic deformation will continue the present investigation of the mechanism of superplasticity and will also address the problem of a mechanical equation of state for homogeneous plastic deformation.

5) In research on the influence of phase transformation on mechanical properties a combination of mechanical testing, Mössbauer spectroscopy, and fracture profile transmission electron microscopy will be used to relate toughness behavior to the extent and nature of transformation in the fracture surface. This research will be supplemented by specific studies of the deformation-induced transformation of austenite. We also hope to employ high resolution Auger spectroscopy to begin study of the chemical consequences of secondary phases.

6) In alloy development for structural applications at cryogenic temperatures, we hope to demonstrate a ferritic Fe-Mn alloy for use to 77K during 1978. We also hope to obtain a thermomechanically-processed low nickel alloy for potential LNG use. Building on basic research on the consequence of deformation-induced austenite we plan to begin research toward improved austenitic steels for use at 4K.

7) In welding research we plan to make, test, and evaluate 9 Ni steel weldments with the several ferritic weld wire compositions that have been proposed as potentially valuable. On the basis of this information we will begin modification of composition and technique to optimize cryogenic weld properties.

8. 1977 PUBLICATIONS AND REPORTS

J. W. Morris, Jr. and Associates

Journals and Books

1. S. H. Chen and J. W. Morris, Jr., Electron Microscopy Study of the Passivating Layer in Fe-Ni Martensite, Met. Trans. A. 8a, (1977).

2. S. Jin, C. K. Syn and J. W. Morris, Jr., The Use of Martensite Reversion in the Design of Tough Ferritic Cryogenic Steels. Proc. of the 1st JIM International Symposium on "New Aspects of Martensitic Transformation," Kobe, Japan, p. 393-397 (1977).

3. S. Jin, D. Huang, G. Thomas and J. W. Morris, Jr., Use of the Reverse Martensitic Transformation and Precipitation to Enhance the Strength and Stability of Austenite, Proc. of the 1st JIM International Symposium on "New Aspects of Martensitic Transformation." Kobe, Japan, p. 387-392, (1977).

4. K. W. Mahin, K. Hanson and J. W. Morris, Jr., Geometric Analysis of Simple Polygranular Microstructures, Bull. Am. Phys. Soc. 22, 284 (1977).

5. E. S. Pundarika, K. Hanson and J. W. Morris, Jr., Kinetics of Clustering Reactions in the Ising Lattice, Bull. Am. Phys. Soc. 22, 302 (1977).

6. K. Hanson and J. W. Morris, Jr., Computer Simulation of Interacting Dislocation Motion Resisted by Point Like Barriers, Bull. Am. Phys. Soc., 22, 443 (1977).

7. E. S. Pundarika, K. Hanson and J. W. Morris, Jr. Theoretical Study of Two-phase Decomposition and Coarsening, Trans. Am. Nuc. Soc. 27, 321 (1977).

8. K. Hanson and J. W. Morris, Jr., Three-Dimensional Analysis of Cellular Microstructures, Trans. Am. Nuc. Soc. 27, 297 (1977).

LBL Reports

1. Keh-Minn Chang, Precipitation-Strengthened Austenitic Fe-Mn-Ti Alloys, (M. S. thesis), LBL-6278, June 1977.

2. Sun-Keun Hwang, The Design of an Fe-12Mn-0.2Ti Alloy Steel for Low Temperature Use, (Ph. D. thesis), LBL-6603, June 1977.

3. E. S. Pundarika, K. Hanson and J. W. Morris, Jr., Theoretical Study of Two-Phase Decomposition and Coarsening, LBL-6613, June 1977.

4. K. Hanson and J. W. Morris, Jr., Three-Dimensional Analysis of Cellular Microstructures by Computer Simulation, LBL-6614, June 1977.

5. S. K. Hwang and J. W. Morris, Jr., The Improvement of Cryogenic Mechanical Properties of Fe-12Mn and Fe-8Mn Alloy Steels Through Thermal/Mechanical Treatments, LBL-6618, July 1977.

6. K. Hanson and J. W. Morris, Jr., Computer Simulation of Interacting Dislocation Motion Resisted by Point Like Barriers, LBL-6636, Aug. 1977.

7. J. W. Morris, Jr. and participants, Materials Science Workshop on Phase Transformations, Stability, and Materials Interactions, LBL-6645, July 1977.

8. S. K. Hwang and J. W. Morris, Jr., The Suppression of Low Temperature Intergranular Brittleness in Ferritic Alloys, LBL-6652, August 1977.

9. J. W. Morris, Jr., S. K. Hwang, K. A. Yushchenko, V. I. Belotzerkovetz and O. G. Kvasnevskii, Fe-Mn Alloys for Cryogenic Use: A Brief Survey of Current Research, LBL-6698, September 1977.

10. F. R. N. Nabarro and E. Kostlan, The Stress Field of a Dislocation Lying in a Plate, LBL-6987, November 1977.

Presentations

1. J. W. Morris, Jr., C. K. Syn and S. Jin, The Effect of Retained Austenite on the Toughness of Fe-8-18Ni Alloys, AIME Annual Meeting, Atlanta, March 6-10, 1977.

2. D. Grivas and J. W. Morris, Jr., Low Stress Creep Properties of Superplastic Alloys, WESTEC '77, Los Angeles, March 14-17, 1977.

3. K. W. Mahin, K. Hanson and J. W. Morris, Jr., Geometric Analysis of Simple Polygranular Microstructure, American Physical Society Conference, San Diego, March 21-24, 1977.

4. E. S. Pundarika, K. Hanson and J. W. Morris, Jr., Kinetics of Clustering Reactions in the Ising Lattice, American Physical Society Conference, San Diego, March 21-24, 1977.

5. K. Hanson and J. W. Morris, Jr., Computer Simulation of Interacting Motion Resisted by Point Like Barriers, American Physical Society Conference, San Diego, March 21-24, 1977.

6. J. W. Morris, Jr., Computer Simulation of Fundamental Reactions in Metallurgy, Solid State Physics Committee Meeting, Lawrence Berkeley Laboratory, March 25, 1977.

7. J. W. Morris, Jr., New Alloy Steels Through Thermal Processing, Golden Gate Welding and Metals Conference, San Francisco, January 1977.

8. J. W. Morris, Jr., New Ferritic Cryogenic Steels, Seminar, Central Research Laboratory Armco Steels Co., Middletown, Ohio, February 1977.

9. J. W. Morris, Jr., Grain Refinement Through Thermal Cycling of Fe-Ni Steels, Research Laboratory, Republic Steel Co., Cleveland, Ohio, February 1977.

10. J. W. Morris, Jr., Education in Materials Science at the University of California, Western Tool Exposition and Conference, Los Angeles, March 1977.

11. J. W. Morris, Jr., Summary Report of the ERDA Workshop on Future Research Directions in Phase Transformation, Stability, and Materials Interactions, ERDA/DPR Overview Meeting on Future Directions for Research in Materials Science, Germantown, Maryland, June 1977.

12. J. W. Morris, Jr., The Design of Tough New Cryogenic Steels, Central Research Laboratories, Daido Steel Co., Nagoya, Japan, June 1977.

13. J. W. Morris, Jr., Microstructure-Property Relations in Fe-Ni Cryogenic Steels, Department of Materials Science, Kyoto Univ., Kyoto, Japan, June 1977.

14. J. W. Morris, Jr., Fe-Mn Alloys For Cryogenic Use: II. Current Research in the U.S. and Japan 2nd International Cryogenic Materials Conf., Boulder, Colorado, August 1977.

15. S. K. Hwang and J. W. Morris, Jr., Suppression of Low Temperature Intergranular Brittleness in Ferritic Fe-Mn Alloys, 2nd International Conference on Cryogenic Materials, Boulder, Colorado, August 1977.

16. S. Chen and A. G. Khachaturyan, Computer Simultation of the Martensitic Transformation, 2nd International Conference on Cryogenic Materials, Boulder, Colorado, August 1977.

17. J. W. Morris, Jr. and A. G. Khachaturyan, Computer Simulation Studies of Spinodal Decomposition and Coarsening, TMS Fall Meeting, Chicago, October 1977.

18. D. H. Klahn, High Strength, Heat Treatable Austenitic Alloys, TMS Fall Meeting, Chicago, October 1977.

19. E. S. Pundarika and K. Hanson, Theoretical Study of Two-Phase Decomposition and Coarsening, Annual Meeting, American Nuclear Society, San Francisco, December 1977.

20. K. Hanson, Three-Dimensional Analysis of Cellular Microstructures, Annual Meeting American Nuclear Society, San Francisco, December 1977.

b. Research in Alloy Design

V. F. Zackay and E. R. Parker, Principal Investigators

1. FUNDAMENTAL INVESTIGATIONS OF CONTINUOUS PRECIPITATION IN AN Fe-Nb CREEP-RESISTANT ALLOY

J. Wert

Ferritic alloys strengthened by precipitation of intermetallic compounds, rather than carbides, have potential application as creep resistant alloys. This is expected because the coarsening rate of intermetallic precipitates should be slower than that of carbide particles, resulting in a more stable microstructure in long-term service applications. However, the precipitation of intermetallic compounds in ferrite usually results in a heavy network of precipitates along the grain boundaries and a precipitate-free zone adjacent to the grain boundaries. Both of these microstructural features are detrimental to the mechanical properties of these alloys; the grain boundary precipitates severely reduce the ductility and the precipitate-free zones adversely affect the creep strength. This investigation is devoted to a study of modifications of the heat treatment procedure that eliminates the precipitate-free zones.

The alloy used in this study had a composition of 2.6 wt.% Nb, the balance being Fe. This study was begun as an extension of previous studies on Fe-Ta alloys.[1,2] The intermetallic precipitate formed in the Fe-Nb alloy was a Laves phase, Fe_2Nb, which had a C14-type hexagonal crystal structure. The upper schematic diagram of Fig. 1 shows the heat treatment normally used to precipitation harden this alloy. The sequence of solution treatment followed by a quench to ambient temperature and subsequent aging is typical of many aging treatments. To avoid quench cracking a relatively slow quench was required—about 40° C/s. Due to the slow quench rate, a heavy network of grain boundary precipitates developed during the quench. In the region adjacent to this boundary precipitate, a Nb-depleted region was formed. The depleted region was observed using the electron microprobe, and its formation has been modeled using computer techniques.

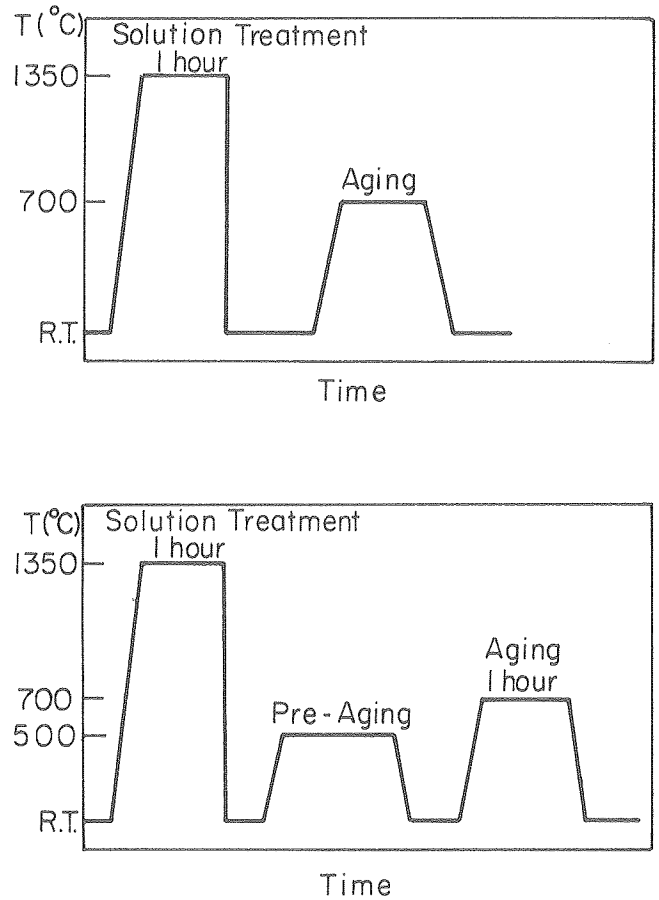

Fig. 1. Schematic heat treatment schedules for precipitation hardening: Normal heat treatment (upper) and modified heat treatment including preaging (lower). (XBL 7710-6240)

Peak hardness was obtained by aging at 700° C for 1 hr. The form of the aging curves suggested that only one precipitation reaction occurred in this alloy. Since only the equilibrium phase was found by x-ray techniques, there was some evidence that no transition phases formed in this alloy. This was in agreement with the observation of previous investigators.[3] The microstructure corresponding to the peak hardness condition is shown in the lower micrograph of Fig. 2. The wide precipitate-free zones resulted from the difficulty of nucleation of the equilibrium precipitate in the regions of lowered Nb concentration.

The heat treatment shown in the lower diagram of Fig. 1 included a pre-aging step at 500° C. There was no change in the hardness nor was any change observed in the microstructure by optical electron microscopy after the pre-aging step. Yet the effect of a 6-hr pre-aging treatment on the microstructure following aging was remarkable, as is shown in the upper micrograph of Fig. 2. The precipitate-free zone was eliminated by using the pre-aging treatment. This was confirmed by electron microscopy. The origin of the pre-aging effect is unclear at this time. Some evidence suggested that it may be related to the clustering phenomenon observed in similar Fe-Mo alloys,[4] although it was certainly not the only possible interpretation of the available evidence. Additional experiments are under way at the present time to establish the origin of this effect. Mechanical tests to evaluate the change in properties are also being conducted. Finally, it is expected that, regardless of the origin of this effect, it can be equally well applied to many other alloys which are strengthened by precipitation of intermetallic compounds.

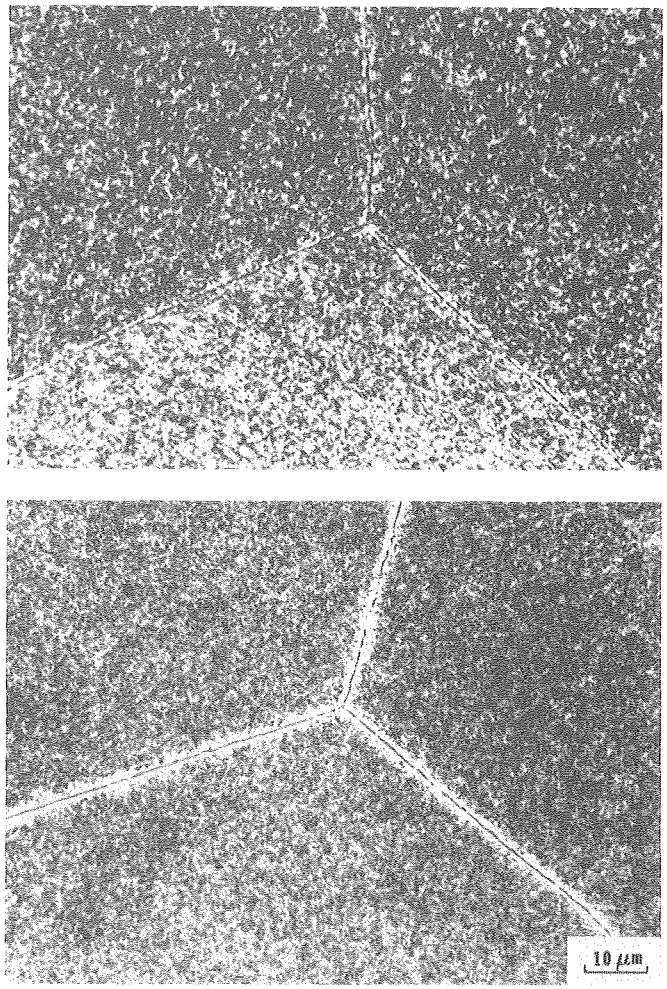

Fig. 2. Optical microstructure of Fe-2.6% Nb alloy. Structure after 6 hr preaging, 1 hr aging (upper). Structure after normal processing of 1 hr aging treatment (lower). (XBB 773-1555)

1. R. Jones, E. R. Parker, V. F. Zackay, Met. Trans. 3, 2835 (1972).
2. D. Bhandarkar, M. S. Bhat, E. R. Parker, V. F. Zackay, Met. Trans. 7A, 753 (1976).
3. Speich, Trans. AIME 224, 850.
4. Marcus, Fine, Schwartz, J. Appl. Physics 38, 12 (1967).

2. MODELING OF WORK HARDENING IN TRANSFORMING ALLOY STEELS

J. Kallend

The mechanical properties of metastable steels are of interest because of the unique combination of strength and ductility which may be obtained in suitably treated alloys. These properties derive from the phase transformation of austenite to martensite which occurs during deformation, leading to a high rate of strain hardening, and consequently postponing the onset of mechanical instability.

In order to understand fully the influence of alloy composition and process variables on the mechanical behavior of TRIP steels, and to develop a useful constitutive equation to describe the behavior, it is desirable to evaluate both the influence of these variables on the kinetics of the martensitic transformation, and the influence of the resultant two-phase microstructure on the mechanical properties. The research described here was directed towards the latter problem.

Previous work[1,2] assumed that the mechanical properties of TRIP steel were determined by a law of mixtures. This law, together with several others, was evaluated on a developmental TRIP steel having the composition 0.325% C, 8.0% Ni, 9.0% Cr, 2.0% Mn. The steel was thermomechanically processed by rolling to 70% reduction at 200, 250, or 450°C. The mechanical properties and kinetics of the phase transformation of these materials have been characterized in a previous study.[3] The models used were:

a. Law of mixtures.
b. Drucker's continum model of constrained deformation.[4]
c. Dispersion hardening, using the Orowan formula.
d. A model based on the development of back stresses in the matrix[5] modified to account for the finite strength of the martensite.

The law of mixtures states that the effective strength of the composite is given by the weighted mean strength or its components, the weighting factor being the volume fraction of each phase.

$$\sigma_e = \sigma_\alpha f_\alpha + \sigma_\gamma \gamma$$

where

σ_α = flow stress of α phase,
α_γ = flow stress of γ phase,
f_α = volume fraction of α phase,
f_γ = volume fraction of γ phase.

This is the expected constitutive law if the deformation of the composite is homogeneous, with no constraint between phases.

Drucker's model relates to the stress required to maintain plastic flow in a soft matrix constrained by hard particles in the form of long rods, and takes the form:

$$\sigma_e = \sigma_\gamma \qquad f_\alpha < 40\%$$
$$\sigma_e = \frac{\sigma_\gamma}{3}(2 + 1.5/g) \qquad 40\% < f_\alpha < 70\%$$
$$\sigma_e = \frac{\sigma_\gamma}{2}(1 + \frac{2.3}{3g} + g) \qquad f_\alpha < 70\%$$

where $g = 2(\frac{1}{\sqrt{f}} - 1)$.

The Orowan model computes the stress required to force a dislocation past an array of non-deforming particles. This is given by:

$$\tau = \frac{Gb}{\ell}$$

where τ is the shear strength of the composite, G is the shear modulus, b is the Burger's vector, and ℓ is the spacing between particles in the slip plane.

The back-stress model is a modification of the law of mixtures, attempting to take account of the constraints between the phases which result from their different strengths. This gives:

$$\sigma_e = \sigma_\gamma f_\gamma + \sigma_\alpha f_\alpha + (\sigma_\alpha - \sigma_\gamma) f_\alpha f_\gamma .$$

In this study the strength of the martensite was calculated from the formula given by Gerberich et al.,[1] and shear stresses and strains were related to tensile stresses and strains using Taylor's value of the orientation factor M = 3.

The results are shown in Fig. 1. The law of mixtures tended to overestimate the strain hardening rate at low strains, but underestimate the rate at higher strains; consequently, the predicted uniform elongations were generally underestimated by this model. The Orowan and back stress models overestimated the strain hardening rate considerably at all strains. The best qualitative fit was given by Drucker's model, based on continuum plasticity. Although it underestimated the strain hardening rate at low strains, and overestimated the Luders strain, it did predict the uniform elongation quite accurately in all cases. From this study it is clear that none of these established models give a good fit to the experimental data over the complete strain range.

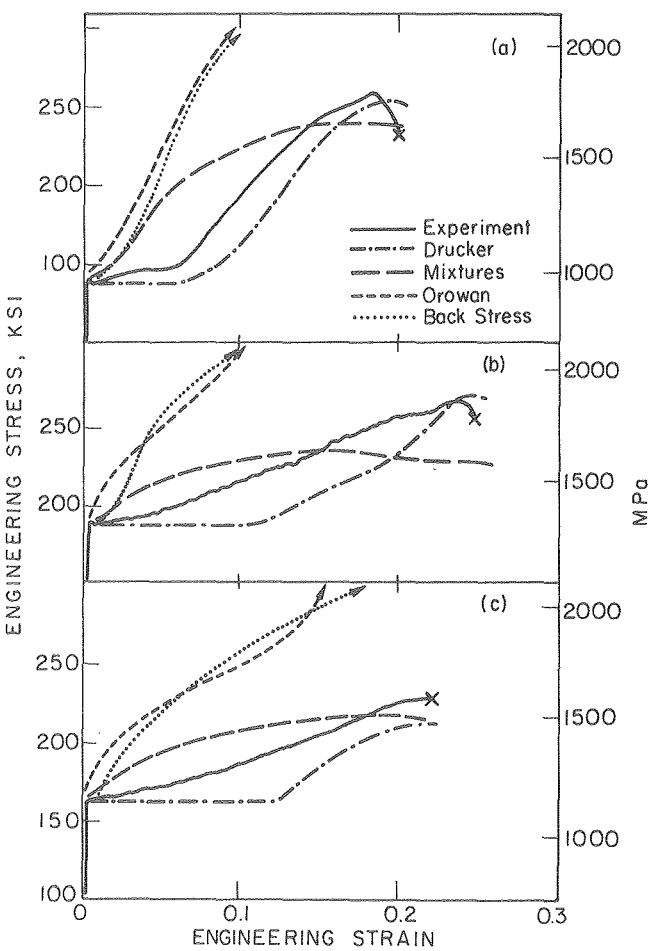

Fig. 1. Engineering stress-strain curves for TRIP steel (0.33C-8Ni-9Cr-2Mn) hot worked 70% at 450°C (top), 250°C (middle) and 250°C (bottom). Predicted curves for each treatment are also shown.
(XBL 7712-6570)

1. W. W. Gerberich, G. Thomas, E. R. Parker and V. F. Zackay, UCRL-20308 (August 1970).
2. M. Acrin, G. B. Olsen and R. A. Gagne, Mat. Sci. and Eng. 23, 33 (1976).
3. D. Bhandarkar, V. F. Zackay and E. R. Parker, Met. Trans. 3, 2619 (1972).
4. D. C. Drucker, Brown Univ. Tech., Report 7, USAEC Contract No. AT(30-1)-2394 (1964).
5. L. M. Brown and W. M. Stobbs, in Constitutive Equations in Plasticity, MIT Press (Cambridge, Mass. 1975) p. 387.

3. INVESTIGATION OF MICROSTRUCTURE AND MECHANICAL PROPERTIES IN TRANSFORMING Fe-Mn-Cr ALLOYS

L. Thompson and G. Haddick

Previous work,[1,2] studying the effect of Cr additions to Fe-Mn alloys, showed that good combinations of strength and ductility could be achieved. With this basis, a series of alloys have been investigated as potential substitutes for conventional stainless steels. The Fe-16%Mn-13%Cr alloy was chosen as the base alloy for this investigation because it possessed the best combination of strength, ductility, and impact resistance. The additions of N, Mo, and Si were made to enhance strength and improve corrosion resistance. Only air cooled microstructures were investigated. Table 1 gives the alloys investigated. The base alloy was found to be a three-phase mixture of austenite (γ), epsilon martensite (ε), and alpha martensite (α). The addition of N led to a stabilization of austenite following air cooling, with the Mo and Si containing steels fully austenitic. The mechanical properties of the modified alloys were enhanced by the nitrogen addition. These steels

Table 1. Influence of composition on volume percent of phases present.

Alloy	Phases γ	ϵ	α
16 Mn - 13 Cr	31	33	36
16 Mn - 13 Cr - 0.13 N	83	17	0
16 Mn - 13 Cr - 0.2 N - 2 Mo	100	0	0
16 Mn - 13 Cr - 0.2 N - 1.5 Si	100	0	0

exhibited higher work hardening rates with an associated increased elongation at room temperature. The increases were attributed to the effect of alloying additions on the relative position of the M_s and M_d temperatures ($\gamma \rightarrow \varepsilon$) with respect to the testing temperature. As expected, testing at decreased temperatures led to reduced ductility. The impact properties are shown in Fig. 1. The modified alloys exhibited good upper shelf energies. However, these properties were degraded as the test temperature approached M_s, as in the tensile test. The Charpy fracture showed a change in mode attributed to fracture along epsilon martensite plates. Transmission electron microscopy revealed the formation of the deleterious epsilon martensite bands after deforma- as shown in Fig. 2.

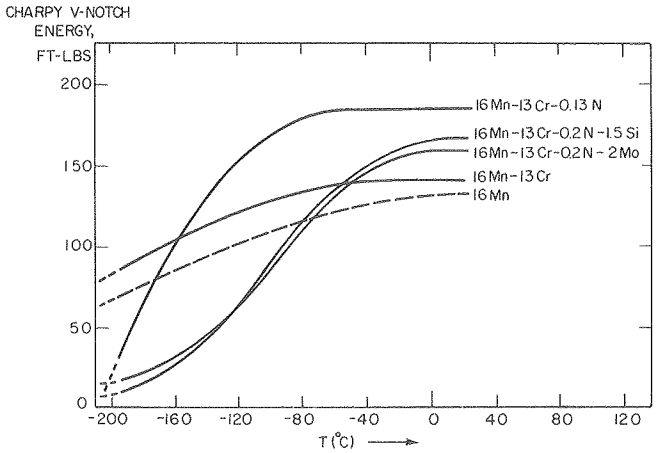

Fig. 1. Charpy impact energies as a function of test temperature for the alloys investigated. (XBL 769-7494)

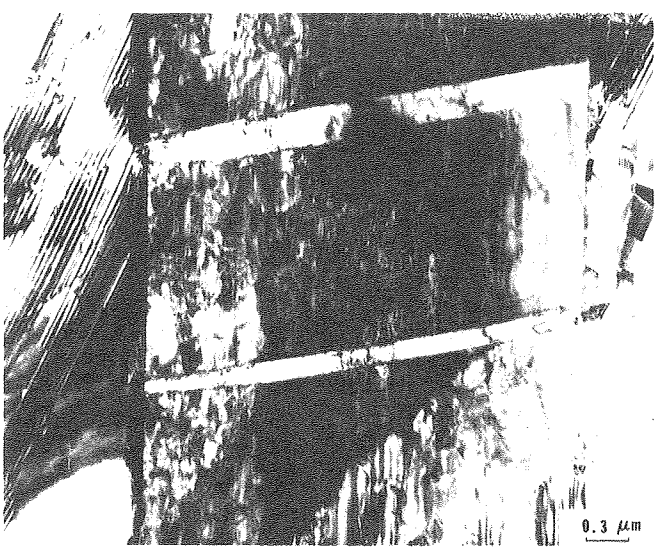

Fig. 2. Transmission electron micrograph showing epsilon martensite formed after deformation in the Cr-Mn steel. (XBB 779-8902)

This study has shown that these new steels have good mechanical properties near room temperature. The steels also exhibited good corrosion performance in certain corrosive environments. The steels did, however, exhibit embrittlement as the test temperature approached the M_s for the $\gamma \rightarrow \varepsilon$ transformation.

---

1. M. J. Schanfein, The Cryogenic Properties of Fe-Mn and Fe-Mn-Cr Alloys, (M.S. thesis), U. C. Berkeley, LBL-2749.
2. L. D. Thompson, The Mechanical Properties and Microstructural Relationships in Fe-Mn-Cr Alloys, (M.S. thesis), U. C. Berkeley, LBL-6234.

4. FUNDAMENTAL INVESTIGATIONS IN STRUCTURE-PROPERTY RELATIONSHIPS IN EUTECTOID STEELS

Y. Mishima

The aim of this study is to characterize and then control the microstructures of interphase precipitation alloys to make them useful for thick wall pressure vessel application. Interphase precipitation has been observed in low carbon steels which contain alloy carbide formers. A very fine dispersion of alloy carbides in a ferrite matrix is developed by direct decomposition of austenite held isothermally or cooled continuously. It has been reported that when vanadium or molybdenum are added to a 0.2% carbon steel, the steel develops a favorable microstructure for mechanical properties. This work has been performed on two systems, iron-carbon-vanadium, and iron-carbon-molybdenum steels. Design criteria for alloy development were established; the new steel must:

a. Develop uniform mechanical properties throughout a thick section using the simplest heat treatment (preferably a continuous cooling process),
b. be weldable requiring no post-weld heat treatment,
c. have a composition close enough to the eutectoid composition to develop uniform microstructures.

Discussions of the two systems follow.

Fe-0.2C-1V-3Ni-Alloy. Work by Honeycombe and his co-workers showed that an Fe-0.2C-1V alloy formed the most favorable structure when it is transformed at relatively high temperatures (600 to 800°C).[1] The addition of 3%Ni was made to lower this transformation temperature regime, promoting a finer precipitation and wider applicability to pressure vessel use. The TTT diagram for this alloy system is shown in Fig. 1. All specimens were austenitized at 1200°C for 15 min to allow vanadium carbide dissolution.

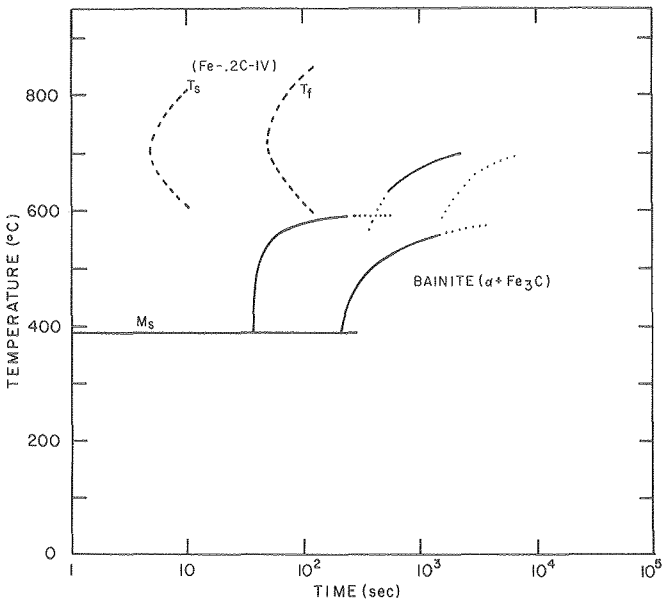

Fig. 1. TTT diagram for Fe-0.2C-1V-3Ni alloy. (XBL 781-6847A)

The diagram clearly shows that the addition of 3%Ni depresses the C-curve expected to be associated with the desirable interphase precipitation. Room temperature Charpy impact properties were measured along with Rockwell hardness (C scale) for the following heat treatments.

Treatments	C_V (ft-lb)	Hardness
a) Isothermally held 30 min 600° C	2	40
b) Isothermally held 15 min 650° C	30	40
c) Isothermally held 30 min 700° C	20	30

However, microstructural observation by TEM showed that there was no interphase precipitation as reported in the Fe-0.2C-1V system. The microstructure corresponding to the alloy transformed at 650°C for 15 min, which exhibited the best combination of hardness and Charpy impact value, is shown in Fig. 2. The structure is not typical of interphase precipitation. Evaluation of microstructure-mechanical property relationships will be made for this alloy for various transformation processes. This will be necessary to develop an alloy meeting the design criteria.

Fe-0.2C-2Mo-2Si Alloys. Because Fe-C-Mo steels also show a favorable eutectoid microstructure, investigations have been initiated in these steel systems. Silicon additions to the base alloy have been made to reduce the eutectoid carbon content and to influence the kinetics of carbide formation. Initial compositions have been chosen and transformation characteristics will be determined. More emphasis will be placed on achieving good properties in material receiving thick-section processing.

1. Proceedings of the Royal Society (London) A322, 191 (1971).

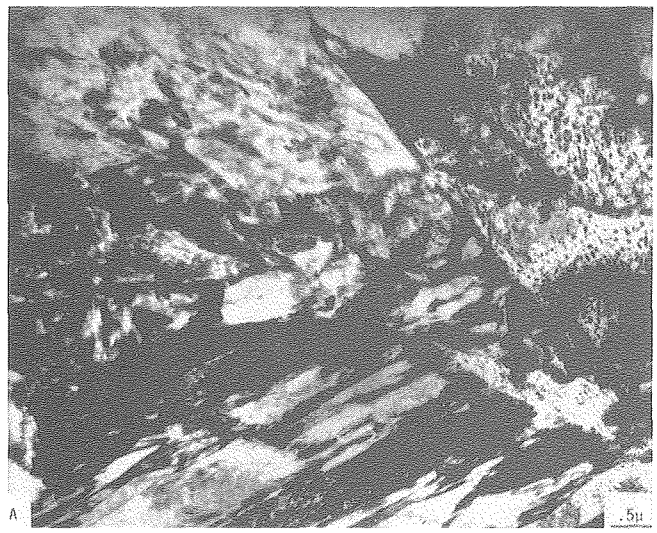

(a)

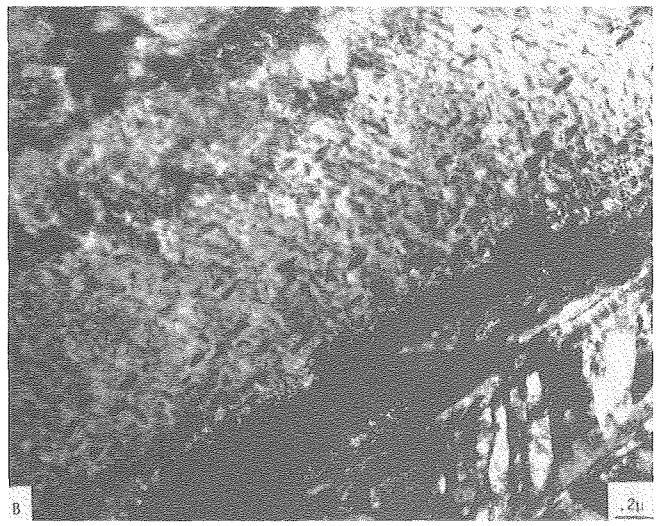

(b)

Fig. 2. Transmission electron micrograph of V-Ni eutectoid steel showing (a) general mixed morphology including carbide precipitation and (b) area of internal carbide precipitation. (XBB 779-8902)

5. RELATIONSHIPS OF PLASTIC STRAIN ENERGY ABSORPTION TO PROPERTIES IN STEELS

R. Turner and G. Haddick

This research has been aimed at evaluating the effectiveness of using plastic deformation in metals to absorb the energy of motion of structures excited by earthquakes. When an earthquake occurs, the resulting ground accelerations can be high enough to set the masses of the structure in motion, inducing large forces throughout the structure. To minimize these forces for economical design, techniques have

been developed that combine the use of a base isolation system and energy absorbing devices. The purpose of this research is to determine how fundamental material properties are related to the response of energy absorbing devices.

The original application of an energy absorbing device, shown in Fig. 1, was made in New Zealand,[1] where the resulting design was optimized for mild steel. The device consisted of a steel bar, restrained at its ends, to which a torque was applied at midspan. The initial tests on this device were run under cyclic strain control. Subsequent tests were made on circular cross-section torsion bars also subjected to cyclic strain control. The materials used in this investigation were 1020 steel and an experimental TRIP steel containing Fe-16Mn-13Cr-1.5-Si-0.1C-0.1N. The tensile test properties of these two steels are listed in Table 1.

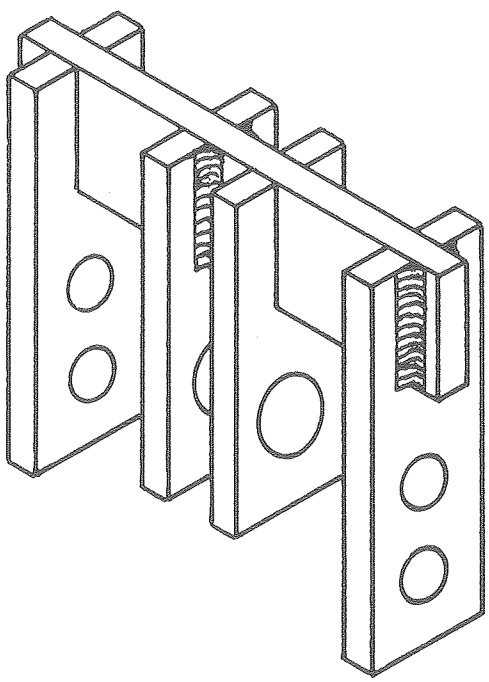

Fig. 1. Energy absorber device constructed of mild steel. Energy was absorbed through plastic twisting of the bar. (XBL 781-4479)

Table 1. Mechanical properties.

	σYS (ksi)	σUTS (ksi)	% El.	% R.A.
1020	48	65	36	59
TRIP Steel	74	147	61	54

Under cyclic deformation, the amount of energy/unit of volume/cycle absorbed by a plastically-deformed material is found from a stress vs. strain hysteresis loop shown schematically in Fig. 2. Important material parameters which influence the area inside the hysteresis loop are 1) the cyclic

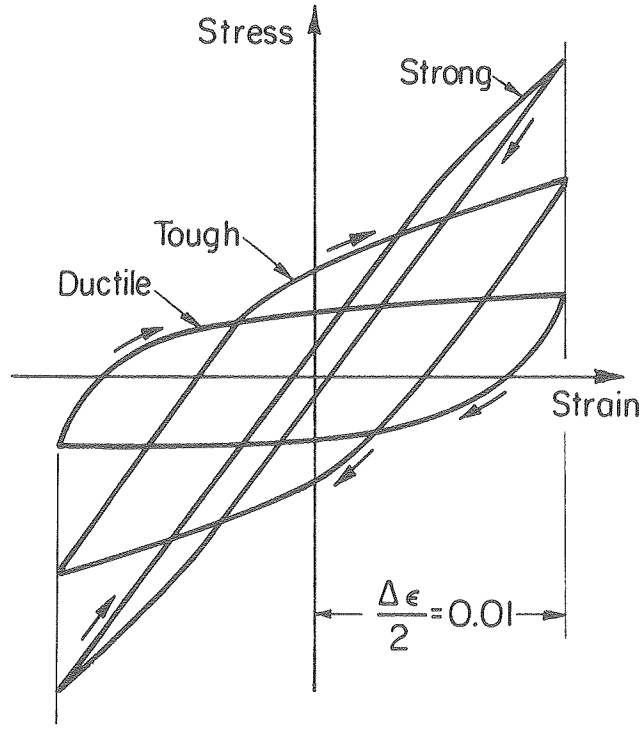

Fig. 2. Hysteresis loops showing idealized stress-strain behavior for different types of materials. (XBL 781-4480A)

yield strength, 2) the work hardening rate, and 3) the total plastic strain. The total work is dependent on the number of loops which at high strains is a function of ductility. Table 2 lists the energy absorbing properties of the two steels along with the life at ± 4% strain. Comparing Tables 1 and 2, it was found that the higher yield strength and ductility were beneficial to the average work per cycle and the cycles to failure. It was also noted from a stress-time history that 1020 steel was cyclically stable after an initial transient hardening while the TRIP alloy showed a very moderate amount of hardening throughout the test. Thus, the slight amount of cyclic hardening shown by the TRIP alloy enhanced the energy absorption and life. Future work is planned to investigate the torsional cyclic response of several materials more completely. This information can then be used to build energy absorbing devices with optimum characteristics.

Table 2. Work done in a cyclic strain controlled test (torsion).

Alloy	Total work done (ft-lbs)	Average work per cycle (ft-lbs)	Cycles to failure
1020	22,000	200	125
TRIP Steel	40,000	220	190

1. P. I. Skinner, J. M. Kelly and A. J. Heine, Earthquake Eng. & Structural Dynamics 3, 289 (1975).

6. MODELING OF THE ELECTROSLAG REFINING PROCESS*

E. Tarapore

Depending on the nature, number and size, nonmetallic inclusions within a steel ingot may have detrimental effects on the mechanical and surface properties of finished products prepared from the ingot. Hence, there has been interest for over a decade in the origins of these inclusions and in ways for removing them. One of the secondary refining processes by which the number and size of nonmetallic inclusions can be reduced is by the Electroslag Refining (ESR) process. However, from a review of the literature, it was concluded that the knowledge of the growth of inclusions and their removal from the molten steel is incomplete. Thus it was proposed to study the growth of nonmetallic inclusions and their removal during electroslag refining.

The object of the research was to determine the relation between impurity levels and inclusion counts in ingots refined by the electroslag process and process variables such as current, power, or melt rate which are typically under the control of the operator. A model was developed that characterized the motion of the molten metal and slag under typical operating conditions. This model can be utilized to predict mass transfer rates which allow a calculation of the impurity levels in the refined ingot.

During ESR, the passage of an electric current through a molten slag, with a higher electrical resistivity than the metal, results in Joule heating of the slag. The unrefined electrode that dips into the slag melts and the molten droplets fall through the slag to collect in a molten metal pool. The refined metal solidifies continuously at its lower surface (due to water cooling of the mold), and is withdrawn steadily. The metal is thereby refined through the intimate contact with the reactive slag. The shapes of the melting electrode and the ingot pool are therefore defined by a dynamic heat and materials balance. Assuming a reasonable geometry for the physical process of ESR, a set of electromagnetic field equations were derived and solved using appropriate boundary conditions. It was possible to obtain fluid flow profiles and turbulence parameters within the ESR unit. Details on the derivation of the equations and their solution for a specific case is reported elsewhere.[1]

---

*Funding by the Army Materials and Mechanics Research Center, Watertown, Massachusetts is acknowledged.

1. E. Tarapore, Fluid Flow in ESR Units, report submitted as part of progress report on a project on "Characterizing Properties of Ultra-high Strength Steels," produced by electroslag refining to Army Materials and Mechanics Research Center, Watertown, Mass.

7. REVIEW OF LOW ALLOY STEEL DEVELOPMENT FOR IMPROVED PROPERTIES

M. S. Bhat and R. M. Horn

Low alloy, ultrahigh strength steels have been commercially important for many decades. In these materials there has always been a compromise in obtaining acceptable strength-toughness combinations. Recent research has been focused on attempts to improve properties such as strength, fracture toughness, and stress corrosion resistance in these steels. A number of different approaches have been taken to improve the toughness without a loss in strength. The most promising of these have been:

a) improving the cleanliness of existing steels,
b) modifying the heat treatment of currently used steels,
c) modifying the composition of the commonly used grades,
d) utilizing new alloy compositions.

A discussion of the research performed at Lawrence Berkeley Laboratory in the first three areas follows.

a) Improvement of the Cleanliness of Steels

An investigation of the properties of an ultrahigh strength steel, 300M, obtained by the ESR process was conducted and the properties obtained were compared to those obtained in a similar steel produced by the VAR process.[1] The properties of both the steels were determined in the quenched and tempered condition. It was found that the steels produced by either process had the same strength levels. However, there was a significant difference in the Charpy impact energies. The room temperature Charpy impact energies are plotted as a function of tempering temperature in Fig. 1. It was observed that the ESR 300M did not exhibit a significant difference in Charpy energies in the transverse and longitudinal directions, whereas there was a substantial difference in the energies with orientation for the VAR 300M. It was also observed that the ESR 300M exhibited higher Charpy energies than did the VAR 300M especially in the transverse direction. These differences between the steels produced by the two processes have been attributed to the lower and finer inclusions present in the ESR 300M and also the finer dendritic macrostructure produced by ESR.

b) Modification of the Heat Treatment of Steels

Most research work in low alloy, ultrahigh strength steels has involved conventional quenching and tempering heat treatments. Although the treatment is relatively simple, it limits the usefulness of the work to section sizes dictated by hardenability considerations. This is a limiting factor for a significant proportion of steel components which are massive. Isothermal and continuous cooling treatments are versatile in the sense that uniform microstructures can be achieved in thicker sections.

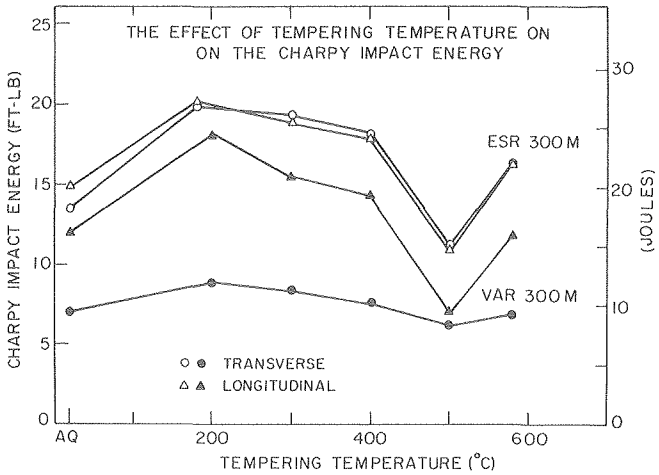

Fig. 1. The effect of tempering temperature on the Charpy impact energy for ESR and VAR 300M.
(XBL 779-6075)

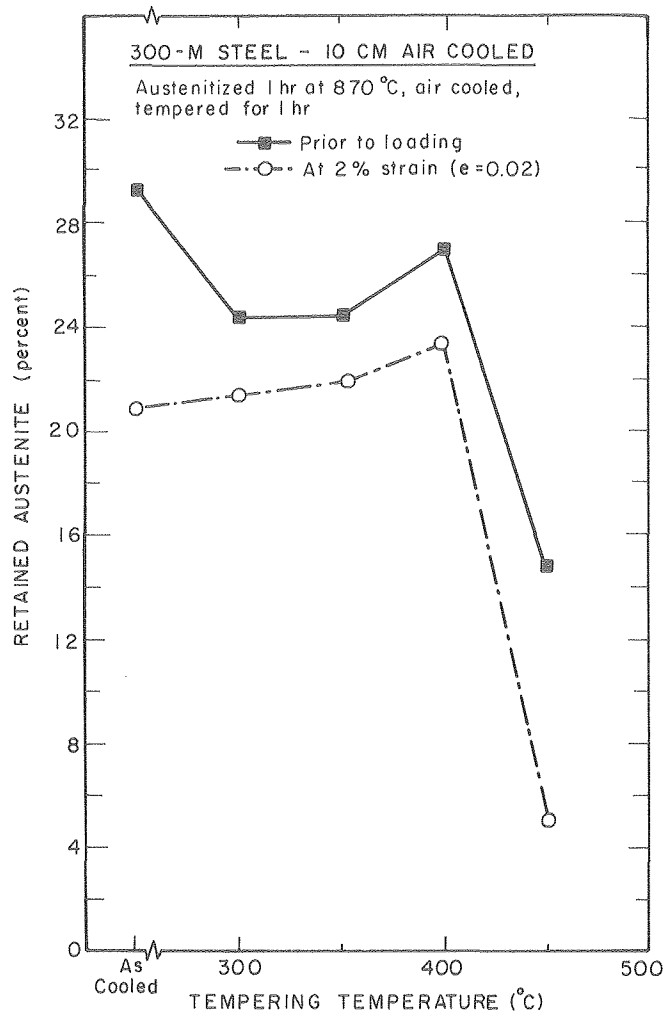

Fig. 2. Retained austenite level as a function of stress and tempering temperature, for 300M steel, cooled to represent a 10 cm slab, normalized.
(XBL 768-7395)

The relationships between microstructure, mechanical, and fracture properties were investigated as a function of section size (up to 15 cm) following air cooling and tempering in 300M steel.[2] A computer model was used to simulate cooling curves obtained in thick sections; this information was utilized to experimentally obtain cooling rates experienced by thick sections and apply them to actual laboratory-size small specimens. The 300M steel studied achieved high strength levels even after very slow cooling. The slow cooling led to high levels of retained austenite (up to 30%). It was found that the stability of this austenite to applied load which changed with tempering treatment, had a major influence on the fracture properties. Specifically, it was determined that if the austenite was stable to stress/strain, the material had good fracture resistance, while if the austenite was unstable, the fracture toughness was poor. This behavior is illustrated in Figs. 2 and 3. Figure 2 shows that on tempering to about 300° C, the stability of the austenite to stress/strain increased and consequently there was an improvement in toughness (Fig. 3). However, beyond about 400° C, the austenite was destabilized by the tempering process itself; there was also a drastic decrease of austenite following tempering at temperatures beyond 400° C. As shown in Fig. 3, there was a large drop in the fracture toughness attendant with this destablization of the austenite. It was concluded that tempered martensite embrittlement which is associated with the precipitation of carbide films was enhanced by the presence of large amounts of unstable austenite.[3] Thus, it was observed that the presence of retained austenite can have a dual effect on toughness. However, proper heat treatment control can lead to good combinations of strength and toughness in thick section steels.

A study similar to the one above has investigated the effect of autenite in isothermally transformed steel in silicon-modified AISI 4330 steel.[4] It was shown that substantial amounts of untransformed austenite were obtained in these steels by combining alloy and heat treatment modification. The amount of austenite could be varied by utilizing the amount of Si in the steel and by isothermally transforming at temperatures above and below the M_S. The stability of the austenite was found to be dependent on the amount of silicon and also on the tempering temperature. (It was found that the stability of the untransformed austenite to stress or strain increased with tempering temperatures up to 350-400° C and then decreased.) The untransformed austenite was retained in the form of thin films around the bainite or martensite laths. The presence of untransformed austenite rich in carbon, obtained by isothermal transformation above the M_S temperature lowered the fracture toughness whereas the austenite obtained by transformation below the M_S (which was less enriched in carbon) appeared to be beneficial to the toughness. It was observed that good combinations of strength and toughness, in isothermally transformed silicon modified 4330 steel could be obtained. A yield

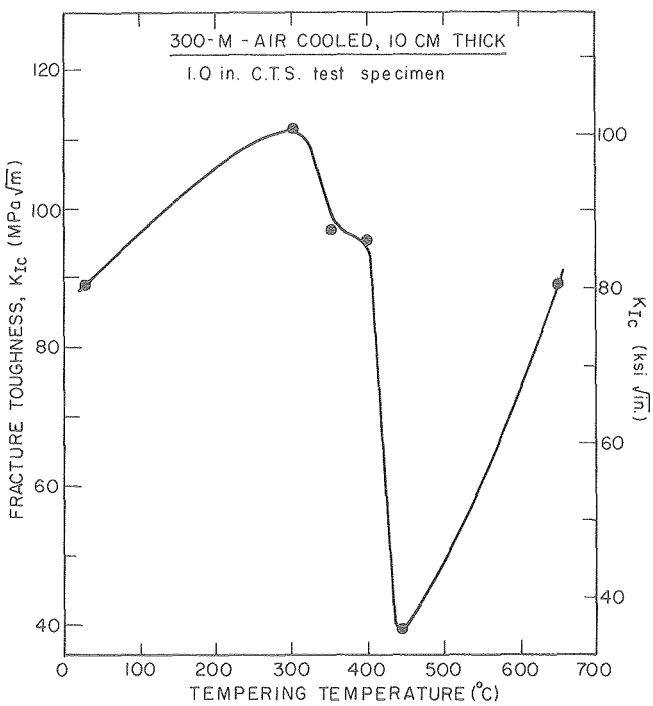

Fig. 3. Fracture toughness vs. tempering temperature for 300-M steel, cooled to represent a 10 cm slab, normalized. (XBL 768-7349)

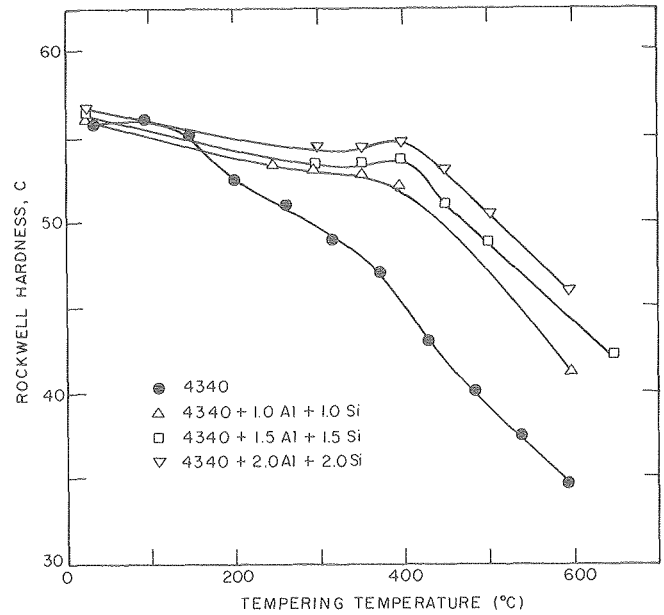

Fig. 4. Plot of Rockwell hardness (R_C) vs. tempering temperature for AISI 4340 and 4340 + Al steels. (XBL 762-6523)

strength—fracture toughness combination of 200 ksi—100 ksi/in. was measured. In addition, isothermal transformation below M_s was shown to give a significant improvement in subcritical crack growth resistance in hostile environments.[5]

c) Modification of the Composition of Commonly Used Grades of Steel

An increase in the fracture toughness at high levels of strength can also be achieved by modifying the composition of an existing steel using inexpensive alloying modifications. Such a study was conducted on the effect of aluminum, and aluminum plus silicon additions to AISI4340 steels.[6] It was observed that the softening which normally occurs on tempering AISI4340 steels beyond 200° C was retarded by the additions of aluminum or combinations of aluminum and silicon, with the combined additions being more effective. The tempering behavior of some of these steels are shown in Fig. 4 from which it is observed that the tempering was retarded to temperatures as high as 600° C. From an investigation of the tempering response and the microstructures, at the electron optical level, of these steels it was concluded that additions of aluminum and combinations of aluminum and silicon to AISI4340 steel resulted in

(1) the extension of the first stage of tempering to higher tempering temperatures.
(2) an increase in the temperature for the second stage of tempering.
(3) the retardation of the third stage of tempering to temperatures greater than about 350-400° C depending upon the alloy content.
(4) an inhibition of the growth rate of carbides.

An example of the microstructure of a 4340+3Al steel tempered at 400° C is shown in Fig. 5. These modified steels exhibited:

(1) an increase in strength and toughness
(2) an extension of the tempered martensite embrittlement range to higher temperatures.

Figure 6 shows a comparison of one of the experimental steels with base 4340 steel showing the mentioned effects. Optimum yield strength-fracture toughness combinations of 245 ksi-80 ksi/in., significantly higher than those achieved in commercial low alloy ultrahigh strength steels, were achieved.

The microstructural study of the modified steels led to the conclusion that optimum combinations of strength and toughness are obtained by the presence of

(1) fine dispersions of carbides in dislocated martensite
(2) retained austenite films at lath boundaries of the "right" stability to stress/strain
(3) smaller prior austenite grain sizes.

No investigations were conducted on new alloy compositions. However, other investigators[7,8] have shown that this approach is also viable for improving

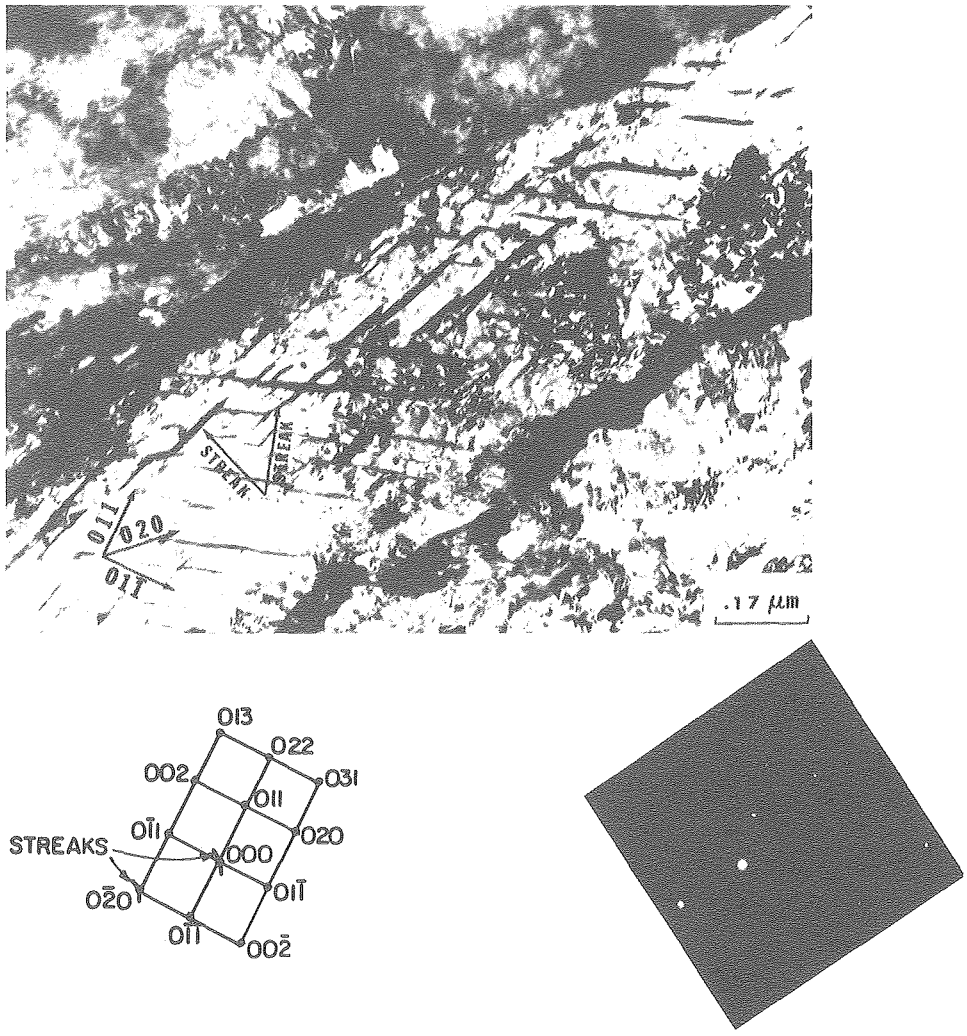

Fig. 5. Transmission electron micrgraph obtained from 4340 + 3A1 steel in the quenched and tempered at 400° C condition. [Close to (100) m orientation]. (XBL 7612-11322A)

properties of steels. Thus, it can be concluded that the toughness of low alloy ultra high strength steels can be improved through proper refining techniques, and that, depending on the particular application, improved combinations of strength and toughness can be obtained through proper alloy modification and heat treatment.

---

1. T. Lechtenberg, (M.S. thesis), LBL-6686. (Partial funding by the Army Materials and Mechanics Research Center, Watertown, Massachusetts is acknowledged.)

2. R. M. Horn, (Ph.D. thesis), LBL-5787, December 1976.
3. R. M. Horn and R. D. Ritchie, accepted by Met. Trans., LBL-6607, November 1977.
4. G. Kohn, (Ph.D. thesis), LBL-5466, November 1976.
5. M. H. Castro Cedẽno, (M.S. thesis), LBL-6012, May 1977.
6. M. S. Bhat, (Ph.D. thesis), LBL-6046, February 1977.
7. E. A. Wylie, (M.S. thesis), LBL-4574, January 1976.
8. G. Thomas, Iron and Steel Inst. 46, 451 (2973).

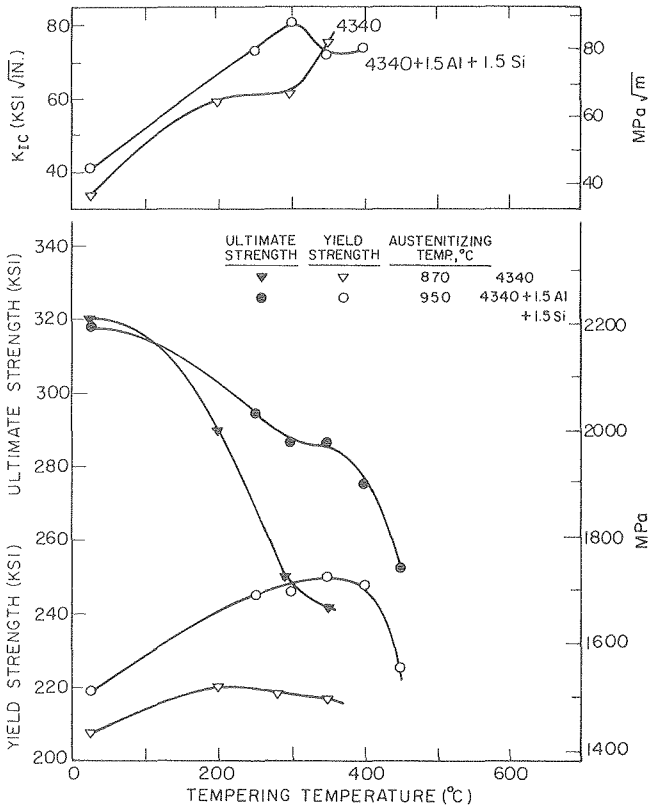

Fig. 6. Fracture toughness, ultimate tensile strength, and 0.2% offset yield strength as a function of tempering temperature for 4340 and 4350 + 1.5Al + 1.5 Si steels. (XBL 762-6525)

Conclusion

This is the Parker/Zackay's last contribution to the Annual Report of the Materials and Molecular Research Division of the Lawrence Berkeley Laboratory. The past decade and a half have been, for us, a rich and rewarding experience. We take this occasion to express our deep gratitude for the pleasure of having worked in MMRD and wish it and all of LBL long and continued success.

8. 1977 PUBLICATIONS AND REPORTS

Earl R. Parker, Victor F. Zackay and Associates

Journals and Books

1. E. R. Parker, Interrelations of Compositions, Transformation Kinetics, Morphology, and Mechanical Properties of Alloy Steels, Met. Trans. 8A, 1025 (1977).

2. R. O. Ritchie, M. Castro-Cedeno, E. R. Parker, and V. F. Zackay: Effects of Silicon Additions and Retained Austenite on Stress Corrosion Cracking Behavior of Commercial Ultra-High Strength Steels in Aqueous Solution, Met. Trans. 9A, January 1978.

3. R. O. Ritchie, Influence of Impurity Segregation on Temper Embrittlement and on Slow Fatigue Crack Growth and Threshold Behavior in 300-M Ultra-High Strength Steel, Met. Trans A 8A, No. 7, 1131 (1977).

4. R. O. Ritchie, B. Francis and W. L. Server, Author's reply to: Discussion of "Evaluation of Toughness on AISI 4340 Steel Austenitized at Low and Higher Temperature," Met. Trans. A 8A, No. 7 1197 (1977).

5. R. O. Ritchie, Effects of Strength and Grain Size on Near-Threshold Fatigue Crack Propagation in Ultra-High Strength Steel, in Proceedings of the 4th International Conference on Fracture, D. M. R. Taplin, Ed., Waterloo, June 1977, vol. 2, pp. 1325-1331.

6. R. O. Ritchie, Near-Threshold Fatigue Crack Propagation in Ultra-High Strength Steel: Influence of Load Ratio in Cyclic Strength, J. of Eng. Mat. and Tech. Trans. of ASME, Series H, Vol. 9i, no. 3 pp. 195-204, July 1977.

7. R, O. Ritchie, Influence of Microstructure on Near-Threshold Fatigue Crack Propagation in Ultra-High Strength Steels, Met. Sciences, vol. 11, no. 8/9, p. 368-381, Aug/Sept. 1977.

8. M. F. Carlson and R. O. Ritchie, On the Effect of Prior Austenite Grain Size on Near-Threshold Fatigue Crack Growth, Scripta Met. 11, no. 12, December 1977.

9. R. O. Ritchie and R. M. Horn, Further Consideration on the Inconsistency in Toughness Evaluation of AISI 4340 Steel Austenitized at Increasing Temperatures, Met. Trans. 9A, no. 3, March 1978.

LBL Reports

1. G. Kohn, Effects of the TRIP Phenomenon on the Toughness of Heat Treatable Alloy Steels, (Ph.D. thesis), LBL-5466, November 1976.

2. R. J. Kar, Optimization of Strength and Toughness in a High-Carbon Steel, (M.S. thesis), LBL-5448, December 1976.

3. N. J. Kar, Interrelationships Between Thermal History and Mechanical Properties of a Secondary Hardening Steel, (M.S. thesis), LBL-5449, December 1976.

4. R. M. Horn, The Influence of Retained Austenite on the Thick-Section Mechanical Properties of a Commercial Low Alloy Ultrahigh Strength Steel, (Ph.D. thesis), LBL-5787, December 1976.

5. Ana-Maria Llopis, Isothermal Transformation Studies on the Effect of Alloying Elements (Mo, Ni, Cr, Mn, Al, Si, Co) on the Kinetics of the Austenite to Bainite Transformation, (Ph.D. thesis), LBL-6068, December 1976.

6. L. D. Thompson, The Mechanical Properties and Microstructural Relationships in Iron-Manganese-Chromium Alloys, (M.S. thesis), LBL-6234, January 1977.

7. M. S. Bhat, The Influence of Al and Al Plus Si Additions on the Mechanical Properties of AISI 4340 Steel, LBL-4920, February 1977.

8. M. S. Bhat, Microstructure and Mechanical Properties of AISI 4340 Steel Modified with Aluminum Plus Silicon, (Ph.D. thesis), LBL-6046, February 1977.

9. Mario Castro-Cedeno, The Effect of Silicon on the Environmental Cracking Behavior of a High Strength Steel, (M.S. thesis), LBL-6012, May 1977.

10. Lorin Brass, The Effect of Microstructure of Ductile Alloys in Solid Particle Erosions, (M.S. thesis), LBL-6277, June 1977.

11. R. M. Horn and R. O. Ritchie, Mechanisms of Tempered Martensite Embrittlement in Ultra-High Strength Steels, LBL-6607, November 1977.

12. T. Lechtenberg, A Comparison of the Microstructure and Mechanical Properties of 300-M Steel Manufactured by the Vacuum Arc Remelt and the Electroslag Remelt Processes, (M.S. thesis), LBL-6686, December 1977.

UCID Reports

1. R. M. Horn, E. R. Parker, V. F. Zackay and A. V. Levy, Low Alloy Steels for Thick Wall Pressure Vessels, Quarterly Report, UCID-3898, February 1977.

2. M. Dilip Bhandarkar, M. S. Bhat, Victor F. Zackay and Earl R. Parker, Wear Resistant Alloys for Coal Handling Equipment, Quarterly Report, UCID-3921, Jan.-March 1977.

3. R. M. Horn, E. R. Parker and V. F. Zackay, Low Alloy Steels for Thick Wall Pressure Vessels, Quarterly Report, UCID-3921, May 1977.

4. R. M. Horn, E. R. Parker and V. F. Zackay, Low Alloy Steels for Thick Wall Pressure Vessels, Quarterly Report, UCID-3943, August 1977.

5. M. S. Bhat, Victor F. Zackay and Earl R. Parker, Wear Resistant Alloys for Coal Handling Equipment, Quarterly Report, UCID-3945, August 1977.

6. R. M. Horn, Design Criteria for Pressure Vessel Steels, Topical Report, UCID-3992, December 1977.

7. R. M. Horn, E. R. Parker and V. F. Zackay, Low Alloy Steels for Thick Wall Pressure Vessels, Yearly Report, UCID-3993, Oct. 1976-Sept. 1977.

8. M. S. Bhat, Victor F. Zackay and Earl R. Parker, Wear Resistant Alloys for Coal Handling Equipment, Yearly Report, UCID-3994, Oct. 1976-Sept. 1977.

Presentations

The following papers were presented at the Annual Meeting of the Metallurgical Society of the AIME held at Atlanta, Georgia from March 6-10, 1977.

1. E. R. Parker, "Interrelations of Composition, Transformation Kinetics, Morphology, and Mechanical Properties of Alloy Steels", The 1977 Institute of Metals Lecture.

2. R. O. Ritchie, M. Castro-Cedeno, V. F. Zackay and E. R. Parker, "Stress-Corrosion Cracking in Ultra-High Strength Steels: Effects of Retained Austenite and Silicon Modifications to AISI4340 Steels."

3. R. M. Horn and R. O. Ritchie, "Effects of Microstructure on Tempered Martensite Embrittlement in AISI4340 and 300-M Alloy Steels."

4. R. O. Ritchie, "Influence of Microstructure and Mean Stress on Near-Threshold Fatigue Crack Propagation in Steels."

5. R. O. Ritchie, "Influence of Impurity Segregation and Temper Embrittlement on Near-Threshold Fatigue Crack Propagation in 300-M Steel."

6. V. F. Zackay, E. R. Parker and G. Thomas, "The Control of Retained Austenite in Alloy Steels."

Paper presented at the WESTIC Conference held at Los Angeles, CA from March 14-17, 1977.

7. L. D. Thompson, E. R. Parker and V. F. Zackay, "The Development of Nickel-Free Austenitic Stainless Steels."

Paper presented at the ASM/OTA/FMS Conference on Materials Substitution held at Chicago on September 27-28, 1977.

8. G. Haddick, L. D. Thompson, E. R. Parker and V. F. Zackay, "The Development of Nickel-Free Austentic Stainless Steels for Ambient and Cryogenic Applications."

Paper presented at the First International Conference on Materials for Coal Conversion and Utilization held at Gaithersburg, Md. from October 11-13, 1977.

9. R. M. Horn, "Developments in Low Alloy Steels for Thick Walled Pressure Vessels."

The following papers were presented at the Fall AIME Meeting held at Chicago, Ill. from October 24-27, 1977.

10. T. Lechtenberg, M. S. Bhat and V. F. Zackay, "Design of Wear Resistant Matrix Steels."

11. N. Kar, M. S. Bhat and V. F. Zackay, "Investigations of Isothermal Transformations in Secondary Hardening Steels."

12. W. M. Garrison, M. S. Bhat and E. R. Parker, "The Effect of Si and Al Additions on the Mechanical Properties of Secondary Hardening Steels."

13. R. J. Kar, E. R. Parker, R. M. Horn and V. F. Zackay, "Modified Low Alloy Pressure Vessel Steels."

14. J. S. Kallend, "Prediction of Yield Loci for Textured Sheets of Cubic Metals."

15. J. A. Wert, E. R. Parker and V. F. Zackay, "Elimination of Precipitate Free Zones in Precipitation Hardening Fe-Nb Alloys."

c. Relations Between Dislocations, Point Defects and Properties of Metal

Jack Washburn, Principal Investigator

1. ECONOMIC UTILIZATION OF SOLAR ENERGY

a. Characterization of Spectrally Selective Black Chrome Surfaces

Carl M. Lampert

The spectral selectivity mechanism of black chrome surface coatings for solar energy collection is being investigated to gain a better understanding of this property and its relationship to microstructure. The work may make it possible to improve this coating or to create new, inexpensive coatings which perform in a similar manner.

Black chrome exhibits excellent energy collection properties with few disadvantages. It has uses for residential heating and exhibits a potential for industrial usage, particularly in process steam production.

Spectral selectivity exists when optical properties of a layered material, consisting of an absorber on a metal, vary greatly from one wavelength region to another, such as from the visible to the infrared regions. As a result of this variation, a surface can efficiently absorb the solar radiation over the visible and near infrared wavelengths, while exhibiting poor radiating properties over far infrared wavelengths. The later wavelength region corresponds to the characteristic emission spectrum over which a hot solar absorber will radiate during its operation. These wavelength relationships are depicted in Fig. 1; superimposed on the energy spectra is the change in optical reflectance for a typical black chrome absorber. Reflectance values can be used to derive other parameters such as solar absorptance and infrared emittance. A selective surface such as black chrome will absorb and retain a greater fraction of the incidence solar energy than a non-selective black painted surface because it loses less energy by radiation.

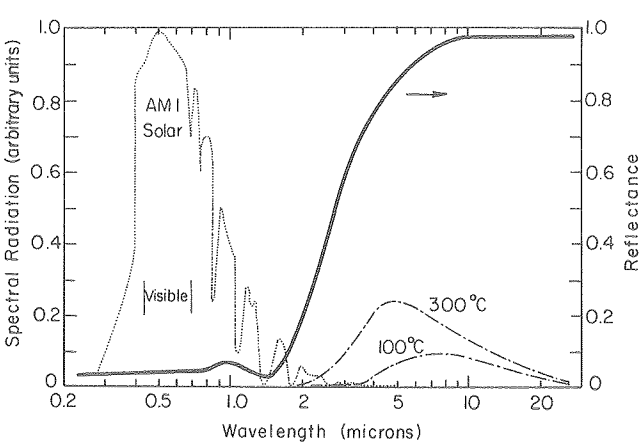

Fig. 1. Wavelength relationships between black chrome spectral reflectance, the solar spectrum (air mass 1) and black body spectra (100°C, 300°C). (XBL 775-5462A)

In the first phase of this study, spectral reflectance measurements were performed on several variations of a black chrome absorber; a schematic cross section is shown in Fig. 2. For reference these samples were compared to a black painted absorber. The best selectivity was found for 0.7 microns of black chrome on nickel plated surfaces and 1.0 micron of black chrome on copper.

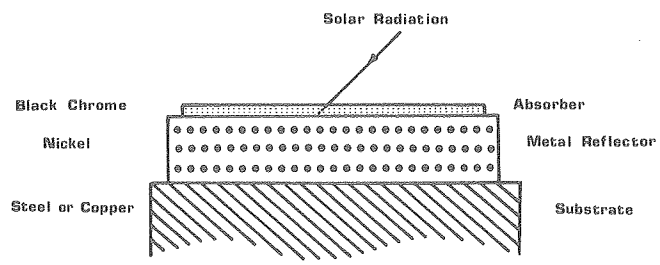

Fig. 2. A cross section of an idealized black chrome-metal tandem selective absorber. The black chrome layer provides the solar absorber and the metal layer gives high reflectance in the thermal infrared wavelengths. (XBL 7712-11144)

In the second phase of the work both scanning and transmission electron microscopy were employed to study the microstructure and chemical composition. It was found that black chrome consists of a very fine distribution of metallic chromium particles (with mean diameter of 139 Å), suspended in an oxide of chromium. These particles are, in turn, agglomerated into larger particles within the 0.05 - 0.3 micron size range. These larger clusters formed a network which constituted the surface coating.

Figure 3(a) and (b) shows two transmission electron microscope photographs of this surface. In (a) a typical bright field micrograph is presented. The large white areas in the picture are holes in the electron microscope foil produced during the thinning process. The dark field picture and diffraction pattern b reveals the fine distribution of chromium particles, appearing as while spots. It was concluded that black chrome has a mechanism of spectral selectivity which is likely to be a combination of multiple scattering, according to a generalized Maxwell-Garnett theory and semiconductor effects. Future work will attempt to correlate changes in this microstructure during annealing with changes in optical properties.

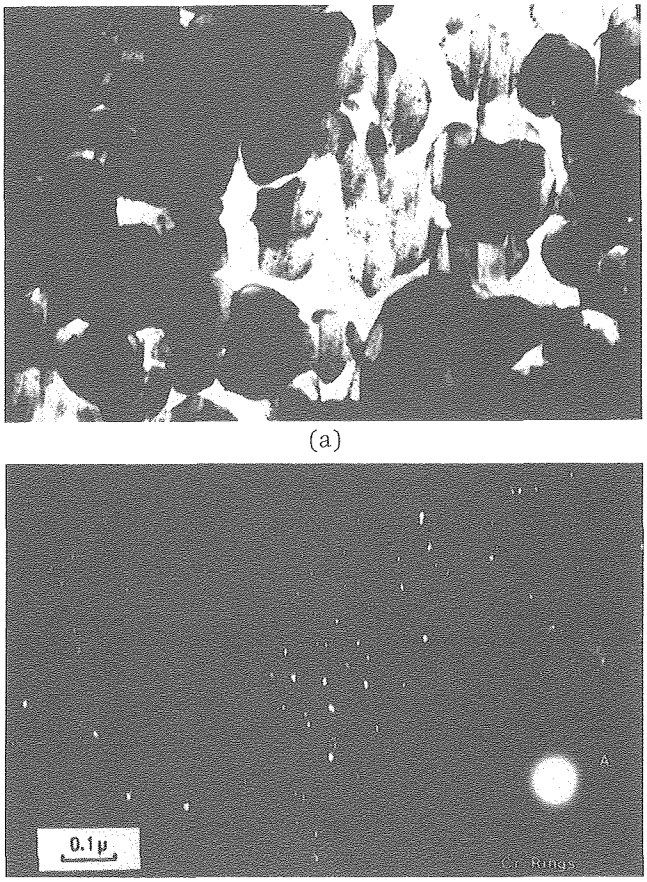

(a)

(b)

Fig. 3. An agglomeration of chromium particles with matrix material viewed by transmission electron microscopy at 100 kV; (a) a bright field showing black chrome islands remaining after ion thinning; (b) dark field of region a, and diffraction pattern, showing metallic chromium particles. (XBB 770-9646)

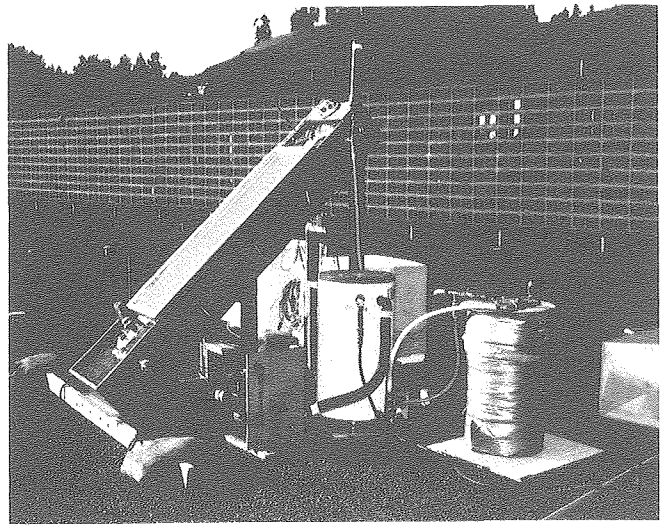

Fig. 4. Solar test collector in operation. (CBB 770-9662)

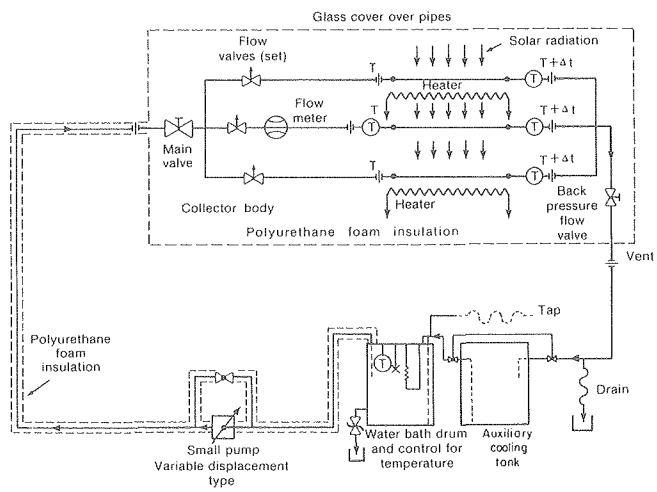

Fig. 5. Flow chart for test collector showing fluid flow and temperature monitoring design details. (XBL 7611-4465A)

b. Solar Test Collector for Evaluation of Collector Coatings

Carl M. Lampert

Our solar test collector was designed for the testing of thermally absorbing coatings under controlled conditions. With this collector, different coatings, including various types of black chrome surfaces, could be evaluated and compared under realistic operating conditions. A photograph of this collector in operation is shown in Fig. 4.

The design consists of a collector fed by a controlled temperature fluid within the range of 25-90°C. This temperature is maintained by a custom electronic controller. A small variable flow pump circulates water through three collector pipes at selected flow rates. Strip heaters coupled with a differential temperature controller compensate for edge losses in the collector. A flow chart is shown in Fig. 5 exemplifying the pertinent details of this design.

Of the many absorbers that were designed, three representatives of black chrome surfaces and one black painted coating were analyzed by the collector in detail, shown in Fig. 6. Collection efficiencies as high as 77 and 75% ($\Delta T = 0$) were obtained, respectively, for 1.0 micron black chrome on copper and nickel plated steel. The highest (a_i/e_i, 20°C) ratio measurements were 20.3 and 18.5 for 0.7 micron black chrome on nickel plated polished steel and 1.0 micron black chrome on copper. The lowest loss coefficients (U_L) ranged from 3.3 - 3.6 W/m^2 °C for all black chrome/metal surfaces with the highest being 8.4 W/m^2 °C for the black paint/metal samples.

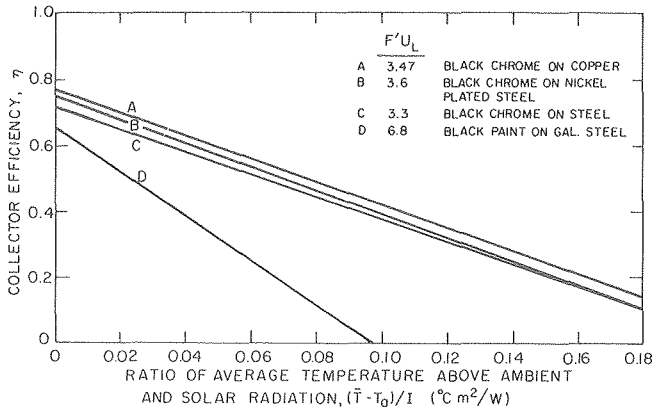

Fig. 6. Comparative efficiencies for four absorber surfaces, measured by the solar test collector. The various slopes represent relative collector losses due to the character of each absorber. The intercept on the abscissa indicates the operating range of each coating. (XBL 774-5328A)

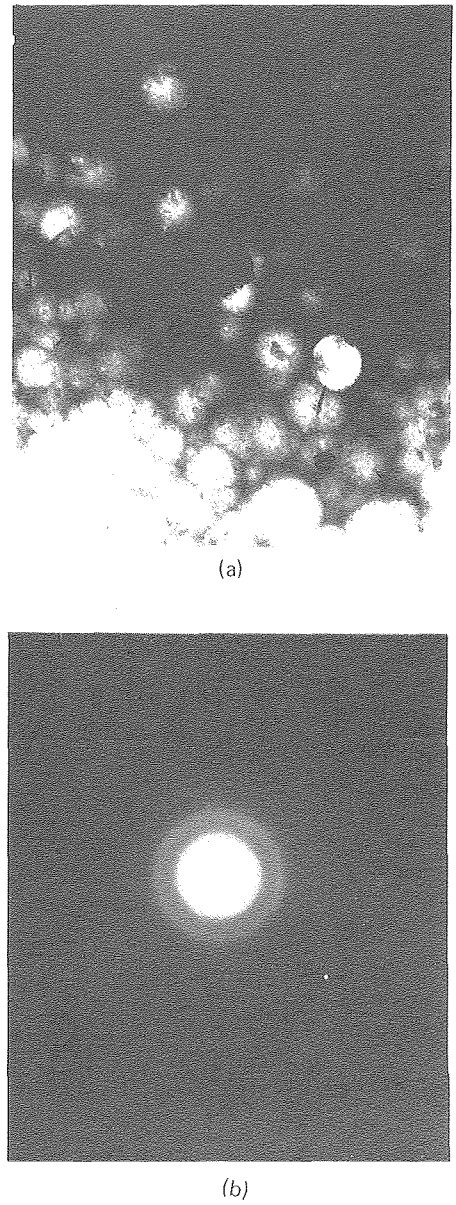

Fig. 7. (a) Transmission electron micrograph of amorphous silicon and (b) its diffraction pattern. (XBB 783-2717)

c. Recrystallization of Evaporated Amorphous Silicon Layers

Donald Huo

We have converted evaporated amorphous Si films into crystalline Si films with a focused electron beam. The films were studied by transmission electron microscopy and x-ray diffraction. These studies indicate that epitaxial films were produced for silicon deposited on silicon and suggest that a crystallization technique using a scanned electron beam focused to a slit image may be useful in preparing large-grain Si films for photovoltaic cells.

Equipment has been developed which permits a narrow electron beam heating zone to be swept across a water cooled moving stage inside a 10^{-7} Torr vacuum system. This will permit migration of the amorphous-crystalline interface in a very steep temperature gradient. It is hoped that conditions can be achieved which will result in growth of large grains at low temperature, thus minimizing diffusion of impurities from the substrate material.

The vacuum apparatus consists of a strainless 18-in. diameter and 30-in. height steel bell jar, pumped by a 6-in. oil diffusion pump with a LN_2 cold trap. Base pressure of this system is routinely in the range of 10^{-7} Torr. Silicon is evaporated from a water-cooled copper crucible by a 10 kV electron beam with a source to substrate distance of 6 inches. The evaportant beam was shuttered mechanically. Figure 7 shows the microstructure of amorphous evaporated thin film and its diffraction pattern. Figure 8 shows the microstructure and diffraction pattern of epigrowth of a thin film deposited on a (111) single crystal silicon substrate after heating to 1250°C for 5 minutes.

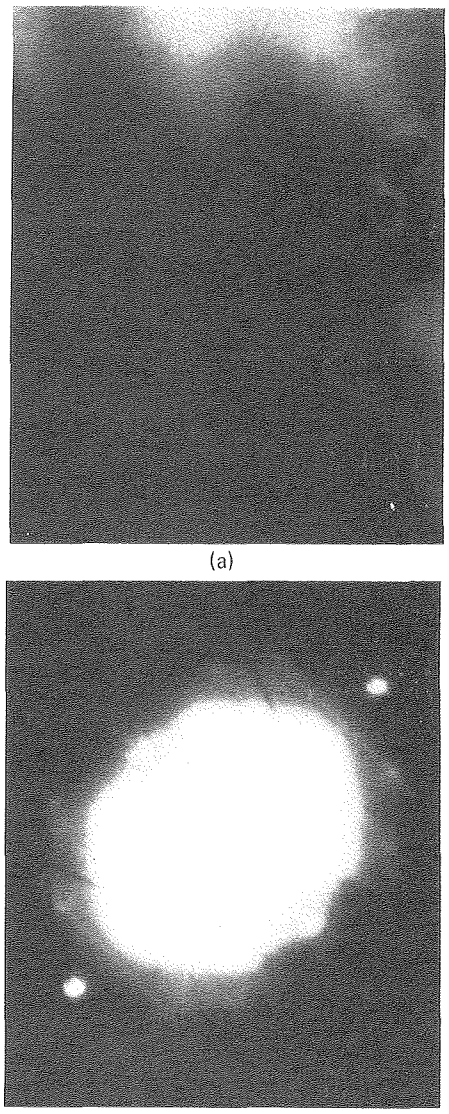

(a)

(b)

Fig. 8. (a) Transmission electron micrograph of epigrowth of amorphous silicon thin film on (111) single crystal silicon substrate heated to 1250°C for 5 minutes and (b) its diffraction pattern.
(XBB 783-2718)

d. Zinc Diphosphide as a Semiconductor for Solar Cell Use

Tom Mowles

If photovoltaic conversion of sunlight to electric power is ever going to make a major contribution to total electric power needs it will probably be a thin film device which can be made on a metal foil substrate by an automated process using cheap abundantly available elements. The efficiency of solar energy conversion to electric power will probably have to be greater than 10%. So far no known technology can meet all of these requirements. It therefore seemed to be worthwhile to make a systematic search of the periodic table for possible new semiconductor materials. Among the many oxides, sulfides and phosphides that were considered monoclinic, ZnP_2 appeared to be one that might be a useful new semiconductor with a chance of being used in a solar cell that could meet all the above conditions:

a) Both elements are currently used in such large quantities that even large scale use in solar cells would hardly be noticed.

b) The direct band gap for ZnP_2 is 1.35 eV, which is an ideal match for the solar spectrum.

c) Crystals of the material are stable in air for long periods at 200°C retaining their black color.

During the past year small crystals of the material have been grown by heating a quartz tube containing the two elements in a temperature gradient, 500°C at the cool end and 1050°C at the hot end. During heating some of the phosphorous evaporates from the charge which has been placed at the hot end and condenses at the cold end; the rest reacts with the zinc, probably forming a mixture of Zn_3P_2 and ZnP_2. On holding at temperature ZnP_2, crystals are nucleated and grow near the center of the tube. At this temperature almost all of them have the black monoclinic structure which is stable at high temperature and metastable at lower temperatures.

The stability and electrical optical properties of these crystals are being investigated to further evaluate their possible usefulness as a solar cell material. The conditions for growth are being studied to determine whether or not it will be possible to deposite the material as a continuous thin film.

2. ION IMPLANTATION IN SILICON

a. On the Nature of the Amorphous Layer

Robert Drosd

It is well known that very high dose ion implantation of silicon can result in an amorphous layer due to severe radiation damage. However, the annealing of this amorphous layer with its complicated dependence on such variables as implant species, implantation dose and temperature, crystal orientation, and thermal history is not well understood. We have looked at the "as-implanted" specimens for differences in structure that may determine the mechanism and rate with which subsequent recrystallization takes place.

Several general features were found in all unannealed specimens. In our experiments the specimens, either of the (100)or (111) orientation, were implanted with P^+ ions at 100 kV, $2\mu A/cm^2$, $2 \times 10^{16}/cm^2$. Two implantation temperatures, 77 and 300 K, were studied. A single voltage 100 kV implant results in a buried amorphous layer sandwiched between a thin crystalline layer at the surface and the underlying crystalline substrate. At the very edge of the wedge shaped TEM specimen a single crystal diffraction pattern is found which confirms that the top-

most layer is crystalline. In thicker parts of the specimen the amorphous material is encountered and the SAD pattern consists of several diffuse rings as well as crystalline spots. In these regions many small (100-200 Å) dark spots are also seen in bright field (light spots in DF). We believe these spots are in the crystalline-amorphous interface since they are not found in specimens where the amorphous layer can be observed alone with the crystalline material stripped away. Also these spots are strongly visible in dark field only when a crystalline reflection is selected rather than a diffuse ring arising from the amorphous material. We feel that these spots arise from crystalline zones, at the amorphous interface, which are highly strained but still of nearly the original orientation.

Although the crystal orientation may strongly effect the annealing behavior of an amorphous layer, we observe no effect on the unannealed microstructure. The density, size, and depth of the dark spots are the same for both orientations studied. The intensity and spacing of the diffuse rings in the diffraction pattern are also unchanged.

The implantation temperature may also strongly effect the annealed structure. However, in the unannealed specimens the only effect of this variable was that for the 77 K implantation the dark spots were somewhat smaller.

It appears that the "as-implanted" microstructure of the amorphous layer is not strongly affected by the implantation conditions, at least for the two variables studied here. This is in sharp contrast to the annealed structures which may undergo radical changes when the implantation temperature or crystal orientation is changed. This seems to rule out the possibility that the different annealed structures are a result of different "as-implanted" structures. Of course there are other important implantation/annealing parameters which we have not yet studied for which the above conclusion may not hold. Further work on these variables is in progress.

b. Defects in (111) and (100) Phosphorus Implanted Wafers

Robert Drosd

During high dose ion implantation of silicon an amorphous layer is formed. For electronic device applications this layer must be annealed to restore electrical properties. A systematic study has been undertaken to categorize and hopefully explain the complex relationships between the annealed structure and the implantation conditions such as crystal orientation, implantation temperature and dose, thermal history, and implant species. Many similar attempts have been made in the past but many have suffered from unawareness of the large number of variables that vitally affect the types of defects created during annealing.

Recently we have observed that for a room temperature implantation of 2×10^{16} P^+/cm^2 that both the (100) and (111) orientations anneal in an identical

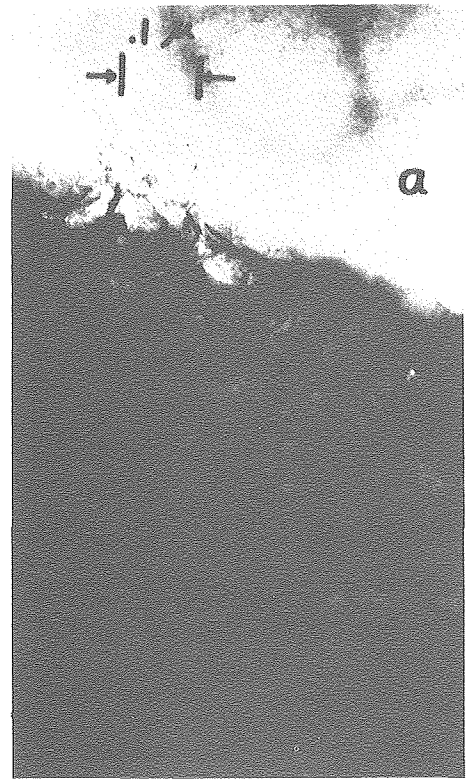

Fig. 1. Bright field micrograph of as-implanted silicon Region (a) shows crytalline layer. As thickness increases in Region (b) the amorphous layer begins to overlap the surface. In Region (c) the amorphous layer is now sandwiched between crystalline material. (XBB 783-2719)

fashion [see Fig. 1 (a) and (b)]. Perfect dislocation loops are nucleated and grow to large sizes where they intersect one another and form a stable network. This is in sharp contrast to the literature where it is found that the annealing mechanism and rate are markedly different for these two orientations. However, we have found that if the implantation takes place at 77 K then the (111) specimens will contain a high density of microtwins while the (100) specimen has only a very low density of faulted dislocation loops [see Fig. 2(c) and (d)]. This observation is in agreement with the literature. This is just one example of the complexities of the annealing behavior of the amorphous layer and demonstrates the necessity to fully specify all implantation conditions to be able to obtain reproducible results.

The above-mentioned microstructure of a low density of faulted dislocation loops would be quite acceptable for electronic device applications but the low temperature implantation that is required for this is inconvenient and expensive. Hence it is of industrial as well as academic interest to understand this type of behavior and devise a simple implantation/annealing procedure that results in a low defect density.

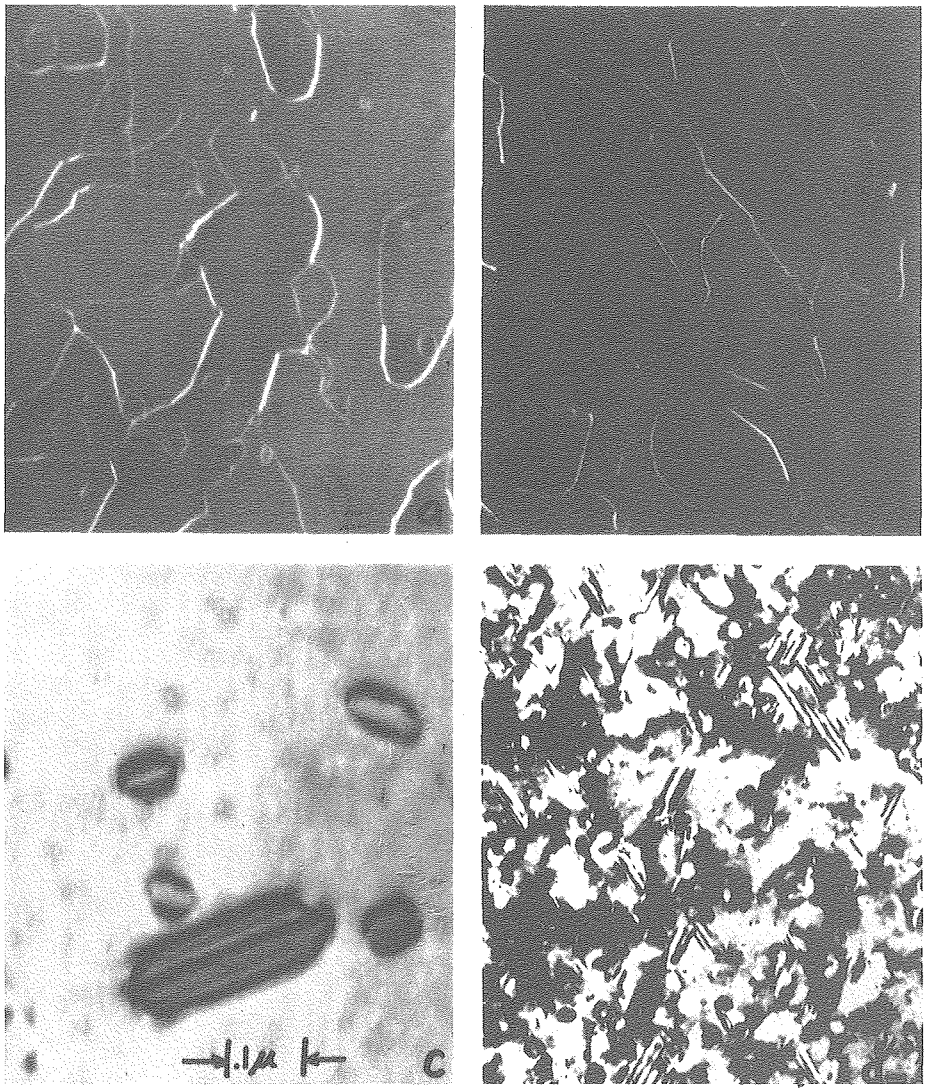

Fig. 2. Microstructures after high temperature annealing (a) weak beam (111) orientation, (b) weak beam (100) orientation, (c) bright field (100) orientation (d) bright field (111) orientation. (XBB 783-2720)

c. A Three-Stage Model for the Development of Secondary Defects in Ion Implanted Silicon

K. Seshan

The model applies to silicon which has been implanted to a dose less than that required to form a continuous amorphous layer so that the integrity of the crystal is never destroyed at any depth. It is suggested that the Frenkel pairs formed by ion impacts result in submicroscopic clusters of vacancy and interstitial type, most of which are stable enough to persist up to 900 K during post-implantation annealing. Upon heating to higher temperatures the smallest clusters emit mobile point defects and the largest clusters grow and covert to dislocation loops. Because interstitials are in excess, due to the presence of the implanted atoms, vacancy loops disappear leaving only interstitial loops. Experimental observations after annealing to above 1100 K confirm that all loops are interstitial type and that the total loop area per unit area corresponds closely to that expected if a number of interstitial atoms equal to the number of implanted atoms are assumed to have formed the loops.

One implication of the above is that, in spite of the high mobility of vacancies and interstitials in the temperatures range considered, the annealing processes in vacuum or dry nitrogen appear to be almost entirely confined to the heavily damaged region which is about 350 Å thick buried about 1000 Å below the surface. It is assumed in the model that during room temperature implantation and during the lowest temperature of post-

implantation annealing, direct recombination of interstitials and vacancies and clustering of both defects predominate and that relatively few defects escape from the immediate vicinity of the heavy damage, even in the second stage almost all the mobile point defects that are formed at the smallest clusters must be trapped after a short migration at another larger cluster.

3. FIELD DESORPTION MICROSCOPY

a. Imaging of Large Molecules

Greg Hirsch

A modification of the relatively new technique of field desorption microscopy may make it possible to obtain shadow images of large organic or biomolecules and therefore get direct information concerning their structure. "Seeing" large molecules has been tried frequently in the past with other techniques such as field ion microscopy, field emission microscopy and transmission electron microscopy with very limited success. The imaging of large molecules by standard field ion microscopy usually fails because the electric field strength must be so high that the molecules are pulled off the surface of the field ion tip. However, by using an irradiated diamond tip we have obtained some limited success; the bonding of an organic molecule to the diamond surface is usually strong.

The idea of the present experiment is to use a material on the field ion tip that field evaporates at an extremely low field strength. The chance that a large molecule will remain on such a surface while atoms are field evaporated around it should be much greater.

During the past year a field ion microscope has been converted into a field desorption microscope by the installation of a chevron microchannel plate which has a useful gain of over 10^7. This permits the observation and photography of even single field evaporated ions. To produce shadow images of large molecules a standard Pt or W field ion tip will be coated with a layer of alkali metal a few hundreds of Å thick. The large molecules can be embedded in the alkali metal.

So far, it has been possible to get desorption images from potassium coated tips. The next step after some contamination problems have been oversome will be an attempt to imbed an organic molecule of known distinctive shape and look for molecular shadows in the desorption patterns. If some atoms field evaporate through the molecule it may even be possible to get some information concerning internal structure.

4. ENVIRONMENTAL RESEARCH

a. Transmission Electron Microscope Study of the Deformation of Asbestos in Relation to Environmental Pollution--An Example Using Automobile Brake Drum Dust

K. Seshan

Asbestos, used in automobile brake drums, is emitted into the atmosphere in a heavily deformed state upon braking. A technique sensitive to this deformation will thus distinguish deformed and undeformed asbestos found in air pollution samples and will help in pollution source identification.

It has been demonstrated[1,2] using dark field transmission electron microscopy that deformed asbestos (Fig. 1) fibers from automobile brake drum dust may be easily distinguished from undeformed natural samples (Fig. 2). Notice that the conventional bright field images do not make this distinction possible. An interesting result of the study is that a wide variety of deformation products--relatively undeformed to almost transformed products--are found in brake drum dust. This is relevant to the controversy in the

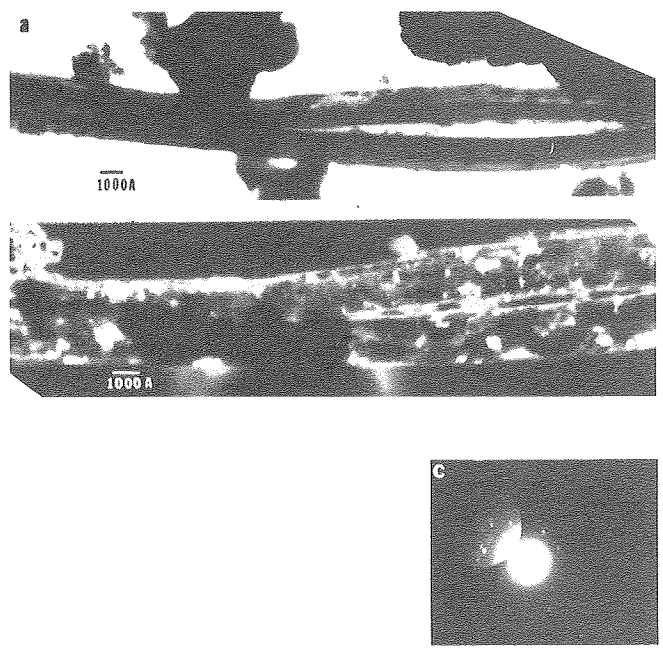

Fig. 1. Deformed asbestos from brake drum dust. (XBB 775-5414)

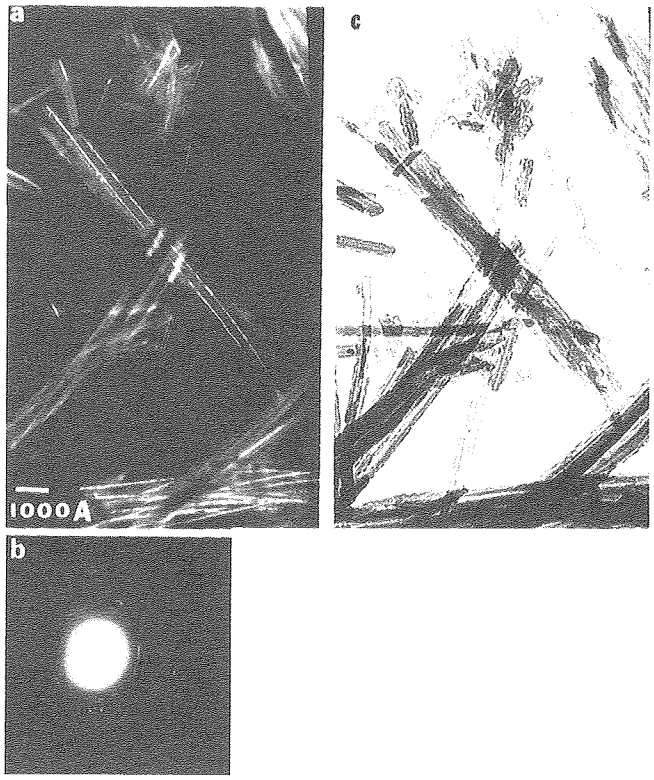

Fig. 2. Undeformed natural asbestos from Calaveras County, CA. (XBB 775-5413)

literature, one group maintaining that asbestos is completely transformed and the other that it is not.[2]

---

1. K. Seshan and G. R. Smith, Characterization of Chrysotile Asbestos in Automobile Brake Drum Dust by TEM, Proc. 35th EMSA Annual Meeting, Boston, G. W. Bailey, Ed., Claitor's Publ. Division, Baton Rouge, 1977, LBL-6211.
2. K. Seshan, On the Utility of Dark Field Electron Microscopy in the Determination of the Degree of Deformation of Chrysotile Asbestos: An Environmental Research Application, to appear in Environmental Research, LBL-6283.

5. RESEARCH PLANS FOR CALENDAR YEAR 1978

Jack Washburn

a. CdS-(CdZn)S-Cu_2S Solar Cell Materials. It is anticipated that successful achievement of inexpensive 10% efficient thin film solar cells based on materials such as CdS, Cu_2S, Zn_3P_2, ZnP_2 or even ternary compounds will require a far more detailed understanding of the behavior of dislocations, impurity atoms, vacancies and their interactions in these crystals than that which presently exists. The quantitative electron microscope techniques which we have successfully applied to in the past to study of dislocation mobilities and diffusion rates in MgO and Cu_2O will be applied to CdS and Cu_2S to begin to build up a background of information concerning defect behavior in these materials.

b. ZnP_2 as a Possible New Solar Cell Material. Conditions for growth of zinc diphosphide as a thin film will be investigated. Electrical Measurements will be correlated with structural perfection of the layers as revealed by transmission electron microscopy.

c. Field Desorption Microscopy. A field ion microscope has been modified by addition of a Chevron microchannel plate so it can be used as a field desorption microscope. By field desorption of a tungsten tip that has been coated with a low melting metal such as potassium it is anticipated that shadow images of large organic or biological molecules adsorbed on the tip can be obtained.

d. Structure and Crystalization of Amorphous Silicon. Amorphous silicon layers produced by ion implantation and by vapour deposition in an electron beam evaporator will be used to study the properties of the amorphous-crystalline interface. Further understanding of the crystallization process may lead to a technique for producing thin silicon layers with large grain size for solar cell use.

e. Spectrally Selective Heat Absorbing Surfaces. Efficient collection of solar energy as heat requires a spectrally selective surface, i.e., one that absorbs in the visible but reflects in the far infrared. The structure of one such surface, electroplated black chrome, has been found to consist of fine chromium metal particles imbedded in an amorphous oxide. Further work is planned on the role of the oxide such as the effect of heat treatments in oxidizing and reducing atmospheres on the spectral selectivity. The structure of black chrome will also be compared with structures of other spectrally selective surfaces in an attempt to further clarify the mechanism of spectral selectivity in these complex surface structures.

6. 1977 PUBLICATIONS AND REPORTS

Jack Washburn and Associates

Journals

1. W. K. Wu and J. Washburn, Rod-like Defects in Ion Implanted Silicon, Crystal Lattice Defects 7, 39 (1977), LBL-4192.

2. K. Seshan, Insensitivity to Tilt of the Electron Diffraction Pattern of Amphibole Asbestos Fibres, Environ. Res. 14, 46 (1977), LBL-4549.

3. H. A. Mohamed and J. Washburn, Deformation Behaviour and Shape Memory Effect of Near Equiatomic NiTi Alloys, J. of Mat. Sci. 12, 469 (1977), LBL-5141.

4. W. K. Wu and J. Washburn, On the Shrinkage of Rod-Shaped Defects in Boron Ion Implanted Silicon, J. Appl. Phys. 48, No. 10, 3742 (1977), LBL-5427.

5. W. K. Wu and J. Washburn, On the Climb of Dislocations in Boron Ion Implanted Silicon, J. Appl. Phys. 48, No. 9, 3747 (1977), LBL-5452.

6. K. Seshan and G. Smith, Characterization of Chrysotile Asbestos in Automobile Brake Drum Dust By Transmission Electron Microscopy, Proc. 35th Annual Electron Microscopy Society of America Meeting, Boston, G. W. Bailey Ed., Claitor's Publishing Division, Baton Rouge, 1977, LBL-6211.

LBL Reports

1. H. A. Mohamed, M. O. Aboelfotch and J. Washburn, On the Mechanism of Martensite Transformation in Near Equiatomic NiTi Alloy, LBL-5143.

2. R. Drosd, The Effect of Temperature and Impurities on the Atomic Displacement Energy During Electron Irradiation, (M.S. thesis), LBL-6075.

3. K. Seshan, On the Utility of Dark Field Electron Microscopy in the Determination of the Degree of Deformation in Chrysotile Asbestos: An Environmental Research Application, LBL-6283.

4. C. M. Lampert, Design of a Solar Test Collector for Evaluation of Selective Absorbers, (M.S. thesis), LBL-6288.

5. C. M. Lampert, Structure of a Black Chrome Solar Selective Surface, LBL-6691.

6. G. Hirsch and J. Washburn, Current Research Towards Possibly Imaging Biological Molecules Using Field Desorption Microscopy and Field Ion Microscopy of Diamond, LBL-6960.

7. Arvind Srivastava, Proton Induced Swelling in Type 316 Stainless Steel, (Ph.D. thesis), LBL-4595.

Papers Presented

1. Krishna Seshan, Application of Electron Microscopy to Problems of Air Pollution, University of Minnesota, Department of Geology and Geophysics, December 20, 1977.

2. Krishna Seshan, Ion Implantation in Silicon, Texas Instruments, Dallas, Texas, August 1977.

d. Erosion-Corrosion Behavior of Materials

Alan V. Levy, Principal Investigator

Introduction

Erosion-corrosion behavior of the materials used in coal gasification process equipment is a major consideration in the design of durable systems which will be capable of economical long-duration operation to convert coal to useable low-, medium-, and high-BTU gas. The simultaneous attack of eroding solid particles and corroding reactive gases has been demonstrated in coal gasification pilot plant operation to cause premature failure of components operating at elevated temperatures. The mechanisms of this attack are complex, requiring that a thorough understanding of each mechanism be gained separately before insight into the combined behavior will be possible.

Erosion behavior has been investigated in both experimental and analytical studies. Mechanisms of low impingement angle and high impingement angle erosion of ductile metals have been defined and provide new insight into material loss in a manner that supports the development of refined analytical models for predicting erosion rates as a function of the several active variables involved in the process. The fluid mechanics of two- and three- dimensional, two-phase flow has been defined in complex computerized analytical expressions that can be used to describe erosion conditions in the actual flow system geometries that occur in coal gasifiers.

The effects of elevated temperature on the erosion behavior of ductile metals to 0.8 of their melting temperatures have been determined. The effect on erosion rate of variations in the microstructure of alloys containing both hard and soft constituents have been determined, dispelling the previously held concept that erosion is primarily a function of the hardness of the alloys. All of these additions to erosion knowledge are important factors in gaining an understanding of how metals can erode under the operating conditions that occur in coal gasifiers.

Corrosion, the other major mechanism that degrades metals in coal gasifier operating environments, has been determined to be primarily a combined oxidation-sulfidation phenomenum. In alloys that contain sufficient quantities of primarily aluminum and/or chromium to form oxide barriers to resist sulfur attack, the competition between their formation and the formation of destructive sulfides has been found to be a delicate balance of the partial pressures of oxygen and sulfur in the gas. The thermodynamic equilibria and kinetics of the formation of binary and ternary compounds of oxides, sulfides, and spinels are being defined by careful exposures of experimental and commercial alloys to gases with controlled activities of oxygen and sulfur. Microscopic examination of the resultant scales and internal reaction products is producing an understanding of the morphologies of the compounds formed that is necessary to determine their susceptibility to erosion by the solid particles that impinge on the surface of coal gasifier components.

The capability of the char particles themselves to chemically attack metals is another facet of the complex degradation mechanism of combined erosion-corrosion. Static corrosion tests of char particles from coal gasification pilot plants in direct contact with metals have indicated that constituents in the char such as FeS and $CaSO_4$ can provide sulfur at activity levels that can severely attack the metals under both oxidizing and reducing conditions. This knowledge adds still another ingredient to the understanding of combined erosion-corrosion attack at elevated temperatures.

Once sufficient understanding of the separate mechanisms of erosion and corrosion of materials used in coal gasifiers is obtained, combined erosion-corrosion experiments can be carried out in a manner that will result in the necessary understanding of the integrated behavior. It is only on the basis of this understanding that materials can be selected, new materials developed, and plant operating conditions set that will result in acceptable performance lives for coal gasifier components.

1. EROSION BEHAVIOR

a. Shallow-Angle Impingement Erosion Mechanism

D. McFadden

The development of an analytical model that describes the erosion of ductile metals by hard angular particles was made by I. Finnie.[1] The model assumed a micro-cutting mechanism and was based upon solving the equations of motion of the tip of the cutting particle to determine the volume of material removed. The resulting expression predicted quite well the shape of the curve as a function of impingement angle for experimental erosion tests up to an angle of about 30°. However, it did not predict the amount of erosion or the dependence of erosion on velocity in an acceptable manner. The purpose of the present investigation was to determine the reasons for the shortcomings of the model and to correct them.

Tests were made using both single and multiple particles to erode surfaces of an FCC metal, 1100-0 aluminum, at room temperature. SiC angular particles, 250-300 μm for the multiple-particle tests and 1100 μm for the single-particle tests, were used at two velocities, 78 and 107 m/s. Angles of impingement from 10° to 90° were used.

The initial model predicted a particle velocity term exponent of 2 while experimental results showed that the exponent, in fact, varied from 2.2 to 2.8, increasing as the angle of impingement, α, increased. As the result of careful observation of the craters formed by single-particle impacts, using SEM analysis not available to Finnie in his original work, it was determined that the equation for angular rotation of the cutting particle should consider the resultant force to be located not at its tip as was originally

assumed, but in the center of the material having contact with the particle. When this was done the analysis produced an effective velocity exponent ranging from 2.2 at an α of 10° to 2.7 at 30°. These results are similar to the experimental results up to an angle of 30°, the limit of applicability of the cutting mechanism for material removal. Furthermore, as is shown in Fig. 1, the modified model was capable of defining the shape of the crater formed by the impact of a single particle.

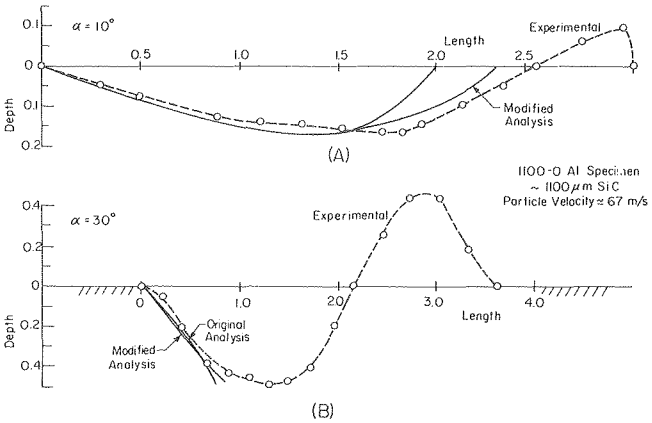

Fig. 1. Single-particle crater profiles for representative experimental results and profiles predicted by original and modified analysis at (A) α = 10° and (B) α = 30°. Results are scaled such that the maximum depth of cut for experimental and predicted results is equal for a given α.
(XBL 775-5530)

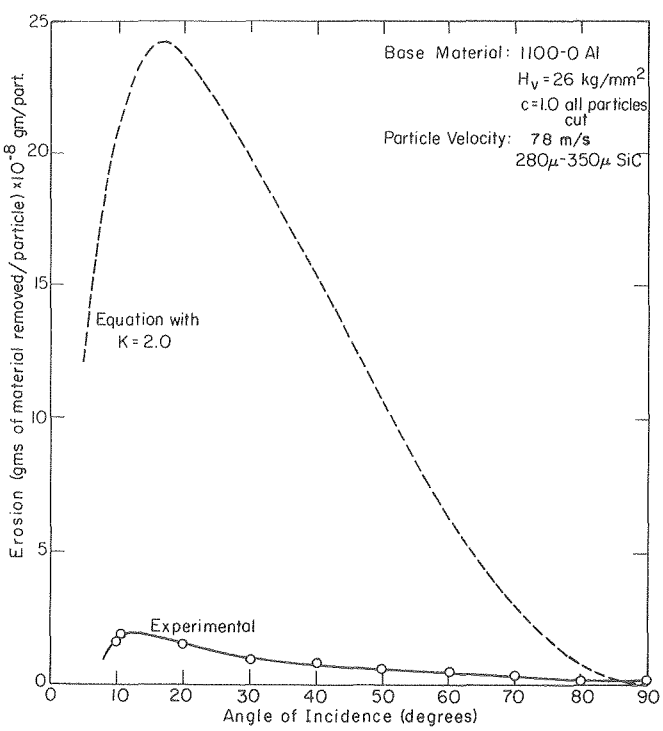

Fig. 2. Plot of erosion per particle (g/part) as a function of angle of incidence (α) for experimental and predicted results. (XBL 775-5523)

To determine the cutting efficiency of the particles, in order to be able to predict quantitative material loss using the analytical model, plots were made of erosion per particle impacted in multiple-particle erosion rather than per weight of particles impacted (Fig. 2). By doing so, it was shown that the model should consider only approximately 10% of the particles as removing material. This percentage corresponds well to the metal-removal efficiency found in abrasive wear studies. The remaining 90% of the particles in both instances displace and roughen the surface.

---

1. I. Finnie, Some Observations on the Erosion of Ductile Metals, Wear 19, 81-90 (1972).

b. Steep-Angle Impingement Erosion Mechanism

R. Mayville

A potential major problem in the development of coal gasification systems is erosion of construction materials by particles of coal and char. While the mechanism of material removal for particles striking materials at shallow impingement angles has been well defined,[1-4] the mechanism for particles striking at steep angles near 90° has thus far not been defined. It is the purpose of this investigation to physically define this erosion mechanism by careful observation of the changes in the microstructure of a surface area being eroded at intervals in the erosion process.

The erosion tests were carried out at room temperature by using 600 μm SiC particles at velocities of 31 and 62 m/s impacting upon an 1100-0 aluminum specimen. This aluminum was selected because its room temperature properties are near the elevated-temperature properties of 310SS, an alloy used in coal gasifiers at operating temperatures to 1000° C.

The specimens are initially eroded at 90° impingement angle through the threshold erosion region. Next, small punch marks are placed in the specimen to use as markers after subsequent erosion. The area is documented photographically over a region approximately 800 by 1600 μm by using the SEM. Then the target area is impacted with 500 to 1000 particles at a time and rephotographed. Changes in the surface features of the area after each erosion interval are observed as to their nature and degree. In addition to the photographic mapping, other metallographic techniques are used to observe the surface at various angles, study cross sections through the surface, and produce SEM stereo pairs for three-dimensional observation. Also, particles of eroded material are recovered to determine their shape and size.

As the result of extensive observations of many erosion areas, it is possible to observe what the sequence of metal movement and removal is. Figure 3 shows four sequential photographs of the same area. It can be seen in going from photo 1 to 2 that a particle has impacted the surface and made a rather flat-bottomed depression in the area above the encircled identification area. In No. 3 another

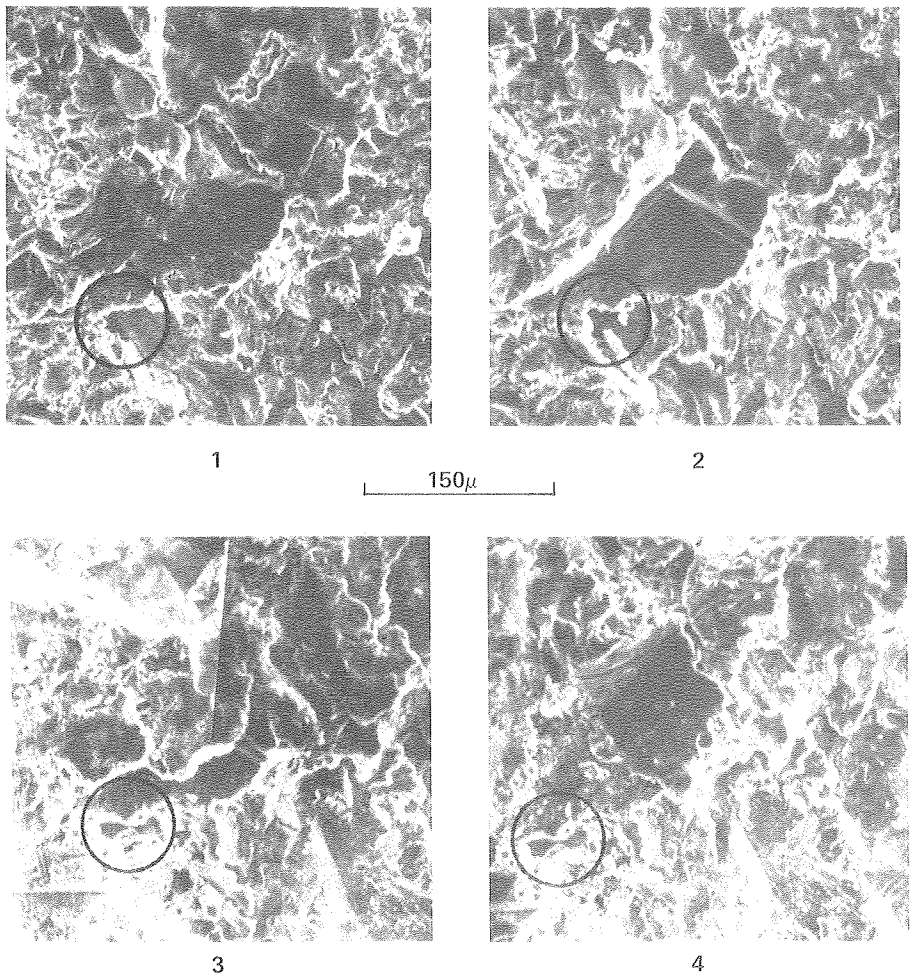

Fig. 3. Photographs of the same spot, each after successive erosion with 600 μm diameter SiC particles at $\alpha = 90°$, $V_0 = 31$ m/s. (XBB 7711-11458A)

particle has extruded material over part of the flat-bottomed depression. In No. 4 further spreading of extruded material has occurred, essentially covering up the first depression and causing a new depression. This depression, extrusion, spreading, depression sequence occurs repeatedly over an eroded surface. Figure 4 shows another view of the spreading out of extruded material in a platelet-like shape. Figure 5 shows a recovered extruded platelet of material, indicating the spread-out flat shape of the material that is removed.

Based on these observations, it appears that steep-impingement-angle erosion occurs by material being extruded out from under impacting particles into platelet-like configurations over the roughened surface of the eroding material. These platelets are not bonded to the material over which they have flowed but only to the immediate area from which they are extruded. As such they are vulnerable to being ejected from the surface by succeeding particle impacts. Using the extrusion mechanism defined in this study, it will now be possible to develop a model for steep-impingement-angle erosion and, with it, be able to predict erosion rates beyond the impingement angle limit of the current microcutting model.[1]

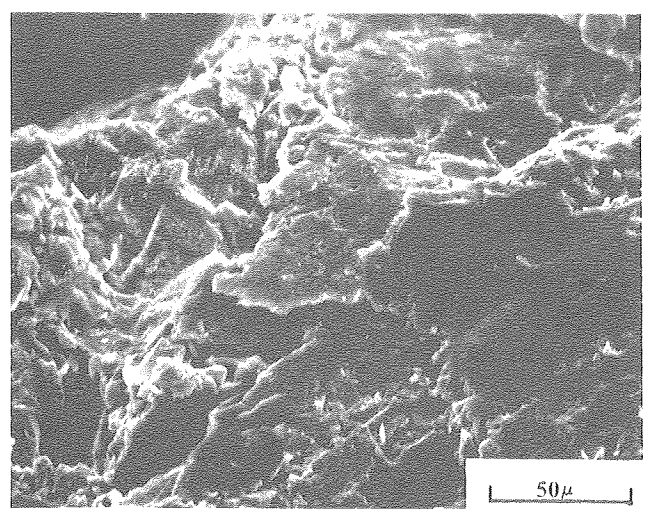

Fig. 4. A layer observed on a specimen eroded at $\alpha = 90°$, with 600 μm diameter SiC particles with $V_0 = 62$ m/s. (Upper part, XBB 770-11459)

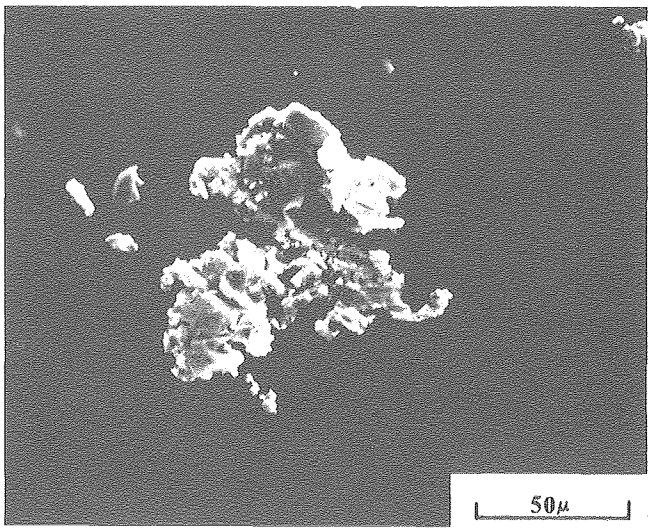

Fig. 5. A piece of aluminum, removed by erosion from an aluminum specimen eroded at $\alpha = 90°$, with 600 μm diameter SiC particle with $V_0 = 62$ m/s. (Upper part, XBB 770-11460)

---

1. I. Finnie, Some Observations on the Erosion of Ductile Metals, Wear 19, 81-90 (1972).
2. R. E. Winter and I. M. Hutchings, Solid Particle Erosion Studies Using Single Angular Particles, Wear 29, 181-194 (1974).
3. G. P. Tilly, A Two Stage Mechanism of Ductile Erosion, Wear 23, 87-96 (1973).
4. D. H. McFadden, Erosion of Ductile Metals by Solid Particles, Lawrence Berkeley Laboratory Report No. 6279, Berkeley, Ca. (1977).

c. One-Dimensional Two-Phase Particulate Flow

D. Kleist

The erosion testing of materials requires a precise set of test conditions to make the resulting data consistent and interpretable. The most important test variable is the velocity of the impacting particles. The purpose of this project was to develop a computer program that takes all of the variables affecting the particle velocity into account and relates the gas pressure setting across the nozzle of the test device to the particle velocity. Using the program, it is possible to reliably achieve a velocity without the need for cut-and-try velocity tests or the imprecise calibration curves of nozzle ΔP vs. particle velocity that have been used in the past.

A computer program for two-phase flow available in the literature using the conservative variable approach incorporating the mutual momentum exchange between phases was used as a starting point. The conservation equations not only account for the mass, momentum, and energy of each phase, but additional equations are also incorporated to relate the mass, momentum, and energy transfer (coupling) between phases. The coupling equations incorporate the equation of state, convective heat transfer between particles and gas, wall friction, particle gas mass flow ratio, particle trajectory aerodynamic drag on the particle due to its relative motion with respect to the gas, and other parameters such as particle size and density, local pressure and temperature, and others. The equations of gas-particle flow are solved by using an iterative solution technique.

The available computer program was modified to generalize its applicability, improve its accuracy, and extend the test operational limits that could be computed. To generalize the program, parameters expressed as constants in the basic program were expanded into terms utilizing input data and information contained within the program. Modification to improve accuracy consisted of developing analytical expressions for the dynamic viscosity and thermal conductivity of the gas as a function of its absolute temperature. The modifications made to expand the limits of computation involved changes to eliminate two extreme conditions which caused the program to become unstable. When the small low-density particles representative of coal char were used in the program and when large pressure differentials across the nozzle (ΔP > 25 psi) were used the program became unstable. Checks were added to the program to prevent the instability.

Experiments were conducted to verify the pressure-vs.-velocity curves predicted by the computer program. Particle velocity measurements were made on an erosion test device using both photographic and rotating disc methods. Glass spheres, steel shot, and SiC powders were used in this tests.

Figure 6 shows the correlation between predicted and test velocities for two different particle sizes.

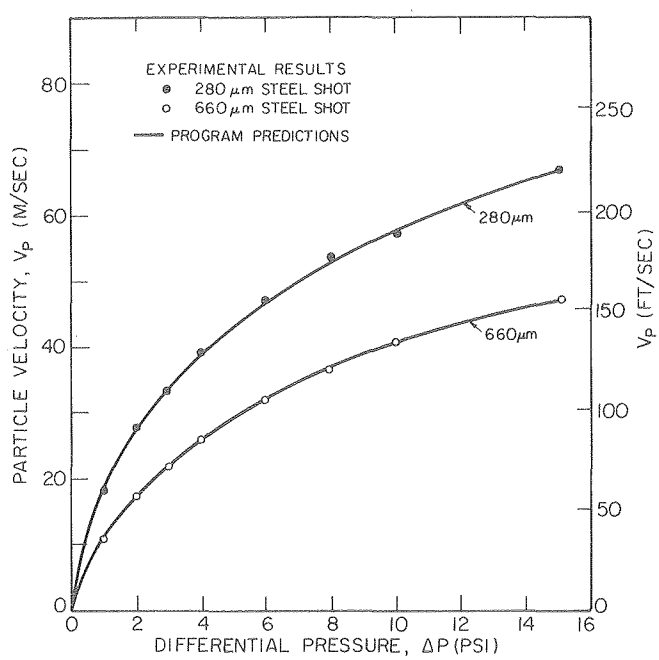

Fig. 6. Variation of particle velocity with particle size for particles of the same material: steel shot, of two different sizes, 280 and 660 μm. (XBL 7710-6169)

Figure 7 shows how well the program predicted velocity when the density of the particles was considerably different. Figure 8 shows the insensitivity of the particle velocity to an order-of-magnitude change in the solids loading in the gas.

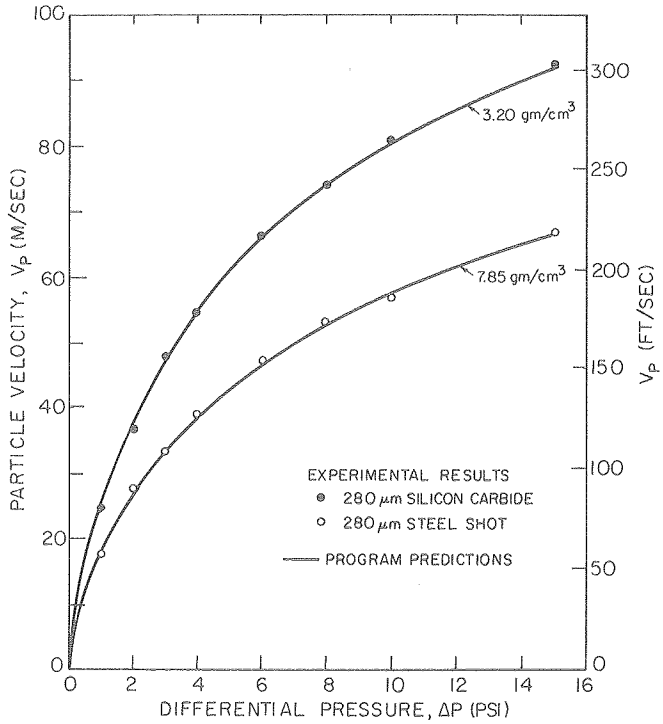

Fig. 7. Variation of particle velocity with particle density for particles of the same size (280 μm) but different materials, SiC and steel shot.
(XBL 7710-6168

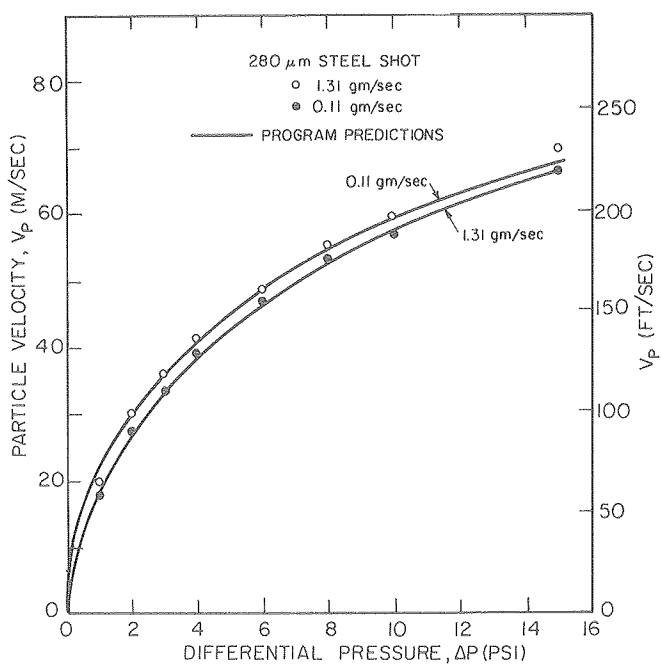

Fig. 8. Variation of particle velocity with particle loading for particles of the same material (steel shot) and same size (280 μm). (XBL 7710-6167)

The development of the computer program and the experimental verification of its accuracy have been a boon to the erosion test program. The program has markedly reduced the total time to carry out a test series over a desired range of operating conditions.

d. Effects of Microstructure of Ductile Alloys on Solid-Particle Erosion

L. Brass

The erosion resistance of ductile metals has usually been directly related to hardness with little consideration of other properties or the microstructure of the alloys. To determine microstructural effects on erosion, two alloys were chosen that allowed microstructural changes to be made without greatly changing their hardness. The alloys used were plain carbon 1075 eutectoid steel in the coarse pearlite, fine perlite, and spheroidized forms and an Al-4.75% Cu alloy heat treated to produce GP zone through θ microstructures. Single-particle and multiple-particle erosion tests were conducted using 240 μm SiC particles at impingement angles of 15°, 30°, and 90° and particle velocities of 100 and 200 fps.

Figure 9 shows the steel microstructures tested and their hardnesses. Figure 10 shows that the lowest steady state erosion rate was exhibited by the softest of the three microstructures, the spheroidized structure. The rate was 1/3 less than that of the pearlite structures. It is also to be noted in Fig. 10 that there is a threshold period prior to achieving a constant erosion rate. It is speculated that during this period the kinetic energy of many of the impacting particles is absorbed by plastic deformation of the steel rather than by physical removal of material. Once the entire eroding surface has been work hardened and roughened, the material-removal efficiency of the impacting particles becomes constant.

Figure 11 is of a single-particle impact crater is a pearlitic steel specimen and shows that surface cracking of the brittle cementite plates occurs to enhance material loss rates. The spheroidized structure isolated the brittle cementite in spheroids in a ductile ferrite matrix and showed no surface cracking. Some cracking did occur in the spheroidal structure ar a depth below the surface of approximately 20 μm. The mechanism of its material loss appeared to be crack formation at the cementite particle-ferrite interface and subsequent propagation by succeeding particle impacts from particle to particle until a platelet of material was formed that separated from the surface.

In the Al-Cu system, the large-precipitate θ' material consistently eroded less than the fine-precipitate GP zone material. There was a consistent reduction in erosion rate as the precipitate size increased from GP zone to θ'', peak hardness and θ' precipitation-hardening states. Figure 12 shows the difference in erosion rates. Through the range of precipitate sizes, the hardness ranged from VHN (1000 g load) of 81 for the GP zone material to 99 at the peak hardness to 74 for the θ condition. The larger precipitates appeared to enhance the

EROSION OF 1075 STEEL

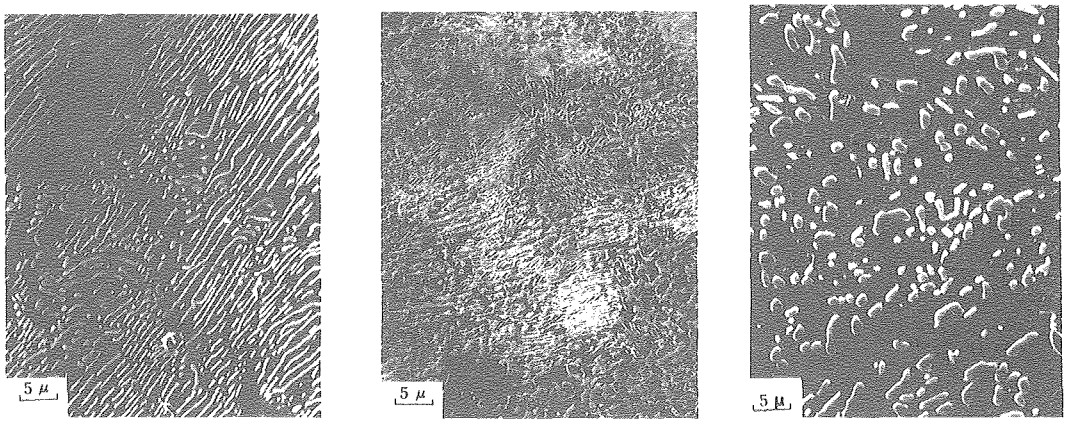

COARSE PEARLITE	FINE PEARLITE	SPHEROIDIZED
Hardness - R_B 90	Hardness - R_B99 (R_C 20)	Hardness - R_B 79
Lamellar Spacing ~ 1 μm	Lamellar Spacing ~ 0.25 μm	Sphere Diameter ~ 1.25 μm

Fig. 9. Scanning electron micrographs of 1075 steel in the coarse pearlite, fine pearlite, and spheroidized microstructures. (XBB 769-8299)

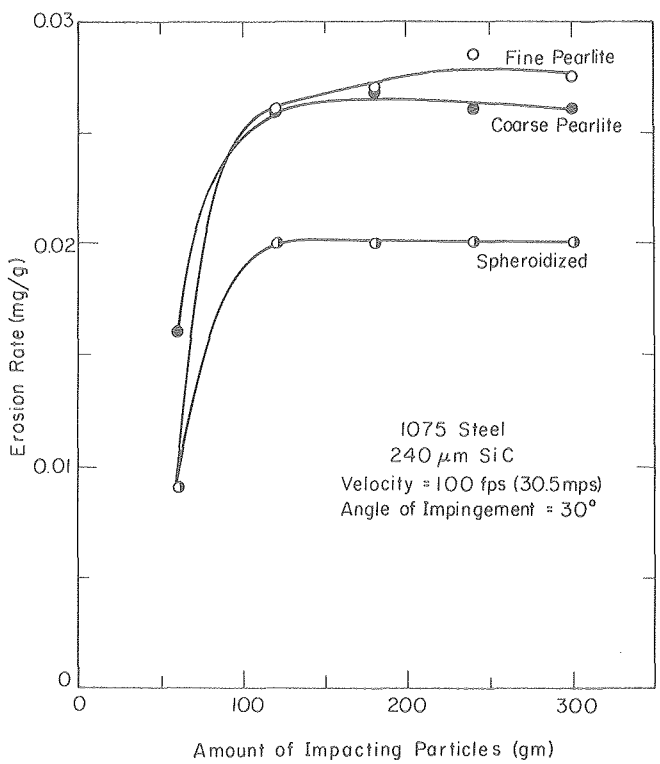

Fig. 10. Plot of erosion rate (mg/g) versus amount of impacting particles (g) for 1075 steel--coarse pearlite, fine pearlite, and spheroidized--using 240 μm diameter SiC. V_p = 30. 5 mps (100 fps), $\alpha = 30°$. (XBL 775-5486)

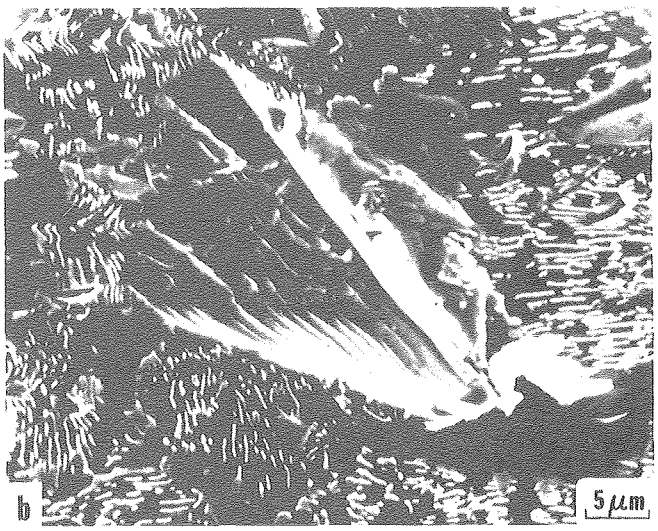

Fig. 11. Photomicrograph of a single-particle impact crater on 1075 steel (coarse pearlite) using 240 μm SiC: V_p = 107 mps (350 fps). (XBB 776-5635)

ability of the ductile matrix material to decrease subsurface crack propagation rates that lead to material loss.

Thus it was found that microstructure plays a major role in determining the susceptibility of a metal to erosion and that higher hardnesses do not necessarily result in greater erosion resistance.

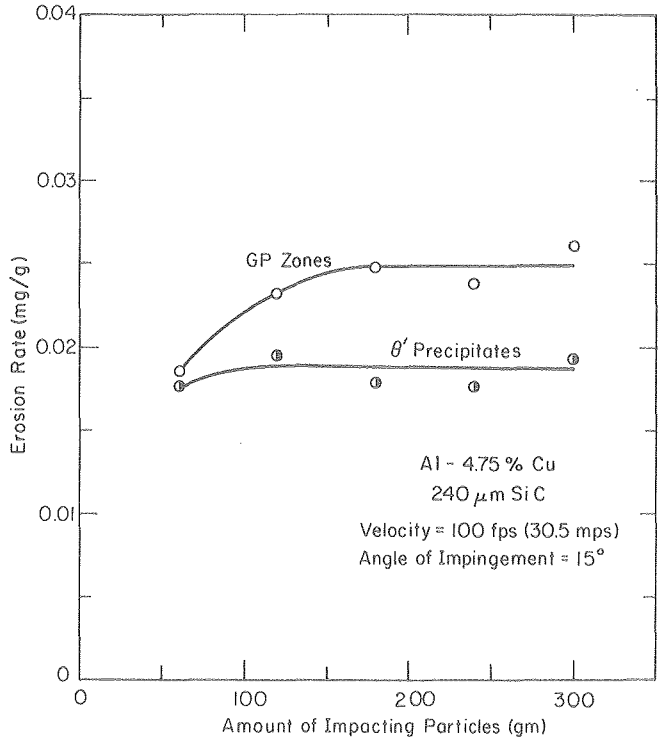

Fig. 12. Reduction in erosion rate with increase in precipitate size. (XBL 775-5474)

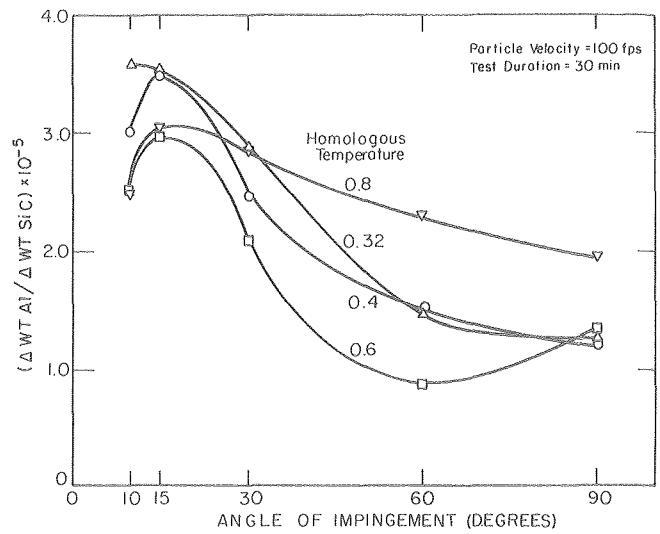

Fig. 13. Erosion rate vs. angle of impingement. (XBL 778-5889)

e. Elevated-Temperature Erosion Behavior of an FCC Metal, 1100-0 Aluminum

P. Doyle

The erosion forces acting on an austenitic stainless steel in a coal gasifier are attacking a material that is operating at elevated temperatures up to 1000°C. In order to gain an initial understanding of elevated-temperature erosion mechanisms, a similar FCC single-phase alloy to an austenitic stainless steel was selected for lower elevated-temperature study. The alloy was 1100-0 aluminum whose mechanical properties in the temperature range from room temperature to near 400°C are similar to those of 310 stainless steel in the 600° to 1000°C range.

Erosion tests were carried out at homologous temperatures of 0.32 (RT), 0.4 (99°C), 0.6 (285°C), and 0.8 (471°C). SiC particles of 250-300 μm in size were carried to the specimens in a nitrogen gas stream at velocities of 100 and 200 fps over a range of impingement angles, α. A 30 minute test duration was used for the 100 fps tests and a 10 minute duration for the 200 fps tests.

At all test temperatures the familiar curve of erosion rate vs. angle of impingement was obtained with a peak erosion rate occurring at about 15°. Figure 13 shows the curves for the 100 fps test series. It can be seen that at the lower three homologous temperatures, which are representative service temperatures for an FCC metal, the erosion rate decreases with increasing temperature. The slope of the 0.8 homologous temperature curve is considerably less than that of the other three, indicating that a different mechanism of erosion may be occurring. At α = 90° the rates for the three lower temperatures were essentially identical, indicating no effect of temperature on normal impact erosion. The difference in the erosion rate between the peak rate and the α = 90° rate for the 0.8 homologous temperature test is approximately 1/2 of that of the lower three temperatures, idicating that the effect of impingement angle is markedly decreased at high temperatures.

The patterns of erosion shown in Fig. 14 indicate a consistent pattern of surface ripples for the α = 10°, 15°, and 30° tests and an alternating depression-and-mound pattern for the 60° and 90° angles. The patterns intensify in depth, and the width of each ripple increases with increasing temperature. Since the rate of erosion is decreasing for the lower three temperatures, it is possible that an increasing amount of plastic flow without corresponding increased metal removal is occurring to consume the kinetic energy of the impacting particles.

The ripple patterns are longer for the 0.8 homologous temperature tests then for the lower temperature tests, which are all approximately the same for each angle. This indicates that at the 0.8 temperature more surface has been affected by the eroding particles, possibly accounting for at least a portion of the increased erosion rate.

Figure 15 shows the cross section of a specimen eroded at 100 fps at 0.6 homologous temperature at 40X and 400X. It can be seen that for α = 30° the ripples have been formed by material that was raised over the original metal surface by multiple impacts, leaving porous cracked areas on the downstream side. The darker areas near the surface are pieces of the eroding SiC particles that have broken off and become embedded in the severely deformed metal. Similar structures were observed at all the impingement angles tested.

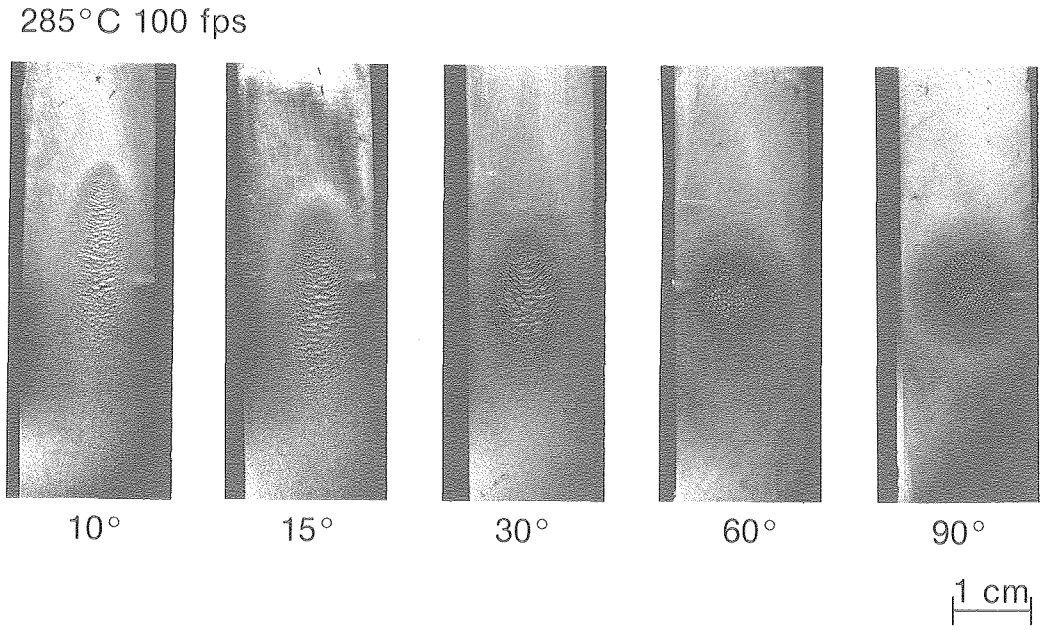

Fig. 14. Erosion patterns on 1100-0 Al from SiC (250 μm) particles.
(XBB 782-2032)

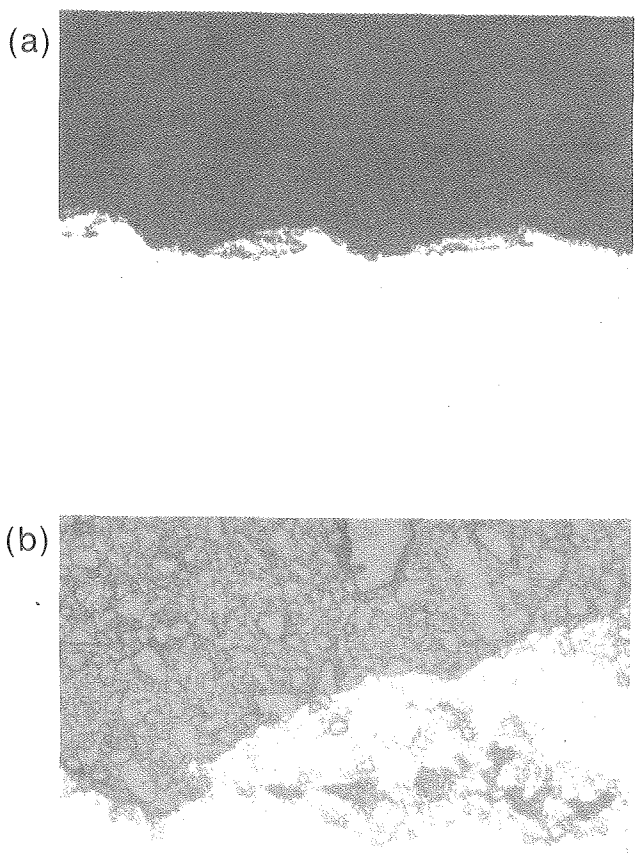

Fig. 15. Cross section of eroded 1100-0 Al; $\alpha = 30°$, V = 100 fps, SiC (250 μm) particles at 285°C. (XBB 783-3205)

The erosion behavior of metals at elevated temperatures introduces several new behavior patterns that do not occur at room temperature. Considerable work is required to understand this behavior in simple systems before introducing the additional complicating factor of reactive gas corrosion into the study of erosion-corrosion behavior of metals in simulated coal gasifier environments.

f. Flow Analysis and Erosion Prediction Near a Stagnation Point

Jonathan A. Laitone

The erosion of material components in energy conversion systems by a two-phase gas-solid particle flow is often the primary mechanism of material degradation. To investigate this type of flow and the subsequent erosion in areas of vorticity such as at corners and steps, a computer model using a vorticity transfer scheme is being developed.

An analytical solution to the gas-solid flow was found for regions near a stagnation point. This analytical solution will be used to determine the accuracy of the computer model in future work.

The analytical solution solves the equations of motion of a dilute particle suspension in a steady inviscid stream. It is assumed that the particles are spherical and do not appreciably affect the gas stream lines. The governing vector equation for the particle in a steady gas stream $\vec{u}$ is:[1]

$$\frac{D\vec{u}_p}{Dt} = \frac{\vec{u}-\vec{u}_p}{\tau},$$

where τ is the momentum equilibration time.

Making a change of variables:

$$z = t/\tau, \quad \lambda_m' = \frac{\lambda_m}{X} = \frac{\tau U_\infty}{X},$$

where λ_m' is the momentum equilibration length parameter for the particle. By inserting the stagnation point gas flow velocity we obtain:

$$\frac{d^2\vec{x}}{dz^2} + \frac{d\vec{x}}{dz} + \lambda_m'\vec{x} = 0.$$

This second-order linear differential equation is readily solved and yields a closed-form solution for the particle trajectories, which are plotted in Fig. 16. It was found that for $\lambda_m \leqslant 0.25$ the particles are completely entrained by the gas and never impact with the wall. Differentiation with respect to time yielded the impact speed of the particles, which is shown in Fig. 17. An unexpected minimum point in the speed was found for $\lambda_m' = 0.4$. The increasing impact speed for very small particles ($\lambda_m' < 0.4$) is due to the gas accelerating away from the stagnation point. A maximum point for speed and erosion was found at $\lambda_m' = 2.0$.

The angle of impact and density distribution was calculated to find the relative erosion along the wall. The results indicated that 400 μm particles can cause substantial erosion away from the stagnation point if the free stream gas velocity is less than 150 cm/s.

The calculated erosion of a ductile metal by 200 μm particles was found to depend on the free stream gas velocity to the 3.83 power. Grant and Tabakoff[2] found, experimentally, exponent values around 4.0 in their work with turbomachinery.

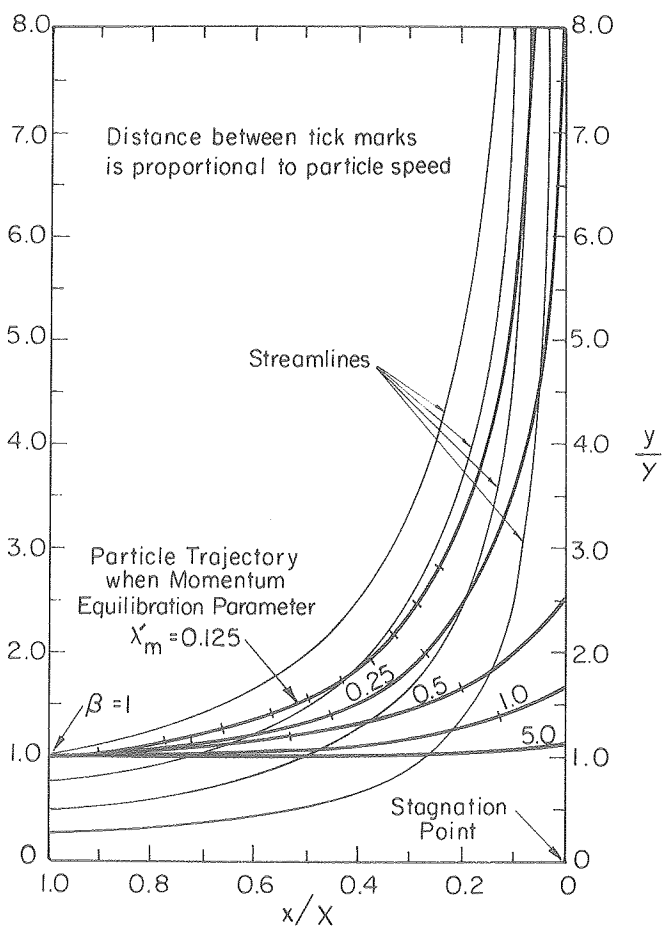

Fig. 16. Particle trajectories. The momentum equilibration parameter indicates the magnitude of a particle's momentum. When $\lambda_m' > 10$ the trajectories are determined by the initial conditions. For $\lambda' \leqslant 0.25$ the particles are completely entrained in the gas flow and never impact with the wall. (XBL 7712-6544)

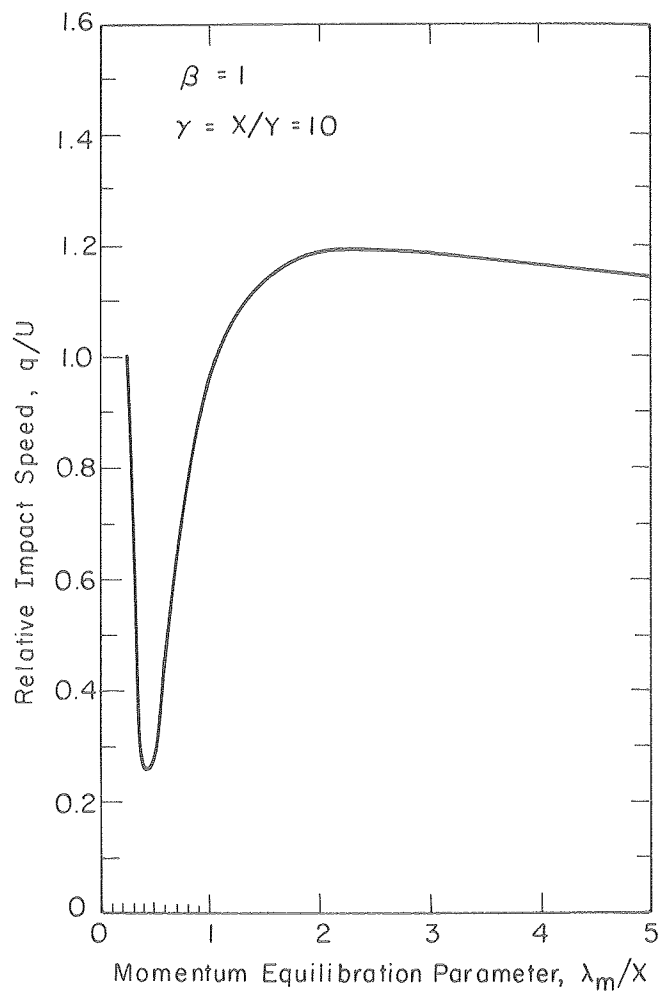

Fig. 17. Relative particle impact speed as a function of the momentum equilibration parameter. The increase in impact speed for $0.25 < \lambda_m' < 0.40$ is due to the gas accelerating away from the stagnation point. (XBL 7712-6546)

The effects of the boundary layer along the wall is being investigated.

---

1. G. I. Taylor, Notes on Possible Equipment and Technique for Experiments on Icing on Aircraft, Aeronautical Research Committee Reports and Memoranda, No. 2024, 1-7 (1940).
2. G. Grant and W. Tabakoff, Erosion Prediction in Turbomachinery Resulting from Environmental Solid Particles, Journal of Aircraft, Vol. 12, No. 5, 471-478 (1975).

g. Two-Phase Three-Dimensional Flow Analysis and Erosion Prediction in a Curved Pipe

W. S. Yeung

The fluid mechanics problem of a dilute gas-particle mixture flowing through a curved pipe has been investigated. The gas is assumed to be inviscid except for the viscous drag effect between the gas and the particle phase. The effect of the particles on the gas streamlines is considered negligible, which is a reasonable assumption when the concentration of particles is sufficiently low. It follows then that the equations of motion for the gas phase are exactly satisfied by a uniform flow in the streamwise direction with no secondary circulation velocity components. The entry conditon into the curved pipe is considered uniform, and dynamic equilibrium is assumed for the mixture.

The main task undertaken has been the solving of the equations of motion for the particle phase. Only the viscous drag force due to relative motion of the two phases was considered, since other (reaction forces) between the gas and particle phases due to various effects are small. Furthermore, the Stoke's drag formula is assumed to be valid throughout the whole particle trajectory. With these simplifying assumptions, the particle equations of motion are written in Lagrangian frame of reference, which constitutes a set of nonlinear, first order, ordinary differential equations. These are solved numerically by using a Runge-Kutta fourth order scheme. From the numerical solutions information can be extracted, such as the impact velocity at the pipe wall and the impingement angle and the local mass flux of particles hitting the wall. The relative erosion rate (in terms of volume of wall material removed) per unit area is then calculated.

The calculated erosion patterns along the central plane of the curve pipe are shown in Fig. 18 for various entry velocities, W. The central plane was chosen, since it is representative of the severe erosion-prone area in pipe bends. It is seen that at high enough entry velocity, the particle trajectories are quite straight and the erosion patterns are similar and confine between the same interval of the bend angle, ϕ. The erosion pattern begins to stretch out to larger bend angles as W decreases. This is easily understood, since at high entry velocities the inertia of the particles dominates over the viscous drag effect, while at low velocities the particles can easily accommodate to the gas streamlines.

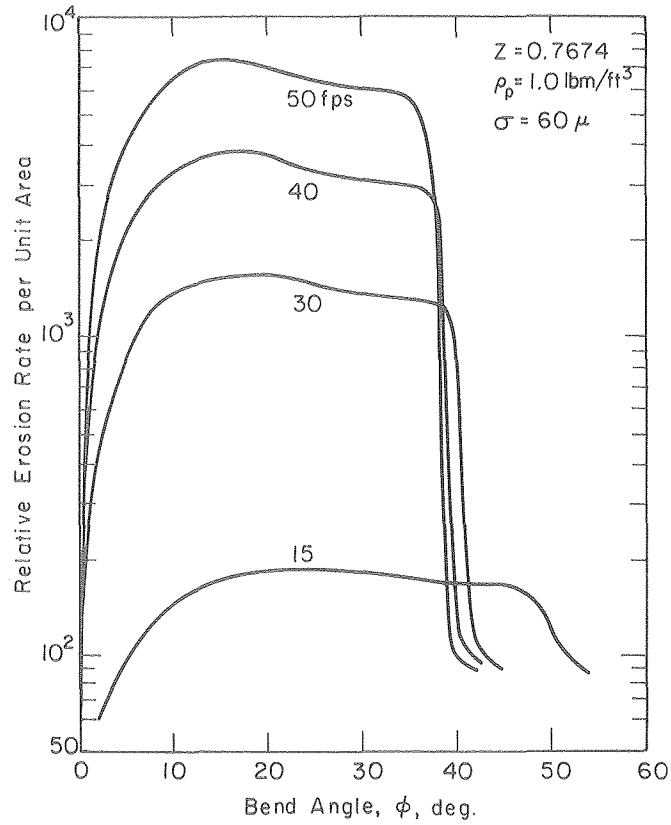

Fig. 18. Relative erosion rate vs. bend angle for various flow velocities in a curved pipe of 20" with a = 1" and R = 11". (XBL 7712-6503)

The dependence of the maximum relative erosion rate, E_{max}, on various parameters, in particular the entry velocity W and the loading ratio in mass of particle per unit mass of gas, Z_L, was studied. The most interesting point is that E_{max} depends more strongly on W at low values of W than at high values of W. The critical entry velocity, W_{crit}, which separates these two regimes of dependence is characteristic of a particular system and geometry. Also, the exponential dependence on W below W_{crit} is a weak function of W itself. For the particular curved pipe and gas-particle mixture in the present study, the following relations are obtained:

$$E_{max} \propto W^3 Z_L \qquad \text{for } W \geqslant 8 \text{ fps},$$

$$E_{max} \propto W^{3.93} Z_L \qquad \text{for } W \leqslant 8 \text{ fps}.$$

h. Diffusion of a Chemical Species Through the Viscous Boundary Layer

Jay Keller

The effects of viscosity on diffusion of a chemical species were investigated. Due to the similarity between the diffusion of mass and the diffusion

of heat an analogy can be drawn allowing the results of heat transfer analysis to be used.

We are interested in the concentration of H_2S at the surface and how the flow field effects this concentration. It can be shown that the equilibrium concentration due to temperature gradients across the flow does not change significantly. So assuming the concentration to be constant the reaction rate at the surface can be found. This is a depletion of H_2S occurring at the surface. Thus this reaction rate gives the mass flux toward the surface. This rate was found to be 3.87×10^{-10} (moles cm/cm^3 sec). The boundary condition to the problem is then one of a constant flux toward the surface. The Nusselt number ($Nu = hd/k_f$) vs. X for turbulent flow and constant flux is plotted in Fig. 32 of Ref.1 (where h = the heat transfer coefficient, d = the pipe diameter, and k_f = the thermal conductivity of the fluid.) By replacing the Nusselt number with the Sherwood number ($Sh = gd/D_i$) and the Prandtl number ($Pr = \nu/\alpha$) with the Schmidt number ($Sc = \nu/D_i$) we can apply this data directly to the mass transfer problem (where g = the mass transfer coefficient, D_i = the mass diffusivity of species i, ν = kinematic viscosity, α = thermal diffusivity.) Reference 1 shows that the Sh decreases from ∞ at the tube entrance asymptotically approaching a value of 300 for fully developed flow. (The Reynolds number ($Re = Ud/\nu$) for this flow is 4.818×10^6 so the Sh number is actually greater than 300, thus this will give a high value of the concentration difference.) Using $M = g\,(\Delta m)$ we find the concentration difference increasing from 0.0 moles/cm^3 at the tube entrance to 3.4×10^{-9} moles/cm^3 for fully developed flow. [Where $\dot{M}$ = the mass flow rate, and Δm_i is the concentration difference of the ith species (bulk concentration at the wall)]. It is thus concluded that the effects of viscosity on the concentration profile are negligible. Indeed the effects of temperature are greater and can be considered simply from an equilibrium composition point of view.

The possibility of creating a concentration difference significant enough to eliminate the formation of FeS was also investigated. The results of transpiration cooling were used and it was found that for a uniform blowing rate of $U_0\rho_0/U_0 = 0.087$ using a gas composition of a typical gasifier with the reactive, agent removed (H_2S), the formation of FeS could be stopped (where U_0 = the average velocity of the pipe flow, ρ_0 = the density of the free stream fluid, U = the blowing velocity, and ρ = the density of the blowing fluid.) Thus it appears possible to control the gas composition at the surface.

Due to the mechanical difficulties involved with uniform injection this type of control may not be feasible. Further research is being conducted to investigate the possibility of controlling the mass composition by intermittent injection rather than uniform injection.

1. Handbook of Heat Transfer, Warren M. Robenow and James P. Hartneff, Eds. (McGraw Hill Book Company, 1973, Chap. 7, p. 7-37.

i. Two-Body Dry Abrasive Wear

H. Hirano

To broaden the understanding of erosion mechanisms, an investigation was undertaken to determine the mechanism of material removal when the particles were restricted in their angular movement. Several sizes of SiC and Al_2O_3 particles ranging from 20 to 260 μm were bonded to a paper which was rotated beneath a stylus of test alloy under a 500 or 1000 g dead weight load. 4340 steel and 7075 aluminum were tested at several heat treatment conditions and their wear rates were related to hardness, strength, and fracture toughness. The hardness range of the aluminum alloy was VHN (kg/mm^2) 102 to 181 and that of the 4340 steel from 318 to 602. Fracture toughness values, Kc (ksi-in.$^{1/2}$), ranged from 23 to 61 for the 7075 aluminum and from 39 to 160 for the 4340 steel.

Figures 19 and 20 show that there was a direct hardness relationship to wear resistance for both

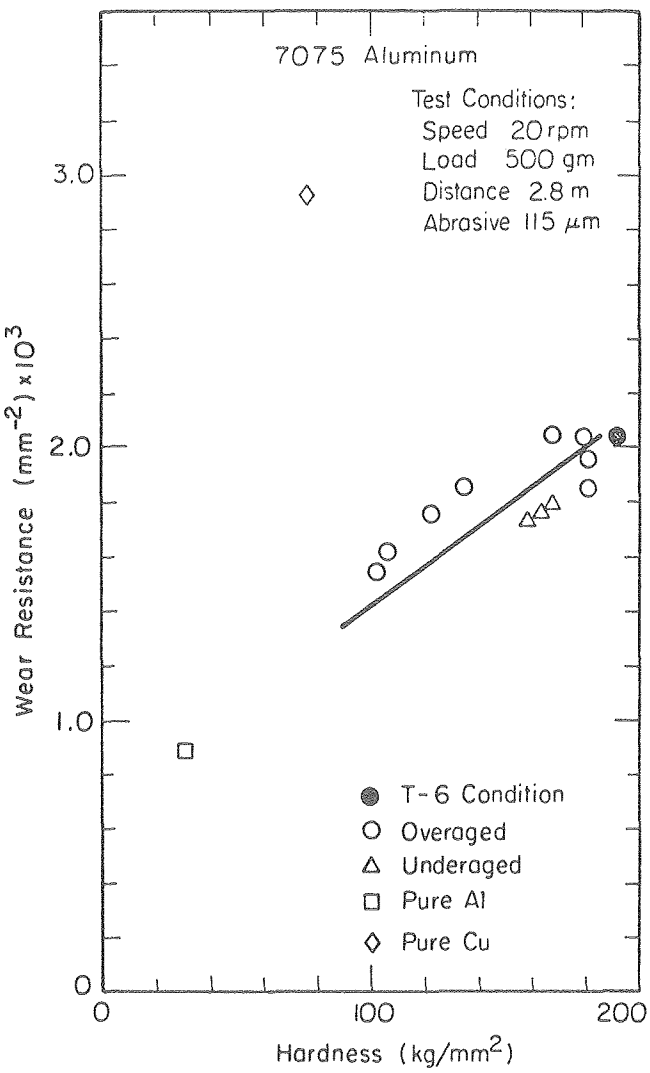

Fig. 19. Wear resistance of 7075 Al vs. hardness. (XBL 7711-6435)

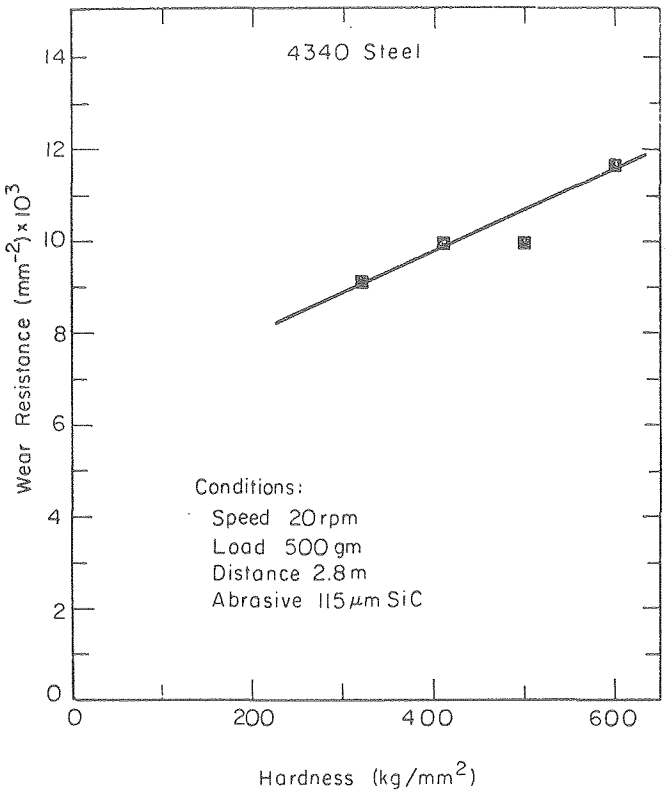

Fig. 20. Wear resistance of 4340 steel vs. hardness. (XBL 7711-6446)

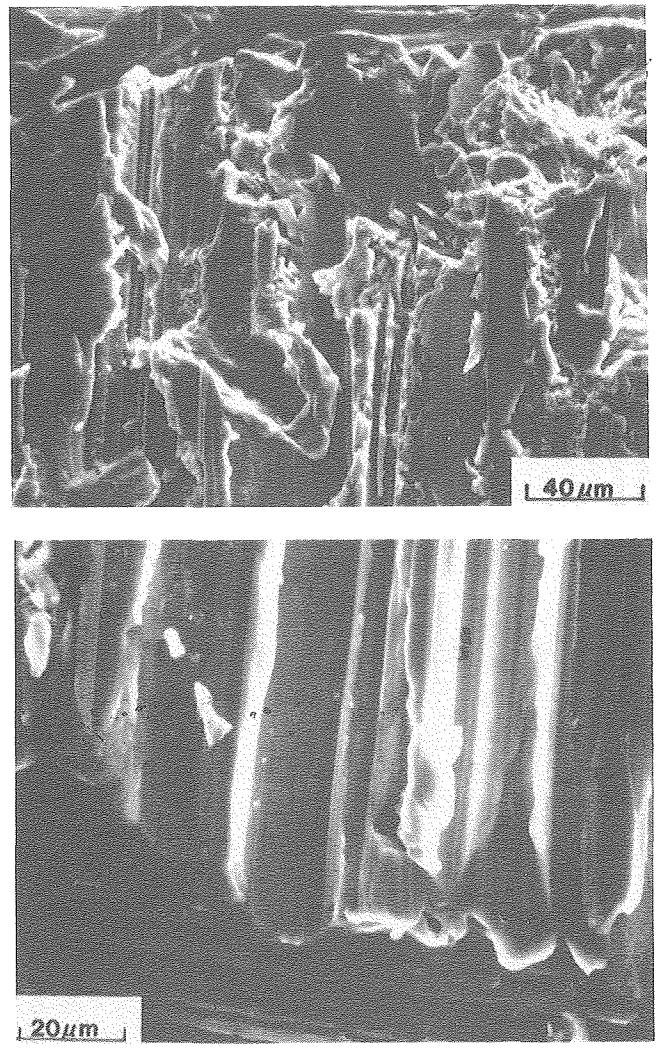

Fig. 21. Upper: 7075-T6 Al (loaded by 1000 g) at the trailing edge.
Lower: 7075-T6 Al (loaded by 1000 g) at the leading edge. (XBB 770-11555)

alloys in two-body wear, unlike that of erosion resistance. There was also a direct relationship between yield strength and wear resistance for both alloys; however, only the 4340 steel indicated some wear relationship with fracture toughness, decreasing as the fracture toughness increased.

The mechanisms of two-body abrasion are considerably different from those of erosion. Figure 21 shows the appearance of the abraded surface at the beginning of the abrasion cycle (bottom photo) and near the end (top photo). Straight cutting with plastic flow of material upwards along the sides of the grooves occurs at the beginning of cutting. At some distance along the abrasion path, the simple cutting is complicated by gouging from particles that have come loose from the abrasive paper, been embedded in the test material, and been subsequently broken loose from it by succeeding, still bonded particles. Also, chips cut from earlier positions in the abrasion path have become welded to the downstream surfaces, creating a jumble of material. The two-body abrasion wear process is seen to have little in common with the erosion process.

2. CORROSION BEHAVIOR

a. Corrosion of Iron-Base Alloys by Coal Char at Elevated Temperatures

B. A. Gordon

Considerable work is being done in gas-phase corrosion of iron-base alloys in the simulated environments of coal gasifiers,[1,2] but so far very little has been done on the attack of alloys by the solid char byproduct of the gasification process.

The char consists of residual fixed carbon, inorganic oxides, and some inorganic sulfur (see Table 1). A serious consideration is whether there is sufficient sulfur present to promote accelerated attack of the alloys used in the gasifier.

Table 1. Composition of typical ash and coal char.

ASH	Percentage
SiO_2	46.3
Al_2O_3	15.2
Fe_2O_3	14.9
CaO	6.5
MgO	1.1
TiO_2	0.6
P_2O_5	0.2
Na_2O	3.0
K_2O	1.8
SO_3	5.4 (as sulfate and sulfide)

Char	Percentage
Fixed carbon	25-50
Ash	45-70
Sulfur	1-5
High boiling tars	< 4

To determine the possibility of sulfidation corrosion, an initial series of experiments was performed in an environment consisting of char obtained from the Synthane process and commercially pure argon at 982°C (1800°F). The experimental alloys chosen were Fe-10Al, Fe-10Al-5Cr, and Fe-10Al-10Cr. The argon contained about 6-10 ppm oxygen, sufficient to promote the formation of a protective Al_2O_3 scale on all three alloys. However, the combination of the carbon in the char and the oxygen in the argon kept the PO_2 about 10^{-19} atm, a level reasonably comparable to that in a gasifier, through the reaction

$$C + 1/2\ O_2 \rightleftarrows CO. \qquad (1)$$

After 100 hours exposure, both the Fe-10Al and Fe-10Al-5Cr underwent massive internal sulfide formation, while the Fe-10Al-10Cr suffered only minor attack and no internal sulfidation. Cross sectioning of the alloys revealed morphologies typified by Fig. 1. Note particularly the internal aluminum-rich sulfides. This type of formation can assist in the breakdown of protective scales with concomitant accelerated internal sulfide penetration.[3]

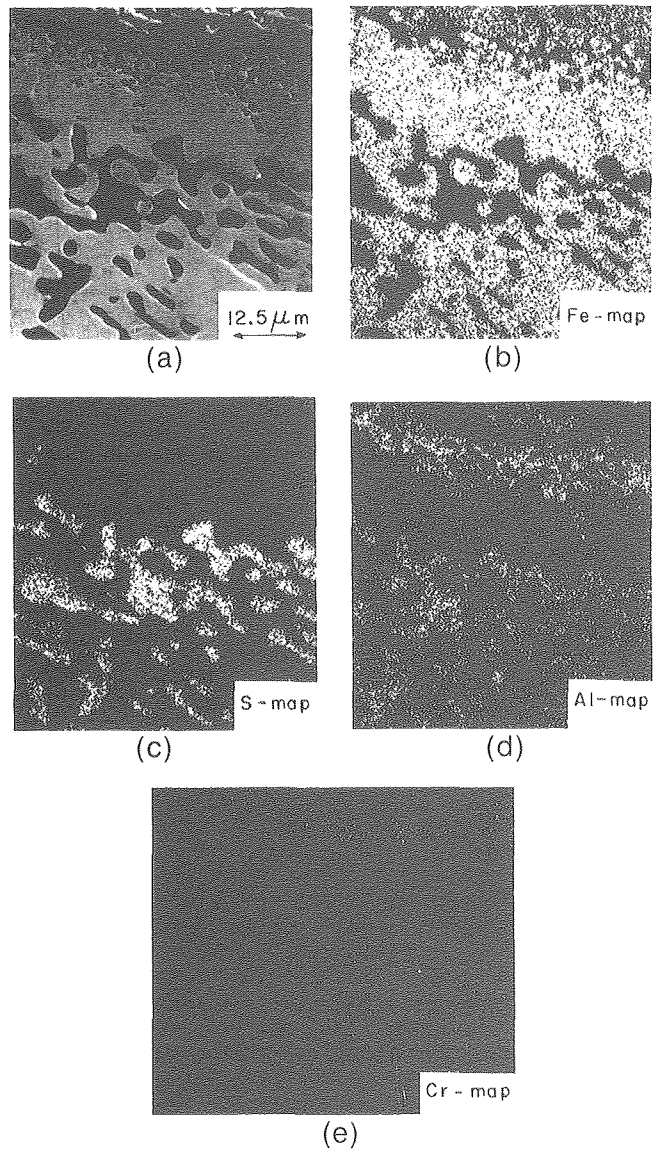

Fig. 1. Cross-section and x-ray mappings of Fe-10Al-5Cr alloy after 100 hours exposure, a) Electorn image, b-e) elemental maps are indicated. Note the four distinct regions in the cross section. 1) lightest gray region is alloy itself, 2) medium gray at top of (a) is a chromium oxide (see e), 3) darker gray below that is aluminum oxide (see c and d), and 4) the dark gray inclusions in bulk of alloy are aluminum-rich sulfides (see c and d). Iron is excluded from the aluminum-containing regions (see b). (XBB 779-8965)

Additional experiments have been performed to clarify the conditions under which char is an aggressive corrodant at 982°C. Simulated char mixtures were made up by using an alumina powder filler and either FeS or $CaSO_4$, two of the principal sulfur-containing constituents in char, to determine whether they were possible sources of sulfur that could attack metals. Alloys were exposed to these mixtures at PO_2's ranging between 10^{-14} and 10^{-19} atm, and the resulting corrosion morphologies were studied.

At PO_2's greater than about 10^{-16} atm, FeS can be oxidized to provide free sulfur for internal attack of the metal the char is in contact with:

$$FeS + 1/2\ O_2(g) \rightleftarrows FeO + 1/2\ S_2(g).$$

At low PO_2's ($< 15^{-16}$ atm) $CaSO_4$ can be reduced to provide free sulfur:

$$CaSO_4 \rightleftarrows CaO + 3/2\ O_2(g) + 1/2\ S_2(g).$$

A study of the morphologies of the scales formed on the test alloys appears to indicate that FeS is the main cause of corrosion from char but that there still is sufficient $CaSO_4$ present to cause some internal attack.

---

1. D. B. Rao and H. Nelson, Sulfidation of 310 Stainless Steel at Sulfur Potentials Encountered in Coal Conversion Systems, NASA TM X-73,166 (September 1976).
2. B. A. Gordon, W. L. Worrell and V. Nagarajan, Thermodynamic Prediction of the Behavior of Fe-Cr-Al Alloys in Coal Gasifier Operating Environments, LBL-7320, December 1977.
3. B. A. Gordon and V. Nagarajan, Corrosion of Re-10Al-Cr Alloys by Coal Char, LBL-6946, October 1977 (accepted by Oxidation of Metals).

b. Combined Oxidation-Sulfidation Behavior of Iron Base Alloys in a Coal Gasifier Environment

V. Nagarajan

Commercially available steels which can be used as internal parts in a coal gasifier develop Cr_2O_3 scales. It has been observed that Cr_2O_3 scales are not good barriers to sulfur diffusion and subsequent sulfide formation and degradation. There is a need to develop alloys that would form other scales like Al_2O_3 and SiO_2, hopefully better barriers to sulfur attack, and to understand their mechanism of sulfur diffusion. A program was undertaken to study the corrosion behavior of Fe base alloys containing Cr, and Si or Al ternary additions.

All of the experimental alloys were vacuum induction melted into 5 lb ingots and rolled to sheet form. They were corroded at 1800°F in an environment simulating the oxygen and sulfur content of the gases in a coal gasifier. The partial pressures of oxygen and sulfur were maintained at 10^{-18} atm and 10^{-6} atm respectively so that FeS along with Cr_2O_3 and Al_2O_3 will be stable. At higher PO_2 levels FeS is not stable and instead oxide spinels like $FeAl_2O_4$ become stable. Since the main aim of this research is to investigate the barrier behavior of simple oxides, the corrosion conditions have been chosen to avoid the formation of oxide spinels.

All the alloys containing 0.5 to 2.0 Si and 18 Cr were extensively corroded within five days in the corrosive environment. Although the onset of catastrophic corrosion was delayed by increasing the Si content, the amount of Si was not found to be sufficient to form a protective SiO_2 subscale. All the alloys developed external Cr_2O_3 scale as the primary barrier interspersed with iron sulfide channels, as iron sulfide was also stable at the surface (see Fig. 2). Since FeS is a highly defective sulfide, rapid transport of metallic species and sulfur occurred through these channels, resulting in catastrophic corrosion of the alloys. To achieve good corrosion resistance it is necessary to prevent the formation of iron sulfide channels.

The alloys containing 2.5 to 7 Al and 18 Cr formed external Al_2O_3-Cr_2O_3 duplex scales and showed good corrosion resistance. The corrosion resistance decreased with increasing Al content. The alloys that contained 10 Al and different amounts of Cr up to 15% formed external Al_2O_3 scales only and exhibited poor corrosion resistance. Figure 3 shows the weight gain per unit area data plotted as a function of time for two alloys that formed external Al_2O_3 scales but which exhibited widely differing corrosion behavior.

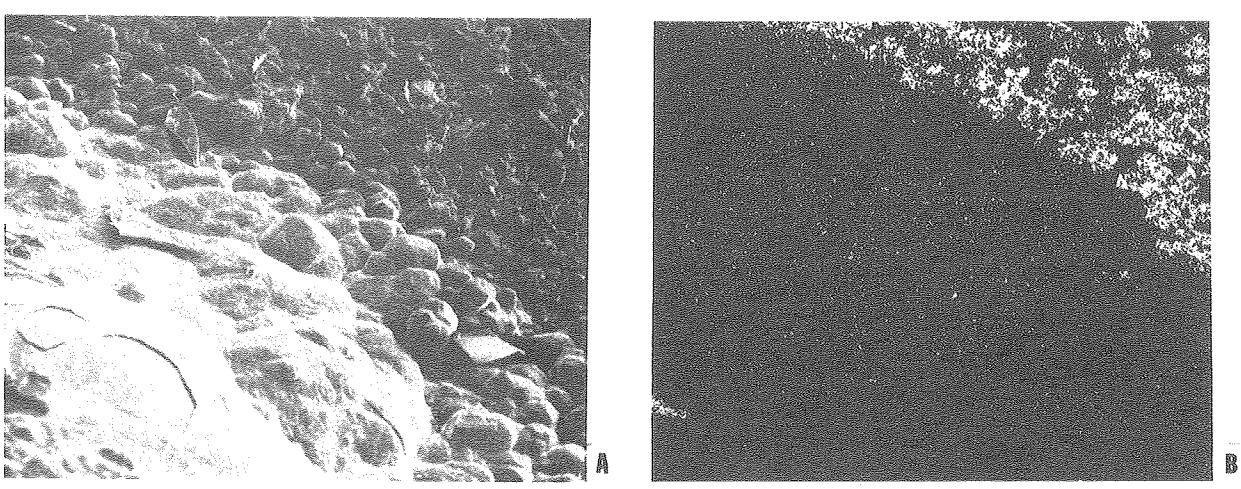

Fig. 2. Fe-18Cr - 1.5Si, corroded for 1 day (200X). (A) Secondary electron image of the outer surface of the corroded specimen. (B) X-ray map for S.
(XBB 770-12691)

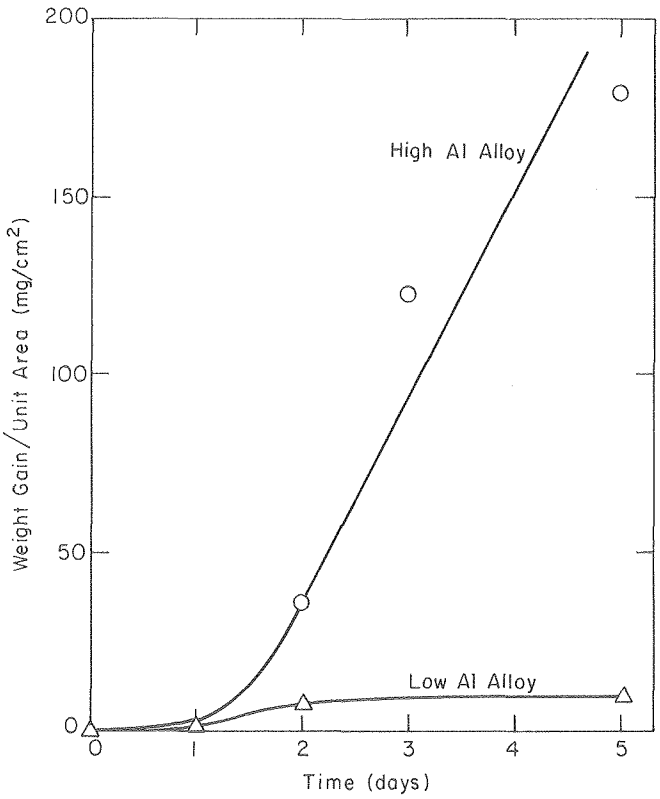

Fig. 3. Shows the weight gain per unit area vs. time plots for two Al_2O_3-forming alloys. (XBL 7712-6569)

Although both the alloys contained similar amounts of chromium the Al content was different, and it was surprising to find the alloy that contained lesser amounts of Al to be more corrosion resistant. This behavior can be rationalized by considering that the duplex Al_2O_3/Cr_2O_3 scale that formed on the low-Al alloys is a far better barrier to sulfur diffusion than the single Al_2O_3 scale that formed on the higher aluminum content alloys. The breakdown of the single Al_2O_3 scale occurred by the formation of Cr-rich sulfides within the oxide scale as shown in Fig. 4.

The conclusions of this investigation are important for alloy designers developing new corrosion resistant alloys for elevated-temperature applications in coal gasifiers. They are:

1) Cr_2O_3 scales are not a barrier to sulfur diffusion in coal gasifier environments. Si additions do not help the Cr_2O_3 become an acceptable barrier material.

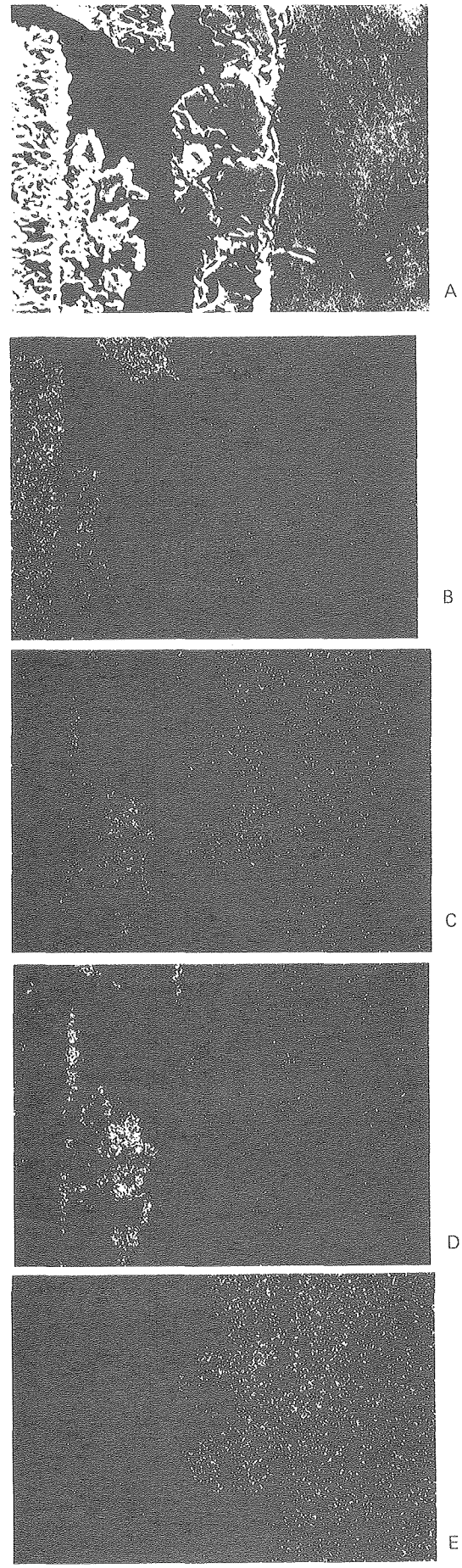

Fig. 4. Fe - 10Al - 15Cr, corroded for 3 days, 130x:
(A) Secondary electron image of the scale/alloy interface.
(B) X-ray map for Al.
(C) X-ray map for Cr.
(D) X-ray map for S.
(E) X-ray map for Fe. (XBB 770-12690)

2) Aluminum-chromium containing alloys with near 18% Cr to form a continuous Cr_2O_3 scale and an optimum amount of aluminum in the range 3-5% to form a continuous Al_2O_3 scale will form a duplex barrier scale that can resist sulfur diffusion, at least for the exposure periods of this study.

3) Aluminum-containing alloys that form primarily a single Al_2O_3 barrier scale, even with significant quantities of Cr also present, do not have resistance to sulfur attack at coal gasifier operating temperatures.

c. Thermodynamic Prediction of the Behavior of Fe-Cr-Al and Fe-Cr-Ni Alloys in Coal Gasification Environments

B. Gordon, W. Worrell and V. Nagarajan

In order to predict the behavior of materials in large-scale coal gasification plants, it will be necessary to understand the corrosion behavior of the alloys. Prediction of the corrosion scales formed under specified coal gasification environments is a necessary initial step in the design of efficient corrosion tests.[1] The thermodynamic stability diagram is a method of plotting the phases formed on an alloy as a function of gas composition. For a given gas phase reaction such as the oxidation of a metal,

$$xM + y/2\ O_2 \rightleftharpoons M_xO_y, \qquad (1)$$

there is an associated free energy, ΔG^r, such that the equilibrium partial pressure of oxygen at which the oxide phase is formed can be calculated, assuming the metal and oxide activities are unity. Similar calculation can be made for the formation of sulfides. When these partial pressures are plotted at constant temperature, a stability diagram such as shown in Fig. 5 is the result.

To construct such a diagram, accurate and consistent thermodynamic data are required. For simple phases such as FeO, Cr_2O_3, etc. such data are available from the JANAF tables.[2] Current work includes the formation and interaction of more complex phases such as $FeCr_2O_4$ and $FeAl_2O_4$ spinels, specifically for the Fe-Cr-Al and Fe-Cr-Ni systems. Data for these phases are not routinely available and are being carefully researched in the literature.[3,4]

Experimental verification of alloy behavior under aggressive conditions is difficult to compare with thermodynamic predictions because of the strong role that kinetics plays in phase formation. Current work compares predicted spinel formation with experiment for the reactions.

$$FeS + 1/2\ O_2 + Cr_2O_3 \rightleftharpoons FeCr_2O_4 + 1/2\ S_2 \qquad (2)$$

and

$$FeS + 1/2\ O_2 + Al_2O_3 \rightleftharpoons FeAl_2O_4 + 1/2\ S_2. \qquad (3)$$

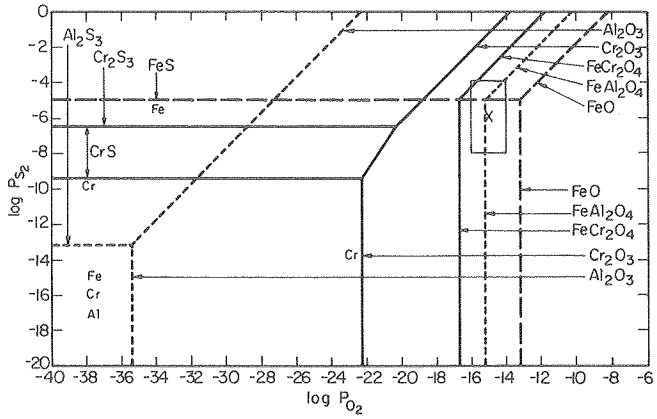

Fig. 5. Fe-Cr-Al system represented at 871°C. Units are atmospheres. The arrows indicate P_{O_2} and P_{S_2} lines at which the specific phase becomes stable. Where arrows overlap, the indicated oxide or sulfide phases are simultaneously stable. For example, at $P_{O_2} = 10^{-20}$ and $P_{S_2} = 10^{-12}$, the stable phases are $FeCr_2O_4$, Cr_2O_3, and Al_2O_3. The rectangular region indicates P_{O_2} and P_{S_2} ranges of typical coal gasifiers corrected for temperature. All metals are at unit activity.

Key: —— —— —— phase boundaries involving only Fe.
---------- phase boundaries involving Al.
———— phase boundaries involving Cr.
(XBL 782-4403)

Such experiments make use of powder mixtures and long exposures to circumvent kinetic influences on the formation of these phases.

---

1. B. A. Gordon, W. L. Worrell and V. Nagarajan, Thermodynamic Predictions of the Behavior of Fe-CrAl Alloys in Coal Gasifier Environments, LBL-7370; to be submitted.
2. JANAF Thermochemical Tables; 2nd edition, NSRDS-WBS 37 (1971).
3. K. T. Jacob and C. B. Alcock, Met. Trans. 6B, 215 (1975).
4. J. C. Chan, C. B. Alcock and K. T. Jacob, Con. Met. Quart. 12, 439 (1973).

d. Influence of Phase Relations on the Sulfidation of 310 Stainless Steel

D. Bhogeswara Rao,* K. T. Jacob,† and Howard G. Nelson‡

The sulfide scales that are formed during the sulfidation of 310 stainless steel are generally multilayered, containing one or two outer layers in addition to a subscale. The number of scales and their compositions varied with the sulfur potential

and the temperature of sulfidation. Micrographs of typical scales are shown in Fig. 6. In two-layered scales, the second outer layer (OL-II), furthest from the alloy, contained primarily phases of the Fe-Ni-S system. The first oyter layer (OL-I), nearest the subscale, contained phases of the Fe-Cr-S system. The subscale consisted of chromium-rich sulfide inclusions in the alloy matrix. The chromium content of OL-I increased with increasing temperature[1] and decreasing sulfur potentials[2] and appeared to control the rate of sulfidation of 310 stainless steel. However, correlations between the compositions of the experimentally observed phases and those that may be theoretically predicted have not been explored. The stability fields of various phases that form on 310 stainless steel have been developed as a function of temperature and partial pressure of sulfur.[3] These constructed stability fields are in excellent agreement with the sulfide phases and compositions determined experimentally.

It has also been observed that during the initial stages, where transient kinetics persisted, the composition of OL-I changed with time at a given surface potential and temperature and finally reached a steady state condition. Initially a chromium-rich sulfide was formed which changed composition during the course of time as more iron went into the solution. This experimentally deduced fact can also be predicted from the stability field diagrams.

A careful microstructural examination of the product layer (OL-I) revealed arrays of alternate sublayers in a slowly cooled sample, as shown in Fig. 7(a). The sublayers are absent when the samples were quenched as shown in Fig. 7(b) and (c). It was determined from the quantative EDAX analysis that the sublayers differed only in the Fe:Cr ratio. These sublayers were absent in the quenched samples. This suggests that the high-temperature phase was separated into two different phases. Such a transformation could be visualized with the help of stability field diagrams.

In certain cases it is not possible to retain some high-temperature sulfide phases by quenching. For example, it was observed from the experiments that the OL-II was composed of a mixture of $(Fe, Ni)_{1-x}S$ monosulfide solid solution and $(Fe,Ni)_9S_8$ pentlandite Fe-Ni alloy.[1] On the basis of the high-temperature stability fields, pentlandite and the associated alloy phase are not high-temperature phases. In order to explore the effect of cooling, a vertical section through the ternary Fe-Ni-S composition-temperature phase relations was developed at a sulfur potential of $1.4 \times 10^{-2} Nm^{-2}$ and is shown in Fig. 8. It can be deduced from this figure that at an experimental temperature of 1150 K, OL-II is composed of iron-rich $(Fe, Ni)_{1-x}S$ phase. On cooling, $(Ni, Fe)_{3\pm x}S_2$ begins to crystallize from the liquid sulfide melt until all the liquid phase is used up. The changes in composition caused by a further decrease in temperature results in the precipitation of some Fe-Ni alloy. Below 850 K pentlandite begins to form as a solid phase from $(Fe, Ni)_{1-x}S$ and $(Ni, Fe)_{3\pm x}S_2$. This example clearly demonstrates the necessity of high-temperature stability field diagrams for the interpretation of corrosion products observed after cooling the specimens to room temperature.

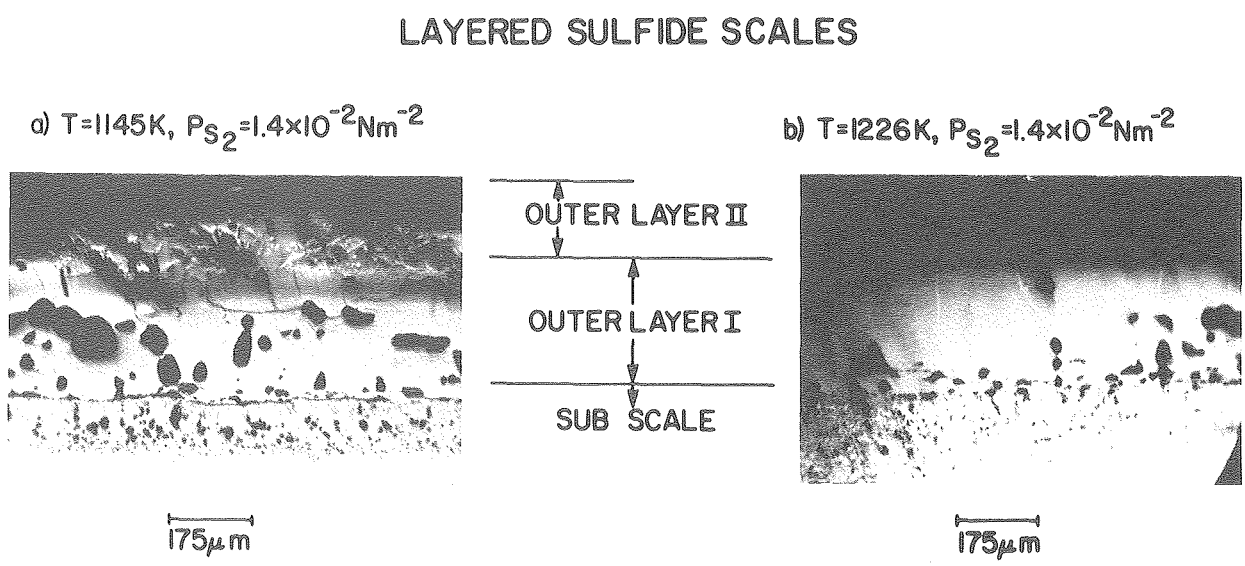

Fig. 6. Multilayered sulfide scales formed during the sulfidation of 310 stainless steel. (XBB 783-3046)

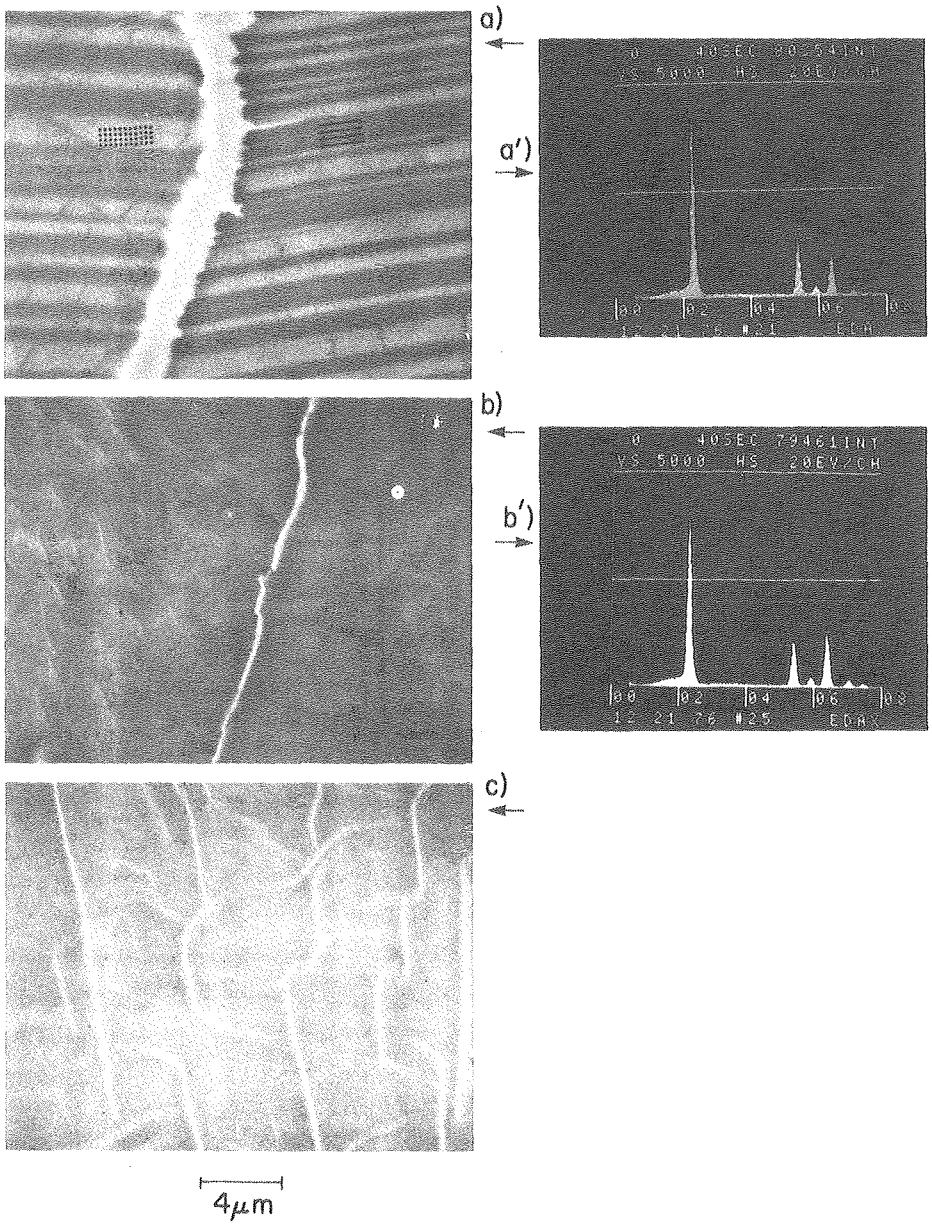

Fig. 7. Effect of cooling rate on the formation of sublayers in OL-1. a) Slowly cooled sample showing the sublayers. b) and c) Disappearance of sublayers in the quenched samples. a') Compositions for the individual sublayers of Fig. 7a. Light grey phase = 14 wt% Cr, 41 wt% Fe, 43 wt% S and 1 wt% Ni. Grey phase = 26 wt% Cr, 27 wt% Fe, 46 wt% S and 0.5 wt% Ni. b') General composition of OL-1 shown in Fig. 7b (19.5 wt% Cr, 33.5 wt% Fe, 2 wt% Ni and 44 wt% S). (XBB 783-3043)

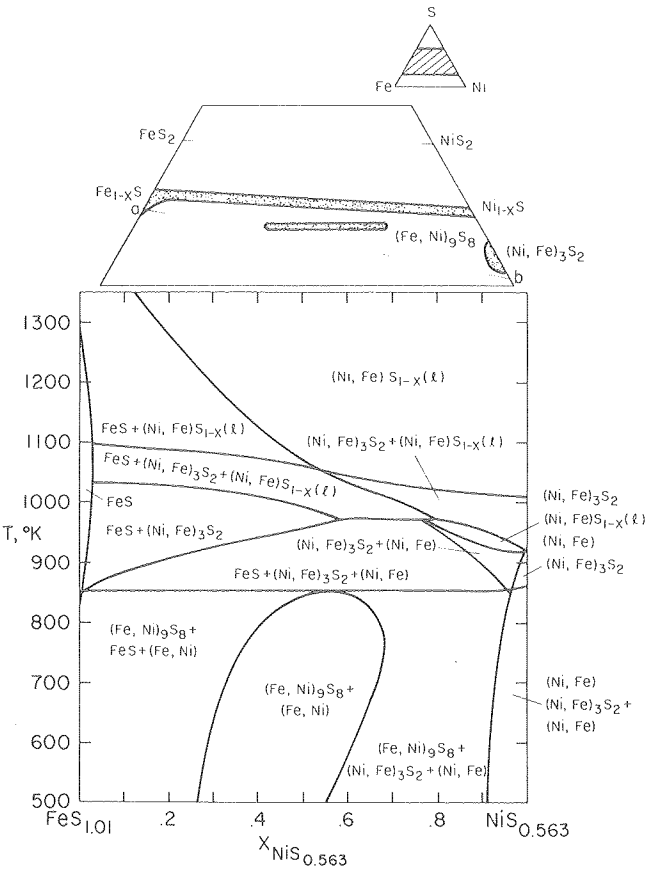

Fig. 8. A vertical section through the Fe-Ni-S composition-temperature phase diagram. The composition of OL-II at 1150 K and $P_{S_2} = 1.4 \times 10^{-2}$ Nm^{-2} falls in section a-b. The points a and b are the compositions of the binary Fe-S and Ni-S phases that exist at 1150 K and $P_{S_2} = 1.4 \times 10^{-2}$ Nm^{-2}. (XBL 783-7647)

---

*Materials and Molecular Research Division, Lawrence Berkeley Laboratory, Berkeley, CA 94720.

†Department of Metallurgy and Materials Science, University of Toronto.

‡Materials and Physical Sciences Branch NASA-Ames Research Center, Moffett Field, CA 94035.

1. D. Bhogeswara Rao and Howard G. Nelson, Influence of Temperature and the Role of Chromium on the Kinetics of Sulfidation of 310 Stainless Steel, in Oxidation of Metals, in press.
2. D. Bhogeswara Rao and Howard G. Nelson, Sulfidation of 310 Stainless Steel at Sulfur Potentials Encountered in Coal Conversion Systems, NASA Technical Memorandum, NASA-TM X-73,166, September 1976, and the Proceedings of the Symposium on Properties of High Temperature Alloys, edited by Z. A. Foroulis and F. S. Pettit, Proceedings Vol. 77-1, The Electrochemical Soc., Inc., Princeton, NH, 464 (1971).
3. K. T. Jacob, D. Bhogeswara Rao and Howard G. Nelson, Influence of Phase Relations in the Fe-Ni-Cr-S System on the Sulfidation of an Austenitic Stainless Steel, in Oxidation of Metals, communicated.

e. Solid State Sulfur Probe for Coal Gasification Systems

K. T. Jacob,* D. Bhogeswara Rao,† and Howard G. Nelson‡

The internal components of coal gasifiers can be severely degraded, depending upon the material and the sulfur content of the reactive gases. Corrosion tests performed in the laboratory involve either well equilibrated gas mixtures or are performed under steady state conditions. In actual operation fluctuations in the gas composition will occur due to such variables as nonuniform distribution of sulfur in the coals. The ability to continuously monitor the sulfur potential in coal gasifiers is of major importance for efficient gasifier operation and for accurate life prediction of construction materials. It was, therefore, decided to study the feasibility of a solid state sulfur probe.

In the absence of an acceptable sulfide electrolyte, analogous to $CaO\text{-}ZrO_2$ or $Y_2O_3\text{-}ThO_2$ for oxygen potential measurements, an alternate approach was followed where CaF_2 was used as a solid electrolyte. The solid electrolyte cell

$$Ar+H_2+H_2S\ /\ CaS+CaF_2+(Pt)//\ CaF_2//\ (Pt)+CaF_2+CaS\ /\ H_2S+H_2+Ar \qquad (1)$$

was constructed and its efficiency determined. The electrodes were designed to convert the sulfur potential gradient across the calcium fluoride electrolyte into an equivalent fluorine potential gradient with the aide of the reaction

$$CaF_2(s) + 1/2S_2(g) \rightarrow GaS(s) + F_2(g). \qquad (2)$$

The emf of the cell can be calculated through the Nernst equation

$$L = \frac{\Delta\mu_{F_2}^{R} - \Delta\mu_{F_2}^{T}}{nF} = \frac{RT}{nF} \ln \frac{P_{F_2}^{R}}{P_{F_2}^{T}} = \frac{RT}{nf} \ln \frac{(P_{H_2S}/P_{H_2})^{R}}{(P_{H_2S}/P_{H_2})^{T}}. \qquad (3)$$

The measured emfs at 1073 and 1173 K are plotted as a function of log P_{H_2S}/P_{H_2} along with the calculated data using Eq. (3). A deviation of not more than 1% was observed between the calculated and experimentally observed (Fig. 9).

The variation of the emf of the cell with temperature was measured for two test gases (Table 1) and is shown in Fig. 10. Again, measured temperature dependence is in agreement with the theoretical value given by the derivative of Eq. (3) with respect to temperature:

$$\frac{dE}{dt} = \frac{R}{nF} \ln \frac{(P_{H_2S}/P_{H_2})^{R}}{(P_{H_2S}/P_{H_2})^{T}}. \qquad (4)$$

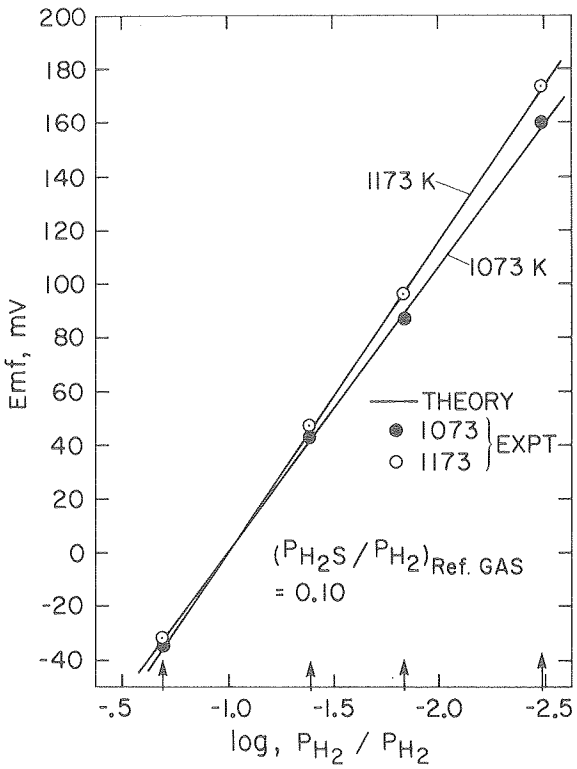

Fig. 9. Variation of the emf with H_2S/H_2 ratio of the test gas at 1073 K and 1173 K. (XBL 783-7646)

Table 1. Composition of the test gas mixtures and the corresponding cell emfs.

Test Gas Number	Composition (vol %)			emf	
	H_2	H_2S	Ar	1073 K	1173K
1	40.6	8.3	51.1	-32	-34
2	50.4	2.05	47.55	43	47
3	54.0	0.79	45.21	87	96
4	55.1	0.18	44.72	160	174
Reference gas	25.2	2.52	72.28	---	---

The response time of the probe was observed to vary from approximately 9 h at 990 K to 25 h at 1225 K. The exact factors affecting the slow response of galvanic cells based on a CaF_2 electrolyte have not yet been determined. The reasons for slow response may be the kinetic factors influencing the electrode reaction (2) or the slow transport of ions in CaF_2. Further investigations are being conducted to improve the response time of the cell.

The conversion of calcium sulfide and/or calcium fluoride into calcium oxide should not be a problem in anticipated coal gasification systems. Suggestions were presented for improving the cell for such commercial operations.[1]

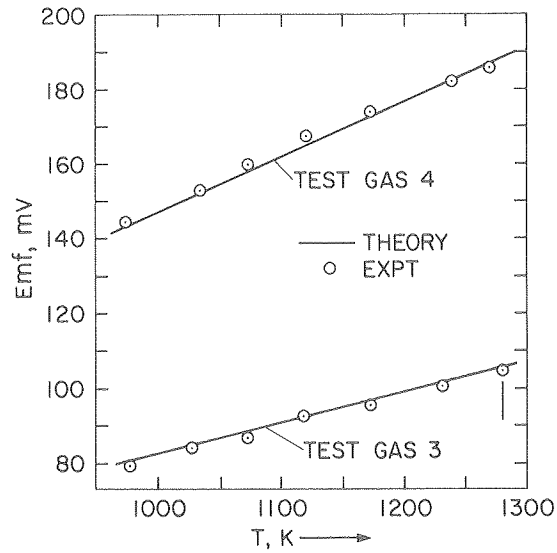

Fig. 10. The temperature dependence of the reversible emf with test gases 3 and 4 passing through the cell. (XBL 783-7645)

*Department of metallurgy and Material Science, University of Toronto.

†Materials and Molecular Research Division, Lawrence Berkeley Laboratory, Berkeley, CA 94720.

‡Materials and Physical Sciences Branch
NASA-Ames Research Center
Moffett Field, CA 94035.

1. K. T. Jacob, D. Bhogeswara Rao and H. G. Nelson, Some Studies on a Solid State Sulfur Probe for Coal Gasification Systems, J. Electrochem. Soc., in press.

f. Sulfidation of 310 Stainless Steel

D. Bhogeswara Rao* and Howard G. Nelson†

The present interest in coal conversion systems require corrosion data for commercial alloys in sulfur-containing gases. Sulfidation attack is particularly severe to the internal components of coal gasifiers where 310 stainless steel is one of the prime candidate materials. The sulfidation problems associated with this austentic stainless steel were investigated over a broad range of sulfur potentials and temperatures, as a part of a continuing program. It was found that chromium content in the product layer is critical to the sulfidation process and controls the rate of sulfidation of 310 stainless steel.

The sulfidation kinetics were determined as a function of temperature at three sulfur potentials: 39 Nm^{-2}, 1.4×10^{-2} Nm^{-2}, and 1.5×10^{-4} Nm^{-2} over the temperature range from 910 to 128 K. Weight gain data obtained at these sulfur potentials and temperatures obeyed a parabolic relationship with the exception of a transient period at the very early

stages of sulfidation.[1] Parabolic rate constants, K'P, were calculated from the curves and plots of the logarithm of the parabolic rate constant as a function of the reciprocal of the absolute temperature are shown in Fig. 11. At a sulfur potential of 39 Nm^{-2} (open circles) the rate of sulfidation increased progressively with increasing temperature and exhibited an activation energy of 125 kJ $mole^{-1}$. At a sulfur potential of 1.5×10^{-4} Nm^{-2} the rate of sulfidation decreased with increasing temperature over the temperature interval studied. At the intermediate sulfur potential, 1.4×10^{-2} Nm^{-2}, the rate of sulfidation increased with increasing temperature up to 1150 K and then decreased with increasing temperature.

A careful anslysis of the corrosion products indicated that the transition in kinetics is associated with a change in scale morphologies as well as composition changes in the Fe-Cr-S layer. In a previous study[2] it was shown from marker experiments that the sulfidation of 310 stainless steel is controlled by the diffusion of metal ions through the sulfide scale. Since the scales are multilayered, diffusion through one of these layers will be the rate-controlling step.

A careful analysis of the results has shown that the sudden decrease in the reaction rate (Fig.11) is associated with a decrease in the Fe:Cr ratio of the product phase (Fe-Cr-S) as shown in Fig. 12. It is seen from Fig. 12 that a sudden change in Fe:Cr ratio occurs at the two lower sulfur potentials, indicating the formation of a new phase which is more protective than the prior phase. A plot of the reaction rate as a function of Fe:Cr ratio for these two sulfur potentials is shown in Fig. 13. The data are reasonably linear at each potential, indicating that diffusion through the Fe-Cr-S layer is the rate-controlling step for which the Fe:Cr ratio is critical. Once this critical composition is reached, the

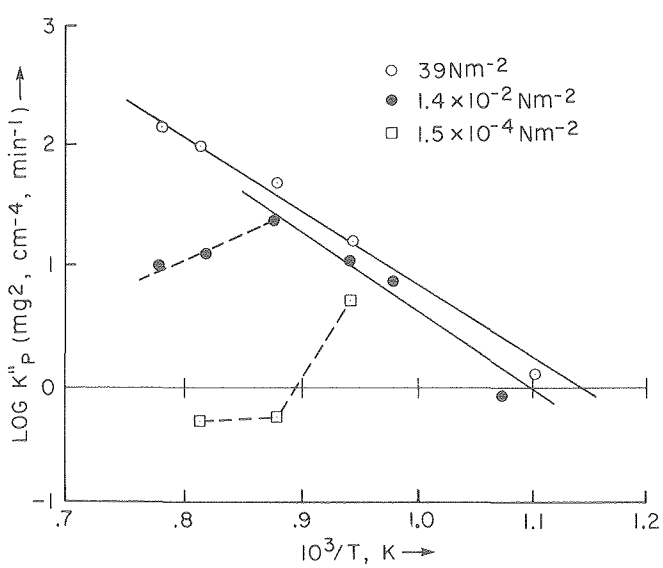

Fig. 11. Influence of temperature on the parabolic rate constant for the sulfidation of 310 stainless steel. (XBL 783-7652)

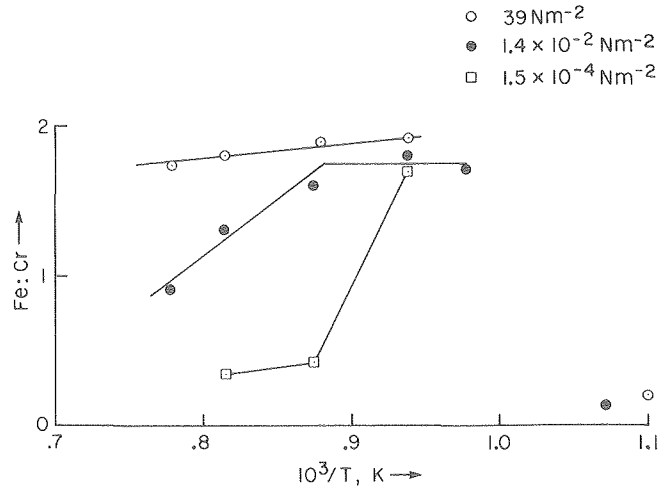

Fig. 12. Fe:Cr ratio of OL-I plotted as a function of the inverse of the absolute temperature. (XBL 783-7644)

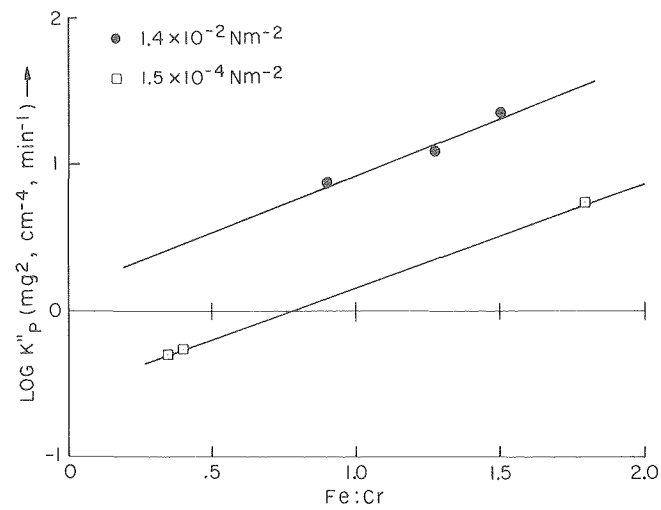

Fig. 13. The dependent of parabolic rate constants on the Fe:Cr ratio of OL-I. (XBL 783-7651)

reaction rate is independent of temperature. The nature of subscale formation is also closely associated with the changes in this composition.[3]

---

*Materials and Molecular Research Division, Lawrence Berkeley Laboratory, Berkeley, CA 94720

†Materials and Physical Sciences Branch, NASA-Ames Research Center, Moffett Field, CA 94035.

1. D. Bhogeswara Rao and Howard G. Nelson, Influence of Temperature and the Role of Chromium on the Kinetics of Sulfidation of 310 Stainless Steel, in Oxidation of Metals, in press.
2. D. Bhogeswara Rao and Howard G. Nelson, Sulfidation of 310 Stainless Steel at Sulfur Potentials

Encountered in Coal Conversion System, NASA Technical Memorandum, NASA-TM X-73,166, September 1976, and the Proceedings of the Symposium on Properties of High Temperature Alloy, edited by Z. A. Foroulis and F. S. Pettit, Proceedings Vol. 77-1 (The Electrochemical Soc., Inc., Princeton, NJ), p. 464 (1977).
3. D. Bhogeswara Rao, K. T. Jacob, R. W. Lindberg and Howard G. Nelson, Factors Influencing the Internal Sulfidation of 310 Stainless Steel, to be published.

g. Stability Fields for the Sulfide Phases in the Fe-Ni-Cr-S System

K. T. Jacob,* D. Bhogeswara Rao,† and Howard G. Nelson‡

Commercial alloys based on Fe-Ni-Cr are being used as construction materials for the internal components of coal gasifiers (e.g., type 310 stainless steel) where sulfidation attack is severe. The ability to predict the structure and composition of sulfide phases would be a major step forward in our understanding of the sulfidation process and of the behavior of alloys in specific environments. Stability field diagrams presently in use are thermodynamic plots of the type shown by Gordon and Worrell.[1] In these diagrams one depicts the stability of a given phase as a function of sulfur and oxygen potential at a constant temperature. Such diagram cannot be used to understand the reaction-path time-dependent variations in the alloy and scale compositions during transient stages. Additionally, these diagrams depict mostly for binary compounds whereas several ternary phases are observed experimentally.[2,3]

To provide a better and more realistic framework for following the sulfidation of Fe-Cr-Ni alloys at high temperatures, the stability fields of various sulfide phases that form on Fe-Cr, Fe-Ni, Ni-Cr, and Fe-Ni-Cr alloys have been developed as a function of temperature and a partial pressure of sulfur. The calculated stability fields in the ternary A-B-S system are displayed on plots of log P_{S_2} vs. the conjugate extensive variable $(n_A/n_A + n_B)$.

Figures 14-15 show calculated stability fields of various sulfide phases that are expected to form in Fe-Cr-S and Fe-Ni-S systems, respectively, at 1275 K. Figure 16 shows the effect of temperature on the stability field of various sulfide phases in the Fe-Cr-S system at a fixed sulfur potential of 1.4×10^{-2} Nm^{-2}.

The construction of these sulfur potential diagrams demand thermodynamic data for all that phases involved. Unfortunately, thermodynamic data for most of the solid solutions were not available in the literature. Current models and correlations were employed[4] to estimate the unknown thermodynamic behavior of solid solutions of sulfides and to supplement the incomplete phase diagram data of geophysical literature.

The stability field plots (Figs. 14-16) are very useful in predicting and correlating the sulfidation of commercial alloys. These kinds of plots have the

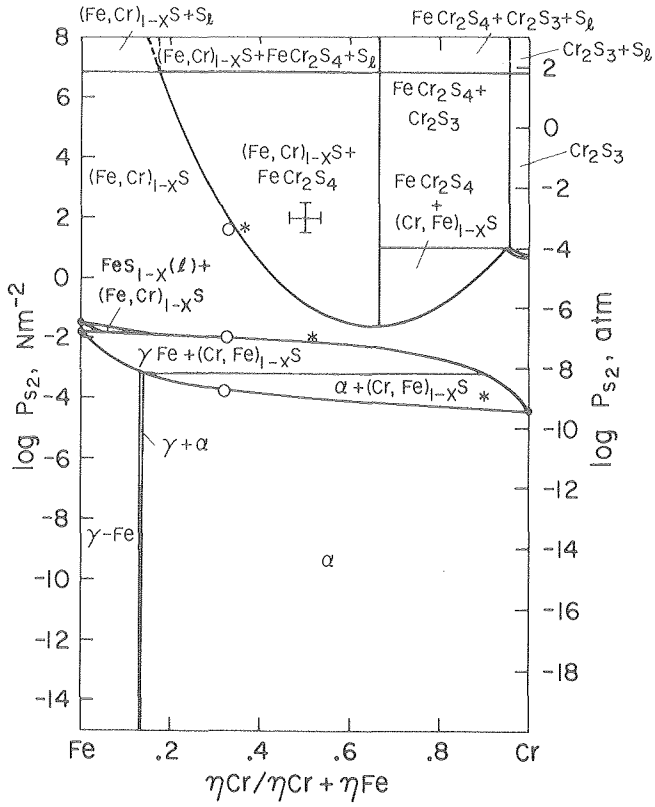

Fig. 14. The stability fields in the Fe-Cr-S system at 1275 K as a function of log P_{S_2}. (XBL 783-7650)

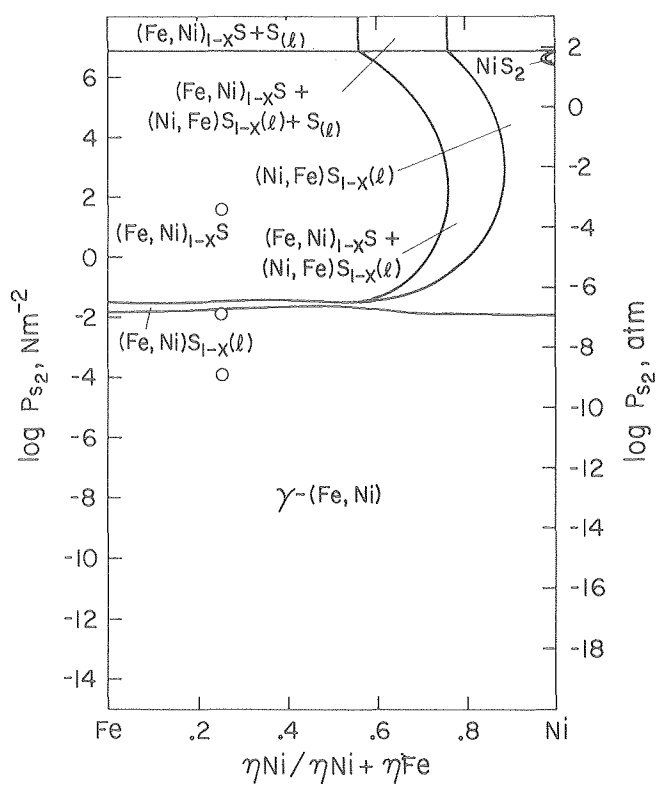

Fig. 15. The stability fields in the Fe-Ni-S system at 1275 K as a function of log P_{S_2}. (XBL 783-7649)

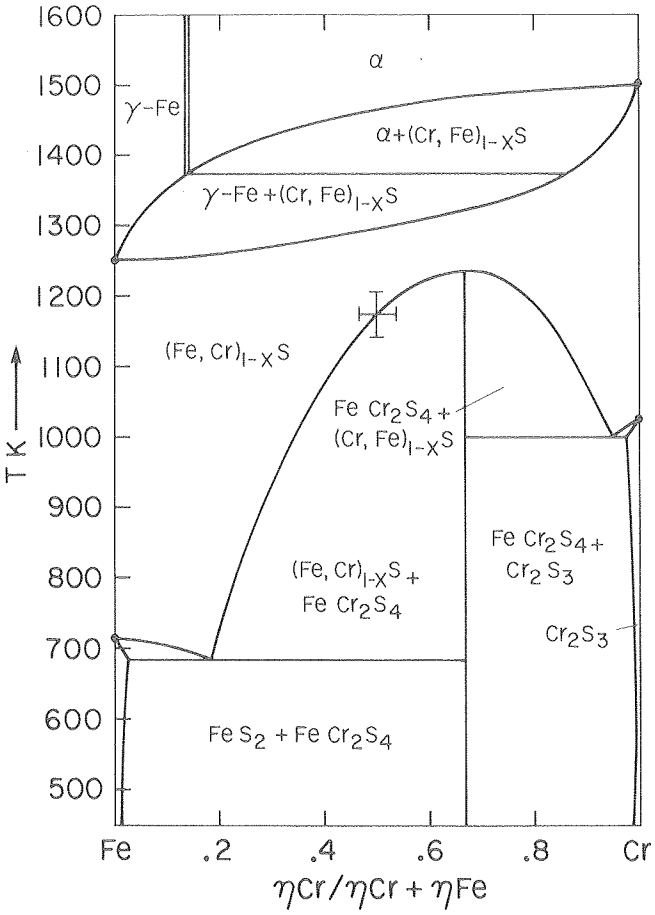

Fig. 16. Effect of temperature on the stability fields of various phases in the Fe-Cr-S system at a fixed sulfur partial pressure ($P_{S_2} = 10^{-2}$ Nm^{-2}). (XBL 783-7648)

advantage over others in that the reaction path could be traced from these diagrams. Similar plots for nickel-based alloys and for multicomponent gaseous environments are being developed.

---

*Department of Metallurgy and Materials Science, University of Toronto.

†Materials and Physical Research Division, Lawrence Berkeley Laboratory, Berkeley, CA 94720.

‡Materials and Physical Sciences Branch, NASA-Ames Research Center, Moffett Field, CA 94035.

1. Bruce A. Gordon, Pourbaix Stability Diagram Development for Stainless Steels in Coal Gasifier Environments, MMRD Annual Report for 1976, LBL-6016.
2. D. Bhogeswara Rao and Howard G. Nelson, Sulfidation of 310 Stainless Steel at Sulfur Potentials Encountered in Coal Conversion Systems, NASA Technical Memorandum, NASA-TM X-73, 166, September 1976, and the Proceedings of the Symposium on Properties of High Temperature Alloys, edited by Z. A. Foroulis and F. S. Pettit, Proceedings Vol. 77-1 (The Electrochemical Soc., Inc., Princeton, NJ), p. 464 (1971).
3. D. Bhogeswara Rao and Howard G. Nelson, Influence of Temperature and the Role of Chromium on the Kinetics of Sulfidation of 310 Stainless Steel, in Oxidation of Metals, in press.
4. K. T. Jacob, D. Bhogeswara Rao and H. G. Nelson, Influence of Phase Relations in the Fe-Ni-Cr-S System on the Sulfifation of An Austenitic Stainless Steel, in Oxidation of Metals (communicated).

h. Oxide Barrier Morphologies of Fe-Cr-Si and Fe-Cr-Al Alloys

R. Miner

In order to obtain a more complete understanding of the barrier behavior of oxide scales subjected to a coal gasification atmosphere, several different iron-base alloys were oxidized at 1800°F in a low P_{O_2} environment (P_{O_2} 10^{-18} atm) and in ambient air (P_{O_2} .2 atm). In order to relate composition and oxidation treatment to corrosion behavior, the surface morphologies of the experimental alloys were examined by using SEM. Composition and phase analysis were determined by using the EDAX and x-ray diffractometer. The cross sections of the air-oxidized specimens were examined by using an optical metallograph and SEM. The materials studied can be classed into two categories, depending on whether the scale formed is chromium oxide (Cr_3O_3) or aluminum oxide (Al_2O_3).

Chromium Oxide Formers. The scale morphology formed on the Fe-18Cr-Si alloys subjected to air oxidation were similar. The scale consisted of a fine granular structure of pure Cr_2O_3. In the low P_{O_2} environment, the oxide developed on the Fe-18Cr-.5Si alloy resembled that formed on the air-oxidized specimens. In addition, nodules of iron oxide were detected protruding through the scale. Figure 17(a) shows the fine granular morphology developed on the Fe-18

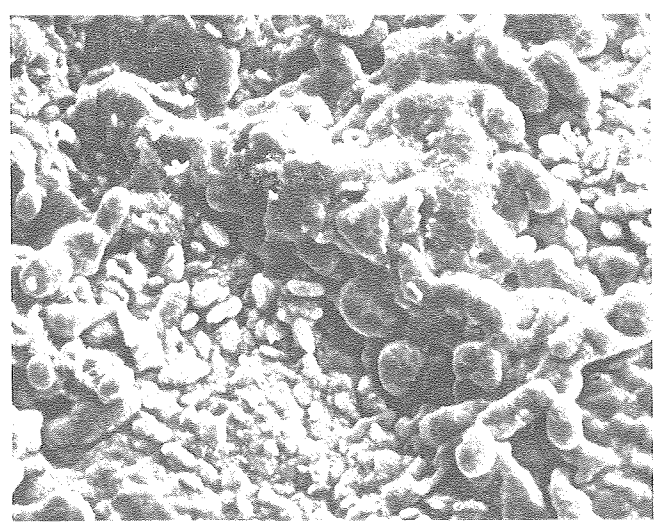

Fig. 17(a). Secondary electron image of the oxide morphology formed on Fe-18Cr-.5Si in low P_{O_2} atmosphere. (XBB 783-3203)

Cr-Si alloys. Figure 17(b) shows the EDAX analysis of the nodule present in Fig. 17(a). As the silicon content increased, the scale morphology developed in the low P_{O_2} environment changed from an aggregate of fine granular oxide pebbles to a foliaceous structure. Nodules of iron were no longer observed. Figure 18 shows the foliaceous structure developed on the silicon-containing alloys in the low P_{O_2} environment. In this figure part of the oxide has spalled from the metal surface, exposing a region rich in SiO_2. In addition to altering the outer CR_2O_3 morphology, increasing the silicon content increased the degree of internal oxidation of silicon. The silicon additions were made in order to enhance the alloy's oxidation resistance due to the formation of an internal layer of SiO_2. A continuous layer of SiO_2 was never formed, as hoped, even after nine days of air oxidation. In the case of Fe-18Cr-.5Si and Fe-18Cr-1.0Si, massive oxidation occurred at the edges and corners of the samples. The corrosion products were found to be Cr_2O_3. The Fe-18Cr-1Al alloy when oxidized in air and in low P_{O_2} atmosphere developed in both instances a fine granular texture of Cr_2O_3, similar to that formed on the air-oxidized Fe-18Cr-Si alloys. Nodules of iron oxide were never observed; however, internal oxidation of aluminum was apparent.

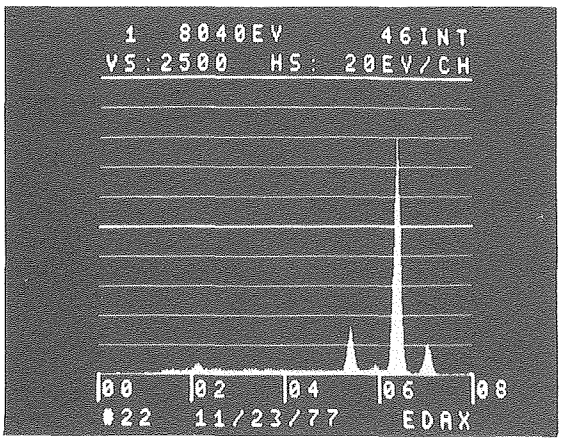

Fig. 17(b). The EDAX analysis of the nodule shown in Fig. 1(a). (XBB 783-3204)

Aluminum Oxide Formers. The morphologies of the oxide formed on the alloys that developed an external scale of Al_2O_3 during oxidation were found to be similar. In general, the scales formed in the low P_{O_2} atmospheres resembled those developed in air. This oxide morphology can best be described as a compact aggregate of spaghetti-like structure extending over the outer surface. Figure 19 depicts the typical spaghetti-like morphology developed on the Fe-18Cr-3Al alloy in air. Upon cooling from temperature, the oxide scale was found to spall readily. On examining the cross sections of the Fe-10Al-Cr alloys, internal precipitates of Al_2O_3 were evident; however, internal oxidation did not occur in the Fe-18Cr=3Al, Fe-18Cr-5Al, or Fe-18Cr-7Al.

The oxidation behavior of the Fe-10Al alloy showed the most contrast. In air the scale resembled that developed on the other aluminum oxide formers. In the low P_{O_2} environment, however, a fine granular texture similar to that developed on the Fe-18Cr-.5Si alloy was observed. In both atmospheres the scale

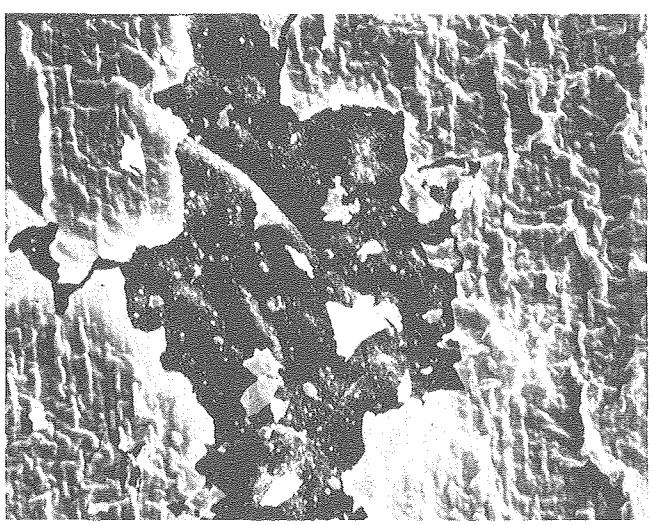

Fig. 18. Secondary electron image of the oxide morphology formed on Fe-18Cr-1Si alloys in low P_{O_2} atmosphere. (XBB 783-3202)

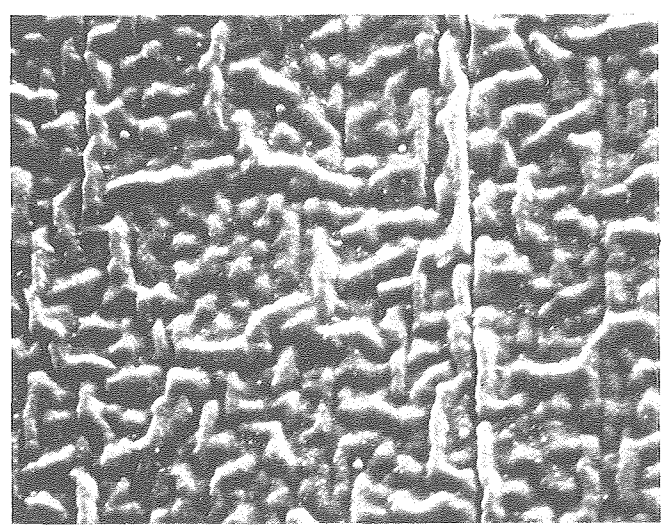

Fig. 19. Secondary electron image of the oxide formed on Fe-18Cr-3Al in low P_{O_2} atmosphere. The spaghetti-like structure is very typical of that observed on most Al_2O_3 formers. (XBB 783-3199)

was pure Al_2O_3. Also, nodules of iron oxide developed in both oxidizing atmospheres. Internal precipitates of oxides were never observed. Figure 20(a) shows the fine granular structure developed in low P_{O_2} atmosphere on the binary alloy. Figure 20(b) shows the relative composition of the nodule protruding through the scale.

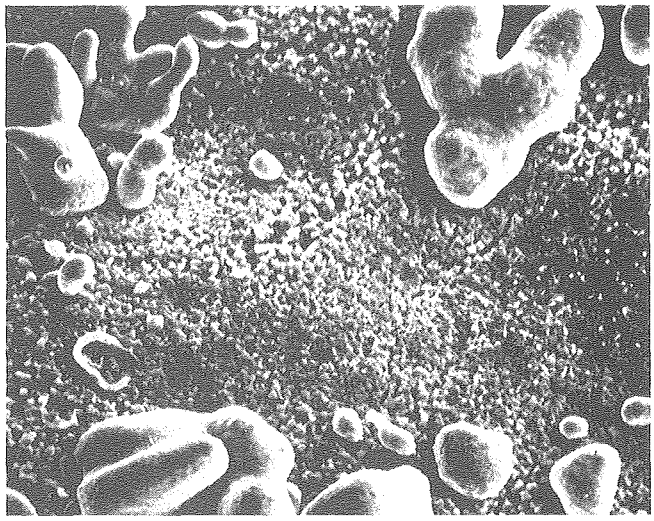

Fig. 20(a). Secondary electron image of the surface oxide formed in low P_{O_2} environments on the Fe-10Al alloy. (XBB 783-3201)

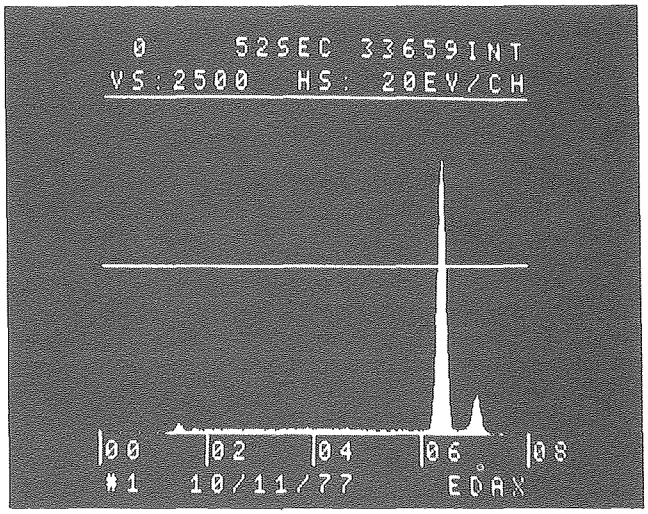

Fig. 20(b). EDAX analysis of the nodule shown in Fig. 4(a). (XBB 783-3200)

i. Corrosion of 310 Stainless Steel in H_2-H_2O-H_2S Mixtures

D. Bhogeswara Rao,* K. T. Jacob,† and Howard G. Nelson‡

The corrosion kinetics of 310 stainless steel was investigated in the gaseous environment of H_2-H_2O-H_2S at 1150 K. The effect of sulfur potential on the reaction rates was determined at a constant oxygen potential of 6×10^{-13} Nm^{-2}. The sulfur potential was varied from 8×10^{-1} Nm^{-2} to 8.6×10^{-3} Nm^{-2}. Weight gain measurments observed with a continuously recording thermobalance were used to evaluate the reaction kinetics. At all sulfur potentials investigated, except for the lowest sulfur potential (8.6×10^{-3} Nm^{-2}), the reaction was found to obey a linear rate law after an initial transient period. The length of the initial transient period was dependent upon sulfur potential with increasing sulfur potential decreasing the transient period. At the lowest sulfur potential studied, the corrosion rate was minimum and obeyed a parabolic rate law. A break in the kinetic curve was observed after a reaction time of about 350 h. The second parabolic rate constant had a slightly higher value than the first.

Scanning electron microscopy and conventional metallography were used to investigate the nature and morphology of the scales. It was found that except for the lowest sulfur potential studied (9.6×10^{-3} Nm^{-2}), the corrosion scales contained multilayered sulfides similar to those observed in pure sulfidation attack. The sulfide layer farthest from the subscale contained phases that belong to the Fe-Ni-S system, which is liquid at the test temperature. The sulfide layer nearest the subscale consisted of phases that belong to the Fe-Cr-S system. The morphology of this layer is again similar to that observed in the sulfidation of 310 stainless steel. Unlike that observed in pure sulfidation, this layer is separated from the subscale by a thin layer of oxide. The oxide phase is similar to the spinel structure, $FeCr_2O_4$, with some amount of dissolved manganese. Because of the oxide layer, the rates of reaction were found to be slower than those observed for pure sulfidation at all sulfur potentials investigated.

At the lowest sulfur potential studied the scale consisted mainly of an oxide layer. Energy dispersive x-rays and x-ray analysis were used to determine quantitatively the compositions of various sulfide and oxide phases. Analysis of the oxide layer indicated that it contained mainly chromium and manganese with small amounts of dissolved iron. Chromium- and manganese-rich sulfides were detected beneath the oxide layer (subscale). At the grain boundaries of the subscale region, the sulfides consisted of chromium, iron, and manganese. Fine discontinuous sulfide inclusions rich in manganese were also detected in the subscale.

When the results are compared with the pure sulfidation of 310 stainless steel in H_2-H_2S mixtures, it can be inferred that at the sulfur potential studied,

the outermost layer (Fe-Ni-S sulfide liquid) is unstable and is absent. The Fe-Cr-S sulfide layer nearest the subscale is the only stable sulfide phase. Under the investigated conditions of simultaneous oxidation-sulfidation, chromium becomes preferentially oxidized, which explains the slow reaction rate. Thermochemical diagrams were developed in an effort to predict and compare the stability and composition of the corrosion products. The corrosion behavior of 310 stainless steel can be deduced from both the experimental results and the thermochemical diagrams.

---

*Materials and Molecular Research Division, Lawrence Berkeley Laboratory, Berkeley, CA 94720.

†Department of Metallurgy and Materials Science, University of Toronto.

‡Materials and Physical Sciences Branch, NASA-Ames Research Center, Moffett Field, CA 94035.

3. RESEARCH PLANS FOR CALENDAR YEAR 1978

Alan V. Levy

Erosion studies will be extended from the pure-metal behavior area into more complex regions that more closely simulate the conditions in coal gasifiers. The erosion behavior of scales formed on metals exposed to the combined oxidizing-sulfidizing environments of a coal gasifier will be determined. Particular emphasis will be placed on gaining an understanding of how combined brittle and ductile materials behave; i.e., a brittle oxide scale formed on a ductile metal matrix. Combined analytical-experimental work will be conducted to adapt the abrasion delamination theory of wear to solid-particle impact erosion. The erosion behavior of surface coatings designed to protect metal surfaces against corrosion environments will be investigated. The major part of the erosion work will be performed at elevated temperatures up to 1000°C.

A continuation of the coal char-metal reaction study will investigate what the composition and state of the reactants are as a function of the source of the char; i.e., various coals from various processes and variations of the test conditions.

Corrosion work will include completion of the initial in-depth study of combined oxidation-sulfidation behavior of 310 stainless steel, development of the stability field diagrams for oxygen-sulfur-alloy systems in two- and three- dimensional representations, determination of the transport properties of anion and cation constituents through oxide barrier scales, and investigation of the effects of pre-oxidation and surface coatings on corrosion of chromia and alumina former alloys. The use of aerodynamic boundary layer control to modify the composition and, hence, the corrosive nature of the reactive gases in a pipe will be investigated.

The combination of erosion and corrosion mechanisms in single tests will also be undertaken. The behavior of ternary alloys in the clean and pre-oxidized states and protective coatings will be studied under oxidizing-sulfidizing conditions with coal char erosive particles.

4. 1977 PUBLICATIONS AND REPORTS

Alan V. Levy and Associates

Journals and Books

1. D. B. Rao and H. Nelson, Sulfidation of 310 Stainless Steel at Sulfur Potentials Encountered in Coal Conversion Systems in Proceedings of the Symposium on Properties of High Temperature Alloys, edited by Z. A. Foroulis and F. S. Pettit, Proceedings Vol. 77-1 (The Electrochemical Society, Inc., Princeton, NJ, p. 464 (1977).

2. D. B. Rao and H. G. Nelson, Influence of Temperature and the Role of Chromium on the Kinetics of Sulfidation of 310 Stainless Steel, in Oxidation of Metals (in press).

3. K. T. Jacob, D. B. Rao and H. G. Nelson, Influence of Phase Relations in the Fe-Ni-Cr-S System on the Sulfidation of an Austenitic Stainless Steel, in Oxidation of Metals (submitted).

4. B. A. Gordon and V. Nagarajan, Corrosion of Fe-10Al-Cr Alloys by Coal Char, in Oxidation of Metals (in press).

5. I. Finnie and D. H. McFadden, On the Velocity Dependence of the Erosion of Ductile Metals by Solid Particles at Low Angles of Incidence, Wear (in press).

6. L. L. Brass and A. V. Levy, The Effects of the Microstructure of Ductile Alloys on Solid Particle Erosion (submitted to Metallurgical Transactions).

7. I. Finnie, A. V. Levy and D. H. McFadden, The Fundamental Mechanisms of the Erosive Wear of Ductile Metals by Solid Particles, ASTM STP (in press).

8. K. T. Jacob, D. B. Rao and H. G. Nelson, Some Studies on a Solid State Sulfur Probe for Coal Gasification Systems, Electrochem. Soc. (in press).

LBL Reports

1. L. L. Brass, The Effects of Microstructure of Ductile Alloys on Solid Particle Erosion (M.S. thesis), LBL-6277.

2. D. H. McFadden, Erosion of Ductile Metals by Solid Particles (M.S. thesis), LBL-6279.

3. D. M. Kleist, One Dimensional-Two Phase Particulate Flow (M.S. thesis), LBL-6967.

4. P. A. Doyle, The Elevated Temperature Erosion of 1100-0 Aluminum by a Gas-Particle Stream, LBL-7327.

5. R. A. Mayville, A Mechanism of Material Removal in Solid Particle Erosion of Ductile Metals, LBL-7333.

6. H. Hirano, An Investigation of Two-Body Abrasive Wear, LBL-7328.

7. J. Laitone, Erosion Prediction Near a Stagnation Point Resulting from Environmental Solid Particles, LBL-6990.

8. W. Yeung, Erosion Prediction from Solid Particle-Gas Flow in a Curved Pipe, LBL-7329.

9. J. Keller, Diffusion of a Chemical Species Through a Viscous Boundary Layer, LBL-7330.

10. V. Nagarajan and A. V. Levy, Elevated Temperature Corrosion Behavior of Iron Base Ternary Alloys that Develop Cr_2O_3 and/or Al_2O_3 Barrier Scales, LBL-7331.

11. B. A. Gordon and W. L. Worrell, Thermodynamic Predictions of the Corrosion of 310 Stainless Steel in Coal Gasification Environments, LBL-7332.

12. B. A. Gordon, W. Worrel and V. Nagarajan, Thermodynamic Predictions of the Behavior of Fe-Cr-Al Alloys in Coal Gasifier Operating Environments, LBL-7320.

Papers Presented

1. A. V. Levy, Erosion-Corrosion of Metals in Coal Gasifier Environments, NACE National Meeting, San Francisco, CA, March 1977.

2. D. B. Rao, H. G. Nelson, and A. V. Levy, Role of Chromium in the Sulfidation of an Austenitic Steel, AIME Meeting, Atlanta, GA., March 1977.

3. A. V. Levy, Erosion-Corrosion Behavior of Metals, Seminar at Ames National Laboratory, Iowa State University, March 1977.

4. I. Finnie and A. V. Levy, Mechanisms of Solid Particle Erosion of Metals at Room and Elevated Temperatures, ASTM Symposium on Erosion of Materials, Vail, CO, October 1977.

3. PHYSICAL PROPERTIES

a. Superconductivity Effects — High Field Superconductivity

Milton R. Pickus, Principal Investigator

1. A NEW A15 MULTIFILAMENTARY SUPERCONDUCTOR BASED ON THE NIOBIUM-ALUMINUM-SILICON SYSTEM

Gary C. Quinn, John Ling-Fai Wang, John T. Holthuis and Milton R. Pickus

At the present time, commercial fabrication of A15 multifilamentary superconductors utilizes the so-called bronze process. This process is effective for a limited number of compounds, notably, Nb_3Sn and V_3Ga. However, it has been found to be ineffective for aluminum-containing compounds which provide the advantages of much higher critical fields and higher critical temperatures. In contrast, the infiltration process developed at MMRD has been used successfully not only for Nb_3Sn but also for Nb_3Al and $Nb_3(Al,Ge)$, and is now reported for the first time for $Nb_3(Al,Si)$.

The infiltrant employed is the binary aluminum-silicon eutectic. In the as-cast condition, this eutectic is quite brittle. Since extremely large deformations are required, this poses a formidable problem. However, thermo-mechanical procedures have been developed that impart to the eutectic extraordinary ductility, so that filaments as small as 1 micron have been obtained. Preliminary data indicate that as the filament size is reduced to this order of magnitude, the superconducting properties are enhanced. Another remarkable characteristic of the aluminum-silicon eutectic is the ease with which it wets and infiltrates niobium. With other infiltrants (Sn, Ga, Al, Al-Ge) infiltration temperatures as much as several hundred °C above the melting point were required for complete infiltration. With high infiltration temperatures, care must be exercised to prevent the formation of brittle intermediate phases, which limit the formability of the composite. It has been demonstrated repeatedly that with the niobium-aluminum-silicon system, complete infiltration takes place at an aluminum-silicon eutectic bath temperature less than 5°C above its melting point—thus eliminating the possibility of any undesirable side reactions.

Still another remarkable observation has been made in working with this system. This relates to the unexpected internal surface chemistry that occurs between extremely fine filaments and the surrounding matrix. In past work on niobium alloy systems containing aluminum, reaction temperatures in excess of 1200°C were required for the formation of the A15 compound. It has now been discovered that the very fine filaments of the aluminum-silicon eutectic interact with the matrix to form the A15 compound at temperatures as low as 850°C. This is of tremendous technological importance, in that it makes possible the incorporation of copper to provide the stability necessary for practical superconductors. This points to a new dimension in the future of very high field superconductors. The procedure employed is shown schematically in Fig. 1.

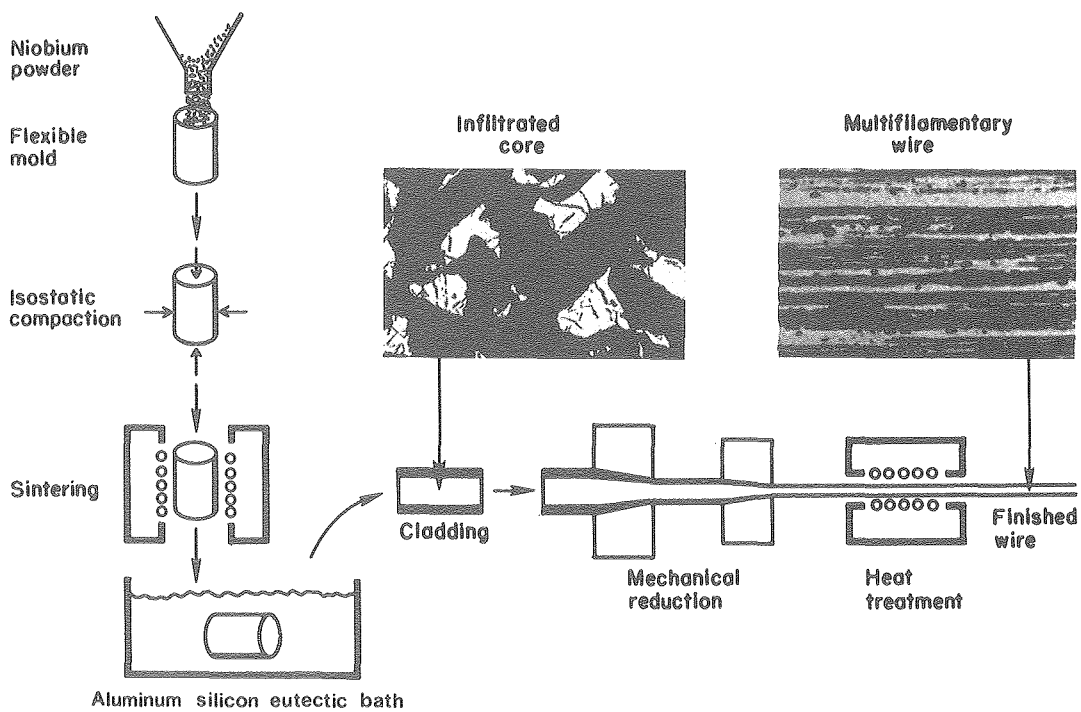

Fig. 1. Infiltration process for multifilamentary niobium-aluminum-silicon superconducting wire. (XBB 770-10876)

2. KINETIC STUDY OF THE FORMATION OF THE A15 COMPOUND $Nb_3(Al_xGe_{1-x})$ USING AN INTERNAL SURFACE AS THE REACTION SITE

Kent Douglas, John Ling-Pai Wang and Milton R. Pickus

The infiltration process developed at MMRD for fabricating multifilamentary superconducting wire has been applied to a study of the reaction kinetics in the niobium-aluminum-germanium system. The versatility of the process allows it to be used for many superconducting systems, including the Nb-Al-Ge system for which the bronze process is ineffective. This system is particularly interesting because of its high critical field and high current carrying capacity.

In previous feasibility studies at this laboratory, it was determined that the superconducting properties of this system were very dependent on the reaction time and temperature used to form the A15 phase. At reaction temperatures of ~1800°C, high critical temperatures, but low current carrying capacities were observed; whereas at temperatures in the 1200-1300°C range the reverse situation was found: Low critical temperatures, but high current carrying capacities. In this earlier work, it was also found that aluminum, from the aluminum-germanium eutectic used as the infiltrant, diffuses quite rapidly into the niobium matrix at the reaction temperatures employed, resulting in the formation of an aluminum deficient A15 phase. These results indicated the need for a kinetic study to determine the nature of the reactions that were occurring in order to establish a scientific basis for controlling the formation of the A15 phase in an optimum manner.

Porous niobium rods infiltrated with the aluminum-germanium eutectic were heated at various temperatures for various lengths of time. From the kinetic studies performed on the samples, it was discovered that a barrier phase of a binary niobium-germanium alloy could be formed which confines the aluminum and allows it to diffuse through the barrier slowly to react with the niobium matrix, forming an aluminum rich A15 phase. The formation of this barrier phase requires a two-step procedure. First, as illustrated in Fig. 1, the sample is held at a temperature which allows a limited reaction between the niobium and aluminum (2) leaving the germanium in a substantially unreacted state (1). Then the temperature is increased moderately to allow the germanium to react with niobium to form the niobium-germanium barrier phase which surrounds the niobium-aluminum alloy (Fig. 2). The aluminum is now constrained from rapidly diffusing into the niobium matrix and the sample is ready for the final heat treatment to form the A15 phase. Figure 3 shows the A15 phase (3) forming at the interface between the barrier phase and the niobium matrix. It is highly significant that with the presence of this barrier phase, it was found that the A15 phase forms at temperatures at least as low as 1000°C. This makes it feasible to use copper as a cladding material to provide conductor stability for the Nb-Al-Ge system. Studies are in progress to determine whether the A15 phase may

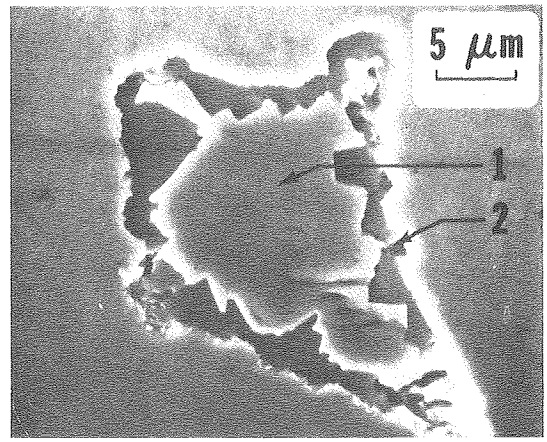

Fig. 1 Scanning electron micrograph of an infiltrated pore following the first heat treatment. 1. Substantially unreacted germanium. 2. Binary niobium-aluminum alloy. (XBB 770-11638)

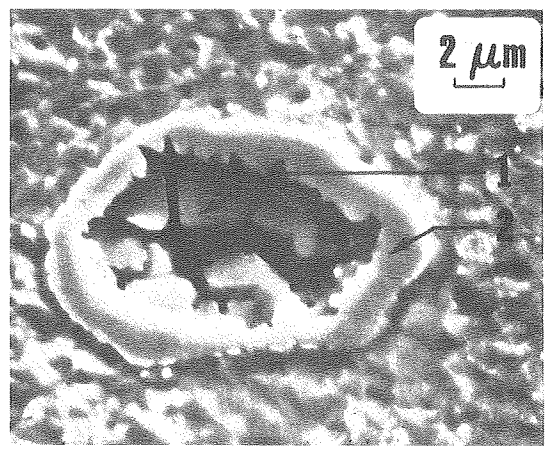

Fig. 2. Scanning electron micrograph of an infiltrated pore following the second heat treatment, showing the diffusion barrier. 1. Niobium-aluminum alloy. 2. Niobium-germanium barrier phase. (XBB 770-11638)

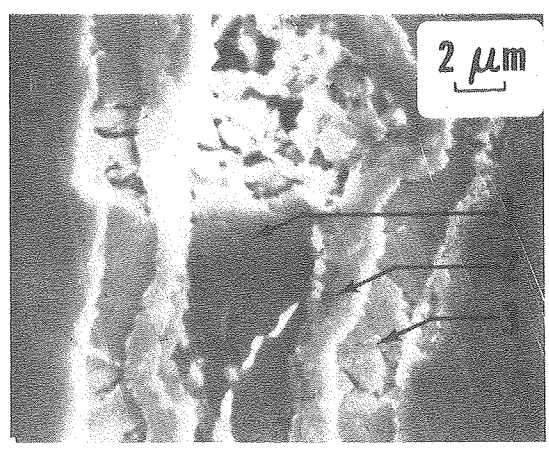

Fig. 3. Scanning electron micrograph of an infiltrated pore after the third heat treatment. 1. Niobium-aluminum alloy. 2. Niobium-germanium barrier phase. 3. A15 phase. (XBB 770-11638)

be formed at even lower temperatures. Apparently, the barrier phase acts as a catalyst to nucleate the A15 compound at the niobium interface. Thermodynamically, one might expect the aluminum to diffuse into the niobium matrix in view of the rather extensive solid solubility range of aluminum in niobium. Surprisingly, analytical results indicate virtually no penetration of aluminum into the niobium matrix.

3. IMPROVED FORMABILITY OF ALUMINUM-GERMANIUM NEAR EUTECTIC COMPOSITIONS THROUGH THE APPLICATION OF SUPERPLASTICITY PRINCIPLES

Gregory J. Pech, John Ling-Fai Wang and Milton R. Pickus

The compound $Nb_3(Al_{0.75}Ge_{0.25})$ is one of the best high field superconductors known. This Laboratory, employing the MMRD infiltration process, was the first to establish the feasibility of fabricating multifilamentary superconducting wire based on this compound. In the course of the work, it was found that problems were encountered due to the poor mechanical workability of the aluminum-germanium eutectic used as the infiltrant. The objective of this investigation was to study the behavior of two aluminum-germanium compositions under conditions that have produced superplasticity in similar binary systems. The compositions studied were 80-20 and 70-30 at.% of aluminum and germanium, the latter being the eutectic composition.

Superplastic behavior is known to occur most commonly in binary systems with a very fine and stable duplex microstructure at temperatures close to a phase transformation, and usually near an eutectic or eutectoid composition. In contrast to the coarse lamellar structure normally obtained, an extremely fine fibrous microstructure (Fig. 1a) was produced by pouring molten aluminum-germanium alloy at less than 950°C into a water cooled copper mold. Although this structure is associated with extreme brittleness, it was found that it could be readily transformed into a stable semi-spheroidal structure by a heat treatment of 30 min at 350°C (Fig. 1b). As a result of this treatment, the Vickers microhardness decreased from 286 to 109.

The deformation behavior of both compositions was studied at various temperatures, using form rolling as the deformation mode. It was found that the 80-20 material could withstand a reduction of 75% at 350°C without cracking. Minor cracking occurred in the 70-30 material in similar tests, but was eliminated through the use of cladding. Although a phase transformation occurs at 424°C in the Al-Ge system, 350°C was chosen as the best deformation temperature due to accelerated grain growth at higher temperatures. A 0.420 in. diam core of 70-30 material was clad in copper, using tantalum as a diffusion barrier. This composite was form rolled at 350°C and then wire drawn at 180°C to a diameter of 0.052 in. In this manner, the aluminum-germanium core was reduced in area by a factor of 441 to a diameter of 0.020 in. Fig. 2).

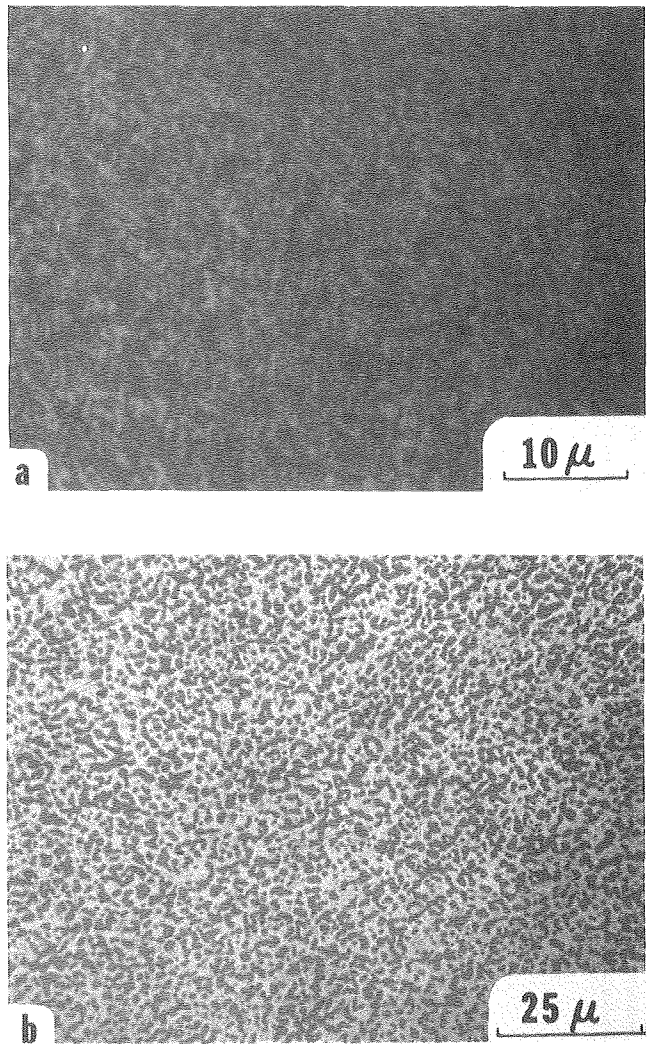

Fig. 1. Microstructure of the aluminum-germanium eutectic composition. a) Fibrous structure of rapidly cooled casting. b) Semi-spheroidal structure achieved by a heat treatment of 30 min at 350°C. (XBB 770-12376)

The application of superplasticity principles to the aluminum-germanium system has proved to be a valuable aid in achieving ductility in an otherwise brittle material. This finding should facilitate the fabrication of multifilamentary niobium-aluminum-germanium superconducting wire.

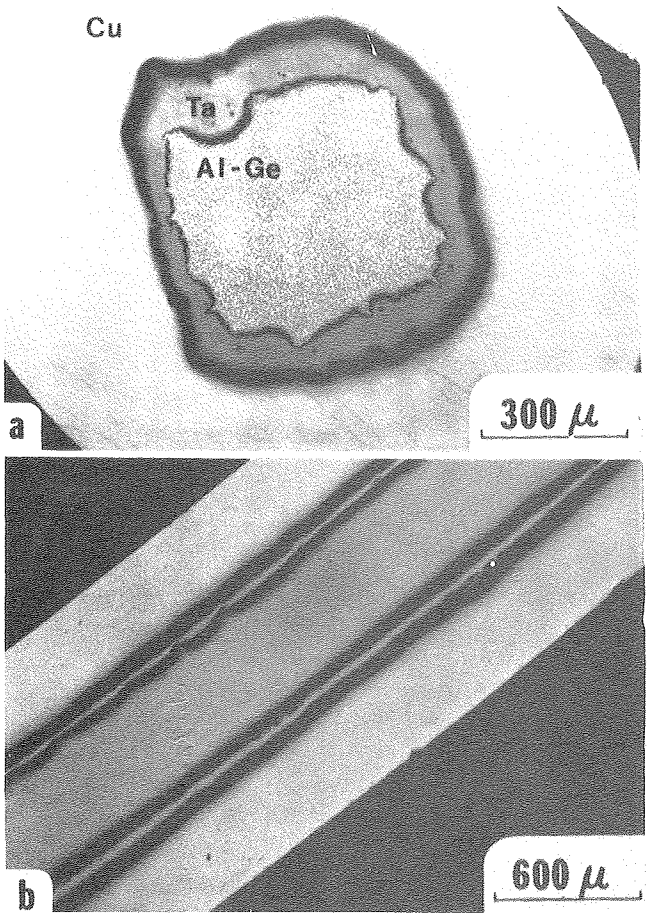

Fig. 2. Clad aluminum-germanium wire of eutectic composition made by form rolling at 350°C followed by wire drawing at 180°C. The aluminum-germanium core was reduced in area by a factor of 441 to a diameter of 0.020 in. a) Transverse section. b) Longitudinal section. (XBB 770-12377)

4. PRELIMINARY INVESTIGATION OF HYDROSTATIC EXTRUSION OF INFILTRATED NIOBIUM-TIN COMPOSITES

Glen E. MacLeod, John Ling-Fai Wang and Milton R. Pickus

In order to obtain long lengths of wire made by the infiltration process for use in winding solenoids, it is necessary to increase either the diameter or the length of the as-infiltrated composites. Work is in progress on both approaches. In this study, an analysis was made of the problems encountered in increasing the diameter from 1/4 in. to 1/2 in. and 3/4 in. A collaborative arrangement was set up with Professor Oleg Sherby's group at Stanford University. This group made available their recently acquired 250,000 psi, 0.750 in. bore hydrostatic extrusion machine (Fig. 1), and their experience with it. The work was greatly facilitated by Professor B. Avitzur of Lehigh University who made available recommendations based on his theoretical analyses of hydrostatic co-extrusion.

The important parameters include the core to sleeve diameter ratio, extrusion die angle, maximum single pass reduction, flow stress ratio and billet-die friction coefficient. A variety of tests were performed to determine the properties of the materials employed in order to optimize these parameters to prevent core or sleeve fracture. A typical billet – in this case, a 0.400 in. diam niobium-tin core and a 0.555 in. O.D. OFHC copper sleeve – is shown in Fig. 2. The successfully extruded billet, representing a single pass reduction in area of 77%, is shown in Fig. 3. In the course of this work, a number of unanticipated problems have become apparent. However, the experience gained should greatly facilitate future work on hydrostatic extrusion.

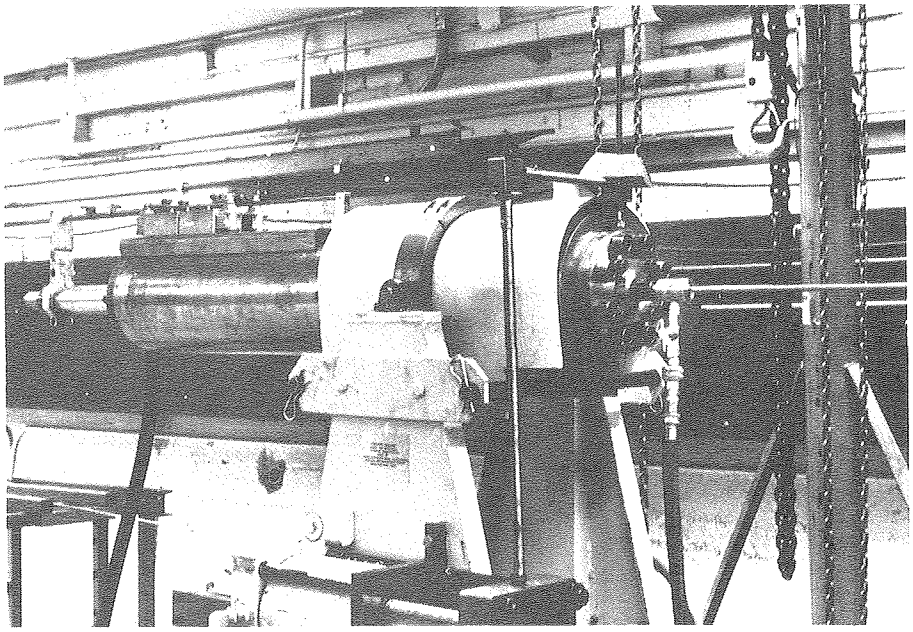

Fig. 1 Side view of hydrostatic extrusion machine. (XBB 776-6085)

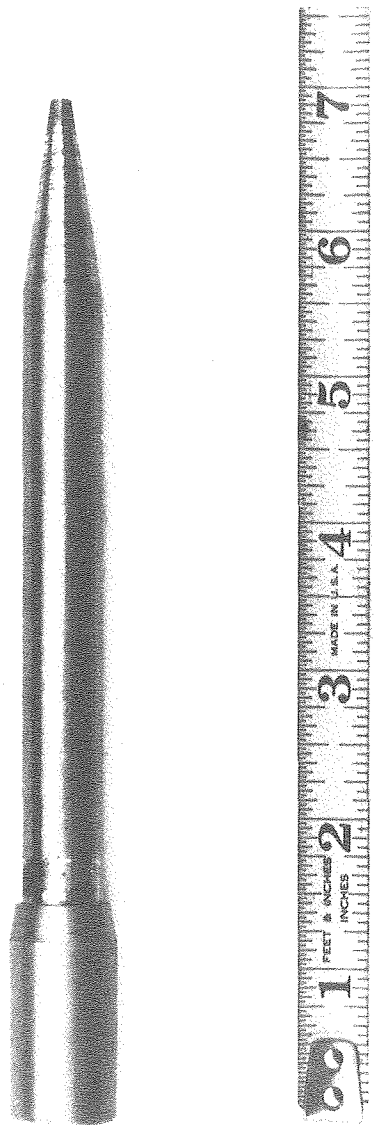

Fig. 2. Composite billet (niobium-tin core and OFHC copper sleeve) ready for extrusion. (XBB 776-6087)

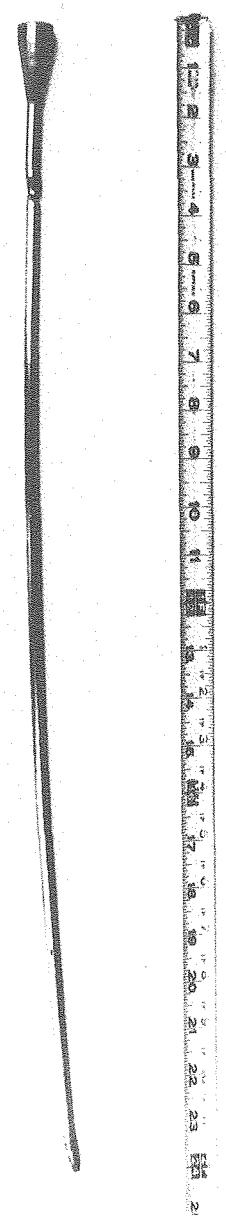

Fig. 3. Hydrostatically extruded billet (77% reduction in area). (XBB 776-6084)

5. AN INVESTIGATION INTO THE PRODUCTION OF METASTABLE Nb_3Ge POWDER VIA THE ROTATING ELECTRODE PROCESS

John P. McCormick, John Ling-Fai Wang and Milton R. Pickus

At the present time, there is no method known for the fabrication of superconducting Nb_3Ge in the form of multifilamentary wire. Among all superconductors, A15 Nb_3Ge holds the record superconducting transition temperature (T_c) and can withstand the highest magnetic fields with the greatest current carrying capacity. Unfortunately, of all the A15 compounds, Nb_3Ge is the most difficult to fabricate in large, uniform amounts. The reason for this lies in the inherent brittleness of Nb-Ge compounds and the thermodynamic instability of A15 type Nb_3Ge at high temperatures. In 1965, nearly stoichiometric Nb_3Ge was produced by the "splat cooling" technique. Since then, it has been found that A15 type stoichiometric Nb_3Ge is a metastable compound, maintaining its crystal structure up to about 1000°C. Thus, once superconducting Nb_3Ge powder is available, the production of wire through powder metallurgy techniques is highly conceivable.

A study was undertaken of the possibility of producing A15 type Nb_3Ge powder via the rotating electrode process (REP) modified to incorporate splat cooling. REP has proven itself economically competitive in the production of large amounts of the reactive metal and prealloyed powders.

Making a niobium-germanium electrode capable of withstanding the thermal shock of the electric arc used in the rotating electrode process proved to be the principal barrier to the project. Utilizing powder metallurgy techniques, a powder composed of a germanium rich niobium compound was produced and combined with pure niobium powder to make an electrode of the desired overall composition which, with precise control of REP parameters, was converted into a mixture of spherical and irregular shapes along with "splats" which are shown in Fig. 1. Many of these electrodes have been employed in the rotating electrode machine while studying the effects of various parameters involved, such as substrate surface condition, power input, electrode to substrate distance and speed of electrode rotation.

The powder produced thus far was predominantly, according to x-ray diffraction studies, of the A15 structure. Analysis with the scanning electron microscope showed the powder to be of two phases, one Ge-rich and the other Ge-deficient, along with a eutectic structure (Fig. 2). Optical microscopy verified high splat cooling rates by the very small grain sizes achieved.

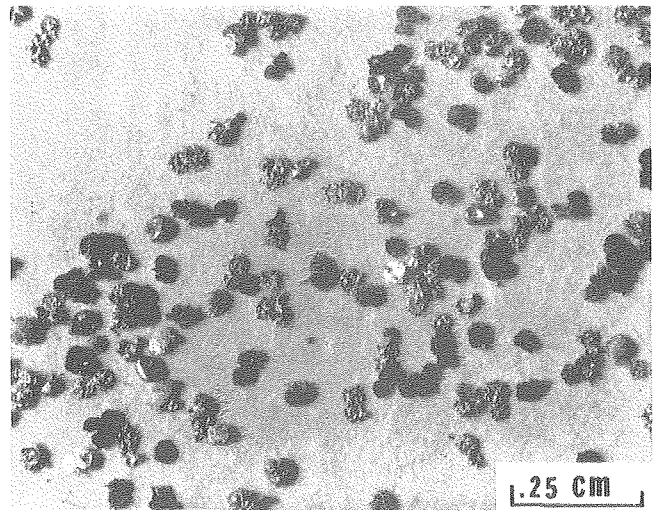

Fig. 1. Optical micrograph of REP splat cooled powder. (XBB 760-10979)

As produced, the REP powder has a low T_c; however, attempts are in progress to improve the ordering of the structure by annealing. Preliminary results in this direction are encouraging.

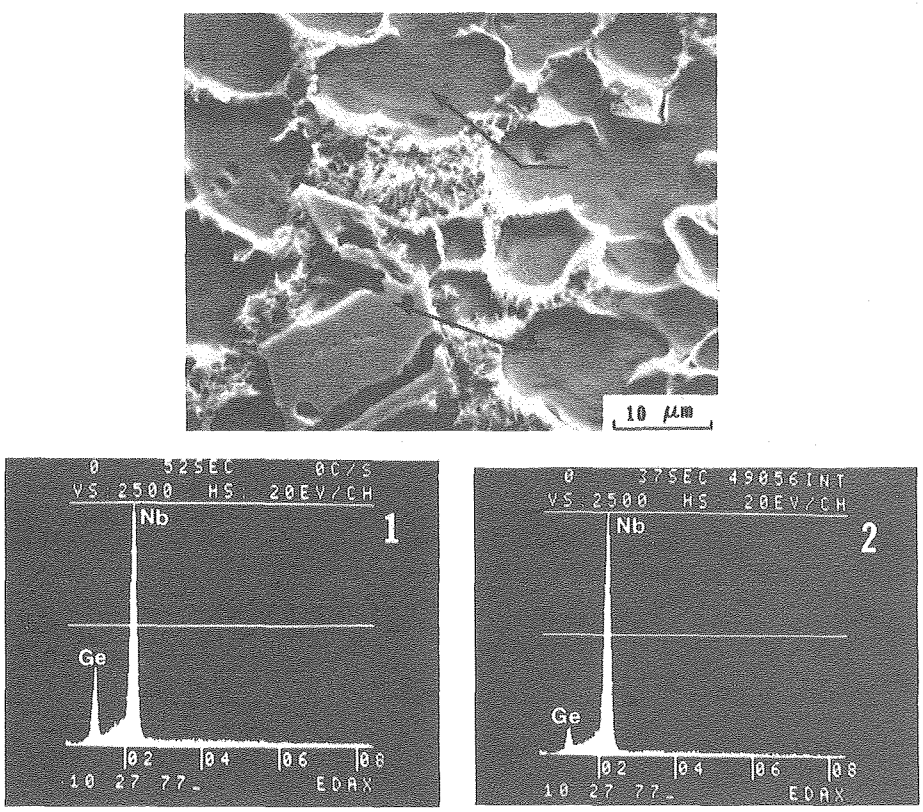

Fig. 2. Scanning electron micrograph of an REP particle with typical EDAX analyses of representative regions. (XBB 760-10981)

6. RESEARCH PLANS FOR CALENDAR YEAR 1978

Milton R. Pickus

The need for more efficient multifilamentary superconductors based on A15 compounds in new energy systems, such as magnetic fusion, is now widely recognized. A number of important new findings that were made in MMRD's program on high field superconducting materials during this past year provide the scientific basis for further research that appears highly promising for the achievement of this goal. In regard to our new niobium-aluminum-silicon multifilamentary conductor, we will utilize the knowledge gained from our study of internal surface chemistry involving very fine filaments to optimize the conditions for forming the A15 compound at temperatures below 1000°C. This is important for two reasons: 1) copper can be used to provide the necessary conductor stability; 2) the lower the temperature of formation of the A15 compound, the greater is the current carrying capacity. We also plan to measure and optimize the superconducting properties of this new superconductor. The aluminum-silicon eutectic used as the infiltrant in our infiltration process is quite brittle as normally prepared. As a result of special mechanical processing procedures we developed, the eutectic becomes so ductile we are able to obtain extremely fine filaments of the order of one micron in size. We were successful in accomplishing much the same thing in regard to the aluminum-germanium eutectic. In the case of the niobium-aluminum-germanium system, we have developed a successful kinetic approach for forming the A15 compound at least as low as 1000°C, again making possible the use of copper for stability. Here too, a special aspect of internal surface chemistry is involved. Our procedure involves the formation of an intermediate phase which not only serves as a necessary diffusion barrier, but apparently functions as a catalyst in nucleating the A15 compound at temperatures much lower than were previously thought possible. In this system, we will determine the conditions for forming the A15 compound that yield the best values of the superconducting properites. Perhaps the most exciting project we will initiate is one that combines all of our recent findings. At the present time, our infiltration process is the only one that has proved successful for producing multifilamentary superconductors based on aluminum-containing A15 compounds – those with the best superconducting properties. On the other hand, the technology for producing niobium-titanium multifilamentary superconductors -- despite their rather inferior superconducting properties -- has been developed by industry over a period of many years to a very high degree of sophistication. Now, as a result of our past year's work, it appears highly probable that this available technology can be applied directly to the niobium-aluminum-germanium and niobium-aluminum-silicon systems. We plan to determine the feasibility of accomplishing this technology transfer. A successful effort would mean there would then be two totally different and new procedures for fabricating these high field superconductors. We would then assess the relative merits of the two approaches.

7. 1977 PUBLICATIONS AND REPORTS

Milton R. Pickus and Associates

Journals

1. R. L. Ciardella, M. P. Dariel, J. Ling-Fai Wang and M. R. Pickus, A Quenched-Age Method for the Fabrication of Nb(Al) Superconductors, IEEE MAG-13(1), 832 (1977), LBL-4953.

2. K. Hemachalam and M. R. Pickus, Studies of Filamentary Nb_3Sn Wires Fabricated by the Infiltration Method, IEEE MAG-13(1), 466 (1977), LBL-4949.

LBL Reports

1. E. Kannatey-Asibu, Jr., Kinetics of Formation of the A15 Phase in the Nb-Al-Ge System, (M.S. thesis), LBL-6266, May 1977.

2. Glen E. MacLeod, An Investigation of Hydrostatic Extrusion and Other Deformation Modes for the Fabrication of Multifilamentary Niobium-Tin Superconductors by a Powder Metallurgy Approach, (M.S. thesis), LBL-6622, June 1977.

3. Gary C. Quinn, A New Multifilamentary Superconductor Based on the Niobium-Aluminum-Silicon System", (M.S. thesis), LBL-6999, December 1977.

4. Gregory J. Pech, Improved Formability of Aluminum-Germanium Near Eutectic Compositions Through the Application of Superplasticity Principles, (M.S. thesis), LBL-7300, December 1977.

5. John P. McCormick, An Investigation into the Production of Metastable Nb_3Ge Powder via the Rotating Electrode Process, (M.S. thesis), LBL-7301, December 1977.

b. Microstructure and Mechanical Behavior of Ceramics; Glass- and Ceramic-Metal Systems

Joseph A. Pask, Principal Investigator

Introduction. A major objective of the research program deals with correlations of character (with emphasis on microstructures and nature of grain boundaries) with mechanical behavior and corrosion resistance at high temperatures, and with determining the factors that play a role in obtaining a ceramic material with a designed character. It involves studies on the mechanisms responsible for the mechanical behavior of single crystals, and on the application of such knowledge to the understanding of the behavior of polycrystalline ceramic materials. It also involves studies on the kinetics and mechanisms of solid state reactions, sintering and distribution of phases in a multiphase system.

The compositions under study--mullite, alumina, spinel, magnesia--are basic materials of industrial ceramics and refractories, and sintering is the basic method for their manufacture. The fundamental approach in these studies with the application of physical and solid state chemistry principles, and dislocation theory lead to the development of principles that should be applicable to other polycrystalline metal, ceramic, and composite materials.

A second objective of this program is concerned with structural and thermodynamic studies of glass-metal and ceramic-metal systems. It involves studies related to wetting, bonding, and the nature of the interfaces between dissimilar phases; to the thermodynamics and kinetics of chemical reactions at such interfaces; and to the kinetics and mechanisms of dissolution and diffusion in glasses. A basic understanding of the nature of interfaces and the mechanisms of reactions at interfaces is critical in studies of all materials.

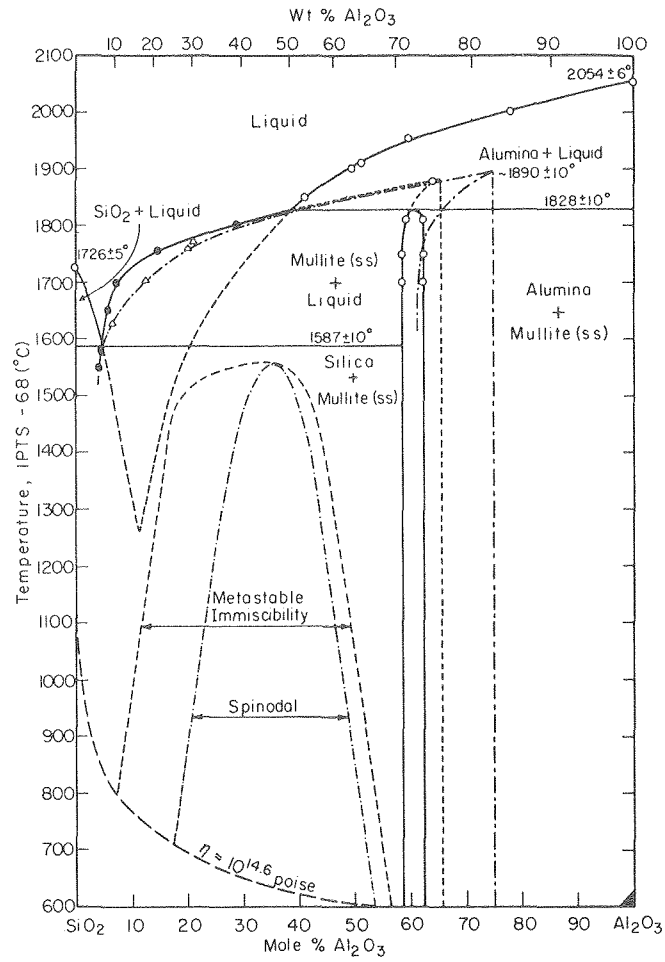

Fig. 1. Stable and metastable phase equilibrium diagram for SiO_2-Al_2O_3 system. (XBL 766-7008)

1. METASTABLE PHASE RELATIONSHIPS IN SYSTEM SiO_2-Al_2O_3

Subhash H. Risbud, Victor F. Draper and Joseph A. Pask

The SiO_2-Al_2O_3 system exhibits a number of metastable phase equilibria because of difficulties related to nucleation of α-Al_2O_3 both from an aluminum silicate melt and from mullite (stoichiometric composition of $3Al_2O_3 \cdot SiO_2$). These difficulties have resulted in disagreements in published phase equilibria diagrams as to whether mullite melts congruently or incongruently. Diffusion couple experiments provide data that indicate that mullite melts incongruently[1] under stable equilibrium conditions and support the phase equilibria shown in Fig. 1.

To further illustrate the nucleation difficulties of α-Al_2O_3, mixtures of SiO_2-Al_2O_3 containing 60 wt% Al_2O_3 of three different particle sizes were heat treated in sealed molybdenum crucibles. The heat treatment consisted of heating to 1725°C in 1 hr, holding at 1725°C for 96 hr, heating to 1855°C in <2 min, holding at 1855°C for 36 hr, and cooling rapidly to room temperature. An x-ray diffraction analysis of the three mixtures showed that mullite was the only crystalline phase present in those with α-Al_2O_3 particles of ~0.03 and ~10 μm, and that both mullite and α-Al_2O_3 were present in the one with α-Al_2O_3 agglomerates of ~45 μm. According to the diagram in Fig. 1, the heating schedule used should have resulted in the presence of α-Al_2O_3 at 1855°C and additional precipitation of mullite on cooling. The absence of α-Al_2O_3 in the first two indicates that the reaction to form mullite at 1725°C was complete and that subsequent heating at 1855°C caused the mullite to melt metastably without nucleation of α-Al_2O_3. The presence of α-Al_2O_3 in the third mixture, on the other hand, indicates that the reaction to form

mullite at 1725°C was not complete and that α-Al_2O_3 persisted with subsequent heating at 1855°C as required by the stable phase equilibrium diagram. The first two mixtures thus are governed by the metastable phase equilibrium diagram for SiO_2-mullite.

A metastable binary phase equilibrium diagram between SiO_2 and Al_2O_3 in the absence of any mullite phase is also shown in Fig. 1 with an eutectic temperature of ~1250 ± 15°C and composition of ~13 mole % Al_2O_3. The liquidi of the proposed metastable system were positioned on the basis of the thermodynamic data calculated from the stable equilibrium diagram of Aksay and Pask.[1] The metastable eutectic temperature was verified experimentally by heating compacts of cristobalite (SiO_2) and corundum (α-Al_2O_3) at a number of temperatures and measuring shrinkage.

---

1. I. A. Aksay and J. A. Pask, Stable and Metastable Equilibria in the SiO_2-Al_2O_3 System, J. Am. Ceram. Soc. 58, [11-12], 507 (1975).

2. MICROSTRUCTURE DEVELOPMENT AND CORRELATION WITH 1200°C STRESS-STRAIN BEHAVIOR OF SINTERED MULLITE*

Michael D. Sacks and Joseph A. Pask

Chemical and phase composition, unfired ("green") density, average particle size of mullite powders (grinding time), contamination from grinding media, and firing schedule (temperature, time and atmosphere) are processing variables or parameters that affect the microstructure of sintered mullite. The stress-strain behavior in compression at 1200°C was found to be sensitive to the nature of the microstructure.

The presence of a second phase appeared to be the most critical factor in determining the high temperature strength. This behavior is partially a function of the difference in mechanical properties of the single phase materials. For example, siliceous glass phase is extremely detrimental to the strength of mullite bodies or compositions at 1200°C because glass flows viscously at this temperature. Figure 1 consists of 1200°C stress-strain curves for mullite bodies ranging in chemical composition from 71.8 to 45.9 wt% Al_2O_3. Since grain size and percent theoretical density remain essentially constant, the reduction in strength and the increasing flow character of the curves reflects the increasing amounts of glass phase (see Fig. 2).

The presence of a second phase also alters the sintering behavior which, in turn, alters microstructural features such as grain size, grain morphology, total porosity, pore size, and distribution of second phase. All of these factors are important in determining high temperature strength. In the presence of a siliceous liquid phase, grain growth leads to the isolation of glass in "pockets." This distribution is beneficial to high temperature strength. Figure 3 shows the

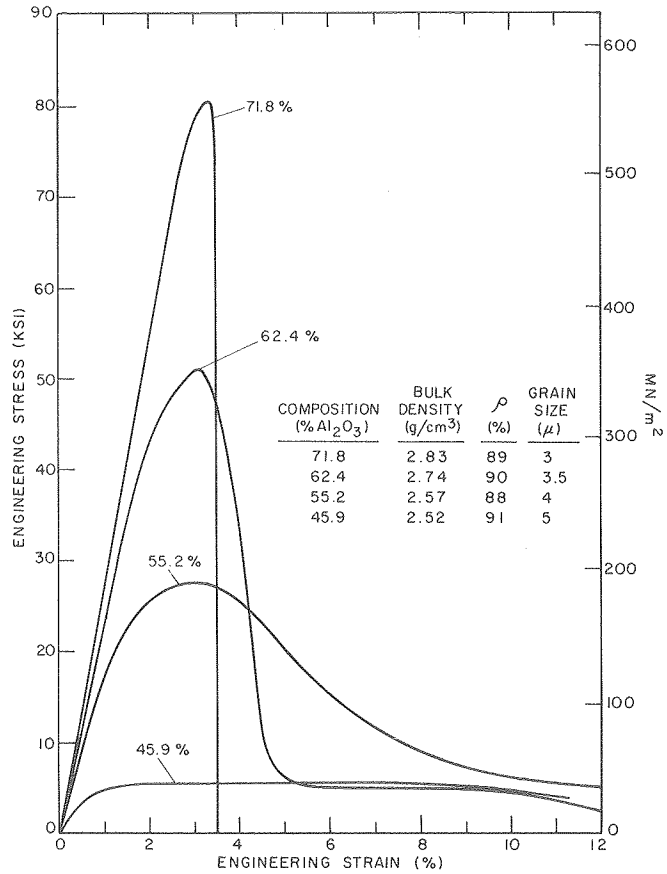

Fig. 1. Stress-strain behavior in compression at 1200°C for compositions ranging from 71.8 to 45.9 wt% Al_2O_3. (XBL 7710-6295)

stress-strain behavior for two identical compositions sintered under different heating schedules. Despite a slightly higher density, the sample fired at ~1570°C has a considerably lower strength due to the presence of a glass "film" around grains as opposed to "pocket-like" distribution for the 1725°C sample (Fig. 4).

The influence of the second phase on microstructure is also dependent upon the firing atmosphere since phase and chemical compositions, and apparently interfacial energies are affected. Densification and grain growth kinetics are thus affected. In samples doped with excess Al_2O_3 increase of sintered density is always adversely affected compared to undoped (71.8 wt% Al_2O_3) samples processed in the same manner up to the firing step. In air firing for a small amount of excess Al_2O_3, strength is improved because of the elimination of small amounts of glass by reaction to form mullite (Fig. 5). In vacuum sintering for an equivalent amount of excess Al_2O_3 strength is not improved, despite glass elimination, because of separation cracks introduced by poor bonding between alumina particles, which remain because of loss of silica, and the mullite matrix (Fig. 6).

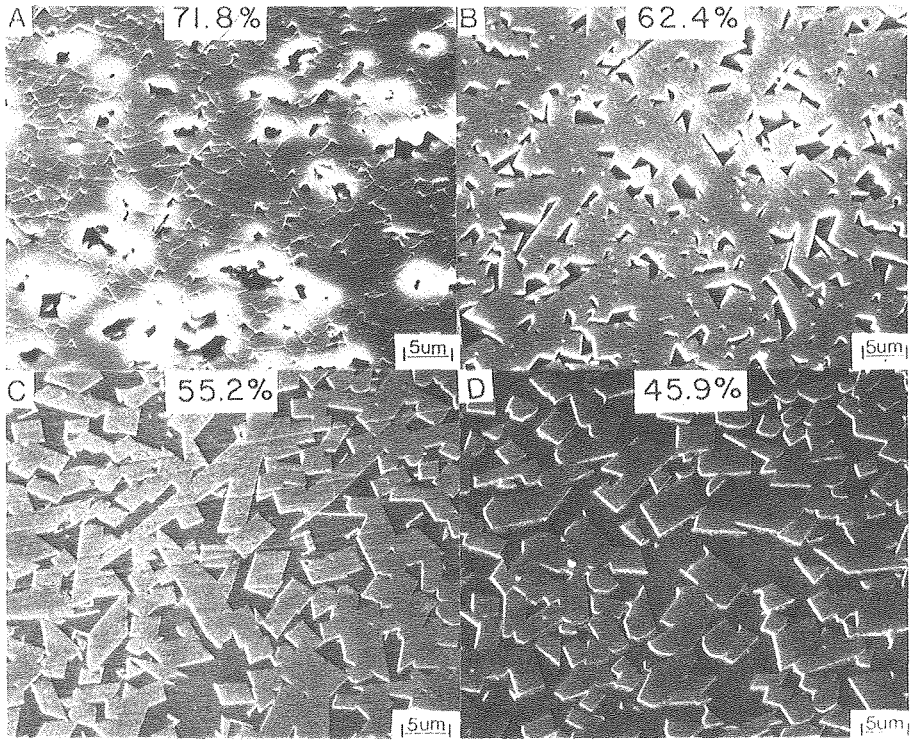

Fig. 2. Photomicrographs illustrating increasing amounts of glass from 71.8 to 45.9 wt% Al_2O_3 compositions. (XBB 770-10642)

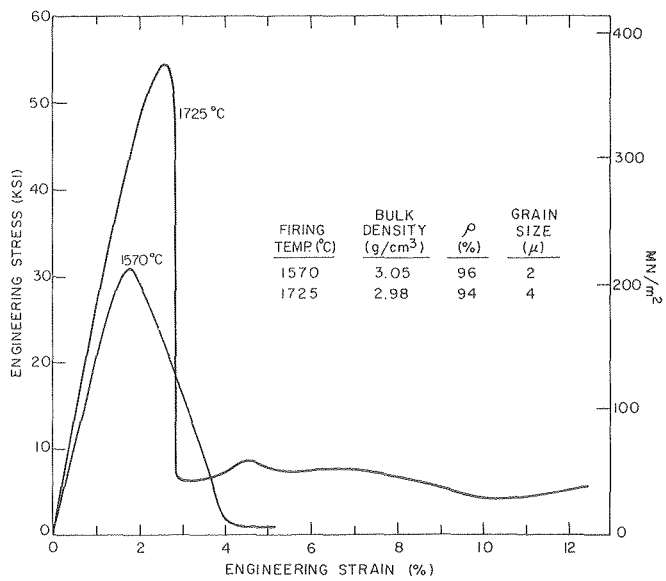

Fig. 3. Stress-strain behavior in compression at 1200°C for identical compositions fired under different heating schedules. (XBL 775-5473)

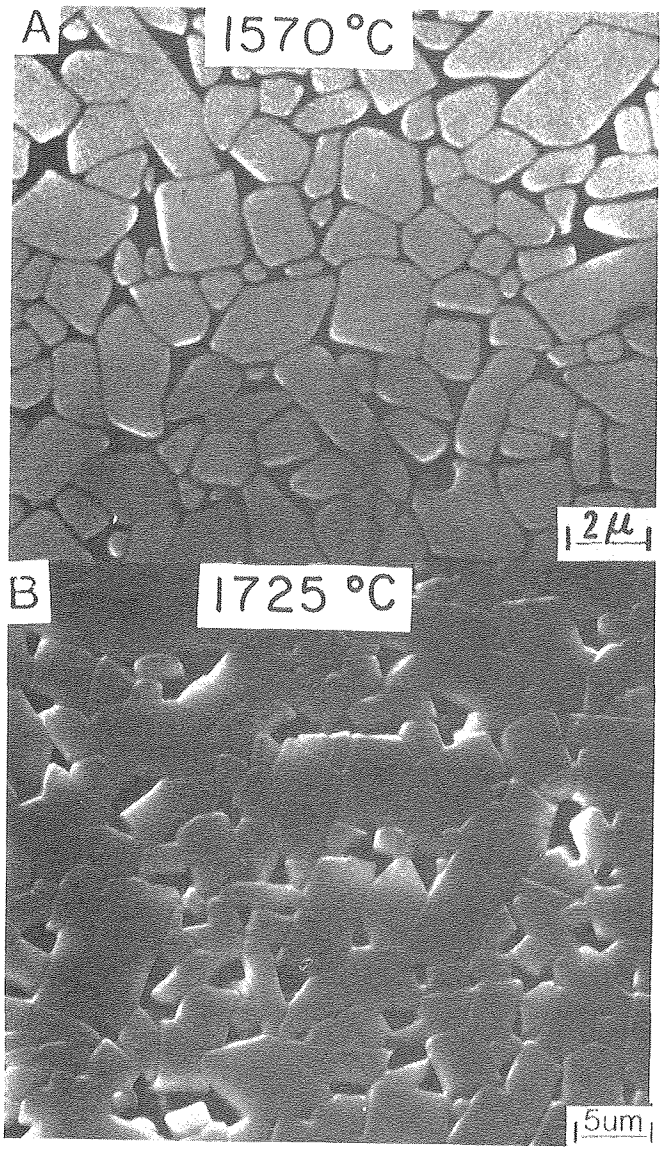

Fig. 4. Photomicrographs illustrating the effect of grain growth on the distribution of the glass phase. The 1200°C stress-strain behavior for these specimens is shown in Fig. 3. (XBB 771-83A)

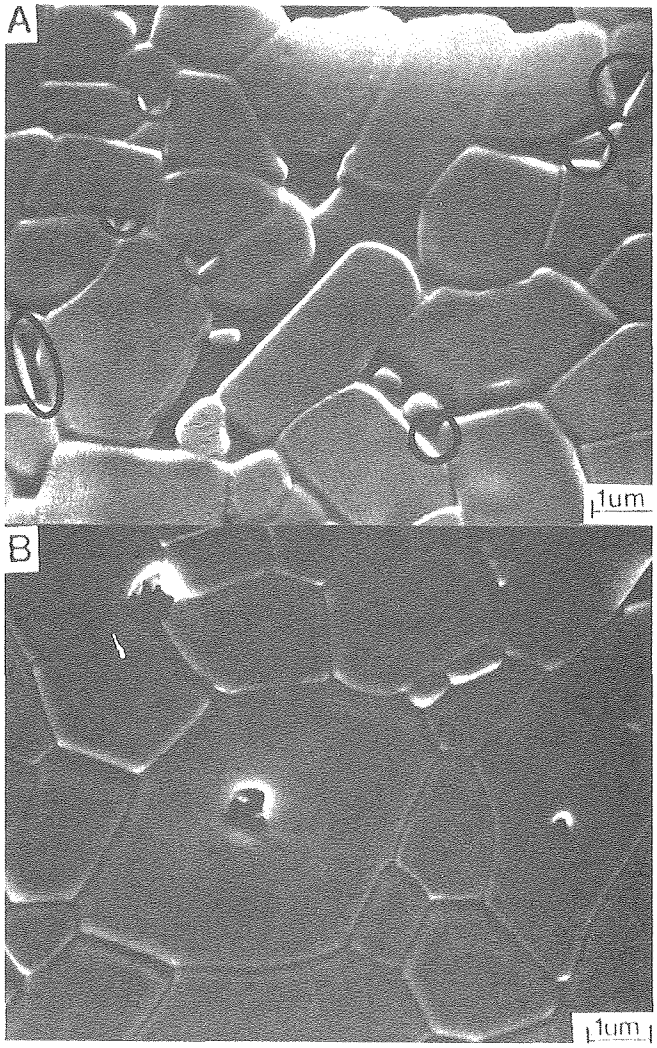

Fig. 5. (A) Undoped 5 hr-ground mullite powder compact fired at ~1710°C for 8 hr in air illustrating presence of glass pockets (circled areas) between grains. (B) Specimens with 15% excess Al_2O_3 fired at ~1710°C for 8 hr in air illustrating the elimination of glass pockets. (XBB 760-10587)

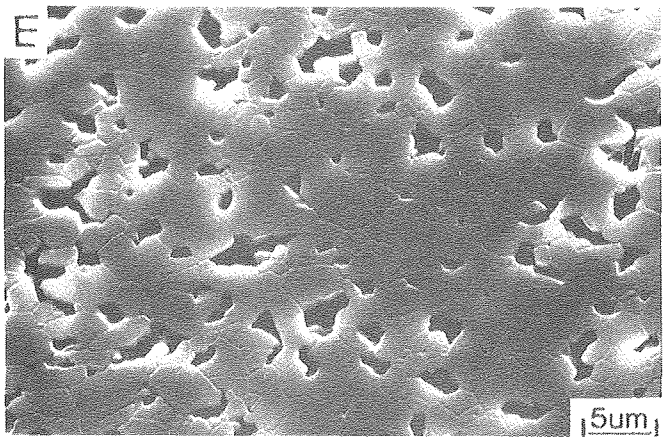

30% EXCESS Al_2O_3 (AIR)

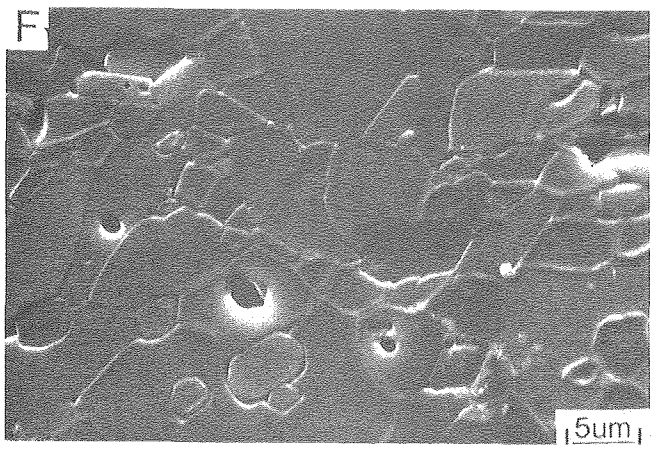

30% EXCESS Al_2O_3 (VACUUM)

Fig. 6. Photomicrographs of identical compacts fired in air (top) and vacuum (bottom). Despite its lower density, the air fired specimen is as strong as the vacuum fired specimen. Al_2O_3 particles are easily discernible in the bottom photomicrograph due to circumferential cracking. (XBB 770-10579)

3. MECHANICAL PROPERTIES OF MULLITE-ALUMINA COMPOSITIONS AT ROOM TEMPERATURE AND 1400°C*

Philip C. Dokko and Joseph A. Pask

Dense, single-phase mullite has been found earlier[1] to have remarkably high compressive strengths at elevated temperatures. Prompted by this observation, this study has been directed to determine 1) how such specimens behave in the presence of tensile stresses introduced in bending and under thermal shock conditions that are of great importance in practical applications, and 2) how the presence of a second phase, primarily alumina, effects their behavior under such conditions.

Single-phase mullite appears to be susceptible to brittle fracture as suggested by data obtained at 1400°C indicating that specimens failed in bending at small fractions of compressive strengths without exhibiting any plastic strains. Thus, the high resistance to deformation-induced fracture in compression was not realized in bending. Under such conditions, no temperature dependence of bending strengths was observed.

When alumina was present as a second phase, effects on strengths were dependent on the test temperature and the amount of alumina. At 1400°C both bending and compressive strengths decreased with increasing alumina up to 50% (Fig. 1) while ductility was enhanced. These effects can be attributed to microcracking due to thermal

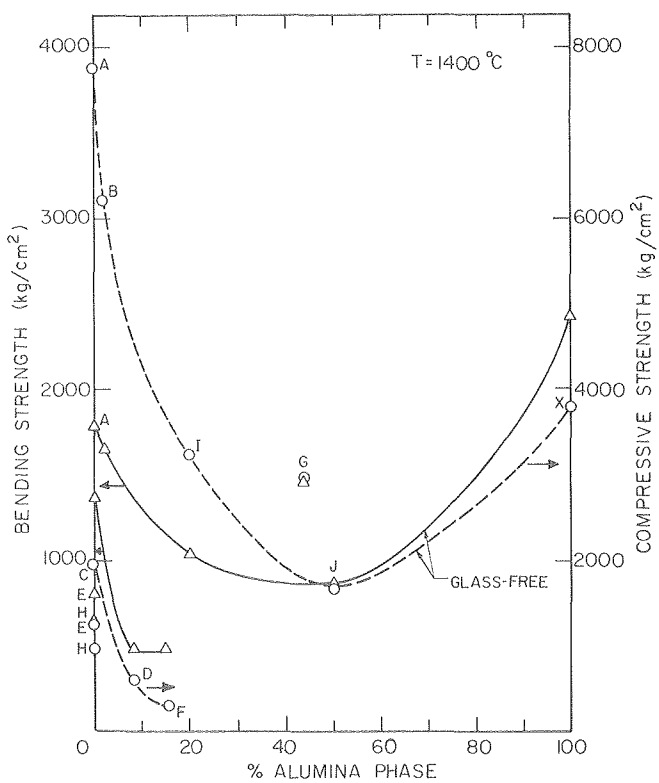

Fig. 1. Effects of increasing alumina on bending and compressive strengths at 1400°C of mullite-alumina series. (XBL 777-5805)

*Supported by NSF.

expansion mismatch which may facilitate deformation by grain boundary sliding. The figure also shows further decrease of strengths due to the presence of a glassy viscous phase because of incomplete reactions to form mullite (specimens C, E, H). At RT, however, bending strength increased with alumina up to 50% (Fig. 2) suggesting that the alumina phase may act as a crack stopper. With

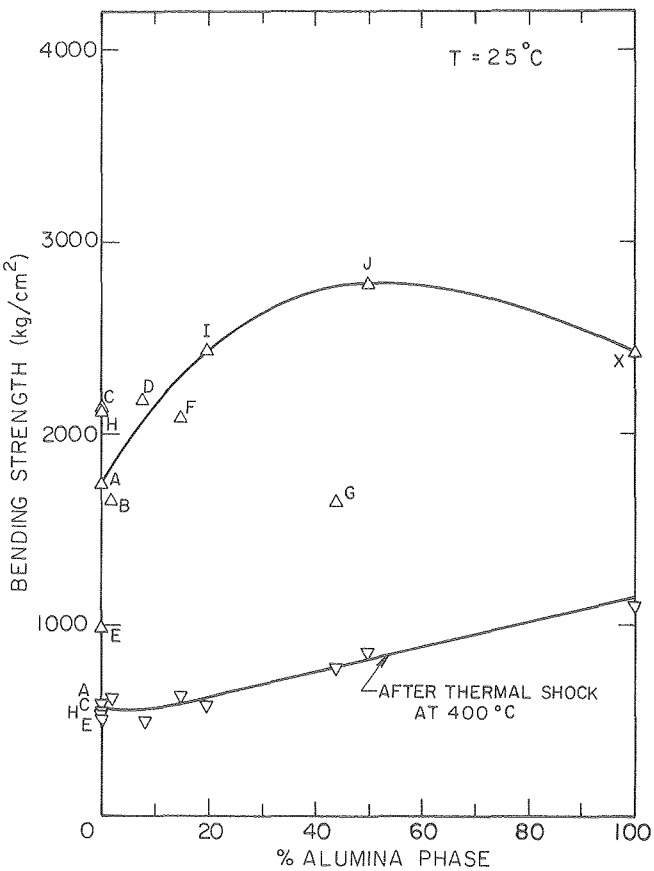

Fig. 2. Effects of increasing alumina in mullite-alumina series on bending strength at RT before and after thermal shock. (XBL 777-5806)

increasing alumina contents from 50 to 100%, bending and compressive strength trends were reversed. On the other hand, the presence of glass that now has the properties of a solid does not have the same damaging effect on strength that it showed at 1400°C.

The bending strengths at RT after a thermal shock at 400°C are also shown in Fig. 2. The strengths are essentially constant regardless of microstructures when alumina less than ~20% is present as a second phase, and the strengths increase with alumina in excess of this amount up to that for a single-phase alumina specimen. In general, however, losses of strength in the range of 50 to 75% occur after thermal shock from 400°C. While no strong relationship is indicated with the limited number of specimens, the presence of glassy phase seems to result in similar reductions of strength after thermal shock.

A point of interest for further study is the reverse behavior of single phase mullite and single phase alumina in compression and bending at 1400°C: mullite is stronger in compression and alumina, in bending. Another point is the need for microstructure modifications to realize improved thermal shock resistance.

---

*Supported by NSF.

1. P. C. Dokko, J. A. Pask and K. S. Mazdiyasni, High-Temperature Mechanical Properties of Mullite under Compression, J. Am. Ceram. Soc. 60, 150 (1977).

4. CORROSIVE RESISTANCE OF MULLITE-ALUMINA COMPOSITIONS*

Stephen Tso and Joseph A. Pask

Gaseous corrosion resistance is one of the requirements for a refractory lining to be used in coal gasification processes. It is known that the glass phase in a refractory has the least such resistance, the mullite is more resistant, and the alumina has the most resistance. Studies are thus in progress to understand and improve the corrosion resistance of the glassy phase. The primary objective is to study the corrosion by H_2 gas. Studies, however, were also undertaken to study the corrosion by HF solutions. Although the corrosion mechanisms are not the same, relative resistance of a glass to corrosion by H_2 or HF is the same. The following reported studies on HF corrosion are thus of value for purposes of evaluation of materials. Portions dealing with kinetics and mechanisms of corrosion of SiO_2 glass are supported by DOE; portions dealing with evaluation of glass compositions for the purpose of developing compositions that will have improved resistance to corrosion are supported by NSF.

Nine glasses were obtained from Corning Glass Co. whose compositions and densities are listed in Table 1. Specimens were prepared as disks 9 mm in diam and 2 mm thick. Reagent grade hydrofluoric acid was obtained with an original 30 M concentration.

A constant temperature bath shaker with a controlled temperature range of 25 to 70°C was used. A shaking frequency of 120 cycles/min was used to provide vigorous agitation. The purpose of such an agitation was to insure that the reaction rate was not diffusion controlled and that the HF solution remained homogeneous during the corrosion runs.

Table 1. Glass Compositions and Densities

	Wt. Proportions			Density
	SiO_2	Al_2O_3	CaO	g/cm^3
SiO_2 Glass	100	0	0	2.20
Glass K	80	20	0	2.31
Glass L	70	30	0	2.42
Glass N	80	20	2	2.30
Glass O	70	30	2	2.38
Glass P	60	40	2	2.61
Glass Q	80	20	5	2.32
Glass R	70	30	5	2.38
Glass S	60	40	5	2.52

The HF concentration effect was studied with 100% SiO_2 glass. A unique activation energy of 5.3 kcal/mole was obtained with HF solution concentrations ranging from 3 to 24M. Figure 1 shows that the glass surface became wavy after reaction with HF acid whose morphology remained unchanged from 2 to 6 hr. The effect of this increase in the surface area on the kinetics was examined. The depth of the cusps was estimated as 10 to 20 μm by stereoscopic examination. The calculated surface area was thus found to be only 4% larger than the projected area.

During reaction no residue was left on the surfaces of any of the glasses. The reaction rates of the glasses were plotted vs the reciprocal of temperature. The reaction rates of the glasses with 2 w/o of CaO and with 20, 30 and 40 w/o of Al_2O_3 with 6M HF acid are plotted in Fig. 2. The reaction rates of the glasses with 30 w/o of Al_2O_3 and with 0, 2 and 5 w/o CaO with 6M HF acid are plotted in Fig. 3. It is seen that the reaction rate increased with the addition of either/both CaO or/and Al_2O_3. The calculated activation energies are: Glass N — 7.34 kcal/mole; O — 8.2, P — 10.7, L — 5.87, and R — 8.5. The values are all larger than that for 100% SiO_2 glass. These results suggest that the addition of Al_2O_3 and CaO weakened the glass structure. CaO is a glass modifier; Al_2O_3 can act both as a glass-modifier and glass-former. Their presence thus increases the number of non-bridging oxygens making them more open to HF attack.

In the case of H_2 corrosion it is expected that relative attacks will occur. In contrast, however, it is also expected that only SiO_2 will be removed leaving residues on the surfaces of the glasses. This residue with proper heat treatment may develop a protective coating against further attack.

*Partially supported by NSF.

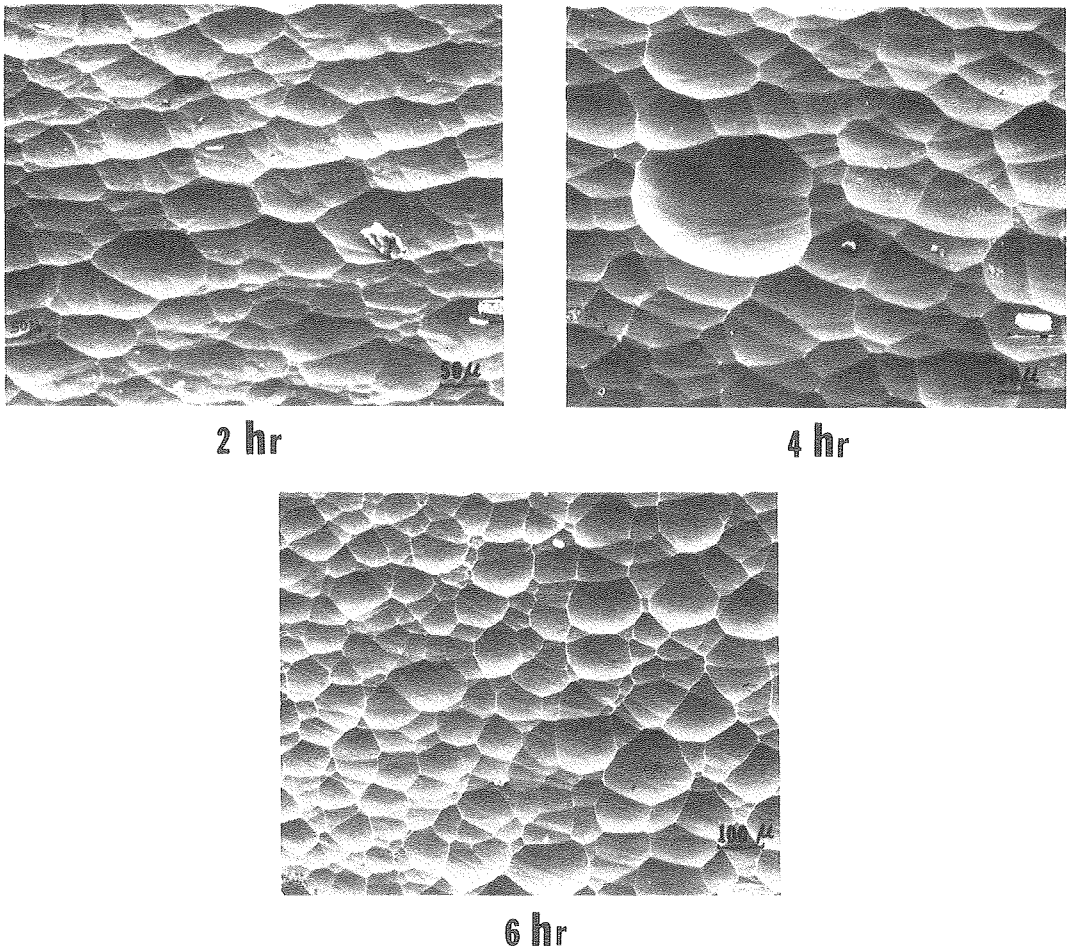

Fig. 1. Morphology of glass surface after exposure to HF acid corrosion.
(XBB 7710-10487)

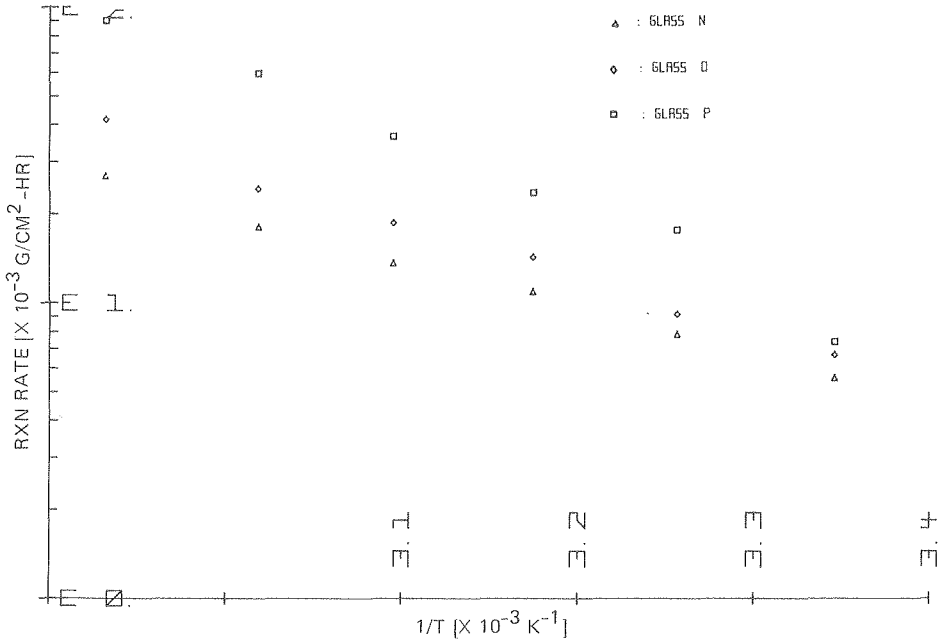

Fig. 2. Reaction rate of glasses containing 2 wt% CaO and 20, 30 and 40 wt% Al_2O_3 on exposure to 6M HF acid vs. 1/T.
(XBL 7710-10332)

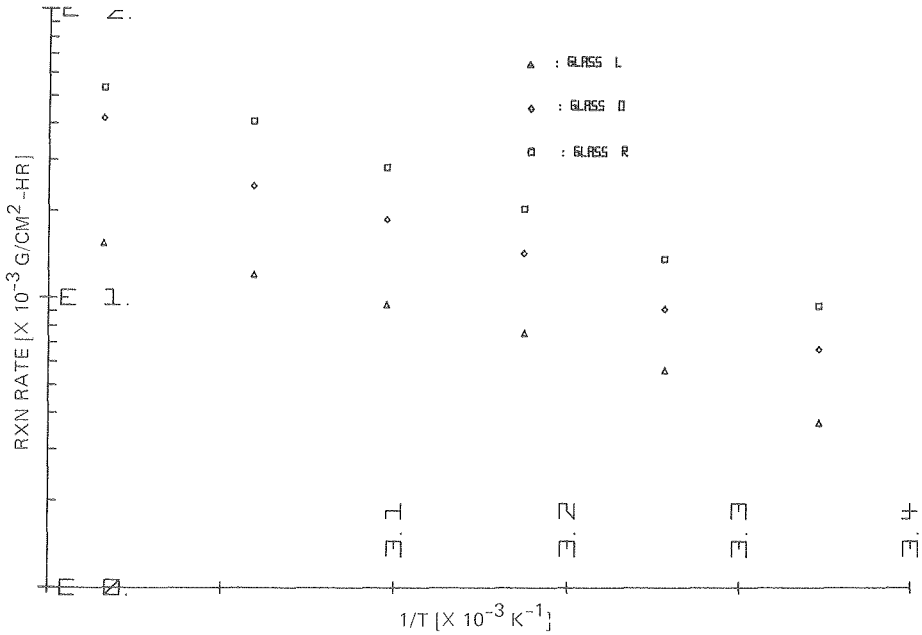

Fig 3. Reaction rate of glasses containing 30 wt% Al_2O_3 and 0, 2 and 5 wt% CaO on exposure to 6M HF acid vs. 1/T.
(XBL 7710-10327)

5. ELASTICITY AND INTERNAL FRICTION IN Al_2O_3-SiO_2 COMPOSITIONS AT ELEVATED TEMPERATURES

Amar P. S. Rana and Joseph A. Pask

The properties of polycrystalline ceramic materials depend to a considerable extent on the relative properties of grains and grain boundaries. Elasticity and internal friction measurements over a range of temperatures by the sonic resonance technique thus is important, since the data can contribute to the development of an understanding of the behavior of grain boundaries under stress at elevated temperatures.

A linear temperature dependence has been observed[1] for Young's modulus of several refractory polycrystalline oxides including aluminum oxide, magnesium oxide, and thorium oxide above room temperature with the exception that a rapid reduction from linearity occurs at high temperatures due to development of internal friction. This effect may be caused by grain boundary slip. For a solid with unique relaxation time[2]

$$E(T) = E(0)-A(1-\tanh(S+R/T))$$

where E(T) is the Young's modulus at temperature T K, E(0) is Young's modulus at 0 K, and A, S and R are constants. Though this equation is strictly true in the region of the equation internal friction peak and for a unique relaxation time, the form of the equation is also valid for a distribution of relaxation times as shown in Fig. 1 for alumina/mullite grain boundary relaxation in a specimen of Al_2O_3 with 2.5 wt% SiO_2. Furthermore, the temperature range over which this equation is valid does not seem to be restricted to the internal friction peak temperature range as seen for single crystal Al_2O_3 data in Fig. 2. It can also be shown that this equation reduces to an empirical equation suggested by Wachtman[3] and later given a theoretical basis by Anderson[4] who proved that an analogous equation holds for bulk modulus. A similar equation has been derived for shear modulus which indicates that the shear modulus decreases much more rapidly with increasing temperature than Young's modulus.

Internal friction is the dissipation energy that occurs when stress and strain are not in phase. Figure 3 shows normalized internal friction (Q^{-1}) as a function of reciprocal absolute temperature (with background substracted) for alumina/mullite grain boundaries. The grain boundary peaks are found to be broader than predicted theoretically.[5] A log normal distribution[5] in relaxation time is used to adequately describe the spectrum of relaxation times governing the grain boundary relaxation. A single relaxation time curve and a curve with a distribution parameter of 0.7 are also shown in Fig. 3. It is experimentally convenient to work with constant inertia rather than constant frequency. A method was developed to correct this frequency effect.

---

1. J. B. Wachtman, Jr. and D. G. Lam, Jr., J. Am. Ceram. Soc. 42, 254 (1959).
2. A. S. Norwick and P. S. Berry, "An Elastic Relaxation in Crystalline Solids," Academic Press, NY, 1972.
3. J. B. Wachtman, Jr., W. E. Tefft, D. G. Lam. and C. S. Epstein, Phys. Rev. 122(6), 1754 (1961).
4. O. L. Anderson, Phys. Rev. 144(2), 553 (1966).
5. A. S. Norwick and B. S. Berry, IBM, J. of Res. and Dev., 297 (1961).

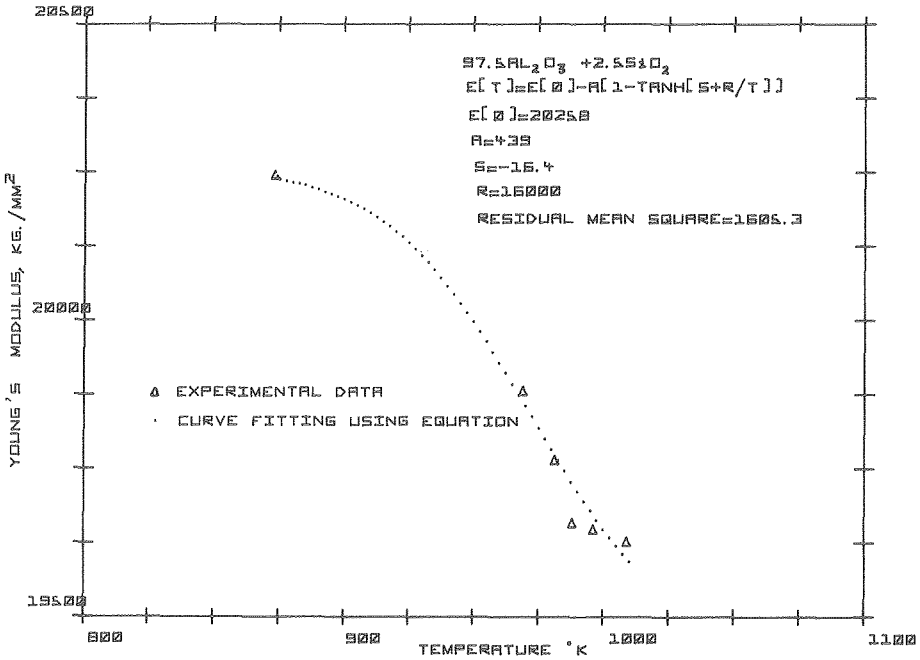

Fig. 1. Temperature dependence of Young's modulus for polycrystalline 97.5 Al_2O_3 + 2.5 SiO_2. (XBL 7710-6251)

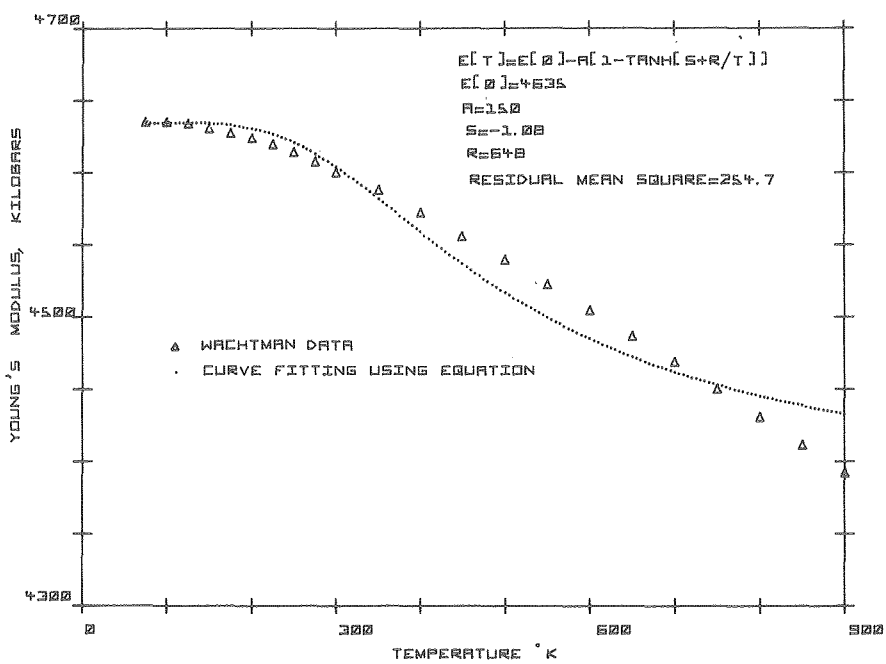

Fig. 2. Temperature dependence of Young's modulus for single-crystal Al_2O_3. (XBL 7710-6252)

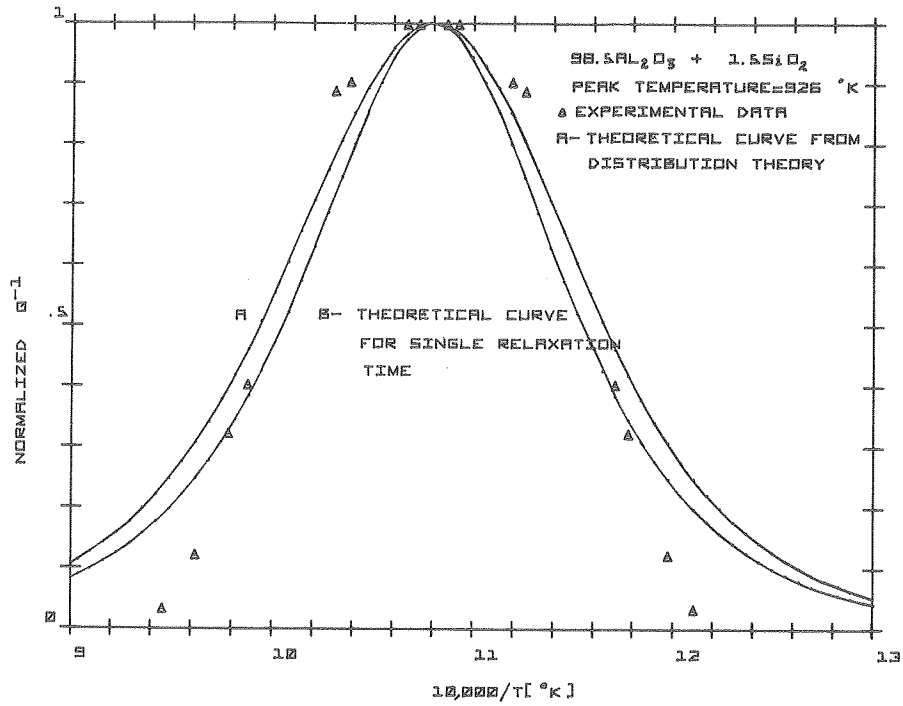

Fig. 3. Normalized internal friction (with background substracted) as a function of reciprocal absolute temperature. (XBL 7710-6253)

6. CHARACTERIZATION AND STRENGTH OF SIALON-TYPE MATERIALS

Paul N. Spencer and Joseph A. Pask

Four sialon-type materials using volcanic ash as a raw material were obtained. These materials are of interest because of their potential high temperature applications. They were characterized and some of their properties were determined. The crystalline portions of the materials were found to be solid solutions of β-Si_3N_4, α-Al_2O_3 and AlN. The specimens, labeled M3 and M4, were identified as β'-Si_3N_4 sialons; M2, as a 15R-AlN polytype sialon; and M1, as a mixture of the two types. The Al/Si ratios for these specimens were 2:3, 1.9:3, 5:1, and 1.5:1, respectively.

Stress-strain curves in compression at a constant strain rate of 0.0002 in./min at 1200°C are shown in Fig. 1, at 1300°C in Fig. 2, and at 1400°C in Fig. 3. M2 is the strongest material retaining a maximum stress of 98.4 ksi at 1400°C, and M1 is the weakest with a maximum stress of 23.8 ksi. This difference is attributed to the presence of an amorphous phase due to incomplete reactions and impurities introduced by the volcanic ash. The specimens showed the same relative order of strength in cross-breaking strength at room temperature. Thermal shock resistance was relatively poor although the coefficients of thermal expansion were of the order of ~3.0×10^{-6}/°C. Good oxidation resistance was exhibited, primarily by the M3 and M4 specimens.

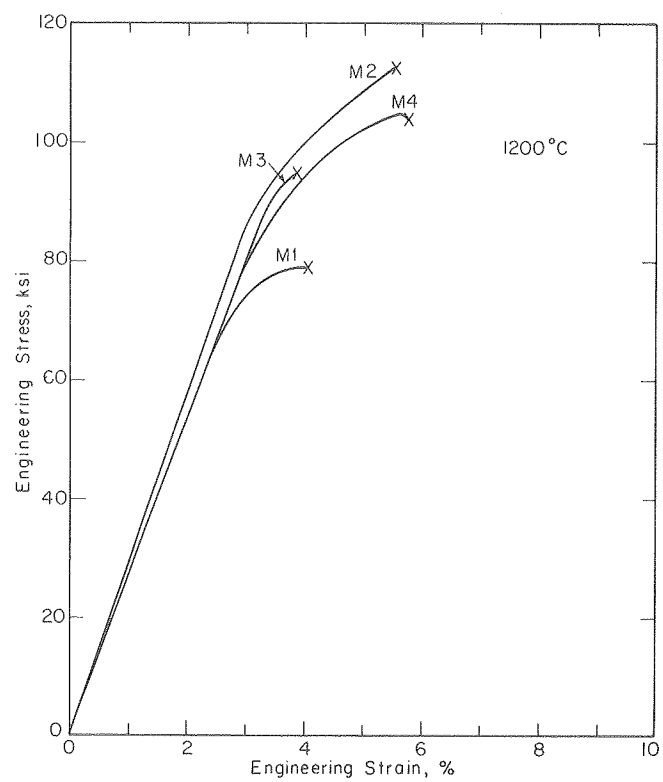

Fig. 1. Stress-strain curves in compression at an applied strain rate of $10^{-5}s^{-1}$ at 1200°C. (XBL 776-5590)

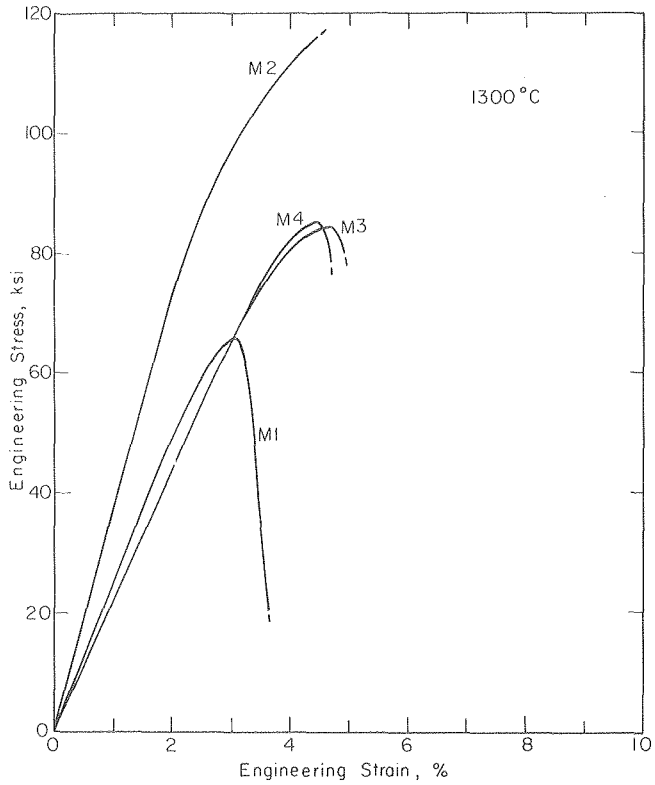

Fig. 2. Stress-strain curves in compression at an applied strain rate of $10^{-5}s^{-1}$ at 1300°C.
(XBL 776-5591)

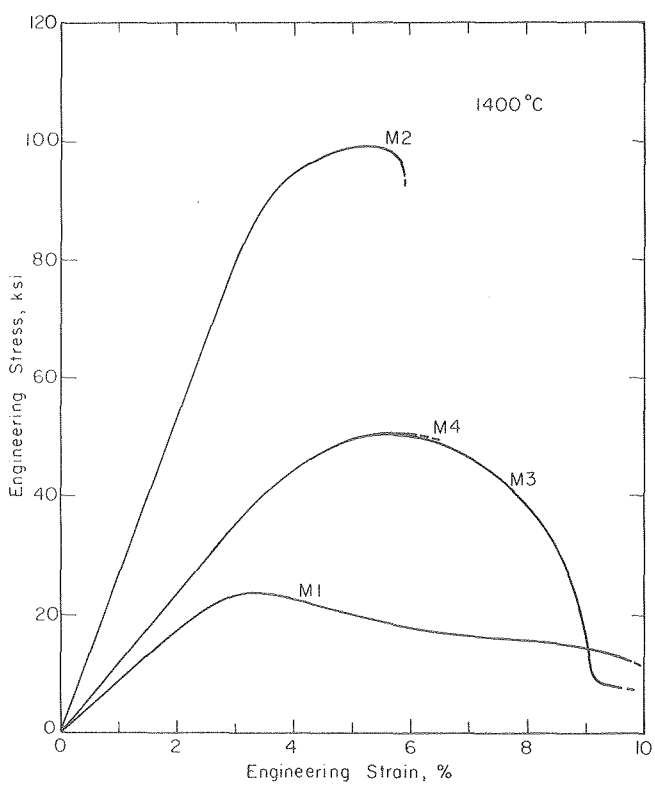

Fig. 3. Stress-strain curves in compression at an applied strain rate of $10^{-5}s^{-1}$ at 1400°C.
(XBL 776-5592)

On the basis of the experiments performed in this study the 15R-AlN polytype showed the best potential for development as a high-strength, high temperature material.

7. HIGH-TEMPERATURE COMPRESSIVE STRESS-STRAIN BEHAVIOR OF MgO

Philip C. Dokko and Joseph A. Pask

Stress-strain curves, obtained at 1200 and 1400°C and at several strain rates, for various types of polycrystalline MgO specimens were analyzed as a function of grain size, grain boundary character and pores, and correlated with those for single crystals. The nature of the grain boundary is generally the most important factor in determining the mechanical behavior of polycrystalline specimens.

Polycrystalline specimens of interest were a) transparent (fully dense) specimens containing residual Li and F (A type, or AP type when annealed with a wrapping in Pt foil), b) less dense specimens hot-pressed without any additive that had fine intragranular pores when annealed sufficiently (B type), and c) sintered specimens that had a visible glassy phase at grain boundaries, notably at triple points (C type). Stress-strain curves for all polycrystalline specimens were bracketed by those for single crystals of ⟨100⟩ and ⟨111⟩ orientations, corresponding to slip on easy (i.e., {110}) and difficult (i.e., {100}) planes, respectively, although a wide range of variation was observed.

Large ductilities (up to ~45% strain) were observed at a low strain rate ($\sim 1 \times 10^{-5}s^{-1}$) for fine-grain transparent specimens, although transparency was lost at early stages of deformation before fracture occurred. Thus, it is concluded that intergranular separation, accentuated by residual Li/F, makes a significant contribution to the observed deformation particularly at a low temperature. Intergranular separation facilitates grain boundary sliding in fine-grain specimens, thus relaxing the need for slip on all five independent systems. Strain softening (or yield drop) was thereby caused while fracture was delayed as grain boundary sliding was accompanied by slip capable of strain hardening. When the diffusion contribution is enhanced by a very small grain size (i.e., short diffusion path), a combination of primary slip and climb throughout the grains, as originally proposed by Groves and Kelly,[1] can cause deformation without premature intergranular separation at a high temperature or a low strain rate. In general, larger ductilities can be achieved with smaller grain sizes not accompanied by excessive segregation of impurities along grain boundaries.

For large grain sizes (> 30 μm) or F-poor grain boundaries where grain boundary sliding is difficult and hence intergranular separation is not an effective accommodation mechanism, deformation takes place predominately by slip on both primary

and secondary planes. The grain boundary effect is reflected in the higher fracture stresses of AP specimens in comparison with A specimens for equivalent intermediate grain sizes, corresponding to less F at grain boundaries in the former specimens (Fig. 1). Under these conditions, intergranular separation must be minimized to increase ductility and fracture stress as indicated by Li/F-free (B type) specimens or by glass-containing (C type) specimens tested at high glass viscosity temperatures, i.e., 1200°C (Fig. 2).

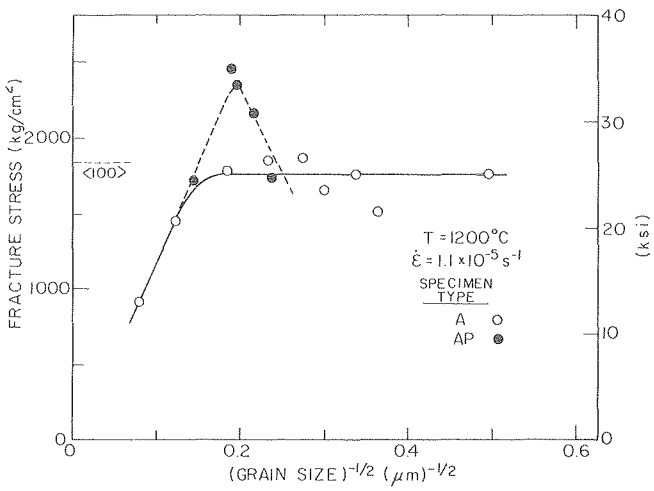

Fig. 1. Dependence of fracture stress at 1200°C on grain size and grain boundary character in transparent MgO specimens. (XBL 777-5721A)

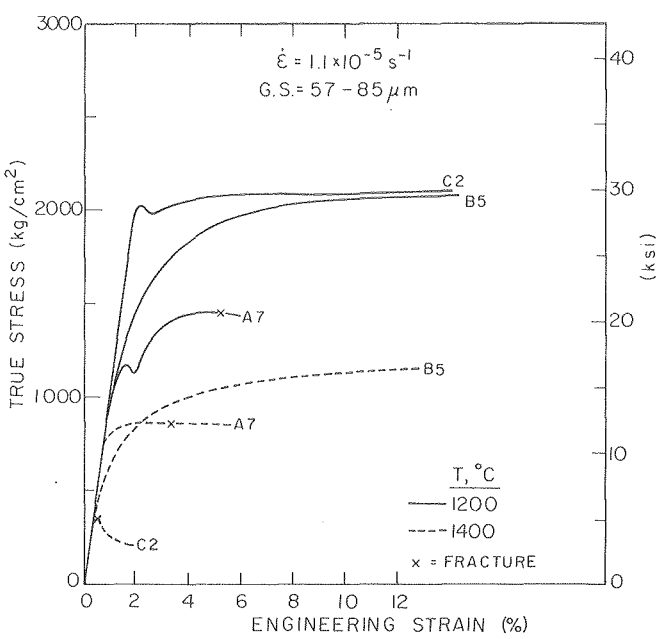

Fig. 2. Stress-strain curves for coarse-grain A, B and C specimens at 1200 and 1400°C (see text for description of specimens). (XBL 777-5726A)

Specimens with clean and strong grain boundaries, such as the sufficiently heat-treated B specimens, show true ductile deformation by wavy slip without intergranular separation. The stress-strain curves show normal strain hardening with no yield drops. Intergranular pores may play a favorable role in providing homogeneous slip. This study has been significant by showing the great sensitivity of the character of the stress-strain curves to the nature of the grain boundaries.

---

1. G. W. Groves and A. Kelly, Change of Shape Due to Dislocation Climb, Phil. Mag. 19, 977 (1969).

8. REACTIONS AND DIFFUSION IN THE SILVER-ARSENIC CHALCOGENIDE GLASS SYSTEM

Glenn A. Holmquist and Joseph A. Pask

Studies have been completed in the determination of reactions and diffusion in the silver-arsenic chalcogenide glass system. An understanding of these reactions is important since Ag is used to make electrical contacts to amorphous As chalcogenide semiconductors.

Diffusion couples were formed by encapsulating amorphous As_2Se_3 and As_2S_3 in Ag by a plating process. Diffusion runs were made at 175°C (below T_g, the glass transition temperature). Ag enters the glass by a redox reaction as Ag^+ by reduction of As from a valence of +3 to +2 or +2 to +1 to maintain charge neutrality in the glass. The reactions for the sulfide and selenide glasses are identical. Ag^+ alone diffuses at this temperature, all other ions being immobile. An example of this behavior is evident in a typical diffusion profile for a couple of As_2Se_3-Ag annealed at 175°C for 5 hr (Fig. 1). It can be seen that the As/Se ratio is invariant at 0.67 across the reaction product and into the bulk glass. The maximum solubility of Ag in these glasses is 44.4 at.%, corresponding to all of the As cations being reduced to the +1 valence. As^{+1} is not reduced to the elemental state. The diffusivity of Ag in As_2Se_3 and As_2S_3 glasses at 175°C is exponentially concentration dependent in the range of 10 to 35 at.% Ag, as shown in Fig. 2. The diffusivities for Ag^+ can be expressed as

$$2 \times 10^{-12} \exp\left[(+0.14 \pm 0.01)(\text{atomic \%Ag})\right] \quad \text{for } As_2Se_3$$

$$4 \times 10^{-14} \exp\left[(+0.23 \pm 0.01)(\text{atomic \%Ag})\right] \quad \text{for } As_2S_3.$$

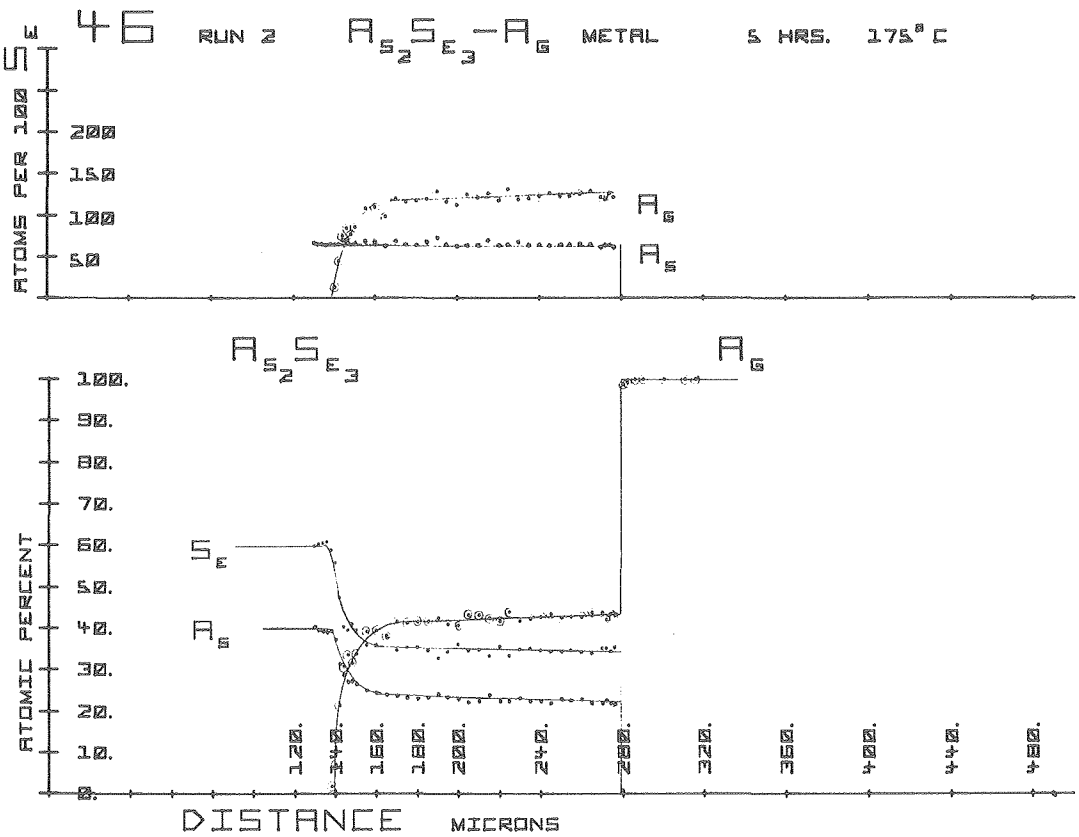

Fig. 1. Diffusion profiles for As_2Se_3-Ag couple in lower plot; corresponding Ag and As atoms per 100 Se atoms in upper plot. (XBL 778-9888)

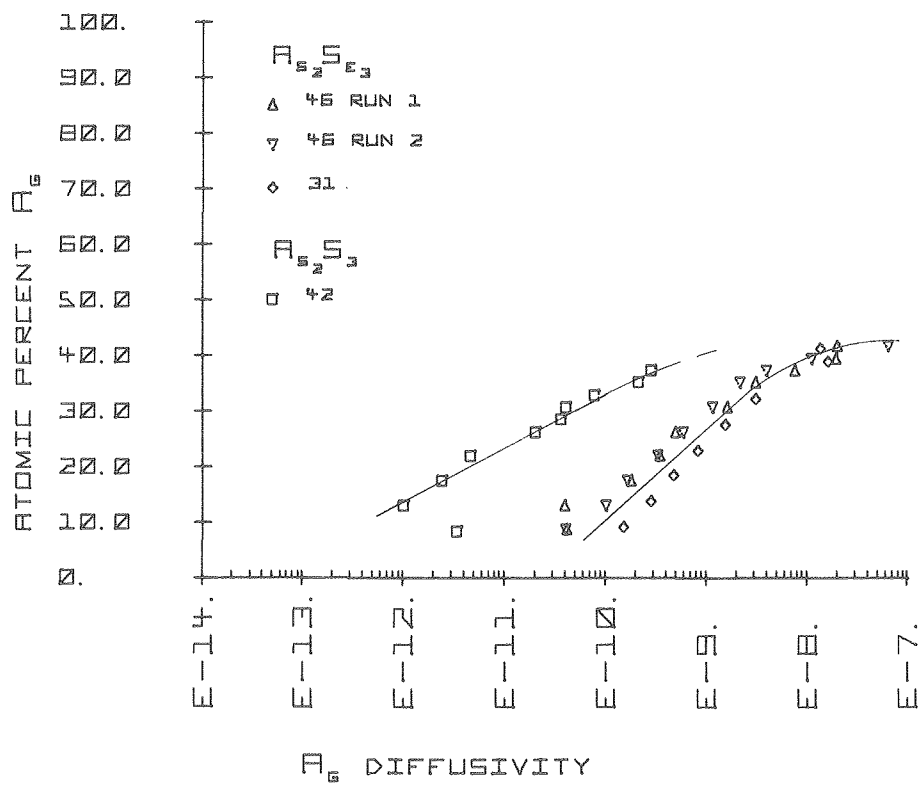

Fig. 2. Ag diffusivity vs. Ag concentration at 175°C in As_2Se_3 and As_2S_3 glasses. (XBL 778-9891)

9. RESEARCH PLANS FOR CALENDAR YEAR 1978

Joseph A. Pask

a. Characterization of Phase Transforamtions in the SiO_2-Al_2O_3 System

Studies will be carried out on nucleation and growth kinetics of mullite from aluminum silicate melts with a wide range of Al_2O_3 contents. The effect of additives such as CaO, Fe_2O_3 and TiO_2 on these kinetics will be explored as well as their effect on the morphology of the mullite grains. Stable and metastable mullites will be characterized by electron transmission microscopy, electron diffraction and x-ray diffraction. The nature of grain boundaries will be explored by high voltage electron transmission microscopy. Phase transformation sequences will be studied in terms of metastable and stable phase relationships.

b. Mechanical Behavior

Internal friction measurements by sonic resonance and oscillation techniques will be made on high Al_2O_3 compositions in the SiO_2-Al_2O_3 system. Efforts will be made to correlate data with the nature of the grain boundary. Variations in the nature of the grain boundary of a given material as determined by these techniques should have correlations with its mechanical behavior.

c. Liquid Phase Sintering

Liquid phase sintering of high alumina compositions will be studied with the use of the hot-stage electron scanning microscope. Correlations of high temperature wetting and spreading characteristics of liquids on Al_2O_3 will be made with the microstructure development, i.e., distribution of phases.

d. Refractories for Coal Gasification Processes

NSF support for a project entitled, "Structure, Strength and Corrosive Resistance of Aluminum Silicate Materials," will continue through the calendar year. The project objective is to develop mullite and mullite-containing compositions and microstructures that have the capability to resist corrosion by H_2-containing atmospheres and to resist erosion conditions encountered in coal gasification processes. Kinetics and mechanisms of the corrosion processes encountered in such microstructure development objectives will also be studied. Mechanical behavior aspects that will be followed are the correlation of microstructure with strength in compression, strength in bending, mechanical toughness, and thermal shock resistance which are considered to be important factors in determining corrosion resistance.

e. Interfaces

Simple binary systems will be utilized to determine conditions under which spreading and wetting of a liquid solution will occur on a solid substrate at high temperatures. Factors that will be involved will be the surface and interfacial energies, and the presence of reactions at interfaces. Similarly, conditions under which the liquid will penetrate grain boundaries in a polycrystalline substrate will be explored.

10. 1977 PUBLICATIONS AND REPORTS

Joseph A. Pask and Associates

Journals and Books

1. Chisato Marumo and Joseph A. Pask, Reactions and Wetting Behavior in the Aluminum-Fused Silica System, J. Materials Sci. 12, 223 (Feb. 1977).

*2. Philip C. Dokko, K. S. Mazdiyasni and Joseph A. Pask, High Temperature Mechanical Properties of Mullite under Compression, J. Am. Ceram. Soc. 60, 150 (March-April 1977).

3. Chisato Marumo and Joseph A. Pask, Reactions and Wetting Behavior in the System AuSi Alloy-αAl_2O_3, J. Am. Ceram. Soc. 60, No. 5-6, 276 (May-June 1977).

4. Ceramic Microstructures '76, Richard M. Fulrath and Joseph A. Pask, Eds. Westview Press, Boulder, Colorado, (1977), p. 907.

5. Carl E. Hoge, Boon Wong and Joseph A. Pask, Dependence of Sintering Characteristics on Thermodynamic and Geometric Factors, in Ceramic Microstructures '76, Richard M. Fulrath and Joseph A. Pask, Eds., Westview Press, Boulder, Colorado, (1977), p. 246.

6. Carl E. Hoge and Joseph A. Pask, Thermodynamic and Geometric Considerations of Solid State Sintering, Ceramurgia International 3, No. 3, 95 (July-September 1977).

7. S. H. Risbud and J. A. Pask, Calculated Thermodynamic Data and Metastable Immiscibility in the System SiO_2-Al_2O_3, J. Am. Ceram. Soc. 60, 418 (September-October 1977), LBL-4190 Rev.

8. Joseph A. Pask, Fundamentals of Wetting and Bonding Between Ceramics and Metals, in Alternatives to Gold Alloys in Dentistry (Proceedings of Conference held at National Institutes of Health, Bethesda, Maryland, January 24-26, 1977) edited by Thomas M. Valega, DHEW Publication No. (NIH) 77-1227, (1977), p. 235, LBL-6028.

LBL Reports

1. Joseph A. Pask, Fundamentals of Wetting and Bonding Between Ceramics and Metals, presented at Workshop at the National Institute of Dental Research, LBL-6028, January 1977.

2. Michael D. Sacks, Correlation of Microstructure of Sintered Mullite Bodies with Their Stress-Strain Behavior in Compression Loading at 1200°C, (M.S. thesis), LBL-6205, March 1977.

3. Paul N. Spencer, Characterization of Sialon-Type Materials, (M.S. thesis), LBL-6612, June 1977.

4. Glenn A. Holmquist, Reactions and Diffusion in the Silver-Arsenic Chalcogenide Glass System, (Ph.D. thesis), LBL-6922, September 1977.

Invitations

1. J. A. Pask, invited participant in Workshop on "Alternatives to Gold Alloys in Dentistry," National Institute of Dental Research, National Institutes of Health, Bethesda, Maryland, January 24-26, 1977.

2. J. A. Pask, presented John Dorn Memorial Lecture at Northwestern University, Chicago, Illinois, May 17, 1977.

3. J. A. Pask, invited lecture in Institut für Werkstoffwissenshaften, Universitat Erlangen-Nurenberg, Erlangen, Germany, August 8-10, 1977.

4. Joseph A. Pask, invited as Guest Scientist at Max-Planck Institut für Metallforshung, Institut für Werkstoffwissenshaften, Pulvermetallurgisches Laboratorium, Stuttgart, Germany, August 14-27, 1977.

5. Joseph A. Pask, Chairman, session on "Research as Business," American Ceramic Society, 30th Pacific Coast Regional Meeting, Los Angeles, California, October 30-November 2, 1977.

6. Joseph A. Pask, Chairman, session on "Fine Particle Science, Technology and Characterization," 14th University Conference on Ceramic Science on "Processing of Crystalline Ceramics," North Carolina State University, Raleigh, North Carolina, November 7-9, 1977.

---

*Supported by NSF.

c. High Temperature Reactions

Alan W. Searcy, Principal Investigator

Introduction. Most of the research described below stems directly or indirectly from a general theory of decomposition reactions that was developed under this project.[1,2]

Articles 1 through 3 describe experiments undertaken to extend our basic understanding of the facts of decomposition reaction kinetics. Articles 4 and 5 describe studies in which the primary objective was to improve our understanding of the kinetics of crystallization and densification of the CaO during $CaCO_3$ decomposition. The earlier basic studies had shown that the background pressure of CO_2 probably markedly influences both surface area and crystallinity.

Articles 6 and 7 describe efforts to use our improved understanding of $CaCO_3$ decomposition in practical applications.

---

1. A. W. Searcy and D. Beruto, J. Phys. Chem. 80, 425 (1976).
2. A. W. Searcy and D. Beruto, J. Phys. Chem., in press.

1. THE KINETICS AND THERMODYNAMICS OF DECOMPOSITION OF DOLOMITE TO A METASTABLE SOLID PRODUCT*

Elizabeth K. Powell and Alan W. Searcy

The decomposition of dolomite, $CaMg(CO_3)_2$, in vacuum has been studied by the torsion effusion and torsion Langmuir techniques. If all steps of the reaction were rapid, measured Langmuir and effusion pressures would be equal. However, because a step in the reaction is slow, the Langmuir pressure was only 1×10^{-4} times the effusion pressure at 850 K. comparison of the two pressures as functions of temperature gives a measure of the irreversibility of the reaction. From torsion Langmuir data, using the second law method, the apparent activation enthalpy and entropy were calculated to be 46.5 kcal and 22.3 cal/degree-mole of CO_2.

Extrapolation of the effusion data to yield pressures for zero orifice area, and therefore presumably equilibrium pressures, gave thermodynamic data which imply that the solid reaction products are metastable by (17,600-8.8T) cal relative to the expected solid products, 1/2 MgO(s) + 1/2 CaO(s). Complete decomposition yields poorly crystalline MgO and CaO of high total surface area, but the decomposition product, when the reaction was 50% complete, did not give coherent x-ray scattering. If the amorphous solid product is assumed to be a supercooled liquid solution of 1/2 MgO + 1/2 CaO, that is a glass, the free energy of formation is predicted to be (18,800-7.4T) cal, in good agreement with the value calculated from our measurements. Anomalously low effusion pressures[1] for the reaction $MgO(s) = MgO(s) + H_2O(g)$, which have puzzled investigators for many years, can also be explained by assuming the solid product is a porous glass.

---

*Accepted for publication in J. Am. Ceram. Soc.

1. E. Kay and N. W. Gregory, J. Phys. Chem. 62, 1079 (1958).

2. TRANSPORT OF GASES THROUGH POROUS OXIDE BARRIERS

Nathan Jacobson, James A. Roberts, Jr., and Alan W. Searcy

Studies of He and CO_2 flow through porous calcium oxide produced by *in situ* decomposition of $CaCO_3$ single crystals were continued. From flow rates, porosity, and porous layer thickness pore diameters were calculated to be about 1 μm on the assumption that the pores can be approximated by linear tubes perpendicular to the direction of flow. This result appeared inconsistent with the fact that pores were not observable by Scanning Electron Microscopy (SEM), and were therefore presumed to be too small, 0.05 μm or less, to resolve with the instrument.

A possibly serious source of error was leakage around the barrier. For this reason BaO barriers from decomposition of $BaCO_3$ single crystals were studied. The BaO so prepared was known to have pores large enough to observe by SEM. Hence the influence of any leak would be less.

Again, Knudsen flow was the primary means of transport for both He and CO_2. The flow of CO_2 and He through BaO was that predicted for equivalent tubular pores of the order of 2 to 3 μm diam. SEM pictures showed a randomly oriented network of pores of approximately 2 to 10 μm diam (Fig. 1).

Because the equivalent tube diameters calculated from the flow data were in good agreement with direct observation by SEM for BaO, the morphology of CaO from $CaCO_3$ decomposition was re-examined using samples which were more carefully protected from water vapor and were fractured immediately before SEM pictures were taken. These pictures showed a series of ridges spaced 1 to 2 μm apart (Fig. 2).

These ridges suggest that CaO is traversed by linear pores of about the diameters expected from the transport measurements.

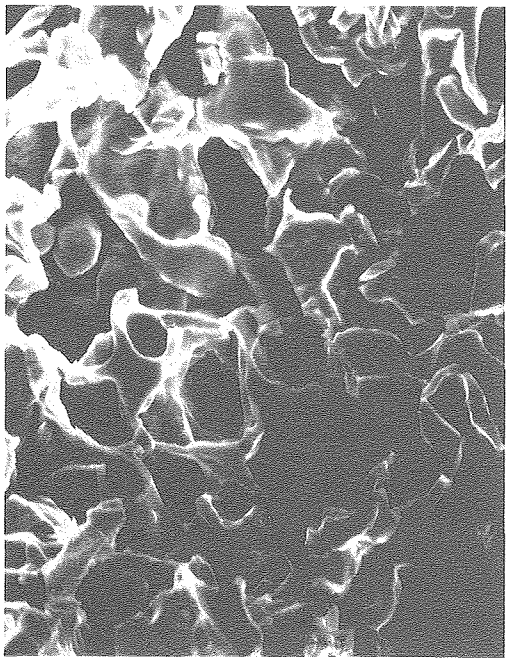

Fig. 1. SEM photograph of pores in BaO from $BaCO_3$ decomposition in vacuum. (XBB 781-367)

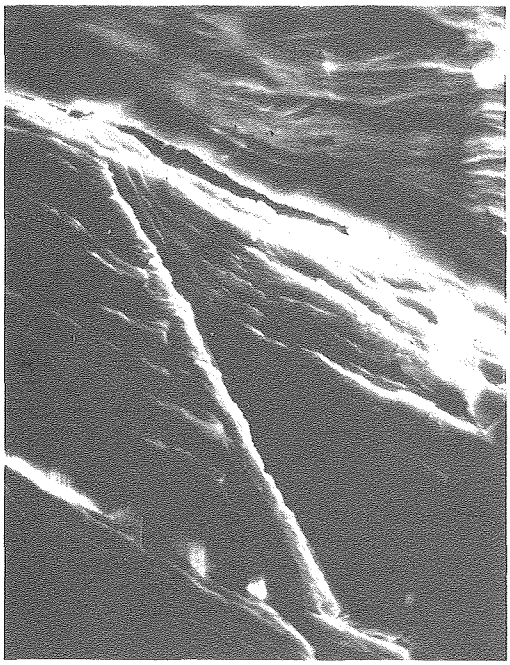

Fig. 2. SEM photograph of ridges which may indicate tubular pores in CaO from $CaCO_3$ decomposition in vacuum. (XBB 781-368)

3. CHARACTERIZATION OF THE GASEOUS AND SOLID PRODUCTS OF ALUMINUM SULFATE DECOMPOSITION*

Gary F. Knutsen and Alan W. Searcy

Sulfate decomposition reactions are more complex than carbonate or hydrate decomposition reactions in that the equilibrium gaseous product of sulfate decompositions is usually a mixture of three molecular species, SO_3, SO_2, and O_2 instead of a single kind of molecule. Lau et al.[1] found that $MgSO_4$ did not readily yield equilibrium pressures of SO_2 and O_2, while $CaSO_4$ yielded the equilibrium gas mixture more readily. They suggested that the lower temperatures used in $MgSO_4$ decomposition might cause the difference.

$Al_2(SO_4)_3$ decomposes at a lower temperature than either of the sulfates studied by Lau et al. Furthermore, we expected that the decomposition of $Al_2(SO_4)_3 \cdot 17H_2O$ first to the anhydrous sulfate and then to Al_2O_3 would yield an amorphous oxide of exceptionally high surface area. Al_2O_3 of such a structure might be useful in a number of applications. For these reasons we have investigated the products of $Al_2(SO_4)_3$ decomposition.

Measurements of SO_2^+/SO_3^+ mass spectrometer ion ratios and of weight losses when $Al_2(SO_4)_3$ is decomposed in an effusion cell show that equilibrium is readily achieved. The experimentally measured decomposition pressures are higher by more than a factor of 4 than would be expected from thermochemical calculations, probably because the heat of formation of $Al_2(SO_4)_3$ is 7 to 9 kcal per mole more positive than had been reported. Measurements of H_2O^+/SO_3^+ mass spectrometer ion intensities as a function of time shows that "anhydrous" aluminum sulfate contains about 0.03 moles of water per mole of sulfate ion.

The solid decomposition product in the range of effusion studies, below 600°C, is an amorphous Al_2O_3 which has a surface area of 165 M^2/g and internal pores that average about 100 Å in diameter.

---

*Accepted for publication in the Journal of the Electrochemical Society.

1. K. H. Lau, D. Cubicciotti and D. L. Hildenbrand, J. Chem. Phys. 66, 4532 (1977).

4. THE INFLUENCE OF VACUUM ON THE STABILITY AND SURFACE AREA OF CaO POWDERS FORMED BY DECOMPOSING $CaCO_3$*

Dario Beruto and Alan W. Searcy

Last year we showed[1] that while decomposition of $CaCO_3$ in air or dry nitrogen yields crystalline CaO, decomposition in vacuum yields poorly crystalline CaO in particles that retain the exterior size and form of the $CaCO_3$ particles from

which the CaO is produced; these CaO particles have high internal porosity. Both the poor crystallinity and the high surface area of the oxide formed in vacuum should make it chemically less stable and could make it kinetically more reactive. Accordingly, we have measured the heat of formation of the CaO formed by vacuum decomposition to obtain a quantitative measure of its thermodynamic stability. We also have investigated the effects of various conditions of preparation on the crystallinity and surface area of CaO powders in order to determine whether or not it may be feasible to prepare high-activity CaO in large quantities.

Heats of reaction with water were measured for commercial CaO, for CaO produced in air, for CaO produced in dry N_2, and for CaO produced by decomposing $CaCO_3$ in vacuum at 580 to 675°C. The heats of reaction of the commercial samples and of the samples produced by $CaCO_3$ decomposition in air or N_2 were found to be 0.5 to 0.6 kcal greater than the accepted values, presumably because of systematic error in our measurements. The heat of solution of CaO prepared in vacuum was 3.0 kcal higher than the accepted value. Therefore, this CaO must have a heat of formation about 2.4 to 2.5 kcal greater than crystalline CaO of low surface area.

Studies by Darroudi and Searcy[2] with single crystals had led us to expect that there might be a critical CO_2 pressure above which $CaCO_3$ decomposed to crystalline CaO and below which it decomposed to poorly crystalline or amorphous CaO. We find, however, that a continuous range of increased surface areas and reduced crystallinity result from decomposing $CaCO_3$ under conditions that favor increasingly rapid removal fo the CO_2 gas that results from the decomposition. Figure 1 shows that the surface area measured by the BET method and the half width of the 100 x-ray diffraction peak (a measure of imperfection) vary together. Surface areas of the order of 1 M^2/g were obtained by decomposing $CaCO_3$ in air or N_2. Areas of 94 M^2/g were obtained by decomposing small samples in high vacuum and the intermediate areas and crystallinities were obtained by decomposing larger samples in poor vacuums. It is evident that for powders the mechanisms of recrystallization and sintering must be closely related, but when single crystals are decomposed in vacuum, recrystallization occurs by a mechanism that does not significantly reduce the surface area.

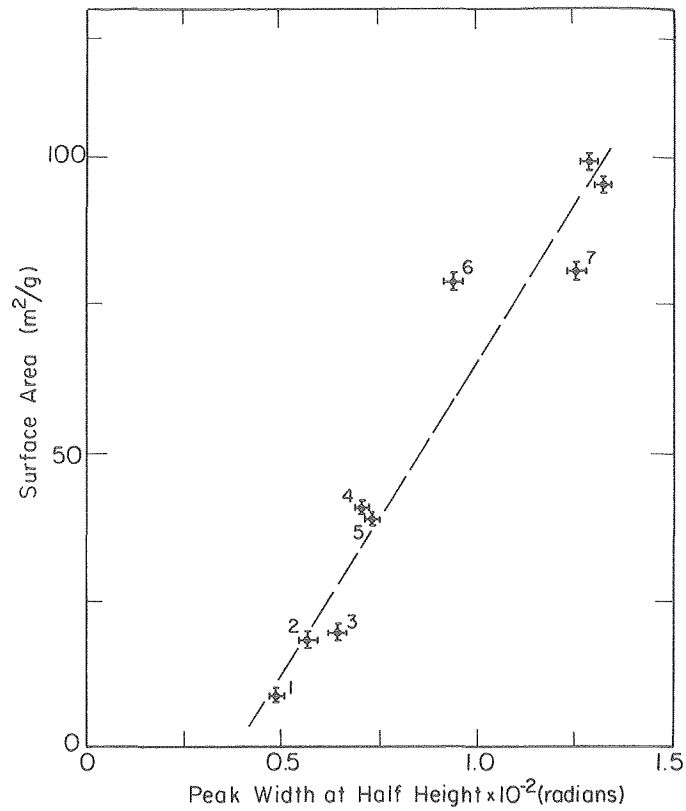

Fig. 1. Variation of surface area of CaO powders with half width of the (100) x-ray peak, a measure of crystal imperfection. (XBL 7712-6629)

5. THE INFLUENCE OF CO_2 PARTIAL PRESSURES AND TIME ON THE STRUCTURE AND MORPHOLOGY OF CALCIUM OXIDE FROM CALCITE DECOMPOSITION

Jay Ewing, Dario Beruto, and Alan W. Searcy

We had several reasons to suspect that the CaO product of partially decomposed $CaCO_3$ might have significantly different properties than found for the CaO after decomposition is complete: 1) Powell and Searcy (article 1 above) have obtained evidence that the solid product present when dolomite $CaMg(CO_3)_2$ is partially decomposed in vacuum differs from the products of complete decomposition. 2) The literature contains repeated allusions to metastable oxide intermediates in decomposition reactions, though the basis for these allusions is not clear. 3) Beruto and Searcy showed that during decomposition of single crystals of $CaCO_3$, a layer of a metastable oxide is present between the undecomposed $CaCO_3$ and a layer of crystalline CaO.[1] The crystalline oxide probably forms by a strain-induced transformation. It is reasonable to expect that an epitaxial layer of CaO on a $CaCO_3$ powder particle is also strained across the solid-solid interface, and may therefore be more reactive.

To study the properties of partially decomposed $CaCO_3$ powders a vacuum torsion furnace was modified with a recording microbalance and gas

*The calorimetric portion of this work was supported by the Centro Studi di Chemica e Chemica Fisica, Universita di Genova.

1. D. Beruto and A. W. Searcy, Nature 263, 221 (1976).
2. T. Darroudi and A. W. Searcy, in MMRD Annual Report 1976, LBL-6016, p. 102.

inlet system to permit dynamic flow of CO_2 at constant pressure. An electronic capacitance manometer permits accurate determination of the pressure. Calcite powders were heated at 973 K to various fractions of decomposition in vacuum or in controlled pressures of CO_2. The product powders were characterized using weight loss, BET surface area measurements, x-ray and scanning electron microscopy.

The surface area of the products of the experiments in vacuum and at 30 to 90 μm CO_2 pressure is plotted in Fig. 1 as functions of mole fraction CaO produced. This graph shows that the molar surface area of the product is constant throughout decomposition, and that the surface area of the product decreases as the back pressure of CO_2 increases. Scanning electron microscopy shows the original morphology of the $CaCO_3$ particles is maintained throughout the decomposition at all CO_2 pressures investigated. X-ray patterns show the oxide product is amorphous when the $CaCO_3$ is decomposed in vacuum, and that the degree of crystallinity increases as the back pressure of CO_2 increases.

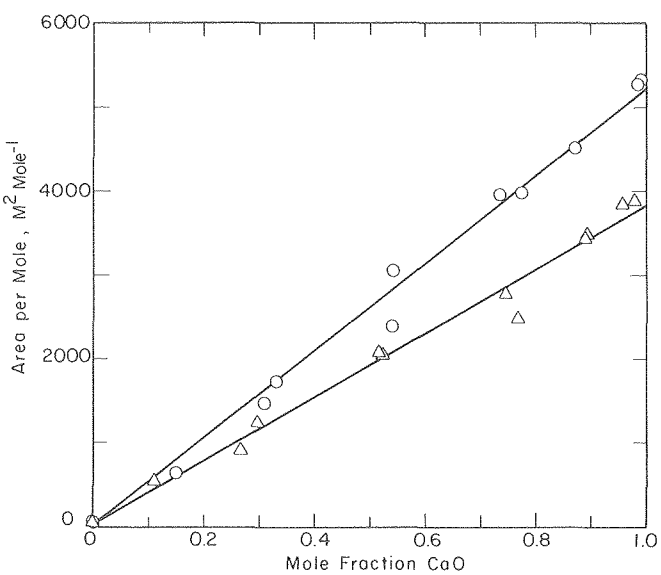

Fig. 1. Variation of the total surface area of $CaCO_3$ powder with the fraction of CaO produced by decomposition. Upper curve--decomposition in vacuum. Lower curve--decomposition in 30 to 90 μm CO_2. (XBL 7712-6630)

These results show clearly that the oxide produced by fractional decomposition of $CaCO_3$ powders is not significantly different in structure or area than the CaO produced by complete decomposition. The conclusion that variations in CO_2 pressures produce the variations in crystallinity and surface areas reported in the previous article is confirmed by these measurements with controlled CO_2 pressures.

---

1. D. Beruto and A. W. Searcy, J. Chem. Soc., Far. Trans. I, 70, 2145 (1974).

6. CATALYSIS OF THE HOT PRESSING OF CALCIUM OXIDE BY CARBON DIOXIDE GAS

Gary F. Knutsen, Dario Beruto and Alan W. Searcy

Our recent studies have shown that when calcite powder was decomposed in vacuum at about 800°C, there was little change in the apparent particle shapes from those of the starting material and very little sintering occurred. However, when calcite was decomposed in air or nitrogen in the same temperature range the product was composed of particles with rounded surfaces and neck areas, which indicated that considerable sintering had taken place. Because sintering occurred at temperatures which were only about 1/3 the melting temperature of clacium oxide, it seemed probable that the CO_2 evolved during $CaCO_3$ decomposition is a sintering catalyst.

Calcite ($CaCO_3$) samples were hot pressed under conditions such that a high partial pressure of CO_2 is maintained while the $CaCO_3$ decomposed. Under these conditions considerable sintering of the calcium oxide occurred at temperatures in the range of 900° to 1000°C. The calcium oxide produced in this manner showed considerable densification and appeared to have undergone almost viscous flow in the regions of CaO farthest from any undecomposed $CaCO_3$ (Fig. 1).

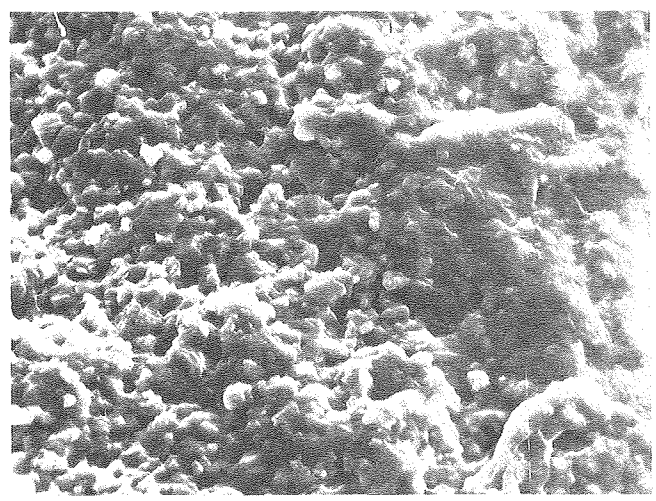

Fig. 1. SEM picture of CaO produced by hot pressing $CaCO_3$. The area to the right is farthest from the undecomposed $CaCO_3$. (XBB 781-369)

In contrast, CaO which had been formed from decomposition of $CaCO_3$ in vacuum and which, therefore, should be thermodynamically more active than ordinary CaO showed no evidence of sintering when hot pressed to between 900 and 1000°C in vacuum. Evidently CO_2 is an effective catalyst for sintering of CaO. Experiments are planned to test whether CO_2 must be initially present in the condensed phase in order to cause catalysis of the oxide sintering or whether CO_2 gas, when introduced after decomposition of the carbonate is complete, is also a catalyst.

7. EVALUATION OF ACTIVE CaO FOR USE IN CEMENTS

Richard Berger and P. Kumar Mehta

Cementing properties can be developed by a reaction between CaO and SiO_2 carried out commercially by heating the solids under hydrothermal conditions. Because the calcium oxide produced by vacuum decomposition of $CaCO_3$ is in a thermodynamically active state and has a higher surface area than oridinary CaO (see article 3 above), it was hoped that the vacuum product might react with water without heating and perhaps produce early setting strengths superior to those otherwise obtained.

To test this possibility, samples of CaO which were made at vacuums that yielded surface areas of the order to 20 M^2/g and ordinary CaO, which has surface areas of the order of 1 M^2/g and is more highly crystalline, were each used as components of cement pastes. Strength development of the pastes were measured, and the rates of hydration of the two kinds of CaO were measured by x-ray diffraction.

There was no practically significant difference in strengths or setting times between the two sets of samples. The x-ray diffraction patterns of the $Ca(OH)_2$ produced from each kind of oxide were sharply crystalline. This observation probably explains why the high activity of the vacuum prepared oxide did not result in a significant difference in setting rates. Beruto and Searcy have shown[1] that the vacuum-produced CaO reacts with water vapor at 140°C to form a poorly crystalline $Ca(OH)_2$. The reaction path that produces a well-crystallized $Ca(OH)_2$ at lower temperatures must be solution of CaO in water followed by precipitation of $Ca(OH)_2$ from the solution. If the precipitation step is rate limiting, the reaction rate would be little influenced by changes in activity or surface area of the CaO.

---

1. D. Beruto and A. W. Searcy, Nature 263, 221 (1976).

8. THERMODYNAMIC PROPERTIES OF SeS GAS

Ming-Der Huang, David J. Meschi and Alan W. Searcy

Mass spectrometry and Knudsen effusion experiments were used to study the equilibrium partial pressure of SeS formed by reaction of S_2 and Se_2 which were produced by thermally decomposing a mixture of In_2S_3 and In_2Se_3 in a Knudsen cell. The heat of formation of SeS(g) by the reaction $1/2\ S_2(g) + 1/2\ Se_2(g) = SeS(g)$ was determined by the second law method to be -0.6 ± 3.0 kcal/mole. The entropy of formation of SeS(g) was calculated from spectrographic data of Ahmed and Barrow[1] to be 1.5 cal/degree-mole at 298 K.

From our data the partial pressure of SeS(g) was calculated to be five times higher than that of $Se_2(g)$ above an ideal solution of 1% CdSe in CdS. This calculation confirms our prediction that SeS(g) is likely to be a major Se impurity carrier in vacuum decomposition of sulfide films in the semiconductor industry.

---

1. F. Ahmed and R. Barrow, J. Phys. B 7, 2256 (1974).

9. RESEARCH PLANS FOR CALENDAR YEAR 1978

Alan W. Searcy

We plan to measure the heats of solution of the products of partially decomposed $CaMg(CO_3)_2$ and $Mg(OH)_2$ in vacuum. The data should confirm or disprove the conclusion from work reported in article 1 above that the solid products may be porous glasses with high positive heats of formation relative to the thermodynamically stable reaction products.

The influence of CO_2 pressure on the morphology and crystal structure of the CaO produced by decomposition of $CaCO_3$ single crystals in vacuum will be studied. The data will test our general theory of decomposition reactions and, by comparison with the measurements for powder decomposition described in article 5, will show if there is an effect of particle size on decomposition kinetics.

The kinetics of decomposition of $SrCO_3$ single crystals will be measured in vacuum and as a function of CO_2 pressure. We hope that $SrCO_3$ will be a simpler substance for theoretical study than $CaCO_3$, which yields a solid product of structure and porosity that is strongly influenced by CO_2 pressure and particle size.

Studies of the variation with CO_2 partial pressure and temperature of the composition of $CaCO_3$, viewed as a pseudobinary phase of CaO and CO_2 should be completed. These measurements will provide data on partial molar thermodynamic properties for a type of inorganic solid for which such data have apparently never been measured.

The rate of decomposition of some sulfates is increased by iron oxides in a manner that suggests that a catalyst is somehow transported from the iron oxide to the interface of the sulfate with a layer of product oxide that grows into each sulfate particle. In an effort to understand this rather surprising effect, we plan to study the catalysis of decomposition of single crystals of $SrSO_4$ by iron oxides and other reagents.

As another means of furthering the theoretical understanding of the mechanisms of sulfate decomposition reactions and of sulfur oxide reactions with oxides, we plan to study the decomposition of SO_3 SO_2 and O_2 as a function of temperature in porous oxide barriers, perhaps with added catalysts, at high temperatures.

We will complete our study of the influence of CO_2 as a catalyst in hot pressing of CaO by measuring the effect on CaO sintering of CO_2 pressures near 1 atmosphere. This experiment should enable us to decide whether CO_2 must be present initially as the carbonate in order to catalize CaO densification or whether it can act by dissolving in, or adsorbing on, the CaO phase after it has already been formed.

We may explore the possibility that an effect equivalent to grinding can be obtained by hydration followed by dehydration of oxides.

10. 1977 PUBLICATIONS AND REPORTS

Alan W. Searcy and Associates

Journals

1. P. Mohazzabi and A. W. Searcy, A Porous Barrier Study of the Temperature Dependence of the Mass Spectrometer Fragmentation Pattern of LiF Monomer, Int. J. of Mass Spectrom. and Ion Phys. 24, 469-70 (1977).

2. James A. Roberts, Jr. and Alan W. Searcy, Anomalous Temperature Dependence for a Partial Vapor Pressure, Science 196, 525 (1977).

3. David J. Meschi, Tushar K. Basu and Alan W. Searcy, Knudsen Flow Through Multiple Barriers, High Temp. Sci. 9, xxx (1977).

LBL Reports

1. E. K. Knauf, The Kinetics and Thermodynamics of Decomposition of Dolomite in Vacuum, (M. S. thesis), LBL-6291, June 1977.

2. G. F. Knutsen, Characterization of the Gaseous and Solid Products of Decomposition of Aluminum Sulfate, (M. S. thesis), LBL-6292, June 1977.

3. E. K. Powell and A. W. Searcy, The Kinetics and Thermodynamics of Decomposition of Dolomite to a Metastable Solid Product, LBL-6668, (1977).

4. A. W. Searcy, Active Oxides, LBL-6669, (1977).

5. M. D. Huang, Thermodynamic Properties of SeS, (M. S. thesis), LBL-6994, December 1977.

Technical Talks and Conferences

1. "A General Theory for Decomposition Reactions and Tests of Its Predictions," Alan W. Searcy, presented at meeting of the Solid State Science Panel, National Research Council, at LBL, Berkeley, March 25, 1977.

2. "Recommendations for Research on Environmental Attack," presented by Alan W. Searcy as a workshop chairman of the ERDA Workshop on Phase Transformations, Stability, and Materials Interactions, LBL, Berkeley, April 20, 1977.

3. "The Kinetics and Thermodynamics of Decomposition of Dolomite," paper by Elizabeth K. Powell and Alan W. Searcy, presented at the Pacific Coast Regional Meeting, American Ceramic Society, Los Angeles, November 1977.

d. Relation of Microstructure to Properties in Ceramics

Richard M. Fulrath, Principal Investigator

Introduction. The physical, chemical, and mechanical properties of ceramic materials are determined by the composition and the manner in which the composition is processed. Unlike metallic alloys that can be treated thermally, mechanically or combinations of both to significantly change their properties, the properties of processed ceramic materials are essentially unchanged by these processes. Therefore, to optimize the properties of existing ceramic materials and develop new materials required for advanced technology generated by raw material and energy shortages, research related to processing and the relation of processing to properties is essential to the progress of ceramic science.

This research effort is divided into four major areas. The first activity is concerned with the densification (sintering) of powder compacts with and without the presence of a liquid phase. A primary tool for these studies has been the MMRD developed capabilities in hot-stage scanning electron microscopy. Both metallic and nonmetallic systems have been studied and include copper, nickel, uranium dioxide, aluminum oxide, iron-copper, and tungsten carbide-cobalt. Presently one study is concentrating on the effect of the stoichiometry of the solid phase when sintering with a liquid phase present. The titanium carbide-nickel system was chosen for this study because of the wide range of solid solution of titanium carbide.

The second major area of investigation is concerned with ferroelectric and piezoelectric ceramics in the lead titanate-lead zirconate system. This system offers a great challenge to understanding ceramic processing because of the high vapor pressure of lead oxide at elevated temperatures. Because of the volatility of PbO at high temperatures it is difficult to control the stoichiometry during processing ceramics in this system. The defects, primarily lead ion and oxygen ion vacancies, created by stoichiometric changes play a major role in determining the electrical properties. Therefore, combining measurements of electrical properties with processing parameter variations and basic studies on compound formation and PbO activity in this system has led to significant advances in developing a better understanding of processing and the role of the defect structure in determining the electrical properties. The present work encompasses two areas. One study is on the mechanism and kinetics of the formation of the compounds lead titanate and lead zirconate and their solid solutions. A second investigation is being pursued to establish the PbO activity in the lead oxide-aluminum oxide system and the equilibrium phase diagram. Two conflicting phase diagrams have been published in literature.

The third major area of investigation is on thick film conductors, a major user of precious metals. The emphasis in this area has been to develop microstructures of thick film systems wherein the precious metal content can be significantly reduced or where base metals can be substituted for noble metals.

The last area of investigation is concerned with the mechanical properties of ceramics, especially the influence of porosity and nature of the surface on the fracture toughness and strength. During the past two years this study has used lead zirconate titanate with induced porosity in a dense fine grained matrix. This work has been concluded and the emphasis now is being directed toward the fracture toughness and strength of alumina, an important ceramic structural material.

The general theme of this total effort is to understand how microstructures are developed in the processing of ceramics and how the microstructure influences the properties.

1. THICK FILM CONDUCTORS

V. K. Nagesh and Richard M. Fulrath

Thick film conductors are one of the basic components of hybrid microcircuits. Application of thick film technology in these circuits is extensive as they are reliable and economical. The following project was undertaken to obtain a basic understanding of the microstructure development of a thick film conductor, to investigate the relationship between its sheet resistivity and the process variables, and to reduce the amount of metal necessary to maintain the desired sheet resistivity.

Conventionally, a thick film conductor is a mixture of precious metal (Au, Pt, Ag or combinations of these with Pd) and powdered glass in an organic vehicle that is printed on a ceramic substrate and subsequently fired. Precious metal is the major phase in these films (80 to 90 w/o) and the glass addition is made to provide bonding of the metal to the substrate. A new process developed by us uses a precious metal content as low as 20 w/o, and still results in a good conducting film.[1] The system under study is lead borosilicate glass-silver. The process involves an acid treatment (0.01N HCl) of the glass particles and subsequent deposition of silver, using thermally decomposable silver resinate in xylene. These silver coated glass particles are then suspended in an organic vehicle, printed on 96 w/o Al_2O_3 substrate and fired at different temperatures and times. With 40 w/o Ag, sheet resistivities are as low as 44 mΩ/□ which are very favorably comparable with the commercial thick film conductors that use up to 90 w/o of the precious metal.

Thick film conductors formulated according to the new process have a microstructure wherein a continuous Ag film exists around the glass particles giving rise to electrical continuity. It is necessary to have Ag strongly bonded to the glass surface to maintain this continuity. Without an acid treatment an insulating film is obtained with similar metal contents. The treatment of glass particles by acid hence is an

important step in the process and its analysis worthwhile.

When the lead borosilicate glass is treated with 0.01 N HCl, lead ions are preferentially replaced by H^+ ions and surface roughening occurs as observed in SEM shown in Fig. 1. This condition facilitates the rapid spreading of silver resinate solution on the glass surface. As the silver resinate solution (in xylene) is essentially a non-conductor with no silver ions, $H^+ \rightleftharpoons Ag^+$ ion exchange reaction appears to be highly improbable at this stage of the process. However, after silver resinate is decomposed (at 210°C), silver oxidizes in the presence of oxygen and H^+ ions at the surface to form Ag^+ ions:

	E° Volts
$O_2 + 4H^+ + 4e^- \rightarrow 2H_2O$	1.229
$4\ (Ag^+ + e^- \rightarrow Ag)$	.800
$O_2 + 4H^+ + 4\ Ag \rightarrow 2\ H_2O + 4\ Ag^+$	.429 V

The saturation of the interface with Ag^+ ions provides good chemical bonding between silver metal and glass.[2]

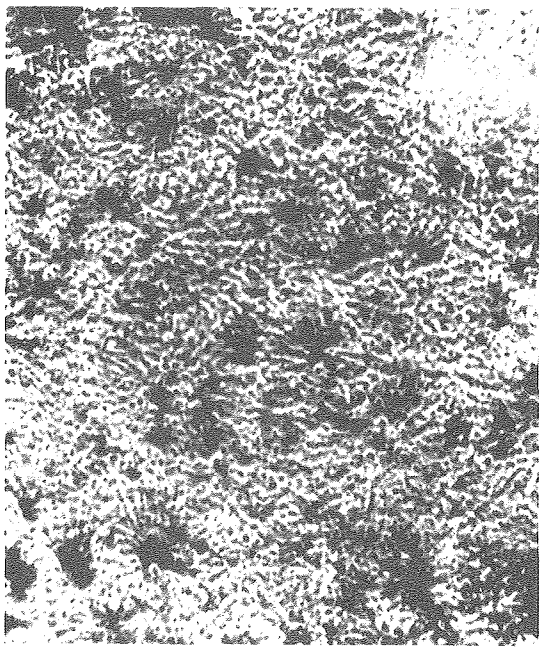

Fig. 1. Surface of etched borosilicate glass observed by SEM. (XBB 765-4532)

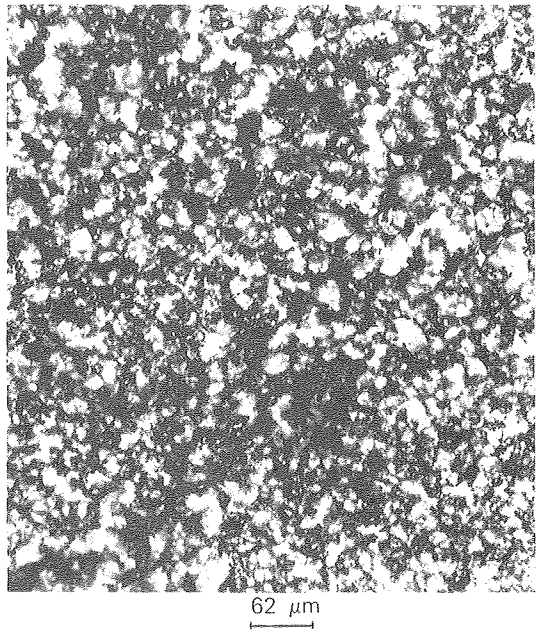

Fig. 2. Transmission optical micrograph of thick film with 25 w/o Ag and surface active glass powder (20-44μ). (XBB 766-4725)

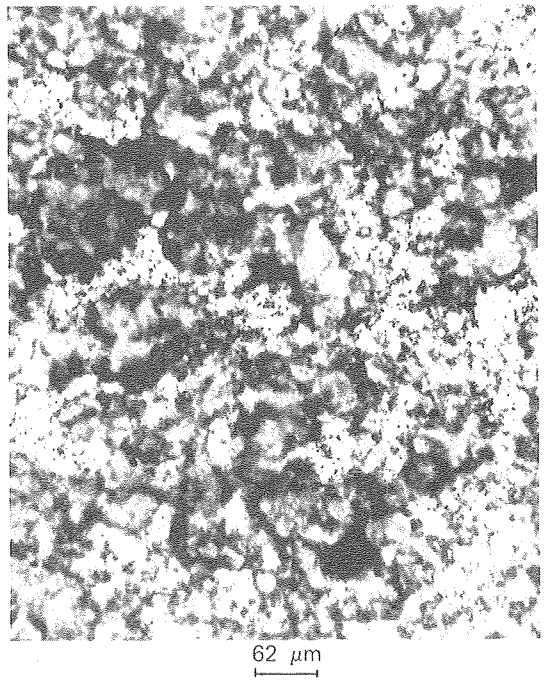

Fig. 3. Transmission optical micrograph of thick film with 25 w/o Ag and surface passive glass powder. (XBB 766-4726)

The microstructure of a thick film conductor using surface activated glass particles is shown in Fig. 2 (metal content 25 w/o). Thick films are not considered to be good conductors (sheet resistivity $> 10^{12}\ \Omega/\square$) when a) H^+ ions are not implanted by acid treatment (Fig. 3), and b) firing is in N_2 atmosphere instead of air atmosphere (Fig. 4). Figure 3 shows discontinuous chain structure of silver (dark phase), and Fig. 4 shows the agglomeration of Ag as seen in a SEM. These observations further support the reaction mechanism suggested above.

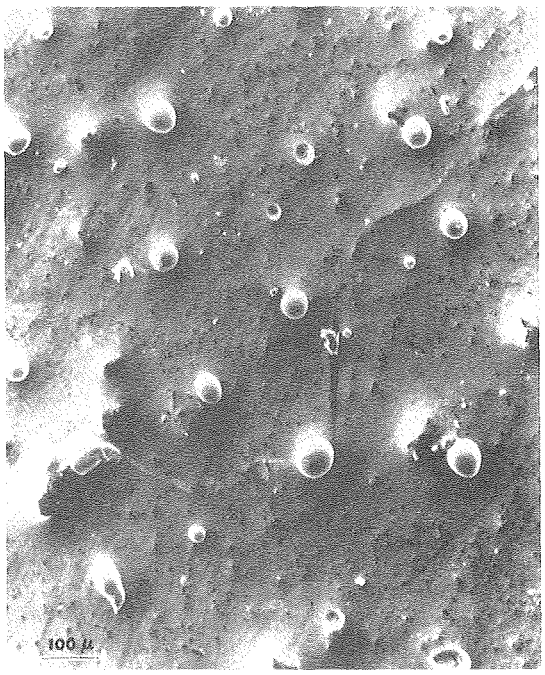

Fig. 4. Scanning electron micrograph of a thick film with 25 w/o Ag and surface active powder fired in N_2. (XBB 781-2)

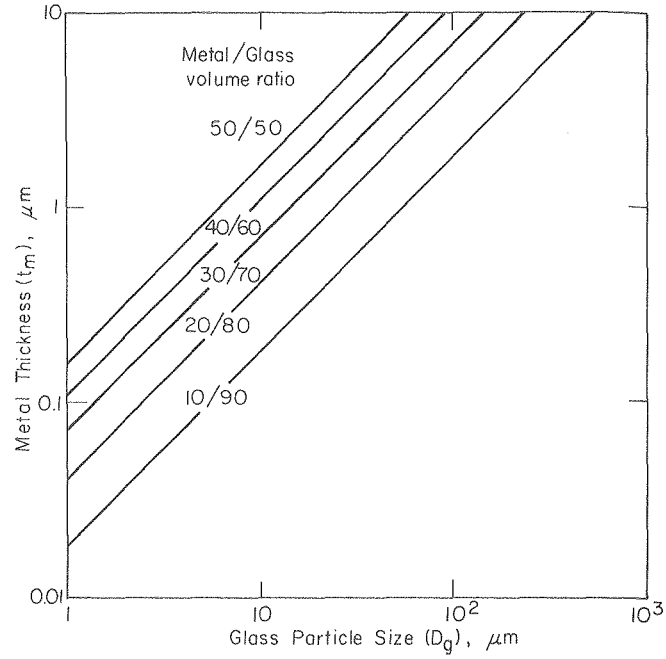

Fig. 5. Variation of metal coating thickness with different glass particle sizes and metal content. (XBL 7710-6293)

In order to calculate the sheet resistivity as a function of the metal content and the glass particle diameter, the following assumptions were made: a) glass particles are spherical with an average diameter when a narrow particle size range is considered, and b) the metal deposited on these glass particles is uniform and of constant thickness (t_m).

Sheet resistivity is defined as the ratio of resistivity to the thickness of the conducting layer. In the microstructure of interest, the conducting layer is a precious metal (Ag in the present case). As the thickness of this layer depends on the metal deposited on the glass particles (t_m), it is important to calculate t_m first. For an average glass particle diameter D_g, glass volume content V_g and metal volume content V_M, the thickness of the metal layer can be given by

$$t_m = \frac{D_g}{6} \frac{V_m}{V_g} \quad . \qquad (1)$$

Figure 5 shows the dependence of deposited metal thickness on glass particle diameter for varying glass/metal volume ratios.

The sheet resistivity of the fired film can now be given by $R_S \propto \rho/t_m$ or $R_S \propto 6\rho V_g/D_g V_m$ by substituting for t_m from Eq. (1), or

$$R_S = \frac{6\rho V_g}{k D_g V_m} \qquad (2)$$

where k is a proportionality constant for a constant thickness of the thick film.

k can be found experimentally and its value is found to be 0.1 for film thicknesses of ~1 mil. The close correlation between the theoretically calculated and the experimental sheet resistivity data is seen in Fig. 6 for varying metal contents. The films are fired in the temperature range 500 to 700°C for times from 8 to 20 min. Dependence

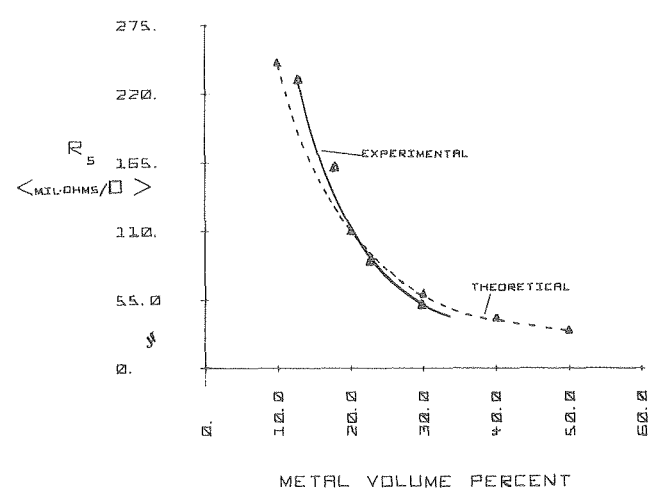

Fig. 6. Variation of sheet resistivity with metal content. (XBL 7710-10282)

of R_s on D_g is yet to be verified. Thus, the expression for R_s gives an indication of the expected sheet resistivities. Films fired at temperatures higher than 750°C essentially were non-conductors. At these temperatures due to the fluidity of the glass and due to the increased solubility of Ag in glass, the glass-metal bonds are possibly weakened leading to segregation of silver. Firing for longer times at lower temperatures would also have similar effects. This effect leads to the breaking of the continuity of the metal chain resulting in non-conductivity.

---

1. V. K. Nagesh, Electrical Conduction in Metal-Glass Composite Materials (M.S. thesis), LBL-5172, June 1976.
2. J. A. Pask and R. M. Fulrath, Fundamentals of Glass-to-Metal Bonding, VIII, Nature of Wetting and Adherence, J. Am. Ceram. Soc. 45, [12], 592 (1962).

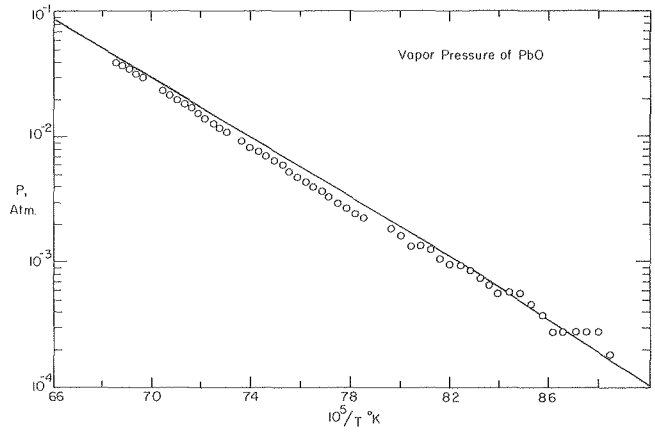

Fig. 1. Vapor pressure of pure PbO as measured by Knudsen effusion-weight loss. (XBL 7610-7627)

2. PHASE EQUILIBRIA IN THE $PbO-Al_2O_3$ SYSTEM

Bob R. Powell, Jr. and Richard M. Fulrath

One of the more serious problems encountered during processing of many ceramics is the vaporization of one or more of the constituents. When this is the case, as it is for lead zirconate-lead titanate (PZT) electronic ceramics, sintering is accomplished without lead oxide loss by use of the packing powder technique, which consists of burying the specimens in a coarse powder having the desired vapor pressure of lead oxide. The vapor pressure of PbO in various PZT systems was determined in this laboratory in 1972.[1,2] This work has been extended to include the $PbO-Al_2O_3$ system because Al_2O_3 is present in the high temperature environment during sintering of PZT as either a structural or container material.

The vapor pressure of PbO in equilibrium with different condensed phases of the $PbO-Al_2O_3$ system was measured as a function of temperature by use of the Knudsen effusion-weight loss technique. In this technique the pressure of PbO is related to the rate of escape of PbO vapor molecules through a small opening in an otherwise closed container. The equation is:

$$P_{PbO} = \frac{dw}{dt} \frac{1}{A_o} \sqrt{\frac{2\pi kT}{m}}$$

where dw/dt is the rate of weight loss, A_o is the effective orifice area and m is the mass of a molecule of PbO. There is no measurable weight loss due to Al_2O_3 evaporation. Monitoring the weight change of a platinum "Knudsen cell" containing reacted PbO and Al_2O_3 yields the vapor pressure data. The measured pressures of pure PbO are compared to the accepted data found in the JANF tables to check the performance of the equipment. This comparison is shown in Fig. 1. The measured pressures for the $PbO-Al_2O_3$ system are plotted in Fig. 2. In this figure, two-phase regions are represented by lines, the straight lines occurring for solids while the curved lines reflect the shift in the liquidus away from the PbO side of the phase diagram with increasing temperature.

The phase diagram in Fig. 2 was constructed from the pressure data and differed from the diagram reported in the literature[3] in that the stabilities of $PbO \cdot 6Al_2O_3$ and $PbO \cdot Al_2O_3$ were increased from 1100 to 1200 and 800 to 1100°C, respectively. Reevaluation of the data of these previous researchers revealed a misinterpretation in their analysis that reinforces our diagram.

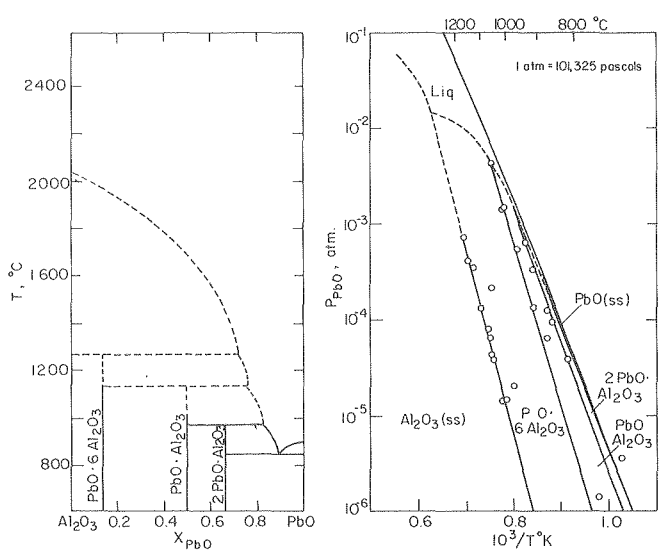

Fig. 2. (Right) vapor pressure of PbO in the $PbO-Al_2O_3$ system; (left) deduced phased diagram for this system. (XBL 7710-6303)

Finally, in Fig. 3, the activity of PbO is plotted in Arrhenius form for the $PbO-Al_2O_3$ system and for the PZT systems. The two lines for the mixtures containing PZT represent the limiting activities of PbO for the solid solution $Pb(Zr,Ti)O_3$. The packing powder used to sinter this material is $PbZrO_3$ and ZrO_2, a two-phase mixture that keeps the PZT samples within the single phase region (the region of optimum electrical properties). Direct exposure of PZT to Al_2O_3 during sintering (1200°C) would result in depletion of PbO from the sample by vapor transport to the Al_2O_3 which has a lower activity. This would stop when the surface of the Al_2O_3 had formed the single phase $PbO{\cdot}6Al_2O_3$. It is possible that PbO diffusion through the Al_2O_3 would also be important.

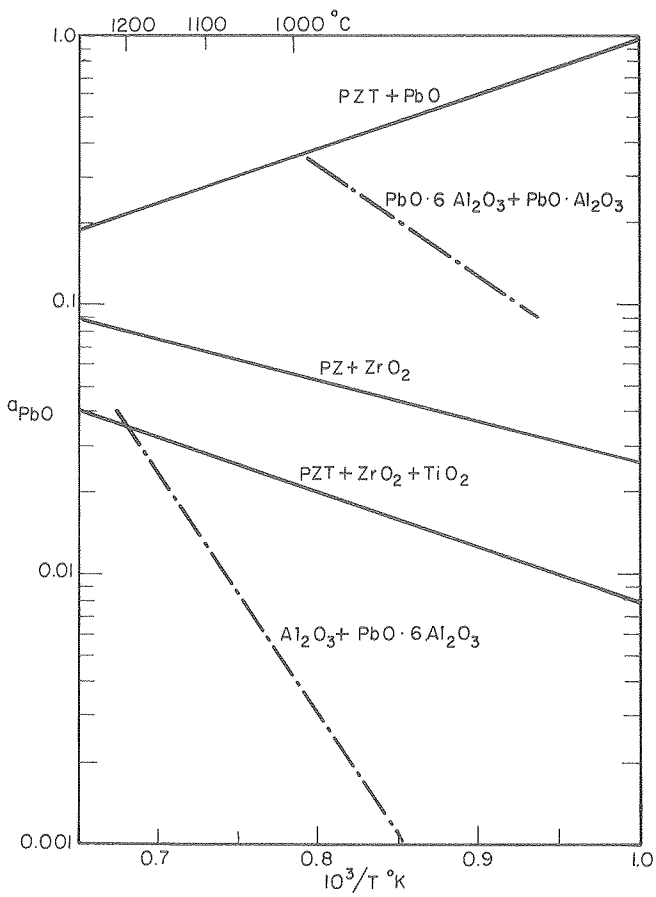

Fig. 3. Activities of PbO for PZT and Al_2O_3 systems. Standard state is the pressure of pure PbO at T K. (XBL 7712-6639)

In the next year the effort will be to gain an understanding of the diffusion of PbO in Al_2O_3 and the kinetics of formation of the intermediate phases. Preliminary results indicate that for the temperatures of interest, grain boundary diffusion is the dominant transport process.

1. Robert L. Holman, (Ph.D. thesis), University of California, July 1972, LBL-880.
2. Robert L. Holman and Richard M. Fulrath, Intrinsic Nonstoichiometry in the Lead Zirconate-Lead Titanate System Determined by Knudsen Effusion, J. of Appl. Phys. 44, [12] 5227 (1973).
3. K. Torkar, H. Krischner and H. Moser, Ber. Deut. Keram. Ges. 43, 259 (1966).

3. KINETICS OF SOLID STATE REACTIONS IN THE $PbO-ZrO_2-TiO_2$ SYSTEM

Sudhir S. Chandratreya and Richard M. Fulrath

The PZT system contains many compositions of considerable technological importance due to their pronounced ferroelectric properties. A number of investigations have been conducted to correlate PZT properties to their composition, various additions and sintering conditions. Reproducibility, however, remains elusive due to lack of standardization in the processing of the ceramics.

One of the first steps in the processing of PZT is "calcination" in which the synthesis of the solid solution of controlled stoichiometry from the powder mixture of PbO, TiO_2 and ZrO_2 takes place. Typically, calcination is done between 800 to 1000°C from a few minutes to several hours with no single standard process being specified. Reports have been made as to the profound effect of calcination conditions on the sinterability[1,2] and electrical properties[3] of the final ceramics. The present study was undertaken to characterize the nature and kinetics of solid state reactions taking place during calcination. The previous report[4] dealt with the investigation of various intermediate reactions leading to the final solid solution. The present report will focus on the kinetic aspects of the solid states reactions, in particular the formation of the two compounds $PbTiO_3$ and $PbZrO_3$ that form the end members of the pseudobinary $(Pb_x(Zr,Ti)_{(1-x)})O_3$ solid solution system. Thermogravimetry (TG) and Differential Thermal Analysis (DTA) were the techniques primarily used towards this end.

The raw materials used were all of high purity and known crystalline form. Two types of TiO_2 were used: the powder for TG was single crystal boule of rutile crushed to the appropriate size range; the powder for DTA was anatase of submicron particle size and high specific surface area (10.7 m^2/g). For DTA, equimolar mixtures of PbO (massicot) and anatase as well as massicot and ZrO_2 (baddeleyite) were milled to the micron size range.

DTA studies were conducted primarily to obtain the apparent activation energy for the solid state formation of $PbTiO_3$ and $PbZrO_3$. Kissinger[5] and Levski[6] have developed a technique whereby an apparent activation energy (E_{act}) can be obtained from the shift of the temperature maximum (T_{max})

of a DTA peak with different values of the heating rate (ϕ). The following relation has been derived[5]

$$\frac{d\left[\ln \frac{\phi}{T^2_{max}}\right]}{d(1/T_{max})} = \frac{E_{act}}{R}$$

A plot of $\ln(\phi/T^2_{max})$ vs $(1/T_{max})$ has the slope $(-E_{act}/R)$. On the basis of data at three heating rates (20°C/min, 10°C/min, 5°C/min) the value of 'E_{act}' was calculated to be 36 kcal/mole for $PbTiO_3$ formation and 101 kcal/mole for $PbZrO_3$ formation. Values reported in literature range from 45 kcal/mole[4] up to 103 kcal/mole[7] for $PbZrO_3$ and 45 kcal/mole[8] for $PbTiO_3$ formation. It is possible that two or more mechanisms with differing activation barriers operate under different experimental conditions leading to divergent values of activation energies. The effect of particle sizes of the reactants, the effectiveness of mixing methods, the compaction techniques could be variables leading to different results. Detailed study of the effect of these variables is presently under way.

TG experiments were conducted on rutile crystals exposed to PbO vapor to monitor progress of $PbTiO_3$ formation. Rutile crystals of various particle sizes were kept in a platinum basket suspended in a platinum crucible containing PbO powder. Isothermal weight gain was monitored for periods up to 24 hours for three different particle size ranges. Fraction of reaction completed (x) was calculated from the weight gain and was plotted vs. time at 900°C for a given size range of rutile. Theoretically, progress of reaction can be plotted if a rate controlling mechanism is assumed. For a non-porous spherical particle of TiO_2 with PbO as the mobile specie if phase boundary reaction is the rate controlling mechanism, the following relations should ideally be obeyed

$$1 - (1 - x)^{1/3} = \frac{kt}{R_o} \exp\left(-\frac{E_{act}}{RT}\right) = k^*t$$

where x is the fractional reaction completed, R_o is the initial particle size of TiO_2, E_{act} is the activation energy, R is the gas constant, and k is the preexponential constant. This relation was also plotted for $k^* = 1.6 \times 10^{-2}$. The correlation with the experimental data was satisfactory. Deviations from the theoretical plot are to be expected considering the variation in value of R_o from 30 up to 37 μm as well as deviation from ideal spherical shape of the actual particles. Similar experiments on rutile of size range 10 to 20 μm and 1 to 10 μm were conducted. Smaller particles, however, indicate larger deviation from theory at higher values of x with better correlation to theory at lower values of x. It is postulated that while the phase boundary reaction is the rate controlling step for larger particles, for smaller particles another mechanism such as diffusion of reactant through product layer or external diffusion of PbO are the rate controlling steps.

The above experiments indicate the complex nature of the solid state reaction kinetics in the PZT system. However, the importance of the study lies in its potential benefits in the manufacture of PZT. For example, if calcination temperature and time are reduced, significant energy and cost saving can be realized. Loss of PbO by volatilization during calcination, a health hazard, can also be minimized leading to better control over stoichiometry of PZT. While under-calcination results in poor properties of the final product, over-calcination can lead to poor sinterability and lack of control over stoichiometry. Proper balance thus should be possible only through better characterization of calcination and related solid state reactions.

---

1. H. Iwasaki, Jap. J. Appl. Phys. 4 (3), 190 (1965).
2. D. A. Buckner and P. D. Wilcox, Bull. Am. Ceram. Soc. 51 (3), 218 (1972).
3. A. E. Robinson and D. Luff, Trans. Brit. Ceram. Soc. 61 (2), 94 (1962).
4. S. S. Chandratreya and R. M. Fulrath, MMRD Annual Report for 1975, p. 109.
5. H. E. Kissinger, J. Res. Natl. Bur. Std. 57, 217 (1956).
6. L. K. Levski, Rus. J. Phys. Chem. 39, 982 (1965).
7. H. Sasaki, J. Am. Ceram. Soc. 47 (10), 515 (1964).
8. A. Mangel and J. Doskocil, Ber. Dt. Keram. Ges. 51 (11), 329 (1974).

4. QUANTIZING THE POLARIZATION OF LEAD ZIRCONATE-TITANATE

Scott Hewett and Richard M. Fulrath

Polycrystalline lead zirconate-titanate (PZT) ceramics are used as piezoelectric materials in several applications. Some of the uses are as sonar transmitters, ultrasonic cleaners, electronic band pass filter elements and even heart pumps. A crucial step in the manufacture of all of these devices is the poling process. Poling consists of applying a strong external electric field in order to leave the ceramic with a net dipole.

The poling process has typically been characterized by the time, temperature and field applied during poling. In this study, the charge displaced during poling was measured and plotted continuously on an x-y plotter as a function of the applied field. Plots were made at various temperatures for the same composition of PZT. A typical family of isothermal curves is shown in Fig. 1 for a composition of $Pb(Zr_{0.52}Ti_{0.48})O_3$ and 1.5% Mn.

Measurement of the planar coupling coefficient for the samples showed no correlation of this piezoelectric effect and the temperature at which

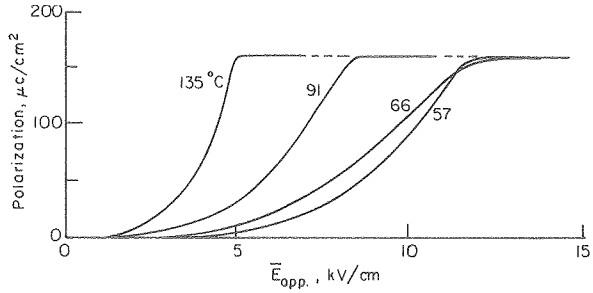

Fig. 1. Polarization vs. applied field at various temperatures for $PZ_{0.52}T_{0.48}$ and 1.5% Mn. (XBL 7712-6537)

the sample was poled or the maximum field applied. All samples reached the same saturation polarization value of 161×10^{-6} coulombs/cm^2. This value is 82% of the maximum polarization estimated for a single crystal of PZT. Most of this saturation polarization is not retained by the sample after the field is removed due to lattice strain energy introduced by the domain switching. The value of remnant polarization is probably on the order of 20 to 30 $\times 10^{-6}$ coulombs/cm^2. The way to increase the remnant polarization, and hence improve the piezoelectric properties of these ceramics would be to relieve the strain associated with domain switching and not by applying higher fields, as these results show.

When the ℓog of the field at saturation is plotted against the reciprocal of the poling temperature, a plot such as Fig. 2 is produced.

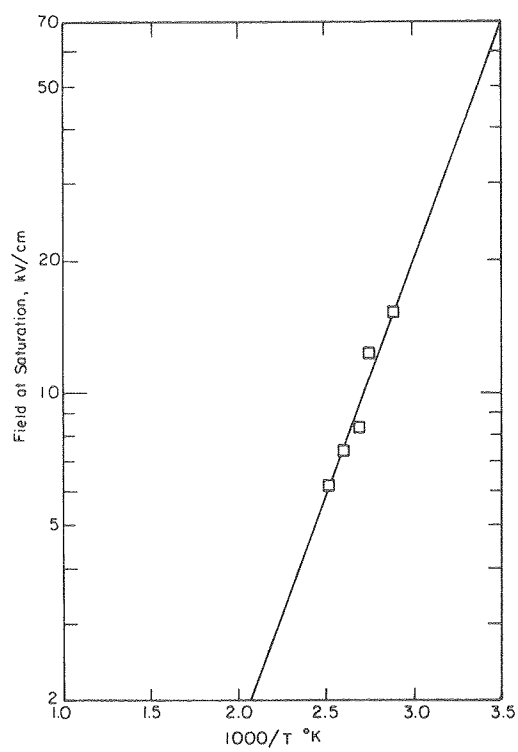

Fig. 2. Field at saturation vs. 1000/T K for $PZ_{0.52}T_{0.48}$ and 1.5% Mn. (XBL 7712-6541)

This type of plot is typical of an activation-type process. From this graph it is possible to predict the field required for saturation polarization to occur at a particular temperature. It should be noted that the field required at room temperature is greater than the dielectric strength of the material and also that these graphs are meaningless above the Curie temperature of the ceramic.

5. EXPERIMENTS IN LIQUID PHASE SINTERING OF Si_3N_4

Jay Wallace and Richard Fulrath

Silicon nitride has been proposed for use in areas where high temperature strength, thermal shock resistance and resistance to oxidation are important. The chief problem at present is processing Si_3N_4 powder to produce dense products which have the high temperature strength that is characteristic of pure Si_3N_4 since current technology requires additives to realize high density. The solution lies in control of the microstructuer; more specifically, control of the grain boundary phase.

Initially the work was to prepare Si_3N_4 samples with a controlled grain boundary phase to be used in room temperature and high temperature bend strength measurements. Fabrication work proceded along two separate lines: 1) additions of volatile liquid phases and 2) additions of silicious glass-ceramics. Due to difficulties in producing dense specimens with a controlled grain boundary phase for strength measurements the effort was aborted.

Volatile liquid phase sintering has been successful with materials such as MgO (LiF liquid) and PZT (PbO liquid). The liquid phase forms at sintering temperatures and allows rearrangement of particles and high atomic mobility to promote rapid densification. As densification continues the void volume decreases and the liquid phase evaporates until, ideally, the body is dense and no liquid phase remains. The proposed requirements for the additions were that the liquid phase would form between 1500 and 1550°C, have a vapor pressure between 10^{-6} and 10^{-4} atmospheres at 1500°C, vaporize congruently and not react with Si_3N_4 to form a compound. Preliminary work showed that several metals, Co, Ni, Sn and Cu, had the required properties but would not wet Si_3N_4; densification of the compact thus was not promoted. Silicon with boron addition did wet Si_3N_4 but required that the sample be fired in a neutral atmosphere to prevent reaction with either O_2 or N_2. It was found, however, that decomposition of Si_3N_4 became a problem when samples were fired in atmospheres other than one atmosphere N_2. The fluorides, starting with LiF, were then tried. Lithium fluoride at 1500°C proved too volatile to promote complete densification before all of the liquid had evaporated. Other fluorides with decreasing volatility, as determined by the Hertz-Knudsen-Langmuir equation, were then selected. MgF_2, CaF_2, SrF_2 and BaF_2 with volume fractions of 0.05 to 0.20 were tried. The BaF_2 addition was the most promising resulting in a final density of

88% for a 10 v/o addition fired at 1550°C in one atmosphere N_2 for 12 hr. X-ray diffraction showed no traces of BaF_2 after firing.

The second objective of the investigation centered on additions of (non-volatile) siliceous glass-ceramics. It was felt that siliceous glass-ceramics would wet Si_3N_4 and form a high strength composite body. The glass ceramic was required to be a liquid at the sintering temperatures, to match the coefficient of thermal expansion of Si_3N_4, and to form a strong fine-grained polycrystalline ceramic with appropriate heat treatment. Initial investigation showed a 5 v/o addition of β-spodumene, $Li_2O{\cdot}Al_2O_3{\cdot}4SiO_2$, could produce a sintered density of 88% of theoretical. Work continued with additions of zero to 10 vol% liquid phase to study the effects of varying the sintering time and temperature. Final density was found to increase with increasing sintering time, temperature and volume fraction liquid. However, reaction of Si_3N_4 with β-spodumene to form solid solutions, sialons and β' Si_3N_4, increased more rapidly than increase of the density. Another glass-ceramic, $3BaO{\cdot}5SiO_2$, was also tried with similar results. Since the reactions to form the solid solutions changed the composition and properties of the grain boundary phase, systematic studies of the strength of the composite body were not undertaken.

6. EFFECT OF SURFACE TREATMENTS ON STRENGTH OF PZT CERAMICS

Dipak R. Biswas and Richard M. Fulrath

In the ceramic industry, surface finishing of the component parts is very important, particularly from the point of view of strength. A wide variety of surface finishes can be generated by grinding, abrading and polishing. The grinding and abrading might produce extrinsic surface cracks whereas polishing might remove some of these cracks. Besides the possibility of extrinsic cracks being generated by the different machining processes, there might be some intrinsic flaws in polycrystalline ceramics. The present work was undertaken to determine the effect of various surface treatments on strength of a highly dense polycrystalline lead zirconate-titanate (PZT) ceramic and its failure mechanism.

In PZT ceramics (average grain size 2 to 5 μm) the grain growth during processing was controlled by doping with 1 mole % niobium oxide. The samples were fabricated[1] by sintering at 1200°C for 8 hr in one atmosphere pressure of oxygen. It was found that a small amount of excess PbO (5.5 w/o in this case) enhances the sintering process. A packing powder ($PbZrO_3$ + 5 w/o ZrO_2) technique was used during the sintering process to prevent PbO loss from the specimen and to maintain the stoichiometry. A wide range of surface treatments were given to the bend specimens after slicing from the sintered disks by using a precision diamond blade. A set of eight specimens were used for each series: a) as cut, b) as cut plus rounded edges (by using a rotating diamond wheel), c) with polished tensile surface, d) with polished tensile surface plus rounded edges and e) with polished tensile surface plus rounded edges plus etch (with HCℓ/HF mixture). All specimens were tested in a four-point bending machine and the fracture origin was detected by using a scanning electron microscope.

It was found from the bend tests that the strength variation (79.30 to 82.70 MN/m^2) with respect to different surface treatments is insignificant. If polishing removed critical surface cracks, the strength should have increased, but in this case there is no change in strength. This behavior indicates that the original surface flaws are not more severe to cause failure. The fracture surfaces are shown in Figs. 1 and 2. In as-cut specimens, the fracture initiation was at the edge of the specimen (Fig. 1a) and/or at the width of the bend specimen (Fig. 1b). Rounding

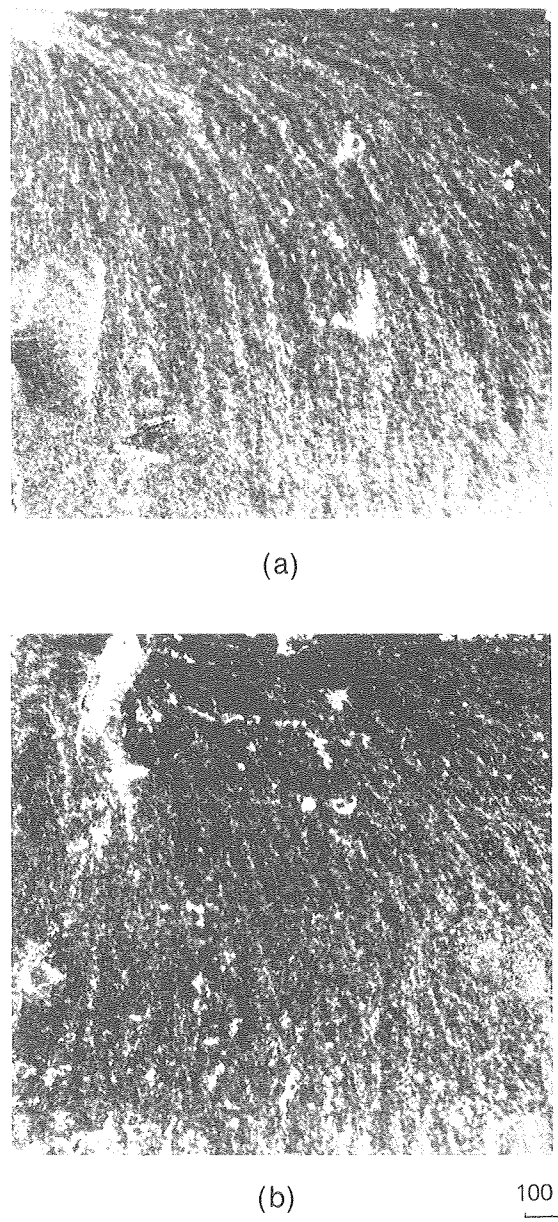

Fig. 1. Fracture surfaces of as-cut specimens. (XBB 770-10389)

off the edges, minimizes the edge failure (Fig. 2a). In case of polished tensile surfaces, polished tensile surfaces plus rounded edges plus etch specimens, the failure occurs (Fig. 2b, 2c, and 2d, respectively) at or near the tensile surface. It is interesting to note that the crack initiation morphology in most cases is very similar and the crack size is quite large (around 200 to 300 μm in length or in depth). This indicates that the failure mechanisms should be the same for all specimens irrespective of various treatments.

It was found that materials with low elastic modulus and high internal friction contain many microcracks.[2] Previous experimental results on this particular ceramic showed that it has a low elastic modulus and a high internal friction. It is thus clearly indicated that this material contains many inherent microcracks. A reason for the existence of microcracks may be attributed to the use of excess PbO to realize a liquid phase sintering mechanism in the fabrication of the PZT ceramics. During sintering, if the excess PbO is not completely evaporated to the packing powder, the remaining PbO during cooling from the sintering temperature remains at the grain boundaries. It may be the source of microcracks because of the thermal expansion differences between PZT and PbO phases. The thermal expansion anisotropy gives rise to boundary stresses that produce the microcracks. Secondly, in presence of excess PbO, rapid densification might occur in a localized region which can lead to stress development that is sufficient to form microcracks in the material. In bending, as the stress level increases, these microcracks are probably linked up to form a large crack that causes the failure.

To support the evidence of having microcracks in the presence of a small amount of excess PbO, a simple experiment was conducted. A small amount of PbO was placed on top of a fired PZT specimen and heated at 950°C (m.p. of PbO is 888°C) for one hour in air. After cooling, the specimens were examined by using the SEM. Large cracks were observed as shown in Fig. 3a and 3b. The liquid PbO penetrates along the grain boundaries or the microcracks; during cooling, because of the thermal expansion difference between the phases, large cracks are produced. Similar experimental evidence for the development of microcracks in

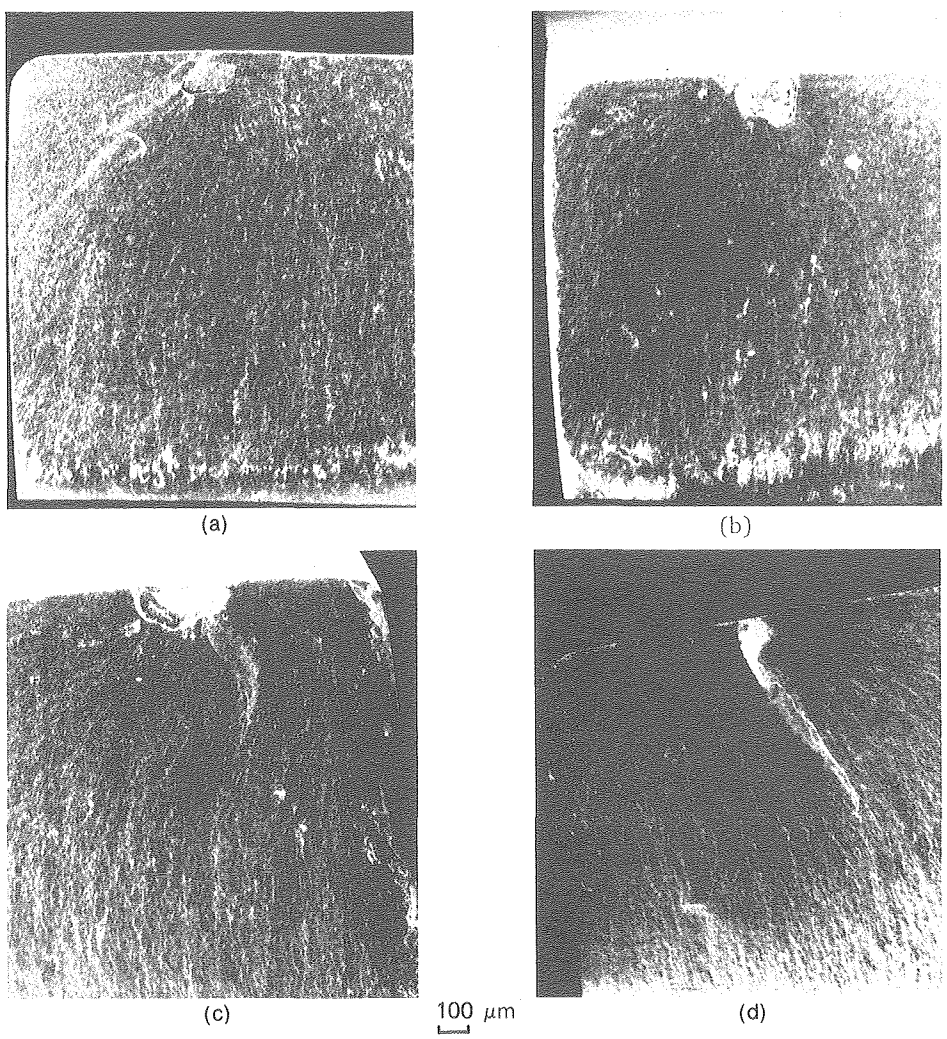

Fig. 2. Fracture surfaces and fracture origin of specimens (a) as-cut plus rounded edges, (b) with polished tensile surface, (c) with polished surface plus rounded edge, and (d) with polished tensile surface plus rounded edges plus etch. (XBB 770-10388)

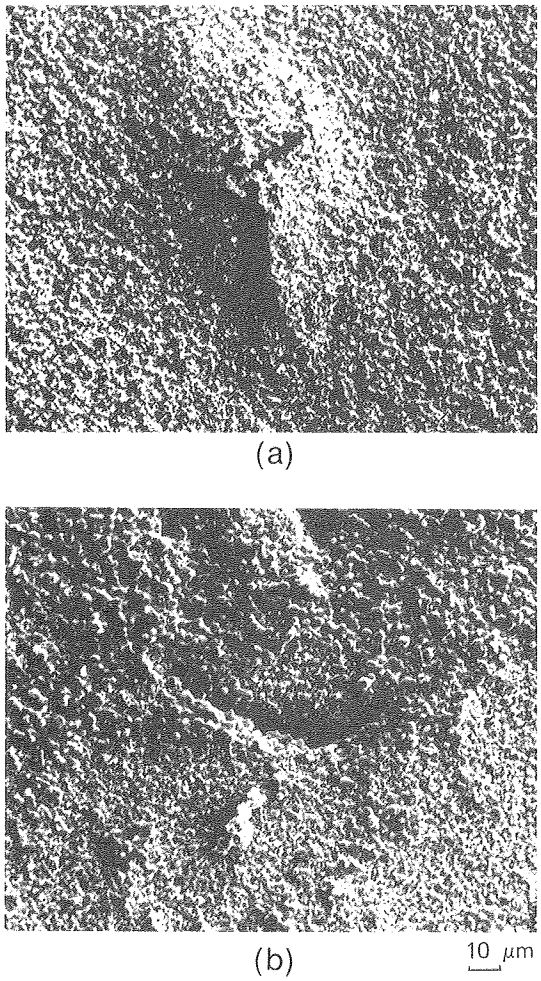

Fig. 3. Large cracks on PZT specimens formed by placement of PbO on surface and heating at 950°C. (XBB 770-10390)

SiC and B compacts was observed by Evans[3] in which B acts as a sintering aid.

From the size of the fracture initiating flaw, the fracture toughness, K_{IC}, was calculated by using the Griffith-Irwin equation:

$$\sigma_f = \frac{Z}{Y} \frac{K_{IC}}{\sqrt{a}} \qquad (1)$$

where σ_f is the fracture stress, a is the flow depth in case of surface flaw, Z is the flaw shape parameter and Y is a dimensionless parameter. An "a" value was measured from flaw configurations, and Z and Y values were taken from Ref. 4. Then, using experimental σ_f values, the K_{IC} value was calculated from Eq. (1) and found to be approximately 1.40 MN $m^{-3/2}$. The experimentally measured[1] K_{IC} value was 1.60 MN $m^{-3/2}$ for this ceramic. Thus, by using the flaw size measurement the calculated fracture toughness value closely matches that obtained experimentally.

Surface finishing might improve the strength of some polycrystalline ceramics if the strength is controlled by extrinsic surface flaws that can be removed by polished or other treatments. In case of PZT, however, which is essentially a two-phase system, surface treatments of bend specimens do not affect the strength because extrinsic flaws generated by machining are less severe than intrinsic microcracks that are produced in presence of a small amount of excess PbO phase.

---

1. D. R. Biswas, Influence of Porosity on the Mechanical Properties of Lead Zirconate-Titanate Ceramics (Ph.D. thesis), U.C. Berkeley, LBL-5479 (1976).
2. J. A. Kuszyk and R. C. Bradt, Influence of Grain Size on Effect of Thermal Expansion Anisotropy in Mg Ti_2O_5, J. Am. Ceram. Soc. 56(8), 420 (1973).
3. A. G. Evans, Rockwell International, Science Center, private communication.
4. G. K. Bansal, Effect of Flaw Shape of Ceramics, J. Am. Ceram. Soc. 59(1-2), 87 (1976).

7. RESEARCH PLANS FOR CALENDAR YEAR 1978

Richard M. Fulrath

Richard M. Fulrath died on July 16, 1977. The programs of study dealing with sintering, processing of PZT ceramics, kinetics and mechanisms of powder reaction, thick film conductors, and mechanical behavior are being supervised by Joseph A. Pask until their completion. Programs dealing with phase equilibria are being supervised by Alan W. Searcy until their completion. It is expected that a new principal investigator, who will also be an academic member of the Department of Materials Science and Mineral Engineering on the campus, will join the ceramic science group sometime during the summer of 1978.

a. Sintering of Powder Compacts

Sintering studies of TiC-Ni compacts both with and without organic binders are continuing. The presence of the carbon from the binder shows a significant effect on the sintering behavior. Kinetics and mechanisms will be evaluated. The hot-stage electron scanning microscope is being used extensively in this study. The ESM will also be used to study mass distribution mechanisms during sintering of different kinds of materials, both in the absence and presence of a liquid phase.

b. Piezoelectric and Ferroelectric Ceramics

Aluminum oxide refractories and containers are extensively used in the production of PZT ceramics. Potential reactions that may affect the stoichiometry of the PZT are thus important to understand. Mechanisms and kinetics of the formation of reaction phases will be determined. Diffusion of PbO in alumina will also be investigated.

Studies on the processing of PZT ceramics will emphasize the effect of the nature of the starting powder on poling properties. Kinetics and mechanisms of the solid state reactions to form PT and PZ are being studied.

c. Thick Film Conductors

Phase distribution in thick film conductors is extremely important in order to realize conductivity with a minimum amount of metal. Fundamentals related to this problem are being studied. Silver is normally used. Attempts to develop conductors with use of cheaper metals will be made.

d. Mechanical Properties of Ceramics

The effect of the nature of the pore structure and distribution in porous alumina bodies on strength, thermal shock, and toughness will be studied. These data will also be correlated with internal friction measurements.

8. 1977 PUBLICATIONS AND REPORTS

Richard M. Fulrath and Associates

Journals and Books

1. J. J. Dih and Richard M. Fulrath, Sintering of Sc-Modified Lead Zirconate-Titanate, J. of Amer. Ceram. Soc. 60 (1-2), Jan.-Feb., 1977, (LBL-5100).

2. O. Vardar, I. Finnie, D. R. Biswas and R. M. Fulrath, Effect of Spherical Pores on the Strength of Polycrystalline Ceramics, Int. J. of Fracture 13(2), 215, April 1977.

3. Dipak R. Biswas, Thermal Energy Storage Using Sodium Sulfate Decahydrate and Water, Solar Energy, Vol. 19, pp. 99-100, Pergamon Press (printed in Great Britain), 1977, (LBL-3998).

4. Ceramic Microstructures '76, Editor with Joseph A. Pask, Westview Press, Boulder, Colorado, 1977, 907 pp.

5. D. R. Biswas and R. M. Fulrath, Mechanical Properties of Porous PNZT Polycrystalline Ceramics, Fracture Mechanics of Ceramics, Vol. 4, R. C. Bradt, D. P. H. Hasselman and F. F. Lange, Eds., Plenum Press, NY-London, 1977, (LBL-6683).

6. G. S. Kino, B. T. Khuri-Yakub, B. R. Tittman, L. Ahlberg, A. G. Evans, D. R. Biswas and R. M. Fulrath, Ultrasonic Failure Prediction in Ceramics, Interdisciplinary Program for Quantitative Flaw Definition, Special Report Third Year Effort, Rockwell International, Science Center, Contract No. F33615-74-C-5180, pp. 232-247, 1977.

LBL Reports

1. David N. K. Wang, Sintering of Al_2O_3 Powder Compact by Hot Stage Scanning Electron Microscopy, (Ph.D. thesis), LBL-5763, January 1977.

2. D. R. Biswas and R. M. Fulrath, Mechanical Properties of Porous PNZT Polycrystalline Ceramics, LBL-6683, November 1977.

e. Structural and Electrical Properties of Composite Materials

Robert H. Bragg, Principal Investigator

Introduction. The objective of our research on carbon materials is to understand the structure and properties of the broad class called hard (difficult to graphitize) carbons. In contrast with the other broad class, soft carbons, the hard carbons do not experience significant grain growth even when heated to temperatures up to 3000°C, nor does the basic graphitic layer structure appear to become well ordered. We chose Glassy Carbon (GC), because it is the most suitable material available for a wide range of physical property measurements and at the same time has numerous technological applications. It happens that GC is also physically hard, and has a compressive strength as high as 70,000 psi.

By the end of CY 1976 we had established that GC actually graphitizes as determined from growth kinetics, with an activation energy of 215 ± 40 kcal/mole, surprisingly close to 260 kcal/mole generally accepted for soft carbons. We had also found that the electrical properties of GC are very similar to those of amorphous semiconductors. The electrical conduction has components due to boundary scattering, hopping conduction, and at low temperatures a Kondo mechanism component. The magnetoresistance, $\Delta\rho/\rho$, was found to be a negative function of a single variable $H/T^{1/2}$ and to increase with increasing heat treatment temperature up to 2800°C, but we had not understood why it is always negative or why it continues to increase. Our investigations of structure, particularly internal pore structure, using the technique of small angle x-ray scattering, had indicated that data capable of a kinetic analysis could be obtained, and while it was possible to obtain the radius of gyration R_g, the more basic structural parameter was the specific surface area S/V because its interpretation is unambiguous. During FY 1977 our studies of structural characterization of GC were intensified and, to expedite data collection the possibilities of using the Stanford Synchrotron Radiation Laboratory small angle scattering facility or the Oak Ridge National Laboratory facility were investigated. Both offer order of magnitude reduction in time required to collect useful data, but the ONRL facility has the further advantage of simultaneous two-dimensional data collection and display, plus appropriate computer programs for data reduction which are already interfaced with the x-ray facility.

We also are investigating composites grown by directional solidification of eutectics because they avoid, or at least reduce difficult problems of fabrication and control of interfacial reactions, and at the same time permit some control of microstructure. The directionally solidified (DS) eutectics are the subject of intensive investigation for application in the hottest parts of gas turbines because they may make significant increases in efficiency possible. We have been investigating the Al-$CuAl_2$ and Al-Si eutectics because they are excellent model systems for the metal-metal and metal-non-metal classes, and the latter is a widely used casting alloy. Both also possess the advantage that there is an abundance of information in the literature concerning the component phases. While these materials can have interesting electrical properties we have concentrated upon mechanical and thermophysical properties. An important finding has been that one can use simple hardness measurements to replace the far more expensive tensile test in many investigations of mechanical properties. A surprising development was the necessity to clarify uncertainty in the literature concerning the interphase relationships between the Al rich, K phase and the $CuAl_2$, θ phase in the Al-$CuAl_2$ eutectic. Work during FY 1977 was concentrated upon texture determination and upon anisotropy in thermal expansion and elastic modulus in this system. Our concern throughout has been to determine to what extent factors, ignored in a simple analytical model used to calculate the properties of composites from knowledge of the individual component phases, must be considered. In the Al-$CuAl_2$ system one can easily, and controllably, change the scale of the microstructure, i.e., the interlamellar spacing λ, by changing the growth rate R. Thus apart from secondary considerations of texture we have concentrated upon finding how the chosen physical property is affected by changes in λ. Results obtained in CY 1977 follow. Most are abridged versions of technical reports, manuscripts in press or to be submitted for publication, M.S. or Ph.D. theses.

1. MICROSTRUCTURE AND KINETICS OF VOID GROWTH IN GLASSY CARBON

S. Bose and R. H. Bragg

The microstructure of glassy carbon (GC) through high resolution electron microscopic lattice imaging is described. Since x-ray diffraction, (XRD) provides a very important technique for structure and microstructure evolution investigations, we have endeavored to standardize a procedure for XRD line profile analysis of GC. The method is presented in brief. Small angle x-ray scattering (SAXS) has been used extensively in characterizing void parameters and their evolution on heat treatment in GC. Pyrolytic graphite (PG) provides a material with oriented pores that are suitable to verify a theory of SAXS from oriented inhomogeneity. The concluding results are also presented.

Microstructure of Glassy Carbon and Kinetics of Void Growth

The structure and properties of non-graphitizing carbons have been the subject of investigation of a large number of workers. Glassy carbon (GC) is a representative of the nongraphitizing class. In our investigation of the microstructure and properties of LMSC GC we have used lattice image in TEM and x-ray analysis.

Glassy carbon heat treated at 2700°C for 10 h was ground to a thickness of 2 mils. A 2 mm disk was then cut ultrasonically. This disk was mounted in an ion-mill using argon gas for about 100 h until it was perforated at the center. The disk was examined on a Philips EM301 electron microscope operated at 100 kV. In the phase contrast mode an aperture was used to allow imaging in the two beam '00.0-00.2' to occur.

A micrograph taken slightly under focus is shown in Fig. 1. The fringes correspond to the (00.2) planes of GC. The fringe separation is 3.4 Å. Fringes are continuous over 50 Å. The fringe pattern resembles the "Jenkins Model"[1] shown in the inset. There are no definite crystallite boundaries. The layers show extensive bending and stacking disorders are encountered at places. The crystallite sizes taken as the distance of continuity of fringes agree very well with values determined from XRD measurements. This work was done in collaboration with U. Dahmen and G. Thomas of MMRD. A paper incorporating this work has been accepted for publication in Journal of American Ceramic Society.

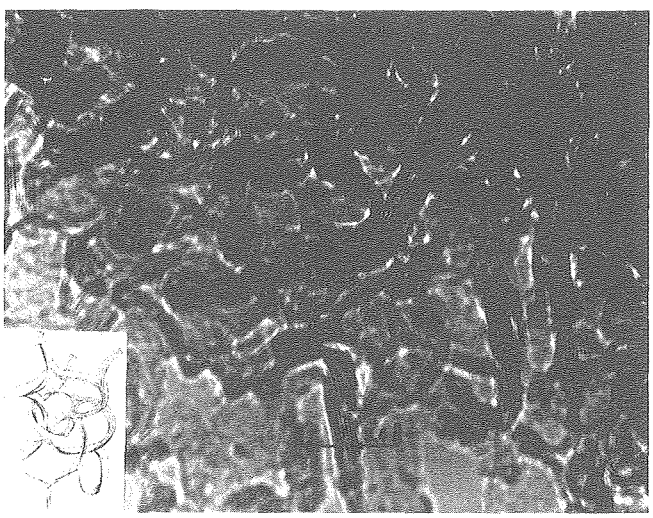

Fig. 1. Lattice image of glassy carbon showing 00.1 planes of 3.4 Å separation. (XBB 778-7454)

One characteristic of the microstructure of GC is the presence of submicroscopic pores. This is evident both from the fact that GC gives rise to strong small angle x-ray scattering (SAXS) and that the density of GC is much smaller than that of graphite even though their crystallographic parameters a and c are not quantitatively very different.

The density of GC as a function of heat treatment time (HTt) at different heat treatment temperatures (HHT) is shown in Fig. 2. It is clear that the total porosity, which causes a reduction in density, remains constant as long as

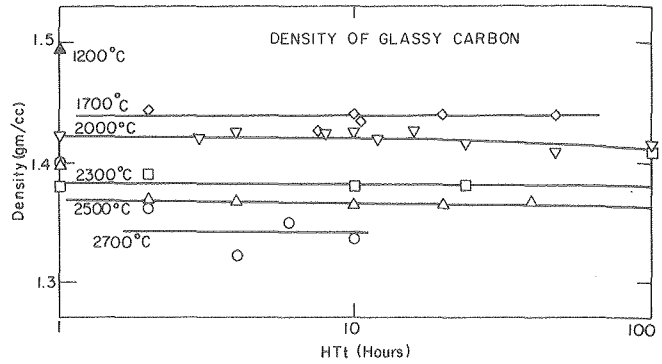

Fig. 2. Density of GC as a function of HTt. (XBL 776-5645)

HTT remains constant. However, raising the HTT increases the total porosity as shown by the decrease in density as in Fig. 3. One important conclusion, therefore, is that the total porosity is a non-kinetic entity.

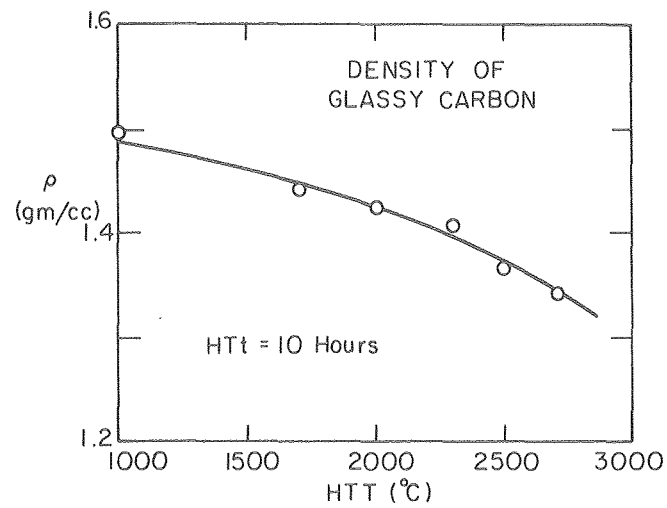

Fig. 3. Density of GC as a function of HTT. (XBL 776-5644)

From SAXS measurements one can determine the specific surface area of the scattering system. In the case of GC this becomes the spectific surface area S/V of voids. S/V was determined for GC as a function of HTt at various HTT. This is shown in Fig. 4. The trend shows that the surface area decreases as HTt increases or as HTT increases. These curves could be fitted into a first order kinetics as shown in Fig. 5. From curve fitting the values of the rate constant k were determined for different HTT. Since k and T are related by an Arhenius type relation, a graph of lnk vs 1/T was made and it gave a straight line with a negative slope as shown in Fig. 6. The activation

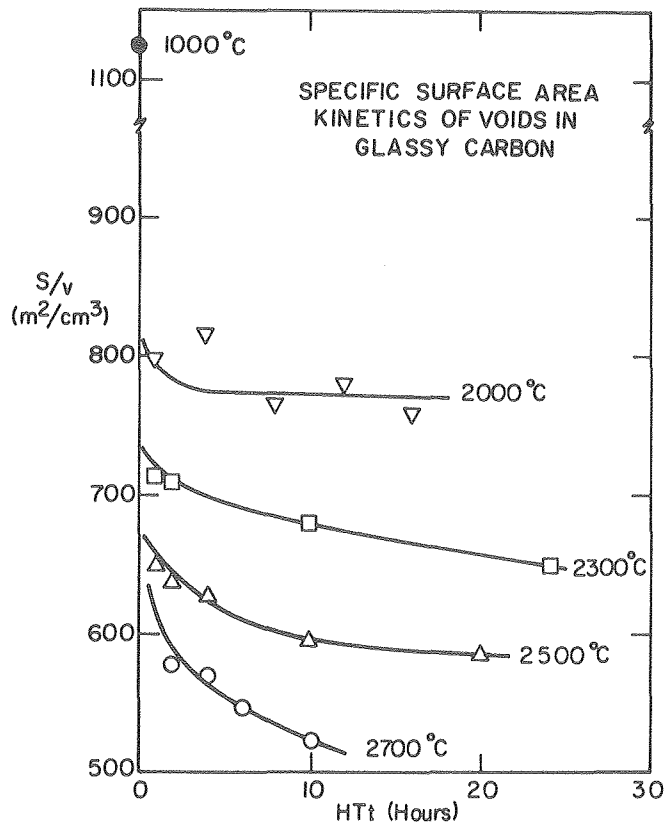

Fig. 4. Specific surface area kinetics of voids in GC. (XBL 776-5641)

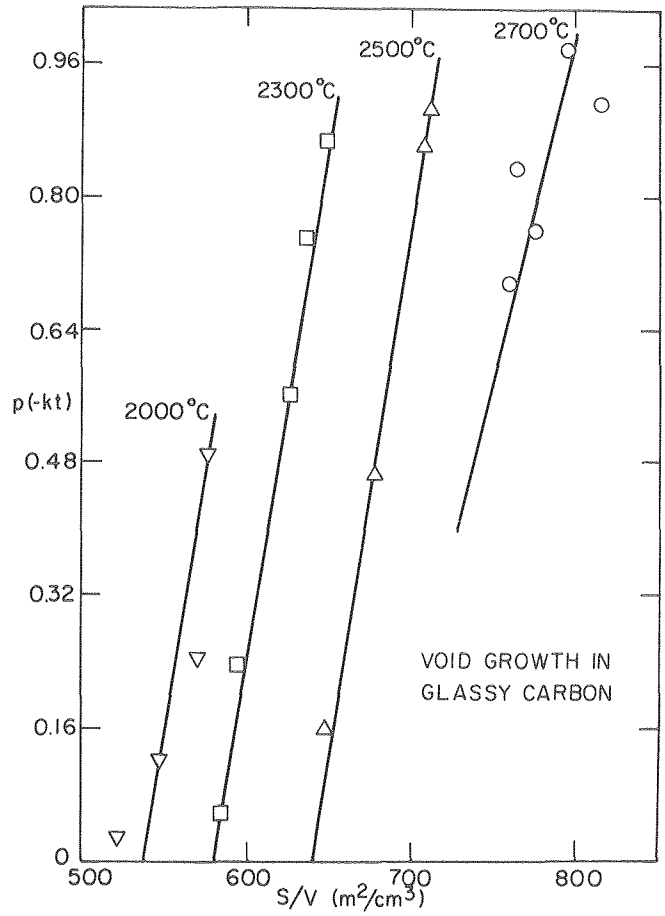

Fig. 5. Rate constants in void growth in GC. (XBL 776-5643)

energy of surface area kinetics came out to be 60 ± 10 kcal/mole. This falls very close to the migration energy 70 kcal/mole of vacancies in graphite. It is, therefore, tempting to try to relate the surface area kinetics to a coarsening mechanism, where smaller pores close while larger ones expand, decreasing the specific surface area. The total porosity change, however, is non-kinetic and must be arising from the thermal expansion of gases trapped in some of the pores, or from the anisotropic thermal expansion resulting in thermal stresses at pore edges and subsequent pore opening. The later mechanism is known to operate in polycrystalline graphite giving rise to the "Mrozowski" cracks.

Procedure for Correcting XRD Line Profile of Glassy Carbon

The procedure for XRD line profile correction of glassy carbon (GC) was standardized. In addition to the routine correction components, it incorporated the removal of small angle x-ray scattering part that often extends to beyond the first interference peak. It is important to note that for the broad peaks characteristic of GC, the Lorentz-Polarization factor is[2] $(1 + \cos^2 2\theta)/\sin^2\theta$. The effect of low sample absorption on the line distortion was analyzed following Keating and Warren[3] and Bragg and Packer,[4] and it was concluded that for the GC samples studied the shift of the 002 peak due to low absorption was insignificant. However, it has been shown that without corrections investigators working with GC can overestimate d_{002} by 0.06 Å. When it is recalled that the range of d_{002} from turbostratic to completely graphitic carbons is only 0.09 Å, it is clear that highly erroneous conclusions can be reached about "degree of graphitization" in GC materials. It also appears that L_a may be underestimated by about 30 to 40% for low heat treatments if corrections are not made. These results are important because of their broad applicability to systems of current technological importance, particularly soft coals. A paper has been submitted for publication in carbon.

Small Angle X-ray Scattering by Pyrolytic Graphite

A theoretical analysis of small angle x-ray scattering (SAXS) from oriented particles was carried out by Hamzeh and Bragg.[5] The preliminary experimental investigation carried out on the oriented voids in pyrolytic graphite (PG) was reported by Bose and Bragg.[6] The SAXS was equivalent to that from oriented ellipsoids of revolution. The pore dimensions determined from "Guinier" and "Porod" regions seem to agree very well. Furthermore, the trend in which the

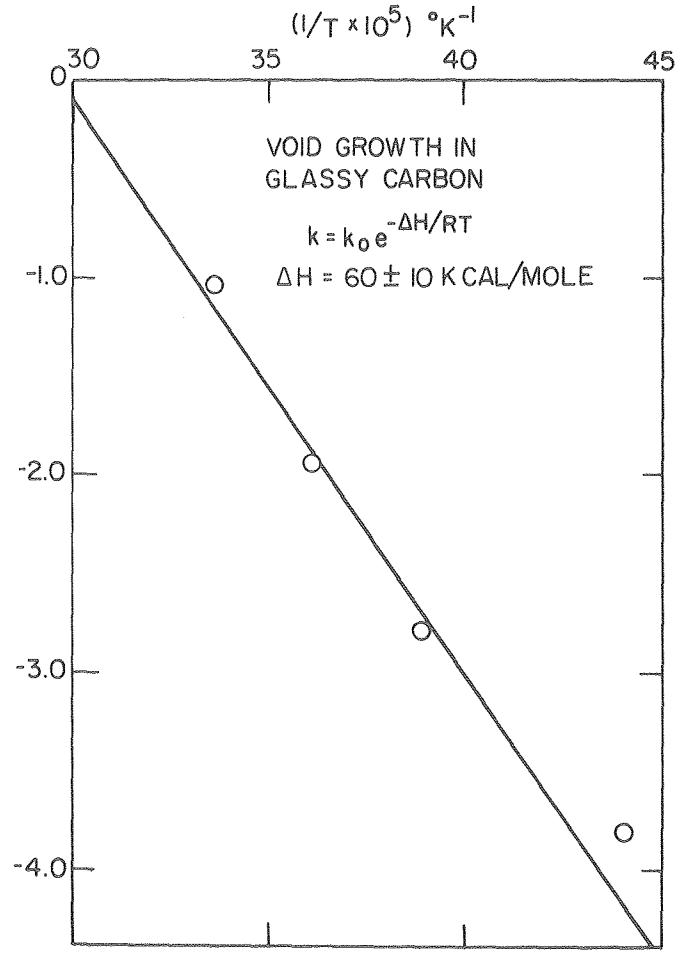

Fig. 6. Activation energy of void growth in GC. (XBL 776-5642)

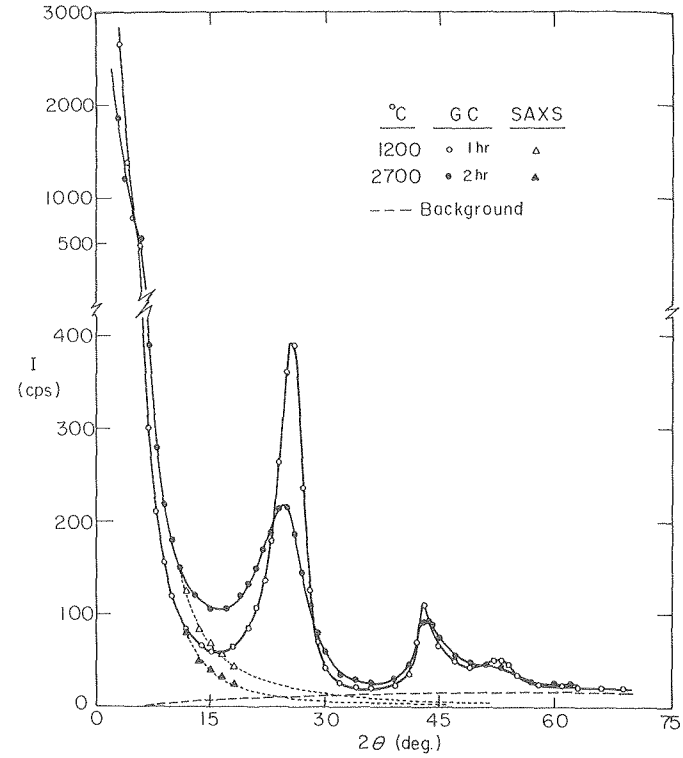

Fig. 7. X-ray diffraction pattern of glassy carbon samples, uncorrected. (XBL 7711-6350)

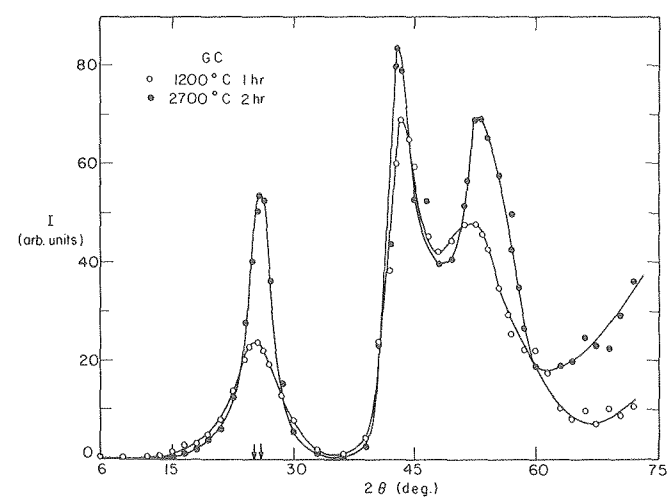

Fig. 8. Corrected line profile of glassy carbon XRD pattern. (XBL 7711-6355)

"Guinier sphere" radius varies with orientation of the pores agrees very well with the theoretical prediction.

A striking demonstration of the asymmetry of the SAXS is shown in Figs. 9 and 10. The data are computer printouts of two-dimensional SAXS data obtained from our PG samples by Hendricks and Lin[7] of Oakridge National Laboratory, using their 10 meter SAXS facility. The connected curves are isointensity contours. The data show clearly that for Fig. 9 the scattering is approximately isotropic while for Fig. 10, the contours are elliptical. These agree qualitatively with our other observations.

Despite the foregoing consistency it cannot be concluded that the voids are ellipsoidal. It is well known that diffraction pattern of an asymmetric object will have a center of symmetry.[8] Thus it is possible, even likely, considering the growth cone structure of PG, that the voids have shapes closer to hemispherical shells than true ellipsoids. These results will be applied in the studies of void growth kinetics of graphitizing carbons planned for FY 1978. A paper has been accepted for publication in Journal of Applied Physics.

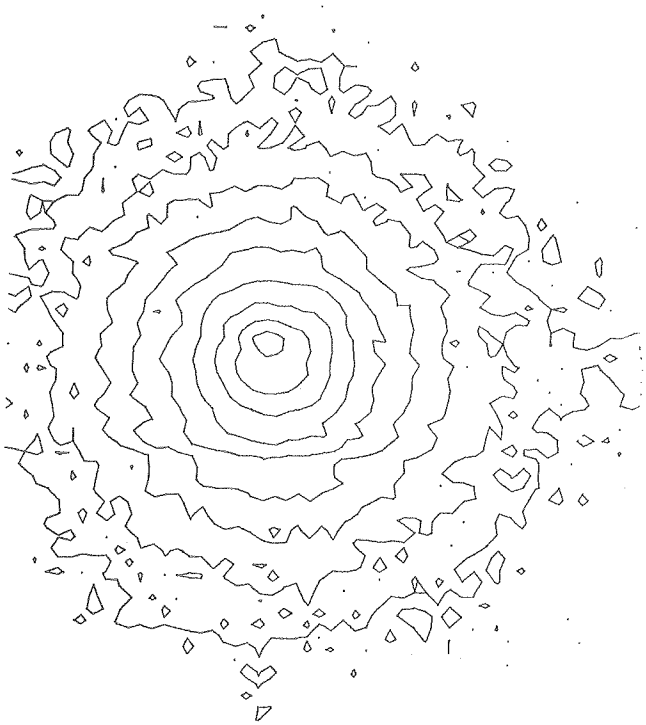

Fig. 9. Circular symmetry of scattering from specimen cut parallel to deposition surface. (XBL 779-2477)

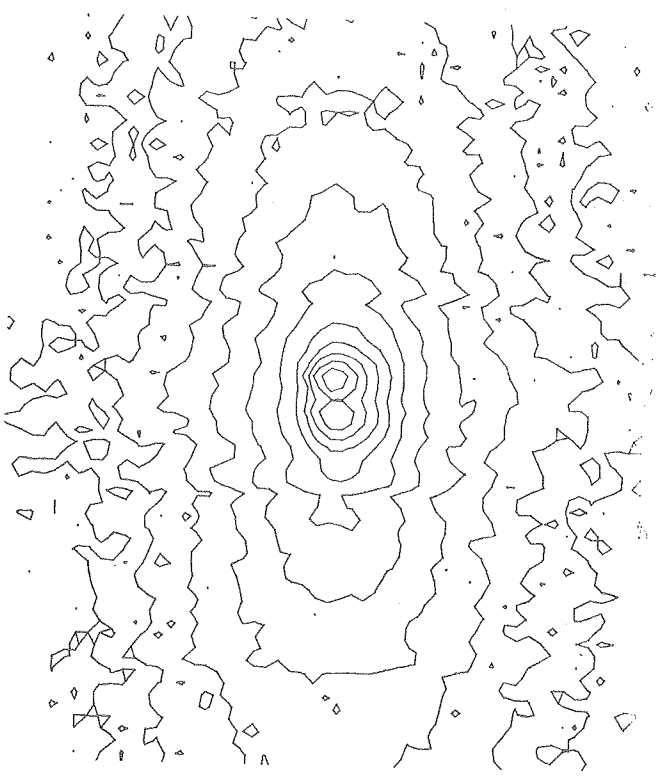

Fig. 10. Elliptical symmetry of scattering from specimen cut normal to deposition surface. (XBL 779-2476)

1. G. M. Jenkins, K. Kawamura and L. L. Ban, Proc. Roy. Soc. (London) A 327, 1571, 501 (1972).
2. J. B. Cohen, Diffraction Methods in Materials Science, MacMillan, New York, 1966, p. 279.
3. D. T. Keating and B. E. Warren, Rev. Sci. Instrum. 23, 519 (1952).
4. R. H. Bragg and C. M. Packer, Rev. Sci. Instrum. 34, 1202 (1963).
5. F. M. Hamzeh and R. H. Bragg, J. Appl. Phys. 45, 3189 (1974), LBL-1874, August 1973.
6. S. Bose and R. H. Bragg, Duetsch Keramische Gesellschaft, Carbon 201, 1976, Baden-Baden.
7. R. W. Hendricks, private communication.
8. G. Harburn, C. A. Taylor and T. R. Welberry, Atlas of Optical Transforms, Cornell University Press, Ithaca, New York (1975) Plate 2 and 31.

2. SMALL ANGLE X-RAY SCATTERING FROM DIFFUSE INTERFACES

S. Bose and R. H. Bragg

Small angle x-ray scattering (SAXS) has been used extensively in the field of materials science to study GP zones, to determine size and surface area of dispersed particles and voids and more recently to follow the early stages of kinetics of spinodal decomposition. However, the power of SAXS in characterizing diffuse precipitate matrix interfaces has remained unused.

The scattering intensity from an electron density $\rho(\bar{u})$ which has sharp interface with its surrounding is given by

$$I(h) = V\langle\rho^2\rangle \int c(r)\, e^{i\bar{h}\cdot\bar{r}}\, dV\bar{r}$$

where C(r) is the correlation function given by

$$C(r) = \frac{1}{V\langle\rho^2\rangle} \int_V \rho(\bar{u})\rho(\bar{u}+\bar{r})\, dV_{\bar{u}} \qquad (1)$$

Following Hoseman and Bagchi[1] and Ruland[2] an electron density $\rho_{diff}(\bar{u})$ with a diffuse interface can be written as a convolution between the sharp electron density and a smoothing function g such as a gaussian. Thus

$$\rho_{diff}(\bar{u}) = \int g(\bar{w})\rho(\bar{w}+\bar{u})\, dV_{\bar{w}} = g(w) * \rho(\bar{u}) \qquad (2)$$

Upon inserting (2) in (1) and taking Fourier transforms of both the sides

$$I_{diff}(h) = I(h)[G(h)]^2$$

where G is the Fourier transform of g, the smoothing function.

Using the inverse Fourier transform one gets the form of g

$$g(\bar{w}) = \left(\frac{1}{2\pi}\right)^3 \int [I_{diff}(h)/I(h)]^{1/2} e^{-i\bar{h}\cdot\bar{w}} dV_{\bar{h}} .$$

This expression cannot be used unless observations are made to considerably large values of h and unless interparticle interference is absent. The second restriction can rarely be overcome. It is safer, therefore, to use the Porod expression and the region of SAXS where it is valid. A simple approximation will be to assume g(w) to be Gaussian. In that case G(R) is also a Gaussian and

$$I_{diff}(h) = I(h) \exp(-k^2h^2/2\pi),$$

where $k/\sqrt{2\pi}$ is a measure of the width of the diffuse boundary. Using Porod expressions and infinitely long and narrow slit approximations

$$I_{diff}(h) = \frac{\pi^2\langle\rho^2\rangle S}{h^3} - k^2 \frac{\pi\langle\rho^2\rangle S}{2} h^2 ,$$

where S is the specific surface area of interface. Thus a plot of $h^3I(h)$ vs h^2 should be a straight line with a negative slope if the interface is diffuse.

Before loss of coherency, spinodally decomposed systems are likely to have diffuse interfaces between the separated phases. However, in the early stages of spinodal decomposition there are thermal fluctuations in concentration comparable to the composition modulation. This is why only later stages of aging should be considered.

The data of Bonfiglioli[3] on Al-20 at.% Ag are plotted in Fig. 1. The composition at room temperature is within the spinodal. The data fall on a straight line with a negative slope. The width of interface is about 14 Å while Guinier radius of minor phase is 80 Å.

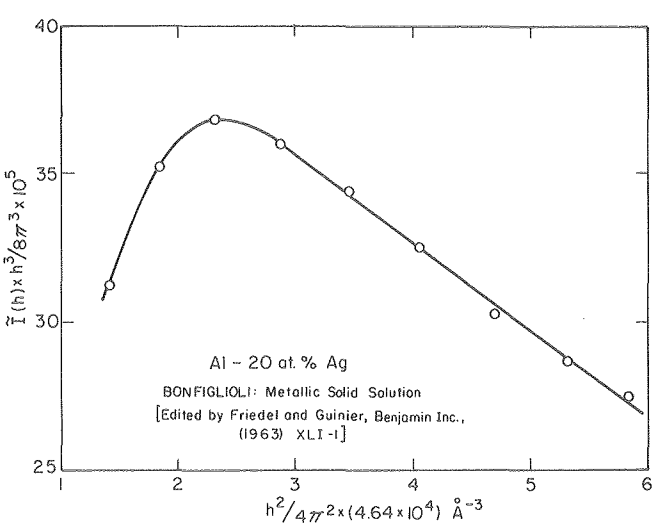

Fig. 1. SAXS from Al-20 at.% Ag showing negative departure from Porod's Law. (XBL 777-5739)

Tomozawa's data[4] on phase separation of Li_2O-SiO_2 glass (shown in Fig. 2, upper two curves) also falls on straight line with a negative slope. The particular composition is fairly within the missibility gap and is likely to have decomposed spinodally. The curve for 9 h annealing at 500°C clearly shows that the phase separation is complete, i.e., the interfaces are no longer diffuse.

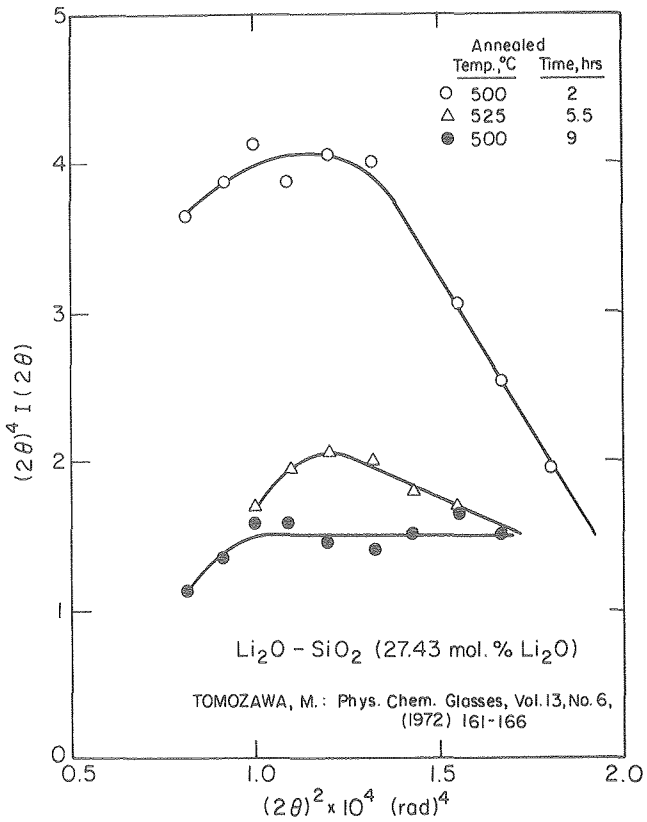

Fig. 2. SAXS from a Li_2O glass showing negative departure from Porod's Law. (XBL 777-5738)

We have used this analysis to resolve questions concerning the nature of the interfaces in GC. A paper has been submitted for publication in Metallurgical Transactions A.

1. R. Hoseman and S. N. Bagchi, Direct Analysis of Diffraction Matter, North-Holland Publishing Co., p. 64 and 605 (1962).
2. W. Ruland, J. Appl. Cryst. 4, 70 (1971).
3. A. F. Bonfiglioli, Metallic Solid Solution, eds. Friedel & Guinier, W. A. Benjamin, Inc. p. XLI-1 (1963).
4. M. Tomozawa, Phys. Chem. Glasses 13, 161 (1972).

3. THE TEXTURE AND INTERPHASE RELATIONSHIPS IN DIRECTIONALLY SOLIDIFIED Al-$CuAl_2$ EUTECTIC ALLOY

Leopoldo Valero and Robert H. Bragg

The Al-$CuAl_2$ eutectic is formed between the K phase which is a substitutional solid solution of Cu in Al (Al-5.7%Cu) with a face centered cubic unit cell, and the θ phase which is an intermetallic compound ($CuAl_2$) with a body centered tetragonal unit cell. The microstructure observed when this eutectic is directionally frozen is characterized by a preferred crystal orientation between the two solid phases stabilized by a selection of a low energy interface during growth. The {111}K ‖ {211}θ interface is apparently such a low energy relationship for this system. Kraft[1] has demonstrated that this relation produces a very good atomic density matching by observing that in the θ phase the stacking sequence parallel to {211} contains four layers of aluminum atoms grouped together forming almost one single plane. All the atoms in this single or "puckered" plane would be close enough to exert a bonding force on the atoms in a neighboring {111} plane of aluminum thus forming a stable low energy interface.

To determine the texture of the eutectic alloy, a specimen was solidified unidirectionally with a growth rate of 12.9 μm/s under a temperature gradient of 70.7°C/cm. A well aligned microstructure with an interlamellar spacing of 2.73 μm was produced (Fig. 1). X-ray data obtained in reflection from the transverse side (normal to the growth direction) with the x-ray diffractometer, showed that the {111}K and the {121}θ planes were strongly reflected and they were selected to obtain the data for the pole figures. The 2θ angles are 38.40° for the {111}K planes and 37.95° for the {121}θ planes when CuK_α radiation is used, and this proximity causes interference, i.e., partial overlapping between the two reflections. To eliminate this problem a method to obtain data for both phases was developed which consisted of recording the line profiles through the region of the overlapping reflections and resolving the pattern into two components (Fig. 2).

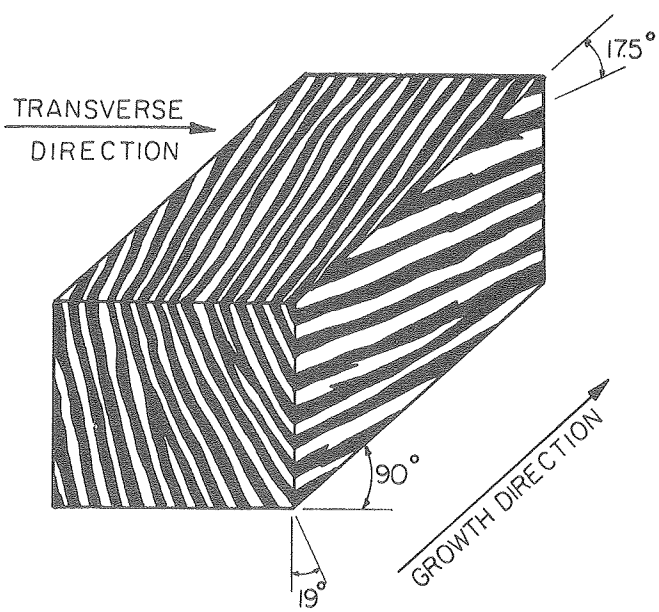

Fig. 1. Sketch of the eutectic grain used in this work, drawn from optical micrographs.
(XBL 7712-6592)

Data for the {111}K and {121}θ phases were analyzed separately; the necessary corrections for absorption were made and for each phase the corrected integrated intensities were converted to "times random" units following the method described by Bragg and Packer.[2] Pole figures for the {111}K phase and for the {121}θ phase were plotted (Figs. 3 and 4). After superimposing the two pole figures (Fig. 5) the following crystallographic relationships were found:

$$(111)K \parallel (2\bar{1}1)\theta$$

$$[1\bar{1}0]K \parallel [1\bar{2}0]\theta \ .$$

Growth direction was close to $[\bar{1}\bar{1}2]K$. By trace analysis it was also possible to determine that the lamellae grew parallel to the $[\bar{1}\bar{2}2]K$ direction.

This work has verified the existence of the interfacial relationship {111}K ‖ {121}θ. Our results are in good agreement with those of Cantor and Chadwick,[3] the only difference being that they reported their results in a general form and we are able to express the relationship by referring to two specific planes. The main discrepancy in the crystallography of this system among different investigators[1,3,4] is due to the exact location of the habit plane. We believe that this discrepancy can be resolved by following the variation of the relationships found here when the growth conditions are changed. The texture in the work is for an intermediate growth rate. We would expect the texture to become sharper as the growth rate is reduced and approach the interphase relationships at thermodynamic equilibrium.

1. R. W. Kraft, Trans. AIME 224, 65 (1962).
2. R. H. Bragg and C. M. Packer, J. of Appl. Phys. 35 (4), 1322 (1964).
3. B. Cantor and G. A. Chadwick, J. of Crystal Growth 23, 12, (1974).
4. I. G. Davies and A. Hellawell, Phil. Mag. 19, 1285 (1969).

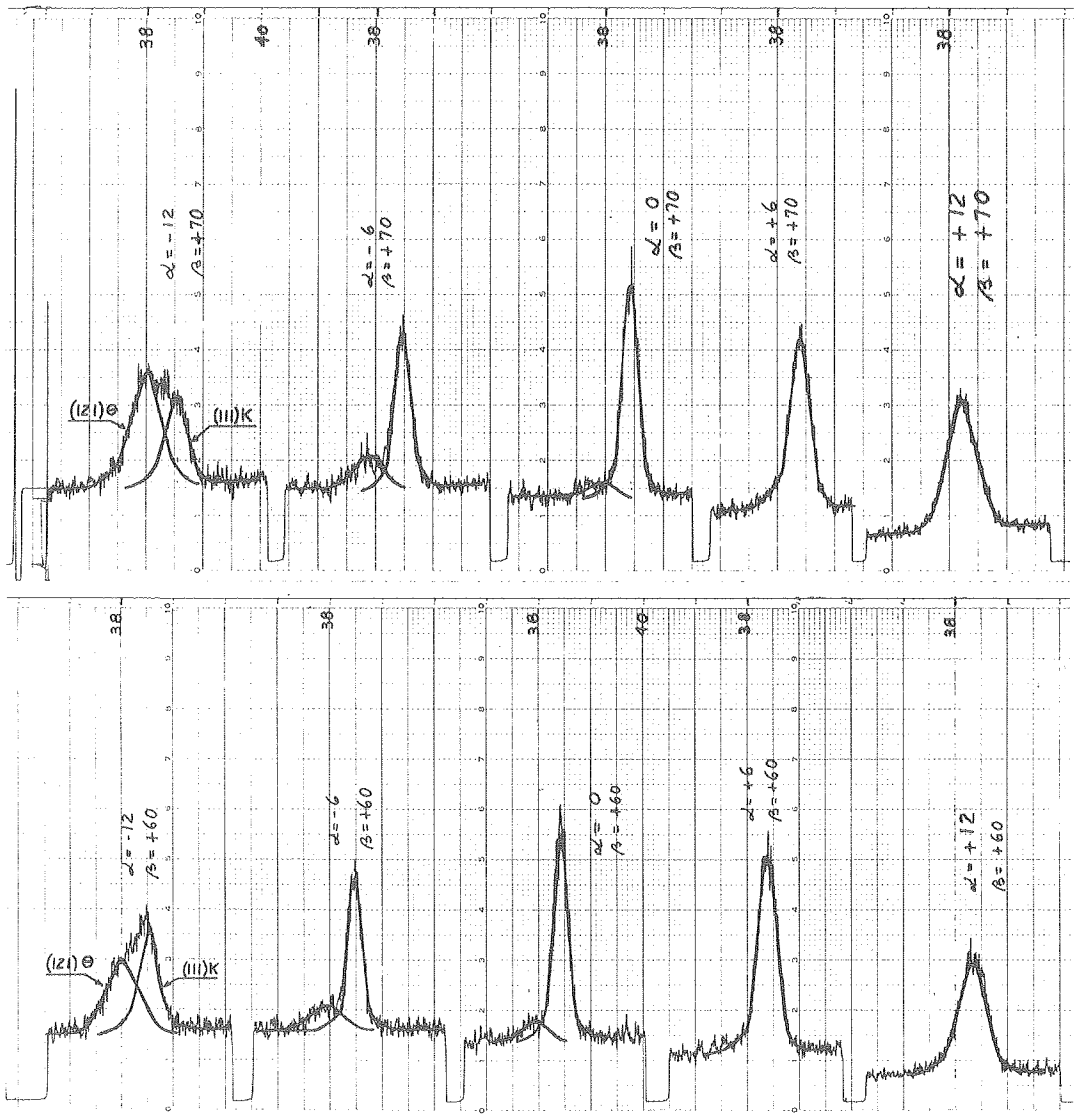

Fig. 2. A set of data showing (a) the merging of the two peaks into one when a=12°, (b) the peak profiles resolved. (XBL 776-9244A)

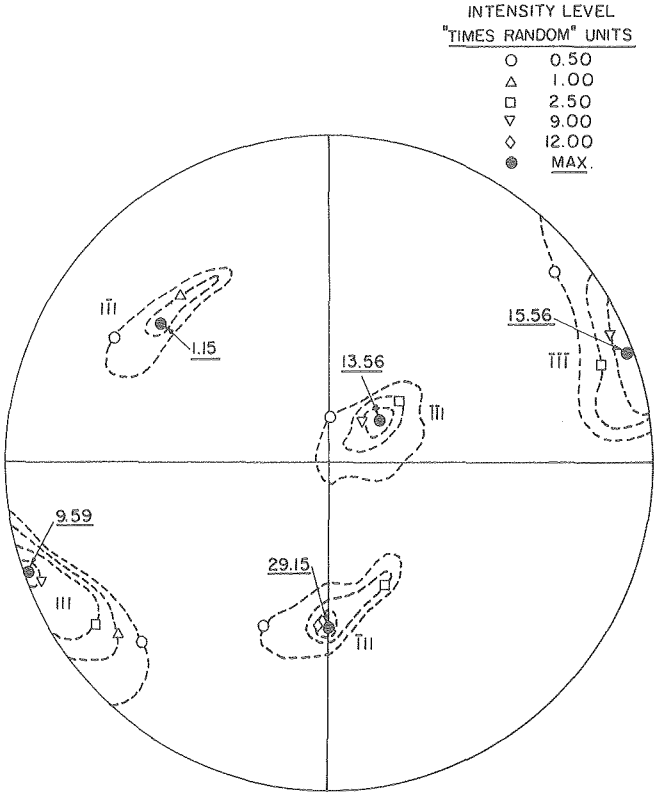

Fig. 3. The {111}K pole figure. (XBL 7712-6600)

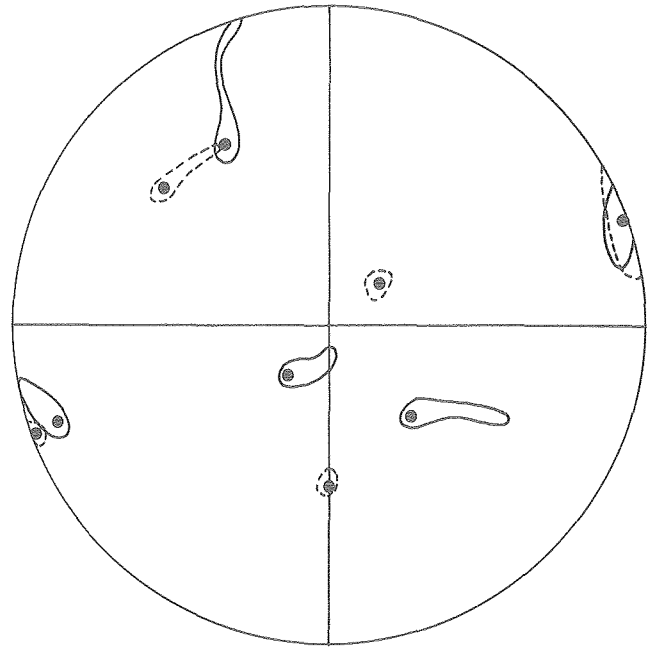

Fig. 5. The two pole figures superimposed showing only the relevant features. (XBL 7712-6602)

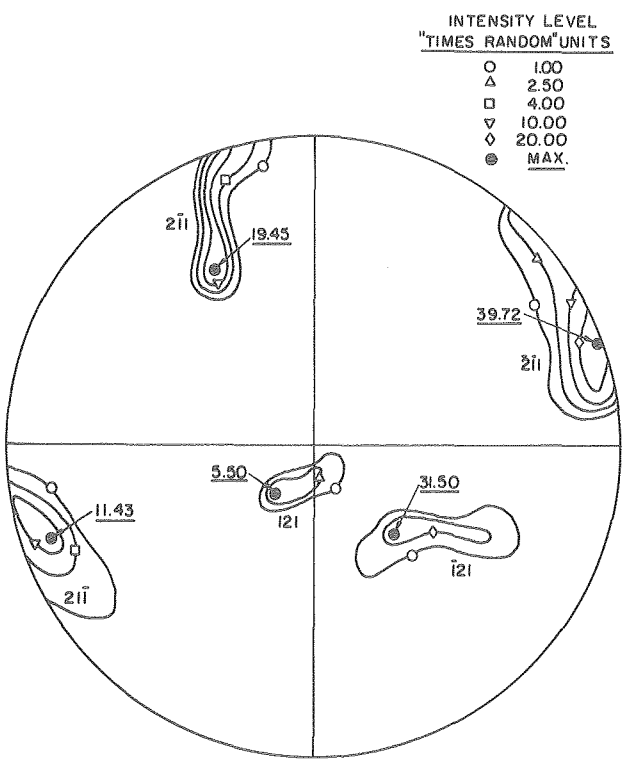

Fig. 4. The {121}θ pole figure. (XBL 7712-6601)

4. THERMAL EXPANSION OF DIRECTIONALLY SOLIDIFIED Al-$CuAl_2$ EUTECTIC

D. Baker and R. H. Bragg

During CY 1977 extensive measurements were made of the thermal expansion of Al-$CuAl_2$ eutectic material directionally solidified under a temperature gradient G at the solid/liquid interface of 45°C/cm at different rates R. The interlamellar spacings λ obtained between the Al-5.7 Cu (K) phase and the $CuAl_2$(θ) phase varied from about 1.4 μm to 7.5 μm. An idealized microstructure that characterizes these materials is shown in Fig. 1.

Specimens were cut so as to make thermal expansion measurements in the three orthogonal directions indicated. The apparatus used was a Theta IIIR dilatometer whose sensitivity in length measurements is quoted to be less than 2×10^{-5} in. It requires cylindrical specimens whose length can be varied but in our case ranged from about 0.5 to 1.5 cm. Preliminary runs were made on specimens 99.999 purity Cu and Al to verify our procedures and the reliability of the apparatus. Data obtained for pure Cu are shown in Fig. 2 wherein the best literature data[1] are also shown. It can be seen that there is a small systematic error in the instrument which is attributed to the thermal expansion of the fused quartz pushrods.

Data obtained for a directionally solidified specimen which contains about 50 vol% K phase are shown in Fig. 3. In this instance several cycles of heating and cooling were employed and significant residual dimensional changes are found. The eutectic melts at 548°C and even the K and θ phases melt in the ranges 660 and 591°C. At 500°C

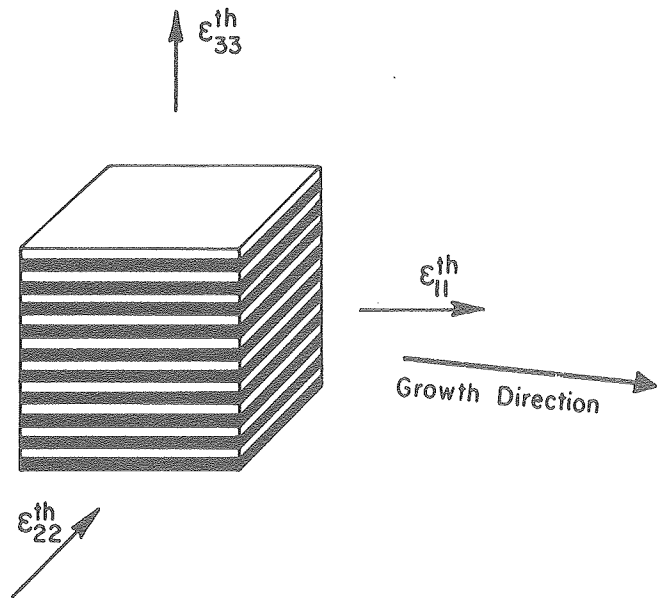

Fig. 1. Coordinates for thermal expansion measurements (idealized crystal). (XBL 773-5200)

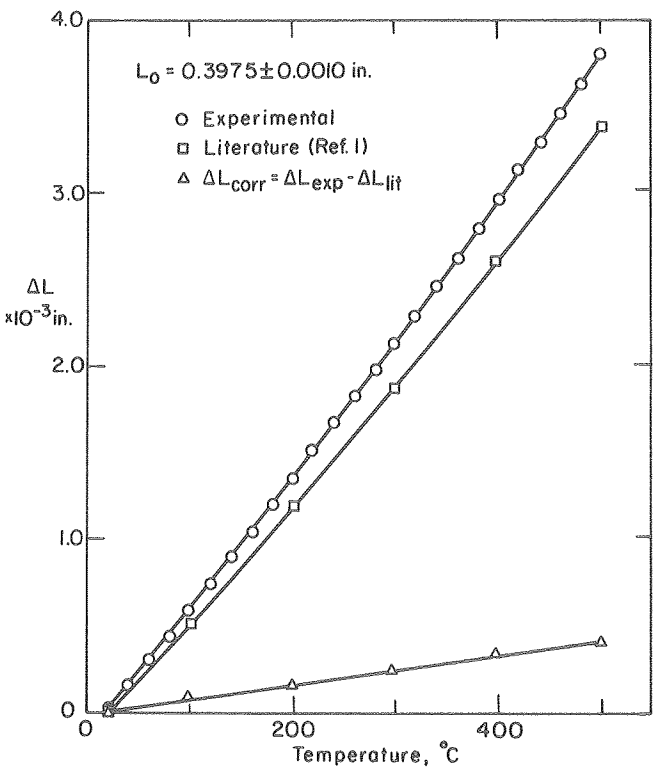

Fig. 2. Thermal expansion of 99.999 copper standard. (XBL 7712-6621)

the eutectic is at 0.93 Tm. Consequently both phases can be expected to undergo some plastic deformation if the eutectic specimens are held at the higher temperatures for appreciable times. Procedures were developed to correct for the

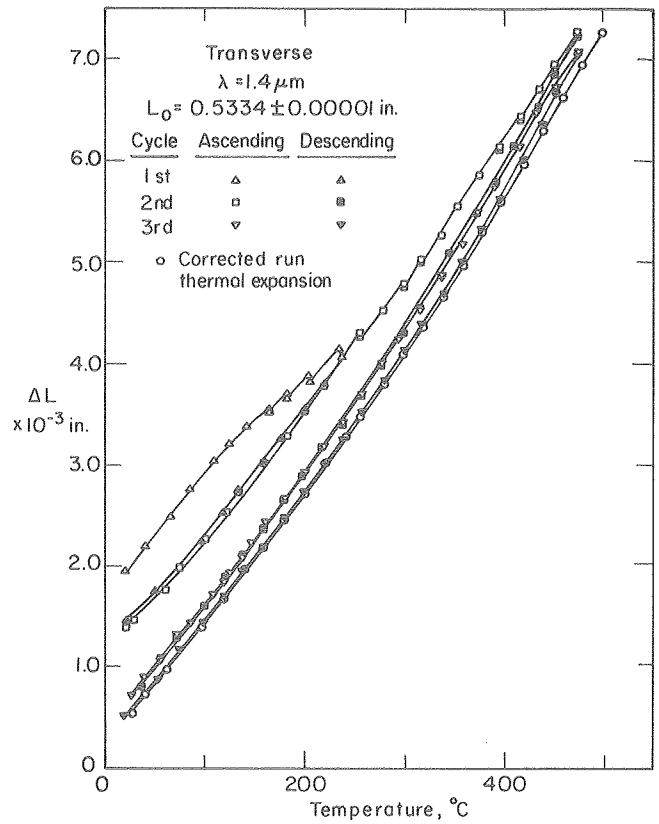

Fig. 3. Cyclic thermal expansion of directionally solidified Al-$CuAl_2$ eutectic. λ = 1.4 μm. (XBL 7712-6622)

residual length changes, and it is felt that the corrected data, while less precise than for higher melting materials (such as Cu for which the homologous temperature is only 0.50 Tm at 500°C), can still be interpreted with confidence.

Results of thermal expansion measurements for material grown at slow, intermediate and fast rates are shown in Figs. 4, 5 and 6. As shown previously the interlamellar spacing λ is related to the growth rate R according to $\lambda^2 R$ = constant. The shaded areas on Fig. 4 represent the estimated uncertainty in the dilatation, ΔL/L, which arises mainly from cumulative errors involved in the correction procedure. In this instance there is no question but that the thermal expansion, i.e., in Fig. 4, longitudinal direction (ε_{11}^{th}) is greater than that in the two directions at right angles to it, and the thermal expansion in the vertical direction (ε_{33}^{th}) is greater than that in the transverse direction (ε_{22}^{th}). This specimen has an interlamellar spacing λ = 7.5 μm. The data of Fig. 5 show anisotropy between longitudinal and transverse directions at temperatures below 400°C. It is not certain that the crossover in ε_{22}^{th} and ε_{33}^{th} at about 450°C is real or an error in recording or correcting the data. This specimen has an interlamellar spacing of λ = 3.5 μm, and it

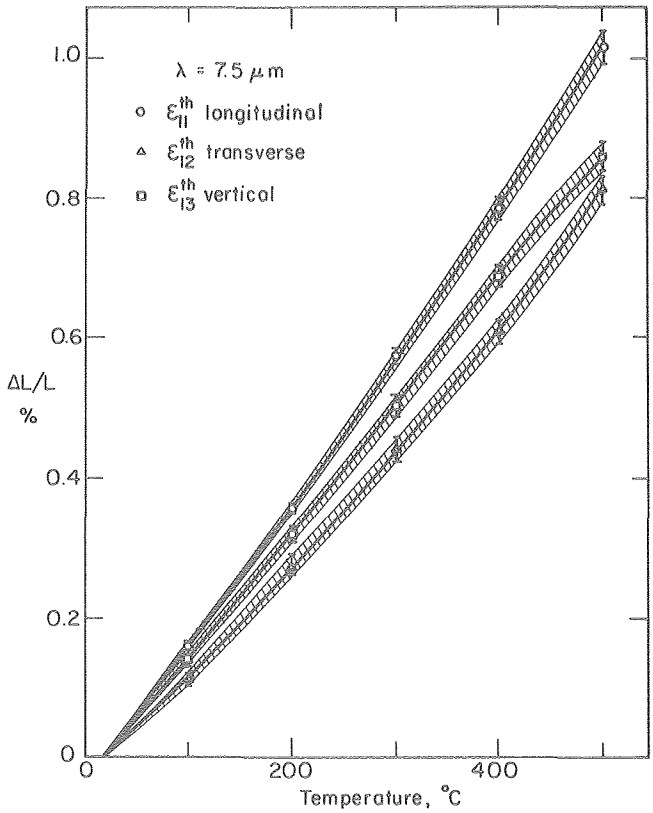

Fig. 4. Thermal expansion of directionally solidified Al-$CuAl_2$ eutectic. λ = 7.5 μm. (XBL 7712-6623)

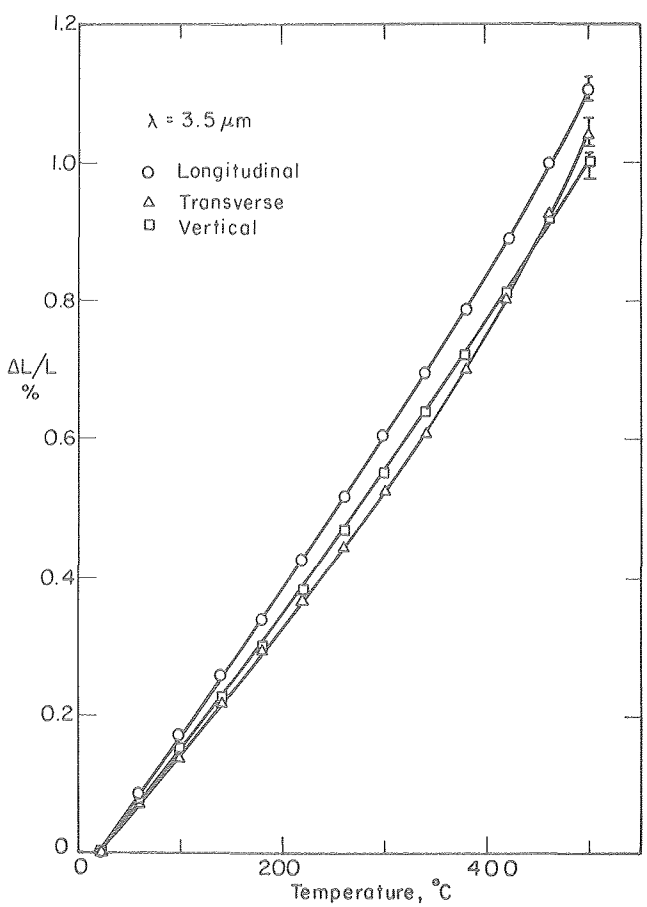

Fig. 5. Thermal expansion of directionally solidified Al-$CuAl_2$ eutectic. λ = 3.5 μm. (XBL 7712-6624)

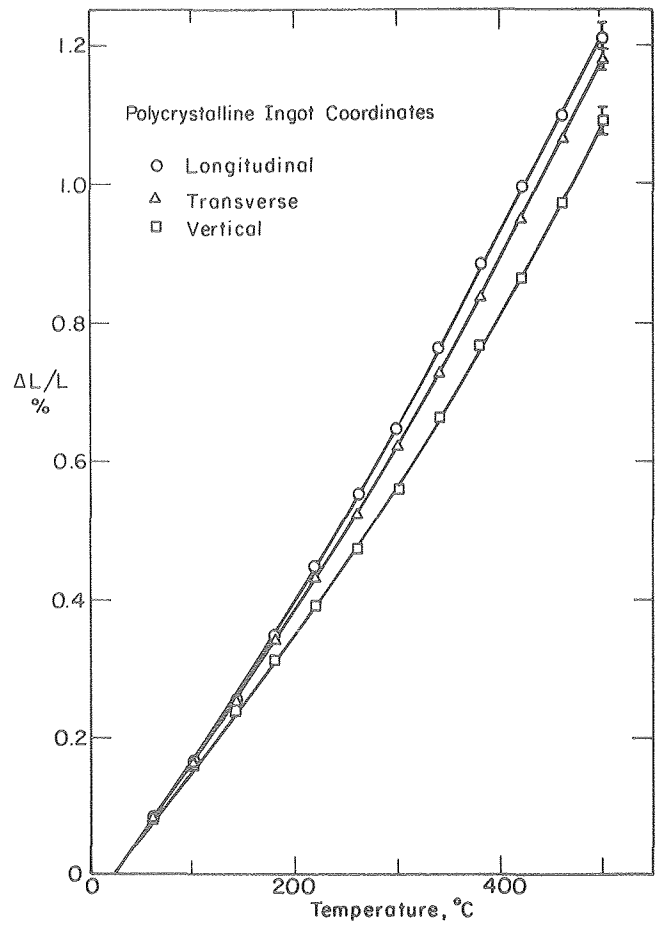

Fig. 6. Thermal expansion of directionally solidified Al-$CuAl_2$ eutectic. λ = 1.4 μm. (XBL 7712-6625)

should be noted that 1) the anisotropy is less pronounced, and 2) the thermal expansion in all directions is greater than was found for λ = 7.5 μm.

The specimen of Fig. 6 had a microstructure much less approximated by Fig. 1 than the other specimens and the distinctions between ε_{22}^{th} pertain exactly only to directions in the ingot material coordinate system rather than crystallographic orientation relationships. Thus in this instance there is less crystallographic significance to the interchange of ε_{22}^{th} and ε_{33}^{th} compared to the order found for λ = 7.5 m (Fig. 4). The most important finding is that in all three directions the thermal expansion is highest of the three growth rates.

It is of importance to examine the data for plausibility. To do this we use a simple model

based upon the rule of mixtures taking account of the anisotropic thermal expansion of the θ phase. This model predicts

$$\varepsilon(\text{longitudinal}) = \varepsilon_{11}^{th} = \left[\frac{(\alpha_k - \alpha_{\theta_{11}})M_\theta v_\theta}{M_\theta v_\theta + M_k v_k} + \alpha_k\right]\Delta T; \quad (1)$$

$$\varepsilon(\text{transverse}) = \varepsilon_{22}^{th} = \left[\frac{(\alpha_k - \alpha_{\theta_{22}})M_\theta v_\theta}{M_\theta v_\theta + M_k v_k} + \alpha_k\right]\Delta T\ ; \quad (2)$$

$$\varepsilon(\text{vertical}) = \varepsilon_{33}^{th} = \left[\alpha_k v_k + \alpha_{\theta_{33}} v_\theta + \frac{\nu v_\theta v_k}{\varepsilon_k v_k + \varepsilon_\theta v_\theta}\ \frac{\varepsilon_k - \varepsilon_\theta}{1-\nu}\left(2\alpha_k - \alpha_{\theta_{11}} - \alpha_{\theta_{22}}\right)\right]\Delta T \quad (3)$$

where $\alpha_{\theta_{ii}}$ and α_k are thermal expansion coefficients, M_θ and M_k are elastic moduli divided by $(1-\nu)$, v_θ and v_k are volume fractions, ν is the Poisson ratio and ΔT is the temperature change. The best available data for calculation are

$\varepsilon_\theta = 14.4 \times 10^{-6}$ psi (Ref. 2); $\nu_\theta = 0.33$ (Ref. 3),

$\varepsilon_k = 10.9 \times 10^{-6}$ psi; $\nu_k = 0.33$,

$\alpha_a = \alpha_{\theta_{100}} = 16.5 \times 10^{-6}/°C$ (Ref. 4) ,

$\alpha_c = \alpha_{\theta_{001}} = 24.5 \times 10^{-6}/°C$ (Ref. 4) ,

$\alpha_k = 27.1 \times 10^{-6}/°C$ (Ref. 5) .

The interphase relationships in the Al-$CuAl_2$ eutectic (see preceding article 3) are closely approximated by

$$(121)_\theta \parallel (111)_k$$

$$\langle 12\bar{3}\rangle_\theta \parallel \langle \bar{1}\bar{1}2\rangle_k$$

and the growth direction is $\langle \bar{1}\bar{1}2\rangle_k$. Thus it is necessary to make appropriate transformations to obtain the components of thermal expansion for the θ phase corresponding to Fig. 1. When these transformations are made it is found that the mean thermal expansion coefficients for the θ phase are

$\alpha_{\theta_{11}} = 22.7 \times 10^{-6}/°C$

$\alpha_{\theta_{33}} = 18.7 \times 10^{-6}/°C$

$\alpha_{\theta_{22}} = 16.5 \times 10^{-6}/°C$.

When these values are combined with the data for the isotropic K phase, and the quantities in the square brackets interpreted as mean thermal expansion coefficients for the composite, i.e., $\varepsilon_{11}^{th} = \overline{\alpha_{ii}}\ \Delta T$, the results in Table 1 are obtained and can be compared with experimental data for $\lambda = 7.5$ μm.

Table 1. Mean thermal expansion coefficients for directionally solidified Al-$CuAl_2$ eutectic, 20-500°C.

	Calculated /°C	Experimental (λ = 7.5 μm)
α_{11}	24.7×10^{-6}	21.2×10^{-6}
α_{22}	21.3×10^{-6}	16.9×10^{-6}
α_{33}	22.6×10^{-6}	17.9×10^{-6}

The model predicts the expected anisotropy. Specifically it predicts that α_{11}^{th} is greater than α_{22}^{th} or α_{33}^{th}, α_{33}^{th} should be greater than α_{11}^{th} but only by about 6%. It should be borne in mind that the model does not take into account the temperature dependence of the elastic module of the K and θ phases (so the calculated α's will be overestimated), nor does it consider the anisotropy in the elastic modulus of the θ phase. The data in the following article 5 indicate that $\varepsilon_{\theta_{11}}$ may be 10% greater than $\varepsilon_{\theta_{22}}$ or $\varepsilon_{\theta_{33}}$, but it is not anticipated that the ranking of the α's will be altered by a more detailed calculation.

The significant findings of this investigation are that the thermal expansion of the composite is anisotropic, is largest for the growth direction than for the two orthogonal directions, both of which are within about 6% of each other, and is a function of λ, being approximately equal to that of the θ phase when λ is large and approaching the rule of mixtures predicted behavior as λ is decreased.

A possible explanation of the observed behavior is as follows: The tensile properties of lamellar composites are known to be a function of λ. A graph of yield stress of tensile strength vs $\lambda^{-1/2}$ has one asymptote at large λ, increases approximately linearly as λ is decreased, and approaches a second asymptote.[6,7] This strongly indicates that the K phase bears more of the load as λ decreases.

It is known that the interfaces in the composite are coherent, i.e., no slip occurs during deformation.[8] Therefore thermal stress can build up at the K-θ interfaces and across both lamellae. Since the yield stress increases as λ decreases the K phase can withstand larger thermal stresses before plastic deformation occurs. That is the thermal expansion of the K phase can conform easily to that of the θ phase for large λ, but should approach rule of mixtures behavior as λ decreases.

Apart from the correctness of the proposed explanation the significance of the experimental findings are important for design purposes, especially if the composite contains one phase which is anisotropic. Since it is well known that the microstructure will coarsen upon prolonged high temperature exposure serious design errors can be made if based upon thermal expansion data obtained from material for which λ is small.

1. Y. S. Touloukian, Thermophysical Properties of High Temperature Solid Materials, Vol. 1, pp. 17-18, 462-463, (1967).
2. A. Pattnaik, A. Lawley, Met. Trans. 2, 1529 (1971).
3. B. Cantor, G. A. Chadwick, J. Mat. Sci. 10, 578 (1971).
4. I. G. Davies, A. Hellawell, Phil. Mag. 19, 1285 (1969).
5. L. Valero, (M. S. thesis), University of California (1977).
6. S. Justi, to be published.
7. G. A. Chadwick, Acta. Met. 24, 1137 (1976).
8. A. S. Yue, F. W. Crossman, A. E. Vidoz, M. I. Jacobson, TMS-AIME 242, 2441 (1968).

5. TENSILE PROPERTIES OF DIRECTIONALLY SOLIDIFIED Al-$CuAl_2$ EUTECTIC

S. Justi and R. H. Bragg

The velocity of sound v in a metallic material is related to the density ρ and the elastic modulus E through

$$v = \sqrt{\frac{E}{\rho}} \quad . \qquad (1)$$

As described in Ref. 1 the elastic modulus can thus be determined by ultrasonic measurements. Compared with finding the elastic modulus through tensile tests the ultrasonic method has the advantages of being both non-destructive and highly accurate.

For measurements the resonant frequency of transverse vibration is usually taken, since it is the lowest of the three possible resonant frequencies, and it has the strongest amplitude. This resonant frequency of transverse vibration ν_t is related to the elastic modulus E by

$$E[kg/mm^2] = 0.96478 \times 10^{-8} \; \frac{M}{b} \left(\frac{L}{a}\right)^3 \times \nu_t^{\,2} \qquad (2)$$

where M is the weight of the prismatic rod in grams, L is the length cm, a is the length cm of the edge which is parallel to the direction of vibration. However it is also possible to calculate the elastic modulus from the resonant frequency of longitudinal vibration, while the resonant frequency of torsional vibration yields the shear modulus.

Rectangular bars of the approximate size 10 cm × 1 cm × 1 cm were cut from directionally solidified ingots using a milling machine. The bars were polished and slightly etched for microscopic inspection of the alignment of the Al and Al_2Cu phases, growth defects, grain boundaries, and other morphological characteristics. An Elastomat, (Reutlingen, Germany) was used for the ultrasonic measurements. The bars were suspended at the nodal points of the fundamental of transverse vibration, which is 0.2242 times the bar length away from the ends (Fig. 1).

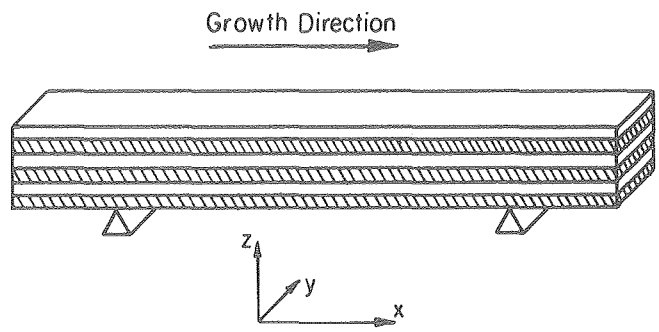

Fig. 1. Setup for ultrasonic elastic modulus measurements. (XBL 7712-6619)

The fundamental resonant frequency of transverse vibration could easily be found. As already mentioned, it is the lowest of the resonant frequencies observed, and usually the strongest. To check its identity the overtones were also recorded. Then the elastic modulus was calculated using Eq. (2). By using this value for the elastic modulus the resonant frequency of longitudinal vibration was calculated, and compared with the resonant frequency for longitudinal vibration found in the ultrasonic test. The calculated value deviated from the measured frequency by less than 0.15%, which demonstrates the high accuracy of the method. The bar was then turned over by 90°, and the procedure was repeated to find the elastic modulus for the y-direction (see Fig. 1). In Fig. 2 the elastic moduli in the y and z directions are plotted vs the growth rate $R^{1/4}$. Although a recent paper[2] concludes that the Al-Al_2Cu eutectic does not show any anisotropic behavior, the results shown in Fig. 2 are contradictory to Ref. 2. The ultrasonic tests in the z direction indicate a higher elastic modulus than in the y direction. Bearing in mind the microstructure as indicated in Fig. 1, the eutectic consists of Al_2Cu platelets in an Al matrix. The

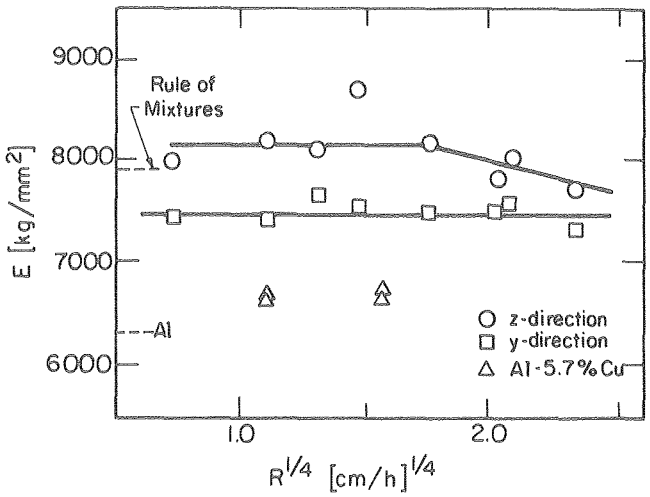

Fig. 2. Elastic modulus of directionally solidified Al-$CuAl_2$ eutectic. Growth rate variable. (XBL 7712-6620)

structure of the matrix is FCC, and ultrasonic tests taken on Al 5.7% Cu alloy for two different growth rates do not show a significant difference of the elastic modulus in the y and z directions, thus indicating, as expected, that the matrix is isotropic. The Al_2Cu phase, however, has a body centered tetragonal structure, and for this phase one would expect anisotropy. If this is the case the eutectic would also be anisotropic. The data found here support this. At high growth rates the eutectic phases are no longer aligned, and an isotropic elastic modulus can be expected. Although the growth rates employed here were not high enough to demonstrate complete isotropy, the data shown in Fig. 2 show that the difference in the elastic modulus for the y and z directions becomes smaller with increasing growth rates. The scatter of data in Fig. 2 is most likely due to microstructural defects (grain boundaries, bands, extra lamellae, etc.) in the bulk of the bars which could not be observed in the microscope prior to testing. The elastic moduli for pure Al and for the eutectic as calculated from the Rule of Mixture (RoM) are also shown in Fig. 2. They are in good agreement with the data found here.

1. F. Foerster, Z. Metallkunde 29, 109 (1937).
2. Y. C. Waung, D. E. Beskos, W. Sachse, J. Mat. Sci. 10, 109 (1975).

6. RESEARCH PLANS FOR CALENDAR YEAR 1978

Robert H. Bragg

Our research findings on GC have far reaching implications for the understanding of both hard and soft carbons. We plan a rapid exploitation via several critical experiments whose rationales are as follows: 1) The non-kinetic density decreases are due to submicroscopic fractures which expose dangling bonds, i.e., unpaired spins. This may explain why the $\Delta\rho/\rho$ increases as the heat treatment temperature is increased. We will test this hypothesis by tensile straining of both GC and PG, i.e., hard and soft carbons and measuring the change in $\Delta\rho/\rho$ induced. The effect of compression will also be investigated.

2) There are reasons to expect that the mobility μ in GC varies at $\mu \sim T^{-1/2}$. Since the expected magnetoresistance behavior is $\Delta\rho/\rho \sim (\mu H)^2$ the $H/T^{1/2}$ single valued function we find would then have a natural explanation. In our previous work measurements of the Hall coefficient R_H were neglected but since $R_H\sigma = \mu$, accurate measurements of R_H and σ, as well as $\Delta\rho/\rho$ are needed. Our electrical measurements during CY 1977 were plagued by a leaky Dewar, but this problem should be resolved during CY 1978, and temperatures less than 8 K (our previous low) should be possible. Extensive electrical measurements for selected heat treatments are planned to test for the $\mu \sim T^{-1/2}$ behavior and to determine if $\Delta\rho/\rho$ saturates. We feel that negative magnetoresistance is associated with paramagnetism and if so $\Delta\rho/\rho$ should saturate at large $H/T^{1/2}$.

3) In GC, graphitization and void growth appear to occur by self-diffusion and vacancy migration mechanisms, respectively. In soft carbons graphitization also occurs via self-diffusion but it is not known how void growth occurs. Using our developments in the characterization of oriented voids in PG we plan to study the kinetics of void growth in PG using the Small Angle Scattering Facility at Oak Ridge National Laboratory for measurements. If GC and PG are found to have the same activation energy for void growth we can conclude that the major difference between hard and soft carbons are the initial steric hindrances.

4) Our results using ion milling techniques of specimen preparation of GC show only diffuse rings in TEM whereas in specimens prepared by crushing, micro size "new" forms of graphite crystals are observed. These have been observed by others in material heated above 2700°C, but we find them in materials which has not been heated above 1800°C. We believe they are artifacts of specimen preparation and plan to clarify this point. Nevertheless we feel that graphite does undergo a phase transformation around 2200°C and plan some in-situ x-ray studies for corroboration. We plan to initiate work on graphite intercalation compounds during CY 1977. Some HOPG base material was obtained for this purpose and we will assembe apparatus for intercalations in CY 1978.

The work on in-situ composites will be phased out. Specifically we will make transmission Laue photographs of the DS Al-$CuAl_2$ eutectics over a full range of λ's to ascertain if gross variations in texture occur. The λ dependence of electrical resistivity will be measured, and exploratory measurements at low temperatures will be made. Finally we will compare hardness and tensile properties to determine if the one-to-one correspondence found for the Al-Si eutectic has a wider applicability.

7. 1977 PUBLICATIONS AND REPORTS

R. H. Bragg and Associates

Journals

1. R. R. Saxena and R. H. Bragg, Negative Magnetoresistance in Glassy Carbon, Phil. Mag. (in press), LBL-5467.

2. R. R. Sexena and R. H. Bragg, Electrical Conduction in Glassy Carbon, J. Non-Crystalline Solids (in press), LBL-5740.

3. S. Bose, U. Dahmen, R. H. Bragg and G. Thomas, Lattice Image of LMSC Glassy Carbon, J. Amer. Ceram. Soc. (in press), LBL-6227.

4. S. Justi and R. H. Bragg, Tensile Properties of Directionally Solidified Al-Si Eutectic, Met. Trans. (in press), LBL-6238.

5. S. Bose and R. H. Bragg, Small Angle Scattering by Oriented Ellipsoidal Voids in Pyrolytic Graphite, J. Appl. Phys. (in press), LBL-6655.

LBL Reports

1. S. Bose and R. H. Bragg, Small Angle Scattering by Diffuse Interfaces, LBL-6656.

2. L. Valero (M. S. thesis) and R. H. Bragg, Texture and Interphase Relationships in Directionally Solidified Al-$CuAl_2$ Eutectic, LBL-7325.

3. D. G. Morrow (M. S. thesis) and R. H. Bragg, Mechanical Properties of Directionally Solidified Al-Si Eutectic, LBL-6036.

Presentations

1. R. H. Bragg, "Advanced Composite Materials", Howard University Colloquium, Washington, D.C., February 1977.

2. R. H. Bragg, "Advances in X-ray Characterization of Amorphous Materials", IBM Watson Research Laboratory Colloquium, Poughkeepsie, N. Y., February 1977.

3. R. H. Bragg, "Structure of Amorphous Carbon", University of Ife, Physics Department Colloquium, Ile-Ife, Nigeria, June 1977.

4. R. H. Bragg, "X-ray Analysis of Disordered Materials", Physics and Chemistry Colloquium, University of the West Indies, Kingston, Jamaica, July 1977.

5. R. H. Bragg, "Workshop on X-ray Quantitative Analysis", Jamaica Bauxite Institute, Kingston, Jamaica, July 1977.

6. R. Saxena, S. Ho and R. H. Bragg, "Negative Magnetoresistance and Electrical Conduction in Glassy Carbon, 13th Biennial Carbon Conference, University of California, Irvine, July 1977.

7. S. Bose, R. Saxena and R. H. Bragg, "X-ray Studies of Graphitization of Glassy Carbon", 13th Biennial CArbon Conference, University of California, Irvine, July 1977.

B. SOLID STATE PHYSICS

1. EXPERIMENTAL SOLID STATE PHYSICS

a. Far Infrared Spectroscopy

Paul L. Richards, Principal Investigator

1. INFRARED SURFACE SPECTROSCOPY

Robert B. Bailey, Shirley Chiang, Takeo Iri and Paul L. Richards

Infrared radiation is a potentially important probe of the structure and composition of solid surfaces. However, because the low energy photons are difficult to detect and their interaction with surface layers is weak, the application of infrared spectroscopy to the analysis of single crystal surfaces has been limited. We have developed a sensitive thermal detection scheme for observing the small infrared absorptions of surface layers and have completed construction of an ultrahigh vacuum system for sample preparation and spectral measurements. Studies of adsorbed chemicals on metal surfaces and of electronic surface states of semiconductors are under way.

Infrared absorption by a layer of surface molecules is less than 1% for even the strongest absorbers. Weaker vibrational transitions of molecules at submonolayer coverages contribute absorptivities of only a few parts per million. Amplitude instabilities in the infrared beam tend to mask such small effects. Conventional optical measurements detect reflected or transmitted power and reduce the effects of instabilities by modulating either the wavelength or polarization state of the radiation. Instead of looking for small changes in a large background signal we measure directly the infrared power absorbed by the sample. A small doped germanium thermometer is attached to the crystal and at liquid helium temperatures the heat generated by 10^{-13} W of absorbed power is easily detected. This technique is most sensitive to surface effects when bulk absorption is small.

Figure 1 shows the infrared spectrum of carbon monoxide adsorbed on an evaporated copper film. The low frequency absorption is associated with CO molecules chemically bonded to surface copper atoms. The sharper line, which coincides with the absorption band in gaseous CO, is due to molecules physically adsorbed on the surface. To produce this spectrum CO was first introduced with the sample at 77 K to form the chemically bonded state. An additional exposure at 1.5 K produce the physically adsorbed species. Following infrared measurements the sample was warmed above room temperature to desorb the molecules and another spectrum was measured. Figure 1 is the difference between the two spectra. This is the first spectrum recorded in our UHV apparatus. When the system is optimized the signal-to-noise ratio should be hundreds of times greater.

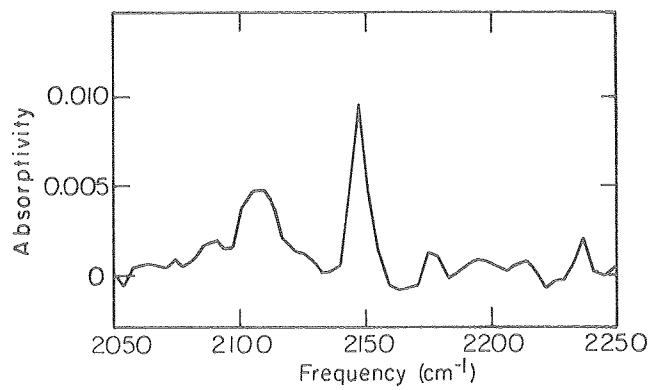

Fig. 1. Infrared spectrum of CO adsorbed on copper. (XBL 7712-6584)

The ultrahigh vacuum chamber constructed for this experiment features a cold finger coupled to a liquid helium cryostat, an ion gun for sample cleaning, and an electron gun for sample heating. Metallic films are deposited from a tungsten filament and gas molecules are introduced from a collimated beam source. The source of the infrared beam is a rapid scan Fourier transform spectrometer interfaced to an on-line computer for data acquisition and analysis. Spectral measurements are made at a sample temperature of 1.5 K. Temperatures up to 1000 K are produced by electron bombardment.

Sensitivity is greatest in our detection scheme if the sample heat capacity is minimized. Polycrystalline metallic samples are prepared by evaporating thin films on low heat capacity sapphire substrates within the UHV system. Thin single crystals of nickel grown epitaxially on sodium chloride substrates are also being prepared for infrared measurements.

2. FAR INFRARED PHOTOCONDUCTIVITY OF UNIAXIALLY STRESSED GERMANIUM

Mark R. Hueschen, Andrei G. Kazanskii and Paul L. Richards

Extrinsic photoconductive detectors, in which infrared photons excite electrons or holes from impurity levels within band gap of a semiconductor

into the conduction or valence band, are easily made from doped germanium or silicon, and are sensitive to radiation from 10 to 120 μm, depending upon the chosen impurity. Photons with wavelengths longer than 120 μm do not have enough energy to free a carrier from even the shallowest impurity levels and must be detected by other means. Bolometers are sensitive at these long wavelengths but have slower response times, so that extension of photoconductive detectors to longer wavelengths is desirable.

This can be accomplished by applying uniaxial stress to a doped germanium detector, which decreases the ionization energy of the donors or acceptors by lifting the degeneracy of the valence band edge. Measurements have been made of the shift of the spectral absorption edge with strain for stresses up to 6.6×10^9 dyne/cm^2 applied along the [100] and [111] directions. Gallium, aluminum, and boron-doped germanium were all used as detectors and operated at temperatures of 2.0 and 7.5 K. Detector dimensions were $1 \times 1 \times 6$ mm with the stress applied along the long dimension.

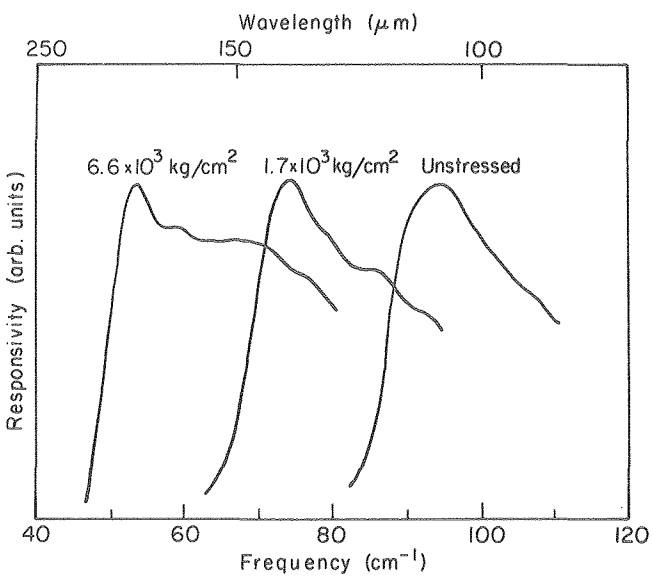

Fig. 1. Shift of the onset of photoconductivity with [100] stress in Ge:Ga. (XBL 775-5536)

These measurements have shown that the decrease in acceptor ionization energy is greatest for stress applied along the [100] direction. The long wavelength cut-off for germanium doped with 2×10^{14} gallium atoms per cm^2 was shifted from the zero stress value of 114 to 200 μm with a stress of 6.6×10^9 dyne/cm^2 along [100]. The measured shifts of the photoconductive threshold at 2 K were combined with published theoretical calculations to give values for the deformation potentials b and d.

When the detectors were operated at 7.5 K, spectral lines were observed at wavelengths longer than the threshold wavelength. These correspond to photoexcitation of the acceptor level followed by thermal ionization. The shift of these lines with stress has been studied and indicates that in general, at high stress ($> 3 \times 10^9$ dyne/cm^2) the ground state is more sensitive to stress than the excited states. In the limit of high stress, the photothermal ionization spectrum of Ge:Ga approaches that of a hydrogenic impurity in a non-degenerate semiconductor.

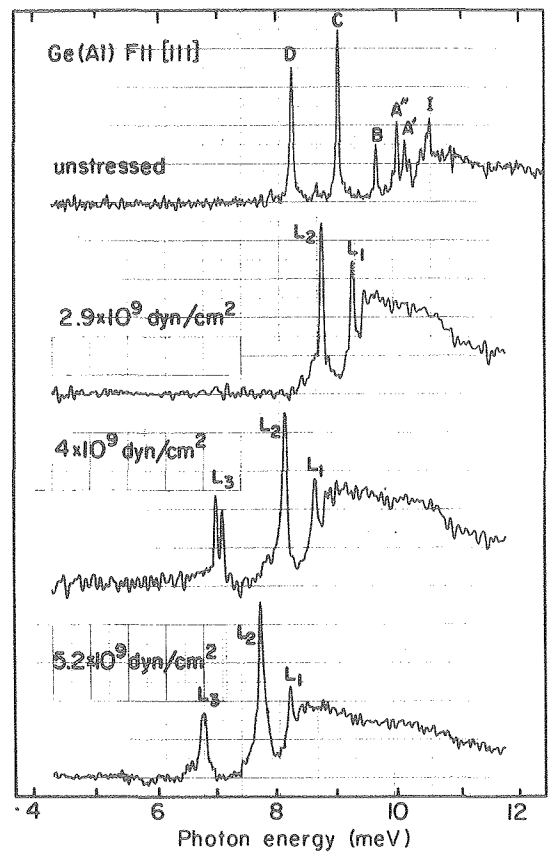

Fig. 2. Photothermal ionization spectra of Al in Ge as a function of [111] stress. The lines change with increasing stress from ones characteristic of the doubly degenerate valence band to those characteristic of a non-degenerate band. (XBL 777-5734)

Another direction of effort is toward the measurement of the responsivity and noise of a stressed gallium-doped germanium photoconductive detector in low background operation. Such a detector may prove very useful in infrared observations from space platforms.

3. FAR INFRARED BOLOMETER DETECTORS

John Clarke, Norman S. Nishioka, Paul L. Richards, David P. Woody and N.-H. Yeh

Over the past five years we have pursued the development of improved thermal (bolometric) detectors of far infrared radiation. This project has now been successfully completed. We have developed techniques which permit us to construct detectors with a variety of parameters which have high optical efficiency and low heat capacity, and which are limited essentially by fundamental thermal fluctuation noise. In low background applications we have achieved at least a two order of magnitude improvement in specific detectivity compared with previously available values at the same operating temperatures.

Two types of detectors have been developed: The superconducting composite bolometer (Clarke, Richards, and Yeh) is available for operation only at ~ 1.3 K. It has especially small inverse frequency noise and is therefore useful for ultimate sensitivity (NEP = 1.7×10^{-15} W/$\sqrt{\text{Hz}}$) at low modulation frequencies (~ 2 Hz). The semiconducting composite bolometer (Nishioka, Richards, and Woody) has been operated at both He^4 temperatures (NEP = 3×10^{-15} W/$\sqrt{\text{Hz}}$, T = 1.2 K, 10 Hz) and at He^3 temperatures (NEP = 6×10^{-16} W/$\sqrt{\text{Hz}}$, T = 0.35 K, 30 Hz). This last detector is the most sensitive infrared bolometer ever made. It is used for the cosmic background measurements described in article 4 below. The He^4 temperature semiconducting composite bolometer is the basis of the surface spectroscopy measurements described in article 1 and the far infrared sky survey described in article 5 below. The absorbing surface of each of the bolometers described above is a $4 \times 4 \times 0.03$ mm slice of Al_2O_3 coated on the reverse side with 200 Ω/□ of Bi. This structure provides high optical efficiency (50%) with low heat capacity in the submillimeter wavelength range.

4. A NEW MEASUREMENT OF THE NEAR-MILLIMETER SPECTRUM OF THE COSMIC BACKGROUND RADIATION

David P. Woody, Norman S. Nishioka and Paul L. Richards

We have made a significant improvement in the determination of the near-millimeter spectrum of the cosmic background radiation (CBR). Our previous observations established that the spectrum of the CBR is that of a 2.9 K blackbody over the frequency range from 4 to 17 cm^{-1} with errors in the measured flux which are typically ± 20%. This frequency range contains 79% of the flux from a 2.9 K blackbody and includes the peak in the Planck spectrum at 6 cm^{-1}. Elementary "Big Bang" cosmology predicts a blackbody spectrum for the CBR, but more detailed scenarios of the evolution of the early universe allow for deviations from an ideal blackbody spectrum. A flight of our liquid helium cooled spectrophotometer on May 3, 1977 produced data which will allow us to decrease the errors in the observed CBR by at least a factor of five in the frequency range from 2 to 17 cm^{-1}. These results will provide new information about the early history of the universe.

The improvement in our data came from several factors. Most important was the use of a ^3He cooled composite bolometer which provides a factor of 50 improvement over our previous ^4He cooled detector. This improvement is particularly important at long wavelengths where the useful response of the spectrophotometer has been extended from 4 to 2 cm^{-1}. The radiation collecting optics have been modified to decrease the contamination from earthshine radiation. The intensity of the atmospheric emission was reduced by a factor two by using a larger balloon to achieve a higher float altitude.

The preliminary data analysis indicates that the expected improved performance of the spectrophotometer was achieved. The observed spectrum of the night sky emission at a resolution of 2 cm^{-1} is shown in Fig. 1a. Atmospheric line emission dominates the spectrum at frequencies above 12 cm^{-1} but the CBR is clearly seen between 2 and 12 cm^{-1}. Even without the removal of the atmospheric emission, the peak in the CBR at ~ 6 cm^{-1} and the Planck high frequency cutoff are clearly visible. Our model for the atmospheric emission has been fitted to the observed spectrum using a preliminary calibration of the instrumental flux responsivity. This best fit model for atmospheric emission is shown in Fig. 1b. The CBR is obtained by subtracting the calculated atmospheric emission from the observed night sky emission and is shown in Fig. 1c. The anomalies remaining at the positions of strong emission lines indicate that higher order corrections need to be applied to the frequency scale of the observed spectrum.

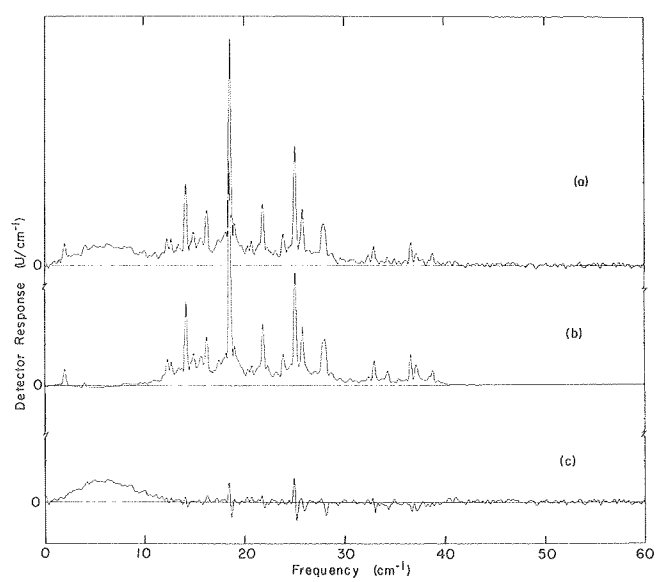

Fig. 1. (a) Night sky emission spectrum; (b) calculated best fit atmospheric emission spectrum; (c) CBR spectrum [residual of (a)-(b)]. (XBL 7712-6580)

To complete the measurement it is necessary to obtain a flux calibration for the instrument so as to convert the detector response plots in Fig. 1 to absolute flux. This is being done by combining flight and laboratory calibrations obtained with blackbody sources with the calculated near-field response of the antenna.

5. FAR INFRARED SKY SURVEY

Stephen E. McBride, Norman S. Nishioka, Paul L. Richards and David P. Woody

Astronomy in the far infrared has always been limited by the lack of sensitive detectors. Our development of new bolometers with greatly improved sensitivity now makes it possible to do many exciting experiments. We are constructing a one-meter Cassegrain balloon telescope to survey the sky and search for sources at far infrared wavelengths. The telescope will be suspended at ~ 45° from the zenith and will rotate at ~ 2 rpm so that each portion of the sky will be observed a minimum of four times during the survey. The survey will have a field of view of 16 arc minutes and will be sensitive to extended sources, several degrees across. Accurate orientational information will be obtained from a photomultiplier with an N shaped mask, which will detect the transit of stars with known positions. Additional orientational information will come from sensitive rate gyros and magnetometers.

Since any radiation from warm objects reaching the detectors would limit their sensitivity, great care has gone into the design of this telescope to insure that it accepts the minimum feasible thermal background radiation. This includes diamond machined metal optics (developed at the Lawrence Livermore Laboratory for the laser fusion program) for the lowest emissivity reflecting surfaces, cold Winstron light concentrators (developed at the Argonne National Laboratory) to define the entrance beam into the cryostat, and careful shielding to minimize background radiation originating from the gondola and from the earth.

There are seven bolometer detectors, each responding to a separate frequency band between 10 cm^{-1} and 1000 cm^{-1}. These frequency bands are isolated by cold filters in the optical path. The outside helium bath temperature of 2 K is too warm for bolometers to function well in the longest wavelength bands. To obtain high responsivity that does not change with time, the bolometers are cooled by a separate helium pot. The pot is pumped by an activated charcoal pump to ~ 1.0 K. The relation of the various parts is shown in Fig. 1.

With the present apparatus floating at an altitude of 30 km, the limiting flux sensitivity should be a few flux units (1 f.u. = 10^{-26} W/m^2 Hz) in the far infrared band. This is orders of magnitude more sensitive than previous surveys. The apparatus is presently in the final stages of construction and testing, and should make its first flight in early 1978.

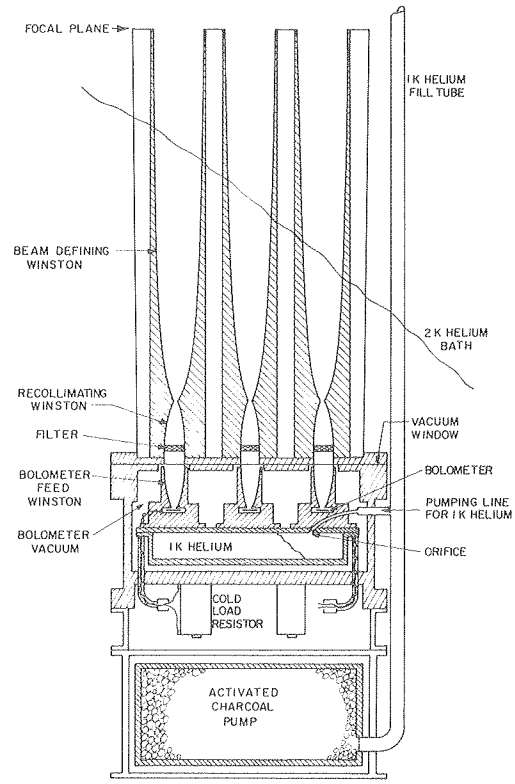

Fig. 1. Diagram of the bottom of the detector system showing the use of Winston light concentrators both to define the optical beam and to concentrate the radiation on the bolometers. The relations between the bolometers, the helium pot, and the charcoal pump are also illustrated. (XBL 7712-6618)

6. NEW POLARIZING INTERFEROMETER

David K. Lambert, Paul L. Richards and Sergio C. Zillio

We have constructed a prototype Martin-Puplett polarizing interferometer for use as a far infrared Fourier spectrometer. This kind of instrument is superior to the conventional Michelson interferometer now in use in most laboratories because a single beam splitter can be used over a very wide frequency range, and because drifts in input signals cannot be confused with interference modulation.

The optical alignment of this instrument proved to be much more difficult than had been anticipated. A theoretical analysis of this problem has yielded a number of results. A complete analysis of the operation of the Martin-Puplett interferometer has been given. A new way to analyze all similar interferometric systems has been found. In particular, we were able to show that using a broad band incoherent source and plane mirrors one may construct an interferometric system to measure the optical transfer function of an optical element as a function of both optical and spatial frequency.

We have arranged for the fabrication of infrared grid polarizers by photolithography at the Hughes Aircraft Corporation. We expect that beam-splitters made from this material will permit operation of the polarizing interferometer over the frequency range from 2 to 800 cm^{-1}. The interferometer drive is being upgraded to permit operation over this very wide frequency range.

7. FAR INFRARED SPECTROSCOPY OF ELECTRONS ON THE SURFACE OF LIQUID HELIUM

David K. Lambert and Paul L. Richards

We have begun measurements of the infrared absorption of electrons trapped on the surface of liquid helium. The electrons are highly mobile along the surface but have a series of discrete energy levels corresponding to the wavefunction perpendicular to the surface. In order to obtain sufficient electrons for many body effects to become important, and external field must be applied normal to the surface.

The measurements are made by passing light from a far infrared molecular laser (pumped by a CO_2 laser) through a far infrared transmittance cavity in which the charged helium surface is contained, and measuring the modulation of the transmitted power at the frequency of a modulation applied to the stark field.

From our measurements of the Stark shift as a function of laser frequency we will obtain detailed information about the liquid gas interface. The structure on the absorption line will provide information regarding the two-dimensional electron fluid.

In addition to our measurements of the far infrared response of the electrons on liquid helium, we also plan to measure the radiofrequency response of the two-dimensional electron gas and to look for similar surface states on other materials on which they have been predicted but not yet observed. Candidate systems for far infrared transitions include liquid hydrogen, liquid neon, and a superfluid helium film on a metal.

8. WHITE MOUNTAIN RADIOMETER

James L. Bonomo, Paul L. Richards and David P. Woody

Far infrared astronomy is a relatively undeveloped field, both because of historically poor detector sensitivity and because of atmospheric absorption. We have constructed a radiometer which is designed to overcome these problems by combining a sensitive composite Ge bolometer detector with a new 1.5 m high altitude telescope. The telescope is located at an altitude of 13,000 ft on White Mountain and so is above much of the atmospheric absorptions.

The radiometer itself incorporates a self-contained He^3 refrigerator to cool the bolometer to ~0.35 K. The optical system is generally similar to that of our sky survey, but with an adjustable cold aperture stope and a set of cold filters to isolate the various windows of atmospheric transmission. The far infrared beam is fed into the radiometer by a wobbling Cassegrain secondary which modulates the intensity of an astronomical source reaching the detector.

The construction of this radiometer was completed this year, and the wobbling secondary mechanism was modified to increase its frequency of operation and angular throw. Preliminary observations which were made from White Mountain during the last observing season allowed us to partially characterize the noise due to atmospheric variations. The first astronomical results are expected from the 1977-78 Winter observing season. Data from this instrument should not only answer important astronomical questions, but should also be extremely useful in checking new sources of far infrared radiation discovered by the sky survey discussed in article 5 above.

This project is being carried out in collaboration with the Berkeley Radio Astronomy Laboratory.

9. SUPERCONDUCTING HETERODYNE RECEIVERS*

John H. Claassen, Paul L. Richards and Tek-Ming Shen

We are evaluating the usefulness of superconducting devices as low noise heterodyne mixers for coherent millimeter wave radiation. New results from this program include a theoretical study of the noise in Josephson junction mixers. Solutions to the appropriate noise driven nonlinear equations were obtained by analog computation. In the range of ambient temperature T and operating frequency ν for which thermal noise is dominant, the calculated single sideband noise temperature is $T_m \simeq 40$ T. At frequencies $h\nu > 2$ kT, the effect of photon noise in the mixer can be approximated by the inclusion of an effective ambient temperature $T_{eff} = h\nu/2k$, so that $T_m \simeq 20\ h\nu/k$.

An experimental study has been completed in which a Nb point contact Josephson effect mixer was evaluated at $\nu = 130$ GHz. The experimental result of $T_m = 180$ K is the best ever reported at such a high frequency and is in very good agreement with the theory.

A superconducting bolometric mixer is being evaluated experimentally at $\nu = 36$ GHz. Preliminary results indicate a conversion efficiency of a few percent and an intermediate frequency bandwidth of ~ 1 MHz. Improved performance is expected as bolometer parameters are optimized.

10. RESEARCH PLANS FOR CALENDAR YEAR 1978

Paul L. Richards

Surface Spectroscopy. The newly constructed ultrahigh vacuum system will be used in measurements of the spectra of a variety of molecules adsorbed on the surface of metals. The first series of measurements will be on evaporated films to test the system performance. Subsequent measurements will be on epitaxially grown 111 Ni films. Development of a cooled spectrometer for emission experiments will be pursued. The overall effort in this area will be expanded significantly compared with 1977.

Photoconductivity in Stressed Gallium Doped Germanium. The properties of the newly discovered long wavelength stressed Ge:Ga photoconductor will be explored in detail. Noise and quantum efficiency will be measured in low infrared background. If good performance is obtained this detector will find important applications in military and astronomical space vehicles.

Infrared Astrophysics. Calibrations will be measured so that the analysis of our cosmic background radiation measurements can be carried out. This will complete our highly successful program of measurements of the spectrum of the cosmic background radiation. Further improvements in our understanding of this fundamental property of the universe will have to wait until the flight of the COBE satellite in 1984.

The apparatus development phase of the sky survey and White Mountain radiometer projects is nearing completion. Both projects should produce valuable data in 1978.

Electrons on the Surface of Liquid Helium. After a long apparatus development phase, data should begin to appear during calendar year 1978.

11. 1977 PUBLICATIONS AND REPORTS

Paul L. Richards and Associates

Journals and Books

1. W. E. Tennant and P. L. Richards, Far Infrared Observation of Antiferromagnetic Resonance of $Mn^{1-x}Zn^{x}F^{2}$, J. Phys. C 10, L365 (1977).

2. P. L. Richards, Telescope and Detector Systems for Submillimeter Line Spectroscopy, Infrared Phys. 17, 241 (1977).

*3. Y. Taur and P. L. Richards, Parametric Amplification and Oscillation at 36 GHz Using a Point Contact Josephson Junction, J. Appl. Phys. 48, 1321 (1977).

*4. Y. Taur and P. L. Richards, A Josephson Effect Parametric Amplifier at 36 GHz, IEEE Trans. Magn. MAG-13, 252 (1977).

5. J. Clarke, P. L. Richards, and N.-H. Yeh, Composite Superconducting Transition Edge Bolometer, Appl. Phys. Lett. 30, 664 (1977).

6. A. G. Kazanskii, P. L. Richards, and E. E. Haller, Far Infrared Photoconductivity of Uniaxially Stressed Ge, Appl. Phys. Lett. 31, 496 (1977).

7. A. G. Kazanskii, P. L. Richards, and E. E. Haller, Photoionization of Acceptors in Uniaxially Stressed Germanium, Solid State Comm. 24, 673 (1977).

8. P. L. Richards, Superconducting Devices for Millimeter and Submillimeter Wavelengths, Proc. of the 1976 SQUID Conference, H. D. Hahlbohm and H. Lübbig, Eds.,(Walter de Gruyter, Berlin-New York, 1977), p. 323.

9. P. L. Richards, Cosmology, McGraw Hill Yearbook of Science and Technology, 1977, p.180.

10. P. L. Richards, The Josephson Junction as a Detector of Microwave and Far Infrared Radiation, Semiconductors and Semimetals, Vol. 12 - Infrared Detectors (II), Willardson and Beer, Eds. (Academic Press, New York, 1977), p. 395.

Reports

1. N. S. Nishioka, P. L. Richards, and D. P. Woody, Composite Bolometer for Submillimeter Wavelengths, to be published in Appl. Opt. 17 (Feb. 1978 issue), LBL-6085.

†2. P. L. Richards and R. Gomer, Optical Imaging in Acoustic NDE, 1977 Materials Research Council Report.

3. D. K. Lambert and P. L. Richards, An Analysis of the Martin-Puplett Interferometer, submitted to Appl. Opt., LBL-6637.

4. D. K. Lambert and P. L. Richards, New Results in the Theory of Plane Mirror Interferometers, submitted to J. Opt. Soc. Am., LBL-6647.

*5. J. H. Claassen and P. L. Richards, Performance Limits of a Josephson Junction Mixer, submitted to J. Appl. Phys.

*6. J. H. Claassen and P. L. Richards, Point Contact Josephson Mixers at 130 GHz, submitted to J. Appl. Phys.

Talks

1. P. L. Richards, Cosmic Background Radiation, Invited Talk, 2nd Int. Conf. on Submillimeter Waves and Their Applications, San Juan, Puerto Rico, December 6-10, 1976.

2. P. L. Richards, J. Clarke, G. I. Hoffer, N.-H. Yeh, and N. S. Nishioka, Composite Bolometers for Submillimeter Wavelengths, ibid.

3. P. L. Richards, Measurements of the Cosmic Background Radiation, colloquium at Iowa State University, Ames, Iowa, January 31, 1977.

4. P. L. Richards, Measurements of the Cosmic Background Radiation, Invited Talk, 2nd Int. Conf. on Fourier Transform Spectroscopy, Columbia, South Carolina, June 20-24, 1977.

5. P. L. Richards, R. B. Bailey, and G. T. Boyd, Techniques for Direct Measurments of Small Absorptivities Using Fourier Transform Spectroscopy, ibid.

---

*Sponsored by the Office of Naval Research.

†Sponsored by the Advance Research Projects Agency.

b. Experimental Solid State Physics and Quantum Electronics

Y. Ron Shen, Principal Investigator

1. STUDY OF SURFACE EXCITON-POLARITONS BY OPTICAL MIXING

Chenson K. Chen, Stanley Kohn, Francesco DeMartini, Marcello Colocci and Y. Ron Shen

Nonlinear optical excitation of surface exciton-polaritons has been experimentally achieved for the first time.[1] From the dispersion and damping characteristics of the surface waves, characteristic parameters of the c-exciton in ZnO were deduced.

$$\varepsilon_\infty = 6.15 \pm 0.01$$

$$\omega_T = 3.421 \pm 0.0001 \text{ eV}$$

$$\varepsilon_0 = 1.72 \pm 0.001$$

$$\Gamma = 0.25 \pm 0.05 \text{ meV}$$

Surface polaritons can exist only in regions of negative dielectric constant of a crystal. For a semi-infinite anisotropic crystal b bounded by an isotropic medium a, the dispersion relation for the surface polariton is given by

$$K_x^2 = (K_x' + iK_x'')^2 = \frac{\omega^2}{c^2}\frac{\varepsilon_a \varepsilon_{bz}(\varepsilon_{bx} - \varepsilon_a)}{\varepsilon_{bx}\varepsilon_{bz} - \varepsilon_a^2} \qquad (1)$$

where ε_{bx} and ε_{bz} are the dielectric constants along $\hat{x}$, the direction of propagation in the surface, and $\hat{z}$, the surface normal, respectively. Surface waves exist when $\varepsilon_{bx} < 0$ and $\varepsilon_{bz} > \varepsilon_a$ or $\varepsilon_{bz} < 0$. From a theoretical treatment of nonlinear optical mixing at crystal interface,[2] we find the surface wave generated by second-harmonic generation ($\omega = 2\omega_1$) to be

$$\underset{\sim}{E}^b(\omega) = \frac{A}{(k_x - K_x') - iK_x''} \times (\hat{x}k_{bz} + \hat{z}k_x)P_x^{(2)} e^{i(k_x v - \omega t) + ik_{bz}z}. \qquad (2)$$

Thus, if one varies $\underset{\sim}{k} \equiv 2\underset{\sim}{k}_1(\omega_1)$ so that $k_x \sim K_x'$, the surface wave will be resonantly excited. Furthermore, in the presence of surface roughness, the radiative output should be proportional to the power of the excited surface wave.

$$I(\omega, k_x) \propto \int |\underset{\sim}{E}^b(\omega)|^2 dxdy \propto \frac{|\underset{\approx}{\chi}^{(2)} : \underset{\sim}{E}(\omega_1)\underset{\sim}{E}(\omega_1)|^2}{(k_x - K_x')^2 + K_x''^2}. \qquad (3)$$

By varying k_x through the resonance condition, both the wavevector K_x' and the damping K_x'' of the surface wave can be determined. And, by measuring K_x at several ω, the dispersion curve of the surface exciton-polariton can be constructed. Then, from fitting experimental data to theory, the parameters characterizing the c-exciton can be deduced.

The experimental setup is shown in Fig. 1. A Q-switched ruby laser was used to pump a dye laser, generating a tuneable laser source near $\omega_1 = 1.71$ ZeV. The beam and linewidth of less than 1.5 cm^{-1}, a diameter of 8 mm, a pulsewidth of 30 ns, and a peak power of about 50 kW. The laser was focused onto the plane surface of ZnO through a f = 25 cm lens. For a given ω_1, k_{1x} was varied by translating the beam parallel to the lens axis. Angular resolution was limited to about 0.5° at the crystal surface.

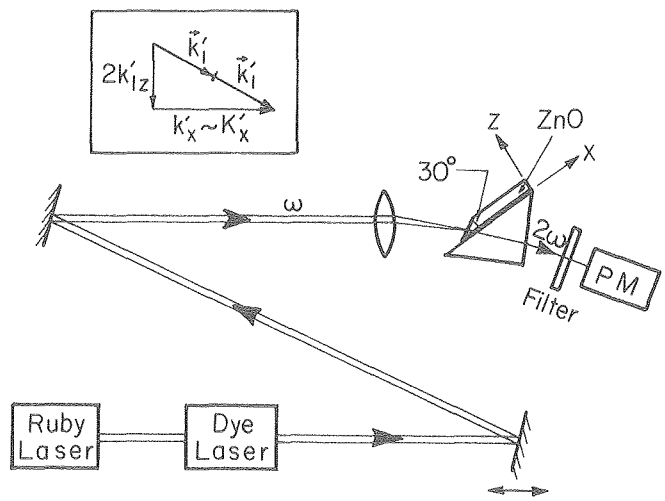

Fig. 1. Experimental setup. The inset shows the wavevector relation. (XBL 772-5095)

The crystal was immersed in superfluid He at 2 K. Initially, we proposed to monitor the output of the surface wave by using a prism to couple out the non-radiative surface wave. The output through prism coupling should have fallen exponentially as the distance between the interface and prism increased. However, the output was independent of the spacing, and we therefore concluded and later experimentally verified that surface roughness coupled out the surface wave. After filtering out the fundamental laser light, the output was monitored by a photomultiplier.

The ZnO crystal had its c-axis along the $\hat{x}$ direction. We studied only surface polaritons associated with the c-exciton, in which the dipole matrix element is allowed only for $\underset{\sim}{E}$ parallel to the c-axis. We used the single oscillator model to describe the process.

$$\varepsilon_{bx} = \varepsilon_\infty - \frac{(\varepsilon_0 - \varepsilon_\infty)\omega_\Gamma^2}{\omega^2 - \omega_T^2 + i\omega\Gamma}$$

$$\varepsilon_{bz} = \varepsilon_\infty$$

where ω_T is the transverse exciton frequency, Γ is the damping constant, $\varepsilon_0 - \varepsilon_\infty$ is proportional to the oscillator strength, and $\varepsilon_\infty > 0$ is the constant background contribution to the dielectric constant. We neglected the anisotropy in $\varepsilon_\infty \left(\frac{|\varepsilon_{\infty x} - \varepsilon_{\infty z}|}{\varepsilon_\infty}\right) < 2\%$. The incoming laser beam was polarized in the plane of incidence (x-z plane) giving rise to a nonlinear polarization

$$P_x^{(2)}(\omega) = \chi_{31}^{(2)} E_z^2(\omega_1) + \chi_{33}^{(2)} E_x^2(\omega_1). \qquad (5)$$

We estimated a maximum output of 10^8 photons per pulse for a smooth crystal surface and optimal prism-interface spacing. However, only 10^4 photons per pulse were observed, supporting the hypothesis that surface roughness was coupling out the surface wave.

For each ω, the experimental results of $I(\omega)$ vs k_x were fitted by a Lorentzian curve, as shown in Fig. 2. K_x' and K_x'' were deduced directly from the

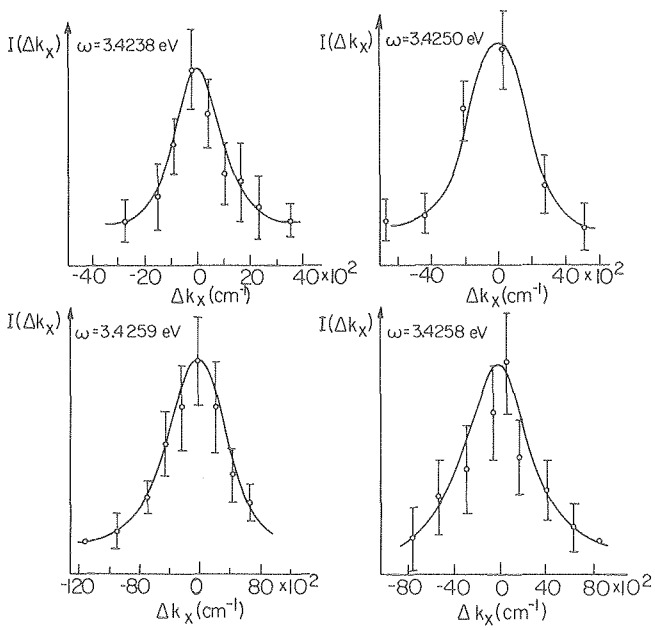

Fig. 2. Experimental results of normalized $I(\omega, \Delta k_x)$ vs Δk_x at four output frequencies. The solid curves are Lorentzian used to fit the data points. (XBL 772-5093)

peak position and halfwidths of the curves. The results are shown in Fig. 3 in comparison with theoretical curves calculated from the dispersion relation of Eq. (1) and ε as in Eq. (4). By least squares fitting the theoretical curves, we obtained values for ε_∞, ε_0, ε_T and Γ as given above. The only serious discrepancy appeared in the value of $(\varepsilon_0 - \varepsilon_\infty)$, a factor of 1.7 lower than previous values found in literature. The larger value of $\varepsilon_0 - \varepsilon_\infty$ shifts the dispersion curve up by about 1 meV. We may question the accuracy of the previous value of $\varepsilon_0 - \varepsilon_\infty$ determined by ATR.[3] Nevertheless, possible causes of the

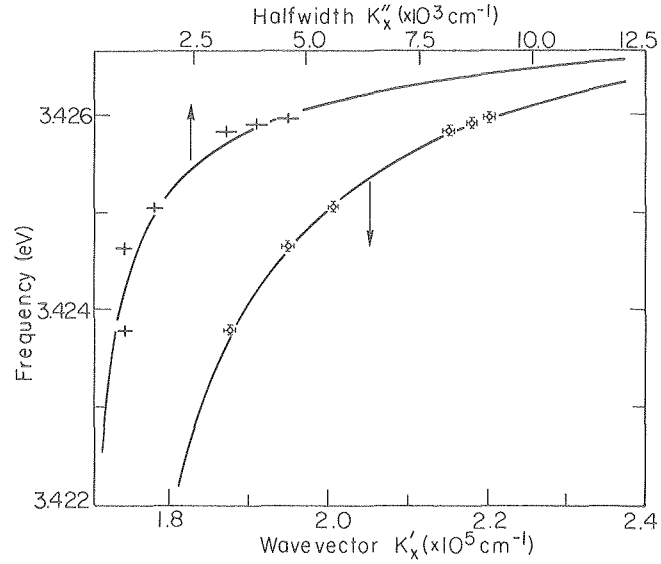

Fig. 3. Measured dispersion and damping characteristics of surface exciton-polaritons in ZnO. (⊹ ——— K_x' vs ω ; + ——— K_x'' vs ω). The solid curves are calculated from Eqs. (1) and (2) using $\varepsilon_\infty = 6.15$, $\varepsilon_0 = 6.172$, $\omega_T = 3.421$ eV, and $\Gamma = 0.25$ MeV. (XBL 772-5094)

shift are 1) surface roughness, which causes a downward shift in the dispersion curve for surface plasmons, and 2) possible surface contamination. However, we believed that our etched sample surface was not sufficiently contaminated to cause any appreciable shift.

Finally, our dispersion curve was 2 meV lower than one measured by Lagois and Fischer[4] using the ATR method. From their paper, 1) we were not sure how accurately the measurement of K_x' was; 2) we were not sure if they accounted for the anisotropy in ZnO; and 3) we did not know how much the uncertain spacing between the prism and crystal shifited their data points. Also, their experiment was conducted at 8 K (ours was at 2 K). We expected that surface roughness would have the same effect, as the crystals were given similar treatment. However, these observations cannot explain the discrepancy to our satisfaction, and we feel more work with controlled surface roughness is necessary to resolve the shifts in the dispersion curve.

Experimental work on the c-exciton is continuing; we plan to deduce the temperature dependence of the c-exciton by measuring the characteristics of the surface wave as a function of temperature. Also, we plan to probe the a and b - excitons, by exciting surface exciton polaritons in the absorption bands of the a, b excitons. In this case, the surface wave is further complicated by spatial dispersion.

In conclusion, we reported the first direct measurement of the damping parameters of surface exciton-polaritons. We have demonstrated that nonlinear optical excitations can be used to study surface exciton-polaritons and provide a very sensitive probe for determining the exciton characteristics.

1. F. DeMartini, M. Colocci, S. Kohn and Y. R. Shen, Phys. Rev. Lett. 38, 1223 (1977).
2. F. DeMartini and Y. R. Shen, Phys. Rev. Lett. 36, 216 (1976).
3. J. Lagois and K. Hummer, Phys. Status Solidi (b) 72, 393 (1975).
4. J. Lagois and B. Fischer, Phys. Rev. Lett. 36, 680 (1976.

2. MULTI-MAGNON LUMINESCENCE IN ANTIFERROMAGNETS

Tai C. Chiang, Pier Salvi, and Y. Ron Shen

Magnon sidebands associated with excitonic absorption and emission in antiferromagnetic systems have long been a subject of extensive theoretical and experimental studies. Among the many antiferromagnets, the fluorides, MnF_2 in particular, have been most thoroughly investigated. Yet work is often limited to one- and two-magnon sidebands. Higher-order magnon sidebands are difficult to observe because they are either too weak or buried in the background. In the luminescence spectrum, strong background usually arises from impurity emission bands. With pulsed excitation and detection, however, long-lived impurity luminescence can be largely suppressed. Using such a technique we have observed luminescence spectra of up to 7 magnon sidebands in MnF_2 and a few less in $KMnF_3$ and $RbMnF_3$ as shown in Figs. 1 and 2.

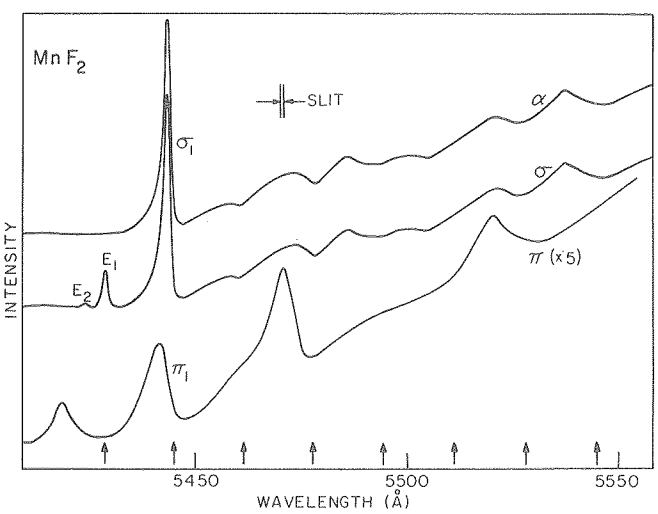

Fig. 1. Polarized intrinsic luminescence spectra of MnF_2. Laser intensity was ~ 20 MW/cm^2 for the α- and σ-polarizations and ~ 30 MW/cm^2 for the π-polarization; laser wavelength λ_ℓ = 5200 Å; laser repetition rate = 6 pps; boxcar gate with 1 μs. Arrows indicate the theoretical cutoff points of the multi-magnon sidebands as explained in the text. (XBL 7712-6587)

In our experiment, the samples were immersed in superfluid liquid helium. A tunable flash-pumped dye laser was used as the excitation source. The laser pulses had a pulsewidth of 0.4 μs and an energy of a few millijoules per pulse. Luminescence

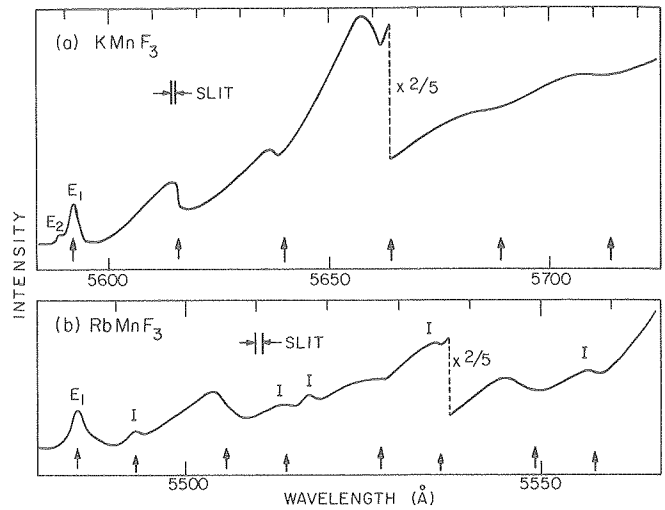

Fig. 2. (a) Unpolarized intrinsic luminescence spectrum of $KMnF_3$ obtained with laser wavelength λ_ℓ = 5130 Å, boxcar gate width = 10 μs, laser repetition rate = 6 pps, and laser intensity = 4 MW/cm^2. Arrows indicate the theoretical cutoff points of the multi-magnon sidebands. (b) Unpolarized luminescence spectrum of $RbMnF_3$ obtained with λ_ℓ= 5230 Å, boxcar gate width = 1 μs, laser repetition rate = 4 pps, and laser intensity = 60 MW/cm^2. Features marked I are due to impurities. Long arrows indicate the intrinsic multi-magnon progression, while short arrows indicate the intrinsic multi-magnon progression starting from the impurity exciton at 5492.7 Å. (XBL 7712-6588)

from a sample was collected with either 90° or backward scattering geometry depending on the sample dimensions and was analyzed by a double monochromator followed by a photomultiplier and a gated PAR-162 boxcar integrator. The gate with an adjustable gate width (1 to 20 μs) was triggered by the exciting laser pulse that was simultaneously monitored for signal normalization. Since the impurity luminescence in the crystals, we were interested in had rather long lifetimes (> 1 ms) we could eliminate most of it by using a relatively short gatewidth (≲ 20 μs). The laser pulse repetition rate was also kept low (≤ 6 pps) in order to suppress the exceptionally intrinsic.

Let us concentrate our theoretical interpretation of the results on MnF_2. The discussion is equally applicable to $KMnF_3$ and $RbMnF_3$. Figure 3a shows schematically the dispersions of magnons and E_1 and E_2 excitons in MnF_2. An E_1 exciton with wavevector $\vec{k}$ can recombine by emitting simultaneously a magnon at $\vec{k}$ and a photon. This gives rise to the one-magnon sideband. It is of course possible for an exciton to emit several magnons and a photon in the recombination. From the perturbation point of view, such a process would appear to be of higher order. This is certainly not true for the observed multi-magnon sidebands since the luminescence peaks in Fig. 1 are generally of comparable magnitude. We can however qualitatively explain the results by the following two-ion local interaction model.

Figure 3b shows the energy level diagrams of three neighboring Mn ions;[1] A and B are nearest neighbors

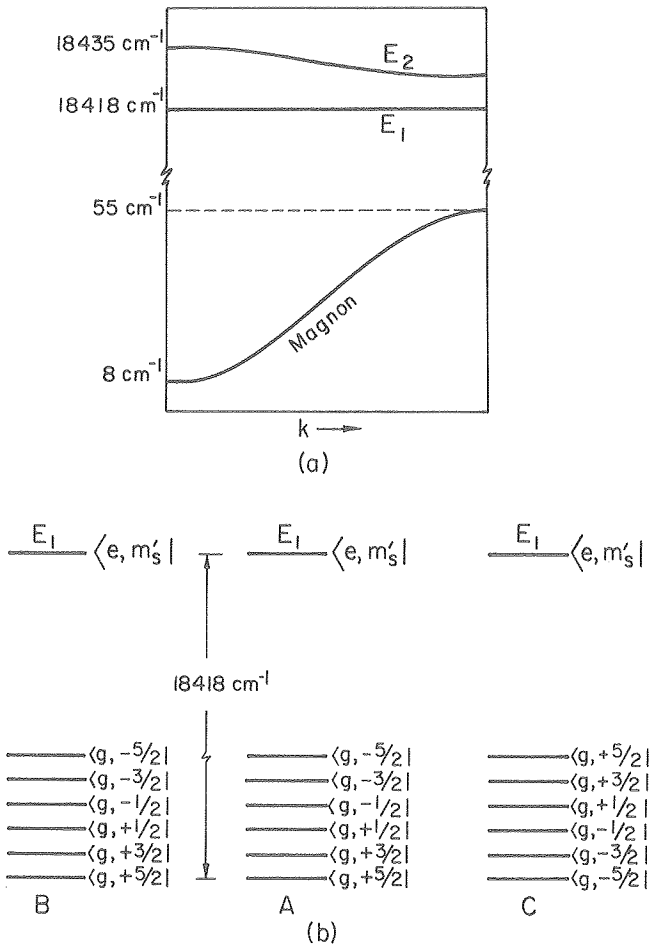

Fig. 3. (a) Schematic dispersion curves of excitons and magnons in MnF_2. (b) Energy level diagrams of three neighboring Mn ions in the molecular field approximation. Ions A and B on the same sublattice; the associated E_1 exciton state $\langle e, m_s' |$ may have a dominant $m_s' = 3/2$ component. Ion C is on the opposite sublattice; the associated E_1 exciton state $\langle e, m_s' |$ may have a dominant $m_s' = -3/2$ component. $\langle e, m_s' |$ and $\langle g, m_s |$ are even-parity states. (XBL 7712-6586)

on the same sublattice while A and C are second nearest neighbors on the opposite sublattices. The ground states $\langle g, m_s |$ of each ion are split by the exchange field into 6 Zeeman sublevels denoted by the spin quantum number $m_s = \pm 5/2, \pm 3/2$, and $\pm 1/2$. The excited state E_1 is a mixed state $\sum_{m_s'} a_{m_s'} \langle e, m_s' |$ with $m_s' = \pm 1/2, \pm 3/2$, although $\langle e, m_s' = 3/2 |$ or $\langle e, m_s' = -3/2 |$ may dominate. In addition to the exchange field, there is also the off-diagonal exchange interaction $J_{ij} S_i^{\pm} S_j^{\mp}$ between ion pairs. We shall treat it as a perturbation. Then, if the Mn ion A is initially excited, the one-magnon sideband emission results from an allowed electronic transition $\langle e, m_s' |_A \rightarrow \langle e', 3/2 |_A$ followed by an exchange spin-flip transition between A and B, $\langle e' 3/2 |_A \langle g, 5/2 |_B \rightarrow \langle g, 5/2 |_A \langle g, 3/2 |_B$, or from the exchange spin-flip $\langle e, m_s' |_A \langle g, 5/2 |_B \rightarrow \langle e', 5/2 |_A \langle g, 3/2 |_B$ followed by the allowed transition $\langle e', 5/2 |_A \rightarrow \langle g, 5/2 |_A$. Either process involves $\Delta m_s = 1$ corresponding to the emission of one magnon. Now, similar physical processes of the same perturbation order can give rise to the n-magnon sidebands with $n \leq 6$. For example, $\langle e, m_s' |_A \rightarrow \langle e', 3/2 |_A$ followed by $\langle e', 3/2 |_A \langle g, -5/2 |_C \rightarrow \langle g, 1/2 |_A \langle g, -3/2 |_C$ via $J_{AC} S_A^- S_C^+$ leads to a three-magnon sideband that can have comparable strength to the one-magnon sideband. Experimentally, the π-polarization spectrum in Fig. 1 even shows a three-magnon sideband stronger than the one-magnon sideband. In a similar manner, the two-magnon sideband can be explained by $\langle e, m_s' |_A \rightarrow \langle e', 1/2 |_A$ followed by $\langle e', 1/2 |_A \langle g, 5/2 |_B \rightarrow \langle g, 3/2 |_A \langle g, 3/2 |_B$ and others; the four-magnon sideband can be explained by $\langle e', 1/2 |_A \rightarrow \langle e', 1/2 |_A$ followed by $\langle e', 1/2 |_A \langle g, -5/2 |_C \rightarrow \langle g, -1/2 |_A \langle g, -3/2 |_C$ and others, etc.

In this model with $J_{ij} S_i^{\pm} S_j^{\mp}$ treated as a perturbation, the n-magnon sidebands with $n > 6$ will have to arise from a higher-order process utilizing $J_{ij} S_i^{\pm} S_j^{\mp}$ more than once. Strictly speaking, we should treat the exchange interaction as a strong coupling Hamiltonian and solve the eigenenergies and eigenstates for a cluster of neighboring Mn ions. If the spin part is isolated from the orbital part, then this is just the sudden approximation model proposed by Bhandari and Falicov.[2] In such a model, all the multi-magnon sidebands are treated on the same footing.

1. E. Strauss, V. Gerhardt, and H. Riederer, J. Luminescence 12, 13, 239 (1976).
2. R. Bhandari and L. M. Falicov, J. Phys. C5, 1445 (1972).

3. SUM-FREQUENCY GENERATION IN Na VAPOR VIA A RESONANT QUADRUPOLE TRANSITION

Donald S. Bethune, Robert W. Smith and Y. Ron Shen

Detailed experiments have been performed to study quadrupole sum-frequency generation (QSFG) in sodium vapor. We have made a complete theoretical treatment of quadrupole sum- and difference-frequency generation that includes the effects of spin-orbit and Zeeman splittings. The predictions of this theory have been experimentally confirmed and its limitations have been determined. Among the limiting effects were field-induced refractive index changes, two-photon saturation, and multi-photon absorption. We have also measured the quadrupole transition matrix element $\langle 3s | 1/2\, z^2 | 4d \rangle$ of sodium using an interference technique involving QSFG. As a generalization of three-wave mixing processes involving a quadrupole transition, we have considered quadrupole difference-frequency generation in cesium vapor.

To observe QSFG we used two flashlamp-pumped dye lasers in a noncollinear geometry focused into a "heat-pipe" oven containing sodium vapor at a density of about 10^{16} atoms/cm^3. One laser (ω_1) was tuned 10 to 100 cm^{-1} below the 3s → 3p transition (16 956.2 cm^{-1}); the other (ω_2) was tuned such that $\omega_1 + \omega_2$ was nearly resonant with the 3s → 4d transition (34 548.8 cm^{-1}). Using the anamolous dispersion of the 3p doublet, phasematching was achieved by varying the angle θ between the two input beams. The elementary theory predicted that the output power at $\omega = \omega_1 + \omega_2$ should be proportional to $N^2 P_1 P_2$, where N is the atomic density and $P_1(P_2)$ is the input power at $\omega_1(\omega_2)$. Figures 1 and 2 show

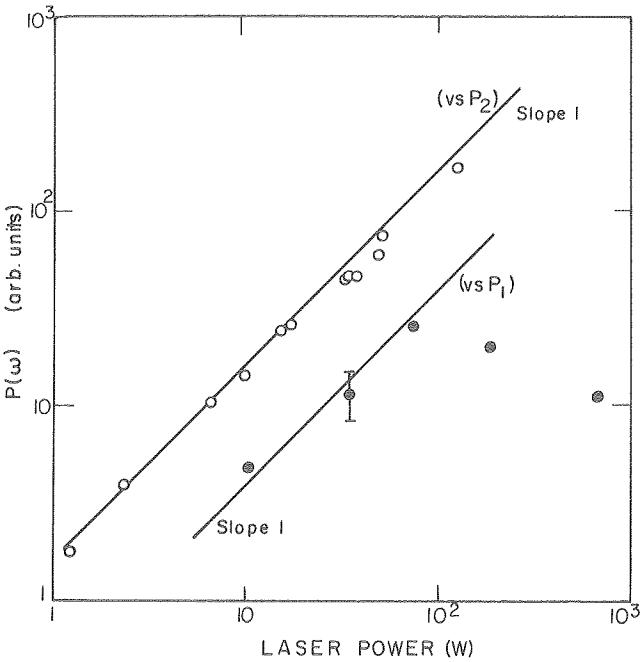

Fig. 1. Normalized output power $P(\omega)/P(\omega_2)$ vs $P(\omega_1)$ and $P(\omega)/P(\omega_1)$ vs $P(\omega_2)$. p = 1 Torr, $\omega_{3p_{1/2}} - \omega_1 = 21.2\ cm^{-1}$.
(XBL 766-7037)

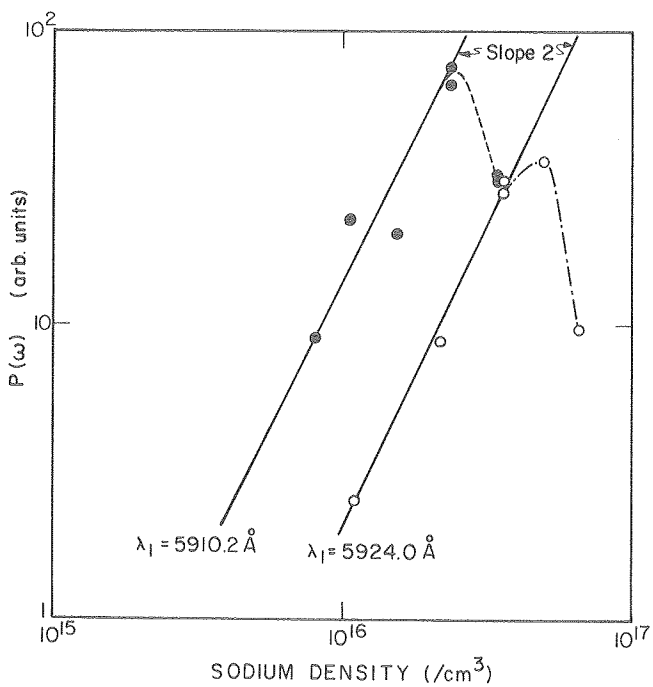

Fig. 2. Phase-matched sum-frequency output $P(\omega)$ as a function of sodium density N at $\omega_{3p_{1/2}} - \omega_1 = 40.8\ cm^{-1}$ and $80.4\ cm^{-1}$. The other parameter fixed in the experiment are $P_1 \sim 2W$, $P_2 \sim 20W$ and $\omega_1 + \omega_2 = \omega_{4d}$.
(XBL 766-7036)

the experimentally determined sum-frequency power $P(\omega)$ vs P_1P_2 and N, respectively. In both cases, the deviation from the simple theory can be satisfactorily explained by consideration of the field-induced refractive index change due to the presence of the field at ω_1. The first effect of this field-induced index is self-defocusing of the input laser beam, which greatly alters the beam size in the beam overlap region. If $\sigma_1 \gg \sigma_2$, where $\sigma_1(\sigma_2)$ is the radius of beam 1(2), the theory predicts that $P(\omega) \propto \sigma_2/\sigma_1$. Thus the output power will decrease as the beam defocuses. Secondly, the induced index change δn_1 alters the phase-matching condition through the dependence of $P(\omega)$ on the wavevector mismatch. This can be written in the form $P(\omega) \propto \exp\ (-\delta n_1^2/1.8 \times 10^{-5})^2)$ in our case. Since $\delta n_1 \sim 10^{-5}$ for $N = 10^{16}\ cm^{-3}$, a detuning of $10\ cm^{-1}$, and an intensity of $10^5\ W/cm^2$, the breaking of the phase-matching condition is the dominant reason for decreased output at high input intensities. The linear dependence of δn_1 on N implies that large densities increase induced index changes. We see that in the high density regime that $P(\omega)$ is no longer proportional to N^2, instead $P(\omega) \propto N^2 \exp(-N^2/\text{constant})$. This type of dependence is shown in Fig. 2. We also noted that, as the product of the intensities I_1I_2 was increased beyond $10^9\ W^2/cm^4$, there was a decrease in $P(\omega)$ and an increase in the resonance linewidth. This was attributed to the saturation of the two-photon transition 3s → 4d (see Fig. 3). Qualitative observations were made

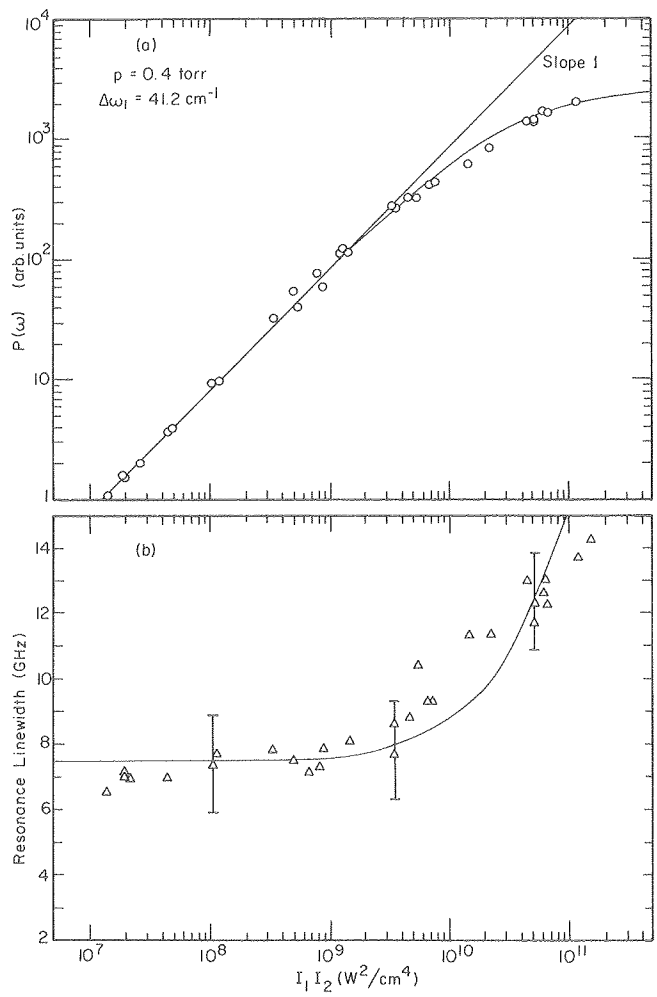

Fig. 3. (a) Sum-frequency power and (b) resonance linewidth as functions of the product of the input intensities I_1I_2. The solid curves are derived theoretically from expressions for the two-photon saturation effects. (XBL 772-5038)

that indicated that the effects of multiphoton ionization were ~ 10% depletion of the ground state population for the highest intensities used in the experiments.

We have also developed a technique to measure atomic quadrupole transition matrix elements relative to dipole matrix elements. The technique uses the interference between quadrupole and dc-field induced sum-frequency generation. The former involves the quadrupole transition while the latter involves only dipole transitions. By varying the applied dc-electric field and monitoring the changing output power, one can deduce that $\langle 3s | 1/2\, z^2 | 4d \rangle = 2.2\ a_0^2$ for sodium. (Here were used the known values of the 3s → 5p and 5p → 4d dipole moments.) This value can be compared to a calculated value of $1.36\ a_0^2$.[1]

Generalizing the theory to the case of quadropole difference-frequency generation (QDFG) we consider the generation of 14.6 μm radiation from Cs vapor. Pumping the $5s \rightarrow 6d_{5/2}$ and $5s \rightarrow 7p_{3/2}$ (2 cm^{-1} below) with 40 kW pump beams, the output should be about 1 W. The possibility of using QDFG as a tunable infrared source is presently under study.

1. E. C. Tull, M. Jackson, R. D. McEachran and M. Cohen, Can. J. Phys. 50, 1169 (1972).

4. THIRD ORDER NONLINEAR OPTICAL SPECTROSCOPY

Alexander Jacobson and Y. Ron Shen

We are conducting a series of experiments to measure the dispersion of the third order nonlinear optical susceptibility tensor $\chi^{(3)}(-\omega,\omega,\Omega,-\Omega)$ of a material as one laser frequency ω approaches, and passes through the other laser frequency Ω. Our experiments are closely related to experiments in coherent Raman spectroscopy, but we look at the resonant enhancement of $\chi^{(3)}$ due to low-frequency excitation modes (e.g., those responsible for Brillouin and Rayleigh-wing scattering) rather than that due to Raman modes. In particular, we hope to demonstrate similar improvements in detection sensitivity, freedom from fluorescence, and high resolution as have been demonstrated in the CARS,[1] RIKES,[2,3] and CW SRS[4] experiments in coherent Raman spectroscopy. If we are successful in the Rayleigh-Brillouin region of the spectrum, we will have further extended the domain in which nonlinear optical methods can supplement or supersede classical spontaneous scattering techniques.

Our current experimental efforts concern the dispersion of $\chi^{(3)}$ due to the reorientation of asymmetric molecules in Kerr liquids. Our setup is similar to that used in Ref. 2 to measure the Raman induced Kerr effect, except that both lasers are narrowband (0.3 cm^{-1}) and tunable, the strong "pump" and weak "probe" intersect in opposite directions, and the spectra are recorded electronically using a photomultiplier and a gated integrator. We can also vary the polarization state of the strong beam. For only the molecular reorientation mechanism, we expect[5,6]

$$\chi_{1212}(-\omega,\omega,\Omega,-\Omega) = \frac{N(\alpha_{\parallel} - \alpha_{\perp})^2}{360kT}\left[1 - \frac{2}{3}\,\frac{1}{1 + i(\Omega - \omega)\tau}\right]$$

$$\chi_{1221}(-\omega,\omega,\Omega,-\Omega) = \frac{N(\alpha_{\parallel} - \alpha_{\perp})^2}{360kT}\left[1 + \frac{1}{1 + i(\Omega - \omega)\tau}\right] \qquad (1)$$

where $\alpha_{\parallel}$ ($\perp$) are the molecular polarizabilities along (perpendicular to) the molecular axis and τ is the orientational relaxation time. For our sample, CS_2, Eq. (1) predicts peak susceptibilities comparable to strong Raman modes like that of benzene.

Our nonlinear spectrometer measures

$$|P_y^{(3)}(\omega)|^2 \propto |\chi_{1212}^{(3)}(-\omega,\omega,\Omega,-\Omega)E_x^*(\Omega)E_y(\Omega) + \chi_{1221}(-\omega,\omega,\Omega,-\Omega)E_x(\Omega)E_y^*(\Omega)|^2\mathscr{P}(\omega) \qquad (2)$$

where $\vec{E}(\Omega)$ is the pump beam field and $\mathscr{P}(\omega)$ is the probe beam power, provided that optical heterodyne terms arising from the interference of the field radiated by the nonlinear polarization $P_y^{(3)}(\omega)$ and a stray transmitted component $E_y(\omega)$ can be neglected.[3] Figure 1 shows some very preliminary results for various polarization states of the strong beam. The discrepancy between theory and agreement in Fig. 1 is attributed to 1) optical heterodyne terms non-negligible, 2) obvious Brillouin peaks not accounted for in Eq. (1) at $\Omega - \omega \simeq 0$, 3) a possible "mixed" polarization state across the strong beam aperture, and 4) impurities in the sample contributing a large nonresonant $\chi^{(3)}$.

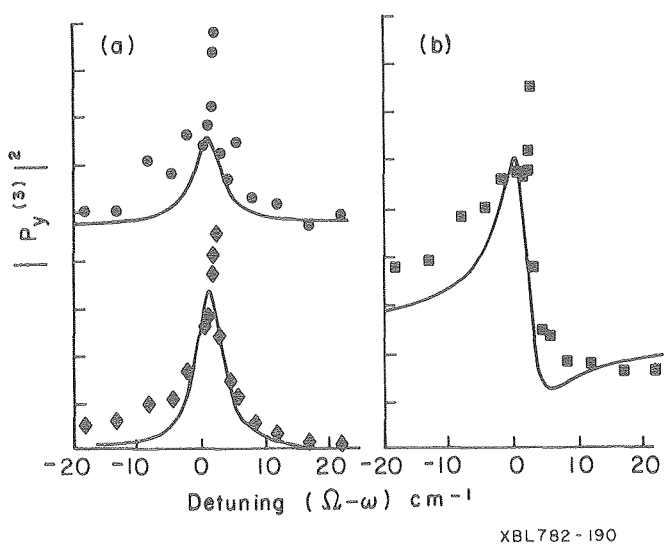

Fig. 1. (a) Upper-curve: optical Kerr signal with linearly polarized pump beam; Lower curve: with circularly polarized pump beam. (b) Optical Kerr signal with elliptically polarized pump beam.

(XBL 782-190)

Our principal experimental difficulty is the length of time necessary to take and analyze data, which is done point by point by hand. This is about

to be overcome by a microprocessor-controlled grating drive that will increase our data rate by a factor of ten to twenty. New linear and logarithmic normalizing electronics will permit displaying the spectrum directly and a recently acquired computer will be used on line to store it for later analysis.

Our future plans include studying the spectrum with even higher resolution near $\Omega - \omega = 0$. Thus, "Brillouin Induced Kerr Effect" will be studied using a pressure scanned laser of linewidth 0.03 - 0.05 cm^{-1}, the components of which have been procured and await assembly.

1. Begley, Harvey, and Byer, App. Phys. Lett. 25, 387 (1974).
2. Heiman, Hellwarth, Levenson, and Martin, Phys. Rev. Lett. 36, 189 (1976).
3. Eesley, Levenson, and Tolles, Optical Heterodyned Coherent Raman Spectroscopy, IEEE JQE, to be published.
4. A Owyoung and E. D. Jones, Opt. Lett. 1, 152 (1977).
5. A. Owyoung, thesis, Calif. Inst. Tech., 1971, unpublished.
6. E. G. Hanson, thesis, Univ. of Calif., Berkeley, 1976, unpublished.

5. USE OF ELLIPSE ROTATION WITHIN A LASER CAVITY FOR PULSE SHAPING

Raymond Hsu and Y. Ron Shen

Q switching allows a sizeable amount of energy to be stored in a ruby laser rod before it is released. But when the cavity is switched to the high Q state, then the energy is dumped in an concontrolled manner. We hope that by introducing an intensity dependent loss into the laser cavity, we will be able to control this energy release. Suitably regulating the intensity at which this nonlinear loss begins to take effect should allow us to stretch the pulse out in a predictable manner. The primary requirements of the lossy medium used in the cavity are threefold: 1) fairly strong linearity, 2) intensity dependence should be easily controlled, and 3) no competing uncontrollable nonlinear losses. We have chosen to use the liquid crytal MBBA as the lossy medium, making use of its property of intensity-induced polarization. MBBA easily meets the first two requirements, especially the second, since we are able to vary both the intensity dependence and the response time of the medium. The response time is controlled by varying the temperature of the MBBA while the intensity dependence is controlled by the setting of the Fresnel rhombs on either side of the MBBA. Two photodiodes are used to sample the cavity intensities $\perp$ and $\parallel$ to the Glen Thomson prism. The parallel component measures cavity intensity while the perpendicular component measures the loss.

We have thus far tested two regimes: 1) the onset of nonlinear loss occurring at an intensity at or above the peak pulse intensity obtainable without the MBBA in the cavity and 2) the onset of nonlinear loss occuring at an intensity well below the peak pulse intensity obtainable without the MBBA in the cavity. Our results for case 1) are as expected—that is, a very mild, barely noticeable, stretching. Our results for case 2) however are significantly different from what is expected. The cavity intensity is reduced by a factor of 15-20 at all FR settings and significant instabilities have been encountered. We suspect the problems can be traced to an additional source of nonlinear loss and are now investigating the problem more closely to determine if these problems can be overcome.

6. BRILLOUIN SCATTERING SPECTROMETER

Tai C. Chiang and Y. Ron Shen

A Brillouin scattering spectrometer has been constructed with a three-pass Fabry-Perot. Discrimination against the elastic scattering background at the Brillouin lines can be reduced to less than 10^{-9}. Electronic feedback is used to stabilize the Fabry-Perot alignment and multiple scanning with multichannel detection is used for signal averaging and spectral recording. Because of the high finesse of the system, the spectrometer can be used to detect Brillouin scattering in materials with a high elastic scattering background such as liquid crystals and non-transparent solids. With the help of a dye laser, resonant Brillouin scattering also becomes possible.

We plan to use the spectrometer together with a dye laser to study resonant Brillouin scattering around excitons or the fundamental energy gap of a number of crystals. Since the Brillouin scattering in solids is generally several orders of magnitude weaker than in liquids, we do not expect to be able to carry out resonant Brillouin study deep in the interband transition. We also plan to study Brillouin scattering in layer compounds and in amorphous solids.

7. DC KERR EFFECTS IN LIQUID CRYSTALLINE MATERIALS

Toni Bischofberger, Robert Yu and Y. Ron Shen

We report the results of our recent measurements on the dc Kerr constants as functions of temperature for seven homologous compounds of p,p'-di-n-alkoxyazoxybenzenes (PAA) ($C_nH_{2n+1}O - C_6H_4 - N_2O - C_6H_4 - OC_nH_{2+1}$ with n = 1, 2, ---, 7). So far as we know, this is the first time the dc Kerr constants for a homologous series of compounds are measured.

The dc Kerr effect was measured at 6328 Å by using a 1-mW He-Ne laser as the light source. A low-frequency sinusoidal wave generator followed by a high-voltage power amplifier were used to drive the Kerr cell. The length of the cell and the separation of the electrodes were L = 1 cm and d = 0.2 cm, respectively. The cell was between a set of crossed polarizers. The beam passing through the analyzer due to induced birefringence in the cell was detected by a photomultiplier and was displayed on an oscilloscope to be measured.

The Kerr constant B of a sample at a given temperature was obtained from the slope of the measured induced birefringence as a linear function of $(E^{dc})^2$. We have obtained B as a function of T for the seven azoxybenzene derivatives with n = 1, 2, ---, 7 denoting the number of methylene groups in the alkyl chain. The results are shown in Fig. 1. We note that PAA (n = 1) is the only homologue whose dc Kerr constant changes in sign in the temperature range we studied. All other compounds in the homologous series have a negative dc Kerr constant, indicating that the permanent-dipole contribution dominates over the induced-dipole part.

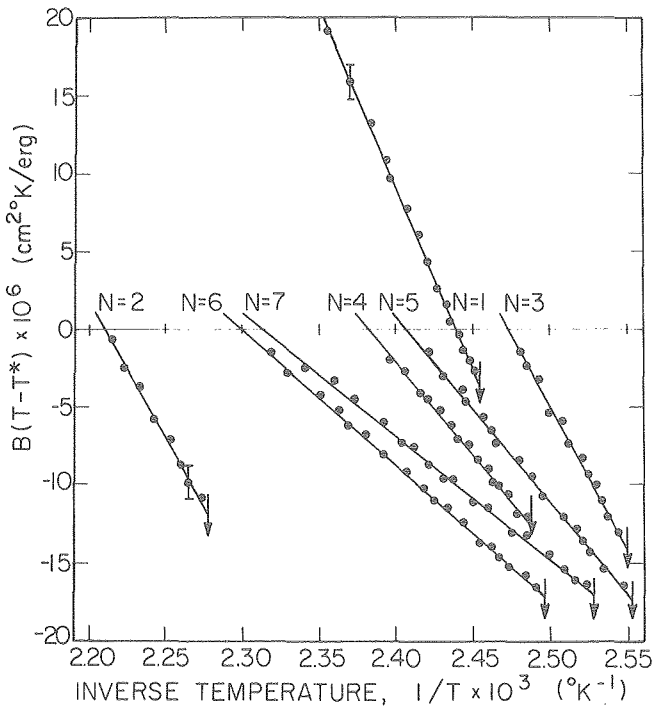

Fig. 1. Experimental results of $(T-T^*)$ B vs T^{-1} for the azoxybenzene derivatives n = 1,2,---, 7. The arrows indicate the isotropic-nematic transition temperature T_k. (XBL 773-5185)

We use the formalism of Landau-de Gennes to describe the dc Kerr effect. We find the Kerr constant to be

$$B = (2\omega/9c)(NhF/n_\omega)(\Delta\chi/a) \times [\Delta\alpha + F\mu^2(3\cos^2\beta - 1)/2kT]/(T - T^*). \quad (1)$$

As seen in the above equation, the induced-dipole part (the $\Delta\alpha$ term) and the permanent-dipole part (the μ^2 term) have different temperature dependence.

It happens that the various parameters N, $\bar{\varepsilon}$, $\Delta\chi$, a, and n_ω, in Eq. (1) are known from our previous measurements for the PAA series. Therefore, from Eq. (1) and the results in Fig. 1, we can deduce the values of $\Delta\alpha$ and $\mu(1 - 3\cos^2\beta)^{1/2}$ for these compounds. They are listed in Table 1 and also plotted as a function of the number n of methylene groups in the alkyl chain in Fig. 2. In Fig. 2, the anisotropy $\Delta\alpha$ in the dc molecular polarizability increases smoothly with increase of the alkyl chain length. No saturation of $\Delta\alpha$ at large n is found. This is in contrast to the behavior of the optical polarizability anisotropy $\Delta\alpha_{opt}$ that shows an obvious saturation at large n. The difference can be explained as follows. Because their lower transition frequencies are closer to the optical frequency, the core (azoxybenzene) electrons contribute much more to the optical $\Delta\alpha_{opt}$ than the bond electrons in the alkyl chains. Therefore, the increase of $\Delta\alpha_{opt}$ with n appears to be saturated. On the other hand, since the transition frequencies of both the core electrons and the bond electrons in the chain are far away from zero frequency, their contributions to the dc $\Delta\alpha$ are not very different and hence the increase of $\Delta\alpha$ with n is unsaturated.

The permanent-dipole factor $\mu(1 - 3\cos^2\beta)^{1/2}$ also shows a smooth increase with the alkyl chain length. Maier and Baumgartner have measured the permanent dipole moment μ of these homologous compounds in highly diluted solution of benzene. Their values are shown in Fig. 3. As expected, μ is essentially independent of the alkyl chains since it is known to come from the N_2O group in the core. Using these values for μ, we can then deduce the angle β. In all cases, we have found a β value that is between 45 and 90°. This is a confirmation on the correctness of our theoretical analysis since otherwise the deduced value of β could be physically unreasonable. We have plotted our values of β as a function of n in Fig. 3.

Table 1. Values of T_k, T^*, T^0, $\Delta\alpha$ and $\mu(1-3\cos^2\beta)^{1/2}$ for azoxybenzene derivatives witn n = 1, 2, ..., 7 deduced from our experiment.

n	1	2	3	4	5	6	7	
T_k	403.8	436.3	393.2	403.2	391.4	396.7	392.6	K
T^*	402.3	432.8	390.5	398.4	387.0	395.7	391.9	K
T^0	409.8	452.5	404.4	419.8	415.5	435.0	432.3	K
$\Delta\alpha \times 10^{24}$	37.0	37.3	39.4	42.3	46.2	50.7	54.0	cm^3
$\mu(1-3\cos^2\beta)^{1/2}$	1.49	1.60	1.61	1.73	1.84	2.01	2.09	Debye

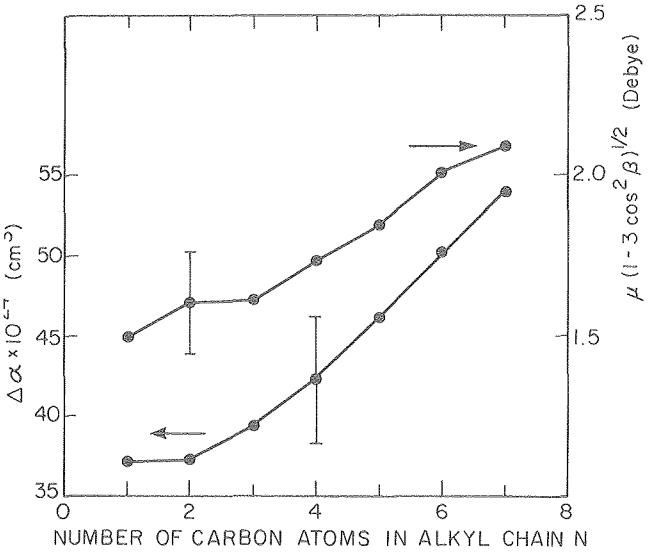

Fig. 2. Variation of $\Delta\alpha$ and $\mu(1-3\cos^2\beta)^{1/2}$ with the number n of carbon atoms in the alkyl chain of $C_nH_{2n+1}O - C_6H_4 - N_2O - C_6H_4 - OC_nH_{2n+1}$. (XBL 773-5188)

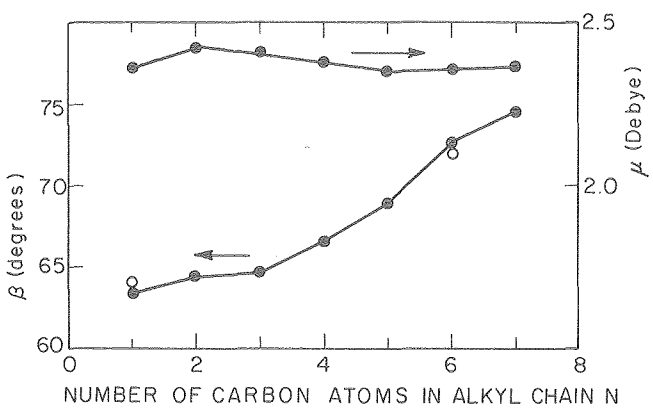

Fig. 3. Variations of the permanent dipole μ and the angle β with the number of carbon atoms in the alkyl chain of $C_nH_{2n+1}O - C_6H_4 - N_2O - C_6H_4 - OC_nH_{2n+1}$. The open circles are values of β obtained from dielectric dispersion measurements. (XBL 773-5187)

For n = 1 and 6, these values are in good agreement with those calculated from the dielectric dispersion measurements (also shown in Fig. 3). For larger n, the angle β between the permanent dipole and the long molecular axis is closer to 90°. The addition of methylene groups to the alkyl chains presumably creates a more balanced average local field at the core to align the permanent dipole more closely towards the normal of the molecular plane.

Since β is larger than 60°, the permanent dipoles like to align the long molecules nearly perpendicular to the applied field while the induced dipoles like to align the molecules parallel to the field. The competition between the two gives rise to the possible change of sign of the dc Kerr constant as it varies with temperature. This is experimentally observed in PAA. For the other homologous compounds, as β increases with n, the permanent-dipole contribution becomes larger and dominates over the induced-dipole contribution leading to the negative Kerr constants in a wide temperature range above T_k.

8. TRANSIENT BEHAVIOR OF A NONLINEAR OPTICAL FABRY-PEROT

Toni Bischofberger and Y. Ron Shen

Because of potential device applications, nonlinear Fabry-Perot (FP) interferometers have recently

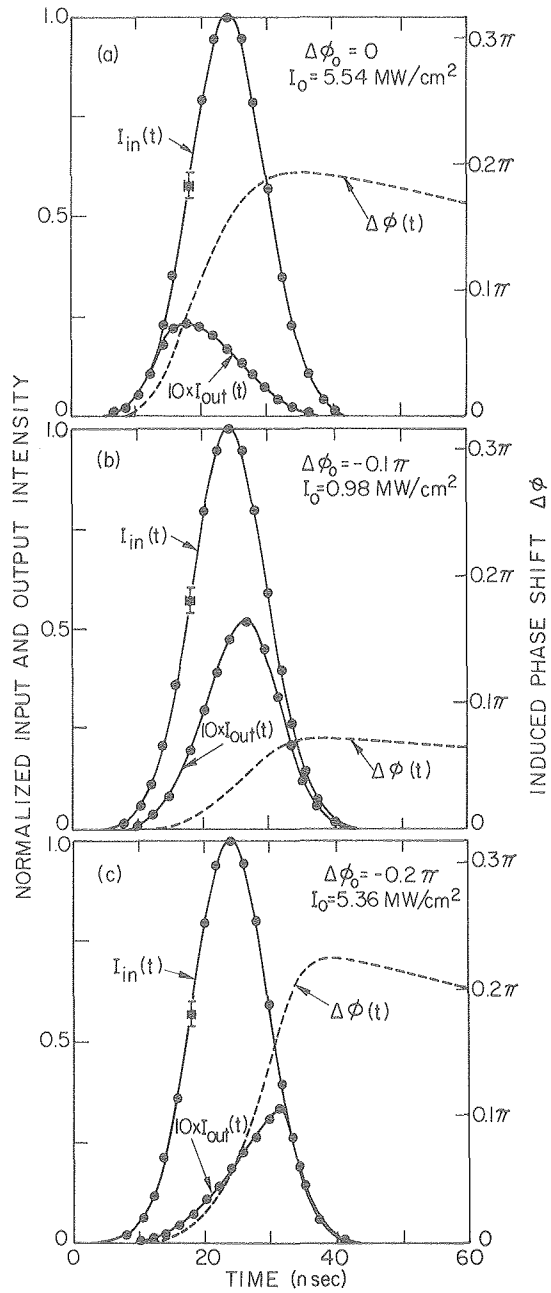

Fig. 1. Measured input and output intensities vs time for three different values of mistunings $\Delta\phi_0$. I_0 is the peak intensity of the input laser pulse $I_{in}(t)$. The solid curves of $I_{in}(t)$ are a least square fits to the measured input pulses. The solid curves of the output pulses $I_{out}(t)$ are calculated. The dashed curves are the corresponding time-dependent field-induced phase shift $\Delta\phi$. (XBL 779-6116)

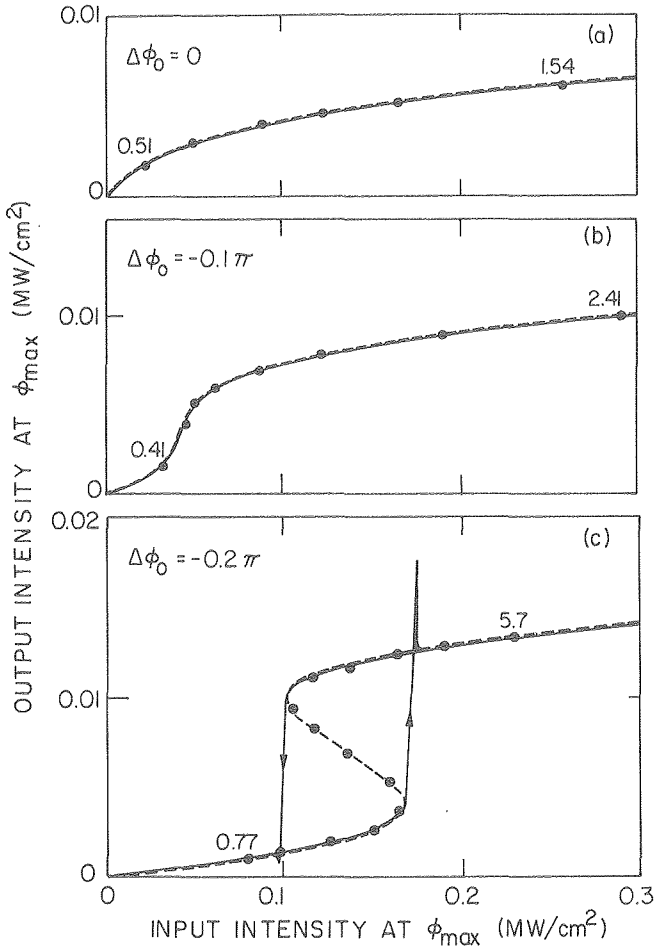

Fig. 2. Input vs output intensities at the maximum field-induced phase shift $\Delta\phi_{max}$ for three values of $\Delta\phi_0$. Each point corresponds to an input pulse with a certain peak intensity as indicated on a few in MW/cm^2. Dashed lines are the steady state characteristic curves for quasi-steady-state operations with τ_D = 2 ps assuming an input pulse with a peak intensity of 0.3 MW/cm^2. The bistable mode of operation in Fig. 2c shows overshoots immediately after switching. (XBL 779-6117)

attracted much attention. Szoke et al.[1] first suggested the use of a nonlinearly absorbing FP for optical limiting, discriminating, and bistable operations. Since then, McCall and coworkers have successfully demonstrated these operations using either sodium vapor or ruby as the nonlinear medium in their FP.[2] They noticed, however, that their observations were dominated by the field-induced refractive index rather than by nonlinear absorption. Nonlinear FP with pure refractive nonlinearity has been proposed and a detailed theoretical analysis for the steady-state operation of an FP filled with nonabsorptive Kerr liquid has been worked out.

We are interested in studying the transient response of a nonlinear FP. We report here the preliminary results of the first such experimental investigation on laser pulse propagation in an FP filled with Kerr liquid—liquid crystal MBBA (n-p-methoxybenzylidene-p-butylaniline) in the isotropic phase at 45° C. The FP cavity was constructed with plane mirrors with d = 1 cm and R = 0.98 and had a finesse of ~13. The Q-switched ruby laser was of single mode with a Gaussian beam radius of 0.13 cm at the FP. It produced a pulse with a pulsewidth of ~ 12 nsec and a peak intensity of ~ 10 MW/cm^2. The input and the output pulses at the FP were measured on two simultaneously triggered Tecktronix 519 oscilloscopes. Measurements were made at the mistunings $\Delta\phi_0$ = 0, -0.1π, and -0.2π ($\phi_0 \equiv \Delta\phi_0$ + multiple of 2π) with varying pulse intensities. Each $\Delta\phi_0$ corresponded to a distinct mode of operation of the nonlinear FP in the steady state.

Figure 1 shoes the typical examples, one for each value of $\Delta\phi_0$. We have developed a theory taking into account both the molecular orientation of the Kerr liquid and the build-up time of the optical field inside the cavity. Figure 1 shows that agreement between theory and experiment is excellent.

We also show that for a sufficiently long orientational relaxation time when the induced phase shift $\Delta\phi$ ($t = t_{max}$) is a maximum, the corresponding output intensity $|E_{out}(t_{max})|^2$ vs the input intensity $|E_{in}(t_{max})|^2$ will yield the characteristic curve for the steady state nonlinear FP. This is shown in Fig. 2 in comparison with the true steady state characteristic (dashed) curves for the three mistuning cases. They show clearly three different modes of operation: a) the power limiter mode, b) the differential gain mode, and c) the bistable or discriminator mode.

1. A. Szoke, V. Daneu, J. Goldhar and N. A. Kurnit, Appl. Phys. Lett. 15, 376 (1969); E. Spiller, J. Appl. Phys. 43, 1673 (1972); J. W. Austin, (Ph.D. thesis), University of Southern California (1972).

2. S. L. McCall, Phys. Rev. A 9, 1515 (1974); H. M. Gibbs, S. L. McCall, and T.N.C. Venkatesan, Phys. Rev. Lett. 36, 1135 (1976); T.N.C. Venkatesan and S. L. McCall, Appl. Phys. Lett. 30, 282 (1977); T.N.C. Venkatesan, (Ph.D thesis), City University of New York (1972).

9. LASER INTERACTION WITH MOLECULAR BEAMS

Aasmund S. Sudbø, Yuan T. Lee and Y. Ron Shen

In collaboration with Prof. Yuan T. Lee's group, we are setting up a molecular beam machine for experiments of laser interaction with atoms or molecules under collisionless condition. The machine will provide a well-collimated molecular beam with density up to 10^{13} molecules per cm^3 or two such beams at 90° with each other. Laser beams can be used to excite one or both molecular beams. They can also be used to probe molecules after the molecules are excited by lasers or collisions. We plan to study the following problems with the machine in the near future:

a) Photoemission spectroscopy of atoms and molecules.
b) Coherent antiStokes Raman spectroscopy to probe excited molecular species.
c) Laser-induced fluorescence or resonant Raman study of atoms or molecules.
d) Molecular dynamics probed by ultrashort laser pulses.

10. THEORY OF MULTIPHOTON DISSOCIATION OF MOLECULES

Edward R. Grant, Peter A. Schulz, Aasmund S. Sudbø, Yuan T. Lee, and Y. Ron Shen

We assume that the multiphoton excitation of a molecule can be described by stepwise incoherent one-photon transitions among a set of equally spaced energy levels; the degeneracy factor of each level is given by corresponding molecular density of states that can be calculated. The excitation is then governed by the following set of rate equations:

$$dN_m/dt = C^a_{m-1} N_{m-1} + C^e_m N_{m+1} - (C^a_m + C^e_{m-1})N_m - K_m N_m . \quad (1)$$

Here, N_m is the population in the mth excited level; K_m is the molecular dissociation rate from the mth level calculated from the RRKM statistical theory for unimolecular dissociation. (For levels below the dissociation energy E_0 we have $K_m = 0$.) C^a_m and C^e_m are respectively the absorption rate from level m to m + 1 and the emission rate from m + 1 to m. For one-photon transitions, we can write

$$C^a_m = \sigma_m \frac{I}{h\nu}, \qquad C^e_m/C^a_m = g_m/g_{m+1} \quad (2)$$

where σ_m is the absorption cross section for m to m + 1 transition, $h\nu$ is the photon energy, I is the laser intensity, and g_m is the degeneracy factor for the mth level.

For a given molecule with σ_m and I(t) specified, the set of rate equations in Eq. (1) can be easily solved on a computer. We have performed such a calculation using SF_6 as an example. The frequencies of the vibrational modes of SF_6 are well known. To find the densities of states, we used exact count at low energies and the Whitten-Rabinovitch formula at higher energies. The dissociation energy E_0 was chosen to be 78 kcal/mole. The spacing between adjacent levels is 944 cm^{-1}. Because of anharmonic coupling among vibrational modes, the absorption cross section σ_m was expected to decrease with increase of m. We assumed that σ_m takes the form

$$\sigma_m = \exp[\alpha m + \beta] \quad (3)$$

where $\alpha = -0.029$ and $\beta = -42.9$ for σ_m in cm^2. These values were chosen so that our numerical results fit the experimentally observed variation of the average number of photons absorbed and the dissociation yield as a function of laser energy fluence.

Figure 1 shows the population distribution at various times calculated with these parameters for a 100-ns 200-MW/cm^2 reactangular laser pulse excitation. Initially only the ground level is populated, but the laser excitation, being a stochastic process, soon distributes the population over many levels. As time goes on, the population is continuously pumped

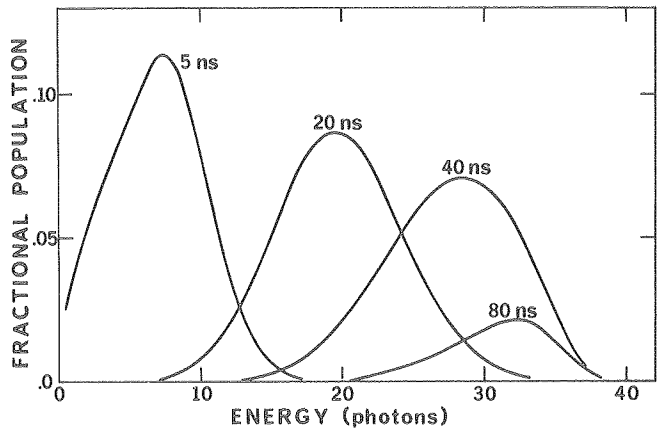

Fig. 1. Population distribution at various times produced by a 100-ns rectangular laser pulse excitation of 200 MW/cm^2. (XBL 779-2428)

up and the distribution curve shifts to higher energies. Correspondingly, the average excitation energy, $\langle n \rangle h\nu$, also increases with time. At $t \sim 20$ ns, the high-energy tail of the distribution curve clearly extends beyond the dissociation level. We should then expect the onset of molecular dissociation. As the laser excitation continuously drives the population distribution upward, the dissociation yield increases rapidly. For those levels well above E_0, the depletion of their population is dominated by the dissociation rate. Consequently, the further up-excitation of the population is restricted, the population at the high-energy tail is heavily depleted by dissociation and the distribution curve becomes asymmetric. The t = 80 ns curve in Fig. 1 clearly exhibits this feature.

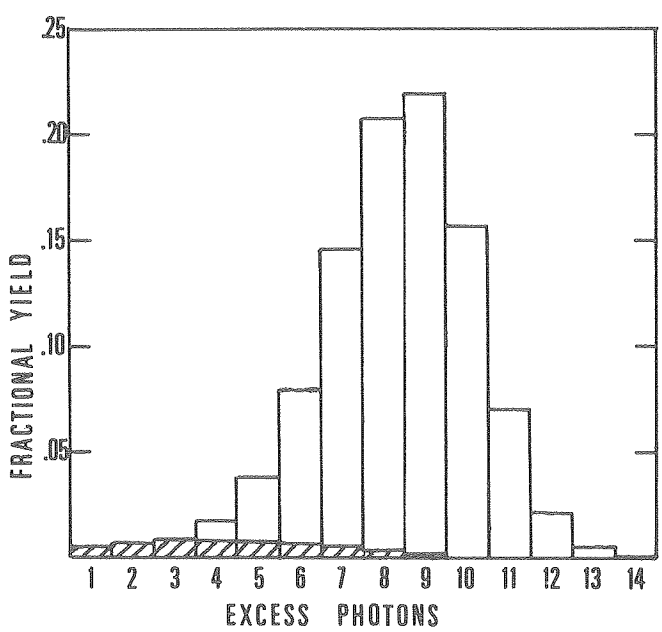

Fig. 2. Calculated dissociation yields form various levels above the dissociation energy during the laser pulse (unshaded region) and after the laser pulse (shaded region) for a 100-ns, 200 MW/cm^2 laser pulse excitation. (XBL 778-9879)

Our model also allows us to calculate the dissociation yield as a function of time. More specifically, we can calculate the dissociation yield per unit time $Y_m(t) = K_m N_m(t)$ from each m level above E_0. In Fig. 2, we show the integrated dissociation yields from each level during and after the laser pulse, respectively. The total dissociation yield is of course the sum of all. As shown in Fig. 2, most of the molecules dissociate during the laser pulse. (More than half dissociate before 2/3 of the laser pulse is over.) They dissociate mainly from those levels 6 to 11 hν above E_0. These results are fairly consistent with the experimental observations. In particular, we can now understand why SF_6 will undergo a two-step dissociation process if the exciting laser pulse is sufficiently long and intense. In the primary dissociation of SF_6 into SF_5 and F, our molecular beam experiment has shown that on the average less than hν of the total excess energy appears as recoil energy of the fragments; the rest is retained by SF_5 in its internal degrees of freedom. With the total excess energy $\gtrsim 6$ hν, this puts SF_5 in the excited quasi-continuum states. Then, if the laser field is still present for a sufficiently long time, the SF_5 fragments can readily absorb additional photons to exceed the threshold for subsequent dissociation into SF_4 + F. Apparently, this can happen for the case shown in Fig. 2.

11. EXPERIMENTS ON MULTIPHOTON DISSOCIATION OF MOLECULES

In collaboration with Prof. Y. T. Lee's group.

See Section on Molecular Beam Laser Isotope Separation, p. 492.

12. RESEARCH PLANS FOR CALENDAR YEAR 1978

Y. Ron Shen

In collaboration with Prof. Y. T. Lee's group, we shall continue our study on the multiphoton dissociation process of polyatomic molecules. Emphasis will be on the dissociation dynamics in various different molecules, on excitations with two lasers, on isotopic selectivity, and on dissociation yield. A number of other projects involving interaction of lasers with molecular beams in collaboration with Prof. Lee's group are in progress or being planned. These include infrared spectroscopy of ions, dynamics of molecular predissociation, laser selective dissociation of van der Waal molecules, picoseond spectroscopy of molecular dynamics, etc.

We plan to continue our work on nonlinear excitation and detection of surface electromagnetic waves in semiconductors and metals. Various geometries will be considered, and effects of overlayers on metal surfaces will be investigated.

We shall test out the sensitivity and resolution capability of our newly developed nonlinear optical spectroscopic technique for detecting low-frequency excitations. We shall apply the techniques on various gases, liquids, and solids.

Three-wave and four-wave mixing experiments will be continued. In particular, we shall evaluate the potential of infrared generation by three-wave mixing using tunable dye lasers. We also intend to try out experiments on resonant coherent Raman scattering from which one expects to learn selective information about electrons, phonons, and electron-phonon interaction.

Brillouin and Raman spectrometers will continuously be used to study various materials. The problem of nonlinear Fabry-Perot as an optical switching device will be investigated. Various linear and nonlinear optical effects in liquid crystals will be studied with partial support from NSF.

13. 1977 PUBLICATIONS AND REPORTS

Y. Ron Shen and Associates

Journals and Books

1. Y. R. Shen, Nonlinear Infrared Generation, Chapter 1, Topic Series of Applied Physics, edited by Y. R. Shen (Springer-Verlag, Berlin, 1977) p. 1.

*2. K. Miyano and Y. R. Shen, Excitation of Stripe Domain Patterns by Propagating Acoustic Waves in an Oriented Nematic Film, Rev. A 15, 2471 (1977).

*3. E. G. Hanson, Y. R. Shen and G. K. L. Wong, Self-Focusing: From Transient to Quasi-Steady State, Optics Comm. 20, 45 (1977).

4. J. R. Morris and Y. R. Shen, Theory of Far Infrared Generation by Optical Mixing, Phys. Rev. A 15, 1153 (1977).

5. J. Camassel, S. Kohn, Y. R. Shen and F. Levy, Modulation Spectroscopy of Semiconducting Group IV-A and IV-B Dichalcogenides, Nuovo Cimento 38B, 185 1977).

6. T. C. Chiang, J. Camassel, J. P. Voichovsky and Y. R. Shen, Resonant Raman Scattering in GaSe and GaS_xSe_{1-x}, Nuovo Cimento 38B, 301 (1977).

7. M. J. Coggiola, P. A. Schulz, Y. T. Lee and Y. R. Shen, A Molecular Beam Study of Multiphoton Dissociation of SF_6, Phys. Rev. Lett. 38, 17 (1977).

8. D. Bethune, R. Smith and Y. R. Shen, Measurement of A Quadrupole and DC-Field-Induced Sum-Frequency Generation, Phys. Rev. Lett. 38,647 (1977).

9. F. DeMartini, M. Colocci, S. E. Kohn and Y. R. Shen, Nonlinear Optical Excitation of Surface Exciton-Polaritons in ZnO, Phys. Rev. Lett. 38, 1223 (1977).

*10. E. G. Hanson, Y. R. Shen and G. K. L. Wong, Experimental Study of Self-Focusing in a Liquid Crystalline Medium, Appl. Phys. 14, 65 (1977).

11. E. R. Grant, M. J. Coggiola, Y. T. Lee, P. A. Schulz, Aa. S. Sudbø and Y. R. Shen, Studies of Multiphoton Dissociation of Polyatomic Molecules with Crossed Laser and Molecular Beams, State-to State Chemistry, ACS Symposium Series 56, 72 (1977).

12. E. R. Grant, P. A. Schulz, Aa. S. Sudbø, M. J. Coggiola, Y. T. Lee and Y. R. Shen, "Multiphoton Dissociation of Polyatomic Molecules Studied with a Molecular Beam" in Laser Spectroscopy III, J. L. Hall and J. L. Carlsten, Eds. (Springer-Verlag, Berlin, 1977) p. 94.

13. Y. R. Shen, "Some Fundamental Aspects of Nonlinear Optics" in Nonlinear Spectroscopy, N. Bloembergen, Ed. (Soc. Italiana di Fisica, Bologna, Italy, Course 64, 1977) p. 170.

14. Y. R. Shen, "Nonlinear Optics in One-Dimensional Periodic Medium" in Nonlinear Spectroscopy, N. Bloembergen, Ed. (Soc. Italiana di Fisica, Bologna, Italy, Course 64, 1977) p. 201.

15. Y. R. Shen, "Nonlinear Optical Study of Pretransitional Behavior in Liquid Crystalline Materials" in Nonlinear Spectroscopy, N. Bloembergen, Ed. (Soc. Italiana di Fisica, Bologna, Italy, Course 64, 1977) p. 210.

Conferences

1. F. DeMartini, M. Colocci, S. E. Kohn and Y. R. Shen, Study of Surface Exciton-Polaritons in ZnO by Nonlinear Optical Excitations, Bull Am. Phys. Soc. 22, 279 (1977).

*2. T. Bischofberger, R. Yu and Y. R. Shen, Low-Frequency Kerr Effect in a Homologous Series of Nematic Compounds, Bull. Am. Phys. Soc. 22, 298 (1977).

3. E. R. Grant, M. J. Coggiola, Y. T. Lee, P. A. Schulz and Y. R. Shen, Dynamics of Infrared Multiphoton Dissociation of SF_6 by Molecular Beam Method, VI International Symposium on Molecular Beams, The Netherlands, April 18-22, 1977.

4. D. Bethune, R. Smith and Y. R. Shen, Second-Order Sum- and Difference-Frequency Generation via Quadrupole Transitions in Atomic Vapor, Fourth Rochester Confernece on Coherence and Quantum Optics, Rochester, N. Y., June 8-10, 1977.

5. E. R. Grant, M. J. Coggiola, P. A. Schulz, Y. T. Lee and Y. R. Shen, A Molecular Beam Study of the Multiphoton Dissociation of SF_6, Am. Chem. Soc. Division of Physical Chemistry National Meeting, New Orleans, Louisiana, March 21-23, 1977.

6. E. R. Grant, M. J. Coggiola, Y. T. Lee, P. A. Schulz, Aa. S. Sudbø and Y. R. Shen, Internal State and Two-Frequency Dependence in Multiphoton Dissociation of Polyatomic Molecules, International Conference on Multiphoton Processes, University of Rochester, Rochester, N. Y., June 6-9, 1977.

7. E. R. Grant, M. J. Coggiola, Y. T. Lee, P. A. Schulz, Aa. S. Sudbø and Y. R. Shen, A Model for the Time Evolution of Multiphoton Absorption and Dissociation, International Conference on Multiphoton Processes, University of Rochester, Rochester, N. Y., June 6-9, 1977.

8. E. R. Grant, P. A. Schultz, Aa. S. Sudbø, M. J. Cogglia, Y. T. Lee and Y. R. Shen, Multiphoton Dissociation of Polyatomic Molecules Studied with a Molecular Beam, Third International Conference on Laser Spectroscopy, Jackson Lake Lodge, Wyoming, July 4-8, 1977.

9. E. R. Grant, P. A. Schulz, As. S. Sudbø, M. J. Coggiola, Y. R. Shen and Y. T. Lee, Molecular Beam Studies on Multiphoton Dissociation of Polyatomic Molecules, International Conference on Multiphoton Processes, University of Rochester, Rochester, N. Y., June 6-9, 1977.

LBL Reports

1. Eric G. Hanson, Nonlinear Optical Effects in Liquid Crystals, (Ph.D. thesis), LBL-6022.

2. E. R. Grant, M. J. Coggiola, Y. T. Lee, P. A. Schulz and Y. R. Shen, Dynamics of Infrared Multiphoton Dissociation of SF_6 Studied by Molecular Beam Method, LBL-6035.

3. Y. R. Shen, Nonlinear Optical Effects, LBL-6091.

4. T. Bischofberger, R. Yu, and Y. R. Shen, Measurement of DC Kerr Constants for a Homologous Series of Nematic Compounds, LBL-6096.

5. E. R. Grant, M. J. Coggiola, Y. T. Lee, P. A. Schulz Aa. S. Sudbø and Y. R. Shen, The Extent of Energy Randomization in the Infrared Multiphonon Dissociation of SF_6 , LBL-6201.

6. D. S. Bethune, Optical Quadrupole Sum-Frequency Generation in Sodium Vapor, (Ph.D. thesis), LBL-6264.

7. J. R. Morris, Optical Difference-Frequency Generation of Far Infrared Radiation, (Ph.D. thesis), LBL-6632.

8. E. R. Grant, P. A. Schulz, As. S. Sudbø, M. J. Coggiola, Y. R. Shen and Y. T. Lee, Molecular Beam Studies on Multiphoton Dissociation of Polyatomic Molecules, LBL-6275.

9. D. Bethune, R. Smith and Y. R. Shen, Sum-Frequency Generation via a Resonant Quadrupole Transition in Sodium, LBL-6672.

10. D. Bethune, R. Smith and Y. R. Shen, Second-Order Sum- and Difference-Frequency Generation via Quadrupole Transitions in Atomic Vapors, LBL-6918.

11. S. E. Kohn, Wavelength Modulation Spectroscopy of Semiconductors, (Ph.D. thesis), LBL-6919.

12. T. Bischofberger and Y. R. Shen, Transient Behavior of a Nonlinear Fabry-Perot, LBL-6924.

13. E. R. Grant, P. A. Schulz, Aa. S. Sudbø, Y. R. Shen and Y. T. Lee, Is Multiphoton Dissociation of Molecules a Statistical Thermal Process, LBL-6656.

14. Aa. S. Sudbø, P. A. Schulz, E. R. Grant, Y. R. Shen and Y. T. Lee, Multiphoton Dissociation Products from Halogenated Hydrocarbons, LBL-6966.

15. T. C. Chiang, P. Salvi, J. Davies and Y. R. Shen, Multi-Magnon Luminescence Sidebands in Antiferromagnets, LBL-6992.

*Partially supported by National Science Foundation.

c. Excited Quantum Fluids in Solids

Carson D. Jeffries, Principal Investigator

Introduction. It has been established, originally by Soviet physicists, that intense optical excitation of semiconductors at low temperatures can lead to the formation of an electron-hole liquid. This is a novel state of matter, having both classical and quantum properties. The electrons and holes formed by the excitation form free excitons, which are bosons. Although it was expected theoretically that a Bose condensation might occur, it was discovered that the exciton "gas" undergoes a gas-liquid phase transition into a conducting electron-hole liquid, somewhat analogous to the ordinary water vapor-fog droplet transition. The liquid forms small electron-hole droplets which can freely move within the crystal up to the velocity of sound. Although the liquid medium is an excited state of the crystal (lifetime $\approx 10^{-4}$ s) it is the first example of a Fermi liquid in a periodic lattice and, as such, has high theoretical interest. It can also be viewed as an anisotropic multi-component plasma of constant density ($\sim 10^{17}$ cm^{-3}), but easily compressible. We have concentrated on detailed and quantitative studies of the liquid in ultrapure germanium: the nucleation process of the droplets, both experimentally and theoretically; the motion, diffusion, and explosion of the droplets; the resonance scattering of free carriers by the droplets, which determines their size (~ 1 μm); the confinement of sizeable volumes (~ 1 mm^3) of the liquid in potential wells of crystal strain, and the measurement of the properties of this strain-confined liquid; observation of magneto-oscillatory behavior characteristic of Fermi systems; measurement of the compressibility of the liquid; observation and theoretical explanation of the deformation of the drops in a magnetic field (magnetostriction); observation of microwave Alfvén wave dimensional resonances in large single drops; and studies of lifetimes, decay mechanisms, and phonon interactions of the droplets. It is known that similar liquids exist in several other semiconductors (Si, GaP, CdSe) and that these excited quantum fluids represent a general and fundamental type of excitation of crystalline solids. Professor C. Kittel is giving us assistance and advice on the theoretical aspects.

1. NUCLEATION PHENOMENA IN ELECTRON-HOLE DROPLET FORMATION

Robert M. Westervelt, Eugene E. Haller, and Carson D. Jeffries

Of prime interest is knowledge of the details of the nucleation of electron-hole drops (EHD) from a gas of free excitons (FE). We have completed both a quantitative nucleation theory and detailed experiments in pure Ge, obtaining good agreement and a basic understanding of this system. Optical pumping excites an electron up into the conduction band edge of the L point in the band structure, leaving a hole at the Γ point; these quickly combine into a FE, detected by its characteristic recombination luminescence at 714 meV. As the excitation power P is increased, a new luminescence line at 709 meV is observed at a well-defined "up-going" threshold power P_+; this is the characteristic recombination luminescence of an EHD. If the excitation is decreased the EHD luminescence persists down to a well-defined "down-going" threshold power P_-. Figure 1 shows data on this remarkable optical hysteresis phenomena: it is due to the existence of surface tension in the droplets and their finite lifetime. To avoid surface effects, sample volume excitation was used, by pumping at 1.52 μm in the indirect gap. Our nucleation theory predicts that in up-going excitation the increase in EHD luminescence is due to an increase in the concentration N of drops of nearly constant size; in down-going excitation, the drop concentration is expected to remain fixed while the size of each drop decreases until a critical power P_c where a droplet will suddenly collapse. That is, once a droplet is nucleated by supersaturation of the exciton gas density to overcome surface tension, it will continue to exist and can be reversibly varied in size by varying the excitation power if $P > P_c$; below P_c, the drop concentration should rapidly decrease to zero. This behavior is borne out by the data of Fig. 2, taken with the excitation power cycle shown in the inset: Power is increased to P_{max}, decreased to an intermediate Power P_2, and increased to a value $P_0 = 1.42$ mW cm^{-2}, just below the drop-formation threshold P_+ of Fig. 1. We find that motion along a down-going hysteresis curve is reversible if $P \gtrsim P_c$, but drops are irreversibly lost if $P \lesssim P_c$.

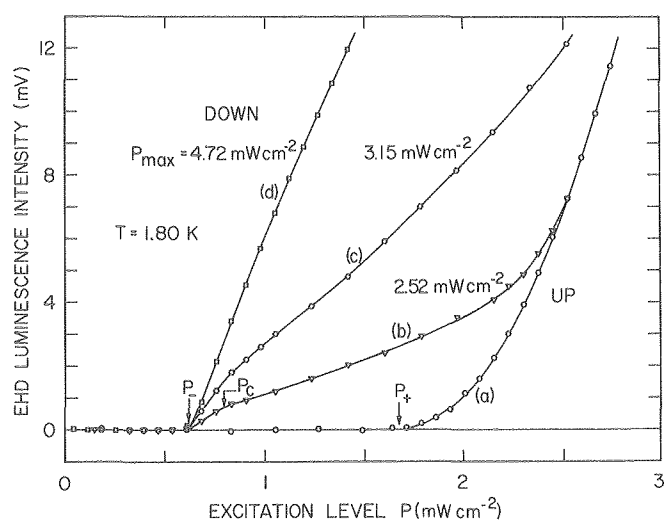

Fig. 1. Luminescence intensity of EHD in pure Ge vs up-going and down-going optical excitation power P, showing clear thresholds P_+ and P_-, and pronounced optical hysteresis, which provides a direct measurement of the droplet surface tension. Droplets collapse below a critical power P_c. (XBL 778-5976)

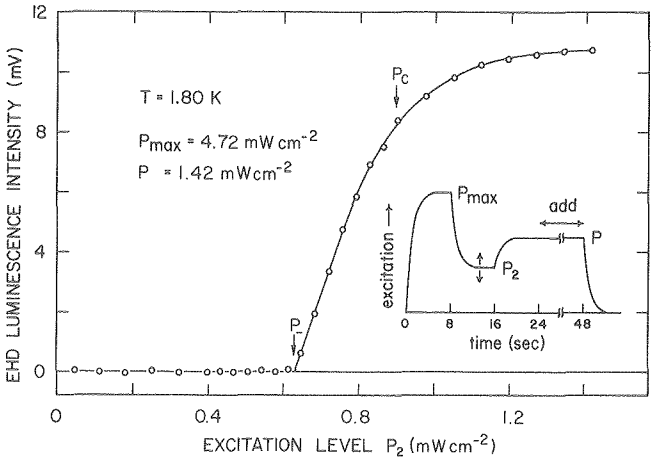

Fig. 2. Luminescence intensity of EHD observed just below drop-formation threshold, following an excitation power cycle that moves reversibly along a down-going hysteresis curve of Fig. 1, and irreversibly if $P < P_c$, where the droplets begin to collapse. At $P = P_-$ the drop concentration has entirely vanished. (XBL 778-5978)

These data clearly indicate the existence of metastable states of the FE-EHD system. For ordinary liquids such as water, metastable supersaturation effects become larger as the temperature is reduced. However, just the opposite is found, experimentally and theoretically, for the electron-hole liquid in Ge at temperatures below 2.1 K: the ratio P_+/P_- is found to decrease and, at 1.25 K, the system reaches equilibrium and the hysteresis disappears entirely, due to the finite EHD lifetime; this is quantitatively understood. However, at higher temperatures the metastable lifetimes are very long indeed. At T = 1.8 K we have measured the time evolution of i) the EHD luminescence reached on up-going excitation to $P = 2.3$ mW/cm^{-2}, just above threshold; and ii) the EHD luminescence at this same excitation power, but reached on down-going excitation from a much higher power. The data are shown in Fig. 3 and display an unusual logarithmic behavior, actually predicted by nucleation theory. The surprising feature is that once a drop is nucleated it persists for a very long time ($\sim 10^4$ s).

Other studies include: an investigation of effects of crystal dislocations and shallow electrically active impurities on excitation thresholds; measurement of a carefully calibrated FE-EHD phase diagram; accurate measurement of the EHD surface energy; measurement of the condensation energy of a free exciton onto a droplet; and a measurement of the EHD radiation enhancement factor, the ratio of the electron density at a hole to the average liquid density--a sensitive measure of the degree of e-h correlation in the liquid. Quite satisfactory agreement between data and theory is found.

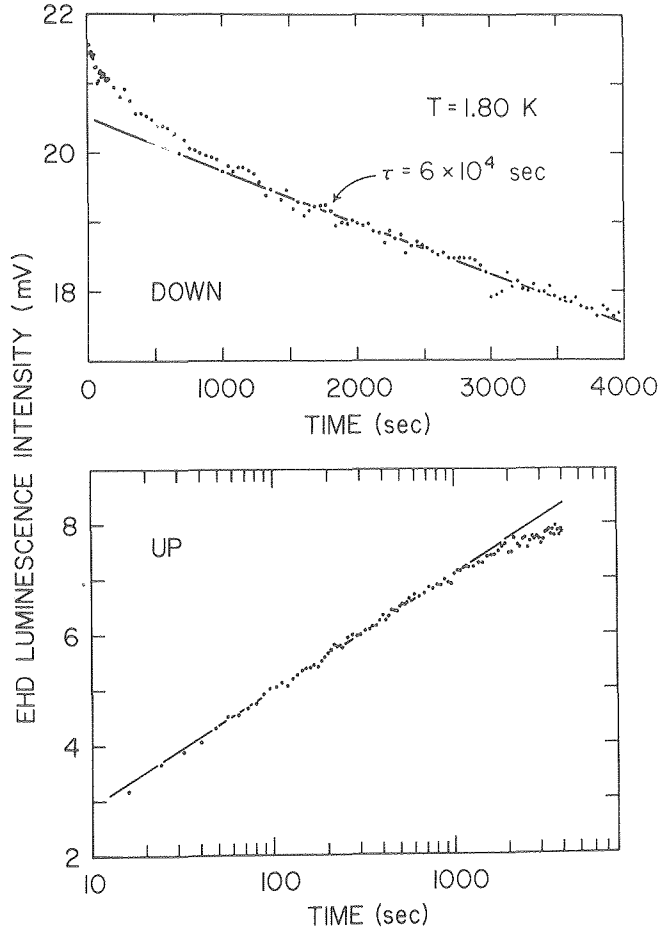

Fig. 3. Metastable time-development of the EHD luminescence in Ge, showing i) logarithmic increase for up-going excitation for very long times and ii) logarithmic and exponential decrease for down-going excitation. (XBL 778-2780)

2. MOTION OF ELECTRON-HOLE DROPLETS IN GERMANIUM

Robert M. Westervelt, Bernard S. Black, and Carson D. Jeffries

The motion of electron-hole droplets in Ge is receiving much attention, both theoretical and experimental. If the droplets are produced by, say, focused laser surface excitation, it is known that free carriers and probably the droplets themselves move rapidly away from the source region with velocities $\sim 10^2$ to 10^5 cm/s. The droplets can be moved by momentum transfer from free carriers, from excitons, and from a flux of hot phonons--the "phonon wind." They are also easily accelerated by crystal strains. Thus it is not surprising that earlier workers have reported values of the diffusion coefficient for droplets ranging from $D = 100$ cm^2/s to $D = 10^{-2}$ cm^2/s. We have used a new and very sensitive method to study

the motion of droplets at low excitation and find that $D \leqslant 10^{-7}$ cm^2/s, many orders lower than the previous results.

The experiment is based on the existence of hysteresis; see Fig. 1 of the previous section. The face of an ultrapure Ge crystal is uniformly illuminated continuously by light at $\lambda = 1.52$ μm, which gives volume excitation of free excitons in the entire crystal, but at a level slightly lower than P_+, the up-going threshold, so that no drops are yet present. Then a laser focused to a narrow stripe image is pulsed once on the crystal face, nucleating droplets in a narrow cylindrical region of the crystal. After the pulse no new droplets may be formed, and those that were formed continue to exist by virtue of surface condensation of the ever-present free excitons at a rate equal to the loss by e-h recombination. An image of the cylindrical droplet region is scanned by a mirror past the slit of a spectrometer, which thus records the EHD recombination radiation as a function of position x perpendicular to the axis of the cylinder. These luminescence profiles are measured periodically at various times t after the laser pulse, with t as long as 2×10^4 s. The results in Fig. 1 show that no statistically significant increase Δx in the full width at half maximum is observed at T = 2.1 K. From this we find $[(\Delta x)^2/t] = D \leqslant 10^{-7}$ cm^2/s. Thus in the ideal case of no spurious motion of droplets caused by phonon wind, strains, and exciton and carrier flux, the droplets do not move, probably because they are slightly bound to crystal impurities or dislocations. At higher temperatures we expect to find them engaging in a hopping motion. Since our method can detect drift velocities as small as $v \approx 10^{-5}$ cm/s, we plan to use it to sensitively measure the motion of droplets under applied forces of all types.

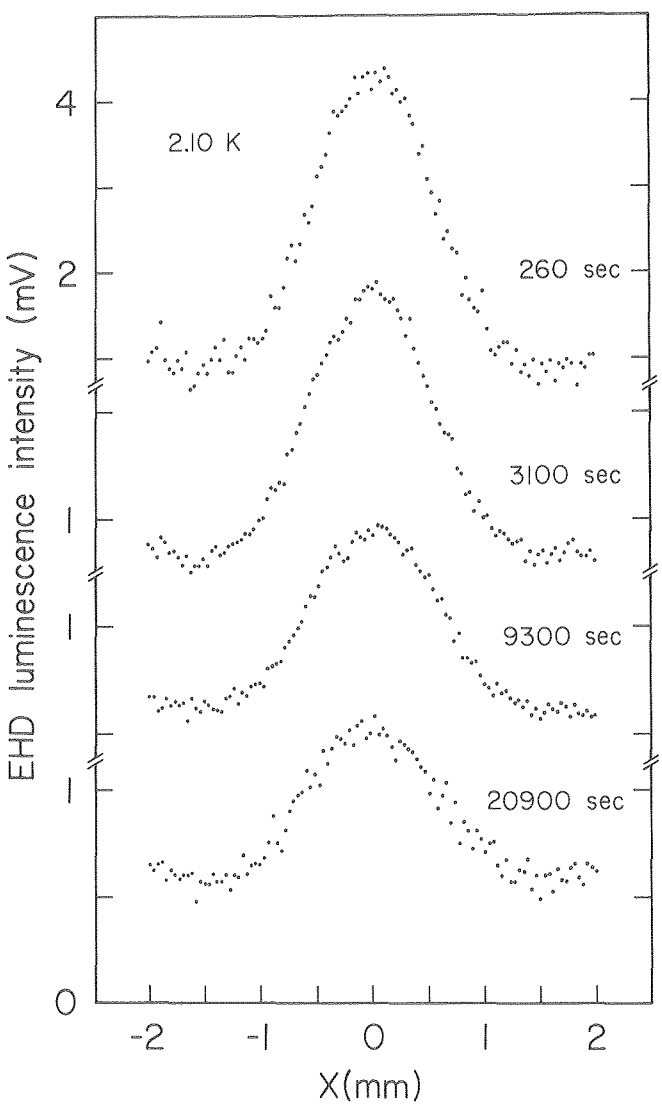

Fig. 1. Luminescence intensity profiles of a cylindrical-shaped volume of electron-hole droplets in Ge, at various times following their formation. These data show that a droplet remains essentially stationary and can be maintained for times as long as six hours. (XBL 781-23)

3. RESONANT SCATTERING OF FREE CARRIERS BY ELECTRON-HOLE DROPS

Laurence Eaves, John Furneaux, Robert Markiewicz, and Carson Jeffries

It is of considerable interest to consider the influence of a cloud of electron-hole drops on the electrical conductivity of the Ge crystal. Figure 1 shows the differential longitudinal magnetoconductivity of an ultrapure crystal at T = 2 K with a magnetic field parallel to the ⟨100⟩ direction, and current probes to measure the conductivity in the same direction. With a moderate excitation power of ≈ 25 mW cm^{-2} only a small fraction of the crystal volume is filled with drops, and the conductivity is mainly due to free carriers outside the drops. The observed extrema of the oscillatory behavior of Fig. 1 are closely periodic in the square root of the magnetic field, with a period $\Delta(B^{1/2}) = 1.24$ $gauss^{1/2}$,

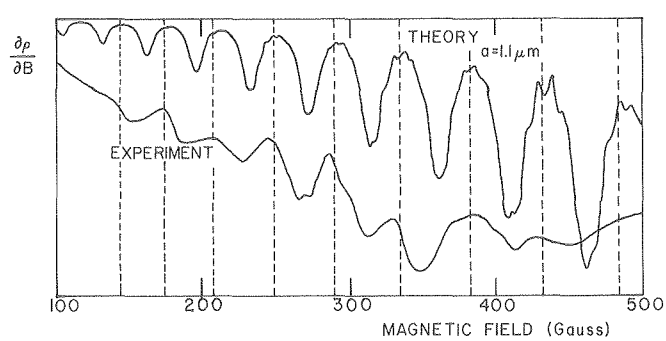

Fig. 1. Measurement and theory for the differential longitudinal magnetoconductivity ($\delta\rho/\delta B$) of a Ge crystal at 2 K, partially filled with electron-hole drops. The period of the resonant oscillations $\Delta(B^{1/2})$ determines the drop radius a = 1.1 μm. (XBL 781-24)

indicated by the dashed vertical lines. This resonant period is directly related to the size of the droplets and yields a droplet radius $a \approx 1.1$ μm.

The resonances are interpreted in terms of a model in which free electrons are scattered by randomly spaced droplets, represented by an attractive, hard edged, square well of radius a and depth $V_0 = 4$ meV, equal to the binding energy inside a drop. The physical origin of the oscillations comes from considerations of the possible elastic transitions for an electron in state $|n,\vec{k}\rangle$. Because of the infinite density of states at the bottom of each Landau level n, the transition rate becomes infinite whenever scattering into the (n+1) band is possible. Thus the scattering time has a saw-tooth variation when plotted against the longitudinal momentum k_z. Extrema in the conductivity occur whenever $B = (\pi/2a)^2 (\hbar/2e) (N+\phi)^2$, where N is an integer and ϕ is a phase factor. The full theoretical result with corrections for electron mass anisotropy is plotted in Fig. 1, for a = 1.1 μm, chosen to give the best fit to the data. This drop radius is consistent with values obtained by Rayleigh-Gans light scattering. The method of resonant carrier scattering is applicable with good sensitivity to much smaller droplets and is an important new and independent method of measuring the sizes of small conducting bodies in solids.

4. PROPERTIES OF THE STRAIN-CONFINED ELECTRON-HOLE LIQUID IN Ge

Robert Markiewicz, John Furneaux, Susan Kelso, James Wolfe, and Carson Jeffries

We have found that it is possible to produce a large volume of liquid in Ge stressed so as to produce a potential well of strain energy in the interior of the crystal, which collects excitons, small droplets, and carriers, where they coalesce into a single large volume, called a γ-drop, with a radius $R \leqslant 0.5$ mm. This is relatively enormous compared to the usual small droplets of a few microns radius in unstressed Ge, here called α-drops, and discussed in Sections 1-3 above. We have studied the properties of the strain-confined liquid from spatial, spectral, and temporal measurements under wide variations in stress, temperature, and excitation level, which determines the γ-drop size. As expected, the e-h pair density n_γ, the exciton condensation energy ϕ_γ, and the e-h lifetime τ_γ are significantly different from EHD in unstressed Ge, which is designated as Ge(4:2), meaning 4 electron valleys and 2 hole bands are occupied. In moderately stressed Ge, only one electron valley is occupied and the configuration is Ge(1:2) for γ-drops.

Figure 1 shows the luminescence spectrum emanating from a strain well, for increasing excitation powers: at low powers only free excitons are observed, but there is a threshold for a second line, that of the electron-hole liquid (EHL) formed in the well; thus, there is a gas-liquid phase transition, just as in unstressed Ge. A careful measurement of the EHL lineshape and width, which is essentially the Fermi energy, yields the e-h pair density. Figure 2(a) shows the theoretically expected lineshape, and the circles of Fig. 2(b) show the best theoretical fit to data at low excitation and at T = 1.8, corresponding to a density $n_\gamma = 0.5 \times 10^{17}$ cm^{-3}, close to that expected theoretically for Ge(1:2), and five times lower than for unstressed Ge, $n_\alpha = 2.3 \times 10^{17}$ cm^{-3}.

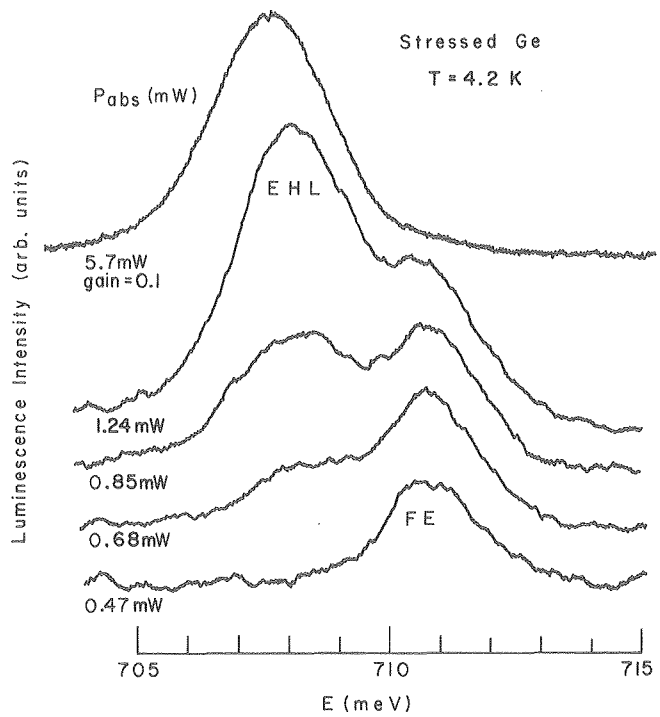

Fig. 1. Luminescence spectrum of radiation from a strain well in Ge, at increasing excitation powers P_{abs}. At low powers only the free excitons (FE) are observed, but there is a threshold for condensation into the electron-hole liquid (EHL).
(XBL 7712-11211)

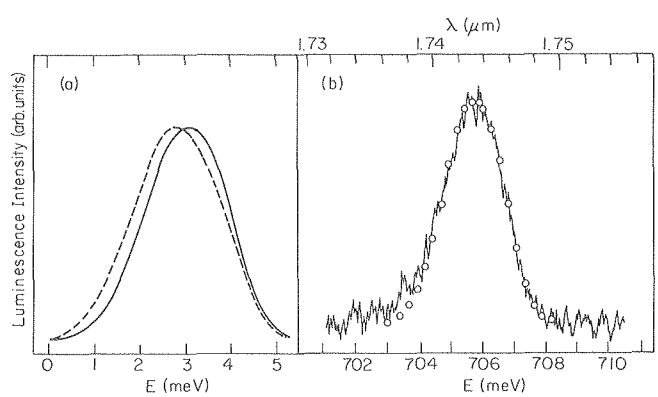

Fig. 2. (a) Theoretical EHL luminescence lineshapes for Ge(1:2): dashed line assumes parabolic hole masses; solid line makes corrections.
(b) Observed spectrum with stress along ⟨111⟩ at T = 2 K; circles are from best-fit theory, and yield liquid density $n_\gamma \approx 0.5 \times 10^{17}$ cm^{-3}.
(XBL 7711-6459)

An independent measurement of n_γ is obtained by observing the magneto-oscillations in the luminescence, Fig. 3, which also measures directly the electron Fermi energy from the period of the oscillations. We find $E_F^e = 2.3 \pm 0.12$ meV, corresponding to $n_\gamma = 0.52 \pm 0.05 \times 10^{17}$ cm^{-3} at T = 1.6 K.

We have measured a 15-fold increase in the EHL lifetime of γ-drops: $\tau_\gamma \approx 530$ μs, vs $\tau_\alpha \approx 36$ μs for small droplets; see Fig. 4(a) and 4(c). The lifetime is principally determined by two processes: i) direct radiation recombination of e-h pairs, with the rate $\tau^{-1} \propto n$; ii) non-radiation auger recombination, with $\tau^{-1} \propto n^2$, or even n^3 in higher order. Our observation that $(\tau_\gamma/\tau_\alpha) > (n_\alpha/n_\gamma)$ suggests that the non-radiation process dominates in α-drops and that the radiation process dominates in γ-drops. Another observed property of γ-drop decay, Fig. 4(b), is that the initial decay is faster, suggesting an initial high liquid density--i.e., compression, discussed in the next Section.

A section of the gas-liquid phase diagram for Ge(1:2) has been measured in the range $3 < T < 4.2$ K by measuring the exciton density at the EHL formation threshold. Figure 5 shows representative data: at a well-defined excitation power the EHL luminescence appears, while the FE gas luminescence becomes saturated: the carriers are all going into the liquid phase. A plot of these data, using a model of an ideal exciton gas but in a strain well, yields the exciton condensation energy $\phi_\gamma \approx 0.9$ meV for Ge(1:2), to be compared to $\phi_\alpha = 1.9$ meV for Ge(4:2). An independent value $\phi_\gamma \approx 1$ meV is obtained by fitting the EHL and FE spectral lineshapes at low excitation. From the phase diagram and the law of corresponding states, we deduce a tentative value of $T_c = 5$ K for the critical temperature of the EHL in Ge(1:2).

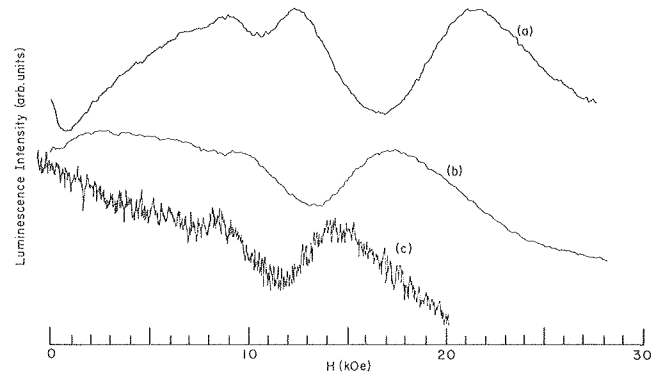

Fig. 3. Magneto-oscillatory luminescence of EHL in stressed Ge: (a) H ∥ ⟨001⟩; (b) H ∥ ⟨110⟩; (c) H ∥ ⟨111⟩. These data directly measure the electron Fermi energy in Ge(1:2). (XBL 7711-6454)

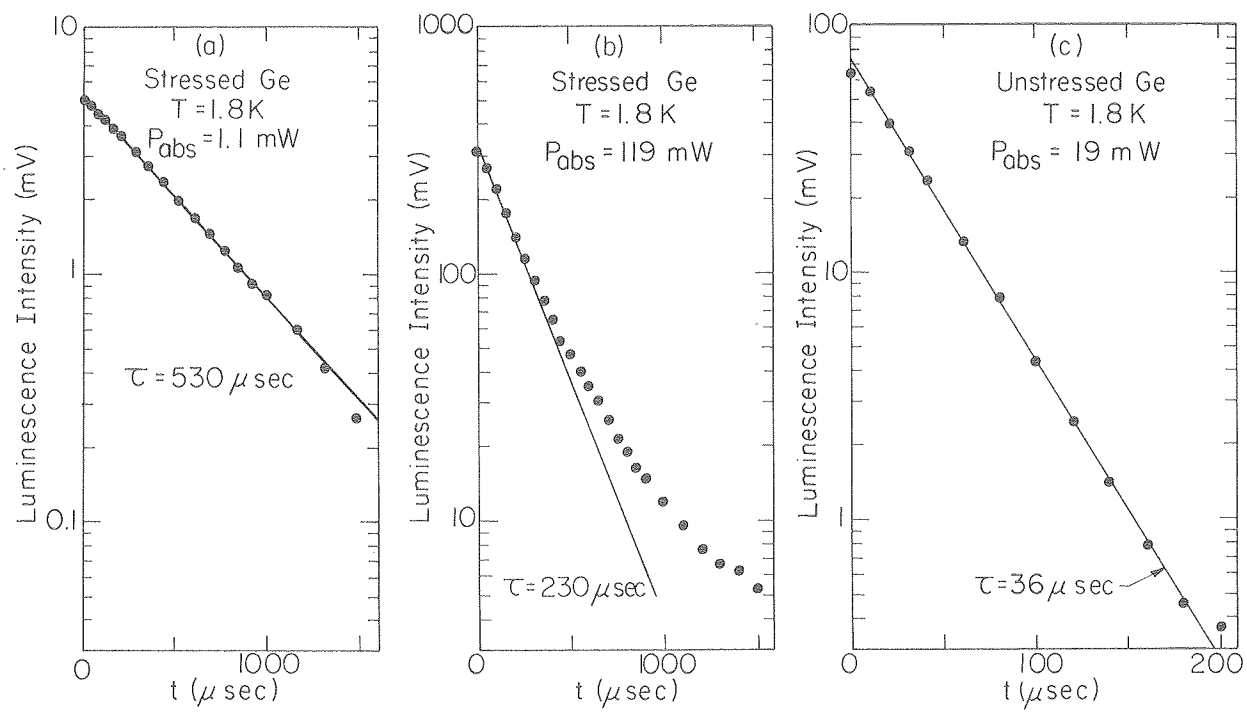

Fig. 4. Luminescence decay of EHL following pulsed excitation. (a) stressed Ge(1:2) at low level of excitation; (b) stressed Ge(1:2) at high level of excitation, showing rapid initial decay due to compression of the liquid; (c) unstressed Ge(4:2). (XBL 777-5692)

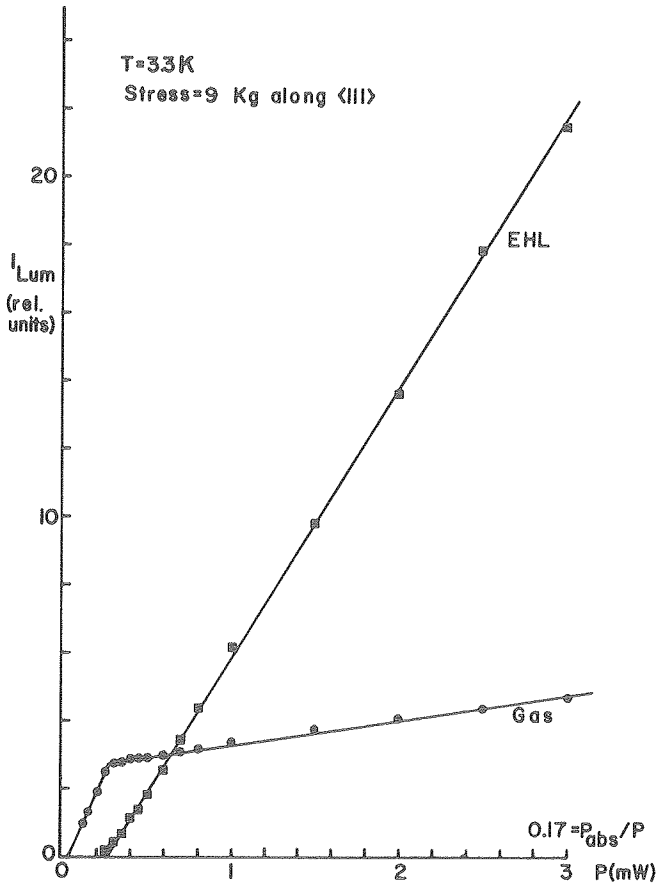

Fig. 5. Luminescence intensity of free exciton gas and electron-hole liquid in a strain potential well in Ge(1:2) versus excitation power. The threshold for EHL formation is at $P \approx 0.2$ mW. These data are used to construct a gas-liquid phase diagram. (XBL 781-26)

5. MEASUREMENT OF COMPRESSIBILITY OF THE ELECTRON-HOLE LIQUID IN Ge

Susan Kelso, Robert Markiewicz, and Carson Jeffries

It is important to measure directly the compressibility of the electron-hole liquid; although it enters indirectly in almost all experiments, it has not been directly measured. The availability of a sizeable volume of electron-hole liquid in a potential well discussed in Section 4 affords a unique experiment: the well is approximately parabolic and is a kind of "bottle" for the liquid, with restoring force given by the gradient of the strain energy $E_S = \alpha r^2$. If the γ-drop is small ($R < 100$ μm) it is experimentally known that the luminescence linewidth ΔE_γ and the decay rate τ_γ^{-1} are not dependent on size, indicating that the liquid e-h pair density n_γ is essentially uniform, and compression is negligible. However, for higher excitation and drop radii, $R > 150$ μm, both ΔE_γ and τ_γ^{-1} begin to increase, indicating that the average density in the γ-drop increases with drop radius. We have examined theoretically possible mechanisms for this. As the γ-drop grows in the strain well, liquid is pushed into regions of lower strain, where the equilibrium density is raised by an amount calculable from uniaxial stress data. A second mechanism is actual compression of the liquid in the well: as the drop grows, liquid is forced into regions of higher energy and the drop can lower its total energy by *increasing* the pair density in the low energy regions near the center of the drop. The first mechanism raises the density at the drop edges, the second mechanism raises the density at the center.

We focus a magnified image of the γ-drop luminescence onto the entrance plane of a spectrometer, and sample the luminescence intensity at different regions of the drop by using slit scanning and box scanning. The evidence is clearly that the density is higher in the drop center and that compression is the important mechanism. We have worked out a detailed theory of the effects of compression, with the results summarized in Fig. 1, which shows the density as a function of drop radius for four drop sizes. If $R = 100$ μm there is only a very small compression, less than 10%; but for $R = 800$ μm, the density at the center is 3 times higher than at the surface--a very sizeable compression.

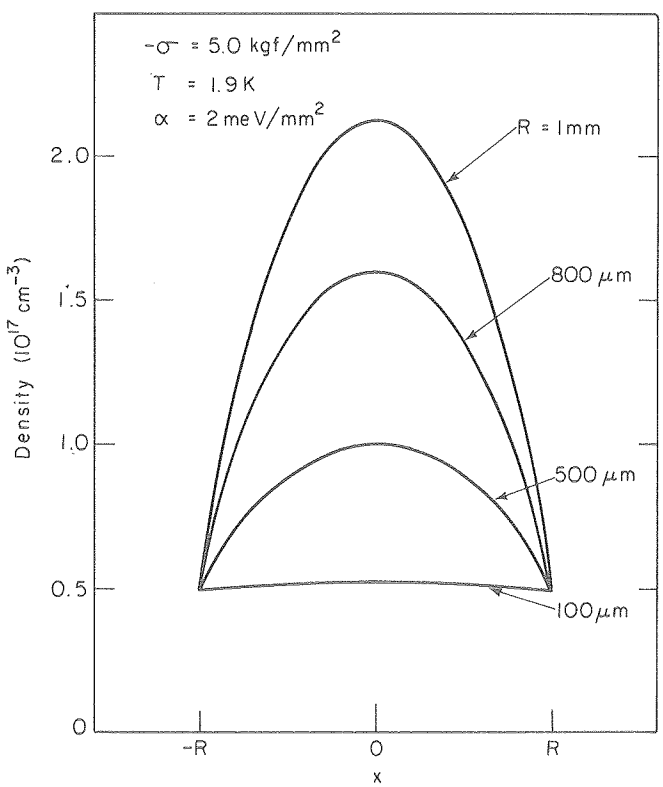

Fig. 1. Predicted density vs radius for strain-confined drops of EHL in Ge for four drop radii R. It is assumed that the well is produced by an inhomogeneous stress σ along the ⟨111⟩ direction and that the well is parabolic, $E_S = \alpha r^2$. (XBL 7711-6386)

Detailed measurements of the radial dependence of the density for a drop of radius R = 700 μm are made by recording the EHL luminescence intensity emanating from the γ-drop in three mutually perpendicular directions, using mirrors and box and slit scans; the data are compiled by Abel transforms to yield the data points of Fig. 2. The solid line is that predicted by the theory for compression and is in good agreement with the data. By measuring the density at the center for various drop sizes, we measure the actual compressibility $K_T \equiv -(\Delta V/\Delta P)V^{-1}$, finding a preliminary value $K_T = 3 \times 10^{-2}$ cm²/dyne for the EHL in Ge(1:2) at T = 1.85 K. This is to be compared to our theoretical value $K_T = 3.7 \times 10^{-2}$ cm²/dyne. We note that the compressibility of the electron-hole liquid is 10^9 larger than that of water; its density is also smaller by roughly the same factor.

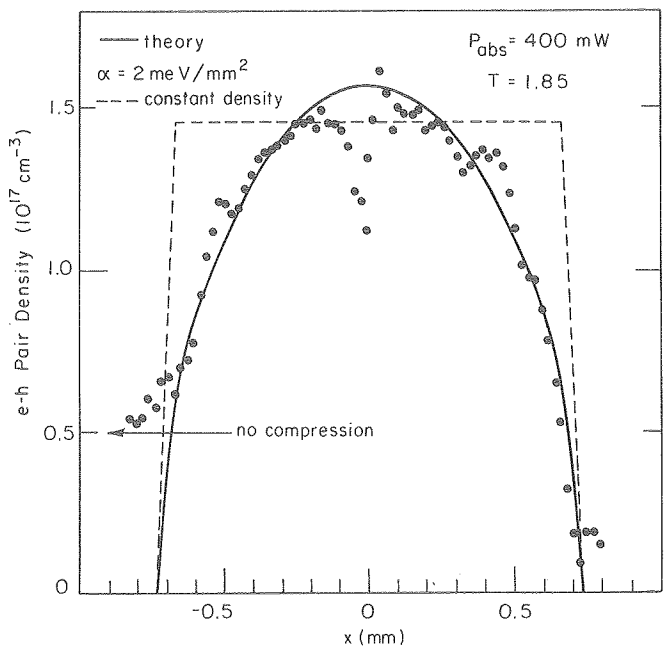

Fig. 2. Measured pair density vs radius for a large strain-confined drop in Ge, obtained by pumping with 400 mW of laser power. A threefold compression in the center is observed, and understood theoretically. (XBL 7711-6387)

6. MAGNETIC PROPERTIES OF ELECTRON-HOLE DROPS

John Furneaux, James Wolfe, Robert Markiewicz, Susan Kelso, and Carson Jeffries

The question of the magnetic properties of an electron-hole drop is very interesting and quite complex. A drop consists of freely moving electrons and holes which ultimately recombine and are replenished by a surface flux of condensing excitons; the carriers in the drop are subject to Lorentz forces when the drop is placed in a magnetic field. The drop medium is also deformable, compressible, viscous, and there is surface tension energy and also strain energy in a potential well. There is a magnetization due to the ordinary Landau diamagnetism of the free carriers, and possibly a spin contribution. The drop, then, is made of some kind of complex dilute magnetic liquid. We ask: what happens to the shape when a magnetic field B is applied? It will change its shape in order to minimize the total energy of all mechanisms. A full magneto-dynamic theory has been developed both for small drops and for large strain-confined drops in Ge, with many novel predictions.

The largest effect, and the most novel, is a new type of dynamic paramagnetism originally suggested by Kaminskii and Pokrovskii: because of the finite lifetime of the carriers inside a drop, there must be a continuous net flow of electrons and holes inward, a "recombination current," to maintain the drop in a steady state, as indicated in Fig. 1(a) for a spherically symmetric surface flux. An applied B field will deflect the electron and holes as shown in Fig. 1(b), which, in effect, produces a net circulating current j as in Fig. 1(c), and magnetization M parallel to B. For spherical symmetry $M = 4\pi n_0 e\omega_c \tau R^5/45c\tau_0$, where R is the drop radius, τ the carrier scattering time, τ_0 the pair recombination lifetime, and $\omega_c = eB/m^*c$, the cyclotron frequency. The drop will change its shape to minimize the magnetic energy $E_M = -1/2\ \vec{M}\cdot\vec{B}$, and to do this it expands perpendicular to the magnetic field to encompass more field lines. A simple measure of this is the oblateness parameter $R_\parallel/R_\perp$, the ratio of drop dimensions parallel and perpendicular to the B field.

We have indeed observed such an effect with $R_\parallel/R_\perp$ as small as 1/3 for a large strain-confined

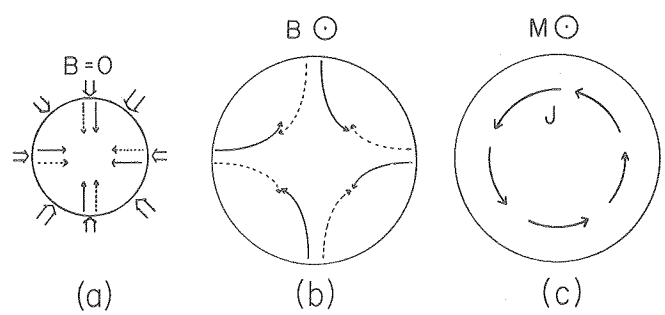

Fig. 1. Schematic illustration of origin of recombination magnetism. (a) Recombination currents in zero magnetic field. Carriers are assumed to be fed into the drop uniformly over the drop surface. (b) In a magnetic field, electrons (solid arrows) and holes (dashed arrows) are deflected in opposite directions. (c) This produces a net azimuthal current, $\vec{j}$, which in turn induces the recombination magnetization $\vec{M}$. Note that the magnetization is paramagnetic, $\vec{M}\cdot\vec{B} > 0$. (XBL 779-4827)

drop. Figure 2(a) shows the Ge crystal mounted to be viewed from face and end directions; Fig. 2(b) is an infrared vidicon image of the EHL recombination luminescence with no applied field showing an approximately spherical drop, obtained at T = 1.7 K by pumping with 50 mW of laser power. In Fig. 2(c), an H field of 20 kOe is applied in the direction shown, and the drop clearly flattens into a pancake with axis along the field. In Fig. 2(d), the field is applied perpendicular to the crystal face and the drop flattens into a pancake with axis along the field, as before. We further find that the primary change in shape occurs for $H \lesssim 10$ kOe and that above this value the distortion saturates. In a given field the distortion is greater for shallow strain wells. The detailed theory can explain all the observed effects in large strain-confined drops, and predicts similar effects in small unstressed droplets, possibly detectable by light scattering. We believe these experiments have firmly established the existence of recombination magnetization.

This deformation, or magnetostriction, in drops in Ge is six orders of magnitude larger than that observed in the semi-metal Bi, which also contains an electron-hole plasma of comparable density (10^{17} cm^{-3}); however, this is its ground state, and so Bi does not possess a recombination magnetization, nor is it so deformable.

The recombination currents usually flatten the drops along the field direction, corresponding to paramagnetism. However, the effect is very sensitive to the boundary conditions of the exciton flux into the drop surface. By orienting the H field along the ⟨111⟩ axis and along the stress direction and by pumping with the laser "off center" so that excitons (or external carriers) impact the drop surface in a narrow channel along the ⟨111⟩ direction, it is possible to reverse the sense of the effective recombination magnetization. In this case we observe cigar-shaped drops, elongated along the magnetic field: the system now displays a dynamic diamagnetization. The detailed magnetohydrodynamic theory takes into account: the incident flux boundary conditions; liquid density variations in magnetic field; compressibility; strain and surface energies; viscosity; and mass anisotropy for Ge. It is reasonably successful in quantitatively explaining the observed exotic magnetic properties of electron-hole drops.

7. ALFVÉN WAVE RESONANCES IN PLASMA SPHERES

Robert Markiewicz and Carson Jeffries

At microwave frequencies and in magnetic fields greater than that for cyclotron resonance, we observe the propagation of Alfvén waves in a large

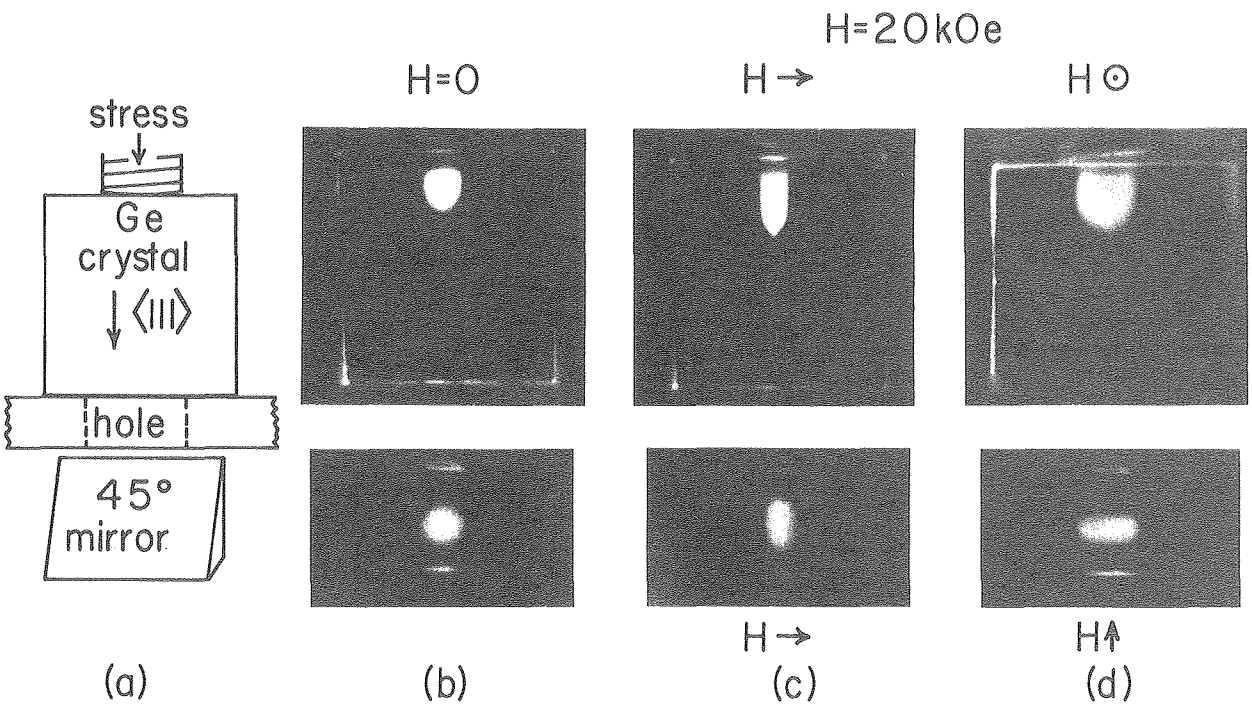

Fig. 2. Observation of recombiantion magnetization in a strain-confined electron-hole drop in Ge. (a) Crystal mounting. (b) Vidicon image of an approximately spherical drop in zero field. (c) Flattening of drop in plane perpendicular to H. (d) Flattening of drop in plane perpendicular to H in another orientation. (XBB 773-2139)

drop of strain-confined electron-hole liquid in Ge. A standing Alfvén wave resonance or magnetoplasma dimensional resonance is observed when a multiple of the Alfvén wavelength $\lambda_A \propto B\sqrt{n}$ becomes comparable to the drop diameter, approximately. In this way we first identified a large drop, estimated the e-h pair density n, and studied the formation and decay of the drop in a strain well. The detailed and difficult theory of Alfvén-wave oscillations in an anisotropic plasma sphere has been studied and two solutions are made. One solution is exact, involving an expansion of the current inside the sphere in a series of orthonormal modes, following a procedure used by Ford and Werner for helicon waves. The second is approximate, based on a perturbation expansion of the induced fields and currents in powers of the drop radius. The approximate solution can be applied to a material having a completely general conductivity tensor, while the exact solution is restricted to situations of high symmetry.

Using these solutions, the resonant microwave power absorption of an electron-hole drop in Ge is calculated explicitly and compared to the size-dependent resonances observed. The new calculations show that both the magnetic and electric microwave fields induce absorption, the magnetic dipole being the most intense, particularly for modest drops ($a < 100$ μm). In stressed Ge(1:2), with the stress and the B field along the ⟨111⟩ axis, the absorbed microwave power predicted by the exact theory is plotted in Fig. 1 vs the B field, with the drop radius a as a parameter. The LM modes are observed with the microwave $\vec{B}_1$ field parallel to $\vec{B}$; the TM ± modes with circularly polarized fields $\vec{B}_1 \perp \vec{B}$. In each case there are a series of well defined dimensional resonance modes a, b, c,... that move to higher fields as the drop size increaxes. The intensity also strongly increases, as $I \propto a^5$, approximately. The width of a resonance ΔB is proportional to the e-h collision rate τ^{-1}, and if τ is independent of B, ΔB is proportional to B for Alfvén waves. Figure 2 shows the exact theoretical prediction for the resonant field B vs drop radius a, for the same modes a,b,c; there is clear evidence of mode crossing. From the approximate solutions it is found that certain of the resonances can have a very strong dependence on the magnetic field orientation with respect to the crystal axes. As a second application of the theory the transition from Alfvén waves (in a material having equal numbers of electrons and holes) to helicon waves (only one carrier type) is studied. The theory is now virtually complete and should be of considerable aid in understanding electromagnetic resonances in electron-hole drops in Ge as well as plasmas in general.

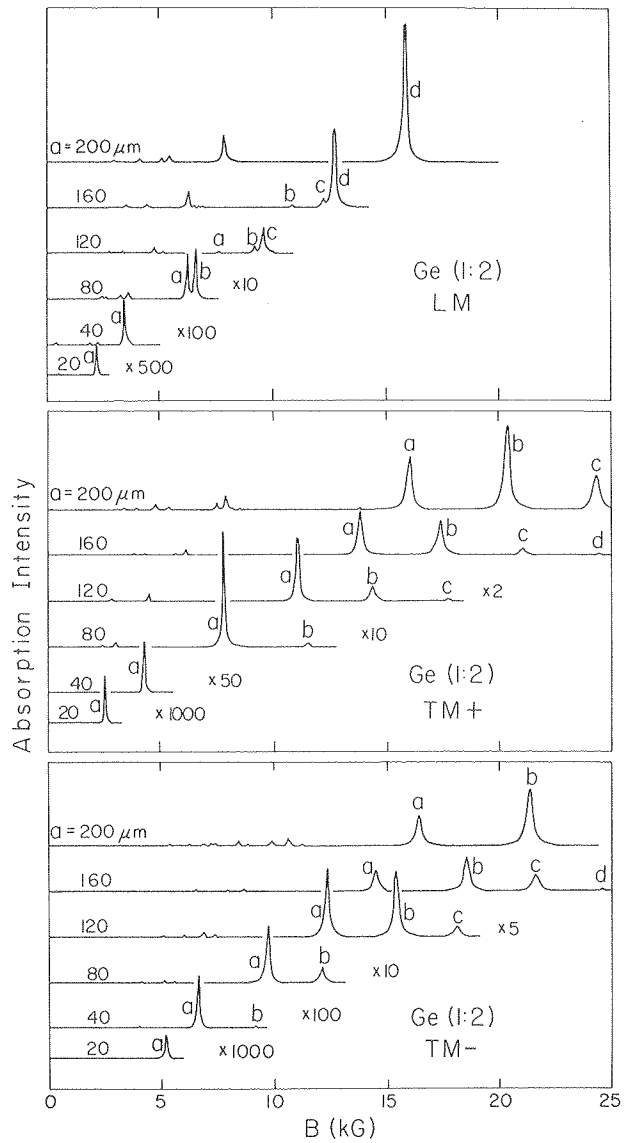

Fig. 1. Predicted microwave power absorption for a spherical electron-hole drop of radius a in strained Ge(1:2) in a magnetic field along the ⟨111⟩ axis. A series of dimensional resonance modes a,b,c,... are shown and occur at different fields dpending on the orientation of the microwave magnetic field B_1. (XBL 7710-6207)

8. RESEARCH PLANS FOR CALENDAR YEAR 1978

Carson Jeffries

There are still many facets of electron-hole liquids to be investigated; frequently experimental surprises occur. We plan to focus on ultrapure Ge, and also to extend the measurements to other materials. The new method of Westervelt discovered in Section 2 above is a breakthrough in the sensitivity to detect very small forces on drops: drift velocities lower by six orders of magnitude than previously reported can be detected. We plan to extend this method in many ways: 1) Study the motion of droplets as a function of crystal impurity doping, dislocations, vacancy clusters, and other defects to determine what are the droplet trapping centers and the binding energy to the center. 2) Work at higher temperatures where it is expected that the droplets will hop off the centers, and a hopping-type of diffusion motion can be observed.

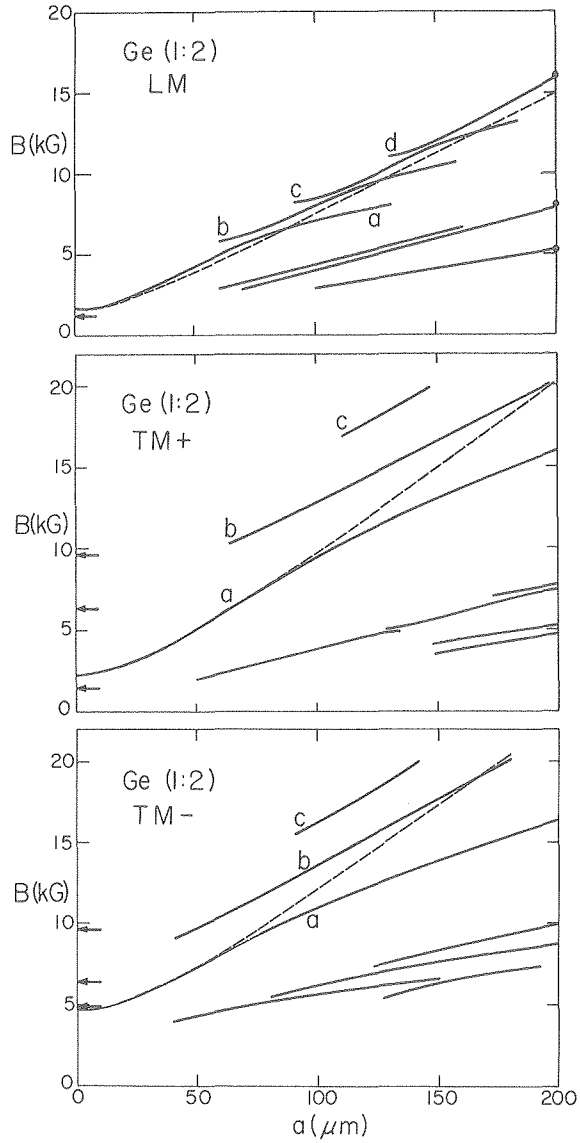

Fig. 2. The resonant field B vs drop radius a for standing Alfvén wave resonance modes in an electron-hole drop in Ge, as in Fig. 1. Mode crossing is evident. (XBL 7710-6208)

3) Study the motion of droplets in small applied electric fields to investigate the change of the droplets; the present experimental evidence is very conflicting. 4) Study the motion of droplets in a crystal temperature gradient, i.e., in a hot phonon flux, to investigate the phonon-wind effect. 5) Similarly, study the effects of exciton wind and free carrier wind on droplets. 6) Study the motion of droplets in magnetic field gradients, where the direction and magnitude of motion will determine whether the droplet is (a) paramagnetic (due to recombination currents) or (b) displays Landau diamagnetism; it has been predicted by our general magnetohydrodynamic theory that there will be a transition between these two cases as the drop size is reduced. 7) Study the motion in a known uniaxial strain gradient; this force is calculable from known deformation potentials and, done simultaneously with other forces, will serve as a calibration of the force, and enable accurate measurements of the droplet-phonon relaxation time. 8) Study further the drag on droplets in a uniform magnetic field analogous to the liquid Na pump effect reported by McGroddy et al. All of these experiments will be done at minimum excitation, actually below threshold using hysteresis, where the drop system is far less perturbed than has heretofore been possible.

A second major objective is to develop and construct ultrahigh-sensitivity infrared detectors in the range 1-4 μm, and use them in a variety of new experiments on electron-hole liquids, excitons, multiexciton complexes, and solid-state spectroscopy in general. Recently astrophysical investigators using very low background photovoltaic InSb detectors, special cooled FET preamplifiers, and thermal and angular screening of background photon fluctuations have achieved sensitivities of 10^{-17} W $Hz^{-1/2}$, which is 3 to 4 orders of magnitude better than detectors used in electron-hole droplet research. We will use such improved detectors in several new experiments: 1) To observe the formation of single small droplets (~1 μm) in unstressed Ge and Si, and to study the formation process and growth by spatial imaging. 2) To observe hysteresis in Si. 3) Perform Rayleigh-Gans scattering at improved sensitivity to measure droplet sizes. 4) To search for spectroscopic evidence at much higher snesitivity for free biexcitons and higher multiexciton complexes.

There is much evidence in the literature that one or more excitons bind to donors and acceptors in Si and Ge--the so-called bound multiexciton complexes. However, the problem is not at all solved: no theory has yet been developed that explains the spectroscopic features. We propose another, experimental, approach: to observe the microwave spin resonance of the donor and its hyperfine structure; then excitons may be bound following light excitation, and the structure should change. This method has been used quite successfully, e.g., in the study of F-centers, and should give very detailed information about the local structure of the multiexciton complex.

The current work on the strain-confined liquid in Ge will be continued and extended to: 1) measurements of the compressibility as a function of temperature; 2) the study of the motion of carriers, excitons and small droplets into the strain well by spatial, temporal, and spectroscopic scanning; 3) similar measurements on other materials. We also plan to use the method of resonant electron scattering to measure the size of small droplets in Si and Ge as a function of temperature and excitation level. This method is very sensitive to very small particles and could be extended to multiexciton complexes. The interaction of electron-hole droplets with the surface of the semiconducting crystal is of very high interest, but has not yet been studied; we will begin this in Ge.

To date, the materials in which electron-hole liquids are experimentally well established or suggested are: Ge, Si, GaAs, GaP, cubic SiC, CdSe, CdS, and ZnO; in some of these the critical

temperatures are in the range 50 to 100 K. It is becoming increasingly evident that this novel state of matter is fairly general and has escaped notice until recently. The liquids are of very high interest, both theoretically and experimentally.

9. 1977 PUBLICATIONS AND REPORTS

Carson Jeffries and Associates

Journals and Conference Proceedings

1. R. S. Markiewicz, J. P. Wolfe, and C. D. Jeffries, Strain-confined Electron-hole Liquid in Germanium, Phys. Rev. B 15, 1988 (1977), LBL-6225.

2. L. Eaves, R. W. Markiewicz, and J. E. Furneaux, A Theoretical Analysis of Resonant Scattering of Free Carriers by Electron-hole Droplets in Germanium, J. Phys. C 10, L531 (1977), LBL-7312.

3. J. L. Staehli, Kinetics of Electron-hole Plasma Condensation in a Saturated Gas of Free Excitons in Pure Germanium, Nuovo Cimento 39B, N.2, 634 (1977).

4. J. P. Wolfe, R. S. Markiewicz, J. E. Furneaux, S. M. Kelso, and C. D. Jeffries, Magnetostriction of an Electron-hole Drop in Ge, Phys. Stat. Sol.(b) 83, 305 (1977), LBL-6049.

5. S. M. Kelso, R. W. Markiewicz, and J. E. Furneaux, Compressibility Effects in the Electron-hole Liquid in a Strain Potential Well in Ge, Bull. Am. Phys. Soc. 22, 269 (1977), LBL-6008 Abstract.

6. J. E. Furneaux, R. S. Markiewicz, and S. M. Kelso, The Phase Diagram of the Electron-hole Liquid in a Strain Potential Well in Ge, Bull. Am. Phys. Soc. 22, 270 (1977), LBL-6009 Abstract.

7. R. S. Markiewicz, Magnetostriction of an Electron-hole Drop (EHD) in a Strain Potential Well in Ge, Bull. Am. Phys. Soc. 22, 270 (1977), LBL-6010 Abstract.

8. R. M. Westervelt and B. S. Black, Motion of Electron-hole Drops in Ge Under Volume Excitation, Bull. Am. Phys. Soc. 22, 269 (1977), LBL-6013 Abstract.

9. A. D. A. Hansen and T. Ohyama, Ultrasonic Absorption by the Electron-hole Liquid in a Strain Potential Well in Ge, Bull. Am. Phys. Soc. 22, 269 (1977), LBL-6014 Abstract.

LBL Reports

1. A. D. A. Hansen, Acoustic Absorption by the Electron-hole Liquid in Germanium (Ph.D. thesis), University of California, Berkeley, 1977, LBL-6340.

2. R. S. Markiewicz, Acoustic Phonon Scattering by Electron-hole Droplets in Ge: Deformation Potentials (in press), LBL-6212.

3. R. S. Markiewicz and S. M. Kelso, Density Variation of the Strain-confined Electron-hole Liquid in Ge (in press), LBL-6245.

4. R. M. Westervelt, Nucleation Phenomena in the Formation of Electron-hole Drops in Ge(Ph.D. thesis), University of California, Berkeley, 1977, LBL-6619.

5. R. S. Markiewicz, Theory of Magnetostriction of Electron-hole Drops in Ge, LBL-6694.

6. J. P. Wolfe, R. S. Markiewicz, S. M. Kelso, J. E. Furneaux, and C. D. Jeffries, Properties of the Strain-confined Electron-hole Liquid in Ge, LBL-6289.

7. R. S. Markiewicz, Alfvén Resonances in Spheres with Applications to Electron-hole Drops, LBL-6942.

d. Superconductivity, Superconducting Devices, and 1/f Noise

John Clarke, Principal Investigator

1. GEOPHYSICS WITH SQUIDS*

T. D. Gamble, W. M. Goubau and J. Clarke

Magnetotellurics is a well-known and widely-used technique for surveying for geothermal sources and mineral deposits. The essential idea is as follows. A fluctuating magnetic field, $\vec{H}(t)$, generated in the ionosphere and magnetosphere is incident on the earth's surface (approximately) as a plane wave. When the fluctuating magnetic field reaches the surface, it penetrates in a direction that is nearly normal to the surface, and decays exponentially with a characteristic length $(2/\mu\mu_0\sigma\omega)^{1/2}$. Here, μ is the permeability of the earth, σ is the electrical conductivity of the earth (which is a function of position), and $\omega/2\pi$ is the frequency of the magnetic field fluctuations. At 1 Hz, this length is typically a few hundred meters. The fluctuating magnetic field induces electric currents in the ground that in turn generate a fluctuating electric field, $\vec{E}(t)$. At each frequency $\omega/2\pi$, the x- and y-components of the magnetic and electric fields in orthogonal directions parallel to the earth's surface are related by

$$E_x(\omega) = z_{xx}(\omega)\, H_x(\omega) + z_{xy}(\omega)\, H_y(\omega), \quad (1)$$

and

$$E_y(\omega) = z_{yx}(\omega)\, H_x(\omega) + z_{yy}(\omega)\, H_y(\omega). \quad (2)$$

The $z(\omega)$ are the elements of the impedance tensor $Z(\omega)$. The goal of magnetotellurics is to measure Z as a function of frequency, and hence to model the resistivity of the ground.

It is evident that Eqs. (1) and (2) contain four unknowns, so that these equations are not sufficient to specify Z. The usual procedure is to multiply each equation in turn by, for example, $E_x^*(\omega)$ and $E_y^*(\omega)$, and to average the resultant products $E_xE_x^*$, etc., over many estimates. One can then solve the four equations so obtained for the $z(\omega)$, for example,

$$z_{xy} = \frac{\overline{H_x H_x^*}\;\overline{E_x H_y^*} - \overline{H_x H_y^*}\;\overline{E_x H_x^*}}{\overline{H_x H_x^*}\;\overline{H_y H_y^*} - \overline{H_x H_y^*}\;\overline{H_y H_x^*}}. \quad (3)$$

In the absence of noise, this procedure yields accurate estimates for the $z(\omega)$. However, in the presence of noise, there may be serious problems. For example, if $E_x = E_{xs} + E_{xn}$, where E_{xs} is the "signal" and E_{xn} is the "noise," then the autopower $\overline{|E_x|^2} = (E_{xs})^2 \times (1 + \overline{|E_{xn}|^2}/\overline{|E_{xs}|^2})$. Since $\overline{|E_{xn}|^2}/\overline{|E_{xs}|^2}$ may be much larger than unity under some circumstances, a large error in z_{xy} may be introduced. Similarly, if the two channels E_x and E_y contain correlated noise, a similar error may be introduced in $\overline{E_x E_y^*}$. The elimination of these errors has been one of the major goals in the magnetotelluric technique.

We have greatly reduced these errors by introducing a remote magnetometer several kilometers from the first. The fields measured by this magnetometer, H_{xr} and H_{yr}, are used to multiply Eqs. (1) and (2) to yield expressions for the $z(\omega)$, for example,

$$z_{xy}^{(r)} = \frac{\overline{E_x H_{xr}^*}\;\overline{H_x H_{yr}^*} - \overline{E_x H_{yr}^*}\;\overline{H_x H_{xr}^*}}{\overline{H_x H_{yr}^*}\;\overline{H_y H_{xr}^*} - \overline{H_y H_{yr}^*}\;\overline{H_x H_{xr}^*}}. \quad (4)$$

Equation (4) contains no autopowers, and, provided the noise at the first magnetometer is uncorrelated with that at the first, there will be no bias errors in the $z(\omega)$.

We have tested this technique in Bear Valley, California. We set up two complete magnetotelluric systems at Upper and Lower La Gloria (see Fig. 1). At each station, the magnetic field fluctuations were measured by a three-axis SQUID magnetometer, and the electric field fluctuations were measured by an array of buried electrodes (see Fig.1). The signals from the Lower La Gloria station were transmitted by FM telemetry to the Upper La Gloria station where all the signals were digitized and recorded on tape. The data were recorded into four overlapping bands, with periods 0.02 to 1 s, 0.33 to 5 s, 3 to 100 s, and 30 to 100 s. In the subsequent data processing, we computed $z(\omega)$ for each station using the standard analysis [Eq.(3)], and using the other station as a magnetic reference. We computed the $z(\omega)$

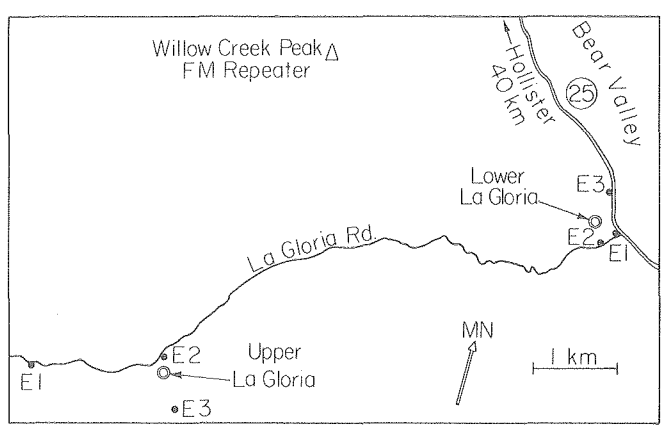

Fig. 1. Map showing magnetotelluric stations at Upper and Lower La Gloria Road in Bear Valley, California. Electrodes are denoted by letter E. Magnetometer locations are indicated by ⓪. Data were transmitted from Lower to Upper La Gloria via the FM repeater. (XBL 7712-6514)

for each station, and, at each frequency, rotated the tensor to maximize $|z_{xy}|^2 + |z_{yx}|^2$. Finally, we computed the apparent resistivities $\rho_x = 0.2\ T\ |z_{xy}|^2$ and $\rho_y = 0.2\ T\ |z_{yx}|^2$, where ρ_x and ρ_y are in Ωm, T is the period in seconds, and z_{xy} and z_{yx} are in units of $(mV/km)\gamma^{-1}$.

The apparent resistivities for the two stations using the two analysis techniques are shown in Figs. 2 and 3. We see at once that the apparent resistivities obtained with the remote reference are much smoother than those using the standard analysis. For example, there is a large dip in the resistivity obtained with the standard analysis at Lower La Gloria [Fig. 3(a)] between 2.5 and 18 s that is completely removed by the remote reference analysis of the same set of data. Furthermore, the values where the four frequency bands overlap are in much better agreement using the remote magnetometer. We believe that almost all of the discrepancies between Figs. 2(a) and 2(b) and Figs. 3(a) and 3(b) are a result of the systematic bias errors inherent in the standard analysis.

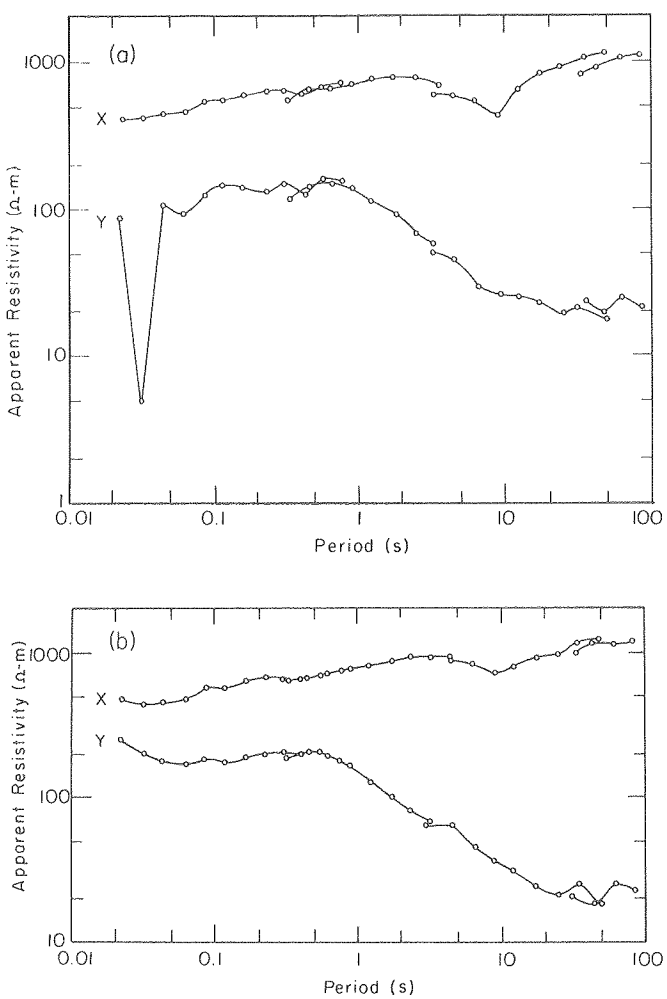

Fig. 2. Apparent resistivities for Upper La Gloria as a function of period: (a) standard analysis; (b) remote reference.
[(a) XBL 7712-6513; (b) XBL 7712-6511]

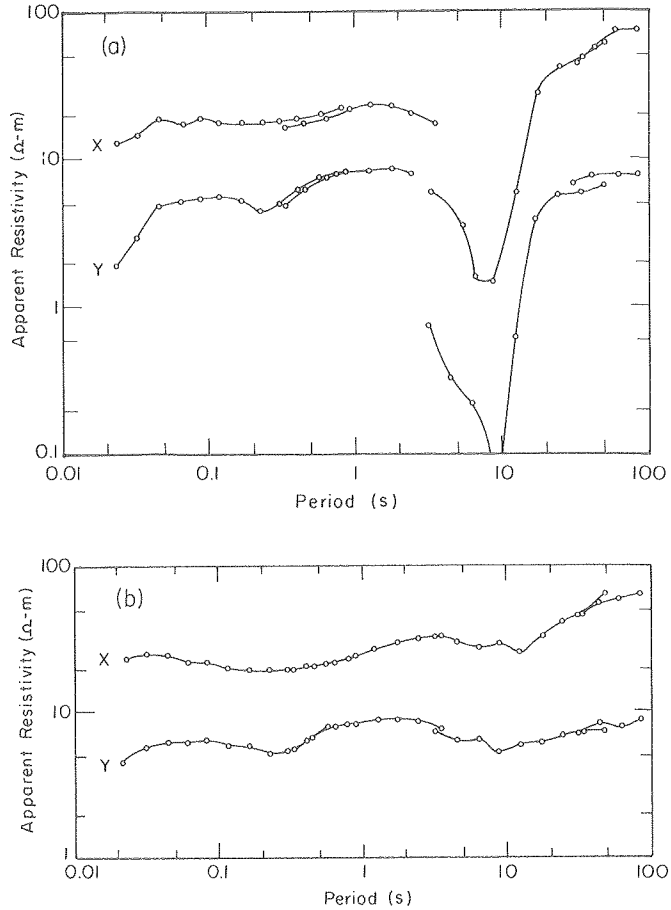

Fig. 3. Apparent resistivities for Lower La Gloria as a function of period: (a) standard analysis; (b) remote reference.
[(a) XBL 7712-6512; (b) XBL 7712-6510]

Our measurements at Bear Valley demonstrate the feasibility of remote-reference magnetotellurics, and show that this technique can significantly improve the reliability of the apparent resistivities obtained. Furthermore, since none of the data need be rejected because of bias errors, the time spent at each station gathering data may be substantially reduced by the use of a remote magnetometer.

We are continuing our evaluation of this new technique.

---

*Supported in part by U. S. G. S.

2. SUPERCONDUCTING THIN-FILM GRADIOMETER AND MAGNETOMETER*

M. B. Ketchen, W. M. Goubau, J. Clarke and G. B. Donaldson

A superconducting gradiometer incorporating a SQUID can be used to detect very small changes in

the gradient of an applied magnetic field. Such devices are important in applications where it is desirable to detect locally generated magnetic signals, which have a relatively high gradient in the presence of large magnetic field fluctuations, for example, those generated by the magnetosphere. Gradiometers thus already have medical applications in magnetocardiology and magnetoencephalography, and have considerable potential for application in geophysics. Previously, all such gradiometers have made use of wire pick-up coils. We have constructed and tested a gradiometer in which the SQUID and superconducting pick-up loops are constructed entirely from thin films.

The dc SQUID is shown in Fig. 1. Four Cr and Au disks were first evaporated onto the substrate, and a 125 μm wide strip of Nb was then sputtered and oxidized. An insulating disk was evaporated onto the midpoint of the Nb, and the SQUID was completed by the evaporation of the Pb films to form two tunnel junctions on the Nb strip. The SQUID is (ideally) insensitive to changes in a uniform magnetic field, but responds to changes in current in the Nb strip. Leads were attached to the Nb and Pb strips. The SQUID was current-biased at a voltage of about 1 μV, and a small 100 kHz flux was applied by means of a coil attached to the substrate. Any 100 kHz voltage developed across the SQUID was amplified by a cooled resonant circuit, further amplified by room temperature electronics, and lock-in detected. The smoothed output of the lock-in was fed back to the coil to flux-lock the SQUID. In this way, the SQUID could detect tiny changes in the current in the Nb strip. A typical power spectrum for the flux noise is shown in Fig. 2. The corresponding rms current noise in the white noise region was 1.7×10^{-10} A $Hz^{-1/2}$. The galvanometer was incorporated into the gradiometer shown in Fig. 3. The 295 × 38 × 38 mm quartz substrate was optically polished on the surface on which the films were deposited. The pick-up loops were of Pb 150-μm wide and 0.5-μm thick, and the diagonal Pb strip was electrically insulated from the Nb strip by a disk of SiO and Ge. The gradiometer could be used in one of two configurations. When the Pb strips were cut at points "A", the pick-up loops were in parallel, whereas when any were cut at "B", the loops were in series. In either case the gradiometer measured the off-diagonal gradient $\partial H_z/\partial x$.

The gradiometer was mounted in a cryostat and first tested in the laboratory. We balanced the gradiometer for fields in the z-direction by adjusting the position of a small balance film (Fig. 3) until a changing field H_z produced a minimum output from the SQUID. The best balance was about 3 ppm. The

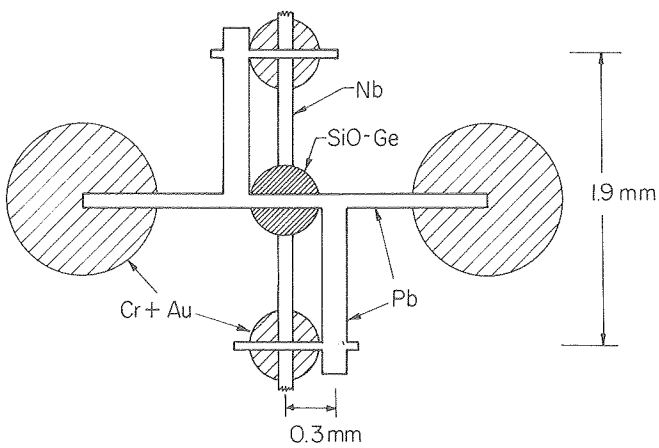

Fig. 1. Configuration of dc SQUID galvanometer. (XBL 7710-6155B)

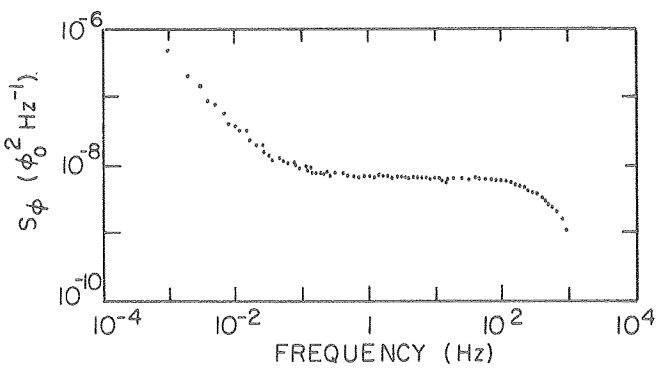

Fig. 2. Flux noise power spectrum of galvanometer. (XBL 767-7244)

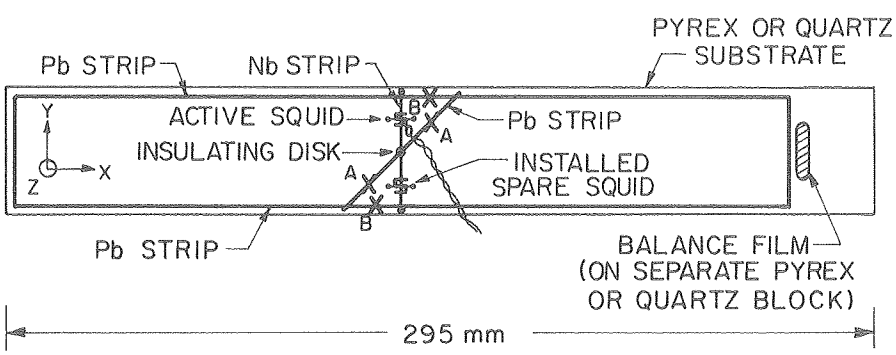

Fig. 3. Configuration of thin-film gradiometer. (XBL 7710-6145B)

intrinsic (unadjusted) balance in the x- and y-direction was about 100 ppm. Subsequently, we tested the series-loop gradiometer at a remote site at which the earth's field could be assumed to be fairly uniform. We balanced the gradiometer by rotating the cryostat about the vertical (x) axis, and adjusting the balance film for minimum response. The optimum balance achieved was 1 ppm. When the gradiometer was rotated through 360° about the x-axis, the output returned to its original value to within an amount corresponding to a balance of 1 ppm, indicating that hysteresis due to the motion of flux pinned in the films was not significant.

We determined the gradient sensitivity by measuring the response to a known flux imbalance between the pick-up loops. With a SQUID resolution of $8 \times 10^{-5} \phi_0$ $Hz^{-1/2}$, the sensitivities of the series- and parallel-loop gradiometers were 3.7×10^{-13}T m^{-1} $Hz^{-1/2}$ and 2.1×10^{-13}T m^{-1} $Hz^{-1/2}$, respectively. These values were in good agreement with our theoretical predictions.

A second type of thin-film device is the planar magnetometer shown in Fig. 4. This SQUID has a sensitivity of about 2×10^{-13}T $Hz^{-1/2}$, and a slewing rate of 2×10^{-4} T s^{-1} at 1 kHz. Thus, it is a factor of 20 less sensitive than our cylindrical SQUIDS, but has a factor of 3 higher slewing rate, a combination that makes it ideal for geophysical applications. The device is particularly easy to fabricate, and three can easily be mounted in an orthogonal array to make a three-axis magnetometer. Our future geophysics magnetometers will probably use SQUIDs of this type.

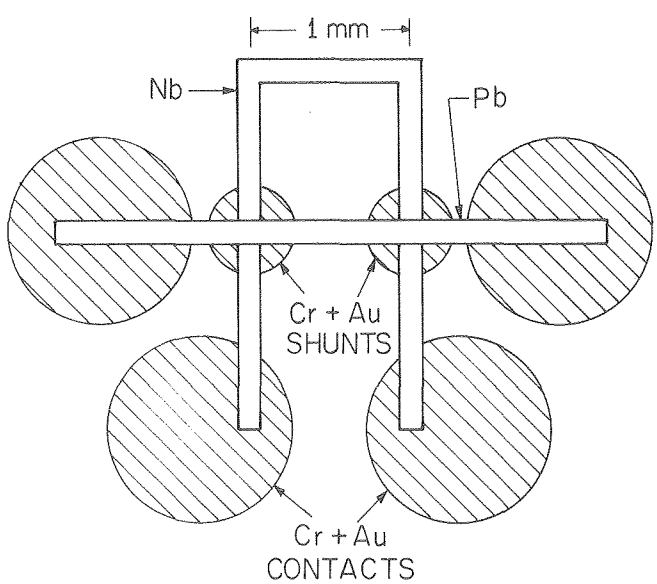

Fig. 4. Configuration of thin-film magnetometer. (XBL 7710-6155A)

We have demonstrated the feasibility of gradiometers fabricated entirely from thin films. In a future design, one would use photolithographic techniques to deposit films with a linewidth (say) 5 μm and with a high degree of symmetry. Gradiometers made in this way should have an improved initial balance in the z-direction, and also in the x- and y-directions. We believe that in the present design the x- and y-balance are limited by the distortion of the magnetic field by the overlapping films in the SQUID, and a reduction in the volume of these films should correspondingly reduce the distortion. Furthermore, if the film widths were reduced by a factor of 30, the resolution of the SQUID, which is proportional to (film width)$^{1/2}$, should be improved by a factor of about 5. With the aid of photolithography, one could also make second derivative gradiometers, which would be particularly suitable for medical applications. Finally we note that this type of gradiometer may be particularly suitable for commercial production, since it involves only thin-film techniques that are well-established in certain industries.

---

*Supported in part by U.S.G.S.

3. MICROWAVE-ENHANCEMENT OF THE SUPERCONDUCTING ENERGY GAP

T. R. Kommers* and J. Clarke

A puzzle in the study of superconducting weak links for almost a decade has been the observation that, under appropriate conditions, microwave irradiation could enhance the critical current of the links. Conversely, microwaves always decreased the critical current of tunnel junctions. A resolution of this apparent contradiction was suggested by Eliashberg and co-workers who showed theoretically that microwaves could enhance the energy gap, Δ, of a superconducting thin film. In this model, photons with energies $\hbar\omega < 2\Delta$ excite quasiparticles from states near the bottom of the excitation spectrum to states of higher energy, thereby making available for occupancy additional pair states with wavevectors near k_F. Since these pair states contribute most strongly to the pairing interaction, this redistribution of pair state occupancy increases the condensation energy, and therefore the energy gap. We have made the first direct observations of this enhancement.

We fabricated Al-Al_2O_3-Al junctions on BaF_2 substrates in a cross-film geometry, and with resistances in the range 1 to 10 Ω. Each sample was mounted in an X-band waveguide near an adjustable short-circuit plunger with the plane of the films parallel to the axis of the waveguide. The sample and waveguide were immersed in a temperature regulated helium bath. The upper curve in Fig. 1 shows the differential resistance, dV/dI, vs. voltage, V, for a sample in the absence of microwaves. The two sharp minima at a and b occur at voltages $(\Delta_> + \Delta_<)/e$ and $(\Delta_> - \Delta_<)/e$, where $\Delta_>$ and $\Delta_<$ are the larger and smaller energy gaps of the two films. The remaining curves in Fig. 1 show the additional structure induced as the 10 GHz (41.4 μV) microwave power was increased. The power levels represent the power delivered to the waveguide. The minima c,d,e, and f

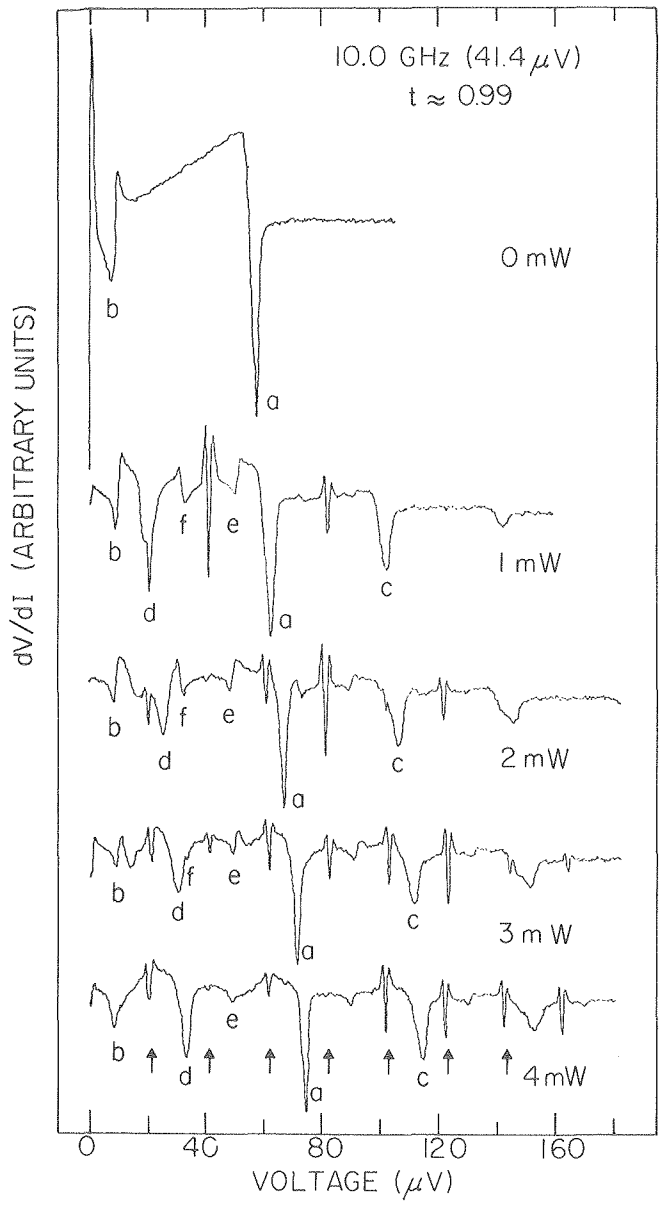

Fig. 1. dV/dI vs. V for Al-Al_2O_3-Al tunnel junction. (XBL 771-5002)

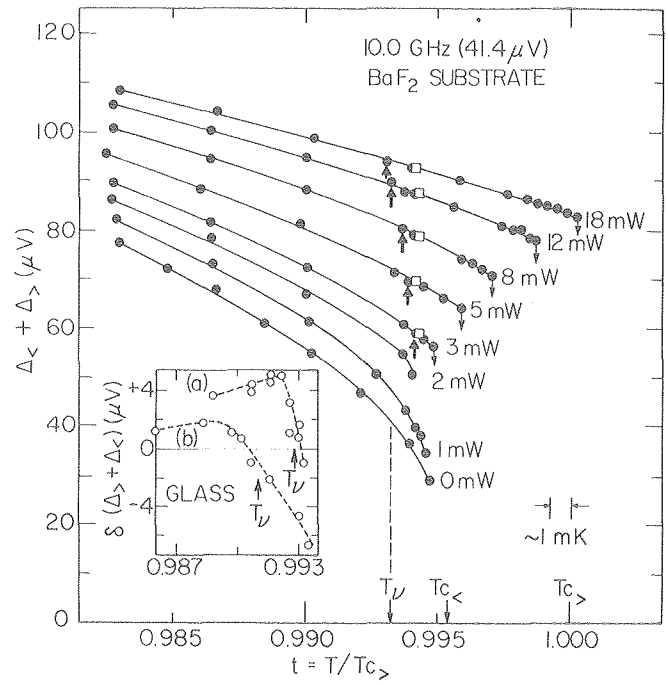

Fig. 2. $(\Delta_> + \Delta_<)$ vs. reduced temperature for several levels of microwave power. Inset shows gap enhancement, $\delta\ (\Delta_> + \Delta_<)$ vs. temperature for (a) 9.9 GHz and (b) 11.9 GHz. (XBL 771-5004)

arose from photon-assisted tunneling, and the structure indicated by arrows was due to microwave-induced Josephson current steps at voltages $n\hbar\omega/2e$ ($n = 0, \pm 1, \pm 2, \ldots$). The voltage at which both types of structures occurred was independent of the microwave power level. The minimum at "a" moved to a progressively higher voltage as the power was increased, while the position of "b" was relatively independent of power. Thus, the average gap, $\langle \Delta \rangle = (\Delta_> + \Delta_<)/2$ was enhanced as the power was increased.

Figure 2 shows the temperature dependence of the average gap for several power levels. These curves were obtained using two methods:

Method I. The temperature was slowly increased from the lowest value keeping the microwave power constant. At the higher power levels, the gap structure abruptly vanished at the temperature $T_\downarrow$ indicated by the downward arrow. Thus, as the temperature was increased at constant microwave power, $2 \langle \Delta \rangle$ was maintained at a value greater than $\hbar\omega$ until a first-order transition to zero gap occurred at $T_\downarrow$. When we subsequently reduced the temperature (keeping the power constant) the gap did not reappear until we reached a temperature $T_\uparrow$ that was lower than $T_\downarrow$. Thus, we observed hysteresis in the plot of $2 \langle \Delta \rangle$ vs. power at constant temperature.

Method II. We increased the microwave power from zero at constant temperature. At temperatures below $T_\square$ (marked □ in Fig. 2), we obtained the same enhanced values as in Method I, whereas, at temperatures $T_\square$ and above, the behavior was quite different. At $T_\square$, there was a small enhancement at lower power levels, but the structure in dV/dI disappeared for powers above 3 mW. At higher temperatures, we observed no enhancement at all. We ascribe this behavior to the fact that the photons were sufficiently energetic ($\hbar\omega > 2\Delta$) to break pairs in this temperature range, so that the microwaves destroyed rather than enhanced the superconductivity. The inset of Fig. 2, in which the change in the average energy gap, $\delta\ (\Delta_> + \Delta_<)$, is plotted vs. temperature for two microwave frequencies, confirms this explanation. T_ν is the temperature at which the microwave energy, $h\nu$, is equal to twice the average equilibrium energy gap. Thus T_ν is the temperature above which we expect substantial pair breaking by the photons. At temperatures well below T_ν, the microwave enhance $\langle \Delta \rangle$, whereas at temperatures well above T_ν, the microwaves depress $\langle \Delta \rangle$, implying that pair breaking sets in.

In preliminary experiments at 3 GHz we obtained similar results. At this frequency, the value of $T_{\downarrow}$ could be as much as 30 mK above the equilibrium transition temperature, so that the transition temperature was considerably enhanced above its equilibrium value. The hysteresis in the plot of $2<\Delta>$ vs. temperature at constant power became even more pronounced. We plan to carry out more experiments at this frequency, to investigate the nature of the phase transition that occurs. We also plan to study other materials, for example, tin.

---

* Deceased.

4. MEASUREMENT OF THE ELECTRON-PHONON RELAXATION RATE IN ALUMINUM

C. C. Chi and J. Clarke

One of the most fundamental properties of a superconductor is the magnitude of the electron-phonon scattering time, τ_o. This time governs most quasiparticle relaxation processes, and an accurate measurement of τ_o is essential to the proper understanding of the nonequilibrium superconducting states. One may estimate τ_o from the quasiparticle recombination time, τ_R. However, the measured value of τ_R may be appreciably larger than the intrinsic value because of phonon-trapping effects. Consequently, we have measured τ_o from the branch relaxation time, τ_Q, which is not affected by phonon trapping.

The sample (inset in Fig. 1) consisted of a 3×3 mm Al-Al_2O_3-Al injection tunnel junction evaporated onto a glass slide. The junction was masked with a 100 nm film of SiO to leave a 1×1 mm window near the middle, and a diagonal Cu strip was evaporated to form an Al-Al_2O_3-Cu detector junction. We passed an injection current, I_i, between the two Al strips at liquid He^4 temperatures, and measured the resultant quasiparticle potential, V_d, developed across the detector junction with a null-balancing SQUID voltmeter. Typical current-voltage characteristics for the injection and detector junctions are shown in Fig. 1. Notice that at high injection voltages, V_d is linear in I_i. Near the transition temperature, T_c, of the Al films, and for values of $V_d >> 2\Delta_{Al}$ (Δ_{Al} is the energy gap in Al), we deduced values of τ_o^{-1} in the second Al film from the result

$$\tau_Q^{-1} = I_i/2N(0)\ g_{NS}(0)\ \Omega\ e^2\ V_d\ . \qquad (1)$$

In Eq. (1), N(0) is the single-spin density of states in Al, $g_{NS}(0)$ is the normalized tunneling conductance of an SN junction at zero voltage, and Ω is the volume of the Al film into which the current I_i is injected. In Fig. 2 we plot $I_i/2N(0)\ g_{NS}(0)\ \Omega\ e^2\ V_d$ vs. $\Delta(T)/k_BT$ for several samples, the characteristics of which are given in Table 1.

To find τ_o, in terms of T_Q, we solved numerically the coupled kinetic equations for quasiparticles that included both elastic and inelastic branch

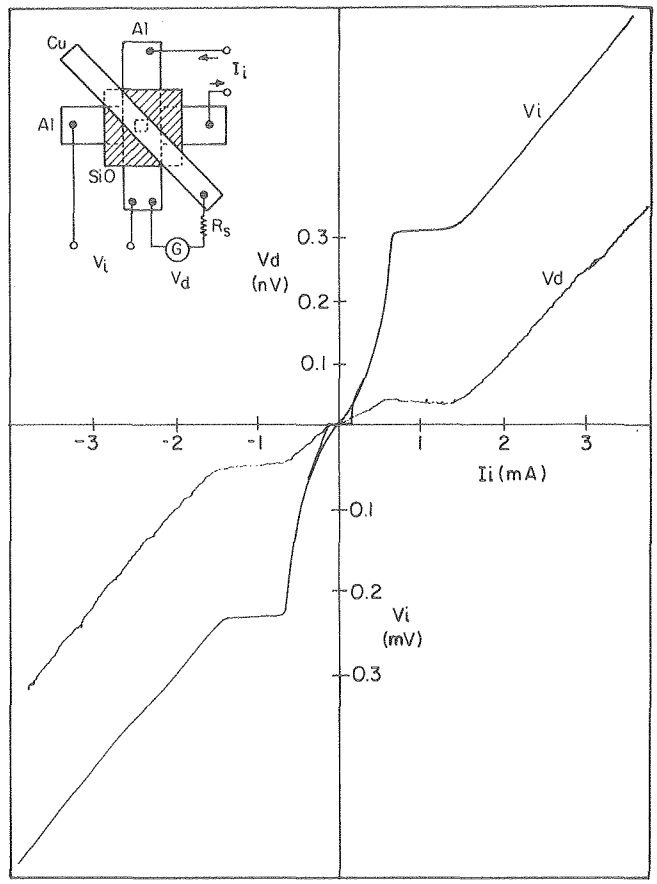

Fig. 1. V_i and V_d vs. I_i for typical sample. Inset shows sample configuration. (XBL 7710-6152)

relaxation processes. Near T_c, we find that the inelastic processes dominate, and the branch relaxation rate is given by

$$\tau_Q^{-1} = 7.8\ \tau_o^{-1}(\Delta/k_BT_c)\ . \qquad (2)$$

As is evident from Fig. 2, the upward curvature of the data indicates that other branch crossing processes become important at larger values of Δ/k_BT_c. This relaxation is due to elastic scattering in the presence of gap anisotropy. We have been able to account fully for this process, and to obtain estimates of the anisotropy.

Table 1 shows the variation of τ_o with T_c and the mean free path, ℓ, of the Al film. For the clean samples, $<\tau_o> = (1.3 \pm 0.2) \times 10^{-7}$ s. As ℓ is reduced, τ_o becomes progressively shorter. This decrease can be largely explained by setting $\tau_o^{-1} \propto T_c^3$, or, equivalently, $\alpha^2F(\omega) = b\omega^2$, where α^2 is the square of the electron-phonon matrix elements, $F(\omega)$ is the phonon density of states, and b is a parameter to be determined. We have used the measured values of τ_o and T_c to calculate the values of b shown in Table 1. We see that b is roughly constant

Table 1. Parameters for samples on which τ_Q was measured.

Sample Number	T_c (K)	ℓ (nm)	τ_o (10^{-7} s)	b (10^{-3} MeV^{-2})
2	1.228	100	1.39	0.63
3	1.231	100	1.32	0.66
4	1.262	90	1.16	0.70
5	1.265	78	1.12	0.72
6	1.253	53	1.56	0.53
7	1.241	49	0.80	1.06
8	1.306	23	0.83	0.88
9	1.411	125	0.64	0.91
10	1.573	6	0.16	2.61
11	1.886	1.1	0.12	2.02
12	2.113	1.0	0.11	1.57

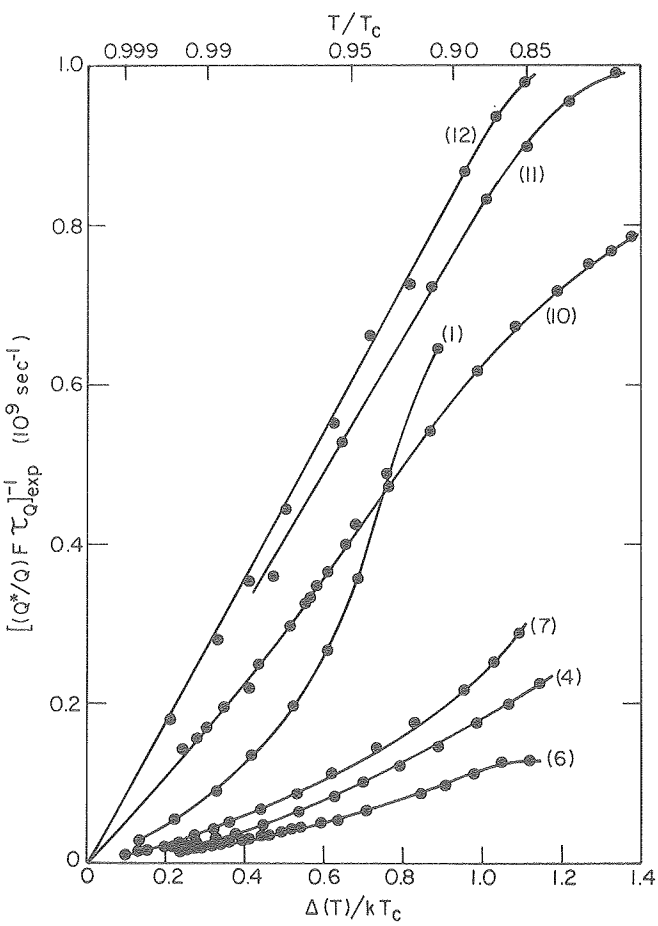

Fig. 2. $I_i/2N(0)\ g_{NS}(0)\ \Omega\ e^2\ V_d$ vs. Δ/k_BT for several samples. (XBL 7710-6149)

for the cleanest samples, but that it increases rapidly by a factor of 2 or 3 as ℓ decreases from about 80 nΩm to about 150 nΩm. For $\ell \gtrsim 150$ nΩm, b is again roughly constant. This rapid change in b is not accompanied by an abrupt change in T_c. Further investigation is required to properly understand the mechanism for the abrupt increase in b.

5. BOUNDARY RESISTANCE OF SNS SANDWICHES AND THE MEASUREMENT OF BRANCH CROSSING TIMES IN LEAD AND TIN

T. Y. Hsiang and J. Clarke

A problem in nonequilibrium superconductivity of long-standing interest has been the mechamism by which an electric current flows across a normal-superconductor (NS) interface. This problem has been tackled by Pippard and co-workers and by Waldram, who have provided a theoretical framework for interpreting their experimental results. We have modified their ideas to extract values for the branch mixing time, τ_Q, in superconductors, as well as to confirm the theory in some detail. These values for τ_Q can be used as derived values for τ_o, the electron-phonon scattering time. This technique is an alternative to the tunnel injection method described in article 4, and provides an important check of the consistency of the two methods.

At an SN inferface, the superconducting energy gap extends into the N-region by virture of the proximity effect. Consider an electron incident on the interface from the N-side. At low temperatures

($T << T_c$), the energy of the electron will be less than the energy gap, Δ, of the superconductor (or possibly than the gap at a point inside the N-metal), and will be Andreev reflected as a hole. Charge conservation is assured by the propagation of pair inside the superconducting region. A normal current incident on the boundary is thus converted to a supercurrent at the point of Andreev reflection. On the other hand, near T_c, the electron is likely to have an energy greater than Δ, and is thus able to propagate into the superconductor, and to carry a normal current into the superconductor. This normal current flows dissipatively in the superconductor, decaying into a supercurrent in a characteristic length $\lambda_Q = (v_F \ell \tau_Q/3)^{1/2}$, where v_F is the Fermi velocity and ℓ is the electronic mean free path. This process gives rise to a boundary resistance that is proportional to the number of electrons transmitted into the superconductor, to the normal state resistivity of the superconducting material, and to τ_Q. As the temperature is lowered, this boundary resistance tends to zero. Thus, by measuring the boundary resistance as a function of temperature, one can deduce λ_Q. To measure τ_Q we made SNS sandwiches in two configurations: One consisted of normal metal foils that were sputtered cleaned and on which superconducting films were evaporated, while the other was made by successive evaporations of the appropriate materials. The samples, usually three at a time, were connected in series with a standard resistance and the input coil of a dc tunnel junction SQUID, and the whole circuit was mounted in a vacuum can surrounded by a Pb shield. We measured the resistance of each sample over the range 1.2 K to T_c. The results for four different samples are shown in Fig. 1. We observe that the resistance rises rapidly as the temperature is increased towards T_c, as we expect. The solid lines in Fig. 1 represent the predictions of the modified Pippard-Waldram theory; only the time, τ_Q, has been used as a fitting parameter. It has been assumed that τ_Q has the form $\tau_Q^0\,\Delta(0)/\Delta(T)$, where τ_Q^0 is independent of temperature. In each case, the fit is excellent over the whole temperature range. The dashed line in each figure represents the best fit obtained using a temperature independent τ_Q^0, and is obviously a much poorer fit to the data than the continuous line. We conclude that $\tau_Q^0\Delta(0)/\Delta(T)$ is the appropriate form for τ_Q, and list the values of τ_Q^0 in Table 1. The values quoted for Sn and Pb are those obtained with 1% In and 1% Bi, respectively, added to reduce the mean free path to a value at which the theory is strictly applicable. Also listed in the Table are the values calculated by Kaplan et al. by solving the kinetic equations for the quasiparticles, and the value obtained for Sn by Clarke and Paterson using tunnel injection. Given the general uncertainties in both the experiments and in the theory, the agreement between the theoretical and experimental values can be considered excellent.

These experiments have demonstrated that the quasiparticle relaxation time appropriate for the decay of quasiparticles injected over a SN interface is the same time that one observes in the tunnel injection experiments. In addition, our results indicate that the theory for the processes involved at the SN interface is quantitatively correct. The measurement of the resistance of SNS sandwiches is thus a relatively straightforward means of measuring τ_Q and thereby determining τ_Q, and could readily be extended to other superconductors.

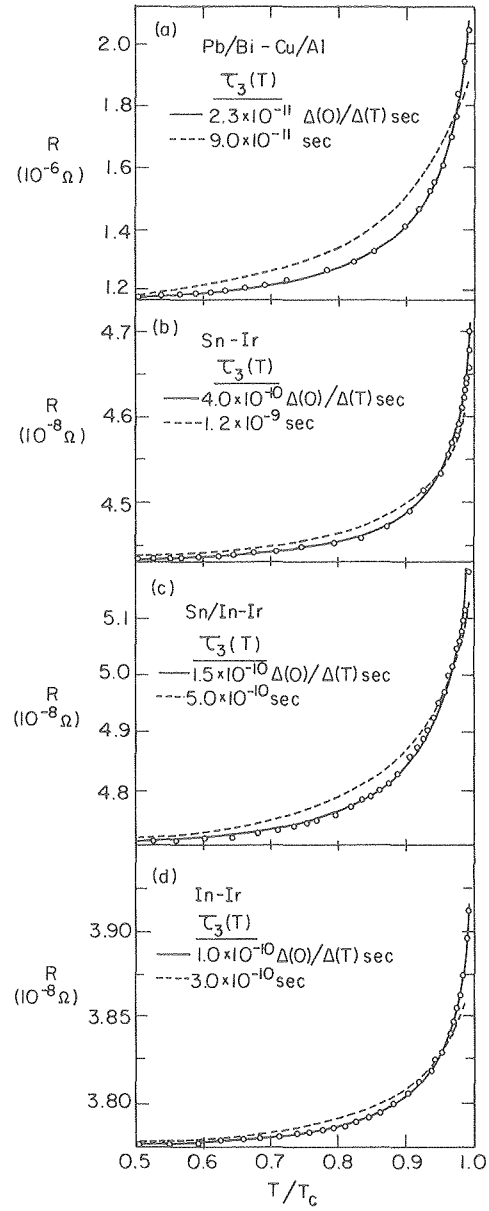

Fig. 1. Measured resistance, R, vs. reduced temperature, T/T_c, for four SNS sandwiches.
(XBL 7711-6409)

6. RESEARCH PLANS FOR CALENDAR YEAR 1978

John Clarke

Geophysics. We propose to exploit our new remote reference technique for performing magnetotelluric surveys. We plan to complete a data processing unit incorporating an LSI-11 microprocessor that should enable us to process magnetotelluric data on-site, and thus quickly assess the quality of the data. We hope to survey several sites, for example, Grass Valley, Nevada, Mt. Hood, Oregon, and Hollister,

Table 1. Values of τ_Q^o.

	Kaplan et al. (sec)	SNS Resistance (sec)	Tunnel Injection (sec)
In	1.0×10^{-10}	1.0×10^{-10}	-
Sn	2.9×10^{-10}	1.5×10^{-10}	1.0×10^{-10}
Pb	2.1×10^{-11}	2.3×10^{-11}	-

California with this equipment. We also plan to perform stringent tests to find the ultimate resolution and reproducibility of our technique.

Another geophysics experiment involves a study of possible magnetic field gradient fluctuations. We know from our magnetotelluric measurements that magnetic "noise" sometimes contaminates our data: It was for this reason that we developed the remote nagnetometer technique. If the magnetic noise is generated near the earth's surface, it may contain a measurable gradient. Thus, by using a superconducting gradiometer that will tend to discriminate against distant magnetic sources, we may be able to locate nearby magnetic sources.

Superconducting Devices. We plan to develop a new generation of dc SQUID devices with increased sensitivity. According to our theory, the energy resolution of a tunnel junction dc SQUID is proportional to the square root of the junction area. Thus, if we can reduce the linear dimensions of our junctions from the present size ($\sim$100 μm) to (say) 5 μm by means of photolithography, we would expect to improve the resolution by a factor of 20. This improvement is badly needed for certain gradiometer applications, and for gravity-wave transducers. In addition, we will attempt to build two-stage SQUID amplifiers in which the second SQUID is used to read out the first. If the first SQUID is cooled to a few mK, the theory predicts that its energy resolution at 1 Hz will be improved by 3 to 4 orders of magnitude to a value that is limited by the uncertainty principle.

Nonequilibrium superconductivity. We expect to maintain a major effort in this area. The work on microwave-induced gap enhancement will be completed. We propose to investigate a new means of gap enhancement by tunnel injection into a superconductor just below its transition. In another experiment we plan to investigate the possible spatial inhomogeneity of a thin superconducting aluminum film irradiated with microwaves or light. The film will have a number of tunnel junctions grown on it at 10 μm intervals (using photolithography) so that we can simultaneously measure the energy gap of the film under varying levels of irradiation. A further possible experiment is the measurement of the branch crossing time, τ_Q, and hence of the electron-phonon time, τ_o, in hard superconductors such as Nb.

1/f noise. Measurements are to be made of the 1/f noise in metals deposited on different substrates. We are particularly interested in the temperature dependence of the noise around room temperature, and in the role of the substrate in the magnitude of the noise. We hope to be able to develop a more microscopic understanding of our thermal fluctuation theory of 1/f noise.

7. 1977 PUBLICATIONS AND REPORTS

John Clarke and Associates

Journals and Books

1. M. B. Ketchen, W. M. Goubau, J. Clarke and G. B. Donaldson, Thin Film DC SQUID Gradiometer, IEEE Trans. Magn. MAG-13, 372 (1977).

2. C. D. Tesche and J. Clarke, A Computer Model for Noise in the DC SQUID, IEEE Trans. Magn. MAG-13, 859 (1977).

3. J. Clarke, Superconducting Quantum Interference Devices, in Superconductor Applications: SQUIDS and Machines, B. B. Schwartz and S. Foner, Eds. (Plenum Press, New York and London, 1977), p. 67.

4. J. Clarke, Current Performance of Superconducting Quantum Interference Devices, in SQUID: Superconducting Quantum Interference Devices and Their Applications, H. D. Halhbohm and H. Lübbig, Eds. (de Gruyter, Berlin, 1977), p. 213.

5. G. B. Donaldson, M. B. Ketchen, J. Clarke and W. M. Goubau, An Integrated Thin Film Gradiometer Based on a DC SQUID, ibid., p. 303.

6. J. Clarke, Summary and Conclusions, ibid., p. 587.

7. T. R. Kommers and J. Clarke, Measurement of Microwave-Enhanced Energy Gap in Superconducting Aluminum by Tunneling, Phys. Rev. Lett. 38, 1091 (1977).

8. J. Clarke, P. L. Richards and N.-H. Yeh, Composite Superconducting Transition Edge Bolometer, Appl. Phys. Lett. 30, 664 (1977).

9. C. D. Tesche and J. Clarke, DC SQUID: Noise and Optimization, J. Low Temp. Phys. 29, 301 (1977).

10. J. Clarke, G. I. Hoffer, P. L. Richards and N.-H Yeh, Superconductive Bolometers for Submillimeter Wavelengths, J. Appl. Phys. 48, 4865 (1977).

11. R. Dalven, Connection Between the Dispersion Relation, Surfaces of Constant Energy, and Energy Bands in Solids, Am. J. Phys. 44, 248 (1976).

12. R. Dalven, Possible Light Scattering Experiment to Detect the Three-Dimensional Wigner Lattice, Phil. Mag. 35, 801 (1977).

LBL Reports

1. J. Clarke, Superconductive Devices (to be published in Encyclopedia of Physics), LBL-6228.

2. M. B. Ketchen and J. Clarke, Low Frequency Noise in Freely Suspended Tin Film at the Superconducting Transition, LBL-6631.

3. M. B. Ketchen and J. Clarke, Temperature Fluctuations in Freely Suspended Tin Films at the Superconducting Transition (submitted to Phys. Rev. B1), LBL-6638.

4. W. M. Goubau, T. D. Gamble and J. Clarke, Magnetotelluric Data Analysis: Removal of Bias (submitted to Geophys.), LBL-6634.

5. T. D. Gamble, W. M. Goubau and J. Clarke, Magnetotelluric Data Analysis: Tests of Methods Using Data Obtained at Grass Valley, Nevada (submitted to Geophys.), LBL-6648.

6. T. D. Gamble, W. M. Goubau, M. B. Ketchen and J. Clarke, Regulator for Controlling Liquid Helium Bath Near 4.2 K (submitted to Rev. Sci. Instrum.), LBL-6676.

7. M. B. Ketchen, J. Clarke, W. M. Goubau and G. B. Donaldson, Superconducting Thin-Film Gradiometer (submitted to J. Appl. Phys.), LBL-6927.

8. M. B. Ketchen, Development and Applications of the Tunnel Junction dc SQUID (Ph.D. thesis), LBL-6086, May 1977.

9. T. Y. Hsiang, Low Frequency Noise in Metal Films at the Superconducting Transition; Resistance in Superconductors—Normal Metal—Superconducting Sandwich and the Quasiparticle Relaxation Time, (Ph.D. thesis), LBL-6611, January 1977.

Papers Presented

1. John Clarke, Principles and Limitations of Superconducting Quantum Interference Devices, Annual Meeting of the APS, Chicago, February 10, 1977.

2. John Clarke and T. R. Kommers, Microwave Enhancement of the Superconducting Energy Gap Observed by Quasiparticle Tunneling (paper given by T. R. Kommers), Meeting of the APS, San Diego, Calif., March 23, 1977.

3. John Clarke and C. C. Chi, Measurement of Quasiparticle Branch-Mixing Time in Superconducting Aluminum (paper given by C. C. Chi), Meeting of the APS, San Diego, Calif., March 23, 1977.

4. John Clarke, Microwave Enhancement of the Energy Gap of Aluminum, Conference on Theory of Transient Effects, San Diego, Calif., March 25, 1977.

5. John Clarke, Microwave Radiation Induced Non-Equilibrium States in Superconductors, invited talk at the Gordon Conference on Quantum Solids and Fluids, Wolfeboro, New Hampshire, July 20, 1977.

2. THEORETICAL SOLID STATE PHYSICS

a. Theoretical Solid State Physics

Marvin L. Cohen, Principal Investigator

1. SURFACE STATES ON CLEAN GERMANIUM AND DIAMOND CRYSTALS*

M. L. Cohen, Steven G. Louie and J. Ihm

We have continued to investigate the electronic structure of clean semiconductor surfaces. The self-consistent pseudopotential method with a slab geometry, which yielded satisfactory results for Si (111) surface, is now employed for the calculations of Ge(111) and diamond (111) surfaces. The local pseudopotential approximation does not work for diamond because p valence electrons of C see a very strong core potential due to the absence of p core orbitals in the C atom. A non-local pseudopotential for C is derived and found to produce an energy band structure of bulk diamond in good agreement with other calculations and experiments. This potential is then used for the diamond surface calculations.

We have obtained the charge densities and the local density of states of Ge and diamond surfaces. Comparing the energy band structure of the bulk and that of the surface, we identified surface states bands. The result for the diamond is illustrated in Fig. 1. The big peak in the local density of states curves presented in Fig. 2 shows that the diamond surface has very strong dangling-bond gap states in the surface region. In this unrelaxed, unreconstructed surface calculation, the Fermi energy (E_F) falls in the gap states so that the surface is metallic. Reconstruction is possible to form a semiconductor surface. The results obtained here will be used as references for the calculations of Ge/metal or diamond/metal interface structures.

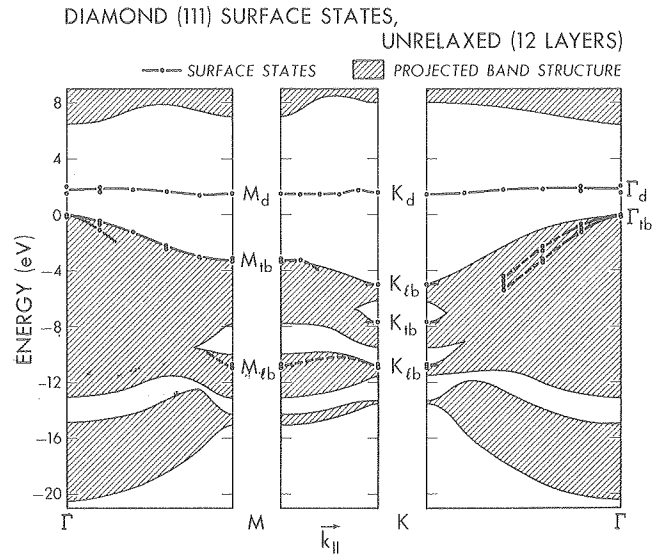

Fig. 1. Two-dimensional band structure of a 12-layer diamond (111) slab along symmetry lines. Various surface states or surface resonances are indicated by heavy lines and are labeled. Dashed lines mean "weak" surface states or resonances which have a long decay length into the bulk. Subscripts represent a "dangling bond (d)," a "transverse back bond (tb)," or a "longitudinal back bond (lb)," respectively. Heavy dots refer to the calculated energy eigenvalues of surface states. As a slab has two surfaces, the surface states come in pairs. Some of them are not completely degenerate due to the finite thickness. The projected band structure is also plotted. A picture of the BZ is inserted. (XBL 782-7115)

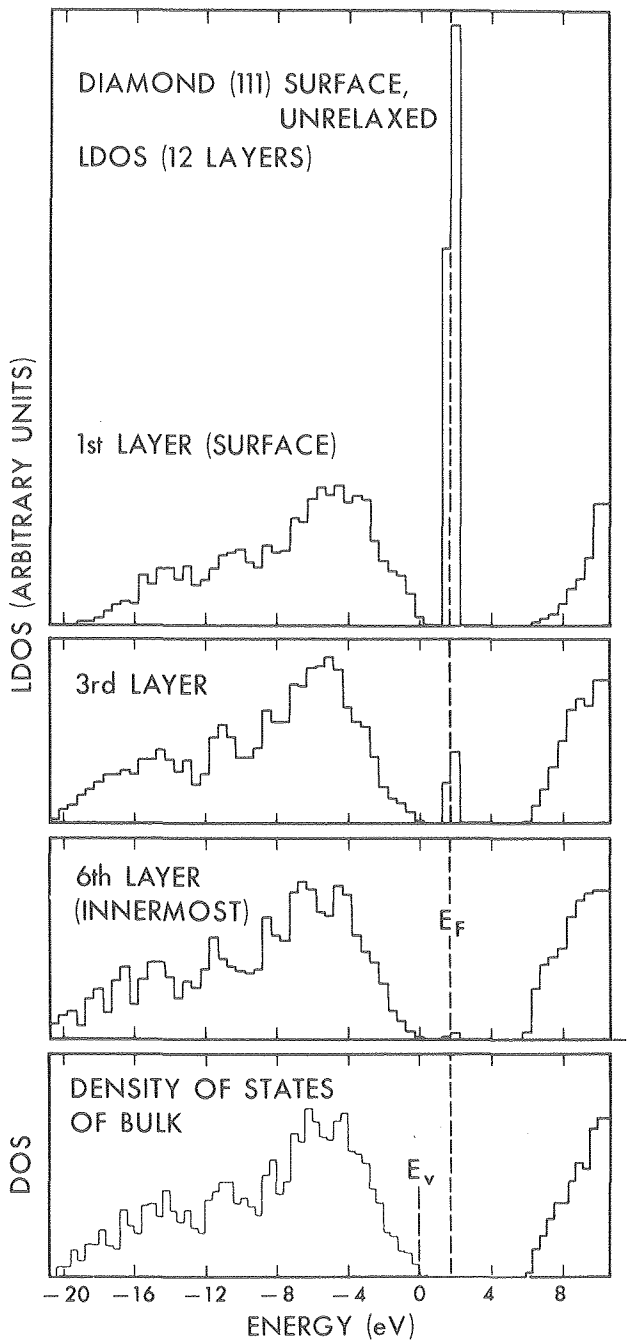

Fig. 2. Local density of states (LDOS) curves for diamond (111) slab. The density of states (DOS) of the bulk calculated is also drawn for comparison. It can be observed that by the 3rd layer the LDOS is very similar to the bulk DOS except for the gap states. (A portion of charges from both sides of the gap participates in forming surface states in the gap.)
(XBL 782-7116)

---

*Partially supported by NSF.

2. RECONSTRUCTION OF SEMICONDUCTOR SURFACES: THE Si (001) SURFACE*

M. L. Cohen, G. P. Kerker and S. G. Louie

It is well known from LEED experiments that most covalent solids show a spontaneous lowering of the symmetry of a surface by reconstruction. This effect can be understood qualitatively from energetic reasons. In order to form the surface one or more bonds have to be broken per surface atom. The broken bonds given rise to surface states near or in the gap between the valence and the conduction bands. The effect of reconstruction is to lower the total energy of the system by splitting these states and shifting them to energies away from the gap. In real space this is accomplished by a rearrangement of the atoms in the surface region that is different from the bulk geometry. Although the structural change can be easily observed in the LEED pattern, it is difficult to determine the atomic positions uniquely from an intensity analysis. A knowledge of the electronic structure can be very useful in order to test the validity of a given structural model.

As an example of present interest we calculated the electronic structure of both the ideal and the reconstructed Si (001) surface self-consistently by using our pseudopotential method described above. The surface of the semi-infinite system was simulated by the surfaces of a 12 layer Si-slab. The ideal unreconstructed surface has two broken bonds per surface atom that give rise to two partially occupied surface bands in the fundamental gap making this surface metallic and therefore unstable against reconstruction. In fact, a (2×1) reconstruction is observed experimentally.

We calculated the electronic structure of the reconstructed surface by adopting a structural model that was claimed to give the best possible fit of the observed LEED intensity data. It assumes that the surface atoms form zig-zag chains along the (100) or (010) direction of the surface plane (Fig. 1). With our method we were able to analyze the electronic structure of this model in terms of the two-dimensional band-structure, the charge density distributions and the local density of states.

We found, as for the ideal case, a metallic surface due to broken bond states. In addition the chain bond states cause a peak in the local density of states at the surface which is not observed in the corresponding photoemission spectrum (Fig. 2).

These results led us to the conclusion that the proposed zig-zag model and its variants can be ruled out as a possible reconstruction of a clean

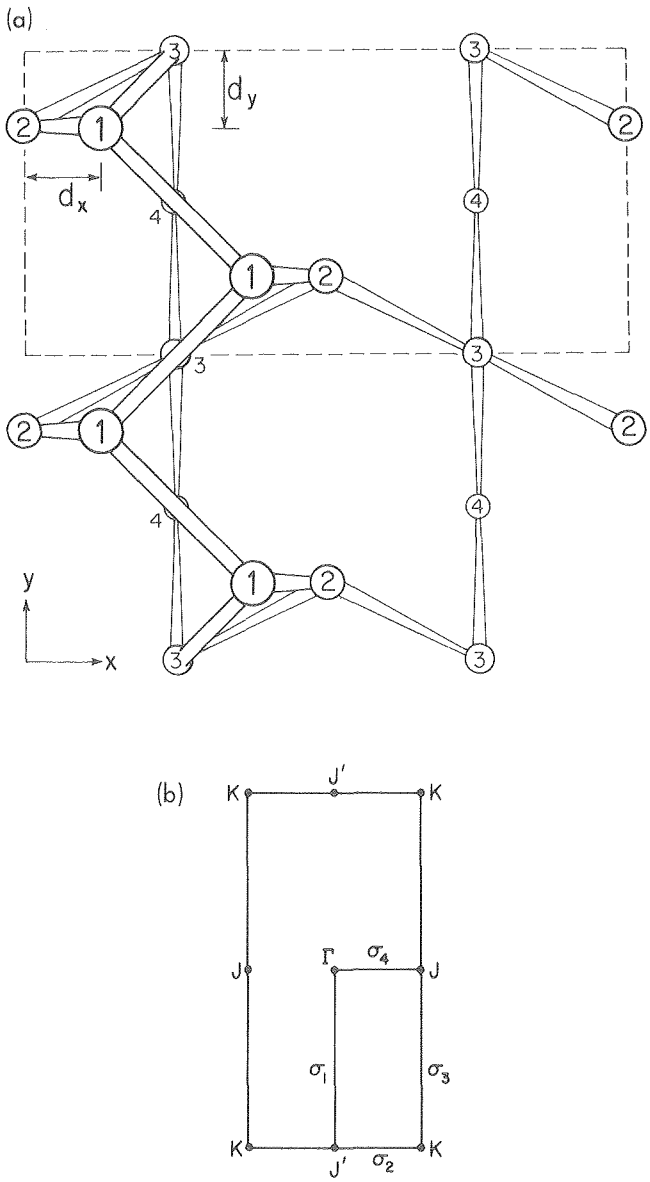

Fig. 1. Orientation of the first four atomic layers of the (2 × 1) reconstructed surface according to the chain model, viewed from the vacuum looking normally into the bulk. The atoms are represented by circles. The number in a circle labels an atomic layer. (XBL 782-7117)

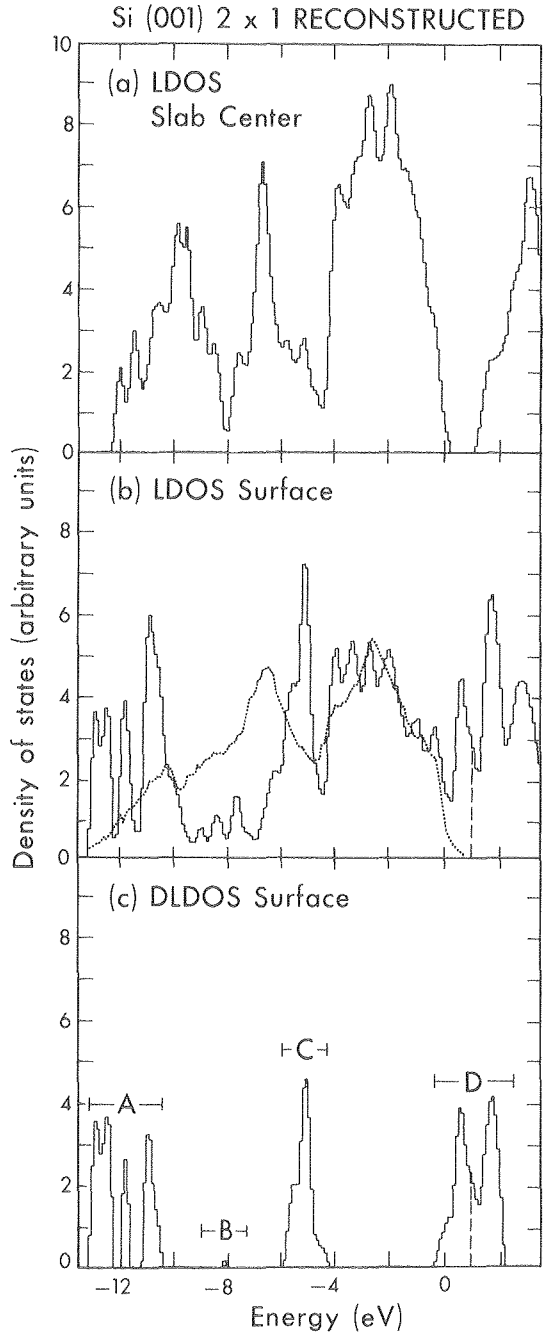

Fig. 2. Calculated local density of states (LDOS) curves for the (2 × 1) reconstructed surface using the chain geometry. Also given in the surface LDOS histogram is the measured photoelectron density (dotted line). Subtracting from the surface LDOS the corresponding values of the slab center LDOS and keeping the positive contributions gives the difference curve of the local density of states (DLDOS) at the surface. It reveals the energy regions where surface states occur. In particular, the chain bond states cause the peak at region C which is characteristic for this geometry. (XBL 782-7114)

Si (001) surface. At present the geometry of this surface is still an open question.

---

*Partially supported by NSF.

3. SURFACE AND BULK ELECTRONIC PROPERTIES OF TRANSITION METALS*

M. L. Cohen, K. M. Ho, S. G. Louie and J. R. Chelikowsky

Because of the partial occupancy of d-states in transition metals, a simple extension of the self-consistent pseudopotential method to these systems isn't possible. The d-states must be treated separately using non-local (angular momentum dependent) potentials. By extending our methods to include the use of these non-local potentials, we have been able to calculate electronic band structures for systems containing transition elements. Transition metals have been studied extensively because of their importance in practical applications (e.g., catalysis) and also because of the interesting properties they exhibit as a result of their partially filled d bands.

Niobium was chosen as the first case to be studied. The ionic pseudopotential was generated by fitting to ionic and atomic data. The resulting potential gives a bulk band structure in good agreement with previous calculations and photoemission experiments. Charge densities were calculated and displayed. These give interesting views of the bonding nature of Nb.

Using the above potential, we performed a self-consistent calculation for the Nb (001) surface. A nine layer periodic slab geometry was used with a vacuum separation of five layers between slabs. The total valence charge density is plotted along the (110) and (100) planes perpendicular to the surface. The charge at the center of the slab is bulk like and shows a distinct d character around the atom.

To investigate the change in the density of states in going from the bulk to the surface, we have plotted the local density of states for each layer of the slab. The local density of states for layers 4 and 5 at the center of the slab is almost bulk like, whereas layer 1 shows surface features in the regions 0 to 2 eV above the Fermi level and at 2 eV below the Fermi level.

To get a better understanding of the distribution of surface states in the two-dimensional surface Brillouin zone, we project the three-dimensional bulk band structure onto the (001) plane. The gaps in the Nb (001) projected band structure are located far away from the zone center and tend to be widest away from high symmetry points. There are two main gaps, one just above the Fermi level between 0 and 3 eV and the other between -1 and -2 eV. Most of the surface states in our calculation appear in these two gaps. We also found strong surface resonances in symmetry gaps along symmetry lines in the two-dimensional surface BZ. (Symmetry gaps are regions along the symmetry lines where states of a given symmetry are forbidden but states with other symmetries may exist.)

*Partially supported by NSF.

4. ELECTRONIC STRUCTURE OF METAL-Ge AND METAL-DIAMOND INTERFACES (SCHOTTKY BARRIERS)*

M. L. Cohen, J. Ihm and S. G. Louie

Interface (IF) problems have been extensively studied in our group using the self-consistent pseudopotential method. This method, which has proved very successful for calculations of the metal-Si and metal-zincblende IFs before, is now applied to similar calculations of metal-Ge and metal-diamond IFs. The origin of the persistent interest in metal-semiconductor IFs is twofold. First, metal-semiconductor IFs are of technical importance for many electronic devices because of their rectifying properties. Second, the barrier height at the metal-semiconductor IFs has been found experimentally to be dependent on ionicity (or gap size) and electronegativity properties of the semiconductor and the metal. Some researchers have claimed that it is a crucial indicator of the covalent-ionic transition among various semiconductors. The physical understanding of these properties is still open questions.

The metal is simulated by a jellium model for the positive background with a charge density equivalent to that of aluminum and the pseudopotential is used for the description of the semiconductor ionic cores. The conduction electrons of the metal and the valence electrons of the semiconductor are free to redistribute self-consistently for the given system. For the metal-Ge (111) IF, the local density of states near the Fermi level is studied in detail to understand the pinning of the Fermi level. As in the case of the metal-Si IF studied previously, a high density of metal induced gap states is found in the gap. Again, we are led to the conclusion that it is this high density of metal induced gap states which are responsible for the pinning of the Fermi level. This results in a small value for the phenomenological index of interface behavior S; we obtained $S = 0.14$ in agreement with experiments. True IF states that are localized at the IF are found only in the gap, but the density of these states are extremely small and the density of states in this region is completely dominated by the metal-induced states. The metal-induced gap states have free electron behavior on the metal side and decay exponentially on the Ge side. The calculated Schottky barrier height, defined to be the difference between the Ge conduction band minimum and the Fermi level is found to be 0.55 ± 0.1 eV in agreement with experiment.

Preliminary results for the metal-diamond (111) IF have been obtained. This calculation is of importance because of its ability to test various theories predicting different S values for this large-gap covalent material. The question of the dependence of S on gap size or ionicity is fundamental to the understanding of the Schottky barrier properties. Our calculations place the diamond Schottky barrier away from $S=0$ but not at the very ionic end of the S vs ionicity curve; S is calculated to be 0.38 ± 0.1. The metal-induced gap states distribution is more or less constant in the large gap thereby giving a relatively low surface density of states in the gap region compared to the Ge and Si Schottky barriers. The

small diamond lattice constant, which is 63 ~ 66% of the Ge or Si lattice constant, contributes to increasing the surface density of states (because of a smaller area per surface atom) by a factor to 2 or more. The net result is still a uniform surface density of states and a value of S of ~0.1 for Si or Ge. The calculated Schottky barrier height, this time taken to be the difference between the Fermi level and the diamond valence band maximum for comparison with experiments done on p-type diamond, is 2.2 eV in agreement with experiment.

---

*Partially supported by NSF.

5. SEMICONDUCTOR-SEMICONDUCTOR INTERFACES AND SUPERLATTICES*

M. L. Cohen and W. E. Pickett

The great technological importance of the properties of the semiconductor-semiconductor interface (IF), or heterojunction, has encouraged detailed theoretical studies on the atomic scale of idealizations of these systems. The idealizations are abrupt IFs, whereas typical heterojunctions are graded over 100 to 300 Å. Recently however, these idealizations have been experimentally realized with IF growth by the molecular beam epitaxy method, in which "superlattices" are constructed by a periodic repetition of IFs. We have done self-consistent calculations on the (110) IFs of AlAs-GaAs, Ge-GaAs and Ge-ZnSe. These systems have been chosen both for their technological interest and in order to study theoretical trends.

These IFs also have small lattice mismatch ($\lesssim 0.2\%$), and experiments suggest that it is valid to ignore the mismatch entirely for many properties. Within this restriction there exists an obvious "ideal" geometry to assume in the calculation, in the absence of experimental information on the actual atomic positions. Although general arguments show that for the polar IFs the ideal geometry is unstable, there are no such restrictions on the non-polar (110) IF and the ideal geometry is expected to be a reasonable first estimate.

The self-consistent pseudopotential method allows a complete study of IF states: their existence, character and their energy density in the IF region. At the AlAs-GaAs IF there are no IF states and negligible density of localized states, i.e., IF resonances. In Ge-GaAs, however, six distinct IF states (bands or partial bands) are found to exist within mutual gaps in the projected band structures of bulk Ge and bulk GaAs. These IF states are shown in Fig. 1, and all lie below the thermal gap. Experimentally no states are found in the gap.

In the Ge-ZnSe system some IF states are also found to exist. Due to the increased difference in ionicity compared with Ge-GaAs, the bulk band structures are less similar, with the result that it is impossible for the gaps in the projected

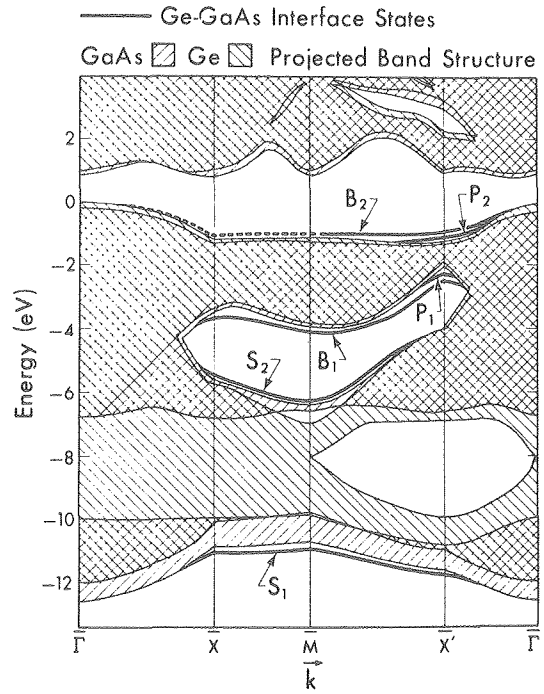

Fig. 1. The interface states of (110) Ge-GaAs relative to the projected band structures of bulk Ge and GaAs from self-consistent calculations. The dispersion of the interface states is denoted by heavy solid lines; heavy dashed lines indicate interface states that have a long decay length into the bulk. Symmetry points (in reduced units) are $\bar{\Gamma} = (0,0)$, $\bar{X} = (1/2,0)$, $\bar{M} = (1/2,1/2)$, $\bar{X}' = (0,1/2)$. The interface states S_1, S_2, B_1, B_2, P_1, P_2, as well as the "stomach" gap (-2 to -6 eV) and the "lower" gap (-7 to -10 eV) are described in the text. (XBL 782-7119)

band structures to overlap as much as in the Ge-GaAs IF. The spectral weight of localized states is shifted from true IF states to resonances. The density of states localized near the IF is larger than in Ge-GaAs but will still be difficult to detect experimentally.

The band edge discontinuities, which are of central importance technologically, are the only experimental data on the IF region that is available. From work on GaAs-$Ga_{1-x}Al_xAs$ superlattices ($x \approx 0.2$) the conduction band discontinuity has been established at $\Delta E_c = (0.15 \pm 0.03)\Delta Eg$ is the difference in direct band gaps. Extrapolating this result to $x = 1$, we find excellent agreement with the calculated result $\Delta E_c = 0.17\ \Delta Eg$. In the Ge-GaAs and Ge-ZnSe IFs the experimental values are somewhat less certain, but the theoretical and experimental values agree to within ~0.2 eV, which is within the combined uncertainties of theory and experiment.

Since the ideal geometry has been used in the calculations it is of interest to inquire whether such IFs are stable against relaxation or reconstruction. In the AlAs-GaAs system the charge density variation across the IF is localized on the cation at the IF, with both the Al-As and Ga-As bonds across the IF being nearly identical to the respective bulk bonds. There is no indication of instability.

At the Ge-GaAs IF the Ge-Ga and Ge-As bonds across the IF, shown in Fig. 2, have no bulk counterparts. These novel bonds suggest unbalanced forces on the atoms at the IF, implying relaxation. These observations apply as well to the Ge-ZnSe IF. Unfortunately there is no experimental information on the interfacial morphology of IFs at present.

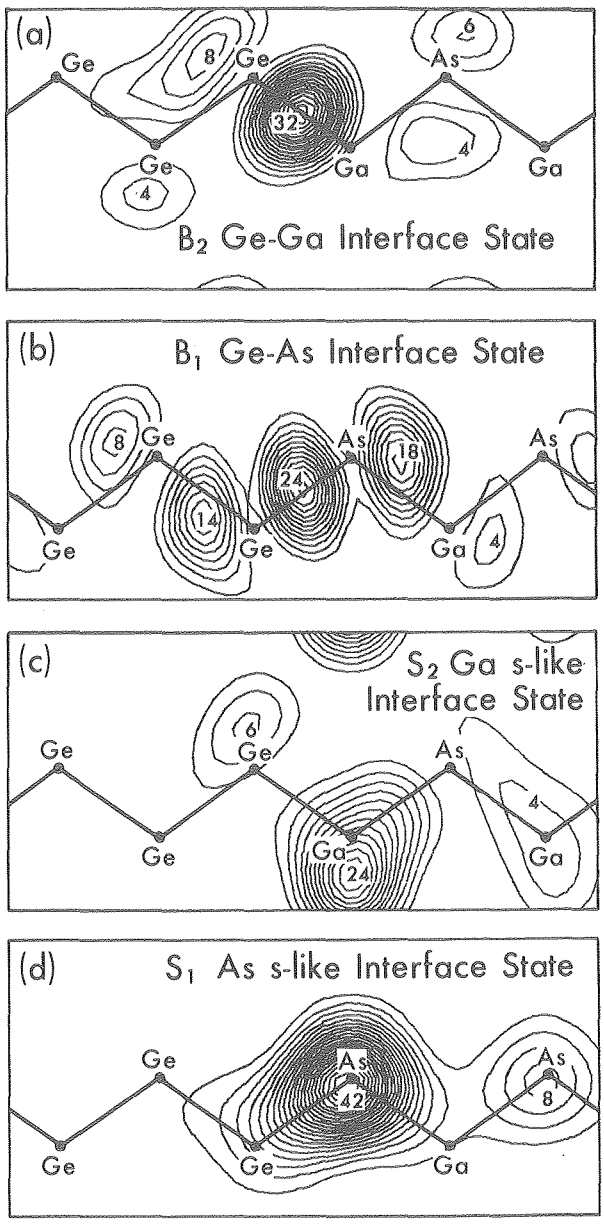

Fig. 2. Contour plots, perpendicular to the interface, of the charge densities of the interface states S_1, S_2, B_1, B_2. Each averaged charge density is normalized to unity; successive contours are separated by 2.0 units. Straight lines denote bond directions. (XBL 782-7118)

If the potential dipole at the IF is sensitive to relaxation, information on the atomic positions could be gained by calculating the band edge discontinuities for various assumed geometries and comparing to experiment values. To study this approach we have considered a simple relaxation in which the distance between the Ge and GaAs atomic planes at the (110) IF is increased by 20%. This is deliberately a substantial overestimate of any relaxation that may actually occur. Even though large distortions of the charge density result from this "relaxation," the potential dipole is found to be quite insensitive, changing by only ~0.1 eV. We conclude that this is not a useful approach for studying atomic structure at the IF.

To study these IFs we have used a superlattice geometry, in which IFs are introduced periodically to form a three-dimensional periodic solid. The IFs are sufficiently well separated so the electronic structure of a single IF is reproduced well, but superlattice effects can also be identified. In our calculations on a 9 layer AlAs-9 layer GaAs superlattice we have noted that, for the two low-energy hole bands, the transverse (to the IF) effective masses may be much different than the bulk values and are likely to be sensitive to the precise superlattice geometry. Superlattices which have been studied experimentally have been of interest because of a longitudinal effective mass m_ℓ that becomes very large ($m_\ell \to \infty$), resulting in localized ("potential well") states which interact only slightly. Transverse masses have not yet been measured experimentally.

*Partially supported by NSF.

6. MOLECULAR ELECTRONIC STATES AND ADSORBATES ON SOLIDS*

M. L. Cohen, K. M. Ho and M. Schlüter

We have applied our method to calculation of equilibrium bond lengths, force constants and binding energies of molecules. As a test case we considered the Si_2 molecule. (A previous calculation using our method gives the molecular energy levels successfully.) We repeated the calculation with higher convergence and with two intermolecular distances. Calculation of the interatomic forces using Hellmann-Feynman Theorem gives an equilibrium bond length of 4.236 a_0, in excellent agreement with experiment. However, the values we obtained for the stretching force constants and binding energy were off by 67% and 83%, respectively. Most other theoretical calculations obtain similar discrepancies for force constant calculations.

A similar calculation was performed for hydrogen adsorbed on the Si (111) surface in the monohydride

configuration. This gives an equilibrium bond length of 2.93 a_0 (which is 5% larger than the Si-H bond length in SiH_5). Again in this case, the calculated stretching force constant for the Si-H was larger than experimental values (by ~40%). It appears that a better determination of the ionic pseudopotential near $q = 0$ is necessary for calculation of properties such as force constants and binding energies which depends critically on the long range interaction of the ions.

The results for spectral features of adsorbates is quite good. Electronic calculations for monohydride and trihydride configurations for hydrogen adsorbed on Si (111) yield abundant information about these systems. Density of states calculations are compared with experiment and spectral features are analyzed using these comparisons.

For Cl adsorbed on Si (111), detailed calculations of the density of states features yield different spectra for Cl adsorbed on covalent and ionic sites. Comparison with experiment gives agreement for Si (111) if the Cl is assumed to be in the covalent configuration. Analysis of data for Cl on Ge (111) suggests that Cl will reside on ionic sites in this material. This is one of the unusual cases where Ge and Si act somewhat differently. Very recent experiments using angular resolved photoemission techniques have mapped the energy dispersion curves for Cl on Si (111). The agreement between the measured spectra and the predicted theoretical spectra is striking.

Calculations on conduction band surface resonances reveal the existence of these states for clean surfaces; however, they are most pronounced for surfaces with adsorbates like Cl. Detailed calculations of dispersion curves and densities of states were performed for these states.

---

*Partially supported by NSF.

7. RESEARCH PLANS FOR CALENDAR YEAR 1978

Marvin L. Cohen

We plan to continue our studies of interfaces with emphasis on semiconductor-semiconductor and semiconductor-insulator interfaces and Schottky barriers.

Some new developments in our techniques have allowed better treatments of localized d-states in transition metals. Work is in progress on M_0 to examine both bulk and surface properties.

A calculation of the local field dielectric function is still in progress. Results for zero wavevector have been used to evaluate the phonon frequencies at long wavelengths for Si. The wavevector-dependent dielectric function should be capable of describing the full phonon dispersion curve; we expect to be able to perform this calculation. The full dielectric matrix will also be used to study the possibility of excitonic superconductivity.

Calculations are under way on the electronic structure of Nb_3Ge and other A15 materials. These materials have the highest known superconducting transition temperatures. We expect to produce electronic charge density plots that should help to describe bonding and charge transfer in these materials. Band structure calculations and density of states curves will also be computed.

A closer analysis of the theory of pseudopotentials is under way. By requiring the pseudopotentials to give both the energy levels in a solid and the atomic levels, it is possible to explore questions related to structure. At present these pseudopotentials are too "strong" to be used easily in band structure calculations, however, new methods are being developed to try to cure this problem.

8. 1977 PUBLICATIONS AND REPORTS

Marvin L. Cohen and Associates

Journals

1. J. R. Chelikowsky, S. G. Louie and M. L. Cohen, Relaxation Effects on the (110) Surface of GaAs, Phys. Rev. B 14, 4724 (1976).

2. P. Thiry, Y. Petroff, R. Pinchaux, J. R. Chelikowsky and M. L. Cohen, Electron-hole Interaction of the d Core Levels in III-V Semiconductors, Solid State Comm. 20, 1107 (1976).

3. M. Schlüter, J. E. Rowe, G. Margaritondo, K. M. Ho and M. L. Cohen, Chemisorption-site Geometry from Polarized Photoemission: Si(111) Cl and Ge (111) Cl, Phys. Rev. Lett. 37, 1632 (1976).

4. S. G. Louie and M. L. Cohen, Some comments on the excitonic mechanism of superconductivity, Superconductivity in d- and f-band Metals, D. H. Douglass, Ed., Plenum Press, N.Y., (1976), p.7.

5. M. Schlüter, S. E. Kohn, C. Y. Fong and M. L. Cohen, Electronic Structure of BiI_3, Phys. Stat. Solidi (b) 78, 737 (1976).

6. J. Camassel, M. Schlüter, S. Kohn, J. P. Voitchovsky, Y. R. Shen and M. L. Cohen, Optical Properties of Layer Compounds GaS_xSe_{1-x}, Proceedings of the 13th International Conference on the Physics of Semiconductors, Rome, Italy (1976), p. 384.

7. D. W. Bullett and M. L. Cohen, Tight-binding Theory of Chemisorption: CO on Ni (100) and (111), Solid State Comm. 21, 157 (1977).

8. K. M. Ho, S. G. Louie, J. R. Chelikowsky and M. L. Cohen, Self-consistent Pseudopotential Calculation of the Electronic Structure of Nb, Phys. Rev. B 15, 1755 (1977).

9. S. G. Louie, J. R. Chelikowsky and M. L. Cohen, Ionicity and the Theory of Schottky Barriers, Phys. Rev. B 15, 2154 (1977).

10. K. M. Ho, M. Schlüter and M. L. Cohen, A Solid-state Approach to SCF-X_α Molecular Equations, Chem. Phys. Lett. 46, 608 (1977).

11. S. G. Louie and M. L. Cohen, Superconducting Transition Temperatures for Weak and Strong Electron-phonon Coupling, Solid State Comm. 22, 1 (1977).

12. K. M. Ho, M. Schlüter and M. L. Cohen, Hydrogen Chemisorption on Si (111), Phys. Rev. B 15, 3888 (1977).

13. S. G. Louie, K. M. Ho, J. R. Chelikowsky and M. L. Cohen, Self-consistent Pseudopotential Calculations for the Ideal (001) Surface of Nb, Phys. Rev. 15, 5627 (1977).

14. D. Bullett and M. L. Cohen, Localized Orbital Approach to Chemisorption I: H on W (100), J. Phys. C 10, 2083 (1977).

15. D. Bullett and M. L. Cohen, Localized Orbital Approach to Chemisorption II: H and CO on Ni and Pt (001), J. Phys. C 10, 2101 (1977).

16. W. E. Pickett, S. G. Louie and M. L. Cohen, Ge-GaAs (110) Interface: A Self-consistent Calculation of Interface States and Electronic Structure, Phys. Rev. Lett. 39, 109 (1977).

17. J. R. Chelikowsky, M. Schlüter and M. L. Cohen, Semi-empirical Pseudopotential Calculations for the Electronic Structure of Polymeric Sulfur Nitride, Phys. Stat. Solidi (b) 82, 357 (1977).

18. L. M. Falicov and M. L. Cohen, The 1977 Nobel Prize in Physics, Science 198, 713 (1977).

Reports

1. G. Kerker, S. G. Louie and M. L. Cohen, Electronic Structure of the Ideal and Reconstructed Si (001) Surface.

2. M. Schlüter and M. L. Cohen, The Nature of Conduction Band Surface Resonances for Si (111) Surfaces with and without Chemisorbed Overlayers.

3. W. E. Pickett, S. G. Louie, and M. L. Cohen, Self-consistent Calculations of Interface States and Electronic Structure of the (110) Interface of Ge-GaAs and AlAs-GaAs.

4. J. Ihm, S. G. Louie, and M. L. Cohen, Self-consistent Pseudopotential Calculations for Ge and Diamond (111) Surfaces.

5. W. E. Pickett and M. L. Cohen, Theoretical Study of Relaxation at the (110) Ge-GaAs Interface.

6. W. E. Pickett and M. L. Cohen, Theoretical Trends in the Abrupt (110) AlAs-GaAs, Ge-GaAs and Ge-ZnSe Interfaces.

7. J. Ihm, S. G. Louie and M. L. Cohen, Pseudopotential Calculations of the Electronic Structure of Germanium and Diamond Schottky Barriers.

8. M. L. Cohen, Electronic Structure of Semiconductor Interfaces.

9. P. K. Larsen, N. V. Smith, M. Schluter, H. H. Farrell, K. M. Ho and M. L. Cohen, Surface Energy Bands and Atomic Position of Cl Chemisorbed on Cleaved Si (111).

10. S. G. Louie and M. L. Cohen, Dielectric Screening and Zone-center Phonons in Si.

11. J. Ihm, S. G. Louie and M. L Cohen, Diamond-Metal Interfaces and the Theory of Schottky Barriers.

12. K. M. Ho, W. E. Pickett and M. L. Cohen,Bonding and Electronic States of Nb_3Ge.

13. P. B. Allen, W. E. Pickett, K. M. Ho and M. L. Cohen, Anomolous Resistivities of A15 Metals--Insights from Band Theory.

C. MATERIALS CHEMISTRY

1. CHEMICAL STRUCTURE

a. High Pressure Chemistry

George Jura, Principal Investigator

1. HEAT CAPACITY OF ALUMINUM AND HEAT DIFFUSIVITY OF SILVER CHLORIDE TO PRESSURES OF 135 kbars

George Jura and Kwang Yul Kim

The technique for the determination of the heat capacities of metals by a microsecond pulse has been developed to the degree that it is now useful as a function of temperature and pressure. Earlier work had solved the problems involved in obtaining results at constant pressure, and the difficulties involved in the variation of pressure have been solved. Data are presented for aluminum at room temperature. As an added bonus, it is possible to determine the heat diffusivity of the surrounding medium as a function of pressure and temperature. It has not as yet been possible to separate the heat capacity and heat conductivity parts of the heat diffusivity. That awaits further work.

Briefly, in the pulse method, a presumed constant current pulse is sent through the sample. The voltage drop across the sample is measured as a function of time. From this data it is possible to determine the quantities of interest.

In our earlier work, it was presumed that the current obtained from our square pulse generator was constant after the rise, about 10 μsec. If the pulse was measured on an oscilloscope, the current was indeed constant to 0.05% after about 25 μsec. It was the assumption that because the current was constant in going to the oscilloscope that it was also constant in going to the sample. This last assumption is erroneous. When the pulse is directed into the scope, the leads are sufficiently short that the transient current can be neglected. However, when the current goes to the sample, the inductance is appreciable, and the length of the leads increases the resistance, and on the time scale on which it is necessary to work to minimize the heat loss, the transient current is appreciable at 60 μsec after the start of the pulse, and its variation with time is important for about the next 200 μsec. Since the data that is required is collected in about 300 μsec, it is evident that a serious error is made if the transient is not considered.

Obviously the transient cannot be measured while the current is rising. However, since according to theory, the rise and decay are related, the rise can be determined from the decay. This is what we have done. The observed voltages on the rise have been corrected for the transient, and the correction is obtained from the decay.

What this means is that the experiments that are performed are changed only in respect to the length of time that measurements are made. The pulse is directed across a variable resistor, of sufficiently high heat capacity that its resistance does not change as the current flows, and whose resistance has been made equal to that of the sample. Voltages are read for several milliseconds. This determines the base or the zero from which all measurements are made. The current is then switched through the sample. After about three milliseconds, the current flows only through the variable resistor. The decay is obtained from these last measurements. The sample and the variable resistors are two arms of a wheatstone bridge, and the actual measurement that is made is the difference between the two voltage drops across these two resistors. The last is necessitated by the fact there is no instrument that will measure the voltage drop across the sample with the necessary accuracy in a sufficiently short period of time.

The results for the heat capacity of aluminum are shown in Fig. 1. If the results are extrapolated back to 1 atm, there is a decrease of

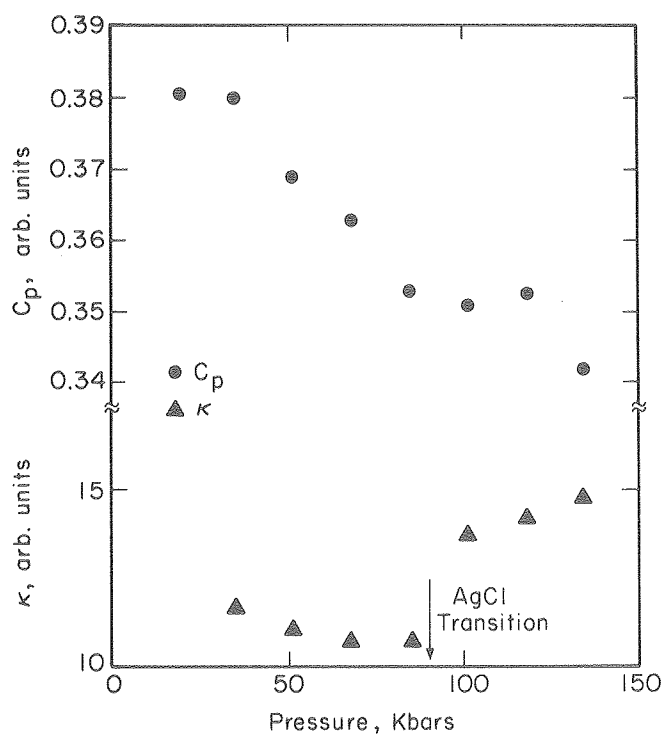

Fig. 1. Heat capacity of aluminum and heat diffusivity of silver chloride as a function of pressure at 25° C. (XBL 781-68)

8.61%. This can be compared to that obtained from an approximation of the Debye temperature from the Bloch-Grueneisen equation for the temperature dependence of the resistance of a one electron metal. This approximation yielded a decrease of 4.8% in the heat capacity for the same change in pressure. The heat diffusivity of silver chloride is also shown in this figure. There are no known comparisons for the numbers that are shown. There is a known polymorphic change in the structure of silver chloride at about 90 kbars. Thus the change in the heat diffusivity is explainable on the above.

The above results have been computed from the equation

$$E = E_o + \frac{I^3 R_o R'}{C_{p_1}} t - \frac{\kappa_2^{1/2}\alpha}{\Gamma(5/2)a} t^{3/2}$$

$$+ \frac{\kappa_2(2\alpha^2-\alpha+2\beta)}{4a^2} t^2 - \frac{\kappa_2^{3/2}(\delta\alpha^3-\delta\alpha^2+16\alpha\beta-\alpha)}{\Gamma(7/2)8a^3} t^{5/2}$$

$$+ O(t^3)$$

where

$$\alpha = \frac{A\kappa_2 a}{C_p \kappa_2} \quad \frac{Aa\rho_2 C_{p_2}}{C_{p_1}}$$

$$\beta = \frac{I^2 R_o' a^2}{\kappa_2}$$

and

a: radius of a wire

$A=\pi a^2$: surface area of the wire

K_2: thermal conductivity of AgCl

C_{p_1}: bulk specific heat of the wire

κ_2: thermal diffusivity of AgCl

$$\kappa_2 = \frac{K_2}{\rho_2 C_{p_2}} .$$

ρ_2: density of AgCl

C_{p_2}: specific heat of AgCl

R_o': temperature coefficient of resistance

In principle, if good enough data were available, it would be possible to decompose the heat diffusivity term into the heat capacity and heat conductivity. This is not possible with the present data. It may become possible when the present 10 bit AD convertor is replaced with a 12 bit interface.

At the present time, data are the averages of about 10 different currents. It is estimated that the heat capacities are good to about 0.5%, and the heat diffusivities to about 7%.

2. RESEARCH PLANS FOR CALENDAR YEAR 1978

George Jura

Measurements will be made on a selected group of metals; iron, gadolinium, and bismuth to start. It is expected that the temperature range investigated will range from 77 to 298 K.

b. Low Temperature Properties of Materials

Norman E. Phillips, Principal Investigator

1. PRESSURE DEPENDENCE OF THE HEAT CAPACITY OF TEFLON AT LOW TEMPERATURES

J. Boyer and N. E. Phillips

Teflon is frequently used, either by itself or in combination with certain fluids, as a pressure-transmitting medium in high pressure clamps of the type frequently used for low-temperature high-pressure measurements and which have been used in this laboratory for heat capacity measurements. At low temperatures and high pressures teflon is indispensable in achieving hydrostatic pressure. The clamp, which must support the large mechanical stresses present at high pressures, is by necessity quite large and consequently contributes the major part of the actual measured heat capacity in any experiment. Thus, to obtain even a few percent accuracy in the heat capacity of the sample, the heat capacity of the calorimeter must be very well characterized. Since teflon is soft and relatively compressible, it can be expected to contribute a significant and strongly pressure-dependent heat capacity to that of the cell.

To provide data to correct measured heat capacities for the heat capacity of teflon, we have measured the pressure dependence of the heat capacity of teflon between 0.5 and 20 K. A 1.771 g sample of teflon was placed in the clamp and pressurized to 6 kbar at room temperature in a hydraulic press. The clamp was then cooled and the pressure at low temperature determined by observing the shift in the superconducting transition[1] of a 5 mil tin disk in contact with the teflon and cell body. The pressure retained in the first pressurization was 5.3 kbar. The heat capacity of the cell and teflon sample was measured by applying a known quantity of heat with a resistance heater while observing the resultant change in temperature with a germanium resistance thermometer. The calorimeter was warmed to room temperature and another pressure locked in and the measurement repeated at the new pressure. The sequence of pressures used was 5.3, 3.6, 0.5, 0.8, and 1.6 kbar. The results suggest a small degree of hysteresis, which could possibly have been avoided by completely releasing the pressure before locking in the new pressure.

The heat capacity of the teflon sample at each pressure was then obtained by subtracting the heat capacity of the empty cell, which had been previously measured, and assuming that the pressure dependence was due only to the teflon sample. At temperatures of less than 1 K the empty cell contributed more than 99% of the measured heat capacity, and the precision of the data is therefore severely limited in the low temperature region. Plots of C/T^3 vs T in Fig. 1 show the strong pressure dependence present in the specific heat of teflon. Also apparent from this figure is the fact that the specific heat of teflon does not approach a T^3 limit at low temperatures. The

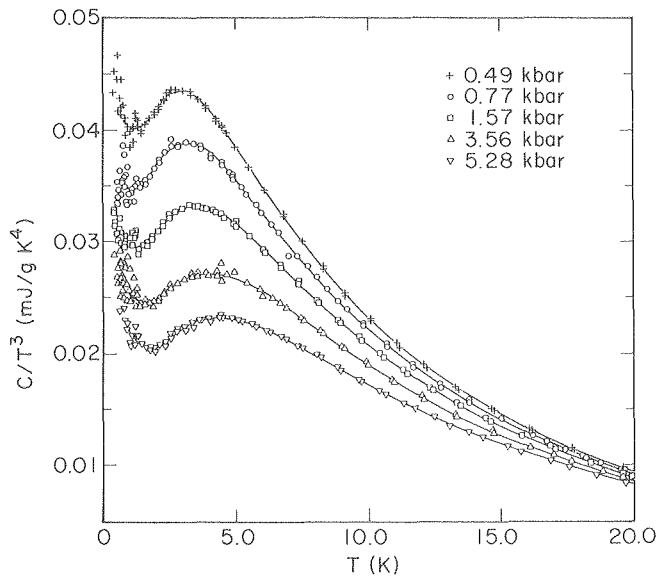

Fig. 1. Plots of C/T^3 vs T for a sample of teflon showing the temperature dependence of the heat capacity at several pressures. (XBL 781-28)

deviations from T^3 behavior below about 1.5 K are probably associated with a linear term which has been found in the heat capacity of many amorphous dielectrics. Figure 2, which presents plots of C vs $\log_{10}P$ for several temperatures, shows that the pressure dependence of the specific heat is logarithmic. The major deviations from logarithmic behavior are apparently associated with uncertainties in assignment of the pressures. The logarithmic behavior is useful for interpolating between measured values but obviously can not be used to interpolate to zero pressure for comparison with other measurements. Least squares analysis of the data to $C(T,P) = C(T,1) + \beta(T) \log P$ generate smooth curves for $C(T,1)$ and $\beta(T)$; however, $C(T,1)$ and $\beta(T)$ are represented best by tabular interpolation rather than polynomials. In the future the measurements will probably be extended to 10 kbar and another sample of teflon of different mass will be measured to check the assumption that the observed pressure dependence was due entirely to the teflon.

---

1. T. F. Smith, C. W. Chu, and M. B. Maple, Cryogenics 9, 53 (1969).

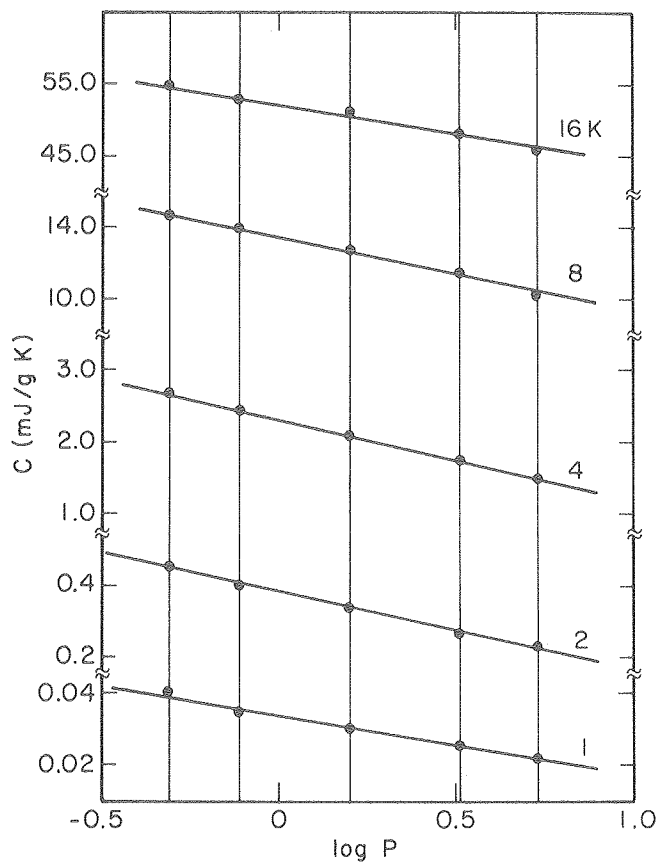

Fig. 2. Plots of C vs $\log_{10}P$ at selected temperatures showing the logarithmic pressure dependence of the heat capacity of teflon. The pressure is measured in kbars. (XBL 781-29)

2. HEAT CAPACITY OF THE SPIN-GLASS CuMn

W. E. Fogle, J. C. Ho, and N. E. Phillips

The heat capacity of dilute magnetic alloys in which the magnetic moments are coupled by the RKKY interaction has attracted attention ever since the discovery[1-3] that it was approximately linear in temperature and independent of concentration. This discovery was made for the CuMn system, which has remained the most thoroughly studied example. It led to theoretical models[4] in which the distribution of internal fields P(H) was constant and scaled with concentration. Several refinements of the earlier theories have been made recently.[5-7]

Some time ago measurements on CuMn samples with concentrations between 0.057 and 1.07% were made in this laboratory by using carbon thermometers calibrated on each run. The measurements extended from 0.06 to 0.8 K. More recently measurements on three samples with concentrations of 96.6, 231, and 960 ppm have been made between 0.06 and 20 K. In the later measurements germanium thermometers were used and calibrated on a magnetic scale that was related to nuclear orientation thermometers at 20 mK and to the ^{4}He scale at and above 1 K. The two sets of measurements together with some older data at higher concentrations and higher temperatures give a very complete picture of the behavior of this system.

To observe the actual temperature dependence of the heat capacity associated with Mn impurity spins, one must eliminate a complication due to the hyperfine heat capacity of the Mn nuclei. This nuclear heat capacity arises from the lifting of the degeneracy of the Mn nuclear levels by the internal hyperfine fields in the alloy. Nuclear orientation experiments by Campbell et al.[8] on dilute solutions of Mn in Cu predict hyperfine fields at the Mn nucleus on the order of 280 kOe. This hyperfine interaction can be shown to lead to a hyperfine heat capacity of the form[9] (for $T \gg T_{max}$ of the anomaly)

$$C_N \approx C_4 T^{-4} + C_2 T^{-2} ,$$

where

$$C_2 = \frac{R}{3} \left(\frac{\mu H_{eff}}{kI}\right)^2 I(I+1)$$

and

$$C_4 = \frac{-R}{30} \left(\frac{\mu H_{eff}}{kI}\right)^4 I(I+1)(2I^2+2I+1) ,$$

R = gas constant, μ = nuclear moment, I = nuclear spin, k = Boltzman's constant.

Our analysis of the hyperfine heat capacity consists of plotting our data on a $(C_{TOT} - C_{Cu})\,T^2$ vs $1/T^2$ plot. If the temperature dependence of the heat capacity at low temperatures is dominated by the nuclear heat capacity, we will observe a straight-line plot whose intercept is C_2 and whose slope is C_4. In practice, at higher temperatures, the data deviate from the expected straight line due to the increasing importance of other terms in the heat capacity. We therefore draw lines on this plot which, considering the scatter in the data at the lowest temperatures, represent upper and lower limits on the hyperfine heat capacity. The only other constraint exercised in the choice of these lines is that the resulting coefficients C_4 and C_2 yield the proper Mn concentration of the alloy.

The results of such an analysis are shown for a typical sample in Fig. 1. On this plot, solid lines are used for clarity to represent the upper and lower limits of the data due to experimental uncertainty in the hyperfine heat capacity. It is clear from such an analysis that the uncertainty in C_N has almost no impact on the temperature dependence of the alloy heat capacity for $T > 0.2$ K.

The magnetic heat capacity is shown in Fig. 2, as C/T vs T, and compared with the original measurements by Zimmerman and Hoare and others by du Chatenier and de Nobel. As expected, there is a broad peak in the heat capacity that shifts

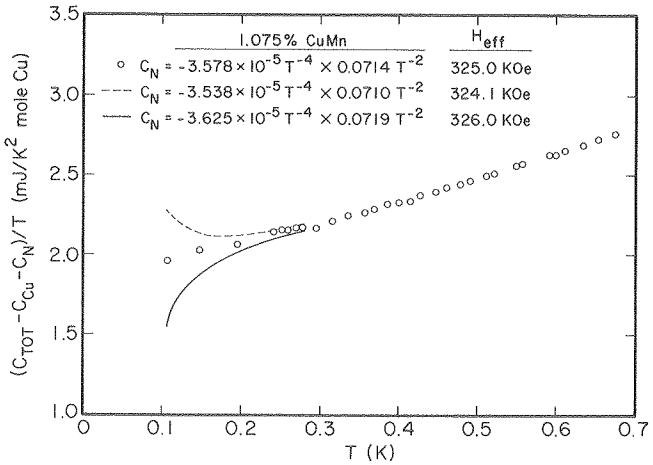

Fig. 1. The effect on the magnetic heat capacity of 1.07% CuMn of different assignments of the hyperfine field. (XBL 781-30)

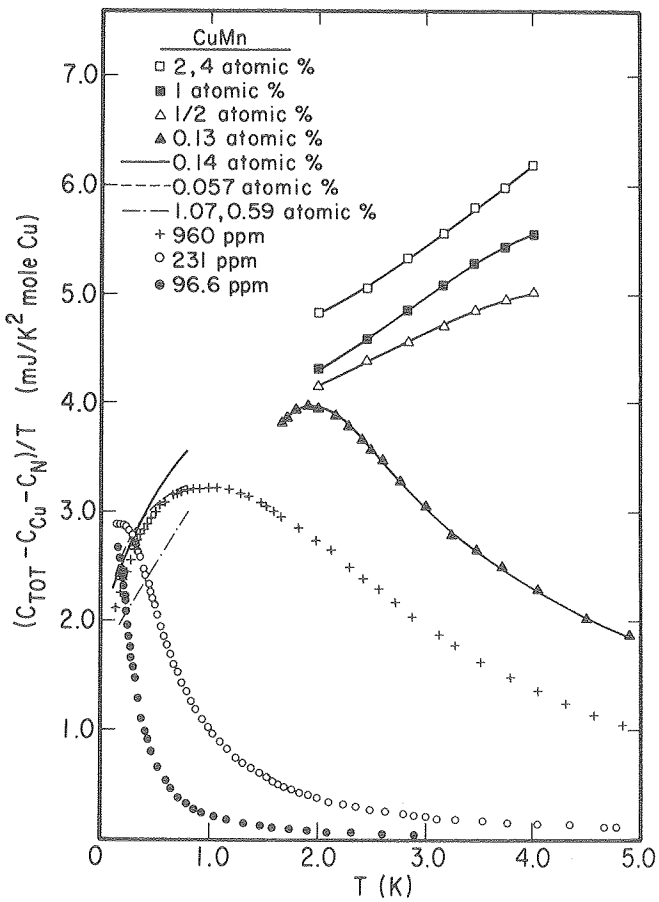

Fig. 2. The magnetic heat capacity of CuMn of various concentrations. The 2%, 4%, 1%, and 1/2% data are from Zimmerman et al.[1] The 0.13% data are from de Nobel et al.[2] The remaining data are from the present work. (XBL 781-31)

to higher temperatures with increasing concentration, and the heat capacity is only weakly concentration-dependent on the low temperature side. This result reflects the dependence of the RKKY coupling on inter spin distance, and hence the concentration dependence of P(H). On the other hand, the temperature dependence of the heat capacity on the low temperature side is much stronger than has generally been recognized: Roughly speaking, there is a T^2 term in the heat capacity that accounts for about 50% of the total at temperatures of the order of 1 K. The shape of the P(H) curve is therefore more complicated than has usually been assumed.

The accuracy with which the concentration dependence of the linear term can be determined is unfortunately limited by the hyperfine heat capacity. However, the data suggest that it is constant within about 10%.

The other interesting feature of Fig. 2 is the high temperature linear term for the 100 and 300 ppm samples. At temperatures above those shown in the figure the 1000 ppm sample shows similar behavior. These linear terms are, very approximately, proportional to concentration and presumably reflect the change in the electronic density of states associated with the magnetic impurity. The magnitude of this effect has not yet been compared with theory.

---

1. J. E. Zimmerman and F. E. Hoare, J. Phys. Chem. Solids 17, 52 (1960).
2. J. de Nobel and F. J. du Chatenier, Physica 25, 969 (1959).
3. F. J. du Chatenier and A. R. Miedema, Physica 32, 403 (1966).
4. W. Marshall, Phys. Rev. 118, 1519 (1960).
5. H. Suhl, Phys. Rev. Lett. 19, 442 (1967).
6. B. Coqblin and B. Blandin, Advan. Phys. 17, 281 (1968).
7. L. L. Hirst, Phys. Kondens. Mat. 11, 255 (1970).
8. I. A. Campbell, J. P. Compton, I. R. Williams, and G. V. H. Wilson, Phys. Rev. Lett. 19, 1319 (1967).
9. O. V. Lounasmaa, in Hyperfine Interactions, edited by A. J. Freeman and R. B. Frankel (Academic Press, New York, 1967), p. 467.

3. RESEARCH PLANS FOR CALENDAR YEAR 1978

Norman E. Phillips

Progress on the establishment of a temperature scale in the millikelvin region has been delayed by problems encountered in the fabrication of coils for susceptibility measurements. The empty coils have both a slowly temperature-dependent mutual inductance over a wide range of temperatures and a sharp peak in the mutual inductance at 1.08 K. The former feature is apparently associated with the niobium wire, but the origin of the latter is as yet entirely unknown. These effects are significant in the calibration of both CMN and nuclear thermometers. It will be necessary to determine the origin of the second effect and the

reproducibility of both before continuing the development of a temperature scale. Once these problems are resolved we will proceed with the comparison of susceptibility thermometers with nuclear orientation thermometers in the millikelvin region.

Measurements on the Tl-Pb-Bl alloy system have resumed and will be continued in 1978. The new measurements will be on ternary alloys for electron/atom ratios other than 4, and on a few binary alloys for which the old samples were found to be inhomogeneous. The results will permit a separation of the effects of disorder and electron/atom ratio on the parameters that determine the superconducting critical temperature. Similar measurements on In-Sn alloys have been initiated and will be continued.

c. Electrochemical Processes

Charles W. Tobias, Principal Investigator

1. FUNDAMENTAL STUDIES OF TRANSPORT PHENOMENA IN ELECTROCHEMICAL REACTORS

a. Studies of the Events Occurring at Gas-Evolving Electrodes

Paul Sides and Charles W. Tobias

The mechanics of bubble growth, coalescence and detachment involves rapid sequential and simultaneous events on electrodes. New techniques designed and implemented in this laboratory to obtain information essential for quantitative characterization of the gas evolution process include the measurements of supersaturation at the surface,[1] time-lapse microphotography of incipient growth of bubbles[2] and motion picture records of coalescence phenomena from behind transparent SnO_2:Sb electrode surfaces.[3] Side views of bubbles are being obtained by observation of bubbles before detachment on a curved cathode surface that allows the measurement of contact angles.

Bubble growth by coalescence before detachment has been clearly observed along artificial grooves. Calculated supersaturation levels obtained from mass transfer theory agree with those calculated by subtracting the gas volume present in bubbles from the total quantity of gas formed in the discharge process. Measurements of cell resistance by the interruptor technique, performed during incipient bubble growth, indicate that the incremental resistance caused by bubbles still attached to the surface may represent a significant component of the overall ohmic resistance.

---

1. C. K. Bon and C. W. Tobias, IMRD Annual Report for 1967, UCRL-18043, p. 51.
2. R. A. Putt and C. W. Tobias, IMRD Annual Report for 1975, LBL-4550, p. 163; also LBL-3989.
3. P. Sides and C. W. Tobias, MMRD Annual Report for 1976, LBL-6016, p. 179.

b. High Rate Electrolysis Processes

A. Dissaux, D. Roha, R. H. Muller and C. W. Tobias

In contrasts to the low space-time-yield of commonly used electrosynthesis processes, the high rate anodic dissolution of metals (ECM) provides cutting rates comparable to mechanical shaping techniques. Past investigations in this laboratory have been directed toward establishing rational methods for the design and operation of ECM.[1] Profiles cut into copper and stainless steel anodes were successfully predicted by a computer implemented modeling procedure.[2] Current efforts are devoted to the examination of shaping refractory compounds (carbides and borides of groups IV-VI B) with or without a "soft" binder (Ni or Co). Here the dissolution chemistry of the dispersed phase and the binder leads to different rates of attack, and consequent variability in surface finish of the work piece. The 20-year-old surplus Hanson van Winkle machine at our disposal is being equipped with more precise controls and instrumentation to measure current densities, electrolyte flow rates, pressure drops and impedances across the interelectrode gap. Hole-sinking experiments performed in carbides and borides indicate that dissolution under transpassive conditions may be carried out using Cl^- or NO_3^- anions. Chlorate leads to oscillatory currents, as observed in the case of copper and steel.

The reverse process, high speed electroforming requires highly efficient ionic transport which, in contrast to ECM, should be achieved by methods other than by high velocity of flow of electrolyte. A review of known techniques for producing thin boundary layers indicates that of the various alternatives available, the use of agitation by dispersed inert solid particles, or vibration of the cathode mandril in the sonic range, may provide satisfactorily uniform distribution of rates, coupled with low energy demand.

---

1. D. Landolt, R. H. Muller and C. W. Tobias, Fundamentals of Electrochemical Machining, Charles L. Faust, Ed., The Electrochemical Society, Princeton, N. J., 1971, pp. 200-207, 300-365.
2. J. B. Riggs, R. H. Muller and C. W. Tobias, Modeling of the Electrochemical Machining Process, vol. 77-1, p. 777, Extended Abstracts, The Electrochemical Society, 1977; also LBL-6019.

2. RESEARCH LEADING TO NEW ELECTROLYTIC PROCESSES

a. Anodic Processes in Propylene Carbonate

Suen-Man Yu and Charles W. Tobias

The demonstrated capability of reversibly depositing and dissolving alkali metals in propylene carbonate solvent containing $MeAlCl_4$ solute offers the possibility of a process technology for the refining of alkali metals from their amalgams.[1] For electrowinning, we need to decompose a potassium compound, e.g., KCL into K and Cl_2, or alternately use a sacrificial anode, such as aluminum, resulting in the overall reaction $Al + 3KCL = AlCl_3 + 3K$. Although aluminum has been shown to passivate in the P.C. electrolytes,[2] it can be dissolved, but only at unreasonably high potentials. To investigate the more interesting halogen liberation reaction, we have undertaken to evaluate the stability of P.C. with respect to anodically evolved elemental chlorine or bromine. A cell employing Nafion membrane to separate the cathode chamber containing the potassium counterelectrode is employed for this purpose. Preliminary results indicate that there is a reaction between chlorine and at least an impurity of P.C., possibly one of the glycols which are present at ppm levels in the purified solvent following vacuum distillation and adsorption on alumina.

Removal of solvent impurities in the ppm range still represents a difficult and, as yet unsolved, problem; identifying an effective practical method for the removal of reactive components constitutes a high priority task.

---

1. C. W. Tobias and J. Jorne, Method for Production of Alkali Metals and Their Alloys, U. W. Patent No. 3,791,945, assigned to USAEC, 1973.
2. R. Atanasoski and C. W. Tobias, MMRD Annual Report for 1976, LBL-6016, p. 180.

3. RESEARCH PLANS FOR CALENDAR YEAR 1978

Charles W. Tobias

a. Investigation of the Dynamics of Gas Evolution

Transparent electrodes SnO_2:Sb will be employed for the observation of nucleation, coalescence, and separation phenomena in the steady state. The effect of surface roughness and electrolyte composition with respect to major and minor constituents (additives) will be evaluated. A superimposed a.c. technique will be developed to monitor the incremental impedance caused by bubbles attached to the surface, and to differentiate this effect from the decreased conductivity caused by bubbles already detached.

b. High Rate Electrode Processes

The surface finish obtained in the dissolution of refractory compounds (carbides and borides of group IV-VI B metals) under ECM conditions will be investigated by SEM. The possibility of using two different electrolytes in succession (one to achieve fast cutting the other to provide smooth finish) will be explored. Special cutting techniques will be sought to produce sharp edges, and to sink very small holes.

Rotating disks and channel flow equipment will be used to evaluate the relative effectiveness of using suspensions of small inert particles to produce boundary layers which are sufficiently thin for high speed electroforming. Preliminary evaluation of the vibration of a planar electrode in the sonic range will be undertaken.

c. Anodic Reactions in Propylene Carbonate

A high resolution gas chromatograph with ionization source will be employed to monitor solvent purity. Following establishment of the stability of P.C. with respect to elemental chlorine and bromine, equilibrium potential measurements will be made of the chlorine and bromine electrodes in P.C. containing $KalCl_4$ and $KalBr_4$, respectively. Kinetic measurements will then be performed using RuO_2/Ti electrodes on the overpotential behavior in practical ranges of current densities. The conditions for use of P.C. for organic halogenation reactions will also be evaluated.

4. 1977 PUBLICATIONS AND REPORTS

Charles W. Tobias and Associates

LBL Reports

1. James B. Riggs, Modeling of the Electrochemical Machining Process (Ph.D. thesis), University of California, Berkeley, LBL-6019, January 1977.

2. F. R. McLarnon, R. H. Muller and C. W. Tobias, Interferometric Study of Forced Convection Mass Transfer Boundary Layers in Laminar Channel Flow, LBL-5797.

Invited Lectures and Papers Presented

1. J. B. Riggs, R. H. Muller and C. W. Tobias, Modeling of the Electrochemical Machining Process, 150th Meeting of the Electrochemical Society, Philadelphia, May 8-13, 1977, Extended Abstract No. 305.

2. F. R. McLarnon, R. H. Muller and C. W. Tobias, Interferometric Study of Combined Forced and Natural Convection, 150th Meeting of the Electrochemical Society, Philadelphia, May 8-18, 1977, Extended Abstract No. 304.

3. C. W. Tobias, The Role of Electrochemical Engineering in Energy Conservation, Keynote address, Fifth Yugoslav Symposium on Electrochemistry, Dubrovnik, June 1-4, 1977.

4. R. T. Atanasoski, H. H. Law and C. W. Tobias, Anodic Dissolution of Aluminum in Propylene Carbonate in the Presence of Alkali Chlorides, Fifth Yugoslav Symposium on Electrochemistry, Dubrovnik, June 1-4, 1977.

5. C. W. Tobias, Modern Problems in Current Distribution, Invited Address, Yugoslav Academy of Sciences, Zagreb, June 6, 1977; University of Banja Luka, June 8, 1977.

6. C. W. Tobias, On the Mechanism of Electrolytic Gas-Evolution, Invited Address, Yugoslav Chemical Society, Belgrad, June 9, 1977.

7. C. W. Tobias, Electrochemical Engineering, Invited Lectures at the American Society for Engineering Education, Summer School for Chemical Engineering Faculty, Snowmass, Colorado, July 31, 1977.

8. C. W. Tobias, The Role of Electrochemical Processes in Energy Conservation, Invited Address, Center of Physical Chemistry, Ministry of Industrial Chemistry, Bucharest, Romania, September 8, 1977; also at the University of Cluj, September 12, 1977.

9. J. B. Riggs, R. H. Muller and C. W. Tobias, Computer Simulation of Electromachining, 28th Meeting of the International Society of Electrochemistry, Druzhba, Bulgaria, September 18-23, 1977.

10. C. Vass and C. W. Tobias, The Effect of Benzotriazol on the Electrodeposition of Copper under Limiting Current Conditions, 28th Meeting of the International Society of Electrochemistry, Druzhba, Bulgaria, September 18-23, 1977.

Book Edited

1. Advances of Electrochemistry and Electrochemical Engineering, Heinz Gerischer and Charles W. Tobias, Eds., Vol. 10, Wiley-Interscience Publishers, New York, 1977.

2. HIGH TEMPERATURE AND SURFACE CHEMISTRY

a. High Temperature Chemistry

Leo Brewer, Principal Investigator

1. THERMODYNAMICS AND PHASE DIAGRAMS OF THE BINARY SYSTEMS OF MOLYBDENUM

L. Brewer

This project consisted of two parts which will be published in 1978 as chapters of the monograph "Atomic Energy Review, Special Issue on Physical Chemical Properties of Molybdenum, Its Compounds and Alloys" (International Atomic Energy Agency, Vienna).

The first part covered the review of available thermodynamic data for any of the binary systems of molybdenum from hydrogen to lawrencium. These data were tested for internal thermodynamic consistency as well as consistency with phase diagram information, and with entropies and enthalpies calculated from available models. Then the acceptable data were supplemented as necessary with estimated values to provide a complete set of thermodynamic data. This was possible for one hundred binary systems. For polonium and astatine, it was felt that available models did not adequately deal with the relativistic effects and could not provide estimates of sufficient accuracy. The resulting thermodynamic data were presented in tabular form in many instances, but for all systems, data were presented in analytical form to allow ready calculation of any desired thermodynamic values. Uncertainties are provided for all data to allow the user to determine the range of possible predicted chemical behavior.

The second chapter dealt with the construction of phase diagrams for any binary system of molybdenum. Any available phase diagram information was checked against the thermodynamic data, and consistency between the thermodynamic data and reliable phase diagram information was insured. Then the final thermodynamic data were used to calculate the portions of the phase diagram for which data were not available. In addition to providing plots of the phase diagrams, analytical equations have been provided for liquidus and solidus boundaries. The temperature range covered was from room temperature to the melting point of molybdenum, although, when significant, the phase boundaries were extended toward the boiling point of molybdenum and analytical equations are given for the boundaries of the gaseous phase regions.

2. HIGH-TEMPERATURE SOLID-ELECTROLYTE CELL AND HIGH-TEMPERATURE GASEOUS EQUILIBRIA STUDIES OF GENERALIZED-LEWIS-ACID-BASE INTERACTIONS IN BINARY METALLIC ALLOYS

G. Bullard, D. Goodman, B. J. Lin, and D. Davis

Previous research[1,2] in our group has demonstrated unusually strong interactions between transition metals of the third to fifth groups, which have unoccupied d orbitals, and transition metals of the ninth to tenth groups, which have non-bonding valence electron pairs. As the contributions from bonding electrons increase markedly from 3d to 4d to 5d, the largest effects are expected with Ir or Pt reacting with Ta, Hf, or the lanthanides and actinides. Enthalpies of solution of one metal in an excess of the other are expected to be more negative than -100 kcal per gram-atom.

Valuable information could be obtained from a titration curve of partial molal Gibbs energy vs molal ratio of the acid and base. Such data could yield information about the variation in behavior as the vacent d orbitals are filled, and one might be able to compare the effect of utilization of d orbitals with the effect of utilization of s and p orbitals.

A high-temperature solid-electrolyte cell could be a way of obtaining the desired titration curve. An example is the cell $Ta\text{-}Ta_2O_5/CSZ/TaIr_x\text{-}Ta_2O_5$ where CSZ is calcia-stabilized zirconia which serves as an oxygen-anion electrolyte. The calcia stabilized the CaF_2 structure and also increases the electrical conductivity of ZrO_2. Measurements of the electrical potential of such a cell as a function of x would yield the desired data. A review of the literature indicated that although this technique has been widely used, more than half of the published data demonstrate serious systematic errors. As just one indication, the temperature coefficients are often quite inconsistent with entropies obtained from low-temperature heat capacity measurements. To ensure that reliable measurements could be made, a systematic study of the response of high temperature cells to important variables was initiated. Because of error introduced by electronic conductivity of the electrolyte when the oxygen partial pressure is too low, the cell

actually studied was M-MO/CSZ/$TaIr_x$-Ta_2O_5, where M was Fe or Ni, or in some instances NbO_2-$NbO_{2.4}$ was used as the reference electrolyte, and values of x were kept large. Also yittrium-stabilized thoria was also used to test the influence of the electrolyte, and to provide the means of extending the titration curve to low values of x corresponding to very low oxygen partial pressures.

These studies have yielded results that will be important for ensuring the reliability of our measurements. A serious error limiting the upper temperature range of the studies results from the diffusion of the minor oxides of the electrolyte, CaO or Y_2O_3, into the electrode region where reaction with Ta_2O_5 produces an insulating ternary oxide. A review of possible oxide additives to ZrO_2, HfO_2, or ThO_2 indicates that La_2O_3 additions might bring about the desired structure and resistivity without impairment due to increase of electronic conductivity or diffusion to form ternary oxides. Studies will be carried out next year to develop methods of controlling the error due to ternary oxide formation.

Another serious source of error that was studied was the effect of gaseous impurities. It is commonly recognized that the gaseous atmosphere can compete with the electrolytic processes in fixing the oxygen chemical potential in the electrode region. It also was found that hydrogen and carbon impurities can also bring about vapor transport reactions resulting in sufficient reduction of the zirconia to introduce error due to electronic conductivity.

Other sources of error are being carefully investigated to ensure reliability of our measurements. As an additional check to ensure that all systematic errors have been controlled, gaseous equilibria of H_2O-H_2 or CO-CO_2 mixtures with metal oxide-alloy mixtures will be measured for the same alloys used in the cell studies.

---

1. L. Brewer, A Most Striking Confirmation of the Engel Metallic Correlation, Acta. Met. 15, 553 (1967).
2. P. R. Wengert and L. Brewer, Transition Metal Alloys of Extraordinary Stability: An Example of Generalized Lewis Acid-Base Interactions in Metallic Systems, Met. Trans. 4, 83-104 (1973).

3. MATRIX ISOLATION SPECTRA*

W. Duley, L. Andrews, and B. Meyer

The spectra of calcium vapor isolated in noble gas matrices have been studied to characterize the spectra of Ca_2. It proved to be rather difficult to assign the observed spectra to reasonable electronic levels of Ca_2, correlating with appropriate atomic levels of Ca, and submission of a manuscript describing the work has been delayed while alternate interpretations have been tested. A satisfactory resolution has been obtained by assignment of the green system of Ca_2 to $^1\Sigma_u^+(^1S+^1D) \leftarrow {}^1\Sigma_g^+$ and the red system to $^1\Sigma_u^+(^1S+^1P) \leftarrow {}^1\Sigma_g^+$. The final manuscript has been accepted for publication in the Journal of Molecular Spectroscopy.

---

*Supported in part by NSF.

4. THERMODYNAMICS OF GASEOUS METAL CLUSTERS

L. Brewer

The current interest in the role of metal clusters on catalyst surfaces has prompted efforts to calculate the stability of gaseous polymeric metal clusters. As the first step in this direction, the thermodynamics of gaseous dimers was examined. A review of available data yielded values showing rather unusual behavior across the transition metals, and the bonding models were examined to understand the variation of bonding energies.

It was found that a minor modification of bonding models used previously[1,2] for the condensed metals fit the observed behavior of the gaseous diatomic molecules. It was necessary to recognize the different bonding behavior of the s and p electrons of the outer valence shell compared to the bonding behavior of the d electrons of the inner shell. The model uses the same variations in bonding as for the condensed metals except for a reduction in bonding ability when the bonding electrons are concentrated between a single pair of atoms, compared to spreading the bonding electrons among many neighbors. This model was used to calculate the dissociation energies of all of the diatomic molecules for which no measurements have been made.

---

1. L. Brewer, Science 161, 115-122 (1968).
2. L. Brewer, Phase Stability in Metals and Alloys, edited by P. Rudman, J. Stringer, and R. I. Jaffe, (McGraw-Hill, New York, 1967), pp. 39-61, 241-9, 344-6, and 560-8.

5. RESEARCH PLANS FOR CALENDAR YEAR 1978

Leo Brewer

The level of activity of measurements of generalized-Lewis-acid-base interactions of transition metals will be considerably expanded. High-temperature solid-electrolyte cell measurements using zirconia, hafnia, and thoria with various oxide additives will be made for tantalum-iridium alloys. In addition, H_2O-H_2 and CO-CO_2 equilibria will be carried out as a check on the cell measurements. The possibility of using nitrogen vapor pressure measurements for metal alloys mixed with metal nitride will be examined.

Matrix isolation studies will be mainly restriced to study of spectra of metallic clusters. The extension of the bonding model used for diatomic molecules to triatomic and larger clusters will be attempted.

An exploration of a collaboration of thermodynamic compilation with the JANAF Tables will be explored at a meeting in January 1978 between Drs. L. Brewer and R. Hultgren of LBL and Dr. M. W. Chase of the JANAF Tables.

6. 1977 PUBLICATIONS AND REPORTS

Leo Brewer and Associates

LBL Reports

1. B. Meyer and B. Mulliken, Sulfur-Wood Composities, Adv. Chem. Series (in press), LBL-4159.

2. B. Meyer and W. Johns, Sulfur in Wood Bonding Systems, accepted for publication in Holzforschung, LBL-6913.

3. B. Meyer, Spectra of Matrix Isolated Metal Atoms and Clusters, submitted to Berichte der Bunsengesellschaft für Physikalische Chemie. (Presented at the Plenary Lecture #2, Int'l. Conf. on Matrix Isolation Spectros., Wester Berlin, 21-24 June 1977, Berlin, Germany.) LBL-6674.

Papers Presented

1. Leo Brewer, speaker at Workshop on Application of Phase Diagrams in Metallurgy and Ceramics, Natl. Bureau of Stnds., 10-12 January 1977.

2. Leo Brewer, principal speaker at California Assc. of Chem. Teachers Conf., San Luis Obispo, 19 February 1977.

3. Leo Brewer, plenary speaker, Electrochemical Society 9-13 October 1977, Atlanta, Georgia.

b. Nuclear Technology Problems

Donald R. Olander, Principal Investigator

1. MOLECULAR BEAM STUDY OF THE KINETICS OF THE FLUORINE-URANIUM DIOXIDE REACTION*

A. Machiels† and D. R. Olander

The reactivity of fluorine with inorganic oxides is of practical importance in several steps of the nuclear fuel cycle and in the performance of hf lasers. The UO_2/F_2 reaction was investigated by impinging a modulated molecular beam of F_2 on a heated single crystal specimen of UO_2 in a high vacuum. Product signals modulated at the same frequency as the incident F_2 beam were detected mass spectrometrically and processed by a lock-in amplifier to extract the amplitude and phase of the product relative to the reactant flux to the solid surface. For F_2 beam intensities equivalent to random gas pressures from 10^{-7} to 10^{-4} Torr and UO_2 temperatures from 1000 to 1800 K, the primary observable product was volatile UF_4. Desorption of atomic fluorine from the surface could not be measured, but was inferred from the data. Above 1600 K, signals arising from the oxyflorides of uranium were detected. No molecular oxygen product was measured mass spectrometrically, which implies that the oxygen produced by the reaction dissolves in the solid rather than excapes to the gas. The overall reaction is:

$$F_2(g) + UO_2(s) \rightarrow UF_4(g) + 2O(\text{sol'n in solid}) \qquad (1)$$

The measured UF_4 phase lags were large (30-80 deg) and very insensitive to modulation frequency, which indicates a substantial influence of bulk and/or surface diffusion of intermediates on the surface chemistry. The UF_4 reaction probabilities and phase lags varied significantly with F_2 beam intensity, which requires nonlinear elementary steps in the surface reaction mechanism.

Figure 1 shows a scanning electron micrograph of the reacted (111) surface. Chemical etching of single crystal UO_2 by fluorine does not produce a smooth (111) surface; rather, the topography consists of regions of planar (111) surfaces about 10 μm in dimension separated by a hill-type structure. This hill/plane morphology persisted after long reaction times and apparently represents an equilibrium surface. Crystals oriented in the (110) and (100) directions resulted in similar surface morphology.

The reaction mechanism that best fit the molecular beam data and was consistent with the observed surface topograph consisted of dissociative adsorption of fluorine on the planar regions of the surface followed by F atom migration to the hills where chemical conversion to UF_4 or desorption of atomic fluorine occurred. The mechanism involves the oxyfloride UOF_2 as a surface intermediate, both on the planar zones and on the reactive hills. Surface migrating fluorine atoms can dissolve in

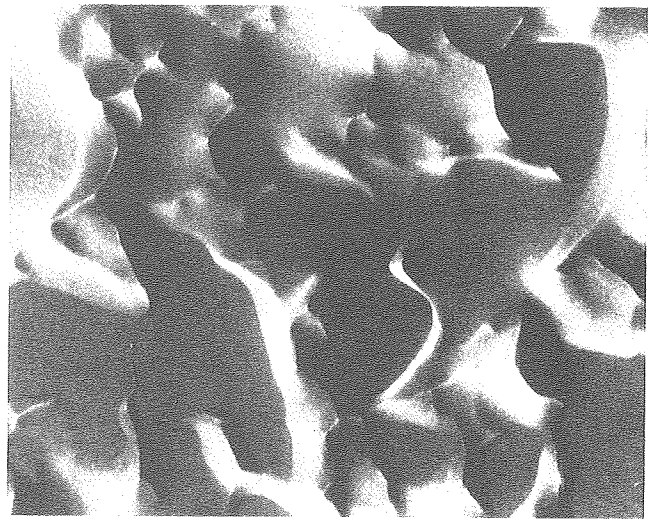

Fig. 1. F_2 - reacted UO_2 surface. (XBB 7510-7931A)

the bulk oxyfluoride and diffuse into the solid. The reactive hill structure is covered with UOF_2, which reacts with adsorbed F atoms reaching it from the planes to produce UF_4:

$$UOF_2 + 2F \rightarrow UF_4(g) + O(\text{sol'n in solid}) \qquad (2)$$

Alternatively, the hill regions provide sites for the desorption step:

$$F \rightarrow F(g) \qquad (3)$$

The nonlinear aspects of the data are due to the second order surface reaction of Eq. (2) and to a coverage dependence of the F_2 sticking probability on the planar zones. Analysis of the data provided a bare surface sticking probability of F_2 on UO_2 of 0.22, a surface diffusion coefficient of F on UO_2 that is quite close to that observed for O on molybdenum,[1] and rate constants for reactions (2) and (3) which exhibit pre-exponential factors expected of bimolecular and unimolecular decomposition reactions, respectively.[2]

---

*Summary of paper published in High Temp. Science.

†Present Address: Nuclear Engineering Program, University of Illinois, Urbana, IL.

1. A. Z. Ullman and R. J. Madix, High Temp. Sci. 6, 342 (1974).
2. R. C. Baetzold and G. A. Somorjai, J. Catal. 45, 94 (1976).

2. A MECHANISTIC INTERPRETATION OF THE H_2O/C REACTION*

D. R. Olander

For many decades, research on the gasification of carbon or graphite by water vapor has been interpreted in terms of a simple two-step mechanism: molecular chemisorption of H_2O to form a strongly bound $C\text{-}H_2O$ complex followed by slow decomposition of this complex to produce H_2 and CO.[1,2] On the basis of a low pressure, flash filament-type experiment, Duval and co-workers have challenged this interpretation,[3] claiming instead that the initial chemisorption step is dissociative and leads to the surface species C-H and C-OH. Our molecular beam investigation of the H_2O-graphite reaction substantiates this interpretation and provides quantitative information on the subsequent reactions that lead either to reconstitution of water by recombination:

$$\text{C-OH} + \text{C-H} \xrightarrow{k_o} 2C_f + H_2O \qquad (1)$$

or reaction to produce H_2 and CO by the sequence:

$$\text{C-H} + \text{C-OH} \xrightarrow{k_1} \text{C-O} + \text{H-C-H} \qquad (2)$$

$$\text{C-O} \xrightarrow{k_{CO}} \text{CO} \qquad (3)$$

$$\text{H-C-H} \xrightarrow{k_{H_2}} C_f + H_2 \ . \qquad (4)$$

In these reactions, C_f denotes a surface carbon atom and C-O and H-C-H represent intermediate surface complexes whose decomposition leads to the stable gaseous products. These complexes are the same as those found in previous studies of the C/O_2 and C/H reactions.[4,5]

Contrary to all previous work, we found that water desorption from graphite is reversible, at least on the millisecond time scale characteristic of modulated molecular beam experiments. This reversibility was demonstrated by isotope exchange experiments in which mixed beams of D_2O and H_2O resulted in formation of HDO, as would be expected from Eq. (1). The older reaction model provides no mechanism by which graphite could catalyze the isotope exchange reaction. We found that the isotope exchange reaction was unactivated, a result which cannot be rationalized with a model that relies upon thermal desorption of a molecular complex $C\text{-}H_2O$. However, it is easy to justify a temperature-independent recombination reaction of the type given by Eq. (1), since the reactants are both surface free radicals and need not present an activation energy barrier to product formation. The absence of a temperature dependence of k_o in Eq. (1) also implies that surface-absorbed H atoms possess the mobility of an ideal two-dimensional gas. Based upon this interpretation, the magnitude of the rate constant k_o can be calculated from kinetic theory. The calculated value of k_o, however, is seven order of magnitude larger than the observed value. This difference is interpreted as a result of the inability of the solid to remove the excitation energy contained in the H_2O molecule produced by reaction (1); unless this excitation can be quickly removed by the solid, the newly-produced water molecule breaks up and the H-OH collision will have been ineffective in producing stable H_2O.

The competing reaction branch given by Eq. (2) was found to be activated, having an activation energy of 170 kJ/mole. This value is in good accord with the dc molecular beam results for the same reaction obtained by Schutze and Schugerl.[6] This step, as well as the subsequent decomposition steps of Eqs. (3) and (4), are irreversible. In addition, the rate constants of reactions (2), (3) and (4) all exhibit characteristic times of the order of milliseconds in the temperature range 2000 to 2500 K and are therefore detectable by the modulated molecular beam method. All earlier studies have found that water vapor is much less reactive towards graphite than is molecular oxygen. This observation, however, needs to be qualified, for it is true only at temperatures below 2000 K. Despite the fact that the sticking (or chemisorption) probability of H_2O on C is larger than that of O_2, the reactivity inversion at about 2000 K is due to the strong temperature dependence of reaction (2). Whereas O_2 chemisorption on graphite is irreversibile, in the sense that once formed, the C-O complex can only decompose to CO, the C-H and C-OH complexes formed upon H_2O chemisorption can react either according to Eq. (1) or Eq. (2). The former reaction, being unactivated, dominates at low temperature; at high temperature, however, reaction (2) effectively competes with reaction (1), and gasification of the solid occurs as readily in H_2O as in O_2 at temperatures above 2000 K.

Despite the complexity of the reaction mechanism revealed by the modulated molecular-beam experiments, the kinetics appear deceptively simple in steady-state experiments. In the latter case, the probability that an incident H_2O molecule produces a CO product molecule is simply:

$$\varepsilon_{CO}^{dc} = \frac{k_1}{k_o + k_1} \eta_o$$

where $\eta_o = 0.15$ is the sticking probability of H_2O and $k_1/(k_o+k_1)$ is the temperature-dependent branching ratio that gives the relative magnitudes of the recombination reaction (1) and the product-forming reaction (2).

---

*Summary of a paper published in J. Chem. Phys.

1. J. M. Thomas, Carbon 8, 413 (1970).
2. R. C. Giberson and J. P. Walker, Carbon 3, 521 (1966).
3. P. Magne, R. Sauvageot and X. Duval, Carbon 11, 485 (1973).
4. D. R. Olander, W. Siekhaus, R. Jones and J. A. Schwarz, J. Chem. Phys. 57, 408 (1972).
5. R. H. Jones, D. R. Olander, W. J. Siekhaus, and

J. A. Schwarz, J. Chem. Phys. 57, 421 (1972).
6. C. Schutze and K. Schugerl, Proc. of the Ninth Int. Symp. on Rarefied Gas Dynamics, M. Becker and M. Fiebig, Eds., (1974), p. E. 11-1.

3. PARTICLE CAVITATION DURING HYDROGEN REDUCTION OF MIXED OXIDE FUEL*

P. E. Hart† and D. R. Olander

The mixed oxide fuel $(U,Pu)O_{2-x}$ is usually prepared from powder blends of the constituents UO_2 and PuO_2, which are sintered and reduced by heating in hydrogen at 1600 to 1700°C. In a recent study of this process,[1] each of the plutonia particles (initial diameters of 50 to 100 μm) was found to have transformed to a spherical shell of dense PuO_{2-x} surrounded by a central cavity that was a substantial fraction of the original particle diameter (Fig. 1).

In rendering $(U,Pu)O_2$ hypostoichiometric, it is generally agreed that the UO_2 component remains essentially stochiometric while the plutonia is reduced. In a powder compact, the PuO_2 particles are separated from the reducing gas by the continuous UO_2 phase. During reduction, oxygen must migrate from the encapsulated plutonia particles through the intervening UO_2 matrix to the gas phase where the oxygen ultimately appears as H_2O. The following reaction mechanism explains the appearance of a cavity at the location of the plutonia particle. Hydrogen dissolves in the UO_2 phase and rapidly diffuses to the plutonia particle. At (or in) the plutonia particle, reduction takes place:

$$H_2 + 2Pu^{+4} + O^{-2} \rightleftharpoons 2Pu^{+3} + H_2O \qquad (1)$$

The H_2O produced by the reaction has a lower diffusivity in UO_2 than does H_2, and its solubility in UO_2 is probably smaller than that of hydrogen as well. If reaction (1) is fast, the rate of reduction of the plutonia particle is controlled by the transport of the reaction product H_2O from the particle through the UO_2 to the ambient gas. If the solubility of H_2O in the oxide is exceeded, a gas bubble containing principally water vapor will be nucleated. The subsequent growth of this bubble is governed by the permeability of UO_2 to water vapor and by the rate at which the cavity volume can expand by vacancy capture or other creep mechanisms.

As PuO_2 is reduced to PuO_{2-x}, the parameter x increases and the water produced diffuses away from the growing bubble, as given by the following oxygen balance on the particle:

$$\frac{4\pi R^3}{3}\frac{dx}{dt} = 4\pi r D_{H_2O} S_{H_2O}(p_{H_2O} - p^{\infty}_{H_2O}) \qquad (2)$$

where R and r are the radii of the initial plutonia particle and of the bubble, respectively. $D_{H_2O}S_{H_2O}$ is the diffusivity-solubility product (i.e., the permeability) of water in UO_2. p_{H_2O} and $p^{\infty}_{H_2O}$ are the water vapor pressures in the bubble and in the ambient reducing gas, respectively.

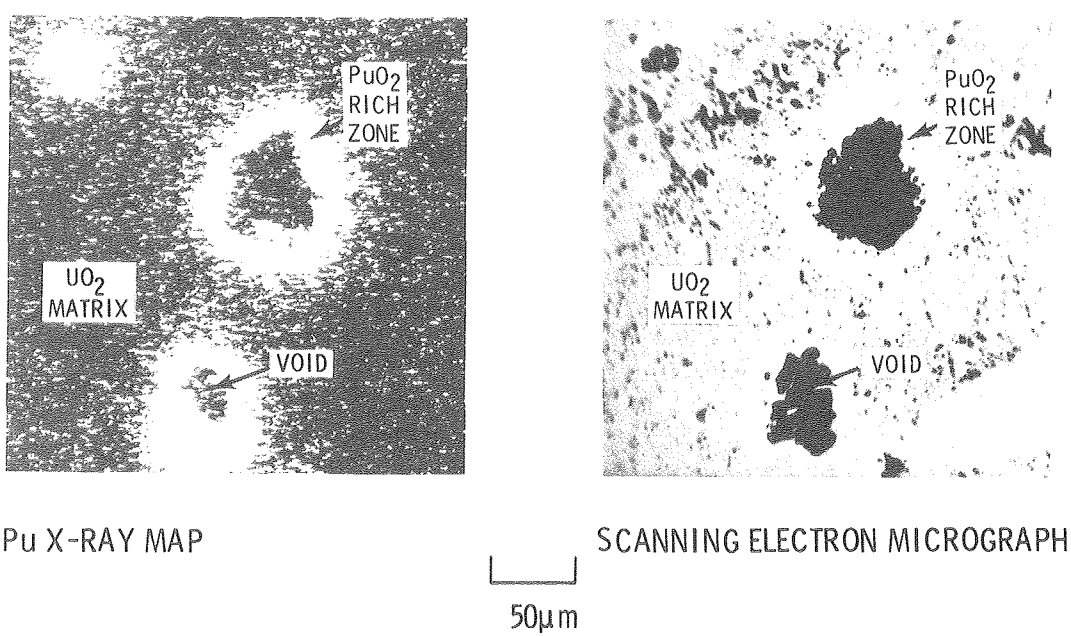

Fig. 1. Plutonia particles in sintered mixed oxide fuel. (XBB 781-221)

Assuming that bubble enlargement is controlled by vacancy diffusion from the bulk solid, the time rate of change of the bubble radius is given by:[2]

$$\frac{dr}{dt} = (p_{H_2O} + p_{H_2} - \frac{2\gamma}{r}) \frac{D_v x_v^{eq}}{rkT} \qquad (3)$$

where $p_{H_2O} + p_{H_2}$ is the total gas pressure in the bubble and γ is the surface tension of UO_2 (or of PuO_2). D_v is the vacancy diffusion coefficient in the oxide and x_v^{eq} is the equilibrium vacancy fraction in the solid. The product $D_v x_v^{eq}$ is the volume self-diffusion coefficient, D_{vol}. Equation (3) is analogous to the growth law of fission gas bubbles with an internal pressure exceeding that required for mechanical equilibrium.

Finally, the assumption of chemical equilibrium between the gas in the bubble and the plutonia surrounding it provides the relation:

$$\frac{p_{H_2O}}{p_{H_2}} = \exp\left[\frac{\frac{1}{2}\Delta\overline{G}_{O_2} - \Delta G^{\circ}_{H_2O}}{kT}\right] \qquad (4)$$

where $\overline{\Delta G_{O_2}}(x)$ is the oxygen potential of PuO_{2-x} and $\Delta G^{\circ}_{H_2O}$ is the standard free energy of formation of H_2O.

Equations (2)-(4) are solved simultaneously to determine the variation of the bubble size and plutonia stoichiometry as a function of sintering time. All parameters of the calculation can be estimated except for the permeability of UO_2 to water. Selecting this quantity as 10^{-5} of the known hydrogen permeability in UO_2, the calculations predict that a water vapor bubble with a diameter 1/4 of that of the initial PuO_2 particle will grow in one hour. After 10^5 h, the bubble grows to twice the size of the original particle. The calculations serve to demonstrate that with reasonable estimates of the physical properties, cavitation of PuO_2 particles during mixed oxide reduction by hydrogen can be qualitatively explained by the proposed model.

---

*Summary of paper submitted to J. Nucl. Mater.

†Battelle Pacific Northwest Laboratories, Richland, Washington.

1. Conducted at Battelle Northwest Laboratories.
2. D. R. Olander, Fundamental Aspects of Nuclear Reactor Fuel Elements, TID-26711-P1 (1976).

4. IN-PILE HOMOGENIZATION OF MIXED-OXIDE FUEL*

B. Mingst† and D. R. Olander

The extent of plutonium homogenization in blended powder mixed-oxide fuel pellets has been the subject of several recent studies.[1-3] The observed intermixing of U and Pu during sintering is thought to arise from classical interdiffusion of the heavy-metal cations. Homogenization during the sintering step of the fuel fabrication process is small but detectable.

When inserted in a reactor, however, homogenization should be accelerated by two phenomena. First, because plutonium is the principal fissile species in the mixed oxide, heat is produced predominantly in the PuO_2 particles (the power density of the PuO_2 is >100 times larger than the average power density in the fuel.)[1] As a result, the temperature in the PuO_2 particles is higher than that of the surrounding UO_2 matrix. This temperature rise increases the cation diffusivity above the value characteristic of the local average temperature, and thus speeds up homogenization. To assess the importance of this effect, the fuel is represented by a unit cell containing a PuO_2 particle of radius R at the center and surrounded by an annulus of UO_2 of radius $\mathcal{R} = R/q_{av}^{1/3}$, where q_{av} is the average plutonium enrichment of the fuel.[2] The composite medium heat conduction problem is solved to yield the temperature difference between the center of the PuO_2 particle and the outer edge of the UO_2 annulus:

$$T(0) - T(\mathcal{R}) = \frac{3.2\times10^{-11}\,\sigma_f N_f \Phi R^2}{3k}\left(\frac{3}{2} - \frac{R}{\mathcal{R}}\right), \qquad (1)$$

where $k \approx 0.03$ W/cm-K is the thermal conductivity of the oxide, σ_f if the fission cross section (of Pu), N_f is the cation density, and Φ is the neutron flux. For a thermal-neutron flux of 3×10^{13} n/cm^2-s, a Pu fission cross section of 800 b, and a fuel containing 5% Pu, the temperature spike produced in a 35-μm-diam PuO_2 particle is <1 K. If the particle is 500 μm in diameter, however, the temperature rise is ~130°C. Since the vast majority of PuO_2 particles in blended mixed-oxide fuel is smaller than 50 μm, the effect of the localized heating on the temperature distribution, and consequently on the homogenization rate, is negligible.

The second in-pile effect on plutonium homogenization is radiation-enhanced diffusion. This results from the greatly increased concentration of lattice vacancies generated by the energetic fission fragments in the fuel. Since U and Pu diffusion probably occurs by a vacancy mechanism on the cation sublattice, the diffusivity can be increased by fission. Generally, radiation enhancement of the diffusion coefficient is treated by adding to the ordinary thermally activated diffusivity in term proportional to the fission rate density:[4]

$$D = D_0 \exp(-E/kT) + C(\sigma_f N_f \Phi q), \qquad (2)$$

where D_0 and E are the preexponential factor and the activation energy of chemical interdiffusion of U and Pu. In the irradiation-enchancement term,

C is a constant and q is the local cation fraction of plutonium. In-pile redistribution of plutonium is governed by Fick's second law with a concentration-dependent diffusion coefficient given by Eq. (2)

$$\frac{\partial q}{\partial t} = \frac{1}{r^2} \frac{\partial}{\partial r} \left(Dr^2 \frac{\partial q}{\partial r} \right) , \qquad (3)$$

which is subject to the initial condition

$$q(r,0) = \begin{cases} 1, & 0 \leqslant r \leqslant R \\ 0, & R \leqslant r \leqslant R \end{cases} \qquad (4)$$

and the boundary condition $(\partial q/\partial r)_R = 0$.

Plutonium concentration distributions were computed as a function of time in-pile by numerical solution of Eq. (3) using the radiation enhancement coefficient $C = 1.3\times10^{-29}$ cm^5/fission given by Marlowe.[5] Thermal diffusion parameters ($D_0 = 0.34$ cm^2/s, E = 460 kJ/mole) were taken from Ref. 6. Figure 1 shows the homogenization time, defined as the time required for the Pu fraction in the center of the PuO_2 particle to be reduced to twice the average Pu fraction in the fuel, plotted as a function of neutron flux for various temperatures. Horizontal lines indicate negligible effect of radiation-enhanced diffusion (i.e., the first term on the right-hand side of Eq. (2) is much larger than the last term). At temperatures $\leqslant$ 1600 K, radiation acts to reduce the homogenization time in the range of neutron fluxes of practical interest. However, the homogenization times at this temperature are so large, the slight radiation enhancement is of little consequence.

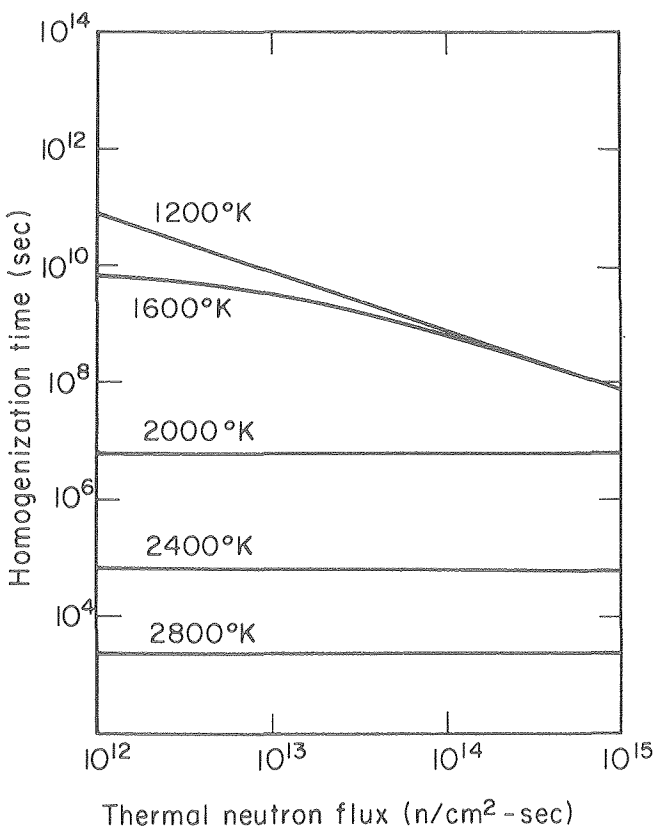

Fig. 1. Homogenization time. (XBL 781-25)

---

*Summary of paper published in Trans. Am. Nucl. Soc.

†Current address: Nuclear Regulatory Commission, Washington, D.C.

1. M. D. Freshley, D. W. Brite, J. L. Daniel and P. E. Hart, paper presented at the ANS Topical Meeting on the Plutonium Fuel Cycle, Miami (May 2-5, 1977).
2. D. R. Olander, J. Nucl. Mater. 60, 237 (1976).
3. P. E. Hart and D. R. Olander, submitted to J. Nucl. Mater.
4. R. S. Nelson, J. Nucl. Mater. 25, 227 (1968).
5. M. O. Marlowe, NEDO-12440 (1973).
6. M. Bober, J. Nucl. Mater. 47, 195 (1973).

5. THE SURFACE CHEMISTRY OF EPITAXIAL SILICON DEPOSITION BY THERMAL CRACKING OF SILANE

R. Behrens,* D. R. Olander and M. Farnaam

Production of epitaxial layers of silicon on a substrate is a widely used and intensively studied process. This technique is utilized extensively in the semiconductor industry and more recently in the fabrication of photovoltaic devices for direct solar energy conversion to electricity. The overall process can be divided into two subprocesses: 1) the surface decomposition of the silicon-bearing gas to produce silicon adatoms, and 2) the incorporation of the silicon adatoms into an epitaxial layer. The second aspect has received the most attention in the literature; the growth process is driven by the supersaturation of the surface with silicon adatoms but does not depend upon their source (i.e., whether produced from a CVD process or by condensation of silicon vapor). The first subprocess contains all the surface chemistry of the overall process, and is the object of the present experiment.

The meager literature on the surface chemistry of the silane cracking reaction:[1-3]

$$SiH_4(g) \rightarrow Si + 2H_2(g)$$

is contradictory and based upon unsophisticated techniques of heterogeneous chemical kinetics (e.g., steady-state measurements of the rate of H_2 production) and rudimentary mechanistic analysis. Our experiment utilizes a modulated molecular-beam method, thereby permitting more

detailed probing of the surface processes by use of phase lag measurements.[4] In addition, use of a mixed reactant containing SiH_4 and SiD_4 provides a means of investigating the H atom rearrangements in the mechanism.

Silane beams with intensities varying from 10^{-5} to 10^{-4} Torr equivalent pressure impinge on a Si(111) target heated resistively to temperatures ranging from 1000 to 1500 K. Modulation frequencies from 10 to 1000 Hz are employed. A complete set of molecular beam data has been obtained (i.e., H_2 reaction probabilities and phase lags as functions of beam intensity, substrate temperature and modulation frequency). However, smooth layer growth was not achieved; instead, islands were found on the surface (Fig. 1). This indicates either an improper

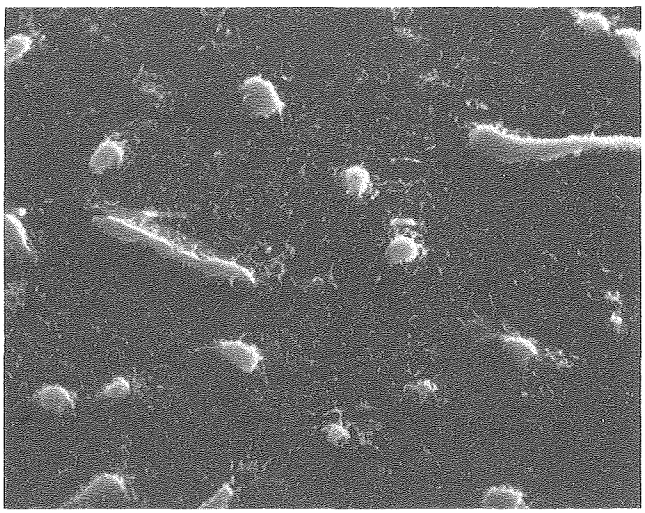

Fig. 1. Island growth on Si(111). (XBB 750-7913)

substrate cleaning procedure or insufficient vacuum. Consequently, the data were not fitted to a detailed reaction mechanism, which will be done only when smooth surfaces result from the experiment. Nevertheless, one feature of the reaction is clear from the data. The reaction product H_2 was observed to have a nonzero phase lag with respect to the incident silane. This means that H_2 is not released instantaneously upon sticking of a SiH_4 molecule on the surface. Sticking may be accompanied by production of hydrogen adatoms which remain on the surface until another H atom is encountered and H_2 is formed. Alternatively, SiH_4 may be adsorbed and migrate as a unit along the surface until it encounters a site favorable for decomposition, at which time H_2 is released.

---

*Current address: Sandia Corporation, Livermore, CA.

1. B. A. Joyce et al., Phil. Mag. 14, 289, 301 (1966) and 15, 1167 (1967).
2. R. C. Henderson et al., Surf. Sci. 30, 310 (1972).
3. R. F. C. Farrow, J. Electrochem. Soc. 121, 899 (1974).
4. R. H. Jones, D. R. Olander, W. J. Siekhaus and J. A. Schwarz, J. Vac. Sci. Technol. 9, 1429 (1972).

6. RETENTION AND RELEASE OF WATER VAPOR BY URANIUM DIOXIDE*

A. Srivastava and D. R. Olander

The uranium dioxide fuel pellets for light water reactors absorb significant quantities of moisture during the many manipulations involved in their fabrication. Unless removed by extensive drying prior to loading into the fuel element, this water will be released during reactor operation and may cause internal hydriding of the cladding.

Previous attempts to measure the quantity of adsorbed water in UO_2 and the kinetics of its release (summarized in Ref. 1) did not solve, or even address, the experimental problem of the trapping of released water by cool walls of the apparatus and the detection device. In addition, the sensitivity of these experiments was so poor that quantities of adsorbed water of technological significance could easily have remained undetected. The present experiment has been designed to overcome these inadequacies.

The samples of sintered UO_2 pellets are subject to an initial vacuum outgassing to remove native moisture and other volatile impurities. The specimens are then exposed to saturated D_2O vapor at room temperature for two days. D_2O is used as a stand-in for H_2O because it can be more easily detected mass spectrometrically. The pellets are then flushed with dry nitrogen at room temperature for one week in order to remove loosely bound D_2O. The remaining water in the pellets is reasonably well trapped, and its subsequent release at high temperature is investigated in the apparatus shown in Fig. 1.

To prevent trapping or decomposition of the released D_2O on metal surfaces, a noble metal crucible is used. The entire upper portion of the assembly is constructed of stainless steel that is maintained at temperatures in excess of 400°C during outgassing of the UO_2 specimen. The released D_2O leaves the furnace assembly via a capillary tube at the top, which permits molecular beam detection by an *in situ* quadrupole mass spectrometer. The molecular beam issuing from the capillary tube into the vacuum is mechanically modulated by a rotating slotted disk before entering the ionizer of the mass spectrometer. Molecular beam sampling completely avoids loss of D_2O by adsorption on walls of the apparatus or the mass spectrometer; lock-in amplification of the D_2O signal from the mass spectrometer affords a two order of magnitude increase in the system sensitivity compared to any previous experimental techniques for measuring water release. The absolute rate of release is determined by periodic comparison of the D_2O signal with that of a calibration gas (neon) that is fed to the furnace assembly at a known flow rate. The sensitivity limit of the molecular beam sampling system has

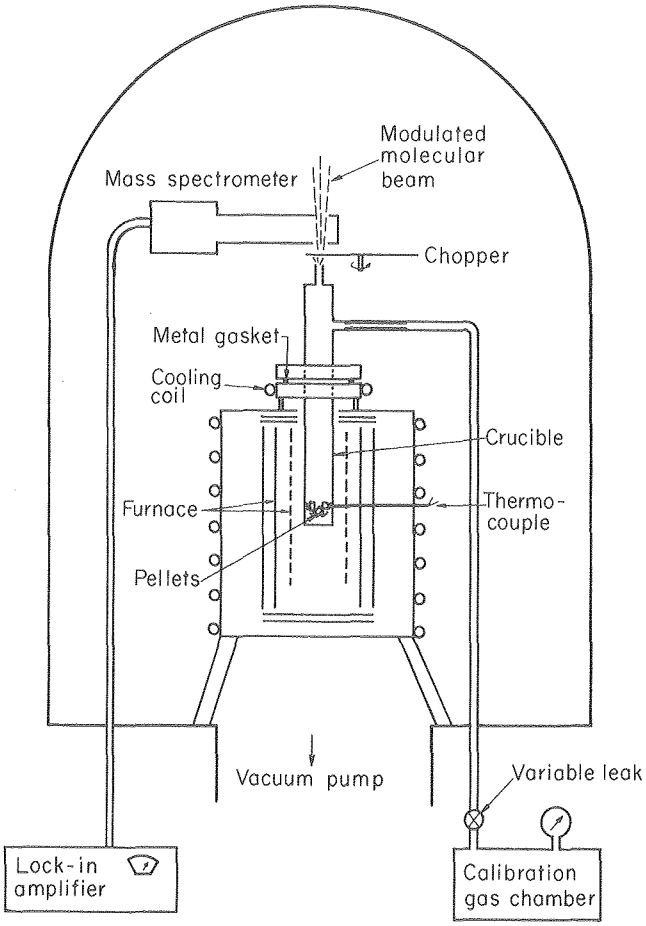

Fig. 1. Apparatus for measurement of gas release from refractory oxides. (XBL 781-2768)

been determined to be a release rate of 10^{-12} g D_2O/s.

Previous attempts to measure water release from UO_2 (Ref. 1) have determined that essentially all release occurs at temperatures below 1000°C within a time span of a few hours. Our results, however, demonstrate that the quantity of water released below 1000°C is rather small (~0.2 μg D_2O/g UO_2) but that release continues for long periods (>150 hours) for temperatures exceeding 1600°C. What the previous investigations undoubtedly measured was the large quantity of loosely bound water that is removed in our experiments by the week-long dry nitrogen flush. The previous investigations have essentially missed entirely the slower release of strongly bound water which takes place at low rates at temperatures greater than 1000°C.

In conducting the release experiment, the temperature was increased by 200°C intervals and held constant for long periods between the changes. At each temperature (in excess of 1000°C), the D_2O release rate is first large, then decreases slowly. Upon raising the sample temperature, a fresh burst of D_2O is observed and the rate then slowly decays. The total quantity of D_2O outgassed from UO_2 up to 1600°C is 12 μg/g UO_2 and there is no evidence that all D_2O has been removed at this temperature.

Experiments of even longer duration and higher temperatures are needed to remove all D_2O from the specimens. Efforts are now being made to model the release process in terms of desorption from internal surfaces in the UO_2 sintered body followed by diffusional escape via interconnected porosity from the solid to the external vacuum. From a practical standpoint, the results of the experiments demonstrate that despite fuel "drying" prior to sealing in the cladding, some water will remain and be released inside the fuel element while it is at elevated temperature in reactor. This water can only be prevented from attacking the zircaloy cladding by the use of getters placed inside the fuel elements during fabrication.

---

*Partially supported by the Electric Power Research Institute.

1. C. E. Beyer and C. R. Hahn, US ERDA Report BNWL-1956 (1977).

7. RESEARCH PLANS FOR CALENDAR YEAR 1978

Donald R. Olander

The molecular beam study of the silane cracking reaction will be redone with properly cleaned crystal targets that do not exhibit island growth upon heating.

The molecular beam investigation of the reaction of atomic hydrogen with ceramic oxides has been troubled by deposition of tungsten from the target holder on the reacting surface. This problem will be attacked by use of new target holder designs.

The study of laser pulsing of UO_2 will investigate the angular distribution of vaporized UO_2, the possibility of droplet ejection and/or formation by condensation in the vapor plume, and emission of ions in the process.

The hydrogen solubility in ceramics study will be performed in two stages; infusion of deuterium into the oxide at high temperature and pressure vessel followed by mass spectrometric measurement of the released deuterium in a vacuum furnace.

The problem of excessive porosity in the specimens used for the study of thermal gradient migrations of solid inclusions in UO_2 will be approached by initial hot-pressing of the samples.

An experiment will be conducted to estimate oxygen diffusion in hypostoichiometric urania by following the rate of weight loss of a UO_2 specimen suspended from a microbalance in a stream of flowing hydrogen.

An experiment to investigate the possibility of radiation-enhancement of iodine stress corrosion cracking of zircaloy has been set up and will begin.

8. 1977 PUBLICATIONS AND REPORTS

Donald R. Olander and Associates

Journals

1. D. R. Olander, Heterogeneous Chemical Kinetics by Modulated Molecular Beam Mass Spectrometry--Limitations of the Technique, J. Colloid and Interface Sci. 58, 169 (1977).

2. A. J. Machiels and D. R. Olander, Investigation of the Tantalum-Fluorine Reaction by Modulated Molecular Beam Mass Spectrometry, Surf. Sci. 65, 325 (1977).

3. D. R. Olander, Particle Cavitation During Hydrogen Reduction of Mixed-Oxide Fuel, Trans. Amer. Nucl. Soc. 26, 167 (1977).

4. A. J. Machiels and D. R. Olander, Molecular Beam Study of the Kinetics of the Fluorine-Uranium Dioxide Reaction, J. High Temp. Sci. 9, 3 (1977).

5. D. R. Olander, T. R. Acharya and A. Z. Ullman, Reactions of Modulated Molecular Beams with Pyrolytic Graphite. IV-Water Vapor, J. Chem. Phys. 67, 3549 (1977).

6. B. Mingst and D. R. Olander, In-Pile Homogenization of Mixed-Oxide Fuel, Trans. Amer. Nucl. Soc. 27, 236 (1977).

Papers Presented

1. A. Machiels, Investigation of the Tantalum-Fluorine Reaction by Modulated Molecular Beam Mass Spectrometry, Electrochemical Society Meeting, Philadelphia, May 8, 1977.

2. D. R. Olander, Particle Cavitation During Hydrogen Reduction of Mixed-Oxide Fuel, American Nuclear Society Meeting, New York, June 20, 1977.

3. D. R. Olander, Kinetics of Fluorination Reactions of Metals and Oxides, ARPA Materials Research Council, La Jolla, CA, July 1977.

4. D. R. Olander, Uranium Enrichment by the Gas Centrifuge, Department of Nuclear Engineering, Nov. 3, 1977.

5. D. R. Olander, In-Pile Homogenization of Mixed-Oxide Fuel, American Nuclear Society Meeting, San Francisco, November 28, 1977.

c. Process Technology of Solid State Materials

Lee F. Donaghey, Principal Investigator*

1. THERMODYNAMIC STUDY OF THE TERNARY LIQUID ALLOY SYSTEM Ga-In-Sb BY SOLID STATE ELECTROCHEMISTRY

Timothy J. Anderson and Lee F. Donaghey

The thermodynamic activity of gallium in selected ternary liquid solutions in the Ga-In-Sb system was studied as part of the current research program to characterize the thermodynamics of solid and liquid alloys in systems of group III and V elements. The group III-V compounds are important semiconductor materials which have particularly important applications in microwave and electro-optical solid state devices. Use of ternary and quaternary solid solutions offers the ability to fabricate devices where both the band gap and the lattice parameter are adjustable over a wide, continuous range. A thermodynamic characterization of these compounds is essential in establishing conditions for optimum device fabrication.

The activity of Ga was measured experimentally in the following solid state electrochemical cell:

$$Pt|C|\ Ga(\ell),In(\ell),Sb(\ell),Ga_2O_3\ \|\ CSZ\ \|\ Ga(\ell),Ga_2O_3|Pt. \quad (1)$$

Various compositions were studied with particular attention given to the psuedo-binary solid solution $Ga_xI_{1-x}Sb$. The gallium activity exhibited moderate negative deviations from ideal solution behavior for all alloys studied.

The results of this study will be used to test different solution models for predicting the phase diagram of the ternary system and optimum conditions for preparing desirable alloy compositions by liquid phase epitaxy.

---

* Present address: Chevron Research Company, Richmond, CA 94802.

2. COMPONENT ACTIVITIES IN In-Sb LIQUID ALLOYS

Timothy J. Anderson and Lee F. Donaghey

Component activities in In-Sb liquid alloys were investigated in the following two high temperature galvanic cells:

$$Pt|C|\ In_xSb_{1-x}(\ell),\ In_2O_3\|CSZ\|In(\ell),In_2O_3|C|Pt \quad (1)$$

and

$$Pt|C|\ In_xSb_{(1-x)}(\ell),\ In_2O_3\ \|CSZ\ \|\ CO,CO_2\ |Pt|. \quad (2)$$

The 15 compositions studied showed moderate negative deviations from Raoult's law over the entire composition range. Analysis of the data showed that the enthalpies of mixing agreed well with the results of calormetric studies when cell 2 utilizing a gaseous reference electrode was employed; the data from cell 1 exhibited a large experimental error due to electrode polarization effects.

In order to compare the results of this study with the In-Sb phase diagram, liquidus temperatures were calculated using the available calorimetric literature data. The derived liquidus temperatures exhibited excellent agreement with the experimentally measured phase diagram.

3. SOLID STATE ELECTROCHEMICAL STUDIES OF GROUP III-V ALLOYS EMPLOYING A CaF_2 SOLID ELECTROLYTE

Timothy J. Anderson and Lee F. Donaghey

Many technologically important semiconducting compounds formed from group III and V elements contain the elements Ga, In and Al. Gallium and indium are amenable to study with solid state electrolytes such as stabilized zirconia and thoria, but alloys containing aluminum are not due to reduction of these electrolytes by aluminum. Thus, in order to investigate alloys of aluminum in solutions of Group III-V elements an alternate approach is needed.

CaF_2 offers the capability of studying aluminum-containing alloys, though this electrolyte presents some experimental difficulties. In the present research program, activities of aluminum are being studied in the following solid state electrochemical cell:

$$Pt|C|Al(\text{in solution}),\ Al_2O_3\|\ CaF_2\|\ Al_2O_3,Al(\ell)|C|Pt. \quad (1)$$

The primary difficulty is the exchange of gaseous fluorides between the electrodes. Figure 1 depicts an experimental cell arrangement that has been developed to significantly reduce this problem. A CaF_2 single crystal is sandwiched between two alumina tubes. The inner and outer compartments contain independent inert gas streams to purge the two cell electrodes. Studies of the $Al_xGa_{1-x}Sb$ system are currently in progress.

4. EROSION PROPERTIES OF REACTIVELY SPUTTERED TITANIUM CARBONITRIDES*

Roger F. Gentile, Kwok K. Chin and Lee F. Donaghey

Titanium nitrides, carbides and carbonitrides are known to exhibit extraordinary hardness. These compounds are of current interest as tool bit coatings and as erosion and corrosion-resistant coatings. Although chemical vapor deposition has

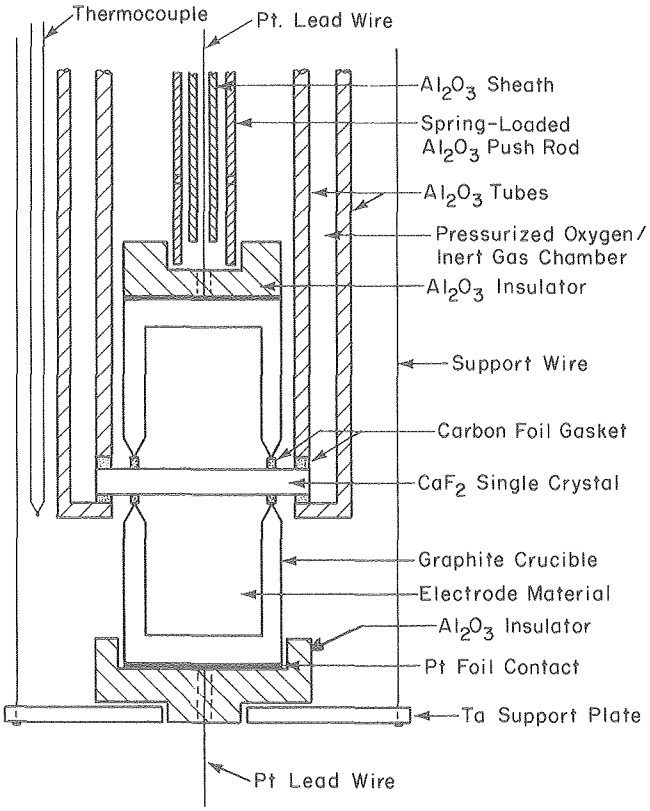

Fig. 1. Electrochemical cell for the study of aluminum activities in solutions of group III and V elements. (XBL 775-8700)

been shown to produce long-wearing tool bits from cemented carbides, the reactive sputtering process offers enhanced adhesion of hard coatings at lower cost on metallic tool bits.

In the present study the mechanical and structural properties of reactively sputtered films of titanium carbonitrides with a wide range of compositions were studied and compared with their erosion properties. The mechanisms of erosion were determined for both amorphous and recrystallized films. TiN films were deposited using nitrogen as a reactive gas, and the effect of substrate bias was studied to determine whether a negative bias voltage applied to the substrate would increase the erosion resistance of TiN films. TiC films were deposited using methane and acetylene as reactive gases. For TiC_xN_y films, acetylene or methane was used together with nitrogen in argon plasmas.

The morphology of reactively sputtered films is exemplified by the scanning electron micrographs of TiC_x films shown in Fig. 1. The annealed samples exhibited grain boundary grooves, with

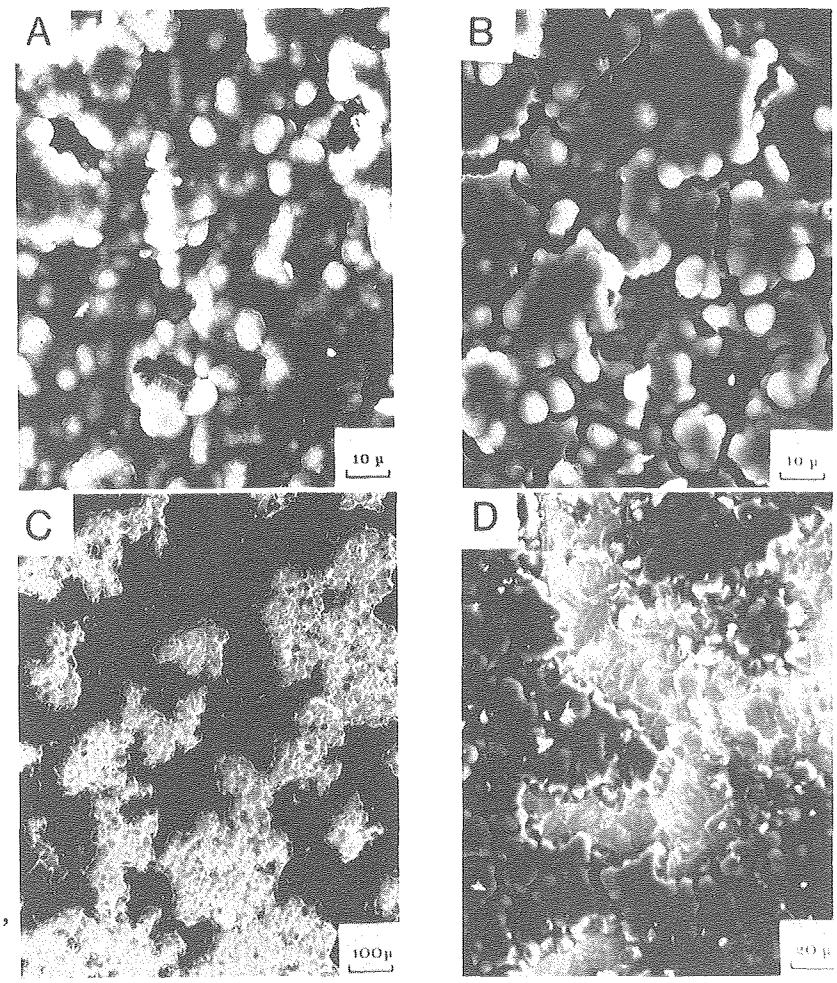

Fig. 1. Surface structure of TiC_x films deposited in 20% C_2H_2, 80% Ar: a) after dep. (1000x), b) after dep. and anneal (1000x), c) after dep. and erosion (100x), d) after dep., anneal and erosion (500x). (XBB 760-11403)

grain size unaffected by annealing. The erosion pattern was similar for both unannealed and annealed films, but the annealing process causes enhanced erosion rates through the removal of sub-grains.

The deposited TiN_y films showed a constant erosion behavior, independent of the plasma gas composition used to deposit them. This result is consistent with a previous study of the deposition rates and chemical composition of TiN_y reactively sputtered films. It appears that the formation of TiN is independent of the nitrogen content of the plasma over a wide range, and that the rate-limiting step is the transport of Ti atoms to the substrate.

*Abstracted from LBL-6255.

5. NUMERICAL SIMULATION OF TRANSPORT PROCESSES IN VERTICAL CYLINDER EPITAXY REACTORS

Charles W. Manke and Lee F. Donaghey

The exploration of transport processes occurring in chemical vapor deposition reactors for the epitaxial growth of silicon from tetrachlorosilane in hydrogen has received considerable attention in the literature, both for the purpose of reactor design and scale-up, and for an improved understanding of experimental phenomena.[1]

In the present study, a numerical method employing a marching integration, finite difference method was used to determine the momentum, temperature, and component molar concentration profiles in the tapered annulus of a vertical cylinder epitaxy reactor for silicon deposition from $SiCl_4$ in H_2. Examples of the results obtained in this study are shown in Fig. 1 for a cylindrical reactor of commercial interest.

The numerical results indicate that boundary layers control the deposition profile in the entrance length of the reactor, while downstream rates are governed by the inlet flow rate and susceptor tilt angle. Results of the study contribute to the understanding of momentum, heat, and mass transfer in the vertical cylinder reactor.

A major objective of reactor design is to develop large capacity reactors which can produce highly uniform deposition over all the substrates in the reactor, reproducible results from run to run, and an economical reactant consumption rate. The present method using numerical methods is extremely useful for developing insight into the silicon deposition process, for providing tests of conditions which optimize the reactor performance, and for providing a basis for scale-up of commercial reactors.

1. C. W. Manke and L. F. Donaghey, J. Electrochem. Soc. 124, 561 (1977).

6. KINETICS OF THE CHEMICAL VAPOR DEPOSITION OF GaAs FROM $Ga(CH_3)_3$ AND AsH_3

Alice L. Lin,* Vy Dao and Lee F. Donaghey

Gallium arsenide has been studied extensively for application in microwave devices, and more recently in low-cost terrestial solar cells. The processing of low-defect density single crystal layers and heteroepitaxial layers is a significantly important step in the preparation of these semiconducting devices.[1-3]

The vapor phase deposition of gallium arsenide from trimethyl gallium (TMG) and arsine has been shown by Manasevit to be a viable alternative to

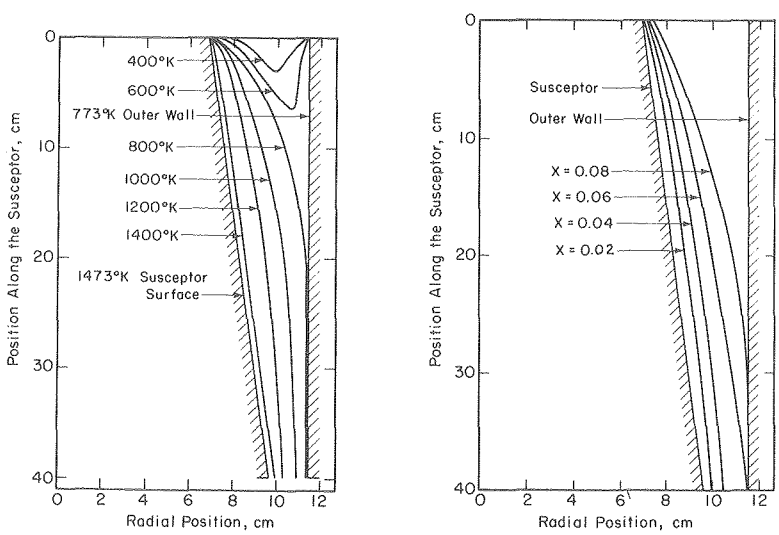

Fig. 1. Simulated temperature isotherms (left) and $SiCl_4$ isoconcentration curves (right) in a vertical cylinder reactor. (XBL 776-9557)

the conventional growth technique using halide transport agents. This method is free of etching species, requires a furnace with only one temperature zone, and offers the possibility of lower growth temperature. Recently, single-crystal GaAs films were successfully prepared by this method in several laboratories. Most of these studies emphasize the surface morphology and electrical properties of the heteroepitaxial GaAs layers deposited on single crystal, insulating substrates rather than the chemical vapor deposition, and no systematic study of the growth kinetics of gallium arsenide from organometallic trimethyl gallium and arsine has been reported.

In this study, growth studies utilizing (100) GaAs substrates showed that growth is linearly dependent on the trimethyl gallium partial pressure in the presence of an excess of arsine. The deposition rate was found to depend on the 0.5 power of the gas flow rate, and on the 0.8 power of the absolute temperature.

A diffusion-controlled model was developed. This model adequately predicts the experimental results for temperatures between 700 and 900°C. At lower temperatures the growth is surface reaction rate controlled. At higher temperatures, decomposition of the GaAs reduces the growth rate.

Defects in the epitaxially grown layers are of two types: hillocks and pits. The hillocks are similar to those observed when GaAs is deposited using chloride transport. Pits are presumed to be produced as a consequence of oxidation of the trimethyl gallium.

---

*Current address: Eastman Kodak, Rochester, NY 14650.

1. R. C. deBernardy and L. F. Donaghey, Preparation of Schottky-Barrier Solar Cells from Polycrystalline GaAs on Molybdenum, LBL-5727, November 1976.
2. R. C. deBernardy and L. F. Donaghey, Chemical Vapor Deposition and Properties of GaAs on Molybdenum Substrates, LBL-5736, December 1976.
3. R. C. deBernardy and L. F. Donaghey, Preparation and Properties of Chemically Vapor Deposited GaAs on Graphite, LBL-5737, December 1976.

7. LOW PRESSURE CHEMICAL VAPOR DEPOSITION OF POLYSILICON

R. J. Gieske, J. J. McMullen, and Lee F. Donaghey

The low pressure chemical vapor deposition of polycrystalline silicon was studied to define the controlling process parameters and the requirements for commercial implementation. Silane and silane-nitrogen mixtures were utilized as source gases in a tubular reactor containing parallel disk substrates oriented with surface normals in the direction of flow. The results of the study showed that the deposition reaction is surface kinetic reaction controlled over the range of temperature studied, 600 to 700°C, that the reaction is first order with respect to silane, and with an activation energy of 1.33×10^5 J/g mole. A gradient in temperature along the reactor tube is sufficient to compensate for reactant depletion and to produce a uniform deposition rate.

8. 1977 PUBLICATIONS AND REPORTS

Lee F. Donaghey and Associates

Journals and Books

1. G. M. Bobba and Lee F. Donaghey, Real-Time Analysis of Gas Chromatographs with a Microcomputer System, J. Chromatog. Sci. 15, 47 (1977).

2. C. W. Manke and Lee F. Donaghey, Analysis of Transport Processes in Vertical Cylinder Epitaxy Reactors, J. Electrochem. Soc. 124, 561 (1977).

3. A. L. Lin and Lee F. Donaghey, Characterization of (111) GaAs and (111) InP Substrates and Homoepitaxial Layers by Divergent X-Ray Beam Diffraction, J. Electronic Materials 6, 383 (1977).

4. T. J. Anderson and Lee F. Donaghey, Solid State Electrochemical Studies of the Standard Gibbs Energy of Formation of β-Gallium Sesquioxide Using a Calcia-Stabilized Zirconia Electrolyte, J. Chem. Thermodynamics 9, 603 (1977).

5. T. J. Anderson and Lee F. Donaghey, Solid State Electrochemical Study of the Standard Gibbs Energy of Formation of Indium Sesquioxide, J. Chem. Thermodynamics 9, 617 (1977).

6. D. Jacobs and Lee F. Donaghey, Microcomputer Implementation of Direct Digital Control Algorithms for Thermal Process Control Applications, Journal of Dynamic Systems, Measurement and Control, Trans. ASME, Series G, Vol. 99, No. 4, pp. 233-240 (1977).

7. Lee F. Donaghey, P. Rai-Choudbury and Richard N. Dauber, Eds., Proc. Sixth International Conference on Chemical Vapor Deposition, The Electrochem. Soc., Princeton, N.J., 1977.

8. C. W. Manke and Lee F. Donaghey, Numerical Simulation of Transport Properties in Vertical Cylinder Reactors, ibid, p. 154, 1977.

9. R. J. Gieske, J. J. McMullen and Lee F. Donaghey, Low Pressure Chemical Vapor Deposition of Polysilicon, ibid, p. 183, 1977.

10. A. L. Lin, V. Dao and Lee F. Donaghey, Kinetics of the Chemical Vapor Deposition of GaAs from $Ga(CH_3)_3$ and AsH_3, ibid, p. 247, 1977.

LBL Reports

1. Roger F. Gentile, Kwok K. Chin and Lee F. Donaghey, Erosion Properties of Reactively Sputtered Titanium Carbonitrides, LBL-6255, May 1977.

Papers Presented

1. C. W. Manke and Lee F. Donaghey, Simulation of Transport Processes in Vertical Cylinder Epitaxy Reactors, 151st Meeting of the Electrochemical Society, Philadelphia, May 8-13, 1977.

2. C. W. Manke and Lee F. Donaghey, Numerical Simulation of Transport Properties in Vertical Cylinder Reactors, 152nd Meeting of the Electrochemical Society, Atlanta, October 9-14, 1977.

3. R. J. Gieske, J. J. McMullen and Lee F. Donaghey, Low Pressure Chemical Vapor Deposition of Polysilicon, 152nd Meeting of the Electrochemical Society, Atlanta, October 9-14, 1977.

4. A. L. Lin, V. Dao and Lee F. Donaghey, Kinetics of the Chemical Vapor Deposition of GaAs from $Ga(CH_3)_3$ and AsH_3, 152nd Meeting of the Electrochemical Society, Atlanta, October 9-14, 1977.

d. Electrochemical Phase Boundaries

Rolf H. Muller, Principal Investigator

1. ELLIPSOMETRY OF ELECTROCHEMICAL INTERFACES

a. Mass-Transport Boundary Layers

Craig G. Smith and Rolf H. Muller

We have recently demonstrated that ellipsometry may be used to determine the concentration of reacting species at an electrode surface.[1,2] In both metal deposition and dissolution, the interfacial concentration can have significant effects on morphology, valence of the electrode process, and the porosity of anodic films. The interest in the ellipsometry of boundary layers is two-fold: 1) as a new technique for the study of mass transport processes at electrodes and 2) to account for the optical effect of boundary layers in the observation of solid films during their growth.

The measurement of interfacial concentrations requires a separation of the optical effect of the mass-transport boundary layer from effects due to changes of the electrode surface, which may be of larger magnitude. Surface changes have caused an uncertainty of about 20% in previous measurements.[3] Improved experimental techniques for the study of transport processes in a flow channel have now been implemented. As before, the cathodic deposition of copper has been chosen as the electrode reaction, but single crystal copper electrodes [(100), (111)] have been used in order to reduce surface roughness. Also, the $CuSO_4$ electrolyte has been deoxygenated and equilibrated with the monovalent cuprous ion in order to reduce corrosion processes. Interfacial concentrations have been determined from the decay of the boundary layers after current interruption by use of our automatic ellipsometer. A new circulation system that provides more stable flow rates of the electrolyte has also been constructed.

Figure 1 shows the measured decrease in the interfacial concentration of Cu^{++}, as a function of flow velocity (shown as Reynolds number) for different current densities. Bulk fluid transport properties have been used in the empirical correlations represented by the solid curves. Deviations of the measurements from the correlations can be explained by the concentration-dependence of transport processes, as has been demonstrated in earlier studies with interferometry.[4]

b. Concentration of Supporting Electrolyte at Electrodes

Craig G. Smith and Rolf H. Muller

Supporting electrolytes serve to increase the solution conductivity and reduce migration effects in electrolytic processes. During electrolysis, two concentration profiles develop near the electrode surface, one for the reacting species and a second for the supporting electrolyte. The interfacial concentration of supporting electrolyte affects the electrode process by altering the chemical environment in which it is conducted.

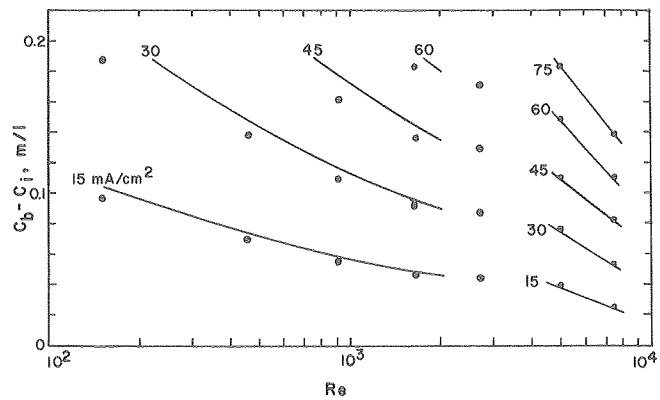

Fig. 1. Decrease in interfacial concentration during Cu deposition from 0.186 M $CuSO_4$. Concentration difference between bulk and interface as function of the flow velocity (shown as Reynolds number). Theoretical predictions for laminar (Re < 2000) and turbulent (Re > 5000) flow given by solid curves. (XBL 7712-10958)

Results were previously reported[5] for the accumulation of H_2SO_4 determined by ellipsometry during the cathodic deposition of copper from stagnant solutions of $CuSO_4$-H_2SO_4. To investigate the influence of convection, measurements have now been conducted in a flow cell.[6] Results are given in Table 1. All measurements were made at limiting current, where the interfacial Cu^{++} concentration is zero, and the H_2SO_4 concentration may be uniquely determined from the refractive index. The change in H_2SO_4 concentration between the interface and the bulk electrolyte relative to the change in $CuSO_4$ concentration, $\Delta C_{H_2SO_4}/\Delta C_{CuSO_4}$, is shown in the last column of Table 1. Computed values for this quantity[7] are 0.43 and 0.16, respectively, for complete and no dissociation of the bisulfate ion. The experimental value of 0.35 indicates that the bisulfate ion is largely but not completely dissociated.

c. Correction for Component Imperfections

Craig G. Smith and Rolf H. Muller

A correction procedure was previously reported[8] that accounts for the optical effects of imperfections in the components of our automatic ellipsometer. These effects are due to strain-induced birefringence, dichroism, or misalignment of azimuth circles. Nineteen imperfection parameters in a linearized model[9] were determined from a series of 24 measurements.

The accuracy of the correction procedure has now been investigated. The effect of optical imperfections is recognized by differences between results obtained for the same specimen in different ellipsometric zones.[10] A perfect correction procedure should remove these

Table 1. Accumulation of supporting electrolyte.

C_{CuSO_4}	$C_{H_2SO_4}$	Re	i	$\Delta C_{H_2SO_4}$	$\Delta C_{H_2SO_4}/\Delta C_{CuSO_4}$
0.176M	3.89M	750	30 mA/cm^2	0.062M	0.35
		6250	65	0.060	0.34
0.193	1.02	1080	40	0.067	0.35
		8600	80	0.071	0.37
0.100	5.83	0	30	0.037	0.37
0.250	5.83	0	60	0.095	0.38

differences. The magnitude of the corrections strongly depends on the values of the measured parameters[9] (relative phase Δ and relative amplitude tan ψ or azimuth angles), as shown in Fig. 2. For this reason, materials with widely different optical properties have been used in this test. Measurements on metallic surfaces were chosen from a large series of experiments conducted over a six-month period after the evaluation of the imperfection parameters. In addition, measurements on oxide surfaces (formed from compressed powders, see Sec. d below) were performed 14 months after the evaluation of the parameters.

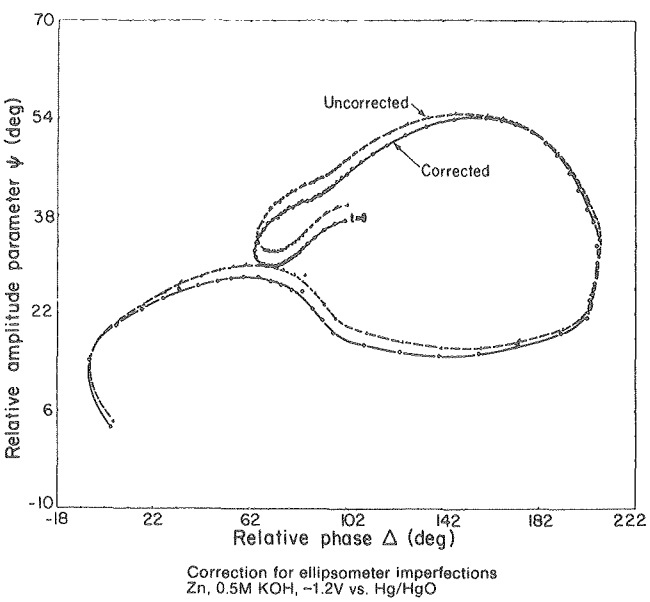

Fig. 2. Effect of component imperfections on the determination of Δ and ψ. Dissolution of Zn (1000 single crystal) at constant potential (-1.2 V vs Hg/HgO) in stagnant 0.5 M KOH. (XBL 7611-9909A)

Table 2 illustrates corrected and uncorrected four-zone measurements for three representative specimens. The corrections to ψ were good for all materials studied, showing remaining differences between zones of only ±0.02 deg where surface anisotropies appear to be small and at most ±0.16 deg for the most highly strained (birefringent) oxide samples. Also, in agreement with theory,[9] the four-zone average of the corrected (ψ) and uncorrected (ψ_0) relative amplitude parameter agree to within experimental error for isotropic surfaces, but disagree for strained surfaces. Differences between corrected four-zone values for the relative phase Δ were at most ±0.25 deg for metal surfaces. The larger differences observed for the compacted oxide samples are indicative of anisotropic properties. The consistency of the corrections over a 14-month period shows that the parameters describing the imperfections remain constant.

d. Optical Constants of Solid Film Materials

Craig G. Smith and Rolf H. Muller

The use of ellipsometry to characterize properties of films often requires a knowledge of the optical constants of film materials. For example, to obtain values for film porosity, the refractive index of the non-porous film material must be known. The optical constants (in general complex numbers) for many materials of electrochemical interest are, however, not available in the literature. We have initiated the use of compressed powders of known composition to independently measure the optical constants of such materials.

A hydraulic press is used to compact materials in the form of powders in a cylindrical stainless steel die. The compacted material replicates the polished surfaces of the end plates. To avoid thermal decomposition of labile compounds, the pressing was done at room temperature. To facilitate removal from the die and subsequent handling of the fragile disks, the powders were pressed inside a brass ring placed on the lower end plate. The use of annealed rings has been

Table 2. Correction of ellipsometer data for component imperfections. Δ_o and ψ_o - values of relative phase and amplitude parameters without correction for imperfections, Δ and ψ - corrected values (degrees).

Material:	Ag, (100) single crystal				Ag_2O				Ag_2O (strained)			
	Δ_o	Δ	ψ_o	ψ	Δ_o	Δ	ψ_o	ψ	Δ_o	Δ	ψ_o	ψ
4-zone results	83.56	82.45	45.75	43.05	11.30	11.95	22.20	22.87	30.48	30.01	17.07	18.56
	82.64	82.37	40.31	43.06	11.38	12.13	23.45	22.83	28.48	27.58	20.05	18.70
	82.40	82.46	42.66	43.05	9.64	9.59	23.65	22.94	33.90	34.01	19.35	18.65
	81.92	82.27	43.49	43.07	10.18	9.83	22.05	22.94	34.30	34.60	17.90	18.65
Average:	82.63	82.39	43.05	43.06	10.62	10.87	22.84	22.89	31.79	31.55	18.59	18.65
	±0.82	±0.10	±2.72	±0.01	±1.74	±1.27	±0.80	±0.05	±2.91	±3.51	±1.49	±0.07

Table 3. Optical constants of solid film materials.

Material	Densities		n-ik		
	specimen	theoretical	present	literature (real part)	ref.
Ag_2O	6.18 g/cm^2	7.14 g/cm^2	2.17-0.28i	2.10†	1
CdO	5.37	8.15	2.50-0.01i	2.49	2
PbO_2	7.58	9.38	2.09-0.32i	2.23	2

†Calculated from literature values for atomic polarizabilities of Ag and O .

1. J.A. Dean, Ed., Lange's Handbook of Chemistry (Mc-Graw-Hill, New York 1973), pp. 10-259.

2. P.E. Liley, Y.S. Touloukian, and W.R. Gambell, Chemical Engineers' Handbook (McGraw-Hill, New York, 4th Ed. 1969) J.H. Perry, Ed., Sec. 3, p. 3-4.

found to minimize the relaxation of elastic deformation which causes strain-induced anisotropies in the samples. Other variables that affect the mechanical properties of the specimens were found to include pressure and the particle size and shape of the powder.

Optical constants determined for three materials by this method are shown in Table 3. Corrections for porosity effects have been based on the difference between the measured density of the compacted specimens and the theoretical density of the same material.

Ellipsometer measurements conducted so far have been performed in air. Subsequent measurements will be made in ultrahigh vacuum to ensure a clean surface. Work is in progress on other materials relating to anodic films.

1. R. H. Muller and C. G. Smith, Surface Sci. 56, 440 (1976).
2. C. G. Smith, Effect of Mass-Transport Boundary Layers on the Ellipsometry of Surfaces, (M.S. thesis), LBL-3903, December 1975.
3. C. G. Smith and R. H. Muller, MMRD Annual Report for 1976, LBL-6016, p. 209.
4. F. R. McLarnon, R. H. Muller and C. W. Tobias, Electrochim. Acta 21, 101 (1976).
5. C. G. Smith and R. H. Muller, 1976 Annual Report, LBL-6016, p. 209.
6. R. H. Muller and C. G. Smith, LBL-7302, in preparation.
7. L. Hseuh and J. Newman, Ind. Eng. Chem. Fund. 10, 615 (1971). J. R. Selman and J. Newman, J. Electrochem. Soc. 118, 1070 (1971).

8. C. G. Smith, J. S. Remer and R. H. Muller, MMRD Annual Report for 1976, LBL-6016, p. 210.
9. C. G. Smith, J. S. Remer and R. H. Muller, LBL-7303, in preparation.
10. R. H. Muller, in Advances in Electrochemistry and Electrochemical Engineering, Vol. 9 (Wiley, New York, 1973) Eds., P. Delahay and C. W. Tobias, pp. 167-226.

2. LASER INTERFEROMETRY OF MASS-TRANSFER BOUNDARY LAYERS

Karrie Hanson, Rolf H. Muller and Charles W. Tobias

Many electrochemical processes are hindered by mass-transfer limitations that require the use of current densities that are lower than desirable for economical operation. It has been shown that local turbulence caused by small obstacles placed near the electrode surface can substantially enhance the average mass transfer to an electrode[1-4] with a minimum increase in pressure drop. The objective of this work is to define optimum size, shape and spacing of flow obstacles by use of laser interferometry to observe local mass-transfer boundary layers below limiting current.

Initial experiments have been concerned with boundary layer decay over an insulator in a flow channel. The results showed that large insulator lengths are required to significantly thin the mass-transfer boundary layer.

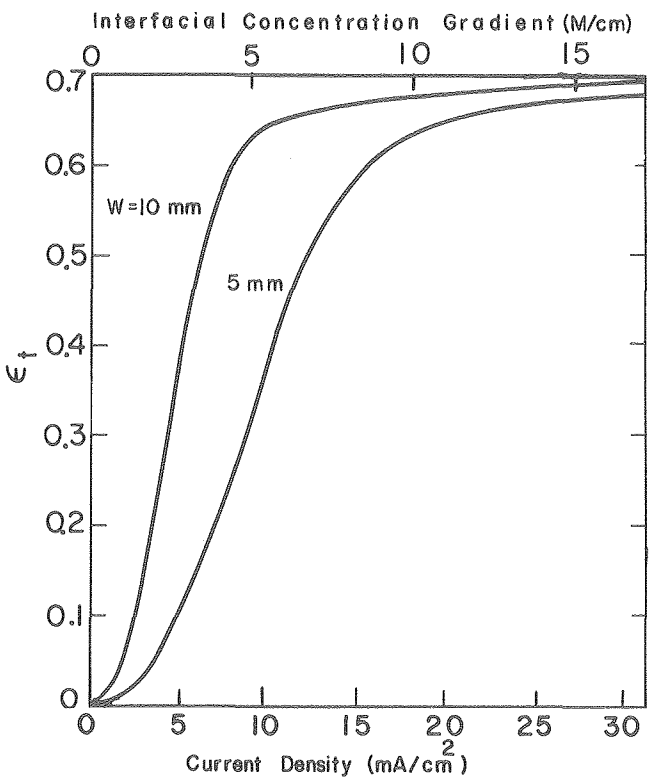

Fig. 1. Relative error in boundary layer thickness due to light-deflection for the new 5-mm wide flow channel compared to the previously used 10-mm channel. At 5 mA/cm^2 the error is reduced to 1/6 of its previous value. (XBL 741-2169B)

To determine the effect of flow obstacles on the mass-transfer boundary layer, a flow channel was designed and constructed. The design was based on a study of optical errors conducted earlier in this laboratory. The cell geometry with a 5-mm channel width was chosen to reduce optical errors encountered in the earlier used 10-mm wide cell (Fig. 1). A similar reduction of electrode separation from 25 to 5 mm has caused a reduction in equivalent flow channel diameter and has reduced the entry length to a third of that of the original channel. The resulting cell is more compact and can therefore by operated more easily and aligned more precisely.

New techniques for the construction of obstacles have been developed, and a specially designed dual-beam, single-mode 5 mW laser has been received for installation in the interferometer. It will provide a more uniform beam and allow greater photographic flexibility.

---

1. F. R. McLarnon (Ph.D. thesis), LBL-3500, December 1974.
2. F. Leitz and L. Marincic, J. Appl. Electrochem. 7, 473 (1977).
3. A. Storck and F. Coeuret, Electrochim. Acta 22, 1155 (1977).
4. F. R. McLarnon, R. H. Muller and C. W. Tobias, J. Electrochem. 122, 1636 (1975).

3. RESEARCH PLANS FOR CALENDAR YEAR 1978

Rolf H. Muller

The use of ellipsometry for the study of metal dissolution processes at high current densities, as encountered in electrochemical machining, will be initiated. Such systems require the simultaneous consideration of several layers in the solid and liquid phase. Alternate experimental methods will be investigated to determine the possible formation of colloidal layers near film-covered electrode surfaces.

The optical constants of a wide range of potential film materials will be determined more reliably by the use of less porous compressed powders in ultrahigh vacuum. The production of controlled surface roughness by powder compaction will be investigated as a new approach to the ellipsometry and modeling of rough surfaces.

The capabilities of the automatic ellipsometer will be extended: A 200 mW argon ion laser light source will provide sufficient reflected intensity for the study of rough surfaces. Facilities for scanning the visible spectrum will be installed for the determination of the spectra of surface layers. The construction of new power supplies for the Faraday cells, which will double the dynamic range of the ellipsometer, presently 55°C for

polarizer and analyzer azimuths, will be completed in order to be able to follow larger surface changes without mechanical adjustments.

The acceleration of ionic mass transport by turbulence induced near an electrode surface will be investigated by interferometry. The effect of different shapes and spacings of flow obstacles will be determined.

4. 1977 PUBLICATIONS AND REPORTS

Rolf H. Muller and Associates

Journals

1. R. H. Muller, Recent Advances in Some Optical Experimental Methods, Electrochim. Acta 22, 951 (1977).

Papers Presented

1. R. H. Muller, Seeing is Believing, Light as a Probe for the Chemist and the Chemical Engineer, Dept. of Chem. Engr. U. C.-Davis, May 23, 1977.

2. J. B. Riggs, R. H. Muller and C. W. Tobias, Modeling of the Electrochemical Machining Process, 150th Meeting of the Electrochemical Society, Philadelphia, May 8-13, 1977, Extended Abstract No. 305.

3. F. R. McLarnon, R. H. Muller and C. W. Tobias, Interferometric Study of Combined Forced and Natural Convection, 150th Meeting of the Electrochemical Society, Philadelphia, May 8-13, 1977, Extended Abstract No. 304.

4. J. B. Riggs, R. H. Muller and C. W. Tobias, Computer Simulation of Electromachining, 28th Meeting of the International Society of Electrochemistry, Druzhba, Bulgaria, September 18-23, 1977.

LBL Reports

1. J. B. Riggs, Modeling of the Electrochemical Machining Process (Ph.D. thesis), LBL-6019, January 1977.

2. F. R. McLarnon, R. H. Muller and C. W. Tobias, Interferometric Study of Forced Convection Mass Transfer Boundary Layers in Laminar Flow, LBL-5797, August 1977.

See also publications in Energy Technology Section, Development of Electrochemical Synthesis and Energy Conversion, J. W. Evans, R. H. Muller, J. Newman C. W. Tobias, Principal Investigators, p. 505 .

e. Solid State and Surface Reaction Studies. Surface Science and Heterogeneous Catalysis

Gabor A. Somorjai, Principal Investigator

1. SURFACE STRUCTURE AND CHEMISORPTION BY LOW-ENERGY ELECTRON DIFFRACTION

a. LEED Intensity Data and Structure Analysis of the (5×14) Reconstructed Pt(100) Surface

Larry L. Kesmodel and Gabor A. Somorjai

It has been known for about 10 years that the (100) surfaces of the 5d metals Ir, Pt, and Au exhibit a reconstruction from the bulk periodicity. It has been suggested that the reconstruction produces a hexagonal close-packed monolayer of surface atoms on top of the underlying square layers. However, there has been no definitive structure analysis to support this model. We have obtained LEED intensity data on several fractional and integral order diffraction beams on the (5×14) reconstructed Pt(100) surface at room temperature. A dynamical intensity analysis of the hexagonal overlayer model of this reconstruction has been initiated. The present results indicate that the top layer of atoms is buckled about 0.8 Å from a perfect planar configuration: this result agrees with elementary considerations of the lattice mismatch and incompressibility of metal-metal bonds. However, the detailed agreement with experiment is not yet sufficiently close to allow a conclusive structure determination.

b. The Surface Structure and Bonding of C_2H_2 and C_2H_4 on the Pt(111) Surface: New Analysis of High-Order Diffraction Beams to Discriminate Between Bonding Models and Surface Species

Larry L. Kesmodel and Gabor A. Somorjai

The adsorption of acetylene (C_2H_2) on the Pt(111) surface at T = 300 K results in a "metastable" state (I) which transforms (irreversibly) upon heating to 350 K to a stable state (II). Both states exhibit (2×2) LEED patterns but are distinguished by their different intensity-voltage profiles. Ethylene (C_2H_4) is found to adsorb at 300 K in a state exhibiting I-V profiles identical to those of (II).

LEED, photoemission spectroscopy and, most recently, high-resolution electron energy loss spectroscopy[1] (HRELS) have been applied to the study of this transformation. The metastable state (I) is generally agreed to be C_2H_2 bonded with the C-C axis parallel to the surface. However, the nature of the stable state (II) derived from either C_2H_2 or C_2H_4 is in question. Ibach et al. have proposed on the basis of HRELS data that $CHCH_3$ is formed.[1]

We have found that analysis of high-order LEED beams is necessary to discriminate on a structural basis between a model for (II) which involves the C-C axis parallel to the surface as opposed to more nearly perpendicular. The analysis of this very recent data is still preliminary but supports the structure shown in Fig. 1 involving a $C\text{-}CH_3$ species rather than $CH{=}CH_3$. Although the hydrogen atom

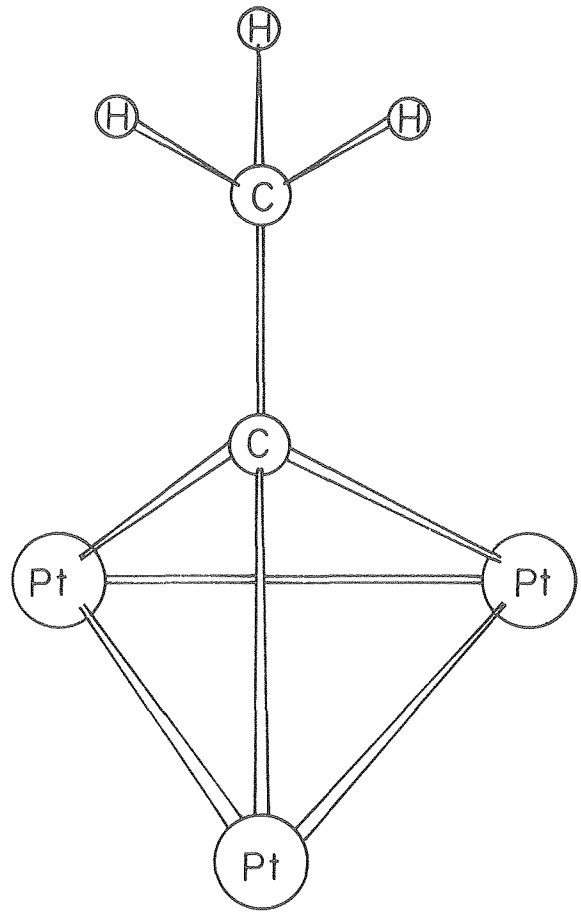

Fig. 1. Proposed structure for $C\text{-}CH_3$ group formed from ethylene or acetylene chemisorption on Pt(111). (XBL 7712-6591)

positions are not readily located with LEED, the $C\text{-}CH_3$ model is to be preferred since no appreciable tilt of the C-C axis is indicated, and a close H-Pt distance of 1.8 Å would favor the $CHCH_3$ model. Importantly, the $C\text{-}CH_3$ model is closely analogous to bonding found in organometallic complexes such as $Co_3(CO)_9CCH_3$. The observed vibrational frequencies for such complexes offer a new interpretation of the HRELS spectra which favors the $C\text{-}CH_3$ model.

1. H. Ibach and S. Lewald, to be published.

c. LEED and Thermal Desorption Studies of Small Molecules (H_2, O_2, CO, CO_2, NO, C_2H_4, C_2H_2, and C) Chemisorbed on the Rhodium (111) and (100) Surfaces

David G. Castner, Brett A. Sexton, and Gabor A. Somorjai

The chemisorption of H_2, O_2, CO, CO_2, NO, C_2H_4, C_2H_2, and C has been studied on the clean Rh(111)

and (100) surfaces. LEED, AES, and thermal desorption were used to determine the surface structures, disordering and desorption temperatures, and displacement and decomposition characteristics for each species. All of the molecules studied readily chemisorbed on both surfaces. A large variety of ordered structures was observed, especially on the (111) surface. The disordering temperatures of most ordered surface structures on the (111) surface were below 100°C. It was necessary to adsorb the gases at 25°C or below in order to obtain well-ordered surface structures. Chemisorbed oxygen was readily removed from the surface by H_2 or CO gas at crystal temperatures above 50°C. CO_2 appeared to dissociate to CO upon adsorption on both rhodium surfaces, as indicated by the identical ordering and desorption characteristics of these two molecules. C_2H_4 and C_2H_2 also had very similar ordering and desorption characteristics, and it is likely that the adsorbed species formed by both molecules is the same. Decomposition of ethylene produced a sequence of ordered carbon surface structures on the (111) face as a result of a bulk-surface carbon equilibrium. The chemisorption properties of rhodium appear to be generally similar to those of iridium, nickel, and palladium.

d. Low-Energy Electron Diffraction, Auger Electron Spectroscopy, and Thermal Desorption Studies of Chemisorbed Carbon Monoxide, Oxygen, Hydrogen, Nitrogen, Ethylene, and Benzene on an Iridium (110) Surface. Correlation with Other Ir Crystal Faces

B. E. Nieuwenhuys and G. A. Somorjai

The interaction of CO, O_2, H_2, N_2, C_2H_4, and C_6H_6 with an Ir(110) surface has been studied by using LEED, Auger electron spectroscopy (AES), and flash desorption mass spectrometry. Adsorption of oxygen at 30°C produces a (1×2) structure, while a C(2×2) structure is formed at 400°C. Two peaks have been detected in the thermal desorption spectrum of oxygen following adsorption at 30°C. The heat of adsorption of hydrogen is slightly higher on Ir(110) than on Ir(111). Carbon monoxide is molecularly adsorbed on clean Ir(110) at 30°C, yielding a (2×1) structure. The CO desorption spectra exhibit two peaks, one around 230°C and the second at about 160°C. At exposures between 250° and 500°C carbon monoxide is dissociatively adsorbed on the surface, yielding a C(2×2) structure and a desorption peak around 600°C. Carbon monoxide is adsorbed on an Ir(110) surface partly covered with oxygen or carbon in a new binding state with a significantly higher desorption temperature than on the clean surface. Carbon monoxide is more easily dissociated on a carbon-contaminated Ir(110) surface than on clean Ir(110). Adsorption of nitrogen could not be detected on either clean or carbon-covered Ir(110) surfaces. The hydrocarbon molecules do not form ordered surface structures on Ir(110). The thermal desorption spectra obtained after adsorption of C_6H_6 or C_2H_4 are similar to those reported previously for Ir(111), consisting mostly of hydrogen. Heating the (110) surface above 700°C in the presence of C_6H_6 or C_2H_4 results in the formation of an ordered carbonaceous overlayer with (1×1) structure. The results are compared with those obtained previously on the Ir(111) and Ir(755) or stepped [6(111)×(100)] surfaces. The CO adsorption results are discussed in relation to data on similar surfaces of other Group VIII metals.

e. The Adsorption of Benzene on the Pt(111) Surface Studied by Low-Energy Electron Diffraction Intensity Measurements and Quantitative Auger Electron Spectroscopy

Peter C. Stair and Gabor A. Somorjai

Benzene when chemisorbed on the Pt(111) crystal face forms an ordered metastable $\begin{vmatrix} 4 & -2 \\ 0 & 4 \end{vmatrix}$ surface structure that transforms, slowly, to a stable $\begin{vmatrix} 4 & -2 \\ 0 & 5 \end{vmatrix}$ surface structure. A complete set of intensity-voltage (I vs V) curves are presented to aid in solving the surface structures of this complex organic molecule. The size of the unit cells and the larger-than-monolayer carbon surface concentrations (determined by quantitative Auger spectroscopy) indicate that most of the adsorbed benzene molecules are inclined at an angle to the surface. The similarity of the I-V profiles for the same diffraction beams from the two structures indicates that the carbon-platinum layer spacing changes very little during the order-order transformation.

f. LEED Study of the Chemisorption of Metal-Organic Molecules on the Ag(111) Crystal Face

Steven Abensohn and Gabor A. Somorjai

Studies of the chemical bonding and surface reactions of metal-organic compounds with metal and oxide supports is of great importance for the construction of polymerization catalysts. We are investigating the adsorption of metallocenes (metal-organic "sandwich compounds") $M(C_5H_5)_2$) on the Ag(111) and TiO_2(110) surfaces with LEED and Auger electron spectroscopy. Ordered monolayer structures have been observed for ferrocene (M=Fe) on the clean silver surface in the temperature range 100 to 240 K. The molecule desorbs below room temperature, indicating weak bonding to the surface.

Chromocene (M=Cr) and cobaltocene (M=Co) exhibit bulk physical properties nearly identical to ferrocene, but display radically different chemical properties. All three compounds melt in the temperature range 172-174°C. Ferrocene is stable on heating to 470°C in air, while chromocene and cobaltocene spontaneously decompose on exposure to oxygen or water at room temperature.

An oven is being constructed to allow the introduction of chromocene and cobaltocene into the ultrahigh vacuum chamber. A comparison of the surface properties of the three metallocenes should yield information about the bonding and reactivity of these compounds with the surface.

g. Chemisorption of CH_3CN, CH_3NC, C_2H_2, C_2H_4, and CH_3CCCH_3 on Ni(111)

John Hemminger, Earl Muetterties, and Gabor A. Somorjai

A clean metal surface has no precise analog in molecular chemistry. The surface is heterogeneous; it presents many binding sites of different structure and bond strength to the incoming molecule. If one considers a well-ordered crystal face of high atomic density like the (111) face of nickel, which has only one or a few binding sites, the structural complexity of the surface is very much reduced. Such a uniform surface resembles a coordinatively unsaturated zerovalent complex. One may also consider coordinatively unsaturated metal clusters as likely models of these more homogeneous surfaces and view the ligand-metal cluster complex as the analog of the surface-adsorbate system.

We would like to probe the relationship between the chemistry of metal cluster-ligand complexes and of the chemical behavior of surfaces of the same metal. We have chosen the (111) crystal face of nickel for this purpose, since the chemistry of zerovalent nickel coordination complexes and of some nickel clusters has been well established. We have studied CH_3CN, CH_3NC, C_2N_2, C_2H_2, C_2H_4, and CH_3CCCH_3 adsorbed on this surface and compared their structures and chemical behavior as ligands in coordination chemistry.

LEED was used to determine surface structure, Auger electron spectroscopy (AES) to obtain surface composition, and thermal desorption to determine the binding states of the molecular species whenever possible. We have carried out displacement reactions to determine relative bond strengths of the various adsorbates on the Ni(111) surface and to compare this with the ligand field strengths in the nickel zerovalent coordination complexes.

From these studies one finds strong correlations between the relative binding energies of adsorbates on Ni(111) and of ligands in nickel complexes. The surface chemistry of these hydrocarbons points out the necessity of comparing the surface to coordinatively unsaturated metal complexes. In particular the surface analog of an oxidative addition reaction appears to be important in the chemistry of CH_3NC on Ni(111). We also find that nickel, unlike platinum, is capable of breaking the CN bond in cyanides. This may be compared to recent work on the thermal decomposition of $Pt(CN)_2$ and $Ni(CN)_2$.

h. LEED-Auger Studies of the Structure and Growth of Thin Metal Films Vapor-Deposited onto Oxide Single-Crystal Surfaces

Frederick Wagner and Gabor A. Somorjai

The growth of films of palladium and gold on α-Al_2O_3(0001), TiO_2 (rutile) (110), and a stepped rutile surface has been studied by LEED and Auger electron spectroscopy. Although α-alumina is an insulator, its clean surfaces can be studied with electron beams of energies greater than 70 eV. At these higher energies each incident electron ejects one or more secondary electrons from the surface and no beam-deflecting negative space charge builds up. However, isolated metal particles on the surface interfere with secondary electron emission; the minimum useable LEED beam energy increases with the amount of metal deposited. After the deposition of two monolayers of palladium, LEED work below 250 eV becomes impossible due to surface charging. Auger spectra of 8-30 monolayer deposits taken with a 3.1 keV incident beam are shifted upwards in energy by up to 400 eV.

No surface charging problems have been encountered during the study of metal deposition onto TiO_2, a 3 eV band gap semiconductor with states in the gap due to Ti^{3+}. LEED patterns of Au and Pd on TiO_2 and on a $(011)\times(0\bar{1}1)$ stepped surface have been obtained by depositing 8-12 equivalent monolayer films on the substrate at 25-450°C and annealing at 700-900°C. The Auger spectra of annealed Pd films show the formation of a Ti-Pd allow, while gold films show no sign of such alloy formation. Most of the LEED patterns are consistent with closest-packed or compressed closest-packed islands of the deposited metal. Films grown on the (110) surface often show fiber structures of random azimuthal orientation, whereas those grown on the stepped surface exhibit more definite azimuthal orientation.

2. ELECTRON SPECTROSCOPY STUDIES OF SOLID SURFACES AND ADSORBATES

a. Construction of High Resolution Electron Energy Loss Spectrometer

Lawrence Dubois and Gabor A. Somorjai

High resolution electron energy loss spectroscopy (HRELS) is a technique that has recently become available for studies of the vibrational spectra of surface atoms and molecules. In this technique a collimated beam of monochromatic electrons is inelastically scattered from a crystal surface and the energy distribution of the specularly reflected beam recorded. The electrons excite surface vibrational modes (surface phonons, adsorbate and adsorbate-substrate vibrations) and will therefore lose energy corresponding to the strength of the vibration involved.

Both theory and experiment have shown that this inelastic scattering process occurs via long-range dipole interactions between the incident electrons and the adsorbed gas molecules. Since only those vibrations that give rise to changing dipole moments prependicular to the surface can be excited, HRELS and infrared spectroscopy provide identical information. However, HRELS has an inherently higher surface sensitivity (<1% of a monolayer) and covers a much larger energy range (0.05-1 eV or 400 to 8000 cm^{-1}). Furthermore, HRELS is the only technique that provides information about how hydrogen is bound to surfaces.

Our spectrometer has recently been completed. Our first detailed experiments will deal with the adsorption of oxygen and CO on Ni(111). This

should provide an excellent test of the theory, since extensive low-energy electron diffraction experiments have been carried out on this system. We will then continue with a study of hydrocarbons adsorbed on this and other catalytically active surfaces.

b. Surface Characterization of $SrTiO_3$ (111) Single-Crystal Face: An ELS, UPS, AES, and LEED Study

Wei Jen Lo and Gabor A. Somorjai

Low-energy electron diffraction (LEED), Auger electron spectroscopy (AES), electron energy loss spectroscopy (ELS), and ultraviolet photoelectron spectroscopy (UPS) were used to study the structure, composition, and electron state distribution of clean strontium titanate single-crystal (111) faces. LEED showed that the surface had a stable (1×1) pattern after annealing the room-temperature Ar-ion bombarded $SrTiO_3$ (111) surface at 600°C. However, the surface after Ar ion sputtering at 600°C resulted in a complex LEED pattern that is completely different from (1×1) structures. AES showed marked variation in the values of Auger Sr(65 eV)/O(510 eV) ratio which increased from 1.5 to 2.8 in going from the $SrTiO_3$ (111)-(1×1) surface to the room-temperature Ar-bombarded surface. For the Ar-ion bombarded $SrTiO_3$ surface at 600°C, the Auger ratio is 4.1.

Electron energy distribution of the $SrTiO_3$ (111) surface has been studied by ELS and UPS. For the Ar-sputtered $SrTiO_3$ (111) surface at room temperature, ELS showed six transitions with energies at 13.1, 10.3, 7.7, 5.6, 3.1, and 1.6 eV, and UPS showed the appearance of -0.6 eV emission in the band gap region. The appearances of the 1.6 eV transition in ELS and the -0.6 band gap emission in UPS indicate the presence of surface Ti^{3+} species. Subsequent annealing did not remove Ti^{3+} species. It was found that the concentration of surface Ti^{3+} species was a function of crystal temperature; it varies reversibly in accordance with the change of crystal temperature.

An ion bombardment of the $SrTiO_3$ surface at 600°C resulted in a Ti^{3+}-free surface that was reflected from the disappearance of 1.6 eV transition in ELS and -0.6 eV emission in UPS. The combination of LEED, AES, ELS, and UPS results indicates that the chemical composition of the $SrTiO_3$ surface is strongly dependent on the surface treatments and plays an important role in determining the surface structure and electron energy distribution.

The comparison of results obtained between TiO_2 and $SrTiO_3$ has been made and gives a reasonable explanation for the difference in their photochemical reactivities.

c. Electron Spectroscopy Studies of the Chemisorption of O_2, H_2, and H_2O on the TiO_2 (100) Surface with Varied Stoichiometry: Evidence for the Photogeneration of Ti^{3+} and Its Importance in Chemisorption

Wei Jen Lo, Yip Wah Chung, and Gabor A. Somorjai

Deposition of a monolayer of titanium on the TiO_2 (100)-(1×3) single-crystal surface produces an oxygen-deficient surface that has the same chemical composition, electronic structure, and chemical reactivities as the Ar-ion sputtered TiO_2 (100) surface. From correlations with studies of oxidation of Ti(0001) single-crystal surfaces, we provide firm evidence for the existence of Ti^{3+} species on the clean oxygen-deficient TiO_2 surface. The chemisorption of O_2, H_2, and H_2O has been studied by ultraviolet photoemission spectroscopy (UPS), electron energy loss spectroscopy (ELS), Auger electron spectroscopy (AES), low-energy electron diffraction (LEED), and thermal desorption on the stoichiometric and Ti^{3+}-rich TiO_2(100) surface. The presence of Ti^{3+} species causes distinct differences in the nature of chemical bonding between the adsorbed molecule and the substrate surface. From the combination of these studies, we conclude that water is adsorbed associatively on the stoichiometric TiO_2 (100)-(1×3) surface, while it tends to disociate into surface hydroxyl groups on the Ti^{3+}-rich surface. UPS and ELS show that while adsorption of H_2O changes the Ti^{3+} to a different oxidation state, illumination by band gap energy photons can regenerate Ti^{3+} species by the reaction $Ti^{4+} + e^- \rightarrow Ti^{3+}$. An attempt has been made to correlate these results on well-characterized surfaces with studies using reduced TiO_2 as a photoanode in the photo-electrochemical cell.

3. MOLECULAR BEAM-SURFACE INTERACTIONS

a. Molecular Beam Study of the Kinetics and Mechanism of H_2-D_2 Exchange on Flat and Stepped Pt(111) Surfaces

Rebecca J. Gale, Miguel Salmeron, and Gabor A. Somorjai

The modulated molecular beam technique has been used to investigate the kinetics and mechanism of hydrogen-deuterium exchange on the Pt(111) and Pt(S)-[6(111)×(111)] surfaces. The Pt(S)-[6(111)×(111)] surface consists of (111) terraces six atoms wide, on the average, separated by monatomic steps of the (111) orientation. Our study of this reaction as a function of angle of incidence on these two surfaces has shown that the reaction probability is enhanced on the stepped surface relative to the flat Pt(111) by as much as an order of magnitude, depending on the angle of incidence of the reactants. Determining the mechanism of the reaction on these two surfaces should help our understanding of this effect.

The amplitude and phase of the HD product signal was monitored as a function of surface temperature, beam modulation frequency, temperature, and pressure, by using a mixed beam of H_2 and D_2 where $H_2 \gg D_2$.

The beam temperature dependence indicates that the activation energy for adsorption of hydrogen is less than 0.4 kcal/mole. From the angle of incidence dependence we have concluded that although there may be a small activation barrier on the Pt(111) surface, adsorption is not activated on the Pt(S)-[6(111)×(111)] surface.

The mechanism of hydrogen-deuterium exchange is complex and follows similar trends on both surfaces. At high surface temperatures, ~200-1000°C, the reaction proceeds via two parallel processes, one of which dominates above ~500°C. Below ~200°C, the reaction proceeds through a series mechanism with several consecutive and distinguishable steps.

At present, the rate constants and pre-exponentials are being extracted by mathematical modeling the experimental data.

4. STUDIES OF CATALYZED SURFACE REACTIONS

a. The Effects of Oxygen Pretreatment on the Selectivity and Rates for Low-Pressure Hydrocarbon Reactions on Single-Crystal Platinum Catalysts

Jean-Paul Biberian, Carol E. Smith, and Gabor A. Somorjai

Recent studies indicate that oxygen pretreatment of a kinked Pt single-crystal catalyst can enhance the low-pressure dehydrogenation and hydrogenation rates of cyclohexene to benzene and cyclohexane, respectively, and also change the selectivity with respect to these two products. The effect of platinum oxidation on cyclohexane dehydrogenation to benzene and n-heptane dehydrocyclization to benzene has also been investigated on this kinked surface. The hydrocarbon reactions have been carried out under flow conditions in the presence of excess hydrogen at total pressures of 10^{-6} to 10^{-5} Torr using a mass spectrometer to monitor reactants and products. Auger electron spectroscopy was used to determine the surface composition, and the surface structure was checked by LEED. These results have been compared to those on the clean and oxygen pretreated surface of a Pt(111) catalyst. It was found that the presence of low-coordination surface sites is important for the effects of surface oxidation on catalytic behavior.

b. Studies of Hydrocarbon Reactions Catalyzed by Platinum at High Pressures

William Gillespie and Gabor A. Somorjai

The use of single-crystal platinum surfaces in reaction studies has provided us with a wealth of exciting information about the fundamentals of various hydrocarbon-reforming reactions. These experiments have utilized the techniques of Auger electron spectroscopy and low-energy electron diffraction to characterize the crystal surface and mass spectrometry to measure reaction kinetics. The major limitation of these studies has been the necessity of performing reactions at pressures of 10^{-4} Torr or less so that existing surface analysis instruments could be used. These pressures, however, are not representative of those used in industrial processes. We have now overcome this limitation through the construction of a new type of instrumentation which allows us to conduct reaction experiments at pressures as high as 100 atmospheres, as well as allowing surface analysis under ultrahigh vacuum conditions. Thus we will be able to establish the link between the results at low pressure and the results one obtains at pressures comparable to those used by industry.

The apparatus consists of an ultrahigh vacuum chamber within which, is a hydraulically operated cell capable of enclosing the platinum crystal in a small volume and isolating it from the rest of the main vacuum chamber. If the cell is in the closed position, reaction studies can be performed by circulating the reactants over the crystal and measuring the formation of products by gas chromatography. With the cell in the open position we are able to characterize the crystal surface by the usual techniques of low-energy electron diffraction and Auger electron spectroscopy. In this way we are able to correlate reactivity and selectivity, under industry-like conditions, with the crystal surface structure and composition before and after reaction.

Our preliminary results indicate that these high-pressure studies will indeed provide us with new information about the intimate details of these hydrocarbon reactions. For example, one reaction of interest is the dehydrocyclization of n-heptane to yield toluene. Although details are still sketchy we have observed that the physical and chemical state of the crystal surface can have a large effect on this reaction. In fact, on the proper platinum surface it is possible to cause this reaction to selectively produce benzene rather than toluene, while on other surfaces the expected product, toluene, is formed very selectively over benzene. Hopefully, by defining the parameters that cause such large changes in selectivity we will be able to control the reaction paths.

c. Heats of Chemisorption of O_2, H_2, CO, CO_2, and N_2 on Polycrystalline and Single-Crystal Transition Metal Surfaces

Isamu Toyoshima and Gabor A. Somorjai

Recent heats of chemisorption of O_2, H_2, CO, CO_2, and N_2 obtained for transition metals are tabulated and summarized. Adsorption studies on single-crystal surfaces show the presence of several binding states on each crystal face. These states have widely different heats of adsorption with the magnitude of ΔH_{ads} varying by more than twofold. Because of this large variation it is not possible to assign a certain heat of adsorption value to a given metal-adsorbate system, although average values may be quoted from the adsorption data obtained for polycrystalline surfaces. The nature and the number of binding states vary from crystal face to crystal face, indicating that the chemical bonding is complex and localized. Trends in the variation of ΔH_{ads} along the periodic table are noted. Correlations of ΔH_{ads} with the binding energies of metal compounds are also indicated from the tabulated data.

5. RESEARCH PLANS FOR CALENDAR YEAR 1978

Gabor A. Somorjai

We shall study the effects of surface additives on the catalytic activities of metals. The effects of oxygen addition to platinum, potasium, and manganese to iron and rhodium will be studied.

The surface crystallography of substituted acetylenes and CO on rhodium and platinum surfaces will be investigated by low-energy electron diffraction and high-resolution electron loss spectroscopy.

The structure and composition of binary alloy clusters (Ag-Pd, Au-Pd) deposited from the vapor on oxide (Al_2O_3, TiO_2) and metal (W, Ta) crystal surfaces will be studied.

The reactivity of platinum monolayers deposited on inert single-crystal substrates will be compared with the reactivity of platinum crystal surfaces.

The photon-assisted reactions of H_2O and CO_2 on $SrTiO_3$ surfaces will be explored.

The pressure dependence of catalyzed hydrocarbon reactions over a range of 10^{-6} - 10^{3} Torr will be explored using platinum surfaces.

6. 1977 PUBLICATIONS AND REPORTS

Gabor A. Somorjai and Associates

Journals and Books

1. G. A. Somorjai, Active Sites in Heterogeneous Catalysis, Adv. Cat. 26, 1 (1977), LBL-4558.

2. L. Chung, W. Siekhaus, and G. A. Somorjai, Studies of Acetylene and Oxygen Adsorption on Silicon Surfaces by Low-Energy Electron Loss Spectroscopy, Surf. Sci. 58, 341 (1976), LBL-4541.

3. P. C. Stair and G. A. Somorjai, The Adsorption of Acetylene on the (111) Crystal Face of Platinum; Detection of Two Chemically Different Adsorption States by Low-Energy Electron Diffraction, Chem. Phys. Lett. 41, 391 (1976), LBL-4975.

4. D. W. Blakely, E. Kozak, B. A. Sexton, and G. A. Somorjai, New Instrumentation and Techniques to Monitor Chemical Surface Reactions on Single Crystals Over a Wide Pressure Range (10^{-8} - 10^{5} Torr) in the Same Apparatus, J. Vac. Sci. Technol. 13, 1162 (1976), LBL-4926.

5. Ch. Steinbruchel and G. A. Somorjai, Limitations of Kinetic Studies of Catalytic Reactions on a Single Crystal Surface at Low Pressures in an Ultrahigh Vacuum System, J. Vac. Sci. Technol. 13, 1162 (1976), LBL-4988.

6. G. A. Somorjai, Atomic and Molecular Processes at Solid Surfaces, Adv. Colloid and Interface Sci. 58, 150 (1977), LBL-5142.

7. B. E. Nieuwenhuys and G. A. Somorjai, Dehydrogenation of Cyclohexane and Dehydrocyclization of n-Heptane Over Single Crystal Surfaces of Iridium, J. Cat. 46, 259 (1977), LBL-5147.

8. J. C. Buchholz and G. A. Somorjai, The Surface Structures of Phthalocyanine Monolayers and Vapor-Grown Films: A LEED Study, J. Chem. Phys. 66, 573 (1977), LBL-4997.

9. Y. W. Chung, W. Siekhaus, and G. A. Somorjai, Electron Energy Loss Spectroscopy Study of the Adsorption of Aluminum on the Silicon (111)-(7×7) Surface, Phys. Rev. B 15, 959 (1976), LBL-4993.

10. R. Mason and G. A. Somorjai, The Reactions of Carbon Monoxide at Coordinatively Unsaturated Sites on a Platinum Surface, Chem. Phys. Lett. 44, 468 (1976).

11. L. E. Firment and G. A. Somorjai, Surface Structures of Normal Paraffins and Cyclohexane Monolayers and Thin Crystals Grown on the (111) Crystal Face of Platinum. A LEED Study, J. Chem. Phys. 66, 2901 (1977), LBL-5443.

12. L. L. Kesmodel, R. C. Baetzold, and G. A. Somorjai, The Surface Structure and Bonding of (2×2) Acetylene Overlayers on Platinum (111): LEED Intensity Analysis, Surf. Sci. 66, 299 (1977), LBL-5407 Rev.

13. S. H. Overbury and G. A. Somorjai, The Surface Composition of Au-Sn Alloys Determined by Auger Electron Spectroscopy, J. Chem. Phys. 66, 3181 (1977), LBL-5430.

14. B. A. Sexton and G. A. Somorjai, The Hydrogenation of CO and CO_2 Over Polycrystalline Rhodium: Correlation of Surface Composition, Kinetics and Product Distributions, J. Cat. 46, 167 (1977), LBL-5178.

15. P. C. Stair and G. A. Somorjai, The Adsorption of Hydrocarbons on Platinum Studied by Low-Energy Electron Diffraction Intensities. The Ordered (2×2) Overlayers of Acetylene and Ethylene on the (111) Crystal Face of Platinum, J. Chem. Phys. 66, 2036 (1977), LBL-5421.

16. G. A. Somorjai, The Surface Chemical Bond, Angew. Chemie 16, 92 (1977), LBL-5451.

17. G. A. Somorjai, Surface Characterization of Ceramic Materials, in Ceramic Microstructures 1976, edited by R. M. Fulrath and J. A. Pask (Westview Press, Boulder, Colorado, 1977), LBL-5475.

18. Y. W. Chung, W. J. Lo, and G. A. Somorjai, LEED and Electron Spectroscopy Studies of the Clean (110) and (100) Titanium Dioxide (Rutile) Crystal Surfaces, Surf. Sci. 64, 588 (1977), LBL-5704.

19. D. W. Blakely and G. A. Somorjai, The Stability and Structure of High Miller Index Platinum Surfaces, Surf. Sci. 65, 419 (1977), LBL-5707.

20. Y. J. Lo, Y. W. Chung, P. C. Stair, L. L. Kesmodel, and G. A. Somorjai, Ultraviolet Photoemission Studies of Acetylene and Ethylene Adsorption on the Pt(111) Surface: Correlations with LEED Studies, Solid State Commun. 22, 335 (1977), LBL-5766.

21. A. Jablonski, S. H. Overbury, and G. A. Somorjai, The Surface Composition of the Gold Palladium Binary Alloy System, Surf. Sci. 65, 578 (1977), LBL-5747.

22. L. L. Kesmodel, P. C. Stair, and G. A. Somorjai, On the Relaxation of the Pt(111) Surface: Results of Dynamical LEED Calculations, Surf. Sci. Lett. 64, 342 (1977), LBL-5768.

23. G. A. Somorjai, Correlations Between the Structure and Reactivity at Solid-Gas and Solid-Liquid Interfaces, J. Electrochem. Soc. 124, 205C (1977), LBL-6045.

24. S. T. Ceyer and G. A. Somorjai, Surface Scattering, Am. Rev. Phys. Chem. 28, (1977), LBL-6230.

25. R. J. Gale, M. Salmeron, and G. A. Somorjai, Variation of Surface Reaction Probability with Reactant Angle of Incidence. A Molecular Beam Study of the Asymmetry of Stepped Platinum Crystal Surfaces for H-H Bond Breaking, Phys. Rev. Lett. 38, 1027 (1977), LBL-6060.

26. G. A. Somorjai, Chemische Binding an Oberflachen, Angew. Chemie 89, 94 (1977), LBL-6260.

27. G. A. Somorjai, Report of the Surface Science Workshop, ERDA, 1977.

Invited Talks

1. G. A. Somorjai, High Resolution Analytic Microscopy, at the High Resolution Electron Microscopy Workshop, Berkeley, California, October 11, 1976.

2. G. A. Somorjai, Surface Crystallography by Low-Energy Electron Diffraction, at the Electrochemical Society Meeting, Las Vegas, Nevada, October 18, 1976.

3. G. A. Somorjai, The Science of Heterogeneous Catalysis, at the University of Illinois, Champaign-Urbana, Illinois, October 27, 1976.

4. G. A. Somorjai, New Techniques for Studies of the Structure and Composition of Solid Surfaces, at the Golden Gate Welding and Metals Conference, San Francisco, California, January 1, 1977.

5. G. A. Somorjai, Recent Achievements and Trends in Catalysis Science, at the National Science Foundation, Washington, D. C., February 3, 1977.

6. G. A. Somorjai, Catalysis by Transition Metals--Pt, Fe, and Rh, at the University of California, Santa Barbara, California, February 10, 1977.

7. G. A. Somorjai, Low-Energy Electron Diffraction, at the Americal Crystallographic Association meeting, Asilomar, California, February 22, 1977.

8. G. A. Somorjai, Active Sites for Heterogeneous Catalysis, University of California, Irvine, California, February 28, 1977.

9. G. A. Somorjai, Surface Crystallography, at the University of British Columbia, Vancouver, B.C., Canada, April 22, 1977.

10. G. A. Somorjai, Catalysis on the Atomic Scale, at the North American Catalysis Society meeting, Pittsburgh, Pa., April 24, 1977.

11. G. A. Somorjai, Active Sites in Heterogeneous Catalysis, at the Shell Development Corporation, Houston, Texas, July 13, 1977.

12. G. A. Somorjai, Structure of Oxide Surfaces, at the Gordon Conference on Solid State Studies in Ceramics, New Hampshire, August 1, 1977.

13. G. A. Somorjai, Structures of Surfaces and Adsorbates by LEED, at the International Conference on Physics of Transition Metals, Toronto, Canada, August 16, 1977.

14. G. A. Somorjai, Energy Conversion and Storage by Heterogeneous Catalysis, at the IUPAC Meeting, Tokyo, Japan, August 26, 1977.

15. G. A. Somorjai, Active Sites for Hydrocarbon Catalysis on Metal Surfaces, at the Japanese Catalysis Society Symposium, Tokyo, Japan, August 30, 1977.

LBL Reports

1. D. Castner, B. A. Sexton, and G. A. Somorjai, LEED and Thermal Desorption Studies of Small Molecules (H_2, O_2, CO, CO_2, NO, C_2H_4, C_2H_2, and C) Chemisorbed on Rhodium (111) and (100) Surfaces, LBL-6299, June 1977.

2. L. L. Kesmodel and G. A. Somorjai, Surface Crystallography by Low-Energy Electron Diffraction, LBL-6299, June 1966.

3. M. Salmeron, R. J. Gale, and G. A. Somorjai, Molecular Beam Study of the H_2-D_2 Exchange Reaction on Stepped Platinum Crystal Surfaces: Dependence on Reactant Angle of Incidence, LBL-6247, June 1977.

4. Y. W. Chung, W. J. Lo, and G. A. Somorjai, Electron Spectroscopy Studies of Light Induced Chemisorption of Oxygen, Hydrogen and Water on the TiO_2(100) Surfaces: Evidence for Photogeneration of Ti^{3+} Species and Its Importantance for Chemisorption, LBL-6257, June 1977.

5. B. E. Nieuwenhuys and G. A. Somorjai, Low-Energy Electron Diffraction, Auger Electron Spectroscopy and Thermal Desorption Studies of Chemisorbed Carbon Monoxide, Oxygen, Hydrogen, Nitrogen, Ethylene and Benzene on an Ir(100) Surface. Correlation with Other Iridium Crystal Faces, LBL-6271, June 1977.

6. P. C. Stair and G. A. Somorjai, The Adsorption of Benzene on the Pt(111) Surface Studied by Low-Energy Electron Diffraction Intensity Measurements and Quantitative Auger Electron Spectroscopy, LBL-6286, June 1977.

7. E. L. Muetterties, J. C. Hemminger, and G. A. Somorjai, A Coordination Chemistry Guide to Structural Studies of Chemisorbed Molecules, LBL-6259, June 1977.

8. Y. W. Chung, W. J. Lo, J. C. Hemminger, and G. A. Somorjai, The Photoassisted Decomposition of Gas Phase Water Adsorbed on $SrTiO_3$, LBL-6627, August 1977.

9. D. W. Dwyer, and G. A. Somorjai, Hydrogenation of CO and CO_2 Over Iron Foils. Correlations of Rate, Product Distribution and Surface Composition, LBL-6658, August 1977.

f. Nuclear Magnetic Resonance*

Alexander Pines,† Principal Investigator

1. MULTIPLE QUANTUM SPECTROSCOPY

D. E. Wemmer, J. Tang, S. Sinton, and A. Pines

Consider a molecule containing N coupled spin -1/2 nuclei. The energy level diagram is shown in Fig. 1. The magnetic quantum number M ranges from N/2 to -N/2. In conventional NMR spectroscopy

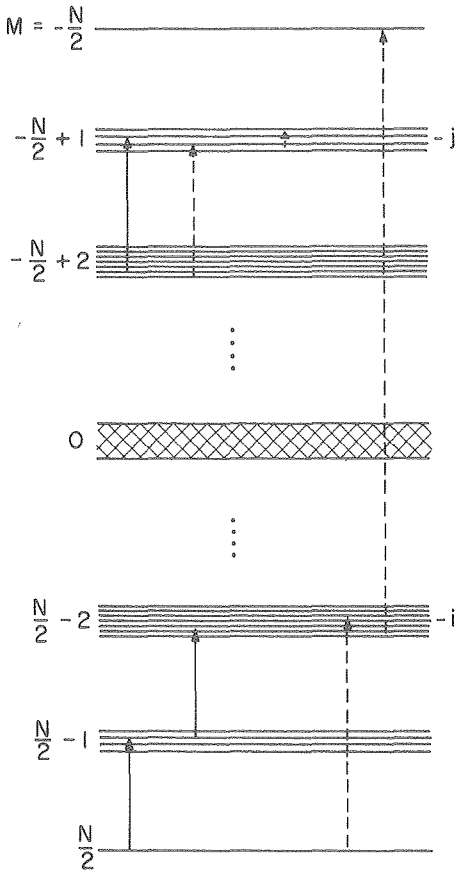

Fig. 1. Energy level diagram of a system of N coupled spin -1/2 nuclei in a large magnetic field. M is the magnetic quantum number. Some typical allowed single quantum transitions are shown as solid arrows, and more typical forbidden ones (n-quantum where n = 0, 1, ...,N) are shown as dashed arrows. There are considerably fewer high order (large n) multiple-quantum transitions. (XBL 7710-10019)

(and other forms of spectroscopy as well) the transitions that are excited and observed are allowed single quantum transitions (ΔM=1). Some illustrative transitions of this are indicated as solid arrows. We have developed further our double quantum experiments, and using a technique we call Fourier Transform Multiple Quantum NMR, we can now excite coherent superpositions of states involving forbidden transitions, e.g., the multiple quantum transitions and other forbidden ones indicated as dashed arrows in Fig. 1. This allows us to obtain n-quantum spectra for n=0,1, ...,

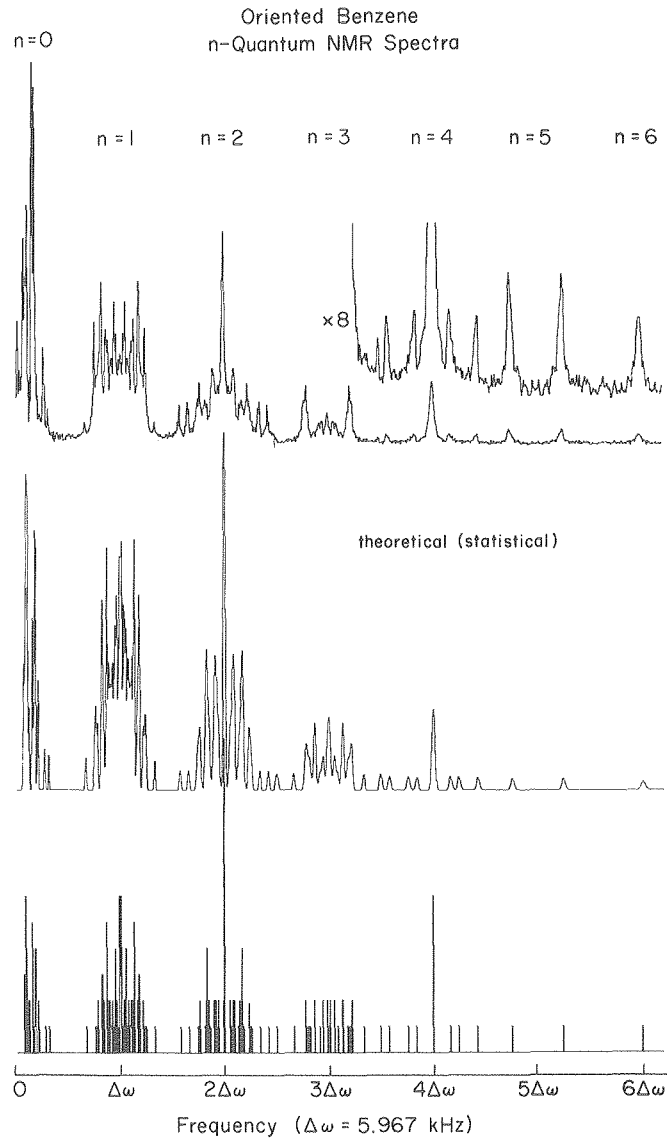

Fig. 2. n-quantum NMR spectra (n = 0, 1,...6) of oriented benzene obtained by Fourier Transform Multiple Quantum NMR. The top is an experimental run. The lower is the theoretical spectrum calculated assuming statistical behavior. The middle trace is the theoretical one broadened by nδω for each n-quantum line where δω is the spectrometer resolution. (XBL 781-6770)

N (clearly the N spins cannot absorb more than N quanta). An example is shown in Fig. 2 performed on the 6-spin proton system of benzene oriented in a liquid crystalline matrix. The n-quantum spectra agree well with those calculated from a statistical model. Significant aspects of this n-quantum spectroscopy include firstly, the possibility of analyzing the high order spectra (high n) when the low ones are too complex. This would alleviate the need for isotopic labeling for molecules with more than 6-8 protons which has been necessary to date. Secondly, correlations of motion could be studied by observing the relaxation of the n-quantum lines. Thirdly, the distribution

over n of the n-quantum coherence is of great theoretical interest.

---

*Supported in part by the National Science Foundation.

†Alfred P. Sloan Foundation Fellow and Camille and Henry Dreyfus Teacher-Scholar.

2. MULTIPLE QUANTUM ECHOES AND SELECTIVE DETECTION

D. E. Wemmer and A. Pines

One of the problems of analyzing proton NMR spectra of oriented systems (i.e., anything other than isotropic fluids, e.g., polymers, surface adsorbed molecules, liquid crystals, membranes, solids ....) for structural and dynamical purposes is the limitation of resolution by magnetic field inhomogeneity. In multiple quantum spectroscopy this is particularly severe since, if the resolution of a normal single quantum line is $\delta\omega$ the corresponding resolution of the n-quantum lines is $n\delta\omega$. We have been able to overcome this problem by Fourier analyzing the time response of spin echoes. This yields extremely high resolution (< 1 Hz) even in the presence of broad magnetic field profiles. An example is shown in Fig. 1. The top is the normal spectrum showing the limited resolution in our magnetic field. The center shows the Fourier transform spin echo spectrum displaying well resolved dipolar splittings and agreeing with the theoretical spectrum for this molecule.

In the presence of the spin echo train the n-quantum spectra are all folded over into the same frequency region (i.e., they will not be separated from each other). It is then necessary to selectively detect the n-quantum spectra. This can be done as follows: assume we make a phase shift of ϕ in the excitation frequency; the

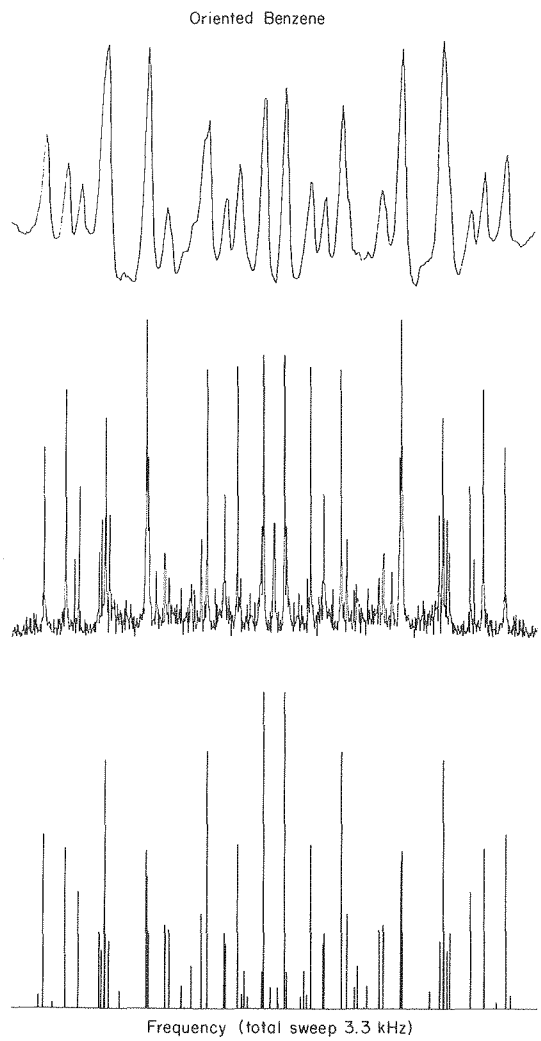

Fig. 1. Illustration of increase of resolution in oriented sample NMR spectrum by Fourier transformation of spin echo train. Top trace is normal Fourier transform spectrum with resolution limited by magnetic instability and non-uniformity. Middle trace is result of Fourier transform spin echo experiment and lower trace is theoretical spectrum. (XBL 781-6769)

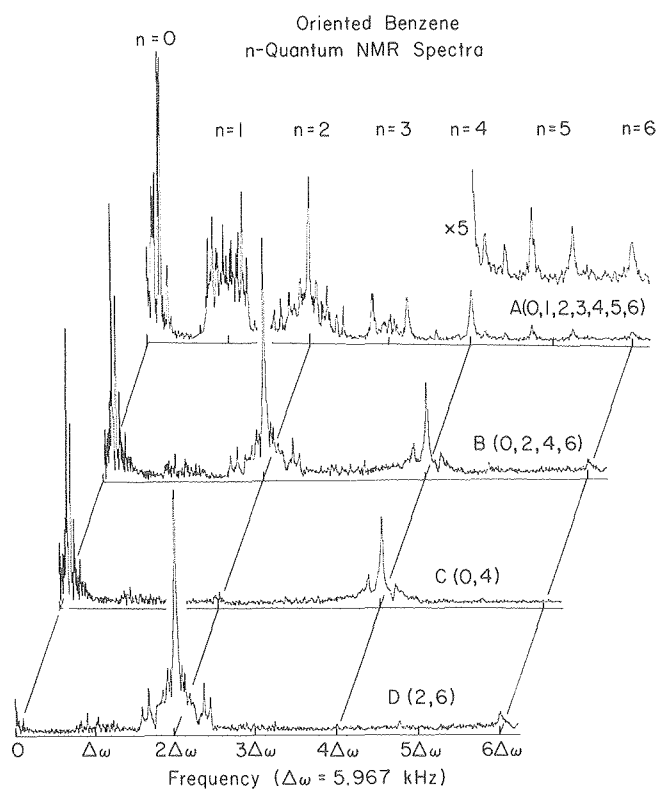

Fig. 2. Demonstration of n-quantum selectivity in Fourier Transform Multiple Quantum NMR. This uses the fact that a phase shift in the excitation of ϕ is "seen" as $n\phi$ by an n-quantum transition. Using this, pulse sequences can be produced to selectively detect different combinations of n-quantum spectra. Sequences A, B, C, D were designed to select the n's indicated in parentheses. (XBL 782-7143)

n-quantum transitions "see" this as $n\phi$. Thus, labeling the n-quantum signal as $I^{(n)}$ we have (taking $I^{(n)}$ $(\phi=0) \equiv I_0^{(n)}$):

$$I^{(n)} = I_0^{(n)} e^{in\phi}$$

and Fourier analyzing the multiple quantum response over ϕ we can separate the n's. An example is shown in Fig. 2 where 4 pulse sequences A, B, C, D were used to detect selectively various groups of n in the multiple quantum spectroscopy of oriented benzene. Thus, the selectivity works quite well and we are now applying this high resolution form of multiple quantum NMR.

3. DISTRIBUTION OF MULTIPLE QUANTUM COHERENCE

S. Mukamel, J. Murdoch and A. Pines

In Fourier Transform Multiple Quantum NMR, a spin system in thermal equilibrium is subjected to a pulse of excitation and the multiple quantum populations and coherences build up with time. The question of the distribution of intensity over the populations and multiple quantum coherences is of interest in many areas (statistical mechanics, chemical reactions, multiphoton ionization, ...). We now have a handle with which to monitor this distribution, namely the overall intensity of the n-quantum spectra for various pumping times. We find that even for only 6 coupled spins, for long enough times, the system behaves ergodically subject to symmetry restrictions (which are obeyed exactly). That is, within each irreducible representation of the molecular symmetry group for long enough times, each n-quantum amplitude and phase is equally probable. This is shown in Fig. 1 which demonstrates that the distribution of coherence depends in a Gaussian fashion on the number of quanta, as expected from a statistical model. The effects of relaxation on this multiple quantum pumping are being studied. Furthermore, attempts to produce non-statistical distributions are under way.

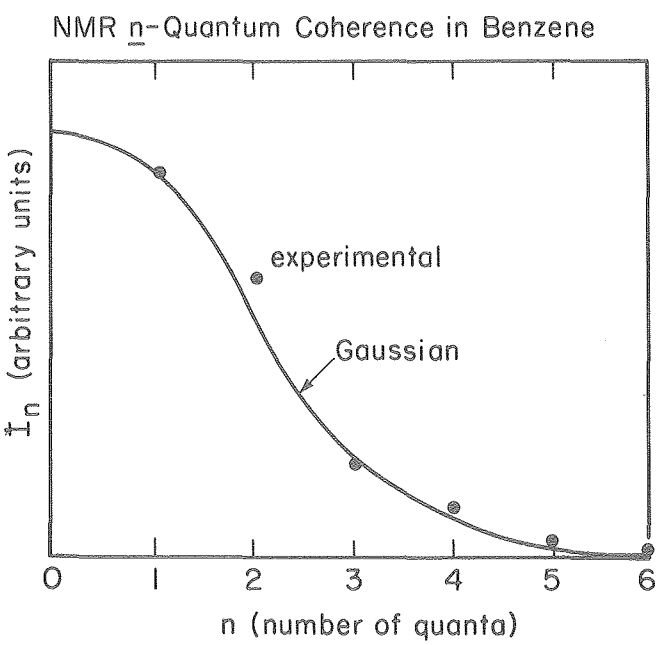

Fig. 1. Statistical behavior of multiple-quantum pumping. The circles were obtained by integrating over ensemble averaged n-quantum spectra. They compare well with a Gaussian model indicating that the system behaves statistically under the constraints of symmetry. Relaxation should strongly affect the behavior. (XBL 781-6894)

4. NMR ANALYSIS OF WHOLE AND PROCESSED COALS*

D. Wemmer, T. Tufano and A. Pines

Together with The Central Research Division of Mobil Oil Company and with EPRI and DOE support,

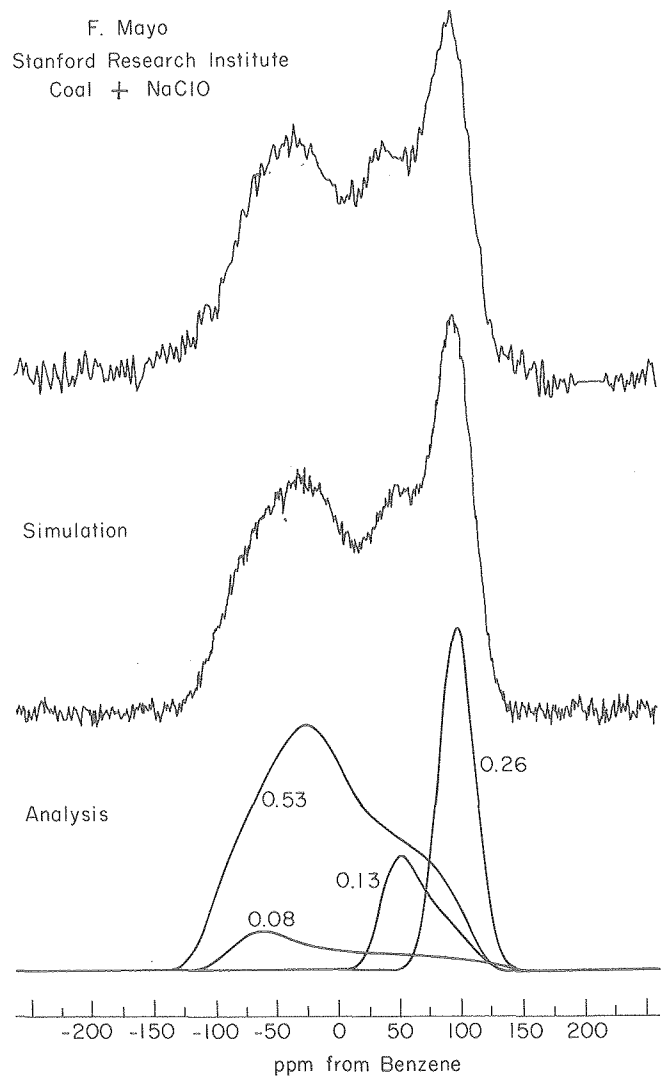

Fig. 1. Analysis of coal and coal processing intermediates by ^{13}C NMR. The top experimental spectrum is decomposed into four functional carbon types (simple aliphatic, oxygen-bonded aliphatic, simple aromatic, condensed aromatic) in the lower trace producing (with some artifically added noise) the computer simulated center spectrum. (XBL 773-8219)

we are characterizing materials used in fuel technology, in particular coal and oil shale. Using solid state NMR techniques we can distinguish four types of carbon functional groups: condensed aromatic, simple aromatic, oxygen bonded aliphatic, and simple aliphatic. This has been used to characterize coals by rank and to understand the changes that occur during processing of the coals. No large scale aromatic condensation is found in coals other than anthracite. The aromatic aliphatic is found to be sensitive to contact time in liquification and an extensive table of characteristic data has been produced. Previously, spectroscopic analysis of whole coal samples in the solid state has been essentially impossible.

Figure 1 shows an example of the analysis of a processed coal by ^{13}C double resonance NMR into the four major constituents. The lineshapes for these constituents are stored in computer and are obtained by analysis of hundreds of model samples with known magnetic shielding and structure. The agreement between the experimental line and the simulated one (noise added artificially for comparison) give us some confidence in this method of analysis. Techniques are now being worked out to analyze deuterium so that the evolution of the chemistry during coal processing can be followed.

*Supported in part by DOE Coal Research Program.

5. SYNTHESIS OF ISOTOPICALLY LABELED LIQUID CRYSTALS

H. Zimmermann, S. Wolfe and A. Pines

By labeling liquid crystal molecules with stable isotopes it is possible to enhance particular NMR signals, remove unwanted couplings by isotopic dilution, and assign otherwise unresolved resonances. Labeling with ^{13}C and deuterium has been accomplished with a variety of techniques and molecules.

Saturated aliphatic hydrocarbon chains have been labeled with controlled percentages of deuterium for use as components of lyotropic phases and as intermediates in the synthesis of chain deuterated thermotropic liquid crystals. Random deuteration to a desired percentage has been achieved by catalytic exchange of alkanoic acids with platinum oxide in a appropriate mixture of D_2O and H_2O. As an example, for studies of aliphatic chain conformation we have synthesized the ^{2}D and ^{13}C labeled liquid crystal shown in Fig. 1.

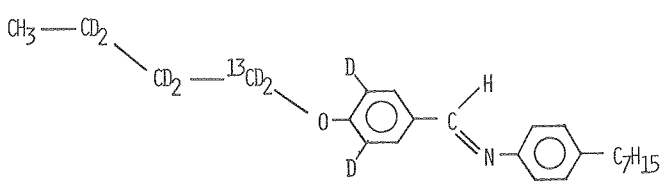

Fig. 1. Example of specifically isotopically labeled liquid crystal molecule. (XBL 782-7149)

6. LOW TEMPERATURE LIQUID CRYSTAL AND PHASE TRANSITIONS

G. Drobny, H. Edzes, and A. Pines

Liquid crystals are composed of long rod-like molecules. They exist in a number of orientationally ordered phases, of which some of the common high temperature forms are shown in Fig. 1. The study of these materials is important since they serve as displays, models for phase transitions and biological membranes, orienting environments for stereochemistry, etc.

The behavior of the smectic-A and smectic-C liquid crystal phases is quite well characterized. On the other hand, the smectic-B phases are not completely understood. For example, the smectic B_C phase is thought to be similar to smectic-C, the molecules tilted with respect to the two-dimensional liquid-like layers as in Fig. 1. It is important to know whether they should behave as smectic-C when rotated in a magnetic field. With the molecules attaining the lowest magnetic energy by coming as close to the field orientation as possible while maintaining the tilt. Furthermore, the question of orientational order about the long molecular axes is still open. We have studied these phases by deuterium NMR of selectively labeled molecules. Figure 2 gives an example of the spectra of 50.7 in the smectic-B_C phase as the sample (after orienting by cooling slowly from the nematic)

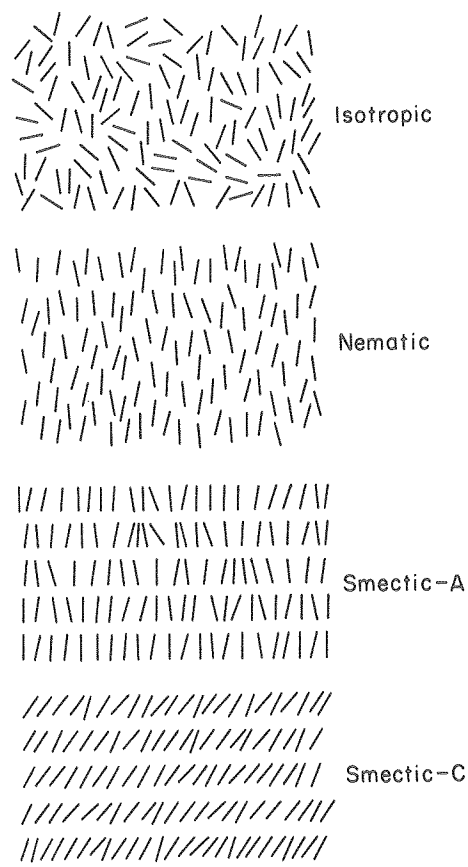

Fig. 1. Some high temperature liquid crystal phases. The smectic B phases sometimes appear at lower temperatures. (XBL 748-7063)

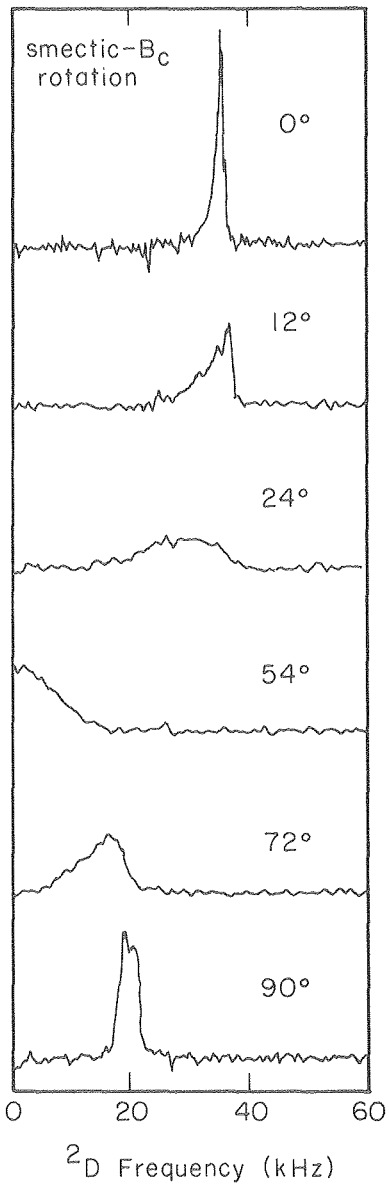

Fig. 2. Behavior of deuterium NMR spectra of methine-d_1 labeled 50.7 in the smectic-B_C phase as the sample is rotated about an axis perpendicular to the magnetic field. The behavior is quite different from smectic-C in which the molecules achieve minimal magnetic energy while maintaining their tilt with respect to the layers. (XBL 782-7142)

is rotated in the magnetic field. The behavior is quite different from smectic-C. From these spectra we find that reorientation of the tilt is not free as in smectic-C. There also is some evidence of biaxial molecular order. A variety of compounds and phases are being studied in this way.

7. CONFORMATION OF ALIPHATIC CHAINS IN LIQUID CRYSTALS

S. Hsi, D. Weitekamp, Z. Luz, and A. Pines

An important question in liquid crystal physics and chemistry is the relationship of molecular structure and conformation to the liquid crystal phase properties. It has been noted, for example, that the aliphatic end chains play a significant role in determining the occurrence and nature of the various nematic and smectic phases. This hydrocarbon chain region of the molecule poses a particularly difficult problem because of the overlapping of resonances and the many possible configurations which the chain can take by rotational isomerization about the carbon-carbon single bonds (Fig. 1). We have studied the conformational structure of the aliphatic end chains in a series of Schiff's base liquid crystals which display a rich variety of mesomorphic phases. For example, p-heptyloxybenzylidene-p-heptylaniline (70.7) has isotropic, smectic-A, smectic-C, smectic-B_A and smectic B_C phases. We assume that the main conformational defect of the chain is a "kink" shown in Fig. 2. Based on a simple model we have made the first quantitative measurement of kink density in a liquid crystal chain using deuterium NMR. The results for the seven-carbon alkoxy chain (specifically labeled) in 70.7 are shown in Fig. 3 for the different phases. The kink probability increases in progressing along the chain from the aromatic core, and is higher in the less

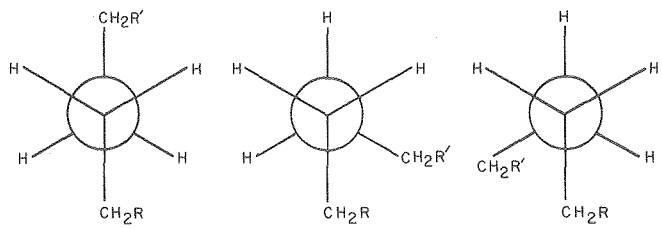

Fig. 1. Projection diagram of possible rotamers at a carbon-carbon single bond in a chain. (XBL 771-7397)

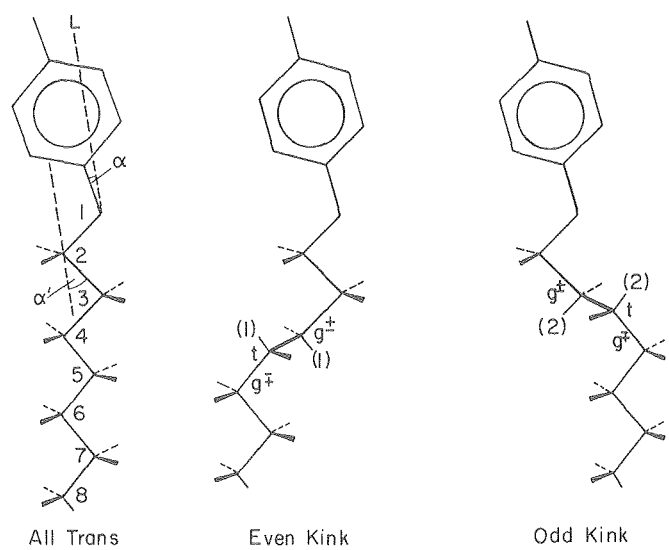

Fig. 2. Conformation diagrams for the all trans, even kink and odd kink of a seven-carbon alkoxy chain. (XBL 778-5951)

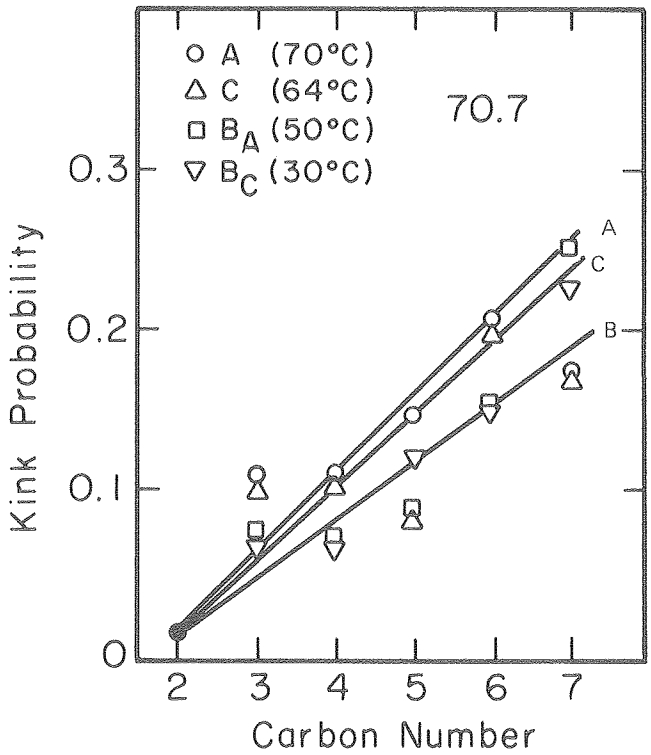

Fig. 3. Calculated kink probabilities in 70.7 for selected temperatures (one for each mesophase) from deuterium NMR. (XBL 782-7141)

structural phases. Applications to systems of biological interest and development of methods to study the dynamics of the kink motion are under way.

8. FERROELECTRIC PHASE TRANSITION IN SQUARIC ACID

D. Wemmer, B. Lamotte, and A. Pines

Squaric acid ($C_4H_2O_4$) is a very interesting material with a two-dimensional hydrogen bonded network shown in Fig. 1. It displays a ferroelectric phase transition in which the hydrogens move in some fashion in the hydrogen bonds. We have observed the phase transition using ^{13}C NMR in powders, supplementing the crystal work of Mehring et al. An important question is whether the transition from the ferroelectric to the paraelectric phase involves a progressively more rapid exchange of protons between molecules or if there exist ferroelectric clusters which exchange very rapidly with paraelectric regions. Our preliminary solid state NMR data support the latter model, and dynamical lineshape studies are under way to precisely characterize the phase transition.

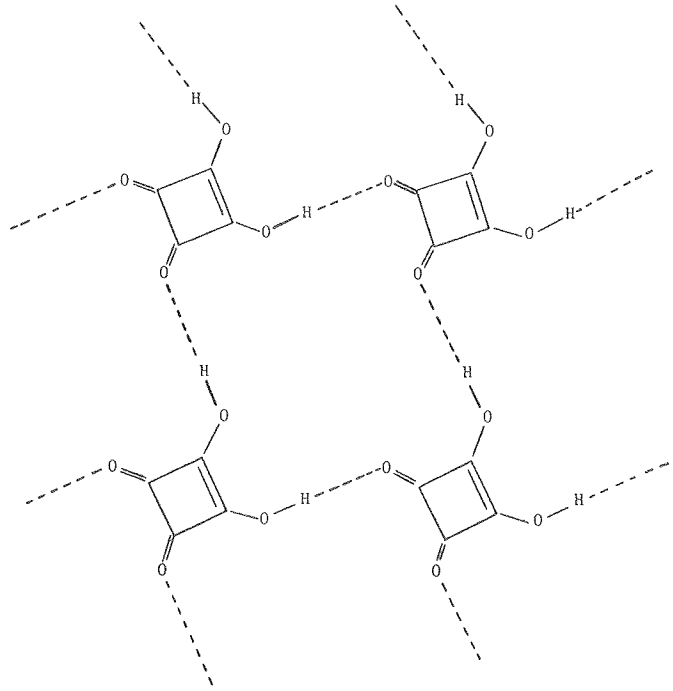

Fig. 1. One plane of squaric acid crystal structure showing two-dimensional eight-vertex hydrogen bond structure. (XBL 782-7152)

9. ENHANCEMENT OF THE MAGNETIC ISOTOPE EFFECT

L. Sterna and A. Pines

Nuclear spin is considered to be a very weak degree of freedom which is unlikely to have any effect on chemical processes. Consider, however, the cyclic photochemical reaction shown in Fig. 1, which is the basis for the CKO theory of CIDNP. A compound is irradiated with UV light to form a triplet radical pair. Triplet-singlet (T-S) intersystem crossing allows the radicals to recombine and undergo photochemical excitation again. If T-S crossing is slow, the radicals will diffuse away from each other and undergo secondary chemical reactions producing other species.

Clearly, there should be a differentiation between ^{13}C and ^{12}C containing radicals in these kinetics due to the hyperfine coupling. We, as well as the Russians, have previously reported the observation of such effects (nuclear magnetic isotope effect) but they were weak. We have now been able to enhance the effect by severely limiting the radical diffusion rate in high viscosity fluids and glasses, thus enabling the physical separation of samples displaying substantial enrichment of ^{13}C by mass and nuclear magnetic resonance spectroscopy.

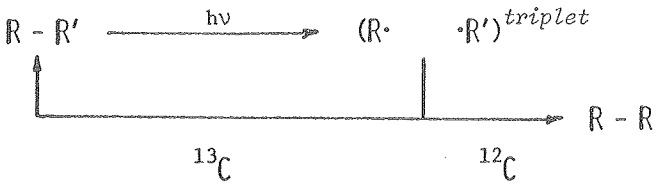

Fig. 1. Photochemical cycle for differentiation between ^{12}C and ^{13}C through the magnetic isotope effect. (XBL 782-7150)

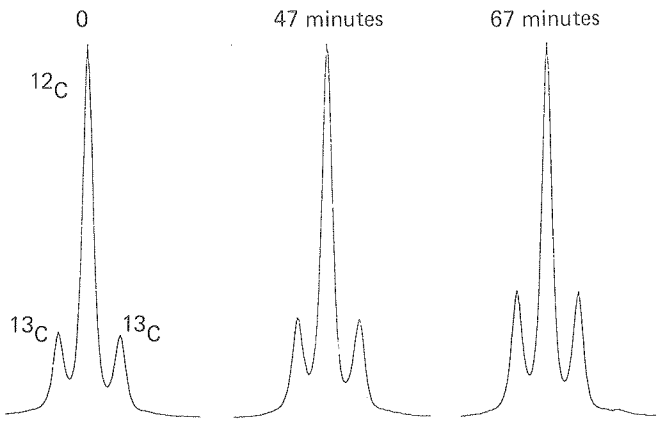

Fig. 2. Proton NMR spectra showing ^{12}C and ^{13}C containing molecules from samples at various intervals of photolysis. (XBL 782-7151)

Table 1.

Viscosity (centipoise)	0.7	7.0	70.0
% ^{13}C enrichment[a]	~ 8	22	36

[a]At 99.2% photolysis conversion.

Figure 2 shows a typical example of the progressive enrichment of ^{13}C in the photolysis of dibenzyl ketone (^{13}CO) at high viscosity. Table 1 summarizes the enhancement effect of viscosity on the isotopic enrichment process. These data explain why the effect has been so weak and erratic under normal viscosity conditions at room temperature. The effect will be studied further in glasses and crystals at low temperatures as well as in the presence of magnetic fields.

10. RESEARCH PLANS FOR CALENDAR YEAR 1978

Alexander Pines

1. Develop selective techniques for n-quantum excitation and detection. Combine this with multiple quantum echoes to produce high resolution multiple quantum spectra. Study the statistics of n-quantum coherence distribution in the presence of relaxation. Develop theory and experiments relating multiple quantum relaxation to correlated microscopic motion.

2. Apply multiple quantum spectroscopy to study the conformation of oriented molecules, in particular liquid crystals. Correlate the molecular conformational properties with the structural and primary characteristic of the liquid crystal phases. If successful, this approach will eliminate the need for extensive and expensive isotopic labeling syntheses.

3. Perform radical pair photochemistry in low temperature glasses and crystals to see the asymptotic limit of the nuclear magnetic isotope effect. Examine the effect of magnetic fields and paramagnetic impurities on the $^{13}C/^{12}C$ isotope enrichment. Extend experiments on other pairs of isotopes

4. Begin experiments on the coupling of nuclear spin to quantized lattice modes. Produce nuclear spin polarization by rotational excitation of low temperature quantum mechanical tunneling methyl group and transfer to protons by spin-rotor interaction.

11. 1977 PUBLICATIONS AND REPORTS

Alexander Pines and Associates

Books and Journals

1. S. Vega and A. Pines, Theory of Double-Quantum Coherence and High Resolution Deuterium NMR in Solids, in Magnetic Resonance and Related Phenomena, K. Hausser Ed., Heidelberg (1977), p. 305.*

2. S. Vega and A. Pines, Operator Formalism for Double Quantum NMR, J. Chem. Phys. 66, 5624 (1977).

3. A. Pines, D. Wemmer, J. Tang and S. Sinton, The 5- and 6-Quantum NMR Spectra of Oriented Benzene, presented at the 1978 APS Meeting, San Francisco, Bull. Am. Phys. Soc. 23, 21 (1978).

4. A. Pines, S. Vega, D. J. Ruben, T. W. Shattuck and D. Wemmer, Double Quantum NMR in Solids, in Magnetic Resonance in Condensed Matter, University of Ljubljana Press, R. Blinc Ed., (1977), p. 127-179.*

Presentations and Invited Lectures*

1. A. Pines, Coherent Multiple Quantum NMR, Annual Meeting of the Western Spectroscopy Association, Asilomar, California, January, 1977, invited talk.

2. A. Pines, Solid State Physics Seminar, University of California, Berkeley, February 1977.

3. D. Wemmer, S. Vega, S. Hsi and H. Zimmermann, Dipole-Dipole Coupling in Fourier Transform Double Quantum NMR, 18th Experimental NMR Conference, April 1977, invited talk.

4. A. Pines, Nuclear Magnetic Resonance with Lots of Photons, Plenary Lecture for the Award Symposium of the American Chemical Society, St. Louis, Missouri, April 1977, invited talk.

5. A. Pines, Chemistry Department, Iowa State University, April 1977, Seminar.

6. J. L. Ackerman and A. Pines, High Resolution Deuterium NMR in Solids, VI International Symposium on Magnetic Resonance, Banff, May 1977, LBL-6081 Abstract.

7. L. Sterna, S. Bustamente, S. Vega and A. Pines, Nuclear Magnetic Isotope Effect, VI International Symposium on Magnetic Resonance, Banff, May 1977, LBL-6082 Abstract.

8. D. Wemmer, S. Vega and A. Pines, Fourier Transform Double-Quantum NMR in Powders, VI International Symposium on Magnetic Resonance, Banff, May 1977, LBL-5783 Abstract.

9. A. Pines, Double Quantum NMR in Solids: Theory and Experiment, University of Waterloo NMR Summer School, Waterloo, Canada, June 1977, invited lectures.

10. S. Vega, Double Quantum Spectroscopy and Deuterium NMR in Solids, Gordon Research Conference, New Hampshire, June 1977, invited talk.

11. A. Pines, Isotope Division, Weizmann Institute of Science, Rehovot, Israel, July, 1977, three lectures on "Photon Dressing Picture of Multiple Quantum Processes."

12. A. Pines, Physics Department, University of Dortmund, West Germany, August 1977, three lectures on "Photon Dressing Picture of Multiple Quantum Processes."

13. A. Pines, Physics Department, Free University of Berlin, Germany, September 1977, Seminar.

14. D. Wemmer and A. Pines, Developments in Fourier Transform Multiple Quantum NMR, 3rd Conference on Molecular Structural Methods in Biological Research, Stanford University, November 1977, invited talk.

LBL Reports

1. A. Pines, S. Vega and M. Mehring, NMR Double Quantum Spin Decoupling in Solids, submitted to Phys. Rev. B, LBL-6984.

2. A. Höhener, Carbon-13 Shielding Tensors in p-Alkoxybenzenes, submitted Chem. Phys. Lett. , LBL-6970.

3. A. Höhener, H. Zimmermann and A. Pines, Comparison of Absolute Order Parameters in Liquid Crystals, Determined with Magnetic Resonance Methods, submitted to Chem. Phys., LBL-6969.

4. D. Suwelack, M. Mehring and A. Pines, Quantitative Aspects of Deuteron (Spin 1) Spin-Decoupling in Solids, submitted to Chem. Phys., LBL-7373.*

5. S. Hsi, H. Zimmermann and Z. Luz, Deuterium Magnetic Resonance of Some Polymorphic Liquid Crystals: The Conformation of the Aliphatic End Chains, submitted to J. Chem. Phys., LBL-6976.

6. A. Pines, Fourier Transform Multiple Quantum NMR, NMR Symposium of the Faraday Division, Queen Elizabeth College, London, December, 1978, LBL-6597 Abstract.*

---

*Also supported in part by Basic Energy 4737.

II.

Chemical Sciences

A. FUNDAMENTAL INTERACTIONS

1. RADIATION SCIENCES

a. Photochemistry of Materials in the Stratosphere

Harold S. Johnston, Principal Investigator

Experimental Studies

1. THE PHOTOCHEMISTRY OF NO_3 AND THE KINETICS OF THE N_2O_5-O_3 SYSTEM*

Richard A. Graham and H. S. Johnston

The kinetics of the nitrogen pentoxide catalyzed decomposition of ozone were studied in the dark and with photolytic light absorbed by the NO_3 radical.[1] Ultraviolet, visible, or infrared absorption cross sections were measured for N_2O_5, HNO_3, NO_2, and NO_3 in this study. The equilibrium constant for $N_2O_5 \rightleftharpoons NO_2 + NO_3$ was found to be: (molecules cm^{-3}, 298-329 K)

$$K = (8.4 \pm 1.8) \times 10^{26} \exp[-11180 \pm 100)/T]$$

The rate constants for several reactions were measured: (cm^3 $molecule^{-1}$ sec^{-1})

$$2\ NO_3 \rightarrow 2\ NO_2 + O_2 \qquad g = (8.5 \pm 2.8) \times 10^{-13} \exp[-(2450 \pm 100)/T]$$

$$O + N_2O_5 \rightarrow \text{products} \qquad m \leq 2 \times 10^{-14}$$

$$O + NO_3 \rightarrow O_2 + NO_2 \qquad n = (1.0 \pm 0.4) \times 10^{-11}$$

By combining the equilibrium constant K with literature values[2,3] of Ke and Kf, rate constants for reactions e and f were evaluated:

$$NO_2 + NO_3 \rightarrow NO + O_2 + NO_2 \qquad e = (2.5 \pm 0.5) \times 10^{-14} \exp[-(1230 \pm 100)/T]$$

$$NO + NO_3 \rightarrow 2\ NO_2 \qquad f = (1.9 \pm 0.4) \times 10^{-11} \text{ at } 297\text{ K}$$

At one atmosphere total pressure, the photolysis of NO_3 occurs with a primary quantum yield less than one in the red region of the spectrum. Under tropospheric conditions with an overhead sun, the solar photolysis constants at 298 K for the two paths of dissociation are consistent with the following values:

$$NO_3 + h\nu \rightarrow NO + O_2 \qquad j_1 = 0.040 \pm 0.02\ sec^{-1}$$

$$NO_3 + h\nu \rightarrow NO_2 + O \qquad j_2 = 0.099 \pm 0.02\ sec^{-1}$$

The average quantum yield for process two was approximately 0.77 for light with wavelengths between 470 and 610 Nm, and that for process one was about 0.23 between 470 and 610 Nm, but only 0.07 in the strong absorption region between 610 and 670 Nm. The photolysis constants may be larger at lower total pressures.

Errors made in previous studies in this laboratory[4,5] are corrected: an infrared absorption ascribed to NO_3 is due to N_2O_5; previously reported visible cross sections for NO_3 were found to be about a factor of four too low and are corrected here.

The photochemistry of NO_3 is potentially important in the balance of ozone in the troposphere and lower stratosphere. If the photolysis products are nitric oxide and oxygen, the net effect is catalytic destruction of ozone:

$$\begin{array}{ll} & NO_3 + h\nu \rightarrow NO + O_2 \\ & NO + O_3 \rightarrow NO_2 + O_2 \\ & NO_2 + O_3 \rightarrow NO_3 + O_2 \\ \hline \text{net:} & 2\ O_3 + h\nu \rightarrow 3\ O_2 \end{array}$$

If the photolysis products are nitrogen dioxide and atomic oxygen, there is no net chemical reaction:

$$\begin{array}{ll} & NO_3 + h\nu \rightarrow NO_2 + O \\ & O + O_2 + M \rightarrow O_3 + M \\ & NO_2 + O_3 \rightarrow NO_3 + O_2 \\ \hline \text{net:} & \text{null reaction} \end{array}$$

The primary goal of this study was to obtain the primary quantum yields for the photolysis of NO_3.

The interactions of the higher oxides of nitrogen and ozone provide a classic case wherein complex laboratory reactions are explainable in terms of sets of elementary reactions.[1,2] The complex reactions are: I. the thermal decomposition of nitrogen pentoxide; II. the reaction of nitrogen pentoxide and nitric oxide; III. the formation of nitrogen pentoxide from nitrogen dioxide and ozone; IV. the nitrogen pentoxode catalyzed decomposition of ozone.

$$\text{I.} \quad 2\ N_2O_5 \rightarrow 4\ NO_2 + O_2$$

$$\text{II.} \quad N_2O_5 + NO \rightarrow 3\ NO_2$$

$$\text{III.} \quad 2\ NO_2 + O_3 \rightarrow N_2O_5 + O_2$$

$$\text{IV.} \quad 2\ O_3 + N_2O_5 \rightarrow 3\ O_2 + N_2O_5$$

These four complex reactions are explained quantitatively by six elementary chemical reactions (A, B, e, f, g, h; see below) involving the nitrate free radical, NO_3.

As a part of the study, it was necessary to determine the optical absorption spectra of several oxides and oxyacids of nitrogen and the rate constants of several elementary reactions. Conventional spectroscopic methods were used to obtain absorption cross sections for various oxides and oxyacids of nitrogen. To obtain absolute cross sections for the NO_3 absorption spectrum, simultaneous molecular modulation measurements were made for NO_3 and N_2O_5 since the formation of one was primarily caused by the disappearance of the other in the system used. Four other photochemical and chemical kinetic studies were made: 1) The rate constant for the reaction between nitrogen dioxide and ozone.[6] 2) The steady-state concentration of the NO_3 radical in the presence of N_2O_5 and O_3. 3) The rate constant for the N_2O_5 catalyzed decomposition of ozone, with and without photolytic illumination of NO_3. 4) The amplitude and phase shift of the molecular modulation of NO_3 with either oxygen or nitrogen as buffer gas and irradiation by red, gold, or green fluorescent lamps.

A diagram of the experimental apparatus is presented in Fig. 1. The reaction cell is a cylindrical quartz tube, 15 cm in diam and 178 cm long. Three aluminum coated, 8.6 cm diam mirrors are mounted in the end caps to give multiple reflections: optical paths of 861, 1717, 2573, and 3429 cm can be selected by an external adjustment screw. Calcium fluoride windows transmit radiation from the far-ultraviolet to approximately 9.5 μ in the infrared. The gas cell is enclosed in an insulated box with walls of six-inch-thick urethane boards faced with one-inch-coated fiberglass boards.

The source beam passes through the reaction cell and then to a McPherson Model 2051 1-m grating monochromator with a 150 line/mm grating and order sorting filters for infrared spectroscopy and a 1200 line/mm grating and colored glass filters for visible and ultraviolet work. As the source beam passes through the cell, it is amplitude modulated with the flashing frequency f of the photolysis lamps (four red, gold, or green 30 W General Electric F30T8 fluorescent lamps) at wavelengths where the reaction species absorb radiation. The modulation information is carried at the sideband frequencies 400 ± f and extracted with lock-in amplification techniques. The higher harmonics of the f cps signal are reducted by the lock-in and filters to less than 2% of the fundamental. A PDP 8/E minicomouter with a programmable clock was interfaced to a multiplexer and a Preston X-Mod 723A digital voltmeter with an accuracy of 1 part in 20,000 and a maximum sampling rate of 100 Hz. Spectra were stored on a dual drive Dectape unit. The modulation signals were simulated with a chemical kinetics program by Whitten.[7] This program uses the Gear method for solving coupled differential equations and is run on Lawrence Berkeley Laboratory's CDC 7600 computer.

The experimental data were interpreted in terms of the following 15-step chemical mechanism:

$$\left.\begin{array}{l} N_2O_5 \xrightarrow{A(M)} NO_2 + NO_3 \\ NO_2 + NO_3 \xrightarrow{B(M)} N_2O_5 \end{array}\right\} \quad K = \frac{A(M)}{B(M)} \qquad (1)$$

$$NO_2 + NO_3 \xrightarrow{e} NO + O_2 + NO_2$$

$$NO + NO_3 \xrightarrow{f} NO_2 + NO_2$$

$$NO_3 + NO_3 \xrightarrow{g} NO_2 + NO_2 + O_2$$

$$NO_2 + O_3 \xrightarrow{h} NO_3 + O_2$$

$$NO + O_3 \xrightarrow{i} NO_2 + O_2$$

$$NO_3 + h\nu\ (vis.) \xrightarrow{j_1} NO + O_2$$

$$NO_3 + h\nu\ (vis.) \xrightarrow{j_2} NO_2 + O$$

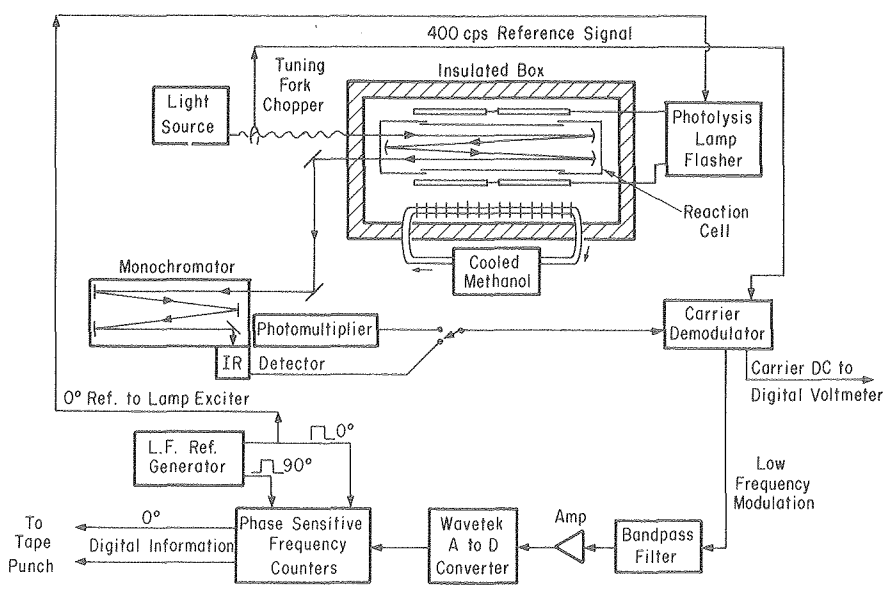

Fig. 1. Schematic diagram of experimental apparatus. (XBL 759-7273)

$$N_2O_5 + O \xrightarrow{m} \text{products}$$

$$NO_3 + O \xrightarrow{n} NO_2 + O_2$$

$$O_3 + h\nu\ (\text{vis}) \xrightarrow{p} O_2 + O$$

$$O_3 + O \xrightarrow{q} O_2 + O_2$$

$$O + O_2 + M \xrightarrow{r} O_3 + M$$

$$NO_3 \text{ on walls} \xrightarrow{w} NO_2 + 1/2\ O_2$$

The full mechanism without light, reactions *A* through *i* plus *w*, involves complex expressions, but they can be solved by a process of successive approximation for $[NO_3]$.[1]

$$[NO_3]_{ss} = \left(\frac{Kh}{2g}\right)^{1/3} [N_2O_5]^{1/3}[O_3]^{1/3}\ \alpha^{1/3} \tag{2}$$

$$-\frac{1}{2}\frac{d[O_3]}{dt} = \frac{1}{2}(Kh)^{2/3}(2g)^{1/3}(\alpha)^{-1/3}[N_2O_5]^{2/3}[O_3]^{2/3} \tag{3}$$

where α is a complex correction factor[1] with values between 0.8 and 1. For the simplified mechanism using the first six elementary reactions, the factor alpha is 1. The equilibrium constant is

$$K = \frac{\left\{-\frac{d[O_3]}{dt}\right\}_{obs} \left\{[NO_3]_{ss}\right\}_{obs}}{\{h\}_{obs} \left\{[O_3]\right\}_{obs} \left\{[N_2O_4]\right\}_{obs}} \tag{4}$$

which depends on five observable quantities and is independent of the complex, correction factor α.

Measurements of the N_2O_5 catalyzed decomposition of ozone were carried out using infrared scanning techniques for monitoring O_3, N_2O_5, and HNO_3. The differential rate of change of ozone was calculated. The rate constant from the central portions of the curves based on Eq. (3) were calculated.

$$\frac{1}{2}(Kh)^{2/3}(2g)^{1/3} = (1.39 \pm 0.19) \times 10^5\ e^{-(9914 \pm 40)/T}\ \text{cm molecules}^{-1/3}\ \text{sec}^{-1}$$

The data from this work are compared to the results of Schumacher and Sprenger[8] on an Arrhenius plot in Fig. 2.

Nitrogen trioxide is a free radical intermediate in the N_2O_5-O_3 system, and its concentration depends on those of O_3 and N_2O_5 and on the rate constants relating the three species. The concentrations of NO_3, O_3, and N_2O_5 were measured under steady-state flow conditions in the UV cell. At three temperatures and over a wide range of concentrations of ozone and nitrogen pentoxide, a total of 136 determinations were made of the steady-state concentration of the NO_3 radical. By means of successive

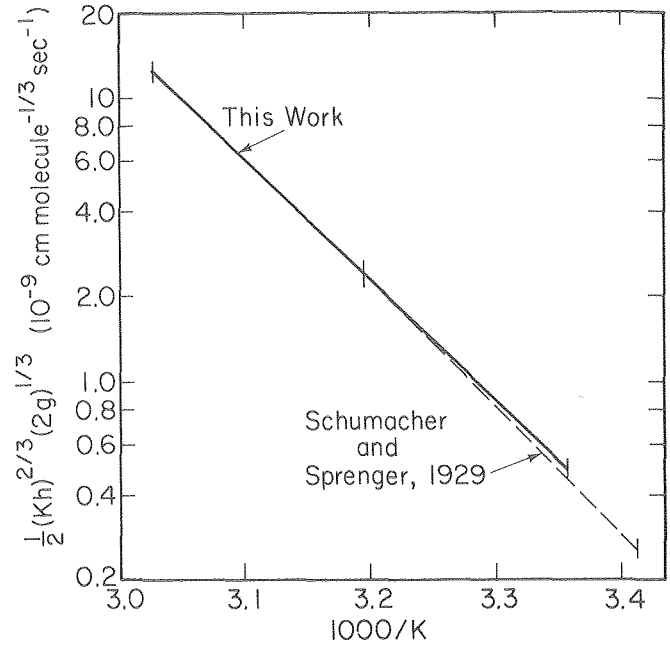

Fig. 2. Arrhenius plot for $\frac{1}{2}(Kh)^{2/3}(2g)^{1/3}$.

(XBL 759-7282)

approximations and the method of least squares, the quantities $(Kh/2g)^{1/3}$ of Eq. (2) were evaluated:

$$(Kh/2g)^{1/3} = (4.04 \pm 0.47) \times 10^8 \exp(-3730 \pm 40)/T \tag{6}$$

molecules$^{1/3}$ cm^{-1}, which is plotted in Fig. 3. Schott and Davidson[9] measured the equilibrium constant *K* and the rate constant *g* at high temperature, Johnston and Yost[10] measured the rate constant *h* near room temperature, and the combined results from these studies for $(Kh/2g)^{1/3}$ are also shown in Fig. 3. The present work differs from the older results by about a factor of three.

The modulation experiments produced several types of kinetic information, including the identification of reaction species, the NO_3 visible absorption cross sections, the primary quantum yields for NO_3 photolysis, and the rate constants for oxygen atoms reacting with NO_3 and N_2O_5. All modulation experiments were performed in a flow system at one atmosphere total pressure. The N_2O_5 modulation was monitored at its 8.03 μ infrared absorption peak. The phase shift for this signal always differed from that for NO_3 by approximately 180°, indicating that NO_3 and N_2O_5 have a reactant-product relationship. The NO_3 modulation amplitude is directly proportional to its primary quantum yield using red, green, and gold lamps. Oxygen was used as the carrier gas in order to suppress possible contribution to the modulation amplitude from oxygen atom reactions with NO_3 and N_2O_5. The quantum yields were calculated from a computer simulation of the reaction system for each set of conditions. The NO_3 absorption spectrum and the quantum yield spectra for two channels of NO_3 photolysis are given by Fig. 4.

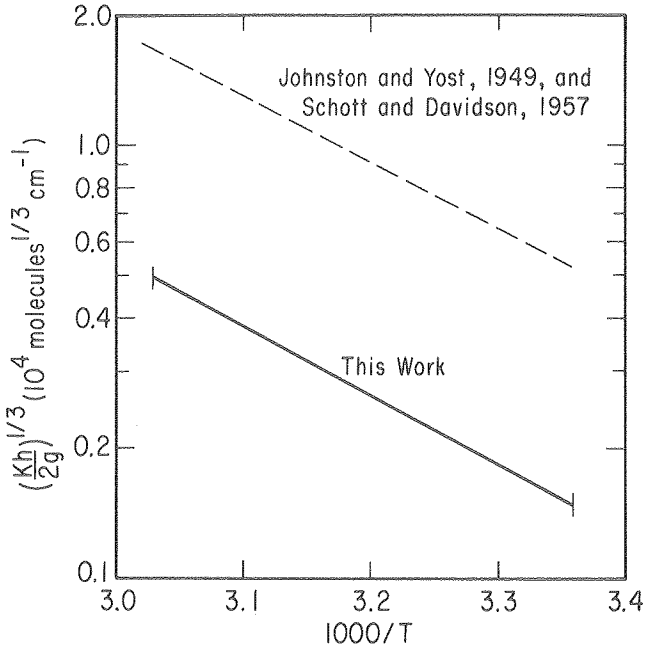

Fig. 3. Arrhenius plot for $(\frac{Kh}{2g})^{1/3}$. (XBL 759-7286)

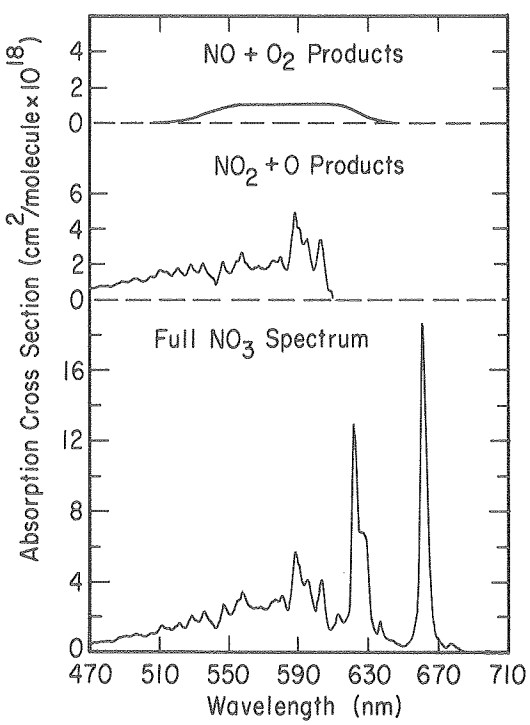

Fig. 4. Separation of the NO_3 spectrum into photochemically active bands with synthetic shapes. (XBL 759-7290)

When nitrogen is substituted for the oxygen carrier gas (which had suppressed the oxygen atom concentration) the changes in modulation amplitudes can be attributed to reactions *m* and *n*. The primary quantum yields for NO_3 were used to calculate the NO_3 modulation amplitudes due to the photolysis reactions j_1 and j_2. The residual amplitudes observed with the nitrogen carrier gas were attributed to reactions *m* and *n*. Computer simulations showed a linear relationship between the rate constants *m* and *n* the calculated modulation amplitudes due to these reactions. The values of *m* and *n* derived in this way are given in Table 1.

The equilibrium constant *K* determined in this research has been used with literature data to calculate rate constants for reactions *B, e, and f* (Table 1).

The quantum yield curves for NO_3 and the complex mechanism were checked by a series of modulation experiments, one example of which is given by Fig. 5. The observed amplitudes and phases of modulation are given together with curves calculated from the complex mechanism and rate constants in Table 1. In general there was satisfactory agreement between calculated and observed quantities.

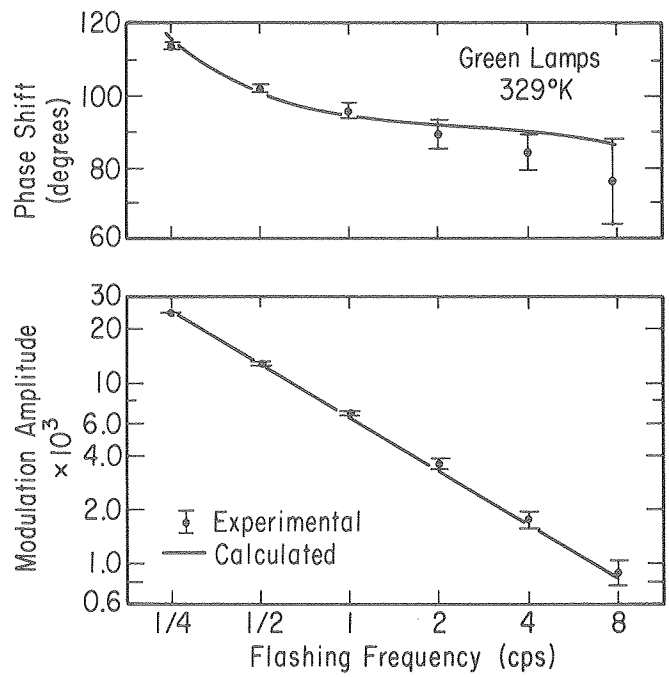

Fig. 5. Modulation amplitudes and phase shifts of NO_3 for green lamp photolysis at 329 K. (XBL 759-7291)

---

*Supported in part by the National Science Foundation and the Climatic Impact Assessment Program.

1. R. A. Graham (Ph.D. thesis), University of California, Berkeley, California, 1975.
2. H. S. Johnston, Gas Phase Reaction Rate Theory, Ronald Press Co., New York, N.Y., pp. 14-32, 1966.

Table 1. Rate constants and NO_3 photolysis constants for eleven reactions in the mechanism, as derived from the literature or obtained in this work.

Quantity	T Range of Observations	A-factor (cm^3 sec^{-1} unless noted)	E_a (degrees K)	Ref
A (1 atm)	273 - 300	1.24×10^{14} sec^{-1}	10,317	11
Ke	338 - 396	2.05×10^{13} sec^{-1}	12,406	12
Kf	297	(0.71 ± 0.014)		3
K	298 - 329	$(8.4 \pm 1.8) \times 10^{26}$ cm^{-3}	11178 ± 100	*
B (1 atm)	273 - 300	$(1.48 \pm 0.33) \times 10^{-13}$	-861 ± 300	*A/K*
e	338 - 396	$(2.5 \pm 0.5) \times 10^{-14}$	1127 ± 100	*Ke/K*
f	297	$(1.87 \pm 0.41) \times 10^{-11}$		*Kf/K*
g	298 - 329	$(8.5 \pm 2.8) \times 10^{-13}$	2450 ± 100	*
h	231 - 298	$(1.34 \pm 0.11) \times 10^{-13}$	2466 ± 30	6
i	198 - 330	$(9. \times 10^{-13})$	1200	13
j_1	Sunlight	(0.040 ± 0.02) sec^{-1}		*
j_2	Sunlight	(0.099 ± 0.02) sec^{-1}		*
m	298	$\leq 2 \times 10^{-14}$		*
n	298 - 329	$(1.0 \pm 0.4) \times 10^{-11}$	0	*
q	220 - 1000	1.9×10^{-11}	2300	13
r	200 - 346	6.6×10^{-35} cm^6 sec^{-1} (M: Ar = 1.0, N_2 = 1.6, O_2 = 1.7)	-510	13

*This work.
Error limits are based on random errors of this study and do not include possible systematic errors.

3. A. B. Harker and H. S. Johnston, J. Phys. Chem. 77, 1153 (1973).
4. F. Cramarossa and H. S. Johnston, J. Chem. Phys. 43, 727 (1965).
5. H. S. Johnston and R. Graham, Can. J. Chem. 52, 1415 (1974).
6. R. A. Graham and H. S. Johnston, J. Chem. Phys. 60, 4628 (1974).
7. G. Z. Whitten, Rate Constant Evaluations Using a New Computer Modeling Scheme, paper presented at ACS National Meeting (Spring, 1974).
8. H. J. Schumacher and G. Sprenger, Z. Physik. Chem. 2B, 266 (1929).
9. G. Schott and N. Davidson, J. Am. Chem. Soc. 80, 1841 (1958).
10. H. S. Johnston and D. M. Yost, J. Chem. Phys. 17, 386 (1949).
11. R. L. Mills and H. S. Johnston, J. Am. Chem. Soc. 73, 938 (1951).
12. H. S. Johnston and Yu-sheng Tao, J. Am. Chem. Soc. 73, 2948 (1951).
13. D. Garvin and R. F. Hampson, Editors, Chemical Kinetics Data Survey, NBSIR 74-430, 1974.

2. PRIMARY PRODUCTS IN THE PHOTOCHEMISTRY OF NITROGEN PENTOXIDE

Peter Connell and H. S. Johnston

There are three possible channels for the photolysis of nitrogen pentoxide by ultraviolet radiation

$$N_2O_5 + h\nu \rightarrow NO + NO_2 + O_2$$
$$\rightarrow N_2O_4 + O \rightarrow 2\ NO_2 + O$$
$$\rightarrow NO_2 + NO_3$$

At 253.7 Nm radiation, steady-source or "DC" photolysis of N_2O_5 in O_2 and in N_2 give results consistent with (2), inconsistent with (1), and ambiquous with respect to (3). From the phase shift of N_2O_5 when photolyzed by intermittent radiation, results are consistent with (1) or (2) or both, but inconsistent with (3). By combining the conclusions from these two experiments, it is found that the primary products of N_2O_5 photolyisis at 253.7 Nm is pathway (2), that is, with production of atomic oxygen.

The photochemistry of N_2O_5 has been studied at 254 Nm under both DC and modulated photolysis. The intent of the project is to provide as direct a determination as possible of the primary products of N_2O_5 photodecomposition, as well as primary quantum yields. Interest in this problem is stimulated by the need for knowledge of the fate of N_2O_5 in the stratossphere. This reservoir for NO_x requires evaluation to allow more accurate diurnal stratospheric modeling.

The 254 Nm Hg line was selected as the photolytic source because of the convenience of obtaining relatively high intensities, in addition to the appearance of a minimum in the cross section of the potentially interfering NO_2 at that wavelength. The N_2O_5 cross section is about 3E-19 cm^2 and the energetically possible and logical pathways are:

$$N_2O_5 + h\nu\ (\lambda = 254\ nm) \rightarrow NO + NO_2 + O_2$$
$$\rightarrow N_2O_4^* + O \rightarrow 2\ NO_2 + O$$
$$\rightarrow NO_2 + NO_3$$

Previous work on this problem appears to be confined to indirect observations of NO_2 appearance by Daniels et al.[1] in 1931 and Murphy[2] in 1969, who agreed on an apparent quantum yield of 0.6 and probable production of an oxygen atom.

The experiment is performed in a 67 liter quartz cell nickel-plated stainless steel end caps (similar to that described by article 1 above). Monitoring of species is accomplished in the infrared using a Nernst glower source, a multipass white cell optical arrangement, a one-meter monochromator and a Ge:Cu photoconductive detector, operated normally at 4.2 K. The entire cell is surrounded by an insulated box and can be cooled to 240 K. Photolysis is accomplished with four germincidal lamps radially distributed. A chlorine gas chemical filter is placed concentric with each lamp to reduce the intensity of the 366 Nm Hg line, which is strongly absorbed with decomposition by NO_2.

The infrared signal is passed to a lock-in amplifier and then, in the case of the modulated photolysis, to up/down digital counters, which evaluate the in- and out-of-phase portions of the modulated N_2O_5 concentrations. The phase angle of the result can distinguish between pathways in which the products of the photolytic event can recombine to reform the reactant (e.g. $N_2O_5 \xrightarrow{h\nu} NO_2 + NO_3$ and those for which the products proceed to other reactions. The amplitude of the signal modulation can be related to the primary photolytic quantum yield. The N_2O_5 chemical system is too complicated to allow analytical solutions to the differential equations describing the chemistry, but accurate numerical models are generated on the CDC-7600 and on our laboratory PDP 11/10 for comparison to experimental results.

Modulation simulation results under various conditions are shown in Table 1, along with the experimentally obtained values. The modulation frequency is restricted to low values in this system to enhance the small amplitudes obtained ($\sim 10^{-4}$). The 8 μ N_2O_5 band shows the modulation phase angle expected in the case of either NO or O atom production in the primary step. The amplitude of the observed modulation indicates a quantum yield on the order of $\sim 0.6 \pm 0.2$.

If the NO production pathway predominates, N_2O_5 would participate in catalytic decomposition of stratospheric ozone by the mechanism:

$$NO_2 + O_3 \rightarrow NO_3 + O_2$$
$$NO_2 + NO_3 \xrightarrow{M} N_2O_5$$
$$N_2O_5 \xrightarrow{h\nu} NO + NO_2 + O_2$$
$$NO + O_3 \rightarrow NO_2 + O_2$$
$$\text{net: } 2\ O_3 \rightarrow 3\ O_2$$

If the O-atom pathway predominates, there is a null cycle so far as ozone is concerned and the N_2O_5 acts as a short term reservoir for NO_x. These two possibilities were distinguished in a DC photolysis flow experiment, in which the approach to steady state of the N_2O_5 concentration was monitored in both N_2 and O_2 carrier gases. No difference would be observed in the NO production case, while the O_2 carrier gas would scavenge the O-atom completely in the other case, resulting in a reduced overall quantum yield for N_2O_5 destruction. The experimental results are shown in Fig. 1, along with numerically produced, predicted curves for the various possibilities. Clearly the combined results of the modulation and DC photolysis experiments point to $2\ NO_2 + O$ as the principal products of N_2O_5 photolysis. The conclusion then is that N_2O_5 is a do-nothing short term sink for stratospheric NO_x, unless it participates in some other reaction schemes than thermal decomposition or photolysis.

Table 1. Calculated and experimental N_2O_5 modulation results.

		$[N_2O_5]$ cc/molecule	$\phi_{N_2O_5}$	Amplitude N_2O_5	$[NO_2]$	ϕ_{NO_2}	Amplitude NO_2
Simulation conditions carrier gas; assumed photo products $\Phi = 1$ 1/4 Hz modulation frequency	1 atm N_2; $NO_2 + NO_3$	9E14	164	7E10	1.1E12	-16	7E10
	1 atm N_2; $NO + NO_2 + O_2$	5E14	86	1.5E11	6.7E14	-99	1.2E11
	1 atm N_2; $NO_2 + NO_2 + O$	6E14	89.4	1.3E11	6E14	-105	1.2E11
	1 atm O_2; $2\ NO_2 + O$	8E14	91.1	2.1E11	1.8E14	-90	4.3E11
	1 atm O_2; $NO + NO_2 + O_2$	5.5E14	95.3	2.8E11	6.6E14	174(2)	8E10
	50 torr O_2; $2\ NO_2 + O$	6E14	85.5	1.76E11	5.6E14	-99	1.9E11
	50 torr O_2; $NO + NO_2 + O_2$	5.4E14	91.3	1.5E11	6.5E14	-90	1.8E11
	50 torr N_2; $2\ NO_2 + O$		Apparently closely similar to 50 torr O_2 case.				
	50 torr N_2; $NO + NO_2 + O_2$		A bug in the program prevents proper evaluation.				
Experimental conditions N_2O_5 observed at 8.028 μm	50 torr N_2	6E14	89 ± 5	1.3 ± (.5) E11		Not observable	
	1 atm O_2	9E14	89 ± 5	1.5 ± 0.5 E11		at present	

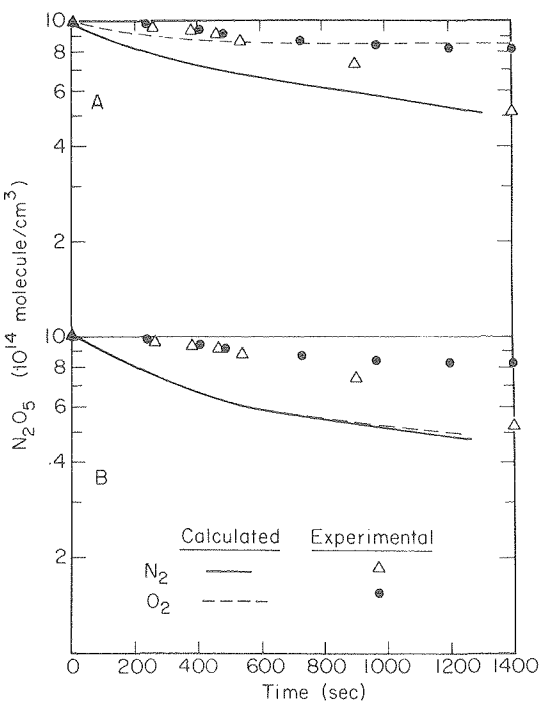

Fig. 1. Calculated and observed photochemical decomposition of N_2O_5 by 253.7 Nm radiation. ---- calculated N_2O_5 in the presence of oxygen; ——— calculated N_2O_5 in the presence of nitrogen; O, experimental points in the presence of O_2; Δ, experimental points in the presence of N_2. A. Calculations based on mechanism: $N_2O_5 + h\nu \rightarrow 2\ NO_2 + O$; B. Calculations based on mechanism: $N_2O_5 + h\nu \rightarrow NO + NO_2 + O_2$. (XBL 782-7015)

1. H. H. Holmes and F. Daniels, J. Am. Chem. Soc. 56, 630 (1934).
2. R. Murphy, (Ph.D. thesis), University of California at Los Angeles, Los Angeles, California, 1969.

3. NITROUS OXIDE ULTRAVIOLET ABSORPTION SPECTRUM AT STRATOSPHERIC TEMPERATURES*

Gary Selwyn, James Podolske and H. S. Johnston

The absorption spectrum of nitrous oxide (N_2O) has been determined at five temperatures from 194 to 302 K and over the wavelength range 173 to 240 Nm. The absorption cross sections as a function of wavelength and temperature are expressed by a nine-term polynomial in a form useful for atmospheric models. The high resolution structure between 173 and 190 Nm has been observed more clearly than by previous studies.

Previously we reported[1] on the near ultraviolet absorption spectrum of nitrous oxide (N_2O) at room temperature, with references to previous literature and a discussion of the resulting lifetime of nitrous oxide in the atmosphere.

Holliday and Rueben[2] found that the ultraviolet absorption cross section for nitrous oxide increased rapidly with increasing temperature from 293 to 953 K over the wavelength range 200 to 270 Nm, and Nicolle and Vodar[3] obtained the ratio of absorption cross sections at 293 to 183 K at wavelengths above 200 Nm. Romand and Mayence[4] reported on near ultraviolet absorption centered at 145 Nm at 291 K. Previous studies have indicated that the spectrum of nitrous oxide may have some weak structure superimposed on the continuous absorption. Zelikoff et al.[5] and Monahan and Walker[6] have found evidence of diffuse bands by optical methods, and Lassettre et al.[7] have observed diffuse bands by electron impact spectra.

Spectra were obtained with a Cary 118C spectrophotometer, fitted with either one of two thermostated cells. A small quartz cell mounted in nitrogen-purged Cary sample compartment was used in the wavelength range 173 to 210 Nm. The optical pathlength was 6.5 cm and each end was closed with a pair of Suprasil windows with a vacuum between them for insulation. The cell was enclosed in an insulating jacket and was cooled by a stream of nitrogen boiled off from a liquid nitrogen dewar. Temperature was measured by a thermocouple. A large stainless steel cell, used over the wavelength range 200 to 240 Nm, had a double-pass optical pathlength of 296 cm, and had a single optically flat, polished Suprasil window coated with MgF_2 to minimize reflective loss around 200 n. A one-to-one focusing mirror inside the cell was also coated with MgF_2 to enhance reflection around 220 to prevent oxidation. The cell was jacketed by an ethanol bath which was cooled by flowing cold methanol through submerged copper coils that encircled the cell. The entire cell was covered with one inch of insulating sponge rubber. The cell had an end-to-end temperature difference of 0.5 K at 243 K and 1 K at 225 K. At low temperatures, a stream of dry nitrogen gas was passed across the window to prevent frost formation.

The analog output of the spectrophotometer was collected and stored by a Fabritek 1074 data collector with a 12 Bit A/D converter and 4000 words of storage. The data were processed by a PDP 8/L minicomputer interfaced with the Fabritek. Data points were taken every 0.2 Nm over the wavelength range studied with a resolution of 0.7 Nm. For high resolution studies, the slits were set at 0.15 mm. The resolution was 0.075 Nm, the time constant was 5 seconds, the scan rate was 0.005 Nm sec^{-1}, and signal averaging on the minicomputer was carried out for four runs. Data points were taken every 0.05 Nm in this case.

Nitrous oxide from a Matheson cylinder was purified by passing through 3A molecular sieve to remove water and then by four successive vacuum distillations with retention of the middle third of each. Purity of the nitrous oxide was confirmed by ultraviolet absorption spectra and high resolution mass spectrometry. Wavelength calibrations were made by observing the rotational structure of the NO absorption doublet at 226 Nm (Ref. 8) and observing the rotational structuring of the Schumann-Runge oxygen bands below 195 Nm (Ref. 9). The absence of photolysis of N_2O by the Cary deuterium discharge lamp was established by the absence of any detectable NO produced during a special six-hour run. The radiation is dispersed before passing through the sample cell, and thus the amount of radiation available for photolysis of N_2O is extremely low.

The cross sections are defined as

$$\sigma = (\log_e Io/I)(CL)^{-1} \qquad (1)$$

where C is concentration in molecules cm^{-3} and L is the optical pathlength in cm. The absorption cross sections for nitrous oxide for radiation between 173 and 240 Nm and at five temperatures between 194 and 302 K. The portion of the data centered about the "stratospheric window" at about 210 Nm is shown in Fig. 1. The ratio of the cross sections between the room temperature value and the value at 225 K is about 2.9 at 240 Nm, about 1.6 at 210 Nm, and about 1.15 at 190 Nm.

At each wavelength the temperature dependence of the spectrum was expressed in the empirical form

$$\sigma(\lambda,T) = A(\lambda)\ \exp[B(\lambda)(T-300)] \qquad (2)$$

The wavelength dependent terms A and B were fit to several empirical functions, the most compact and efficient of which was

$$\ln \sigma(\lambda,T) = A_1 + A_2\lambda + A_3\lambda^2 + A_4\lambda^3 + A_5\lambda^4 + (T-300)\ \exp(B_1 + B_2\lambda + B_3\lambda^2 + B_4\lambda^3) \qquad (3)$$

The nine parameters were fit by a nonlinear, least-squares, minimization routine to give the coefficients (where λ is given in Nm)

$A_1 = 68.21023$	$B_1 = 123.4014$
$A_2 = -4.071805$	$B_2 = -2.116255$
$A_3 = 4.301146 \times 10^{-2}$	$B_3 = 1.111572 \times 10^{-2}$
$A_4 = -1.777846 \times 10^{-4}$	$B_4 = -1.881058 \times 10^{-5}$
$A_5 = 2.520672 \times 10^{-7}$	

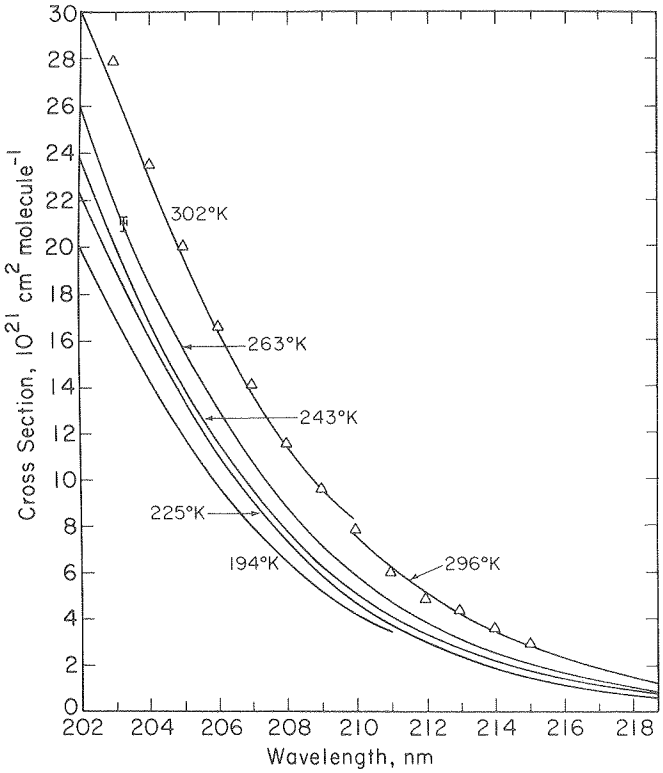

Fig. 1. Cross section, $cm^2 \times 10^{21}$ vs wavelength, Nm for five temperatures—this work, Δ data points of Zelikoff, Watanabe and Inn (1953). Note the discontinuity at 210 Nm due to two different "room temperature." The estimated standard deviation of wavelength (± 2%) is indicated by the cross on the 263 K CURVE. Resolution 0.7 Nm. (XBL 782-7017)

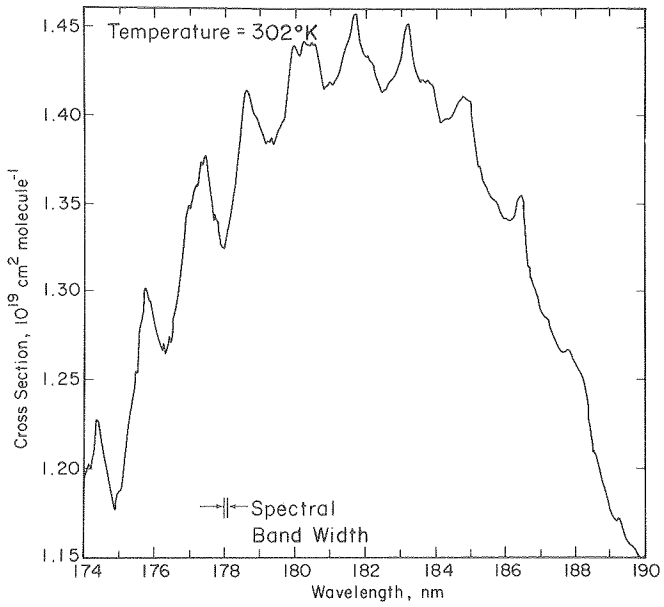

Fig. 2. High resolution spectrum in the structured region. Cross section, $cm^2 \times 10^{19}$ vs wavelength, Nm. Temperature = 302 K. Pressure is 44 Torr N_2O. Resolution 0.075 Nm. (XBL 782-7018)

The estimated standard deviation is about 4%.

The high resolution data at 302 K and 44 Torr N_2 are given by Fig. 2. A vibrational progression superimposed on a continuous spectrum is more clearly defined here than in previous studies. At low temperatures this spectral structure is less prominent than at room temperature.

The basis for the temperature dependence of the nitrous oxide spectrum is concisely stated by Monahan and Walker:[10] "The $^1\Delta[\leftarrow X^1\Sigma]$ transition is orbitally forbidden but vibronically allowed by bending." The excited bending states of nitrous oxide have much larger Franck-Condon overlap with the upper statt than does the (000) mode of the ground state molecule. The population of excited bending states (010, 020, ···) increases with temperature, as does the absorption cross section for ultraviolet radiation. With a fundamental bending frequency of 589 cm^{-1}, about 2.5% of the molecules are in the (010) bending mode at 194 K. At 296 K there are about 11% in the (010) mode, and 1.5% in the (020) vibrational state.

---

*Supported in part by the National Science Foundation.

1. H. S. Johnston and G. S. Selwyn, Geophys. Res. Lett. 2, 549 (1975).
2. Holliday and Rueben, Faraday Soc. Trans. 64, 1735 (1968).
3. Nicolle and Vodar, Comptes Rendus 210, 142 (1940).
4. Romand and Mayence, Comptes Rendus 228, 998 (1949).
5. M. Zelikoff, K. Watanabe and E.C.Y. Inn, J. Chem. Phys. 21, 1643 (1953).
6. Monahan and Walker, J. Chem. Phys. 63, 1676 (1975).
7. E. N. Lassettre, A. Skerbele, M. A. Dillon and K. J. Ross, J. Chem. Phys. 48, 5066 (1968).
8. G. Herzberg, Electronic Spectra and Electronic Structure of Diatomic Molecules, Vol. I, Second Edition, (Van Nostrand Reinhold, New York, N.Y., (1950).
9. H. P. Knauss and S. S. Ballard, Phys. Rev. 48, 796 (1935).

4. KINETIC ENERGY AND WAVELENGTH DEPENDENCE OF THE REACTION OF NITRIC OXIDE WITH OZONE

Marta Kowalczyk, Carol Kahler, Y. T. Lee and H. S. Johnston

The reaction of $NO + O_3 \rightarrow NO_2 + O_2$ has been one of the most intensely studied reactions in recent years since it is important in the kinetics of atmospheric pollution, and is a very convenient system to study the effect of infrared laser and magnetic state selection on the dynamics of the reaction.[1-3] We have undertaken to study several aspects of this reaction using a crossed beam configuration. The product NO_2 emerges from this reaction partially in the ground electronic state, but vibrationally excited and partially in an electronically excited state which chemiluminesces with a lifetime up to 70 microseconds. Using molecular beams rather than standard gas phase techniques insures single collision conditions for the reaction, eliminating complications due to collisional quenching of the long lived electronically excited NO_2. A better control of the collision kinetic energy also becomes possible.

The first set of experiments was a study of the effect of kinetic energy on the chemiluminescent channel of the reaction.[4] The NO beam was supersonically expanded through one differential pumping chamber to the collision center. The energy of the beam was varied by using different seeding ratios of the NO in helium for high energies, NO in argon for low energies, as well as by heating and cooling the gas mixtures directly before expansion into the vacuum chamber. Beam energies thus available are virtually continuous from 0.5 to 15 kcal/mole. The ozone reactant was directly expanded from a silica gel substrate, which was pumped to remove excess oxygen, through an absorption concentration monitor and introduced directly above the collision center. The reactants then collide in the vacuum chamber emitting a visible-near infrared chemiluminescence. This chemiluminescence was spatially filtered to eliminate stray light not originating from the collision center and detected with a PMT having a gallium arsenide photocathode. The signal was handled with standard photon counting techniques then sent to a dual channel gated scaler synchronized to a mechanical chopper in front of the NO beam.

Figure 1 shows a typical result for 10% NO in He which highlights the intermediate energy range studied. At room temperature, indicated by the arrow, the signal to background was typically 5:1 and the signal to noise 180:1. The NO beam energy was changed by varying the temperature from 120 to 430 K. At the lower collision energies studied, we were able to see the chemiluminescence rise from the reaction threshold. Time-of-flight analysis was done to determine the energies of the collision. An example of one done for 10% NO/He at room temperature is given by the dashed curve in the insert. When one compares the velocity distribution with the Maxwellian one (solid line), one sees that the supersonic beam has three times the peak velocity, but only one-third the velocity spread. This narrow velocity spread enables us to determine the collision energy more precisely.

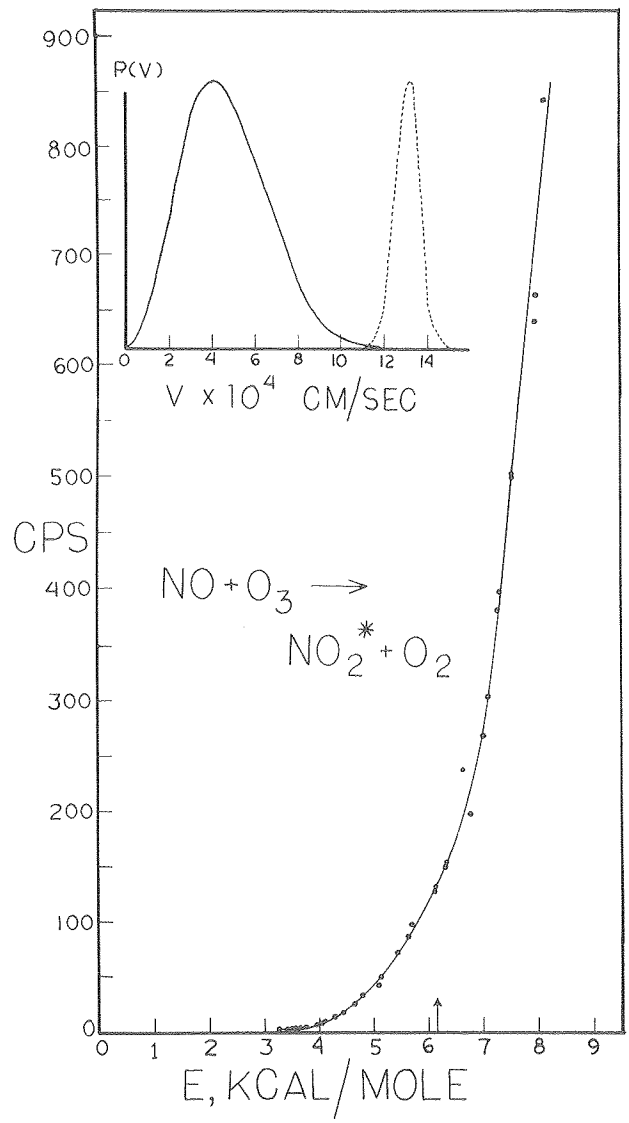

Fig. 1. Chemiluminescence signal as a function of NO beam energy for 10% NO in He. Insert gives velocity distributions at room temperature; ----- experimental NO beam determined by TOF; ——— calculated Maxwell-Boltzmann. (XBL782-7016)

Presently in progress is a study of the wavelength dependence of the chemiluminescence.[2,3] This will be done at two different beam energies to enable us to determine whether the excess translational energy shows up proportionately in the product as electronically excited NO_2, or ends up in some other mode. An extension of these experiments is planned for the future. Specifically, we will study the effect of spin-orbit state of the reactant NO on the chemiluminescent channel.[5] We may also try to determine the branching ratio of ground to excited state product for various collision energies and for both spin-orbit states of NO.

---

1. M. A. A. Clyne, B. A. Thrush and R. P. Wayne, Trans. Faraday Soc. 60, 359 (1964).

2. P. N. Clough and B. A. Thrush, Trans. Faraday Soc. 63, 915 (1967).

3. W. Braun, M. J. Kurylo, A. Kaldor and R. P. Wayne, J. Chem. Phys. 61, 461 (1974).

4. A. E. Redpath and M. Menzinger, Can. J. Chem. 49, 3063 (1971).

5. A. E. Redpath and M. Menzinger, J. Chem. Phys. 62, 1987 (1975).

Theoretical Studies

5. THE ORIGIN OF NITROUS OXIDE IN SMOKE STACKS FROM HIGH TEMPERATURE COMBUSTION

David Littlejohn and H. S. Johnston

Tropospheric nitrous oxide plays an important role in stratospheric chemistry. It diffuses into the stratosphere where it reacts with singlet oxygen by photolysis and by chemical reaction. The nitric oxide so produced is a major factor in the natural stratospheric ozone balance.[1]

The manufacture of nitrogen fertilizer, which has expanded at an exponential rate since 1950, now fixes nitrogen at a rate comparable to the natural rate.[2,3] Estimates are in the range of 25 to 50%. Eventually, this increased rate of nitrogen fixation is expected to increase the rate of production of tropospheric nitrous oxide, but the mechanism and time scale are regarded as very uncertain.

Recently Pierotti and Rasmussen[4] found that power plants are significant ground-based sources of nitrous oxide. They found 3.1 to 37.6 parts per million by volume (ppmv) of nitrous oxide in the exhaust gases of three power plants. The power plant burning coal had a substantially higher yield of nitrous oxide than the two that burned natural gas. The concentrations observed in the smoke stacks are a factor of 10 to 100 above ambient tropospheric nitrous oxide levels. From the observed nitrous oxide concentrations and the power plant operating conditions, Pierotti and Rasmussen estimate that 1.0×10^3 tons of nitrous oxide are produced for each million tons (M ton) of coal burned, and 2.0×10^2 tons of nitrous oxide are produced for each billion cubic meters of natural gas burned. From worldwide production of coal and gas, they estimate that 3.5 M ton per year of nitrous oxide are produced from power plant combustion.

Hahn and Junge[5] used an atmospheric model, a model for production of nitrous oxide from fixed nitrogen, and this source of nitrous oxide from combustion. They assume exponential increase of nitrogen fertilizers at a rate of 6% per year until the year 2000 and then no further increase. They assume a 3.7% per year increase in combustion of fossil fuels until the year 2050 and then no further increase. Their predicted increase of atmospheric nitrous oxide over the next century is shown in Fig. 1. This model predicts an increase of atmospheric nitrous oxide by 100 to 150% over the next century. The natural nitrous oxide cycle is sufficiently uncertain at this time that this prediction itself is uncertain by about an order of magnitude.[6]

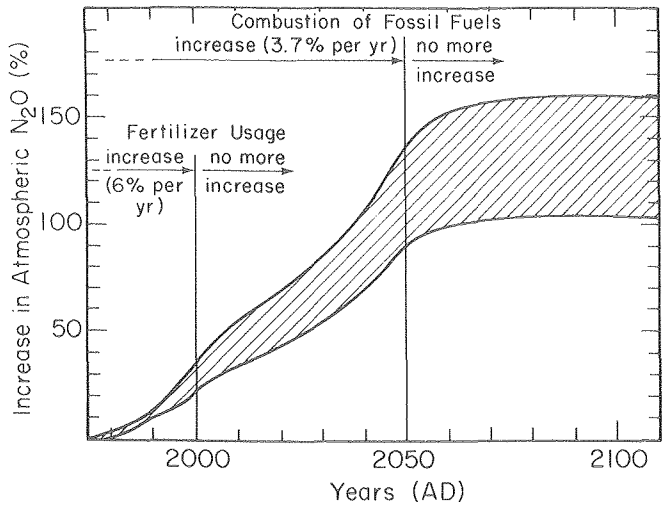

Fig. 1. Hahn and Junge's prediction of increasing atmospheric nitrous oxide from nitrogen fertilizer and from combustion over the next century. (XBL782-7019)

If a human activity promises more or less to double on the global scale a natural atmospheric species that plays an important natural role, then it is very important that the mechanism be understood, regardless of whether the predicted effects are good, bad, or indifferent. This study is a preliminary attempt to understand the chemical mechanism for production of N_2O from high temperature combustion. Nitrous oxide is an unstable molecule, and it thermally decomposes to N_2 and O_2 at temperatures between 600 and 1000°K. It is also produced and destroyed by several reactions as summarized in Table 1.

Table 1. List of reactions producing and destroying nitrous oxide.

$$N_2 + O + M \rightleftharpoons N_2O + M$$

$$NO + NO \rightleftharpoons N_2O + O$$

$$N_2 + O_2 \rightleftharpoons N_2O + O$$

$$N + NO_2 \rightarrow N_2O + O$$

$$N_2 + O(^1D) + M \rightarrow N_2O + M$$

$$N_2O + O(^1D) \rightarrow N_2 + O_2$$

$$N_2O + O(^1D) \rightarrow NO + NO$$

In a combustion process, a substantial amount of atomic oxygen is produced and sudden quenching of the high temperature may "freeze out" some nitrous oxide by way of

$$O + N_2 + M \rightarrow N_2O + M.$$

This process was favored by Pierotti and Rasmussen and by Pratt and Malte.[7] From Table 1, one sees that other reactions also, upon temperature quenching, might leave some nitrous oxide. On the other hand, the nitrous oxide might be formed by combustion of ammonia or bound nitrogen in coal.

We carried out a numerical experiment to see if known chemical reactions with reported rate constants are sufficient to produce the observed amount of nitrous oxide when the temperature is quenched at various assumed rates. The question asked is whether "hot air" reactions are sufficient or whether other mechanisms perhaps involving bound nitrogen in fuels must be invoked. We used our Chemical Kinetics Computer program, which uses the Gear method for solving simultaneous differential equations to give concentrations of chemical species with time. There are 39 reactions in the simulations involving atomic and molecular nitrogen and oxygen and oxides of nitrogen.

The first exploratory calculations involve reactions at constant volume, instead of the more nearly realistic condition of constant pressure. No explicit consideration was given to the fuel, carbon or hydrogen-containing compounds. No effort was made to model the actual combustion process, but only "hot air" reactions were considered. Air was assumed to be heated at various rates, to a plateau temperature of various assumed value and duration, and then the temperature was quenched at various rates. The "freeze out" of nitrous oxide, as well as nitric oxide NO was noted.

Runs were done with maximum temperatures from 1500 to 3500 K and cooling rates of 10^4 to 10^8K/s. The largest maximum temperatures and largest cooling rates were much greater than would be observed in combustion. Figure 2 shows the effect of different cooling rates on nitrous oxide concentration. The species were in equilibrium at 2000 K before cooling was initiated. Figure 3 shows the effect of total concentration on nitrous oxide concentration. Since the program does not change total concentration with temperature, the lower concentration levels would give more realistic results than the maximum concentration shown. Figure 4 shows the change in concentration of N_2O, NO, NO_2 and O_3 as cooling occurs.

Variation of the rate constants within their uncertainty did not change nitrous oxide concentrations more than a factor of two. As mentioned by Pratt and Malte,[2] the reaction of $N_2 + O + M \rightarrow N_2O + M$ was found to be most important in nitrous oxide production, and the reverse reaction was most important in nitrous oxide destruction. The results of our calculations indicate that less than 10% of the nitrous oxide observed by Pierotti and Rasmussen is caused by the heating of air. A combination of very high maximum temperatures and very fast cooling rates were needed to produce the observed nitrous oxide concentrations. These conditions would not be expected in combustion.

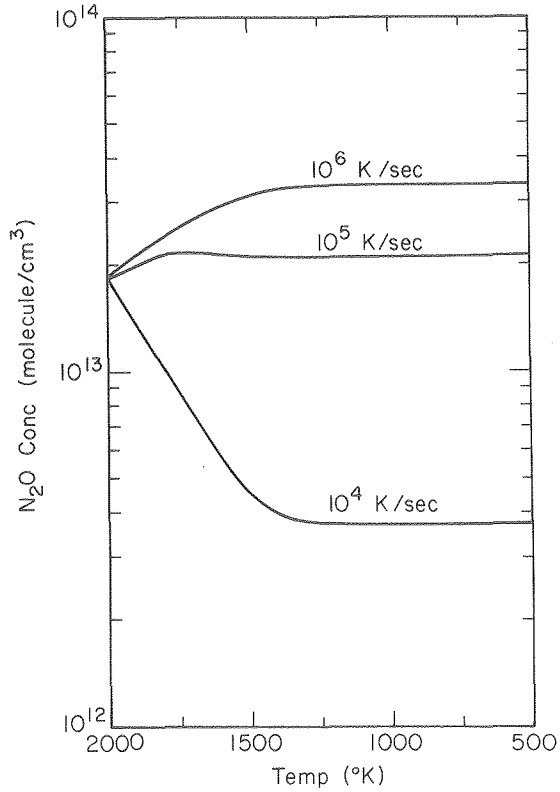

Fig. 2. Remaining nitrous oxide as a function of temperature for three assumed rates of cooling. Initial condition 2000 K, 2.4×10^{19} molecules cm^{-3} total concentration. (XBL 782-7013)

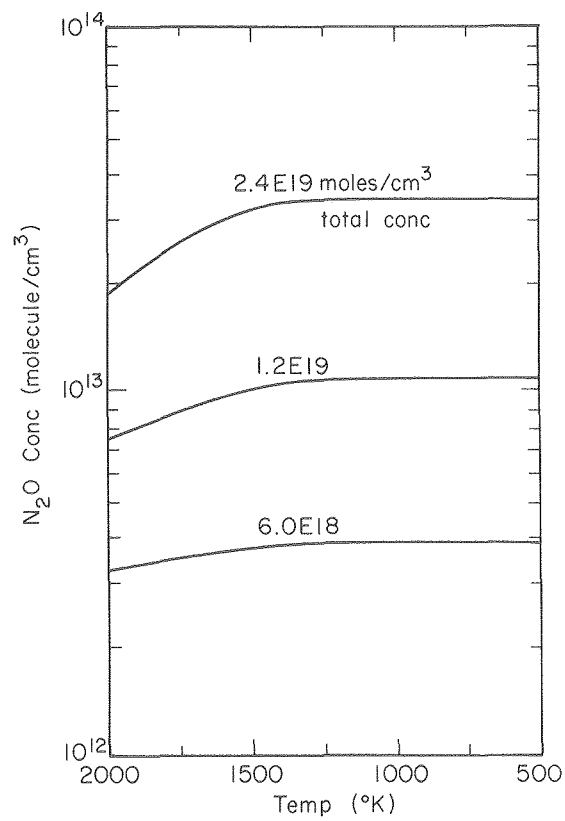

Fig. 3. Remaining nitrous oxide from 10^6 degree sec^{-1} cooling rate as a function of total air concentration. (XBL 782-7014)

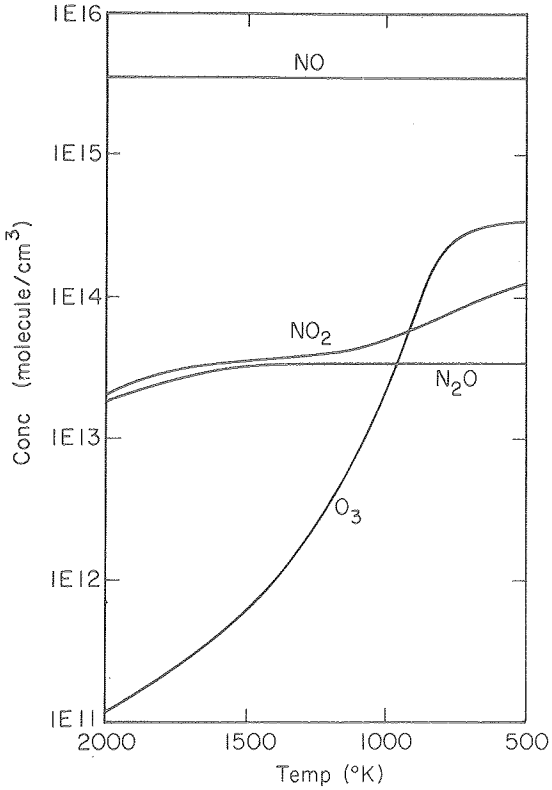

Fig. 4. Concentration of N_2O, NO, NO_2 and O_3 as a function of temperature with a cooling rate of 10^6 degree sec^{-1} and initial air concentration of 2.4×10^{19} molecules cm^{-3}. (XBL 782-7012)

The tentative conclusion is that "hot air" chemistry alone, as presently understood, may not be sufficient to produce the high mole fraction of N_2O observed by Pierotti and Rasmussen in the smoke stack of power plants. It appears that some other processes involving C, H, or N in the fuel may be necessary to account for the observed nitrous oxide. Further work is planned on this system.

6. INTERPRETATION OF OBSERVED TRACE SPECIES IN THE STRATOSPHERE

H. S. Johnston and James Podolske

Although stratospheric photochemistry is indeed complex, there exist some valid simplifying considerations. Chemical species in the stratosphere may be classified as major (N_2, O_2, Ar), minor (O_3, CH_4, H_2O, CO_2, parts per million), and trace (NO, NO_2, HO, HOO, Cl, ClO; etc., parts per billion or less). Consider the reaction of nitric oxide and ozone

$$NO + O_3 \rightarrow NO_2 + O_2.$$

If this reaction occurred as a one-way reaction, the trace species would have only a very weak effect

	NO	O_3
Before	10^{-9}	10^{-6}
After	0	0.999×10^{-6}.

Only if the trace species interacts in a cyclic manner, with ozone

$$NO + O_3 \rightarrow NO_2 + O_2$$
$$O_3 + h\nu \rightarrow O_2 + O$$
$$NO_2 + O \rightarrow NO + O_2$$
$$\text{net: } 2\,O_3 \rightarrow 3\,O_2$$

can it have a significant direct effect on ozone

	NO	O_3
Before	10^{-9}	10^{-6}
After one cycle	10^{-9}	0.998×10^{-6}
After two cycles	10^{-9}	0.996×10^{-6}
...		
After 100 cycles	10^{-9}	0.8×10^{-6}.
...		

In general, free radicals, HO_x, NO_x, ClX, interact with odd oxygen to change odd oxygen by + or - one unit. From the fundamental properties of odd and even numbers, it requires two such processes to convert odd oxygen to even oxygen or even oxygen to odd oxygen. The situation is summarized in Fig. 1. If free radical R_1 is converted to free radical R_2 in a process that decreases odd oxygen by one unit ($\Delta = -1$), the cycling of R_2 back to R_1 must involve either an increase ($\Delta = +1$) or a decrease ($\Delta = -1$) of odd oxygen. An increase cancels the decrease of the initial step, and one has a null cycle. A decrease of odd oxygen in the return loop completes a catalytic cycle ($\Delta = -2$) that destroys ozone. Two steps of

1. P. J. Crutzen, J. Geophys. Res. 76, 7311 (1971).
2. C. C. Delwiche, Sci. American 223, 137 (1970).
3. Council for Agricultural Science and Technology, Report 33, 33 pp., Iowa State University, January 1976.
4. D. Pierotti and R. A. Rasmussen, Geophys. Res. Lett. 3, 265 (1976).
5. J. Hahn and C. Junge, Z. Naturforsch. 32, 190 (1977).
6. H. S. Johnston, J. Geophys. Res. 82, 1767 (1977).
7. D. T. Pratt and P. C. Malte, AIChE Symp. Ser. 71, 150 (1975).

COMPLEXITY

Hundreds of Reactions, Scores of Free Radicals Valid, Partial Simplification

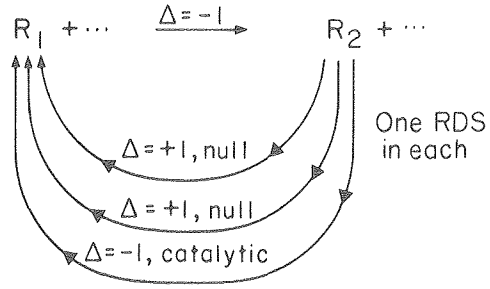

Effect of radical is minute, unless cycled. If cycled, each cycle is either catalytic or null. Rate-Determining steps in catalytic cycles are uniquely important.

Fig. 1. Graphical summary of wherein null and catalytic cycles are the components of stratospheric photochemistry of ozone. The transformed differential equation identifies the rate-determining steps in all catalytic cycles. (XBL782-7020)

$\Delta = +1$ would constitute catalytic formation of odd oxygen. These cycles can be entered at any step. In each cycle there is a rate-determining step, RDS. The rate determining steps in catalytic cycles are uniquely important.

This study gives the first systematic demonstration that one can take the complete (50 term, more or less) differential equation for odd oxygen and derive from it the rate-determining steps of catalytic cycles or consumptive sequences that produce P or cause the loss L of odd oxygen. If one tries to construct the significant cycles by inspection of the mechanism, there are uncertainties both with respect to duplication and omission of processes. By starting with the differential equation, by utilizing group theory of odd and even numbers, and by transforming the differential equation to the irreducible form, one can discover the essential chemical components of these very complex systems, namely the sequences and cycles that change odd oxygen by -2, 0, +2, +4 ···. By comparing terms in the differential equation with atmospheric observations, tables of rate constants, and model calculations, one can separate the complete equation into one that concerns dominant processes and minor ones. This differential equation identifies the important cycles and sequences in the natural ozone balance. These cycles and sequences are listed below.

The first term, $2\ J_1$ in the differential is the rate determining step in the sequence that converts oxygen to ozone

$$j_1 \qquad O_2 + h\nu \rightarrow O + O$$

$$2(O + O_2 + M \rightarrow O_3 + M)$$

$$\text{net:} \qquad 3\ O_2 + h\nu \rightarrow 2\ O_3$$

This sequence represents the dominant source of atmospheric ozone.

The terms $(4\ J_{12} + 2\ J_{13} + 2\ K_{43} - 2\ K_{38})$ in the differential equation represent the methane-NO_x-smog reaction, including the effect of branching, between methane, formaldehyde, and carbon dioxide. Maximum ozone production occurs, namely 4 per CH_4 consumed, if the sequence is

$$CH_3 \xrightarrow{k_{35}} CH_3OO \rightarrow CH_3O \rightarrow H_2CO$$

$$\xrightarrow{j_{12}} H + HCO \rightarrow CO \rightarrow CO_2 .$$

Two ozones are produced per methane consumed if the sequence is either

$$CH_3 \xrightarrow{k_{38}} H_2CO \xrightarrow{j_{12}} H + HCO \rightarrow CO \rightarrow CO_2$$

or

$$CH_3 \xrightarrow{k_{35}} CH_3OO \rightarrow CH_3O \rightarrow H_2CO \xrightarrow{j_{13}} H_2 + CO \rightarrow CO_2$$

$$\xrightarrow{k_{34}} HCO \rightarrow CO \rightarrow CO_2 .$$

No ozone is produced per methane consumed if the sequence is

$$CH_3 \xrightarrow{k_{38}} H_2CO \xrightarrow{j_{13}} H_2 + CO .$$

The formation of ozone from the methane-smog reaction can be written as

$$\left(\frac{d[O_3]}{dt}\right)_{smog} = \left(4\ j_{12} + 2\ j_{13} + 2\ k_{43}[HO]\right)[H_2CO] - 2\ k_{38}[CH_3][O_2] .$$

The concentration of formaldehyde and methyl radicals can be eliminated by means of steady-state relations to give a more readily interpreted expression

$$\left(\frac{d[O_3]}{dt}\right)_{smog} = 2\ A\left(1 + \frac{j_{12}}{j_{12} + j_{13} + k_{43}[HO]} - \frac{k_{38}}{k_{35}[M] + k_{38}}\right)$$

where

$$A = \left(k_{11}[O(^1D)] + k_{30}[HO] + k_{51}[Cl]\right)[CH_4]$$

is the total rate of production of methyl radicals from methane.

The methane-smog reactions are catalytic in NO_x and in HO_x, but represent consumption of methane as a fuel to produce ozone, carbon dioxide, and water

as products. The amount of ozone produced is limited by the amount of methane consumed. These cycles are lengthy and it requires another cycle for each branching path. These cycles have been written out in full but are not included here.

The loss of ozone from O_x reactions involves three couplets of reactions for which the rate determining steps are K_2, K_{44} and K_{61}.

$$k_2 \quad \begin{array}{l} O_3 + h\nu \rightarrow O_2 + O \\ O_3 + O \rightarrow O_2 + O_2 \\ \hline \text{net: } 2\,O_3 + h\nu \rightarrow 3\,O_2 \end{array}$$

$$k_{44} \quad \begin{array}{l} O_3 + h\nu \rightarrow O_2 + O(^1D) \\ O_3 + O(^1D) \rightarrow O_2 + O_2 \\ \hline \text{net: } 2\,O_3 + h\nu \rightarrow 3\,O_2 \end{array}$$

$$k_{61} \quad \begin{array}{l} 2(O_2 + h\nu \rightarrow O_2 + O) \\ O + O + M \rightarrow O_2 + M \\ \hline \text{net: } 2\,O_3 + 2\,h\nu \rightarrow 3\,O_2 \end{array} .$$

The loss of ozone to NO_x reactions involves two catalytic cycles with rate determining steps K_4 and J_{10}.

$$k_4 \quad \begin{array}{l} NO + O_3 \rightarrow NO_2 + O_2 \\ O_3 + h\nu \rightarrow O_2 + O \\ NO_2 + O \rightarrow NO + O_2 \\ \hline \text{net: } 2\,O_3 + h\nu \rightarrow 3\,O_2 \end{array}$$

$$j_{10} \quad \begin{array}{l} NO + O_3 \rightarrow NO_2 + O_2 \\ NO_2 + O_3 \rightarrow NO_3 + O_2 \\ NO_3 + h\nu \rightarrow NO + O_2 \\ \hline \text{net: } 2\,O_3 + h\nu \rightarrow 3\,O_2 \end{array} .$$

The loss of ozone due to HO_x involves five catalytic cycles where the rate determining steps are K_{14}, K_{15}, K_{17}, K_{18}, and K_{19}:

$$k_{14} \quad \begin{array}{l} HO + O_3 \rightarrow HOO + O_2 \\ HOO + O_3 \rightarrow HO + O_2 + O_2 \\ \hline \text{net: } 2\,O_3 \rightarrow 3\,O_2 \end{array}$$

$$k_{15} \quad \begin{array}{l} HO + O_3 \rightarrow HOO + O_2 \\ O_3 + h\nu \rightarrow O_2 + O \\ HOO + O \rightarrow HO + O_2 \\ \hline \text{net: } 2\,O_3 + h\nu \rightarrow 3\,O_2 \end{array}$$

$$k_{17} \quad \begin{array}{l} O_3 + h\nu \rightarrow O_2 + O \\ HO + O \rightarrow H + O_2 \\ H + O_3 \rightarrow HO + O_2 \\ \hline \text{net: } 2\,O_3 + h\nu \rightarrow 3\,O_2 \end{array}$$

$$k_{18} \quad \begin{array}{l} O_3 + h\nu \rightarrow O_2 + O(^1D) \\ O(^1D) + H_2O \rightarrow 2\,HO \\ HO + O_3 \rightarrow HOO + O_2 \\ HO + H_2O_2 \rightarrow H_2O + HOO \\ HOO + HOO \rightarrow H_2O_2 + O_2 \\ \hline \text{net: } 2\,O_3 + h\nu \rightarrow 3\,O_2 \end{array}$$

$$k_{19} \quad \begin{array}{l} O_3 + h\nu \rightarrow O_2 + O(^1D) \\ O(^1D) + H_2O \rightarrow 2\,HO \\ HO + O_3 \rightarrow HOO + O_2 \\ HO + HOO \rightarrow H_2O + O_2 \\ \hline \text{net: } 2\,O_3 + h\nu \rightarrow 3\,O_2 \end{array} .$$

The last two cycles are interesting in that the rate-determining steps do not involve odd oxygen: $HO + HOO \rightarrow H_2O + O_2$ and $HOO + HOO \rightarrow H_2O_2 + O_2$. However, these reactions measure the amount of $O(^1D)$ lost by $O(^1D) + H_2O \rightarrow 2\,HO$ that is not reconverted to odd oxygen, for example by $2\,HO \rightarrow H_2O + O$. It can also be shown from the complete differential equation, that even if HOO is produced from methane oxidation, its loss through K_{18} or K_{19} constitutes a net loss of odd oxygen.

There is one important catalytic cycle involving chlorine and chlorine oxide that destroys ozone,

$$k_{47} \quad \begin{array}{l} Cl + O_3 \rightarrow ClO + O_2 \\ O_3 + h\nu \rightarrow O_2 + O \\ ClO + O \rightarrow Cl + O_2 \\ \hline \text{net: } 2\,O_3 + h\nu \rightarrow 3\,O_2 \end{array} .$$

In the differential equation there are several other minor processes involving nitrogen atoms, N_2O, and other species, which can be shown to be very slow compared to the cases given above. Thus every term in the differential equation can be identified as the rate-determining step in a sequence or cycle that produces two molecules of ozone from three molecules of oxygen or causes the loss of two molecules of ozone.

The rate of ozone production was calculated for each hour of the day and averaged for 59° N, July 22, which corresponds to the time of and latitude of

measurement by Evans et al.[1] The results are given in Fig. 2, including two methods of treating Rayleigh scattering. Similar calculations were made for noon conditions at 30° N, in July, October and December, and these calculations are plotted in Fig. 3.

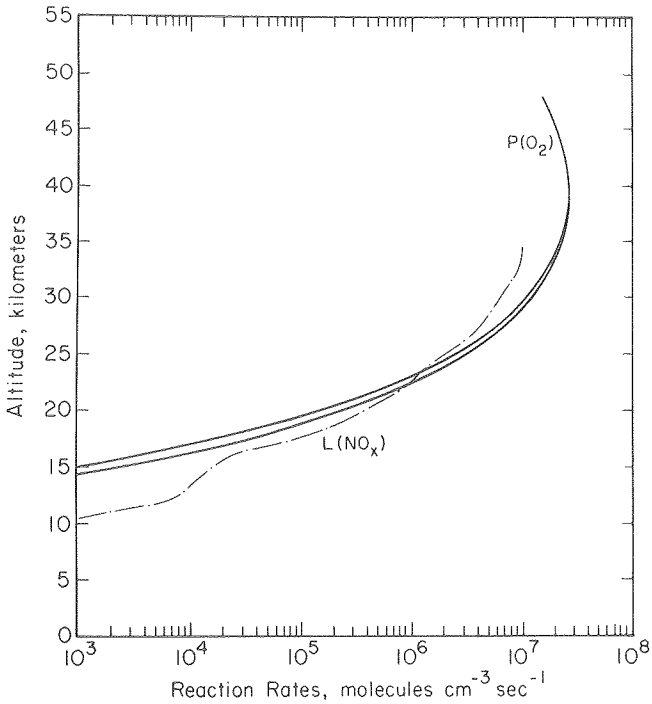

Fig. 2. Rate of ozone destruction L(NO_x) by observed NO_2 (Ref. 1) and calculated atomic oxygen compared with rate of ozone production P(O_2) under same conditions. July 22, noon, solar angle 38.4°, latitude 59° N. (XBL 782-7021)

Ozone is produced from methane at twice the rate of formation of methyl radicals and an additional factor that depends on the branching of formaldehyde potolysis. Methane has been observed in the stratosphere by several groups, and the results were reviewed by Ackerman et al.[2] Anderson observed hydroxyl radicals between 30 and 42 km. As a good approximation, the rate of production of ozone from methane in the middle stratosphere is

$$P_{O_x}(CH_4) = 2.4\ k_{30}[HO]_{OBS}[CH_4]_{OBS}.$$

These rates are entered on Fig. 3. It is evident that the methane-smog reaction is a minor source of ozone in the middle and upper stratosphere. Measured values of hydroxyl radical concentrations are needed in the 10 to 25 km range to establish the rate of ozone and water formation from methane in this region.

Anderson[3] measured the concentration of atomic oxygen in situ in the stratosphere on November 25, 32° N, 56° solar angle. Using the standard winter distribution of ozone and temperature for 30° N, we calculated the atomic oxygen concentration with a

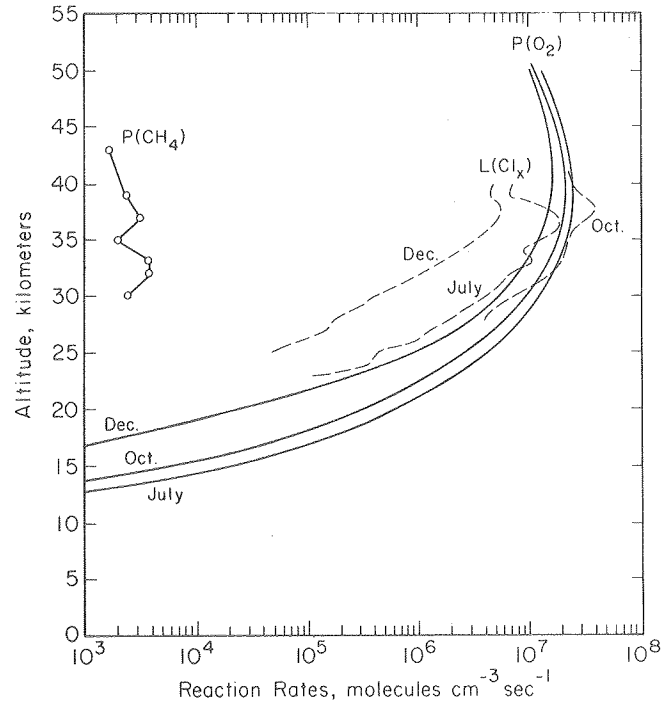

Fig. 3. Production of ozone from O_2 photolysis, P(O_2), as calculated from solar radiation and standard ozone profiles. Destruction of ozone by ClX, L(ClX), as calculated from observed ClO (Ref. 4) and calculated atomic oxygen. Production of ozone from methane-smog reaction P(CH_4) as calculated from observed methane and hydroxyl radicals. (XBL 782-7022)

56° solar angle. Using the standard winter distribution of ozone and temperature for 30° N, we calculated profile of atomic oxygen is plotted in Fig. 4 together with the concentrations observed by Anderson. There appears to be fairly good agreement between calculated and observed atomic oxygen but since the ozone profile is a standard one rather than the simultaneously observed actual one, the agreement or lack of it in Fig. 2 is not highly significant.

The only important reaction whereby odd oxygen is destroyed by odd-oxygen species is 2 $k_3[O][O_3]$. Under conditions by Evans et al.[1] observed ozone and temperature profiles the oxygen-atom concentrations were calculated for 59° N, July 22 noon, are multiplied by the observed ozone concentrations and the rate constant to give the rates of ozone loss L by this process from 10 to 48 km, Fig. 5. These rates are based on observed stratospheric ozone and temperature and on a single-step calculation, namely, the calculated concentration of oxygen atoms. In view of the directness of this calculation, these rates of ozone destruction by O_x reactions are very nearly "observed." This "instantaneous rate" is much closer to observations than the corresponding rate in a model calculation.

The important reaction whereby ozone is destroyed by the oxides of nitrogen is 2 $k_4[O][NO_2]$. Evans et al.[1] observed nitrogen dioxide from a balloon by sighting on the sun at a 90° angle before sunset.

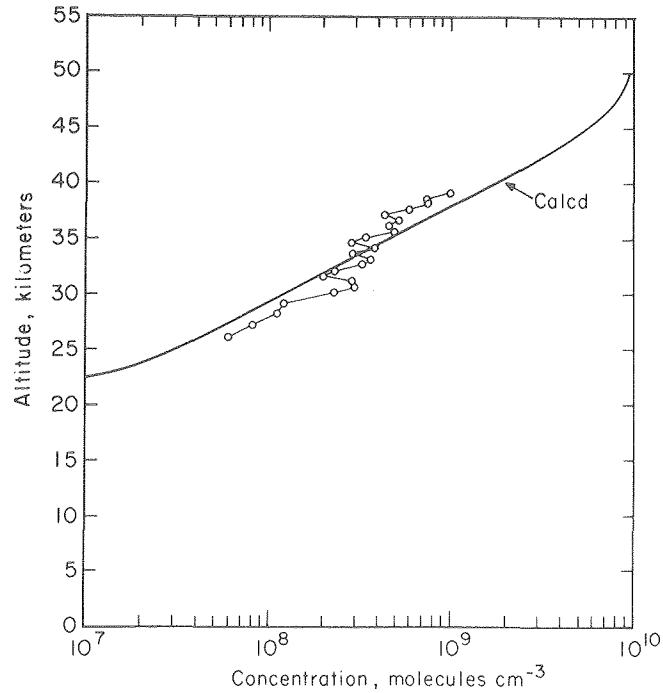

Fig. 4. Observed atomic oxygen (Ref. 3) and calculated atomic oxygen based on standard ozone profile, November 25, 32° N, 56° solar angle. (XBL 782-7023)

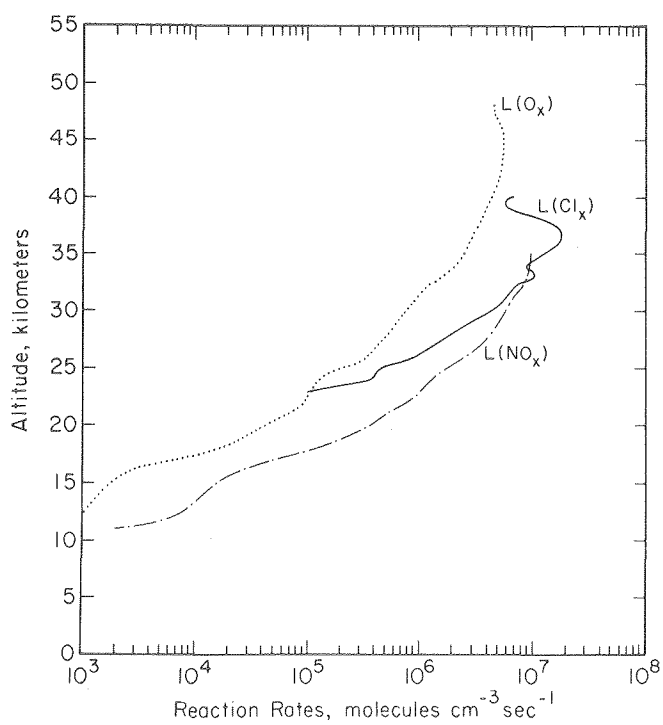

Fig. 5. Comparison of ozone loss rates, based on observed ozone, Evans observed NO_2, Anderson mid-value observed ClO, and on calculated atomic oxygen. Noon. O_x and NO_x, 60° N; ClX, 32° N. (XBL 782-7024)

Evans et al. provided elevation-dependent corrections that convert their observed NO_2 profile to either the day time or the 24-hour average profile. The corrected noon time NO_2 profile is multiplied by calculated oxygen atom concentrations and 2 k_4 to give the rate of ozone destruction by NO_x. This rate is plotted in Figs. 2 and 5.

The rate of ozone production P from 2 $j_1[O_2]$ and ozone loss L from 2 $k_2[O][NO_2]$ are compared in Fig. 2. At noon, 59° N, July 22, NO_x as reported by Evans destroys ozone at about 50 to 60% of the rate of formation between 30 and 35 km, about 60 to 80% between 25 and 30 km, and about 100 to 200% between 20 and 25 km. The ratio between column loss, 20 to 35 km, and column production over the same range is 1.14.

Anderson et al.[4] have reported three in situ measurements of stratospheric ClO, taken on 28 July 1976, 2 October 1976, and 8 December 1976. All were made at 32° N and close to local noon. We used standard ozone distributions for 30° N and for July, September, and January. We based our calculations on solar angles 11°, 34°, and 53°. We calculated oxygen atom concentrations, rates of ozone production P by photolysis of oxygen, and rates of ozone loss L by ClX catalysis. The rates of ozone production and loss for each of the three measurements are given in Fig. 3. A notable aspect about the measured ClO concentration is the wide variability from one case to another. At 40 km, the October value is four times the July or December values. At 35 km the concentrations for Oct/July/Dec vary as 4.7/2.3/0.8. At 30 km these ratios are 5.3/3.0/0.37.

The ratio of integrated ozone loss by ClX to integrated ozone production over the ranges of ClO observations is 0.45 for the July values of ClO, 1.27 for the October values, and 0.25 for the December data.

The integrated loss due to O_x reactions between 25 and 35 km is 10% the integrated ozone photochemical production over the same range. The corresponding figure is 7% for HO_x reactions over the same range, based on model calculations. On the basis of Evans observed NO_2 and O_3, ozone destruction by NO_x relative to ozone formation is 57%. With Anderson middle value of ClO, the profile measured in July, ClX destroys ozone at 40% of its formation rate between 25 and 35 km. In terms of relative rate of ozone destruction and formation between 25 and 35 km, the roles of O_x, HO_x, NO_x (mid values) and ClX (mid values) are as follows:

O_x	0.10
HO_x	0.07
NO_x	0.57
ClX	0.40.

From measured concentrations of NO_2 and ClO, it appears that the principal agents in destroying ozone in the natural stratosphere are the oxides of nitrogen and free radicals containing chlorine. Both appear to be highly important, with O_x and HO_x being distinctly less important in the mid-stratosphere "ozone formation region." From the mid-values of published measurements of NO_2 and ClO, it appears that the NO_2, ClO, and O_3 are sufficient to destroy

ozone as fast as it is formed in the range 23 to 35 km. There is no need to invoke any new or unknown sink for ozone in this region, if the mid-values of measured NO_2 and ClO are representative of the global average.

This study is another application of the "method of instantaneous rates." [5,6] This method takes atmospheric measurements, and in a simple, separable, one-step calculation derives consequences. In certain cases, firm conclusions (within the accuracy of the atmospheric measurements) can be reached concerning components of the total problem, long before the total problem itself is solved. This method does not displace model calculations, but it is supplementary to such calculations. This method is especially useful in the interpretation of atmospheric observations, in the design of programs of future atmospheric observations, and in finding the meaning of the mountains of computer printout from model calculations.

---

1. W. F. J. Evans, J. B. Kerr, D. I. Wardle, J. C. McConnell, B. A. Ridby and H. I. Schiff, Atmosphere 14, 189 (1976).
2. M. D. Rimout Ackerman and C. Muller, Aeromica Acta 180, 1 (1977).
3. J. G. Anderson, Geophys. Res. Lett. 2, 231-234 (1975).
4. J. G. Anderson, J. J. Margitan and D. H. Stedman, Science 198, 501 (1977).
5. H. S. Johnston and G. Whitten, Pure Appl. Geophys. 106-108, 1468 (1973).
6. H. S. Johnston, Rev. Geophys. Space Phys. 13, 637 (1975).

7. RESEARCH PLANS FOR CALENDAR YEAR 1978

a. Primary Products and Quantum Yields in Pulsed Laser Photolysis

Frank Magnotta and David Littlejohn

By the method of pulsed, tunable, doubled, dye laser photolysis and resonance-fluorescence detection, primary products and quantum yields will be studied for the following photochemical reactants: NO_2 (calibration, detection of NO and O); NO_3 (detection of NO and O); N_2O_5 (detection of NO and O); HNO_3 (detection of HO and O).

b. Completion of the Study of $O(^1D)$ Quantum Yield from Ozone as a Function of Wavelength and Temperature

John Girman

Ozone is being flash photolyzed at various wavelengths between 300 and 330 Nm by a doubled tunable dye laser. The singlet oxygen atom $O(^1D)$ reacts very rapidly with molecular oxygen to produce excited singlet sigma molecular oxygen, which slowly emits characteristic visible radiation. The quantity of $O(^1D)$ produced is measured by this emitted radiation. The wavelength and temperature dependence of the $O(^1D)$ production is being studied.

c. Studies of HOO Reactions in the Molecular Modulation Apparatus

James Podolske

Our remodeled, long-path, infrared or ultraviolet molecular modulation spectrometer will be used to study the photochemistry and kinetics of the HOO radical, which can be detected by its intense diffuse ultraviolet spectrum or by its sharp near infrared electronic spectrum. Reactions of particular interest are: $HOO + HOO \rightarrow H_2O_2 + O_2$, $HOO + HO \rightarrow H_2O + O_2$, $HOO + O_3 \rightarrow HO + O_2 + O_2$.

d. Reactions of Peroxy-Nitric Acid

Carleton Truesdale

Peroxy-nitric acid is in rapid equilibrium with its dissociation products HOO and NO_2

$$HOONO_2 \rightleftharpoons HOO + NO_2.$$

An added substance that reacts rapidly with HOO causes the irreversible decomposition of peroxy-nitric acid, for example

$$\begin{array}{ll} & HOO + NO \rightarrow HO + NO_2 \\ & HO + NO_2 \rightarrow HNO_3 \\ \hline \text{net:} & HOONO_2 + NO \rightarrow HNO_3 + NO_2 \end{array}$$

We plan to added other substances of interest such as ozone or olefins to get information about the reactivity of the HOO radicals.

e. Fluorescence and Other Spectroscopic Studies of Nitrous Oxide in the Vacuum Ultraviolet Spectral Region

Gary Selwyn

Moderately high resolution vacuum ultraviolet spectra of N_2O show some unexpectedly sharp fine structures. This spectrum is being studied both in absorption and by excitation of long-wavelength fluorescence.

f. Infrared Emission from Fast Cyclic Photochemical Reactions

David Littlejohn

The fastest reaction of ozone in the atmosphere is its null cycle

$$\begin{array}{ll} & O_3 + h\nu \rightarrow O_2 + O \\ & O + O_2 + M \rightarrow O_3 + M \\ \hline \text{net:} & \text{null} \end{array}$$

The fastest reactions of nitrogen dioxide in the atmosphere is its null cycle

$$NO_2 + h\nu \rightarrow NO + O$$

$$O + O_2 + M \rightarrow O_3 + M$$

$$NO + O_3 \rightarrow NO_2 + O_2$$

net: null

The cycled molecules O_3 and NO_2 are reformed in highly excited vibrational states. We plan to study infrared emission from $O_3(v^*)$ and $NO_2(v^*)$ under upper atmospheric conditions, both to study the vibrational cascading mechanism and to see if there is significant extra chemical reactivity in these excited molecules.

g. Theoretical and Interpretive Studies

H. S. Johnston, M. Kowalczyk, J. Podolske and D. Littlejohn

By now there are enough observations of atmospheric nitrous oxide to provide an estimate of the global distribution from the ground to the upper stratosphere. With our method of "instantaneous rates" we are studying the locus of photolysis and chemical reactions of N_2O, based on the observed distribution. As new measurements of atmospheric HO, HOO, ClO, and NO_2 are produced, we plan to carry out :instantaneous rate" interpretations of these data. We plan to continue investigating the chemical mechanism for the formation of nitrous oxide from combustion. Our chemical kinetics computer program will be extended to include variation of temperature under constant pressure conditions.

8. 1977 PUBLICATIONS AND REPORTS

Harold S. Johnston and Associates

Journals and Articles

1. H. S. Johnston, Analysis of the Independent Variables in the Perturbation of Stratospheric Ozone by Nitrogen Fertilizers, J. of Geophys. Res. 82, 1767 (1977), LBL-5488.

2. H. S. Johnston and H. Nelson, Comment on "NO_x Catalytic Ozone Destruction: Sensitivity to Rate Coefficients" by W. H. Duewer, D. J. Wuebbles, H. W. Ellsaesser, and J. S. Chang, J. of Geophys. Res. 82, 2593 (1977).

3. H. S. Johnston, Expected Short-Term Local Effect of Nuclear Bombs on Stratospheric Ozone, J. of Geophys. Res. 82, 3119 (1977), LBL-5460.

4. G. Selwyn, J. Pdolske and H. S. Johnston, Nitrous Oxide Ultraviolet Absorption Spectrum at Stratospheric Temperatures, Geophys. Res. Lett. 4, 427 (1977), LBL-6284.

Presented Papers

1. "Stratospheric Ozone," Naval Reserve Laboratory Meeting, Washington, D.C., April 1977.

2. "Atmospheric Nitrous Oxide," Marcel Nicolet Honorary Symposium, The Queen's University, Belfast, North Ireland, July 7, 1977.

3. "Calculated and Observed Distributions of Stratospheric Trace Species," Fifth International Symposium on Gas Kinetics, University of Manchester, Institute of Science and Technology, Manchester, England, July 12-14, 1977.

LBL Reports

1. Richard A. Graham and Harold S. Johnston, The Photochemistry of NO_3 and the Kinetics of the N_2O_5-O_3 System, LBL-6276, May 1977.

b. Radiation Chemistry of Heavy Particles

*Michael E. Jayko**

1. INTRODUCTION

Michael E. Jayko

*The following people have collaborated on this project:

- A. Appleby, visiting scientist from Rutgers University
- E. Christman, visiting scientist from Rutgers University
- A. Chatterjee, Biomedical Division, Donner Laboratory
- J. Magee, Biomedical Division, Donner Laboratory
- H. Sokol, Materials and Molecular Research Division.

Dr. Warren Garrison, who was the principal investigator in radiation chemistry, retired in June of this year after serving many years in this position.

The radiation chemistry of aqueous systems under irradiation with carbon, neon and argon beams from the Bevalac has been investigated. The study was undertaken as part of a program to determine the chemical properties of accelerated heavy particles. Systems were chosen that were well established in radiation chemistry and were most likely to provide basic data for the illumination of heavy-particle tracks. This is part of a larger program that is designed to better understand the processes involved in energy absorption from the initial physical effects that are complete in approximately 10^{-12} s and the biological effects that occur from several minutes to several years after irradiation.

Initial products in irradiated aqueous systems are hydrated electrons (e^-_{aq}), H atoms, OH radicals, and H_3O^+ ions produced in the particle track. These intermediates result in the primary molecular products H_2 and H_2O_2, and primary radical products, which are the ones that escape the initial track. The intermediates are formed in high concentration in the track; their initial concentration distribution is dependent on the quality of the radiation, i.e., the particle, its LET, charge, etc. These products can be studied with classical radiation chemistry systems using scavengers, taking into consideration that certain assumptions made for low LET radiation may not be valid when 10^2 to 10^3 eV/A are being absorbed. When large amounts of energy are deposited in small volumes (for example more than 50 eV/A), it is reasonable to assume additional effects are being produced.

Chemical systems were irradiated in cells designed to obtain measurable yields of product in the shortest irradiation time within the constraints imposed by the Bevalac. Cells were used in matched sets with quartz windows 1.65 to 1.80 mm thick, 3.2 cm in diameter, necks 10 cm long with ground glass stoppers, a depth of 1 cm, and containing 8.3 ml of target solution. Two techniques were used to irradiate the cells simultaneously: 1) the entire Bragg curve was measured in some cases using up to 16 cells, or 2) the beam was degraded before entering the first cell by the variable water column. Initially the location of the Bragg peak was determined experimentally; however, by using a factor of 1.838 to compare the relative stopping power of water and quartz the Bragg peak could be placed at any desired position to within ± 0.5 mm.

At present the uncertainties in the value of G are greater than ± 5%. The greatest contribution to this uncertainty is the lack of quantitative knowledge of nuclear fragmentation of the incident beam. It is not possible at this time to extract beams of lower energy from the Bevalac; a water column is currently used to reduce the beam energy and this introduces nuclear fragmentation. In any case, at the present time we cannot be entirely free of nuclear fragmentation since even without the water column the beam must penetrate 2 g/cm^2 of absorbing material before it gets to the first ion chamber. The range and shape of the Bragg curves may change under actual experimental conditions and since the dose we calculate for each cell is a product of the entrance dose and the relative ionization at the point in the Bragg curve corresponding to the location of the cell of interest, these variations must be considered very carefully.

We have so far studied five different systems for each of the three particles: carbon, neon, and argon.

Table 1. System studied.

$FeSO_4(10^{-2}M)/H_2SO_4(0.4M)/air$
$FeSO_4(10^{-2}M)/H_2SO_4(0.4M)/N_2$
$HCOONa(5x10^{-3}M)/air$
$NaBr(10^{-3}M)/air$
C_2H_5OH (0.025M)/$NaNO_3$(0.0025M)/N_2

The first two systems are at low pH and the ferric oxidation yields (expressed in molecules/100 eV deposited) are related to the primary H_2O_2, OH, H, and hydrated electron yields as shown in Eqs. (1) and (2).[1,2]

$$G\,(Fe^{3+})O_2 = 2G_{H_2O_2} + G_{OH} + 3G_H + 3\,G_{e^-_{aq}} \qquad (1)$$

$$G\,(Fe^{3+})N_2 = 2G_{H_2O_2} + G_{OH} + G_H + G_{e^-_{aq}} \qquad (2)$$

The total reducing radical yield is derived from Eq. (3).

$$G_H + G_{e^-_{aq}} = \tfrac{1}{2}\left[G\,(Fe^{3+})O_2 - G(Fe^{3+})N_2\right] \qquad (3)$$

The water decomposition yield is derived from Eq. (4).

$$G_{H_2O} = 2G_{H_2O_2} + G_{OH} = \tfrac{1}{2}\left[3G\ Fe^{3+}N_2 - GFe^{3+}O_2\right] \qquad (4)$$

In aerated sodium formate, hydrogen peroxide measured is formed according to Eq. (5)[2]

$$G(H_2O_2)_{HCOO^-} = G_{H_2O_2} + \tfrac{1}{2}\,G_{OH} + \tfrac{1}{2}\,G_{e^-_{aq}} + \tfrac{1}{2}G_H \qquad (5)$$

In sodium bromide the OH radical reacts differently:[4]

$$G(H_2O_2)_{Br^-} = G_{H_2O_2} - \tfrac{1}{2}G_{OH} + \tfrac{1}{2}G_H + \tfrac{1}{2}G_{e^-_{aq}} \qquad (6)$$

Thus the difference between the observed yields of the formate and the bromide systems is equal to the yield of the OH radical.

In deaerated ethanol/nitrate solutions the hydrated electron reacts to convert the nitrate anion to nitrite:[5]

$$G\ NO_2^- = f\ G_{e^-_{aq}} \qquad (7)$$

The factor f depends on the concentration of ethanol and nitrate, but in the system used it is essentially equal to the hydrated electron yield.

Using the systems so far studied, we can derive the OH and hydrated electron yield in neutral solution and the reducing radical and water decomposition yield in acidic solution.

Figure 1 shows the preliminary results for the two ferrous sulfate systems. The yields are plotted against the mean ion energy for each of the 1-cm sample cells. The G values are calculated from the slopes of linear plots of chemical yield vs dose, each plot having at least four data points. Between two and six runs were made, and this data represents the averages; the error bars represent one standard deviation.

For all ions the ferric yield decreases as the beam energy decreases and there is a reduction in yield as the Z increases. Figure 2 shows the H_2O_2 yield from formate behaving similarly but the H_2O_2 from bromide solutions is less dependent. This is to be expected qualitatively since H_2O_2 yields in the bromide systems are greatly affected by the molecular H_2O_2 yield. It has been shown previously that molecular H_2O_2 is less dependent on ionization density than the radical yields and that it increases slightly with ionization density.

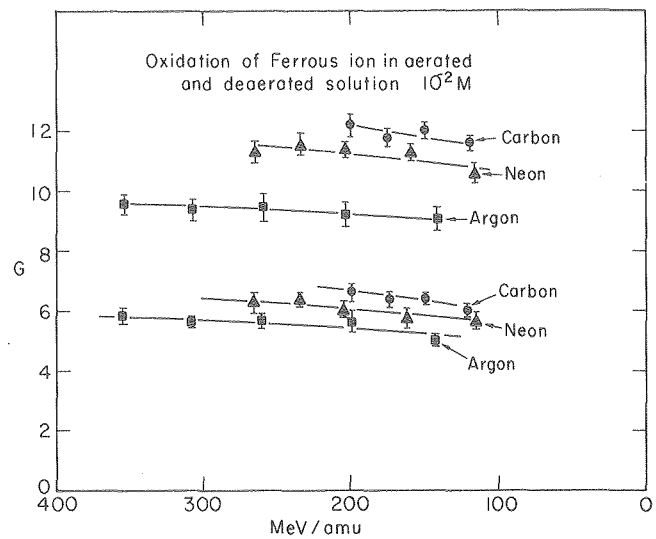

Fig. 1. Preliminary results for the two ferrous sulfate systems: the top group is aerated; the bottom group is deaerated. (XBL 775-3388)

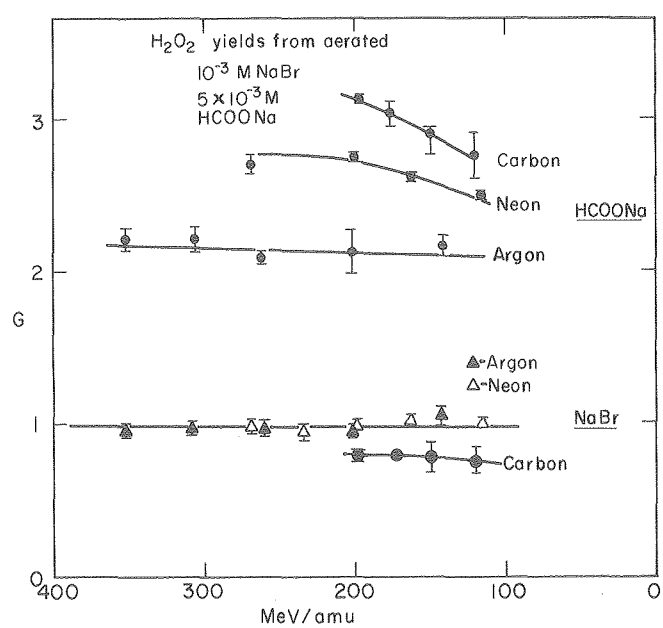

Fig. 2. Hydrogen peroxide yields from aerated HCOONa (top) and NaBr (bottom). (XBL 775-3384)

The nitrate yields from oxygen-free ethanol/nitrate solutions are shown in Fig. 3. This is essentially the hydrated electron yield.

With this information we can derive some individual primary yields or combinations of them. For example, Fig. 4 shows the quantity calculated in Eq. (3), which, according to classical radiation chemistry, gives the yield of reducing free radicals that escape the spurs. The thick lines are from the experimental values; the thin lines represent a confidence interval of one standard deviation (± 5 - 7%).

The difference between the H_2O_2 yields of the neutral formate and bromide solutions is shown in Fig. 5. According to generally accepted reaction mechanisms for these two systems, this difference should be equal to the OH radical yield.

Figure 6 shows the total water decomposition yield using Eq. (4) errors are greater (± 8%) since this is a difference between numbers of a similar magnitude.

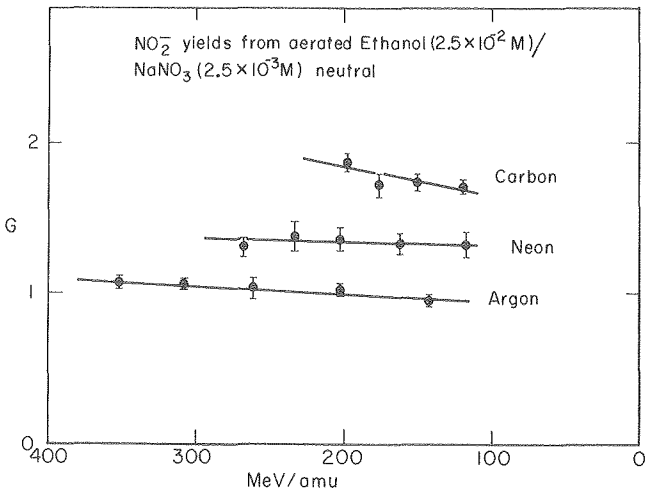

Fig. 3. NO_2^- yields from deaerated ethanol (2.5×10^{-2} M)/$NaNO_3$ (2.5×10^{-3} M) neutral. (XBL 775-3386)

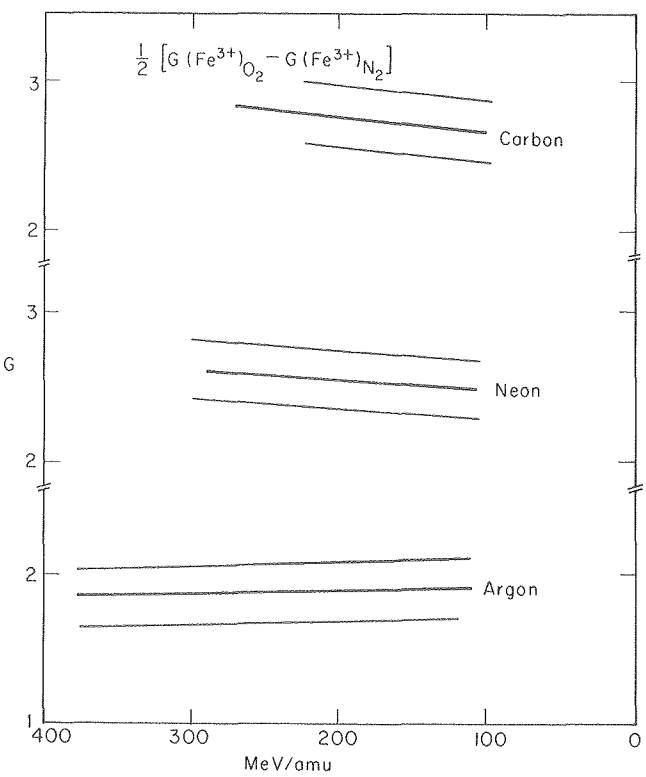

Fig. 4. The yield of reducing free radicals that escape the spurs. (XBL 7710-3897)

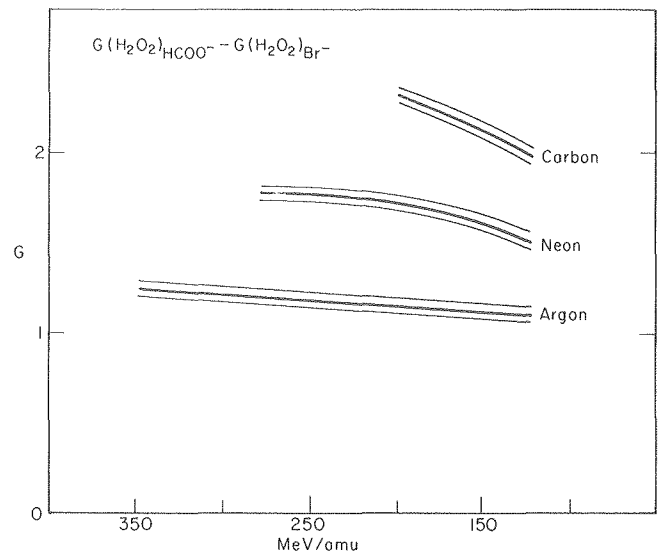

Fig. 5. OH radical yield. (XBL 7710-3896)

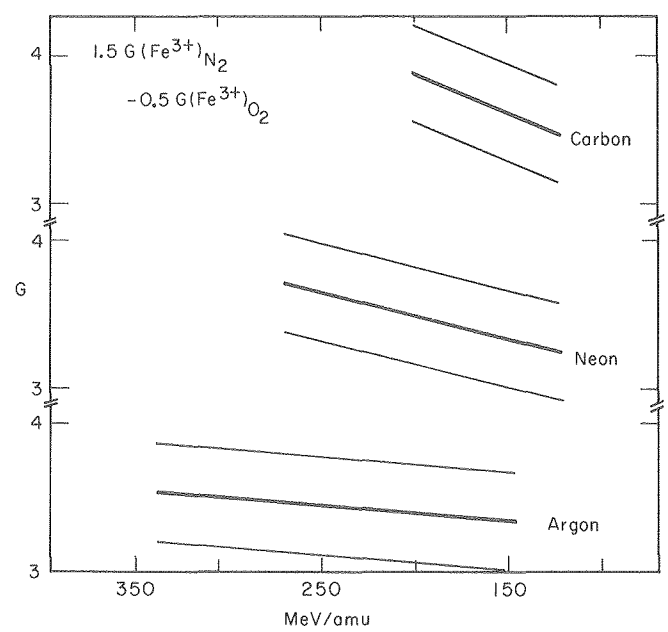

Fig. 6. Total water decomposition in acid. (XBL 778-3681)

The observed decrease in radical yields as the beam penetrates is consistent with what has been seen previously for lower Z and is what one expects qualitatively. As an ion slows down its rate of energy loss increases and less energetic secondaries are produced. Radical recombinations are favored so the radical yields tend to decrease, as do the yields of those products that are principally derived from radicals, such as ferric ion, nitrite, and H_2O_2 from formate solutions. More highly charged particles of the same velocity will produce more secondary electrons per unit path length traveled, with more liklihood of radical overlap and recombination with fewer radicals available for reaction with solutes.

---

1. Robert H. Schuler and Augustine O. Allen. Radiation Chemistry Studies with Cyclotron Beams of Variable Energy: Yields in Aerated Ferrous Sulfate Solutions, J. Amer. Chem. Soc. 79, 1565 (1957).
2. Edwin J. Hart, Warren J. Ramler and Sol R. Rocklin, Chemical Yields of Ionizing Particles in Aqueous Solutions: Effect of Energy of Protons and Deuterons, Rad. Research 4, 378 (1956).
3. A. R. Anderson and Edwin J. Hart, Molecular Product and Free Radical Yields in the Decomposition of Water by Protons, Deuterons, and Helium Ions, Rad. Research 14, 689 (1961).
4. Augustine O. Allen and Richard A. Holroyd, Preoxide Yield in the Gamma Irradiation of Air-Saturated Water, J. Amer. Chem. Soc. 77, 5852 (1955).
5. Z. D. Draganic and I. G. Draganic, Studies on the Formation of Primary Yields of Hydroxyl Radical and Hydrated Electron in the Gamma-Radiolysis of Water, J. Phys. Chem. 77, 765 (1973).

2. 1977 PUBLICATIONS AND REPORTS

Michael E. Jayko and Associates

1. Michael Jayko, Edward Christman, Aloke Chatterjee and Alan Appleby, Radiation Chemistry of Accelerated Heavy Particles. I. Experimental Arrangements and Results for the Fricke Dosimeter, Radiation Research Society Meeting, San Juan, Puerto Rico, May 8-12, 1977.

2. Alan Appleby, Michael Jayko, Edward Christman and Aloke Chatterjee, Radiation Chemistry of Accelerated Heavy Particles. II. Yields of Primary Species in Water, Radiation Research Society Meeting, San Juan, Puerto Rico, May 8-12 1977.

3. Aloke Chatterjee, John L. Magee and Michael Jayko, Radiation Chemistry of Accelerated Heavy Particles. III. Model Calculations of Chemical Yields, Radiation Research Society Meeting, San Juan, Puerto Rico, May 8-12,1977.

4. Harvey Sokol, Detection of N-acetylglycine, N-acetylglycylglycine, and N-acetylglycylglycylglycine by Paper Chromatography, LBL-6954, October 1977.

5. Harvey Sokol and Warren Garrison, Determination of Pyruvic and Glycylic Acids in the Presence of Acetaldehyde, Anal. Chim. Acta 89, 407 (1977).

6. Michael E. Jayko, Alan Appleby, Edward Christman, Aloke Chatterjee and John L. Magee, Radiation Chemistry of Particles Accelerated by the Bevalac, LBL-6681.

c. Photon-Assisted Surface Reactions on Well-Characterized Surfaces

Gabor A. Somorjai, Principal Investigator

1. LIGHT-ASSISTED SURFACE REACTIONS: THERMODYNAMICALLY UPHILL CATALYSIS

John Hemminger, Roger Carr and Gabor A. Somorjai

Several semiconductors have been shown to be effective photoassisted catalysts for thermochemically uphill reactions. TiO_2, GaP and $SrTiO_3$ as well as other materials have been shown to be capable of the photoassisted electrolysis of water when used as electrodes in solution. An electrochemical cell, utilizing $SrTiO_3$ as the anode, photolytically decomposes water without an external voltage when band gap radiation is incident of the $SrTiO_3$ (band gap ~3.2 eV).

The mechanism of the photoassisted decomposition of water on $SrTiO_3$ involves the production of electrons and holes in the $SrTiO_3$ with band gap radiation. These electrons and holes then assist the reaction at the solid surfaces. However, at present little is known of the detailed mechanism of this process.

We have modified a commercial LEED, AES surface analysis system by the addition of an isolation cell for the crystal. This allows us to run photoassisted reactions on well-characterized surfaces at up to 1 atm pressure. We are presently using this apparatus to explore the possibility of using $SrTiO_3$ to photoassist several thermochemically uphill reactions in the gas phase.

For example:

$$C + 2H_2O + h\nu \rightarrow CO_2 + 2H_2$$

$$CO_2 + 2H_2O + h\nu \rightarrow CH_3OH + 3/2O_2$$

$$\rightarrow CH_4 + 2O_2$$

$$H_2O + h\nu \rightarrow H_2 + 1/2O_2$$

$$N_2 + 3H_2O + h\nu \rightarrow 2NH_3 + 3/2O_2$$

By studying the kinetics of these reactions as well as the effects of surface preparation, we hope to be able to better understand the detailed mechanisms of photoassisted catalytic reactions at semiconductor surfaces.

Using this knowledge we should be able to develop materials with suitable surface structure and composition to optimize the photo-assisted reaction rates and product distributions.

2. SPECTRAL SENSITIZATION OF SEMICONDUCTOR SURFACES BY ORGANIC DYES

Roger Carr and Gabor A. Somorjai

Wide band-gap semiconductors such as TiO_2 and $SrTiO_3$ resist corrosion in photoelectrochemical cells, but can convert only short wavelength light into useable electric currents. Additional currents may be injected into the semiconductor by an organic dye with spectral response in longer wavelengths. Indeed we have found that dye, crystal violet, appears to enhance the photoconductivity of $SrTiO_3$. It is likely that other dyes and other semiconductors will be found to exhibit this behavior; dyes are presently used to sensitize silver halides and ZnO. If it is possible to design sensitized ohotoelectrodes, we shall be able to carry out non-biological (inorganic) photosynthesis, using a substantial portion of the solar spectrum. We study the adsorption of organic dyes and their photoresponse on $SrTiO_3$ crystal surfaces in ultrahigh vacuum, and characterize our surfaces well, using Auger electron spectroscopy; this procedure eliminates many of the problems encountered in studies of organic photosensitization of electrochemical cells (solid-liquid interfaces) and reveals much about the detailed mechanisms of the photoresponse.

3. RESEARCH PLANS FOR CALENDAR YEAR 1978

Gabor A. Somorjai

The photon-assisted reactions of CO_2, H_2O and N_2 will be explored using a large variety of semiconductor oxide surfaces. The metal contacts necessary to carry out photon-chemical reactions will be changed from platinum to the use of other transition metals: nickel, rhodium and iron.

4. 1977 PUBLICATIONS AND REPORTS

Gabor A. Somorjai and Associates

Journal

1. Y. W. Chung, W. J. Lo and G. A. Somorjai, LEED and Electron Spectroscopy Studies of the Clean (110) and (100) Titanium Dioxide (Rutile) Crystal Surfaces, Surf. Sci. 64, 588 (1977), LBL-5704.

Talks

1. G. A. Somorjai, Recent Achievements and Trends in Catalysis Science, at the National Science Foundation, Washington, D.C., February 3, 1977.

2. G. A. Somorjai, Catalysis by Transition Metals--Pt, Fe and Rh, at the University of California, Santa Barbara, California, February 10, 1977.

3. G. A. Somorjai, Active Sites for Heterogeneous Catalysis, at the University of California, Irvine, California, February 28, 1977.

4. G. A. Somorjai, Structure of Oxide Surfaces, at the Gordon Conference on Solid State Studies in Deramics, New Hampshire, August 1, 1977.

5. G. A. Somorjai, Energy Conversion and Storage by Heterogeneous Catalysis, at the IUPAC Meeting, Tokyo, Japan, August 26, 1977.

LBL Reports

1. Y. W. Chung, W. J. Lo and G. A. Somorjai, Electron Spectroscopy Studies of Light Induced Chemisorption of Oxygen, Hydrogen and Water on the $TiO_2(100)$ Surfaces: Evidence for Photogeneration of Ti^{+3} Species and Its Importance for Chemisorption, LBL-6257, June 1977.

2. Y. W. Chung, W. J. Lo, J. C. Hemminger and G. A. Somorjai, The Photoassisted Decomposition of Gas Phase Water Adsorbed on $SrTiO_3$, LBL-6627, August 1977.

2. CHEMICAL PHYSICS

a. Energy Transfer and Structural Studies of Molecules on Surfaces

Charles B. Harris, Principal Investigator

1. INTRODUCTION

Charles B. Harris

In the past year our laboratory has been engaged in developing several new methods for investigating a variety of problems associated with the electronic and molecular structure of molecules adsorbed on single-crystal metal surfaces. The first of these is scanning ellipsometric spectroscopy applied to physi- and chemisorption of molecules on Ni(111) at low temperatures. We have built an ultrahigh vacuum chamber capable of operating over a range of 4 to 450 K, maintaining a background pressure of better than 10^{-11} Torr. In addition it has associated with it the standard surface techniques of LEED, Auger, and quadrupole mass spectra so that the results of the ellipsometric experiments can be correlated with the composition and strucutre of the adlayer. In addition, we have solved the coupled boundary value equations to determine the optimum geometry in the experiments and to assess what sort of signal-to-noise we can expect for various coverages of molecules having different oscillator strengths in their transitions. This project has involved a considerable amount of instrumentation and is now completely operational. The results from a variety of experiments on Ni(111) are presented in Sections 2a through 2e of this report.

The second area that we have been developing is the use of picosecond spectroscopy for studying energy transfer and relaxation processes in condensed phase and on metal and semiconductor surfaces. For these studies we have constructed a selected single-pulse Nd laser having transform-limited pulses of 5 ps. Results on vibrational energy transfer and relaxation in liquid and solid phases are presented in Section 3. The important questions to ascertain in condensed phase are whether or not energy transfer processes in solids at room temperature reflect the periodic potential of the solid or whether thermal motion gives rise to energy transfer processes similar to those in liquids.

Finally we are continuing some research in the area of energy transfer processes of molecular solids using the coherent spin resonance techniques that have been developed in the laboratories over the past three years. The advances in this area speak for themselves, as most of the published work from this laboratory in the past three years has been associated with this project.

2. THE SPECTROSCOPY OF MOLECULES ADSORBED ON METAL SURFACES

a. Temperature-Dependent Studies of Nickel (111) Surface Oxidation and Reconstruction

C. B. Harris, A. R. Gallo, H. J. Robota and D. A. Zwemer

Oxidation and corrosion are among the most familiar and important surface chemical processes for metals. In the past year we have begun an investigation of the oxidation of the nickel (111) surface by O_2, NO, and NO_2 and have been able, for the first time, to observe separately the different stages of the oxidation process, e.g., deposition, reaction, surface reconstruction. Our experimental method combines optical ellipsometry with ultrahigh vacuum surface analysis techniques and a variable temperature sample probe. Ellipsometry is the measurement of the state of polarization of light reflected from a surface and gives both the thickness and refractive index of an overlayer on that surface continuously and nondestructively.

A major thrust of our first experimental work has been to correlate the results of ellipsometry with other surface-sensitive techniques. The ultrahigh vacuum chamber with LEED and Auger electron optics allows us to reproducibly clean, characterize, and maintain single-crystal surfaces, and to compare our results with those of other investigators using complementary techniques. By LEED and XPS it has been shown that initial oxygen exposure to Ni(111) forms a (2×2) overlayer up to one-quarter monolayer coverage, and further exposure forms a $(\sqrt{3}\times\sqrt{3})$ R30° overlayer up to one-third of a monolayer. Figure 1 shows the change in Δ, an ellipsometric parameter which is linear in overlayer thickness here, for oxygen exposure. The initial rise represents the formation of the (2×2) overlayer, and the slower increase shows the more unfavorable compression of the adsorbate surface structure to $(\sqrt{3}\times\sqrt{3})$ R30°. The first stage may be fit to a Langmuir adsorption curve in order to calibrate the oxygen flux at the surface. This experiment establishes that we can with great sensitivity observe an already well-characterized oxidation process and relate our results to the results of other complementary techniques.

More importantly, the techniques can provide new information. Oxidation consists of several possible

successive steps: deposition (physisorption or condensation of the oxidant), chemisorption, decomposition of the oxidant, and surface reconstruction of either the metal or an oxide overlayer. At room temperature as in Fig. 1 for O_2 or Fig. 2 for NO_2, the steps cannot be elucidated. Our experiments involve cooling the metal surface to liquid helium temperatures, depositing the oxidant in thicknesses from partial monolayer to hundreds of layers, and allowing the crystal to warm up slowly. The steps in the oxidation process with the lowest activation energy will tend to occur at the lowest temperatures, and so the individual steps will be separated in temperature. Also, at low temperatures we can produce the high surface concentrations corresponding to real systems in nature. Our experimental results for NO and NO_2 are in Figs. 3 and 4, respectively.

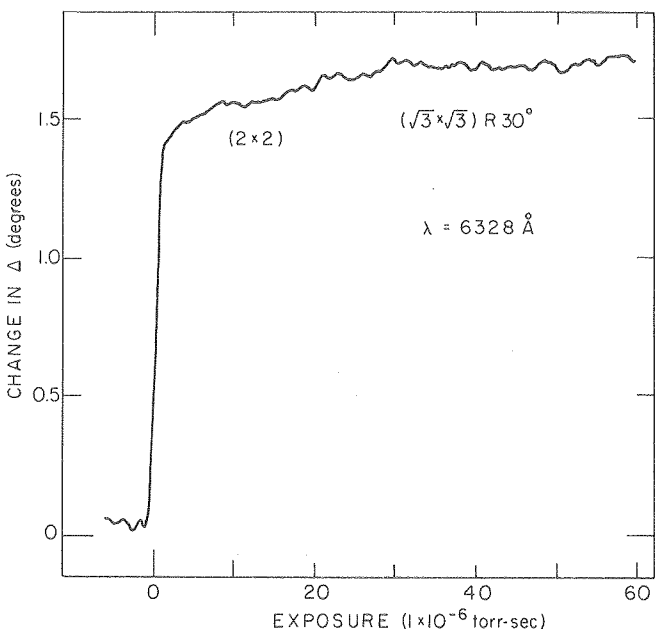

Fig. 1. Change in surface optical parameter Δ during extended exposure of Ni(111) surface of O_2 at 280 K. Observed LEED surface structures are indicated. The initial increase in Δ, which is linear in overlayer thickness, obeys Langmuir adsorption kinetics. (XBL 7711-6432)

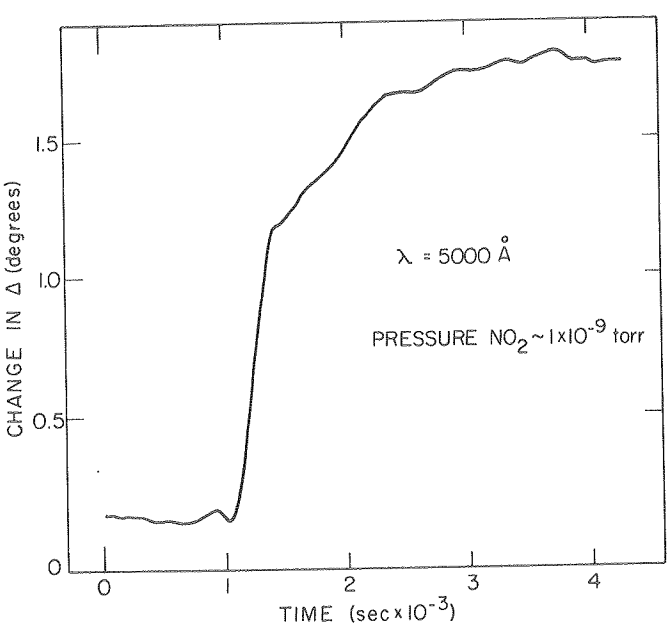

Fig. 2. Change in Δ during exposure of Ni(111) to NO_2 at 280 K. (XBL 7711-6425)

Several conclusions can already be drawn from the data shown here.

(1) Several different effects can be observed in each graph. The sharp initial rise is the deposition; the sublimation of the condensed oxidant is the major drop on warming. The other changes, all of which are experimentally reproducible, represent other processes such as dimerization, chemisorption, or decomposition (which will be discussed in the next section), reconstruction, etc. Note that they have been at least partially resolved in time and are separately amenable to investigation not only by ellipsometry, but by all surface techniques.

(2) The final state is different from the initial clean state, and the final state, which Auger shows in each case to be an oxide layer, is thicker

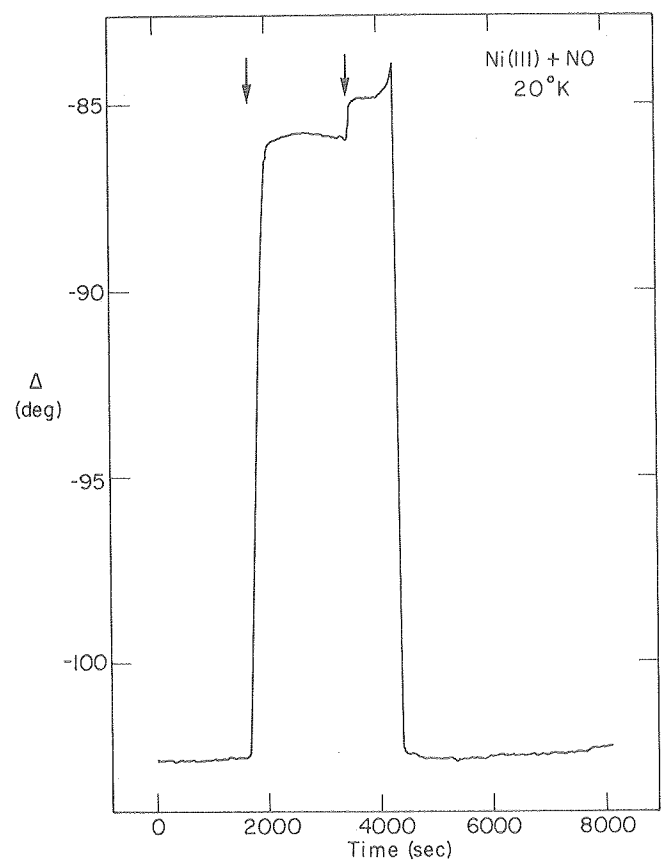

Fig. 3. Change in Δ for deposition of NO on Ni(111) at 20 K and subsequent warming. The two arrows indicate introduction of NO to vacuum system and cut-off of coolant flow to sample. (XBL 779-6109)

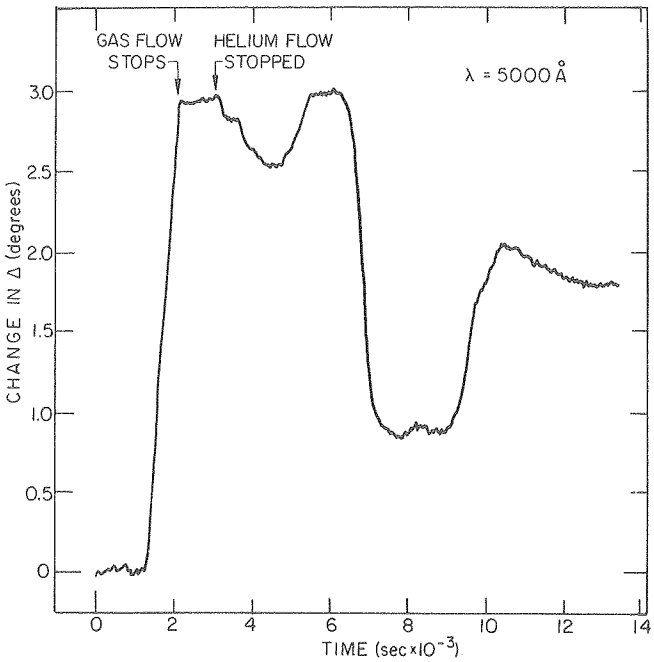

Fig. 4. Change in Δ for deposition of NO on Ni(111) at 20K and subsequent warming. Temperature range is ~20 - 170K. (XBL 7711-6431)

for NO_2 than for NO or O_2 (not shown). On the other hand, the final state for NO_2 in Figs. 2 and 4 is about the same, indicating that the oxidation processes we observe at low temperatures are the same, although faster, at room temperature.

(3) The final abrupt change in Fig. 4 represents an increase in the overlayer thickness from 2 to 7 Å. No new material is being deposited on the surface, so this change indicates a surface reconstruction, perhaps the dissolving of surface oxygen into the bulk. A similar state in the NO and O_2 systems has not been unambiguously established.

The next section will give additional examples to elucidate separate stages of the oxidation process.

b. Catalytic Decomposition of Nitrogen Oxides: Investigations Using Ellipsometry, LEED, and Auger Electron Spectroscopy

C. B. Harris, A. R. Gallo, H. J. Robota and D. A. Zwemer

In the past year we have applied the techniques of spectroscopic ellipsometry to study the well-characterized catalytic decomposition of the nickel (111) surface. These studies complement information available from other surface sensitive techniques, such as LEED, XPS, UPS, and AES. However, our experimental technique allows two important degrees of freedom: (1) by looking at the real part of the complex dielectric function of the adsorbed layer, one is not restricted to wavelengths where specific species absorb light, and (2) by our capability to cool the nickel substrate to liquid helium temperatures (see part 2e for details) we can physisorb the gases of interest. This is a state of weak interaction between the substrate and adsorbed layer which provides few reactive pathways.

From XPS and LEED studies, it is known that NO_2 decomposes upon adsorption on the nickel (111) surface at room temperature. We have been able to observe this reaction ellipsometrically. Figure 2 of the preceding paper is a plot of Δ, a parameter describing the phase change of linearly polarized light upon reflection from a surface, vs. exposure time of NO_2 on a clean nickel surface. The reproducible shift in Δ is indicative of a new state on the surface. Auger analysis of this state, however, shows large oxygen and nickel peaks, with little or no nitrogen present.

When the experiment is repeated on a cooled (20 K) clean Ni surface, the NO_2 remains intact, physisorbed to the nickel surface. Upon warming the crystal slowly, we observe (see Fig. 4 preceding paper) a series of changes in Δ not present in the room temperature deposition, although the final states are the same. We attribute these changes to intermediate steps in the decomposition of NO_2. An expanded view of the rise in Δ after the initial state warms up is shown on Fig. 5. A plot of the logarithm of δΔ, which for low coverage is proportional to concentration vs. 1/T (Fig. 6), gives us an activation energy of about 2 kcal/mole. It is conceivable that this activation

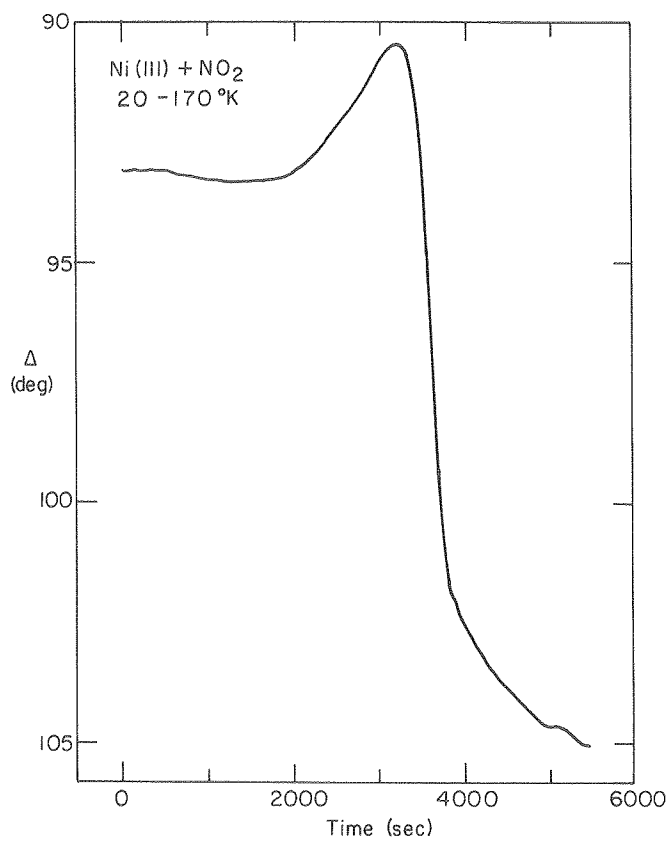

Fig. 5. Change in Δ during warming of NO_2 overlayer on Ni(111) shows rise ascribed to NO_2 reorientation and drop ascribed to NO_2 sublimation from surface. (XBL 7712-6615)

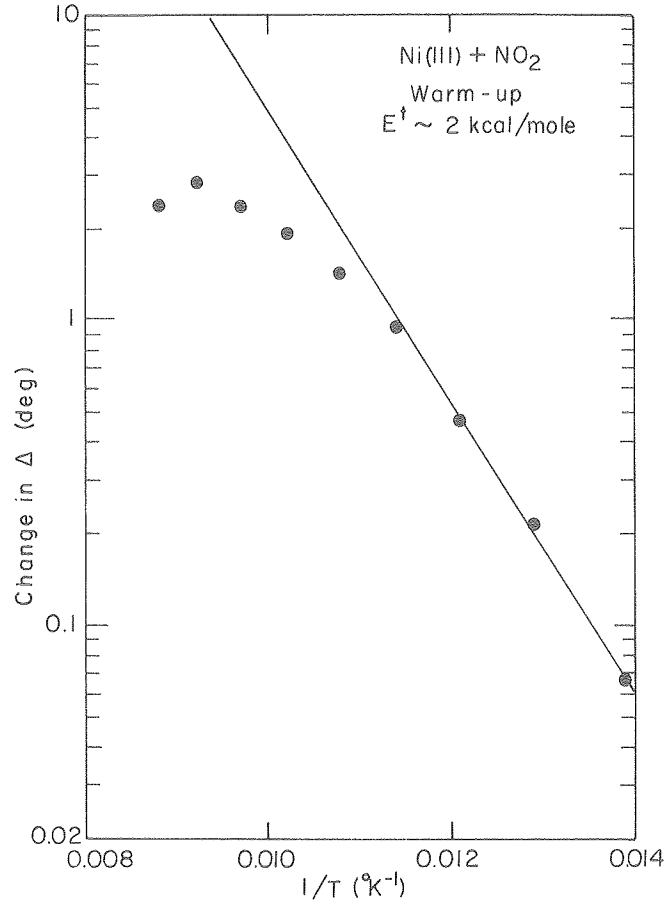

Fig. 6. Rise in Δ from Fig. 1 is analyzed to obtain activation energy E^+. Fall-off at higher temperatures represents onset of overlayer sublimation. (XBL 7712-6617)

energy is due to the orientation and mobility of the still intact NO_2 molecule on the surface. The sharp drop in Δ at about 7000 seconds correlates well with the calculated boiling point of NO_2 at the chamber pressure.

In an effort to further characterize the intermediate steps of the NO_2 decomposition, we have investigated the enthalpy of reaction for the possible final products of the decomposition. Those which are consistent with the experimental observations are:

(a) $4\ Ni + 2\ NO_2 \rightarrow N_2 + 4\ NiO$ $\Delta H = -246$ k cal,

(b) $4\ Ni + 3\ No_2 \rightarrow 3/2 N_2 + O_2 + 4\ NiO$ $\Delta H = -255$ k cal.

In both cases the nitrogen would simply desorb from the surface at the temperatures involved.

Thermodynamically, it is possible to name an NO intermediate as well:

$Ni + NO_2 \rightarrow NO + NiO$ $\Delta H = -44$ kcal.

There is evidence from XPS and UPS studies that this is a likely pathway, although it has not been confirmed. To investigate this possibility, we repeated the ellipsometer experiments with NO physisorbed on nickel (111); (see Fig. 3 of preceding paper).

These studies indicate that NO results in a final state quite different from that of NO_2: (1) Auger analysis of the final state shows no oxygen or nitrogen, and (2) the final drop in Δ to the initial state indicates a simple desorption of the unreacted gas. An expanded view of the rise of Δ upon warming is shown in Fig. 7. It is interesting to note that a log (δΔ) vs. 1/T for NO shows an activation energy of about 1 kcal/mole, a factor of 2 lower than for NO_2, (cf. Fig. 8). This supports the idea that there is a surface orientation and mobility of the adsorbed molecule, as NO has a much smaller van der Waals radius than NO_2.

c. Visible and UV Spectroscopic Ellipsometry: Excited States of Adsorbed Aromatic Molecules

C. B. Harris, A. R. Gallo, H. J. Robota and D. A. Zwemer

Traditionally most of our knowledge about molecular orbitals and bonds has been obtained by ultraviolet and visible spectroscopy. To this day however, there has been a surprisingly small effort to

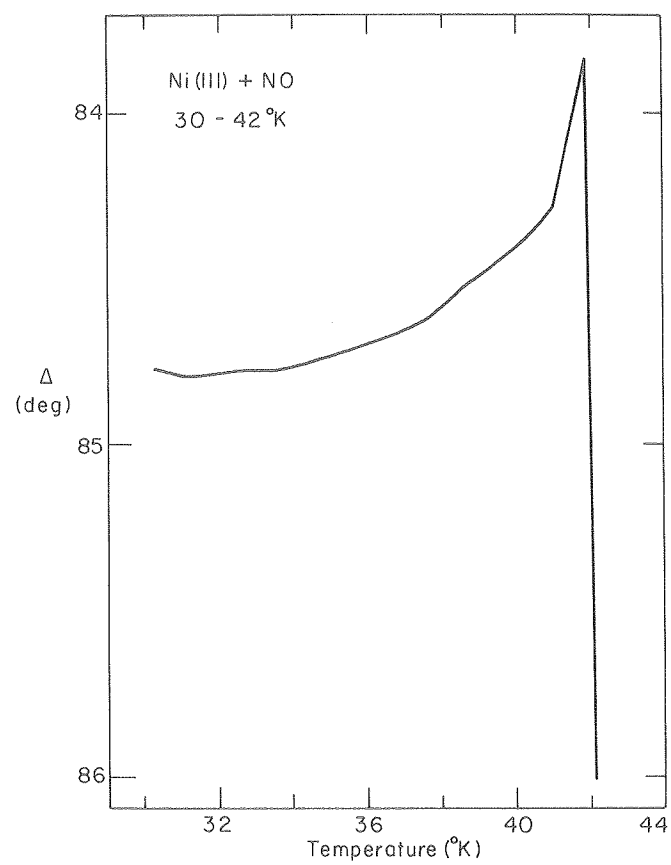

Fig. 7. Change in Δ during warming of NO overlayer on Ni(111) shows rise and sharp fall on sublimation of NO from surface. (XBL 7712-6614)

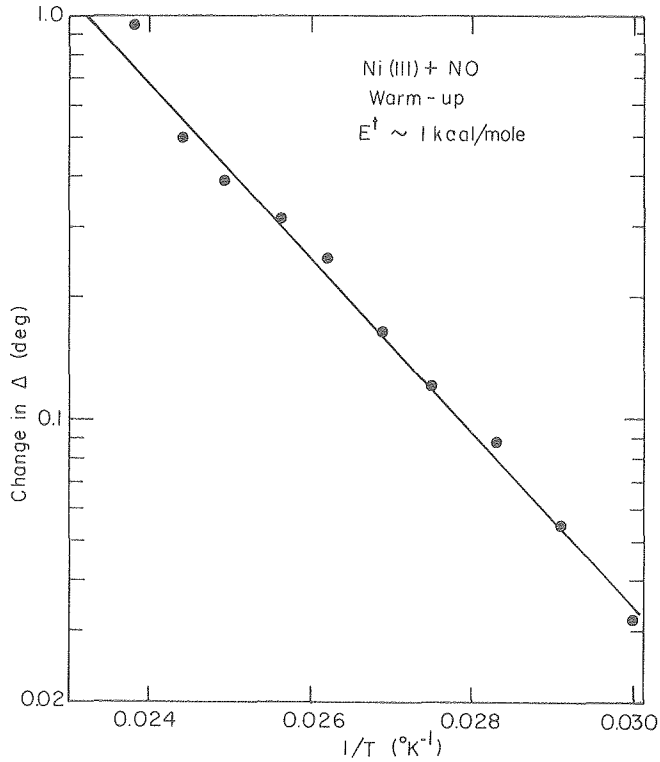

Fig. 8. Analysis of rise in Fig. 3 for NO on Ni(111). Activation energy observed is smaller than in NO_2-Ni system. (XBL 7712-6616)

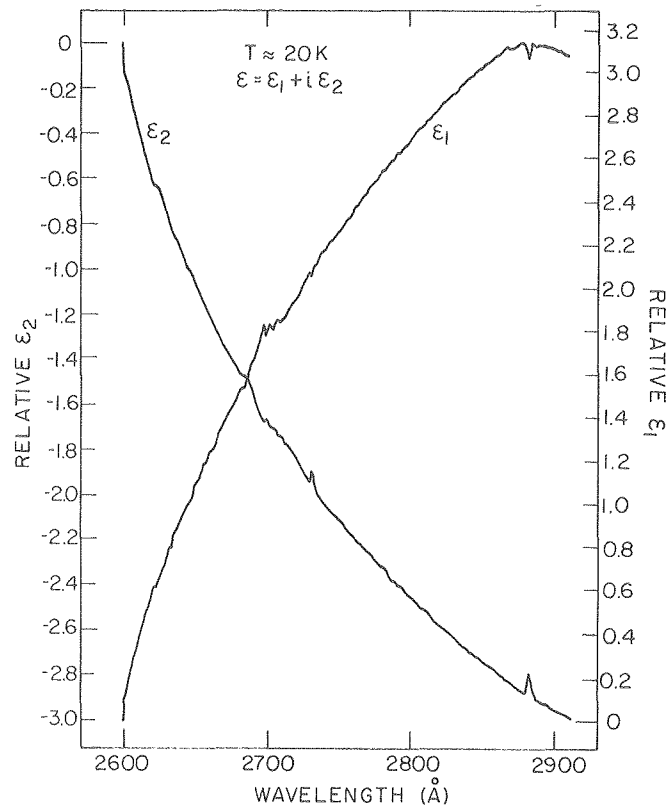

Fig. 9. Real (ε_1) and imaginary (ε_2) components of dielectric constant of bare Ni(111) surface between 2600 and 2900 Å. (XBL 7711-6429)

use this region of the spectrum to probe the properties of molecules adsorbed on various metal and semiconductor surfaces. In part, this is due to the extreme tedium of conventional reflection and ellipsometric techniques, as well as their relatively narrow spectral region of operation. The lack of energy resolution and the destructive nature of the higher energy surface-sensitive techniques such as LEED, XPS and AES has also been a deterent. The technique of rotating analyzer ellipsometry (see part 2e) is rapidly filling in the void and promises to be a powerful tool in studying the electronically excited states of molecules adsorbed on surfaces.

Figure 9 shows the wavelength dependent dielectric constant for a clean Ni(111) surface cooled to 20 K from 260-290 nm. Figure 10 shows the same region after deposition.

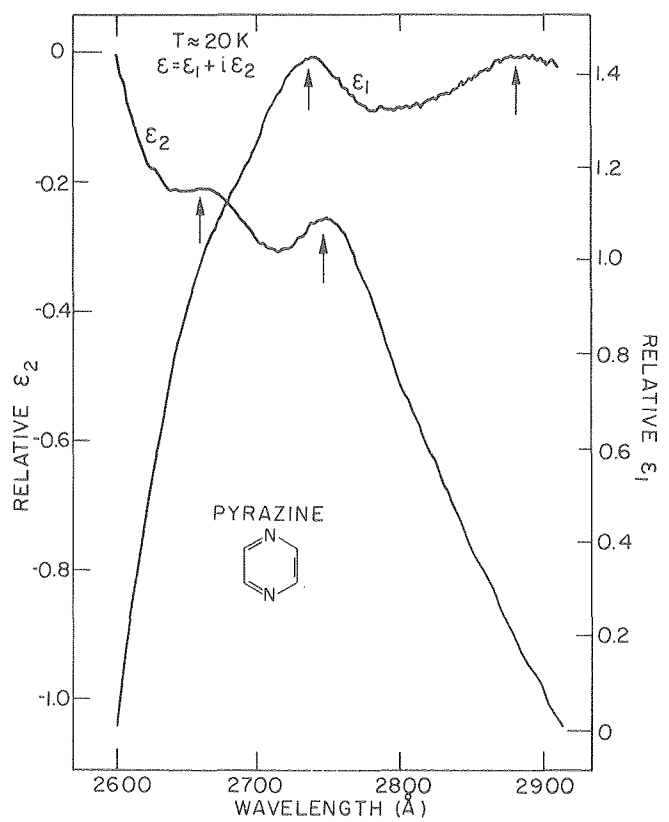

Fig. 10. Effective dielectric constant of Ni(111) surface plus 20 Å thick pyrazine overlayer. Broad features at 2750 and 2660 Å are ascribed to pyrazine $\pi\pi^*$ transition. Spectrum was taken at 20 K. (XBL 7711-6427)

d. Linewidth Studies of Radiationless Energy Transfer at Metal-Adsorbate Interfaces

C. B. Harris, A. R. Gallo, H. J. Robota and D. A. Zwemer

The adsorption of an organic molecule on a metal surface opens up new channels for deactivation of the molecule's excited states by energy transfer to modes of the metal surface. Spectroscopic ellipsometry is the first technique capable of monitoring

these processes directly, by extracting lifetimes from absorption lineshapes that carry information about the radiationless relaxation processes available to the excited state. Previous lifetime studies have required special dyes at long distances from the surface; our technique can be extended to well-characterized systems of interest to the surface or catalytic chemist.

Preliminary studies of pyrazine on nickel (111) surfaces at low temperatures have shown several remarkable effects. At 20 K, no appreciable broadening of the $\pi\pi^*$ singlet transition at 3300 Å is observed as the coverage is varied from partial monolayer to several monolayers (Fig. 11). This is unexpected if it is assumed that the first monolayer will transfer energy to the surface faster and have a shorter lifetime than successive layers. This may indicate either efficient long-range (~ 30 Å) transfer or an effect of the disordered physisorbtive binding at this temperature. The observed halfwidth is about 400 cm^{-1}, corresponding to a lifetime of $\sim 10^{-15}$ seconds, much shorter than the free-molecule radiative lifetime, for a homogeneous lineshape. Of course, the linewidth may be broadened by environmental splitting at different adsorption sites. To

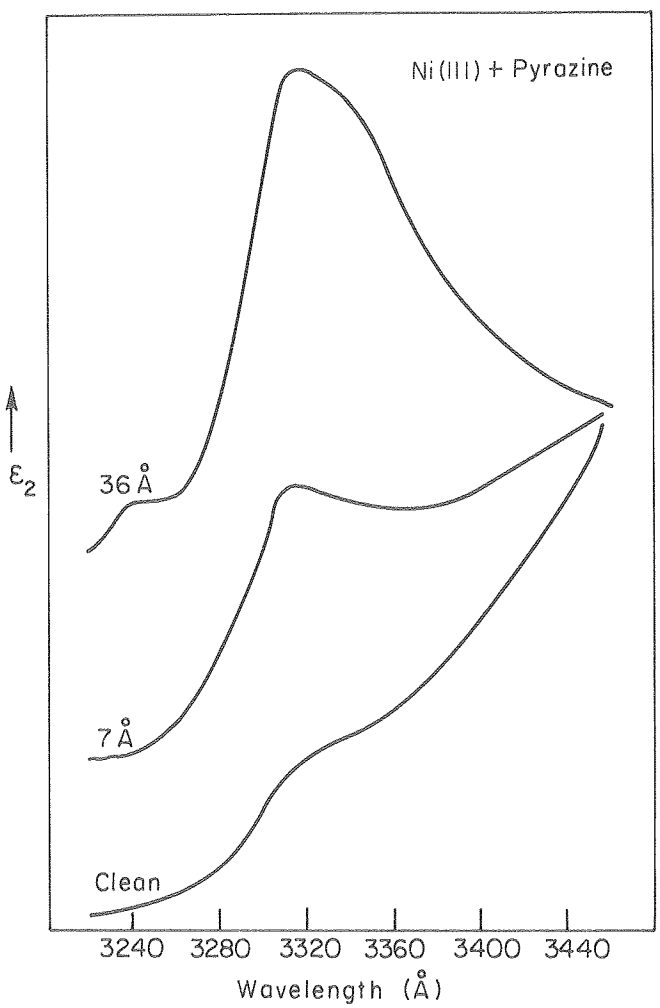

Fig. 11. Overlayer thickness dependence of pyrazine $^1n\pi^*$ transition on Ni(111). Weak feature in clean spectrum is attributed to Ni d-band transitions. (XBL 7712-6555)

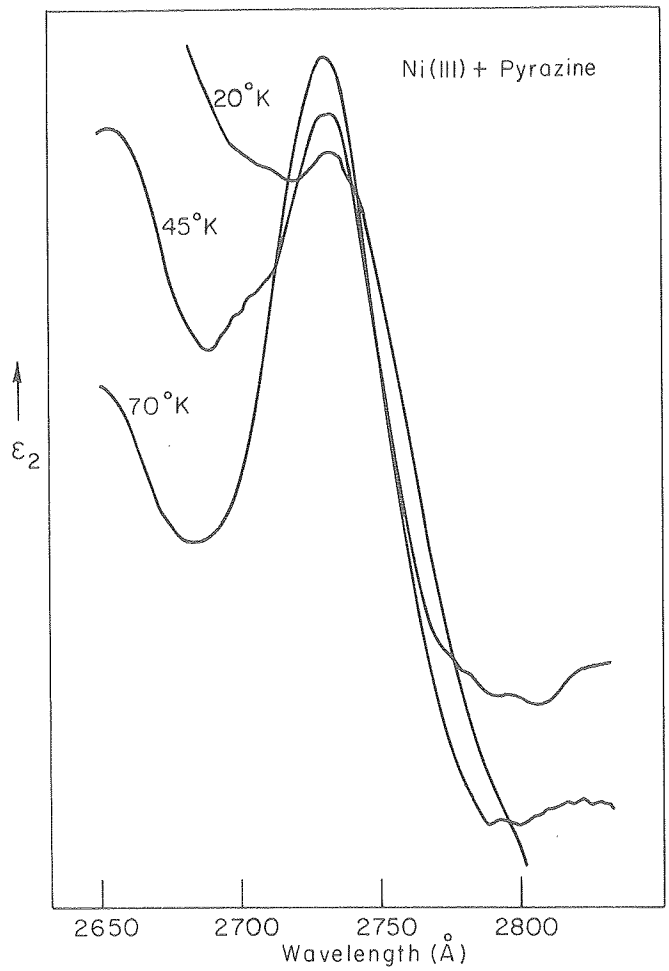

Fig. 12. Temperature dependence of ε_2 for pyrazine $^1\pi\pi^*$ transition on Ni(111). (XBL 7712-6554)

study these effects, the temperature dependence of the $\pi\pi^*$ transition was observed. Thin films of pyrazine are known to order on the microscopic level at 77 K. As the temperature increases from 20 to 77 K, the spectral lines become more easily resolvable and more prominent above the baseline (Fig. 12), although accurate linewidths are difficult to measure because of the sloping baseline. This behavior is reversible; that is, it is not due to the ordering of a disordered overlayer deposited at the lowest temperature. We are presently trying to interpret this unusual behavior in terms of (i) migration between different surface site and (ii) fluctuation and differences in the interaction between metal and adsorbate at higher temperatures.

e. Instrumentation and Software for Spectroscopic Ellipsometry of Well-Characterized Surfaces

C. B. Harris, A. R. Gallo, H. J. Robota and D. A. Zwemer

In the past year, we have completed and tested a rotating analyzer photometric ellipsometer to be

used for spectroscopic studies of well-characterized single-crystal oriented metal and semiconductor surfaces under ultrahigh vacuum conditions. The combined experimental system allows great versatility and control over many variables for the development of new techniques in the study of adsorbed molecules on surfaces.

The rotating analyzer ellipsometer is used to measure the shift in the state of polarization of linearly polarized light upon reflection from an overlayer-covered surface. In general this allows the calculation of (1) the real part of the sample index of refraction, which is related to the electrical conductivity, (2) the imaginary part of the index of refraction, which is related to the adsorption coefficient, and thus identifies the orbitals involved in surface bonding, and (3) the thickness of the adsorbed layer.

Figure 13 is a schematic drawing of the ellipsometer system. The input leg consists of a xenon high pressure arc lamp and a 3/4 meter monochromator. The state of polarization of the quasimonochromatic incident beam is then selected by a calcite rhomb mounted on a computer-controlled stepping motor. The reflected beam from the sample surface then passes through another rotating rhomb axially mounted in a frequency-stabilized synchronous motor with an optically encoded reference, and is detected by a photomultiplier tube. The optical system is interfaced to an LSI-11 minicomputer which allows data acquisition and reduction of the digitized time-dependent transmitted light intensity. The strengths of the system are its wavelength independence over a large (visible-ultraviolet) spectral range, its high speed and sample averaging capability, and its precision, greater than 1 part in 10^4, all of which were obstacles in previously used ellipsometer systems.

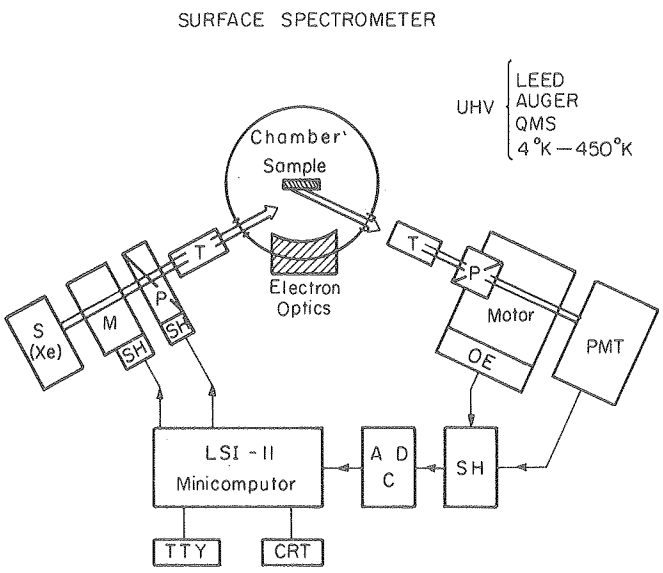

Fig. 13. Diagram of ultrahigh vacuum ellipsometry apparatus. Optical path consists of xenon arc source (S), 1 m monochromator (M) with stepping motor (SH), polarizer (P), telescope (T), sample in vacuum chamber, telescope, rotating polarizer mounted in shaft of motor with optical encoder (OE) reference, and photomultiplier tube (PMT), which is interfaced through a sample-and-hold circuit (SH) and an A/D converter (ADC) to an LSI-11 minicomputer for data analysis. (XBL 7612-7951)

The UHV chamber (see Fig. 14 used in these studies) allows the cleaning and full characterization of the crystal samples by means of low-energy electron diffraction, Auger electron spectroscopy, and mass spectroscopy. Base pressures of the order of 10^{-11} Torr keep the prepared samples free from contamination during data acquisition (several hours). Variable sample temperature is achieved by a liquid-helium-cooled cold tip in the range 4-450 K, allowing the study of epitaxially grown layers. The flexibility of the chamber allows the system to be used for laser and electron beam excited fluorescence and phosphorescence, as well as reflection spectroscopy.

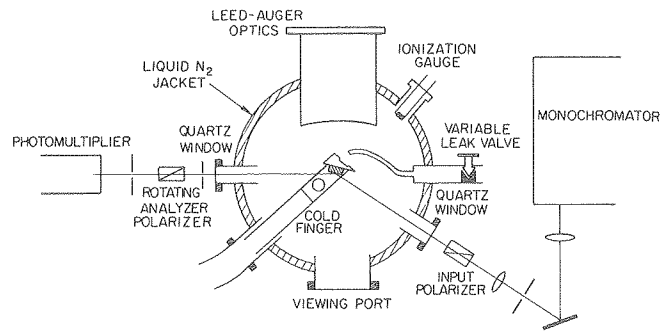

Fig. 14. Detail of ultrahigh vacuum chamber. Chamber also contains facilities for ion sputtering, annealing, and mass spectroscopy of desorbed gases. (XBL 7711-6434)

3. ENERGY TRANSFER STUDIES IN CONDENSED PHASES AND PICOSECOND LASER SPECTROSCOPY

a. The Origin of Optical Dephasing Times and Lineshape Functions for Electronic Transitions to Localized and Delocalized States in Solids*

C. B. Harris

Over the years a great deal of effort has been expended trying to relate the linewidths of optical transitions in molecular solids to phonon interactions with Frenkel exciton states. It has usually been assumed that phonon-exciton scattering times can be obtained directly from the homogeneous linewidths and that the coherent nature of the exciton state can be established to a first approximation, from the ratio of the linewidth vs. the intermolecular interaction which gives rise to the band dispersion. This has recently been shown to be erroneous. Although coherent optical experiments have been brought to bear on some of the problems associated with relaxation processes in solids, no clear understanding of the mechanism for optical dephasing times (homogeneous T_2 processes), absorption linewidths, and k-scattering in the band states has emerged from these studies.

A simple and straightforward, although approximate, theory for the dephasing times of the homogeneous component of the optical absorption linewidth to localized states and to the $k = 0$ levels of the exciton states has been developed.

To understand the optical absorption lineshape function and its relation to exciton coherence, we have to understand two features of the phonon-exciton interaction. First, one must know whether or not the interaction of a phonon with the exciton state scatters the initial $k = 0$ state (k_0) to another k' state ($k_0 \neq k'$) or whether the optic phonon is simply absorbed and re-emitted without an appreciable change in q, a process that would not cause a significant change in k_0. Secondly, one must know how fluctuations between the ground zero point energy (oo) and the phonon state (oq) are related to fluctuations between the exciton $k = 0$ state, ($k_0 0$), and the states (kq) via the scattering events, since these can contribute to the transition dipole moment autocorrelation function between (oo) and ($k_0 0$). It is in this respect that the theory deviates significantly from previous lineshape theories. The effect of specific scattering mechanism on the transition dipole moment can be understood more easily if one investigates the simpler case of a localized excited state interacting with the vibrations or phonons of a single mode.

Consider the case illustrated in Fig. 1. The total Hamiltonian for the system is represented by a zeroth-order Hamiltonian $\mathcal{H}_0$, a perturbation Hamiltonian $\mathcal{H}_p$, and an exchange Hamiltonian $\mathcal{H}_{ex}$. Zeroth-order states are simply the eigenstates of electronic and vibrational (or phonon) excitations at a site N. These are given as

$$\mathcal{H}_0 = \sum_n \varepsilon_f \, a_n^\dagger a_n + \sum_m \omega \, (b_m^\dagger b_m + 1/2), \qquad (1)$$

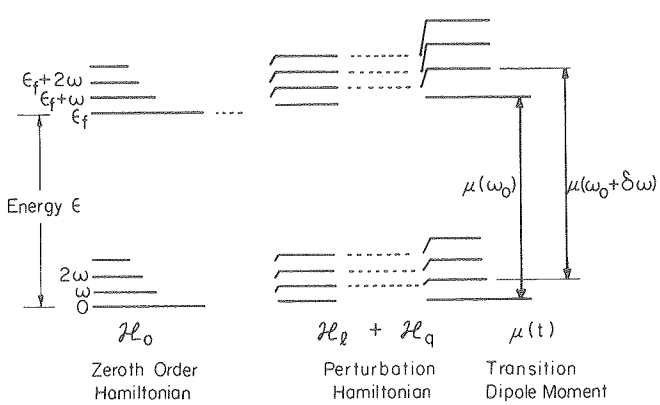

Fig. 1. Schematic representation of the effect linear and quadratic terms in the Hamiltonian have on introducing frequency shifts in the optical spectra when transitions are coupled by phonon or vibrational exchange. As discussed in the text, dephasing of the optical transition dipole moment autocorrelation results from a random frequency modulation at ω_0 by an amount $\delta\omega$. (XBL 776-5597)

where a_n refers to electronic coordinates and b_m refers to vibrational coordinates. For simplicity, the perturbation Hamiltonian is taken to be composed of only linear and quadratic interactions and is given as:

$$\mathcal{H}_p = \mathcal{H}_\ell + \mathcal{H}_q \qquad (2)$$

$$\mathcal{H}_\ell = \sum_n K \, a_n^\dagger a_n \, (b_n^\dagger + b_n) \qquad (3)$$

and

$$\mathcal{H}_q = \sum_n C \, a_n^\dagger a_n \, (b_n^\dagger + b_n)^2 . \qquad (4)$$

Finally, the exchange Hamiltonian is given by the intermolecular exchange of vibrational (or phonon) energy between sites. It should be noted that exchange conserves both energy and the total number of particles. It is given by:

$$\mathcal{H}_{ex} = \sum_{n,m}{}' \; J_{nm} \, b_n^\dagger b_m \qquad (5)$$

where J_{nm} is a measure of the intermolecular coupling and the prime denotes the fact that the sum is over only states $n \neq m$.

For the above Hamiltonian it can be shown that

$$[\mathcal{H}_0, \mathcal{H}_{ex}] = 0 \qquad (6a)$$

$$[\mathcal{H}_q, \mathcal{H}_{ex}] \neq 0 \qquad (6b)$$

$$[\mathcal{H}_\ell, \mathcal{H}_{ex}]_{as} = 0 \qquad (6c)$$

$$[\mathcal{H}_\ell, \mathcal{H}_{ex}]_{s} \neq 0 . \qquad (6d)$$

The physical interpretation of the commutator relationships is that random frequency modulation is introduced into the electronic and vibronic transitions by vibrational or phonon exchange from the quadratic terms in the Hamiltonian. Although the linear perturbation does not commute with $\mathcal{H}_{ex}$ for symmetric modes (s), no frequency modulation results from linear coupling to symmetric modes [or asymmetric (as) modes] because the commutator is a simple momentum operator. Finally, intermolecular vibrational or phonon exchange has no direct effect on the absorbed or emitted photons associated with the radiation field at the energy of the electronic origin and thus the exchange Hamiltonian also commutes with $\vec{\mu}$, i.e.,

$$[\vec{\mu}, \mathcal{H}_{ex}] = 0, \qquad (7)$$

where $\vec{\mu}$ is the electric transition dipole moment operator.

If one extends this model for optical dephasing processes in localized states to exciton states, the exciton exchange Hamiltonian must be added, i.e.,

$$\mathcal{H}_e' = \sum_{nm} \beta_{nm} a_n^\dagger a_m. \qquad (8)$$

The result is that a band of exciton k states are formed in addition to the localized and delocalized phonon-exciton states (cf. Fig. 2). However, in the limit of small bandwidth the physical character of the problem remains essentially the same as described above. Basically, one expects specific coupling terms in the perturbation Hamiltonian between the proper symmetrized Bloch functions to also cause optical dephasing in the transition from (oo) to the $k = 0$ state of the band ($k_0 0$) when phonon exchange is included. This is illustrated diagrammatically in Fig. 2.

In this model the dynamics of how phonon scattering causes line broadening can be quantitatively resolved by considering the effects of exchange between both the exciton state ($k_0 0$) and the phonon-promoted state ($k_0 q$), and between (oo) and (oq). This approach is valid for a simple two-state scattering process in all limits that are Markoffian and can be derived from exchange theory. The significant feature of exchange theory that is relevant to the present case is that whenever two modes interact, an excitation of one mode can result in a line broadening and frequency shift of the other mode when the excitation returns to the initial state, bringing with it phase memory of the upper state's transition dipole moment.

The application of exchange theory to the optical absorption at $k = 0$ or optical dephasing times (in the case of photon echo experiments) is schematically illustrated in Fig. 3. The lowest phonon or vibrational branch in the ground state is taken to be at an energy ω, while in the excited state it is ω', and for simplicity only one mode is assumed to be responsible for dephasing of the optical transition in a given temperature range. This gives rise to frequency difference $\delta\omega$, which is a direct result of the quadratic terms of the perturbation Hamiltonian for both symmetric and asymmetric modes. The difference is given as $\delta\omega = \omega' - \omega$. Simply stated, the

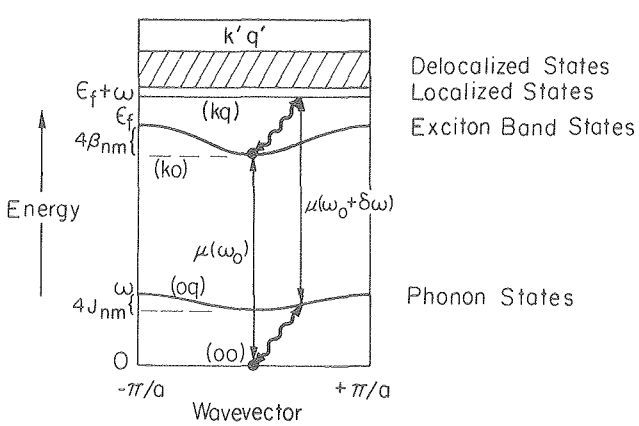

Fig. 2. Schematic representation of one-dimensional phonon branches and exciton bands. (00) represents the ground state, (oq) is the lowest optic phonon branch, (k0) represents the phononless exciton band while (k'q') represent the delocalized scattering states. (XBL 776-5596)

optical transitions (oo) → ($k_0 0$) and (oq) → ($k_0 q$) will have different frequencies because the phonon energy in the excited state is different from that in the ground state.

Under these conditions, one expects the homogeneous portion of the lineshape function at ω_0 to become exchange-averaged with the transition at $\omega_0 + \delta\omega$ at a temperature where the occupation of the phonon or vibrational states causes the fluctuations of the transition dipole moment autocorrelation function at ω_0 to become comparable to $\delta\omega$. In such cases, one expects both a line broadening and frequency shift with temperature to either higher or lower frequency, depending on the sign of $\delta\omega$. This is illustrated diagrammatically in Fig. 3. The effect of the frequency shift, $\delta\omega$, is to generate a random frequency modulation of the transition at ω_0 at a rate determined by the phonon exchange Hamiltonian $\mathcal{H}_{ex}$. If one assumes that the exchange is a stochastic process, the results can be cast into the more familiar rate relationships which satisfy detail balance.

The phonon "absorption rate" from (oo) to (oq) is given by W_+ and the "lifetime" in (oq) is given by τ which is simply $(W_-)^{-1}$, the emission rate.

Quantitatively, the lineshape function for the transition from (oo) to ($k_0 0$) is given by Fourier transform of the electric dipole autocorrelation function including exchange, i.e.,

$$I(\omega) = \int_{-\infty}^{\infty} \exp(i\omega t) \langle \mu(t) \rangle \langle (o) \rangle \, dt. \qquad (9)$$

When the interaction that is responsible for the frequency shift does not appreciably mix the phonon branch with the $k = 0$ exciton state, then the off-diagonal elements are small and the effect of scattering at rates W_+ and W_- (τ^{-1}) can be written in terms of a time-dependent frequency $\omega_0(t)$.

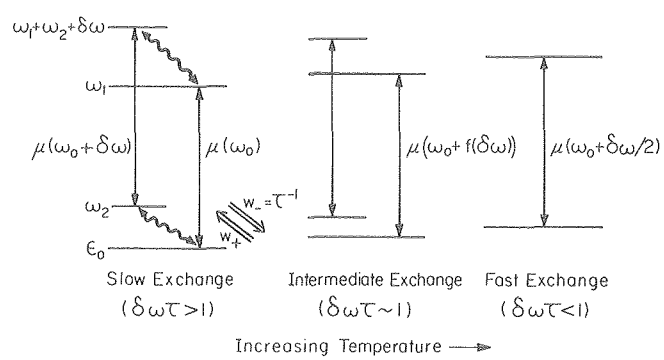

Fig. 3. Schematic representation of the absorption and emission of a phonon by the ground and exciton ($k_0 0$) state. The absorption rate is given by the W_+ while the emission rate is given by W_-. τ is the lifetime in the state ($k_0 q$) or (oq). Such a process exchange averages the electric dipole transition moment $\langle 00|\mu(t)|k_0 0\rangle$ at a frequency ω_0 with $\langle 0q|\mu(t)|k_0 q\rangle$ at a frequency $\omega_0 + \delta\omega$ with increasing temperature as illustrated. $\delta\omega$ is given by the difference of the phonon energy in excited state (ω') and ground state (ω). (XBL 777-5821)

Near $\omega = \omega_o$, $I(\omega)$ can be approximated by a Lorentz lineshape function by setting $\omega - \delta\omega/2 \approx -\delta\omega$. This form is

$$I(\omega) = \frac{W_+\tau^2(\delta\omega)^2/[D(1+W_+\tau)]}{[(\omega'+\delta\omega/2 - W_+\tau\delta\omega/D)]^2 + W_+^2[\delta\omega^2\tau^2]^2/D^2}, \qquad (10)$$

where $D = 1 + (\delta\omega)^2\tau^2$. The characteristic feature of this lineshape function is that it contains both a line-broadening term and a frequency shift term. The lineshape function can be reexpressed in terms of an effective relaxation time and frequency. The effective relaxation time is given by:

$$(T_{eff})^{-1} = W_+(\delta\omega)^2\tau^2/[1 + (\delta\omega)^2\tau^2], \qquad (11)$$

while the effective frequency is given by

$$(\omega)_e = \omega_o + (\delta\omega W_+\tau)/[1 + (\delta\omega)^2\tau^2] \qquad (12)$$

The lineshape function in terms of the effective relaxation time and frequency is given as

$$I(\omega) = \frac{1}{1 + (\omega_e - \omega)^2 (T_{eff})^2}. \qquad (13)$$

In the terminology of rates, the lineshape function (or dephasing time) resulting from phonon absorption and emission processes,

$$(k_oC) + (oq) \underset{W_-}{\overset{W_+}{\rightleftharpoons}} (k_oq) \qquad (14)$$

and

$$(00) + (oq) \underset{W_-}{\overset{W_+}{\rightleftharpoons}} (oq), \qquad (15)$$

can now be simply derived. For phonons, the relationship between W_+, the absorption rate, τ, the lifetime in (k_oq) or (oq), and the Planck distribution function $\langle n(\omega)\rangle$ is

$$W_+\tau = \frac{\langle n(\omega)\rangle}{\langle n(\omega)\rangle + 1}. \qquad (16)$$

This satisfies detail balance and is given by the Boltzmann equation:

$$W_+\tau = \exp(-\omega/kT), \qquad (17)$$

where ω is the energy of the phonon branch given by $\mathcal{H}_o + \mathcal{H}_p$ that is absorbed by the $k=0$ state of the exciton or by (oo). Because the Planck distribution function falls to small values for temperature where $\omega > kT$, the most effective phonons would be those at low energy having a large J_{nm}. Inserting Eq. (17) into the $T=0$ equations (11) and (12) and rearranging, expressions for the temperature-dependent portion of the effective relaxation time and the frequency shift are obtained. These are given by

$$(T_{eff})^{-1} = \delta\omega^2\tau \left[\frac{1}{[1+(\delta\omega\tau)^2]}\right]\left[\exp(-\omega/kT)\right] \qquad (18)$$

and

$$\Delta_{eff} = \delta\omega \left[\frac{1}{[1+(\delta\omega\tau)^2]}\right]\left[\exp(-\omega/kT)\right], \qquad (19)$$

respectively.

The development presented above allows a measure of the exciton coherence time to be evaluated from the temperature-dependent lineshape function [Eq.10] in favorable cases. The utility of the approach is that it provides a semi-quantitative measure of the scattering rate with a particular phonon when the phonon branches are well enough separated in energy. In cases where the change of the occupation number of the phonon branch responsible for scattering the exciton over a given temperature range is changing rapidly relative to other phonon branches, W_+ can be determined from the analysis of the lineshape function in the intermediate exchange region ($\delta\omega \approx 1$). As the Boltzmann factor approaches unity for a particular phonon mode, the line would, in principle, narrow to a high temperature limit similar to that given by the exchange theories developed for magnetic resonance. In most cases, however, narrowing with increasing temperature might be difficult to observe since higher harmonics or other modes begin to contribute to the exchange average of the optical transition linewidth, causing a further increase in the linewidth with increasing temperature. However, when the lineshape function can be analyzed in trems of exchange, one obtains the contributions the individual phonon modes have on the transition dipole moment autocorrelation function. As a result, one measures the effect a particular phonon mode has on the localization of the coherent exciton wavepacket. It is important to stress that only certain modes will affect the transition dipole moment autocorrelation function because of symmetry restrictions, and thus the interpretation of the lineshape function in terms of the exciton coherence can only be valid when one demonstrates that the scattering rate from one mode dominates all others at a particular temperature.

---

*Partially supported by NSF.

b. Interpretation of the Optical Dephasing Time and Lineshape Function in the $S_0 \rightarrow T_1$ Exciton Transitions of 1, 4-Dibromonaphthalene*

C. B. Harris

The lineshape function for the $S_0 \rightarrow T_1$ absorption in 1, 4 dibromonaphthalene (DBN) has been analyzed in terms of exchange theory. It was shown that the dominant optical dephasing mechanism for the electric dipole transition to the $k=0$ state in the band results from the absorption and emission of a low energy optic phonon. This process dephases the optical absorption because of frequency differences of

the phonon in the ground and excited state. In addition, it was shown how to extract the energy of the phonon responsible for dephasing, the phonon absorption rate, and the lifetime in the phonon promoted state from the data. The analysis of the data for DBN shows that very little dephasing of the optical transition occurs before ≈ 15 K but from 15 K to ~ 40 K the singlet-triplet transitions to site I (20,192 cm^{-1}) and site II (20245 cm^{-1}) are dephased by absorption and emission of an ~ 38 cm^{-1} and 45 cm^{-1} phonon respectively. The phonon absorption rates by the K = 0 state in the exciton band are similar for both sites, being 5×10^6 s^{-1} and 3×10^5 s^{-1} at 4 K and 7×10^{11} s^{-1} at 30 K for sites I and II respectively. Finally, the lifetimes in the phonon-promoted state for sites I and II are 0.23 and 0.28 ps over the range 15-40 K.

---

*Partially supported by NSF.

c. Picosecond Studies of Vibrational Dephasing

C. B. Harris, P. A. Cornelius and R. M. Shelby

Until the application of picosecond laser techniques (von der Linde, Laubereau, and Kaiser, 1971) the only experimental probe of vibrational relaxation was the indirect one of vibrational lineshape analysis. However, a variety of mechanisms can contribute to the observed linewidth, including inhomogeneous line broadening, vibrational energy relaxation or redistribution among the other degrees of freedom, as well as so-called "pure dephasing" which can result from interactions that modulate the vibrational phase without causing redistribution of the energy. The use of picosecond techniques offers the possibility of separately investigating these contributions.

The ability to coherently excite vibrations of an ensemble of molecules by using stimulated Raman scattering of intense laser pulses provides the basis for a direct measurement of vibrational dephasing times using picosecond laser spectroscopy. The excitation process is coherent, because the stimulated emission of stokes radiation results in a driving field which excites molecules to a well-defined linear superposition of vibrational states with identical phases (except for phase shifts due to the velocity of light in the medium). These excited molecules posses the ability to interact with a picosecond probe pulse to produce a coherent beam of anti-stokes scattered light. This coherent anti-stokes scattering is emitted toward the direction in space for which the anti-stokes signal can be expressed in terms of conditons on the wave vectors of excitation, probe, stokes, and anti-stokes radiation as depicted in Fig. 4. As has been shown (Laubereau, Wochner, and Kaiser, 1976), by experimentally restricting the allowed directions of these wave vectors one can probe a narrow band of frequencies and therefore measure the homogeneous contribution to vibrational dephasing in the presence of inhomogeneous broadening.

Although the existence of an inhomogeneous vibrational line in a room temperature liquid may seem somewhat surprising, we have obtained picosecond

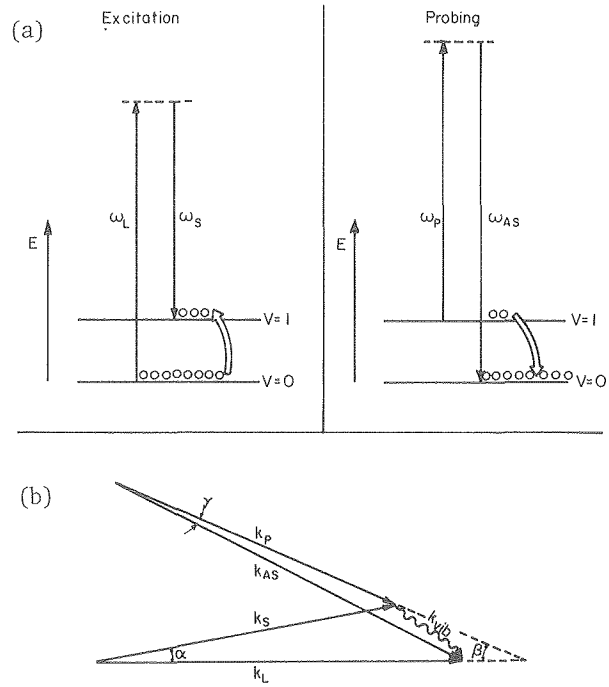

Fig. 4. (a) Energy levels involved in Raman excitation and probing are the ground state (v = 0 and a vibrationally excited state (v = 1). Excitation involves scattering events in which a laser photon (frequency = ω_L) is absorbed and a Stokes photon (frequency = ω_S) emitted, thus transferring population from v = 0 to v = 1. In the probing process, photons are absorbed from the probe pulse and anti-Stokes photons are emitted (frequencies ω_p and ω_{AS}, respectively). Thus the amount of vibrational excitation remaining in v = 1 can be measured by the intensity of the scattered signal. (b) The wavevector geometry necessary to observe coherent anti-Stokes scattering is shown. k_{vib} is the wavevector of the vibrational excitation prepared by stimulated Raman scattering. (XBL 7612-7944)

results for the 2912 cm^{-1} Raman band of p-xylene that indicate the presence of inhomogeneous broadening. These data were obtained using well-characterized, fully coherent 5300 Å picosecond pulses produced by a mode-locked Nd-glass laser system (Fig. 5). The experimental setup used for the measurement is shown in Fig. 6. To demonstrate the technique, data obtained in these laboratories for the C-H stretching vibration of ethanol; 1,1,1-trichloroethane; and p-xylene are shown in Figs, 7, 8, and 9. Because of its short dephasing time (T_2 = 0.5 ps) the ethanol data can be used to determine the shape of the picosecond laser pulse. The pulse shape determined in this experiment can then be use to determine the dephasing time for the other two samples, using a similar fitting process. This allows the determination of T_2 values that are on the order of or somewhat smaller than the pulse width as well as longer decay times. For the case of 1, 1, 1-trichloroethane, the value determined in this manner (T_2 = 3.5 ps) is well within the estimated experimental error of a factor of 2 of the literature value (T_2 = 2.6 ps; Laubereau, von der Linde, and Kaiser, 1972).

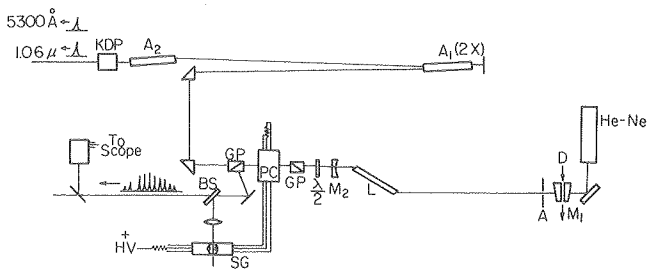

Fig. 5. The laser oscillator is formed by a resonant cavity consisting of reflectors M_1 and M_2, and the Brewster-angled Nd: glass laser rod, L. The aperture, A, selects for TEM_{00} mode, and the laser is mode-locked by a saturable dye, D, whose flow is indicated schematically. The laser system is aligned with a 5.0 mW helium-neon laser. The pulse selection system consists of an ultrafast shutter formed by two Glan-Thompson polarizers, GP, and a Pockel's cell, PC, which is energized by a spark gap triggered by the rejected pulse train, SG. The single 1.06 μm pulse traverses the amplifier rod, A_1, twice and the seond amplifier, A_2, once. It then passes through a saturable dye cell (not shown), which serves to remove any low-intensity background radiation which might be present. Generation of a second harmonic pulse at 5300 Å is possible in a KDP (potassium dihydrogen phosphate) crystal. (XBL 7612-7942)

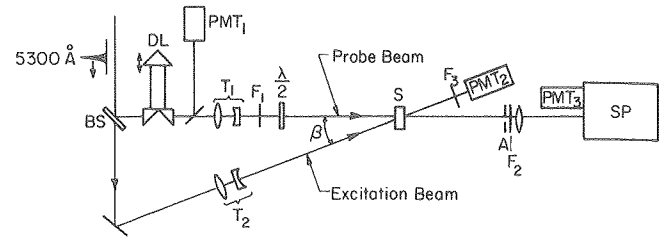

Fig. 6. Diagram of the setup used for the dephasing time measurement. BS = beam splitter; DL = optical delay line; T_1 and T_2 = Gallilean telescopes; F_1, F_2, and F_3 = filters; $\lambda/2$ = quartz half-wave plate; PMT_1, PMT_2, and PMT_3 = photomultiplier tubes which monitor the laser intensity, Stokes intensity, and anti-Stokes intensity respectively; S = sample ; SP = 3/4 m spectrometer; A = aperture. (Ref: von der Linde Laubereau and Kaiser, Phys. Rev. Lett. 26, 954 (1971). (XBL 7612-7941)

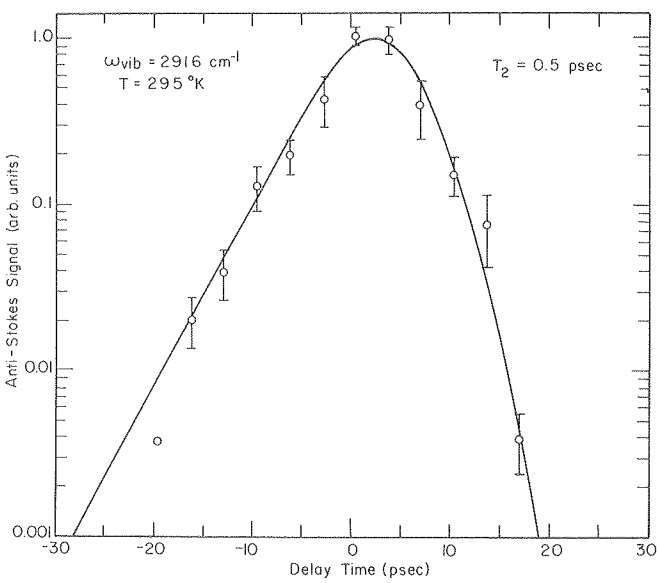

Fig. 7. The coherent anti-Stokes scattering data for the C-H stretching mode of ethanol. The normalized anti-Stokes signal is plotted as a function of probe pulse delay time. The theoretical fit indicates that our laser pulse intensity can be represented as a Gaussian rise [$I_1 = I_0 \exp(-(t/6.34\ \text{ps})^2$ for $t \leq 0$] and an exponentially falling tail [$I_1 = I_0$ sech $(t/3.94\ \text{ps})$ for $t \geq 0$]. (XBL 7612-7950)

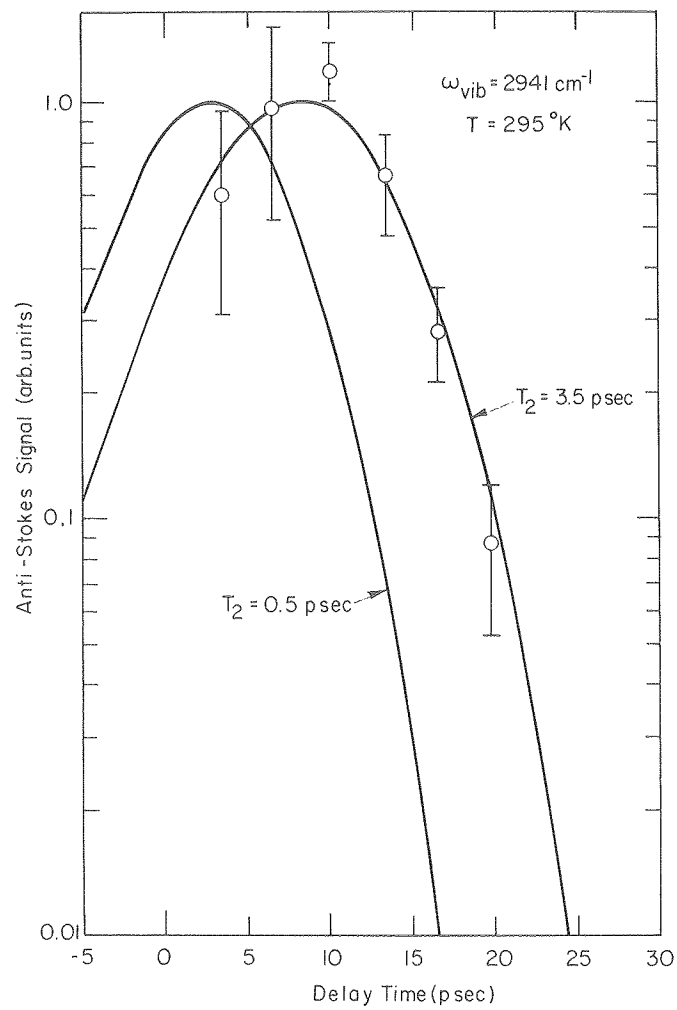

Fig. 8. The coherent anti-Stokes data for the 2941 cm^{-1} vibration of 1, 1, 1-trichloroethane is shown. The data can be fit by assuming a value of $T_2 = 3.5$ ps, which is to be compared with the accepted value of 2.6 ps. The calculated curve expected for a dephasing time of 0.5 ps (e.g., ethanol) is also shown for comparison. (XBL 7711-6481)

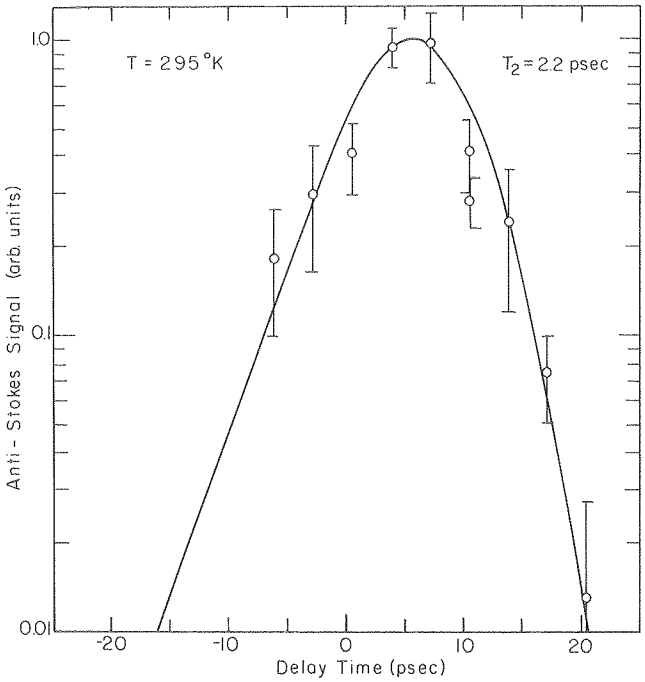

Fig. 9. Coherent anti-Stokes data for the 2912 cm^{-1} vibration of p-xylene. The value of T_2 determined in this case is 2.2 ps. (XBL 7612-7948)

The value for p-xylene, however (T_2 = 2.2 ps), is a factor of 4 larger than that predicted by the spontaneous Raman linewidth of ~ 20 cm^{-1} (see Fig. 10). Theoretical calculations of stimulated Raman excitation for inhomogeneous lines suggest that this discrepancy may indicate the presence of inhomogeneous broadening. This idea is supported by the low temperature Raman spectrum of p-xylene (Fig. 11) which shows that the 2912 cm^{-1} band is made up of several spectral components which may be incompletely average together even in the room temperature liquid. This averaging process is related to the exchange mechamism of vibrational dephasing discussed below.

The homogeneous dephasing time can be measured by using the restricted wavevector geometry mentioned above. These studies are currently in progress.

d. Theory of Vibrational Energy Exchange in Polyatomic Solids and Liquids*

C. B. Harris, P. A. Cornelius and R. M. Shelby

Studies of vibrational lineshapes and the corresponding dephasing and relaxation processes can give a great deal of information about vibrational dynamics and an increased understanding of the interactions between a vibrating molecule and excitations of its surroundings. These interactions result in a finite correlation time for the vibrational motion due to a variety of mechanisms. These include inhomogeneous line broadening, vibrational energy relaxation and redistribution, as well as so-called "pure dephasing" which results from interactions which modulate the vibrational phase without causing energy redistribution.

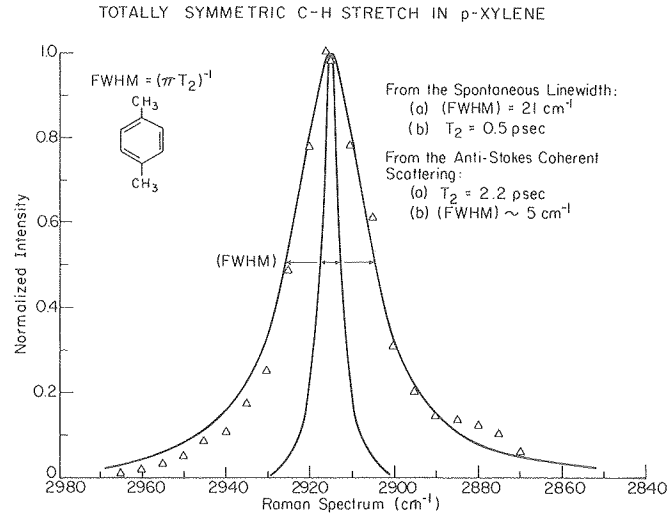

Fig. 10. The spontaneous Raman lineshape function (triangles) and the linewidth expected from the picosecond results are compared. The solid lines represent Lorentzian lineshape functions. The factor of 4 discrepancy cannot be accounted for by experimental error and may be the result of an inhomogeneous line. (XBL 773-5230)

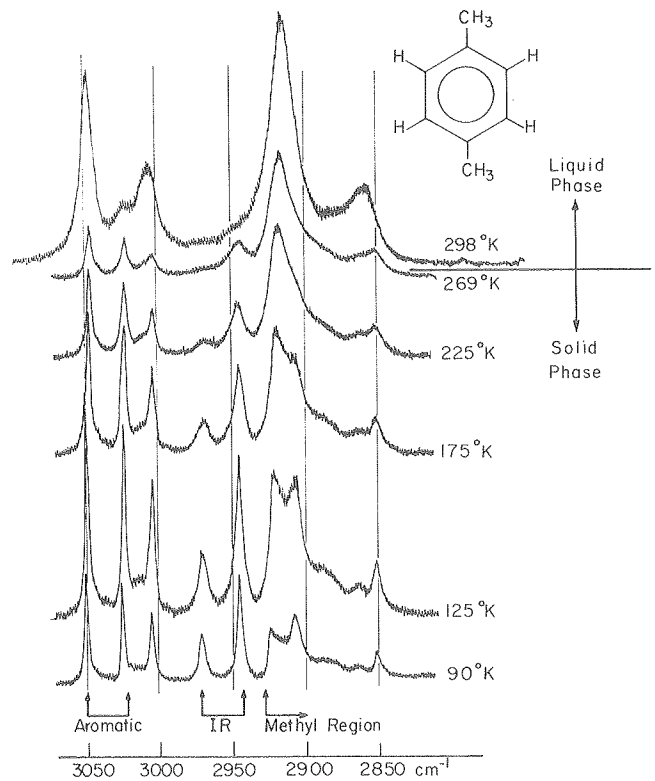

Fig. 11. The temperature-dependent Raman spectrum of xylene shows a number of interesting effects, many of which are only partially understood at this time. The point to note is that the picosecond data at room temperature in the liquid phase correspond to the harmonics of the C-H bending modes on the methyl groups. At low temperature it appears as if there are several spectral components in the region below 2925 cm^{-1} that may not be completely averaged at room temperature, thus leading to an inhomogeneous line. (XBL 777-5858)

One such mechanism that has been overlooked results from the exchange of vibrational energy among low frequency intramolecular modes of polyatomic molecules. In such process, anharmonic coupling causes intramolecular interactions between different vibrational modes to be much stronger than interactions between these modes and the surroundings. Thus, excitation and de-excitation of low frequency modes by this exchange process causes dephasing by effectively modulating the vibrational frequency. We have developed a theory that is capable of calculating the effects of this modulation on vibrational dephasing, as reflected in the Raman lineshape function. This formalism correctly takes into account the phase memory of the modulation and makes it possible in favorable cases to extract rates of energy exchange in the dominant dephasing channels as well as a measure of the intramolecular anharmonic coupling.

The basic ideas of this theory are depicted by the vibrational energy level scheme of a typical polyatomic molecule shown in Fig. 12. The key idea is the partitioning of the degrees of freedom of the molecule and surroundings (excluding the vibrational mode whose dephasing we wish to calculate, hereafter called mode A) into two groups, the exchanging modes and the reservoir. The exchanging modes are those modes that interact strongly with mode A such that their excitation shifts its frequency (e.g., from ω_0 to $\omega_0 + \delta\omega_j$; see Fig. 12). Excitation and de-excitation of the exchanging modes can occur due to either resonant energy transfer from neighboring molecules or by interaction with the thermalized reservoir modes. It is the rate of the resulting frequency modulation of mode A relative to the amplitude of the modulation that determines the importance of phase memory. As shown in Fig. 12, the rates are given by W_+ and W_- and the amplitude or frequency shift by $\delta\omega$.

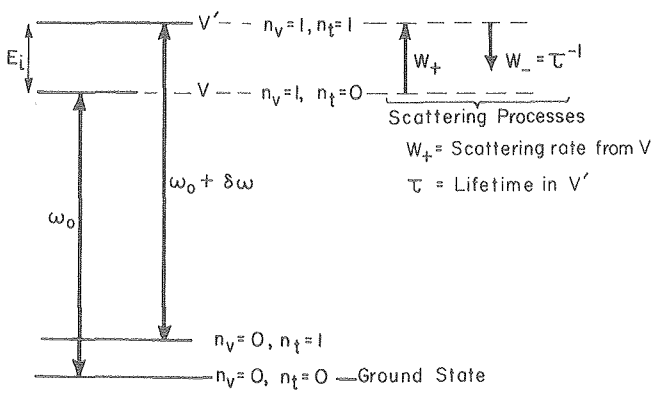

Fig. 12. Energy levels for vibrational exchange between two modes denoted by V and V'. A vibrational mode of frequency ω_0 and vibrational quantum number n_V interacts with some low frequency mode, shifting the frequency by $\delta\omega$. Excitation and de-excitation of the exchanging mode occur with the rates W_+ and W_-. The resulting modulation of the vibrational frequency is similar to the modulation of the Larmor frequency in the two-site exchange problem in NMR. The exchange process manifests itself in the Raman spectrum through the vibrational correlation function. (XBL 774-5291)

This frequency shift, $\delta\omega$, arises as a result of the intramolecular anharmonic coupling between mode A and the exchanging mode. To illustrate this, the anharmonic vibrational potential is expanded as a power series:

$$V_{anh} = \sum_i K_i Q_i^2 + \sum C_{ijk}\, Q_i Q_j Q_k + \sum_{ijkl} C_{ijkl}\, Q_i Q_j Q_k Q_l, \tag{1}$$

where the Q's are vibrational normal coordinates in the harmonic approximation. A perturbation calculation of $\delta\omega$ shows that the largest contribution comes from the $C_{1122}Q_1^2Q_2^2$ term in the above expansion, and is given by $\delta\omega = 4C_{1122}$. This gives values of $\delta\omega$ on the order of a few cm^{-1} to tens of cm^{-1}.

To solve the equations of motion of the exchanging molecule and determine the vibrational lineshape, we have used a reduced-density matrix technique in the limit of Markoffian random excitation and de-excitation of the exchanging modes. This procedure gives an expression for the vibrational correlation function similar to that obtained earlier by others for the case of exchange in magnetic resonance:

$$\langle Q(t)\, Q(0) \rangle = \underset{\sim}{1} \cdot \exp(i\underset{\approx}{\omega}_V + \underset{\approx}{\pi}) \cdot \underset{\sim}{W}, \tag{2}$$

where the matrices ω_V and π incorporate the different values of the vibrational frequency (e.g., ω_0 and $\omega_0 + \delta\omega$) and the rates of transition (e.g., W_+ and W_-) respectively. W is a column vector which gives the average distribution of frequencies and 1 is a row vector whose elements are all unity. The lineshape which corresponds to this result is plotted as a function of temperature in Fig. 13 and is given analytically

$$I(\omega) = \frac{W_+(\delta\omega)^2 / (1 + W_+/W_-)}{[\omega'^2 - (\delta\omega/2)^2]^2 + [W_-(\omega' + \delta\omega/2) + W_-(\omega' - \delta\omega/2)]^2}, \tag{3}$$

where $\omega' = \omega - \omega_0 - \delta\omega/2$. The important point to notice is that the partial retention of phase memory which occurs in the intermediate exchange regime (i.e., $W_+, W_- \approx \delta\omega$) causes a temperature-dependent linewidth and effective Raman frequency.

These effects can be experimentally observed and are the signature of the vibrational exchange mechanism of dephasing. They form the basis for analyses of experimental lineshapes to determine exchange rates and frequency shifts. Physically, the exchange rates are related to the rate of intermolecular resonant energy transfer and to the interaction of the molecule with degrees of freedom of the macroscopic system. The frequency shift is related to the strength of the intramolecular anharmonic coupling. Thus, this type of analysis is a good probe for these particular features of the vibrational dynamics.

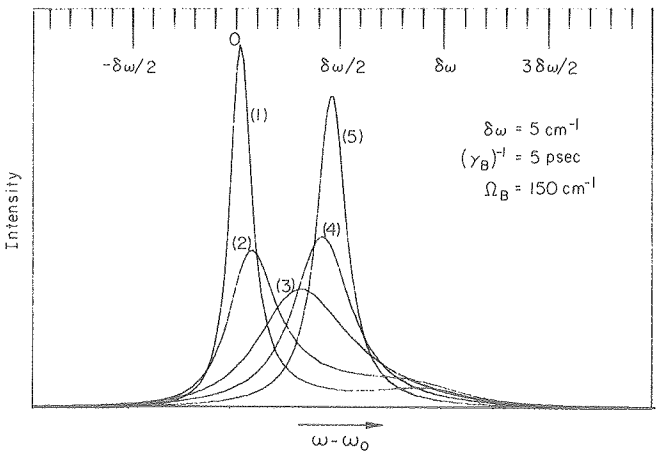

Fig. 13. This figure is shown as an example of the temperature dependence of the exchange lineshape (Eq.3) for the parameters shown in the figure. The five curves correspond to the following temperatures: Curve #1 = 150 K, curve #2 = 250 K, curve #3 = 500 K, curve #4 = 800 K, and curve #5 = 1500 K. For this calculation the exchange rates were given by $W_+ = \gamma_B(n(\Omega_B))$ and $W_- = \gamma_B[n(\Omega_B)+1]$, where $\Omega_B = 150$ cm^{-1}. (XBL 7711-6474)

---

*Partially supported by NSF.

e. Observation of Vibrational Energy Exchange by Spontaneous Raman Spectroscopy*

C. B. Harris, P. A. Cornelius and R. M. Shelby

A vibrationally excited molecule in a condensed phase can be under the influence of numerous interactions, both inter- and intramolecular. Such a situation is very difficult to analyze theoretically, and a few experimental techniques allow one to distinguish among the various effects that may be important. For example, a Raman linewidth can be a composite of contributions from population relaxation (T_1), dephasing (T_2), and inhomogeneous broadening. These components are, traditionally, not directly separable. However, in our recent work we have demonstrated that another effect, namely energy exchange, may facilitate the interpretation of Raman lineshapes in a fundamental way. When this exchange phenomenon makes a significant contribution to a Raman lineshape, it can be utilized to obtain information regarding coupling of intramolecular modes, lifetimes of low-energy vibrational modes, and characterization of important dephasing channels for high-energy vibrational modes.

In another section of this report, we present the theoretical aspect of this problem. The present discussion concentrates on experimental applications of the theory we have developed. The theory predicts that, when a strong anharmonic coupling exists between modes (in our case, a high-frequency one and a low-frequency one), the Raman lineshape should exhibit a temperature-dependent width and peak frequency. Statistical analysis of lineshape data as a function of temperature can be employed to extract the following parameters: (1) the lifetime (τ) of the first excited state of the low-frequency mode; (2) the size of the coupling ($\delta\omega$) between the two modes; (3) the scattering rate (W_+) from the ground state of the low-frequency mode; and (4) the energy difference between the ground and first excited state of the low-energy mode (this appears as an "activation energy" for the line-broadening and frequency shift). Of particular interest are (1) and (4) above. The lifetime, τ, that is measured in these experiments represents a pure population relaxation time (T_1)--a quantity difficult to measure by any direct means. The activation energy motion of the molecule is important for dephasing of that mode, again providing information about intramolecular dynamics which is otherwise difficult to obtain.

The molecule we have chosen for detailed study is 1,2,4,5-tetramethyl benzene (durene). The Raman spectrum of the C-H stretch region of this molecule is shown in Fig. 14. As is readily seen, five lines in this part of the spectrum exhibit significant broadening and frequency shifts over this temperature range. Extensive computer analysis of the lineshape data over a number of temperatures has enabled us to evaluate the parameters discussed above.

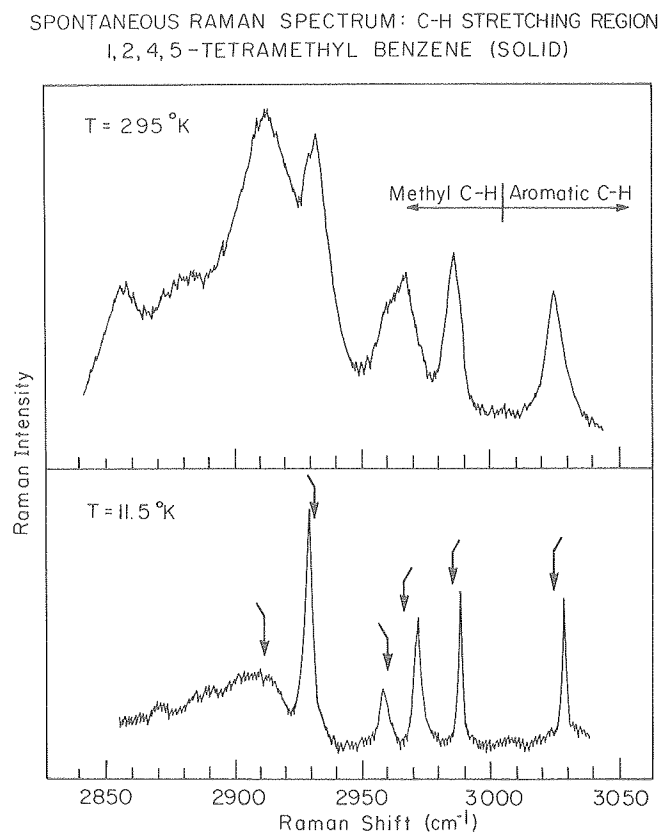

Fig. 14. The five bands which become very sharp at low temperatures are assigned as C-H stretches. The line near 3930 cm^{-1} corresponds to the aromatic ring protons, and the other four lines, the methyl group protons. The arrows in the lower panel indicate the magnitude of frequency shifts which occur when the sample is warmed to room temperature. (XBL 773-5179A)

These results are summarized in Fig. 15. An interesting facet of this problem can be seen from a consideration of the measured activation energies. Four of the five modes studied have an activation energy that matches the energy of some low-frequency motion of the molecule. Thus it appears that a given high-energy mode selects one of the low-energy modes as the dominant channel for dephasing. One can account for this selectivity on the basis of steric considerations. For example, the mode at 3027.5 cm^{-1} (symmetric ring-photon stretch) is dephased by a methyl rocking motion--the one motion that brings the neighboring methyl groups closest to the ring protons. In similar fashion, we have been able to account for the other observed matchings of low- and high-frequency modes.

Currently, several other substituted benzenes are under study in a similar way. For example, in Fig. 11 of Section c above we present the temperature dependence of the Raman spectrum of xylene, in the same C-H stretch region. Several lines exhibit the type of temperature dependence characteristic of exchange, and these data are currently under analysis.

VIBRATIONAL DEPHASING RATES FOR THE RAMAN ACTIVE C-H STRETCHES IN 1,2,4,5 TETRAMETHYLBENZENE (DURENE)

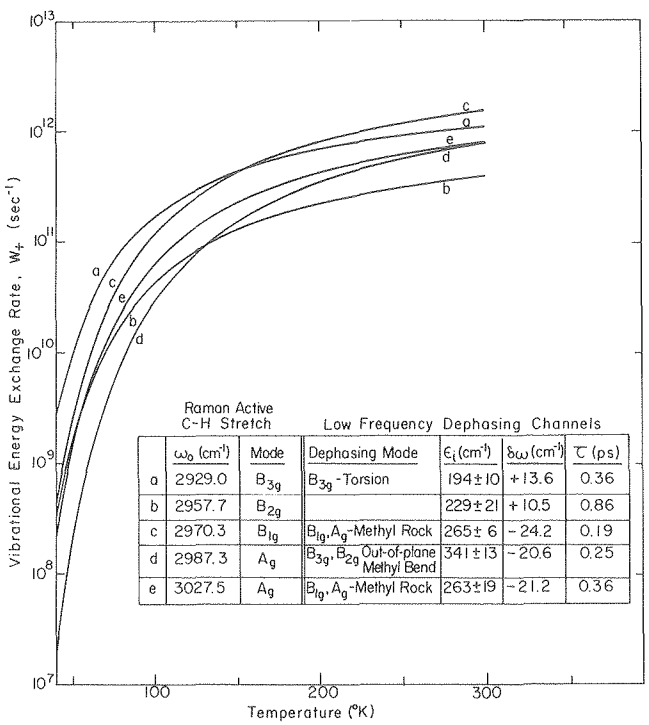

	ω_0 (cm^{-1})	Mode	Dephasing Mode	ϵ_i (cm^{-1})	$\delta\omega$ (cm^{-1})	τ (ps)
a	2929.0	B_{3g}	B_{3g}-Torsion	194±10	+13.6	0.36
b	2957.7	B_{2g}		229±21	+10.5	0.86
c	2970.3	B_{1g}	B_{1g},A_g-Methyl Rock	265±6	-24.2	0.19
d	2987.3	A_g	B_{3g},B_{2g} Out-of-plane Methyl Bend	341±13	-20.6	0.25
e	3027.5	A_g	B_{1g},A_g-Methyl Rock	263±19	-21.2	0.36

Fig. 15. The exchange rate W_+ is shown for the five durene lines indicated in the inset. The assumption is made that the rate $W_- = \tau^{-1}$ is constant over this temperature range. The effects of the exchange are observed for temperatures above about 100° K as the intermediate exchange region is beginning to be approached. The inset shows possible assignments for the C-H stretching modes, the dephasing (exchanging) modes which are thought to be important in the exchange process, and the values of the parameters determined by the fitting process. These include the effective activation energy, ϵ_i, the frequency shift due to the perturbation H_p, $\delta\omega$, and the lifetime in the upper state, τ. (XBL 777-5848)

It should be emphasized that the only experimental input necessary for the type of analysis sketched here is the Raman lineshape temperature dependence. On the basis of this alone, it has been possible to build up a detailed picture of the intramolecular dynamics for the modes we have considered. This application suggests that the technique may find frequent use in future energy transfer studies.

---

*Partially supported by NSF.

4. COHERENT SPECTROSCOPY IN EXCITED TRIPLET STATES

a. Coherent Averaging in Excited Triplet States via Rotary Echoes*

C. B. Harris and M. E. Tarrasch

For pulsed NMR experiments satisfying certain cyclic criteria, it can be shown that the spin system may be described by a time-independent average Hamiltonian $\bar{\mathcal{H}}$, equal to a time-weighted average of the Hamiltonians the system sees as a result of each rf pulse. We have used this formalism to elucidate features of electron spin coherence techniques in excited triplet states.

The rotary echo is a fairly simple two-pulse sequence in which each pulse is of length τ, but the second ("refocusing") pulse is 180° phase-shifted from the first pulse. Unlike other optically detected coherence experiments, no probe pulse is required, since the echo is manifested as a population difference rather than as a transverse magnetization. The phase shift removes applied field ($\mathbf{H}_1$) inhomogeneities and results in a signal waveform resembling two back-to-back transient nutations, much as a spin echo removes static field ($\mathbf{H}_0$) inhomogeneities and looks like back-to-back free-induction decays.

To apply average Hamiltonian theory, we consider a two-level system (since only two of the three triplet sublevels are coupled by the field) with a general relaxation Hamiltonian:

$$\mathcal{H}_R = \begin{bmatrix} H_{yy} & H_{yx} \\ H_{xy} & H_{xx} \end{bmatrix} . \qquad (1)$$

After a general pulse of angle θ, the spins' relaxation Hamiltonian, $\mathcal{H}_R(\theta)$, can be calculated. The average Hamiltonian over a pulse of angle Θ is:

$$\bar{\mathcal{H}}_R = \frac{1}{\Theta} \int_0^{\Theta} \mathcal{H}_R(\theta)\, d\theta . \qquad (2)$$

If we neglect spin-lattice relaxation ($T_1 = \infty$), we can set $H_{xy} = H_{yx} = 0$ and this integral yields, for both 0 and 180° pulses:

$$\bar{\mathcal{H}}_R = \frac{1}{2}\begin{bmatrix} H_{xx}+H_{yy} & 0 \\ 0 & H_{xx}+H_{yy} \end{bmatrix}. \qquad (3)$$

The diagonal terms are now equal, which corresponds physically to adding the same energy term (1/2) $(H_{xx}+H_{yy})$ to the energy of each sublevel coupled by the microwaves. Since this term is assumed to vary over different sites in the sample, the rotary echo can be seen to eliminate the effects of an inhomogeneous distribution of local relaxation fields. This is illustrated in Fig. 1.

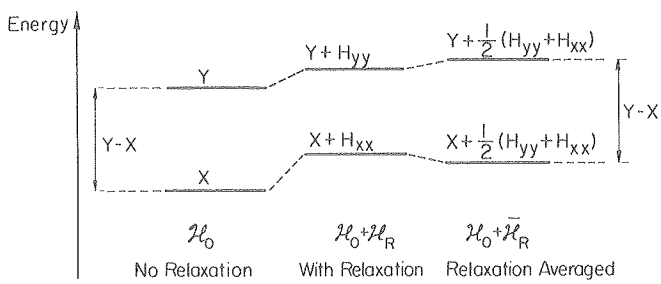

Fig. 1. Schematic representation of relaxation averaging by rotary echoes. The zero-field $|y\rangle \leftrightarrow |x\rangle$ transition occurs at energy Y-X for an isolated triplet state but is shifted and broadened by the inclusion of relaxation to a new energy $Y-X+H_{yy}-H_{xx}$. Application of the rotary echo removes the effect of relaxation by by coherent averaging.
(XBL 7711-6492)

We can perform a similar calculation for an off-resonance applied field ($\Delta\omega \neq 0$) to examine the detrimental effects of going off-resonance. The results for the initial 0° pulse only is shown, since the refocusing pulse calculation is too unwieldly:

$$\mathcal{H}_R(\Delta\omega \neq 0) = \frac{1}{2}\begin{bmatrix} H_{yy}\left[1+\left(\frac{\Delta\omega}{\bar{\omega}}\right)^2\right] + H_{xx}\frac{\omega_1}{\bar{\omega}}^2 & \frac{i\Delta\omega\omega_1}{\bar{\omega}^2}(H_{yy}-H_{xx}) \\ \frac{i\Delta\omega\omega_1}{\bar{\omega}^2}(H_{xx}-H_{yy}) & H_{yy}\left(\frac{\omega_1}{\bar{\omega}}\right)^2 + H_{xx}\left[1+\left(\frac{\Delta\omega}{\bar{\omega}}\right)\right]^2 \end{bmatrix}. \qquad (4)$$

We see that even though $\mathcal{H}_R$ is diagonal, $\bar{\mathcal{H}}_R$ is not. This implies that an effective T_1 process is occurring, since the off-resonance condition results in a different average spin polarization than that for $\Delta\omega=0$. Transverse relaxation (T_2) processes are not eliminated (as for $\Delta\omega=0$), but are partially averaged. If a local field has strength A, off-resonance rotary echoes will reduce the relaxation linewidth by a factor of roughly $\Delta\omega/\bar{\omega}$. This may also be seen by a simple geometric argument, as illustrated in Fig. 2: the angle $\underset{\sim}{H}_{eff}$ makes with the r_2 axis is $\alpha = \arctan(\Delta\omega/\omega_1)$. Therefore, any field $\underset{\sim}{A}$ along the r_3 axis has a projection of $A \sin\alpha = A\,(\Delta\omega/\bar{\omega})$ along $\underset{\sim}{H}_{eff}$. It can be shown that rotary echoes average fields perpendicular to $\underset{\sim}{H}_{eff}$, but not parallel to $\underset{\sim}{H}_{eff}$, for an arbitrary choice of phase and resonance offset $\Delta\omega$. Thus $A(\Delta\omega/\omega)$, the component of $\underset{\sim}{A}$ parallel to $\underset{\sim}{H}_{eff}$, represents the reduction in relaxation field strength due to off-resonance averaging and is similar to the rigorous result obtained above.

Perhaps the most significant aspect of coherent averaging in excited triplet states is that the result for $\bar{\mathcal{H}}_R$ is the same for many of the coherence experiments, including transient nutations, spin locking, and Carr- Purcell-Meiboom-Gill spin echoes,

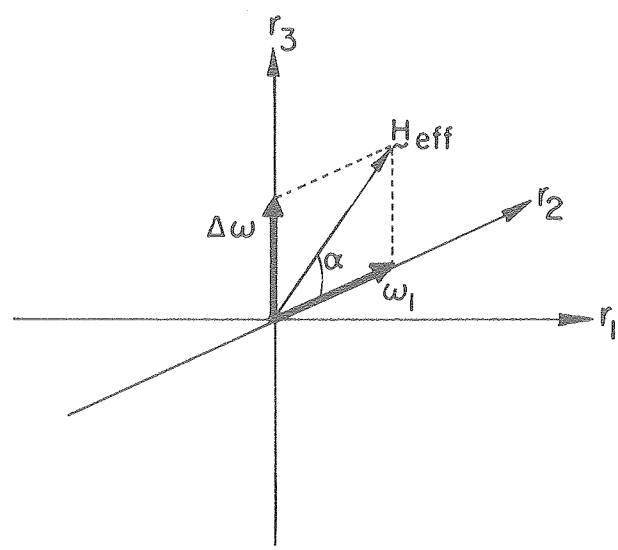

Fig. 2. Definition of the angle α in r-space.
(XBL 7711-6490)

even though the relaxation times obtained can vary over five orders of magnitude, depending on the coherence technique used. This allows us to separate the averaging properties from the geometrical considerations and quantitatively compare the relaxation times in terms of the geometrical relations between the psuedomagnetization $\underset{\sim}{r}$ and the effective driving field $\underset{\sim}{H}_{eff}$.

---

*Partially supported by NSF.

b. Off-Resonance Effects in Rotary Echoes*

C. B. Harris and M. E. Tarrasch

The formation of an echo in r-space depends on the constructive interference of the r-vectors associated with each ensemble of two-level systems. Therefore, the echo intensity is dependent on the ability of the r-vectors to refocus along the r_3 axis at time 2τ and is affected strongly by off-resonance driving fields. As an approach to this problem, we have used the equations of motion for the r-vector to numerically simulate rotary echo decays. We consider first a delta-function absorption line with an off-resonance driving field. Figure 3 shows the echo maximum decay one would observe as a function of the echo time 2τ; these curves like all the curves in this section, do not represent the echo waveform. [In all of these calculations, $r_3(\tau=0)$ has been set equal to 1.0 and ω_1 has been set at 5 MHz.] Clearly, beats are noticeable for $\Delta\omega \gtrsim 0.5$ MHz. The amplitude and frequency of the beats is determined by the magnitude of $\bar{\omega}$ and the angle α (see Fig. 2 of preceding paper). As $\Delta\omega$ increases, $\bar{\omega}$ also increases, causing a higher frequency beat to be superimposed on the decay. The heat amplitude is given generally by $8\cos^2\alpha - 8\cos^4\alpha$ a maximum for $\alpha = \pi/4$, which can result in complete inversion of the echo signal for special values of τ.

One may now incorporate the effects of population "feeding and decay" kinetics, since the lowest triplet state is continuously being populated by the first singlet state and depleted to the ground singlet state during the rotary echo. Dynamic processes, such as exciton-trap interactions, are also taken into account by this calculation, and are in fact more likely to affect rotary echoes than lifetime effects, because they can occur on a more rapid time scale.

Figure 4 shows an example of decay curves for a given $\Delta\omega$ (1 MHz) and variable kinetic parameters determined by the choice $r_3(t=0) = 1.0$ and k_A, the average triplet sublevel decay rate. As k_A approaches the beat frequency, the decay curves become damped to a steady-state r_3 value dependent on $\Delta\omega$. Thus, the rotary echo is a useful probe of processes in molecular solids which occur on the time scale of $10^4 - 10^6$ s^{-1}. Triplet lifetimes ($k_A \sim 10^2$ s^{-1}) are too slow to affect the decay curves and would be obscured by other dephasing events (spin diffusion, inhomogeneous broadening, etc.)

Finally, the effects of inhomogeneous broadening in the absence of spin diffusion can be simulated by taking the equations for a single r-vector and numerically integrating across the resonance line. Figures 5 and 6 show the rotary echo decays for Gaussian and Lorentzian lineshapes, respectively, with equal FWHM's of 3 MHz. Because the integration limits are 5 FWHM's on both sides of the center frequency, the Lorentzian decays have noticeably incorrect (~ 5%) normalization and are thus more qualitative in nature. Inhomogeneous broadening shows up a damping of the echo intensity dependent on the parameters $\Delta\omega$ and $(T_2^*)^{-1}$ αFWHM. For a given FWHM, the damping rate increases as $\Delta\omega$ increases and thus the destructive interference of the various r-vectors associated with the homogeneous isochromats in the

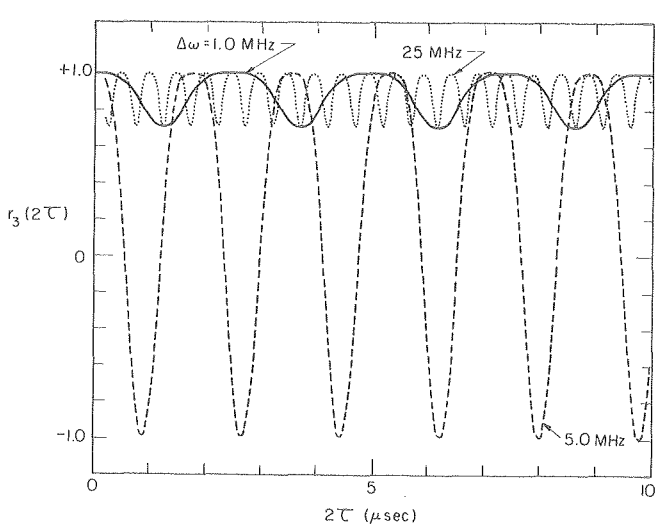

Fig. 3. r_3 component of the pseudomagnetization at at the time of the rotary echo formation for a single isochromat. The curve represents the echo intensity as the pulse length τ is increased. (XBL 7711-6493)

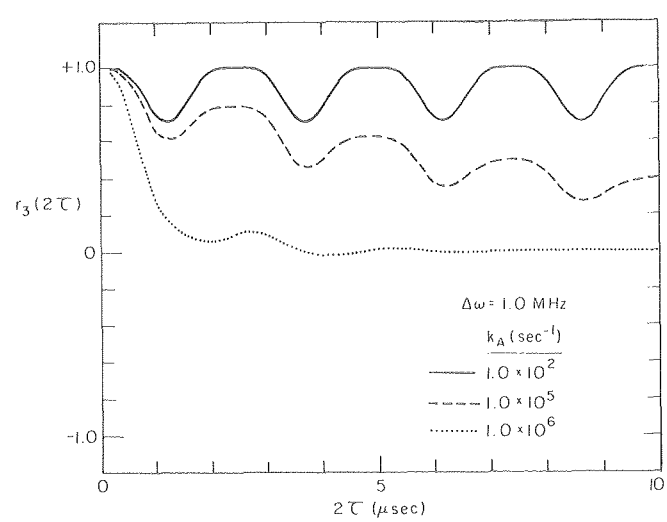

Fig. 4. Off-resonance echo maximum intensity for a single isochromat as a function of pulse length τ and decay rate k_A. The resonance offset $\Delta\omega$ is set equal to 1 MHz. (XBL 7711-6498)

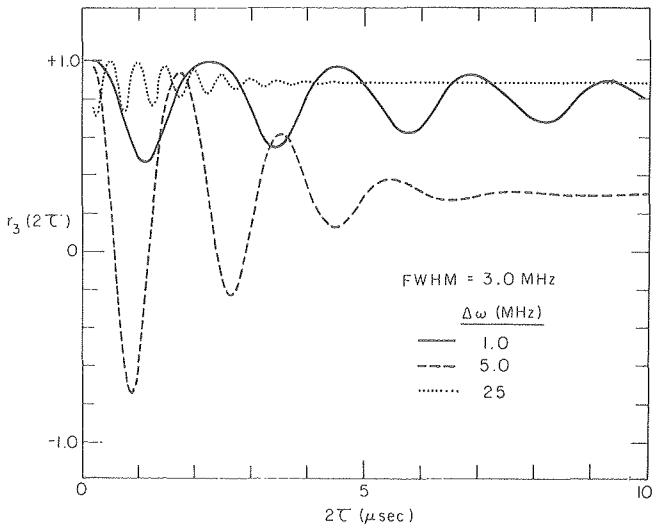

Fig. 5. Off-resonance echo maximum intensity for Gaussian lineshape as a function of τ and Δω. The FWHM is fixed at 3 MHz. (XBL 7711-6495)

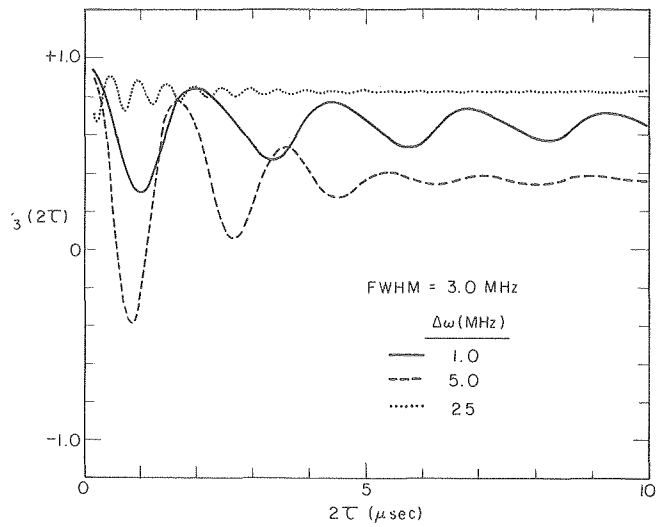

Fig. 6. Off-resonance echo maximum intensity for Lorentzian lineshape as a function of τ and Δω. The FWHM is fixed at 3 MHz. (XBL 7711-6494)

line is more efficient as more of the isochromats are off-resonance.

The rotary echo is particularly sensitive to imperfections in the driving field, since the field is on during the entire course of the experiment. This is verified by the preceding examples of off-resonance rotary echos in which beats are predicted to be superimposed on the echo maxima decay. One must therefore be careful in experiments to ensure that $\Delta\omega = 0$ in order to avoid these oscillations which obscure the measurement of relaxation times.

*Partially supported by NSF.

c. Rotary Echoes in Excited Triplet States: Experimental

C. B. Harris and M. E. Tarrasch

Rotary echoes in excited triplet states has not been a widely used coherence technique, because the conditions under which the echo decay reflects processes of interest are fairly stringent. If the echo is to be used to measure dynamic processes like trap-exciton band or trap-vibronic level interactions, the decay rates due these processes must be significantly faster than rates of time-dependent nuclear processes. Dynamic processes which take place on the millisecond time scale are more amenable to study by a technique like spin locking which is not sensitive to nuclear spin diffusion or inhomogeneous broadening.

We have been engaged in a series of rotary echo experiments on various 1,2,4,5-tetrachlorobenzene (TCB) systems to learn about spin diffusion rates, detrapping rates, and other interactions in molecular solids. The observed decays exhibit large amounts of scatter, making quantitative estimates of rate processes impossible. Generally, decay times ($T_{2\rho}$) were temperature-independent and ranged from 5 to 40 μs, depending on the system studied. The temperature independence is indicative of a process such as nuclear spin flips which change the local fields at the triplet electrons. There is no apparent correlation between the approximate $T_{2\rho}$ values and the particular TCB system studied.

The scatter in the data has recently been resolved as arising from beats superimposed on the echo decay. By calculating the echo intensity for an inhomogeneous line on-resonance and displaying it as in Section 4b, we clearly see that inhomogeneous broadening will distort the decay of the rotary echo. Figure 7 illustrates the on-resonance echo decay as a function of the inhomogeneous linewidth. Because most data points were taken at regularly spaced values of τ

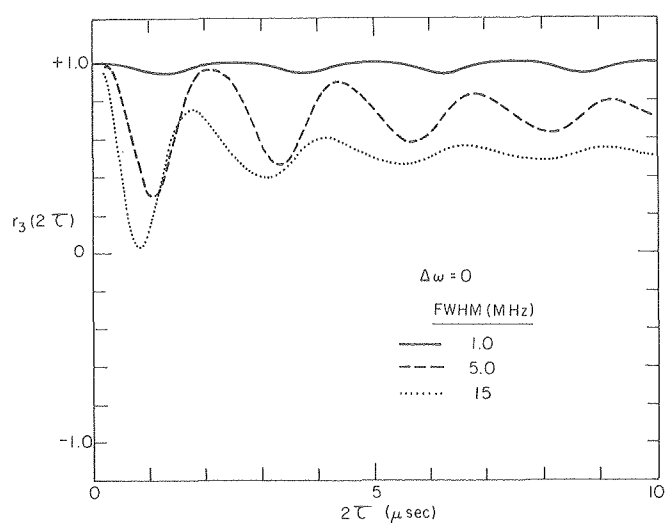

Fig. 7. Echo maximum intensity for Gaussian lineshape as a function of τ and FWHM. The driving field is on-resonance. (XBL 7711-6497)

chosen purely for experimental convenience and without knowledge of the beat pattern, data for rotary echoes have been difficult to treat.

Physically, the appearance of beats is a consequence of two features: (1) even though $\Delta\omega = 0$, all the spins are off-resonance by an amount depending on their position in the line; and (2) the applied field is "on" continuously during the experiment, and one cannot make the approximation used for short pulses ($\theta = \pi/2, \pi$) that all the isochromats nutate through θ about the same effective field. Because of these characteristics, the rotary echo is the only cyclic coherence experiment that exhibits these beats for on-resonance driving fields.

To observe these beats experimentally requires that the resonance line have a FWHM large enough ($\gtrsim 2$ MHz) to make the beat amplitude overcome experimental error and S/N problems; if the FWHM is very large ($\gtrsim 15$ MHz) and τ is chosen too long, the beats will be damped out and thus unobservable. This last point is illustrated by the dotted curve in Fig. 7, for which the oscillations disappear by $2\tau \sim 8\ \mu s$ for a 15-MHz-wide Gaussian line. TCB systems are ideal cases to study, since the FWHM for TCB/durene mixed crystals is about 3.5 MHz. We are currently in the process of obtaining detailed echo decays for this system to verify the predictions of this calculation.

d. Energy Transfer Processes in Substitutionally Disordered One-Dimensional Solids

C. B. Harris and D. A. Zwemer

To completely understand Frenkel exciton propagation in substitutionally disordered systems, knowledge of the lattice vibrations is just as important as knowledge of the exciton energy levels. A chemical impurity with different mass and intermolecular force constants creates a phonon mode localized about the impurity and a node in the delocalized host phonons at the impurity. Exciton propagation at the impurity is governed by processes such as thermal detrapping and thermally activated tunneling, which are in turn governed by the population of the local phonon modes. In the past year we have made the first study of the coupling between localized and delocalized phonon modes in a molecular solid.

Our probe is the spin dephasing rate of a trapped exciton at a chemically induced y trap in 1,2,4,5-tetrachlorobenzene (TCB), a pseudo-one-dimensional exciton conductor. The y trap is a perturbed TCB molecule 45 cm^{-1} below the host exciton band and lying adjacent to a chemical impurity. When the impurity energy levels are not accessible to the exciton, we have shown by optically detected spin locking that trapped excitations are thermally promoted to a vibrationally excited state of the trap 25 cm^{-1} higher in energy. This localized phonon level is in near-resonance with a 26 cm^{-1} phonon in the pure host, but the promotion rate, which is extracted from the dephasing rate in the limit of intermediate exchange, is extremely slow, about 100 s^{-1} at 4.2 K. In contrast, promotion to a similar local phonon level of para-benzoquinone in an isotopically mixed system where the perturbation of the lattice phonon structure is much less, is about 10^4 times faster. Depending on the nature of the chemical impurity producing the y trap, excitation may be transferred to a low lying impurity state rather than a localized phonon mode. Although the activation energy for transfer is much less, the pre-exponential factor representing coupling between the initial and final states is about the same. This shows that, in these systems, the coupling between delocalized and local phonon modes is the limiting step in energy transfer.

5. THERMAL MODULATION SPECTROSCOPY

a. Heat Pulse Propagation in Molecular Crystals at Low Temperatures

C. B. Harris and A. R. Burns

One of the primary motivations for research in the area of high frequency phonon propagation at low temperatures lies on the fact that there are a number of important phonon-induced energy transfer processes in a wide variety of materials. In particular, the numerous studies of exciton migration in aromatic molecular crystals have demonstrated the need for a detailed description of the phonon-induced delocalization of "trapped" excitations. A thorough study of the frequency dependences and the resonance absorption cross sections of such phonon interactions will certainly lead one to a greater understanding of the specific dynamics involved. In this part (a), the heat pulse method of generating high frequency phonons will be discussed with special attention to the problem of describing in detail the transmission factors for the phonon propagation. The specific application of the heat pulse technique to the study of excited triplet energy transfer phenomenon in molecular crystals will be discussed in part (b).

In order to characterize the frequency distribution of a pulse of high frequency (10^{11}-10^{12}Hz) phonons, two basic parameters must be known: (1) the effective temperature of the source; and (2) the mean free path of the phonons from the source. The first parameter is easily obtained by a blackbody phonon radiation relation which is completely analogous to the electromagnetic case described by the Stefan-Boltzmann equation. The effective temperature can be calculated from the input power at the heating source and the radiation constant. The second requirement entails a knowledge of the thermal conductance of the transmitting medium; in this case, it is a molecular crystal lattice. If the propagation of the radiated phonons is essentially unobstructed, then the frequency spectrum of the phonons will always be a function of the source temperature. In the event of extensive phonon scattering, the original frequency distribution will be lost and the subsequent analysis of phonon absorption processes will be most difficult.

The limit of free phonon propagation is usually referred to as ballistic thermal transport. When scattering dominates the propagation, the thermal transport is described by the classical diffusion limit. In the framework of these two limits,

one may assign a mean free path ℓ for the phonons traveling with a mean velocity $\bar{v}$ between scattering events:

$$K_s = 1/3\ C_s\ \bar{v}\ \ell. \qquad (1)$$

In the above equation, K_s is defined as the thermal conductivity of the medium and C_s is the heat capacity per unit volume.

The molar heat capacity of 1,2,4,5-tetrachlorobenzene (TCB) in the temperature range 0.5-7.0 K was determined by using a measurment technique developed by Prof. Phillips. The data shown in Fig. 1 indicate a reasonable fit to the expected Debye T^3 dependence, and thus yield a reliable value for $\bar{v} = 1.58 \times 10^5$ cm/s.

The thermal conductivity of the medium is determined by the heat pulse method, where the sample is situated in between a heater (source) and a bolometer (detector). The heater and bolometer are thin films of nichrome and germanium, respectively, which are vacuum evaporated onto separate quartz substrates and then bonded to the faces of the sample as shown in Fig. 2. The thermal coupling of the metal films to the crystal is accomplished by a thin layer of Dow-Silicone grease. The grease-mediated intefacial conductance K_B is unfortunately too low to observe the actual transit time of a short phonon pulse. However, this problem can be circumvented if one measures the thermal rise time τ_R of the crystal lattice. The rise time is a function of the sample heat capacity and the total thermal conductance K_{tot} between the heater and the bolometer:

$$\tau_R = C/K_{tot},$$
$$1/K_{tot} = 1/K_S + 2/K_B. \qquad (2)$$

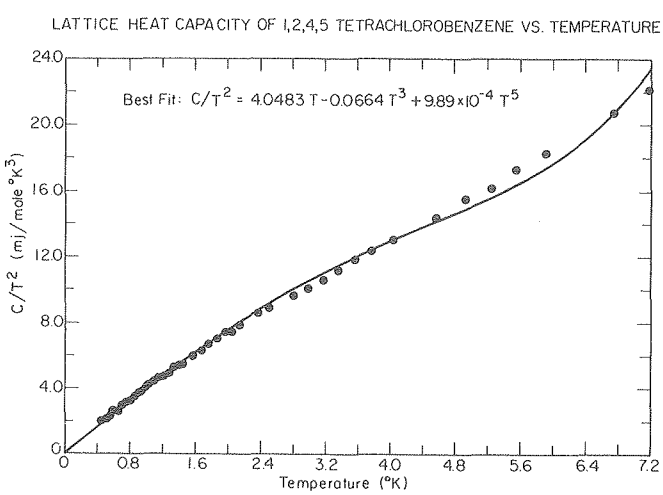

Fig. 1. Molar heat capacity of tetrachlorobenzene. The best fit was obtained by a least-squares analysis. (XBL 7612-7965)

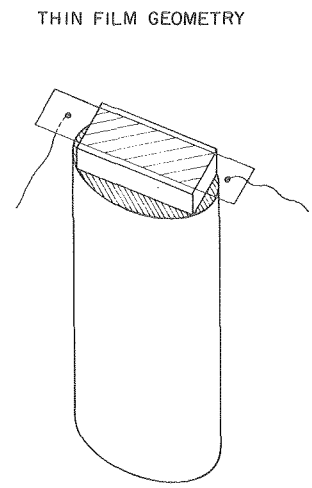

Fig. 2. A thin slab of single crystal TCB sandwiched between the heater film (bottom) and detector film (top). The electrical connections to the heater film are made by evaporated gold films running down the side of the glass rod. The germanium detector film is connected to a constant current supply by way of solder connections to chrome-gold contact pads adjacent to the germanium. (XBL 7612-7961A)

The factor of 2 appearing in the K_B term is there because one must take account of both the heater/crystal interface and the identical crystal/bolometer interface. The rise time of the crystal lattice is found by analyzing the exponential form, $\Delta T_{max}\,[1-\exp(-t/\tau_R)]$, of the bolometer signal. A typical bolometer signal is shown in Fig. 3. The values of τ_R in the temperature range 1.5-2.2 K are depicted in Fig. 4 for a 0.025-cm-thick crystal having a cross-sectional area of 0.06 cm^2.

If one assumes that the mean free path ℓ is equal to the crystal thickness, then K_S can be calculated from Eq. (1) and K_B can be calculated from Eqs. (2).

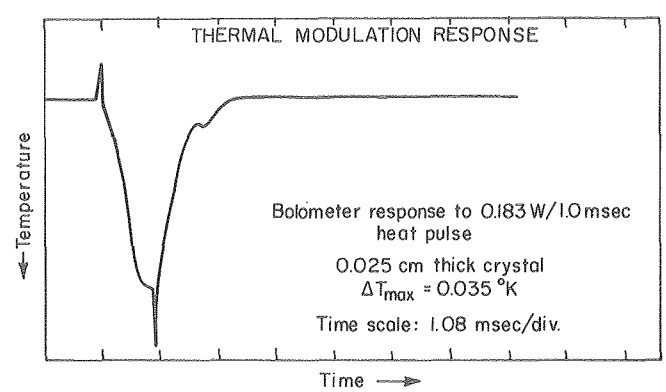

Fig. 3. Electrical response to the temperature change experienced by the germanium bolometer film. The sharp peaks are pick-up from the leading and trailing edges of the electrical pulse used to generate the heat pulse. (XBL 7612-5960A)

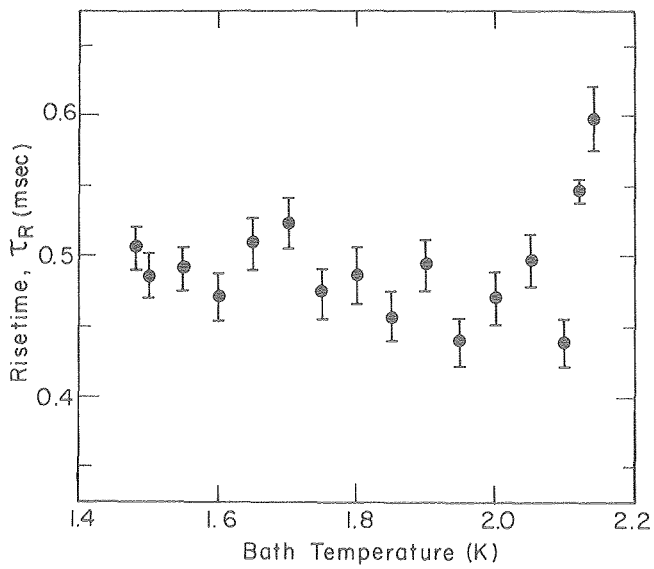

Fig. 4. Temperature dependence of the exponential risetime of the bolometer signal. (XBL 7710-6246)

The results of these calculations are shown in Fig. 5. From the comparison of the K_B results ($0.0034T^{3.2}$W/K cm^2) with those cited in the literature for conventional steady-state measurements ($0.0037T^3$W/K cm^2) on Dow Silicone grease interfaces, one can see that the agreement is certainly close enough to conclue that ℓ is indeed equal to the crystal thickness.

Thus the propagation of the heat pulse-generated phonons is ballistic at these temperatures. This conclusion enables one to characterize the spectral distribution in terms of the heater temperature. The bolometer will detect phonons of all frequencies and thus it is insensitive to the spectral distribution. However, most of the phonons emitted by the heater, which is at an effective temperature T_H, are centered around a maximal frequency $\nu_{max} = 2\ KT_H/h$. The half-width of this distribution (see Fig. 6) is also roughly proportional to KT_H/h. If the response of the bolometer to the heat pulse is primarily due to the absorption of the phonons in the spectral maximum region, it can be shown that the modulation depth of the signal ΔT_{max} will be linearly proportional to the input power. This can be seen in Fig. 7 for two pulse widths. It appears that the 0.10 ms

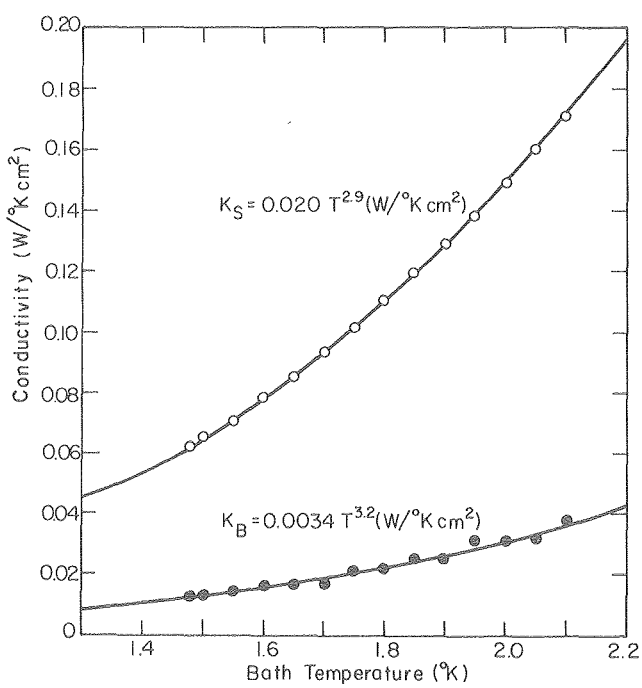

Fig. 5. Lattice conductivity of tetrachlorobenzene and the crystal/heater interface conductivity. (XBL 7612-7959A)

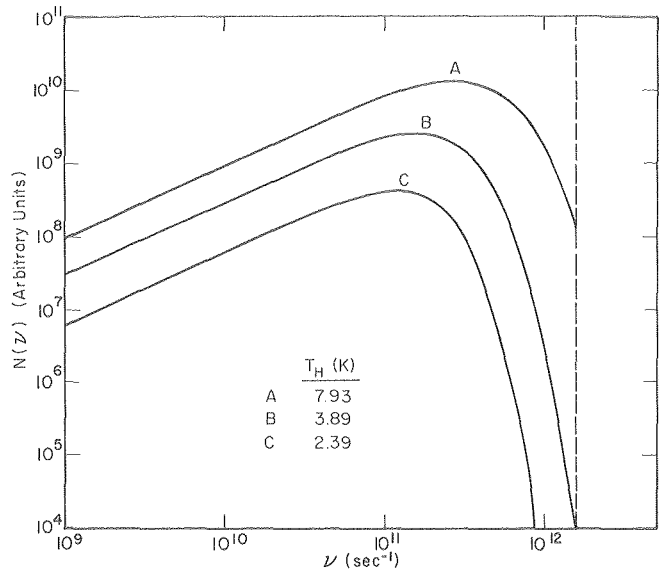

Fig. 6. Calculated phonon flux emitted by an ideal blackbody source at various temperatures T_H. The bath temperature is 2.0 K. (XBL 7710-6250)

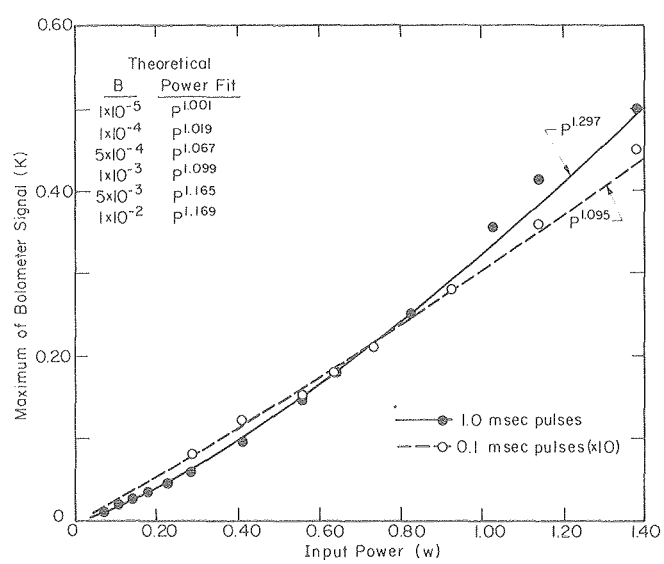

Fig. 7. Power dependence of the bolometer modulation depth ΔT_{max} at constant bath temperature (2.0 K). (XBL 7710-6249)

pulses obey the linear power dependence, whereas the 1.0 ms pulses do not quite behave in the expected manner. One possible explanation for this discrepancy is that the 1.0 ms pulses contain a larger-than-expected amount of higher frequency modes with respect to the spectral maximum. Another possible explanation is that the crystal is being overheated by the longer pulses and the diminished thermal contact with the bath due to the presence of the bolometer film.

b. A Study of Resonant Phonon Absorption by Traps in Molecular Crystals Using the Heat Pulse Technique

C. B. Harris and A. R. Burns

As was discussed in the preceding section, the spectrum of phonons created at the heater film is a broad band centered about 2 KT_H/h. Individual phonon frequencies cannot be selected unless they are specifically absorbed in an energy transfer process occurring in the transmission medium. One such process, shown in Fig. 8, is the phonon-assisted promotion of a "trapped" excited triplet state τ to a higher energy state within an exciton band. If one monitors the population decay of this localized state during the propagation time of a heat pulse, then one can calculate the kinetics of the absorption event with the transmission factors discussed in the preceding section.

In TCB there exists a localized state (X-trap) 17.3 cm^{-1} lower in energy than the top of the exciton band. Since the width of the exciton band, 4β, is equal to 1.3 cm^{-1}, one would expect that some of the phonons propagating in the lattice which have energies in the range of 16.0-17.3 cm^{-1} will be absorbed in the promotion event. The intensity of phosphorescence emission from the X-trap is equal to nk_{ave}, where n is the number of localized states and k_{ave} is the average radiative emission constant.

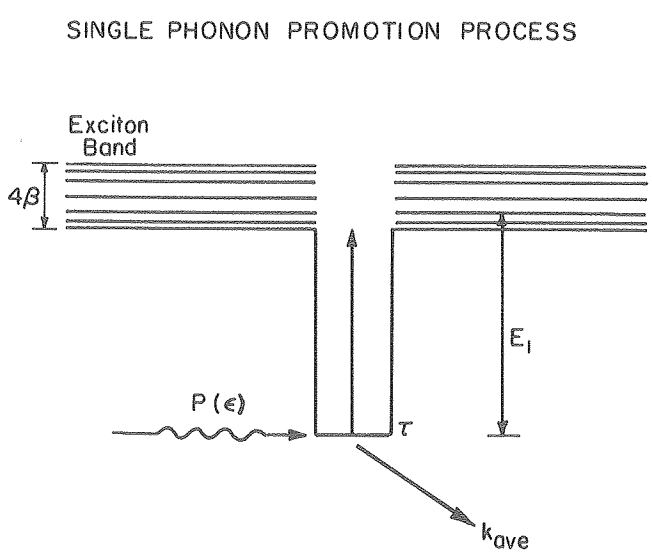

Fig. 8. Kinetic model of the phonon-assisted promotion of the localized (τ) triplet state to the exciton band. (XBL 7612-6249)

Thus any change in the population n due to the absorption of 16.0-17.3 cm^{-1} phonons can be optically detected through the phosphorescence modulation. This can be easily seen in Fig. 9 and 10, where the steady-state phosphorescence intensity is markedly temperature dependent. The curves in Fig. 3 are calculated from a partition function that incorporates Δ, 4β, and the number of band states N. For any given crystal, the average number of band states is unique, although N is usually in the range of 10^4 - 10^5 states for extensively zone-refined material.

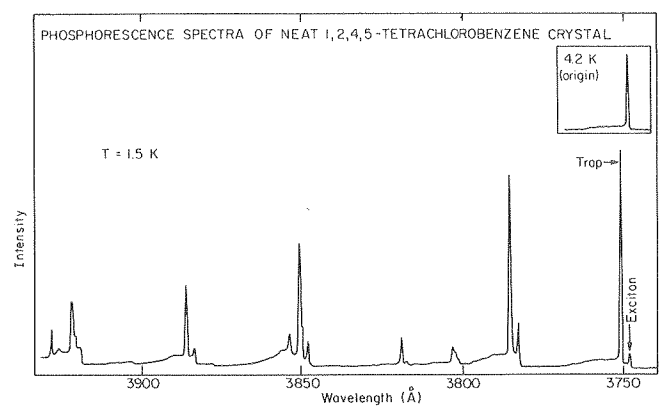

Fig. 9. Phosphorescence emission from extensively zone-refined TCB at 1.5 and 4.2 K. The A_g emission origin is at 3748 Å and B_{2g} emission is at 3781 Å. (XBL 757-6637)

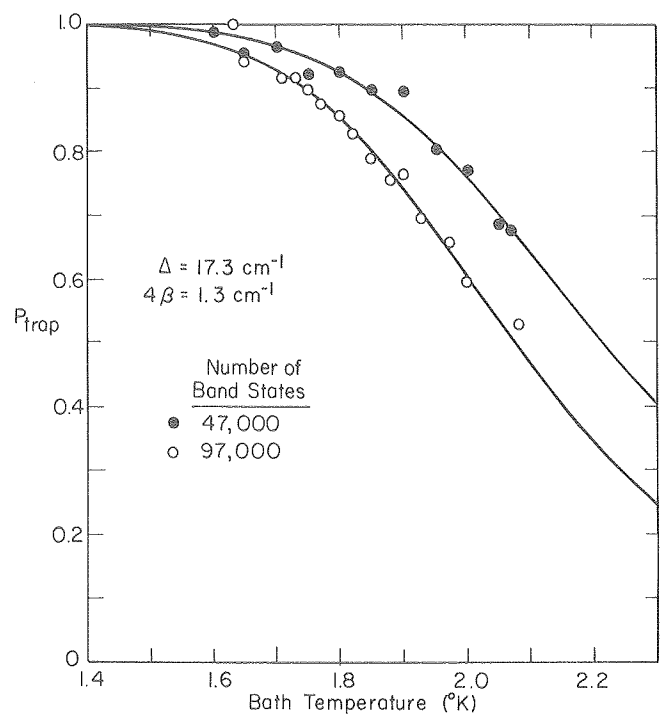

Fig. 10. Normalized phosphorescence emission intensity from the X-trap origin in two TCB crystals. The curves represent fits to the data by using an excitation partition function. (XBL 7712-6621)

When a heat pulse is applied to this system, the change in light intensity of the trap emission will be proportional to the density of the heat pulse phonons. An example of the time-resolved heat pulse modulation is shown in Figs. 11 and 12. It is evident that the rate of decay of the trap population is governed by the thermal conductance of the lattice and the crystal/heater interface. However, the modulation depth $\Delta I_{max}/I_{ss}$ is also a function of the number of available band states and the degree of coupling between the phonon and the localized states. Thus one can define a relative phonon absorption cross section ϕ, which is the ratio of the modulation depth to the resonant phonon flux F:

$$\phi = \frac{(\Delta I_{max}/I_{ss})}{F} . \qquad (1)$$

The total acoustic power P_a of the heat pulse in the crystal is proportional to the product of the input power P_i and the thermal conductance K_{tot} away from the heater surface:

$$P_a \propto K_{tot} P_i = K_{tot} B \, (T_H^4 - T_B^4). \qquad (2)$$

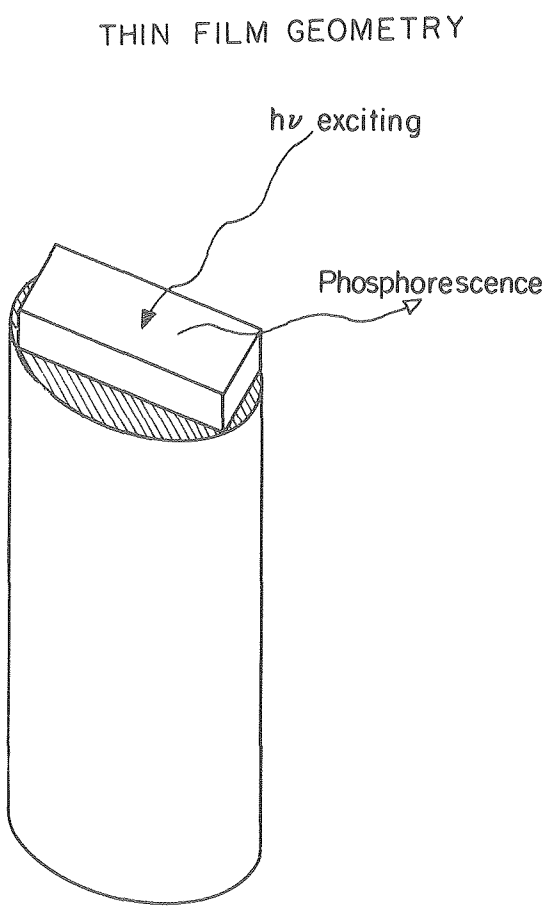

Fig. 11. The phosphorescence emitted by the crystal is monitored at a 90° angle to the exciting light. The heater film is identical to that shown in Fig. 2 of the preceding paper. (XBL 7612-7961B)

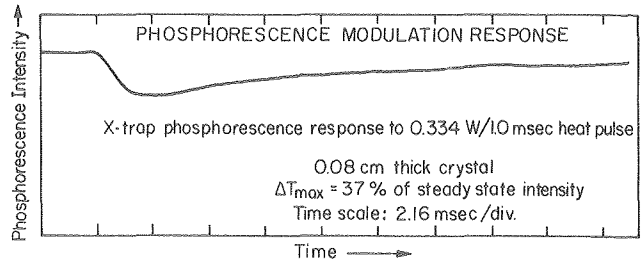

Fig. 12. Decrease in the phosphorescence intensity of the X-trap emission during the course of a heat pulse. The long relaxation back to the steady-state intensity is due to the combined slow rates of retrapping and singlet-to-triplet energy conversion ("feeding"). (XBL 7612-5960B)

The proportionality factor B is analogous to the Stephan-Boltzmann constant for electromagnetic radiation from a blackbody. For phonons of frequency ν, the net flux from the heater film at temperature T_H into the crystal which is at a bath temperature T_B is given by:

$$F(\nu, T_H, T_B) \cong K_{tot} \, \nu^2 \left[\frac{1}{\exp(h\nu/kT_H)-1} - \frac{1}{\exp(h\nu/kT_B)-1} \right]. \qquad (3)$$

Since one is concerned with the total flux F of the resonance phonons in a range ν to ν', during a pulse width of Δt, Eq. (3) must be integrated with respect to frequency:

$$\int_{\nu}^{\nu'} F_\nu(\nu, T_H, T_B) d\nu = K_{tot} \left[\mathscr{F}(T_H)\Big|_{\nu}^{\nu'} - \mathscr{F}(T_B)\Big|_{\nu}^{\nu'} \right], \qquad (4)$$

$$\mathscr{F}(T) = \frac{-kT}{h} \exp(-h\nu/kT) \left[\nu^2 + \frac{2KT}{h} + 2\left(\frac{kT}{h}\right)^2 \right]. \qquad (5)$$

As one would expect, the net flux F is a function of the input power. However, the power dependence $F(P_i)$ differs from one frequency interval to the next in the phonon spectral distribution. One can see this dependence only if the results of several traps having different depths are compared. In Fig. 13 we show the results of the phosphorescence modulation ofthe X-trap and the two isotopic traps hd- and h_2-TCB in d_2 - TCB. A complete analysis of these results is found in Tables 1 and 2. The X-trap results indicate a fairly definite dependence of the cross section ϕ on the number of available band states. Also the results clearly show that the phosphorescence modulation is independent of which triplet sublevel is monitored (the A_g or the B_{2g} emission).

The most interesting feature of the results presented here is that the absorption cross sections for the isotopic traps are much greater than that for the X-trap, especially considering the fact that the number of band states available to the isotopic

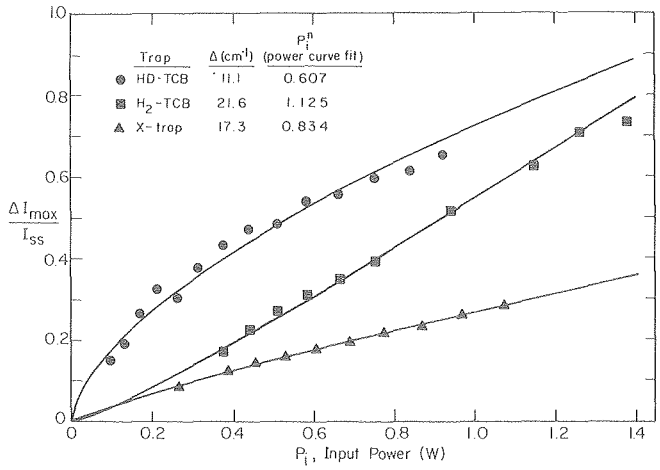

Fig. 13. Power dependence of the phosphorescence modulation for three different traps in the TCB lattice. The pulse widths are all 1.0 ms, the bath temperature is kept at 2.0 K, and the exciton band width is 1.3 cm^{-1}. A complete analysis of the data appears in Tables 1 and 2. (XBL 7712-6628)

traps is three orders of magnitude less. Thus these experiments reveal a fundamental difference in the mechanism for the two phonon-mediated processes.

6. REMOTE SATELLITE COMPUTER SYSTEMS DEVELOPMENT

C. B. Harris and J. L. Chao

In our latest effort to computerize the laboratory's experiments, a network system has been developed to expand our computer facilities. This network, called the Remote-11 system, consists of a host computer and up to four remote satellites and three remote terminals.

The network allows rather inexpensive, yet fast LSI-11 microcomputers to provide dedicated real-time laboratory applications, while allowing them to share the extensive and rather costly peripherals that support the complete Remote-11 system.

Table 1. Heat pulse transmission parameters, TCB.

Sample[a]	Bath temp. (K)	Thickness (cm)	C[b] (Nj/K)	τ_R[c] (ms)	K_{tot} (mW/K)	K_B (mW/K)
A	2.0	0.080	1.26	0.449	2.80	2.90
B	2.0	0.039	0.61	0.183	3.44	4.12
C	2.0	0.050	0.79	0.263	2.99	3.28
C,B_{2g}	2.0	0.050	0.79	0.251	3.02	3.30
C	1.75	0.050	0.54	0.262	2.04	2.23
C,B_{2g}	1.75	0.050	0.54	0.282	1.90	2.06
C	1.48	0.050	0.33	0.211	1.56	1.74
C,B_{2g}	1.48	0.050	0.33	0.234	1.40	1.55
D,hd	2.0	0.024	0.38	0.406	0.93	1.05
D,h_2	2.0	0.024	0.38	0.336	1.12	1.31

[a]Emission to electronic origin, unless indicated by B_{2g}.
[b]Values ± 5%.
[c]Values ± 10%.

Table 2. Phosphorescence modulation results, TCB.

Sample[a]	Bath temp.	Δ (cm^{-1})	Band States[b]	B (MW/K^4)	Power Range (ω)	Calc. T_H Range (K)	P_i^{n}[c]	φ(norm)
A	2.0	17.3	72,000	0.15	0.19-1.89	0.02-10.60	0.741	1.00
B	2.0	17.3	50,000	0.43	0.28-2.20	5.09- 8.46	0.900	0.694
C	2.0	17.3	47,000	0.22	0.27-1.08	5.93- 8.38	0.834	0.502
C,B_{2g}	2.0	17.3	47,000	0.24	0.33-0.97	6.10- 7.98	0.852	0.496
C	1.75	17.3	47,000	0.10	0.27-0.97	7.21- 9.93	0.709	0.744
C,B_{2g}	1.75	17.3	47,000	0.30	0.27-1.08	5.50- 7.75	0.909	0.638
C	1.48	17.3	47,000	0.15	0.33-1.08	6.85- 9.21	0.754	0.839
C,B_{2g}	1.48	17.3	47,000	0.22	0.27-1.08	5.92- 8.37	0.852	0.820
D, hd	2.0	11.1	<100	0.21	0.09-0.94	4.64- 8.12	0.607	2.27
D, h_2	2.0	21.6	<100	0.38	0.38-1.38	5.63- 7.77	1.125	2.28

[a]Emission to electronic origin, unless indicated by B_{2g}.
[b]Values ± 500 states, except last two.
[c]Standard deviation of slopes ≈ 1%.

Remote-11 is supported by DEC as a software package available for the RT-11 system based on the PDP-11 family of computers. This software was modified to support the LSI-11 microcomputers for which we structured the system. The hardware modifications were rather straightforward; users are connected to the host through asynchronous serial interface boards that have been properly configured for the proper register and vector addresses.

Management of the host is provided through the RT-11 Foreground/Background monitor. This monitor allows high priority servicing of Remote-11 system requests from all users in the foreground while offering background execution to a single remote user with low priority. The distinction between users is of one of two kinds, the first being a satellite microprocessor that can be loaded to execute a program, the second being a terminal connected directly to the host through which files may be edited or programs executed in the background.

The major consideration in relying on the Remote-11 system network to support the laboratory's experiments, is that of substantial savings on peripherals which would otherwise be duplicated. In particular, the RT-11 system is a disk-based system for which a disk drive singly approaches the price of a complete LSI microcomputer. Secondly, only in this way can we use the LSI-11 microcomputer to provide the dedicated real-time with floppy diskettes capable of storing over 250K bytes of data for later data reduction.

It is interesting to note that this sytem is so versatile that while a remote satellite could be collecting data on to a disk in real-time, the data reduction could then be performed simultaneously in either the background of the host, or even in a second remote satellite.

The Remote-11 system is rather simple to adapt to if the user is already familiar with programming under the RT-11 system. Programs run in the satellite are down-line-loaded in the standard PDP-11 ABSOLUTE LOADER format using DAP and DDCMP communications protocols.

We are presently using the RT-11 system for high speed data collection of ellipsometric parameters from our surface experiment as well as for the data acquisition and manipulation from the stimulated Raman emission from a picosecond experiment collected using an Optical Multichannel Analyzer (OMA).

Peripherals which the Remote-11 system supports include a Tektronix graphics terminal and hard copy plotter, a digital multi-meter, a high speed reader and punch, as well as a fancy teletype console. Each satellite will also be equipped with multiplexed A/D converters.

We are presently interfacting the Optical Multichannel Analyzer (OMA) to determine the temperature dependence of high resolution phosphorescence lineshapes from crystals. This "state of the art" optical multichannel analyzer requires a computer for both control and data acquisition. The requirements for data acquisition from the OMA are high speed data storage as well as display of the lineshape. We have also successfully interfaced a multichannel analyzer for real-time display of the data as well as implementing a 2-D oscilloscope for real-time two-dimensional display of the image.

A more complicated experiment involves using the OMA to perform time-resolved spectroscopy on a sample whose lineshape exhibits "hole burning" due to the absorption of light from a pulsed tuneable dye laser. This kind of experiment requires a greal deal of data handled through the Remote-11 disk system.

7. RESEARCH PLANS FOR CALENDAR YEAR 1978

Charles B. Harris

a. Surface Studies of Nitrogen Oxides on Ni(111)

Further avenues to pursue in the study of catalytic decomposition of oxides of nitrogen include: (1) the studies of the kinetics of the decomposition to develop models for the mechanism, (2) the study of the dependence of the surface role in the decomposition; this can most easily be achieved by similar studies on the high-Miller-index faces of nickel, and (3) the study of the decomposition on different metal substrates; this would provide valuable information as to the role of the metal substrates' electronic structure in catalysis.

b. The Development of Infrared Ellipsometry for Studying Catalytic Pathways

We propose the development of a set of experiments to directly measure the reaction pathways and activation energies for reactions of adsorbed molecules on metal surfaces. The experiments involve the use of infrared ellipsometry, which would follow individual vibrational modes during the course of a reaction. Conventional methods for determining activation energies, such as thermal desorption and work function measurements, are not useful in most cases in identifying chemical reaction channels directly on the surface, the mode or nature of the molecular binding to the substrate, or the site selectivity of the process. The infrared spectrum of an adsorbed molecule from ellipsometry is a direct measure of the strength and nature of the surface interaction and can be used to follow the specifics of a reaction. The technique is extremely sensitive, easily capable of detecting less than 1% of a monlayer. It does not induce surface decomposition, unlike the various electron beam techniques, and can be used with insulator substrates without the problems of space charge formation.

Preliminary ellipsometric studies in the visible and ultraviolet have shown major changes in the interactions of various small oxidizing molecules on single-crystal nickel (111) surfaces. The studies have included O_2, NO, and most importantly NO_2, a major constituent of smog and atmospheric systems, and an important molecule in metallic corrosion and oxidation. Detailed information about the reaction pathways can be anticipated from IR ellipsometric studies.

The experiments require the building of an ultrahigh vacuum system with stringent geometrical constraints for infrared optics. The system is to have

a capability for a wide temperature range of the sample substrate, as well as support equipment to clean, characterize, and monitor the surface composition in situ. The key innovations of the system are: (1) the ability to physisorb and adlayer at low temperatures, (2) the ability to monitor the reaction from the physisorbed to chemisorbed state upon warming of the sample via IR ellipsometry, and (3) thereby directly measuring the activation energy for individual channels in a complex reaction. Therein lies the importance of the development of this tool for surface studies.

c. Spectroscopy of Molecules Adsorbed on Metal Surfaces

The development of surface spectroscopy for studying the changes in the electronic and molecular structure of aromatic hydrocarbons adsorbed on metal surfaces will be an important objective for the 1978 program. We are studying aromatic hydrocarbons on nickel (111) and nickel step surfaces with the objective of finding site-selective transitions that can be used to identify molecules adsorbed at the site-selective surface states and for studying energy transfer from the molecular to the surface states. In addition we will initiate a series of related experiments to look at electron beam damage of adlayers on metal surfaces, using the combined techniques of LEED and scanning spectroscopic ellipsometry.

8. 1977 PUBLICATIONS AND REPORTS

Charles B. Harris and Associates

Journals and Books

1. C. B. Harris, R. M. Shelby and P. A. Cornelius, Effects of Energy Exchange on Vibrational Dephasing Times in Raman Scattering, Phys. Rev. Lett. 38, 24, 1415 (1977).

2. C. B. Harris, The Origin of Optical Dephasing Times and Lineshape Functions for Electronic Transitions to Localized and Delocalized States in Solids, J. Chem. Phys. 67, 12, 5607 (1977).

3. C. B. Harris, Interpretation of the Optical Dephasing Time and Lineshape Function in the $S_0 \rightarrow T_1$ Exciton Transitions of 1,4 Dibromonapthalene, Chem. Phys. Lett. 52, 1 (1977).

4. M. E. Tarrasch, C. R. Chen and C. B. Harris, The Use of Coherent Spectroscopy in the Study of Intramolecular Tunneling Processes in Excited Triplet States, Chem. Phys. Lett. 48, 3 (1977).

5. C. B. Harris, Discussions on Radiationless Processes, Dynamical Interpretation of Electronic and Vibrational Dephasing Processes in Solids and Liquids, 1977.

6. C. B. Harris, The Study of Energy Transfer Processes in Solids Using Optically Detected Electron Spin Coherence Techniques, Proceedings of the Third Specialized Colloque Ampere, Optical Techniques in Magnetic Resonance Spectroscopy, 1977.

7. C. B. Harris and W. G. Breiland, Coherent Spectroscopy in Electronically Excited States, in Laser and Coherence Spectroscopy, edited by J. I. Steinfeld (Plenum, New York, 1977), pp. 373-450.

Lectures by C. B. Harris

1. Chemistry Colloquium, University of Michigan, "Coherent Spectroscopy and Energy Transfer Processes in Solids," Ann Arbor, Michigan, Jan. 1977.

2. IBM Colloquium, San Jose, California, "Scanning Spectroscopic Ellipsometry on Metal Surfaces," Feb. 1977.

3. Gordon Research Conference on the Chemistry and Physics of Solids, "Coherent Exciton Migration in Solids: The Determination of the Coherence Length and Times at Low Temperatures," New Hampshire, June 1977.

4. Eighth Molecular Crystal Symposium, "Origin of Optical Dephasing Process in Electronic Transition," Santa Barbara, June 1977.

5. Radiationless Processes, General Discussion Meeting, "Dynamical Interpretation of Electronic and Vibrational Dephasing Processes in Solids and Liquids," Breukelen, The Netherlands, Aug. 1977.

6. Third Specialized Colloque Ampere, Optical Techniques in Magnetic Resonance Spectroscopy, "The Study of Energy Transfer Processes in Solids Using Optically Detected Electron Spin Coherence Techniques," Trinity College, Dublin, Ireland, Aug. 1977.

7. Physics Colloquium, Physikalisches Institut, Universitat Stuttgart, "Origin of Optical and Vibrational Dephasing Processes in Condensed Phase," Sept. 1977.

8. Physical Chemistry Seminar, University of California, Berkeley, California, "The Origin of Vibrational Dephasing Processes in Infrared and Raman Spectroscopy," Oct. 1977.

9. Solid State Physics Colloquium, University of California, Berkeley, "The Origin of Vibrational Dephasing in Condensed Phase Raman Scattering," Nov. 1977.

LBL Reports

1. M. T. Lewellyn, Studies of Energy Transfer Processes in Triplet States Using Optically Detected Magnetic Resonance (Ph.D. thesis), LBL-6601, 1977.

2. D. A. Zwemer and C. B. Harris, Energy Transfer in One-Dimensional Substitutionally Disordered Systems. I. The Effects of Coherence, Tunneling and Thermal Promotion, LBL-5793, 1977.

3. A. R. Burns and C. B. Harris, Heat Pulses in Molecular Crystals. I. Heat Pulse Transmission, LBL-6953, 1977.

4. H. C. Brenner, J. C. Brock and C. B. Harris, Energy Exchange in a Coherently Coupled Ensemble, LBL-6663, 1977.

5. M. T. Lewellyn and C. B. Harris, Energy Transfer Processes Above and Below 2.17° K in 1,2,4,5-Tetrachlorobenzene Mixed Crystals, LBL-7305, 1977.

6. M. T. Lewellyn and C. B. Harris, Coherent Triplet Exciton Migration in Isotopically Mixed Crystals of 1,2,4,5-Tetrachlorobenzene, LBL-7306, 1977.

7. M. E. Tarrasch and C. B. Harris, Coherent Averaging of Electron Spins by Rotary Echoes in Excited Triplet States, LBL-7307, 1977.

8. D. A. Zwemer and C. B. Harris, Impurity-Induced Trap Structure and Dynamics in a Pseudo-One-Dimensional Molecular Solid, LBL-7308, 1977.

9. R. M. Shelby, C. B. Harris, and P. A. Cornelius, The Origin of Vibrational Dephasing of Polyatomic Molecules in Condensed Phases, LBL-7309, 1977.

10. C. B. Harris, R. M. Shelby and P. A. Cornelius, Exchange Model for Vibrational Dephasing of Polyatomic Molecules in Condensed Media, LBL-7310, 1977.

11. P. A. Cornelius, C. B. Harris and R. M. Shelby, Vibrational Dephasing of Durene in Condensed Phase, LBL-7311, 1977.

b. Physical Chemistry with Emphasis on Thermodynamic Properties

Kenneth S. Pitzer, Principal Investigator

1. EFFECTIVE POTENTIALS BASED ON RELATIVISTIC WAVEFUNCTIONS

Yoon S. Lee, Walter C. Ermler and Kenneth S. Pitzer

Many properties of molecules with heavy atoms may not be properly calculated unless the relativistic effects are included. All electron self-consistent-field (SCF) calculations of those molecules, however, are exceedingly costly even without relativistic effects because of the large number of two-electron integrals that arise. One of the promising ways to handle this problem is to treat only the valence electrons explicitly using a frozen core approximation. This usually involves the substitution of the effect of the core electrons with some form of effective potentials or EP's. In order to include the effect of relativity, we derive our EP from the numerical Dirac-Hartree-Fock calculations of atoms using the Phillips-Kleinman transformation. Since valence electrons are essentially nonrelativistic in the valence space and the pseudo-orbital transformation tends to decrease the importance of the small components as was shown in last year's report, the formulation of our EP is almost the same as that in the nonrelativistic case except for the j-dependency of the EP. This arises from the spin-orbit splittings in the original DHF (relativistic) atomic calculations.

The numerical EP for an atom with many valence electrons are obtained by solving the following equation for each angular quantum number v,

$$[-\frac{1}{2}\nabla^2 - \frac{Z}{r} + U_v^{EP}(r) + W(\chi_v^T, \chi_{v'}^T)]\,\chi_v^T = \varepsilon_v \chi_v^T \qquad (1)$$

where $-1/2\ \nabla^2$ is the kinetic energy operator, Z the nuclear charge, r the distance from the nucleus, $U_v^{EP}(r)$ is the radial part of the EP of the symmetry v, $W(\chi_v^T, \chi_{v'}^T)$ the sum of Coulomb and exchange interactions of a given two-component pseudo-orbital, χ_v^T, with all other valence pseudo-orbitals, $\chi_{v'}^T$, and ε_v is the eigenvalue of the v orbital.

Two-component pseudo-orbitals, $\chi_{v'}^T$, are selected from the linear combinations of the large components of the relativistic atomic spinors (four-component) with the same angular momentum. We select the pseudo-orbital that is nodeless and most similar to the original valence orbital in the outer portion of the atom. When all the pseudo-orbitals are available, Eq. (1) can be solved for for each angular momentum to generate the complete EP, U^{EP}, which may be expressed as

$$U^{EP} \approx U_L^{EP}(r) + \sum_{\ell=0}^{L-1} \sum_{j=|\ell-\frac{1}{2}|}^{\ell+\frac{1}{2}} \sum_{m=-j}^{j} \times\ |\ell j m\rangle [U_{\ell j}^{EP}(r) - U_L^{EP}(r)]\ \langle \ell j m| \qquad (2)$$

where L is the smallest angular quantum number not present in the core orbitals. In Eq. (2), angular projections are defined in terms of the j-dependent angular basis, $|\ell j m\rangle$'s, acting on two-component wavefunctions. The assumption, implicit in the above expression, is that the radial parts of EP are same for all orbitals having higher angular quantum numbers than are present in the core. This seems to be reasonable since electrons in those orbitals spend little time in the core region. The EP of Au (Fig. 1) shows that potentials are quite different for $p_{1/2}$ and $p_{3/2}$ even in the outer range (R > 1.5 a.u.) while they become indistinguishable for $g_{7/2}$ and $g_{9/2}$. It may be noted that EP's depend on the choice of the pseudo-orbital transformations and the definition of valence space.

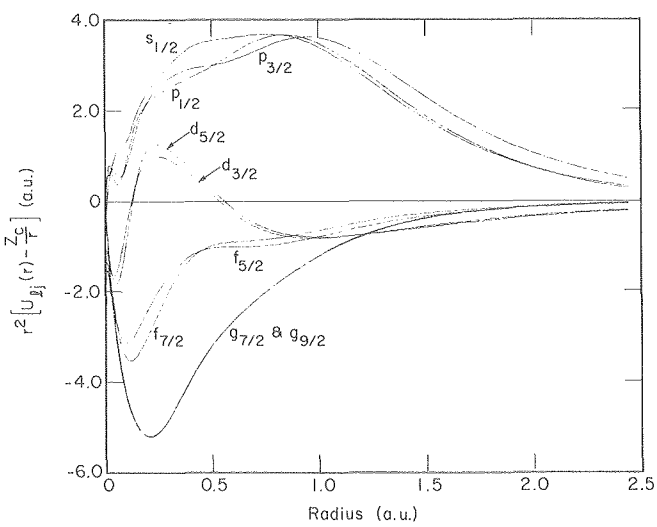

Fig. 1. Effective core potentials of Au (11-valence electrons). (XBL 776-8923)

In order to test the EP, the atomic program is modified to include the EP, and to be appropriate for the jj-coupling scheme. Many excited and ionic states of Xe and Au have been studied and seem to yield reasonable results. Gold has been treated as a 1-, 11-, 17-, 19-, or 33- valence electron

Table 1. Calculations with EP for Au with various assignments between valence and core electrons (a.u.).

		Orbital Energies $-\varepsilon$							
	-T.E.	$4f_{7/2}$	$4f_{9/2}$	$5s_{1/2}$	$5p_{1/2}$	$5p_{3/2}$	$5d_{5/2}$	$5d_{7/2}$	$6s_{1/2}$
DHF	19018.1992	3.8675	3.7202	4.6873	3.1893	2.5588	0.4934	0.4286	0.2919
1-elec	.2912								.2912
11-elec	35.3827						.4932	.4254	.2936
17-elec	109.4704				3.2294	2.5473	.5106	.4368	.2985
19-elec	145.2199			4.6462	3.2661	2.5843	.4856	.4176	.3395
33-elec	610.9816	3.9555	3.8123	4.6494	3.2376	2.5760	.4972	.4254	.3438

atom. The ground state calculations of Au shown in Table 1 indicate that the DHF results are reasonably reproduced except for the 6s of 19- and 33-valence electron cases where 6s orbitals have to be obtained as excited orbitals from the 5s potentials. This difficulty is not too critical at present since Au appears to be well represented as an 11-valence electron atom in the detailed analysis of excited and ionic states. Similar results are expected for other heavy atoms. Our atomic program has the versatility of taking alternate forms of EP's with either Slater or Gaussian basis sets that may be optimized for molecular calculations.

The direct application of the EP requires the molecular formalism to be based on j-dependent atomic bases. A molecular program, which utilizes the Slater basis functions and EP's, is being developed and will be tested for the diatomic molecules formed from Cu, Ag, Au, and Hg.

2. POTENTIAL CURVES FOR Xe_2, Xe_2^+, and Xe_2^* BASED ON EFFECTIVE POTENTIALS

Walter C. Ermler, Yoon S. Lee, and Kenneth S. Pitzer (with the collaboration of Nicholas W. Winter of L.L.L.)

All-valence-electron self-consistent-field (SCF) calculations were carried out for the ground $^1\Sigma_g^+$ state of Xe_2, the four states of Xe_2^+ corresponding to the removal of an electron from each of the outer molecular orbitals ($^2\Sigma_u^+$, $^2\Pi_g$, $^2\Pi_u$, and $^2\Sigma_g^+$), and the eight states resulting from the addition of an electron to the lowest Rydberg MO relative to each of these ions ($^{1,3}\Sigma_u^+$, $^{1,3}\Pi_g$, $^{1,3}\Pi_u$, $^{1,3}\Sigma_g^+$).

The calculations used standard programs appropriate for the LS-coupling scheme. The method described in article 1 was used to generate EP's for the Xe atom. These EP's were cast into a form appropriate for L-S coupling by averaging the respective ℓ - 1/2 and ℓ + 1/2 components. To gauge the effects of the inclusion of the mass-velocity and Darwin terms in the Hamiltonian, EP's for Xe were obtained in an analogous manner using the numerical (nonrelativistic) Hartree-Fock wavefunctions for Xe. Comparisons of the averaged relativistic (AREP) and nonrelativistic (NREP) results are shown in Fig. 1. Although some other differences may be noted, the calculations indicate that the principal relativistic effect is a change in the 5s orbital energy from -0.94 to -1.00 a.u. The use of the relativistic EP's in calculations on Xe dimers resulted in only an insignificant shift in the equilibrium bond lengths. Consequently, it appears that, while there is a rather large spin-orbit interaction in Xe, other relativistic effects are unimportant; and that the 5s electrons are not strongly participating in the Xe-Xe interaction.

To account for the predominance of Hund's case c type coupling in electronic states of Xe_2^+ and Xe_2^* an empirical model[1] was used whereby the experimental atomic splittings are used to define the matrix elements of the spin-orbit Hamiltonian. This matrix is then added to the diagonal matrix of the appropriate interacting electronic states and the roots of this matrix are determined for each point on the respective SCF curves. Thus, the spin-orbit interaction is assumed to be atom-like at all internuclear distances.

The 23 potential energy curves derived from the 13 SCF curves are plotted in Fig. 2. The Xe_2^+ curves have been shifted vertically such that the experimental (rather than the SCF) ionization potentials of the Xe atom are reproduced. Note that

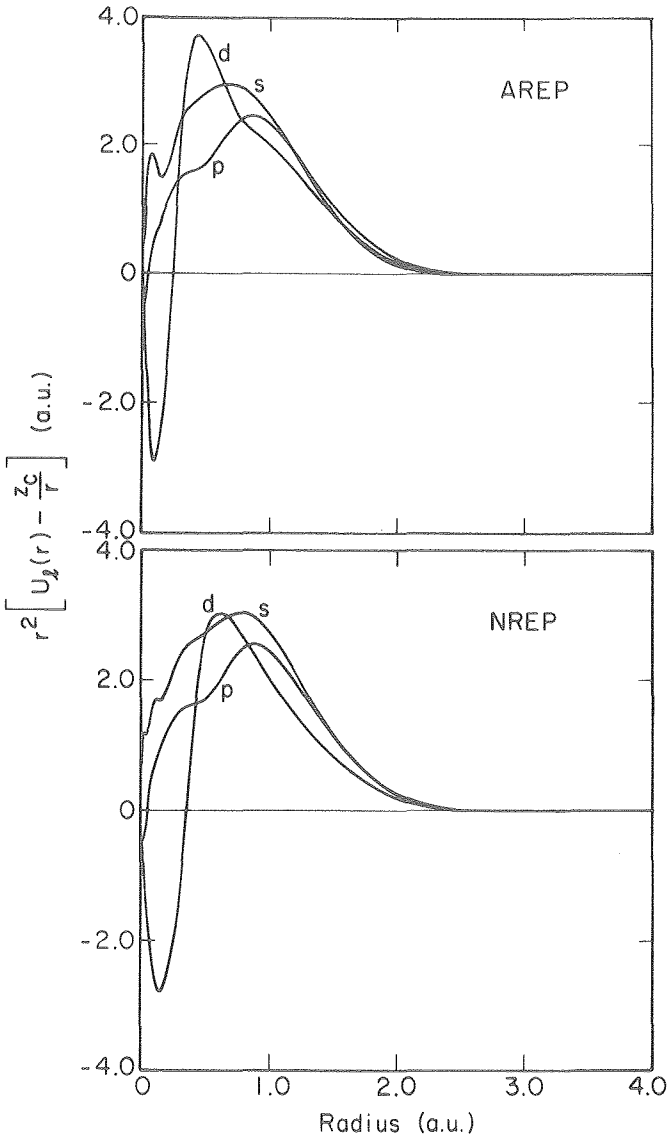

Fig. 1. Effective core potentials of Xe.
(XBL 782-7092)

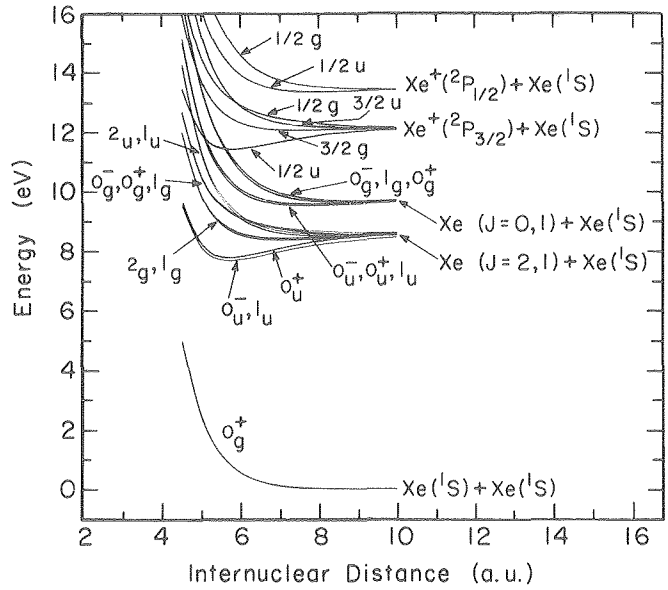

Fig. 2. Xe_2 potential energy curves.
(XBL 782-7091)

the Xe_2^* curves are generally parallel to the corresponding Xe_2^+ curves and that the repulsive sections of the upper Xe_2^* curves intersect the ground state curve of Xe_2^+ in the neighborhood of its minimum.

Calculated spectroscopic constants for the ground $(1/2)_u$ state of Xe_2^+ are R_e = 3.08 Å, D_e = 0.70 eV, ω_e = 110.4 cm^{-1}, $\omega_e x_e$ = 0.5 cm^{-1}, B_e = 0.0270 cm^{-1}, and α_e = 0.00013 cm^{-1}; observed values are R_e = 3.2 Å and D_e = 1.03 eV.[2] Constants computed for the bound states of Xe_2^* are nearly the same as those for the $(1/2)_u$ state of Xe_2^+. Vertical transition energies from R_e of the $(1/2)_u$ state to the $(3/2)_g$, $(1/2)_g$, and the upper $(1/2)_u$ states of Xe_2^+ are 1.03, 1.67, and 3.56 eV, respectively. The transition energies from the 0_u^+ and 1_u states (at R_e) of Xe_2^* to the repulsive wall of the ground state are 6.99 and 6.82 eV, respectively. The former transition is observed at 7.21 eV.[3]

It should be noted that the SCF potential energy curves for the Xe_2^+ and Xe_2^* states do not dissociate properly to Xe^+ + Xe or Xe^* + Xe but to wavefunctions that are averages of the optimum MO's for each species.[4] However, in rare gas dimers it has been found that errors of this type are cancelled to a large degree by errors of the same magnitude that arise due to the neglect of molecular extra correlation energy. Indeed, the spectroscopic constants are in close agreement with all-electron CI calculations[5] on Xe_2^+, although the EP leads to a somewhat smaller value of R_e.

The upper portion of Fig. 2 is incomplete by the omission of higher Rydberg states of Xe_2^*. There will be avoided crossings of states of the same symmetry at the higher energies as has been noted by others.[1,6]

1. J. S. Cohen and B. Schneider, J. Chem. Phys. 61, 3230 (1974).
2. P. M. Dehmer and J. L. Dehmer, J. Chem. Phys. 67, 1774 (1977).
3. C. K. Rhodes, IEEE J. Quantum Electron. 10, 153 (1974).
4. T. L. Gilbert and A. C. Wahl, J. Chem. Phys. 55, 5247 (1971).
5. W. R. Wadt, J. Chem. Phys. (in press).
6. R. S. Mulliken, Radiation Res. 59, 357 (1974).

3. THERMODYNAMIC PROPERTIES OF AQUEOUS SOLUTIONS OF RARE EARTH CHLORIDES, NITRATES AND PERCHLORATES

Kenneth S. Pitzer, John R. Peterson and Leonard F. Silvester

In a very extensive series of papers Spedding and associates have presented various thermodynamic

data for the nitrates, chlorides, and perchlorates of most of the rare earths. While excellent comparative treatments of the results for any one series are given in these papers, it seemed to us to be of some interest to fit a general array of these data to a single type of equation. We have considered the osmotic coefficient, the heat of dilution, and the volumetric data for all of the chlorides, perchlorates, and nitrates. Thus, in effect, we consider the Gibbs energy and its temperature and pressure derivatives. Activity coefficients may be calculated from these results.

It was hoped that the trends of the parameters along the rare earth series would yield more reliable and interesting structural information than were obtained by Spedding and his associates in their direct examination of the original data. Our results in this respect are discussed below. The parameters obtained are also useful for various thermodynamic calculations and will be especially valuable for mixtures where the other components have been treated in the same system.

The equations for activity and osmotic coefficients and for enthalpies have been published.[1] For the volumetric properties the derivation is similar to that for the enthalphy, but the measured property is the density rather than the heat of dilution and this yields the absolute rather than the relative apparent molal volume. The additional term, the partial molal volume of the solute at infinite dilution $\bar{V}°$, must be evaluated. One has, then,

$$\phi_V = \bar{V}° + \nu|z_M z_X|(A_V/3b)\ \ell n\ (1+bI^{1/2}) - 2\nu_M\nu_X\ RT(mB^V_{MX} + m^2\ C^V_{MX}) \quad (1)$$

where

$$B^V_{MX} = (\partial\beta^{(0)}_{MX}/\partial P)_{I,T} + (\partial\beta^{(1)}_{MX}/\partial P)_{I,T} \times (2/\alpha^2 I)\ [1-(1+\alpha I^{1/2})\ \exp(-\alpha I^{1/2})] \quad (2)$$

$$C^V_{MX} = \frac{1}{2}\ (\nu_M\nu_X)^{1/2}\ (\partial C^\phi_{MX}/\partial P)_{I,T} \quad (3)$$

The density is related to the apparent molal volume by the expression

$$d = \frac{1000+M_2 m}{(1000/d_o)+\phi V m} \quad (4)$$

where d_0 is the density of the pure solvent and M_2 the molecular weight of the solute. The Debye-Hückel parameter for volume is

$$A_V = -3A_\phi\ RT[3(\partial\ell nD/\partial P)_T + (\partial\ell nV_W/\partial P)_T] \quad (5)$$

where the last term is the negative of the compressibility of the solvent. The equations for the volume and the dielectric constant for water that were adopted earlier were used to calculate A_V. The value of A_V is 2.626 cc $kg^{1/2}$ $mole^{-1/2}$ for water at 25°C.

The specific parameters for each rare earth salt were evaluated by least squares from the original data of Spedding et al.[2] together with any other published data[3] which was judged to be of comparable accuracy. For the chlorides good fits were obtained up to the highest concentrations, frequently saturation. For the perchlorates and especially for the nitrates, it was possible to get good fits only up to about 2M and the final calculations were based only on data up to this maximum molality for these salts.

The details of this evaluation process and the resulting tables of parameters are available in Report LBL-6399 and will be published soon.

It is interesting to note the magnitude of the temperature and pressure derivatives in relation to the parent functions. For the important parameters 3/2 $\beta^{(0)}$, which is of the order unity, the temperature derivative is less than 0.0004 K^{-1}. Consequently, a 25° change in temperature causes less than 1% change in $\beta^{(0)}$ or 2% change in γ at 1 M. The pressure derivative is less than 0.00006 atm^{-1}; hence a 160 atm change causes less than 1% change in $\beta^{(0)}$. The Debye-Hückel coefficient is somewhat more sensitive to temperature, with 25° causing a 4% change, but is even less sensitive to pressure. Thus the properties of these solutions do not change rapidly with temperature or pressure, and the dominant effect is the change of Debye-Hückel parameter with temperature.

The more significant parameters are shown as a function of the ionic radius of the positive ion in Figs. 1-3. The radii of Templeton and Dauben[4] are used for the rare earths. Many of these figures show the s-shaped curves noted before by Spedding and others and often attributed to a change in the inner-sphere hydration number of the cation. It is assumed that the inner sphere contains nine water molecules from La to Nd and eight water molecules from Tb to Lu with a transition between Nd and Tb. The trend with radius of the primary parameter for short-range pairwise interaction $\beta^{(0)}$ is shown in Figs. 2 and 3. The larger absolute value for perchlorates than chlorides indicates a more repulsive interaction for the perchlorate anion. The trend over a wider range of radii in Fig. 3 indicates that $\beta^{(0)}$ decreases with increase in radius. Thus the trend from Tb to Nd appears to be normal and the regions Lu and Dy and Pr to La anomalous. This is in contrast to the explanation for $\bar{V}°$ values where the middle group of rare earths Tb to Nd was said to be the anomalous region.

Additional figures are given in our full report together with further discussion. This research was supported, in part, also by the Geoscience program at LBL.

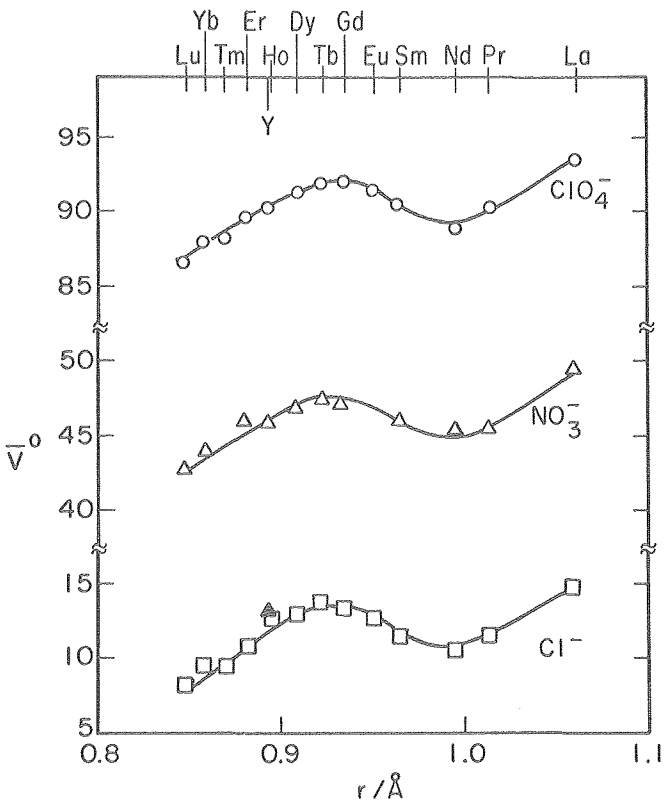

Fig. 1. The partial molal volume at zero molality for rare earth salts as a function of cation radius. (XBL 782-7090)

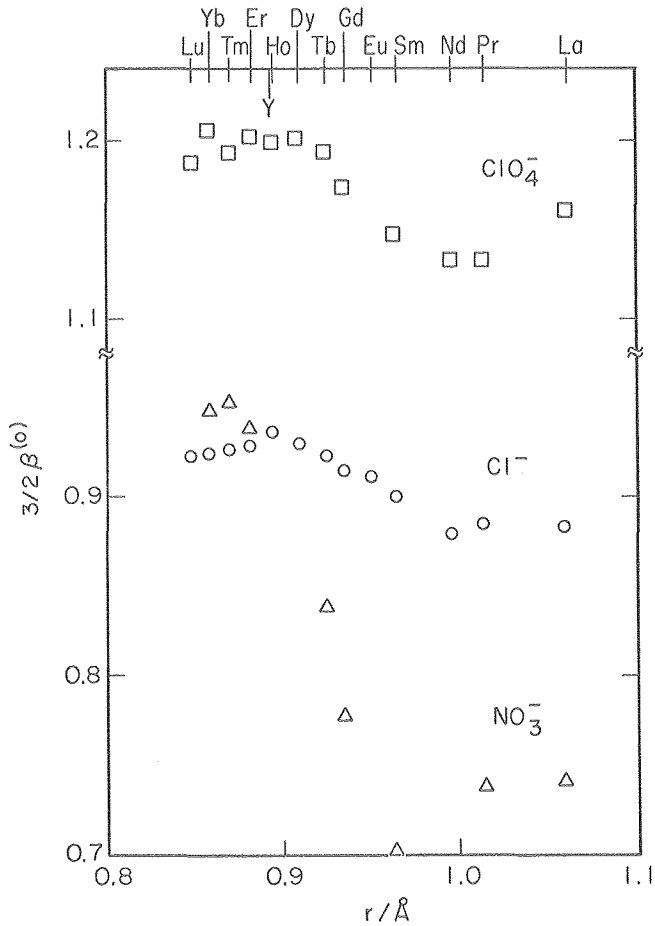

Fig. 2. The pairwise short-range interaction parameter $\beta^{(0)}$ as a function of cation radius for rare earth salts. Chlorides are shown as circles, nitrates as triangles, and perchlorates as squares. (XBL 782-7093)

1. L. F. Silvester and K. S. Pitzer, J. Phys. Chem. 81, 1822 (1977).
2. F. H. Spedding et al., J. Chem. Eng. Data 22, 58, 142, 187, 337 (1977) and earlier papers therein cited.
3. R. A. Robinson and R. M. Stokes, "Electrolyte Solutions", 2nd ed. (revised) Butterworths, London, 1965.
4. D. H. Templeton and C. H. Dauben, J. Am. Chem. Soc. 76, 5237 (1954).

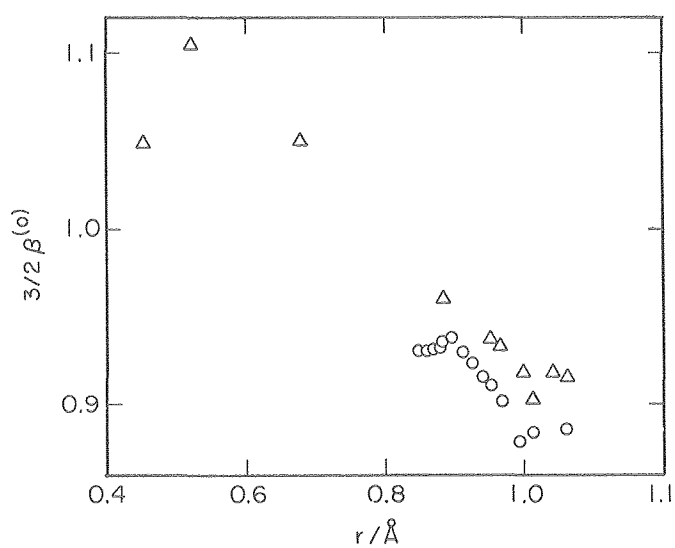

Fig. 3. The pairwise short-range interaction parameter $\beta^{(0)}$ for a series of +3 ion chlorides as function of cation radius. The current results are shown as circles; previous results as triangles. (XBL 782-7089)

4. THERMODYNAMICS OF ELECTROLYTES; ENTHALPHY AND THE EFFECT OF TEMPERATURE ON ACTIVITY COEFFICIENTS

Leonard F. Silvester and Kenneth S. Pitzer

While the thermodynamic relationship between the partial molal enthalphy and the temperature derivative of the activity coefficient is well-known, it is convenient to use the same basic equation for both. Then the temperature derivative of each parameter in the equation for the activity coefficient is just the corresponding

parameter for the enthalphy equation. We have derived the detailed equations in connection with our analysis[1] of the properties of aqueous NaCl to 300°C. For most solutes we have only heat of dilution data at or near 25°C. In the present paper these data for 84 electrolytes are fitted to the enthalphy equation corresponding to the equations used in papers II[2] and III[3] of this series for the osmotic and activity coefficients for 237 solutes. The parameters given below allow the convenient calculation of properties at other temperatures not too different from 25°C.

It was shown in paper IV[4] that this system of equations was convenient and effective for mixed electrolytes and that the important parameters were those for pure electrolytes. Thus the results of this paper will allow calculations of mixed electrolyte properties at temperatures other than 25°C.

The equation for the apparent molal enthalpy is

$$\phi_L = \nu|z_M z_X|(A_H/3b)\ \ln(1+bI^{1/2}) - 2\nu_M\nu_X\ RT^2[mB^L_{MX}+m^2(\nu_M z_M)\ C^L_{MX}] \quad (1)$$

where

$$B^L_{MX} = (\partial B_{MX}/\partial T)_{I,P} \quad (2)$$

$$B_{MX} = \beta^{(0)}_{MX} + (2\beta^{(1)}_{MX}/\alpha_1^2 I) \times [1-(1+\alpha_1 I^{1/2})\ \exp(-\alpha_1 I^{1/2})] + (2\beta^{(2)}_{MX}/\alpha_2^2 I)[1-(1+\alpha_2 I^{1/2})\ \exp(-\alpha_2 I^{1/2})] \quad (3)$$

$$C^L_{MX} = (\partial C^\phi_{MX}/\partial T)_P/2|z_M z_X|^{1/2}. \quad (4)$$

The quantity A_H is the Debye-Hückel coefficient for enthalphy

$$A_H = 6RT^2(\partial A_\phi/\partial T)_P = -9A_\phi\ RT^2[T^{-1} + (\partial \ln D/\partial T)_P + \alpha_w/3] \quad (5)$$

where $\alpha_w = (\partial \ln V/\partial T)_P$ is the coefficient of thermal expansion of water. At 25°C, $A_H/RT = 1.1773$.

The data for heat of dilution for 1-1 aqueous electrolytes were reviewed as of 1964 by Parker[5] who also considered heat capacity and heat of solution data. For the solutions considered by Parker, most of our results do not differ significantly, but we did base our calculations on the original data. Our contribution is in the compactness of the results and their direct usefulness in calculating activity coefficients at temperatures other than 25°C.

In addition to the 1-1 electrolytes considered by Parker, we made a reasonable effort to consider most available data for higher valence electrolytes.

In some cases there are heat of solution results for various concentrations and these yield, in effect, also heat of dilution data. The treatment of these heat of solution data yield also the ΔH°_S of solution at zero molality.

Values of the temperature derivatives of $\beta^{(0)}$, $\beta^{(1)}$, and $\beta^{(2)}$ and/or C^ϕ where applicable, are listed in tables that will be given in detail in Report LBL-7009 and will be published.

The most important conclusion is that these temperature effects are small. Thus for 1-1 electrolytes where $\beta^{(0)}$ and $\beta^{(1)}$ are commonly of the magnitude of one tenth or a few tenths, their derivatives are of the order 10^{-3}. Hence a temperature change of a few degrees or even ten or twenty degrees causes little change in these parameters. Beyond that range one must also consider the effect of the second derivative or of the heat capacity of the solution.

This research also received support through the Geoscience program at LBL.

1. L. F. Silvester and K. S. Pitzer, J. Phys. Chem. 81, 1822 (1977).
2. K. S. Pitzer and G. Mayorga, J. Phys. Chem. 77, 2300 (1973).
3. K. S. Pitzer and G. Mayorga, J. Solution Chem. 3, 539 (1974).
4. K. S. Pitzer and J. J. Kim, J. Am. Chem. Soc. 96, 5701 (1974).
5. V. B. Parker, Thermal Properties of Squeous Uni-univalent Electrolytes, Nat. Std. Ref. Data Series, Nat. Bur. Stds., Washington, 1965.

5. RESEARCH PLANS FOR CALENDAR YEAR 1978

Kenneth S. Pitzer

The development of a quantum chemistry for heavy atoms, which has proceeded successfully through quantitative calculations for atoms, will be directed toward calculations for molecules. This will require the development of a new general set of equations and computer programs for molecules in j-j coupling (or ω-ω coupling). As soon as this is completed we will proceed to particular cases of interest beginning with diatomic molecules. As a parallel effort, and in collaboration with LLL, we are making more approximate calculations within the L-S coupling framework for examples

where the spin-orbit effects are not too large. The work of this type on Xe_2^*, etc., is reported above, and other cases are being considered.

In the work on the thermodynamics and statistical mechanics of electrolytes, attention will be given a) to the properties of high-valence compounds, b) to mixed electrolytes at high temperatures, and c) to solid-solution equilibria of geochemical interest. Both theoretical and experimental work will be included. This activity also receives some support from the Geoscience program at LBL.

6. 1977 PUBLICATIONS AND REPORTS

Kenneth S. Pitzer and Associates

Journals

1. Janice J. Kim and Kenneth S. Pitzer, Crystal Field Effects on Oxygen in Solid Methane and the Catalysis of Spin-Species Conversion of Methane, J. Chem. Phys. 66, 2400 (1977), LBL-5476.

2. Kenneth S. Pitzer, Rabindra N. Roy and Leonard F. Silvester, Thermodynamics of Electrolytes. VII. Sulfuric Acid, J. Am. Chem. Soc. 99, 4930 (1977), LBL-5970.

3. Leonard F. Silvester and Kenneth S. Pitzer, Thermodynamics of Electrolytes. VIII. High Temperature Properties, including Enthalpy and Heat Capacity, with Application to NaCl, J. Phys. 81, 1822 (1977), LBL-6217.

4. Kenneth S. Pitzer, Electrolyte Theory - Improvements since Debye and Hückel, Acc. of Chem. Res., 10, 371 (1977), LBL-6218.

5. Yoon S. Lee, Walter C. Ermler and Kenneth S. Pitzer, ab initio Effective Core Potentials Including Relativistic Effects. I. Formalism and Applications to the Xe and Au Atoms, LBL-6285 J. Chem. Phys. 67, 5861 (1977), LBL-6285.

LBL Reports

1. Kenneth S. Pitzer, The Origin of the Acentric Factor, LBL-5969. (A Chapter for a book to be published by the Am. Chem. Soc., in late 1977 or early 1978.)

2. Kenneth S. Pitzer, John R. Peterson and Leonard F. Silvester, Thermodynamics of Electrolytes. IX. Rare Earth Chlorides, Nitrates, and Perchlorates, LBL-6399 (J. Soln. Chem.)

3. Yoon Sup Lee, ab initio Effective Core Potentials Including Relativistic Effects and Their Applications to the Electronic Structure Calculations of Heavy Atoms and Molecules, (Ph.D. thesis), LBL-6962.

4. Leonard F. Silvester and Kenneth S. Pitzer, Thermodynamics of Electrolytes. X. Enthalpy and the Effect of Temperature on the Activity Coefficients, LBL-7009 (J. Soln. Chem.)

c. Chemical Dynamics Studies

Bruce H. Mahan, Principal Investigator

1. TRANSPORT IN GASES: AN ALTERNATIVE TREATMENT*

Bruce H. Mahan

In this primarily pedagogical article, we show how the coefficients of diffusion, viscosity, thermal conductivity, and electrical conductivity can be obtained in terms of the collisional relaxation time for gaseous systems. The approach has the advantage of avoiding the questionable geometric arguments of mean free path theory, emphasizing the nonequilibrium nature of the transport process, and providing explicit, if approximate, expressions for the nonequilibrium distribution functions.

*Abstracted from LBL-6267, accepted for publication in the J. of Chem. Ed.

2. LASER INDUCED FLUORESCENCE OF GASEOUS IONS

Richard Davis, Frederick Grieman and Bruce H. Mahan

Important applications of ion-molecule reaction kinetics have been made in the areas of mass spectrometry,[1] plasma chemistry,[2] combustion,[3] radiation chemistry,[4] atmospheric chemistry,[5] ion solvation,[3] and the chemistry of interstellar matter.[6] In order to systematize, explain, and anticipate ion-molecule chemistry, knowledge of the molecular structure and electronic states of gaseous ions is needed. Some of this necessary information has been provided by photoelectron spectroscopy. However, photoelectron spectroscopy rarely reveals the rotational levels of ions, and is applied only with considerable difficulty to ions of reactive or unstable molecules.

Direct optical spectroscopy of gaseous ions would supply the required information. While the emission spectra of approximately 30 diatomic ions have been obtained, the absorption spectra of only 6 of these are known. For polyatomic ions, the situation is much worse, with the emission spectra of only 6 ions known, and the absorption of only 4 ions detected.

We have developed a method for obtaining the absorption spectra of mass selected gaseous ions by laser induced fluorescence. Ions are formed by irradiating a low pressure gas with a pulse of electrons. A three-dimensional quadrupole trap[7] is used to confine the ions. The trap can be operated so as to retain ions of all masses, or in a mass-selective mode. In the latter case, after a time sufficient for mass selection to occur (~1 ms), the ions are irradiated with a 10 ns light pulse from a tunable dye laser. If the laser is tuned to an absorption frequency of the ions, approximately 10^4 ions can become electronically excited. The radiation from those that fluoresce is detected by a gated photomultiplier and recorded. An electrical pulse is then applied to the trap to drive the ions to a detector, where their number is determined. The production-selection-fluorescence-detection sequence is repeated 10 to 40 times per second.

We have recently detected one vibrational band of the $B\ ^2\Sigma_u^+ - X\ ^2\Sigma_g^+$ transition of N_2^+ in preliminary experiments with our apparatus. This spectrum is well-known from conventional optical spectroscopy. Its detection shows that our apparatus is operating within the design specifications, and should be capable of detecting the spectra of small polyatomic ions with sufficient sensitivity and resolution to permit structural parameters to be derived from rotational analyses. The apparatus can also be used to obtain the internal state population distribution of ions formed in ion-molecule reactions as well as electron impact induced fragmentations.

1. L. Friedman and B. Reuben, Adv. Chem. Phys. 19, 33 (1971).
2. M. Venuglopalan, Ed., Reactions Under Plasma Conditions, Vol. 2 (Wiley-Interscience, New York, 1971).
3. J. L. Franklin, Ed., Ion Molecule Reactions, Vols. 1,2. (Plenum, New York, 1952).
4. L. G. Christophoru, Atomic and Molecular Radiation Physics, (Wiley-Interscience, New York, 1971).
5. E. W. McDaniel, V. Cermak, A. Dalgarno, E. Ferguson and L. Friedman, Ion-Molecule Reactions, (Interscience, New York, 1970).
6. W. Klemperer, Nature 227, 1230 (1970).
7. P. H. Dawson and N. R. Whetten, Adv. Electronics and Electron Phys. 27, 59 (1969).

3. DYNAMICS OF THE F^+-H_2 REACTION

James M. Farrar, Steven G. Hansen and Bruce H. Mahan

Work is continuing on the reaction $F^+(H_2,H)HF^+$. This system is particularly interesting in that the reactants F^+ and H_2 constitute an excited state of the system that does not correlate adiabatically with accessible bound states of HF^+. Nevertheless, HF^+ is observed as a product when the collision energy is less than approximately 5 eV. The general features of the potential energy surfaces derived by qualitative consideration of the occupied molecular orbitals have been largely confirmed by the ab initio calculation of Schaefer and Ungemach, and enforce the conclusion that as long as H_2 remains near its equilibrium internuclear separation, there are no crossings of the $F^+ + H_2$ surface with those that lead to $HF^+ + H$.

Consideration of correlation diagrams with distorted H_2 molecules indicate that the surfaces that lead to the experimentally observed product HF^+ may be accessible in these situations. This

requirement may also account for the small reaction cross section and its disappearance at high collision energies. These possibilities are being explored in collaboration with H. F. Schaefer and S. R. Ungemach.

4. DYNAMICS OF CO_2^+-D_2 COLLISIONS AT LOW ENERGIES

Steven G. Hansen and Bruce H. Mahan

Earlier work by Mahan and Schubart[1] has shown that the reaction $CO_2^+(D_2,D)DCO_2^+$ proceeds principally by a direct interaction mechanism at relative energies higher than 2.0 eV. However, the product velocity vector distributions in the low energy regime were broad and showed considerable intensity near the center-of-mass velocity, thereby indicating that a possible transition to a long lived $D_2CO_2^+$ collision complex mechanism would be found at lower relative energies.

We have investigated this reaction at relative energies of 1.4 eV and below. When CO_2^+ is prepared by a microwave discharge through a CO_2-He mixture, a procedure that typically produces ions in their electronic ground state, the velocity vector distributions of DCO_2^+ are nearly symmetric about the center-of-mass velocity. This indicates that at low relative energies, the reaction proceeds predominately through the formation and decay of a long lived $D_2CO_2^+$ complex.

Somewhat different results are obtained when CO_2^+ is produced by the impact of 150 eV electrons on CO_2. Even at collision energies as low as 0.28 eV, the velocity vector distribution of DCO_2^+ is asymmetric about the center of mass. This indicates that high energy electron impact on CO_2 produces significant amounts of CO_2^+ in a metastable electronically excited state. The reaction of this metastable CO_2^+ with D_2 then occurs directly on a potential energy surface that does not contain a potential energy well that corresponds to a $D_2CO_2^+$ collision complex.

The reaction $CO_2^+(D_2,OD)DCO^+$ was also investigated by Mahan and Schubart.[1] Although it has virtually the same overall energetics as the $CO_2^+(D_2,D)$ DCO_2^+ reaction, it has a much smaller cross section in the 2 to 10 eV relative energy range, and had never been detected in experiments at thermal energies. Mahan and Schubart[1] speculated that a potential energy barrier might prevent DCO^+ formation, but would not interfere with DCO_2^+ formation. We have shown in our recent experiments that there is a threshold for DCO^+ formation at approximately 1.4 eV energy. If DCO_2^+ and DCO^+ both come from the decay of a common $D_2CO_2^+$ intermediate, our findings suggest that the barrier to DCO^+ formation is in the exit channel of the potential energy surface.

---

1. B. H. Mahan and P. J. Schubart, J. Chem. Phys. 66, 3155 (1977).

5. RESEARCH PLANS FOR CALENDAR YEAR 1978

Bruce H. Mahan

With our laser induced fluorescence technique we shall pursue the visible and ultraviolet spectroscopy of light triatomic ions such as H_2O^+, CH_2^+, and NH_2^+. We will attempt to use this device to obtain radiative lifetimes and vibrational state distributions of ions formed by various fragmentation and reaction processes. The connection between electronic structure and chemical reactivity will be further explored by completing our work on the F^+-H_2 systems, and starting work on the reactions of CF^+, S^+, and P^+ with H_2. The energy spread of our low energy beam apparatus will be improved by the addition of a velocity filter, and redesigned ion sources. This will permit the resolution of vibrational states of the products in certain favorable cases. Modifications to improve the performance of our high energy ion-molecule collision apparatus will be completed, and tests of our sequential impulse model for high energy reactions will be made by studying the high energy scattering of C^+ and Cl^+ by H_2.

6. 1977 PUBLICATIONS AND REPORTS

Bruce H. Mahan and Associates

Journals

1. C. Y. Ng, D. J. Trevor, B. H. Mahan and Y. T. Lee, Photoionization Study of the Xe_2 van der Waals Molecule, J. Chem. Phys. 65, 4327 (1976).

2. B. H. Mahan, W. E. W. Ruska and J. S. Winn, Sequential Impulse Model of Direct Reactions, J. Chem. Phys. 65, 3889 (1976).

3. B. H. Mahan and W. E. W. Ruska, Dynamics of the Reaction of N^+ with H_2. IV. Reactive Scattering at Relative Energies Above 6 eV, J. Chem. Phys. 65, 5045 (1976).

4. C. Y. Ng, D. J. Trevor, B. H. Mahan and Y. T. Lee, Photoionization Studied of the Kr_2 and Ar_2 van der Waals Molecules, J. Chem. Phys. 66, 446 (1977).

5. B. H. Mahan and P. J. Schubart, Dynamics of CO_2^+-D_2 Collisions, J. Chem. Phys. 66, 3155 (1977).

6. C. Y. Ng, P. W. Tiedemann, B. H. Mahan and Y. T. Lee, The Binding Energy Between NO and NO^+, J. Chem. Phys. 66, 3985 (1977).

7. C. Y. Ng, P. W. Tiedemann, B. H. Mahan and Y. T. Lee, Photoionization Studies of the Diatomic Heteronuclear Rare Gas Molecules XeKr, XeAr, and KrAr, J. Chem. Phys. 66, 5737 (1977).

LBL Reports

1. B. H. Mahan, Transport in Gases: An Alternative Treatment, J. Chem. Ed. (in press), LBL-6267, 1977.

2. B. H. Mahan, H. F. Schaefer III and S. R. Ungemach, Some Features of the Potential Energy Surfaces for the $F^+ + H_2$ Ion-Molecule Reaction, J. Chem. Phys. (in press), LBL-6679, 1977.

d. Theory of Low Energy Atomic and Molecular Collisions

William H. Miller, Principal Investigator

1. PENNING IONIZATION OF H_2 BY He^{*}†

A. P. Hickman,‡ A. D. Isaacson and W. H. Miller

Recent experiments[1,2] dealing with the Penning ionization of closed shell species by He^*(1s2s ^1S and ^3S), e.g.,

$$He^* + Ar \rightarrow He + Ar^+ + e^-$$

$$+ H_2 \rightarrow He + H_2^+ + e^- ,$$

indicate interesting differences between ionization by singlet and triplet metastable helium. Specifically, the interaction potential between He^* and its closed shell collision partners is deduced to be an (expected) repulsive curve for $He^*(^3S)$, but for $He^*(^1S)$ the experiments suggest that it has a relative maximum. There has been no satisfactory explanation of why this structure should appear, and if it does, why it is present for the singlet but not for the triplet.

We have earlier calculated[3] the interaction potential for $He^*(^3S) + H_2$, and this work reports similar calculations for the case of singlet He^*, the goal being to see if the anomalous structure can be found, and if so, understood. Figure 1 shows our results. For C_{2v} geometry one sees that this structure in the potential curve does exist, but not for the collinear ($C_{\infty v}$) orientation.

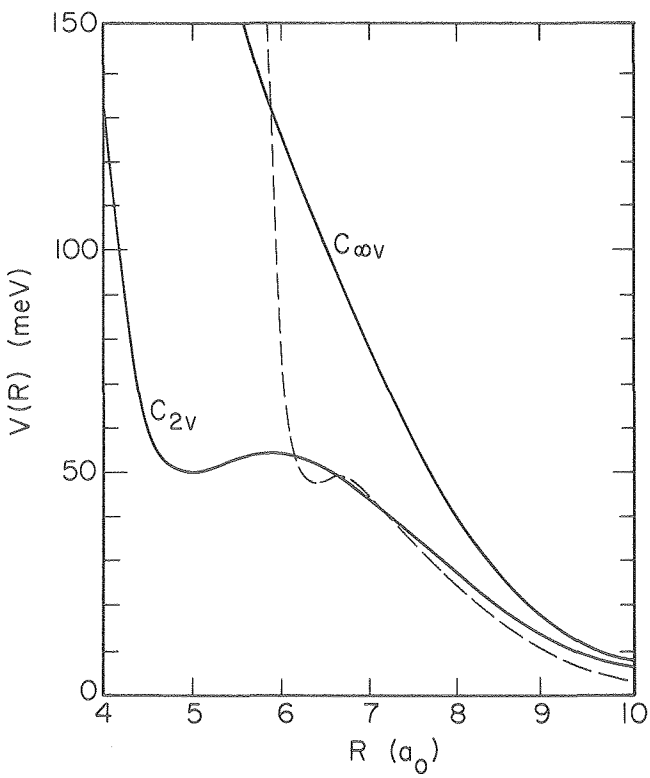

Fig. 1. The two solid curves are the present results for the He^*(1s2s ^1S)-H_2 interaction potential for perpendicular (C_{2v}) and collinear ($C_{\infty v}$) approaches. R is the distance between He and the center of mass of H_2, and the H-H distance is fixed at its equilibrium value 1.4 a_0. The units of energy are milli-electron volts and of distance are Bohr radii. The dashed curve is the effective spherically symmetric potential of Ref. 2.
(XBL 773-7927)

Analysis of the electronic wavefunction shows clearly that the anomalous structure arises from interaction between the 1s2s ^1S and 1s2s ^1P states of helium. For large R the electronic states correspond to the outer electron being in an s or in a p orbital, while for small R the adiabatic states are essentially s-p hybrids. The transition from atomic states to s-p hybrids takes place over a small region of internuclear distance, and this is the origin of the structure in the potential curve. A similar effect is not significant for the triplet case because the atomic splitting of 1s2s ^3S and 1s2p ^3P states of helium is about twice the size of that for the singlet case, and the triplet states thus interact only weakly.

Also shown in Fig. 1 is the effective spherically symmetric potential deduced[4] from experimental measurements. There is qualitative agreement, but more accurate scattering calculations are necessary before the analysis of the data is meaningful.

---

†Abstracted from J. Chem. Phys. 67, 370 (1977).

‡Non-LBL employee.

1. M. T. Leu and P. E. Siska, J. Chem. Phys. 60, 2179, 4082 (1974).
2. B. Brutschy, H. Haberland, H. Morgner and K. Schmidt, Phys. Rev. Lett. 36, 1299 (1976).
3. A. P. Hickman, A. D. Isaacson, and W. H. Miller, J. Chem. Phys. 66, 1483 (1977).
4. R. Altpeter, H. Haberland, W. Kunz, P. Oesterlin and K. Schmidt, J. Chem. Phys. 67, 836 (1977).

2. UNIFIED TREATMENT OF PENNING IONIZATION AND EXCITATION TRANSFER*

W. H. Miller and H. Morgner

Penning ionization,

$$A^* + B \rightarrow A + B^+ + e^-, \qquad (1)$$

and excitation transfer

$$A^* + B \rightarrow A + B^*, \qquad (2)$$

are usually treated by different theoretical approaches. One reason for this is that reactions (1) and (2) are usually detected by different experimental means: in (1) the ions[1] or electrons[2] are detected, while in (2) the excited state B^* usually radiates so that photons are detected.[3]

In some cases, however, it is useful to consider both processes in a unified manner; this is partic-

ularly true if both channels exist for one set of reactants. This paper develops a semiclassical theory for this unified approach.

Referring to Fig. 1, suppose the potential curve for A^*-B lies above that for A-B^+ at large R, but below it for small R. Within the Born Oppenheimer approximation, therefore, reaction (1) takes place at large R ($R > R_+$), while only reaction (2) is possible at small R ($R < R_+$). The important theoretical point we show is that $\Gamma(R)$, the autoionization rate for $R > R_+$, is not zero at $R = R_+$ and in fact is a continuous function even for $R < R_+$. We then show that the cross-section formulae developed earlier by Miller[4] for Penning ionization, reaction (1), can also be applied to the case of reaction (2). For the case depicted in Fig. 1, therefore, both reactions (1) and (2) take place, and our semiclassical theory--which is only a slight generalization of our earlier work[4]--allows one to calculate the cross sections for both reactions.

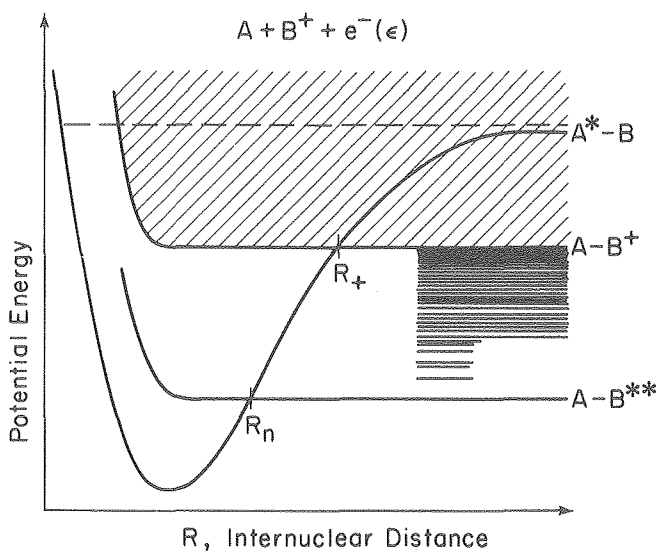

Fig. 1. Sketch of the potential curve for A^*-B. For $R > R_+$ it is embedded in a continuum of curves of the type A-B^+ + e^-, and for $R < R_+$ it crosses the infinite family of curves of the type A-B^{**}, B^{**} being a Rydberg state of B. (XBL 777-9640)

A particular system to which this situation applies is

$$He^+ + F^- \rightarrow He + F^+ + e^-$$
$$\rightarrow He + F^* .$$

We calculated the relevant potential energy curves and the autoionization rate function $\Gamma(R)$, as shown in Figs. 2 and 3. Figure 4 shows the cross sections, as a function of collision energy, for ionization (i.e., final state He + F^+ + e^-) and for excitation transfer [i.e., final states He + $F^*(2p^4np)$]. The lowest excited state of F is the most likely product, but the ionization cross section is not negligible.

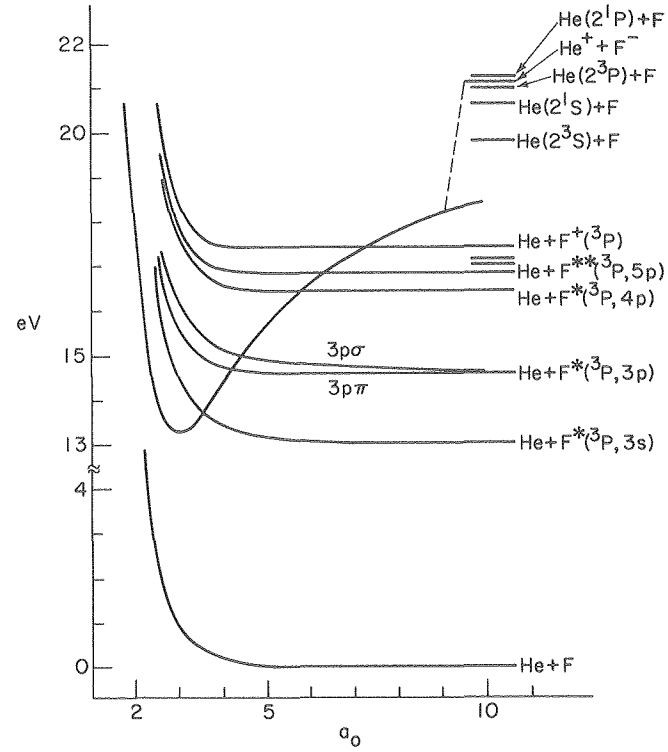

Fig. 2. Semiquantitative potential energy curves for $^2\Sigma$ states of He-F, and for the ground state of He-F^+. (XBL 777-9642)

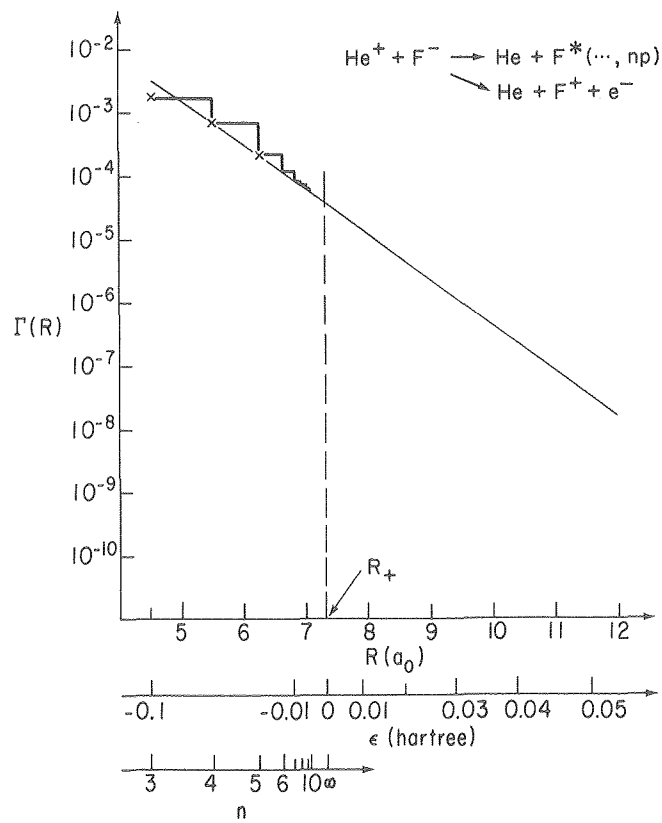

Fig. 3. The width function $\Gamma(R)$ (in hartrees) as determined from $\Gamma(R) = 2\pi\rho(\varepsilon)\,|\langle\chi_\varepsilon|\underline{\phi}_x\rangle|^2\,|H_{AB}(R)|^2$. (XBL 777-9644)

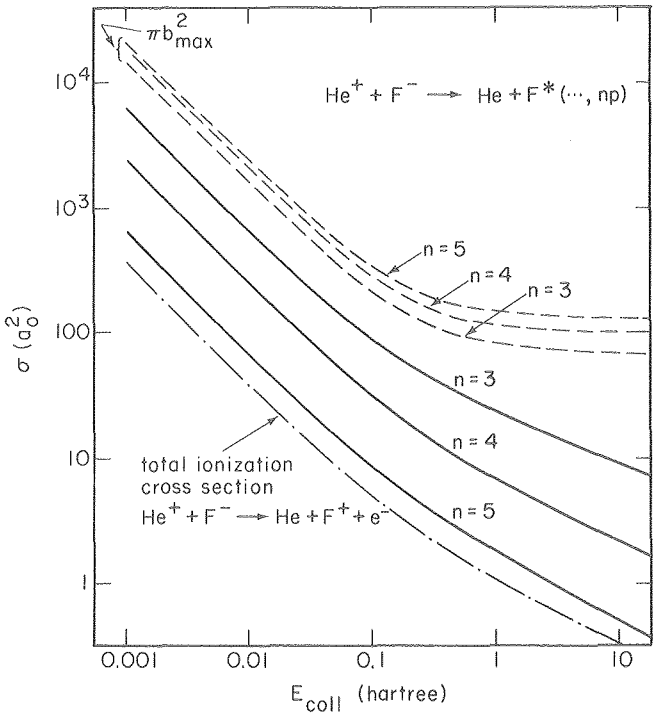

Fig. 4. Total cross sections for the reactions $He^+ + F^- \rightarrow He + F^{**}(n)$, $He + F^+ + e^-$, as a function of collision energy. (XBL 777-9645)

*Abstracted from J. Chem. Phys. 67, 4923 (1977).

1. See, for example, E. Illenberger, A. Niehaus, A. Phys. B 20, 33 (1975).
2. For a review, see A Niehaus, Ber. Bunsenges. Phys. Chem. 77, 632 (1973).
3. See, for example, W. Lee, R. M. Martin, J. Chem. Phys. 64, 678 (1976).
4. W. H. Miller, J. Chem. Phys. 52, 3563 (1970).

3. SEMICLASSICAL DESCRIPTION OF INTERFERENCE EFFECTS IN ROTATIONAL STATE DISTRIBUTIONS*†

C. W. McCurdy and W. H. Miller

Although classical mechanics describes many features of molecular collision phenomena quite well, one must go beyond it in order to include intrinsically quantum mechanical effects such as interference and tunneling. The general semiclassical approach known as classical S-matrix theory[1] allows one to incorporate these quantum features while at the same time retaining a classical mechanical description of the mechanics itself.

An interesting illustration of this theory is the case of rotational excitation of an "almost homonuclear" diatomic molecule. Consider the excitation of diatom BC by the atom A:

$$A + BC(j_1) \rightarrow A + BC(j_2),$$

where j is the rotational quantum number. If BC is homonuclear (i.e., B ≡ C), then it is well-known that $\Delta j \equiv j_2 - j_1$ must be even, whereas there is no such restriction on Δj if BC is heteronuclear. More quantitatively, suppose the interaction potential between A and BC has the form

$$V(R,\gamma) = V_0(R)\ [1 + a_1 P_1(\cos\gamma) + a_2 P_2(\cos\gamma)]$$

where R is the distance from A to the center of mass of BC and γ is the angle between this coordinate and the axis of the molecule; P_1 and P_2 are Legendre polynomials. If $a_1 = 0$, the diatom is homonuclear, i.e., the potential is unchanged by the replacement $\gamma \rightarrow \pi - \gamma$ (which corresponds to interchanging B and C); if $a_1 \neq 0$, the molecule is heteronuclear.

The rigorous selection rule thus implies that the cross section $\sigma(j_2 \leftarrow j_1)$ is zero for odd Δj if $a_1 = 0$, but is nonzero if $a_1 \neq 0$. The semiclassical analysis shows moreover that this transition is continuous; i.e., if $|a_1| << 1$, then σ (odd Δj) << σ (even Δj).

Figure 1 shows an example of the calculations that illustrate this "weak selection rule." The solid line connects the results for the homonuclear case ($a_1 = 0$), and the dashed line the results for a_1 small but finite. Figure 2 shows similar results for larger values of a_1. One sees here that

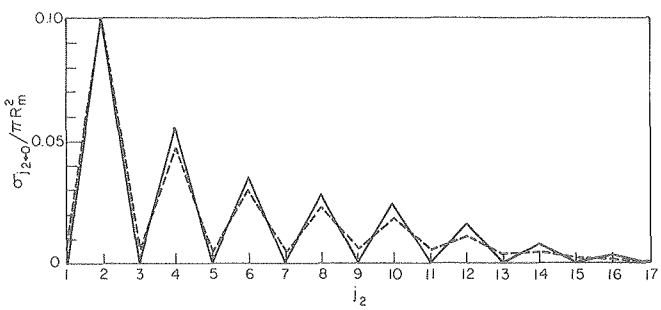

Fig. 1. Cross sections for rotationally inelastic transitions $j_1 = 0 \rightarrow j_2$. The solid line connects values for the homonuclear case $a_1 = 0$, $a_2 = 1.2$, and the dashed line the values for the "almost homonuclear" case $a_1 = 0.15$, $a_2 = 1.2$. (XBL 773-5181)

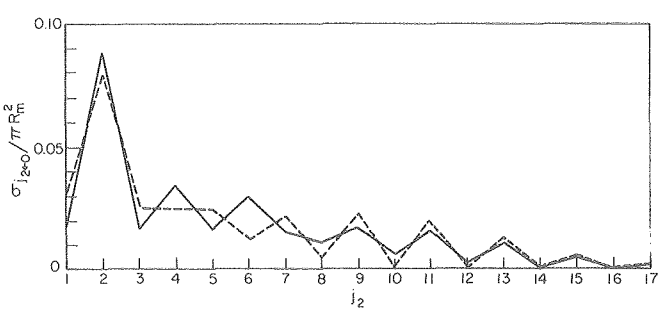

Fig. 2. Same as Fig. 1 except the anisotropy parameters are $(a_1,a_2) = (0.3, 1.2)$ (solid line) and $(a_1,a_2) = (0.4, 1.2)$ (dashed line). (XBL 773-5182)

the odd anisotropy is so large that the interference has been shifted in phase for large Δj; i.e., for small Δj, the ordinary propensity is seen, σ (odd Δj) $< \sigma$ (even Δj), but for large Δj it is inverted, σ (odd Δj) $> \sigma$ (even Δj). For anisotropies this large it no longer makes sense to think of this as a remnant of the homonuclear selection rule, but simply an interference effect in the rotational state distribution.

---

*Abstracted from J. Chem. Phys. 67, 463 (1977).

†Supported by the National Science Foundation.

1. W. H. Miller, Acct. Chem. Res. 4, 161 (1971); Adv. Chem. Phys. 25, 69 (1974).

4. SEMICLASSICAL EIGENVALUES FOR FINITE INTERVALS*

J. E. Adams and W. H. Miller

The well-known Bohr-Sommerfeld eigenvalue condition,

$$(n + \tfrac{1}{2})\pi = \int_{x_<}^{x_>} dx \sqrt{\frac{2m}{\hbar^2}[E-V(x)]} \quad , \qquad (1)$$

$n = 0,1,2,3,\ldots$, is applicable when the domain of the potential is the entire x-axis $(-\infty,\infty)$. If the potential is defined only on the semi-infinite interval $(0,\infty)$, then the above equation is modified by the replacement,

$$V(x) \to V(x) + \Delta V(x) \quad , \qquad (2)$$

where

$$\Delta V(x) = \frac{\hbar^2}{8mx^2} \quad . \qquad (3)$$

This is known as the Langer modification.[1]

For potential functions defined on a finite interval (a,b) Eq. (1) is also inappropriate, and we have derived the appropriate modification for this situation. The modification is the same form as Eq. (2), but where here

$$\Delta V(x) = \frac{\hbar^2}{8m} \frac{\left(\frac{\pi}{b-a}\right)^2}{\cos^2\left[\frac{\pi}{b-a}\left(x - \frac{a+b}{2}\right)\right]} \quad . \qquad (4)$$

It is easy to show that Eq. (4) has the Langer form in the limits $x \to a$, or $x \to b$:

$$\lim_{x\to a} \Delta V(x) = \frac{\hbar^2}{8m(x-a)^2}$$

$$\lim_{x\to b} \Delta V(x) = \frac{\hbar^2}{8m(b-x)^2} \quad ,$$

and if the interval (a,b) becomes $(0,\infty)$, then

$$\Delta V(x) = \frac{\hbar^2}{8mx^2} \quad ,$$

the Langer form is recovered precisely.

To illustrate and test this result we consider the harmonic oscillator defined on the interval $(-L/2, L/2)$; i.e., the potential is $+\infty$ for $|x| > L/2$. (This specific example has relevance to frequency doubling in wave guides.) For $m = \hbar = 1$ the eigenvalues have the following limits for large and small values of L,

$$\lim_{L\to\infty} E_n = (n + \tfrac{1}{2})\omega \qquad (5)$$

$$\lim_{L\to 0} E_n = \frac{1}{2}\left[\frac{(n+1)\pi}{L}\right]^2 \quad , \qquad (6)$$

for $n = 0,1,2,\ldots$ For intermediate values of L we have carried out calculations to compare the results of Eqs. (1) and (4) to the exact quantum mechanical results[2] for this problem.

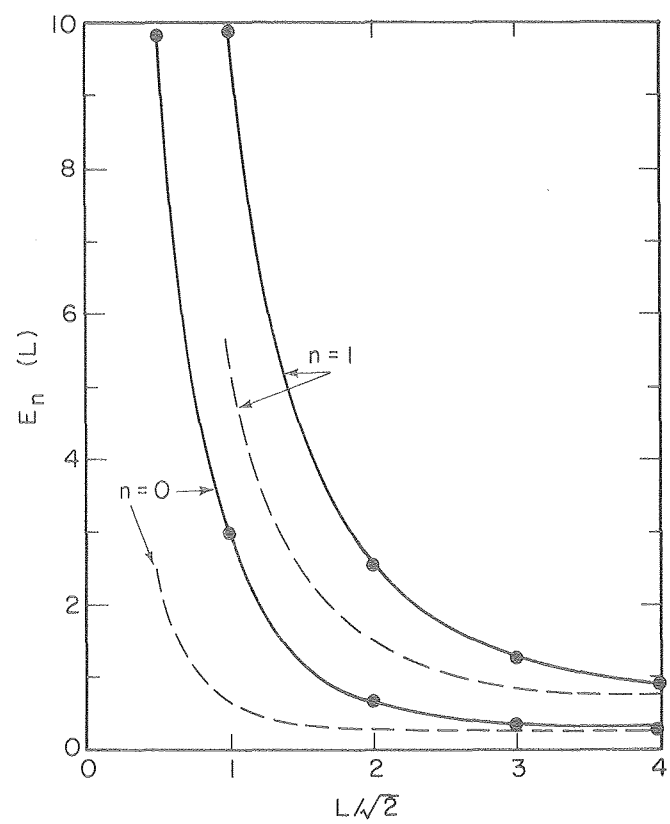

Fig. 1. Eigenvalues of the ground (n = 0) and first excited state (n = 1) for a harmonic oscillator of frequency $\omega = 1/2$ in a box of length L. The points represent the exact quantum mechanical values of Ref. 2, the solid curves the values calculated via the modified WKB quantum condition, and the dashed lines the results given by the ordinary unmodified WKB quantum condition. (XBL 778-2852)

Figure 1 shows the lowest two eigenvalues as a function of L. The modified WKB eigenvalues are in excellent agreement with the correct quantum mechanical values for all L, while the unmodified WKB values are quite poor for small L.

*Abstracted from J. Chem. Phys. 67, 5775 (1977).

1. R. E. Langer, Phys. Rev. 51, 669 (1937).
2. A Consortini and B. R. Frieden, Nuovo Cimento 35, 153 (1976).

5. SEMICLASSICAL PHASE SPACE DISTRIBUTIONS*

R. M. Stratt and W. H. Miller

A previously obtained[1] semiclassical expression for the canonical distribution function $\rho(\underset{\sim}{p},\underset{\sim}{q})$ is investigated for several examples of the type that are of interest for chemical applications.

The expression for the distribution in coordinate space $\rho(\underset{\sim}{q})$ is

$$\rho(\underset{\sim}{q}) = h^{-N}\int d\underset{\sim}{p}\; e^{-\frac{2}{\hbar}\int_0^{\hbar\beta/2} d\tau\, H(\underset{\sim}{p}(\tau),\underset{\sim}{q}(\tau))}, \qquad (1)$$

where $H(\underset{\sim}{p},\underset{\sim}{q}) = \underset{\sim}{p}^2/2m + V(\underset{\sim}{q})$, is the classical Hamiltonian, and $\underset{\sim}{p}(\tau),\underset{\sim}{q}(\tau)$ is the trajectory determined by the equations of motion

$$\underset{\sim}{q}'(\tau) = \underset{\sim}{p}/m \qquad (2a)$$

$$\underset{\sim}{p}'(\tau) = \frac{\partial V(\underset{\sim}{q})}{\partial \underset{\sim}{q}}, \qquad (2b)$$

with initial conditions

$$\underset{\sim}{q}(0) = \underset{\sim}{q} \qquad (3a)$$

$$\underset{\sim}{p}(0) = \underset{\sim}{p}. \qquad (3b)$$

The partition function Q is given by

$$Q = \int d\underset{\sim}{q}\; \rho(\underset{\sim}{q}). \qquad (4)$$

Figure 1 shows a comparison of the classical, quantum, and semiclassical partition function for a particle in a box of length L as a function of the reduced parameter $\theta = L/\hbar\sqrt{2mkT}$. The semiclassical approximation is seen to include quantum effects to some extent, but it is far from quantitative at very low temperatures. This is an example of the difficulty that semiclassical methods usually have with discontinuous potentials.

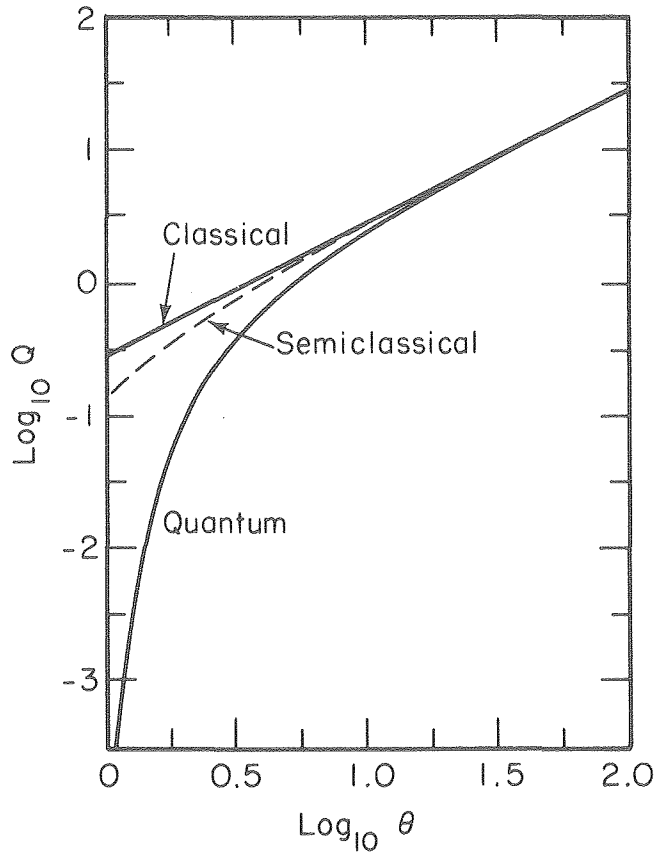

Fig. 1. Partition function for a particle in a box; $\theta = L\sqrt{2mkT}/\hbar$. (XBL 777-9632)

Figure 2 shows a similar comparison for a Morse oscillator. Here the semiclassical approximation is in quantitative agreement with the quantum re-

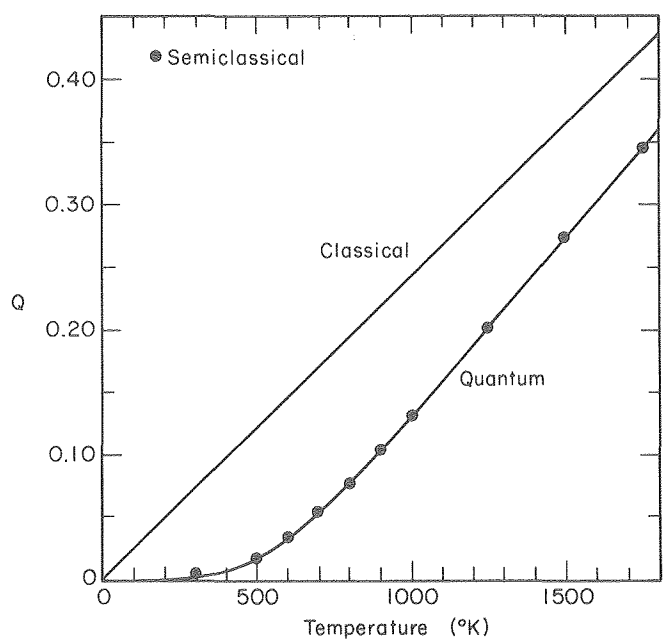

Fig. 2. Partition function for a Morse oscillator (T_{char} = 4184 K). (XBL 777-9634)

sult for all temperatures. The semiclassical model is thus much more accurate for this smooth potential function.

Finally, Fig. 3 shows the radial distribution function for two helium atoms interacting via a

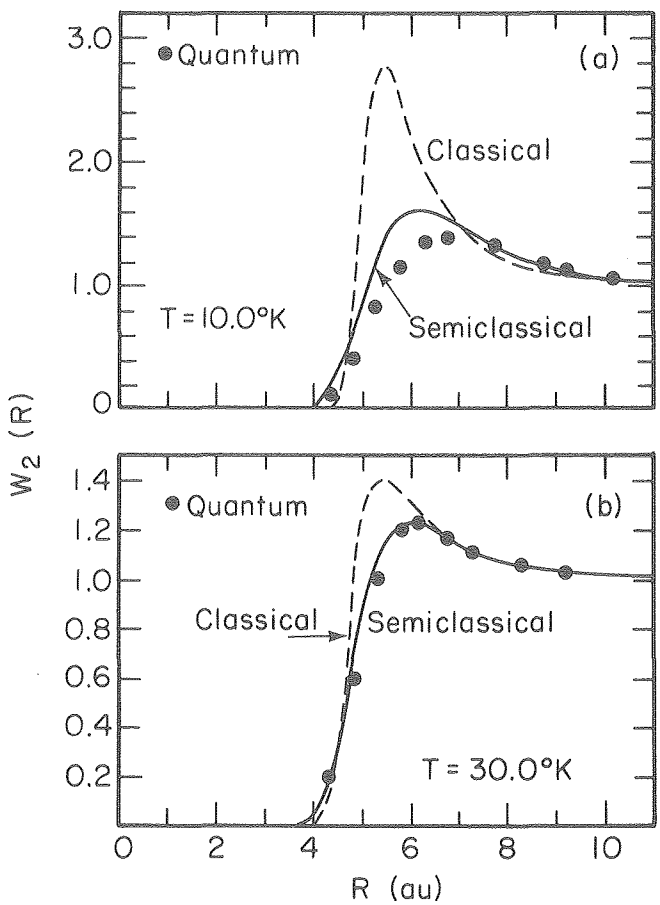

Fig. 3. Two particle radial distribution function for He^4 in a Lennard-Jones potential. Distance is in atomic units (σ = 4.83 a.u.). (XBL 777-9636)

Lennard-Jones potential. At the lower temperature, 10K, the quantum corrections to the classical result are sizeable, and the semiclassical approximation does a good job of describing them. At 30K the quantum effects are smaller and the semiclassical approximation even more accurate.

In general, the semiclassical model does a good job of describing the quantum effects in the canonical distribution function when the interaction potential is smooth. It could thus be a useful approach for exploring these effects in more complex systems.

*Abstracted from J. Chem. Phys. 67, 5894 (1977).

1. W. H. Miller, J. Chem. Phys. 58, 1664 (1973).

6. RESEARCH PLANS FOR CALENDAR YEAR 1978

William H. Miller

In addition to continuing interest in various aspects of semiclassical theory, there are several new topics that we are planning to investigate.

Classical Liouville Equation

Classical mechanics is an adequate description of molecular dynamics for many purposes. In collision problems the essential task is to map an initial phase space distribution onto a final one, and this is normally accomplished by sampling the initial distribution (usually by Monte Carlo methods) and then integrating Hamilton's equations to follow the individual trajectories of the system from reactants to products. The same goal can be achieved somewhat more concisely (in principle) by solving the classical Liouville equation for the phase space distribution function. This effectively maps the initial distribution function onto the final one in one step.

We have already solved some of the formal problems that have obstructed this approach in the past and plan to apply the equations we have obtained to specific examples to see how useful the approach may be.

Quantum Mechnical Reactive Scattering

A number of years ago (1969) I developed a formalism for carrying out quantum mechanical reactive scattering. It has many attractive features but has never been seriously applied. We have recently thought of some particular tricks that make it even more appealing and plan to apply it first to some test cases and, if encouraged, to some reactions of interest.

The most important feature of this approach is its complete generality. It does not rely on the use of "natural collision coordinates" that must be tailored to each specific problem, and in some cases are not possible to use at all.

Infrared Laser Induced Chemistry

This is a very popular topic these days. In its simplest version the laser is used to excite the reactant species vibrationally and the reaction usually proceeds much faster with vibrationally excited products. One of the best known examples is

$$K + HCl(v) \rightarrow KCl + H,$$

for which the cross section is much larger for v = 1 than for v = 0. To be effective, therefore, the laser must be in the frequency region that excites HBr from the v = 0 to the v = 1 vibrational state.

We have recently realized that an infrared laser can promote a chemical reaction even if the reactants are infrared inactive. In $H + H_2 \rightarrow H_2 + H$,

for example, there is a nonzero dipole moment when the three atoms are in the transition state region of the potential energy surface. Furthermore, the dipole moment changes with the asymmetric stretch (i.e., motion along the reaction coordinate) and can thus absorb energy from a radiation field. The symmetric stretch, on the other hand, is infrared inactive. The system thus absorbs energy selectively in the particular degree of freedom most effective in making the reaction go. Test calculations for this and other reactions are being begun.

7. 1977 PUBLICATIONS AND REPORTS

W. H. Miller and Associates

Journals

1. N. C. Handy, S. M. Colwell and W. H. Miller, Semiclassical Methods for Vibrational Energy Levels of Triatomic Molecules, Faraday Disc. Chem. Soc. 62, 29 (1977).

2. W. H. Miller, Semiclassical Theory for Non-Separable Systems: Construction of 'Good' Action-Angle Variables for Reaction Rate Constants, Faraday Disc. Chem. Soc. 62, 40 (1977), LBL-4991.

3. A. P. Hickman, A. D. Isaacson and W. H. Miller, Feshbach Projection Operator Calculation of the Potential Energy Surfaces and Autoionization Lifetimes for He(2^3S)-H and He(2^3S)-H_2, J. Chem. Phys. 66, 1483 (1977), LBL-5484.

4. A. P. Hickman, A. D. Isaacson, and W. H. Miller, Penning Ionization of H_2 by He(2^3S): Quantum Mechanical Scattering Calculations Within the Rigid-Rotor Approximation, J. Chem. Phys. 66, 1492 (1977), LBL-5483.

5. A. D. Isaacson, A. P. Hickman and W. H. Miller, Penning Ionization of H_2 by He^*: Calculation of Anomalous Structure in the Singlet Interaction Potential, J. Chem. Phys. 67, 370 (1977), LBL-6083.

6. C. W. McCurdy and W. H. Miller, Interference Effects in Rotational State Distributions; Propensity and Inverse Propensity, J. Chem. Phys. 67, 463 (1977), LBL-6093.

7. W. H. Miller and H. Morgner, A Uniform Treatment of Penning Ionization and Excitation Transfer, J. Chem. Phys. 67, 4923 (1977), LBL-6653.

8. P. K. Pearson, R. R. Lucchese, W. H. Miller and H. F. Schaefer, Theoretical Chemistry via Minicomputer, Minicomputers and Large Scale Computations, P. Lykos, Ed., ACS Symp. Series 57, 171 (1977).

9. J. E. Adams and W. H. Miller, Semiclassical Eigenvalues for Potential Functions Defined on a Finite Interval, J. Chem. Phys. 67, 5775 (1977), LBL-6630.

10. R. M. Stratt and W. H. Miller, A Phase Space Sampling Approach to Equilibrium Semiclassical Statistical Mechanics, J. Chem. Phys. 67, 5894 (1977), LBL-6646.

11. C. W. McCurdy and W. H. Miller, A New Helicity Representation for Reactive Atom-Diatom Collisions, ACS Symp. Ser. 56, 239 (1977).

Meetings and Invited Lectures

1. W. H. Miller, Recent Developments in Semiclassical Scattering Theory, Invited lecture at the Canadian Symposium on Theoretical Chemistry, June 19-25, 1977, University of New Brunswick, Fredericton, Canada.

2. W. H. Miller, Semiclassical Mechanics of Molecular Collisions, Organizer and speaker at the Monie A. Ferst Award Symposium honoring Professor E. Bright Wilson, Jr., Georgia Institute of Technology, Atlanta, May 25, 1977.

3. W. H. Miller, Semiclassical Theory of Collision Processes, Invited lecture at the Gordon Research Conference on Few Body Problems in Chemistry and Physics, Kimball Union Academy, Meriden, New Hampshire, August 15-19, 1977.

4. Papers at the Xth International Conference on the Physics of Electronic and Atomic Collisions, Paris, July 21-27, 1977:
(a) A. P. Hickman, A. D. Isaacson, and W. H. Miller, Penning Ionization of H_2 by He(2^1S): Calculation of Energy Surface, Width, and Cross Sections, p. 309 of Abstracts.
(b) F. T. Smith and W. H. Miller, A Bessel Function Representation for Semiclassical Perturbation Scattering, p. 772 of Abstracts.
(c) A. P. Hickman, F. T. Smith, and W. H. Miller, Semiclassical Perturbation Scattering Theory: Comparison of Vibrational Excitation of CO and N_2 by Li^+, p. 484 of Abstracts.

e. Photoelectron Spectroscopy

David A. Shirley, Principal Investigator

1. THERMAL DIFFUSE SCATTERING IN PHOTOEMISSION: A NEW EFFECT*

R. S. Williams, P. S. Whener, J. Stohr,† and D. A. Shirley

For any scattering mechanism occurring in a crystalline solid, the conservation of crystal momentum for the scattering process arises due to the assumption that infinite three-dimensional periodicity exists in the solid. Any breakdown in the crystalline symmetry allows scattering not conserving crystal momentum to occur. The presence of phonon modes in a crystal disrupts the perfect periodicity of a lattice and thus opens inelastic (i.e., phonon assisted) channels to the scattering process. We have observed this effect in photoemission for the first time in a study of the temperature dependence of angle-resolved photoelectron spectra of a copper single-crystal surface.

The temperature and energy dependence of the momentum conservation rules for elastically scattered radiation (e.g., x-rays, neutrons, or electrons) by a crystal lattice is governed by the Debye-Waller factor

$$f = \exp\left[-\langle(\vec{q}\cdot\Delta\vec{r})^2\rangle\right] \quad . \qquad (1)$$

Here $\vec{q} = \vec{k}_f - \vec{k}_j$ is the difference between the wavevectors of the incident ($\vec{k}_j$) and scattered ($\vec{k}_f$) radiation, and $\Delta\vec{r}$ is the instantaneous thermal displacement of an atom from the equilibrium lattice position. In a simple one-electron picture, photoemission can be viewed as a scattering process. The initial state involves a photon with wavevector $\vec{k}_{h\nu}$ and a bound (e.g., a valence) electron with wavevector $\vec{k}_i$ ($\vec{k}_j = \vec{k}_{h\nu} + \vec{k}_i$), while the final state is characterized by the photoelectron with wavevector $\vec{k}_f$. The diffraction law $\vec{k}_f - k_j = \vec{G}$, where $\vec{G}$ is a reciprocal lattice vector describing the elastic scattering of radiation by a crystal lattice, also describes the direct transition requirement in photoemission. Hence, one would expect the intensity of direct-transition features in ARP spectra to exhibit a temperature and energy dependence in accordance with Eq. (1).

In this approximation, the indirect transition channel in photoemission corresponds closely to x-ray temperature-diffuse scattering.[1] The connection between x-ray diffraction and ARP is revealed by an evaluation of the photoexcitation matrix element including the time average over the atomic thermal displacements,

$$|\langle\phi^f(\vec{r})|\vec{A}\cdot\vec{p}|\phi^i(\vec{r})\rangle|^2 \sim f\,\sigma_{if}(\vec{k}_f) \times \left\{\delta(\vec{q}-\vec{G}) + \left(1-\delta(\vec{q}-\vec{G})\right) \times \left[\phi_1\frac{|\vec{q}|^2}{|\vec{q}-\vec{G}|^2}(k_BT) + \phi_2|\vec{q}|^4(k_BT)^2 + \ldots\right]\right\} . \qquad (2)$$

This expression was derived assuming LCAO tight-binding initial-state and plane-wave final-state wavefunctions.[2] Here, $\sigma_{if}(\vec{k}_f)$ is an atomic-type matrix element, k_B the Boltzmann constant, and T the temperature. The quantities ϕ_1 and ϕ_2 involve sums over phonon modes familiar from first- and second-order temperature-diffuse scattering.[1]

To elucidate the effect of temperature on the ARP spectrum we consider normal photoemission from a Cu(110) single crystal. At room temperature we found that photoemission from Cu in the ultraviolet (UPS) regime is dominated by direct transition processes.[3] The band-6 peak at $E_B \sim 0.5$ for $h\nu = 45$ eV is an extremely sensitive indicator of the direct transition channel because it can only originate from transitions in a very small region

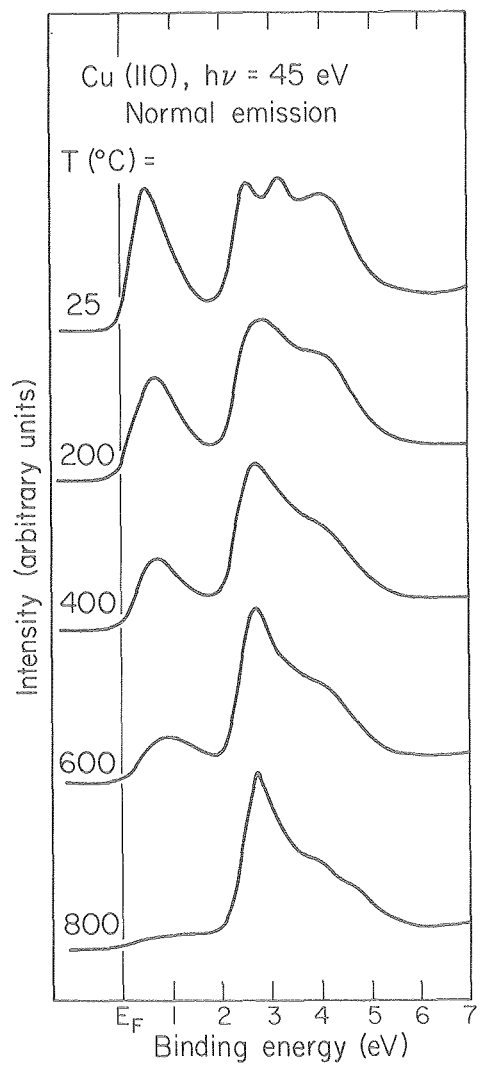

Fig. 1. Temperature dependence of the normal photoemission spectrum from a Cu(110) crystal at $h\nu = 45$ eV. Emission near 0.5 eV binding energy is due almost entirely to initial states of the 6th valence band on the ΓK line of the Brillouin Zone. (XBL 774-818)

of the Brillouin Zone (BZ). As phonon-assisted processes become more important with increasing temperature, this peak (Fig. 1) decreases dramatically in intensity. Figure 1 also shows that as the temperature is raised the shape of the d-band changes as well; the d-band peak becomes asymmetric, with more intensity at the top of the bands, until, at 800°C, the spectrum resembles that of polycrystalline copper for $h\nu$ = 40-50 eV.[4] For copper, a single electron-phonon interaction can change the electron wavevector by a large amount, but since the energy transfer is small, more of the $\vec{k}$ states in the BZ are sampled without greatly disrupting their energy distribution. This increase in the number of different states that can contribute to the photoemission spectrum washed out structure due to bands with a large amount of dispersion (in particular the band 6 feature in Fig. 1.).

In follows that the direct-transition model describes ARP studies at ultraviolet energies only if the temperature is low enough to suppress phonon-assisted indirect transitions. Thermal mean-square displacements of atoms in crystals approach their limiting zero-temperature values for temperatures somewhat below the Debye temperature of the material in question. Thus, a general rule for assuming a minimum amount of thermal momentum broadening is to collect ARP spectra at temperatures below the surface Debye temperature of the material studied.

Because the Debye-Waller factor determines the fraction of the $\vec{k}$-conserving direct transitions, the direct transition process is less important at x-ray energies than at UPS energies. In fact, since $|\vec{q}|$ is about 5 times larger at $h\nu$ = 1486.6 eV (Al Kα radiation) then at $h\nu$ = 45 eV, it is expected from Eq. (1) that room temperature XPS spectra are dominated by the phonon-assisted indirect transition process. Valence-band spectra of Au single crystals yield identical results at $h\nu$ = 1253.6 eV (Mg Kα) and 1486.6 eV for photoemission along the [001] and [111] directions.[5] These experimental findings lead to the conclusion that the entire BZ is being sampled at high ($\gtrsim$ 1000 eV) photon energies. The angular dependence observed in XPS spectra arises from the photoexcitation matrix element $\sigma_{if}(\vec{k}_f)$ in Eq. (2).

---

*From LBL-6213.

†Present address: Stanford Synchrotron Radiation Laboratory, P.O. Box 4349, Stanford, CA 94305.

1. B. E. Warren, X-ray Diffraction (Addison-Wesley, Reading, MA, 1969), p. 159.
2. R. S. Williams, P. S. Wehner, J. Stohr, and D. A. Shirley, Phys. Rev. Lett. 39, 302 (1977).
3. J. Stöhr, P. S. Wehner, R. S. Williams, G. Apai, and D. A. Shirley, Phys. Rev. B 16, 302 (1977).
4. J. Stöhr, F. F. McFeely, G. Apai, P. S. Wehner, and D. A. Shirley, Phys. Rev. B 14, 4431 (1976).
5. P. S. Wehner, G. Apai, J. Stöhr, unpublished results.

2. THE BAND-6 RESONANCE IN ANGLE-RESOLVED PHOTOEMISSION FROM Cu(110): DIRECT DETERMINATION OF TOTAL VALENCE-BAND DISPERSION RELATIONS*

P. S. Wehner, R. S. Williams, J. Stöhr,† G. Apai, and D. A. Shirley

The interpretation of angle-resolved photoemission spectra in terms of electronic band structure has suffered from a lack of detailed information on how the crystal momentum $\vec{q}$ of the photoexcited electron inside the crystal is related to the momentum $\vec{p}$ of the free electron outside the crystal. Normal photoemission avoids this problem because electron refraction at the surface is zero and the propagation direction of the electron inside and outside the crystal is the same. Thus the detailed relationship between $\vec{q}$ and $\vec{p}$ need not be considered. Using this fact, we have demonstrated that photon-energy-dependent normal photoemission, employed over a sufficiently large energy range, is a very effective method for investigating the details of the bulk band structure, along the photoemission direction.[1,2]

For this study a single crystal of copper with a (110) orientation was used. The crystal was cleaned in situ by argon-ion bombardment and annealed to remove surface damage. Photoemission measurements were carried out at a pressure of ~5 × 10^{-10} Torr in the experimental geometry shown in Fig. 1 of Ref. 3. The crystal was azimuthally oriented such that the surface normal, the [111] and [11$\bar{1}$] crystalline directions lay in the horizontal plane. The electron-analyzer resolution was ~0.2 eV, and the monochromator resolution ranged between 0.01 eV ($h\nu$ = 32 eV) and ~0.2 eV ($h\nu$ = 160 eV).

Experimental spectra are shown in Fig. 1. The The most striking feature in Fig. 1 is the intense peak, which we shall term the band-6 resonance, in the "s-p" band region between the Fermi level (E_F) and about 2 eV binding energy (E_B), which appears for 43 eV $\leqslant h\nu \leqslant$ 52 eV. In contrast to previously published Cu spectra,[3] this feature is completely new and initially quite surprising. The intensity of this peak is comparable with that of the "d" band peaks between 2 eV $\leqslant E_B \leqslant$ 5.5 eV. Also, it shows strong dispersion, ranging from E_B = 0.4 eV at $h\nu$ = 43 eV to E_B = 1.7 eV at $h\nu$ = 52 eV. The "s-p" intensity vanishes in the energy range 70 eV $\leqslant h\nu \leqslant$ 120 eV and shows another maximum around $h\nu$ = 140 eV. At $h\nu$ = 160 eV it has diminished again. The "d" band region also exhibits strong changes in both peak positions and intensities. The d-bandwidth narrows from ~2.5 eV FWHM at low energies to ~1.5 eV in the range 70 eV $\leqslant h\nu \leqslant$ 120 eV, then broadens to ~2.5 eV at the highest energies.

The observed peak positions can be related directly to the initial state band structure as shown in Fig. 2. Figure 2a illustrates that for photoemission along the [110] direction the final-state photoelectron wavevector $\vec{q}$ in the repeated zone scheme lies along the Γ-K-X direction. By

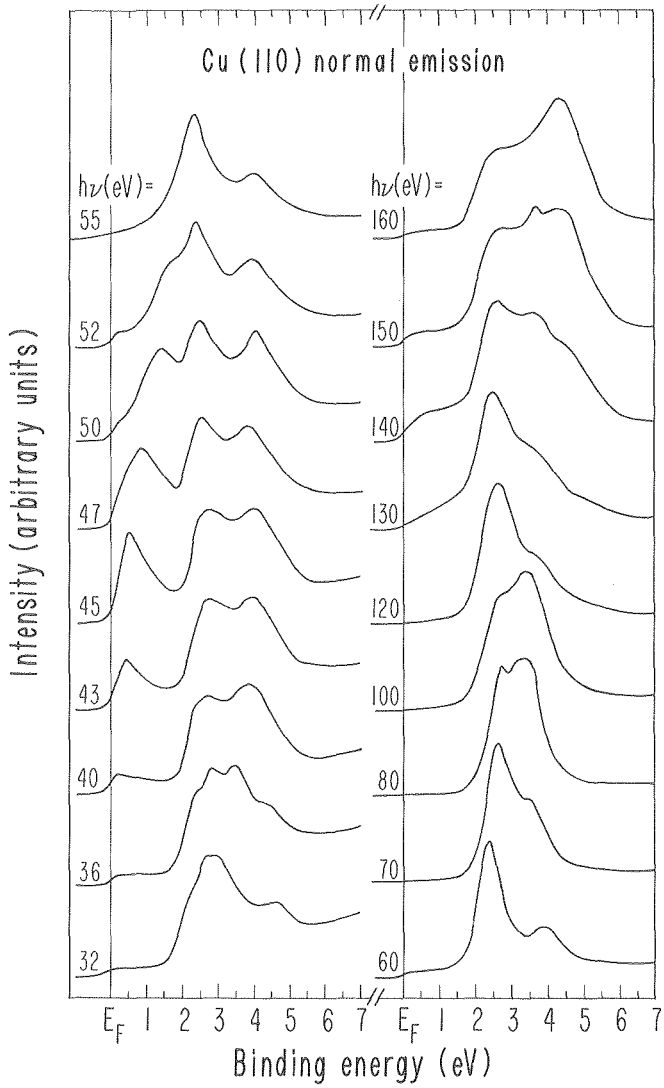

Fig. 1. Photoemission spectra from the valence bands of Cu(110) single crystals in the range 32 eV $\leqslant h\nu \leqslant$ 160 eV. Electrons were collected normal to the (110) face with an angular resolution of $\pm(5 \pm 1)°$. Peak A is the peak between E_F and 2 eV in the $h\nu$ = 43-52 eV spectra. (XBL 772-390)

varying the photon energy the endpoint of $\vec{q}$ will thus sweep through the zone along this line. Figure 2b shows Burdick's[4] valence band structure for Cu along KΓK. Superimposed are the observed peak positions $E_{ex}(h\nu)$ relative to the E_F (cf. Fig. 1). The location of the experimental points in Fig. 2b was derived as follows. From the measured peak positions, relative to the E_F, the final state energy $E_f = E_{ex}(h\nu)$ was calculated. The magnitude of the final state wavevector was then determined from the free-electron dispersion relation $|\vec{q}| = (2m\, E_f/\hbar^2)^{1/2}$, where the zero of the free-electron scale was taken to be the bottom of the free-electron-like bands in Burdick's band structure. The relation $\vec{q} = \vec{k} + \vec{G}$ where $\vec{G}$ is a reciprocal lattice vector, then yields $\vec{k}$ in the first Brillouin Zone (BZ) and the corresponding values $E_{ex}(\vec{k})$ are plotted as bars in Fig. 2b. Figure 2c relates the horizontal scale in Fig. 2b to the corresponding photon energy in eV, assuming an initial state energy of 3.5 eV (middle of "d" band).

Comparison of our experimental peak positions with Burdick's band structure in Fig. 2b reveals generally good agreement. One striking result is the complete agreement of the energy dependence of the pronounded "s-p" band resonance in Fig. 1 with the dispersion of the uppermost band between K and Γ in Fig. 2b. The appearance of an s-p band at only certain photon energies is explained as well. Only when photoemission occurs in a part of the zone where a band exists near the E_F is an s-p band observed. The peak positions in the "d" band region 2 eV $\leqslant$ BE $\leqslant$ 5.5 eV also follow Burdick's band structure. For example, the four-peak structure at $h\nu$ = 36 eV corresponds exactly to the band structure near $k_x = k_y = -0.65$ in Fig. 2b. The two-peak structure at energies around 80 eV matches the bands close to the Γ point. At $h\nu$ = 150 eV, two wider peaks and a sharp middle peak are observed, in full agreement with the bands at $k_x = k_y = 0.6$.

A closer examination of Figs. 1 and 2, however, reveals two interesting facts: 1) a band exists between 6 eV $\leqslant E_B \leqslant$ 9 eV in the band structure but no peaks are observed at a E_B greater than 6 eV; and 2) for photon energies near 130 eV, the same portion of the BZ is sampled as at $h\nu$ = 45 eV but, in contrast to the $h\nu$ = 45 eV spectrum, no strong peak is observed in the s-p region of the spectrum.

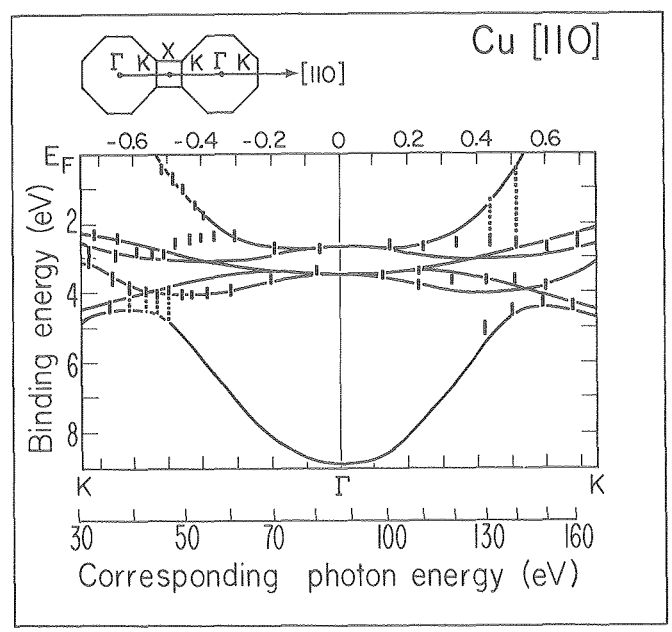

Fig. 2. a) (001) projection of the three-dimensional Brillouin Zone of a fcc lattice in the repeated zone scheme. b) Burdick's band structure from the Fermi level (E_F) to 9 eV binding energy along the UXU and KΓK direction in a repeated zone scheme. The bars are the peak positions of Fig. 1. c) The lower scale establishes a correspondence between the wavevector in Fig. 3b and the experimental photon energies as discussed in the text. (XBL 7712-10950)

The first observation is readily explained by the relative cross section of 4s and 3d wavefunctions (a tight-binding calcualtion shows the comparison of the states spanning the range 6 eV $\leqslant E_B \leqslant$ 9 eV to be almost completely "s" in character). The second observation can be attributed to the increased volume sampled in the BZ because of the smaller inelastic mean free path in the 130-140 eV region ($\lambda_e \sim 3$Å) as compared to that around 45 eV ($\lambda_e \sim 8$Å), and the increased radius of the cylinder detected in k space. While this broadening is small for electron energies near 45 eV, it amounts to ~10% of the width of the BZ in the range 130-140 eV. This amount of broadening is sufficient to smear out the sharp peak (an intense shoulder is observed) in the s-p band because of the steepness of the band from which this structure arises (see Fig. 2b). Indeed, momentum broadening in the final state poses a serious problem in the use of photon-energy-dependent ARP studies (as employed here) to map out the details of the bulk band structure.

We close by noting that the effective photon energy in which dispersion relations can be determined is rather narrow. At the lowest energies (~ 10 ev) band-structure effects distort the free-electron nature of the final states. There is a usable region (roughly 20-80 eV) in which the electron mean free paths are still relatively long, permitting sharp features to be observed. At higher energies (~100 eV) the broad minimum in the electron-mean-free-path relation is approached, and k-broadening obviates sharp structure in the spectrum. Fortunately the intermediate region is usually wide enough to permit studying the entire first BZ.

---

*From LBL-6066; to be published in Physical Review B.

†Present address: Stanford Synchrotron Radiation Laboratory, P. O. Box 4349, Stanford, CA 94305.

1. J. Stöhr, P. S. Wehner, R. S. Williams, G. Apai, and D. A. Shirley, to be published.
2. D. A. Shirley, J. Stöhr, P. S. Wehner, R. S. Williams, and G. Apai, to be published in Physica Scripta.
3. J. Stöhr, G. Apai, P. S. Wehner, F. F. McFeely, R. S. Williams, and D. A. Shirley, Phys. Rev. B 14, 5144 (1976).
4. G. A. Burdick, Phys. Rev. 129, 138 (1963).

3. ELECTRON REFRACTION INTO VACUUM FROM ANGLE-RESOLVED PHOTOEMISSION*

R. S. Williams, P. S. Wehner, J. Stöhr,† and D. A. Shirley

Photoemission from solids is generally considered to proceed in a three-step process: photoexcitation of an electron to an unbound state, transport of the hot electron to the sample surface, and escape of the electron into vacuum. The interpretation of experimental photoemission data has been almost entirely in terms of the photoexcitation step, relegating the transport and escape phenomena to nearly constant effects which do not significantly affect the data. In an attempt to better understand the complete photoemission process, we have performed the first direct measurements of the refraction angles of photoelectrons crossing a solid-vacuum interface. Such determinations are crucial in the interpretation of angle-resolved photoemission (ARP) spectra collected in off-normal photoelectron emission orientations.

For this study, the "band six" peak which has been observed for $h\nu$ = 45 eV in normal photoemission from Cu(110) was chosen. This resonance arises from a direct transition involving the valence band (VB) closest to the Fermi level (E_F) at $\vec{k}$ = (-0.5, -0.5, 0), in units of $2\pi/a$ (where a is the lattice constant of Cu). Photoelectrons created by this transition travel along the [110] direction inside the crystal and thus provide a sensitive indicator for directional effects in ARP.

The conservation laws determining the behavior of an off-normal photoemitted electron as it transverses the solid-vacuum interface en route to the analyzer have been discussed in detail by Mahan.[1] If $\vec{q}$ is the wavevector of the photoelectron inside the crystal, it is related to the free electron wavevector $\vec{p}$ outside the crystal by the following relationships:

$$\vec{p}_{\parallel} = \vec{q}_{\parallel} \qquad (1)$$

$$\left(\hbar^2/2m\right)|p_{\perp}|^2 = \left(\hbar^2/2m^*\right)|q_{\perp}|^2 - V_o \qquad (2)$$

Here $p_{\perp}$ and $q_{\perp}$ are the surface normal components of $\vec{p}$ and $\vec{q}$, while $\vec{p}_{\parallel}$ and $\vec{q}_{\parallel}$ are the parallel components. V_o denotes the inner potential, the energy difference between the zero of energy inside the crystal and the vacuum level. As seen from Eqs. (1) and (2), electron refraction in this simple model depends on both the ratio of the effective mass of the electron (m^*) inside the crystal to that outside (m-the free electron value) (transport step) and the magnitude of the inner potential (escape step). The angle Θ between the emerging photoelectron and the surface normal $\vec{n}$ becomes

$$\Theta = \arcsin[(m^*(E + V_o)/mE)^{1/2}\sin\Theta'] \quad , \qquad (3)$$

where Θ' is the angle between the photoelectron and $\vec{n}$ inside the crystal and E is the measured kinetic energy of the detected photoelectron. The validity of Eq. (3) in photoemission has been assumed in the past for $m^* = m$.

The inner potential V_o is usually taken as the sum of the work function for the particular surface in question and the separation between the zero of energy for the free electron bands and the Fermi level (8.9 eV in copper), which yields a V_o of ~13.8 eV. This value of V_o forms an upper limit for the inner potential seen by hot electrons.[2] Using V_o determined above and $m^* = m$ we may predict the surface refraction for photoelectrons with a particular $\vec{k}_f$ inside the sample. In particular, for electrons originating from the

band-six peak in copper in the [110] direction at 45 eV, Eq. (1) predicts refraction angles ($\Theta - \Theta'$) of 10° and 7° for photoemission from (100) and (111) surfaces, respectively.

In order to measure these refraction angles, ARP spectra were collected as a function of emission angle from (100) and (111) Cu surfaces around the [110] crystalline direction. Figures 1 and 2 show the spectra collected. In each figure the spectrum which maximizes the "band six" peak intensity with respect to the total valence band intensity represents the external projection of the [110] photoemission inside the crystal. The measured refraction angles from these spectra, 16° and 12° for emission from the (100) and (111) crystal faces respectively, is much larger than predicted above.

Since $\hbar^2k^2/2m$ is effectively a measured quantity, and V_0 is taken to be fixed, the data can be fit by Eqs. (1) and (2) only by increasing m^*. An effective mass of $m^* = 1.15$ m (and $V_0 = 13.8$ eV) yields $\Theta = 6.17°$ and 45.5° for the (100) and (111) faces, respectively. That m^* may assume a value other than the free-electron value for the final state photoelectron in the solid is quite likely due to the strong mixing of the final state bands of Cu in this energy regime calculated by Pendry.[3] Furthermore, Moruzzi et al. find that a value of $m^* = 1.08$ m for hot electrons 20 eV above the Fermi level allows a good fit of their calculated Cu band structure to photoemission data.[4]

These studies are expanding our knowledge of the photoemission process beyond the first step of a three-step process and leading to considerable insight into the nature of the hot electron final states of photoemission. Previously, band structure studies of crystalline solids by photoemission have been limited to normal photoelectron emission orientations to avoid the problem of electron refraction. Increased understanding of the transport and escape of photoelectrons will enable

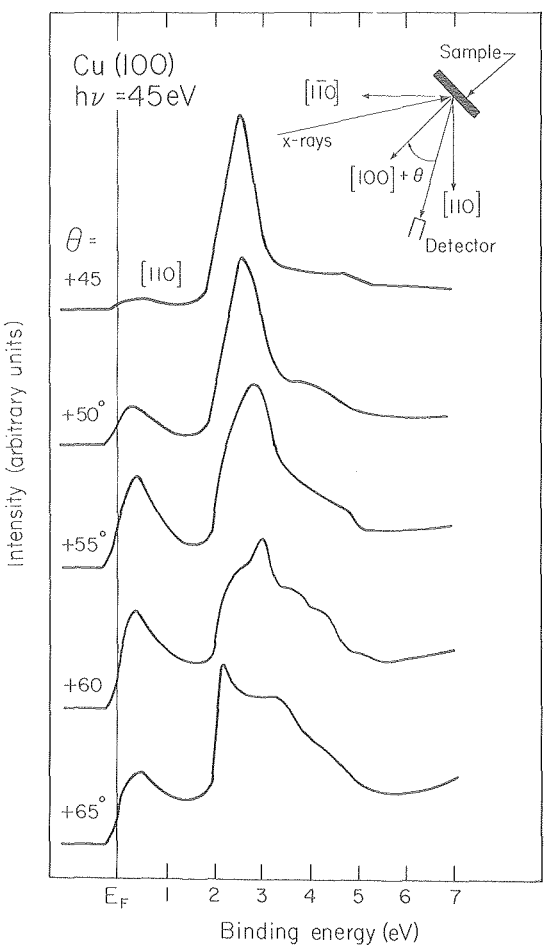

Fig. 1. ARP spectra obtained as a function of Θ from a Cu(100) crystal surface. The experimental geometry is shown in the insert. The "band six" peak intensity (0.5 eV E$_B$) is maximized at an angle 15° closer to the surface of the crystal than the external projection of the [110] axis (labeled spectrum). (XBL 775-1060)

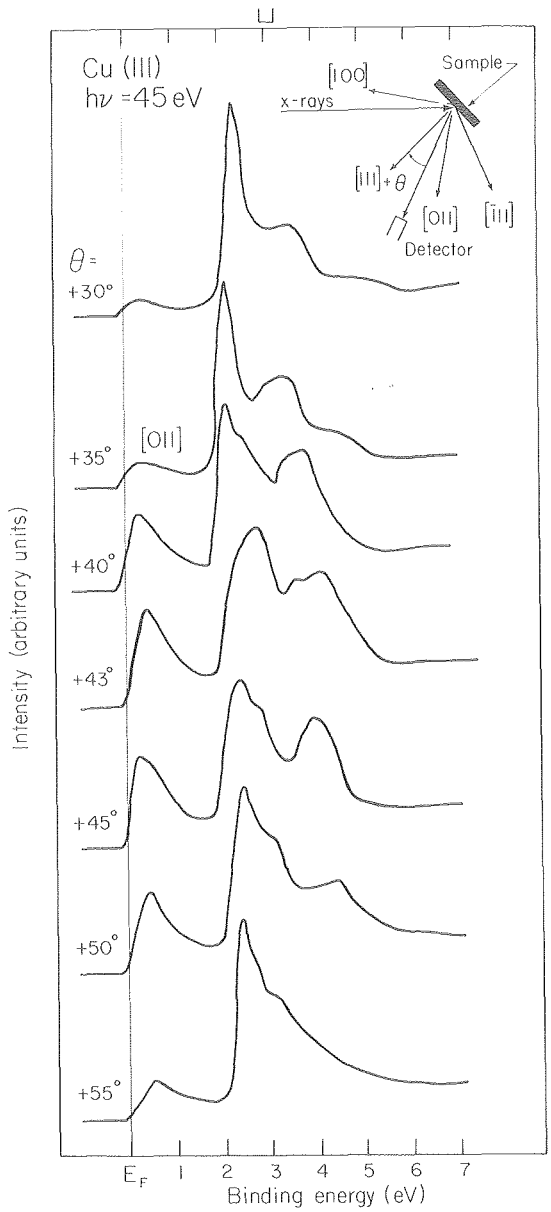

Fig. 2. ARP spectra as a function of Θ from a Cu(111) face. The effects of electron refraction are again clearly evident. (XBL 775-1061)

detailed band structure studies using a single face of a crystaline solid.

---

*Condensed version of LBL-6040, submitted to Surface Science.

†Present address: Stanford Synchrotron Radiation Laboratory, P. O. Box 4349, Stanford, CA 94305.

1. G. D. Mahan, Phys. Rev. B 2, 4334 (1970).
2. L. Hedin and B. I. Lundquist, J. Phys. C 4, 2064 (1971).
3. J. B. Pendry, J. Phys. C 2, 2273 (1969).
4. V. L. Moruzzi, P. M. Marcus, and J. A. Knapp, to be published.

the use of two inherently different models. The surface sensitivity of electron spectroscopy has led most investigators to interpret their results in terms of a one-dimensional density of state (ODDOS) model.[4,5] In this model, only the energy and $\vec{k}_{\parallel}$, the component of crystal momentum parallel to the surface, are conserved, and the observed spectra are predicted to reflect the ODDOS along that $\vec{k}_{\parallel}$ direction. Other workers have emphasized a direct transition model in which photoemission is treated as a bulk process, with strict conservation of energy and of all three components of crystal momentum.[6,7] Recent results[6] from this laboratory have demonstrated that direct transitions from valence band initial states into final states at energies given by the plane-wave dispersion relation adequately describe the peak positions in ARP spectra obtained from copper single crystals.

4. EVIDENCE FOR THE ITINERANT ELECTRON MODEL OF FERROMAGNETISM AND FOR SURFACE PHOTOEMISSION FROM ANGLE-RESOLVED PHOTOEMISSION STUDIES OF IRON*

S. D. Kevan, P. S. Wehner, and D. A. Shirley

The itinerant electron theory of ferromagnetism is widely accepted as describing the situation in the iron group ferromagnets on the basis of a variety of evidence. For example, de Haas-van Alphen studies show two Fermi surfaces-- for the majority and minority bands--in iron, cobalt, and nickel.[1] It is highly desirable to characterize the itinerant nature of the 3d electrons more completely throughout the valence bands, as well as at the Fermi energy E_F. In particular, direct observation of the exchange splitting throughout the Brillouin Zone would be valuable. Photoemission is clearly the method of choice for this problem. Although the exchange splitting has been the subject of numerous photoemission experiments in the past,[2] the information obtained was limited. In a really definitive study, it would be desirable to observe separate peaks arising from majority and minority spin bands and to follow their dispersion relations through the zone. We have undertaken such a study on iron. We report here our first results, which:
1) exhibit for the first time continuous dispersion of separate peaks due to majority and minority bands, and 2) give clear evidence for polarization-dependent surface photoemission, as predicted by Kliewer.[3]

Angle-resolved photoemission (ARP) experiments were performed on the (001) face of an iron single crystal at the HeI photon energy of 21.2 eV. An atomically clean surface was prepared in situ by repeated and simultaneous argon-ion bombardment and heating. The experimental geometry and results are shown in Fig. 1. Spectra were taken at the normal emission angle ($\Theta = 0°$) and in 5° increments off normal emission toward the [101] axis ($\phi = 0°$) or "backward" toward the [$\bar{1}$01] axis ($\phi = 180°$). The unpolarized light beam was incident in the plane containing the [100] and [001] directions, at a constant angle of 35° from the analyzer acceptance direction.

In the past, the interpretation of ARP spectra of three-dimensional lattices has been confused by

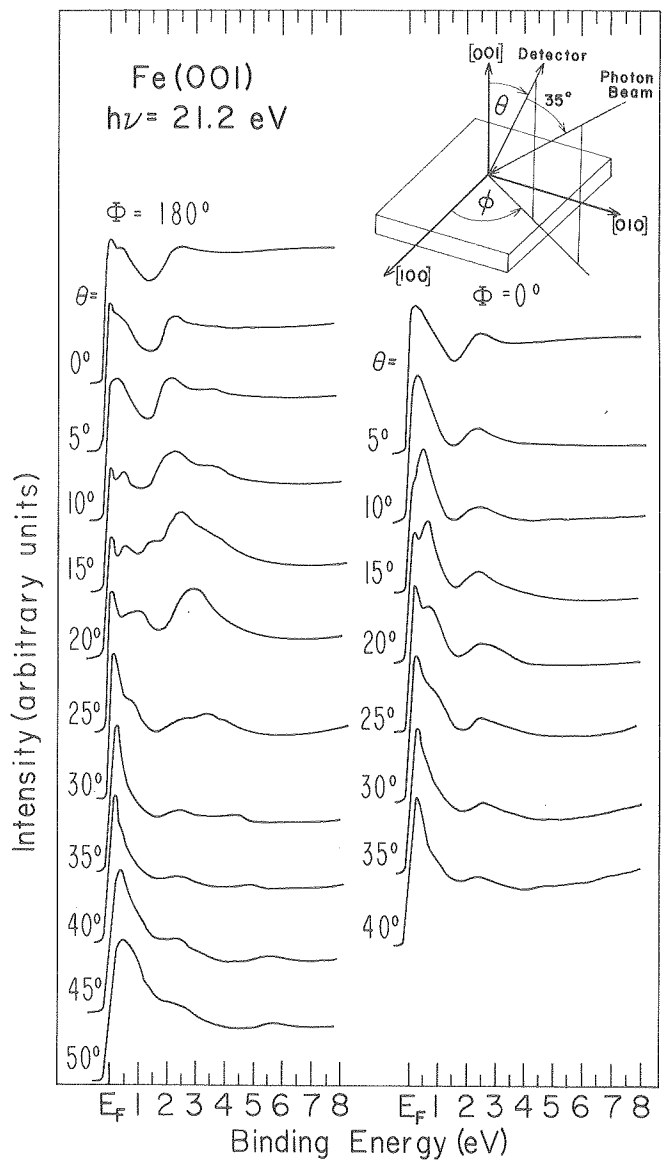

Fig. 1. Experimental geometry and spectra. Note that the angle between light incidence and electron emission is fixed at 35°. Θ and ϕ are the spherical polar and azimuthal angles, respectively, measuring the electron emission direction with respect to the sample normal. (XBL 7710-6935)

In Fig. 2 we show the results of a similar direct-transition calculation on iron, for the conditions applicable to this work. The values of the initial state momenta $\vec{k}_i$ were calculated assuming direct conservation of crystal momentum. Band energies were calculated at these $\vec{k}_i$ by use of the interpolation scheme of Baker and Smith,[8] which was fitted to Callaway's[9] majority and minority spin bands independently. Also shown in Fig. 2 are the peak positions taken from our $\phi = 180°$ spectra. Agreement between theory and

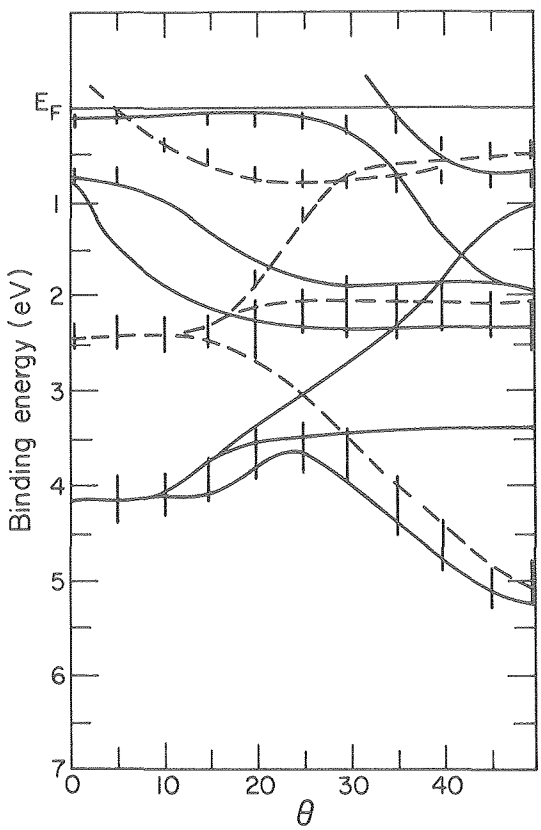

Fig. 2. Direct transition calculations for peak positions as functions of Θ for $\phi = 0°$ or $180°$, with the experimental peak positions superimposed. Corrections have been made for finite angular resolution and refraction of the photoelectrons at the surface. (XBL 779-2338)

experiment is good, considering the approximations used to generate the first principles band structure and those inherent in our use of the interpolation scheme. We conclude that the agreement shown in Fig. 2 demonstrates clearly, for the first time, that majority and minority bands follow different dispersion relations continuously through the zone. The absence of some predicted peaks is probably due to cross-sectional effects. The fact that the fit continues to be quite good at the highest values of Θ, where one would expect the greatest surface sensitivity, leads us to conclude that the broadening in $k_\perp$ due to the variation in the sampling depth is unimportant in this study.

In addition to the finite mean-free-path of the excited electron, p-polarized light also leads to an uncertainty in $k_\perp$ and has been discussed at length by Kliewer.[3] The important parameter determining the amount of uncertainty in $k_\perp$ is the magnitude of the component of the vector potential $\vec{A}$ perpendicular to the surface, $A_\perp$. Since the relative positions of the photon beam and the analyzer are fixed in our apparatus, it is apparent that for fixed Θ this quantity is significantly greater for our $\phi = 0°$ spectra than for our $\phi = 180°$ spectra. On this basis, we expect our $\phi = 0°$ spectra to exhibit more ODDOS structure than our $\phi = 180°$ spectra. In fact, an ODDOS calculation similar to that used by Grandke et al.[6] for PbS predicts a peak at $E_B = 0.5$ eV and complicated structure at $E_B = 1.5 - 2.5$ eV for all values of Θ, in good qualitative agreement with the data for $\phi = 0°$. However, the calculation does not fit the spectra in overall detail. Because our measurements were made at two azimuthal angles, $\phi = 0°$ and $\phi = 180°$, we can make direct comparisons between pairs of spectra with the same Θ values and thus equivalent angles between the crystalline axes and the electron propagation direction. On this basis, we conclude that the "surface photoeffect" predicted by Kliewer[3] has been observed in our $\phi = 0°$ spectra, and that it is responsible for the $E_B = 0.5$ eV peak in these spectra. Because of the magnitude of the effect it seems probable that surface photoemission and bulk photoemission have been present in previous ARP studies in which the role of the photon polarization was neglected.

In summary, we can draw the following conclusions from this research:

1. Distinct, continuous dispersion relations for majority and minority spin bands have been observed throughout the d-bands of iron for the first time. This provides strong support for the itinerant electron model of ferromagnetism.

2. Although direct transitions are of primary importance in predicting peak positions in ARP spectra of iron for near-normal incidence light, p-polarization leads to $k_\perp$-broadening and surface photoemission, as predicted by Kliewer.[3] Clear evidence for this effect was obtained in the form of spectra taken at $\phi = 0°$ which exhibited ODDOS characteristics.

3. Electron refraction at the surface, which was implicit in all of our direct transition calculations, is important and must be taken into account.

Finally, off-normal ARP has been treated systematically and rigorously in this work, by carrying out appropriate interpolation calculations. To our knowledge this represents the first approach of this kind in metals. The significance of this approach is that it allows the experimenter to study dispersion relations along arbitrary directions in the Brillouin Zone, using a single photon energy, rather than being confined to a single value of k along those symmetry lines for which band structure calculations are available.

---

*From LBL-6943; submitted to Solid State Communications.

1. N. F. Mott, Advan. Phys. 13, 325 (1964);

C. Herring, Magnetism, edited by G. T. Rado and H. Suhl (Academic Press, New York, 1964), Vol. IV; D. Shoenberg, Progress in Low Temperature Physics, edited by C. J. Gorter (North-Holland Publishing Co., Amsterdam, 1957), Vol. 2, p. 226; A. V. Gold, J. Appl. Phys. 39, 768 (1968).
2. D. E. Eastman, Electron Spectroscopy, edited by D. A. Shirley (North-Holland Publishing Co., Amsterdam, 1972), p. 487; S. Hufner and G. K. Wertheim, Phys. Lett. 47A, 349 (1974); M. Pessa, P. Heimann, and H. Neddermeyer, Phys. Rev. B 8, 3488 (1976); P. Heimann and H. Neddermeyer, J. Phys. F 6, L257 (1976).
3. K. L. Kliewer, Phys. Rev. B 14, 1412 (1976).
4. B. Feuerbacher and R. F. Willis, J. Phys. C 9, 169 (1976).
5. T. Grandke and L. Ley, Phys. Rev. B 16, 832 (1977), and T. Grandke, L. Ley, and M. Cardona, Phys. Rev. Lett. 38, 1033 (1977).
6. J. Stöhr, P. S. Wehner, R. S. Williams, G. Apai, and D. A. Shirley, submitted to Phys. Rev. B.
7. L. F. Wagner, Z. Hussain, and C. S. Fadley, Solid State Commun. 21, 257 (1976).
8. S. K. Baker and P. V. Smith, J. Phys. F 7, 781 (1977).
9. J. Callaway and C. S. Wang, Phys. Rev. B 16, 2095 (1977).

5. TEMPERATURE INDEPENDENCE OF THE ANGLE-RESOLVED X-RAY PHOTOEMISSION SPECTRA OF GOLD AND PLATINUM VALENCE BANDS*

O. B. Dabbousi,† P. S. Wehner, and D. A. Shirley

Strong angular variations have been reported in the valence-band angle-resolved x-ray photoemission (ARXPS) spectra of copper and gold single crystals.[1-5] Two models were proposed to explain the observed behavior. A direct-transition model[1,2] predicted that ARXPS would sample only a small volume in the first Brillouin Zone, while a "matrix-element" model[3-5] interpreted ARXPS as sampling the valence bands widely throughout the Zone. A detailed comparison of both models with experiment showed[5] that the matrix-element model gave good agreement, while the direct-transition model failed. Recently, a compelling reason for breakdown of the direct-transition model--namely, thermal diffuse scattering--has been suggested by Shevchik[6] and confirmed experimentally at intermediate energy (45 eV) for copper.[7] If thermal diffuse scattering were the only reason for the failure of the direct-transition model to predict ARXPS spectra, then the direct-transition processes should be substantially restored by cooling the sample to liquid nitrogen temperatures. We have carried out low temperature ARXPS studies on gold and platinum that were designed to test this question.

With thermal diffuse scattering taken into account, the angle-resolved photoemission cross section is given as the sum of the two terms: a k-conserving direct-transition term and an atomic term.[6,7] The relative contributions of these two terms are related to the Debye-Waller factor, which can be expressed as

$$f = \exp[-\langle(\vec{q} \cdot \Delta\vec{r}_T)^2\rangle] \quad . \qquad (1)$$

It can be shown that the direct-transition component $[\sigma(\vec{q}-\vec{G})$ should increase in importance, relative to the phonon-assisted component, as the temperature is lowered. For gold, using bulk mean-square displacement values derived from x-ray measurements,[8] we calculated a Debye-Waller factor of 0.063 for T = 293 K and 0.393 for T = 93 K. For platinum, the Debye-Waller factor is approximately 0.23 for T = 293 K and 0.58 for T = 93 K. Hence, a very substantial enhancement of the direct-transition contribution to the spectrum would be expected upon cooling the samples to the liquid-nitrogen temperature range.

A gold single crystal was cut to produce two samples: one with a (111) surface orientation and the second with a (100) surface orientation. A platinum sample with a (111) surface orientation was also prepared. The samples were polished, etched, and checked for damage using back-reflection Laue patterns. The samples were place on a specially-built low-temperature probe in a Hewlett-Packard 5950A ESCA spectrometer and irradiated with monochromatized AlKα radiation (1486.6 eV). The probe was rotated to allow analysis of electrons emitted along the [100] direction from the (111)-cut crystals and along the [111] direction form the (100)-cut crystal.

Our experimental results are compared with theory in Figs. 1 and 2. In each case the lowest (solid) curve is the experimental room-temperature result, and the top (dot-dashed) curve is a theoretical low temperature curve, calculated on the direct-transition model. By using the experimental room-temperature curves in the calculation, and looking for any changes in the spectra on cooling in the direction of the calculated low temperature spectra, we have a very sensitive experiment to detect partial restoration of the direct-transition model.

No changes were observed in the gold ARXPS spectra at low temperature. The middle (dashed) experimental low temperature curve for gold in Fig. 1 is identical to the room-temperature curve, within the accuracy of our measurements. It is in marked disagreement with the predicted curve.

For platinum [100], which was run as a confirmatory experiment, the conclusion is exactly the same, although several experimental parameters are quite different from the gold case. The Debye-Waller factors are larger for Pt than for Au at both ambient and low temperatures. In addition, because of the different lattice constant, a different part of the Brillouin Zone would be sampled in the AlKα spectra of Pt, according to the direct-transition model. As Fig. 2 shows, there would be a very large change in the spectrum with temperature according to this model, whereas none whatever is observed.

The direct-transition model as formulated by Wagner et al.[9] has had considerable success in the UPS energy regime. Shevchik's thermal diffuse scattering model[6] also appears to describe the breakdown of the direct-transition model for large

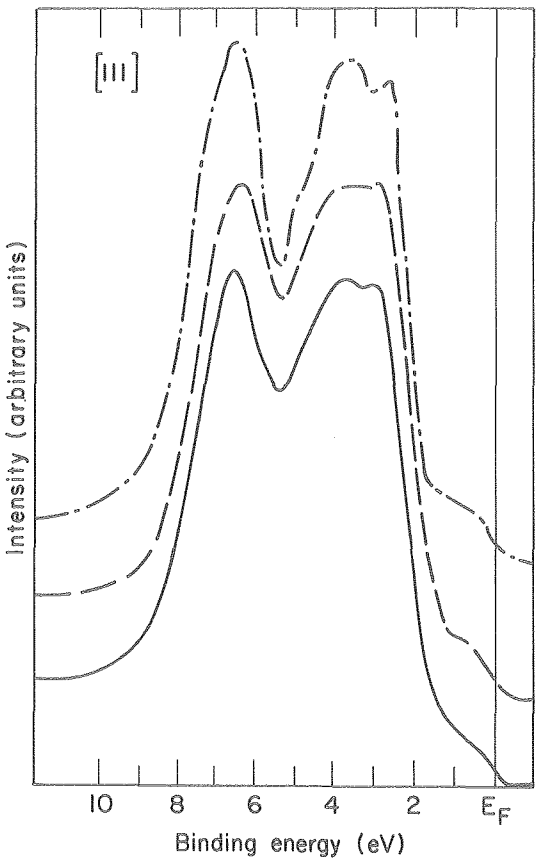

Fig. 1. Angle-resolved x-ray photoemission spectra for Au valence band electrons along the [111] crystalline direction. The lowest (full) curve is the experimental spectrum at room temperature. The middle (dashed) curve is the experimental spectrum at liquid nitrogen temperature. The top curve is the expected spectrum at liquid nitrogen temperature, based on the direct-transition model. The curves are offset for clarity. (XBL 7710-2021)

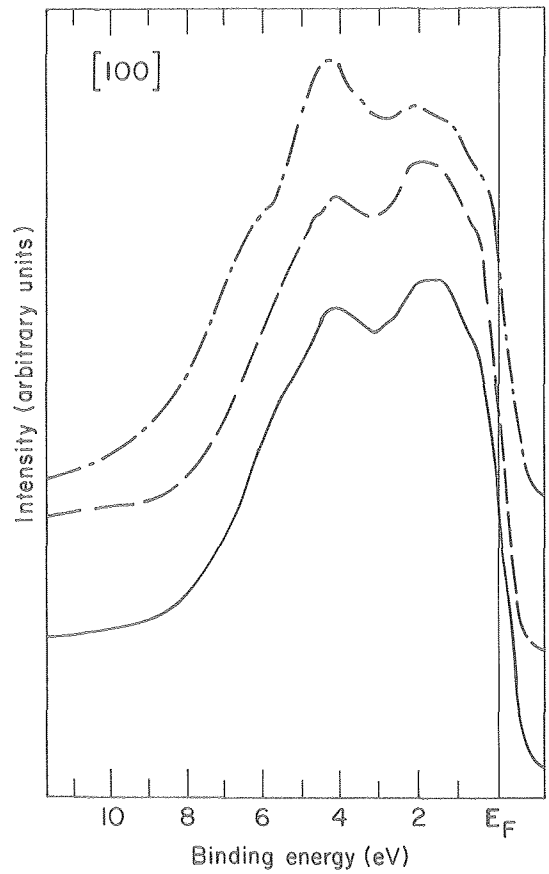

Fig. 2. Angle-resolved x-ray photoemission spectra for Pt valence band electrons along the [100] direction. The format is the same as in Fig. 1. (XBL 7710-2019)

values of $\langle (\vec{q}\cdot\Delta\vec{r})^2 \rangle$ in the UPS regime. However, the present results indicate that the converse is not true in the XPS energy regime; i.e., that lowering the temperature does not substantially restore the direct-transition model in angle-resolved XPS. Rather, the "matrix-element" model,[3-5] which relies on the assumption that ARXPS samples the zone thoroughly enough that the spectra are predicted by integrating over the zone, appears to predict the low temperature spectra as well. This integration implies that the [100] and [111] spectra are very nearly given by the e_g and t_{2g} projections, respectively, as has been found for copper and gold.[5] This may well also be true for platinum, although our data do not provide a critical test of this point.

We believe that the complexity of the final states--i.e., band mixing combined with the very high density of final states--is responsible for the failure of the direct-transition model to be restored in ARXPS at low temperatures. As a reminder of how complex the final-state spectrum is at XPS energies, we have plotted in Fig. 3 the empty-band states near 1500 eV. We note that this

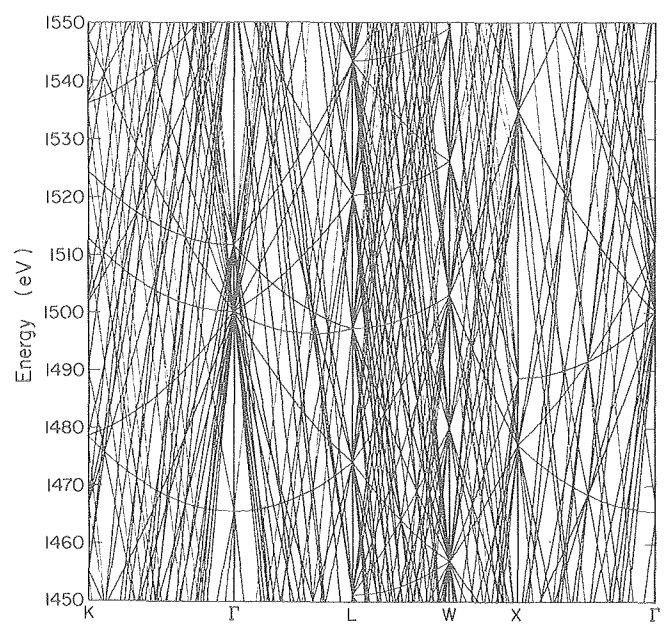

Fig. 3. High energy bands of Cu in the free electron approximation, along symmetry directions. (XBL 7712-11079)

plot is actually unrealistically favorable to the direct-transition model. Band mixing would remove many degeneracies (producing more bands) and would make many of the bands shown much flatter.

---

*From LBL-6911; submitted to Solid-State Communications.

†Permanent address: Dept. of Physics, University of Petroleum and Minerals, Dhahran, Saudi Arabia.

1. J. Baird, L. F. Wagner, and C. S. Fadley, Phys. Rev. Lett. 37, 111 (1976).
2. L. F. Wagner, Z. Hussain, C. S. Fadley, and R. J. Baird, Solid State Commun. 21, 453 (1977).
3. F. R. McFeely, J. Stöhr, G. Apai, P. S. Wehner, and D. A. Shirley, Phys. Rev. B 14, 3273 (1976).
4. G. Apai, J. Stöhr, R. S. Williams, P. S. Wehner, S. P. Kowalczyk, and D. A. Shirley, Phys. Rev. B 15, 584 (1977).
5. P. S. Wehner, J. Stöhr, G. Apai, F. R. McFeely, and D. A. Shirley, Phys. Rev. Lett. 38, 169 (1977).
6. N. J. Shevchik, private communication to D. A. Shirley, March 1977.
7. R. S. Williams, P. S. Wehner, J. Stöhr, and D. A. Shirley, Phys. Rev. Lett. 39, 302 (1977).
8. C. H. McGillavry, G. D. Riech, and K. Lonsdale, editors, International Tables for X-ray Crystallography, Vol. III (The Knyoch Press, Birmingham, England, 1972), p. 237.
9. L. F. Wagner, Z. Hussain, and C. S. Fadley, Solid State Commun. 21, 257 (1977).

6. MOLECULAR-ORBITAL PHOTOEMISSION ENHANCEMENT IN ADSORBATES AT SUBSTRATE COOPER MINIMUM ENERGIES*

P. S. Wehner, R. S. Williams, G. Apai,† J. Stöhr,‡ and D. A. Shirley

Cooper and Fano[1] predicted minima in the atomic photoemission cross section if the initial-state wavefunction exhibits a radial node. In such cases the cross section may vary strongly over a small energy range. We have investigated whether such effects can be observed in photoemission from valence bands in solids. We have studied the energy dependence of the d-band intensity in Cu (3d, no radial node), Ag (4d, one radial node), and Au (5d, two radial nodes) in the range $40\ \text{eV} \leqslant h\nu \leqslant 250\ \text{eV}$.

Results for Cu,[2] Ag,[3] and Au[4] are shown in Fig. 1. The energy dependence of the d-band intensity is significantly different for the three metals. The d-band intensity varies the least for Cu, with a maximum around 130 eV. For Ag a strong intensity is observed with a maximum around 60 eV and a minimum at 140 eV. The intensity changes most drastically, by a factor of ~10, between 100 eV and 130 eV. The Au valence band also exhibits its maximum intensity at low photon energy ($\lesssim 40$ eV) with a pronounced decrease, by a factor of 30, between 70 eV and 160 eV.

As discussed in Ref. 3 the measured d-band intensities should be approximately proportional to the photoionization cross sections for the 3d, 4d, and 5d levels in atomic Cu, Ag, and Au, respectively. The selection rules for electric dipole transitions ($\Delta\ell = \pm 1$) connect a d initial state to p- and f-partial-wave final states. The important variations in Fig. 1 can be discussed in terms of the $d \to f$ channel, which is dominant (relative to $d \to p$) at high energies (>20 eV).[1] Above threshold the d-band intensities first exhibit maxima which occur in the order Au 5d (<40 eV), Ag 4d (≈60 eV), and Cu 3d (≈130 eV). Such maxima have also been observed in absorption measurements above the d-threshold.[5] The reason for this shift in maximum cross section is that, close to threshold, the f radial final-state function is restrained to be far from the nucleus by the centrifugal barrier $\ell(\ell+1)/r^2$; thus, little overlap is possible with the initial state d-function. As the kinetic energy increases the εf wavefunction begins to have greater overlap with the d-function, creating a larger cross section. Because the orbital radial expectation values decrease in the order 5d > 4d > 3d, maximum overlap, and hence a maximum in cross section beyond threshold, will occur in the same order, as observed. At higher energies the d-band intensity decreases steeply to a minimum for Ag

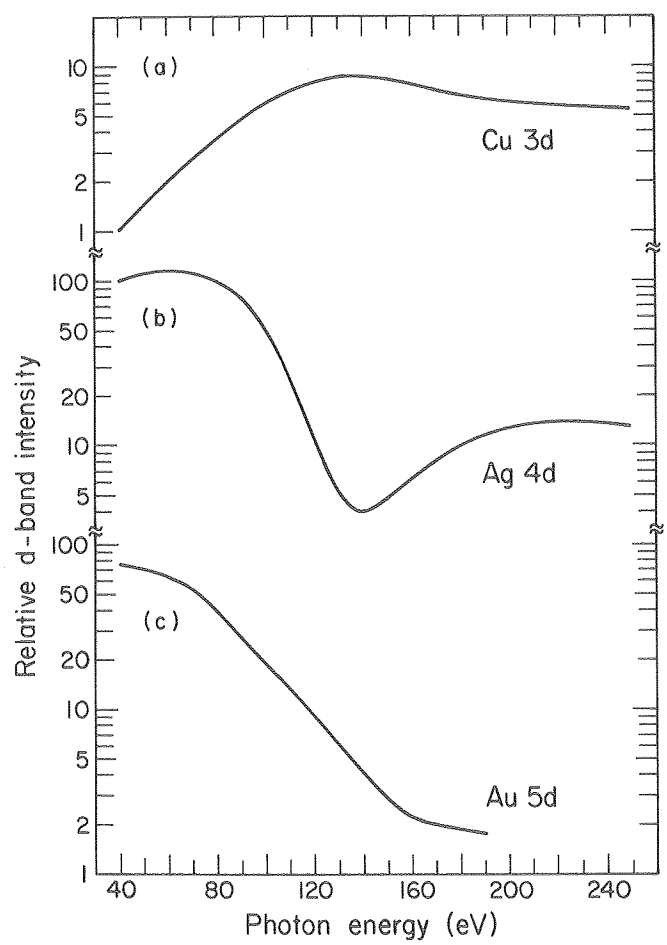

Fig. 1. Relative d-band intensity of Cu, Ag, and Au as a function of photon energy. Curves have been corrected for the collecting efficiency of the cylindrical mirror analyzer, the transmission of the monochromator, and inelastic background. (XBL 777-1372)

and Au. These so-called Cooper minima arise from a change of sign in the radial dipole matrix element associated with the d → f channel. The photoexcitation cross section, which is proportional to the sum of the squares of the p and f channel radial matrix elements, will exhibit a minimum at the energy for which one of the matrix elements vanishes. In general, a minimum in the cross section can occur provided the initial-state wavefunction has at least one node. As compared to the 4d function in Ag (one node) the 5d function in Au has two radial nodes and the 5d → εf matrix element approaches zero more gradually. In this case the Cooper minimum is smeared out.

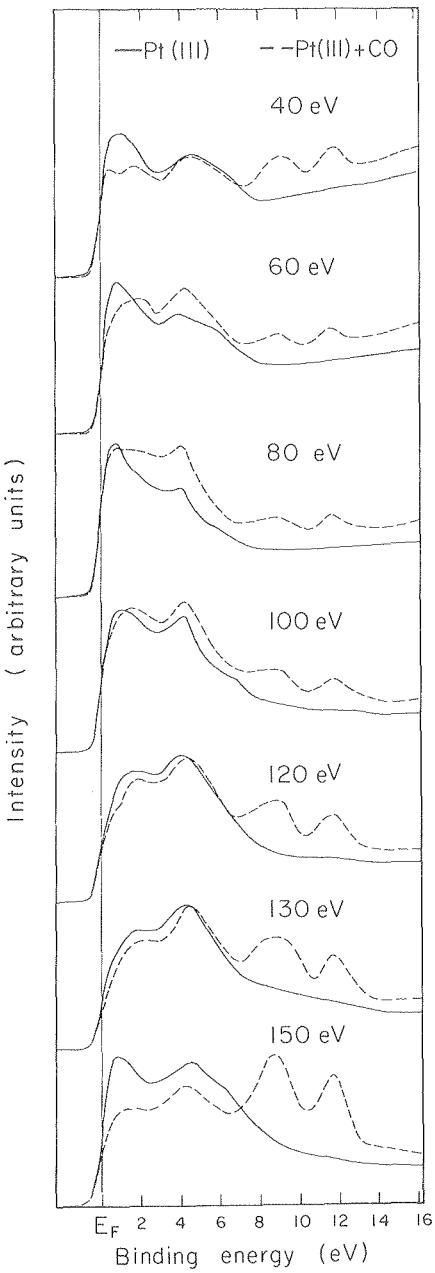

Fig. 2. Photoemission spectra of clean Pt(111) and Pt(111) + 5L CO in the energy range 40 eV ≤ hν ≤ 150 eV. Experimental resolution was 0.8 eV. Note increase in the intensity of the CO-derived peaks (at ~8.7 eV and 11.8 eV E_B) as hν is increased to 150 eV. (XBL 764-2733)

We have reported photoemission studies of CO on Pt(111) in the range 40-150 eV.[6] These can be discussed together with earlier studies by Gustafsson et al.[7] of CO on Ni and Pd. Our main goal is to assess the value of photoemission experiments on an adsorbate-substrate system using variable photon energies not accessible with laboratory sources. Another purpose of this study is to learn how the photoemission spectrum of CO on d-band metals is modulated by cross-section effects, as a continuation of the studies on clean d-band metals, and to select the most appropriate energy range for angle-resolved studies on adsorbates.

Experimental results for clean Pt(111) and Pt(111) + 5L CO are displayed in Fig. 2 as solid and dashed curves, respectively. (1L = 1 Langmuir = 1×10^{-6} Torr sec exposure). Common features of all spectra are the two peaks at ~8.7 eV and ~11.8 eV E_B relative to the E_F, attributed to the (5σ + 1π) and 4σ CO molecular orbitals, respectively. The CO spectral intensity relative to the Pt VB, while low for hν ≤ 100 eV, increases steeply at higher energies and is about a factor of 4 stronger at 150 eV than around 80 eV. Figure 3 shows quantitatively how the intensity ratio of the (5σ + 1π) CO peak and the Pt 5d VB changes with photon energy.

We attribute this adsorbate relative intensity enhancement above 100 eV to the steep decrease of the Pt 5d intensity between 100 eV and 150 eV,

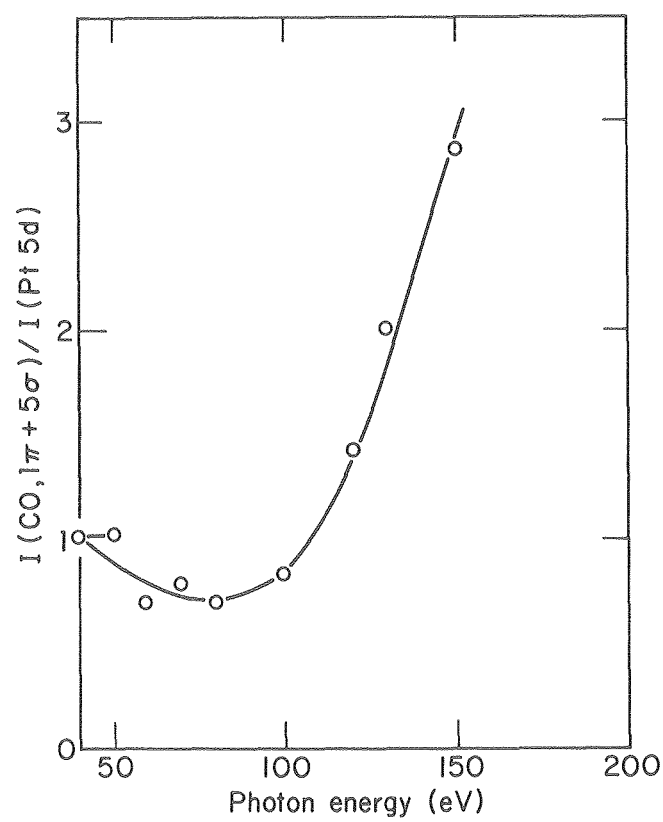

Fig. 3. Relative intensity of the (5σ + 1π) CO peak at ~8.7 eV E_B to the Pt valence band intensity as a function of photon energy. (XBL 763-2484)

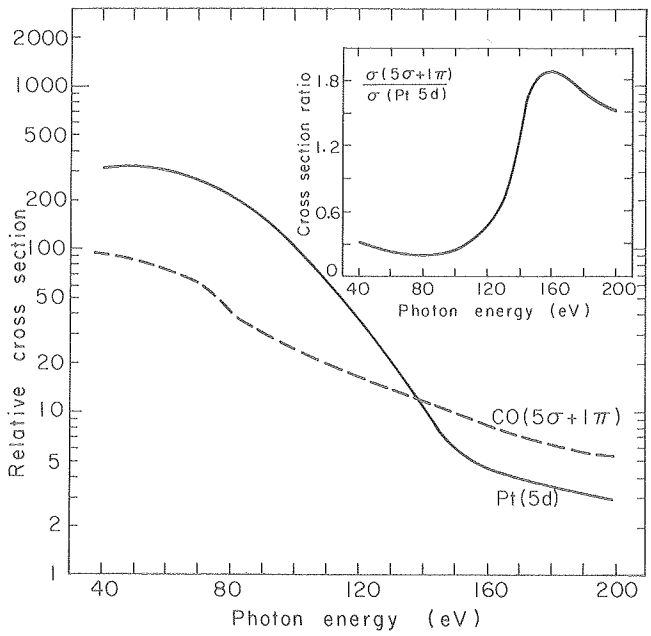

Fig. 4. Plot of the theoretical CO ($5\sigma + 1\pi$) cross section from Ref. 8 and the experimental Pt valence band intensity (Ref. 6). The resultant ratio is plotted as a function of photon energy in the insert on a linear scale. (XBL 764-2786)

as shown in Fig. 4. The energy dependence of the Pt VB intensity was measured in the same way as that of Cu, Ag, and Au discussed above, and the Au (cf. Fig. 1) and Pt 5d cross sections show a very similar dependence. In Fig. 4 we have also plotted the theoretical differential photoionization cross section of the ($5\sigma + 1\pi$) molecular orbitals of CO as a function of incident photon energy. Although we realize the limitations of a plane-wave (PW) final-state calculation for CO for quantitative comparison with experimental cross sections, we have used the PW CO cross sections[8] shown in Fig. 4, for lack of any more reliable theoretical values, to predict the ratio of the integrated ($5\sigma + 1\pi$) CO peak intensity relative to the Pt 5d VB intensity. The results, shown inserted on a linear scale in Fig. 4, are in qualitative agreement with the experimental results in Fig. 3.

The above approach can also account qualitatively for the relative cross sections of CO on Ni and Pd. Gustafsson et al.[7] found that the relative adsorbate signal falls off much more rapidly for CO on Ni than for CO on Pd. Ni is a 3d VB metal and should exhibit an increase in photoemission intensity to $h\nu \approx 120$ eV, then a more gradual monotonic decrease in photoemission intensity with increasing photon energy, much like Cu (see Fig. 1). For this case the CO spectral intensity falls off more rapidly than the Ni VB intensity, particularly for $h\nu < 120$ eV, giving a steep monotonic decrease of the adsorbate signal relative to that of the substrate. On the other hand Pd is a 4d VB metal with a radial node in the 4d wavefunction and should exhibit a Cooper minimum similar to the 4d VB of Ag (see Fig. 1). We attribute the increase in relative adsorbate emission for Pd at $h\nu > 80$ eV to this Cooper minimum. The restriction of their photon energy to $h\nu \leqslant 100$ eV precludes Gustafsson et al. from observing the full extent of MO enhancement. Figure 5 compares the experimental data ($h\nu \leqslant 100$ eV) of Gustafsson et al. for the ratios $\sigma_{CO}(1\pi + 5\sigma)/\sigma_{Ni}(3d)$ and $\sigma_{CO}(1\pi + 5\sigma)/\sigma_{Pd}(4d)$ with the ratios derived from PW theoretical CO cross sections[8] and our experimental intensities for clean Cu and Ag (Fig. 1). The data have been normalized at $h\nu = 40$ eV. The agreement over the photon energy range 40-100 eV substantiates the qualitative arguments we have previously invoked. An extension of the calculated ratio for Ag and CO cross sections allow us to predict enhanced CO/Pd ratio results for photon energies up to 150 eV, as shown in Fig. 6. Our results indicate that studies of molecular orbitals of adsorbates such as CO on 4d or 5d VB substrates will benefit from synchrotron studies at high photon energies because of the enhancement of relative adsorbate spectral intensity.

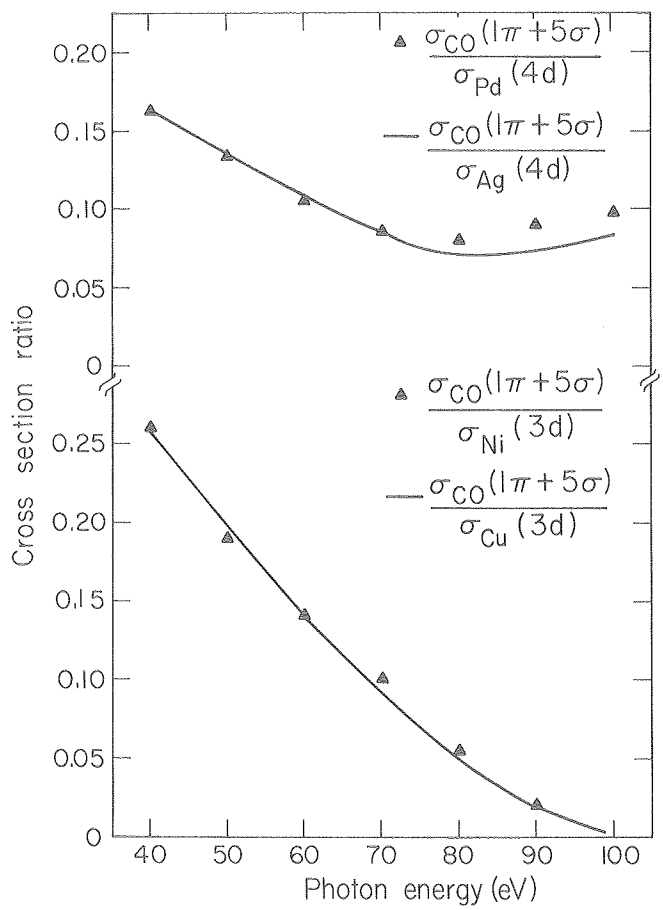

Fig. 5. The experimental results from Ref. 7 for the ratio of the CO peak ($5\sigma + 1\pi$) with respect to the Ni VB and Pd VB (triangles) are compared with the ratio formed from the theoretical ($5\sigma + 1\pi$) cross sections from Ref. 8 and the experimental cross sections for Cu VB and Ag VB (solid curves). (XBL 775-1023)

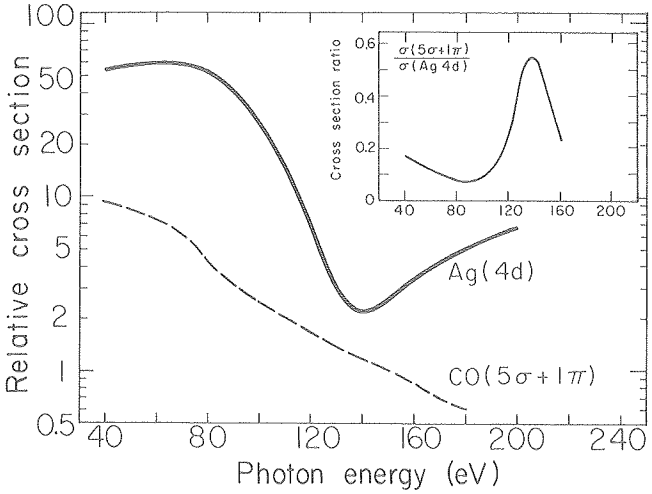

Fig. 6. The relative cross section of the Ag VB (Ref. 3) and the CO (5σ + 1π) molecular orbitals (Ref. 8) in the photon energy range 40 eV ≤ hν ≤ 180 eV. The resultant ratio is plotted as a function of photon energy in the insert on a linear scale. (XBL 776-1114)

---

*From LBL-6650. To be published in Physica Scripta.

†Present address: Eastman Kodak Company, Rochester, NY 14650.

‡Present address: Stanford Synchrotron Radiation Laboratory, P. O. Box 4349, Stanford, CA 94305.

1. J. W. Cooper, Phys. Rev. Lett. 13, 762 (1964); U. Fano and J. W. Cooper, Rev. Mod. Phys. 40, 441 (1968).
2. D. A. Shirley, J. Stöhr, P. S. Wehner, R. S. Williams, and G. Apai, Physica Scripta, to be published.
3. P. S. Wehner, J. Stöhr, G. Apai, F. R. McFeely, R. S. Williams, and D. A. Shirley, Phys. Rev. B 14, 2411 (1976).
4. J. Stöhr, G. Apai, P. S. Wehner, F. R. McFeely, R. S. Williams, and D. A. Shirley, Phys. Rev. B 14, 5144 (1976).
5. R. Haensel, G. Kunz, T. Sasaki, B. Sonntag, App. Phys. 7, 301 (1968); F. C. Brown, Solid State Phys. 29, 1 (1974).
6. G. Apai, P. S. Wehner, J. Stöhr, R. S. Williams, and D. A. Shirley, Solid State Commun. 20, 1141 (1976).
7. T. Gustafsson, E. W. Plummer, D. E. Eastman, and J. L. Freeouf, Solid State Commun. 17, 391 (1975).
8. J. W. Rabalais, T. P. Debies, J. L. Berkosky, J. J. Huang, and F. O. Ellison, J. Chem. Phys. 61, 516 (1974).

7. DIRECT OBSERVATION OF PHOTOELECTRON LOW-ENERGY ELECTRON DIFFRACTION (PLEED) AT HIGH PHOTON ENERGIES*

J. Stöhr,† P. S. Wehner, R. S. Williams, G. Apai,‡ and D. A. Shirley

Low-energy electron diffraction (LEED) has been the technique of choice to characterize the crystallographic structure of clean and adsorbate-covered surfaces.[1] However, several factors have kept this technique from being more than a surface characterization tool in most cases. First, LEED studies of adsorbed molecules have been hampered by radiation damage and dissociation of adsorbates by the electron beam.[2] Electrons tend to be more damaging than photons because they have a higher probability per incident particle of exciting a valence electron, the beams have a greater flux, and the radiation is concentrated closer to the surface, with a high degree of collimation.[1] Secondly, LEED scattering requires ordered domains ~500 Å in diameter because of limitations on the coherence width of the electron beam. Thus, studies of low-coverage adsorbate overlayers and amorphous or disordered materials are difficult. The most severe problem, however, lies in the analysis of the scattered LEED intensities due to strong multiple-scattering effects.

Some of these problems are eliminated by studying photoelectron diffraction[3,4] rather than LEED. As illustrated classically in Fig. 1 for the case of CO on a substrate, a photoelectron can make its way

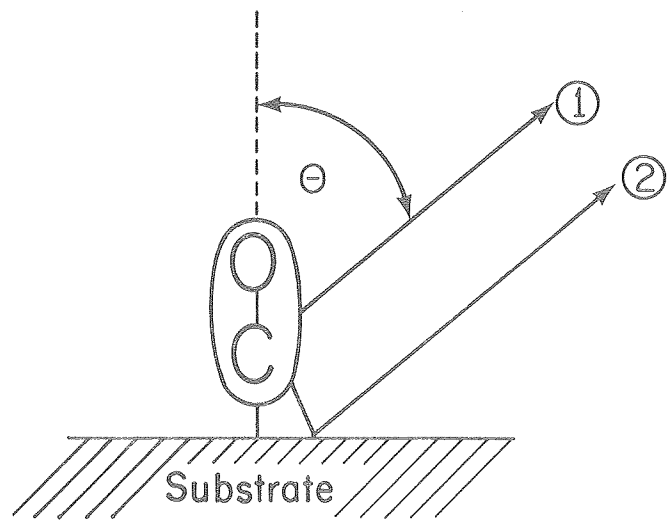

Fig. 1. Schematic illustration of two processes that may contribute to the photoemission process: 1) photoelectrons originating from the molecule and making a direct path of the detector, and 2) indirect emission after backscattering from the substrate. (XBL 7611-4377)

to the detector either directly (channel 1) or by scattering from the atoms of the substrate (channel 2). Quantum-mechanically, the two channels correspond to the primary photoelectron wave and the backscattered wave from the substrate. It has been predicted theoretically that interference of these waves can significantly alter the photoemission angular distributions. It is clear that photoelectron diffraction not only avoids the radiation damage problem of LEED but is also applicable to isolated adsorbate units or materials lacking long-range order. Furthermore, by using synchrotron radiation the photoelectron kinetic energy may be tuned to maximize either channel 1 or 2. This way photoemission from valence orbitals of adsorbates may yield the bonding coordination via channel 1 and the site geometry via channel 2. Photoemission from adsorbate core levels provides an additional check of the site geometry via channel 2 and, in the case of an adsorbed molecule, may also determine the molecular orientation via channel 1 through polarization selection rules.[5] As yet, photoelectron diffraction has not been applied experimentally to this purpose, but in the following we present some data for CO on Pt(111) which appear to indicate for the first time the importance of final-state interference effects.

Several angle-resolved photoemission spectra for Pt(111) + 4L CO are shown in Fig. 2. Common features of all spectra are the two peaks at ~9.2 eV (A) and ~11.8 eV (B) which are assigned to the ($1\pi + 5\sigma$) and 4σ CO molecular orbitals, respectively. Peaks A and B show strong variations with Θ, the angle between the crystal normal and the photoelectron propagation direction. The polarized nature of synchrotron radiation leads to an enhancement of the angular dependence at $h\nu$ = 40 eV. This is clearly shown in Fig. 3,

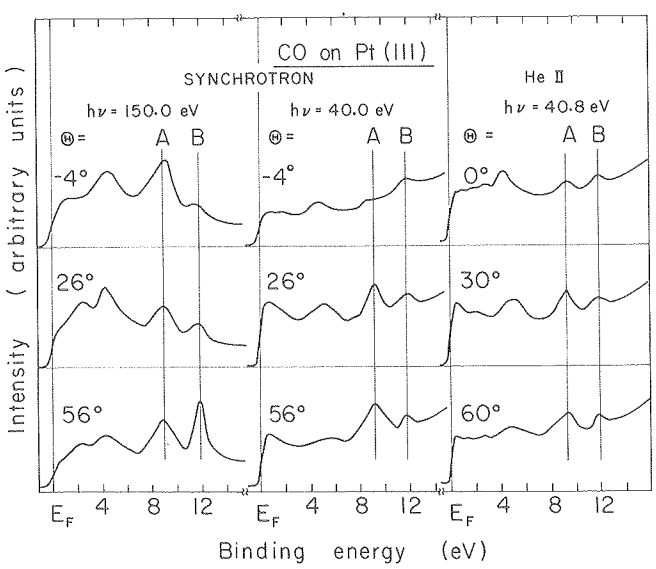

Fig. 2. Comparison of experimental spectra of CO on Pt(111) using 150 eV and 40 eV synchrotron radiation and 40.8 eV HeII radiation as a function of the photoemission angle Θ, as defined in Fig. 3b and c. Note the strong variation in the CO peak intensity of A and B with a change in angle or photon energy. (XBL 7610-4180)

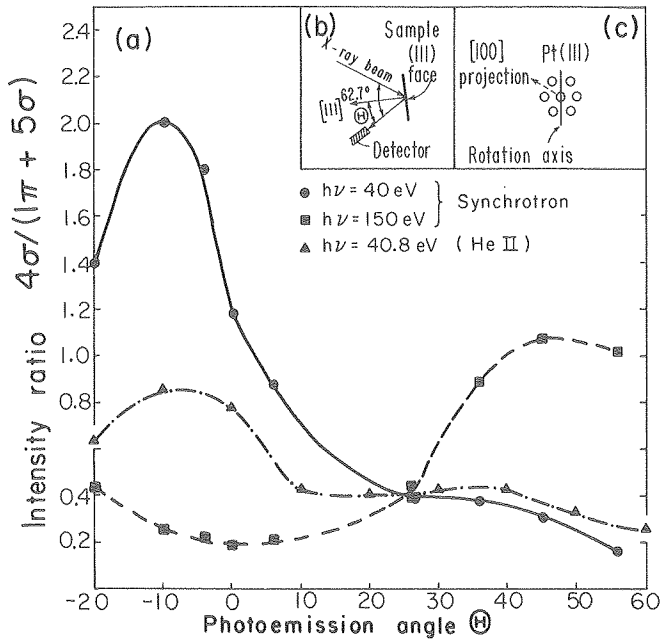

Fig. 3. Plot of the measured intensity ratio $4\sigma/(1\pi + 5\sigma)$ for two different light sources (HeII and synchrotron) and photon energies (~40 eV and 150 eV). All spectra were taken in the same geometry as shown in Fig. 3b and c. The difference between the intensity ratio derived from HeII and synchrotron radiation spectra is due to the polarized nature of the synchrotron light. The dramatic inversion of the ratio $4\sigma/(1\pi + 5\sigma)$ between 40 eV and 150 eV may indicate the importance of final-state scattering effects. (XBL 769-4026)

which also gives details of the crystalline orientation with repect to the photon beam and the detector (Fig. 3b,c). Figure 3 shows that the molecular orbitals of CO are not only more intense with respect to the VB at 150 eV than at 40 eV but also that there is a dramatic reversal in the angular variation of relative MO peak intensities.

Figure 4 shows the relative peak intensities and the ratio $4\sigma/(1\pi + 5\sigma)$ for normal photoemission and for a 45° electron take-off angle over the entire 40-150 eV range. For normal emission, the 4σ and the ($1\pi + 5\sigma$) peak intensities show modulations in the range 40-150 eV, while the energy dependence is relatively smooth for a 45° electron take-off angle.

The observed modulations indicate the importance of final-state interference effects, which have theoretically been shown to vary strongly with both energy and photoemission angle.[4] For a molecule on a substrate, however, final-state interference effects exist not only between channels 1 and 2, but channel 1 itself contains interference effects resulting from intramolecular scattering within the molecule. Intramolecular final-state interference effects are included in SW Xα calculations and have been found theoretically[6] and experimentally[7] to lead to cross-section resonances at energies not too far (~10-20 eV) above threshold. Without a detailed SW Xα calculation for an oriented (gas

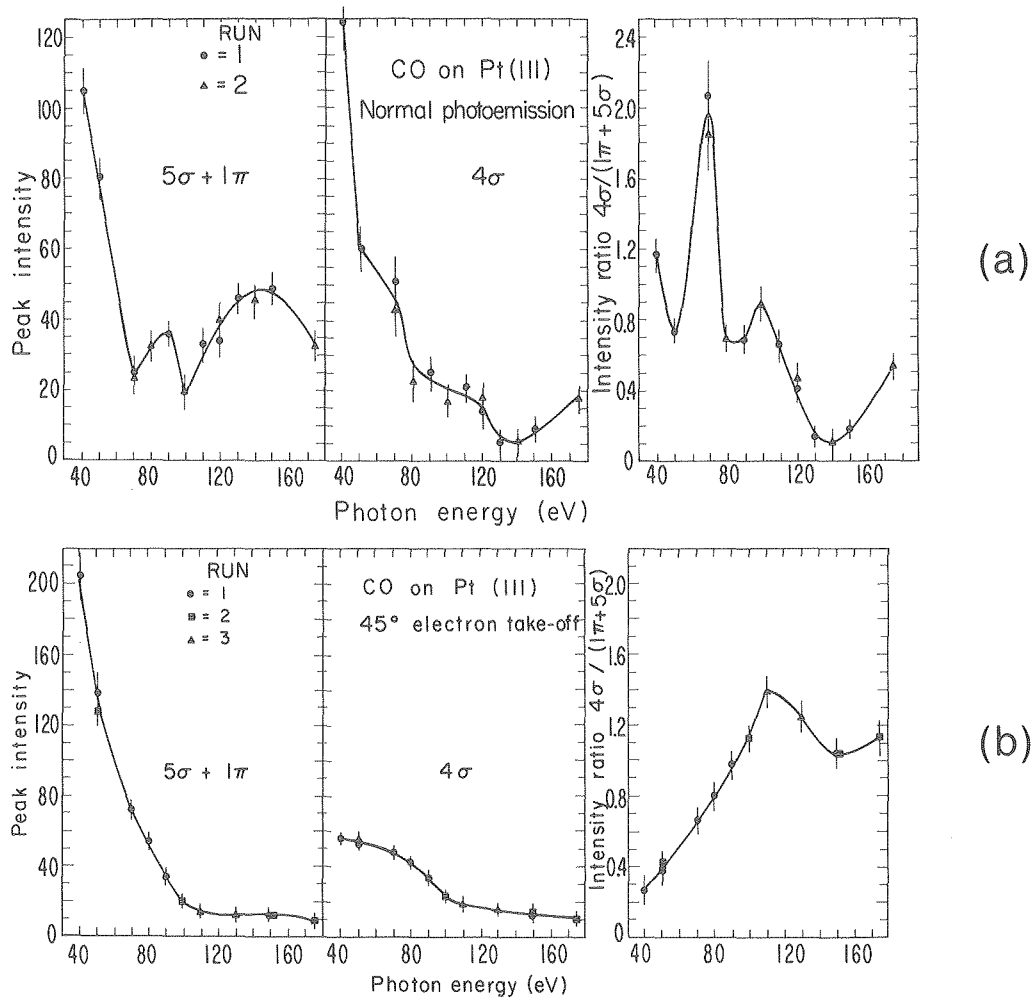

Fig. 4. (a) Integrated intensity from CO (1π + 5σ) and CO 4σ adsorbate MO levels as a function of photon energy. The geometry is the same as described in Fig. 3b and c. The right-hand panel shows the ratio for 4σ/(1π + 5σ) as a function of photon energy. Photoelectrons were measured at a normal emission angle. (b) Integrated intensity from CO (1π + 5σ) and CO 4σ adsorbate MO levels as a function of photon energy for a 45° electron take-off angle. The right-hand panel shows the ratio similarly to Fig. 4a. (XBL 774-8535)

phase) molecule at higher (> 40 eV) energies, the origin of the resonances in Fig. 4 and the reversal in angular photoemission distributions in Fig. 3 therefore cannot be interpreted quantitatively. Analysis of the observed intensities should yield information about the conformation of CO on Pt(111) and improve our general understanding of final-state scattering effects.

---

*From LBL-6650; to be published in Physica Scripta.

†Present address: Stanford Synchrotron Radiation Laboratory, P.O. Box 4349, Stanford, CA 94305.

‡Present address: Eastman Kodak Co., Rochester, NY 14650.

1. C. B. Duke, in Advances in Chemical Physics, Vol. XXVII, edited by I. Prigogine and S. A. Rice (Interscience).

2. J. C. Tracy, J. Chem. Phys. 56, 2736 (1972).

3. A. Liebsch, Phys. Rev. Lett. 32, 1203 (1974); A. Liebsch, Phys. Rev. B 15, 544 (1976).

4. S. Y. Tong and M. A. Van Hove, Solid State Commun. 19, 543 (1976) and references therein.

5. D. Dill, J. Siegel, and J. L. Dehmer, J. Chem. Phys. 65, 3158 (1976).

6. J. W. Davenport, Phys. Rev. Lett. 36, 945 (1976).

7. C. L. Allyn, T. Gustafsson, and E. W. Plummer, Chem. Phys. Lett. 47, 127 (1977).

8. D-ORBITAL DIRECTED PHOTOEMISSION IN MnF_2*

P. M. A. Sherwood,† F. R. McFeely,‡ S. P. Kowalczyk,§ and D. A. Shirley

Angle-resolved x-ray photoemission (ARXPS) has recently been shown to yield strong directional variations in valence-band spectra with respect to the crystalline axes of single-crystal samples.[1,2] Two approximate models have been proposed to explain the variation of the d-band spectrum. The direct-transition model[1] attributes the effect entirely to lattice periodicity, while the transition matrix-element model[2] emphasizes the local symmetry of the d orbitals. The direct-transition model has been shown to be incorrect.[2,3] While the matrix-element model fits experimental spectra of noble metals well,[2] it remained to be shown that this model, which is based on a "crystal field" picture, really would work for a substance in which the crystal field model is applicable; i.e., an ionic lattice. Of course the model must pass the test if it is to be taken seriously; otherwise, another explanation should be sought for its fit of the nobel-metal ARXPS spectra.

The ideal lattice for this test of the matrix-element model would be one in which transition-metal d-orbitals of t_{2g} and e_g symmetry would be clearly recognizable in the spectrum and separable in energy. A more subtle, but equally important, requirement is that the octahedral axes of the transition-metal complexes must be oriented either parallel (the ideal case) or at least in such a way that the microscopic t_{2g}-e_g asymmetry would be preserved in part in the macroscopic crystal. To understand this problem, consider a crystal with two octahedral complexes in a unit cell, oriented such that the [001] direction of one complex coincides with the [111] direction of the other. Then in this common direction photoelectrons will emerge from the e_g orbitals of the first complex and the t_{2g} orbitals of the second, largely cancelling the sought-after effect, d-orbital directed photoemission. Many crystal structures have cancellation problems of this kind, but a careful search revealed that MnF_2 provides a satisfactory compromise among the various requirements noted above, and it was chosen for this study.

A single crystal of MnF_2 was cleaved along the (111) face and oriented using the Laue back-reflection method. The crystal was mounted on a holder which allowed it to be rotated under vacuum with the (111) crystal face exposed to the x rays. The axis of rotation lay at right angles to the z axis and parallel to this face. The crystal holder was placed in the spectrometer in one of two orientations. In the first, which we shall term the "z+" orientation, the crystal z direction made an angle $\Theta < 90$ with the outgoing photoelectrons accepted in the analyzer. In the second orientation, which we call z-, Θ lay between 90° and 180°. The exact arrangement is shown in Fig. 1.

Application of the "matrix-element" model[2] to MnF_2, which has the rutile structure, is achieved by writing out the expected photoelectron angular distribution for the two types of octahedra in the lattice, then adding them after appropriate

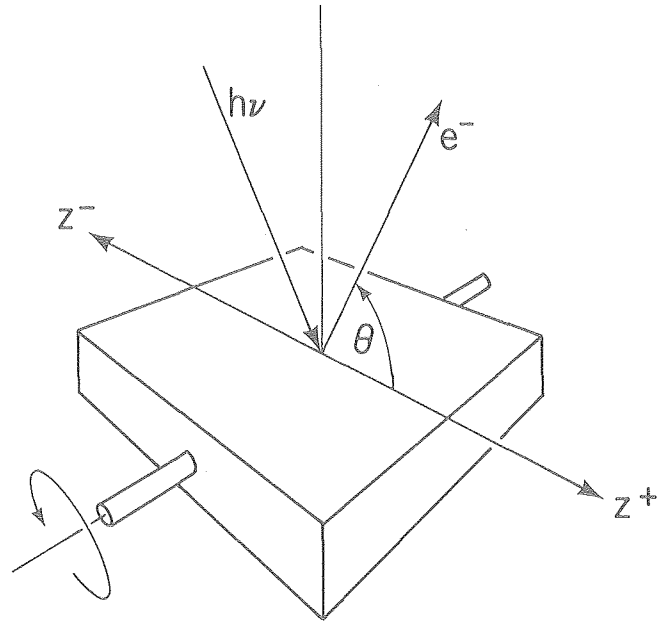

Fig. 1. The manganese fluoride single-crystal geometry. The crystal was held in two ways, with the (111) crystal face exposed to the x-ray beam. The crystal z direction lies in the plane of the (111) face and at right angles to the axis about which the crystal is rotated to change the angle Θ. (XBL 7712-11451)

rotational transformations. The angular distributions, assuming plane-wave final states, for the t_{2g} and e_g directions of a single octahedron can be written:[2]

$$PED_{eg} \propto \left[\frac{15}{4\pi}\right]\left[\frac{1}{4}\sin^4\Theta\ \left(\cos^2\phi-\sin^2\phi\right)^2 + \frac{1}{3}\left(\frac{3}{2}\cos^2\Theta-\frac{1}{2}\right)^2\right]$$

$$PED_{t_{2g}} \propto \left[\frac{15}{4\pi}\right]\left[\sin^4\Theta\ \sin^2\phi\ \cos^2\phi\ \sin^2\Theta\ \cos^2\Theta\ \cos^2\phi\right]\cdot + \sin^2\Theta\ \cos^2\Theta\ \sin^2\phi\ +$$

Figure 2 shows how the intensities of t_{2g} and e_g contributions to the Mn(3d) peaks vary with the experimental angle Θ in Fig. 1 (not to be confused with Θ in the above equation). Although there was a good deal of cancellation between the two types of octahedra, as discussed above, a substantial anisotropy was still predicted by the model.

The spectra showed two partially resolved components of the Mn(3d) peak, which were assigned t_{2g} and e_g character. Spectra at six values of Θ were consistent with the intensity variation shown in Fig. 2. This provides strong support for the "matrix-element" model of ARXPS.

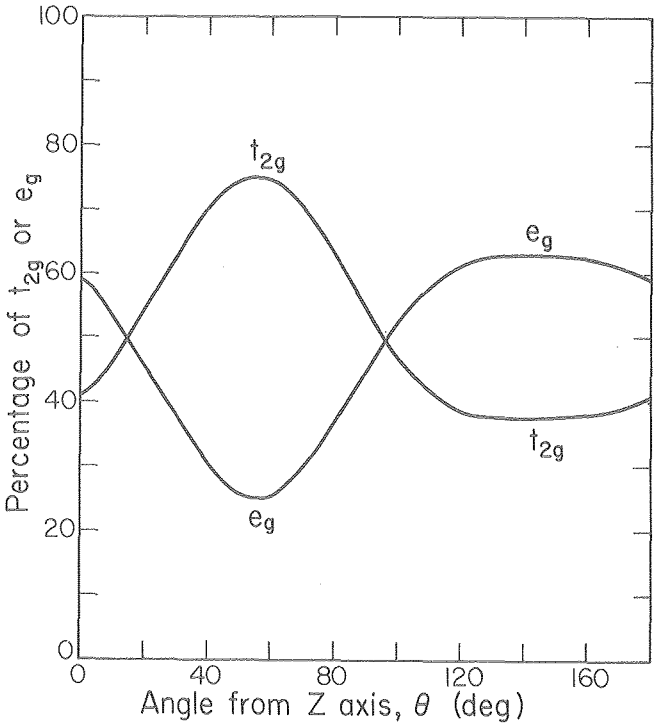

Fig. 2. Graph showing how the amount of t_{2g} and e_g character in the Mn(3d) peak varies as the angle θ is varied, according to the theory described in the text. (XBL 7712-11450)

---

*From LBL-6947.

†Present address: Dept. of Inorganic Chemistry, Univ. of Newcastle upon Tyne, Newcastle upon Tyne, England.

‡Present address: Dept. of Chemistry, Massachusetts Institute of Technology, Cambridge, MA 02139.

§Present address: Max-Planck Institut, 7000 Stuttgart 80, W. Germany.

1. R. J. Baird, L. F. Wagner, and C. S. Fadley, Phys. Rev. Lett. 37, 111 (1976).
2. P. S. Wehner, J. Stöhr, G. Apai, F. R. McFeely, and D. A. Shirley, Phys. Rev. Lett. 38, 169 (1977).
3. Reference 2 shows that the direct-transition model predicts ARXPS spectra incorrectly. Report 1 of this series shows that ARXPS transitions are not direct at room temperature. Report 5 shows that direct transition are not restored at low temperatures.

9. THE RELATION BETWEEN SATELLITE PEAKS IN X-RAY EMISSION AND IN X-RAY PHOTOEMISSION SPECTRA*

R. L. Martin,† S. P. Kowalczyk,‡ and D. A. Shirley

In this report a unified model is reported that explains the satellite structures observed in x-ray emission spectroscopy (XES) and x-ray photoelectron spectroscopy (XPS). This model accounts for electron correlation by the use of configuration interaction, rather than the heuristic "shake-up" approach, and actual eigenstates of the system are considered. The XPS final state plus its correlation states serve as the initial states in XES. The final XES states consist of the main state plus its satellites. Two situations are discussed, differing in whether the final XES states have holes in core or valence shells. For core-to-core XES transitions, the correlation-state structure is almost identical in initial and final states. Large satellite intensites may be observed in XPS, in accord with experiment. In core-to-valence XES transitions, the satellite structure should be similar to that observed in XPS, also in accord with experiment. Detailed CI calculations for the 3s spectra of Ar have been compared with experiment.

Figure 1 shows a hypothetical state diagram for an ionic species. The states labeled P_1 and P_2 are two of the primary ionic states of the system; associated with each of them is a satellite state, S_1 or S_2. In a photoemission experiment all four of these states can be reached, and the intensity of, e.g., S_1 relative to P_1 will be governed by the projections of their respective wavefunctions onto the hypothetical "frozen-orbital" primary ionic state, defined by removing the photoelectron from the initial (neutral) ground states without allowing the passive orbitals to relax (i.e., as in Koopmans' model).

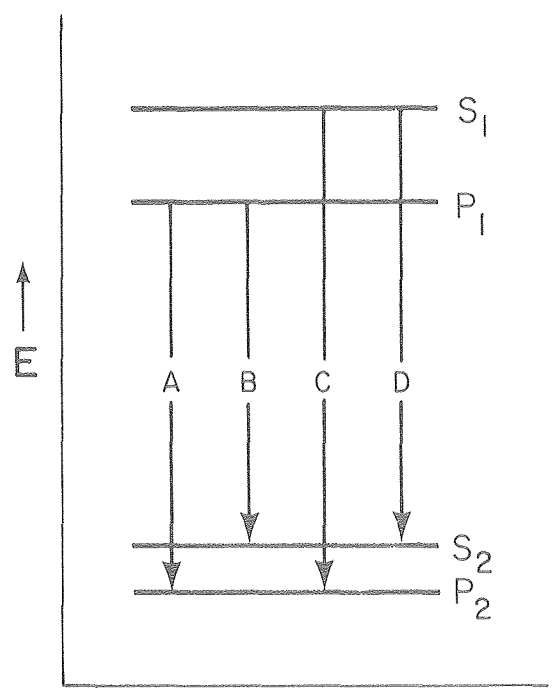

Fig. 1. A hypothetical ionic state diagram. The states labeled P_1 and P_2 are two of the primary ionic states of the system; associated with each of them is a satellite state, S_1 or S_2. The x-ray emission transition labeled A produces the diagram line, while B corresponds to a semi-Auger peak. Processes C and D are similar, but originate from decay of the satellite state S_1. (XBL 773-656)

Turning to the XES process, decay of the ionic states P_1 and S_1 via x-ray emission leads to four distinct possibilities. The transition labeled A in Fig. 1 produces the diagram line, while B corresponds to a "semi-Auger" peak. Processes C and D are similar, but originate from decay of the satellite state S_1.

For the purpose of discussing the relative intensities of the transitions, it is useful to distinguish the case in which P_1 and P_2 are both core-hole states from that in which P_1 is a core-hole state and P_2 is a valence-hole state. The satellite states S_1 and S_2 can be described in terms of rearrangements in the valence shell. Because the main effect of a core hole is manifest through an increase in the effective in-core charge, any two core holes will affect the valence shells in a similar way. It follows that channels A and D in Fig. 1 will be relatively strong, while B and C will be weak. Because A and D will also have similar x-ray transition energies, they will tend to appear as one line, and no intense satellite will be expected in XES, even though one is observed in XPS.

For core-to-valence transition the same theoretical approach yields the different result that satellites of similar intensity will be expected in XES and XPS. This follows because of the detailed similarity between an XES transition down from a core-hole state to a valence-hole final state and the transition up from the atomic or molecular ground state to the same final state. In both types of transition final ionic-state configuration interaction dominates the spectral structure.

The 3s hole state of the argon atom is a prototypical case. Luyken[1] surmised from the optical spectrum that the main final-state correlation effect involves the excitation of $3s^1 3p^6(^2S)$ to $3s^2 3p^4 nd(^2S)$. A more direct experimental verification of this mixing is, of course, provided by the strong satellites observed in the 3s photoelectron and $L_{2,3}$ x-ray emission spectra. The mechanism by which this interaction is felt in photoemission is illustrated diagrammatically in Fig. 2. Because of the importance of

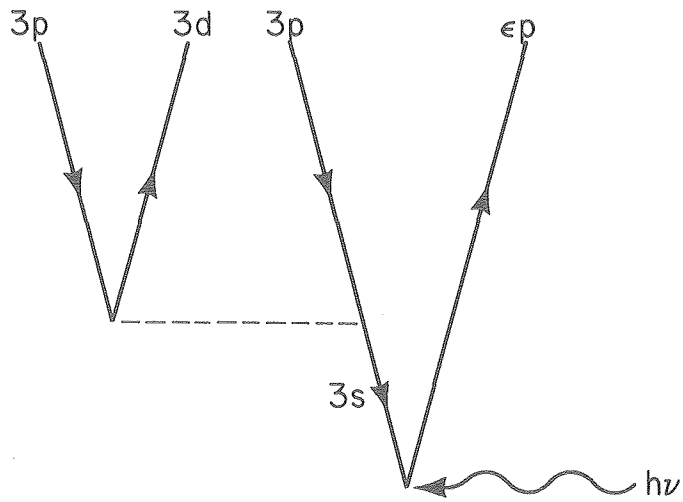

Fig. 2. Diagrammatic representation of the configuration-interaction effect in photoemission from the argon 3s shell. Time proceeds upward and holes are denoted by arrowheads pointing backward. (XBL 778-1769A)

this case we carried out a detailed CI calculation on the relevant states of Ar and Ar^+, using the theoretical framework discussed earlier.[2] The transition intensities for XES and XPS were then calculated rigorously.

The results for the ^2S satellite intensities are reproduced along with the experimental results of Spears et al.[3] in the second and third columns of Table 1. A comparison shows that while the agreement is quite satisfactory for the first two states, the computed intensity for the $3s^2 3p^4 4d$ satellite is much too high. The reason for this behavior comes from the fact that there is a strong interaction not only between the primary hole state and the Rydberg channels, but also with the shake-off continuum bases on $3s^2 3p^4 \epsilon d$. This behavior was surmised in the earlier work of Luyken[1] and observed in calculations of photoionization cross sections.[4] Thus the disagreement between experimental and theoretical intensities

Table 1. Argon XPS and XES satellite intensities.

	$(I/I_o)_{XPS}$		$(I/I_o)_{XES}$	
Final State	Expt	Theory	Expt	Theory
$3s^1 3p^6$	100%	100%	100% (219.2, 221.4 eV)	100% (223.2 eV)
$3s^2 3p^4 4s$	3 ± 2% (8.1 eV)	2.5% (8.8 eV)		3.6% (8.8)
$3s^2 3p^4 3d$	17 ± 2% (9.4)	14.4% (10.4)	35% (11 eV)	14.7% (10.4)
$3s^2 3p^4 4d$	6 ± 3% (11.9)	15.1% (13.0)		14.8% (13.0)
$3s^2 3p^4 5s$	———	0.6% (14.8)		0.5% (14.8)

of this state is not due to a flaw in our model, but rather to the inability at present to deal adequately with Rydberg orbitals.

Finally, we summarize this discussion of XES transitions in the form of a set of rules below.

1. Core-Core XES Transitions

If the XPS structure arises from an excited state of the same symmetry as the primary ionic state, no type B and C satellites should be observed in XES. Furthermore, the type D satellite should be very nearly equal in energy to the diagram line and may not be resolved from it. This type of behavior has been noted and commented on by Asada et al.[5] in the Kβ spectrum of NiF_2. While there are intense satellites in the Ni(2p) XPS spectrum, they are not observed in XES.

2. Core-Valence XES Transitions

In this case, the type B (semi-Auger) satellites should have nearly the same relative intensity as the pertinent "shake-up" structure in XPS. The type C and D satellites should be weaker than the corresponding structure in XPS, primarily due to the reduced initial-state population.

---

*From LBL-5445; to be published in Journal of Chemical Physics.

†Present address: Dept. of Chemistry, University of Washington, Seattle, WA 98195.

‡Present address: Max-Planck Institut, 7000 Stuttgart 80, W. Germany.

1. B. F. J. Luyken, Physica 60, 432 (1972); B. F. J. Luyken, F. J. De Heer, and R. Ch. Baas, Physica 61, 200 (1972).
2. R. L. Martin and D. A. Shirley, Phys. Rev. A 13, 1475 (1976).
3. D. P. Spears, H. J. Fischbeck, and T. A. Carlson, Phys. Rev. A 9, 1603 (1974).
4. M. Ya Amusia, V. K. Ivanov, N. A. Cherepkov, and L. V. Chernysheva, Phys. Lett. A 40, 361 (1972).
5. S. Asada, C. Satoko, and S. Sugano, J. Phys. Soc. Japan 37, 855 (1975).

10. ABSORPTION SPECTROSCOPY IN THE CARBON 1s SHELL: CHEMICAL SHIFTS IN KYNAR AND EXAFS IN GRAPHITE

D. Denley, J. Stöhr,* R. S. Williams, P. Perfetti,† and D. A. Shirley

The photon energy range 200-1000 eV which has previously been inaccessible, is nonetheless of considerable chemical and biological interest. Within the region there are the K-edges of the low Z elements C (284 eV), N (399 eV), O (532 eV), and F (686 eV). We are concerned here with the first and last of these, carbon and fluorine, and in particular the fine structure in the K-edge absorption spectra in thin films of graphite and Kynar $(-CH_2-CF_2-)_n$.

Absorption experiments were performed on the 4° line of the Stanford Synchrotron Radiation Laboratory which utilizes a grazing incidence monochromator[1] that can yield polarized monochromatic radiation at energies in the range 32-1000 eV.

Absorption spectra at the carbon K-edge were taken for three graphitic samples: evaporated carbon foils, evaporated carbon foils that had been annealed at 1100°C under vacuum, and a thin sample cleaved from a crystal of stress-annealed monochromator graphite. The main differences in the three samples are in crystallite size and orientation. The evaporated foils generally have a crystallite size of ≥ 10 Å and no discernable orientation.[2] The foils which are subsequently annealed have a crystallite size of ~ 250 Å as determined by transmission electron microscopy and are known to show preferential ordering with the c-axis becoming normal to the foil surface plane.[3] The monochromator graphite is a well-ordered mosaic of crystallites, with the graphite planes parallel to the surface plane. While the $\vec{a}$ and $\vec{b}$ in-plane crystal axes do not maintain their orientation throughout a sample, monochromator graphite is otherwise quite similar to single-crystal graphite.[4]

The edge spectra for the three materials are shown in Fig. 1. There are two two main features, the low energy edge at 281.5 eV and a second edge at 288.0 eV. The main difference among the samples is in the intensity of the low energy edge, which decreased in going from the evaporated to the annealed foil and finally the monochromator graphite. We believe this effect can be understood as polarization effect due to the crystalline anisotropies in graphite.

Graphite forms weakly interacting planes, each plane being composed of a hexagonal net (Fig. 2). The bonding within a plane is composed of $sp^2\sigma$ bonds and π bonds arising from the p_z orbitals directed out of the plane. The resulting band structure as calculated by Painter and Ellis[5] using a variational LCAO method shows two critical points at Q_{2g}^{-} and Q_{1u}^{+}, which lie at 2.4 eV and

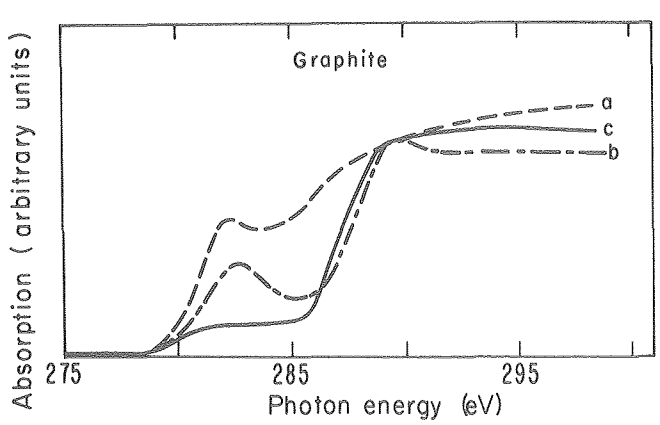

Fig. 1. Absorption spectra for three forms of graphite at the K-edge: a) microcrystalline graphite; b) polycrystalline graphite; c) monochromator graphite. (XBL 7712-11088A)

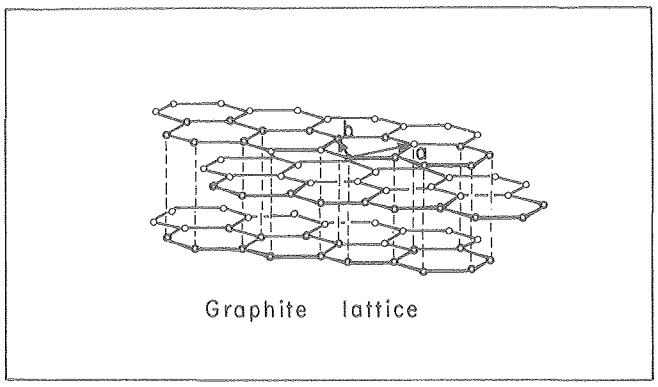

Fig. 2. Graphite lattice with the two basal plane lattice vectors shown. (XBL 7712-11091)

9.5 eV above the Fermi level (E_F) respectively. The two representations at Q have odd and even symmetry respectively for reflections across the plane of the hexagonal net. The result is that for $\vec{E}$ parallel to the c-axis, transitions from the 1s core level to Q^+_{1u} are forbidden, while for $\vec{E}_\perp$ c-axis, transitions to Q^-_{2g} are forbidden. While the former case cannot be observed in our experiments, the latter case occurs naturally as the c-axis of the crystallites in the three samples become progressively more aligned with the film surface plane, which also contains $\vec{E}$ in our experiments. The above results provide a confirmation of the electron diffraction results of the behavior of evaporated graphite upon annealing and show excellent agreement with the calculated values for the gap $Q^+_{1u} - Q^-_{2g}$.

Other kinds of information are available by studying the absorption fine structure above the K-edge. In Fig. 3 we show a spectrum of an annealed graphite foil which we believe displays the first EXAFS structure above the carbon K-edge in a solid material. In the simple single scattering theory, the EXAFS signal is given by

$$\chi(k) = \frac{1}{k} \sum_i \frac{N_i}{r_i^2} F(k) \sin (2kr_i + \phi_a(k) + \phi_b(k) - \pi) \times e^{-2\sigma_i^2 k^2} e^{-2r_i/\lambda(k)}$$

where $k = \{2m/\hbar^2 (E - E_F + E_B)\}^{1/2}$ is the electron wavevector in the material with reference to the Fermi level (E_F) after correcting for the inner potential E_B. The sum is taken over the nearby nearest neighbor shells of N_i neighbors at a distance r_i. The scattering amplitude F(k) and the absorbing and backscattering phase shifts ϕ_a and ϕ_b respectively are generally available from theoretical calculations.[6,7] The Debye-Waller factor $e^{-2\sigma_i^2 k^2}$ was nearly unity in our case, and $\lambda(k)$ is the energy-dependent electron mean free path.

We have found that upon taking for $\lambda(k)$ a suitable parametrization of the "universal curve"[8] and summing over shells up to ~3.5 times the nearest neighbor distance, that a gratifying agreement is reached. With our confirmation of the calculated scattering parameters for carbon we can now proceed to analyze recently obtained data for polymer films for data on interatomic spacings that are otherwise difficult to obtain.

In addition to EXAFS in the polymers, one other effect has been measured in the polymers and in particular for Kynar $(-CH_2-CF_2-)_n$. In Fig. 4 existence of the two inequivalent carbons, one halogenated, the other not, is clearly indicated by chemical shifts in the K-edge to two values (284.5 ± 0.5 eV and 289.5 ± 0.5 eV) separated by 5 ± 1 eV. We feel that the good agreement with photoemission data[8] of 4.5 eV separation proves absorption spectroscopy for chemical analysis (ASCA) to be both a competitive and complementary technique to ESCA.

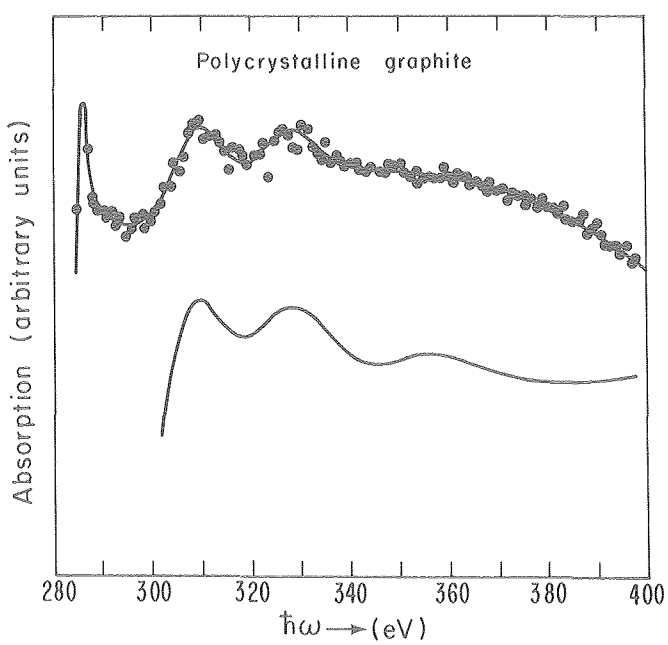

Fig. 3. Above: Experimental absorption spectra of polycrystalline graphite above the edge. Below: Calculated EXAFS spectra. (XBL 7712-11090)

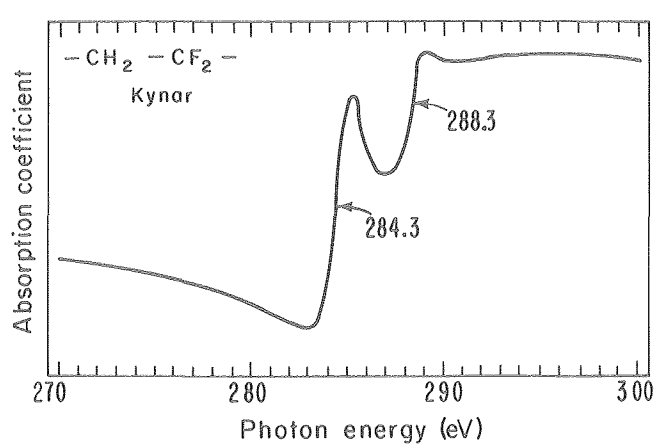

Fig. 4. K-edge spectra of Kynar polymer. (XBL 7712-11089A)

*Present address: Stanford Synchrotron Radiation Laboratory, P.O. Box 4349, Stanford, CA 94305.

†On leave from the Italian National Coucil of Research, Rome, Italy.

1. F. C. Brown, R. Z. Bachrach, S. B. M. Hagström, N. Lien, and C. H. Pruett in Proceedings of the Fourth International Conference on Vacuum Ultraviolet Radiation Physics, Hamburg, July, 1974, edited by E. Koch, R. Haensel, and C. Knuz (Pergamon, Vieweg, 1974), p. 785.
2. G. M. Jenkins, J. A. Turnball, and G. K. Williamson, J. Nucl. Mat. 7, 215 (1962).
3. T. Evans and P. F. James, Proc. Roy. Soc. (London) A277, 260 (1964).
4. A. W. Moore in Chemistry and Physics of Carbon, edited by Philip L. Walker, Jr. and Peter A. Thrower (Marcel Dekker, 1973), p. 105.
5. G. S. Painter and D. E. Ellis, Phys. Rev. B 1, 4747 (1970).
6. P. A. Lee, Boon-Keng Teo, and A. L. Simons, J. Am. Chem. Soc., to be published.
7. Steven Trent Manson, Phys. Rev. 182, 97 (1969).
8. I. Lindau and W. E. Spicer, J. Electron Spectrosc. 35, 117 (1974).

11. TIME-RESOLVED FLUORESCENCE OF XeF* FROM THE VUV PHOTODISSOCIATION $XeF_2 \rightarrow XeF^* + F$ INDUCED BY SYNCHROTRON RADIATION

E. D. Poliakoff, M. G. White, R. A. Rosenberg, and D. A. Shirley

Many spectroscopic studies of XeF_2 and XeF have been undertaken,[1-7] but have yielded little information on the photodissociative states of XeF_2. Since XeF^* $(B^2\Sigma_{1/2}) \rightarrow XeF(X^2\Sigma_{1/2}) + h\nu$ is an important lasing transition, it is desirable to understand the mechanisms which funnel electronically excited molecules of XeF_2 into important lasing levels of XeF^*.

In this report, we discuss the time-resolved excitation spectroscopy of photodissociative states of XeF_2. In this experiment we have monitored fluorescence from the XeF^* fragment produced in the photolysis as a function of the excitation photon energy. In addition, we demonstrate for the first time that synchrotron radiation at Stanford Synchrotron Radiation Laboratory (SSRL) is a versatile radiation source for studying photodissociation.

The experimental apparatus has been described in detail elsewhere.[8] For these studies, a plexiglass filter, which absorbed the radiation from the $D^2\Pi_{1/2}$ state[9] (see Fig. 1), was placed in front of the fluorescence phototube (RCA 8850). For the time-resolved excitation spectra, a standard coincidence circuit was used[10] such that photons arriving at the detector within 30 ns of the excitation pulse were counted.

The time-gated excitation spectrum, shown in Fig. 2, demonstrates heretofore unobserved fine structure. Because the onset of the fine structure

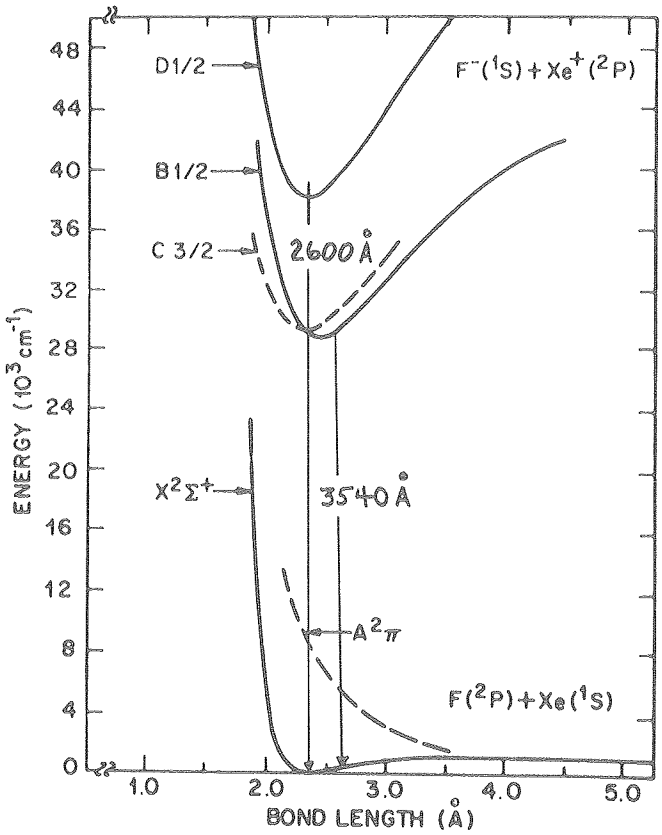

Fig. 1. Potential curves of XeF. (XBL 7710-10246A)

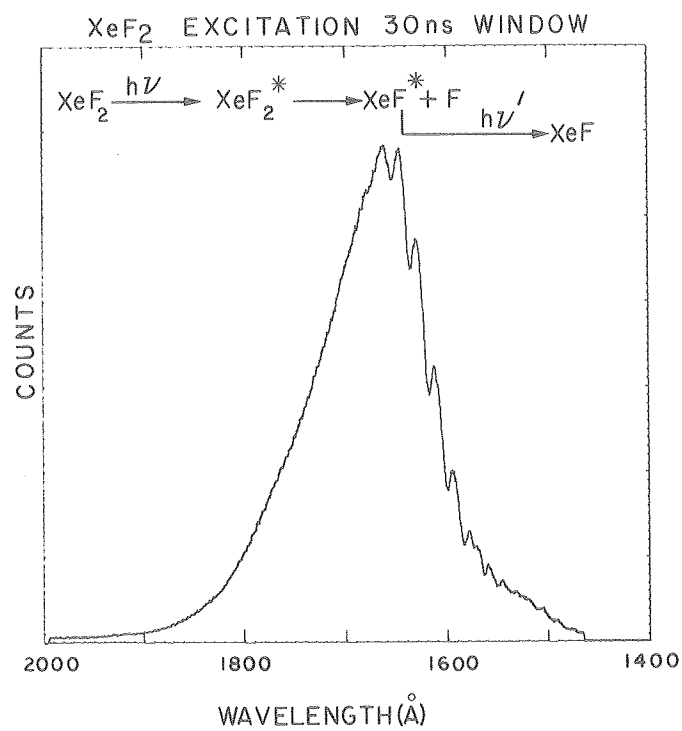

Fig. 2. XeF_2 time-gated excitation spectrum. (XBL 7711-11329)

is so abrupt, we infer that the overall band shown in Fig. 2 is a superposition of two bands, one with discrete structure and one without. The spacings between peaks is ~600 cm^{-1}. The decay curve shown in Fig. 3 ($\lambda_{excitation}$ = 1622 Å) was fitted via least-squares to a function of the form

$$I(t) = A + Be^{-t/\tau_1} + Ce^{-t/\tau_2} ,$$

yielding decay constants of 11.4 and 41.2 ns. The decay curve generated with an excitation wavelength of 1726 Å (not shown) again resulted in a two-exponential decay, with decay constants of 10.9 and 44.5 ns.

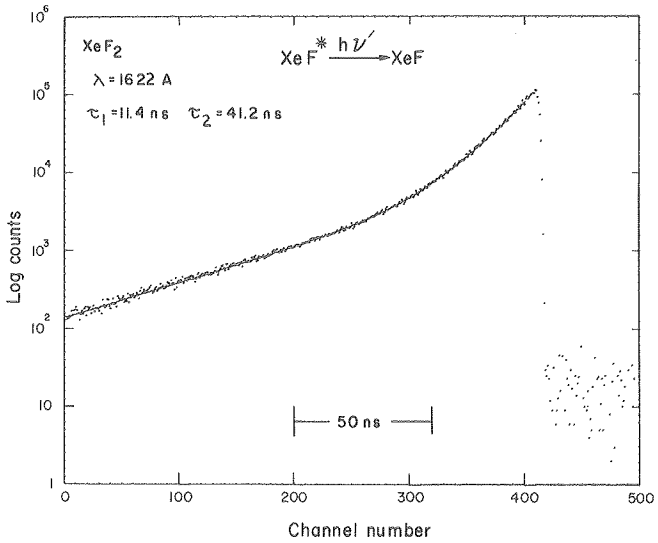

Fig. 3. XeF* decay curve. (XBL 7711-11331)

It is apparent that at least two states of XeF* are being populated because a two-component decay is observed. Photons from the $A^2\Pi \rightarrow X^2\Sigma^+_{1/2}$ transition are in the infrared and cannot be detected by our phototube. In addition, direct transitions from the $D^2\Pi_{1/2}$ to the $X^2\Sigma^+_{1/2}$ levels are filtered out by the plexiglass filter. Cascading processes from the $D^2\Pi_{1/2}$ manifold seem unlikely because the same two-component decay is observed whether or not the excitation energy exceeds the threshold for production of XeF* $D^2\Pi_{1/2}$ (the threshold corresponds to λ = 1692 Å).

Thus the two decay components must be due to the $B^2\Sigma_{1/2}$ and $C^2\Pi_{3/2}$ states. Burnham and Harris have measured the decay rate of the $B^2\Sigma_{1/2}$ and found a lifetime at 2.6 Torr of 11.5 ns,[11] in good agreement with our short-lived component. Hence, we assign the long-lived component to the $C^2\Pi_{3/2}$ state. At present, we cannot distinguish between direct fluorescence of the $C^2\Pi_{3/2}$ state and cascading processes through the $B^2\Sigma_{1/2}$ state.

The 30 ns time gate was chosen on the basis of the aforementioned decay curves, allowing detection of most of the direct $B^2\Sigma_{1/2}$ fluorescence, while discriminating against photons originating from the decay of the $C^2\Pi_{3/2}$ state.

Pack[13] and Jortner[14] have suggested that direct photodissociation of linear symmetric triatomics can lead to discrete structure in absorption spectra, the origin of the structures being a bound potential for motions perpindicular to the reaction coordinate for dissociation.

To our knowledge, this is the first observation of such discrete structure in a symmetric triatomic. Further experiments using synchrotron radiation are planned to elucidate the mechanisms involved in this process.

---

1. U. Nielsen and W. H. E. Schwarz, Chem. Phys. 13, 195 (1976).
2. H. C. Brashears, Jr., D. W. Setser, and D. Desmarteau, Chem. Phys. Lett. 48, 84 (1977).
3. J. E. Velazco, J. H. Kolts, D. W. Setser, and J. A. Coxon, Chem. Phys. Lett. 46, 99 (1977).
4. J. Tellinghuisen, G. C. Tisone, J. M. Hoffman, and A. K. Hays, J. Chem. Phys. 64, 4796 (1976).
5. J. Tellinghuisen, A. K. Hays, J. M. Hoffman, and G. C. Tisone, J. Chem. Phys. 65, 4473 (1976).
6. M. V. McCusker, unpublished.
7. J. Goodmand and L. E. Brus, J. Chem. Phys. 65, 3808 (1976).
8. E. Matthias, R. A. Rosenberg, E. D. Poliakoff, M. G. White, S.-T. Lee, and D. A. Shirley, Chem. Phys. Lett., in press.
9. J. G. Calvert and J. N. Pitts, in Photochemistry (Wiley & Sons, New York, 1966), p. 748.
10. K. Monahan and V. Rehn, unpublished.
11. R. Burnham and N. W. Harris, J. Chem. Phys. 66, 2742 (1977).
12. F. Schreiner, G. N. McDonald, and C. L. Chernick, J. Phys. Chem. 72, 1162 (1968).
13. R. T. Pack, J. Chem. Phys. 65, 4765 (1976).
14. J. A. Beswick and J. Jortner, Chem. Phys. 24, 1 (1977).

12. VUV STUDIES FOR λ < 1000 Å: TIME-RESOLVED SPECTROSCOPY IN N_2^+

R. A. Rosenberg, M. G. White, E. D. Poliakoff, and D. A. Shirley

Time-resolved spectroscopy in the VUV region has been severely limited due to the lack of tunable light sources with good timing characteristics. Although tunable laboratory light sources are available for wavelengths greater than 1050 Å (the LiF cutoff), none have the timing characteristics of synchrotron radiation, a feature which we have exploited in our previous work using light from the Stanford Synchrotron Radiation Laboratory (SSRL).[1] In order to extend this gas phase work to an area where there are no conventional tunable light sources, a window material with good transmission properties in this region had to be incorporated into the apparatus. The achievement of this allows us to extend our spectroscopic studies to include ions, inner-shell phenomena, and photoelectron spectroscopy of gases. This

report presents the first results of this work: the lifetime of the first vibrational level of the $B^2\Sigma_u^+$ state of N_2^+.

A 1500 Å Al window (obtained from Luxel Corp.) was found to possess the best overall characteristics for this work. Its transmission (see Fig. 1) sets a low energy limit of approximately 17 eV and is transparent up to 80 eV. In addition, it is able to withstand pressure differentials up to 3 Torr. The extreme thinness of the windows and the ultrahigh vacuum (UHV) conditions in the SSRL beam lines dictated extreme caution both in the design and the operation of the equipment used in conjunction with the windown. Our previous apparatus[1a] was modified to include a special chamber for the window and a sophisticated interlock system. Design of the interlocks was based upon the need for maintaining the UHV integrity of the beam line in the eventuality of either the window breaking or a condition that could possibly lead to the rupture of the window occurring. This necessitated, among other things, the installation of a special gas handling system and a fast-closing gate valve on the UHV side of the window.

The lifetimes of the $B^2\Sigma_u^+$ state of N_2^+ have been studied by a variety of methods (see Table 1) making this an ideal choice for our initial study.

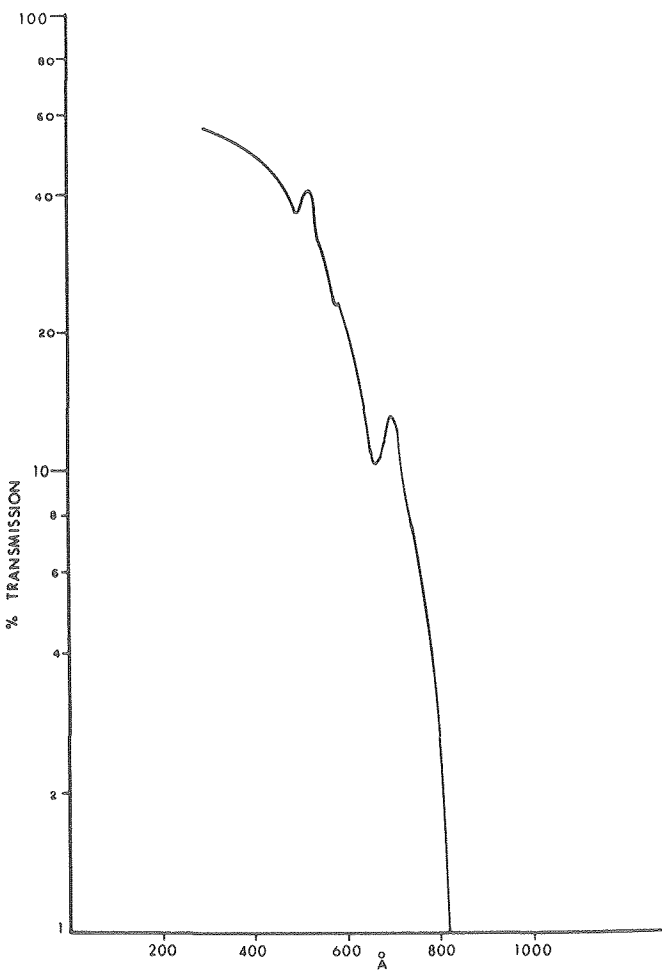

Fig. 1. Transmission of a 1500 Å Al window.[10] (XBL 778-2808)

Table 1. Lifetimes of the $B^2\Sigma_u^+$ (v'=0) of N_2^+.

Author	Lifetime (ns)	Method
This work	61.86 ± 0.21	pulsed photon excitation
Smith et al.[3]	60.6 ± 0.6	inelastic electron-photon coincidence
Bloch and Turner[4]	69	photoelectron-photon coincidence
Bingham[5]	61.0 ± 0.9	pulse proton excitation
Head[6]	58.6 ± 5	beam-gas
Gray et al.[7]	61.3 ± 1.6	pulsed electron excitation
Johnson and Flowler[8]	59.2 ± 4.0	pulsed discharge excitation
Hesser[9]	59.2 ± 6.0	phase shift (electrons)

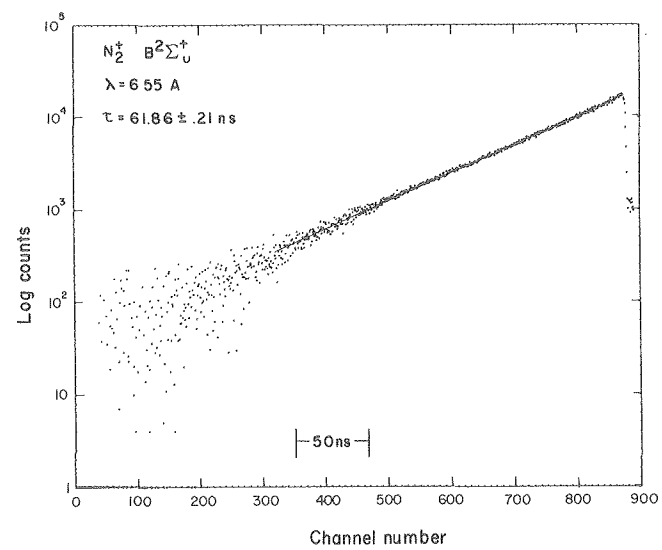

Fig. 2. Decay curve of N_2^+ $B^2\Sigma_u^+$ fitted with a single exponential. (XBL 7711-11330)

Experiments were performed on the 8° beam line at SSRL. The important experimental parameters of this facility have been described previously.[1a] Lifetimes were taken at a N_2 pressure of 5×10^{-3} Torr, low enough to avoid collisional effects and any risk to the window. Excitation was done at 655 Å, above the threshold for production of N_2^+ $B^2\Sigma_u^+$ (v' = 0),[3] but below the limit of the v' = 1 vibrational level.[2] Use of a visible PM tube (RCA 8850) limited the detected radiation to $\lambda > 2600$ Å, so that no prompt or Rayleigh scattered signal is seen in the decay curve.

From Table 1 it can be seen that our lifetime (61.86 ± 0.21 ns), which we believe to be the most

accurate, agrees well with others. Passing this threshold proves this higher energy extension of our work is both feasible and productive, thus opening up vast new areas of experimentation for the future.

1. a) E. Matthias, R. A. Rosenberg, E. D. Poliakoff, M. G. White, S.-T. Lee, and D. A. Shirley, Chem. Phys. Lett. 52, 239 (1977). b) E. Matthias, M. G. White, E. D. Poliakoff, R. A. Rosenberg, S.-T. Lee, and D. A. Shirley, Chem. Phys. Lett., to be published. c) E. D. Poliakoff, M. G. White, R. A. Rosenberg, S.-T. Lee, E. Matthias, and D. A. Shirley, J. Chem. Phys., submitted for publication.
2. Forrest R. Gillmore, J. Quant, Spectrosc. Radiation Transfer 5, 369 (1965).
3. A. J. Smith, F. H. Read, and R. E. Imhof, J. Phys. B 8, 2869 (1975).
4. M. Bloch and D. W. Turner, Chem. Phys. Lett. 30, 344 (1975).
5. F. W. Bingham, Bull. Am. Phys. Soc. 18, 609 (1973).
6. C. E. Head, Phys. Lett. 34A, 92 (1971).
7. D. Gray, J. L. Morack, and T. D. Roberts, Phys. Lett. 37A, 25 (1971).
8. A. W. Johnson and R. G. Fowler, J. Chem. Phys. 53, 65 (1970).
9. J. E. Hesser, J. Chem. Phys. 48, 2518 (1968).
10. From James A. Kinsinger, William L. Stebbings, Richard A. Valenzi, and James W. Taylor, Anal. Chem. 44, 773 (1972).

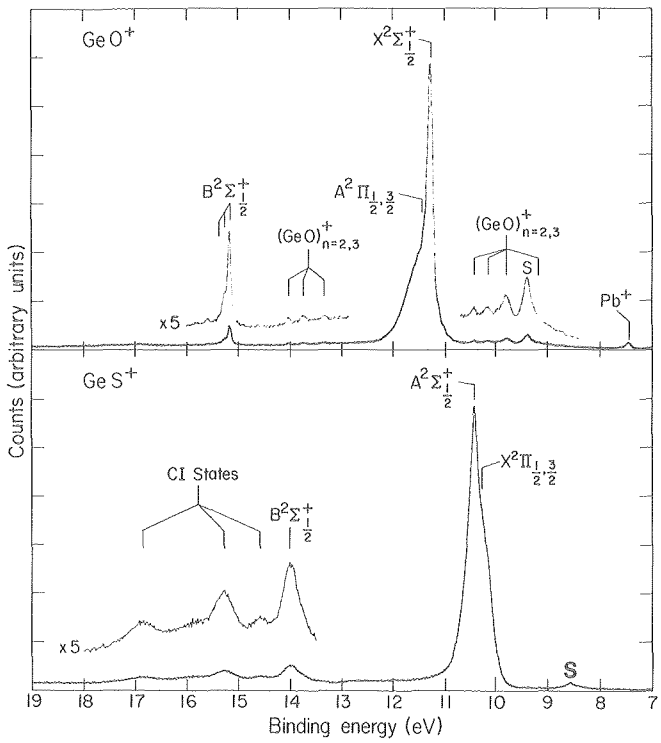

Fig. 1. HeI photoelectron spectra of GeO^+ and GeS^+. The peaks marked S are due to ionization by the HeI β line and those marked CI states are correlation satellites discussed in the text. (XBL 7712-11403)

13. MOLECULAR ORBITAL STRUCTURE OF THE IV-VI DIATOMICS FROM PHOTOELECTRON SPECTROSCOPY

M. G. White, R. A. Rosenberg, S.-T. Lee,* and D. A. Shirley

Considerable effort in ultraviolet photoelectron spectroscopy (UPS) has been focused on the systematic trends observed in the electronic structure of valence isoelectronic molecules as one proceeds down the Periodic Table. In the case of the Group VI homonuclear diatomics (O_2, S_2, Se_2, Te_2), the overall intensities and relative energy ordering of the valence molecular orbitals are similar to one another.[1] As the atomic number of the chalcogenide increases, however, spin-orbit interactions dominate, resulting in large splittings between the Ω substates and non-statistical intensity ratios.[2] To investigate these effects further, we have recently studied the valence electronic structure of several heavy Group IV-VI diatomic molecules by UPS.

The HeI photoelectron spectra of the GeX (X = O, S, Se, Te) and the SnX (X = Se, Te) molecular series are shown in Figs. 1-3, with the assignments of the prominent bands labeled. The spectra were recorded on a modified Perkin-Elmer PS-18 photoelectron spectrometer[3] operating at a nominal energy resolution of ~90 meV (FWHM). The temperatures at which the spectra were recorded are: GeO (550°C), GeS (380°C), GeSe (405°C), GeTe (550°C), SnSe (640°C), and SnTe (650°C). At

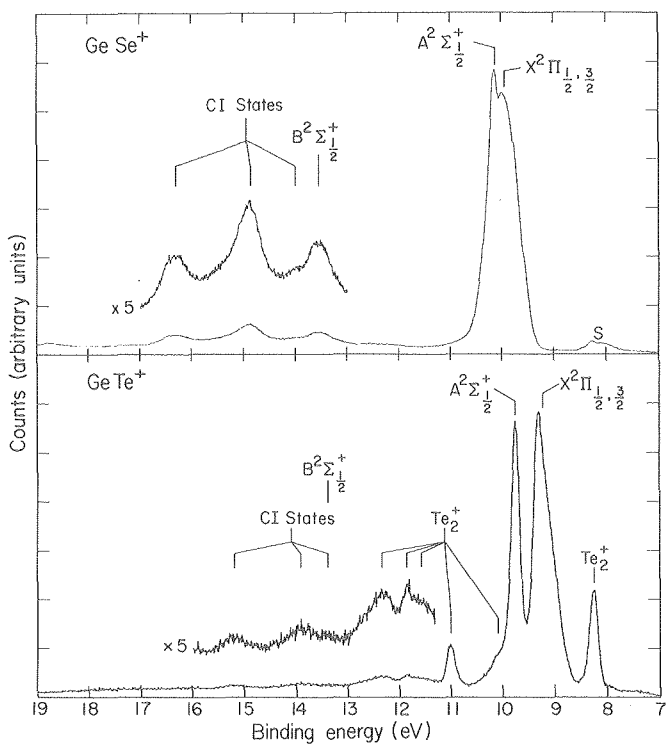

Fig. 2. HeI photoelectron spectra of $GeSe^+$ and $GeTe^+$. The peaks marked S are due to ionization by the HeI β line and those marked CI states are correlation satellites discussed in the text. (XBL 7712-11404)

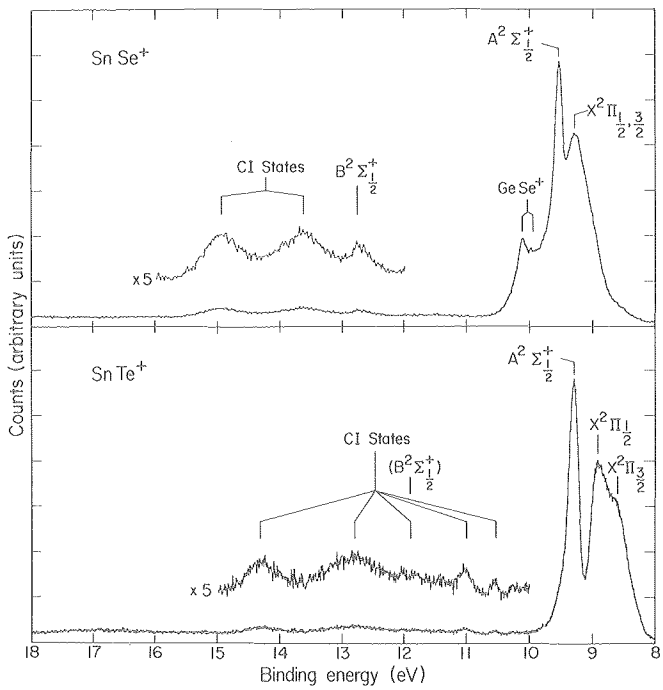

Fig. 3. HeI photoelectron spectra of $SnSe^+$ and $SnTe^+$. The peaks marked S are due to ionization by the HeI β line and those marked CI states are correlation satellites as discussed in the text. (XBL 7712-11405)

these temperatures, mass spectroscopic data for the GeX[4] and the SnX[5] vapors show that the MX(g) diatomic species is the principal component. The spectra of GeO^+ and $GeTe^+$ also contain bands from the less abundant species, $(GeO)^+_{n=2,3}$ and Te_2^+, respectively. The spectra of GeS^+, $GeSe^+$, and $SnTe^+$ are similar to those observed in the previous work of Wu and Fehlner.[6]

Assignments and experimental binding energies for the GeX and SnX molecules are summarized in Table 1. Peak assignments were based on CNDO semi-empirical SCF-MO calculations, band shape and intensity arguments, and comparison to the UPS data of the light homologues, CO, CS, and SiO.[7] The MO scheme of the highest occupied orbitals for the IV-VI diatomics studied was found to be (except for GeO^+):

$$(1\sigma)^2(2\sigma)^2(3\sigma)^2(1\pi)^4 ,$$

where the MO ordering only considers the outer valence electrons and where the 1σ MO lies too high in energy to be observed with HeI (21.2 eV) photons. Photoionization from the 1π MO gives rise to the spin-orbit partners $^2\Pi_{1/2}$ and $^2\Pi_{3/2}$, with the Ω = 3/2 level at lower binding energy. For the case of $SnTe^+$ the spin-orbit splitting is substantial and the $^2\Pi_{1/2}$ and $^2\Pi_{3/2}$ components are easily resolved. From the photoelectron band shapes of the $^2\Sigma^+(3\sigma)^{-1}$ and $^2\Pi(1\pi)^{-1}$ states, the

Table 1. Experimental and theoretical I.P.'s for the GeX (X = O, S, Se, Te) and SnX (X = Se, Te) molecules.

Molecule	Ionic State	Experimental I.P. (eV) This Work[a]	Wu & Fehlner[b]	Theory (eV)[c]
GeO	X $^2\Sigma^+_{1/2}$	11.25(1)	——	11.61
	A $^2\Pi_{1/2,3/2}$ $\nu' \sim 740 \pm 70$ cm^{-1}	11.40(5)	——	12.16
	B $^2\Sigma^+_{1/2}$ $\nu' \sim 694 \pm 150$ cm^{-1}	15.16(2)	——	15.21
GeS	X $^2\Pi_{1/2,3/2}$	10.36(5)	10.28	10.17
	A $^2\Sigma^+_{1/2}$	10.43(2)	10.39	10.24
	B $^2\Sigma^+_{1/2}$	14.00(4)	——	14.40
	CI STATE	14.6(1)	——	——
	CI STATE	15.28(5)	——	——
	CI STATE	18.86(6)	——	——

(continued)

Table 1. (Continued)

Molecule	Ionic State	Experimental I.P. (ev) This Work[a]	Wu & Fehlner[b]	Theory (eV)[c]
GeSe	X $^2\Pi_{3/2}$	(9.87)	——	10.14
	X $^2\Pi_{1/2}$	9.95(5)	9.95	
	A $^2\Sigma^+_{1/2}$	10.16(1)	10.20	10.37
	B $^2\Sigma^+_{1/2}$	13.56(5)	13.4	13.92
	CI STATE	14.0(1)	——	——
	CI STATE	14.88(5)	14.9	——
	CI STATE	16.31(5)	——	——
GeTe	X $^2\Pi_{3/2}$	(9.09)	——	8.67
	X $^2\Pi_{1/2}$	9.32(2)	——	
	A $^2\Sigma^+_{1/2}$	9.76(1)	——	9.55
	(B $^2\Sigma^+_{1/2}$)	13.3(1)	——	13.56
	CI STATE	13.88(6)	——	——
	CI STATE	15.20(5)	——	——
SnSe	X $^2\Pi_{3/2}$	(9.0)	——	9.30
	X $^2\Pi_{1/2}$	9.26(3)	——	
	A $^2\Sigma^+_{1/2}$	9.56(1)	——	9.77
	B $^2\Sigma^+_{1/2}$	12.7(1)	——	12.89
	CI STATE	13.65(5)	——	——
	CI STATE	14.99(5)	——	——
SnTe	X $^2\Pi_{3/2}$	8.61(4)	8.65	8.58
	X $^2\Pi_{1/2}$	8.91(2)	8.95	
	A $^2\Sigma^+_{1/2}$	9.30(1)	9.39	9.57
	CI STATE	10.55(5)	——	——
	CI STATE	11.02(5)	——	——
	(B $^2\Sigma^+_{1/2}$)	11.9(1)	——	12.48

(continued)

Table 1. (Continued)

CI STATE	12.8(1)	——	——
CI STATE	14.33(5)	——	——

a) Vertical ionization potentials. Uncertainties are specified in parentheses.

b) Ref. 6.

c) Koopmans' theorem ionization potentials. Empirically reduced by 0.85 to reflect final ionic state relaxation.

3σ and 1π MO's can be characterized as non-bonding and bonding, respectively. At higher binding energies a single ionization band corresponding to the $B^2\Sigma^+(2\sigma)^{-1}$ ionic state is predicted, and is observed at 15.2 eV for GeO^+. The spectra of the heavier GeX^+ ions and the SnX^+ ions, however, show several weak ionization bands in this energy range. These states are tentatively assigned to configuration-interaction (CI) satellites[8] due to many-electron correlation effects with the $(2\sigma)^{-1}$ primary hole states. The intensities of these states are consistent with the low cross section of the 4s and 5s atomic orbitals of Ge and Sn, respectively, of which the 2σ MO is largely composed. A complete analysis of this structure is severely hampered by the lack of additional information on the highly excited ionic states of these molecules. This situation is further complicated by the fact that these molecular ions are best described by Hunds' case (c) coupling in which Ω = 1/2 excited ionic states($^2\Sigma^-_{1/2}$, $^2\Pi_{1/2}$, $^2\Delta_{1/2}$, etc.) in this energy range may interact with the $(2\sigma)^{-1}$ hole state.

As the atomic number of the chalcogenide increases within the GeX and SnX series, the separation between the $^2\Pi_{1/2,3/2}$ and $^2\Sigma^+$ levels increases. A similar trend has also been observed within the valence isoelectronic Group V-V series in which the $^2\Pi/^2\Sigma^+$ ordering reverses between N_2^+ and P_2^+ [9] and their separation increases in going to Bi_2^+.[10] In addition, we note that the $^2\Pi(1\pi)^{-1}$ ionization band becomes narrower and sharper as one proceeds down the GeX series. These trends can be interpreted on the basis of the calculated charge distributions of 3σ and 1π wavefunctions given in Table 2. The 1π MO is predominately localized (~75%) on the chalcogenide, while the 3σ MO has significant contributions from the atomic orbitals of both atoms. Hence, as one proceeds down the GeX or SnX series, the ionization potentials of the $(3\sigma)^{-1}$ and $(1\pi)^{-1}$ levels decrease, following the decrease in ionization potential of the chalcogenide. The 1π MO energy will decrease faster, however, since it has the proportionally higher Group VI atomic character. The narrowing of the $^2\Pi$ ionization band in the GeX^+ series indicates a decrease in the IV-VI π-type interaction, as suggested by Wu and Fehlner.[6] The overall decrease in the 1π MO overlap populations (see Table 2) with increasing molecular weight supports this contention.

Table 2. Bonding properties of the 3σ and 1π MO's.

Molecule	Atomic Character (%) 3σ IV	3σ VI	1π IV	1π VI	MO Overlap Populations 3σ	1π
GeO	66	34	31	69	.0196	.1397
GeS	51	49	24	76	.1150	.1861
GeSe	58	42	26	74	.0833	.1855
GeTe	52	48	25	75	.1140	.1587
SnSe	65	35	24	76	.0839	.1504
SnTe	58	42	22	78	.1153	.1298

For the heavier members of the GeX and SnX series the spin-orbit interactions become appreciable. Hence, the ionic states of these molecules are more appropriately described by (ω,ω) [Hunds' case (c)] rather than (Λ,Σ) [Hunds' case (a)] coupling scheme. In this coupling scheme, the closely spaced $^2\Sigma^+_{1/2}(3\sigma)^{-1}$ and $^2\Pi_{1/2}(1\pi)^{-1}$ are expected to interact most strongly. The resulting Ω = 1/2 states can be expressed as linear combinations of the (Λ,Σ) states, i.e.,

$$\Phi(\Omega = 1/2) = a\Phi(^2\Sigma^+_{1/2}) + b\Phi(^2\Pi_{1/2}) \quad .$$

To estimate the importance of these final ionic state interactions, an approximate spin-orbit model was employed. The molecular spin-orbit operator was approximated as

$$\mathcal{H}_{so} = \sum_A \sum_i \zeta_A^{eff} \vec{\ell}_{iA} \cdot \vec{s}_i \quad , \qquad (1)$$

where the sums over A and i refer to atomic centers and electrons, respectively, and where ζ_A^{eff} is the effective atomic spin-orbit coupling constant as defined by Grimm.[11] In a $|\Lambda S\Sigma\Omega\rangle$ basis the non-zero matrix elements are

$$\langle {}^2\Pi_{3/2}|\mathcal{H}_{so}|{}^2\Pi_{3/2}\rangle = \langle 1\pi\text{-}\alpha|\mathcal{H}_{so}|1\pi\text{-}\alpha\rangle = +\ 1/2\ A \ , \qquad (2)$$

$$\langle {}^2\Pi_{1/2}|\mathcal{H}_{so}|{}^2\Pi_{1/2}\rangle = \langle 1\pi\text{+}\beta|\mathcal{H}_{so}|1\pi\text{+}\beta\rangle = -\ 1/2\ A \ , \qquad (3)$$

$$\langle {}^2\Sigma^+_{1/2}|\mathcal{H}_{so}|{}^2\Pi_{1/2}\rangle = \langle 3\sigma\beta|\mathcal{H}_{so}|1\pi\text{+}\beta\rangle \ , \qquad (4)$$

where A is proportional to the spin-orbit splitting within an electronic term. The 3σ and 1π wave-

functions were taken from the molecular orbital calculation of the ground state as a Koopman's approximation to the hole state wavefunctions. The values of ζ_A^{eff}, and the appropriate matrix elements as well as the calculated spin-orbit splittings are summarized in Table 3. Overall, the predicted $^2\Pi_{1/2}/^2\Pi_{3/2}$ separations are in reasonable agreement with experiment. This indicates the importance of including such spin-orbit terms to obtain an accurate description of the ionic states of relativistic molecules.

Table 3. Summary of spin-orbit calculations (MeV).

Molecule	ζ_{IV}^{eff} [a]	ζ_{VI}^{eff} [b]	A	ε	$^2\Pi_{1/2} - {}^2\Pi_{3/2}$ Theory	Expt
GeO	134	20	49	19	51	45
GeS	131	54	72	5	71	(73)
GeSe	127	232	204	-60	161	80
GeTe	127	521	423	-183	288	230
SnSe	312	232	251	15	250	(260)
SnTe	312	521	475	135	390	300

[a] For the Group IV atoms, $\zeta_{IV,p}$ and $\zeta^{+}_{IV,p}$ obtained from Landé Interval rule for the lowest multiplets of the ns^2np^2 and ns^2np configurations, respectively.

[b] The oxygen and sulfur atomic s-o parameters taken from Ref. 11. For Se and Te the intermediate coupling values for $\zeta_{VI,p}$ were used. See S.-T. Lee, S. Süzer, and D. A. Shirley, Chem. Phys. Lett. 41, 25 (1976).

---

*Present address: Eastman Kodak Research Laboratories, Rochester, NY 14615.

1. J. M. Dyke, L. Golob, N. Jonathan, and A. Morris, J. C. S. Faraday II, 71, 1026 (1975); J. Berkowitz, J. Chem. Phys. 62, 4074 (1975).
2. S.-T. Lee, S. Süzer, and D. A. Shirley, Chem. Phys. Lett. 41, 25 (1976).
3. S. Süzer, M. S. Banna, and D. A. Shirley, J. Chem. Phys. 63, 3473 (1975).
4. J. Drowart, F. Degreve, G. Verhaegen, and R. Colin, Trans. Faraday Soc. 61, 1075 (1965); V. I. Davydov, and N. P. Diev. J. Inorg. Chem. USSR 119, 31 (1957); L. Ch'ün-Hua, A. S. Pachinkin, and A. V. Novoselova, Russ. J. Inorg. Chem. 7, 496 (1962).
5. C. Hirayama, Y. Ichikawa, and A. M. DeRoo, J. Phys. Chem. 67, 1039 (1963).
6. M. Wu and T. P. Fehlner, J. Amer. Chem. Soc. 98, 7578 (1976).
7. N. Jonathan, A. Morris, M. Okuda, K. J. Ross, and D. J. Smith, Disc. Faraday Soc. 54, 48 (1972); D. Bulgin, J. Dyke, F. Goodfellow, N. Jonathan, E. Lee, and A. Morris, J. Elect. Spectrosc. 12, 67 (1977).
8. R. L. Martin and D. A. Shirley, J. Chem. Phys. 64, 3685 (1976); S. T. Manson, J. Elect. Spectrosc. 9, 21 (1976).
9. A. W. Potts, K. G. Glenn, and W. C. Price, Disc. Faraday Soc. 54, 66 (1972).
10. S. Süzer S.-T. Lee, and D. A. Shirley, J. Chem. Phys. 65, 412 (1976).
11. F. A. Grimm, J. Elect. Spectrosc. 2, 475 (1973).

14. RADIATION DAMAGE STUDIES BY X-RAY PHOTOELECTRON SPECTROSCOPY. I. ELECTRON-IRRADIATED $LiNO_3$ AND Li_2SO_4 *

T. Sasaki,† R. S. Williams, J. S. Wong,‡ and D. A. Shirley

X-ray photoelectron spectroscopy (XPS) has been applied to the study of radiation damage on the surfaces of $LiNO_3$ and Li_2SO_4 single crystals that were free of carbon contamination. Irradiations were performed in situ at room temperature with 0.3 - 1.6 keV electrons. The products, assigned from chemical shifts in the binding energies of core levels, were: $LiNO_2$ and Li_2O from irradiated $LiNO_3$; and Li_2SO_3, elemental sulfur, Li_2S, Li_2O, and adsorbed oxygen species from irradiated Li_2SO_4, respectively. Heavy irradiations of the Li_2SO_4 sample showed that the final products of the radiation decomposition are Li_2O and Li_2S. Furthermore, analysis of peak intensities in the XPS spectra allowed a quantitative analysis of the surface layer radiation damage caused by the electron bombardments.

Radiation damage studies by XPS are of some general importance both intrinsically and because of the detrimental effects of XPS measurements on samples unstable to the source x rays. The main advantage of this method is that it can in principle provide useful information about molecular products as well as radical species from their chemical shifts. Also, the chemical fate of the alkali-metal ions, which have been neglected in previous radiation damage studies by other methods, can be elucidated.

In the application of XPS to this series of radiation damage studies, the following points were especially taken into consideration: (1) The spectrometer should be designed to detect a given chemical shift with good energy resolution. Monochromatization of the x rays is desirable. (2) The XPS measurement should be done under UHV conditions to minimize surface contamination with hydrocarbons, oxygen, water vapor, etc. (3) Low-energy electrons or ions should be employed as a radiation source because they produce damage on the sample surface far more efficiently than soft x rays in a photoelectron spectrometer. (4) In situ irradiation under high-vacuum conditions is indispensable for the prevention of chemical reactions between the products and their surroundings.

The $LiNO_3$ sample was irradiated with 1 keV electrons. A two-hour irradiation at 1 mA filament current did not change the color of the sample surface. Figures 1a and 1b are spectra before and after the electron irradiation, respectively, and are normalized to the intensity of the parent $LiNO_3$.

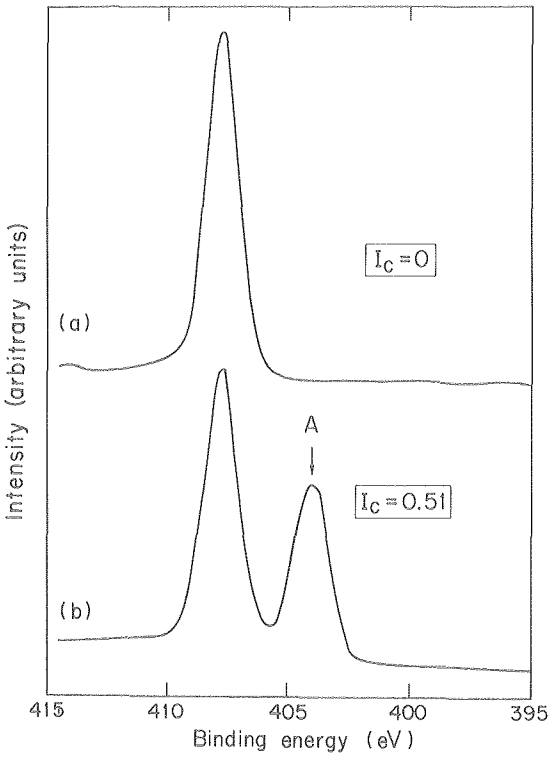

Fig. 1. Spectral changes in the N(1s) region of irradiated $LiNO_3$. Peak A is assigned to product NO_2^-. I_c is in units of coulomb/cm^2. (XBL 7710-6852)

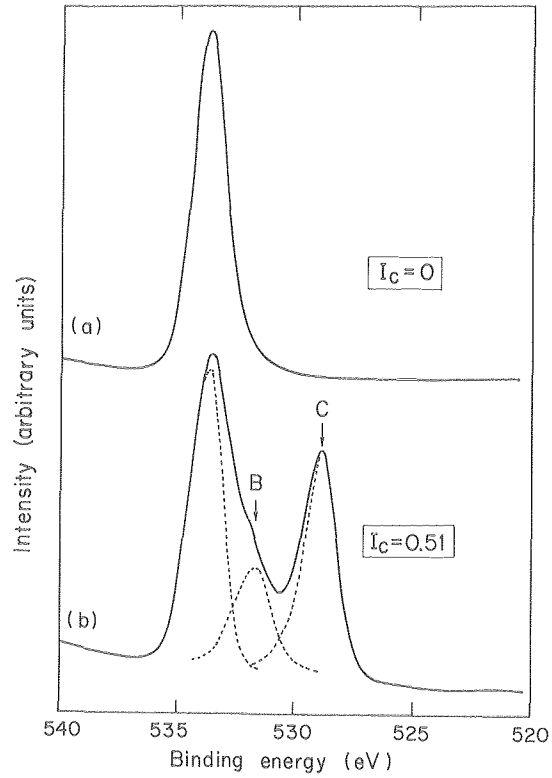

Fig. 2. Spectral changes in the O(1s) region of irradiated $LiNO_3$. Peak B is assigned to product NO_2^- and Peak C to product Li_2O. (XBL 7710-6851)

Irradiation causes the appearance of peak A, with a binding energy lower by 3.6 eV than that of the parent. The product was so stable chemically that further radiation decomposition was not observed upon continued irradiation. Since the position of the N(1s) product peak did not change with total radiation dose, the chemical form of the product can be inferred from its chemical shift. By comparison with the -3.3 eV shift in the N(1s) energy of $NaNO_2$ from that of $NaNO_3$,[1] the observed product is probably NO_2^-. This is consistent with the generally agreed overall reaction in crystalline nitrates irradiated at room temperature:

$$MNO_3 \rightarrow MNO_2 + 1/2\ O_2\ .$$

Because only one nitrogen-containing product was observed, peak A cannot be associated with such radicals as NO_2 and/or NO_3.

Figure 2 presents the spectral changes in the O(1s) region. The broken lines in Fig. 2b were obtained by computer deconvolution in which three Gaussians were employed. There are two new peaks, B and C. Because the presence of NO_2^- has been confirmed in Fig. 1, the appearance of the O(1s) line from the same ion is expected. Peak B, with binding energy 1.85 eV less than that of the parent, is attributed to NO_2^-. This assignment is supported by a quantitative analysis of the product yield. Computer deconvolution showed that the O(1s) intensity of NO_2^- relative to the parent is 0.44, while the relative N(1s) intensity of NO_2^- is 0.64. The correction by stoichiometry yields 0.66 (=0.44 × 3/2) for the latter, which agrees very well with the NO_2^- product yield from the N(1s) intensity. On the other hand peak C, which is located at a position lower by 4.6 eV than the parent, arises from one of the products ubiquitous on the surfaces of irradiated lithium oxyanion salts. We assign this to an O(1s) peak from Li_2O.

Bombardment of the Li_2SO_4 crystal with a 1.4 keV electron beam caused a gradual black coloration which increased with irradiation time and was insensitive to photobleaching. Figure 3 shows the spectral change in the S(2p) region. The absolute total intensity decreased with irradiation time, and the relative S(2p) intensities in Figs. 3b and 3c were 0.84 and 0.58 times that in Fig. 3a, respectively. After electron irradiation, the S(2p) line split into peaks attributable to three different chemical forms, labeled D, E, and F. Comparisons of the present chemical shifts with the published data for the S(2p) binding energy yield the oxidation states of the sulfur products. The chemical forms of the products are identified as shown in brackets in the first column of Table 1.

For quantitative analysis, the relative intensities of the S(2p) peaks are plotted against the total current density of the incident electrons in Fig. 4. The initial slopes of these curves have been used to estimate approximate G-values. In the heavy irradiations, the increasing rate of sulfide yield is far larger than that of the SO_3^{2-} yield, and is slightly larger than the decreasing rate of the parent. This means that sulfide is one of the common radiation products from both SO_4^{2-} and SO_3^{3-}. The relative concentrations as a function of radiation dose of SO_4^{2-}

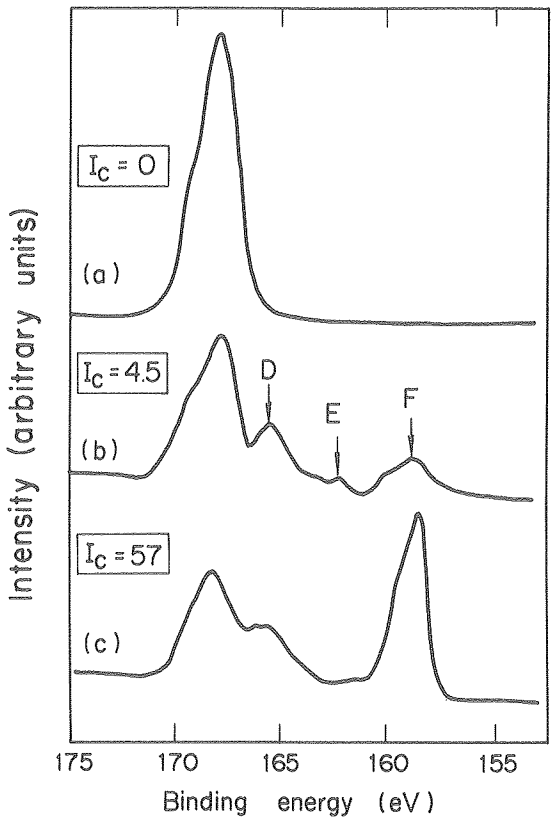

Fig. 3. Spectral changes in the S(2p) region of irradiated Li_2SO_4. Each peak is a $2p_{1/2}$-$2p_{3/2}$ doublet only partially resolved. Peak D is assigned to product SO_3^{2-}, Peak E to elemental sulfur, and Peak F to S^{2-} (see Table 1). (XBL 7710-6845)

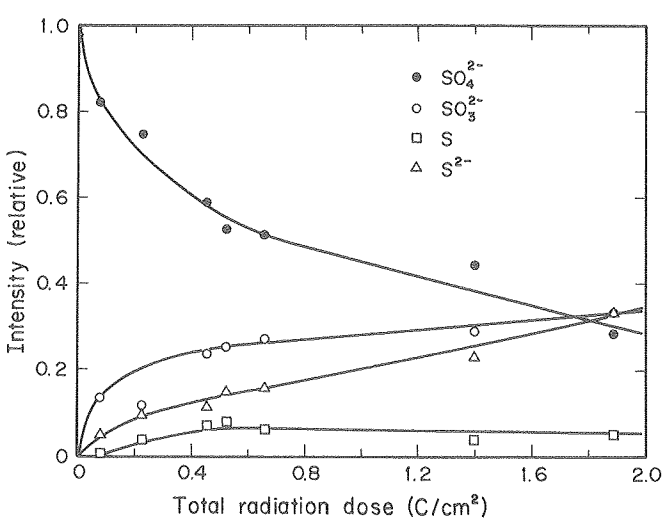

Fig. 4. Relative S(2p) intensities of the products on the irradiated Li_2SO_4 surface vs total radiation dose. (XBL 7710-6854)

Table 1. The $S2p_{3/2}$ binding energies and G-values of the products.

Chemical forms	E(ev)	ΔE(ev)	G (±50%)
SO_4^{2-}	168.1	0	-4.1×10^{-3}
D (SO_3^{2-})	165.5	2.6	3.4×10^{-3}
E (elemental)	162.2	5.9	8.4×10^{-5}
F (S^{2-})	158.8	9.3	6.4×10^{-4}
Sum of products			4.1×10^{-3}

and SO_3^{2-} were independently checked by monitoring the respective O(1s) intensities from these species. The agreement with Fig. 4 was within a few percent, so the measurements are self-consistent.

An estimate of the absolute yields of the products is especially important, because little is known about the formation of molecular species in solids. For this purpose the G-values (the number of molecules produced or decomposed per 100 eV of radiation absorbed) should be determined. Because the incident electrons penetrate far beyond the depth detected in XPS measurements, the quantity obtained in this study is different from the G-value usually adopted in radiation chemistry, but it provides important information about the nature of the radiation damage in the surface layers. Obtaining the differential energy loss of the bombarding electrons by a semi-empirical method[1] allows the determination of the G-values listed in Table 1. The G-value of -4.1×10^{-3} for radiation decompostiion of SO_4^{2-} means that in order to achieve a 20% decomposition of the surface layer of a Li_2SO_4 crystal with a 1.4 keV electron beam, a radiation dose equivalent to 1100 electrons per surface sulfate ion is required.

---

*From LBL-6220, submitted to Journal of Chemical Physics.

†Present address: Chemistry Division, Japan Atomic Energy Research Institute, Tokai-mura, Ibaraki-ken, 319-11, Japan.

‡Present address: Department of Chemistry, University of California, Berkeley, CA 94720.

1. T. Tabata, R. Ito, and S. Okabe, Nucl. Instr. Method 103, 85 (1972).

15. RADIATION DAMAGE STUDIES BY X-RAY PHOTOELECTRON SPECTROSCOPY. II. ELECTRON IRRADIATED Li_2CrO_4 AND Li_2WO_4*

T. Sasaki,† R. S. Williams, J. S. Wong,‡ and D. A. Shirley

In further studies of in situ radiation damage by XPS, lithium salts of the Group VI oxyanions $CrO_4^{=}$ and $WO_4^{=}$ were studied as anhydrous single crystals. The results for the two salts are discussed separately below.

Irradiation of $LiCrO_4$ with 1 keV electrons for 10 minutes at 1 mA electron gun filament current induced considerable changes in both the core-level and valence-band spectra, while exposure to source x rays for as long as 40 hours caused only very small changes. Figure 1 shows the spectral changes in the Cr(2p) region. All spectra were normalized to the intensity of the highest peak, and the total incident charge is indicated by I_c in units of 10^{-1} coulomb/cm^2. As seen in Fig. 1a, a small feature appears at a binding energy lower by ~2.8 eV than the main peak position of $Cr(2p)_{3/2}$. As this spectrum was recorded after exposure to source x rays for 24 hours, this feature is due to x-ray induced reduction. This feature is conspicuously enhanced by electron irradiation and about 80% of the CrO_4^{2-} undergoes radiation-induced reduction following a total dose equal to I_c = 14.3 of 1.4 keV electrons. The oxidation state of the product is inferred to be +3 by comparison of the chemical shift with values reported for various inorganic chromium compounds. From our measurements, the spin-orbit splittings between $Cr(2p)_{1/2}$ and $Cr(2p)_{3/2}$ are 9.1 eV for CrO_4^{2-} and 9.8 eV for Cr(III). Such an increase in the splitting energy with a decrease in the oxidation state of chromium has been found in previous work.[1]

The assignment of the product is also supported by spectral changes in the Cr(3s) region, shown in Fig. 2. In spite of the 80% reduction shown by the Cr(2p) lines, Fig. 2b appears to show that a considerable amount of CrO_4^{2-} remained. This is due to a multiplet splitting in the 3s level, which is well-known for compounds of transition metals possessing unpaired 3d electrons.[2] Cr(III) has three unpaired electrons in the 3d shell, while Cr(VI) in CrO_4^{2-} has none. The splitting energy of the 3s level increases with the number of unpaired electrons, and we can expect ~4 eV for the 3s splitting of Cr(III). The splitting of 3.8 eV observed here is in good agreement with this expectation. Assuming that ionization of the 3s shell results in only one (exchange-split) electron configuration for the final state, the theoretical intensity ratio of the two peaks is predicted to be 0.6 from the multiplicity ratio. The observed value of 0.7, which was obtained after correcting for the remaining CrO_4^{2-} contribution in the high-energy peak, is consistent with this estimate.

The valence band region as a function of radiation dose is displayed in Fig. 3. The $4t_2$ and $5a_1$ orbitals are mainly O(2s) in character,

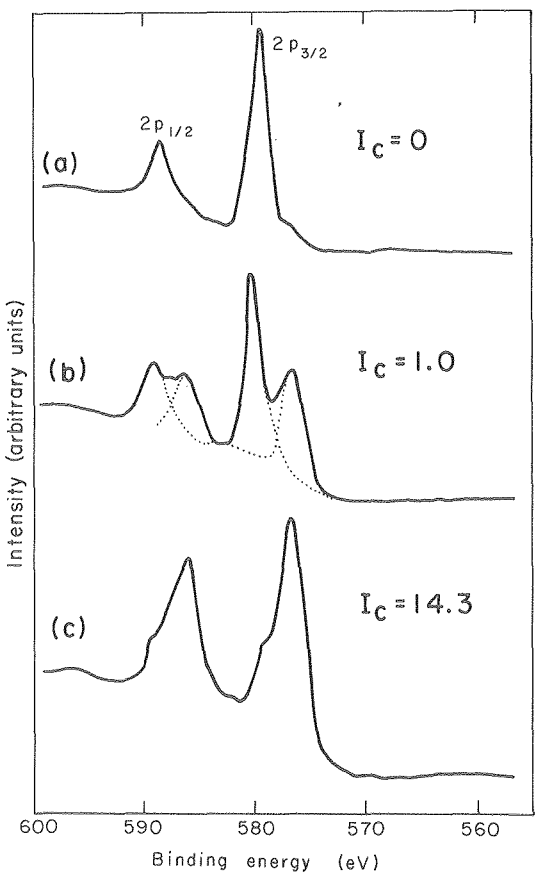

Fig. 1. Spectral changes in the Cr(2p) region of electron-irradiated Li_2CrO_4. The units of I_c are coulomb/cm^2. (XBL 7612-11157)

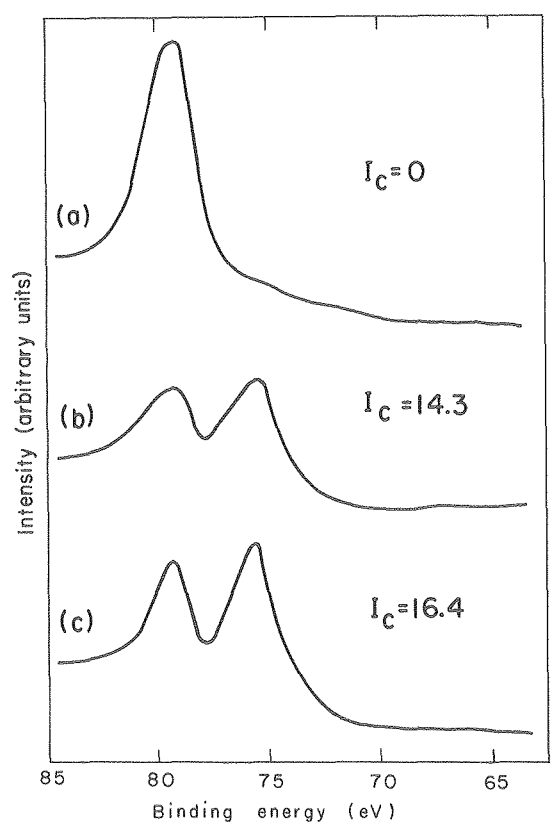

Fig. 2. Spectral changes in the Cr(3s) region of irradiated Li_2CrO_4. (XBL 7612-11153)

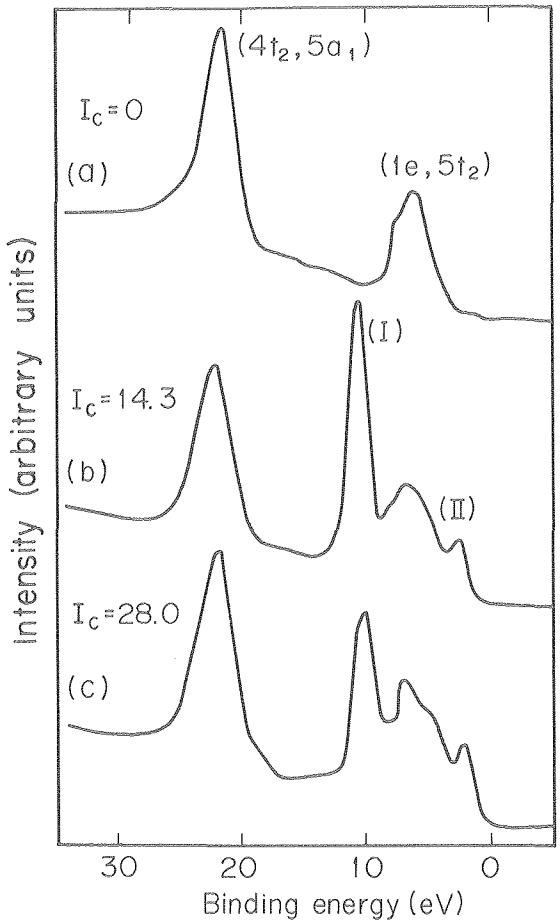

Fig. 3. Spectral changes in the valence band region of irradiated Li_2CrO_4. (XBL 7710-6853)

and the 1e and $5t_2$ orbitals have O(2p) character. After irradiation, two new peaks (I) and (II) appear at 10.3 and 2.4 eV, respectively. The absolute intensity of peak (I) initially increases with total radiation dose and then decreases under heavy irradiation, while the intensity of peak (II) does not change with respect to the 1e, $5t_2$ peak as shown in Figs. 4b and 4c. Peak (I) has a FWHM of 1.8 eV and arises from O(2p) orbitals in the product. Since heavy irradiation caused a decrease in the intensity of this peak, it is attributed to molecular oxygen absorbed on the sample surface. Thus the broadening of the peaks from O(2s)-derived orbitals from 2.7 eV FWHM in Fig. 4a to 3.3 eV in Fig. 4c is attributable to additional O(2s) contributions from atomic oxygen. The decrease in intensity of peak I may be explained by formation of molecular oxygen, which is lost to the vacuum. On the other hand, peak (II) is assigned to the Cr(3d)-derived orbitals of the product. Photopeaks in this position from non-bonding orbitals have been previously observed for both Cr(III) and Cr(IV) compounds.[1]

From the above observations we conclude the main products are lithium chromite ($LiCrO_2$) and molecularly adsorbed oxygen. $LiCrO_2$ is expected to be a more stable chemical form than Cr_2O_3 in the presence of Li^+. This assignment is also based on the observation that neither O(1s) nor Li(1s) attributable to Li_2O, which were observed in irradiated $LiNO_3$ and Li_2SO_4, appear in irradiated Li_2CrO_4.

The importance of the G-value estimated from XPS data was stressed in the preceding report. It is interesting to compare the surface G-value determined for decomposition of Li_2CrO_4 ($G = -1.3 \times 10^{-2}$) with related data. Debuyst and co-workers[3] obtained G-values of the order of 10^{-4} for the yield of total radicals, including CrO_2^-, and of 2×10^{-5} for CrO_3^- formation in K_2CrO_4 single crystals irradiated with ^{60}Co gamma rays at room temperature. Since our surface G-value, which in fact is a lower limit, is two orders of magnitude larger than the bulk values, the surface must be far more sensitive to ionizing radiation than the bulk.

Electron irradiation did not cause visible changes in the Li_2WO_4 surface. The most evident change in the XPS spectra was a time-dependent shift in the core-level peaks. The spectral changes in the O(1s) and W(4f) regions of the sample irradiated by 1 keV electrons are shown in Fig. 4. Just after irradiation the O(1s) and W(4f) regions shift toward lower binding energy by 1.8 and 2.2 eV, respectively. These shifts decrease with the passage of time, and after 20 hours the original peak positions are nearly recovered. Because all the core-level peaks, including $W(4p)_{3/2}$ ($E_b \approx 429$ eV) and $W(4d)_{5/2}$ ($E_b \approx 249$ eV), shift to lower binding energy and require almost the same time for recovery, the phenomena can not be attributed to formation of unstable products.

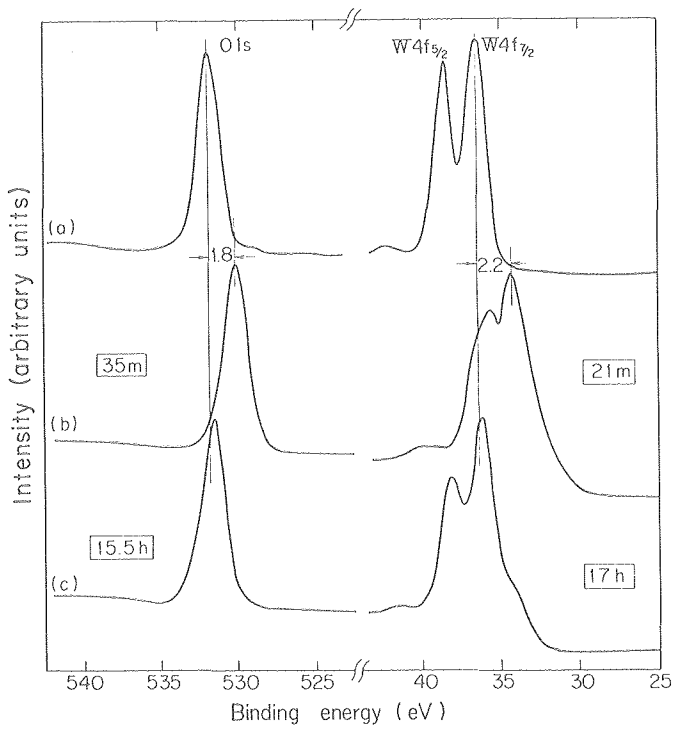

Fig. 4. Time-dependent changes in the O(1s) and W(4f) regions of Li_2WO_4 irradiated with 1 keV electrons for a total exposure of 0.51 coulomb/cm^2. (XBL 7710-6848)

The direction of the spectral shift means that photoelectrons gain kinetic energy during emission. This can be interpreted in terms of surface charging. The spectral shift is caused by acceleration arising from the electric field induced between the positively charged sample surface and a negatively charged region around the terminal site of the incident electrons. This would explain a larger energy shift for the W(4f) peak than for the O(1s) peak, because photoelectrons from the W(4f) shell have a larger escape depth, corresponding to a longer acceleration distance. The induced field strength in the surface layer of irradiation Li_2WO_4 is estimated to be 1×10^7 V/cm from the magnitude of the energy shift and the mean free path of the photoelectrons. The peak broadening of W(4f) in Fig. 4b is presumably due to differences in the acceleration distance along the mean free path. The spectral evolution in Fig. 4c indicates a gradual neutralization of the surface charges. It is noteworthy that the time-dependent shift is characteristic only of irradiated Li_2WO_4; such phenomena have not been observed for the other ten oxyanion samples we have examined to date.

Another distinguishable change in the W(4f) region is a broadening with a small shoulder to the low-energy side, as seen in Fig. 4c. Similar trends were also observed for the W(4p) and W(4d) lines. This broadening arises from the formation of reduced tungsten species. The spectral shape of W(4f) in Fig. 4c is very similar to the observation by De Angelis et al.[4] for $Na_{0.547}WO_3$, which was exposed to AlKα x rays for 8 hours. They resolved their spectrum into three components: W(IV), W(V), W(VI), and the sum of their satellites to higher binding energy. A similar computer fit has been performed on our spectrum for W(4f), as shown in Fig. 5. The fit indicates a 26% transformation of WO_4^{2-}, into reduced species. While computer fits of partially resolved spectra are never as satisfying as actually resolving the lines, we note that the $4f_{7/2}$ peak of W(V) appears as a readily observable shoulder on the W(VI) $4f_{7/2}$ peak in Fig. 5, and even the weak W(IV) $4f_{7/2}$ peak gives rise to a visible shoulder.

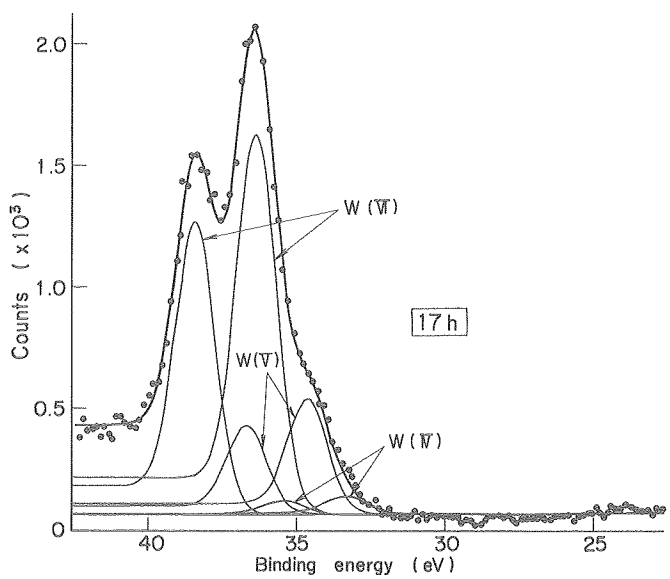

Fig. 5. Deconvolution of the W(4f) region. The spectrum is the same as that shown in Fig. 4c. (XBL 7710-6847)

---

*Brief version of LBL-6296; submitted to Journal of Chemical Physics.

†Present address: Chemistry Division, Japan Atomic Energy Research Institute, Tokai-mura, Ibaraki-ken, 319-11, Japan.

‡Present address: Department of Chemistry, University of California, Berkeley, CA 94720.

1. J. C. Helmer, J. Electron Spectrosc. 1, 259 (1972/1973).
2. D. A. Shirley, Adv. Chem. Phys. 23, 85 (1973).
3. R. Debuyst, D. J. Apers, and P. C. Capron, Inorg. Nucl. Chem. 35, 1541 (1972).
4. B. A. DeAngelis and M. Schiavello, Chem. Phys. Lett. 38, 155 (1976).

16. MOLECULAR BEAM PHOTOELECTRON SPECTROSCOPY*

Dennis Trevor

Ultraviolet HeI photoelectron spectra of most permanent gases have been measured. Unstable species such as free radicals, Van der Waals' complexes, ions, and excited states have only recently begun to be studied. Several new techniques have been developed to examine such systems. However, each technique has relied upon high resolution or modulation methods to study these minor components. These methods have been somewhat successful, but only with considerable sacrifice in intensity. Coincidence photoelectron-photoion spectrometry should be an ideal technique to apply to these systems because of its very high selectivity. Previous coincidence spectrometers have suffered from poor signal-to-noise ratios, preventing their application to these systems.

We are nearing completion of the first supersonic molecular beam photoelectron-photoion coincidence spectrometer. Our objective is to study exotic species, produced only in supersonic expansion or in collision-free environments. The high selectivity of the coincidence experiment enables the study of minor components without several restrictions on sensitivity.

The spectrometer (Fig. 1) consists of a supersonic molecular beam pumping system allowing for complete interchangeability with the many different beam sources in operation in the laboratory of Y. T. Lee. These sources produce useable supersonic beams, of atoms (by thermal dissociation), Van der Waals' complexes (by high pressure expansion), and many other exotic species. The spectrometer's HeI capillary discharge lamp has been shown to produce an average photon flux of $\sim 10^{11}$ photons/s while being pulsed at a variable

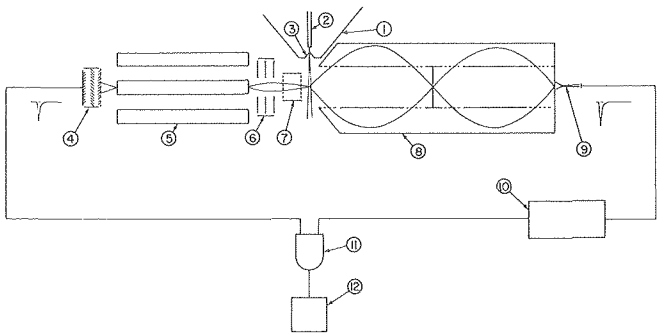

Fig. 1. Molecular beam photoelectron photoion coincidence spectrometer schematic: HeI discharge lamp points into the page (not shown), (1) differential pumping chamber, (2) nozzle, (3) skimmer, (4) ion detector, (5) quadrupole mass filter, (6) ion lens system, (7) ion space focusing grid system, (8) CMA, (9) electron detector, (10) delay line, (11) coincidence gate, (12) scaler and associated electronics. (XBL 7712-11448)

frequency up to 100 kHz with a duty cycle of ~1%. At present we are optimizing the photon pulse character of the lamp. The photoelectrons are energy-analyzed with a commercial (Physical Electronics Industries Model 15-250) double-pass cylindrical mirror analyzer with a transmission of ~1% and a measured energy resolution ($\Delta E/E$) of ~1% for our diffuse source. Due to refraction effects of the hemispherical grids and the low density of these three-dimensional sources, higher resolution operation requires a severe loss of intensity. For higher resolution studies we will be using a differentially-pumped 180° hemispherical analyzer with a "zoom" lens system and multi-channel detection. The photoions will be analyzed by time-of-flight and quadrupole mass spectrometry, with arrival-time distributions giving a measure of their kinetic energies. The quadrupole mass filter will be used for high mass resolution studies. When this is not necessary, reducing the dc potential will alow it to be used only as a high mass pass filter.

At present we have a fully operational supersonic beam source system, pulsable HeI resonance lamp, and photoelectron energy analyzer. Within the next fiscal year we hope to finish construction of the mass spectrometer and hemispherical energy analyzer multichannel system.

---

*This project is being carried out under the joint direction of Y. T. Lee and D. A. Shirley.

17. VALENCE-BAND STUDIES OF LIQUID METALS

K. A. Mills, P. S. Wehner, and D. A. Shirley

The electronic structure of liquid metals is a question of considerable technological and theoretical interest, and one may expect photoemission to prove of equal utility in studying such systems, as it does for solids. Nevertheless, comparatively little work has been done along these lines, in part due to the experimental difficulties involved, and in part due to the lack of a theoretical framework for interpreting the results. The recent development[1] of formalisms based on multiple scattering and other methods, however, makes the time right for such studies.

We report here HeII photoemission spectra for liquid and solid Ga and In. In the case of In, studies using HeI and lower energy radiation have been reported in the literature;[2,3] we shall discuss these presently.

Samples were prepared from 7 nines Eagle-Pitcher semiconductor grade Ga and 5 nines ROC/RIC In ingot. Initial attempts to obtain spectra by direct melting of these materials showed significant oxide contamination.* Accordingly, the following procedure was used for both metals. In an N_2 purged glove bag, the metal was repeatedly frozen and thawed in a pyrex container, the surface layer being discarded each time. An aliquot from the center of the final melt was transferred to a quartz crucible with a tungsten grounding ribbon; this assembly was transferred under N_2 to the spectrometer where it was mounted on a manipulator and inserted, again under nitrogen. Samples prepared in this way had a highly specular surface in both cases.

Spectra were taken in an all metal /glass UHV chamber using a CMA analyzer, with a stated resolution of 0.09 eV. Pressures were in the low 10^{-9} region during all runs. Both liquid and solid samples showed initial oxide contamination, but were easily cleaned by Ar bombardment. AES was used to monitor cleanliness,† but we found the PES spectrum to be more sensitive to the presence of oxide. The criterion for cleanliness was identical spectra after two successive bombardments, once the oxide peak had been attenuated essentially to zero. Sample cleanliness gradually degraded with time; results here are the sum of several runs terminated at first sign of contamination, with subsequent cleaning prior to repetition. The solid samples were at R.T. (as was the supercooled Ga) and the liquids were held in the range of 20-40°C above the M.P. using a Chromel-Alumal TC and a magnetically non-inductive heater.

The spectra are shown in Figs. 1 and 2. The Ga solid and supercooled results are preliminary due to the possibility of slight oxide contamination, and insufficient statistics (around one-half the counts of other runs). We see the characteristic 3d doublet for Ga and 4d doublet for In; the primary peaks are due to HeII (40.8 eV) radiation and the remaining to higher energy HeII resonances. As can be seen, the core level BE's are identical within our resolution. In addition, the line widths and shapes, which are indicative of relaxation and many-body effects in the condensed phase, are again virtually identical. It was shown[4] in Li that the dominant contribution to the 1s hole lifetime is hole-phonon coupling, and that the inherent width of this state is 0.04 eV. Since the d electrons in Ga and In are less tightly bound

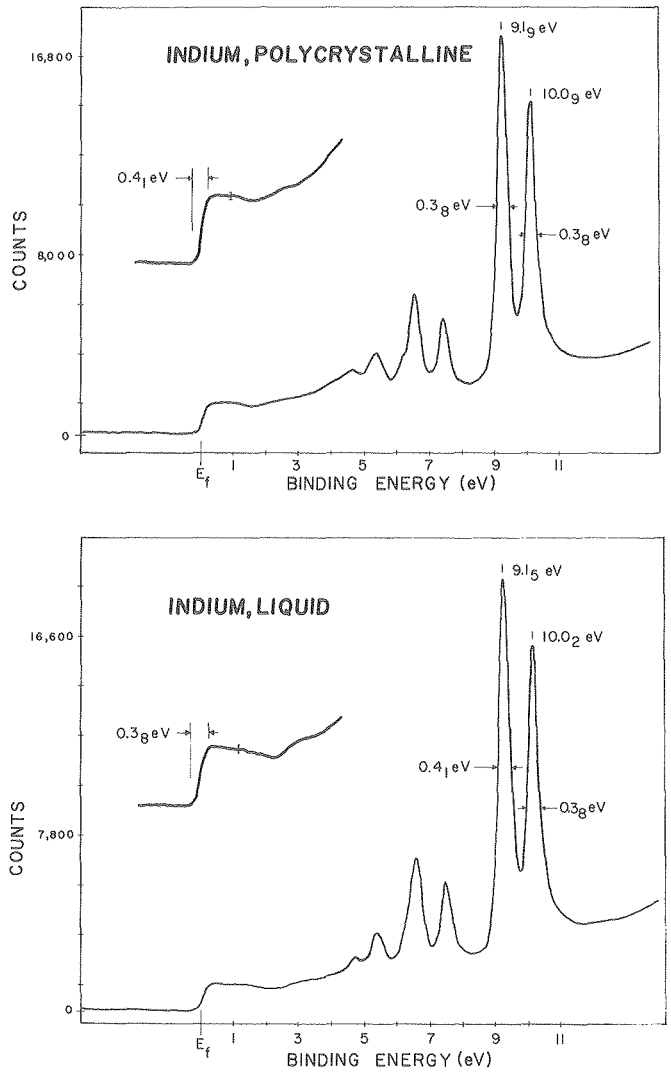

Fig. 1. (XBL 774-8562)

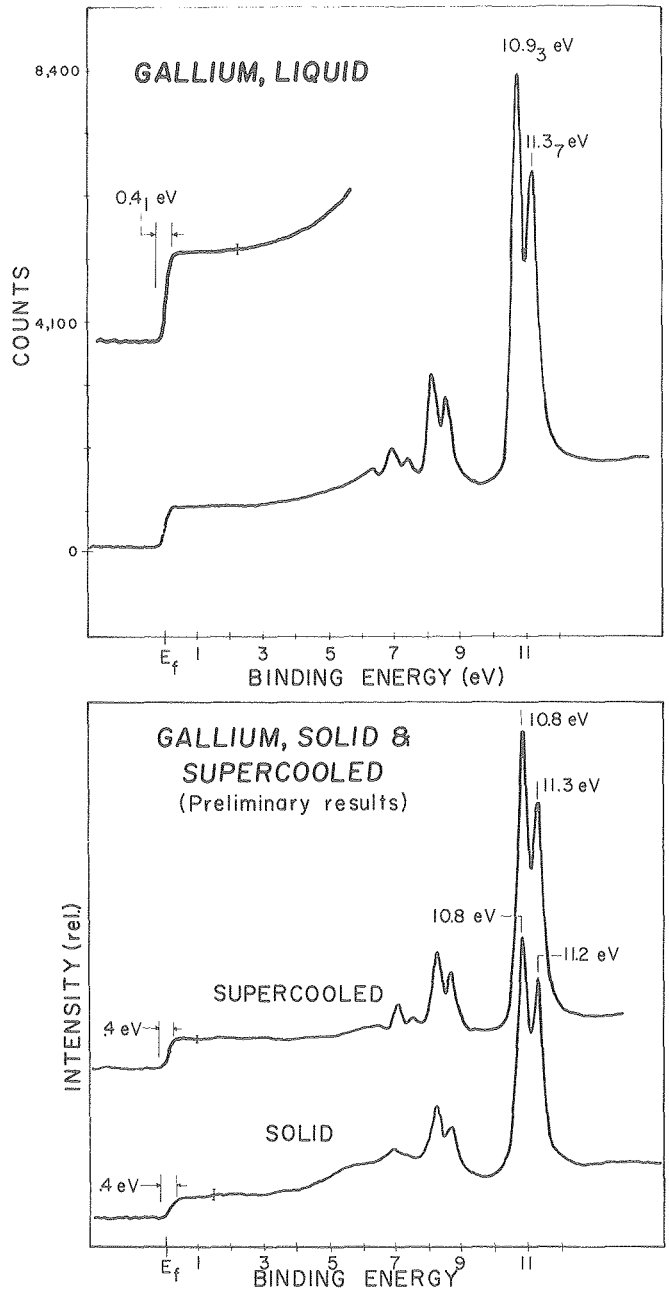

Fig. 2. (XBL 774-8559)

than the Li 1s, we expect their inherent hole widths to also be of this order. Apparently, then, the hole-medium coupling in the liquid and solid are quite similar, or at least produce the same lifetimes.‡

The valence bands similarly show virtually no change from solid to liquid, although we note that the higher d resonances made it impossible to unambiguously assign a band width. Nevertheless, if one assumes a sloping inelastic tail, the results for liquid Ga and In both indicate a very free-electron-like VBDOS. One important result is that for In we seem not to observe the dip at ~2.5 eV BE seen in Refs. 2 and 3. This is in accord with the theoretical predictions (see Fig. 3); it is hard to say whether this is a photon-energy-dependent (i.e., sampling depth) effect or is due to contamination in the previous studies. It would be very interesting to obtain systematic variable energy spectra for these metals; if in fact one is seeing a change in the VBDOS with hν, this would lend support to some recent theoretical work that assumes the existence of significant structure for liquid metal surfaces relative to the bulk.[5]

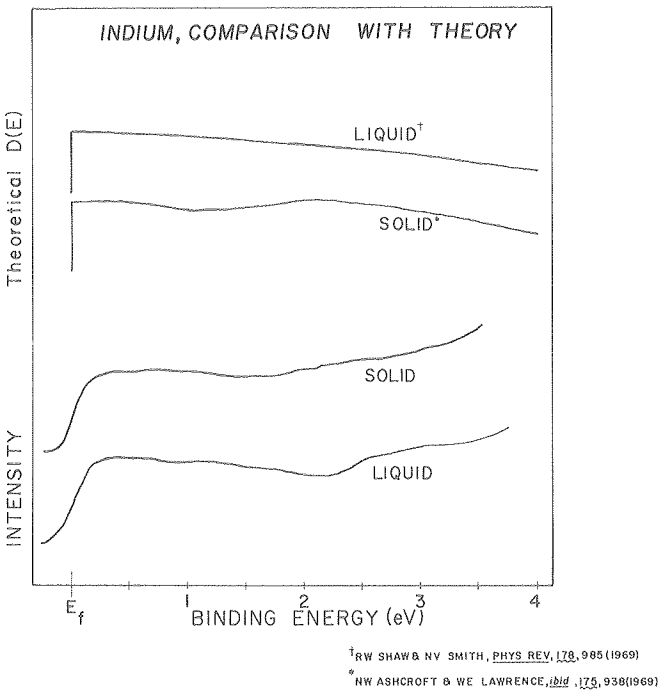

Fig. 3. (XBL 774-8558)

---

*Visible as scum on surface, and in spectrum [O(2p) at ~4 eV B.E.].

†Estimated sensitivity a few hundredths of a monolayer.

‡We note that the Li results were for x ray excitation, so that the electron E_K was considerably higher there. Nevertheless, for HeII radiation we feel the photoelectron is far enough above threshold to make our comparison meaningful.

1. See, for example, L. E. Ballentine, in S. A. Rice and I. Prigogine, eds., Adv. Chem. Phys. XXXI, 263 (1974); L. M. Roth, Phys. Rev. B 11, 3769 (1975).
2. R. Y. Koyama and W. E. Spicer, Phys. Rev. B 4, 4318 (1971).
3. C. Novus, D. C. Rodway, and G. P. Williams, in Proc. 2nd Conf. Prop. Liq. Metals, Tokyo, 1972.
4. Y. Baer, P. H. Citrin, and G. K. Wertheim, Phys. Rev. Lett. 37, 40 (1976).
5. J. W. Allen and S. A. Rice, private communication.

18. RESEARCH PLANS FOR CALENDAR YEAR 1978

David A. Shirley

Our electron spectroscopic research in 1978 will be tied to the development of new synchrotron radiation facilities at the Stanford Synchrotron Radiation Laboratory (SSRL) as well as that of new kinds of apparatus at Lawrence Berkeley Laboratory.

An angle-resolved movable spectrometer will be through the construction stage early in 1978. It will be used both at LBL and at SSRL for the study of electronic structures of clean metal surfaces and for elucidating molecular orbital structure of adsorbates on surfaces.

Surface densities of states of liquid metals and alloys will be studied further to elucidate the effect of loss of long-range order. This research is the principal project planned for the magnetic spectrometer.

Van der Waals' molecules and other clusters will be studied in the molecular beam machine. This project should yield interesting results in a new area of research in 1978.

In the vacuum-ultraviolet energy range, absorption and fluorescence studies of molecular species will be pursued, with emphasis on time-resolved spectroscopy and relaxation phenomena. Energy analysis will be initiated in the fluorescence channel. Angle-resolved photoemission experiments on gases at SSRL will be initiated.

The newly established EXAFS (extended x-ray absorption fine structure) capability in the 300 eV region at SSRL will be employed to study a variety of phenomena related to surface and adsorbate structure.

19. 1977 PUBLICATIONS AND REPORTS

David A. Shirley and Associates

Journals

1. G. Apai, J. Stöhr, R. S. Williams, P. S. Wehner, S. P. Kowalczyk, and D. A. Shirley, Angle-Resolved Photoemission from Cu Single Crystals Using Al Kα Radiation, Phys. Rev. B 15, 584 (1977).

2. R. L. Martin, S. P. Kowalczyk, F. R. McFeely, L. Ley, and D. A. Shirley, Core-Electron Binding Energies of the First Thirty Elements, Phys. Rev. B 15, 544 (1977).

3. P. S. Wehner, J. Stöhr, G. Apai, F. R. McFeely, and D. A. Shirley, Evidence for D-Orbital-Directed X-ray Photoemission, Phys. Rev. Lett. 38, 169 (1977).

4. S.-T. Lee, R. A. Rosenberg, E. Matthias, and D. A. Shirley, Glow Discharge Lamps as Electron Sources for Electron Impact Excitation, J. Electron Spectrosc. Rel. Phen. 10, 203 (1977).

5. R. S. Williams and D. A. Shirley, Comparison of Final State Approximations in the Calculation of Total and Differential Photoemission Cross Sections of Neon, J. Chem. Phys. 66, 2378 (1977).

6. S.-T. Lee, Ş. Süzer, E. Matthias, R. A. Rosenberg, and D. A. Shirley, Configuration Interaction Effects in the Atomic Photoelectron Spectra of Ba, Sm, Eu, and Yb, J. Chem. Phys. 66, 2496 (1977).

7. G. P. Schwartz and D. A. Shirley, Rare-Earth Valence-State Studies of the Series RIn_3 and RSn_3 Derived from Quadrupole Coupling Constants, Hyperfine Interactions 3, 67 (1977).

8. H. H. Rinneberg, G. P. Schwartz, and D. A. Shirley, PAC Studies of Spin Deviations, Pressure Induced Hyperfine Field Shifts, and Temperature Variation of Supertransferred Hyperfine Fields, Hyperfine Interactions 3, 97 (1977).

9. D. A. Shirley, S.-T. Lee, Ş. Süzer, R. L. Martin, E. Matthias, and R. A. Rosenberg, Electron Correlation in Atoms from Photoelectron Spectroscopy, in Atomic Physics 5 (1977), edited by R. Marrus, M. Prior, and H. Shugart (Plenum Publishing Corp., New York, NY), pp. 313-323.

10. S. P. Kowalczyk, L. Ley, F. R. McFeely, and D. A. Shirley, X-ray Photoelectron Spectroscopic Studies of the Electronic Structure of Transition-Metal Difluorides, Phys. Rev. B 15, 4997 (1977).

11. R. L. Martin and D. A. Shirley, Many-Electron Theory of Photoemission, in Electron Spectroscopy: Theory, Techniques and Applications, edited by C. R. Brundle and A. D. Baker (Academic Press, New York, 1977), Vol. 1, Chap. 2, p. 75.

12. S. P. Kowalczyk, F. R. McFeely, L. Ley, V. T. Gritsyna, and D. A. Shirley, The Electronic Structure of $SrTiO_3$ and Some Simple Related Oxides (MgO, Al_2O_3, SrO, TiO_2), Solid State Commun. 23, 161 (1977).

13. R. S. Williams, P. S. Wehner, J. Stöhr, and D. A. Shirley, Thermally Induced Breakdown of the Direct-Transition Model in Copper, Phys. Rev. Lett. 39, 302 (1977).

14. B. E. Mills and D. A. Shirley, X-ray Photoemission Spectra of the 2s Valence Orbitals in Cyclic Alkanes in Relation to Valence Bands of Amorphous Group 4 and 5 Elements, J. Am. Chem. Soc. 99, 5885 (1977).

Invited Talks

1. D. A. Shirley, Surface and Adsorbate Studies by Angle-Resolved Photoemission, Xerox Palo Alto Research Center, January 14, 1977.

2. D. A. Shirley, Angle-Resolved Photoemission Applied to Surface and Adsorbate Electronic Structure, Chemistry Department, University of Chicago, January 24, 1977.

3. D. A. Shirley, Photoemission Studies of Surfaces and Adsorbates, Department of Chemistry, University of California, Santa Barbara, February 3, 1977.

4. D. A. Shirley, Valence Bands of Solids, Departments of Materials Science, Chemistry, and Physics, University of Utah, February 24, 1977.

5. D. A. Shirley, Absorption, Fluorescence, and Photoemission Studies Using Synchrotron Radiation, Chemistry Department, Texas A and M, March 8, 1977.

6. D. A. Shirley, Electron Correlation Effects from Photoelectron Spectroscopy, Chemistry Department, University of California, Davis, March 15, 1977.

7. D. A. Shirley, The Electronic Structure of Surfaces, ERDA Materials Science Workshop on Surface Science, MMRD/LBL, March 17, 1977.

8. D. A. Shirley, New Experiments at the Stanford Synchrotron Radiation Project, Spring 1977 Meeting of the Solid-State Science Committee of NAS/NRC, held at MMRD/LBL, March 25, 1977.

9. D. A. Shirley, Angle-Resolved Photoemission from Noble Metals and Adsorbates Using Synchrotron Radiation, Symposium on Electron Spectroscopy, University of Uppsala, Institute of Physics, Uppsala, Sweden, May 9, 1977.

10. D. A. Shirley, A Summary of the Conference, Symposium on Electron Spectroscopy, University of Uppsala, Institute of Physics, Uppsala, Sweden, May 11, 1977.

11. D. A. Shirley, Correlation Effects in Photoelectron Spectrometry of Atoms, Opening Talk of the Fifth International Conference on Vacuum Ultraviolet and Radiation Physics, Montpellier, France, September 5, 1977.

12. D. A. Shirley, Charge Distributions and Molecular Orbital Character from ESCA, Journées de Chimie Organique d'Orsay, University of Orsay, France, September 9, 1977.

13. D. A. Shirley, Solid-State Band Structure Photoemission Studies with High-Energy Synchrotron Radiation, Free University of Berlin, September 19, 1977.

14. D. A. Shirley, New Applications of Synchrotron Radiation in the VUV and Soft X-ray Range, University of Namur, Belgium, September 21, 1977.

15. D. A. Shirley, New Applications of Synchrotron Radiation, Physical Chemistry Seminar, University of California, Berkeley, September 29, 1977.

16. D. A. Shirley, Some New Experiments with Synchrotron Radiation in the VUV and Soft X-ray Regions, Department of Chemistry, University of California, Irvine, October 24, 1977.

17. D. A. Shirley, Some New Applications of Synchrotron Radiation in the VUV and Soft X-ray Range, Department of Chemistry, University of California, Los Angeles, November 15, 1977.

LBL Reports

1. R. L. Martin, S. P. Kowalczyk, and D. A. Shirley, The Relation Between Satellite Peaks in X-ray Emission and X-ray Photoemission Spectra, LBL-5445.

2. S. P. Kowalczyk, G. Apai, G. Kaindl, F. R. McFeely, L. Ley, and D. A. Shirley, An X-ray Photoemission Investigation of the Density of States of β'-NiAl, LBL-5744.

3. R. S. Williams, S. P. Kowalczyk, P. S. Wehner, G. Apai, J. Stöhr, and D. A. Shirley, Angle- and Energy-Dependent Core-Level Photoelectron Energy Loss Studies in Al and In, LBL-6027.

4. J. Stöhr, P. S. Wehner, R. S. Williams, G. Apai, and D. A. Shirley, Bulk Versus Surface Effects in Normal Photoemission from Cu(110) in the Range 32 eV $\leqslant h\nu \leqslant$ 160 eV, LBL-6066.

5. L. Ley, O. B. Dabbousi, S. P. Kowalczyk, F. R. McFeely, and D. A. Shirley, X-ray Photoemission Spectra of the Valence Bands of the 3d Transition Metals, Sc to Fe, LBL-6208.

6. T. Sasaki, R. S. Williams, J. S. Wong, and D. A. Shirley, Radiation Damage Studies by X-ray Photoelectron Spectroscopy. I. Electron Irradiated $LiNO_3$ and Li_2SO_4, LBL-6220.

7. D. A. Shirley, Many-Electron and Final-State Effects: Beyond the One-Electron Picture, LBL-6244.

8. J. Stöhr, R. S. Williams, G. Apai, P. S. Wehner, and D. A. Shirley, Carbon K-Edge Absorption Fine Structure of Graphite and Some Polymers, LBL-6257.

9. J. Stöhr, R. S. Williams, P. S. Wehner, and D. A. Shirley, Temperature and Photon-Energy Induced Breakdown of the Direct-Transition Model in Cu, LBL-6258.

10. T. Sasaki, R. S. Williams, J. S. Wong, and D. A. Shirley, Radiation Damage Studies by X-ray Photoelectron Spectroscopy. II. Electron Irradiated Li_2CrO_4 and Li_2WO_4, LBL-6296.

11. E. Matthias, R. A. Rosenberg, E. D. Poliakoff, M. G. White, S.-T. Lee, and D. A. Shirley, Time-Resolved VUV Spectroscopy Using Synchrotron Radiation. I. Fluorescent Lifetimes of Atomic Kr and Xe, LBL-6605.

12. D. A. Shirley, J. Stöhr, P. S. Wehner, R. S. Williams, and G. Apai, Photoemission from Noble Metals and Adsorbates Using Synchrotron Radiation, LBL-6650.

13. E. Matthias, S.-T. Lee, M. G. White, E. D. Poliakoff, R. A. Rosenberg, and D. A. Shirley, Time-Resolved VUV Spectroscopy Using Synchrotron Radiation. II. Zeeman Beats in Resonance Fluorescence of the $^3P_1$ States in Kr and Xe, LBL-6651.

14. E. D. Poliakoff, M. G. White, R. A. Rosenberg, S.-T. Lee, E. Matthias, and D. A. Shirley, Time-Resolved VUV Spectroscopy Using Synchrotron Radiation. III. Radiative Decay Measurements of Electronically Excited States of Xe_2, LBL-6687.

15. D. A. Shirley, Correlation Effects in Photoelectron Spectrometry of Atoms, LBL-6900.

16. O. B. Dabbousi, P. S. Wehner, and D. A. Shirley, Temperature and Photon-Energy Induced Breakdown of the Direct-Transition Model in Copper, LBL-6911.

17. R. S. Williams, P. S. Wehner, J. Stöhr, and D. A. Shirley, Electron Refraction and Light Polarization Effects in Angle-Resolved Photoemission Spectra of Cu Surfaces Using 45 eV Radiation, LBL-6940.

18. S. D. Kevan, P. S. Wehner, and D. A. Shirley, Evidence for the Itinerant Electron Model of Ferromagnetism and for Surface Photoemission from Angle-Resolved Photoemission Studies of Iron, LBL-6943.

19. P. M. A. Sherwood, F. R. McFeely, S. P. Kowalczyk, and D. A. Shirley, D-Orbital Directed Photoemission from Manganese Fluoride Single Crystals Using Al Kα Radiation, LBL-6947.

20. P. M. A. Sherwood and D. A. Shirley, Crystal-Field and Band-Broadening Effects on the Apparent 4d Spin-Orbit Splitting in Cadium Photoelectron Spectra, LBL-7316.

21. Gustav Richard Apai II, Photoemission Studies of Clean and Adsorbate Covered Metal Surfaces Using Synchrotron and UV Radiation Sources (Ph.D. thesis), LBL-6906.

f. Crossed Molecular Beams

Yuan T. Lee, Principal Investigator

1. ATOMIC OXYGEN SOURCE DEVELOPMENT AND A STUDY OF THE O + ICl → IO + Cl REACTION

Steven J. Sibner and Richard J. Buss

The long term stability and reproducibility of our high pressure radiofrequency discharge beam source for the production of ground state oxygen atoms has been improved to the point where reactive crossed beam scattering experiments have been successfully carried out. Product angular distributions and time-of-flight velocity distributions have been obtained for reactions with three iodine containing compounds: ICl, C_2H_5I, and CF_3I. When a full analysis of all three systems is completed, we hope to refine the IO bond strength value proposed by Grice,[1] $D_0(IO) = 53 \pm 3$ kcal/mole. The previous spectroscopic value was $D_0(IO) = 42 \pm 5$ kcal/mole.[2] Our preliminary results fall within Grice's error limits. The reactants in the O + ICl reaction approach on a triplet potential energy surface. The possibility that a surface crossing might occur to a singlet surface, yielding ClO + I as the reaction products, was also investigated. However, no ClO product was detected. All three experiments were carried out at a collision energy of approximately 3.3 kcal/mole. The energetics for the reactions studied are:

	ΔD_o (kcal/mole)	
$O + ICl \longrightarrow \underline{IO} + Cl$	3.4	(1)
$O + C_2H_5I \longrightarrow \underline{IO} + C_2H_5$	0.0	(2)
$O + CF_3I \longrightarrow \underline{IO} + CF_3$	-0.2	(3)
$O + CH_3I \not\longrightarrow \underline{IO} + CH_3$	-3.3	(4)

Reaction (4) was also attempted but no IO product was detected.

In this article the analysis of the energetics and dynamics of the O + ICl → IO + Cl reaction will be discussed. The reaction is found to proceed via a long-lived collision complex whose IO product translational energy distribution can be described by RRKM-AM statistical theory (within the current uncertainties of the reaction energetics). The ICl was seeded in argon to a translational velocity of 4.95×10^4 cm/s and a Mach number of 7. The oxygen atoms were produced in our radiofrequency discharge beam source with a peak translational velocity of 1.29×10^5 cm/s and a Mach number of 4. Table 1 lists typical dissociation characteristics of the discharge source for two different nozzles. Molecular dissociation is always found to be greater than 80% and to depend weakly on RF power and nozzle pressure. The gas mixture used in these experiments was 95% argon/5% O_2.

Figure 1 shows the lab angular distribution and the most probable Newton diagram for the O + ICl reaction. Significant lab intensity appears on both

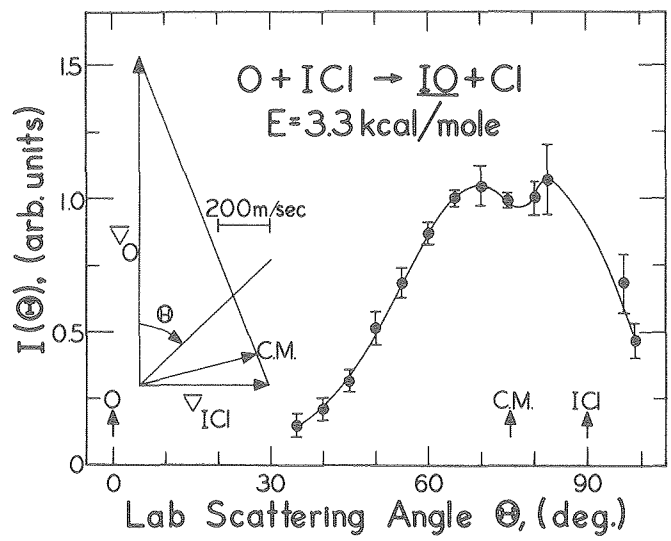

Fig. 1. Angular distribution of reactively scattered IO product. (XBL 7712-10934)

Table 1. Molecular oxygen dissociation characteristics.

	Pressure (torr)	RF Power (watts)	Dissociation (percent)
Nozzle A	190	115	87.6
	190	120	88.1
	190	150	92.6
Nozzle B	100	110	88.5
	150	110	85.2
	180	110	80.7

sides of the center-of-mass angle that is approximately 15° from the halogen beam direction. Cross-correlation time-of-flight (TOF) spectra taken at eight lab angles were combined with this angular distribution to give a center-of-mass contour map that is shown in Fig. 2. Both the forward (with respect to the oxygen beam direction) and backward scattered peaks are observed to peak along the relative velocity vector indicating the importance of angular momentum considerations for this reaction. The symmetry of the map is indicative of a long-lived collision complex. The forward peak has a much higher information content than the backward peak since it is composed of six angles at which TOF spectra were taken in a low noise environment (far from the halogen beam). Hence further discussions in this report on the energetics of this reaction will be based exclusively on information from the forward scattered IO product peak.

Figure 3 compares the calculated best-fit flux distribution with the experimentally determined flux distributions for all eight angles at which TOF spectra were taken. These best fit distributions were deconvoluted and used in the construction of the canonical contour map described earlier. For the reaction under study the anisotropy ratio for the center-of-mass angular distribution, $I(\theta=0°)/I(\theta=90°)$, was found to be approximately 2.5. The contour map and anisotropy ratio obtained for our reaction at a collision energy of 3.3 kcal/mole are similar in form to Herschbach's[3] $O + Br_2$ and Grice's[4] $O + I_2$, ICl results, which were obtained with effusive atomic oxygen beams.

A product translational energy distribution was computed using information in the forward peak of the contour map. This is shown in Fig. 4. The RRKM-AM[5] statistical predictions are also shown when E' = 6.7 kcal/mole and E' = 8.7 kcal/mole are assumed available for product translation (E' = collision energy + reaction exoergicity). The lower of these E' values assumes Grice's IO bond strength of 53 ± 3 kcal/mole. These two curves appear to define lower and upper bounds for the experimental P(E') distribution when the maximum exit centrifugal barrier of RRKM-AM theory, B_m', is set at 0.75 kcal/mole. When final bounds are calculated for the CF_3I and C_2H_5I reactions a composite IO bond strength will be determined. $D_0(IO) = 54 \pm 1.5$ kcal/mole appears consistent with the P(E') distribution determined in this experiment.

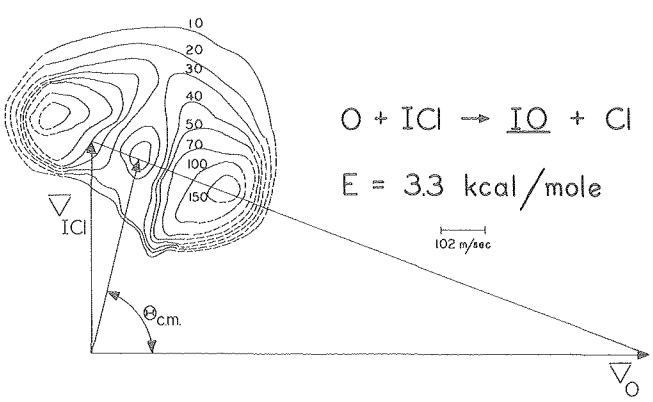

Fig. 2. Contour map of the IO product flux density in the center-of-mass coordinate system produced in the reaction O + ICl. (XBL 7712-10948)

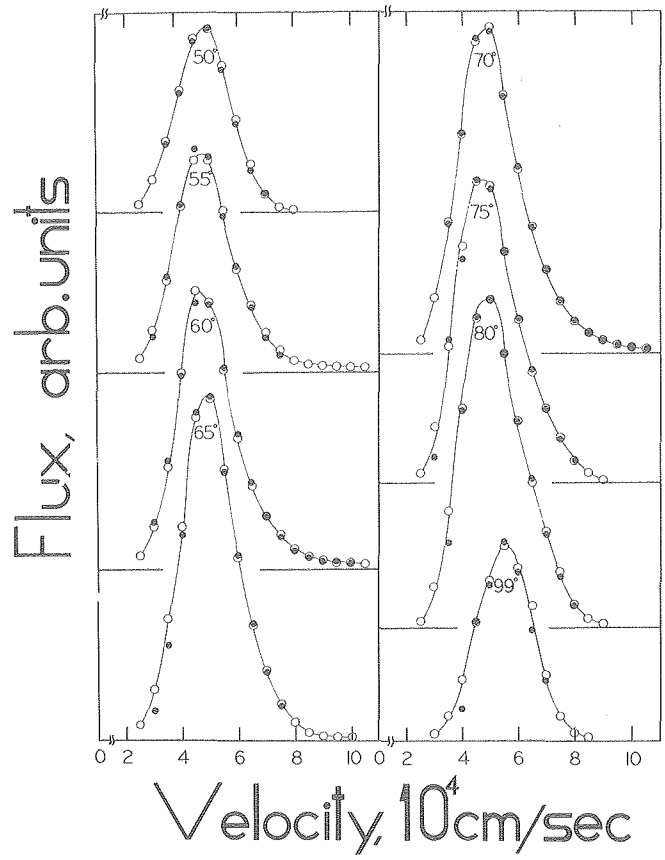

Fig. 3. Flux distributions for reactively scattering IO at eight laboratory angles. ● Experimental distributions obtained from cross-correlation TOF; ○ Calculated best-fit distributions. (XBL 7712-10949)

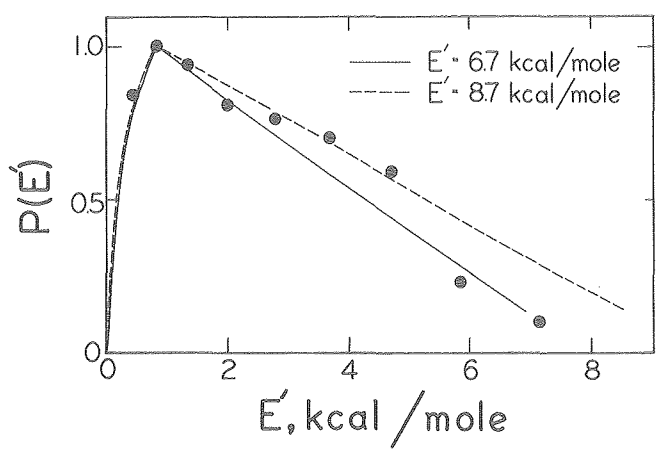

Fig. 4. Experimental product translational energy distribution (●) and calculated RRKM-AM distributions for the reaction O + ICl at a collision energy of 3.3 kcal/mole. (XBL 7712-10931)

In summary, our atomic oxygen reactive scattering program has begun successfully and will now proceed on to the study of combustion reactions with unsaturated hydrocarbons. We hope to determine the product channels and dynamics for these systems. Hopefully these studies will add significantly to our knowledge of the combustion process, since the products from these reactions are highly reactive free radicals that participate in subsequent chain branching reactions.

---

1. D. St. A. G. Radlein, J. C. Whitehead and R. Grice, Nature 253, 37 (1975).

2. R. A. Durie and D. A. Ramsay, Can. J. Phys. 36, 45 (1958).

3. D. D. Parrish and D. R. Herschbach, J. Am. Chem. Soc. 95, 6133 (1973).

4. D. St. A. G. Radlein, J. C. Whitehead and R. Grice, Mol. Phys. 29, 1813 (1975).

5. S. A. Safron, N. D. Weinstein, D. R. Herschbach and J. C. Tully, Chem. Phys. Lett. 12, 564 (1972).

2. REACTIONS OF O + C_2H_5I AND O + CF_3I

R. J. Buss and S. J. Sibener

Recent studies of energy randomization in long lived complexes have suggested that coupling between high and low frequency vibrations may be sufficiently weak as to prohibit the complete redistribution of energy. In the reactions of chlorine atoms with several bromo-olefins, both the vibrational and translational energy distributions exhibit nonstatistical behavior. Using the technique of crossed molecular beams, we have obtained product translational energy distributions for the iodine abstraction reactions:

$$O + C_2H_5I \longrightarrow IO + C_2H_5 \qquad (1)$$

$$O + CF_3I \longrightarrow IO + CF_3. \qquad (2)$$

While the IO product velocity distribution from reaction (2) agrees well with statistical predictions, that for reaction (1) deviates from the theoretical.

The oxygen atom beam was produced by RF discharge of a mixture of 5% O_2 in argon, at about 200 Torr pressure. The peak velocity was measured to be 1.29×10^5 cm/s and the mach number about 4. The ethyl iodide was run at vapor pressure from a 316 K oil bath, which produced a peak velocity of 6.5×10^4 cm/s and mach number 10. With 250 Torr CF_3I behind the 0.13 mm nozzle, the peak velocity was 3.4×10^4 cm/s and the mach number, 6.4. The collision energy for both systems was about 3.3 kcal/mole.

The laboratory angular distributions are shown in Fig. 1, with error bars giving the 95% confidence limit for twelve scans. The IO product, mass 143, peaks at the center of mass, as expected from the

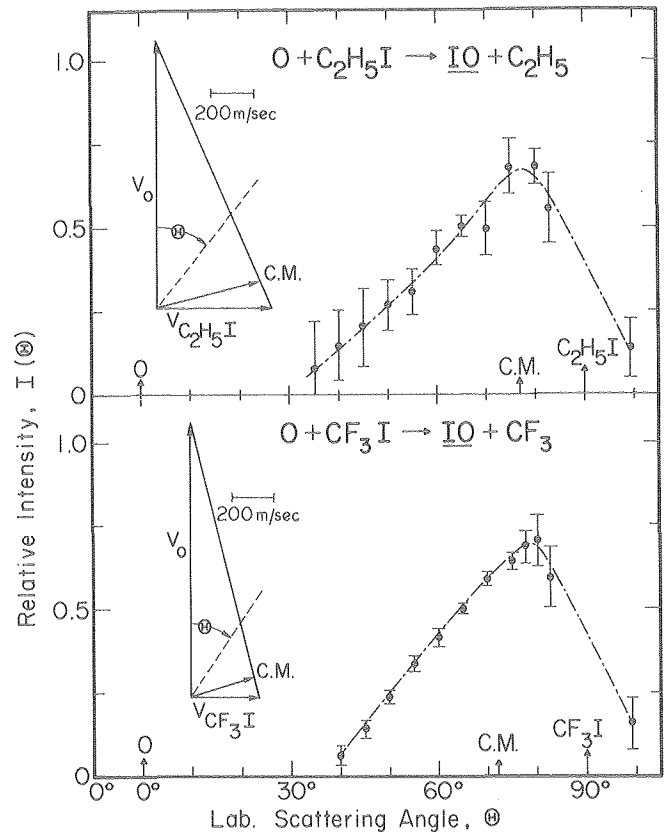

Fig. 1. Experimental laboratory angular distributions of IO product from the reaction of oxygen atoms with C_2H_5I and CF_3I. (XBL 7712-10935)

relative mass of the two fragments and the low exoergicity of the reaction. In both systems the information on the backward scattered product is insufficient to establish the presence of forward/backward symmetry. Velocity information obtained by cross-correlation time of flight of the product was used to produce the translational energy distributions shown in Figs. 2 and 3. It is significant that both distributions begin at zero energy, hence the products do not descend a repulsive barrier in the exit channel.

Shown in Fig. 2 are three RRKM calculations in which the exoergicity is varied. Angular momentum has been treated as described by Safron et al.[1] The agreement of the observed data is such that bounds can be set on the energetics of the reaction, $\Delta H = 0 \pm 1$ kcal/mole. Using published data for the ΔH_f of CF_3I and CF_3[2] we obtain an IO bond energy 53 ± 1 kcal/mole, in good agreement with that deduced from the reaction of O + ICl.[3]

The full RRKM calculation for the C_2H_5I reaction, with all vibrational modes assumed to be active and the IO bond energy 54 kcal/mole, is shown in Fig. 3. Substantially more translational energy is observed in the products than is predicted. Even when the exoergicity is assumed to be 4 kcal/mole (dashed

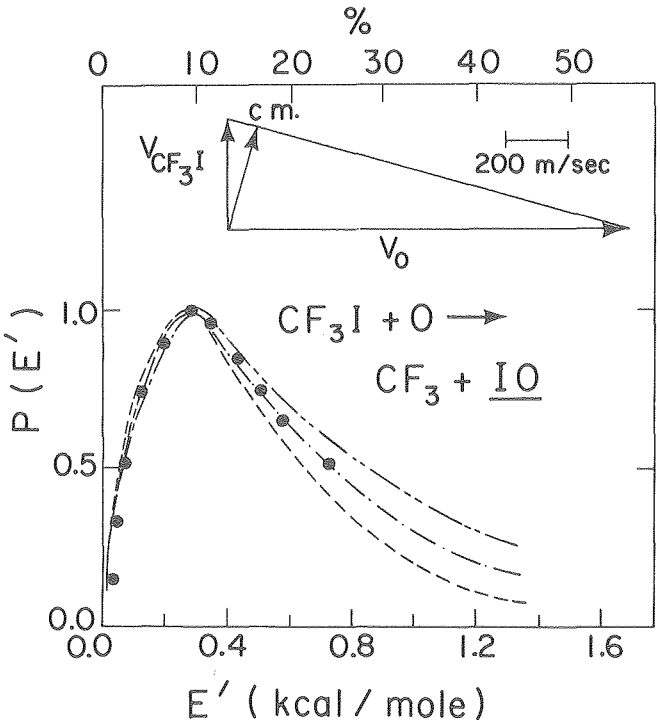

Fig. 2. ● Observed product translational energy distribution of IO.

- - - - - RRKM Calculation ΔH = + 1.0

— - — RRKM Calculation ΔH = 0.0

— - - — RRKM Calculation ΔH = 1.0

(XBL 7712-11072)

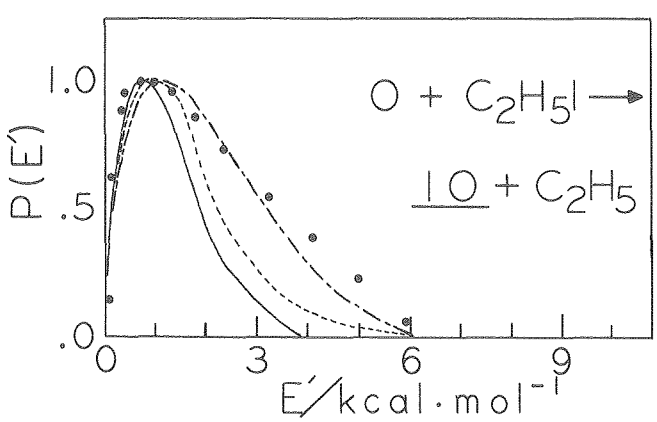

Fig. 3. ● Observed product translation energy distribution of IO.

——— RRKM Calculation ΔH = - 1.0
21 Active Vibrations

- - - - - RRKM Calculation ΔH = - 4.0
21 Active Vibrations

— - — RRKM Calculation ΔH = - 4.0
7 Active Vibrations

(XBL 7712-10965)

curve in Fig. 3) the distribution is considerably narrower than that observed. The RRKM calculation in which hydrogen modes have been removed is in modest agreement with our data. It is of interest to note that for this latter molecule without hydrogen modes, the RRKM lifetime is 0.01 ps, which is far shorter than a rotational period. Indeed it should be difficult for energy to randomize in the time scale of a single vibrational period.

These two reactions provide an interesting comparison. Although the energetics are quite similar, the reaction dynamics are altered by the internal frequency dispersion. It would appear that energy sharing by the hydrogen modes in C_2H_5I is prohibited by the large frequency difference.

---

1. S. A. Safron, N. D. Weinstein, D. R. Herschbach and J. C. Tully, Chem. Phys. Lett. 12, 564 (1972).
2. H. M. Rosenstock, K. Draxl, B. W. Steiner and J. T. Herron, J. of Phys. and Chem. Ref. Data, Vol. 6, 1977, Suppl. No. 1.
3. See preceding article No. 1 in this series.

3. SUBSTITUTION REACTION OF Cl + BROMOPROPENE

R. J. Buss and S. J. Sibener

In chemiluminescence studies of chlorine reacting with bromine-substituted olefins,[1] the product vibrational energy distribution has been shown to be nonstatistical. Calculations in which the energy of the long-lived complex is assumed to be randomly distributed over the internal degrees of freedom, predict more energy in the high frequency modes of the product than is actually observed. This suggests that coupling between the hydrogen modes and the skeletal modes of the complex is sufficiently weak that these high frequency ones do not share the energy released in the collisional activation. A recent study of the $Cl + C_2H_3Br \rightarrow Br + C_2H_3Cl$ in crossed molecular beams[2] has shown that the product translational energy distribution does not agree with that predicted by the statistical theory. More energy appears as product translational than would be expected if all internal degrees of freedom are active in the complex. We have now used crossed molecular beams to look at the product angular and velocity distributions in the reactions of chlorine atoms with the three olefins: 1-bromopropene, 2-bromopropene and allyl bromide. The product translational energy of all three is found to be higher than the statistical theories predict.

The chlorine atoms were produced in a resistively heated graphite oven previously described.[3] Time-of-flight analysis was used to determine the beam's peak velocity, 1.29×10^5 cm/s and its mach number 9.0. The bromo-olefin beams were produced from the vapor pressure above the liquid in an ice bath with argon added to bring the total pressure to 250 Torr. The beams had mach numbers of 11.0. The beams collide at 90°

giving a collision energy of 6.3 kcal/mole. The observed angular distributions are shown in Fig. 1, together with a typical Newton diagram. The error bars are 95% confidence limits on twelve, 100-second scans. The product mass 76.0 was detected as a weak contaminant of the olefin beam, and elastic scattering prevented observation of product scattered backward from the center-of-mass direction. Fractional distillation of the olefin failed to remove the contaminant. Velocity distributions were obtained at 5° intervals using the cross-correlation time-of-flight wheel with counting times of one to three hours at each angle. The product translational energy distributions are shown in Fig. 2.

The results of several statistical calculations are also shown in Fig. 2. Because the addition of bromine to olefins is known to proceed without an activation barrier, the analysis is not complicated by the existence of an exit channel barrier. The energetics of these three reactions (shown in Fig.3) are quite similar. Using group contributions to the internal energy[4] the exoergicity is estimated to be 12.5 kcal/mole and the complex is more stable than the reactants by 18.0 kcal/mole. The RRKM calculations with all internal degrees of freedom active are shown as solid lines in Fig. 2. These distributions peak at lower energy and are far narrower than those observed. The dashed curves are the RRKM calculations in which the hydrogen modes have been removed. In the reactions of 1-bromo and 2-bromopropene, these calculated distributions agree quite well with the observed data. This suggests that the lifetime of the complex is short enough that the energy initially released in formation of

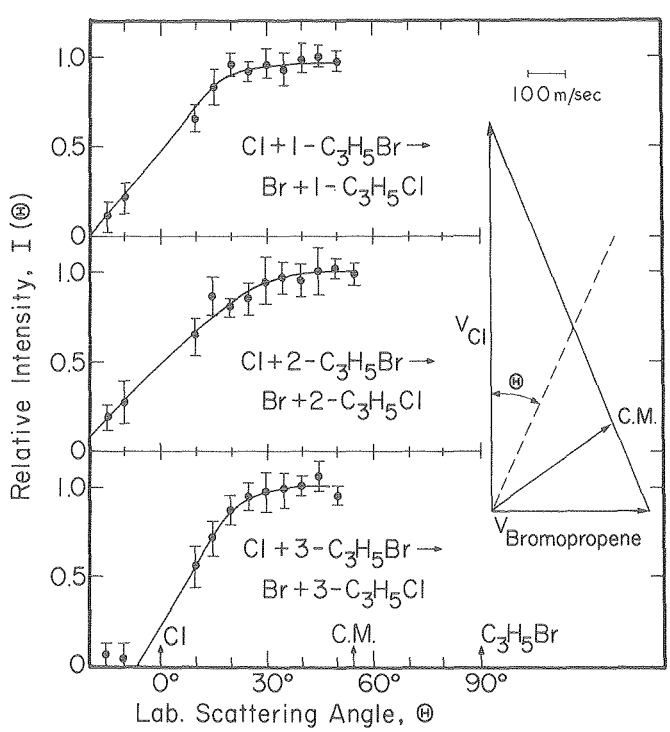

Fig. 1. Experimental laboratory angular distributions of chloropropene produced in the reaction of Cl + C_3H_5Br at collision energy 6.3 kcal/mole.

(XBL 7712-10933)

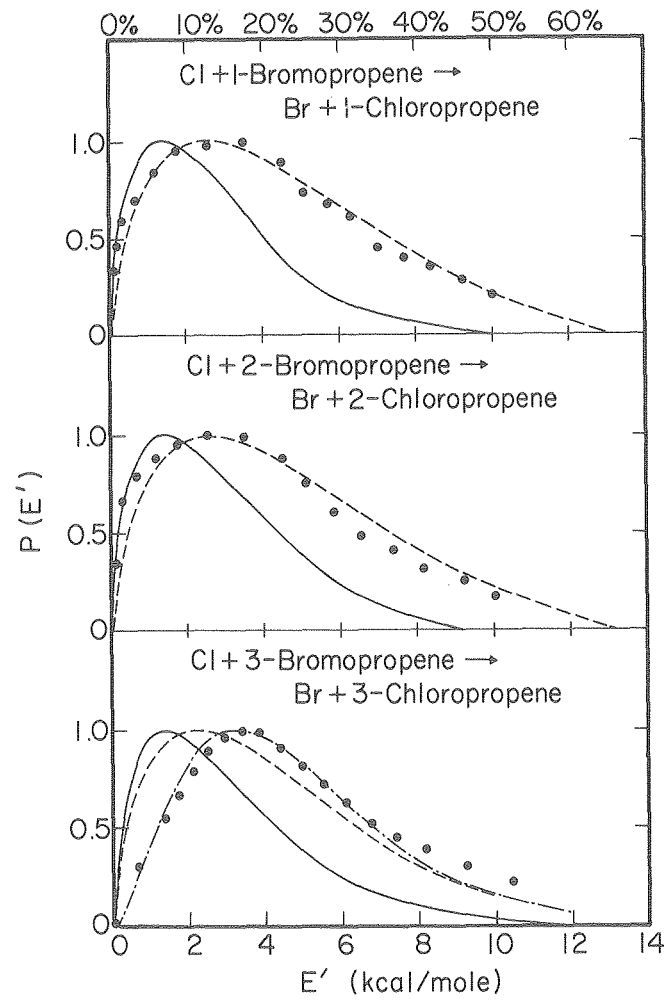

Fig. 2. ● Experimental product translational energy distribution.

——— RRKM-AM Calculation 24 Active Vibrations
– – – – – RRKM-AM Calculation 9 Active Vibrations
— — — — RRKM-Am with modified angular momentum treatment 24 Active Vibrations

(XBL 7712-10906)

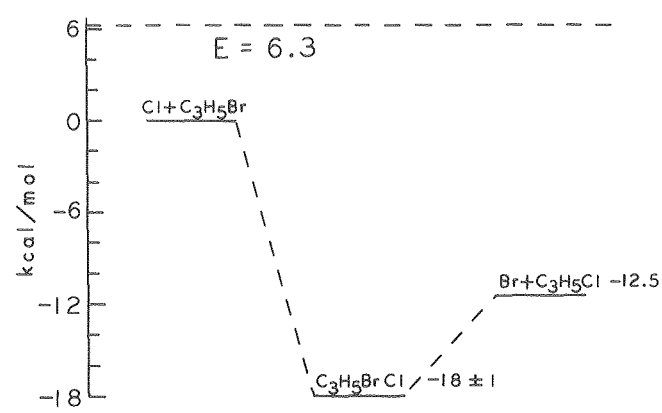

Fig. 3. Energetics of the reaction Cl + C_3H_5Br → Br + C_3H_5Cl.

(XBL 7712-10929)

the carbon chlorine bond remains in the vibrations of the heavy atoms. This description is inadequate to explain the three-bromopropene results.

The angular momentum in these reactions is treated according to the method proposed by Safron et al.[5] The model assumes that for a loose complex the distribution of angular momentum will be linear in impact parameter up to a maximum value and zero thereafter. This approximation might be expected to be satisfactory for complexes in which the reactive site is coincident with the center of mass. In the reaction of chlorine with three-bromopropene, the chlorine must attack the double bond which is considerably removed from the center of mass. Thus the angular momentum of the complexes might be considerably higher, on the average, than the linear approximation can allow. When the distribution of angular momentum in the complexes is changed to $P(b) = b^n$, with $n > 1$, the theory will predict more energy going to translation. In Fig. 2 the calculated distribution for $n = 3$ with all vibrations active gives a reasonably good fit to the data.

It is clear that the RRKM-AM calculation does not predict the correct product translational energy. This observation supports the results of the chemiluminescence experiments. As with the vinyl bromide reaction, there remains some doubt whether the angular momentum treatment is adequate for these reactions. We hope to answer this question by lowering the collision eneegy, thereby reducing the effect of angular momentum to a minimum.

---

1. J. F. Durana and J. D. McDonald, J. Chem. Phys. 64, 2518 (1976).

2. M. Coggiola, R. Buss and Y. T. Lee, unpublished results.

3. James Joseph Valentini, Reactive Scattering of Halogen Molecules, (Ph.D. thesis), LBL-5746, November 1976.

4. S. W. Benson, Thermochemical Kinetics, John Wiley and Sons, Inc., New York, 1968.

5. S. A. Safron, N. D. Weinstein, D. R. Herschbach and J. C. Tully, Chem. Phys. Lett. 12, 564 (1972).

4. IMPROVED POTENTIALS FOR Ar-Kr AND Ar-Xe

C. H. Becker and R. J. Buss

The study of interatomic potentials for rare gas pairs has become extensive in the last few years.[1] Yet the least well-known systems are heavier asymmetric pairs: Ar-Kr and Ar-Xe. We report differential cross section [$I(\theta)$] measurements at thermal energies for these systems and use this data, together with existing second virial coefficient data, [$B(T)$], to obtain accurate potential energy functions as a function of internuclear distance [$V(r)$].

The experiments were performed by crossing two supersonic beams of rare gas atoms and detecting the lighter gas in-plane scattering by a rotatable universal detector. Apparatus details are given elsewhere.[2] Two collision energies were studied; the argon beam was produced at room temperature and at approximately 2040 K by a resistively heated graphite oven/nozzle;[3] the Kr and Xe beams were at room temperature using a quartz nozzle. The supersonic beam velocity peaks and distributions were monitored by time-of-flight technique. The velocity spread of the beam ranges from 8 to 15% FWHM depending on temperature and operating conditions.

Analysis proceeds by assuming a flexible analytic form for the interatomic potential; we use a Morse function of well depth ε for $r \leq r_m$ (minimum position), another Morse function at $r > r_m$, then a Hermite polynomial spline function leading to the long range Van der Waals terms (MMHV potential):

$$f(x) = V(r)/E \qquad x = r/r_m \qquad c_i = c_i/(\varepsilon r_m^i)$$

$$\begin{aligned}
f(x) &= \exp[2\beta_1(1-x)]-2\exp[\beta_1(1-x)] && 0 < x \leq 1 \\
&= \exp[2\beta_2(1-x)]-2\exp[\beta_2(1-x)] && 1 < x \leq x_1 \\
&= b_1 + (x-x_1)[b_2+(x-x_1)\, b_3 \\
&\qquad + (x-x_1)b_4\,] && x_1 < x < x_2 \\
&= c_6\, X^{-6} + c_8\, X^{-8} + c_{10}\, X^{-10} && x_2 \leq x < \infty
\end{aligned}$$

With a given potential the differential cross sections [$I(\theta)$] were calculated by the Rayleigh-Faxen-Holtsmark partial wave expansion utilizing JWKB phase shifts. Comparison with experiment for goodness of fit criteria was made by calculating

$$\chi^2 = \sum_{i=1}^{N} \left(\frac{I_i^{expt} - \alpha I_i^{calc}}{\sigma_i} \right)^2 ,$$

where I_i is at scattering angle θ_i, N is the number of data points, σ_i is one standard deviation in the data at θ_i, and α is a normalization constant necessary because our I_i^{expt} are relative values. The value of α is determined by minimization of χ^2.

The fitting of the potential to the $I(\theta)$ data is carried out with the low energy $I(\theta)$ by a nonlinear least squares technique due to Marquardt.[4] Very accurate C_6 constants are given by Starkschall and Gordon.[5] Good estimates of C_8 and C_{10} were taken from Cohen and Pack's[6] work (using their lower bounds). The value of x^2 was chosen after examining its affect on the calculated $I(\theta)$; it is consistent with the theoretical prediction of the location of electron overlap. The values of ε, r_m. β_2, and

$f(x_1)$ were simultaneously varied starting with a reasonable first guess. Here $f(x_1)$ is the functional value at the Morse-spline joining point, fixing x_1. Then the effect of β_1 [repulsive part of V(r)] was examined using the high energy I(θ) and B(T). These results for β_1 were in turn used in the nonlinear least squares fitting and the new results checked with B(T) and the high energy I(θ). This process was continued until a confidence in parameter convergence was reached. All I(θ) calculations take into account beam-detector resolution and beam velocity spread. No less than nine Newton diagrams were used in any calculation.

The final potential parameters are given in Table 1 and the comparison of the calculated second virial coefficient, B(T), with experiment[7] is in Table 2. First and second quantum corrections[8] to classical B(T) calculations were used. Comparison of I(θ) calculated and experiment is shown in Fig. 1. The potentials are shown in Fig. 2.

Due to the energy range of these experiments the given V(r) can be considered valid only up to approximately 13 kcal/mole on the repulsive walls. More complete potentials can be constructed by using Hartree-Fock self-consistent-field theory or Thomas-Fermi-Dirac statistical theory evaluation of the repulsive wall. Alternatively, new estimates of A and b for the repulsive Born-Mayer form V(v) = A exp(-br) can easily be evaluated following the method of Tang and Toennies,[9] using only the values of ε, R_m, and van der Waals constants.

Table 1. MMHV potential parameters for Ar-Kr and Ar-Xe.

	Ar - Kr	Ar - Xe
ε(kcal/mole)	.33749	.37859
r_m (Å)	3.83145	4.01028
r_o (Å)	3.42287	3.58263
β_1	6.4	6.5
β_2	6.77887	6.33309
C_6 (kcal/mole Å^6)	1304.	1957.
C_8 (kcal/mole Å^8)	7293.	12005.
C_{10} (kcal/mole Å^{10})	51241.	93502.
$f(x_1)$	-.82407	-.75192
X_1	1.08021	1.10884
X_2	1.45000	1.45000
b_1	-.82407	-.75192
b_2	3.30144	3.16650
b_3	-5.22773	-5.52469
b_4	3.11383	3.80547

Table 2. Experimental[7] and calculated values of second viral coefficients B(T) cc/mole.

	T(°K)	B_{expt}	B_{calc}	$B_{expt}-B_{calc}$
	148.15	-1.3127E + 02	-1.2963E + 02	-1.644
	173.15	-9.8850E + 01	-9.7269E + 01	-1.581
Ar - Kr	198.15	-7.5900E + 01	-7.5143E + 01	-.757
	223.15	-5.9600E + 01	-5.9102E + 01	-.498
	273.15	-3.7240E + 01	-3.7480E + 01	.240
	323.15	-2.3430E + 01	-2.3652E + 01	.222
	standard deviation = 1.0106			
	173.15	-1.4124E + 02	-1.4051E + 02	-.729
	198.15	-1.0802E + 02	-1.0945E + 02	1.429
Ar - Xe	223.15	-8.6500E + 01	-8.7129E + 01	.629
	273.15	-5.6220E + 01	-5.7299E + 01	1.079
	323.15	-3.6740E + 01	-3.8367E + 01	1.627
	standard deviation = 1.1646			

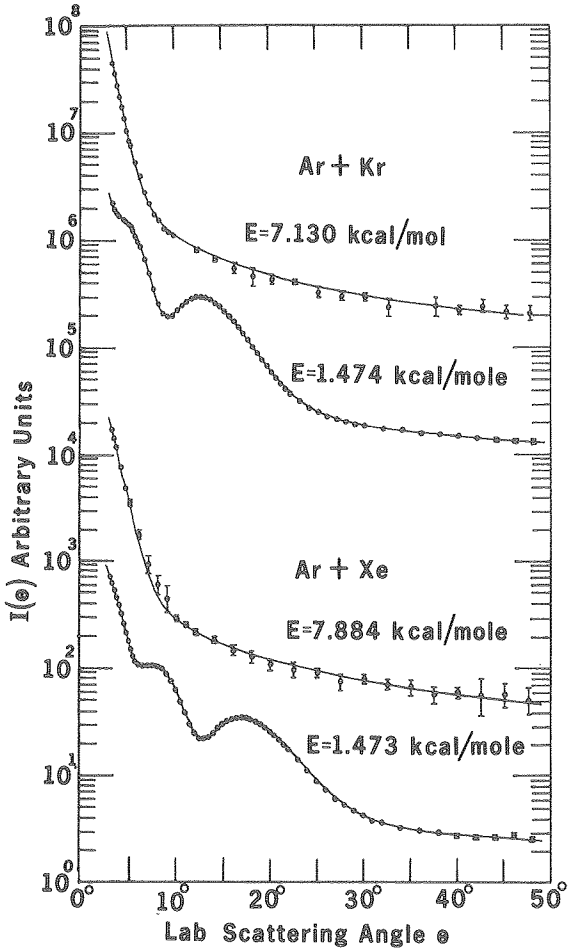

Fig. 1. Experimental and calculated values of the differential cross sections I(θ) for Ar-Kr and Ar-Xe. (XBL 7712-10938)

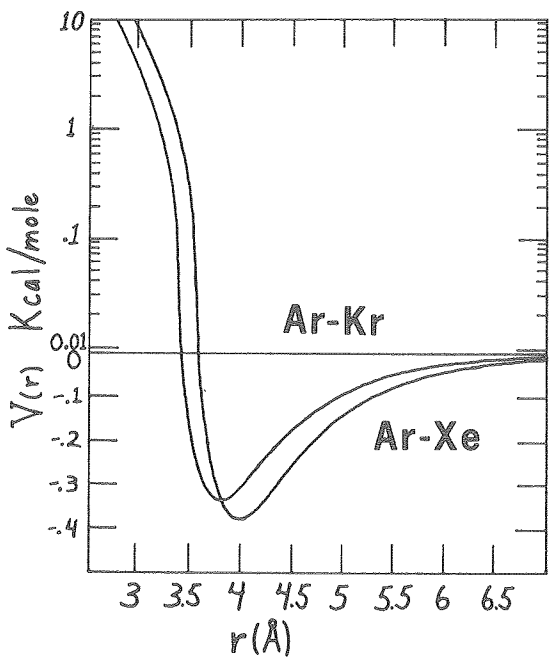

Fig. 2. Derived interatomic potential functions V(r) for Ar-Kr and Ar-Xe. (XBL 7712-10922)

1. See, e.g., J. M. Farrar, T. O. Schafer and Y. T. Lee, AIP Conference Proceedings No. 11, Transport Phenomena (1973), and references cited.

2. J. M. Parson, P. E. Siska and Y. T. Lee, J. Chem. Phys. 56, 1511 I1972); Y. T. Lee, J. D. McDonald, P. R. LeBreton and D. R. Herschbach, Rev. Sci. Instrum. 40, 1402 (1969).

3. J. J. Valentini, M. J. Coggiola and Y. T. Lee, Rev. Sci. Instrum. 48, 58 (1977).

4. D. W. Marquardt, J. Soc. Ind. Appl. Math 11, 431 (1963).

5. G. Starkschall and R. G. Gordon, J. Chem. Phys. 54, 663 (1971).

6. J. S. Cohen and R. T. Pack, J. Chem. Phys. 61, 2372 (1974).

7. J. Brewer, U. S. Bureau of Standards, AD663-448, (1967).

8. J. O. Hirschfelder, C. F. Curtiss and R. B. Bird, Molecular Theory of Gases and Liquids (Wilery, New York, 1964), Chap. 6.

9. K. T. Tang and J. P. Toennies, J. Chem. Phys. 66, 1496 (1977).

5. PROTON AFFINITIES OF HYDROGEN FLUORIDE AND ITS CLUSTERS DETERMINED IN MOLECULAR BEAM—PHOTOIONIZATION EXPERIMENTS*

P. W. Tiedemann, S. T. Ceyer and C. Y. Ng

The proton affinity of a compound is defined as the negative of the enthalpy variation in the process

$$A + H^+ \longrightarrow AH^+ \qquad PA(A) = -\Delta H$$

When gas-phase proton affinities became available many processes in solution involving proton transfer could be rationalized, since previously it was not known to what extent the solvent could change the intrinsic properties of the reactants.[1] Also, thermochemical quantities for unstable neutrals have been obtained using proton affinity scales.[2]

Proton affinities have been determined mainly through appearance potential measurements and the qualitative occurrence-nonoccurrence of proton transfer reactions. The first method suffers from the difficulty of finding a suitable precursor molecule from which the protonated species of interest can be formed in its ground state; the second method provides only relative proton affinities.

In this laboratory it was found that van der Waals dimers produced in the supersonic expansion of a gas of hydrogen containing molecules constitute excellent precursors for the protonated species of these molecules. The protonated molecules are formed by photoionization of the van der Waals dimers and from the threshold energy for this process the proton affinity of the molecule under consideration can be obtained.

The apparatus used in these experiments consists of a differentially pumped supersonic beam source and a windowless vacuum ultraviolet source whose light is dispersed in a 1m near normal incidence

monochromator; the light beam crosses the molecular beam and the ions produced are mass analyzed in a quadrupole filter and detected using pulse counting techniques.[3]

An HF beam was produced by expanding the gas from 400 Torr through a 0.13 mm nozzle. Besides the dimer, $(HF)_2$, evidence for larger clusters, up to $(HF)_5$ was obtained. The following processes were observed:

$$HF + h\nu \longrightarrow HF^+ + e^-$$

$$(HF)_n + h\nu \longrightarrow (HF)_{n-1}H^+ + F + e^-$$

$$n = 1 - 5$$

It is noteworthy that no signal for ionized polymers, $(HF)_n^+$, was observed, only for protonated species, $(HF)_nH^+$. Figure 1 shows the photoionization efficiency curves, i.e., ion flux divided by photon flux as a function of wavelength, for the various processes observed. (Inclusion of data for n = 5 didn't seem justified due to the comparatively larger uncertainties in the data for this case.) In order to verify that H_2F^+ is a fragment that only comes from $(HF)_2$, temperature studies in which the nozzle was heated were carried out. Above 200°C the molecular beam contains only HF and $(HF)_2$; above 300°C only the monomer is present. The thresholds measured at elevated nozzle temperatures agree well with those obtained at room temperature.

The ionization potential of HF was found to be 15.98 ± 0.04 eV, in agreement with previous measurements.[4] The appearance potential of H_2F^+ is 15.65 ± 0.04 eV. Previous evidence[5,6] leads to the assumption that H_2F^+ is formed by dissociative ionization of $(HF)_2$. Near threshold one of the HF molecules in the $(HF)_2$ van der Waals complex is ionized to the $^2\pi$ state; the rise in the photoionization efficiency curve at 661 Å is due to formation of HF^+ in the complex in the $^2\Sigma^+$ excited state of HF^+.[4] This rise can also be seen in the protonated dimer and trimer curves. Using the dissociation energy of $(HF)_2$ into HF molecules[7] and the dissociative ionization energy of HF into H^+ and F,[4] the proton affinity of HF is calculated as 4.09 ± 0.06 eV or 94.3 ± 1.4 kcal/mole. This is illustrated in more detail in Fig. 2, which includes the energetics for the higher clusters. The proton affinity can be considered as the solvation energy of a proton by one hydrogen fluoride molecule. Figure 2 shows that attachment of additional HF molecules to the proton lowers the energy of the system by successively smaller amounts. Thus, the solvation energy of a proton by one HF molecule is 94.3 ± 1.4 kcal/mole, by two HF molecules the solvation energy is 119 ± 3 kcal/mole and by three molecules, 134 ± 5 kcal/mole. From the energy diagram in Fig. 2 it is also possible to calculate the proton affinity of the HF dimer (113 ± 2 kcal/mole) and of the trimer (121 ± 4 kcal/mole).

In order to relate the proton affinity of HF to proton affinities of other compounds, for which many tables have recently appeared in the literature,[8,9] the 0 K value determined has to be converted to 298 K, yielding 95.5 ± 1.4 kcal/mole. (The heat capacity of H_2F^+ as a function of temperature has been approximated by that of the isoelectronic species H_2O.)[10]

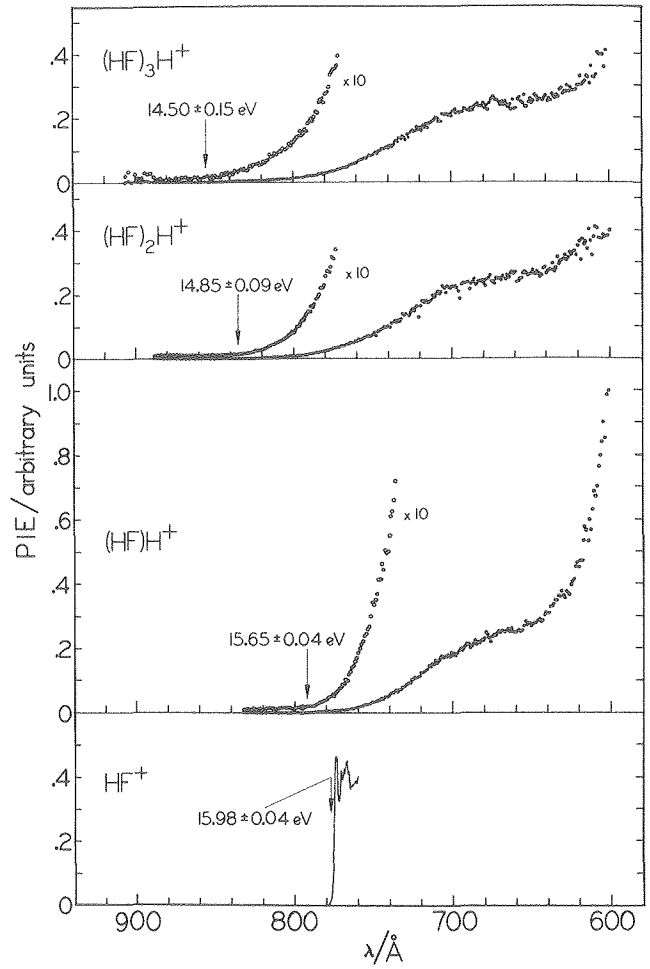

Fig. 1. Photoionization efficiency curves for HF^+, H_2F^+, $(HF)_2H^+$ and $(HF)_3H^+$. (XBL 779-4881)

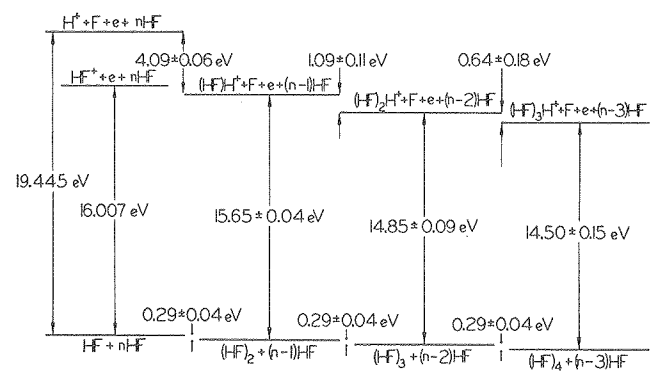

Fig. 2. Energy diagram for the HF system upon photoionization. (XBL 779-4880)

Ion cyclotron resonance studies led to an HF proton affinity of 112 ± 2 kcal/mole.[11] The reason for the disagreement between this result and the present one is not clear, mainly in light of the good agreement in the H_2O[5] and NH_3[6] cases. Since no $(HF)_2^+$ is observed, excess energy might be involved in the H_2F^+ formation, leading to a higher threshold for H_2F^+ appearance and thus to a lower proton affinity for HF. (In the water and ammonia systems $(H_2O)_2^+$ and $(NH_3)_2^+$ were observed.) This possibility is being

further investigated and in the course of these experiments the molecular beam-photoionization method will certainly provide more interesting and valuable thermochemical data.

---

*This work was carried out in collaboration with Professor Bruce H. Mahan's group.

1. J. F. Wolf, P. G. Harch and R. W. Taft, J. Am. Chem. Soc. 97, 2904 (1975).
2. D. J. DeFrees, R. T. McIver, Jr. and W. J. Hehre, J. Am. Chem. Soc. 99, 3853 (1977).
3. C. Y. Ng, B. H. Mahan and Y. T. Lee, J. Chem. Phys. 65, 1956 (1976).
4. J. Berkowitz, W. A. Chupka, P. M. Guyon, J. H. Holloway and R. Spohr, J. Chem. Phys. 54, 5165 (1971).
5. D. J. Trevor, P. L. Kronebusch, C. Y. Ng and Y. T. Lee, MMRD Annual Report for 1976, Lawrence Berkeley Laboratory, University of California, p.365.
6. See following article No. 6.
7. G. C. Pimentel and A. L. McClellan, The Hydrogen Bond, H. W. Freeman Co., San Francisco, 1960, p.212.
8. R. Yamdagni and P. Kebarle, J. Am. Chem. Soc. 98, 1320 (1976).
9. J. F. Wolf, R. H. Staley, I. Koppel, M. Taagepera, R. T. McIver, Jr., J. L. Beauchamp and R. W. Taft, J. Am. Chem. Soc. 99, 5417 (1977).
10. JANAF Thermochemical Tables, Nat. Stand. Ref. Data Ser. 37, NBS, US, June 1971.
11. M. S. Foster and J. L. Beauchamp, Inorg. Chem. 14, 1229 (1975).

6. THERMOCHEMICAL QUANTITIES OF NH_3 AND ITS CLUSTERS*

P. W. Tiedemann and S. T. Ceyer

Photoionization studies of clusters of NH_3 were performed in a similar manner to the HF studies. The NH_3 cluster beam was formed by expansion of neat NH_3 at about 1000 Torr through a 0.003 in. diam nozzle. The photoion yield curves for $(NH_3)_2^+$, NH_4^+, $(NH_3)_2H^+$, $(NH_3)_3H^+$ are shown in Figs. 1 and 2. Unlike the HF polymers, stable parent ions $(NH_3)_n^+$ n = 2 - 6 were observed due to a stronger chemical interaction between the nitrogen lone pair of the neutral and the ion. From a measure of the difference of the ionization potential of the monomer[1] and that of the dimer and a value for the neutral-neutral NH_3 interaction[2] the NH_3 ion-neutral interaction well depth is at least 18.36 ± 1.8 kcal. When the internal energy of the dimer species is increased by 0.052 eV, the onset of the NH_4^+ fragment is observed. The appearance potential of the fragment ion is used to calculate the proton affinity of NH_3 via the thermochemical cycle shown below.

$NH_3 + NH_3 \longrightarrow (NH_3)_2$	-4.0 ± .5	
$(NH_3)_2 \longrightarrow NH_4^+ + NH_2 + e$	221.1 ± .4	
$NH_2 + H \longrightarrow NH_3$	-106.0 ± 1.1	(Ref. 3)
$H^+ \longrightarrow H$	-313.6	
$NH_3 + H^+ \longrightarrow NH_4^+$	-202.5 ± 2.0 kcal	

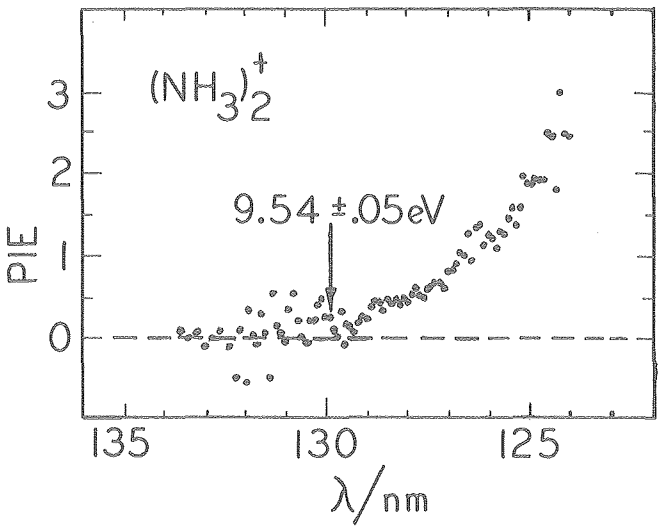

Fig. 1. Photoionization efficiency of $(NH_3)_2^+$ normalized at 1160 Å. (XBL 7712-10928)

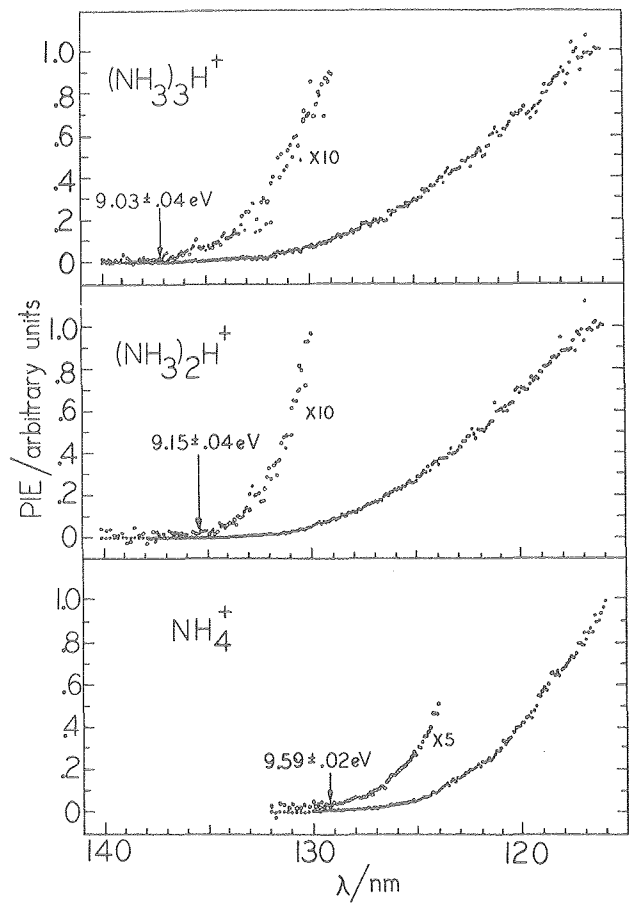

Fig. 2. Ion yields of NH_4^+, $(NH_3)_2H^+$ and $(NH_3)_3H^+$ normalized at 1160 Å. (XBL 7712-10939)

The proton affinity becomes 203.9 kcal when corrected to 298 K. This value compares favorably with the proton affinity value of 202.3 obtained by recent equilibrium proton transfer experiments at 298

K.[4] The previously accepted value for the proton affinity of NH_3 was 207 ± 3 kcal/mole. Appearance potential measurements of the higher polymers, $(NH_3)_2H^+$ a fragment from $(NH_3)_3^+$ and $(NH_3)_3H^+$ a fragment from $(NH_3)_4^+$ were also carried out. These values as well as the neutral-neutral ammonia interaction allow the solvation energy of an ammonium ion or the protonated dimer species by an ammonia molecule to be calculated via the cycles shown below.

$(NH_3)_3 \longrightarrow (NH_3)_2H^+ + NH_2 + e$	211.0	± .8
$NH_4^+ + NH_2 + e \longrightarrow (NH_3)_2$	-221.0	± .4
$(NH_3)_2 + NH_3 \longrightarrow (NH_3)_3$	-4.0	± 1.0
$NH_4^+ + NH_3 \longrightarrow (NH_3)_2H^+$	-14.0	± 2.2
$(NH_3)_4 \longrightarrow (NH_3)_3H^+ + NH_2 + e$	208.3	± 1.0
$(NH_3)_2H^+ + NH_2 + e \longrightarrow (NH_3)_3$	-211.0	± 0.8
$(NH_3)_3 + NH_3 \longrightarrow (NH_3)_4$	-4.0	± 1.0
$(NH_3)_2H^+ + NH_3 \longrightarrow (NH_3)_3H^+$	-7.0	± 2.8

A plot of the log of the photoion fragmentation efficiency of NH_4^+ vs log $(E-E_{threshold})$ is shown in Fig. 3 for the threshold region. There is a distinct change in slope at $\lambda = 1274$ Å that corresponds to the calculated threshold for photodissociation of $(NH_3)_3$ into NH_4^+, NH_3 and NH_2. Similarly, a distinct change in slope of the threshold behavior of $(NH_4^+)NH_3$ occurs upon photodissociation of $(NH_3)_4$ into $(NH_4^+)(NH_3)$, NH_3 and NH_2. Thus the solvation energies for the ammonium ion that are calculated from experimental thresholds are consistent with the observed increases in photoion fragmentation efficiency of the next lower polymer ion. Our solvation energies, however, do not agree well with the gas phase equilibrium solvation energies obtained for the ammonium ion in a high pressure ion source mass spectrometer (Table 1).[5] If one assumes that the difference in energies is due to vibrational excitation of the resulting ion in the photoionization experiments and that the kinetic energy of the electron is zero then the $NH_4^+(NH_3)_2$ produced will have (42.3 - 21) = 21.3 kcal of excitation energy. This value is larger than the dissociation energy of 17.5 kcal for $NH_4^+(NH_3)_2$ measured by Kebarle. Thus, the two sets of values are inconsistent, the reason for which is not clear at this time.

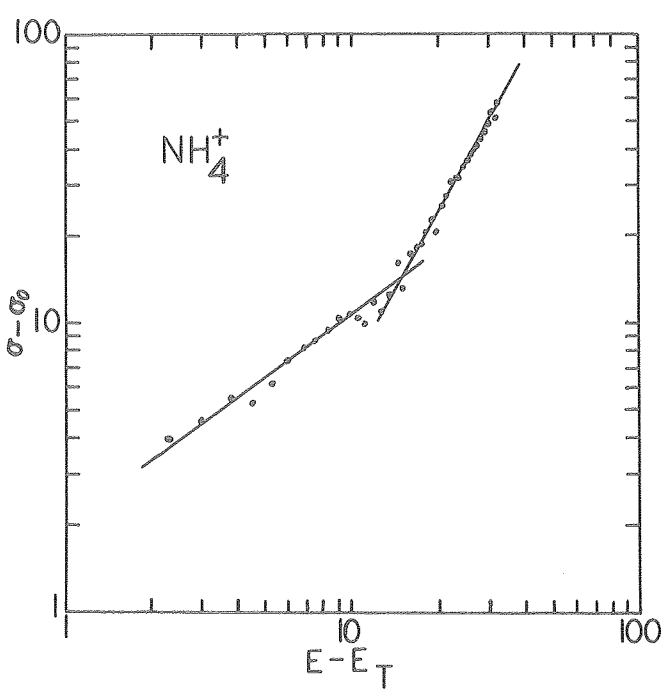

Fig. 3. Log $(\sigma - \sigma_B)$ where σ = photoionization efficiency, σ_B = baseline vs log $(E - E_T)$ where E_T = threshold energy for NH_4 formation. (XBL 7712-10924)

Table 1.

$$NH_4^+(NH_3)_n \longrightarrow NH_4^+(NH_3)_{n-1} + NH_3$$

n, n-1	ΔH^o_o (kcal/mol) This work	ΔH^o_{298} (kcal/mol) Literature[5]
1, 0	14 ± 2.8	24.8 ± 0.4
2, 1	7 ± 2.8	17.5 ± 0.2

*This work was carried out in collaboration with Professor Bruce H. Mahan's group.

1. H. M. Rosenstock, K. Draxl, B. W. Steiner, and J. T. Herron, J. Phys. Chem. Ref. Data 6, Suppl. 1, 1977.
2. G. C. Pimental and A. L. McClellan, The Hydrogen Bond, W. H. Freeman Co., San Francisco, 1960, p. 221.
3. D. K. Bohme, R. S. Hemsworth and H. W. Rundle, J. Chem. Phys. 59, 77 (1973).
4. J. F. Wolf, R. H. Staley, I. Koppel, M. Taagepera, R. T. McIver, Jr., J. L. Beauchamp and R. W. Taft, J. Am. Chem. Soc. 99, 5417 (1977).
5. J. D. Payzant, A. J. Cunningham and P. Kebarle, Can. J. Chem. 51, 3242 (1973).

7. PHOTOIONIZATION STUDIES OF $(C_2H_4)_2$ and $(C_2H_4)_3$*

S. T. Ceyer and P. W. Tiedemann

In most exothermic ion-molecule reactions, the total energy of the system is often large compared to the activation energy barriers along the reaction coordinate for rearrangments or decompositions. This condition prevents the determination of these barriers and the stabilities of reaction complexes in

an experiment involving two-body collisions. However, if the initial reactant is an ion-cluster, not only can one determine the stability of the ion cluster from the threshold energy of formation, but also the highest barrier can be determined provided that the vibrational degrees of freedom could be excited precisely to overcome the potential energy barrier of chemical reactions. We have formed the ion cluster by photoionization of polymers produced by adiabatic expansion in a beam. For example, photoionization of $(C_2H_4)_2$ can be viewed as ionization of only one of the C_2H_4 molecules. Once ionized, further excitation of the dimer allows the zero kinetic energy ion-molecule reaction to proceed. Fragmentation of the dimer ion is a common pathway.

The $(C_2H_4)_2$ and $(C_2H_4)_3$ systems were investigated and their photoion yield and photoion fragment yield curves are shown in Figs. 1 and 2. The appearance potentials for $(C_2H_4)_2^+$ and $(C_2H_4)_3^+$ along with the ionization potential of C_2H_4[1] and the neutral interaction energy of 0.42 ± 0.03 kcal[2,3] yield the $(C_2H_4)^+$ C_2H_4 well depth as 18.2 ± 0.7 kcal and the $(C_2H_4)_2^+$ C_2H_4 well depth as 4.2 ± 1.0 kcal.

$2C_2H_4 \longrightarrow (C_2H_4)_2$	$-.42 \pm 0.03$	
$(C_2H_4)_2 \longrightarrow (C_2H_4)_2^+ + e$	224.3 ± 0.5	
$C_2H_4^+ + e \longrightarrow C_2H_4$	-242.1 ± 0.2	
$C_2H_4 + C_2H_4^+ \quad (C_2H_4)_2^+$	-18.2 ± 0.7	kcal
$(C_2H_4)_2 + C_2H_4 \longrightarrow (C_2H_4)_3$	$-.42 \pm 0.03$	
$(C_2H_4)_3 \longrightarrow (C_2H_4)_3^+ + e$	220.5 ± 0.5	
$(C_2H_4)_2^+ + e \longrightarrow (C_2H_4)_2$	-224.3 ± 0.5	
$(C_2H_4)_2^+ + C_2H_4 \longrightarrow (C_2H_4)_3^+$	-4.2 ± 1.0	kcal

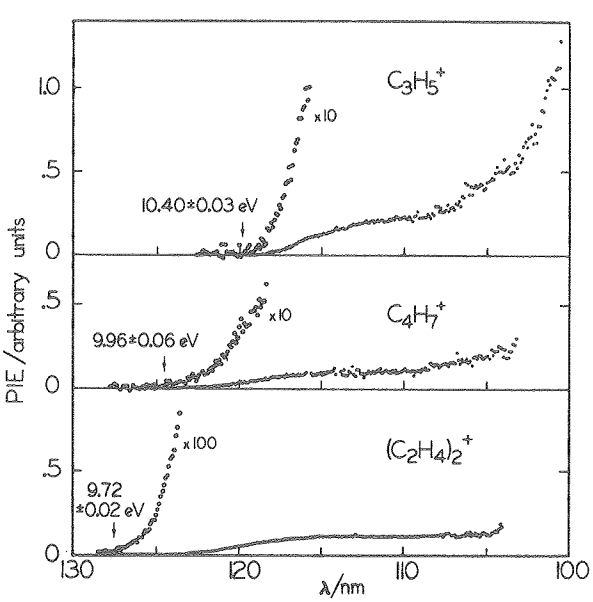

Fig. 1. Photoionization efficiency of $(C_2H_4)_2^+$, $C_3H_5^+$ and $C_4H_7^+$. (XBL 779-4878)

With increased internal excitation both the dimer and the trimer exhibit H atom and CH_3 elimination. The experimental appearance potential for $C_4H_7^+$ yields 206 kcal as its heat of formation in good agreement with tabulated values.[2] Thus, there exists no activation energy barrier for H atom elimination. The experimental appearance potential for $C_3H_5^+$ indicates that there is an activation energy barrier for CH_3 elimination of 15.6 kcal or 8.4 kcal for the reverse reaction employing 226 kcal as the heat of formation of $C_3H_5^+$.[2] This barrier could only be elucidated at zero relative kinetic energy of the ion and molecule. A proposed reaction coordinate is shown in Fig. 3.[4]

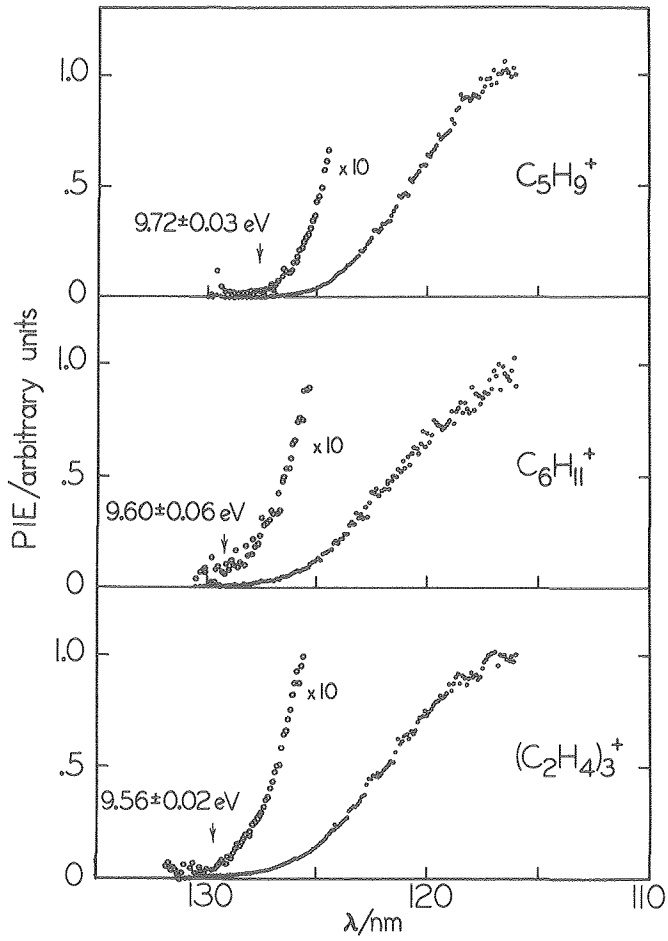

Fig. 2. Photoionization efficiency of $(C_2H_4)_3^+$, $C_5H_9^+$ and $C_6H_{11}^+$. (XBL 779-4879)

The photoionization fragments from the trimer appear to be $C_3H_5^+$ and $C_4H_7^+$ fragments solvated by another ethylene. That is, calculation of the activation energy barrier for the reverse reactions from the experimental appearance potential as compared to tabulated values for the heat of formation of $C_6H_{11}^+$ and $C_5H_9^+$ would yield a barrier unrealistically large. Therefore, the trimer upon ionization does not rearrange into one ion but remains as a solvated complex. From the measured appearance potentials, the well depths of $(C_3H_5^+)(C_2H_4)$ and $(C_4H_7^+)(C_2H_4)$ are calculated as 16.2 ± 1.5 kcal and 8.7 ± 1.9 kcal, respectively. A proposed reaction coordinate is shown in Fig. 4.

The intensity of the photoionization fragments was measured as a function of stagnation pressure and is shown in Fig. 5. The fragments originating from the dimers and trimers can be seen to be clearly separated in stagnation pressure indicating that there is little contamination of the fragments from higher polymers. In addition, the $C_3H_5^+$ and $C_5H_9^+$ fragments peak at much lower pressure than their corresponding parent ions. This may indicate the

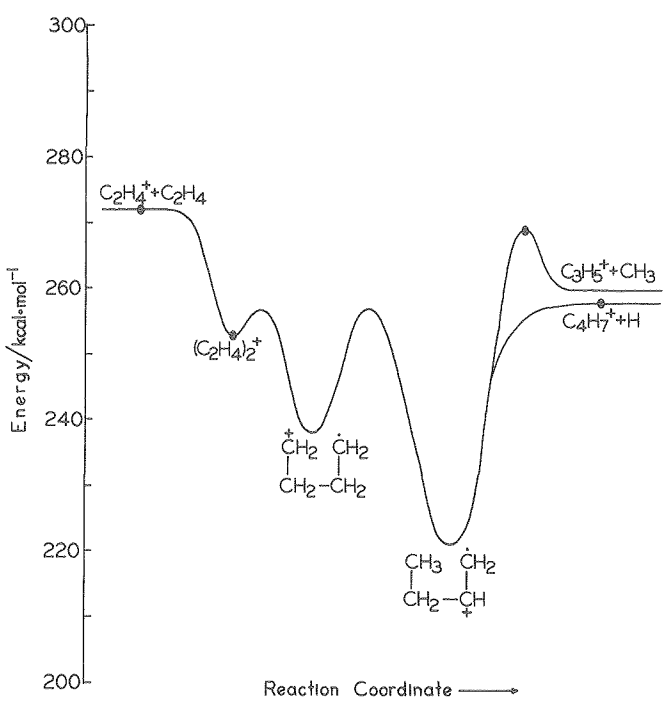

Fig. 3. Reaction coordinate for $(C_2H_4)_2^+$ decomposition. Solid dots indicate experimental values. (XBL 7710-6833)

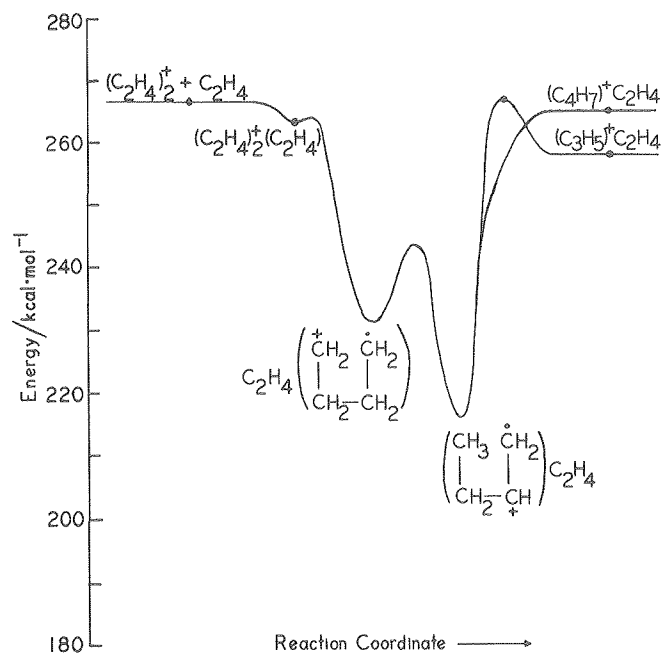

Fig. 4. Reaction coordinate for $(C_2H_4)_3^+$ decomposition. Solid dots indicate experimental values. (XBL 7712-10947)

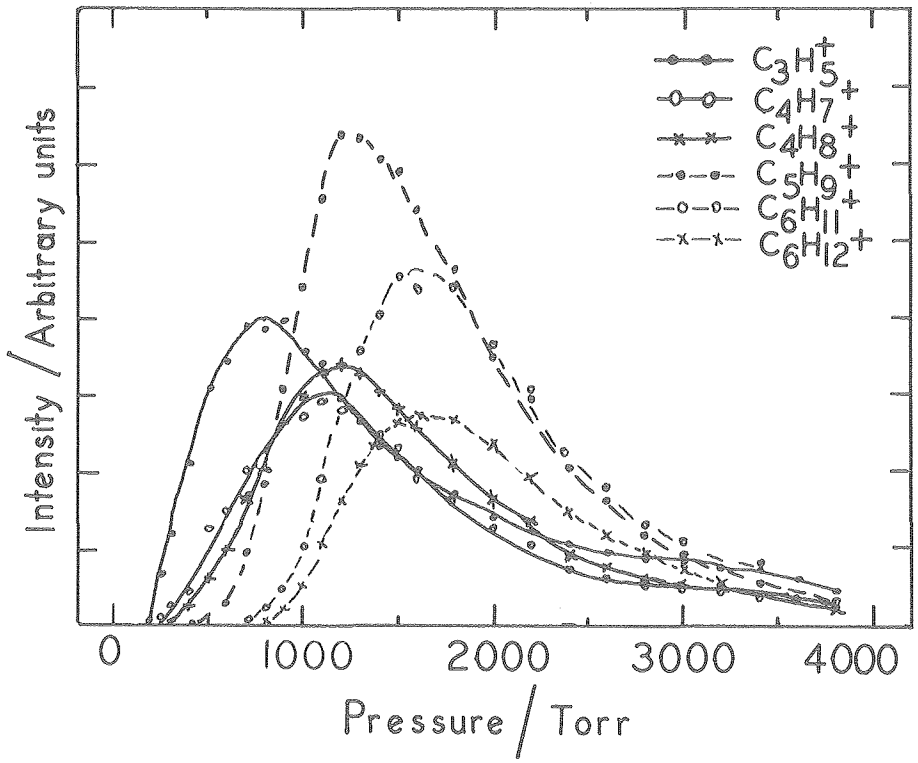

Fig. 5. Intensity of dimers, trimers and fragments at zero order vs pressure of 13% C_2H_4 in Ar behind the nozzle. (XBL 7712-10925)

presence of two discrete van der Waals structures of the neutral dimer and trimer formed in the expansion. A T-shaped dimer fragmenting exclusively to $C_3H_5^+$ would have a larger cross section for collision and thus attenuation would occur at lower stagnation pressures. The $C_4H_7^+$ and $C_4H_8^+$ ions may be formed from an ethylene dimer structure of two parallel planes, a structure that would have a smaller collision cross section. Further investigations are required in order to more fully investigate the structure of van der Waals polymers.

---

*This work was carried out in collaboration with Professor Bruce H. Mahan's group.

1. H. M. Rosenstock, K. Draxl, B. W. Steiner and J. T. Heron, J. Phys. Chem. Ref. Data 6, Suppl. 1 (1977).

2. L. W. Flynn and G. Thodos, Am. Inst. Chem. Eng. J. 8, 362 (1962).

3. J. O. Hirschfelder, C. F. Curtis and R. B. Bird, Molecular Theory of Gases and Liquids (Wiley, New York, 1954).

4. P. R. LeBreton, A. D. Williamson, J. L. Beauchamp and W. T. Huntress, J. Chem. Phys. 62, 1623 (1975).

8. DECOMPOSITION CHANNELS IN MULTIPHOTON DISSOCIATION*

Aa. S. Sudbo, P. A. Schulz and E. R. Grant

The recent interest in multiphoton dissociation (MPD) of polyatomic molecules has revealed quite a bit of confusion as to what the major dissociation channels of some molecules are,[1-5] and whether the dissociation process can be described by a statistical, e.g., RRKM, theory of unimolecular reactions.[4-8] In a gas cell experiment an experimenter often finds great difficulties in answering questions such as: do vibrationally excited molecules react with one another; how do reactions involving free radicals produced in the dissociation proceed; can these radicals decompose further in the presence of the laser field; and does the detection method used actually probe the primary dissociation channel.

Using the molecular beam setup previously described,[9] we have overcome most of these difficulties. We have studied MPD of a number of compounds, mainly halogenated methanes, ethanes and ethylenes, and identified their major dissociation channels. To identify an MPD product, we realize that a unique set of ratios between mass spectrometer signals of various ion fragments must first be established for a given molecular species or radical, and preferably the velocity distributions of the dissociation products should be measured and checked for consistency. In our setup, we could measure both angular and time-of-flight distributions for the fragments, and perform

this check. The low density of molecules in the beam and the extremely low duty cycle in our experiment prevented us from observing the competing minor channels that have very small branching ratios (< 0.1).

In Table 1 we give a list of the molecules we have studied, together with the results and a few parameters describing the experimental conditions. The purpose of heating the nozzle in some of the experiments was to increase the hot-band absorption and thus shift the absorption frequency to a value more easily attainable by our CO_2 TEA laser. A more extensive presentation and analysis of our data will be given elsewhere; here we present only the qualitative results.

The simplest compounds studied were the numbers of the CF_3X series, X = Cl, Br, I. The fragments of MPD were CF_3, detected in the mass spectrometer mainly as CF_2^+ and CF^+, both with identical velocity distributions, and X with a different distribution. The velocity distributions of CF_3 (detected as CF_2^+ and CF^+) and X were correlated by the conservation of linear momentum in the dissociation process. The ratios between the mass spectrometer signals of CF_3^+, CF_2^+ and CF^+ were determined for each of the three cases. The ratios were independent of laser energy fluence and the product translational energy (within the stated uncertainties). With an ionizing electron energy of 200 eV in the mass spectrometer, the ratios were

X	CF_3^+		CF_2^+		CF^+
Cl	0.2 ± 0.2	:	2.4 ± 0.2	:	1.0
Br	0.2 ± 0.3	:	2.4 ± 0.1	:	1.0
I	0.7 ± 0.2	:	2.6 ± 0.2	:	1.0

The species CF_2Cl_2, CF_2Br_2, C_2HCl_3 also mainly dissociate through the rupture of a carbon halogen bond. Molecular elimination forming $CF_2 + Cl_2$ and $CF_2 + Br_2$ from CF_2Cl_2 and CF_2Br_2 were found not to be the major dissociation channels.[1,2] For $CFCl_3$, however, as previously reported for SF_6,[8] we observed an ionization pattern that depended on laser energy fluence and the product translational energy. At moderate ($\approx$ 5 J/cm^2) laser energy fluence the products could be identified as $CFCl_2$ and Cl, through the observation of the ions $CFCl_2^+$ and Cl^+. Our result agreed with Hudgens' observation,[1] but not with

Table 1

Molecule, Fragments and Observed Ions	Absorption Frequency (cm^{-1})	Exciting Frequency (cm^{-1})	Beam Nozzle Temperature °C
$CF_3Cl \rightarrow CF_3 + Cl$ (Cl^+, CF_2^+)	1106	1090.0	240°C
$CF_3Br \rightarrow CF_3 + Br$ (Br^+, CF_2^+)	1082	1078.6	25°C
$CF_3I \rightarrow CF_3 + I$ (I^+, CF_2^+)	1076	1073.3	25°C
$CF_2Cl_2 \rightarrow CF_2Cl + Cl$ (Cl^+, CF_2Cl^+)	1098, 923	1089.0, 925.1	25°C, 310°C
$CF_2Br_2 \rightarrow CF_2Br + Br$ (Br^+, CF_2Br^+)	1090	1084.6	25°C
$CHF_2Cl \rightarrow CF_2 + HCl$ (HCl^+, CF_2^+)	1116, 1160	1082.3	280°C
$CHFCl_2 \rightarrow CFCl + HCl$ (HCl^+, $CFCl^+$)	1070	1055.6	290°C
$CFCl_3 \rightarrow CFCl_2 + Cl$ (Cl^+, $CFCl_2^+$) $\rightarrow CFCl + Cl$ ($CFCl^+$)	1090	1074.6	25°C
$CHClCF_2 \rightarrow C_2F_2 + HCl$ (HCl^+) $\rightarrow CHCF_2 + Cl$ ($CHCF_2^+$)	970	967.7	25°C
$C_2HCl_3 \rightarrow C_2HCl_2 + Cl$ ($C_2HCl_2^+$)	930	929.1	80°C
$CF_3CF_2Cl \rightarrow CF_3CF_2 + Cl$ (Cl^+, $C_2F_4^+$) $\rightarrow CF_3 + CF_2Cl$ (CF_2Cl^+)	982	978.5	25°C
$CH_3CF_2Cl \rightarrow CH_2CF_2 + HCl$ (HCl^+, CF^+)	963	956.2	280°C
$CH_3CCl_3 \rightarrow CH_2CCl_2 + HCl$ (HCl^+, CH_2CCl^+)	1075	1073.3	25°C
$SF_6 \rightarrow SF_5 + F$ (SF_3^+, SF_2^+) $\rightarrow SF_4 + F$ (SF_3^+, SF_2^+)	948	944.2	25°C
$N_2F_4 \rightarrow 2NF_2$ (NF_2^+, NF^+)	998	975.9	25°C

Dever and Grunwald's conclusion of $CFCl_3 \rightarrow CFCl + Cl_2$.[4] However, at higher energy fluence (> 20 J/cm^2), products with very high translational energy showed appreciably less relative fraction of $CFCl_2^+$ as compared to $CFCl^+$, indicating that $CFCl_2$ dissociated further to form CFCl and Cl. No F^+ or Cl_2^+ could be detected throughout this experiment.

Similar analysis has been performed for the other molecules listed in Table 1. Here we will just briefly comment on the general features we have observed. A number of our systems showed hydrogen halide (i.e., HCl) elimination (in some cases expected on the basis of observed pyrolytic unimolecular reactions). The translational energy distribution of HCl in all cases, with the exception of $CHCl:CF_2$, indicated an exit potential energy barrier of the order of a few kcal/mole.

Especially interesting cases are some of the compounds containing two carbon atoms, because we observed competing dissociation channels. They were inferred on the basis of observation of fragments in the mass spectrometer that could not have all been present if there were only one channel, and also from their unique velocity distribution. Table 1 lists some of the obseved fragment ions for these molecules. None of our observations seemed to contradict the assumption that dissociation always proceeds through the channel(s) with the lowest dissociation threshold, i.e., the endoergicity plus exit potential energy barrier.

In conclusion we have found that our experimental results, including the velocity distributions of fragments that will be reported elsewhere, strongly support the idea that multiphoton dissociation of molecules produces fragments mainly through the lowest-energy dissociation channel, as one would expect for molecules with randomly distributed excitation energy. Our data is not as yet fully analyzed, but so far, we have not seen any evidence that the process is qualitatively different from what can be adequately described by a statistical theory of unimolecular reactions.

---

*This work was carried out in collaboration with Professor Y. Ron Shen's group.

1 J. W. Hudgens, preprint, submitted to J. Chem. Phys.
2. D. S. King and J. C. Stephenson, Chem. Phys. Lett. 51, 48 (1977).
3. S. Mukamel and J. Ross, J. Chem. Phys. 66, 5235 (1977).
4. D. F. Dever and E. Grunwald, J. Am. Chem. Soc. 98, 5055 (1976).
5. I. Oref and B. S. Rabinovitch, preprint, submitted to J. Phys. Chem.
6. J. G. Black, E. Yablonovitch, N. Bloembergen and S. Mukamel in "Multiphoton Processes," J. M. Eberly and P. Lambropoulos, Eds. (Wiley, New York, 1977).
7. J. L. Lyman, J. Chem. Phys. 67, 1868 (1977).
8. E. R. Grant, P. A. Schulz, Aa. S. Sudbo, Y. T. Lee and Y. R. Shen, in "Multiphoton Processes," J. H. Eberly and P. Lambropoulos, Eds. (Wiley, New York, 1977).
9. M. J. Coggiola, P. A. Schulz, Y. T. Lee and Y. R. Shen, Phys. Rev. Lett. 38, 17 (1977).

9. A PHENOMENOLOGICAL MODEL FOR MULTIPHOTON DISSOCIATION*

E. R. Grant, P. A. Schulz and Aa. S. Sudbo

In the many theoretical approaches to multiphoton dissociation, one is often faced with models of great complexity with many parameters that are not all equally readily available from theory or independent experiments. We have constructed a simple model that seems to be able to describe adequately the dissociation for the case of a short exciting laser pulse, i.e., a pulse such that the dissociation yield is determined by the total energy fluence of the pulse, and not by the intensity. In most of the experiments done so far, this is the case. Then we feel justified in making the following approximations: Ignore the initial few coherent steps in the excitation of the molecule, since the effect of their influence would be strongly dependent on intensity. Furthermore, in analogy with the derivation of Fermi's Golden Rule, once the molecule is excited to a region of high density of vibrational states, we can picture the excitation as molecules undergoind absorption and stimulated emission, between neighboring states on a ladder of states spaced equally apart, an energy equal to the photon energy. This excitation is incoherent, and can be described by a standard Master equation, where also the decay of dissociative states can be incorporated straight forwardly. The excitation is governed by the following set of rate equations:

$$dN_m/dt = C^a_{m-1} N_{m-1} + C^3_m N_{m+1} - (C^a_m + C^e_{m-1}) N_m - K_m N_m \qquad (1)$$

Here, N_m is the population in the mth excited level; K_m is the molecular dissociation rate from the mth level calculated from the RRKM statistical theory for unimolecular dissociation.[1] For levels below the dissociation energy E_0 we have $K_m = 0$. C^a_m and C^e_m are, respectively, the absorption rate from level m to m+1 and the emission rate from m+1 to m. For one-photon transitions, we can write

$$C^a_m = \sigma_m \frac{I}{h\nu}, \quad C^e_m/C^a_m = g_m/g_{m+1} \qquad (2)$$

where σ_m is the absorption cross section for m to m+1 transition, $h\nu$ is the photon energy, I is the laser intensity, and g_m is the degeneracy factor for the mth level.

We used this model, with a two parameter formula for the effective cross section for stimulated emission and absorption (each weighted by the appropriate density of vibrational states as obtained from a semiclassical count) that was adjusted for the model to fit two independent experimental results on SF_6;

and with rate constants obtained from a statistical (RRKM) theory for unimolecular decomposition for SF_6. The resulting set of some 50 first-order coupled linear differential equations can easily be solved on a computer.

In Fig. 1 we see how the population distribution evolves in time when SF_6 molecules are excited by a 100 ns long, 200MW/cm^2 square laser pulse, which is a reasonable representation of commonly prepared experimental conditions. The population spreads slowly until, as it moves up in energy, the high energy tail starts to be depleted by dissociation, and finally almost all the molecules are dissociated. Figure 2 shows how the excess vibrational energy (as referred to the dissociation threshold) is distributed in the dissociation products. If one then uses a statistical (RRKM) theory to predict the translational energy distribution in the fragments (here SF_5 and F), this distribution is in good agreement with our measurements[2] of translational energy released in the dissociation. The resulting high vibrational excitation of the SF_5 fragment, also seems to support our observation that SF_5 can be further excited to dissociate into SF_4 +F.

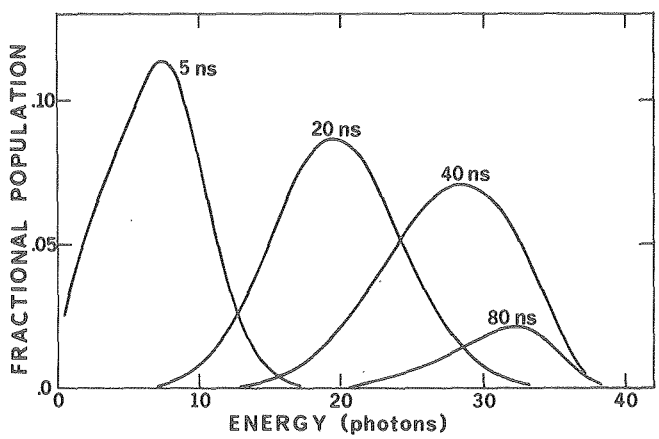

Fig. 1. Population distribution at various times produced by a 100 ns rectangular laser pulse excitation of 200 MW/cm^2. (XBL 779-2428)

In addition to the good qualitative description of, and the reasonable quantitative agreement with the experimental results, we want to point out that according to our model, laser heating is not equivalent to thermal heating. The latter gives a much too broad energy distribution for a given average excitation energy—in particular the high energy tail is always depleted by dissociation, and is definitely nonthermal. This is shown in Fig. 3. The laser-excited distribution curve with $\langle n \rangle = 20$ was obtained from our model calculation at $t \simeq 20$ ns. The thermal distribution with T = 2200 K has an average excitation energy of $\langle n \rangle h\nu \cong 20\ h\nu$, while the other with T = 1800 K has its characteristic temperature obtained from the equipartition theorem 15 kT = 20 $h\nu$.

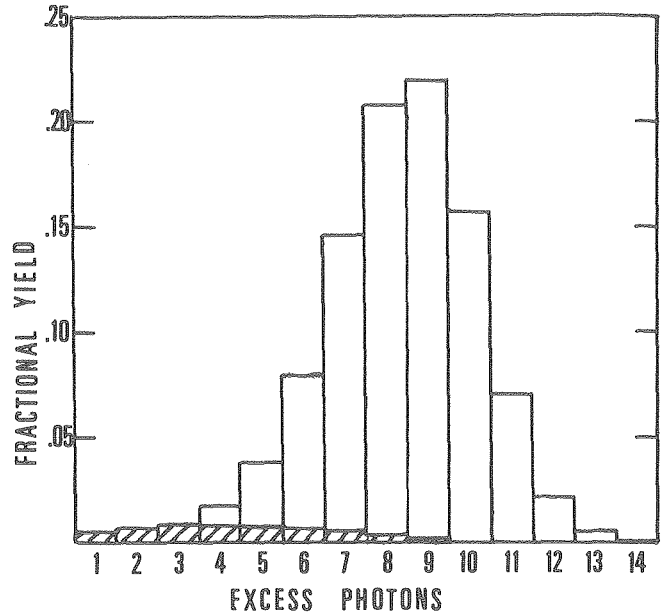

Fig. 2. Calculated dissociation yields from various levels above the dissociation energy during the laser pulse (unshaded region) and after the laser pulse (shaded region) for a 100-ns, 200 MW/cm^2 laser pulse excitation. (XBL 778-9879)

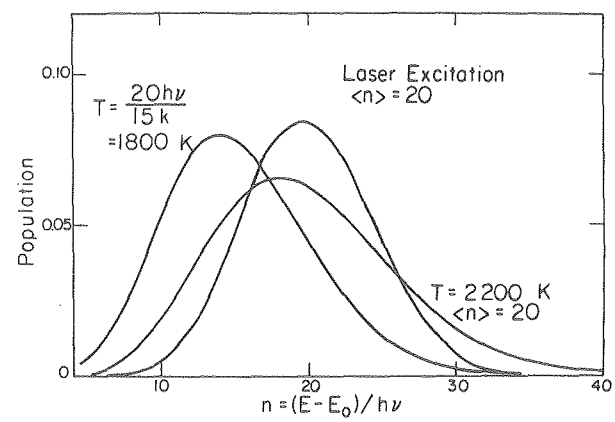

Fig. 3. Comparison of a laser-excited population distributions with $\langle n \rangle = 20$ and the other with T = 1800 K obtained from the equipartition theorem T = 20 $h\nu$/15k. (XBL 777-5750A)

---

*This work was carried out in collaboration with Professor Y. R. Shen's group.

1. E. R. Grant, P. A. Schulz, Aa. S. Sudbo, Y. R. Shen and Y. T. Lee, Phys. Rev. Lett. 40, 115 (1978).
2. E. R. Grant, M. J. Coggiola, P. A. Schulz, Aa. S. Sudbo, Y. R. Shen and Y. T. Lee, Chem. Phys. Lett. 52, 595 (1977).

10. CHEMILUMINESCENCE OF $NO + O_3 \rightarrow NO_2^* + O_2^\dagger$

Carol Kahler and Marta Kowalczyk

The chemiluminescence-laser fluorescence crossed molecular beam machine described in last year's annual report has undergone some improvement. The light collecting optics were redesigned and a careful alignment carried out. The new system (Fig. 1) uses four quartz lenses mounted on a precision machined optical rail. The first two lenses collect the light from the collision center and focus it onto an iris that blocks all light except that coming from the collision center. The second pair of lenses focus the light from the iris onto a photomultiplier tube or a polychromator coupled to an optical multichannel analyzer. The collision center in the machine was located using the intersection of the primary and secondary beam axes and the laser beam axis. By placing a 3-mm filament at the collision center, we have positioned the lenses and determined that the optical system is well aligned.

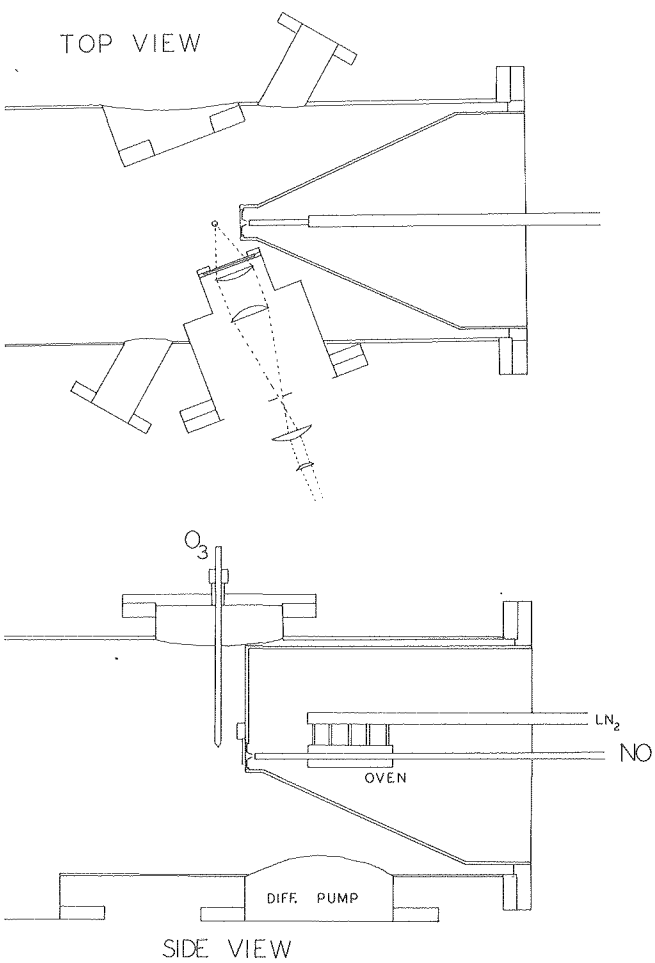

Fig. 1. Experimental setup for determination of collision energy dependence of the $NO + O_3$ reaction chemiluminescence. (XBL 7712-10937)

The first experiment we have worked on since redesigning the lens system is the study of the bimolecular chemiluminescent reaction of $NO + O_3$. There are quite a few papers in the literature concerning this reaction. The reaction is exoergic by 48 kcal/mole and has two pathways:[1] $NO + O_3 \rightarrow NO_2(^2A_1) + O_2$ and $NO + O_3 \rightarrow NO_2^*(^2B_1) + O_2$ with the subsequent emission of light by $NO_2^*(^2B_1)$ in the 5900 Å → 31000 Å region of the spectrum. It has been found that the two pathways have similar pre-exponential factors bit different activation energies and that about 90% of the NO_2 formed is formed in the $^2A_1$ state at room temperature.[1] The question of primary interest to us is whether one of the two spin-orbit states of NO, $^2\pi_{1/2}$ (ground) and $^2\pi_{3/2}$ (121.1 cm^{-1} above ground), is responsible for the chemiluminescent pathway. Work has been done on this by Redpath and Menzinger.[3] They used a seeded supersonic NO beam and a scattering chamber (77 K) filled with ozone. The collision energy was changed by changing seeding ratios and nozzle temperature. They observed that at a given collision energy, there was an increase in chemiluminescence with an increase in nozzle temperature. Since they assumed that the spin-orbit temperature of NO would equal the energy spread temperature of NO down to 177 K and that therefore the population of $NO(^2\pi_{3/2})$ goes up with nozzle temperature, Menzinger and Redpath concluded that $NO(^2\pi_{3/2})$ must be primarily responsible for the chemiluminescent pathway. It has since been discovered by Reuss et al.,[4] that the spin-orbit states of NO relax completely in a supersonic expansion. Our experiment will therefore consist of two parts, one using a supersonic NO beam to check collision energy dependence of the chemiluminescence, the second part using an effusive NO beam to observe any $\pi_{1/2}/\pi_{3/2}$ dependence.

Figure 1 shows the experimental setup. We cross one chopped supersonic beam source at 90° with an effusive beam source. The background pressure in the reaction chamber is maintained at $\sim 2 \times 10^{-5}$ Torr (single collision conditions) with both beams running. The light emitted at the collision center is focused by the lens system onto the photocathode of a dry ice cooled RCA C31034 photomultiplier tube. The signal from the tube is amplified, discriminated, and sent into a dual channel scalar. In part one of the experiment we measure the light emitted from the reaction as a function of collision energy. We use three seeded mixtures (1%, 10% NO in He, 24% NO in Ar) and pure NO in the supersonic source. The gas is first run through a silica gel trap in a dry ice/isopropanol bath to remove impurities before going into the nozzle at ~ 400 Torr. The ozone from our ozonizer is stored on silica gel in a dry ice/isopropanol bath and comes off the silica gel at 10 to 15 Torr. It then goes through an ozone monitor and into the effusive beam source. The supersonic source has the capability of being cooled to - 140° C and heated to 140° C which, combined with our different seeding ratios, gives us calculated collision energies of from 2 to 16 kcal/mole.

We have completed the measurement of undispersed light as a function of collision energy. The signal-to-noise ratio peaked at 156 and we had counting rates of up to 630 counts/s. The data near the reaction threshold is shown in Fig. 2. We have also done time of flight measurements on both our beams, although we have not finished analyzing the data and

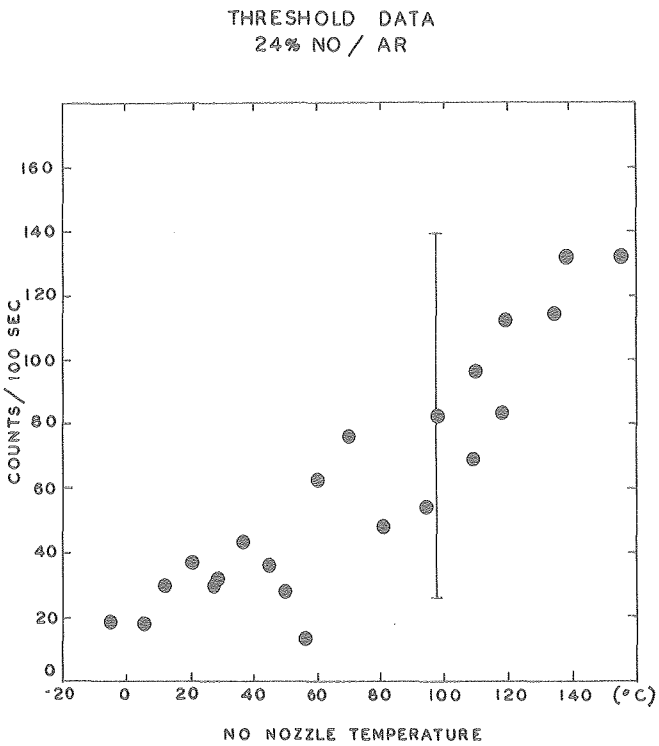

Fig. 2. Undispersed chemiluminescence from $NO + O_3$ near the reaction threshold. (XBL 7712-10923)

cannot yet report on the true collision energies. Before we are done with this experimental configuration we will measure the chemiluminescence dispersed at low resolution at several collision energies and also check for NO dimers in the beam that could react with the ozone.[5]

In the second part of the experiment we will measure light emitted as a function of NO spin-orbit populations. An effusive NO beam source is currently being constructed that will have the same cooling and heating capabilities as the supersonic source. We will calculate the $^2\pi_{1/2}/^2\pi_{3/2}$ population ratio as a function of nozzle temperature. We will measure the undispersed and dispersed chemiluminescence as a function of the population ratio and again take time-of-flight measurements to determine the collison energy of the beams.

---

†This program is carried out in collaboration with Professor Harold Johnston's group.

1. Clyne, Thrush and Wayne, Trans. Faraday Soc. 60, 359 (1964).
2. Clough and Thrush, Faraday Soc. 63, 915 (1967).
3. Redpath and Menzinger, J. Chem. Phys. 62, 1987 (1975).
4. Reuss et al., Nymegen, The Netherlands, private communication.
5. Golumb and Good, J. Chem. Phys. 49, 4176 (1968).

11. RESEARCH PLANS FOR CALENDAR YEAR 1978

Yuan T. Lee

Reactions of oxygen atoms with unsaturated hydrocarbons is the area of research that we will spend our major effort in the coming year. With a high intensity monoenergetic oxygen atom beam source that was developed during the last year and using an O^{18} isotope, a series of reactions that play very important roles in combustion processes will be investigated in great detail. Reactions of oxygen atoms with unsaturated hydrocarbons will be the first series.

The completion of two new molecular beam machines will expand our program in the investigation of the spectroscopy of molecule ions and molecular energy transfer processes. In collaboration with Dr. Y. R. Shen's group, a sophisticated infrared absorption spectrometer for molecule ions based on an entirely new concept using mass spectrometers and a tunable infrared laser will be completed early next year. From the absorption spectra, we hope to derive valuable information on the structure of many molecule ions. A high resolution universal crossed molecular beams apparatus is in the final stage of testing. This machine will have a higher performance and a higher resolution than any other universal molecular beams machine in our laboratories. Energy transfer processes and the dynamics of photodissociation, especially those molecules of atmospheric importance, will be studied with this new machine.

Two state selected chemical reactions, $Li + HF$ ($V = 1$, $J = 2, 3, 4$) $\rightarrow LiF + H$ are $He + H_2^+$ ($V = 0, 1, 2, 3$) $\rightarrow HeH^+ + H$, will be studied in a crossed molecular beams experiment. State selection will be accomplished by a CW chemical laser excitation for HF and by autoionization processes for H_2^+ using dispersed vacuum UV photons. These studies are intended for the better understanding of the reaction dynamics from first principles.

The investigations on the dynamics of infrared multiphoton processes and on the energetics of molecule ions by molecular beam photoionization, carried out in collaboration with Dr. Y. R. Shen's and Dr. B. H. Mahan's groups will be continued next year. The investigations in multiphoton processes will stress the dynamics of excitation and the behavior of highly excited molecules. Energetics of molecule ions will be investigated extensively using van der Waal's molecules as precursors in photoionization experiments.

The other areas of research that will be covered during the next year are the chemistry of radical molecules, high energy reactive scatterings of endoergic reactions, various elementary processes involving the interaction of lasers and molecules and the investigation of the interaction potentials of open shell atoms.

12. 1977 PUBLICATIONS AND REPORTS

Yuan T. Lee and Associates

Journals

1. J. J. Valentini, M. J. Coggiola and Y. T. Lee, Supersonic Atomic and Molecular Halogen Nozzle Beam Source, Rev. Sci. Instrum. 48, 58 (1977).

2. M. J. Coggiola, P. A. Schulz, Y. R. Shen and Y. T. Lee, Molecular Beam Study of Multiphoton Dissociation of SF_6, Phys. Rev. Lett. 38, 17 (1977).

3. C. Y. Ng, P. W. Tiedemann, B. H. Mahan and Y. T. Lee, The Binding Energy Between NO and NO^+, J. Chem. Phys. 66, 3985 (1977).

4. C. Y. Ng, D. J. Trevor, B. H. Mahan and Y. T. Lee, Photoionization Studies of the Kr_2 and Ar_2 van der Waals Molecules, J. Chem. Phys. 66, 446 (1977).

5. C. Y. Ng, P. W. Tiedemann, B. H. Mahan and Y. T. Lee, Photoionization Studies of the Diatomic Heteronuclear Rare Gas Molecules XeKr, XeAr, and KrAr, J. Chem. Phys. 66, 5737 (1977).

6. E. R. Grant, M. J. Coggiola, Y. T. Lee, P. A. Schulz, Aa. S. Sudbo and Y. R. Shen, Studies of Multiphoton Dissociation of Polyatomic Molecules with Crossed Laser and Molecular Beams, State-to-State Chemistry, ACS Symposium Series, P. R. Brooks and E. F. Hayes, Eds. [Amer. Chem. Soc. 56, 72 (1977)].

7. E. R. Grant, P. A. Schulz, Aa. S. Sudbo, Y. T. Lee and Y. R. Shen, Molecular Beam Studies on Multiphoton Dissociation of Polyatomic Molecules, Multiphoton Process, J. H. Eberly and P. Lambropoulos, Eds. (Wiley, New York, 1977).

8. E. R. Grant, P. A. Schulz, Aa. S. Sudbo, M. J. Coggiola, Y. T. Lee and Y. R. Shen, Multiphoton Dissociation of Polyatomic Molecules Studied with a Molecular Beam, Laser Spectroscopy, J. L. Hall and J. L. Carlsten, Eds., Springer Series in Opt. Sci. Vol. 7 (Springer-Verlag, NY., Heidelberg 1977).

9. C. Y. Ng, D. J. Trevor, P. W. Tiedemann, S. T. Ceyer, P. L. Kronebusch, B. H. Mahan and Y. T. Lee, Photoionization of Dimeric Polyatomic Molecules: Proton Affinities of H_2O and HF, J. Chem. Phys. 67, 4235 (1977).

LBL Reports

1. E. R. Grant, M. J. Coggiola, P. A. Schulz, Y. T. Lee and Y. R. Shen, Dynamics of Infrared Multiphoton Dissociation of SF_6 by Molecular Beam Method, VI International Symposium on Molecular Beams, Noordjwijerkout, The Netherlands, April 18-22, 1977, LBL-6035.

2. E. R. Grant, M. J. Coggiola, P. A. Schulz, Aa. S. Sudbo, Y. T. Lee and Y. R. Shen, The Extent of Energy Radomization in the Infrared Multiphoton Dissociation of SF_6, submitted to Chem. Phys. Lett., August 1977, LBL-6201.

3. J. M. Farrar, A. L. J. Burgmans, J. M. Parson, R. B. Walker and Y. T. Lee, Crossed Molecular Beam Study Rotational Excitation of HD($J=0\rightarrow 1$) in Collisions with He, VI International Symposium on Molecular Beams, Noordjwijerkout, The Netherlands, April 1977, LBL-6214.

4. E. R. Grant, P. A. Schulz, Aa. S. Sudbo, M. J. Coggiola, Y. R. Shen and Y. T. Lee, Molecular Beam Studies on Multiphoton Dissociation of Polyatomic Molecules, International Conference on Multiphoton Processes, University of Rochester, New York, June 6-9, 1977, LBL-6275.

5. James J. Valentini, Daniel J. Auerbach and Yuan T. Lee, A Crossed Molecular Beam Study of the Translational Energy Dependence of $Cl + Br_2 \rightarrow BrCl + Br$ Reaction, submitted to J. of Chem. Phys., July 1977, LBL-5719.

6. E. R. Grant, P. A. Schulz, Aa. S. Sudbo, Y. R. Shen and Y. T. Lee, Is Multiphoton Dissociation of Molecules a Statistical Thermal Process?, submitted to Phys. Rev. Lett., August 1977, LBL-6659.

7. Aa. S. Sudbo, P. A. Schulz, E. R. Grant, Y. R. Shen and Y. T. Lee, Multiphoton Dissociation Products from Halogenated Hydrocarbons, submitted to J. Chem. Phys. as a Communication, November 1977, LBL-6966.

Presentations

1. Y. T. Lee, Molecular Beam Studies on the Dynamics of Infrared Multiphoton Dissociation of Polyatomic Molecules, University of California, Berkeley, Department of Chemistry, February 8, 1977.

2. Y. T. Lee, Dynamics of Multiphoton Dissociation of SF_6 by Molecular Beam Method, 2nd Winter Colloquium on Laser Induced Chemistry, Park City, Utah, February 13-16, 1977.

3. E. R. Grant, Infrared Multiphoton Dissociation of SF_6 by Molecular Beam Method, Department of Chemistry, Cornell University, February 14, 1977.

4. E. R. Grant, Molecular Beam Studies of Multiphoton Dissociation of SF_6, Department of Chemistry, Dartmouth University, February 15, 1977.

5. C. Y. Ng, Photoionization Studies by the Molecular Beams Method, Department of Chemistry, Iowa State University, March 8, 1977.

6. E. R. Grant, Studies of Multiphoton Dissociation of Polyatomic Molecules with Crossed Laser and Molecular Beams, ACS Symposium on "State to State Chemistry" New Orleans, Louisiana, March 21-23, 1977.

7. Y. T. Lee, Molecular Beam Studies on Reaction Dynamics, Project SQUID Annual Meeting, La Jolla, California, March 22-25, 1977.

8. C. Y. Ng, Photoionization of van der Waals Molecules, Department of Chemistry, University of Wisconsin, March 29, 1977.

9. Y. T. Lee, Dynamics of Infrared Multiphoton Dissociation of SF_6 by Molecular Beam Method, VI International Symposium on Molecular Beams, Noordwijkerhout, Netherlands, April 1977.

10. J. M. Farrar, Crossed Molecular Beam Study on Rotational Excitation of HD($J=0\rightarrow1$) in Collisions with He, VI International Symposium on Molecular Beams, Noordwijkerhout, Netherlands, April 1977

11. Y. T. Lee, Molecular Beam Studies on Photoionization of van der Waal's Molecules, N. V. Philip's Gloeilampenfabrieken Research Laboratories, Eindhoven, The Netherlands, April 27, 1977.

12. Y. T. Lee, Photodissociation and Photoionization by Molecular Beams Method, Fakultat f. Physik der Universität, Bielefeld, West Germany, May 2, 1977.

13. Y. T. Lee, Molecular Beam Studies on Multiphoton Dissociation of Polyatomic Molecules, Hahn-Meitner-Institut, West Berlin, West Germany, May 4, 1977.

14. Y. T. Lee, Recent Studies on Interaction of Photons with Molecules by Molecular Beams Method, Max-Planck-Institute fur Strömungsforschung, Göttingen, West Germany, May 6, 1977.

15. Y. T. Lee, Dynamics of Multiphoton Dissociation of Polyatomic Molecules, Max-Planck Institut, Abt. Laser Forschung, Garching, West Germany, May 10, 1977.

16. Y. T. Lee, Photoionization and IR Multiphoton Dissociation of Molecules by the Molecular Beam Method, Naval Research Laboratory, Washington, D.C., May 13, 1977.

17. Y. T. Lee, Molecular Beam Studies on Infrared Multiphoton Dissociation of SF_6, International Conference on Multiphoton Processes, Rochester, New York, June 6-9, 1977.

18. E. R. Grant, Internal State and Two Frequency Dependence in Multiphoton Dissociation of Polyatomic Molecules, International Conference on Multiphoton Processes, Rochester, New York, June 6-9, 1977.

19. P. A. Schulz, A Model for the Time Evolution of Multiphoton Absorption and Dissociation, International Conference on Multiphoton Processes, Rochester, New York, June 6-9, 1977.

20. Y. T. Lee, Dynamics of Infrared Multiphoton Excitation and Dissociation of Polyatomic Molecules, JILA-Battelle Laser Workshop, Seattle, Washington, August 22, 1977.

21. P. W. Tiedemann, A Molecular Beam Study of Polymer Photoionization, 1977 Pacific Conference on Chemistry and Spectroscopy, Anaheim, California, October 12-14, 1977.

22. Y. T. Lee, Molecular Beam Studies on the Dynamics of Multiphoton Dissociation of Polyatomic Molecules, Department of Chemistry, University of California, Santa Cruz, California, October 19, 1977.

g. Molecular Electronic Structure Theory

Henry F. Schaefer III, Principal Investigator

1. ENERGY SEPARATION BETWEEN THE OPEN (C_{2v}) AND CLOSED (D_{3h}) FORMS OF OZONE*

Robert R. Lucchese and Henry F. Schaefer III

One of the most important recent discoveries of theoretical chemists is the existence of a bound, low-lying cyclic (D_{3h}) isomer of O_3. The normal open (or C_{2v}) form, with equilibrium geometry r(O-O) = 1.278 Å, θ(OOO) = 116.8°, has of course been known for many years. However, the energy separation between the C_{2v} and D_{3h} isomers continues to be a rather volatile quantity.

For reasons of brevity we cite here only the more recent and reliable results. To date, the largest basis set used to probe the open-closed energy separation (called ΔE hereafter) problem is the standard double-zeta-plus-polarization set employed by Siu and Hayes. Although they did not consider the effects of electron correlation, their self-consistent-field (SCF) ΔE value of 9.9 kcal is probably within a few kcal of the Hartree-Fock limit. In an earlier paper, Hayes and Siu stated their belief that correlation effects should increase the Hartree-Fock value of ΔE, i.e., that there is more correlation energy associated with open or normal form of ozone. In their excellent paper on the electronic spectrum of O_3, Hay, Dunning, and Goddard conclude that ΔE is > 32 kcal. However, it appears that the methods used to calculate ΔE were considerably less reliable than employed in the rest of that important paper. The cyclic isomer of O_3 was discovered by Peyerimhoff and Buenker, and their more recent study employs configuration interaction (CI) including roughly 200 configurations. Using a double-zeta basis augmented by s-type bond functions between each pair of O atoms, Shih, Buenker, and Peyerimhoff (SBP) predict ΔE to be 16.1 kcal. The most recent theoretical study, by Burton and Harvey, added s, p_x, p_y, and p_z bond functions to a poorly contracted double-zeta basis and used the PNO-CEPA method to predict a ΔE value of 4.6 kcal.

Since state-of-the-art ab initio methods should be capable of more precision than the 30 kcal range seen above, we decided to markedly improve upon previous theoretical studies. The predictively reliable O(9s5p1d/4s2p1d) double-zeta-plus-polarization basis was used, with the set of six d-like functions having Gaussian orbital exponent α = 0.8. Although this same basis has been used in SCF studies by Rothenberg and Schaefer, Siu and Hayes, and Hay, Dunning, and Goddard, it has not been applied including correlation effects to the open-closed energy difference problem. For the open isomer, the experimental geometry was assumed, while for the closed form the generally accepted O-O separation of ~1.44 Å was used.[1]

CI was carried out using the recently developed BERKELEY system of programs. The correlated wavefunctions were constructed from singly and doubly excited $^1A_1$ configurations relative to the Hartree-Fock reference configurations

$$\text{open:} \quad 1a_1^2 1b_2^2 2a_1^2 3a_1^2 2b_2^2 4a_1^2 5a_1^2 3b_2^2 1b_1^2 4b_2^2 6a_1^2 1a_2^2 \,, \quad (1)$$

$$\text{closed:} \quad 1a_1^2 1b_2^2 2a_1^2 3a_1^2 2b_2^2 4a_1^2 5a_1^2 3b_2^2 1b_1^2 6a_1^2 1a_2^2 2b_1^2 \,. \quad (2)$$

Two series of CI calculations were performed differing in the number of "core" SCF orbitals held doubly-occupied in all configurations. In the first series six molecular orbitals were frozen, and in the second only the (three oxygen 1s-like) $1a_1$, $2a_1$, and $1b_2$ SCF orbitals were constrained to be doubly-occupied. In the latter case it was necessary to exclude the six highest improved virtual orbitals from the CI.

Our results are summarized in Table 1. From the total energies given there it may be seen that the SCF energy difference is 6.8 kcal, a result which should be within ±3 kcal of the true Hartree-Fock ΔE value for the chosen geometries. Both CI treatments predict, as suggested first by Hayes and Siu, that correlation is more important for the C_{2v} than the D_{3h} isomer. The final pair of calculations should be the most reliable, since significantly lower total energies are obtained. The latter prediction must be corrected for the effects of higher (triple, quadruple, etc.) spinorbital excitations, especially unlinked clusters, which should be more important for the open form. Although there are fairly elaborate methods for approximately including these effects, one of the most useful is the simple formula derived by Davidson. By applying this to the final two calculations in Table 1, the predicted open-closed separation is increased to 21.8 kcal. Another small correction will arise, since the closed form (with presumably a larger symmetric stretching frequency) will have somewhat more zero-point vibrational energy. Thus we arrive at our final estimate for ΔE of 22±5 kcal. Hence we conclude that nearly all the observable properties of ozone may be explained without reference to the cyclic isomer.

Finally we note that our prediction is rather close to that of Shih, Buenker, and Peyerimhoff. However, this agreement must be considered somewhat fortuitous since their smaller basis predicts the closed form to lie 7 kcal below the open at the SCF level. Thus the contribution of correlation effects is less than suggested by their results.

Table 1. Summary of configuration interaction (CI) results for the open (C_{2v}) and closed (D_{3h}) isomers of ozone. (The SCF total energies were -224.30971 and -224.29887 hartrees, respectively.)

Isomer	SCF Orbitals Doubly Occupied	Virtual Orbitals Excluded	$^1A_1$ Configurations	Total Energy (hartrees)	ΔE (kcal/mole)
Open	6	0	6131	-224.65832	16.2
Closed	6	0	6005	-224.63248	
Open	3	6	9644	-224.80065	17.8
Closed	3	6	9493	-224.77229	

*From LBL-6062; J. Chem. Phys. 67, 848 (1977).

1. Using the 9493 configuration wavefunction, the equilibrium geometry of the cyclic form is predicted to be r_e(O-O) = 1.422 Å. The total energy is now -224.77289 hartrees, only 0.4 kcal below that obtained at the assumed O-O separation of 1.44 Å.

2. METAL-CARBENE COMPLEXES AND THE POSSIBLE ROLE OF HYDROXYCARBENE IN FORMALDEHYDE LASER PHOTOCHEMISTRY*

Robert R. Lucchese and Henry F. Schaefer III

Hydroxycarbene CHOH is probably the most important very simple carbene that has not been characterized experimentally. First, one would like to relate the properties of hydroxycarbene to those of other simple carbenes (e.g., CH_2, CHF, CHCl, CHBr, and CHCN) for which experimental data are available. Secondly, CHOH may be considered the simplest alkoxycarbene

and alkoxycarbenes have proven extremely difficult to prepare via conventional synthetic methods. Third, the Fischer-type transition metal carbenes

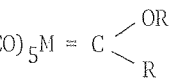

which have been one of the most exciting developments in organometallic chemistry during the past decade, contain the alkoxycarbene fragment. In fact, as related by Fischer in his Nobel address, the very first metal carbene complexes prepared were of the hydroxy variety

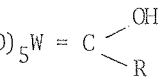

And, in fact, metal carbene complexes are even today considered the most realistic source of the extremely reactive alkoxycarbene radicals. When the carbene ligand is split off from the metal, it appears that a hydrogen shift occurs almost immediately, yielding an aldehyde product. A simple example of this process would be

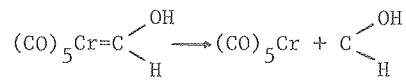

(1)

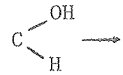

(2)

Our interest in hydroxycarbene arose from recent experimental studies (some of the most important by Dr. C. B. Moore of MMRD, LBL) of the laser photodissociation of formaldehyde. Despite the simplicity of this system and the sophistication of the experimental techniques employed, there is still no adequate molecular explanation of the experimental results. Specifically, neither triplet formaldehyde T_1 nor the excited vibrational manifold of the ground state S_0 can be satisfactorily invoked as the intermediate I for the observed process

$$H_2CO(S_0) \xrightarrow{h\nu} H_2CO(S_1) \longrightarrow I \longrightarrow H_2 + CO. \quad (3)$$

However, if some hitherto unrecognized molecular species were involved in the photodissociation, a coherent picture might emerge. One conceivable such "intermediate state" would be hydroxycarbene, which is of course an isomer of formaldehyde. Here we wish to point out that experiments on Fischer-type carbenes lend credence to this hypothesis. As shown in (1) and (2) it is accepted by organometallic chemists that hydroxycarbenes spontaneously undergo isomerization to yield formaldehyde. It must be noted of course that the hydroxycarbene in (1) may possess as internal energy some of the exothermicity resulting from the rupture of the metal-carbene bond. Nevertheless, it seems likely that there is a relatively small activation energy for rearrangement (2). This

conclusion is supported by detailed theoretical studies, incorporating the effects of electron correlation, of the related vinylidene rearrangement

$$CH_2{=}C: \longrightarrow HC{\equiv}CH \ , \qquad (4)$$

for which a barrier of no more than 8 kcal/mole is predicted.

If there is only a small barrier associated with (2), then from microscopic reversibility we know that formaldehyde may be converted to hydroxycarbene with an amount of energy only slightly greater than the energy difference between the two isomers. The second purpose of this paper then is to evaluate this energy difference by using reliable theoretical techniques. This problem has been addressed in a different context by Altmann, Csizmadia, Yates, and Yates, and we build on their research in the present study.

Using the standard Huzinaga-Dunning double-zeta (DZ) basis set, we first determined the equilibrium geometries of triplet and singlet hydroxycarbene within the single-configuration self-consistent-field (SCF) approximation. This process was immensely simplified by having at our disposal the theoretical structures obtained by Altmann using a slightly smaller basis set, and in fact the two sets of structures are nearly indistinguishable. We note here one of Altmann's primary conclusions, namely that singlet hydroxycarbene has stable cis and trans forms (both planar), whereas the triplet state has only one stable geometry, gauche. Relative to the $^1A_1$ ground state of formaldehyde, the S_0 trans, S_0 cis, and T_1 gauche states of HCOH lie at 46.5, 54.2, and 48.2 kcal, respectively. Some idea of the reliability of these results may be gleaned from the S_0-T_1 separation in formaldehyde, which is known experimentally to be 72.0 kcal/mole. In the present SCF calculations $\Delta E(S_0\text{-}T_1)$ is predicted to be 35.5 kcal. This difference of 36.5 kcal, which is also apparent in the Altmann study, is sufficiently large to bring into serious question the validity of such theoretical predictions.

For this reason, we decided to consider the effects of electron correlation, using configuration interaction (CI). Since the DZ SCF geometries should be quite reliable, no geometry search was attempted in the CI studies. All but the final CI included all Slater determinants differing by one or two spinorbitals from the appropriate SCF reference configuration. This procedure was adopted with the restrictions (spelled out in Table 1) that certain SCF orbitals were held frozen (i.e., doubly-occupied in all Slater determinants) and some of the highest improved virtual orbitals deleted from the CI. The CI treatments thus described ranged from 1628 to 5697 Slater determinants. In the final and most reliable set of calculations, Slater determinants were selected (e.g., 5,561 from a total of 57,870 for triplet hydroxycarbene) using the cumulative perturbation theory method of Raffenetti, Hsu, and Shavitt.

Our results are summarized in Table 1 and show that the final CI treatment predicts the formaldehyde S_0-T_1 separation to be only 3 kcal less than known experimentally. This and the extensive CI methods employed suggest that the predictions in the final theoretical column should be quite reliable.

Table 1. Summary of energetic predictions for H_2CO and HCOH, using different theoretical methods. (The total energies obtained for the formaldehyde ground state were -113.8307, -113.9933, -114.0353, -113.8936, -114.0417, -114.0744, and -114.1338 hartrees.)

Species	[Relative Energy (kcal/mole)]							
	DZ SCF	DZ CI[a]	DZ CI[b]	DZ+P SCF	DZ+P CI[a]	DZ+P CI[b]	DZ+P CI[c]	Experiment
Formaldehyde S_0	0.0	0.0	0.0	0.0	0.0	0.0	0.0	0.0
Formadelhyde T_1	35.5	56.2	58.6	48.4	66.2	67.1	68.9	72.0
Hydroxycarbene S_0 trans	46.5	53.2	54.1	47.9	54.2	53.0	51.7	-
Hycroxycarbene S_0 cis	54.2	60.0	60.8	53.8	58.7	57.6	57.5	-
Hydroxycarbene T_1 gauche	48.2	66.7	-	55.9	72.6	-	73.0	-

[a]The three lowest SCF orbitals were held doubly-occupied, and 13 virtual orbitals included in the CI.

[b]The two lowest (essentially C and O 1s) orbitals were held doubly-occupied, and 14 virtual orbitals included in the CI.

[c]The two lowest orbitals were held doubly-occupied, all virtual orbitals included in the CI, and determinants selected by perturbation theory.

The most important finding here is that the S_0 trans, S_0 cis, and T_1 gauche electronic states of hydroxycarbene all lie below the formaldehyde S_1 state (80.6 kcal). Thus all three are energetically accessible during the photodissociation (3) of H_2CO. S_0 trans CHOH is a particularly attractive candidate for I [in Eq. (3) above] since it lies ~29 kcal below S_1 H_2CO, and is also favored from least-motion considerations.

Finally we must emphasize that the present energy surface results by no means demonstrate that hydroxycarbene is the "intermediate state" in the laser photodissociation of formaldehyde. What we have shown is that this possibility is quite feasible energetically. Rather detailed theoretical dynamical studies and/or additional experiments will be needed to unravel the H_2CO photodissociation mechanism. It remains a formidable challenge to both theory and experiment.

*From LBL-6063; J. Amer. Chem. Soc. 100, 298 (1978).

3. THE FUZZY INTERFACE BETWEEN SURFACE CHEMISTRY, HETEROGENEOUS CATALYSIS, AND ORGANOMETALLIC CHEMISTRY*

Henry F. Schaefer III

Each of the three areas of surface chemistry, catalysis, and organometallic chemistry is well-established and currently fluorishing. However, for some time chemists have suspected an underlying relationship between the three, and this relationship or "fuzzy interface" is the subject of the present account. It seems clear, and has often been mentioned in the literature and even in undergraduate texts, that the transition metal-organic fragment chemical bond is the key to linking the three disciplines. Unfortunately, however, few scientists have been willing to comment beyond this broad generality. Two striking exceptions to this noncommittal posture should be cited here. Based on his experimental studies, Muetterties has advanced a detailed thesis that discrete metal cluster complexes [e.g., $(C_5H_5)_3Mn_3(NO)_4$] may be considered "models of the surface structure of a metal where there has been extensive chemisorption of molecules, radicals or atoms." Second is the theoretical work of Goddard, who is engaged in an ambitious study of the methanation of CO on nickel surfaces modeled by finite clusters Ni_n.

I have felt for some time that these three fields have suffered from a lack of sufficient thermochemical and structural information. After all, one of the tremendous strengths of organic chemistry is the existence of well-established and reliable values for the bond energies and bond lengths of C-C single, double, and triple bonds. Building blocks of this nature allow the facile correlation of vast amounts of chemical data. In contrast, if one asks for comparable information on transition metal to carbon bonds, he is likely to come away empty-handed. Therefore one of the aims of both theorists and experimentalists should be a more fundamental understanding of bonding in organometallic systems. In fact, there is a substantial experimental effort now in progress along these lines, particularly by chemists using gas phase transition metal atoms for chemical synthesis. Among the most important contributors have been Skell Timms, Ozin, and Klabunde. A particularly important recent paper is that of Ozin and co-workers, who have synthesized and taken the infrared spectra of the $Cu(C_2H_4)$, $Cu(C_2H_4)_2$, and $Cu(C_2H_4)_3$ species. Such studies are extremely important, since they hold out the possibility of a detailed understanding of the nature of the unadorned metal-organic fragment entities. Thus far these experiments have not yielded either precise structures or bond energies, although these are expected to be forthcoming. In the meantime, the setting is ripe for theoretical studies of the type described in this review.

Before moving on, let us review very briefly the goals of the three disciplines in question, in what might be considered the "region of overlap." In surface chemistry one traditionally attempts to study infinite, perfectly ordered structures, e.g., the (111) surface of platinum. One of the most exciting recent developments is the emergence of low-energy electron diffraction (LEED) as a technique capable of determining the structures of chemisorbed polyatomic molecules. The first example, acetylene on Pt(111), was reported in 1976 by Somorjai and co-workers. More generally the study of how chemical reactions occur on perfect surfaces is often considered a first step in the understanding of heterogeneous catalysis. This analogy becomes more realistic when irregularities are added to the surface, for example, steps, kinks, edges, and ledges. An extremely important recent realization is that stepped surfaces are vastly more effective than perfect surfaces as catalysts for gas phase chemical reactions, the most carefully studied example being the $H_2 + D_2$ exchange reaction.

Heterogeneous catalysis, as carried out industrially, is extremely complicated in molecular terms. Perhaps best known is the Fisher-Tropsch synthesis, in which H_2 and CO are passed over metallic catalysts at 200° to 300°C to produce hydrocarbons ranging from C_1 to C_{40}. The four metals that show significant activity in the Fischer-Tropsch synthesis are iron, cobalt, nickel, and ruthenium, and these require varying degrees of promotion and supporting. Although the structure of metallic catalysts is the subject of a certain amount of controversy, it appears that even small metal clusters can display catalytic behavior. Most strikingly Hamilton and Logel at Kodak have shown that the Au_2 dimer and Ag_4 tetramer facilitate the photographic process. Work by Boudart, Anderson, Sinfelt, and others suggests that typical industrial metallic catalysts consist of finely divided, irregular particles of 100 or more metal atoms. This is clearly quite different from an ideal metal surface.

Perhaps best known to the readers are the homogeneous (i.e., in solution) catalysts of organometallic chemistry. These have been known for some time, the most widely-recognized being Wilkinson's catalyst, $RhCl(PPh_3)_3$ or tris(triphenylphosphine) chlororhodium(I). Wilkinson's catalyst represented the first rapid

and practical system for the homogeneous reduction of olefins and acetylenes under ordinary conditions. The two most frequently cited disadvantages of homogeneous (vs. heterogeneous) catalysis are the practical problem of separation of products from reactants and catalyst, and the apparent inability to reduce nitrogen and carbon monoxide. The latter disparity with the Fischer-Tropsch synthesis is particularly obvious. However, two important recent advances should be noted. First, Chatt and co-workers have succeeded in the reduction of N_2 to NH_3 under mild conditions, for example when cis-$[W(N_2)_2(PMe_2Ph)_4]$ is treated with sulphuric acid in methanol solution. Chatt's process is particularly intriguing since it appears to go against Muetterties thesis that mononuclear metal complexes should not be particularly effective as catalysts. In another extremely important communication, the homogeneous reduction of CO to CH_4 has been reported by the discrete clusters $Os_3(CO)_{12}$ and $Ir_4(CO)_{12}$. Although the reaction rates observed by Muetterties and co-workers were relatively low, selectivity (not present in the Fischer-Tropsch process) was a distinctive feature, with no hydrocarbons besides methane being detected. These and other recent discoveries (e.g., concerning the role of metal-carbene complexes in olefin metathesis, discussed briefly here) suggest for the future an increasingly important role for homogeneous catalysis.

Some discussion should be devoted to the choice of theoretical methods adopted here. Seemingly since time began, theoreticians have been forced to choose between Scylla and Charybdis. Namely, does one use simple, sometimes unreliable, methods to study molecules that have actually been prepared in the laboratory; or does one accept more rigorous quantum mechanical methods and settle on smaller systems which hopefully serve as models for the chemical system in question? As the full text of this review makes clear, we have adopted the latter philosophy, using ab initio molecular electronic structure theory. This path has the well-documented comfort of showing that, as larger basis sets and more extensive configuration interaction are employed, one eventually reaches prediction of genuine chemical accuracy. However, the choice is a difficult one and it should be noted here that the simpler methods have been applied, often successfully, to numerous problems in surface chemistry, catalysis, and organometallic chemistry.

*Abstracted from Accounts of Chemical Research 10, 287 (1977); LBL-6032.

4. ELECTRON CORRELATION EFFECTS ON THE EXCITATION ENERGIES OF THE LOWEST TRIPLET STATES OF GLYOXAL*

Clifford E. Dykstra, Robert R. Lucchese, and Henry F. Schaefer III

In an attempt to understand the ordering of excited states of glyoxal, the ^1A_g ground state and low-lying triplet states, ^3A_u, ^3B_u, and ^3B_g, have been studied with ab initio correlated wavefunctions. A double-zeta basis set was used in the configuration interaction calculations, and ~6,000 Slater determinants were selected for each electronic state. The predicted CI adiabatic excitation energies T_e are 21,800 cm^{-1} (^3A_u), 25,100 cm^{-1}(^3B_u), and 29,300 cm^{-1} (^3B_g). The effects of d functions and higher (than double) excitations (unlinked clusters) have also been evaluated. For the ^3B_u state, both d functions and higher excitations raise the predicted T_e value, by perhaps as much as 5,000 cm^{-1}. For the ^3B_g state, d functions raise the predicted excitation energy but higher excitations have the opposite effect. It is concluded that the excitation energy of the ^3B_u state is dramatically increased by correlation effects, while T_e for the ^3A_u and ^3B_g states is markedly decreased by correlation. Our results are summarized in Fig. 1.

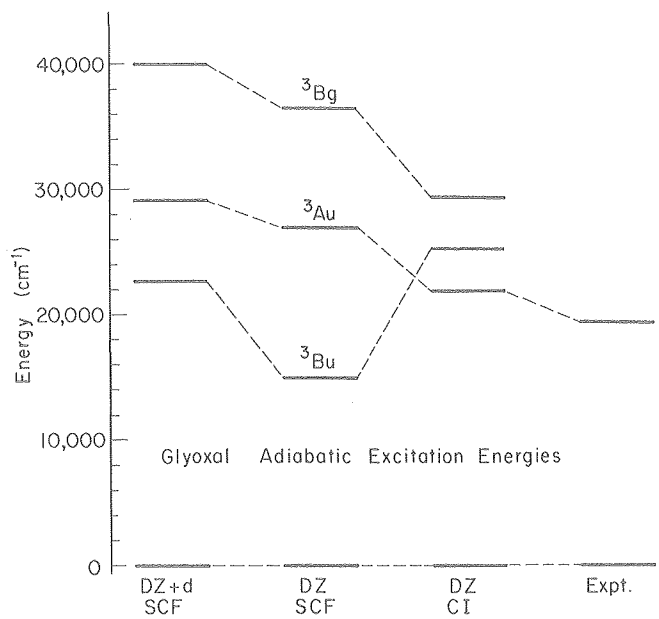

Fig. 1. Adiabatic excitation energies T_e for the three lowest triplet states of glyoxal. The three different levels of theory plotted on the x axis are described in the text. DZ refers to a double-zeta basis set, SCF implies the use of self-consistent-field theory, and CI is an abbreviation for the configuration interaction method.
(XBL 775-3502)

*Abstracted from J. Chem. Phys. 67, 2422 (1977); LBL-6273.

5. SOME FEATURES OF THE POTENTIAL ENERGY SURFACES FOR THE $F^+ + H_2$ ION-MOLECULE REACTION*

Bruce H. Mahan, Henry F. Schaefer III, and Steven R. Ungemach

During the past five years, molecular beam and theoretical studies have yielded a great deal of important information concerning the dynamics of

the $C^+ + H_2$ and $N^+ + H_2$ ion-molecule reactions. These systems are in some ways more interesting than typical neutral reactions, which can often be understood in terms of a single potential energy surface. At low energies both the C^+ and N^+ reactions with molecular hydrogen can be largely explained in terms of C_{2v} or near-C_{2v} orientations of approach. The reagents may approach each other on a potential surface ($^2B_2$ for CH_2^+ and $^3A_2$ for NH_2^+) which is significantly atrractive [e.g., $D_e(N^+-H_2) \sim 60$ kcal]. This surface is in turn connected to the ground state surface ($^2A_1$ for CH_2^+ and $^3B_1$ for NH_2^+) when the approaching heavy ion is moved off the H_2 perpendicular bisector, lowering the symmetry to C_s. The resulting complex formation leads to products $CH^+ + H$ or $NH^+ + H$.

In the present note we present comparable theoretical results for the $F^+ + H_2$ system. On first glance this reaction might appear quite analogous to $N^+ + H_2$, since F^+ with four 2p electrons is related to N^+ (two 2p electrons) in its particle-hole equivalence. However, there are some equally obvious differences between the $F^+ + H_2$ and $N^+ + H_2$ systems. For example, $N^+ + H_2$ is the energetic ground state of the separated system, while $F^+ + H_2$ actually lies 46 kcal above $F + H_2^+$. Furthermore, even in combination with a reasonable understanding of the C^+ and N^+ reactions, a correlation diagram[1] (see Fig. 1) for the $F^+ + H_2$ system does not make the route to the observed products $HF^+ + H$ apparent.

As in Pearson's work on $C^+ + H_2$ and ours on $N^+ + N_2$, a double-zeta-plus-polarization basis set was adopted in conjunction with configuration interaction (CI). The CI included all singly- and doubly-excited configurations relative to one or two reference configurations. Thus it seems reasonable to expect the present theoretical results to be qualitatively valid.

In Fig. 2 we present the triplet part of a "vertical" ab initio analogue to the empirical correlation diagram seen in Fig. 1. The C_{2v} results were obtained at $r_e(F-H) = 0.963$ Å, $\theta_e(HFH) = 112.1°$, the CI equilibrium geometry of the ground state $^1A_1$ FH_2^+ ion, and the $D_{\infty h}$ results at $r_e(F-H) = 0.959$ Å, the lowest point on the linear symmetric HFH^+ potential surface. It is apparent that all the excited states of the FH_2^+ system lie very high in relative energy near the ground state equilibrium geometry. We must conclude that the important features of the FH_2^+ potential surfaces occur much "earlier" in the approach of F to H_2^+ or of F^+ to H_2.

The critical region of configuration space for the C_{2v} $F^+ - H_2$ surfaces is clearly that "adjacent to" the reactants. This region is seen in Fig. 3, which illustrates the approaches of F to H_2^+ and of F^+ to H_2. We were initially surprised[2] to find that the $^3A_2$ state, which is so strongly bound for $N^+ - H_2$, has only relatively weak long-range attractive character for $F^+ - H_2$. Specifically, we find a potential minimum of only ~0.8 kcal, occurring at $r(F-H) = 2.9$ Å, $\theta(HFH) = 15°$. As predicted in Fig. 1, the $^3B_1$ and $^3B_2$ states are

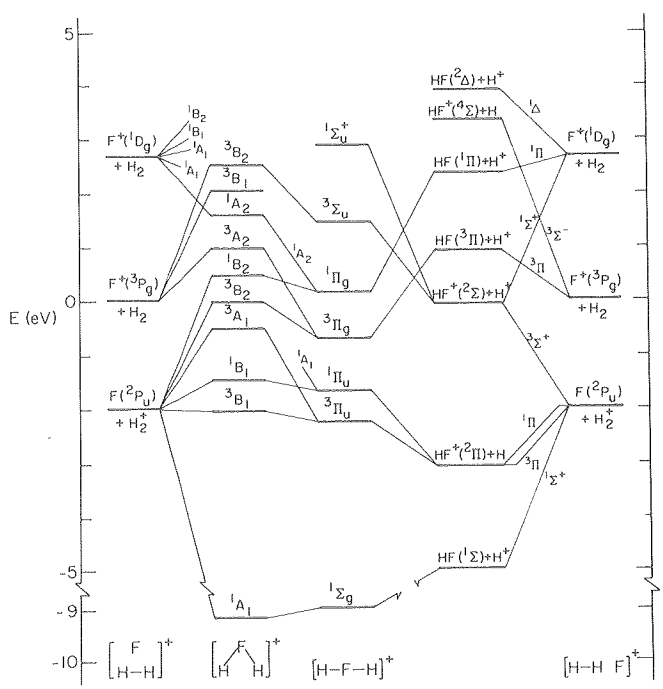

Fig. 1. Empirical correlation diagram for the ($F^+ + H_2$, $F + H_2^+$) system. (XBL 783-7509)

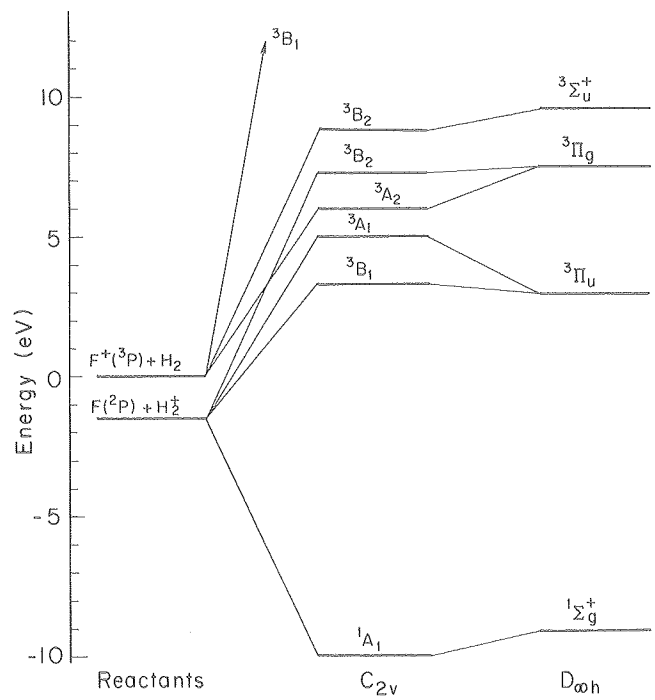

Fig. 2. Ab initio correlation diagram for the ($F^+ + H_2$, $F + H_2^+$) system. The C_{2v} results refer to the ground state FH_2^+ equilibrium geometry, i.e., they are vertical excitation energies. Similarly the $D_{\infty h}$ results were all obtained at $r_e(H-F) = 0.959$ Å, the optimum for the linear symmetric ground state. Note that the second $^3B_1$ state is very high, lying off the scale of the present figure. (XBL 778-3703)

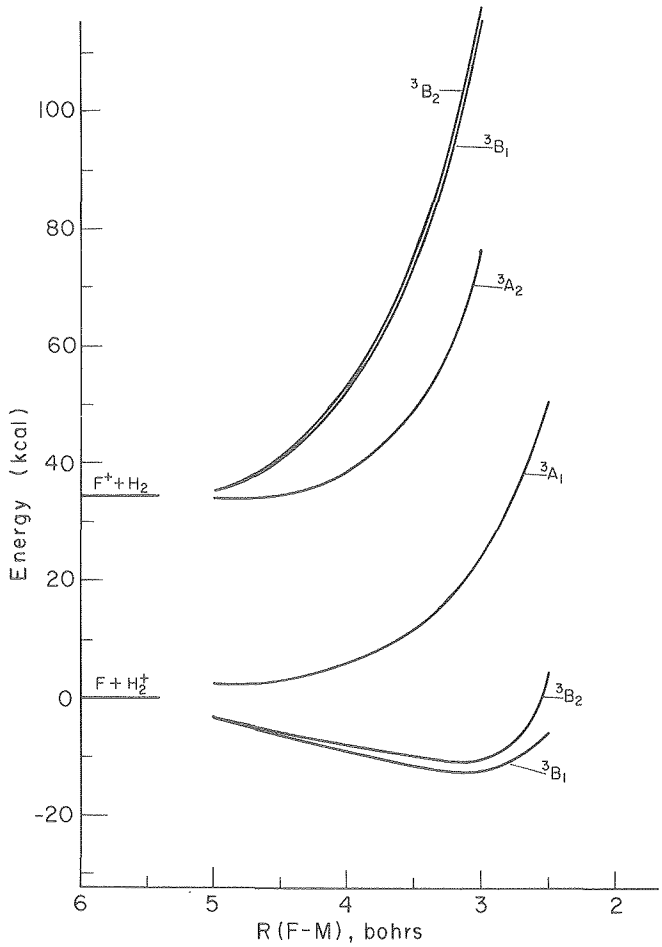

Fig. 3. Potential-energy curves for the C_{2v} approach of F to H_2^+ with fixed bond distance r(H-H) = 1.04 Å; and of F^+ to H_2(r = 0.74 Å). (XBL 778-3702)

even less attractive. Thus it would appear that C_{2v} or near-C_{2v} approaches of F^+ to H_2 cannot lead to reaction. This certainly confirms the conclusion that $F^+ + H_2$ is a completely different kind of reaction than $N^+ + H_2$.

Turning to the surfaces arising from $F + H_2^+$, Fig. 3 makes apparent the very strongly attractive characterof the $^1A_1$ ground state. More interesting, in the present context, are the three triplet states, which have the same spin as the separated $F^+(^3P_g) + H_2$. As predicted in Fig. 1, $^3B_1$ is the lowest of these, with an equilibrium geometry of r_e(F-H) = 1.67 Å, θ_e(HFH) = 31.6°, corresponding to an $F^+ - H_2$ dissociation energy of 17.5 kcal. The $^3B_2$ and $^3A_1$ states are reversed from the empirical correlation diagram, the $^3B_2$ being significantly bound, by 14.5 kcal, with its potential minimum at r_e(F-H) = 1.72 Å, θ_e(HFH) = 30.3°.

The possible significance of the $^3B_1$ and $^3B_2$ minima lies in the fact that the ground state $^1A_1$ surface can lead only to $HF + H^+$ products, i.e., not to $HF^+ + H$, the products observed experimentally. It is not inconceivable that a suitable C_s distortion of these two minima might lead to products $HF^+ + H$ without a noticeable barrier. However, it is at least equally likely that there is a low-energy pathway to HF^+ associated with $C_{\infty v}$ or near-$C_{\infty v}$ approaches $(F\text{-}H\text{-}H)^+$.

---

*From LBL-6679

1. This correlation diagram was constructed prior to the theoretical calculations reported here, to aid in the interpretation of molecular beam studies by S. G. Hanson and B. H. Mahan (unpublished).
2. In retrospect, however, it is clear that the origin of the small-bond-angle states of CH_2^+, NH_2^+, and OH_2^+ is related (in the sense of Walsh's rules) to their singly-occupied $1b_2$ orbital. However, for FH_2^+, the dominance of the singly-occupied $1b_2$ orbital is countered by the energertically unfavorable $4a_1$ orbital, not occupied in OH_2^+.

6. RESEARCH PLANS FOR CALENDAR YEAR 1978

Henry F. Schaefer III

We hope to complete a number of studies in the organometallic chemistry-surface chemistry area, beginning with the examination of chemisorption of a number (e.g., C_2H_2, CO, and N_2) of molecules on the (0001) beryllium metal surface. In light of the most recent experimental results of Somorjai, Kesmodel, and co-workers, we are particularly anxious to explore the relative energies of acetylene (HC≡CH) and vinylidene ($C{=}CH_2$) at various sites on this model surface, which has the first two layers isostructural with platinum(111). Other research in this general area will include a comprehensive study of the transition metal hydrides MH_4 (M = Ti, V, Cr, Mn, Fe, Co, Ni) and a study of the structures and energetics of singlet and triplet silaethylene $SiH_2{=}CH_2$. We plan to investigate a number of aluminum systems, including Al-C_2H_4, Al-C_2H_2, and Al-H_2O. For the former two, the competition between π-bonded forms and σ-bonded radicals (analogous to the vinyl and ethyl radicals) is particularly pertinent to the organometallic-surface-catalysis analogy.

7. 1977 PUBLICATIONS AND REPORTS

Henry F. Schaefer III and Associates

Journals and Books

1. C. W. Bauschlicher, Jr., Henry F. Schaefer III, and P. S. Bagus, Structure and Energetics of Simple Carbenes. CH_2, CHF, CHCl, CHBr, CF_2, CCl_2, J. Amer. Chem. Soc. 99, 7106 (1977), LBL-4945.

2. C. F. Bender, J. H. Meadows, and H. F. Schaefer III, Potential Energy Surfaces for Ion-Molecule Reactions. Intersection of the $^3A_2$ and $^3B_1$ Surfaces of NH_2^+, Faraday Discussions of the Chemical Society 62, 59 (1977), LBL-5114.

3. C. E. Dykstra and H. F. Schaefer III, Instructional Approach to Molecular Electronic Structure Theory, J. Chem. Ed. 54, 310 (1977).

4. R. R. Lucchese and H. F. Schaefer III, Dicyanocarbene: Triplet and Singlet Structures and Energetics, J. Amer. Chem. Soc. 99, 13 (1977), LBL-5168.

5. C. E. Dykstra, H. F. Schaefer III, and W. Meyer, Electron Correlation in Small Metal Clusters. Application of a Theory of Self-Consistent Electron Pairs to the Be_4 System, J. Chem. Phys. 65, 5141 (1976), LBL-5184.

6. C. W. Bauschlicher, Jr., K. Haber, H. F. Schaefer III, and C. F. Bender, Concerted Non-Least-Motion Pathway for the Singlet Methylene Insertion Reaction $CH_2(^1A_1) + H_2 \rightarrow CH_4$, J. Amer. Chem. Soc. 99, 3610 (1977), LBL-5194.

7. B. R. Brooks and H. F. Schaefer III, A Model Transition Metal Carbene System. $MnCH_2$, Mol. Phys. 34, 193 (1977), LBL-5416.

8. W. C. Swope and H. F. Schaefer III, Model Studies of π-Bonded Organometallic Systems $Mn\text{-}C_2H_2$ and $Mn\text{-}C_2H_4$, Mol. Phys. 34, 1037 (1977), LBL-5422.

9. S. R. Ungemach, H. F. Schaefer III, and B. Liu, Concerning Ab Initio Potential Energy Surfaces for $F + H_2$, Faraday Discussions of the Chemical Society 62, 330 (1977), LBL-5482.

10. M. Trenary, H. F. Schaeffer III, and P. Kollman, A Novel Class of Molecular Complexes: $Li\text{-}NH_3$, $Li\text{-}H_2O$, Li-HF, $Li\text{-}H_2S$, $Na\text{-}H_2O$ and Na-NF, J. Am. Chem. Soc. 99, 3885 (1977).

11. S. R. Ungemach, H. F. Schaefer III, and B. Liu, Theoretical Dipole Moment Function of the $X\ ^1\Sigma^+$ State of HI, J. Mol. Spectrosc. 66, 99 (1977), LBL-6949.

12. R. R. Lucchese and H. F. Schaefer III, Energy Separation Between the Open (C_{2v}) and Closed (D_{3h}) Forms of Ozone, J. Chem. Phys. 67, 848 (1977), LBL-6062.

13. N. R. Carlsen and H. F. Schaefer III, Open (C_{2v}) and Closed (D_{3h}) Forms of the S_3 Molecule, Thiozone, Chem. Phys. Lett. 48, 390 (1977).

14. H. F. Schaefer III, The Fuzzy Interface Between Surface Chemistry, Heterogeneous Catalysis, and Organometallic Chemistry, Accounts Chem. Res. 10, 289 (1977), LBL-6032.

15. P. K. Pearson, R. R. Lucchese, W. H. Miller, and H. F. Schaefer III, Theoretical Chemistry via Minicomputer, American Chemical Society, Symposium Series, Vol. 57, Editor Peter Lykos, 1977.

16. C. E. Dykstra, R. R. Lucchese, and H. F. Schaefer III, Electron Correlation Effects on the Excitation Energies of the Lowest Triplet States of Glyoxal, J. Chem. Phys. 67, 2422 (1977), LBL-6278.

17. C. E. Dykstra, M. Hereld, R. R. Lucchese, H. F. Schaefer III, and W. Meyer, Molecular Structure of the Methyl Anion CH_3^-. An investigation of the Effects of Electron Correlation Using the Theory of Self-Consistent Electron Pairs (SCEP), J. Chem. Phys. 67, 4071 (1977).

18. R. R. Lucchese, H. F. Schaefer III, and C. E. Dykstra, Excitation Energies of the $n \rightarrow \pi^*\ ^3A''$ and $\pi \rightarrow \pi\ ^3A'$ States of Acrolein, Chem. Phys. Lett. 51, 600 (1977).

19. L. Radom and H. F. Schaefer III, On the Limits of Stability of Multiply Charged Monocyclic Aromatic Cations: $C_3H_3^+$, $C_4H_4^{2+}$, $C_5H_5^{3+}$, $C_6H_6^{4+}$, $C_7H_7^+$, $C_8H_8^{2+}$, $C_9H_9^{3+}$, J. Am. Chem. Soc. 99, 7522 (1977).

20. R. R. Lucchese and H. F. Schaefer III, Extensive Configuration Interaction (CI) Studies of the Methylene Singlet-Triplet Separation, J. Am. Chem. Soc. 99, 6765 (1977).

21. H. F. Schaefer, editor, Methods of Electronic Structure Theory, Volume 3 of Modern Theoretical Chemistry (Plenum Press, New York, 1977), 462 pp.

22. H. F. Schaefer, editor, Methods of Electronic Structure Theory, Volume 4 of Modern Theoretical Chemistry (Plenum Press, New York, 1977), 461 pp.

23. C. E. Dykstra, An Examination of the Brueckner Condition for the Selection of Molecular Orbitals in Correlated Wavefunctions, Chem. Phys. Lett. 45, 466 (1977), LBL-5446.

24. D. S. Marynick, Ab Initio Self-Consistent Field Studies of Metal-Phosphate Complexes, J. Mol. Struct. 36, 339 (1977).

25. C. E. Dykstra, Internal Rotation in the Ground Electronic State of Allene, J. Am. Chem. Soc. 99, 2060 (1977), LBL-5480.

26. C. E. Dykstra, Self-Consistent Electron Pair Theory for Certain Types of Open Shell Wavefunctions, J. Chem. Phys. 67, 4716 (1977).

Invited Talks

1. H. F. Schaefer III, Department of Chemistry, University of Western Australia, Perth, Australia, February 1977.

2. H. F. Schaefer III, Department of Chemistry, Murdoch University, Perth, Australia, February 1977.

3. H. F. Schaefer III, Department of Chemistry, Tel-Aviv University, Tel-Aviv, Israel, March 1977.

4. H. F. Schaefer III, Department of Chemistry, The Hebrew University, Jerusalem, Israel, March 1977.

5. H. F. Schaefer III, Laboratoire de Chimie Theorique, University of Paris, Orsay, France, March 1977.

6. H. F. Schaefer III, Department of Chemistry, Kaiserslautern University, West Germany, April 1977.

7. H. F. Schaefer III, invited speaker at "Symposium on Minicomputers and Large Scale Scientific Computations," Chemical Institute of Canada/American Chemical Society, Montreal, Quebec, May 29-June 2, 1977.

8. H. F. Schaefer III, invited speaker at American Chemical Society Symposium on "The Reliability of Quantum Chemical Predictions," Chicago, Illinois, August 28-September 2, 1977.

9. H. F. Schaefer III, Department of Chemistry, University of Nebraska, Lincoln, Nebraska, September 1977.

10. H. F. Schaefer III, invited speaker, "Linus Pauling Award Symposium," Northwest Section, American Chemical Society, University of Oregon, Eugene, Oregon, November 4-5, 1977.

LBL Reports

1. C. F. Bender and H. F. Schaefer III, Potential Energy Surfaces for Fluorine Hydrogen Systems, Advances in Chemistry, (in press) LBL-5779.

2. R. R. Lucchese and H. F. Schaefer III, Metal-Carbene Complexes and the Possible Role of Hydroxycarbene in Formaldehyde Laser Photochemistry, J. Am. Chem. Soc., LBL-6063.

3. H. F. Schaefer III, XeF: Chemically Bound?, LBL-6298.

4. C. F. Bender and H. F. Schaefer III, Ionic Excited States of Ne_2F, Chem. Phys. Lett., LBL-6950.

5. B. H. Mahan, S. R. Ungemach, H. F. Schaefer III, Some Features of the Potential Energy Surfaces for the $F^+ + H_2$ Ion-Molecule Reaction, J. Chem. Phys., LBL-6679.

3. ATOMIC PHYSICS

a. Low Energy Atomic Physics

Howard A. Shugart, Principal Investigator

Introduction. Our Atomic Physics Group studies experimentally the interactions of electromagnetic radiation (x rays, light, microwaves) with free single atoms, molecules, or ions. Electromagnetic radiation generally carries information from the atomic system or acts as a probe of the atomic system under investigation. The purpose of such research ranges from the very practical development of advanced technology or commercial processes to the purely scientific discovery or testing of basic physical concepts. In the reports which follow, laser developments and isotope selective schemes represent technological advances, while thallium spectroscopy (neutral weak interactions) and the $^3S_1$ Li^+ lifetime studies exemplify investigations of two current, puzzling, and forefront questions in atomic physics.

1. LASER DEVELOPMENTS

E. Commins, S. Chu, R. Conti and P. Bucksbaum

Many applications for lasers require operation with characteristics quite different from those available in commercial instruments. This situation frequently necessitates extensive developmental work which advances the state-of-the-art. In the thallium spectroscopy reported below stringent conditions on high power, narrow bandwidth and high repetition rates has resulted in several developments:

Injection locking. A narrow-band continuous wave (CW) dye laser, driven by an argon ion pump laser was used to supply a reference signal for amplification by our flash-lamp pumped dye laser at 585 nm. This procedure is termed injection locking of the pulsed dye laser. The effect of injection locking was definitely observed and studies continue toward the goal of producing high power, single mode laser pulses at high repetition rates in a reliable way.

Intracavity doubling. Ultraviolet light was generated at 292.7 nm by using a short ADA crystal as a doubling element inside the cavity of our CW dye laser. The efficiency of power conversion to 292.7 nm light was comparable to the best efforts recently reported in the literature. When pumping with 4 watts (all lines) with an Argon laser roughly 1 milliwatt of tunable narrow band ultraviolet light was generated.

Improved operation of flash-lamp pumped pulsed dye lasers. The following substantial improvements in flash lamp pumped dye lasers were made during the past year. First a new-design, aluminized pyrex double elliptical reflector was developed successfully. This design makes much more efficient use of pump light from the flash lamps, can easily be fabricated, and is immune to deterioration of polished aluminum reflectors used in commercial instruments. A second improvement in control of the laser occurred when thyratron firing of the flash lamps was used in place of spark gap firing. This substitution essentially eliminated annoying timing jitter. Finally flash lamps are now "simmered" at ~ 800 ma between pulses. This procedure eliminates the need for prepulsing, results in more reproducible pulses, and much longer flashlamp lifetimes. These improvements give longer life and a factor of 10 more power in less than 1/2 the bandwidth of the best available commercial units.

2. THALLIUM SPECTROSCOPY AND NEUTRAL WEAK INTERACTIONS

E. Commins, S. Chu, R. Conti and P. Bucksbaum

A year ago, we reported measurements made on the extremely weak forbidden M1 transition $6^2P_{1/2}$ - $7^2P_{1/2}$ (292.7 nm) in atomic thallium ($Z = 81$) vapor. This result obtained with our Model 1 apparatus was preparatory to searching for circular dichroism effects which should arise from the existence of parity-violating neutral, weak electron-nucleon interactions predicted by gauge theories.

During the past year, the second version of our experimental apparatus (Model 2) was completed. This included a number of distinct features: a) new cell design with double electrodes, b) on-line computer handling of data, and c) overall gain in signal of a factor of 50 compared to original apparatus.

The Model 2 apparatus was used to search for parity violation in neutral weak currents. Observations lasting a total of 24 hr have gotten us to within an order of magnitude of the sensitivity required to test the Weinberg-Salam gauge model predictions.

Rather than continue with these observations, we decided to change to a new method (Model 3) which offers much better sensitivity and signal strength. In Model 3, a second infrared transition is used to optically pump Tl atoms from the $7^2P_{1/2}$ state to the $8^2S_{1/2}$ state. Fluorescence is then observed in the decay of $8^2S_{1/2}$ atoms to the $6^2P_{3/2}$ level (323 nm). The infrared optical pumping at 2.18 nm is achieved by use of an optical parametric oscillator driven by a second flash lamp pumped pulse dye laser in synchronism with the first one.

This scheme has been tested in detail with the Model 3 cell in a new stainless steel oven, and it works satisfactorily. At the time of writing we are just at the point of beginning to take data with the Model 3 system. An overall gain in sensitivity of a

factor of 50 or so compared to the Model 2 system is anticipated. This should provide a definitive test of the Weinberg-Salam model.

Theoretical analysis of parity non-conservation effects in Tl and Cs was completed and published in Physical Review.[1,2]

---

1. D. V. Neuffer and E. D. Commins, Phys. Rev. A 16, 844 (1977).

2. D. V. Neuffer and E. D. Commins, Phys. Rev. A 16, 1760 (1977).

3. EXPERIMENTS ON STORED IONS

Michael H. Prior and Randall D. Knight

Lifetime of the $(1s2s)^3S_1$ State of Li^+

The $(1s2s)^3S_1$ state of He-like ions decays to the $1s^2\ ^1S_0$ ground state by so called forbidden magnetic dipole radiative decay. This decay has been studied in the multicharged ions S^{+15}, Cl^{+16} and Ar^{+17} by the beam-foil time-of-flight technique and an unexplained non-exponential decay curve has been observed in each case. In an effort to extend the study of this decay over a wider range of nuclear charge, we are currently studying it in Li^+ ($Z = 3$) where theory predicts a radiative lifetime of $\tau = 49$ s. Our technique is markedly different from the beam-foil method and hence our observations will help to establish whether the peculiar behavior seen in S^{+15}, Cl^{+16} and Ar^{+17} is a real property of the decay of this state or an uncorrected experimental artifact.

Our method consists of the excitation and confinement of $(1s2s)\ ^3S_1\ Li^+$ ions inside a radiofrequency quadrupole ion-trap. After ionization and excitation by electron impact on a Li atomic beam, the decay of the $^3S_1$ ions is studied by one of three methods. We also measure the decay of the total number of Li^+ ions (most of which are in the ground state) as a function of storage time.

The decay of $^3S_1\ Li^+$ ions has been observed by a) counting spontaneously emitted magnetic dipole photons ($\lambda = 210$Å) vs. time after filling the trap, and b) by a laser quenching technique in which photons from a dye laser are tuned to excite the $(1s2s)\ ^3S_1$ to $(1s2p)\ ^3P_1$ transition at $\lambda = 5485$ Å. The $^3P_1$ state (see Fig. 1) then decays predominantly (99.9%) back to $^3S_1$ but has a small probability, ~ 0.1%, for decay to the ion's ground state with the emission of a 204 Å photon. Thus on the average after absorption of about 1000 photons at 5485 Å, each $^3S_1$ ion will have decay to the ground state and produce one 204 Å photon which we count. With about 100 mW of laser power we find that we can completely remove all the $^3S_1$ population in a few tenths of a second. This time is much less than the $^3S_1$ mean life and the mean life for ion loss from the trap so that the integrated number of laser induced counts is essentially an instantaneous measure of the number of $^3S_1$ ions in the trap.

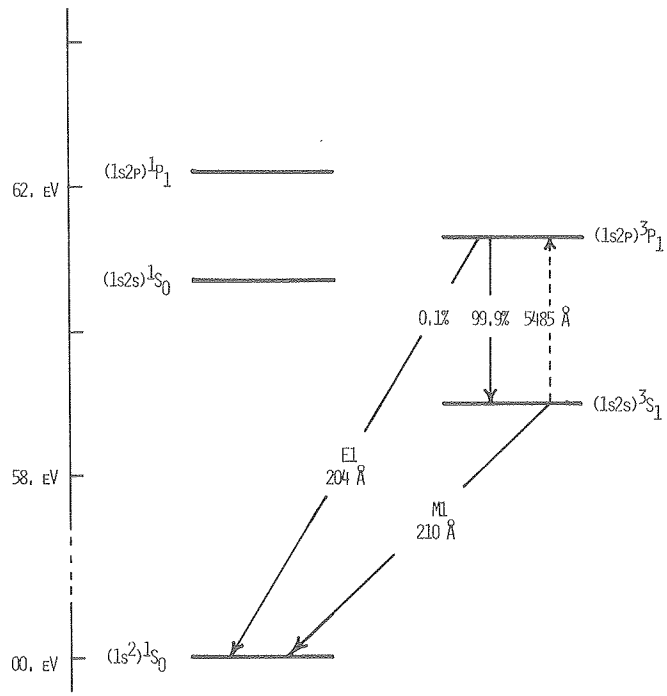

Fig. 1. Energy level diagram of the lowest states of Li^+. $^3S_1$ ions decay spontaneously by M1 emission at 210 Å. The laser excites the upward transition at 5485 Å (dashed line). This transfers all of the $^3S_1$ ions into the ground state via the weak E1 fluorescence at 204 Å. (XBL 781-6903)

Accumulation of laser induced counts vs. the time at which the laser is switched into the trap volume produces a decay curve for the $^3S_1$ population.

Both methods a) and b) produce curves which yield the total mean lifetime of $^3S_1$ ions, a third technique c) yields the radiative lifetime only. This consists of counting spontaneous M1 photons for a period T_1 which is short compared to the $^3S_1$ total mean lifetime; the number of counts collected is $C_1 = \varepsilon_1 \Gamma_r N T_1$ where ε_1 is a detector geometry and efficiency factor, Γ_r is the radiative decay rate, and N, the number of $^3S_1$ ions. After T_1 the laser is switched into the trap, and the integrated laser counts are accumulated. This gives $C_2 = \varepsilon_2 N$, and thus one has $\Gamma_r = (C_1\varepsilon_2)/(C_2\varepsilon_1\tau_1)$. ε_2 is not necessarily equal to ε_1 because of a number of effects most of which are probably not large ($\lesssim$ 10% but which have not yet been totally explored. These are: 1) variation of detector efficiency at 210 Å vs. 204 Å; 2) possible difference in the angular distribution and polarization of spontaneous and laser induced photons caused by impact alignment and optical pumping.

Figures 2, 3 and 4 show examples of our data by the various methods. Our current status is that by both methods a) and b) we measure a total mean life for $^3S_1$ decay of 5 ± 2 s and by method c) we obtain a radiative lifetime $\tau_r = \Gamma_r^{-1} = 50$ s which is in agreement with τ_r(theory) = 49 s but has not been corrected for possible ε_2, ε_1 differences. We do not believe such a correction will shorten τ_r to less than 25 s, and thus we conclude that there is an additional loss mechanism for $^3S_1$ ions other than spontaneous radiative decay in our apparatus. The fact that we observe considerably more laser

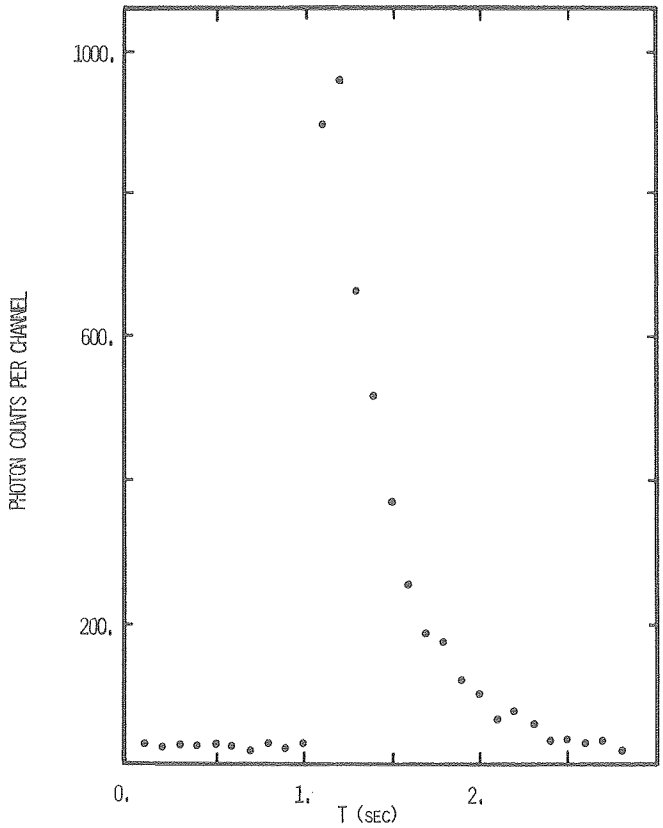

Fig. 2. Example of the laser quenching of $^3S_1$ Li^+ ions. Counts shown up to 1 s are from spontaneous M1 decay, the laser is switched on at 1 s and the ensuing counts are the E1 photons at 204 Å. The ratio of the spontaneous count rate ($T \leq 1$ s) to the integrated laser induced counts is a measure of the M1 decay rate. (XBL 781-6904)

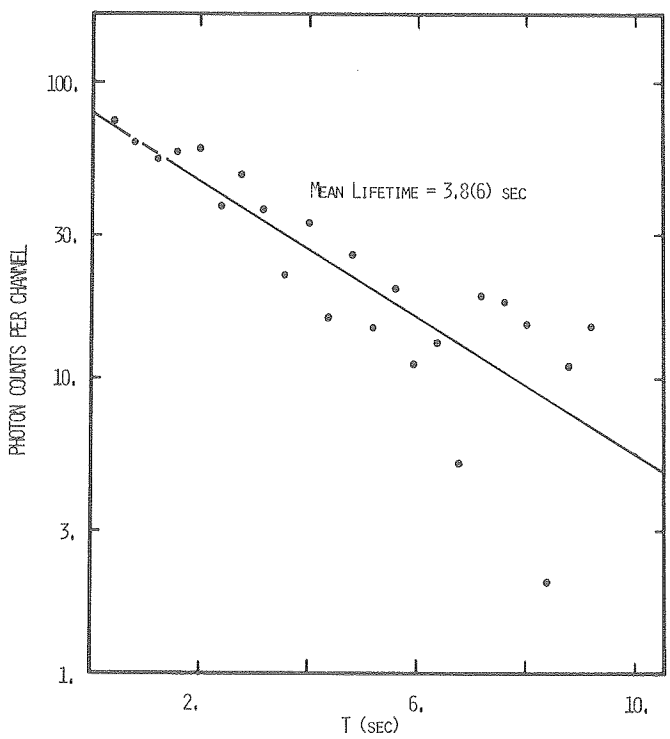

Fig. 3. Decay curve obtained by accumulating spontaneous M1 photons vs. time after filling trap with Li^+ ions. (XBL 781-6905)

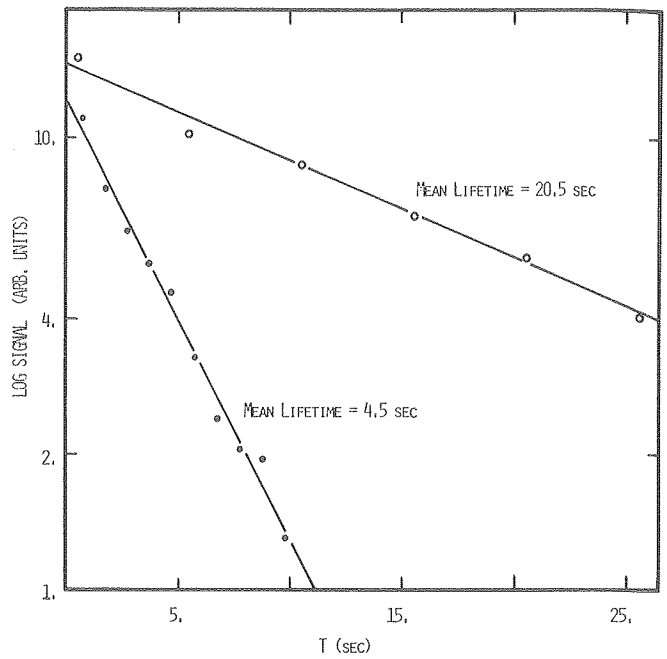

Fig. 4. Decay curves for all Li^+ ions in trap (upper curve) and $^3S_1$ Li^+ ions (lower curve) as measured by accumulation of laser induced counts vs. time of application of the laser beam to the trap volume. (XBL 781-6906)

induced counts than would be obtained from integration of the spontaneous decay curve indicates that the additional loss mechanism does not produce countable photons. During all these studies the ion storage lifetime (mean lifetime for ion loss from the trap) was 15 to 25 s. Possible candidates for the additional loss mechanism are: 1) shortened ion storage lifetime for $^3S_1$ ions due to velocity dependent metastability exchange cross section with ground state ions; 2) charge exchange and/or ion-molecule reactions on background gas molecules (background pressure is $\approx 10^{-9}$ Torr).

We plan to examine these possibilities by varying the trap parameters and background gas pressure and composition.

4. ATOMIC ABSORPTION SPECTROSCOPY

Tetsuo Hadeishi and Associates

Three separate projects have been pursued during the past year which cover different applications of atomic absorption spectroscopy. The first project has as its goal the discovery of an efficient and economical way of separating uranium isotopes by using a simple apparatus. The basic idea involves the general property that chemical reactions are more rapid with atoms in excited states than with atoms in the ground state. Thus an experiment was designed to vaporize uranium at approximately 2700°C and to excite optically one uranium isotope to resonant states using light containing two watts of power in a linewidth of 4.5 GHz. The excited iso-

tope preferentially reacts with various gases such as H_2, Cl_2 or I_2 to form a compound which is separated simply from the system. Two preliminary reports[1,2] on the initial aspects of this scheme have been written. The present status of the research is as follows: An efficient uranium vaporization furnace was constructed which was capable of total absorption of resonant laser light. We have measured the line shape and many other relevant properties of the system. One of the most important findings so far is the vaporization properties of uranium from different furnace materials. This work has established limits and constraints on the type of vaporization furnace needed in a real scale separation apparatus. Subsequent stages of the separation scheme are currently under investigation.

The second project funded by the Division of Biological and Environmental Research (DOE) is concerned with developing a general purpose molecular detector which is sensitive and specific. At present, there is no such device. Recently, we have developed a molecular detector which would, in principle, detect all the organometallic compounds that are soluble. This was accomplished by coupling a high pressure liquid chromatograph (HPLC) with a Zeeman Atomic Absorption Spectrometer (ZAA). The HPLC separates molecular species while the ZAA detects the concentration of metal present in the molecules. This idea was tested and preliminary findings submitted to Nature.[3] Another area of activity under this funding deals with optical detection of molecules is a three-dimensional space. At present the important application is for diagnostics of the nitrogen compounds in combustion processes.

The third project funded by the National Science Foundation concerns the final stage of development of the Zeeman Atomic Absorption Spectrometer. After four years of research and development, we have achieved the status that almost any element can now be detected in the ZAA spectrometer. This accomplishment resulted because of the development of an intense, stable source of optical resonance radiation from any atomic species. The new lamp works on the principle of a new discovery of two-dimensional plasma confinement owing to crossed electric and magnetic fields. We have named this new light source the MAGNETICALLY CONFINED ARC DISCHARGE LAMP.

---

1. T. Hadeishi, Dissociation of Uranocene by Collision With Metastable States of Noble Gas Atoms Detected by Forward Level Crossing, ICPEAC, July 21-27, 1977, U. of Paris Sud, 91405 Orsay.
2. T. Hadeishi and T. Andersen, New Technique for Uranium Resonance Absorption by Means of a Zeeman Tuned Magnetically Confined Arc Discharge Lamp, accepted for publication by Optics Communication.
3. H. Koizami, T. Hadeishi, and R. McLaughlin, Species Determination of Organometallic Compounds Using Zeeman Atomic Absorption Spectroscopy With Liquid Chromatography, submitted to Nature.

5. RESEARCH PLANS FOR CALENDAR YEAR 1978

Howard A. Shugart

During 1978 our group's effort will be concentrated in three principal areas of research. The important search for weak neutral currents in atomic physics should reach the point where a definitive test of current gauge theories is possible. Concommitant with this study will be continued development of laser techniques which improve the power and stability of optical and ultraviolet lasers. In the subject of ion trapping, we will seek to understand the unknown nonradiative decay mechanism which seems to depopulate metastable $^3S_1$ Li^+ but does not affect ground state Li^+ ions. A search for any parameter which might help resolve the problem will be made. We also plan to replace the current trap with a new electrostatic trap. This should establish if a property of the ion or of the trap is responsible for the unexplained behavior of the decay. Finally, atomic absorption studies will provide further information on the optical isotope separation techniques and on practical means of detecting trace atoms or molecules.

6. 1977 PUBLICATIONS AND REPORTS

Howard A. Shugart and Associates

Journals

1. S. Chu, E. D. Commins and R. Conti, Observation of the $6^2P_{1/2}$ - $7^2P_{1/2}$ M1 Transition in Atomic Thallium Vapor, Phys. Lett. 60A, 96 (1977), LBL-6236.

2. David V. Neuffer and Eugene D. Commins, Calculation of Parity Violating Effects in the $6^2P_{1/2}$ - $7^2P_{1/2}$ Forbidden M1 Transition in Thallium, Phys. Rev. A 16, 844 (1977).

3. S. Chu and E. Commins, An Aluminum Coated Pyrex Double Ellipse Laser Cavity, Applied Optics 16, 2619 (1977), LBL-6031.

4. M. H. Prior and E. C. Wang, Hyperfine Structure of the 2s State of ^3He, Phys. Rev. A 16, No. 1, 6 (July 1977).

5. David V. Neuffer and Eugene D. Commins, Calculation of Parity Nonconserving Effects in Forbidden M1 Transitions in Cesium, Phys. Rev. A 16, 1760 (1977), LBL-6261.

6. M. H. Prior and E. C. Wang, Hyperfine Structure of 2s ^3He, Phys. Rev. A 16, 6 (1977), LBL-6026.

7. R. Marrus, M. H. Prior and H. A. Shugart, Editors, Atomic Physics 5, Plenum Press (New York) 1977.

8. Atilla Ozmen, Ahsanul Huq and Howard A. Shugart, Ground State g_J of Atomic Lithium, Bull. Am. Phys. Soc. 22, 623 (1977), LBL-6121 Abs.

9. M. H. Prior and R. D. Knight, Laser Quenching of the Metastable $n = 2$ $^3S_1$ State of Stored Li^+ Ions, Bull. Am. Phys. Soc. 22, 1319 (1977), LBL-6952 Abs.

Reports

1. T. Hadeishi, Dissociation of Uranocene by Collisions With Metastable States of Noble Gas Atoms (Detected by Forward Level Crossing), ICPEAC Meeting, July 21-27, 1977, Univ. of Paris Sud, 91405 Orsay.

2. T. Incesu, Ahsanul Huq and Howard A. Shugart, The g_J- Factor of Metastable $^5S_2$ Atomic Oxygen Using a Time-of-Flight, Atomic Beam Magnetic Resonance Method, July 25, 1977, LBL-6643.

3. T. Hadeishi and T. Andersen, New Technique for Uranium Resonance Absorption by Means of a Zeeman Tuned Magnetically Confined Arc Discharge Lamp, to be published in Optics Communication.

4. H. Koizami, T. Hadeishi, and R. McLaughlin, Species Determination of Organometallic Compounds Using Zeeman Atomic Absorption Spectroscopy With Liquid Chromatography, submitted to Nature.

5. S. Chu, Observation of the Forbidden Magnetic Dipole Transition $6^2P_{1/2} \rightarrow 7^2P_{1/2}$ in Atomic Thallium, (Ph.D. thesis), October 1976, LBL-5731.

6. David B. Neuffer, Calculation of Parity Violating Effects in the $6^2P_{1/2} - 7^2P_{1/2}$ Forbidden M1 Transition in Thallium, (Ph.D. thesis) May 1977, LBL-6237.

7. M. H. Prior, Electrostatic Ion Analyzer (EIA) Feb. 1977, patent application.

Publicity Articles

1. Ted Hadeishi, New Device Identifies Elements, Currents, June 17, 1977.

2. T. Hadeishi, Element Identifying Made Easy, Oakland Tribune, Wednesday, June 29, 1977, p. 7.

3. T. Hadeishi, LBL Scientist Hadeishi Invents Instant Indicator to Check for Gold in Rocks or Mercury in Food, ERDA News, June 27, 1977.

4. T. Hadeishi, Business Week, Dec. 5, 1977.

Invited Colloquia:

1. E. Commins, Weak Interaction Research in Atomic Physics

Stanford University	May 24, 1977
	Nov. 9, 1977
	Nov. 22, 1977
Oregon State University	May 3, 1977
Ben Lee Memorial International Conference on Parity Violation	Oct. 20, 1977
University of Michigan	Nov. 30, 1977
University of Chicago	Dec. 1, 1977

2. M. H. Prior, Lifetime of Metastable $^3S_1$ Li^+
Oregon State University Nov. 21, 1977

b. Studies on Highly Stripped Heavy Ions

Richard Marrus, Principal Investigator

1. OSCILLATOR STRENGTHS OF LOW-LYING TRANSITIONS OF Li-LIKE AND Be-LIKE IRON (Z = 26)

H. Gould, D. MacDonald and R. Marrus

We have completed measurements of the oscillator strengths of the lowest-lying resonance transitions, $2s^2S_{1/2}$ - $2p^2P_{1/2,3/2}$, in lithium-like Fe XXIV and have made a preliminary measurement of the oscillator strength of the transition $(2s)^2$ $^1S_0$ - 2s2p $^3P_1$ in beryllium-like Fe XXIII.

Lines from low-lying transitions of highly-charged ions of the Li and Be isoelectronic sequences appear prominently in the spectra of hot plasmas, both those of astrophysical interest associated with solar flares,[1,2] and those associated with the controlled fusion program.[3] Spectral wavelengths are used to identify the ions present; knowledge of oscillator strengths is required for determination of the ion concentration[4] and the electron temperature and density.[5] Further, these simple systems with small cores should be susceptible to successful theoretical treatment. In particular, for sufficiently high effective nuclear charge, relativistic contributions to calculated oscillator strengths are expected[6] to be large enough to be experimentally discernible. Calculated[6] oscillator strengths of the 2s $^2S_{1/2}$ - 2p $^2P^o_{1/2,3/2}$ doublet in Li-like Fe XXIV contain relativistic contributions of 6 and 37%, respectively, of the nonrelativistic values; the nonzero oscillator strength of the $2s^2$ $^1S_0$ - 2s2p $^3P^o_1$ transition in Be-like Fe XXIII is entirely due to relativistic effects. Hence, these measurements provide a test of whether these calculationsl techniques may be used with confidence in regions not presently accessible to experiment.

A 491 MeV Fe^{+17} beam (60 particle nanoamps) from the Lawrence Berkeley Laboratory SuperHILAC was magnetically deflected into our apparatus and passed through a carbon foil (206 μg/cm^2 for the Li-like Fe, and 40 μm/cm^2 for the Be-like Fe) mounted on a movable support that had about one-half meter total travel. A 0.95 cm collimator mounted immediately upstream from the region viewed by the spectrometer (used in the standard "side-on" viewing configuration) insured that light detected by the spectrometer was emitted by ions that subsequently struck the downstream Faraday cup. The spectrometer (McPherson Model 247, with stepping motor drive and a 2.2 meter, 600 ℓ/mm grating) was operated with an 82° angle of incidence, a 3.17 mm wide grating mask slit and a blaze wavelength of 210 Å; for an entrance slit width of 500 μ, the beam length viewed was 2.1 mm. The photon detector (Bendix Channeltron Model 4700) was placed behind a repelling (-300 volts) grid followed by a grounded grid to exclude charged particles. Calibration constants for the spectrometer were obtained from spectral scans over the 225 to 305 Å region containing the first five members of the He II Lyman series from a stationary hollow cathode source (calibration uncertainty = ±0.2 Å).

Spectral scans over the regions of interest are shown in Fig. 1. These data were fitted[7] with Gaussian line shapes; the quoted uncertainties have been calculated from twice the statistical uncertainty (typically 0.3 Å) associated with the Gaussian fitting added in quadrature to the 0.2 Å uncertainty associated with the calibration. There is good agreement with known accurate wavelengths obtained from solar flare spectra.[2] We identify the line at 271.2 ± 0.6 Å as the previously unreported 1s2s $^3S_1$ - 1s2p $^3P^o_2$ transition in He-like Fe XXV; a scaling of the terms used by Davis[8] for Ar XVII yields a predicted wavelength of 271.0 Å, in agreement with our measured value.

Decay curves from which the mean lives of the 2p $^3P^o_{1/2,3/2}$ levels in Fe XXIV were obtained are shown in Figs. 2a and 2b. These data were obtained by the following procedure: for each foil position, with the spectrometer set on the particular spectral line center, the number of counts registered by the detector and the time elapsed during collection of a specified amount of charge in the Faraday cup were recorded (the dark current was ≈ 0.1 count/s). At the same foil position, background data were acquired by making similar measurements about 10 Å above and below the line center. The number of detector counts recorded (corrected for average background and dark current) vs foil position is plotted in Figs. 2a and 2b. A single exponential has been least squares fitted to the data in each case; the quoted uncertainties in the mean lives have been obtained by adding in quadrature the uncertainty (1%) in beam velocity and twice the statistical uncertainty (≈ 68% confidence level) associated with the least squares fit.

The results of these measurements are compared with theoretical predictions in Table 1 and Fig. 3a. The oscillator strengths, f_{ik}, were calculated using the usual formula

$$f_{ik} = 1.50 \times 10^{-16} \lambda^2 \frac{g_k}{g_i} \frac{1}{\tau_k}$$

where the transition wavelength[1] λ is in Å, g_k and g_i are the statistical weights of the upper and lower states, respectively, and τ_k is the mean life of the upper state in seconds ($1/\tau_k$ is the transition probability A_{ik}, since the decay is unbranched) measured in this work. It is apparent that the relativistic calculations of Armstrong et al.[6] and Kim and Declaux[9] in the dipole "length" gauge are in excellent agreement with our measurements.

The result of our measurement is compared with theory in Table 1 and Fig. 3b. The relativistic The relativistic dipole "velocity" gauge calculation

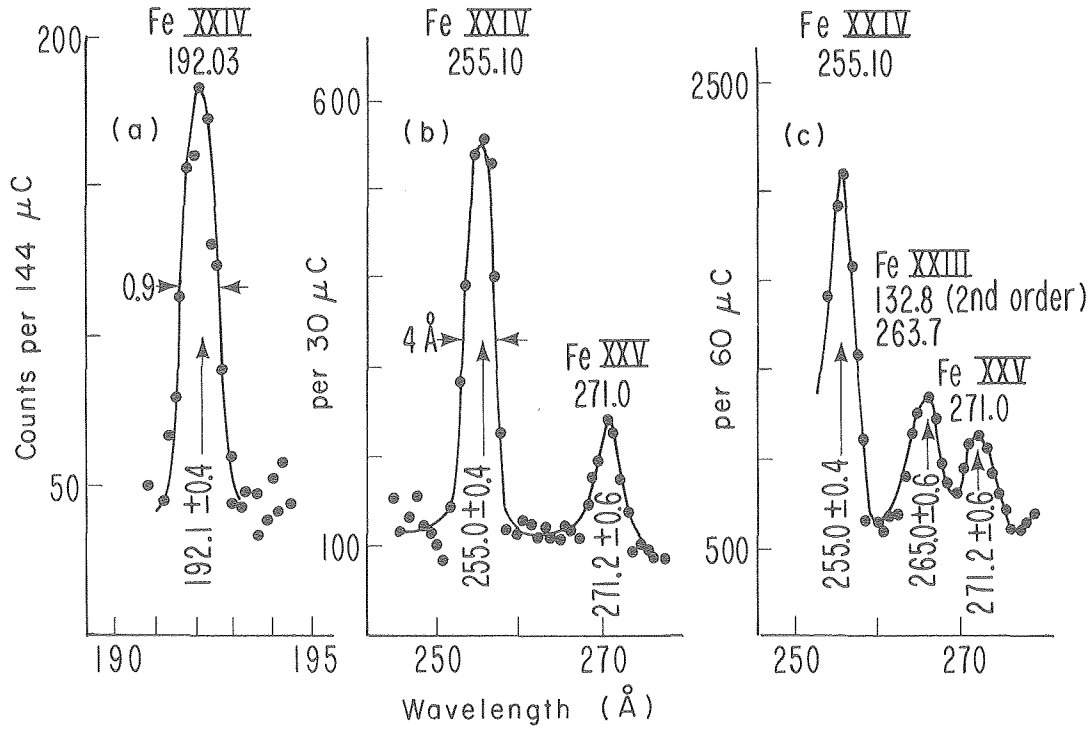

Fig. 1. Spectral scans of the post-foil beam for a 491 MeV Fe^{+17} beam incident on a carbon foil. (a) Scan of the 2s $^2S_{1/2}$ - 2p $^2P^o_{3/2}$ resonance line from Li-like Fe XXIV (120 μ slits and 206 μg/cm^2 foil). (b) Scan of the 2s $^2S_{1/2}$ - 2p $^2P^o_{1/2}$ resonance line from Fe XXIV and the previously unreported line at 271.2 ± 0.6 Å that we attribute to the 1s2s $^3S_1$ - 1s2p $^3P^o_2$ transition in He-like Fe XXV (500 μ slits and 206 μg/cm^2 foil). (c) Scan over the region shown in (b) (foil thickness = 40 μg/cm^2). The feature at 265 Å is attributed to a blend of the first and second order lines from Be-like Fe XXIII (132.8 Å from 2s^2 $^1S_0$ - 2s2p $^1P^o_1$ and 263.7 Å from 2s^2 $^1S_0$ - 2s2p $^3P^o_1$). (XBL782-191)

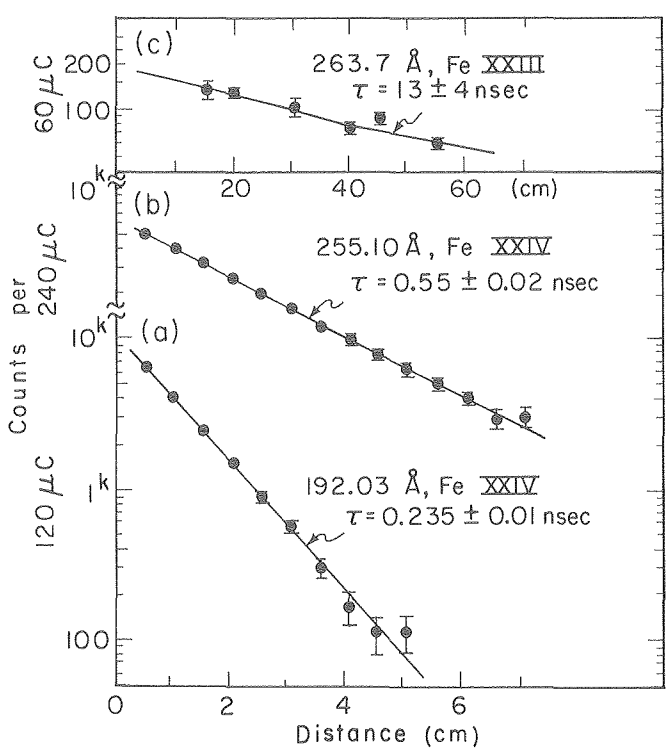

Fig. 2. Measured decay curves for determination of the mean lives of (a) the 2p $^2P^o_{3/2}$ level of Fe XXIV; (b) the 2p $^2P^o_{1/2}$ level of Fe XXIV; and (c) the 2s2p $^3P^o_1$ level of Fe XXIII. (XBL 782-201)

Table 1. Comparison of experimental and theoretical values of oscillator strengths.

Ion	Transition observed	λ (Å)[a]	Measured lifetime (ns) of upper level[b]	Experimental oscillator strength[b]	Calculated relativistic oscillator strengths[c] f_L	f_V
Fe XXIV	$2s\ ^2S_{1/2} - 2p\ ^2P^o_{1/2}$	255.10	0.55 ± 0.02	0.018 ± 0.001	0.018 (0.017)	0.020 (0.017)
Fe XXIV	$2s\ ^2S_{1/2} - 2p\ ^2P^o_{3/2}$	192.03	0.235±0.01	0.047 ± 0.002	0.048 (0.035)	0.053 (0.035)
Fe XXIII	$2s^2\ ^1S_0 - 2s2p\ ^3P^o_1$	263.74	13 ± 4	0.0024±0.0007	0.0015	0.0024 0.0015[d]

[a] Ref. 2.

[b] This work.

[c] Ref. 6; f_L and f_V are "length" and "velocity" calculations; values in parentheses are nonrelativistic.

[d] Ref. 10.

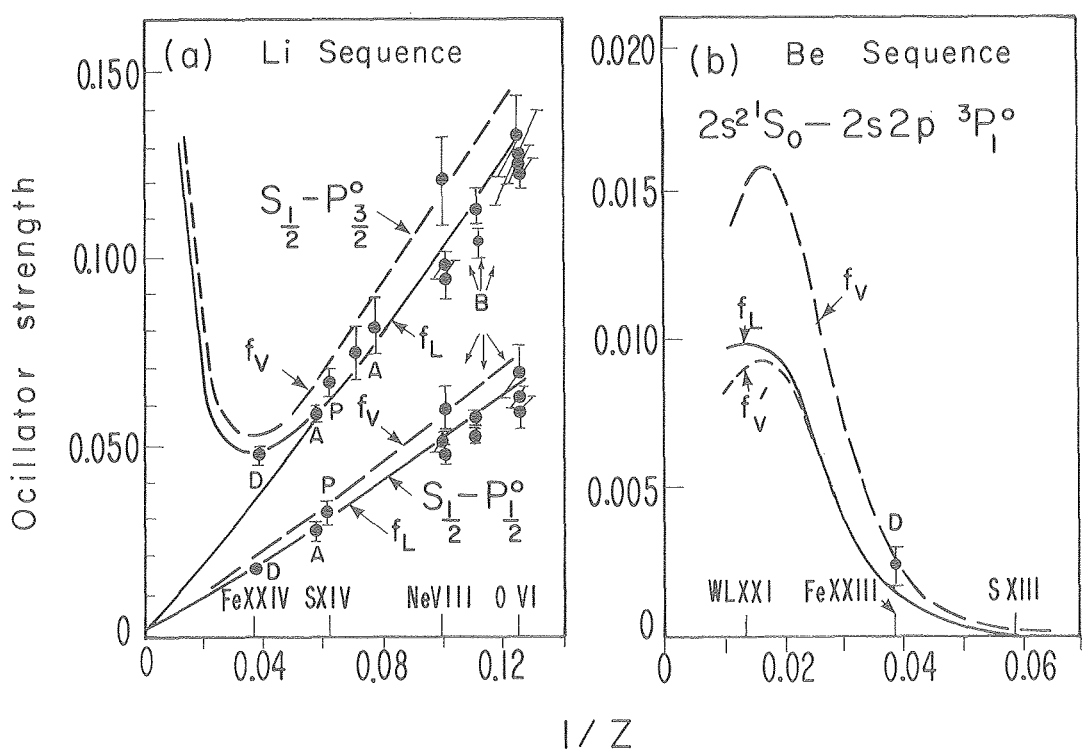

Fig. 3. Comparison of theoretical and experimental oxcillator strengths of: (a) the $2s\ ^2S_{1/2} - 2p\ ^2P^o_{1/2,3/2}$ resonance transitions for ions of the Li isoelectronic sequence [the middle solid curve through the origin is nonrelativistic theory;[7,10] the remainder of the curves are relativistic theory[7,9] with subscripts V and L denoting dipole "velocity" and "length" calculations. The experimental points are D (this work), P (Ref. 3), A (Ref. 5), and B (Ref. 8)]; and (b) the $2s^2\ ^1S_0 - 2s2p\ ^3P^o_1$ intersystem transition for ions of the Be isoelectronic sequence (theoretical curves labeled f_V and f_L are from Ref. 7; that labeled f_V' is from Ref. 10. The experimental point D is from this work.) (Z = atomic number.) (XBL782-192)

of Armstrong et al.[7] appears to be in good agreement with our measurement. This agreement may be misleading in view of the fact that a similar relativistic calculation by Cheng and Johnson[10] (which includes certain "exchange overlap" terms neglected by Armstrong et al.)[7] obtains good agreement between oscillator strengths calculated in "length" and "velocity" gauges. Their results do not agree with our measurements but do agree with the "length" gauge calculations of Armstrong et al. Thus it appears there is actually a discrepancy between theoretical and experimental results in this case. Theoretical inaccuracies may be caused by the fact that the calculated values rely heavily on the relativistic spin-orbit mixing of the 2s2p $^1P_1^o$ and 2s2p $^3P_1^o$ levels and are therefore strongly dependent on the calculated 2s2p $^1P_1^o$ lifetime; recent measurements in sulphur indicate a 20% discrepancy between the measured and predicted 2s2p $^1P_1^o$ lifetime. On the experimental side, it should be noted that we regard our measured value in this case to be much less reliable than those given above due to the obvious shortsomings of poor statistics, the small number of data points and the fact that we followed the decay curve for less than one mean life. We report the result because it appears to be of considerable interest.

1. G. D. Sandlin, G. E. Brueckner, V. E. Scherrer and R. Tousey, Astrophys. J. 205, L47 (1976).
2. K. G. Widing and J. D. Purcell, Astrophys. J. 204, L151 (1976); K. G. Widing, Astrophys. J. 197, L33 (1975); W. M. Neupert and M. Swartz, Astrophys. J. 191, 261 (1974); W. M. Neupert, Phil. Trans. Roy. Soc. London A 270, 143 (1971) and Ref. 1 above.
3. U. Feldman, G. A. Doschek, D. K. Prinz and D. J. Nagel, J. Appl. Phys. 47, 1341 (1976); E. Hinnov, Phys. Rev. A 14, 1533 (1976).
4. P. L. Smith, Nucl. Instrum & Meth. 110, 395 (1973).
5. U. Feldman and G. A. Doschek, J. Opt. Soc. Am. 67, 726 (1977).
6. L. Armstrong, Jr., W. R. Fielder and D. L. Lin, Phys. Rev. A 14, 1114 (1976).
7. D. Zurstadt, GAUS2Z Program (1969), Argonne National Laboratory, Argonne, Illinois 60439.
8. W. A. Davis and R. Marrus, Phys. Rev. A 15, 1963 (1977).
9. Y.-K. Kim and J. P. Declaux, Phys. Rev. Lett. 36, 139 (1976).
10. K. T. Cheng and W. R. Johnson, Phys. Rev. A 15, 1326 (1977).

2. QUENCHING OF THE METASTABLE STATE OF HYDROGEN-LIKE ARGON IN AN EXTERNAL ELECTRIC FIELD

H. A. Gould and R. Marrus

During calendar 1977, work continued on the experiment to make a precision test of the Bethe-Lamb theory of Stark quenching of the $2S_{1/2}$ state of hydrogen-like argon in an external electric field. The most important goal of this experiment is to obtain a precision value of the Lamb shift in the highest Z hydrogenic system studied to date (Ar^{+17}). At the 1% level such a measurement will provide a new test of the theory of the Lamb shift.

The basic method of the experiment is to measure the lifetime of the metastable state in a strong, external electric field. From the measured lifetime, the predictions of the Bethe-Lamb theory can be checked and values of the Lamb shift deduced. During calendar 1977, extensive data were taken on argon beams accelerated by the Berkeley SuperHILAC to 340 MeV. These ions were excited to the metastable state of the hydrogenic ion by passing the beam through thin carbon foils. The spectrum emitted by these foil-excited ions was viewed by Si(Li) detectors. There are two possible decay modes for these ions, a two-photon electric dipole (2E1) mode and a single-photon (E1) mode which is sometimes referred to as quench radiation. The 2E1 mode gives rise to a continuous x-ray spectrum with an end-point energy equal to the $2S_{1/2}$ - $1S_{1/2}$ energy separation (3.34 keV) while the quench peak is a distinct line at the $2S_{1/2}$ - $1S_{1/2}$ energy separation. Both of these modes are in evidence in the observed spectrum (see Fig. 1) and each gives experimental

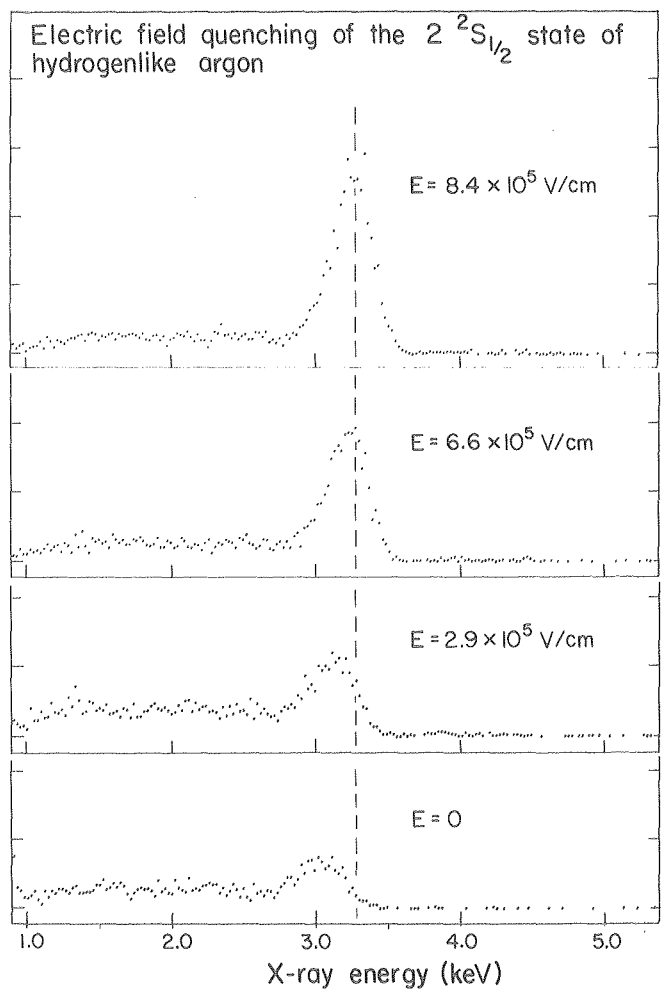

Fig. 1. Spectrum of the $2S_{1/2}$ state decaying in the presence of an external electric field. (XBL 767-8583)

information about the lifetime. Most important, the lifetime information provided by each is sensitive to different systematic errors, and hence provide an important check on the internal consistency of the data.

During calendar 1977 a substantial amount of data analysis was completed. Possible systematic effects due to:

- electronic dead time
- geometrical corrections
- counts in the quench peak from decays of helium-like ions
- nonlinear normalization effects
- structure in the velocity distribution of the beam
- variation of the detector efficiency with x-ray energy
- Doppler shifts arising from beam bending effects
- cascading effects in the 2E1 spectrum

were studied in detail and eliminated as sources of uncertainty.

As a result of these studies, a value of the Lamb shift has been obtianed with an accuracy of $1\frac{1}{2}$%. This is already sufficient to distinguish between two discrepant calculations (due to P. Mohr and G. Erickson). Our result is in good agreement with the calculation of Mohr. We have further identified that the most serious remaining systematic effect in the lifetimes determined from the 2E1 data comes from helium-like counts resulting from radiative decay of the 2^1S_0 state. We plan to eliminate this by doing coincidence measurements that will unambiguously establish the fraction of counts that arise from decay of the 2^1S_0 state. The most serious systematic effect that influences the lifetimes determined from the quench peak data arises from transitions from the $2p_{1/2}$ and $2p_{3/2}$ states. These counts are unresolved by our detectors and arise from cascades from highly-excited states populated by the beam-foil excitation process. We are planning a direct measurement of the fraction of counts due to cascades.

When the measurements described in the preceding paragraph are completed (early 1978), we anticipate an ultimate accuracy in the Lamb shift of 1% or better.

3. SINGLE PHOTON DECAY OF METASTABLE $2S_{1/2}$ STATE IN HYDROGEN-LIKE ATOMS

A. H. Gould and R. Marrus

Although this decay mode was predicted over 30 years ago by Breit and Teller[1] it has not as yet been observed. Recently there has been a great deal of theoretical interest in this decay since it has been shown to be especially sensitive to a possible parity-violating interaction in the atomic Hamiltonian. Hence, we have initiated experiments to search for this transition.

An attempt was made to observe this M1 decay in a foil-excited Fe beam. A Doppler-tuned spectrometer[2] was used to provide high energy resolution capable of distinguishing the x rays from helium-like transitions. A strong signal was obtained at the expected energy. However, subsequent measurements showed that a large part of this signal results from cascade transitions through the nearby $2p_{1/2}$ state. Experiments are currently being planned to remove the cascade contribution.

---

1. G. Briet and E. Teller, Astrophys. J. 91, 215 (1940).
2. R. Marrus and R. W. Schmieder, Nucl. Instrum. Meth. 110, 459 (1973).

4. THEORETICAL STUDY OF ELECTRIC-FIELD INDUCED DECAYS

P. J. Mohr and R. Marrus

The theory of electric field induced decays has been studied starting from the bound-state interaction picture of quantum electrodynamics. It is found that the problem is amenable to a solution if a small number of assumptions of a very general nature are made. As a result of the solutions one obtains a rigorous formula for the decay rate of the hydrogenic $2S_{1/2}$ state in an external field, and an accurate prediction for the angular distribution of the decay photons relative to the electric field direction.

It is further predicted that there should be a large asymmetry in the angular distribution that results from an M1-electric field interference term in the matrix element. This has important consequence for several experiments that are now in progress.

5. RESEARCH PLANS FOR CALENDAR YEAR 1978

Richard Marrus

a. Complete Measurements on the Stark Quenching Experiments. The study of the remaining systematic effects in the Stark quenching experiments can be completed in about one week of running at the SuperHILAC. These measurements (scheduled for the second week in February 1978) should give a value for the Lamb shift at the 1% level.

b. Study of Resonance Transitions in Helium-like Mo. Our success with the grazing-incidence spectrometer for studying UV transitions in iron leads us to attempt similar studies in Mo. The wavelengths and oscillator strengths of these lines are important in diagnostics of fusion plasmas.

c. Theoretical Investigation of Energy Levels and Transition Probabilities in Highly-ionized Atoms. We have already shown that these transition rates are strongly affected by radiative corrections

to the energy levels. For example, in helium-like krypton, the level shifts lead to a change of more than 10% in the decay rate for $2^3P_0 \rightarrow 2^3S_1$, and the effect increases rapidly with increasing Z. Further investigations of radiative corrections to decay rates is being undertaken in order to determine the decays for which these effects are important. In a parallel effort, we are working on development of new computational techniques that are necessary in order to carry out rigorous calculations of the structure and decay rates of highly ionized ions. Techniques already developed to calculate the radiative corrections and Lamb shift in high-Z hydrogenic atoms need further refinement in order to deal with situations in which two bound-electron propagation functions appear in expressions for the energy levels and radiative corrections. Preliminary investigations suggest that the necessary improvements are possible.

6. 1977 PUBLICATIONS AND REPORTS

Richard Marrus and Associates

1. P. J. Mohr, Atomic Physics Tests of Quantum Electrodynamics, in Atomic Physics 5, R. Marrus, M. H. Prior, and H. A. Shugart, Eds. (Plenum Press, New York, 1977), p. 37; invited paper presented at the Fifth International Conference on Atomic Physics, Berkeley, July 1976.

2. P. J. Mohr and Stanley J. Brodsky, Quantum Electrodynamics of Strong and Supercritical Fields, in Topics in Current Physics, Vol. 5: Structure and Collisions of Ions and Atoms, I. A. Sellin, Ed. (Springer-Verlag, Berlin, to be published).

3. P. J. Mohr, Status of the Theory of the Lamb Shift in Hydrogenic Atoms, Abstract for an invited paper at the Knoxville Meeting of the American Physical Society, Division of Electron and Atomic Physics, December 5-7, 1977; Bull. Am. Phys. Soc. 22, 1314 (1977).

4. P. J. Mohr, Lamb Shift in High-Z Ions and Atoms, Abstract for an invited paper at the Annual Meeting of the American Physical Society, January 23-26, 1978, San Francisco (to be published in the Bulletin).

5. A. H. Gould and R. Marrus, Quenching of the Metastable State of Hydrogen-like Argon (Z = 18) in an External Electric Field, Abstract for an invited paper at the Knoxville Meeting of the American Physical Society, Division of Electron and Atomic Physics, December 5-7, 1977; Bull. Am. Phys. Soc. 22, 1315 (1977).

6. R. Marrus, Forbidden Decay Modes of One- and Two-Electron Ions, in Cargèse Lectures in Physics, Vol. 7, M. Levy, Ed. (Gordon and Breach, 1977).

4. CHEMICAL ENERGY

a. Formation of Oxyacids of Sulfur From SO_2

Robert E. Connick, Principal Investigator

1. THE RAMAN SPECTRUM OF HSO_3^- AND $S_2O_5^=$--ISOTOPE EFFECTS

B. Meyer, L. Peter and C. Shaskey-Rosenlund*

Both disulfite ion, $S_2O_5^{2-}$, and bisulfite ion, HSO_3^-, form widely used and common salts, and their correct molecular weight and elemental analysis have been known since Rammelsberg[1] investigated them. X-ray studies of $K_2S_2O_5$ [2,3] and $(NH_4)_2S_2O_5$ [4] have shown that the disulfite ion contains SO_2 and SO_3 groups joined by a S-S bond and with a plane of symmetry for the ion. The nature of the $S_2O_5^=$ species in aqueous solution is still subject to some uncertainty although Herlinger and Long[5] have interpreted Raman data in terms of the structure found in solids. From Raman data it is known[6,7] that HSO_3^- has the hydrogen attached to the sulfur.

The purpose of this work was to prepare all alkali metal salts of disulfite and/or bisulfite and to employ isotopic substitution of hydrogen, sulfur, and oxygen to identify fundamental frequencies and improve their assignment. Furthermore, we were interested in identifying the S-S stretch. Such an identification has both theoretical and practical interest, as it yields information about the structure of the ion, the S-S and S-O coupling in the molecule, and serves to develop an analytical tool for monitoring formation and dissociation of this molecule, which in aqueous solution is in equilibrium with the bisulfite ion. The equilibrium constant and kinetics of this system are not yet fully understood, despite their practical importance in SO_2 abatement and other applications.[8]

Measurements have been made of the Raman frequencies of six solid disulfites, two solid bisulfites and of an aqueous solution saturated with potassium disulfite. The frequencies of four isotopic species of cesium bisulfite are listed in Table 1. Also listed are the relative intensities and the isotope shifts. In all compounds at least eight peaks are observed that can be readily identified as components of the six fundamentals of HSO_3^-, which has C_{3V} symmetry. In the deuterated salts, the appearance of the spectrum is drastically changed, because two strong lines are strongly shifted and change relative positions with partners. In all other salts the spectra are qualitatively unchanged.

The spectra of isotopic potassium disulfites are shown in Table 2.

Bisulfite, HSO_3^-. The structural parameters of bisulfite are not yet known, but Simon and co-workers[6,7] have concluded from their Raman studies that bisulfites have approximately a pyramidal C_{3V} structure. An XYZ_3 molecule with C_{3V} symmetry is expected to have six Raman active fundamental frequencies: Three A_1 and three E

Table 1. Raman spectra of HSO_3^- in $CsHSO_3$.

$CsH^{32}S^{16}O_3$		$CsD^{32}S^{16}O_3$		$CsH^{34}S^{16}O_3$		$CsH^{32}S^{18}O_3$	
ν	rel. int.	ν	% shift	ν	% shift	ν	% shift
508.5	m	500.5	1.6	506.5	0.4	484	4.8
518.5	w	511	1.4	517	0.3	493	4.9
625.5	vw	619	1.0	618.5	1.1	608	2.8
1038	s	1035	0.3	1034.5	0.3	986.5	5.0
1122.5	s	832	25.9	1122.5	0	1112	0.9
1193	w	1193	0	1177.5	1.2	1163	2.5
1247.5	vw	1247	0	1231	1.3	1217	2.6
1253.5	vw			1238	1.2		
2573	s	1871.5	27.3	2570	0.1	2572.5	0

s=strong, m=medium, w=weak, vw=very weak

Table 2. Raman spectra of $S_2O_5^{2-}$ in $K_2S_2O_5$.

$K_2{}^{32}S_2{}^{16}O_5$		$K_2{}^{34}S_2{}^{16}O_5$		$K_2{}^{32}S_2{}^{18}O_5$	
ν	rel. int.	ν	% shift	ν	% shift
217.5	m	216	0.7	206	5.3
244.5	vs	242	1.0	236.5	3.1
317.5	m	316.5	0.3	303	4.6
434	s	428.5	1.3	420	3.2
516	w	513.5	0.5	492	4.6
557	w	551	1.0	536.5	3.7
642.5	vw	633.5	1.4	627	2.4
652.5	s	642	1.6	635	2.7
970	w	964	0.6	928	4.3
1060	s	1052.5	0.7	1014.5	4.3
1088.5	m	1076	1.1	1052	3.4
1178.5	m	1163.5	1.3	1141	3.2

vs=very strong, s=strong, m=medium, w=weak, vw=very weak

modes that combine to form three pairs of bands, a symmetric and an asymmetric S-O stretching mode, a symmetric and an asymmetric S-O bending mode, and the stretching and bending mode of H-S. The six observed bands account for all six fundamentals.

The strong deuterium isotope shifts identify the 2573 and 1122.5 cm^{-1} bands as the H-S stretch and bend, respectively, and of the A_1 and E modes. The 1038 cm^{-1} band is assigned to the A_1 symmetric stretch for S-O bonds and the group around 1200 cm^{-1} to the corresponding E mode asymmetric stretch. The intensity and isotope effects substantiate the assignment. The bands at 625.5 and 508.5 cm^{-1} correspond to S-O deformation modes and are assigned to A_1 and E, respectively. The latter assignment and that of all bands is confirmed by excellent agreement of the Teller-Redlich product rule for the two different symmetry groups.

Disulfite, $S_2O_5^{2-}$. The analysis of the difulfite spectrum is more difficult than that of bisulfite, because the molecule is more complex, and only 13 of the 15 expected frequencies are known. Herlinger and Long[5] have made a partial vibrational analysis, based primarily on Raman depolarization ratios of the aquated ion. Previtali and Baggio[9] used the x-ray structure[4] and the Raman work of Herlinger and Long to compute nine force constants and the corresponding potential energy distribution.

It is seen from Table 2 that the ^{18}O and ^{34}S isotope shifts are quite appreciable but do not vary greatly. Consequently it is not easy to use them in a qualitative fashion to make band assignments, particularly since the normal coordinate treatment of Baggio[9] indicates that there is a great deal of mixing in the normal modes. To proceed further it will be necessary to use a normal coordinate analysis to calculate isotope effects for comparison with the experimental values.

---

*Work done partly at Berkeley and partly at the University of Washington, Seattle.

1. C. Rammelsberg, Pogg. Ann. Phys. and Chem. 143, 2450 (1846).
2. W. Zachariasen, Phys. Rev. 40, 923 (1932).
3. I. Lindqvist and M. Mörtsell, Acta Cryst. 10, 406 (1957).
4. S. Baggio, Acta Cryst. B 27, 517 (1971).
5. A. W. Herlinger and T. V. Long, Inorg. Chem. 8, 2661 (1969).
6. A. Simon and K. Waldmann, Z. physik. Chem. 204, 235 (1955); A. Simon and K. Waldmann, Z. physik. Chem. 204, 235 (1955); A. Simon and K. Waldmann, Z. anorg. Chem. 281, 113, 135 (1955).
7. A. Simon and W. Schmidt, Z. Electrochem. 64, 737 (1960).
8. B. Meyer, Sulfur, Energy, and Environment, Elsevier, Amsterdam, 1977.
9. C. M. Previtali and S. Baggio, Rev. Latinoamer. Quim 7, 54 (1976).

2. CHEMICAL DYNAMICS OF METAL COMPLEXES--THE BIS-IMINODIACETATE COMPLEX OF NICKEL ION

R. E. Connick and Kevin Klotter

For several years this laboratory has been concerned with the kinetics of water exchange between water solvent and water coordinated to a partially chelated paramagnetic transition metal ion.[1] The polydentate ligands have been α-aminopolycarboxylates that quite strongly bind to metal ions in aqueous solution to form coordination complexes. In the course of measurements of the solvent water exchange rates from such complexes by broadline ^{17}O nuclear magnetic resonance, the lability of the ligands themselves became apparent and deserving of further study. The dynamics of such systems are of general interest whenever complexed metal ions are present.

Our solvent water exchange studies by NMR have been done by observing the line broadening and chemical shift effects of paramagnetic complexes in aqueous solution on the ^{17}O resonance of the solvent using the continuous wave technique. The availability of a large bore superconducting Fourier transform NMR spectrometer operating at 42 kG has made possible the observation of ^{1}H, ^{13}C, and ^{17}O resonance signals from the ligands, both complexed and uncomplexed.

Bis-iminodiacetate nickelate(II) ($Ni(IDA)_2^{=}$) has been the subject of much interest.[2] Early continuous wave ^{1}H NMR spectra provided structural information about this paramagnetic complex in solution through the large chemical shifts observed. Uncertainty in the proper assignment of groups of overlapping proton resonances, however, led to ambiguity in the value of the cis-trans isomer equilibrium. Since the ^{13}C spectra of NiEDTA had

been observed earlier by other workers, and 25 mm diameter sample tubes were available for use in the 42 kG system, the isomer distribution was studied by observing the much more widely shifted carbon resonances arising from the bound ligands of the bis complex.

The iminodiacetate ligand has the structural formula

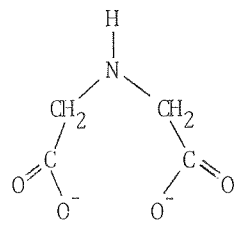

with identical pairs of carboxylate carbons and methylene carbons. On forming the bis complex with nickelous ion the trans isomer should show two ^{13}C resonances corresponding to these pairs. The cis complex, however, should show four ^{13}C resonances because the partners in the pairs are no longer identical. Experimentally it was found that three resonances were observed in the carboxylate carbon region, two of which appeared to have the same area and a third which was considerably smaller. In the methylene region incompletely resolved resonances were observed. Interpreting the two strong carboxylate resonaces as the cis species one calculates a cis/trans ratio of ca. 7 based on the integrated areas.

Repetition of the earlier proton work, with the present apparatus and on a 270 mc instrument yielded somewhat better resolution of the curves but still insufficient for identifying the isomers. A recently acquired curve fitting routine for the 42 kG spectrometer's computer system may help to unravel the proton ambiguities, including determination of relaxation mechanisms.

Variable temperature ^{1}H and ^{13}C spectra are also being used in the bis-iminodiacetato nickelate system to determine the rate and mechanism of intramolecular cis/trans isomerization. The aforementioned problems in the proton spectra prevent any clean-cut interpretation of the data as the intramolecule rearrangement processes become fast enough to cause coalescences and shifts. Again, careful ^{13}C variable temperature spectra and lineshape analysis provide a much more reliable value of the racemization rate and activation energy and yield information on the rearrangement mechanism. The initial results indicate that both the cis and the trans carboxylate ^{13}C resonances start to broaden in the same temperature region. The simplest interpretation would be that isomerization is proceeding by interconversion of cis to trans and vice versa, as for example by the twist mechanism.

Finally, solutions highly concentrated in $Ni(IDA)_2^{=}$ containing ligands highly enriched with ^{17}O in the carboxylate group have been used for the direct observation of the resonance of the nonbonded oxygen nucleus in the coordinated carboxylate groups of the chelated ligands. The variable temperature behavior of this resonance should provide a direct measurement of the rate of exchange of the two carboxylate oxygens between the coordinated and non-coordinated positions, a quantity that has been estimated indirectly by the observation of bulk water resonances.[1] Although not all experimental difficulties pertaining to this ^{17}O NMR variable temperature measurement have been solved, the determination of this effect is in progress.

---

1. T. N. Rowland, Oxygen-17 NMR Studies of the Rate of Water Exchange from Partially Complexed Nickel Ion, (Ph.D. thesis), LBL-3122, October 1975; Jack Vriesenga, unpublished work in this laboratory.
2. L. Pratt and B. B. Smith, Trans. Faraday Soc. 65, 915 (1969); L. E. Erickson, F. F-L. Ho, and C. N. Reilley, Inorg. Chem. 9, 1148 (1970); D. S. Everhart and R. F. Evilia, Inorg. Chem. 14, 2755 (1975).

3. RESEARCH PLANS FOR CALENDAR YEAR 1978

R. E. Connick

Investigations will be continued on the aqueous chemistry of sulfur dioxide and related compounds with an emphasis on the identification of species, measurement of equilibrium constants and studies of rates of reaction, particularly oxidation by oxygen. The ionization of sulfur dioxide will be determined spectrophotometrically for a variety of conditions, yielding both equilibrium data and values of activity coefficients for such systems. Investigation of previously unidentified species in $HSO_3^- - SO_2$ solutions will be continued using Raman and UV absorption measurements. The rate of exchange of oxygen atoms between water and HSO_3^- will be investigated by means of ^{17}O NMR. Studies will be made of the chain reaction oxidation of HSO_3^- by oxygen in order to obtain reliable rate data under controlled conditions. All of these results are of importance in the scrubber processes for removing sulfur dioxide from stack gases from fossil fuel combustion. Some of the results are pertinent to atmospheric pollution problems.

The study of the dynamics of the metal chelate bis-iminodiacetate nickel(II) will be completed and correlations of the rate behavior will be made for this and similar metal--amino acid-like complexes. A rather complete picture of the dynamics of these systems is beginning to emerge--a matter of interest whereever metal ion complexes are encountered, such as in fuel processing, waste disposal, many enzyme systems, etc.

Slow but continuous progress is being made on the computer modeling of the replacement reaction in the first coordination sphere of a metal ion.

b. Conversion of Coal to Clean Liquid and Gaseous Fuels

Gabor A. Somorjai and Alexis T. Bell, Principal Investigators

1. HYDROGENATION OF CO AND CO_2 OVER IRON FOILS. CORRELATIONS OF RATE, PRODUCT DISTRIBUTION AND SURFACE COMPOSITION

D. J. Dwyer and G. A. Somorjai

The hydrogenation of CO and CO_2 over polycrystalline iron foils has been investigated under highly controlled conditions (6 atm, 3:1 H_2:CO, 300°C). The surface composition of the foil before and after high pressure reaction was determined by Auger electron spectroscopy. The H_2/CO reaction produced C_1-C_5 hydrocarbons in detectable quantities. In this reaction the initially clean iron surface was rapidly covered by a monolayer of carbonaceous material that appeared to be the active surface. The specific methanation rate on this surface was 1.9 molecules $site^{-1}$ sec^{-1} with an activation energy of 27±2 kcal $mole^{-1}$. The H_2/CO_2 reaction produced almost exclusively methane (97 mole %) and at a higher rate (10.9 molecules $site^{-1}$ sec^{-1}) than the H_2/CO reaction. The initially clean iron foil was oxidized during the H_2/CO reaction. In both the H_2/CO and the H_2/CO_2 reactions the active surfaces were eventually poisoned by excessive deposition of carbon. The carbon-poisoned surfaces produced only methane but at much slower rates than the active surfaces. It appears that clean iron is not the catalyst that is used industrially to carry out the hydrogenation of CO, since very different product distributions are obtained in our studies as compared to the industrial catalyst. The effect of promoters such as potassium and the activity of iron carbides and oxycarbides are being explored at present.

2. STUDIES OF FISCHER-TROPSCH SYNTHESIS ON SUPPORTED RUTHENIUM CATALYSTS

J. G. Ekerdt, S. C. Kellner, G. Low, and A. T. Bell

The synthesis of hydrocarbons from CO-H_2 mixtures was studied by using a silica-supported-ruthenium catalyst. Product composition was determined by gas chromatography, and the structure of adsorbed species present on the catalyst surface was established by infrared spectroscopy. Working at a total pressure of 1 atm and with H_2/CO ratios between 2 and 20, methane was observed as the primary product. Small concentrations of ethane were detected as well, and the selectivity towards C_2H_6 increased rapidly as the H_2/CO ratio approached 2. Infrared spectra recorded under reaction conditions showed only a single band associated with chemisorbed CO. The position of the band shifted from 2030 to 2010 cm^{-1} as the H_2/CO ratio was increased. This trend suggests that adsorbed H atoms contribute electrons to surface Ru atoms, thereby enhancing the back donation of electrons at adsorbed CO. Back donation was also observed from C atoms produced on the Ru surface through a dissociation of CO.

Studies of the kinetics of CH_4 synthesis showed that the rate could be correlated by the ratio of H_2/CO concentrations over the catalyst. However, it was observed that the catalyst activity declined with time, the decline being most rapid for reaction mixtures in which H_2/CO was low. Reactivation of the catalyst could be achieved by heating it in hydrogen.

The role of carbon deposited on the catalyst during the reaction of CO and H_2 was studied by following the product composition obtained when H_2 was passed over the catalyst at the end of a run. Plots of the partial pressures of CO and CH_4 (normalized to unity at t = 0) in the effluent are illustrated in Figs. 1 and 2 as functions of time. The elimination of CO from the reactor is rapid and coincides with the disappearance of

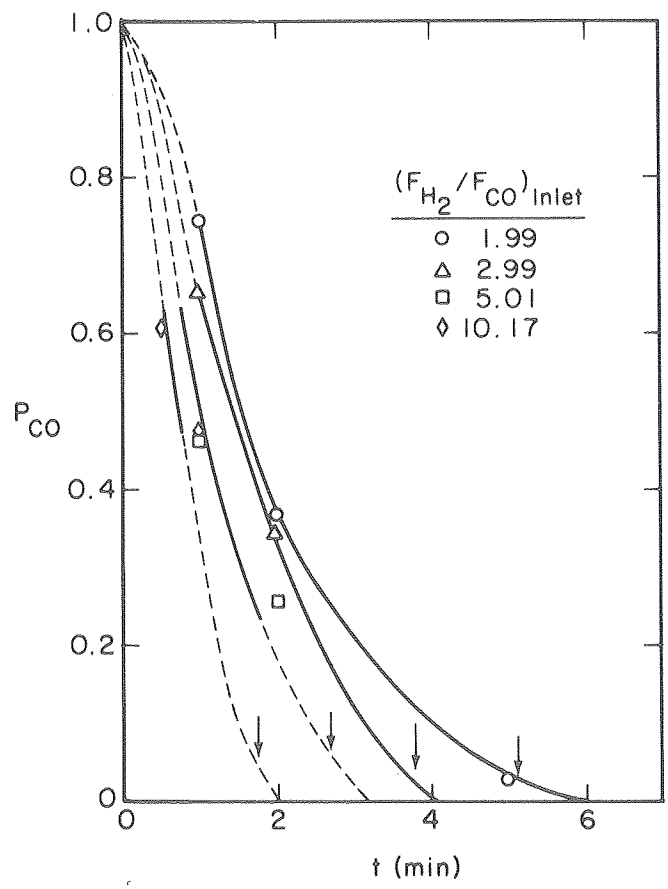

Fig. 1. Normalized partial pressure of CO in the reactor effluent during catalyst reactivation with H_2 at 275°C. (XBL 783-7512)

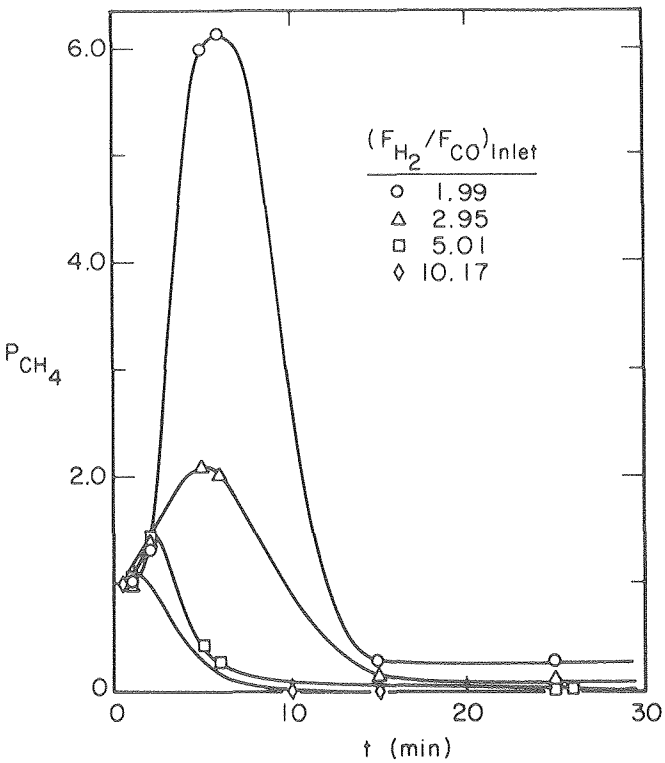

Fig. 2. Normalized partial pressure of CH_4 in the reactor effluent during catalyst reactivation with H_2 at 275°C. (XBL 783-7511)

the CO band from the infrared spectrum, as inicated by the arrows in Fig. 1. A most notable result is that the CH_4 production at first exceeds that observed under steady state conditions and then continues at a noticeable level well beyond the point where CO is present in the gas phase or on the Ru surface. The amount of CH_4 produced during these experiments is equivalent to several monolayers of carbon.

Current results suggest that under reaction conditions the catalyst surface is covered almost exclusively by CO and that H_2 competes with CO for the remaining vacant sites. The adsorption of H_2 promotes a weakening of the CO bond and may facilitate CO dissociation. That CO dissociation occurs is evident from the large amounts of carbon present on the surface, and it appears that this carbon plays an active role in the synthesis of CH_4. Oligomerization of carbon atoms to form graphite is a competing reaction and is the most likely cause of catalyst deactivation.

In a separate series of experiments, thermal desorption spectroscopy is being used to investigate the chemisorption and reaction of CO and H_2 on Ru catalysts. From these studies it has been established that carbon monoxide adsorbs in two states with binding energies of 17 and 25 kcal/mole, while hydrogen chemisorbs in a single state with a binding energy of 28 kcal/mole. During the desorption of CO a part of the adsorbate dissociates to produce adsorbed carbon atoms. This carbon can be removed from the surface by heating in H_2. Allowing the C atoms to remain on the surface reduces the pre-exponential for CO desorption but does not alter the activation energy for CO desorption. Further studies are now in progress to evaluate the roles of chemisorbed CO and C in the formation of CH_4 and higher molecular weight hydrocarbons on Ru catalysts.

3. NOVEL TRANSITION-METAL CLUSTER CATALYSTS IN HYDROGENATION, HYDROGENOLYSIS, AND METHANATION*

R. E. Colborn, J. R. Fritch, D. K. Mitchell, P. Perkins, E. S. Strauss, and K. P. C. Vollhardt

Polyfunctional ligands are being explored as potential matrices for transition-metal cluster formation to be used in catalytic hydrogenation and hydrogenolysis of benzenoids, hydroaromatics, and coal.

In an attempt to improve the homogeneous catalytic hydrogenating power of η^3-allyl cobalt complexes in benzenoid hydrocarbon hydrogenation, several oligoallyl cobalt complexes were prepared and their catalytic activity investigated. The synthetic approach involved nucleophilic displacement reactions of $NaCo[P(OMe)_3]_4$ on suitable oligoallyl halides: 3-bromo-1,5,9-cyclododecatriene; 3,7,11-tribromo-1,5,9-cyclododecatriene; 1,3,5-tris(bromomethyl)benzene; 1,3,5-tris(3-bromo-1-propenyl)benzene; 2,3-bis(bromomethyl)buta-1,3-diene; and ally iodide. Extremely air-sensitive organe-red products were isolated in all cases by column chromatography under nitrogen. Characterization by spectral techniques allowed the identification of complexes 1 and 2, present as respective mixtures of isomers. Attempts at crystallization proved unsuccessful. Attempts to convert 2 into a trinuclear cobalt cluster led to decomposition. Both 1 and 2 are powerful catalysts

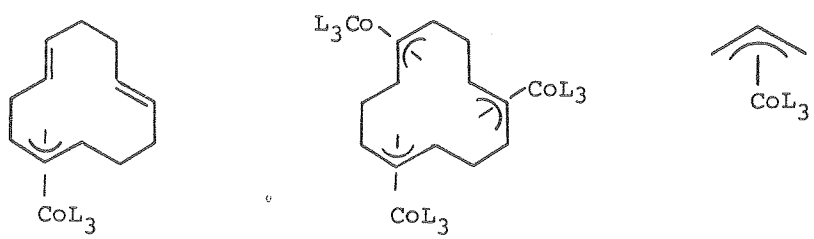

1 2 L = $P(OMe)_3$ 3

in the hydrogenation of benzene to cyclohexane under mild conditions (room temperature, normal pressure). Catalyst life time is, however, limited as in the case of 3, the first homogeneous benzene hydrogenation catalyst known (E. L. Muetterties et al.). The hydrogenation of dried and oxygen-free 20-mesh Illinois #6 coal using catalysts 1-3 led to only limited hydrogen uptake, again due to limited catalyst life time.

We have completed the physical and chemical characterization of hexaradialene (hexamethylene benzene) 5 generated by the respective gas phase thermolysis of 1,5,9-cyclododecatriyne 4; 2,4,6-tris(bromomethyl)mesitylene 6; and a variety of other hydrocarbon precursors. Compound 5 should prove to be an attractive ligand to transition metals en route to mixed-metal clusters. It also constitutes one of the most abundant structural moieties found in polycyclic benzenoid compounds and coal. Its electronic structure and chemical reactivity is therefore of interest. The ^{1}H-NMR spectrum shows a sharp singlet at $\tau = 4.69$, whereas the proton-decoupled ^{13}C-NMR spectrum exhibits two absorptions at 145.0 and 110.0 ppm. The ^{13}C-H coupling constant has a value of 159 Hz. These data show that despite benzenoid topology 5 does not sustain a diamagnetic ring current and is best regarded as a methylene cyclohexane derivative. Hydrogenation occurs rapidly to give hexamethylbenzene. The relative ease of formation of 5 from various hydrocarbon precursors suggests that structures of similar topology might occur in coal depolymerization, coal pyrolysis, and metal surface catalyzed hydroreforming processes.

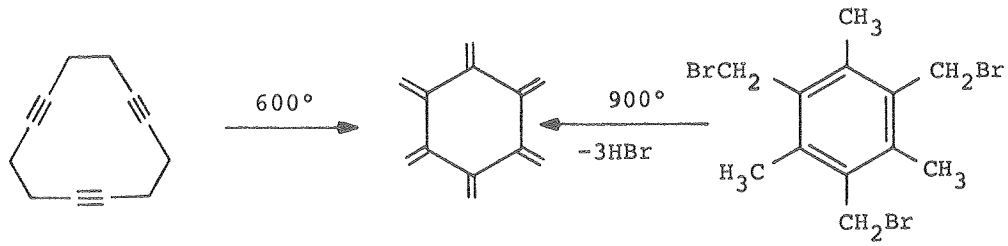

4 5 6

In an approach to the synthesis of topologically novel linear clusters of type 8 we have investigated synthetic routes to a metal complexed form of tricyclooctatetraene 7, a highly unusual ligand both for its inherent strain and its potential anti-aromaticity. During the course of these studies we discovered a completely novel, unprecedented, and fascinating gas phase rearrangement of complex 9 to cleanly give 10. An attractive intermediate in this rearrangement is complex 11 with the desired tricyclooctatetraene moiety as a ligand. The stability of the cyclopentadienyl and cyclobutadienyl ligand bonds under the conditions of the rearrangement suggest a novel approach to cluster synthesis by gas phase thermolytic chemistry.

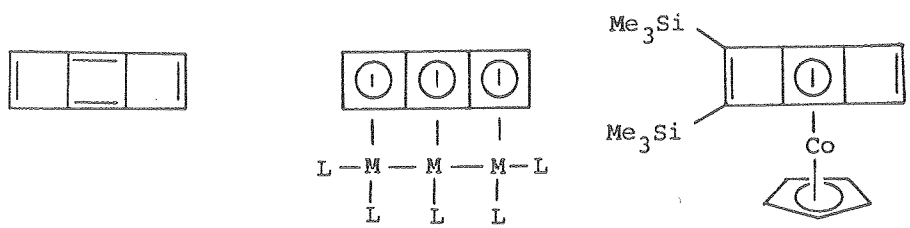

7 8 11

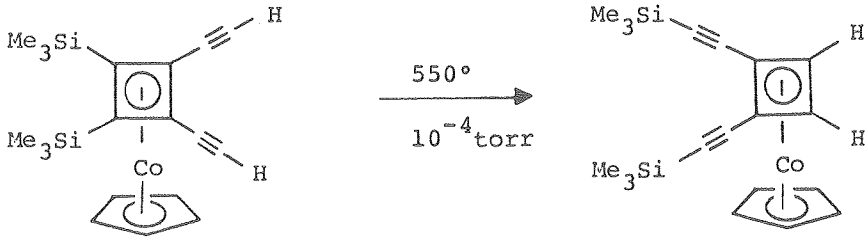

9 10

*Partially supported by NSF, NIH, PRF, and the A.P. Sloan Foundation.

4. ACTIVATED BENZENOID HYDROCARBONS*

W. G. L. Aalbersberg, P. Perkins, and
K. P. C. Vollhardt

We are continuing the investigation of activated polycyclic benzenoid hydrocarbon chemistry in an effort to gain further understanding of benzenoid aromaticity, the mechanism of hydrogenation of coal molecules, the mechanism of coal depolymerization and the nature of intermediates therein, and the mechanism of mutagenesis and carcinogenesis by coal structures.

Iodine-catalyzed photooxygenation of stilbene derivative 12 gives rise to two novel activated phenanthrenes, 13 and 14. The chemical and physical properties (see Fig. 1 for electronic spectrum) point to considerable reactivity and a π-electronic framework reflecting the strain-related distortion of the benzenoid topology.

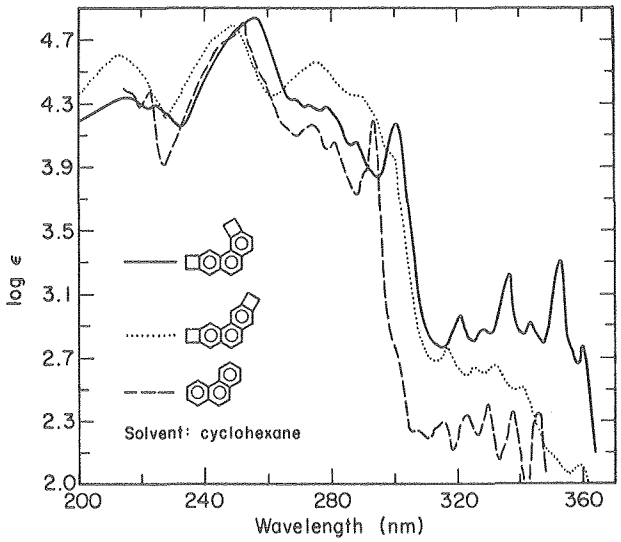

Fig. 1. Electronic spectra of phenanthrenes in cyclohexane solvent. (XBL 784-525)

A layered benzenoid structure 16 is obtained on pyrolysis of hydrocarbon 15. The diastereomer 16 is generated exclusively, no trace of the chiral stereosiomer 17 being detectable. Compound 16 might be regarded as a model for layered

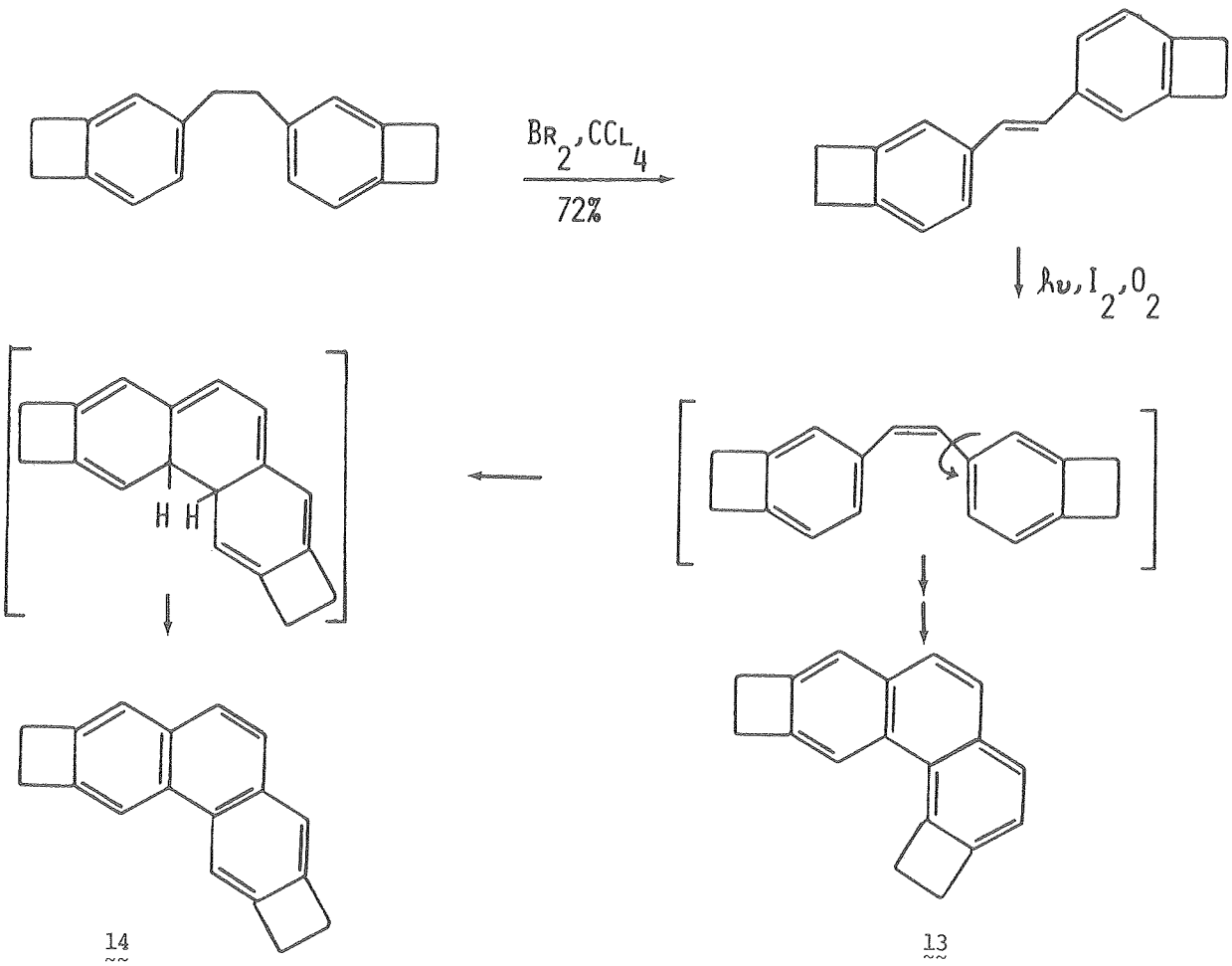

asphaltene structures derived from coal. Interestingly, fast hydrogenation rather than hydrogenolysis occurs under mild conditions (room temperature, normal pressure) to give 18. At higher pressures further hydrogen uptake to 19 is observed. Oxidation with peracids occurs instantly

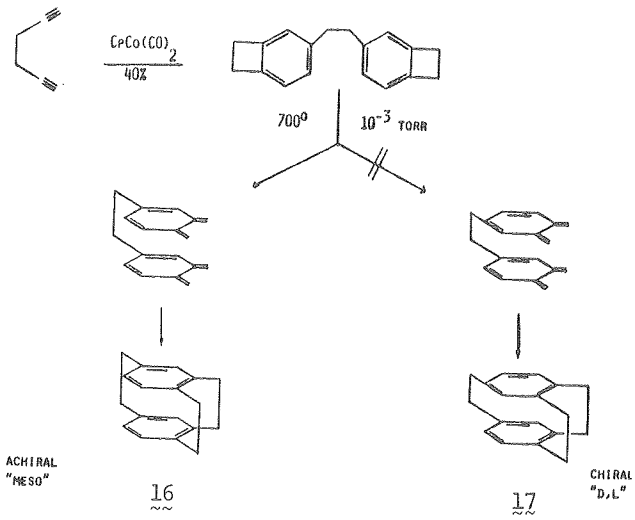

to give a mixture of products. The available evidence indicates that π-electronic interactions in layered benzenoids might play an important role in the general chemistry of coal-derived hydrocarbon mixtures.

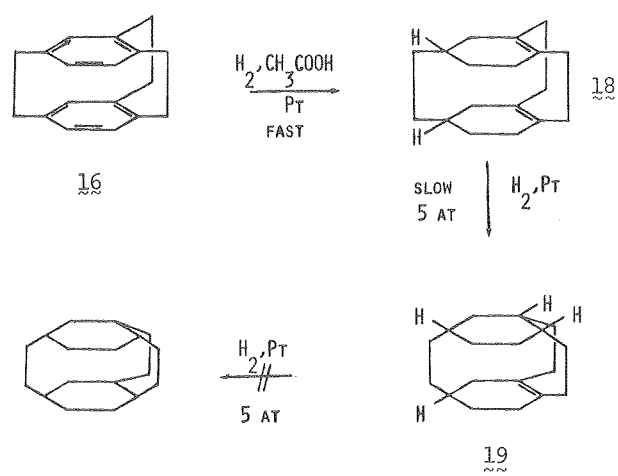

The potential mutagenicity of 13, 14, and 16 is currently being probed by using the Ames test.

*Supported in part by NSF, NIH, PRF, and the A. P. Sloan Foundation.

5. RESEARCH PLANS FOR CALENDAR YEAR 1978

Gabor A. Somorjai and Alexis T. Bell

Studies of the effects of additives (K,Mn) on the rates and product distribution in CO hydrogenation reaction on iron and rhodium.

Studies of the structure sensitivity of CO hydrogenation by using various crystal faces of iron and rhodium.

Studies of hydrocarbon reactions on iron and rhodium to elucidate the mechanism of CO hydrogenation.

Studies of iron carbides and oxycarbides to test their catalytic activity as compared to the metal surfaces.

Investigations of hydrocarbon synthesis on supported ruthenium will be extended up to pressures of 20 atm to examine the production of high-molecular-weight products. Emphasis will be placed on establishing conditions favoring the formation of C_5 to C_{12} compounds. In the course of this work infrared spectroscopy will be used to look for hydrocarbon precursors on the catalyst surface.

The chemistry of carbon atoms on the surface of ruthenium catalysts will be studied to establish their role in the synthesis of hydrocarbons. Particular interest will be devoted towards establishing whether chain growth occurs via oligomerization of CH_x groups or by CO insertion into Ru-CH_x bonds.

The effect of alkali metal oxide additives on the activity and selectivity of ruthenium catalysts will be examined.

We will further probe the potential of novel polyfunctional ligands as matrices for transition metal cluster synthesis.

We will embark on an exploratory program aimed at utilizing gas phase pyrolyses of metal carbonyls as a source of novel homogeneous catalysts and catalyst surfaces. The potential of these compounds in catalytic hydrogenation, hydrogenolysis, methanation, Fischer-Tropsch, and methanol synthesis will be explored.

The nature of our polymer-supported methanation catalyst will be investigated. The scope of methanation and Fischer-Tropsch catalysis, catalyst life-time, and response to catalyst poisons should be scrutinized. We will initiate a search for homogeneous analogs.

6. 1977 PUBLICATIONS AND REPORTS

Gabor A. Somorjai, Alexis T. Bell, and Associates

Journals

1. D. W. Blakely, E. Kozak, B. A. Sexton, and G. A. Somorjai, New Instrumentation and Techniques to Monitor Chemical Surface Reactions on Single Crystals Over a Wide Pressure Range (10^{-8}-10^{-5} Torr) in the Same Apparatus, J. Vac. Sci. Technol. 13, 1091 (1976) LBL-4926.

2. Ch. Steinbruchel and G. A. Somorjai, Limitations of Kinetic Studies of Catalytic Reactions on a Single Crystal Surface at Low Pressures in an Ultrahigh Vacuum System, J. Vac. Sci. Technol. 13, 1162 (1976), LBL-4988.

3. B. A. Sexton and G. A. Somorjai, The Hydrogenation of CO and CO_2 Over Polycrystalline Rhodium: Correlation of Surface Composition, Kinetics and Product Distributions, J. Catalysis 46, 167 (1977), LBL-5178.

4. K. P. C. Vollhardt, Transition Metal Catalyzed Acetylene Cyclizations in Organic Synthesis, Acc. Chem. Res., 10, 1 (1977).

5. K. P. C. Vollhardt and L. S. Yee, 1,2-Bis(trimethylsilyl)benzocyclobutadiene, a Paratropic 8Π-Electron System, J. Amer. Chem. Soc. 99, 2010 (1977).

6. W. G. L. Aalbersberg and K. P. C. Vollhardt, Retention of Stereochemistry in the Extrusion of Sulfur Monoxide from Thiirane Oxides. Synthesis and Thermal Decomposition of cis and trans-Dideuteriothiirane Oxide, J. Amer. Chem. Soc. 99, 2792 (1977).

7. R. L. Hillard III and K. P. C. Vollhardt, Substituted Benzocyclobutenes, Indans, and Tetralins via Cobalt Catalyzed Co-oligomerization of α,ω -Diynes with Substituted Acetylenes. Formation and Synthetic Utility of Trimethylsilylated Benzocycloalkenes, J. Amer. Chem. Soc. 99, 4058 (1977).

8. R. L. Hillard III and K. P. C. Vollhardt, 3,4-Bis(trimethyl)silylbenzocyclobutene. Synthesis by Acetylene Cotrimerization and Conversion to Cyclobuta[1,2-c]benzyne, Angew. Chem. 89, 413 (1977); Angew. Chem. Internat. Edn. 16, 399 (1977).

9. A. Naiman and K. P. C. Vollhardt, A Cobalt-Catalyzed One-Step Synthesis of Annulated Pyridines, Angew. Chem. 89, 758 (1977); Angew. Chem. Internat. Edn. 16, 708 (1977).

10. R. L. Funk and K. P. C. Vollhardt, A Cobalt-Catalyzed Steroid Synthesis, J. Amer. Chem. Soc. 99, 5483 (1977).

11. K. P. C. Vollhardt, Cobalt-Katalysierte Acetylen-Cyclisierungen, Nachr. Chem. Tech. 25, 584 (1977).

12. A. J. Barkovich, E. S. Strauss, and K. P. C. Vollhardt, Hexaradialene, J. Amer. Chem. Soc. 99, 8321 (1977).

13. J. C. Smart and C. J. Curtis, Bridging Ligands in Organometallic Chemistry. 1. η^5:η^5-Fulvalene Complexes of Molybdenum Carbonyl, Inorg. Chem. 16, 1788 (1977).

14. J. C. Smart and B. L. Pinsky, The Synthesis and Characterization of Bis(fulvalene) dinickel, in Three Oxidation Levels, J. Am. Chem. Soc. 99, 956 (1977).

15. J. C. Smart and C. J. Curtis, The Synthesis and Characterizatio of Bis(fulvalene) dimolybdenum and Its Monocarbonyl Adduct, J. Am. Chem. Soc. 99, 956 (1977).

Invited Talks and Papers Presented

1. G. A. Somorjai, Recent Achievements and Trends in Catalysis Science, at the National Science Foundation, Washington, D. C., February 3, 1977.

2. G. A. Somorjai, Catalysis by Transition Metals--Pt, Fe, and Rh, at U. C. Santa Barbara, California, February 10, 1977.

3. G. A. Somorjai, Active Sites for Heterogeneous Catalysis, at U. C. Irvine, Irvine, California, February 28, 1977.

4. G. A. Somorjai, Catalysis on the Atomic Scale, at the North American Catalysis Society meeting, Pittsburgh, PA, April 24, 1977.

5. G. A. Somorjai, Active Sites in Heterogeneous Catalysis, at the Shell Development Corporation, Houston, Texas, July 13, 1977.

6. G. A. Somorjai, Energy Conversion and Storage by Heterogeneous Catalysis, at the IUPAC Meeting, Tokyo, Japan, August 26, 1977.

7. A. T. Bell, Infrared Spectroscopy Applied to Catalysis, at Air Products and Chemicals, Inc., Allentown, PA, March 1977.

8. A. T. Bell, Applied Chemical Kinetics, at ASEE Summer School for Chemical Engineering Faculty, Snowmass Village, Colorado, August 1977.

9. A. T. Bell, Infrared Spectroscopy Applied to Studies of Catalytic Reactions, at the Michigan Catalysis Society, Detroit, Michigan, September 1977.

10. A. T. Bell, Infrared Spectroscopy Applied to Studies of Catalytic Reactions, at the Chemical Engineering Department, Brigham Young University, Provo, Utah, September 1977.

11. A. T. Bell Infrared Spectroscopy Applied to Studies of Catalytic Reactions, at the Institut de Recherches sur la Catalyse, Villeurbanne, France, September 1977.

12. A. T. Bell, The Search for New Coal Liquefaction Catalysts, at the Materials and Molecular Research Division, Lawrence Berkeley Laboratory, Berkeley, California, October 1977.

13. K. P. C. Vollhardt, U. C. Riverside, Riverside, California, January 26, 1977.

14. K. P. C. Vollhardt, University of Washington, Seattle, Washington, February 4, 1977.

15. K. P. C. Vollhardt, University of Oregon, Eugene, Oregon, February 7, 1977.

16. K. P. C. Vollhardt, U. C. Los Angeles, Los Angeles, California, March 10, 1977.

17. K. P. C. Vollhardt, 173rd ACS National Meeting, New Orleans, Louisiana, March 20-25, 1977.

18. K. P. C. Vollhardt, University of Nevada, Reno, Nevada, March 25, 1977.

19. K. P. C. Vollhardt, Syntex Corporation, Palo Alto, California, April 5, 1977.

20. K. P. C. Vollhardt, University of Nebraska, Lincoln, Nebraska, April 14, 1977.

21. K. P. C. Vollhardt, Plenary Lecturer, Symposium on Natural Products Synthesis, 32nd ACS Northwest Regional Meeting, Portland, Oregon, June 15-17, 1977.

22. K. P. C. Vollhardt, 1st Annual Workshop in Organometallic Chemistry, Rochester, New York, July 5-8, 1977.

23. K. P. C. Vollhardt, 18th International Conference on Coordination Chemistry, San Paulo, Brazil, July 18-23, 1977.

24. K. P. C. Vollhardt, 3rd International Symposium on Novel Aromatic Compounds, San Francisco, California, August 22-26, 1977.

25. K. P. C. Vollhardt, 26th IUPAC Congress, Tokyo, Japan, September 4-11, 1977.

26. K. P. C. Vollhardt, 8th International Conference on Organometallic Chemistry, Kyoto, Japan, September 12-16, 1977.

27. K. P. C. Vollhardt, University of Colorado, Boulder, Colorado, October 3, 1977.

28. K. P. C. Vollhardt, NSF Research Initiation Support Grant Lecturer, University of Colorado, Boulder, Colorado, October 3, 5, 1977.

29. K. P. C. Vollhardt, Colorado State University, Fort Collins, Colorado, October 4, 1977.

30. K. P. C. Vollhardt, University of Colorado, Boulder, Colorado, October 5, 1977.

31. K. P. C. Vollhardt, Pacific Conference on Chemistry and Spectroscopy, Anaheim, California, October 12-14, 1977.

32. K. P. C. Vollhardt, Plenary Lecturer, Symposium on Organometallic Chemistry, 1977, Pacific Conference on Chemistry and Spectroscopy, Anaheim, California, October 12-14, 1977.

33. K. P. C. Vollhardt, U. C. Irvine, Irvine, California, October 17, 1977.

34. K. P. C. Vollhardt, Princeton University, Princeton, New Jersey, October 26, 1977.

35. K. P. C. Vollhardt, Columbia University, New York, New York, October 27, 1977.

36. K. P. C. Vollhardt, E. I. DuPont de Nemours and Co., Wilmington, Delaware, October 28, 1977.

37. K. P. C. Vollhardt, U. C. Santa Barbara, Santa Barbara, California, November 9, 1977.

LBL Reports

1. D. Castner, B. A. Sexton, and G. A. Somorjai, LEED and Thermal Desorption Studies of Small Molecules (H_2, O_2, CO, CO_2, NO, C_2H_4, C_2H_2, and C) Chemisorbed on Rhodium (111) and (100) Surfaces, LBL-6299, June 1977.

2. D. J. Dwyer and G. A. Somorjai, Hydrogenation of CO and CO_2 Over Iron Foils. Correlations of Rate, Product Distribution and Surface Composition, LBL-6558, August 1977.

c. Synthetic and Physical Chemistry

William L. Jolly, Principal Investigator

1. X-RAY PHOTOELECTRON SPECTROSCOPY*

a. Use of Oxygen 1s Binding Energies and Multiplicity-Weighted C-O Stretching Frequencies to Measure Back-Bonding in Transition Metal Carbonyl Complexes†

William L. Jolly, Steven C. Avanzino and Richard R. Rietz

Back-bonding in a transition metal carbonyl involves a decrease in the C-O bond order of the carbon monoxide ligand

$$^{-}M - C \equiv O^{+} \leftrightarrow M{=}C{=}O.$$

Because a decrease of bond order corresponds to a decrease of bond strength, the C-O stretching frequencies (or the derived force constants) of transition metal carbonyls have commonly been used to measure the degree of back-bonding. Unfortunately there are very few other physical properties which can be used to measure back-bonding and which are correlated with the stretching frequencies or force constants. Carbon-13 NMR chemical shifts have been shown to be related to the degree of back-bonding in carbonyls, but good correlations with C-O stretching frequencies have been obtained only for restricted sets of compounds, in which the structures are very similar.

Because back-bonding in a carbonyl involves a shift of negative charge from the metal atom to the oxygen atoms of the CO ligands, we anticipated that O 1s binding energies would be closely correlated with back-bonding. During the last few years we have measured these binding energies for a wide variety of transition metal-carbonyl complexes in which the CO ligands are terminally bound. One would expect a correlation of the O 1s binding energies with the corresponding C-O stretching force constants, Unfortunately the force constants have not been calculated for all the molecules and could not be readily calculated without some rather poor approximations. As an alternative to the use of force constants, we have used the multiplicity-weighted averages of the C-O stretching frequencies, $\langle \nu_{CO} \rangle$. These values were calculated from literature assignments of the frequencies bh giving a weight of 2 to those of E symmetry, and a weight of 3 to those of T symmetry. A plot of E_B(O 1s) vs. $\langle \nu_{CO} \rangle$, given in Fig. 1, shows that these quantities are closely correlated. The straight line through the points corresponds to the equation $E_B(O\ 1s) = 0.0146 \langle \nu_{CO} \rangle + 510.00$. We believe that this correlation is strong evidence that both E_B(O 1s) and $\langle \nu_{CO} \rangle$ can be used to measure back-bonding in carbonyl complexes.

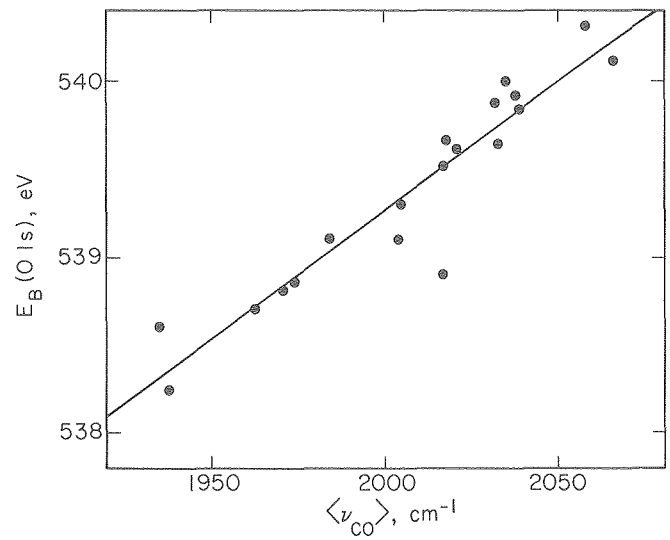

Fig. 1. Oxygen 1s binding energies for carbonyl complexes vs. the multiplicity-weighted C-O stretching frequencies. (XBL 7610-4840B)

b. The Correlation of Core Replacement Energies with Nonbonding s Electron Density*

William L. Jolly, Christina Gin and David B. Adams

The equivalent cores approximation was first used in x-ray photoelectron spectroscopy to predict chemical shifts in core electron binding energies.[1-3] This and many subsequent applications of the approximation have recently been reviewed.[4] The essence of the approximation may be expressed as follows: The energy of the process in which an electron is transferred from a core level of an atom to the nucleus of the atom is independent of the chemical environment of the atom. In the case of an ion $M(Z)^{+}$ containing an atom of atomic number Z, this process may be represented thus:

$$M(Z)^{+} \rightarrow M(Z - 1)^{*+}. \qquad (1)$$

The asterisk is used to indicate a core vacancy. Although Eq. (1) is balanced with respect to electrons, protons, and neutrons (assuming the elements of atomic number Z and Z - 1 have the same mass number), it is not balanced with respect to the elements involved, as in a normal chemical reaction. However, we can convert it into a balanced chemical reaction, and change its energy by a constant amount, by the appropriate addition of the species corresponding to the elements of atomic number Z and Z - 1 in their standard states.

---

*This work was partly supported by a National Science Foundation grant.

†Abstracted from Inorg. Chem. 16, 964 (1977).

$$\text{Element}(Z-1)_{\text{std. state}} + M(Z)^{+} \rightarrow \text{Element}(Z)_{\text{std. state}} + M(Z-1)^{*+}. \quad (2)$$

According to the equivalent cores approximation, the energy of reaction (2) is the same for all ions $M(Z)^{+}$; we shall refer to the energy of this reaction as the core replacement energy, and shall give it the symbol Δ_Z. It can be shown that a core replacement energy can be calculated from a binding energy and appropriate thermodynamic data. Thus the core replacement energy Δ_N can be calculated from the C 1s binding energy for methane and the heats of formation of NH_4^+ and CH_4:

$$C_{\text{graphite}} + NH_4^{+} \rightarrow \frac{1}{2} N_2 + CH_4^{*+},$$

$$\Delta_N = E_B(CH_4) + \Delta H_f^{\circ}(CH_4) - \Delta H_f^{\circ}(NH_4^{+})$$

$$= 290.88 - 0.78 - 6.61 = 283.49 \text{ eV}.$$

Value of Δ_N calculated from data for nine different nitrogren-containing cations and the isoelectronic carbon compounds (including NH_4^+/CH_4) are given in Table 1. The first eight values are very close to their average value, 283.68 eV (average deviation

Table 1. Core replacement energies for nitrogen-containing cations.

Compounds	E_B(C 1s) (eV)	Δ_N (eV)
NHF_3^+/CHF_3	299.1	282.9
NO_2^+/CO_2	297.71	282.69
HN_2^+/HCN	293.5	283.9
$HCNH^+/C_2H_2$	291.14	283.86
NH_4^+/CH_4	290.88	283.49
$CH_3NH_3^+/C_2H_6$	290.74	283.39
$C_5H_5NH^+/C_6H_6$	290.42	283.46
CH_3CNH^+/CH_3CCH	290.40	283.71
NO^+/CO	296.24	284.90

± 0.17 eV, standard deviation 0.21 eV). The last value, calculated from data for NO^+ and carbon monoxide, is 1.22 eV greater than the average of the other values. There is no reason to doubt the accuracy of any of the quantities involved in calculating Δ_N for NO^+/CO, and we believe the large difference is real. We conclude that Δ_Z is not exactly constant for all compounds of a given element and that it can shift by amounts considerably greater than experimental error. The question is, what sort of chemical information can be obtained from the observed shifts in core replacement energy?

The core replacement reaction, involving the transfer of an electron from a core to a nucleus, should not change much on going from one compound to another as long as the differences in electron density of the atom in question are mainly outside the region of the core. However, if the atom has a relatively high electron density at the nucleus (because, for example, of nonbonding valence electrons with considerable s character), the core replacement energy will be relatively endothermic--i.e., more positive. On this basis we can explain the very high Δ_N for NO^+/CO. The nitrogen atom of NO^+ differs from those of the other nitrogen cations in that it has a nonbonding pair of valence electrons. Nonbonding electrons generally have a much higher fraction of s character than bonding electrons; hence, the nitrogen atom of NO^+ has an abnormally high electron density at its nucleus. Of course, the carbon atom of carbon monoxide also has an abnormally high s electron density.

The effect of the s character of nonbonding electrons on core replacement energy can be seen in the data for oxygen-containing cations shown in Table 2. We have separated the compounds into two groups. The first group consists of compounds in which the non-

Table 2. Core replacement energies for oxygen-containing cations.

Compounds	E_B(N 1s) (eV)	Δ_O (eV)
OF_2^+/NF_2	413.0	400.0
O_2^+/NO	410.6	399.5
NO^+/N_2	409.95	399.75
$NO_2^+/^*NNO$	408.5	399.4
HCO^+/HCN	406.8	399.7
CH_3CO^+/CH_3CN	405.41	399.73
CH_2CHCO^+/CH_2CHCN	405.28	398.97
O_3^+/NO_2	412.9	399.4
OH_3^+/NH_3	405.60	398.88
$CH_3OH_2^+/CH_3NH_2$	405.2	399.0
$(CH_3)_2OH^+/(CH_3)_2NH$	405.0	398.9

bonding electrons on the oxygen atom would be expected to have a relatively high fraction of s character, and the second group consists of compounds expected to have relatively low s character in the oxygen nonbonding electrons. The average Δ_O value for the first group is 399.63 eV and that for the second is 399.04. The difference of 0.59 between the average Δ_O values for the two groups is in the expected direction and has a magnitude considerably greater than could be explained by experimental error.

Core replacement energies can be used as indicators of electron density at nuclei and, in the case of atoms with nonbonding valence s electrons, can give information about the hybridization of the atomic orbitals.

---

*Abstracted from Chem. Phys. Lett. 46, 220 (1977).

1. W. L. Jolly and D. N. Hendrickson, J. Am. Chem. Soc. 92, 1863 (1970).
2. W. L. Jolly, J. Am. Chem. Soc. 92, 3260 (1970).
3. W. L. Jolly, in Electron Spectroscopy, edited by D. A. Shirley (North-Holland, Amsterdam, 1972, pp. 629-645.
4. W. L. Jolly, in Electron Spectroscopy; Theory, Techniques and Applictions, Vol. 1, edited by C. R. Brundle and A. D. Baker (Academic Press, New York, 1977), pp. 119-149.

c. The Estimation of Heats of Formation of Gaseous Cations from Core Electron Binding Energies *

William L. Jolly and Christina Gin

The "core replacement energy" of an atom in a gaseous species is equal to a core binding energy plus the difference between the heats of formation of two isoelectronic species, and it is essentially a constant quantity for the atom, almost independent of the nature of the gaseous species. Core replacement energies for several elements are given in Table 3. Core binding energies and heats of formation of gaseous molecules have been combined with the appropriate core replacement energies to estimate the heats of formation of 156 gaseous cations. Most of these estimated values are believed to be accurate to ± 10 kcal mol^{-1} or less.

Table 3. Recommended values of core replacement energies.

Element in cation	Core level for which E_B required	Δ (eV)	Uncertainty in Δ, (eV)
C	B 1s	186.89	0.73
N	C 1s	283.68	0.21
O (high s density)	N 1s	399.63	0.29
O (low s density)	N 1s	399.04	0.24
F	O 1s	529.60	0.66
P	Si $2p_{3/2}$	99.29	---
S	P $2p_{3/2}$	127.6	1.0
Cl	S $2p_{3/2}$	160.1	1.1

The heats of formation of several cations can be estimated by the method which we have outlined by using two or more completely independent sets of data. For example, the heat of formation of NF_4^+ can be estimated either from data for CF_4 or from data for ONF_3. The results of such estimations, summarized in Table 4, serve as an indicator of the general reliability of the method. The average deviation between the independently estimated heats of formation in Table 4 is ± 13 kcal mol^{-1}.

Table 4. Heats of formation of cations calculated from more than one core binding energy.

Cation	Compound whose E_B and ΔH_f° are used to calculate ΔH_f°	ΔH_f° (kcal mol^{-1})
NF_4^+	CF_4	198
	ONF_3	214
NH_2CHF^+	NH_2CHO	139
	CH_2CHF	142
PF_4^+	SiF_4	-94
	POF_3	-77
PCl_4^+	$SiCl_4$	103
	$PSCl_3$	115
SOF_3^+	SO_2F_2	70
	POF_3	67
	NSF_3	66
ClO_2F_2	SO_2F_2	225
	ClO_3F	262

*Abstracted from Intl. J. Spectr. Ion Phys. 25, 27-37 (1977).

d. The Core Electron Binding Energies of Cyclotriphosphazenes and Cyclotetraphosphazenes*

S. C. Avanzino, W. L. Jolly, T. F. Schaaf and H. R. Allcock

The cyclophosphazenes are often cited as examples of inorganic aromatic systems. A large number of experimental data, including structural parameters, ionization potentials, and mass spectrometric fragmentation patterns, have been interpreted in terms of the presence of delocalized π bonding in the rings. Any increase in the degree of this π bonding involves the transfer of negative formal charge from the ring nitrogen atoms to the phosphorus atoms or to substituent groups on the phosphorus atoms. Therefore the atomic core electron binding energies should be sensitive to the degree of π bonding.

In this study we have used x-ray photoelectron spectroscopy to determine the core electron binding energies of $(NPF_2)_3$, $(NPF_2)_4$, $(NPCl_2)_3$, $(NPCl_2)_4$, and $[NP(CH_3)_2]_4$ in the gas phase in an attempt to provide experimental information related to the bonding arrangements in these compounds. On going from $(NPF_2)_4$ to $(NPF_2)_3$ or from $(NPCl_2)_4$ to $(NPCl_2)_3$, the binding energies increase by only 0.22 eV or less. This near-constancy of the binding energies suggests that the degree of π bonding is similar in the trimers and tetramers. We believe that resonance structures such as the following are good representations of the bonding in both the trimers and the tetramers. The N-P-N and X-P-X bond angles are essentially the same

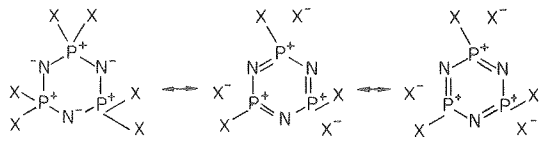

in all the phosphazenes (~120 and ~ 100°, respectively), indicating that the hybridization of the phosphorus orbitals is relatively constant. The N-P-N bond angles cannot be increased further without decreasing the X-P-X bond angles, which are already so small that X-X repulsions are very great.

*Abstracted from Inorg. Chem. 16, 2046 (1977).

e. A Reversal of the Usual Binding Energy-vs.-Charge Relationship. The Carbon 1s Binding Energies of Bis(cyclopentadienyl) Metal Complexes in the Gas Phase*

Albert A. Bakke, William L. Jolly and Theodore F. Schaaf

The carbon 1s binding energies of solid bis(cyclopentadienyl) complexes of first-row transition metals have been measured by several investigators.[1-3] The experimental uncertainty of the binding energies (ca. ± 0.3 eV) was so great that no significant correlation of the binding energy with metal atomic number was possible. In this study we determined, by gas phase x-ray photoelectron spectroscopy, the carbon is binding energies of these compounds, as well as bis(cyclopentadienyl)magnesium and bis(fulvalene)diiron, with an experimental uncertainty of ± 0.05 eV. Our measured binding energies are given in Table 5.

Table 5. Calculated carbon atom charges in bis(cyclopentadienyl) metal compounds.[a]

Compound	$E_B(c)$ (eV)	k'	ℓ'	Q_C
$Mg(C_5H_5)_2$	290.12	1.2(6)	289.7(3)	+0.3(5)
$Cr(C_5H_5)_2$	290.13	-2.9(6)	288.9(3)	-0.4(2)
$Mn(C_5H_5)_2$	290.17	2.0(7)	290.0(4)	+0.1(3)
$Fe(C_5H_5)_2$	290.03	-5.8(3)	288.2(1)	-0.31
$Co(C_5H_5)_2$	289.82	-4.3(4)	288.7(3)	-0.3(1)
$Ni(C_5H_5)_2$	289.85	-2.2(6)	289.2(4)	-0.3(3)

[a]The parenthesized numbers indicate the uncertainty in the last digit. The uncertainties were calculated by using the reported standard deviations of the structural parameters and our estimated uncertainty of ±0.05 eV in the binding energies.

We have interpreted these binding energies by using the point-charge potential equation

$$E_B(A) = kQ_A + V + \ell - E_R, \quad V = \sum_{i \neq A} (Q_i/r_{iA}). \qquad (1)$$

Here $E_B(A)$ is the binding energy for a particular core level in atom A, Q_A and Q_i are the charges on atoms A and i, r_{iA} is the distance between the nuclei of atoms i and A, ℓ is a constant, and E_R is the electronic relaxation energy associated with the core ionization. Because all the compounds have similar sandwich structures, it is a reasonable approximation to assume that the electronic relaxation energies E_R associated with the carbon 1s ionization are equal. After making appropriate substitutions, we can write, for the C 1s ionization of a bis(cyclopentadienyl) complex, the relation

$$E_B(C) = k'Q_C + \ell',$$

where k' and ℓ' are parameters which can be calculated for each compound. The calculated values of k', ℓ', and Q_C, are given in Table 5.

In a bis(cyclopentadienyl) complex, ten carbon atoms are bonded to one metal atom. Any change in the nature of the metal-ligand bonding causes the metal atom charge to change about ten times as much as, and in the opposite direction to, the carbon atom charge. Consequently there is a near cancellation of the kQ_A and V terms in Eq. (1), and the values of k' are quite small. Indeed some of the k' values are negative. Thus we have examples of the rare situation in which a change in the charge of an atom corresponds to a change of opposite sign in the binding energy.

Because of the relative insensitivity of the carbon 1s binding energy to the carbon atom charge, the data of Table 5 cannot be used to compare the ionic character of the metal-ligand bonds. The calculated Q_C values in Table 5 are too uncertain to draw meaningful conclusions.

*Abstracted from J. Electron Spectros. Related Phenom. 11, 339-342 (1977).

1. D. T. Clark and D. B. Adams, Chem. Commun. 740 (1971); Chem. Phys. Lett. 10, 121 (1971).
2. M. Barber, J. A. Conner, L. M. R. Derrick, M. B. Hall and I. H. Hillier, J. Chem. Soc. Faraday Trans. II, 559 (1973).
3. C. J. Groenenboom, G. Sawatsky, H. J. D. Miejer and F. Jellinek, J. Organomet. Chem. 76, C4 (1974).

f. ESCA Spectra of Trimethylenemethaneiron Tricarbonyl and Butadieneiron Tricarbonyl*

J. W. Koepke, W. L. Jolly, G. M. Bancroft, P. Å. Malmquist and K. Siegbahn

The trimethylenemethane diradical (I) has been the subject of considerable theoretical speculation. It

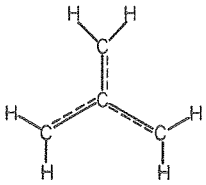

I

has been detected only at low concentrations as an unstable intermediate. An ab initio calculation by Yarkony and Schaefer[1] indicated that the central carbon has a charge of +0.62, comparable to the charge of the carbon atom in CHF_3. Although trimethylenemethane itself is too unstable to allow investigation of its charge distribution by ESCA, we have studied the ESCA spectrum of the relatively stable complex trimethylenemethaneiron tricarbonyl. For comparison we have also studied the structural isomer butadieiron tricarbonyl.

Savariault and Labarre[2] reported, on the basis of CNDO/2 calculations, that the bonds between the iron atom and the three CH_2 groups of trimethylenemethaneiron tricarbonyl are much stronger than the bond between the iron atom and the central carbon. They calculated atomic charges of +0.67 for the iron atom, +0.09 for the carbonyl carbon atoms, -0.30 for the CH_2 carbon atoms, and +0.17 for the central carbon atom, and explained the weak bond between the iron atom and the central carbon atom in terms of electrostatic repulsion. We hoped that measurement of the carbon 1s binding energies of the compound would give enough information regarding the charge distribution in the molecule to test these calculations. Trimethylenemethane has been implicated as an intermediate in several reactions, and our results will determine whether ESCA can serve as a tool to search for trimethylenemethane intermediates on catalyst surfaces.

The C 1s spectra are shown in Figs. 2 and 3. The peaks are easily assigned by comparison with the binding energies of other organometallic compounds and by intensity considerations. The peaks at 293.17 eV in Fig. 2 and at 293.03 eV in Fig. 3 are in the region typical of metal carbonyls and can be confidently assigned to the CO groups in the compounds. In Fig. 2, the relatively weak peak at 291.47 eV is undoubtedly due to the central carbon, and the 290.18 eV peak is due to the CH_2 group. The CO peaks in both spectra and the central carbon peak in Fig. 2 have lost considerable intensity to shake up bands at higher energy.

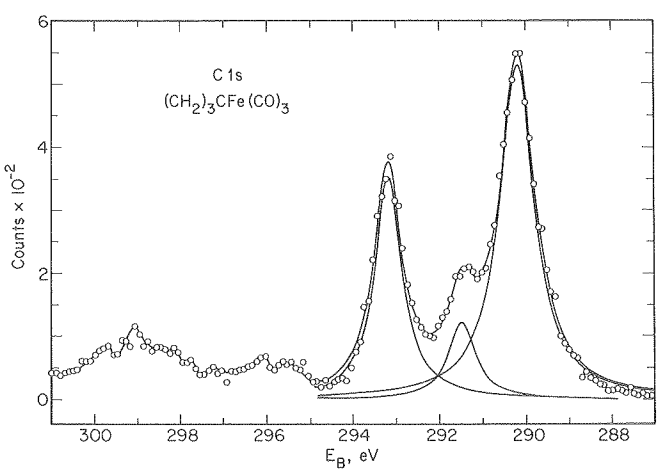

Fig. 2. Carbon 1s spectrum of trimethylenemethaneiron tricarbonyl, deconvoluted using Lorentzian curves. The relative intensities of the three peaks are 2.96:1:5.72. (XBL 782-7223)

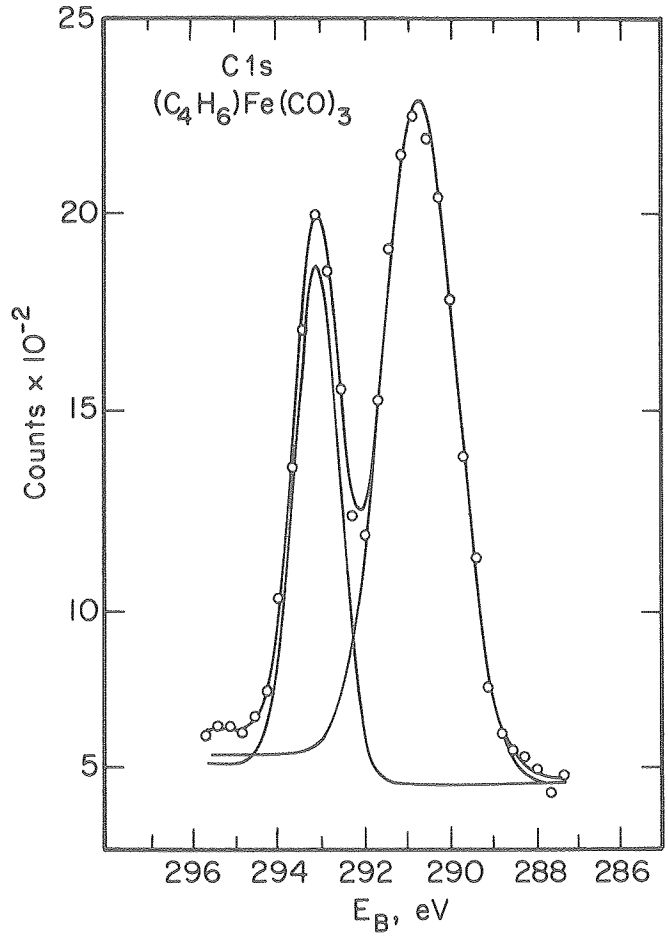

Fig. 3. Carbon 1s spectrum of butadieneiron carbonyl, deconvoluted using Gaussian curves. The relative intensities of the peaks are 1:2.16. (XBL 782-7224)

A very simple interpretation of the C 1s binding energies (ignoring relaxation energies) would put the charge of the central carbon atom of the trimethylenemethane group between those of the CO carbon atoms and the CH_2 carbon atoms. This charge distribution is not at all consistent with the calculations of Savariaut and Labarre. However, by taking account of relaxation energies, we can show that the data are consistent with a very positively charged central carbon atom in the trimethylenemethane group. The bonding in trimethylenemethaneiron tricarbonyl can be crudely represented by valence bond structure II. This structure is somewhat misleading because it does not show any back-bonding to the three carbonyl groups.

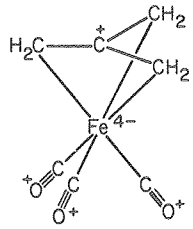

II

However, the representation of the bonding to the trimethylenemethane group, which also shows no back-bonding, is probably reasonably accurate, in view of the fact that back-bonding to carbonyl groups is generally recognized to be much greater than that to olefins and other unsaturated organic ligands. The core ionization of a ligand atom causes an increase in the amount of back-bonding to the ligand if the back-bonding effects a shift of negative formal charge to the core-ionized atom. This increase in the degree of back-bonding corresponds to an extraordinarily large relaxation energy associated with the core ionization and causes the binding energy associated with the core ionization to be lower than otherwise expected. Now let us consider the trimethylenemethane group, in view of these facts. Back-bonding to this group can be represented by structure III, in which negative formal charge has

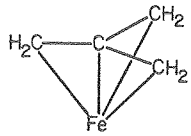

III

been transferred from the iron atom to the central carbon atom. There is no change in the formal charges of the CH_2 carbon atoms (at least this is so if structure II is accepted as the non-back-bonded structure); hence, one expects no extraordinarily large relaxation energy associated with the CH_2 C 1s ionization. On the other hand, one expects an extraordinarily large relaxation energy in the C 1s ionization of the central carbon atom. In other words, the binding energy of the central carbon atom is lower than would be expected on the basis of its ground-state charge. Thus the C 1s spectrum is consistent with a high positive charge on the central carbon atom, possibly higher than that of the carbonyl carbon atoms.

---

*Abstracted from Inorg. Chem. 16, 2659 (1977).

1. D. R. Yarkony and H. F. Schaefer, J. Am. Chem. Soc. 96, 3754 (1974).
2. J.-M. Savariault and J.-F. Labarre, Inorg. Chim. Acta 19, 153 (1976).

2. SYNTHETIC AND MECHANISTIC STUDIES

a. A Kinetic Study of the Hydrolysis of 2-Germaacetate in Neutral and Alkaline Solutions*

Duck J. Yang and William L. Jolly

In neutral and alkaline solutions, the 2-germaacetate ion decomposes to give germane and bicarbonate (or carbonate): $GeH_3CO_2^- + H_2O \rightarrow GeH_4 + HCO_3^-$. The rate of this decarboxylation is pH-independent and is first order in the germaacetate ion. The rate constant at 60° and ionic strength 1.0 is 1.62×10^{-5} s^{-1}; the activation energy is 28.6 kcal/mol. In strongly alkaline solutions (expecially at hydroxide concentrations above 1 M), a second decomposition reaction, producing hydrogen and the insoluble brown polymer $H_2Ge_2O_3 \cdot xH_2O$, competes with the decarboxylation: $2GeH_3CO_2^- + 2OH^- + (3+x) \rightarrow 6H_2 + H_2Ge_2O_3 \cdot xH_2O + 2CO_3^{2-}$. The rate of the latter reaction is first order in germaacetate ion and is inversely proportional to the Hammett acidity function h_- (i.e., first order in hydroxide ion); $-d\ln(GeH_3CO_2^-)/dt = k_2/h_-$. At 60° in 1 M NaOH, $k_2 = 2.5 \times 10^{-19}$ M s^{-1}; the activation energy is 20.8 kcal/mol.

The germane-producing reaction is analogous to the decarboxylation of an organic carboxylate ion, RCO_2^-:

$$RCO_2^- \xrightarrow{\text{slow}} R^- + CO_2$$

$$R^- + H_2O \xrightarrow{\text{fast}} RH + OH^-.$$

One would expect the rate of the slow step to be closely correlated with the protonic acidity of RH. In fact such correlation can be seen in the fact that the 2-germaacetate and trichloroacetate ions undergo decarboxylation under comparable conditions. The pK germane (~25) is close to that of chloroform (~24). Although the above mechanism is reasonable for the germane-producing decomposition of 2-germaacetate, it should be pointed out that our data are also consistent with a four-center mechanism involving initial attack of a water molecule:

$$H_3GeCO_2^- + H_2O \rightarrow \left[\begin{array}{c} H_3Ge \cdots CO_2 \\ \vdots \quad\quad \vdots \\ H \cdots O \\ \quad\quad H \end{array}\right]^- \rightarrow GeH_4 + HCO_3^-.$$

The base-catalyzed hydrogen-producing reaction is somewhat analogous to the well-known base-catalyzed hydrolyses of silicon hydride derivatives. The latter reactions involve the attack of hydroxide ion on the silicon atom, with displacement of hydride ion. These reactions may be S_N2 processes, or they may involve fleeting pentacoordinate intermediates. It seems reasonable to assume the same sort of process

in the case of the 2-germaacetate ion, corresponding to the following mechanism;

$$GeH_3CO_2^- + OH^- \xrightarrow{slow} HOGeH_2CO_2^- + H^-$$

$$H^- + H_2O \xrightarrow{fast} H_2 + OH^-$$

$$HOGeH_2CO_2^- + OH^- + 2\ H_2O \xrightarrow{fast} (HO)_3GeH + CO_3^{2-} + 2\ H_2$$

$$2\ (HO)_3GeH + (x-3)H_2O \xrightarrow{fast} H_2Ge_2O_3 \cdot xH_2O\ .$$

Complete hydrolysis to germanate(IV) does not immediately occur because of precipitation of the insoluble polymer $H_2Ge_2O_3 \cdot xH_2O$ after the evolution of three moles of hydrogen per germanium atom and the hydrolytic cleavage of the Ge-C bond.

---

*Abstracted from Inorg. Chem. 16, 2834 (1977).

b. The Conversion of Hydrous Germanium(II) Oxide to Germynyl Sesquioxide, $(HGe)_2O_3$*

Duck J. Yang, William L. Jolly and Anthony O'Keefe

Germanium(II) hydroxide [hydrous germanium(II) oxide] is a white, yellow, or brown noncrystalline material, only slightly soluble in water and alkaline solutions, having no definite stoichiometry, and generally represented by the formula $Ge(OH)_2$ or $GeO \cdot xH_2O$. We have found that digestion of a suspension of either yellow or brown germanium(II) hydroxide in aqueous sodium hydroxide solutions yields a dark brown insoluble compound that has properties distinctly different from those of the starting hydroxide. The compound, after being thoroughly washed and dried in vacuo at room temperature, is a dark-brown pyrophoric powder with a composition close to $(HGe)_2O_3$. The empirical formula and properties of the compound suggest that it is a polymer consisting of Ge-H groups linked by oxygen atoms, i.e., "germynyl sesquioxide."

Infrared spectra indicate that $(HGe)_2O_3$ is structurally different from various forms of germanium(II) hydroxide that not been treated with hydroxide solutions. Bands near 2000, 835, and 760 cm^{-1} are characteristic of Ge-H stretching, vibrations of a germanium-oxygen network of the type

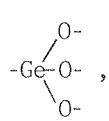

and Ge-H deformation, respectively.

When ordinary germanium(II) hydroxide is heated in vacuo to 400°, the principal reaction is the dehydration to GeO, although a small amount of hydrogen gas is evolved during the process:

$$Ge(OH)_2 \longrightarrow GeO + H_2O.$$

On the other hand, when germynyl sesquioxide is similarly heated, most of the hydrogen in the compound is evolved as hydrogen gas, and the residue is a mixture of GeO and GeO_2:

$$(HGe)_2O_3 \longrightarrow H_2 + GeO + GeO_2.$$

The solubility of germanium(II) hydroxide in water and in sodium hydroxide solutions has been studied by various workers. The results are somewhat discordant; however, there is general agreement that the solubility is very low, i.e., < 0.03 M. We believe that previous workers have not fully recognized that the nature of the solid phase changes at a measureable rate when germanium(II) hydroxide is suspended in alkaline solutions, that the rate of this change is a function of hydroxide concentration, and that consequently the measured solubility changes with hydroxide concentration and with time. Our solubility data indicate that ordinary germanium(II) hydroxide reacts with the hydroxide ion to form a soluble species, perhaps a complex such as $OGeH(OH)_2^-$. The conversion of $Ge(OH)_2$ to the relatively insoluble $(HGe)_2O_3$ appears to be catalyzed by this dissolved species or by hydroxide ions, perhaps through a mechanism such as the following:

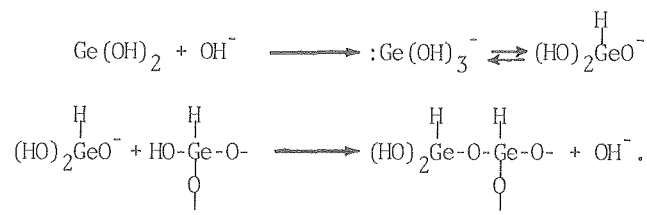

---

*Abstracted from Inorg. Chem. 16, 2980 (1977).

c. Thermal Decomposition of Nitrosyl Cyanide*

John D. Illige and William L. Jolly

Since the recent first synthesis of nitrosyl cyanide,[1,2] several physical chemical studies have been carried out on the compound, but relatively little is known about its chemical behavior. Nitrosyl cyanide undergoes both photochemical and thermal decomposition. In this study we mainly investigated the stoichiometry of the thermal decomposition. By isotopic tracer studies we also obtained some information about the mechanism of the reaction.

Nitrosyl cyanide decomposes at 75° C, with reaction times of 10 days, to form equimolar amounts of N_2, N_2O, CO_2, and $(CN)_2$, according to the equation

$$3\ ONCN \longrightarrow N_2 + N_2O + CO_2 + (CN)_2\ .$$

In low pressure runs, a significant amount of NO and an equivalent extra amount of $(CN)_2$ forms. Apparently at low pressures the following side reaction occurs to an important extent:

$$ONCN \longrightarrow NO + \frac{1}{2}\ (CN)_2\ .$$

In studies of the decomposition of ONCN having the terminal nitrogen atom labeled with ^{15}N, the distribution of ^{15}N, among the nitrogen-containing products was determined mass spectrometrically. The data show that most of the labeled nitrogen ends up as the two nitrogen atoms of cyanogen and the terminal nitrogen atom of nitrous oxide. However, small amounts of singly labeled $(CN)_2$ and N_2 form, and the amount of labeled N_2 is always greater than the amount of unlabeled N_2O. The data as a whole can be quantitatively accounted for in terms of two concurrent mechanisms. We propose the principal mechanism

$$2\ ONCN \longrightarrow 2\ NO + (CN)_2, \qquad (1)$$

$$NO + ONCN \longrightarrow N_2O + OCN, \qquad (2)$$

$$NO + OCN \longrightarrow CO_2 + N_2. \qquad (3)$$

Reaction (1) is quite reasonable as the initiation step in view of the very low C-N bond dissociation energy of nitrosyl cyanide. Reactions (2) can be envisaged as taking place in either of two ways. In the first way, the NO molecule essentially plucks off the terminal nitrogen atom from the ONCN molecule to form the fulminate radical, ONC:

$$ONCN + NO \longrightarrow ONC\cdots N\cdots NO \longrightarrow ONC + NNO.$$

This radical rapidly rearranges to the more stable cyanate radical, OCN. When labeled ONCN is used, this first way leads to labeled N_2O and unlabeled OCN. In the second way, the NO and ONCN molecules react by a four-center process:

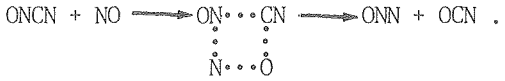

When labeled ONCN is used, the second way yields unlabeled N_2O and labeled OCN. Reaction (3) is probably a four-center process.

According to the first mechanism, the use of terminally labeled ONCN should yield only doubly labeled cyanogen, and the amount of labeled N_2 should equal the amount of unlabeled N_2O. To account for the fact that the observed data deviate from these predictions, we propose that the following mechanism occurs concurrently with, but to a lesser extent than, the first mechanism:

$$NO + ONCN \longrightarrow N_2O + OCN, \qquad (2)$$

$$OCN + ONCN \longrightarrow NO_2 + (CN)_2, \qquad (4)$$

$$NO_2 + ONCN \longrightarrow CO_2 + N_2 + NO. \qquad (5)$$

This mechanism consists of three chain-propagating steps, involving the chain carriers NO, OCN, and NO_2. Reactions (1) and (3) can serve as the chain-initiating and -terminating steps, respectively, of this mechanism. It should be noted that the first step of the second mechanism [reaction (2)] is the same as the second step of the first mechanism. The second step [reaction (4)] is probably a four-center process; it yields singly labeled $(CN)_2$ when the OCN is unlabeled and the ONCN is labeled. The third step [reaction(5)] may occur directly as a complicated multicenter process or may actually be a two-step process, involving nitryl cyanide as an intermediate.

---

*Abstracted from Inorg. Chem. 16, 2637 (1977).

1. P. Horsewood and G. W. Kirby, Chem. Commun. 1139 I1971).
2. R. Dickinson, G. W. Kirby, J. G. Sweeny and K. K. Tyler, J. Chem. Soc., Chem. Commun. 241 (1973).

d. The Reduction of Organic Compounds with the Hydroxyborohydride Ion*

Janice W. Reed and William L. Jolly

The hydroxyborohydride ion, BH_3OH^-, is formed during the hydrolysis of the borohydride ion, BH_4^-.[1,2] In the reduction of esters by aqueous borohydride solutions, Kirsch and Lee[3] observed an increase in the rate of reduction when the borohydride solutions were allowed to age before adding the esters, and they proposed that the increased reducing power of the aged solutions was due to the formation of the BH_3OH^- ion. By use of a quenching flow reactor described in a previous publication,[4] it is possible to prepare alkaline solutions containing the BH_3OH^- ion in concentrations as high as 0.35 M. The half-life of BH_3OH^- in such solutions is 3.9 hours at 20° and pH ≥ 12.5. To determine the utility of the BH_3OH^- ion as a reducing agent, we have studied the reduction of esters, nitriles, nitro compounds, ketones, and alkyl halides.

In cold solutions the BH_3OH^- ion reduces esters that are reduced by $NaBH_4$ only at elevated temperatures, e.g., in refluxing methanol. Benzonitrile is reduced by cold aqueous BH_3OH^-, whereas reduction of similar nitriles by $NaBH_4$ requires special conditions, such as the presence of $AlCl_3$. Aqueous BH_3OH^- reduces nitrobenzene all the way to aniline rather than just to azoxybenzene, as in the reduction by $NaBH_4$. At 0° it reduces ketones as readily as $NaBH_4$ does at room temperature. We attempted the reduction of 1-chlorooctane, 1-iodooctane, and benzhydryl chloride with BH_3OH^-, but were unable to isolate any hydrocarbons. Thus the hydroxyborohydride ion has a reducing power intermediate between that of the rather powerful lithium aluminum hydride and the rather mild and selective sodium borohydride.

---

*Abstracted from J. Org. Chem. (in press).

1. J. A. Gardiner and J. W. Collat, Inorg. Chem. 4, 1208 (1965); J. A. Gardiner and J. W. Collat, J. Am. Chem. Soc. 86, 3165 (1965); J. A. Gardiner and J. W. Collat, J. Am. Chem. Soc. 87, 1692 (1965).
2. F. T. Wang and W. L. Jolly, Inorg. Chem. 11, 1933 (1972).
3. J. F. Kirsch and W. N. Lee, Paper S64 presented at the 154th meeting of the American Chemical Society, Chicago, Illinois, 1967.
4. J. W. Reed, H. H. Ho, and W. L. Jolly, J. Am. Chem. Soc. 96, 1248 (1974).

3. RESEARCH PLANS FOR CALENDAR YEAR 1978

William L. Jolly

a. X-Ray Photoelectron Spectroscopy. Preliminary studies indicate that it is possible to obtain XPS spectra of species dissolved in glycerin at room temperature. Glycerin has a very low vapor pressure, and many ionic compounds can be dissolved in it. We plan to extend these studies to a wide variety of dissolved compounds and to exploit this technique as an analytical method for dissolved species.

By a careful least-squares analysis of the oxygen 1s spectrum of $Fe(CO)_5$, we believe that we can resolve the band into two peaks corresponding to the axial and equatorial CO groups. This result means that quite subtle changes in the degree of back-bonding in metal carbonyls can be determined by XPS, and the results will help the interpretation of XPS spectra of CO adsorbed on metals and catalytic surfaces.

We plan to study a variety of transition metal coordination compounds to elucidate the nature of the metal-ligand bonds. One of the first ligands that we will concentrate on is the nitrosyl group, NO. Nitrosyl and carbonyl complexes are involved in automotive exhaust catalysts. We also plan to study "mixed-valence" compounds to help clarify the interactions between the metal atoms in such compounds.

b. Synthetic and Mechanistic Studies. We are continuing our characterization of diaminoborane, $BH(NH_2)_2$. We hope to clarify the decompostion reaction, which yields what appears to be a polymeric material of composition $(BHNH)_x$.

We hope to replace the hydrogen atoms in the two-dimensional polymers $(SiH)_2O_3$ and $(GeH)_2O_3$ with other groups, such as alkyl groups, SiR_3 groups, etc. The resulting compounds may have physical and chemical properties that will make them useful as structural materials.

4. 1977 PUBLICATIONS AND REPORTS

William L. Jolly and Associates

Journals and Book

1. W. L. Jolly, S. C. Avanzino and R. R. Rietz, Use of 1s Binding Energies and Multiplicity-Weighted C-O Stretching Frequencies to Measure Back-Bonding in Transition Metal Carbonyl Complexes, Inorg. Chem. 16, 964 (1977), LBL-5708.

2. W. L. Jolly, C. Gin and D. B. Adams, The Correlation of Core Replacement Energies with Nonbonding s Electron Density, Chem. Phys. Lett. 46, 220 (1977), LBL-5726.

3. W. L. Jolly and C. Gin, The Estimation of Heats of Formation of Gaseous Cations from Core Electron Binding Energies, Intl. J. Mass Spectr. Ion Phys. 25, 27 (1977), LBL-5728.

4. S. C Avanzino, W. L. Jolly, T. F. Schaaf and H. R. Allcock, The Core Electron Binding Energies of Cyclotriphosphazenes and Cyclotetraphosphazenes, Inorg. Chem. 16, 2046 (1977), LBL-5790.

5. J. D. Illige and W. L. Jolly, The Thermal Decomposition of Nitrosyl Cyanide, Inorg. Chem. 16, 2637 (1977), LBL-5769.

6. A. A. Bakke, W. L. Jolly and T. F. Schaaf, A Reversal of the Usual Binding Energy-vs.-Charge Relationships. The Carbon 1s Binding Energies of Bis(cyclopentadienyl) Metal Complexes in the Gas Phase, J. Electron Spectrosc. Rel. Phenom. 11, 339 (1977), LBL-5785.

7. J. W. Koepke, W. L. Jolly, G. M. Bancroft, P. Å. Malmquist, and K. Siegbahn, ESCA Spectra of Trimethylenemethaneiron Tricarbonyl and Butadieneiron Tricarbonyl, Inorg. Chem. 16, 2659 (1977), LBL-6616.

8. D. J. Yang and W. L. Jolly, A Kinetic Study of the Hydrolysis of 2-Germaacetate in Neutral and Alkaline Solutions, Inorg. Chem. 16, 2834 (1977) LBL-6055.

9. D. Y. Yang, W. L. Jolly, and A. O'Keefe, The Conversion of Hydrous Germanium(II) Oxide to Germynyl Sesquioxide, $(HGe)_2O_3$, Inorg. Chem. 16, 2980 (1977), LBL-6256.

10. W. L. Jolly, Inorganic Applications of X-Ray Photoelectron Spectroscopy, Topics in Current Chem. 71, 149 (1977), LBL-5705.

11. W. L. Jolly, The Application of X-Ray Photoelectron Spectroscopy in Inorganic Chemistry, Chap. 3 in Electron Spectroscopy: Theory, Techniques and Applications, Vol. 1, edited by C. R. Brundle and A. D. Baker (Academic Press, London, 1977), pp. 119-149, LBL-6623.

12. J. W. Reed and W. L. Jolly, The Reduction of Organic Compounds with the Hydroxyborohydride Ion, J. Org. Chem. (in press), LBL-6200.

Papers Presented

1. William L. Jolly, X-Ray Photoelectron Spectroscopy of Metal Carbonyl Compounds, at 18th International Conference on Coordination Chemistry, São Paulo, Brazil, Uly 20, 1977.

2. William L. Jolly, The Study of Back-Bonding by X-Ray Photoelectron Spectroscopy (invited symposium talk), at American Chemical Society Meeting, Chicago, III, Aug. 27, 1977.

d. Electrochemical Systems

John Newman, Principal Investigator

1. VAPOR-LIQUID EQUILIBRIA IN MULTICOMPONENT AQUEOUS SOLUTIONS OF VOLATILE ELECTROLYTES*

Thomas J. Edwards, John Newman and John M. Prausnitz

The phase equilibria of volatile weak electrolytes in aqueous solutions have become of major importance to chemical engineers due to social and economic considerations. The solutions of interest vary over a wide range of concentration and composition, including on the one hand extremely dilute wastestreams of ammonia, carbon dioxide, and hydrogen sulfide, and on the other, concentrated solutions of ammonia.

A static experimental apparatus has been constructed[1] to measure vapor-liquid equilibria of aqueous solutions containing one or more volatile weak electrolytes at high solute concentrations at temperatures to 150°C. Both phases are sampled and analyzed using gas-liquid chromatography. Preliminary data for the ammonia-carbon dioxide-water system were obtained.

A molecular-thermodynamic correlation has been established for calculating the thermodynamics of aqueous solutions containing one or more volatile weak electrolytes: ammonia, carbon dioxide, hydrogen sulfide, sulfur dioxide, and hydrogen cyanide. The correlation holds from 0 to 170°C and for total solute concentrations to 10 molal. To represent activities of these high concentrations, activity coefficients are expressed as a function of molality. Required parameters, obtained from data reduction or estimated from correlations, are presented. An engineering-oriented computer program has been written for the calculation of vapor-liquid equilibria of multisolute systems.

A new expression has been proposed for representing the effect of composition on the activity coefficients of water and ammonia. At a fixed temperature, only one adjustable constant is required to give good representation of the experimental partial pressure of ammonia over the entire composition range. A new thermodynamic consistency test is applied to literature values for the ammonia-water system.

*Funded by National Science Foundation.

1. Thomas Edwards (Ph.D. thesis), University of California, Berkeley, October 1977.

2. CORROSION OF IRON-BASED ALLOYS BY COAL CHAR

Bruce A. Gordon, John Newman and Alan V. Levy

One of the by-products of coal processing is coal char, a light friable material made up of ash, unprocessed carbon, and a mixture of inorganic sulfides and sulfates. Preliminary screening experiments indicated that at the operating temperatures of a coal gasifier, char contains sufficient fixed sulfur to corrode iron-base alloys. More detailed experiments indicated that at oxygen partial pressures of less than 10^{-19} atmosphere, any sulfidation that occurs is due to reduction of sulfates in the char, specifically $CaSO_4$. At oxygen partial pressure of more than 10^{-17}, the sulfidation would be due to oxidation of the sulfides, specifically FeS.

3. SIMULTANEOUS REACTIONS ON A ROTATING-DISK ELECTRODE

Ralph White and John Newman

A model of simultaneous reactions on a rotating-disk electrode operating in a well-supported electrolyte is presented and applied to copper deposition from an acidified copper sulfate solutions with simultaneous formation of dissolved hydrogen.[1] The effects of mass transfer, nonlinear kinetics, and nonuniform ohmic potential drop are included in the model. The governing equations are used to develop a parameter that can be used to characterize a side reaction relative to a main reaction. In the model the diffusion coefficients and other physical properties of the solution are assumed to depend only on the solution temperature (25°C) and bulk composition. It is also assumed that the disk surface remains smooth during metal deposition. In essence, this work extends Newman's earlier model[2] to include multiple electrode reactions.

The governing equations can be used to derive a parameter that is characteristic of a side reaction relative to a main reaction:

$$\Delta U_s = U_{m,ref} - U_{s,ref} - \frac{RT}{\alpha_{cs}F} \ln \left| \frac{i_{os,ref}}{i_{m,lim}} \right| + \frac{RT}{\alpha_{cm}F} \ln \left| \frac{i_{om,ref}}{i_{m,lim}} \right| , \quad (1)$$

where the α_c's are cathodic transfer coefficients and the U's are open-circuit cell potentials, evaluated at specified reference concentrations, relative to a reference electrode of a given kind. The exchange current densities $i_{oj,ref}$ of the reactions, based on reference concentrations, are as important as the open-circuit potentials in determining the influence of the side reaction. Another significant parameter is the dimensionless limiting current density

$$N = \Gamma(4/3) \frac{n_m F r_o}{s_{Rm} RT \kappa_\infty} i_{m,lim} ,$$

which governs the magnitude of the variation of the solution potential $\tilde{\Phi}$ from the center to the edge of the electrode.

The main reaction in this study is

$$Cu^{++} + 2e^- \rightarrow Cu \qquad (2)$$

and the side reaction is

$$H^+ + e^- \rightarrow \frac{1}{2} H_2 \ . \qquad (3)$$

Predicted and measured[3] current-potential curves for this system are shown in Fig. 1. Figure 2 shows how the shape of the current-potential curve depends on N and ΔU_s. Here the abscissa involves a modified electrode potential given by

$$V_m = U_{m,ref} - \frac{RT}{\alpha_{cm} F} \ln \left| \frac{i_{m,lim}}{i_{om,ref}} \right| \ .$$

Distortion of the limiting-current plateau exists even for N = 0 and becomes more pronounced as N increases for a given ΔU_s or as ΔU_s decreases for a given N. For the driving forces shown in Fig. 2, flat-plateau limiting-current curves are predicted, however, for N = 0 and $\Delta U_s > 0.5$ V.

Figures 3 and 4 contain the radial current, surface concentration, and potential distributions for the case presented in Fig. 2 with N = 50 and $V - V_m - \tilde{\Phi}_o(r = 0) = -0.0739$ V.

Figure 3 demonstrates that the main reaction current density can be below its limiting value at the center of the disk while hydrogen gas bubbles may be formed at the edge, since the dissolved hydrogen concentration exceeds its saturation value there by a factor of about 2.388.

The potential distribution labeled "Actual" in Fig. 4 is the reason for the nonuniform distributions in Fig. 3. The potential changes by about 0.236 V from the center to the edge of the disk because of the disk's nonuniform accessibility from

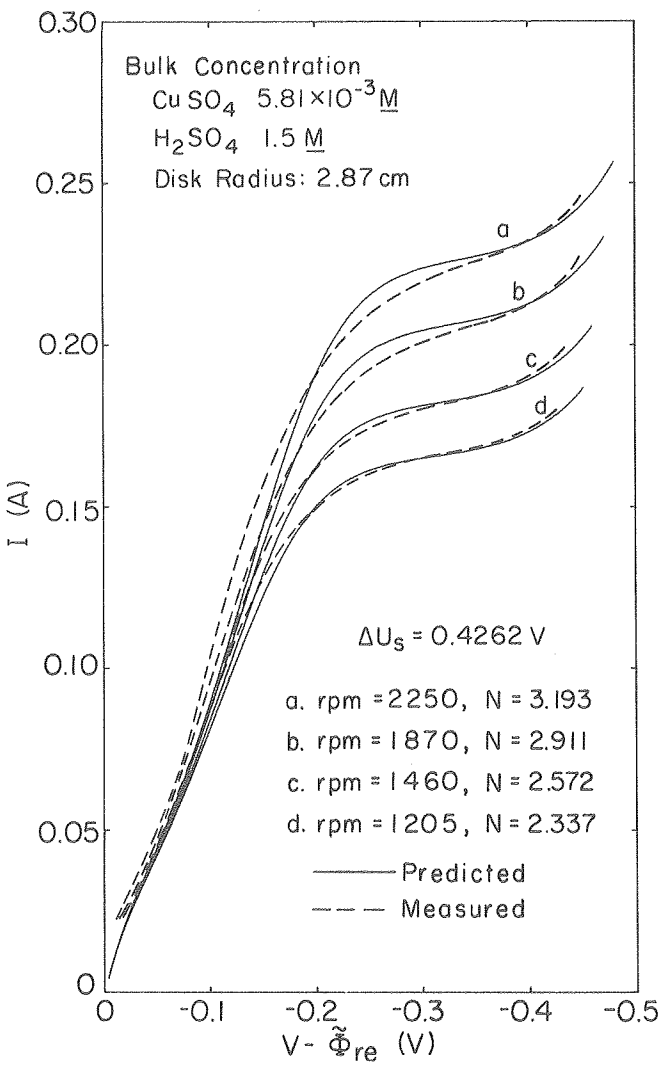

Fig. 1. Comparison of predicted and measured[2] limiting current curves for copper deposition with simultaneous formation of dissolved hydrogen. The reference electrode was a copper wire located in the bulk solution; its position in the experimental cell was approximated in the model by placing it in the plane of the disk, 5 cm from the axis of rotation. (XBL 771-4940)

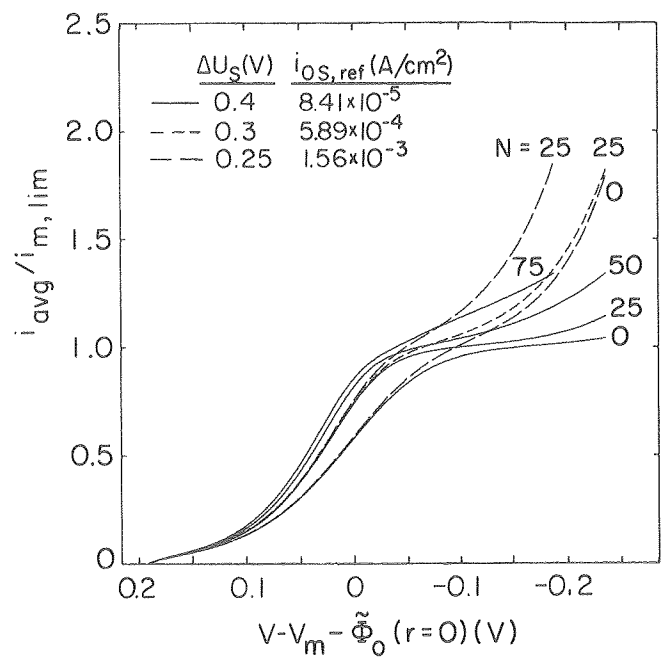

Fig. 2. Simulated current-potential curves for copper deposition with simultaneous dissolved hydrogen formation, where the anodic portion of the side reaction is negligible and the anodic portion of the main reaction is significant only near the open-circuit potential. The reference exchange current density for the main reaction is $i_{om,ref} = 3 \times 10^{-3}$ A/cm^2. (XBL 771-4939)

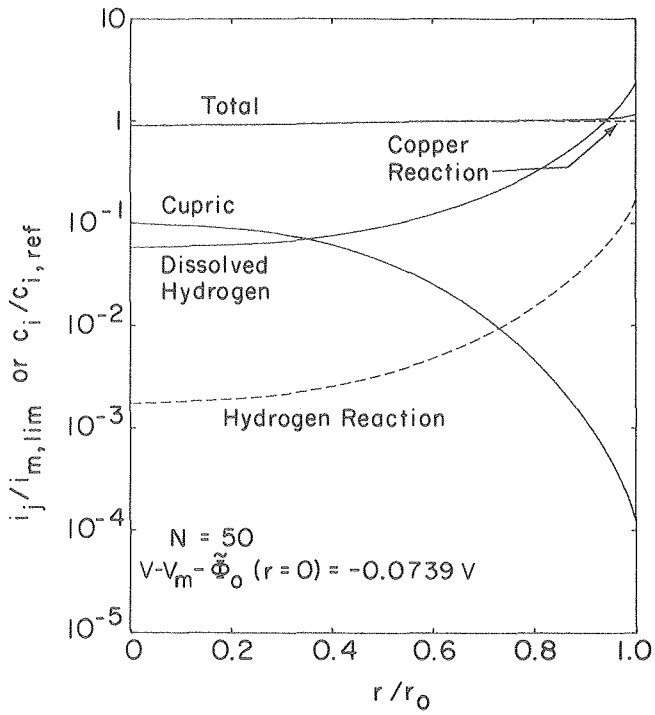

Fig. 3. Radial current and surface concentration distributions. The reference concentration of the cupric species is the bulk value; that for hydrogen is the solubility. Hence, the solution is somewhat supersaturated in hydrogen toward the edge of the electrode. (XBL 771-4937)

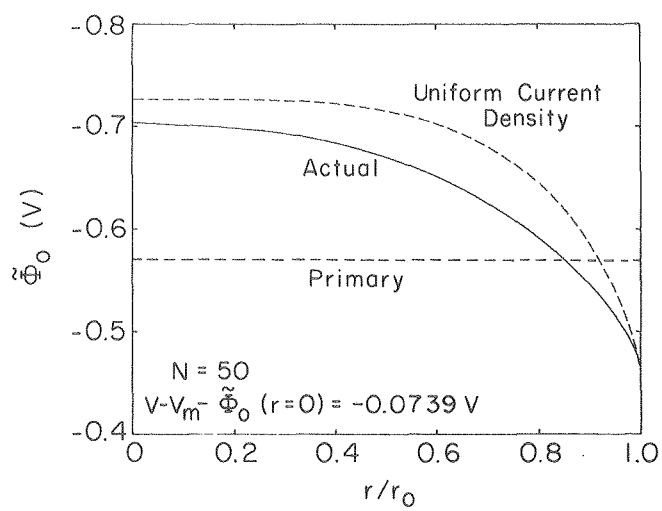

Fig. 4. Radial potential distributions. (XBL 771-4938)

an ohmic standpoint. The potential labeled "Primary" was obtained from[4]

$$\tilde{\Phi}_o = I/4\kappa_\infty r_o \ .$$

Finally, Fig. 1 illustrates that limiting-current curve plateau distortion can exist even for a relatively small value of N and a relatively large value of ΔU_s.

---

1. Ralph White, (Ph.D. thesis), University of California, Berkeley, LBL-6094, March 1977.
2. John Newman, Current Distribution on a Rotating Disk Below the Limiting Current, J. Electrochem. Soc. 113, 1235 (1966).
3. Charles M. Mohr, Jr. and John Newman, Mass Transfer to a Rotating Disk in Transition Flow, J. Electrochem. Soc. 123, 1687 (1976).
4. John Newman, Resistance for Flow of Current to a Disk, J. Electrochem. Soc. 113, 501 (1966).

4. A MODEL FOR THE ANODIC DISSOLUTION OF IRON IN H_2SO_4

Clarence Law and John Newman

A model, which assumes a continuous transition of iron from the active to the passive state, has been obtained that yields a z shaped current-potential curve. The calculations are based on the secondary current distribution of a disk electrode modified to reflect the formation of a passive layer. Epelboin et al.[1] have measured the i-V curve of a rotating disk electrode in H_2SO_4. Agreement is obtained between their data and this model. The significance of the z shaped polarization curve is discussed in terms of the ohmic potential variation, film coverage, and kinetic parameters.

---

1. I. Epelboin, C. Gabrielli, M. Keddam, J. C. Lestrade and H. Takenouti, J. Electrochem. Soc. 119, 1632 (1972).

5. RING ELECTRODES

Peter Pierini and John Newman

The primary and secondary current distributions and the primary resistance for ring electrodes have been calculated.[1] Current distributions, including mass transfer effects, for various potential dependent heterogeneous kinetics are computed for a representative set of rotating ring electrode geometries.

---

1. Peter Pierini and John Newman, Ring Electrodes, LBL-6235, April 1977.

6. MASS TRANSFER IN TURBULENT AND TRANSITIONAL FLOW AT RING ELECTRODES

Peter Pierini and John Newman

Rotating ring electrodes were used to collect data on mass transfer rates for three different electrode geometries. The measurements basically confirm those of Daguenet[1] and also Deslouis and Keddam[2] taken at the limiting current for transitional and turbulent flows. Data were also collected for operating conditions below the limiting current. The polarization curves are being used as the basis to verify an extension of the modeling technique of Pierini and Newman.[3] The mass transfer information is 0 comparable to that of Mohr and Newman[4] and is being used to eliminate the integration of mass transfer boundary layers across laminar, transitional and turbulent zones.

---

1. M. Daguenet, Int. J. Heat Mass Transfer 11, 1581 (1968).
2. C. Deslouis and M. Keddam, Ibid 16, 1763 (1973).
3. P. Pierini and J. Newman, Ring Electrodes, LBL-6235, April 1977.
4. C. M. Mohr, Jr. and J. Newman, J. Electrochem. Soc. 123, 1687 (1976).

7. POTENTIAL DISTRIBUTIONS IN FINITE CELL GEOMETRIES

Peter Pierini and John Newman

Much work has been expended in computing potential and current distributions for rotating disk electrodes. An even larger volume of work has been conducted experimentally with the device. The mathematical solutions of Laplaces equation which have been used to describe the potential distributions assume cells of infinite dimension. Large cells and small disks are approximated well by this assumption but there exist small deviations that are measureable.[1] The method of Newman and Harrar[2] has been extended to compute these deviations for cylindrical cells.

---

1. B. Miller and M. I. Bellavance, J. Electrochem. Soc. 120, 42 (1973).
2. J. Newman and J. Harrar, ibid. 120, 1043 (1973).

8. RESEARCH PLANS FOR CALENDAR YEAR 1978

John Newman

A mathematical model that describes the behavior of high temperature batteries will be applied to the Li,Al/LiCl,KCl/FeS_x system. Digital simulations for individual electrodes and the separator will be combined to predict the characteristics of the battery as a whole. A high pressure, porous flow-through electrode will be used to study the effect of pressure on the current efficiency of the removal of lead from a dilute waste stream. Corrosion of iron under conditions of low pH, high pH, and presence of Cl^- will be studied experimentally. These experiments will provide a basis to test the numerical simulation developed for a corroding iron disk.

Fundamental study of mass-transfer limited reactions in packed beds will be continued. The periodically constricted tube model of a bed will be used to predict high Péclet number mass transfer coefficients. An experimental correlation will be developed. The development of numerical simulations for photovoltaic devices, as well as simulations for the primary current distribution on thick rings and banded rings, will be continued.

9. 1977 PUBLICATIONS AND REPORTS

John Newman and Associates

Journals

1. Peter W. Appel and John Newman, Application of the Limiting Current Method to Mass Transfer in Packed Beds at Very Low Reynolds Numbers, AIChE J. 22, 979 (1976).

2. Donald N. Hanson and John Newman, Calculation of Distillation Columns at the Optimum Feed Plate Location, Ind. Eng. Chem. Process Design and Development 16, 223 (1977).

3. Ralph White, James A. Trainham, John Newman and Thomas W. Chapman, Potential-Selective Deposition of Copper from Chloride Solutions Containing Iron, J. Electrochem. Soc. 124, 669 (1977).

4. Peter Pierini and John Newman, Current Distribution on a Rotating Ring-Disk Electrode Below the Limiting Current, J. Electrochem. Soc. 124, 701 (1977).

5. John Van Zee and John Newman, Electrochemical Removal of Silver Ions from Photographic Fixing Solutions Using a Porous Flow-Through Electrode, J. Electrochem. Soc. 124, 706 (1977).

6. Peter Fedkiw and John Newman, Mass Transfer at High Péclet Numbers for Creeping Flow in a Packed-Bed Reactor, AIChE J. 23, 255 (1977).

7. Thomas J. Edwards and John Newman, Effect of Diffusional Resistance Upon Gas Chromatography in Capillary Columns, Macromolecules 10, 609 (1977).

8. J. A. Trainham and J. Newman, A Thermodynamic Estimation of the Minimum Concentration Attainable in a Flow-Through Porous Electrode Reactor 7, 287 (1977).

9. Ralph While and John Newman, Simultaneous Reactions on a Rotating-Disk Electrode, J. Electroanal. Chem. 82, 173 (1977).

10. James A. Trainham and John Newman, A Flow-Through Porous Electrode Model: Application to Metal-Ion Removal from Dilute Streams, J. Electrochem. Soc. 124, 1528 (1977).

11. John Newman, D. N. Hanson and K. Vetter, Potential Distribution in a Corroding Pit, Electrochim Acta 22, 829 (1977).

12. John Newman, Simultaneous Reactions at Disk and Porous Electrodes, Electrochim. Acta 22, 903 (1977).

13. Peter Appel and John Newman, Radially Dependent Convective Warburg Problem for a Rotating Disk, J. Electrochem. Soc. 124, 1864 (1977).

14. William Tiedemann, John Newman and Frank DeSua, Potential Distribution in the Lead-Acid Battery Grid, D. H. Collins, Ed., Power Sources 6, (London: Academic Press, 1977), p. 15.

Papers Presented

1. John Newman, Summary of Lawrence Berkeley Laboratory Programs on Battery Support Research and Development, ERDA Battery Contractor's Coordination Meeting, Germantown, Maryland, January 27, 1977.

2. Ralph White and John Newman, Simultaneous Reactions on a Rotating Disk Electrode, (Ralph White presented the paper), Philadelphia Meeting of the Electrochemical Society, May 13, 1977.

3. T. J. Edwards, J. M. Prausnitz, and J. Newman, Vapor-Liquid Equilibria for Multicomponent Aqueous Solutions of Volatile Electrolytes, (Edwards presented the paper), New York Meeting of the American Institute of Chemical Engineers, November 16, 1977.

Theses

1. Ralph Edward White, Simultaneous Reactions on a Rotating-Disk Electrode (Ph.D. thesis), LBL-6094, March 1977.

2. Thomas James Edwards, Vapor-Liquid Equilibria in Multicomponent Aqueous Solutions of Volatile Electrolytes (Ph.D. thesis), October 1977.

LBL Reports

1. Peter Fedkiw and John Newman, Mass Transfer at High Péclet Numbers for Creeping Flow in a Packed-Bed Reactor, LBL-5406 Rev., December 1976.

2. Ralph White and John Newman, Simultaneous Reactions on a Rotating-Disk Electrode, LBL-6018, January 1977.

3. James Trainham and John Newman, A Flow-Through Porous Electrode Model: Application to Metal-Ion Removal from Dilute Streams, LBL-6041, January 1977.

4. Peter Appel and John Newman, Radially Dependent Convective Warburg Problem for a Rotating Disk, LBL-6053, February 1977.

5. Peter Fedkiw and John Newman, Low Péclet Number Behavior of the Transfer Rate in Packed Beds, LBL-6074, March 1977.

6. James Trainham and John Newman, The Effect of Electrode Placement and Finite Matrix Conductivity on the Performance of Flow-Through Porous Electrodes, LBL-6260, May 1977.

7. Peter Pierini and John Newman, Ring Electrodes, LBL-6235, April 1977.

8. Bruce A. Gordon and V. Magarajan, Corrosion of Fe-10Al-Cr Alloys by Coal Char, LBL-6946, October 1977.

e. Delocalized-Electron Solids and High-Energy Oxidizers

Neil Bartlett, Principal Investigator

1. GRAPHITE AND BORON-NITRIDE SALTS

Barry McQuillan, Eugene McGarren, Richard N. Biagioni and Neil Bartlett

Attempts to make salts of BN other than $(BN)_4SO_3F$ have, so far, failed. Layer boron nitride interacts with oxidizing fluorides (to yield BF_3 and N_2). Most of our work has involved oxidation of graphite and the synthetic and structural work have had, as their main focus, the settling of the question of the validity of the salt formulation $C_x^+X^-$ for the strong-acid-anion intercalates. Thus while certain of the intercalates of graphite with AsF_5 have recently been described[1] as having electrical conductivity superior to that of graphite, information on the nature of the intercalated AsF_3 has remained meager. It has even been recently suggested[2] that the intercalated species were largely molecular AsF_5. This appeared to be contrary to the behavior one anticipates for the strong oxidizer AsF_5. Moreover, our work with the oxidizer SO_3F, in which both $C_{12}SO_3F$ and $(BN)_4SO_3F$ had been achieved, persuaded us that salt formulations were appropriate for the fluorosulfates (i.e., $C_{12}^+SO_3F^-$ and $(BN)_4^+SO_3F^-$) and by extension would also be appropriate for intercalates of the higher ionization potential anions AsF_6^-, PtF_6^-, IrF_6^- and OsF_6^-. It seemed probable that the AsF_5 oxidation of graphite produced at least some AsF_6^-. Our investigation of the graphite/AsF_5 first stage material and our synthesis of the simple AsF_6^- graphite intercalate[3] are described in Sec. (a).

The synthesis of the hexafluorometallates (MF_6^- = Os, Ir, Pt) was undertaken for two reasons. The first was to obtain a series of salts containing nearly isodimensional intercalated species, MF_6, of graded electron affinity (PtF_6 having the highest known molecular electron affinity and IrF_6 and OsF_6 having electron affinities successively ~ 1 eV less). The second was to use magnetic susceptibility measurements, as an adjunct to x-ray diffraction studies, to settle the constitution of the salts. These transition-metal studies are reported in Sec. (b).

a. Arsenic Fluoride Intercalates

Treatment of pyrolytic graphite with arsenic pentafluoride yielded material of approximate composition $C_{10}AsF_5$. This is a blue solid and corresponds to the material first described by Selig and his coworkers.[4]

Single crystals of graphite (previously characterized by x-ray precession photography) were similarly treated with AsF_5 and overpressure of two or three atmospheres of the gas was maintained over the crystal by enclosing the crystal and gas in a quartz capillary. The crystal (usually smaller than 1 mm diam) was held steady in the capillary by quartz "wool." By slow intercalation much order can be maintained and there is a good possibility that adequate intensity data can eventually be collected to show the disposition of the arsenic fluoride species with respect to the graphite lattice. It appears that the unit cell of the first stage graphite/AsF_5 material is at least pseudohexagonal (it may be truly so) with $a_o = 4.92$, $c_o = 16.20$ Å, V = 340.03 Å. The observed 00ℓ reflections have $\ell = 2n$ and it seems probable that the gallery height in the intercalate (i.e., the spacing between adjacent carbon sheets) is 8.10 Å. This is appropriate spacing for an octahedral AsF_6^- species fitted between graphite sheets of thickness ~ 3.4 Å.

A parallel study of graphite oxidized by $O_2^+AsF_6^-$ was also made. The oxidation:

$$\text{graphite} + O_2^+AsF_6^- \longrightarrow \text{graphite}^+AsF_6^- + O_2\uparrow$$

was carried out, at ~ -20°, using SO_2ClF as a dispersive agent and solvent (in which the O_2AsF_6 is only slightly soluble). Gravimetric work, using pyrolytic graphite, has established that a first stage material of limiting composition C_8AsF_6 is generated when an excess of O_2AsF_6 is used. Single crystals of graphite were similarly converted to a first stage material and proved to be hexagonal (or pseudohexagonal) with $a_o = 4.92$ and $c_o = 8.10$, V = 170 Å^3. Indeed, but for the superlattice reflexions that require a doubling of c_o in $C_{10}AsF_5$, the precession photographs for C_8AsF_6 were very nearly the same as for $C_{10}AsF_5$.

The a_o value for the unit cell of the $C_8^+AsF_6^-$ salt is twice that of graphite ($a_o = 2.456$ Å) and this indicates that the carbon network has essentially the same dimensions as in the unoxidized carbon. The doubling of a_o on intercalation may be seen from Fig. 1. It is reasonable to assume that the AsF_6^- species are centered, with respect to the graphite network, as shown in Fig. 2. If, as is presently indicated, $c_o = 8.10$ Å and not a simple multiple of it, then this implies an eclipsing of the graphite sheets. Since the graphite sheets are not eclipsed in graphite, there would have to be a massive reorganization in forming the C_8AsF_6 salt if our present unit cell is confirmed.

The unit cell of C_8AsF_6 also implies close packing of the AsF_6^- species. The unit cell volume of 170 Å^3 can be divided into a carbon network component and an AsF_6^- component. Since the unit cell contains 8 carbon atoms and since, from the graphite unit cell, the volume occupied by 4 carbon atoms of graphite is 35 Å^3, we can conclude that the volume available for the AsF_6^- is ~ 100 Å^3. But this is the effective packing volume for hexafluoride molecules [see Sec. (b)] and in $IF_6^+AsF_6^-$ $V_{\text{formula unit}}$ = 214 Å^3. The C_8AsF_6 stoichiometry probably therefore represents a packing limit rather than a graphite oxidation limit.

The similarity of the C_8AsF_6 and $C_{10}AsF_5$ x-ray data suggested that the gallery dimensions were being determined by a common species: AsF_6^-. X-ray K-shell absorption-edge spectra for the two materials when compared with like spectra of AsF_6^- salts and a spectrum of As_2O_3 confirm this view and show that the

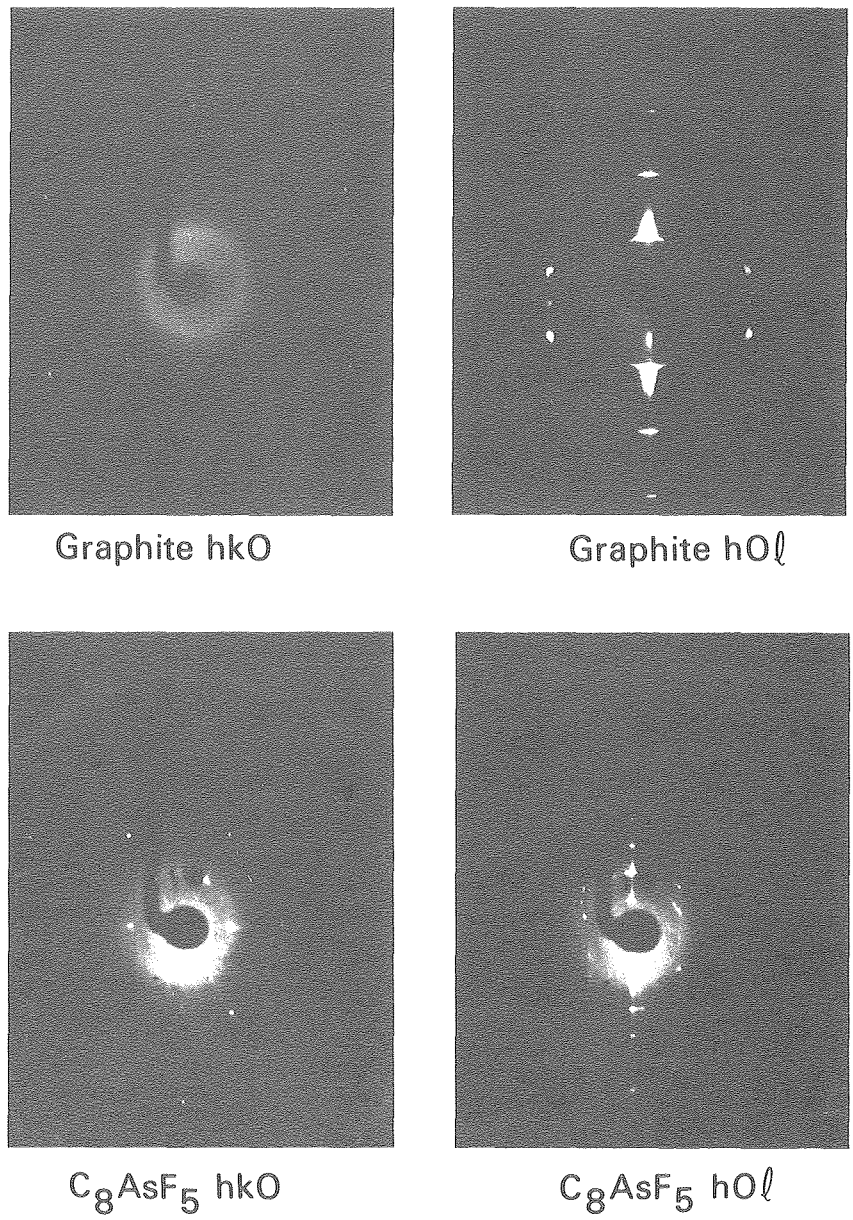

Fig. 1. Single-crystal x-ray precision photographs of graphite and first-stage graphite-AsF_5 intercalate. (XBB 782-2045)

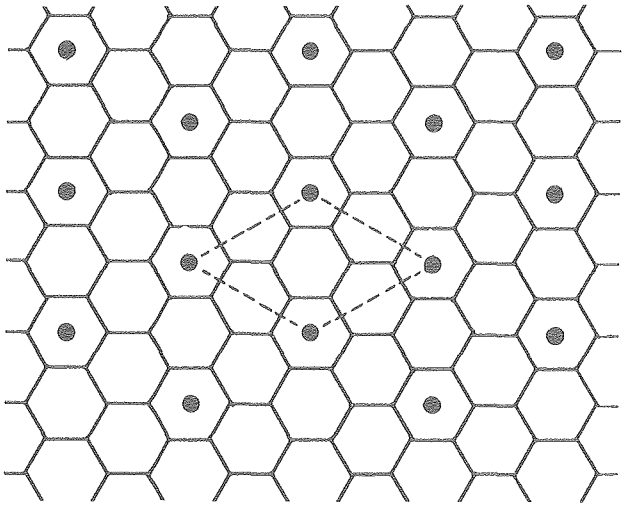

Fig. 2. A probable $C_8^+MF_6^-$ salt unit cell. ● represents center of MF_6^- location. (XBL 782-7236)

AsF_5 must oxidize the graphite according to the equation:

$$3\ AsF_5 + 2\ e^- \longrightarrow 2\ AsF_6^- + AsF_3.$$

The spectra are shown in Fig. 3. Note that the pre-absorption edge feature, in $C_{10}AsF_5$, attributable to As(III) has half the intensity of the feature attributable to AsF_6^-.

b. Metal Hexafluoride Intercalations

The electron affinities of the hexafluorides of osmium, iridium and platinum are estimated to be:

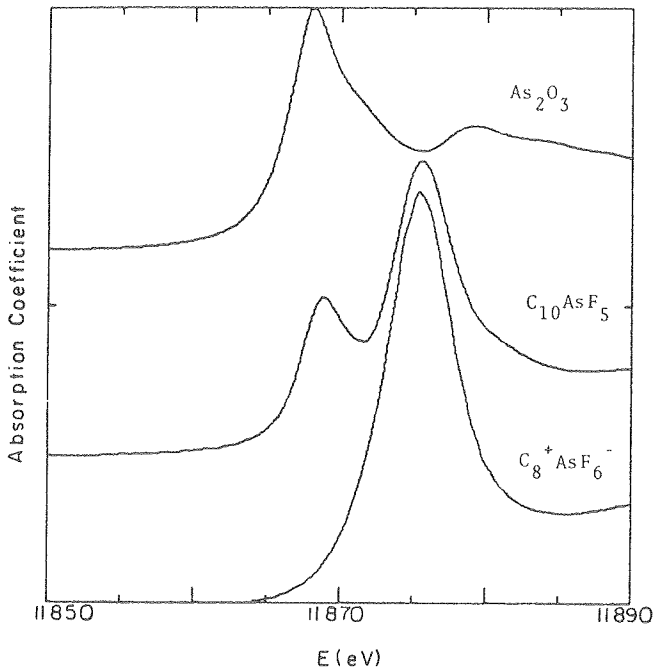

Fig. 3. X-ray K-shell absorption-edge spectra of $C_8^+AsF_6^-$, $C_{10}AsF_5$ and As_2O_3. (XBL 7710-6305)

OsF_6, 165; IrF_6, 190 and PtF_6, 215 kcal/mole^{-1}, these being based, for the last value on calorimetry and a lattice energy estimate for $O_2^+PtF_6^-$ and, for the others, on interpolation between the PtF_6 value and the more certain value for $E(WF_6) = 104$ kcal/mole^{-1} from the work of Cooper et al.[5] Although these values may be subject to considerable error, the known chemistry leaves no doubt about the trend and about the outstanding oxidizer capability of the PtF_6.

Graphite intercalates each of OsF_6 and IrF_6 at room temperature to form first stage materials (blue) of composition C_8MF_6. Both are stable under vacuum to at least 250°. At ~500° C_8IrF_6 ignites spontaneously: $C_8IrF_6 \rightarrow (CF)_n + Ir_{(m)} + CF_4 + C_2F_6$, etc.

Single crystal work has shown that C_8OsF_6 can be made in a highly ordered state and the unit cell is very like that given for C_8AsF_6. Again the symmetry appears to be hexagonal with $a_o = 4.92$ Å and $c_o = 8.1$ Å. It is not possible at this time to rule out a simple multiple of the given c_o value but no superlattice features have yet been discerned. So far, no single crystal data have been obtained for the iridium and platinum cases and attempts to produce them by introducing the vapors into single crystals of graphite have resulted in complete loss of ab plane order.

The magnetic data for the osmium and iridium salts have been obtained and show that the metals are quinquevalent. Thus C_8OsF_6 magnetic susceptibility obeys a Curie-Weiss relationship and has a magnetic moment similar to that of the simple cubic salt $SF_3^+OsF_6^-$. Similarly, C_8IrF_6 shows a temperature independent paramagnetism ($\chi_M \approx 7.5 \times 10^{-4}$ c.g.s units above 17 K) akin to that of the $A^+IrF_6^-$ (A = K, Cs, NO) salts.

These magnetic results, combined with the x-ray diffraction findings are fully in accord with the formulation $C_8^+MF_6^-$ for the Os and Ir cases. Magnetic results for C_xPtF_6 are not yet available and are of interest because the remarkable oxidizing capability of PtF_6 even allows for the possibility of there being some PtF_6^{2-} present. As we have seen, all gallery space in the C_8MF_6 compounds has been used up, hence a doubly negative anion would allow greater electron withdrawal from the graphite than any system hitherto.

Conclusion. In C_8MF_6 (M = As, Os, Ir) the structural and magnetic data confirm the salt formulation $C_8^+MF_6^-$ and combined with x-ray K-shell absorption-edge spectra show that the first stage graphite/AsF_5 intercalate is also a salt with 2/3 of the arsenic present as AsF_6^-. Thus any interpretation of the physical properties of these salts (particularly the very high electrical ab plane conductivities of C_xAsF_5) must recognize the substantial electron withdrawal from the π electron system of the carbon network.

---

1. E. R. Falardeau, G. M. T. Foley, C. Zeller and F. L. Vogel, J. C. S. Chem. Communs., 389 (1977).
2. J. E. Fisher, Electronic Properties of Graphite Intercalation Compounds, Physics and Chemistry of Materials with Layered Structures, F. Levy, D. Reidel, Eds., Dordrecht Holland 1977, Vol. 5 (in press). L. B. Ebert and H. Selig in Abstracts Franco-American Conference on Intercalation Compounds of Graphite, May 23-27, La Napoule, France.
3. N. Bartlett, R. N. Biagioni, B. W. McQuillan, A. S. Robertson and A. C. Thompson, submitted to J. C. S. Chem. Communs. (1977).
4. J. Binenboym, H. Selig, S. Sarig, J. Inorg. Nucl. Chem. 38, 2313 (1976).
5. C. D. Cooper, R. N. Compton and P. W. Reinhardt, Abstracts of Papers for the IXth International Conference on the Physics of Electronic and Atomic Collisions, J. S. Risley, and R. Geballe, Eds., Vol. 2, p. 922, Seattle, Wash., 24-30 July (1975).

2. SALTS DERIVED FROM $C_5F_5N^+$ AND OTHER AROMATICS

Francis Tanzella, T. J. Richardson and Neil Bartlett

The salts $C_5F_5N^+AsF_6^-$ and $C_5F_5N^+Sb_2F_{11}^-$ have been prepared from SO_2ClF solutions of C_5F_5N interacting with the appropriate O_2^+ salt at -45°:

$$C_5F_5N + O_2AsF_6 \longrightarrow C_5F_5N^+AsF_6^- + O_2\uparrow.$$

$$C_5F_5N + O_2Sb_2F_{11} \longrightarrow C_5F_5N^+Sb_2F_{11}^- + O_2\uparrow$$

The salts are blue and are thermally unstable above -22°. They are paramagnetic and the solids give broad intense ESR signals centered at g = 2.0032. As yet we have no knowledge of the temperature dependence

of the magnetic susceptibility. Thermal decomposition takes the course:

$$2\ C_5F_5N^+AsF_6^- \longrightarrow C_5F_5N{\cdot}AsF_5 + C_5F_7N{\cdot}AsF_5$$

The AsF_5 adducts are colorless and the C_5F_7N adduct is extensively dissociated at room temperature. A ^{19}F NMR spectrum of C_5F_7N shows that the only C_5F_7N isomer obtained is perfluoro-1-azacyclo-hexa-1,3-diene (A). This pyrolysis probably involves fluoride ion transfer to the cation to generate the $C_5F_6N^{\cdot}$ radical:

and this radical probably interacts with another cation:

$$C_5F_6N + C_5F_5N^+AsF_6^- \longrightarrow C_5F_6N^+AsF_6^- + C_5F_5N$$

and the new salt in time undergoes F^- transfer from anion to cation:

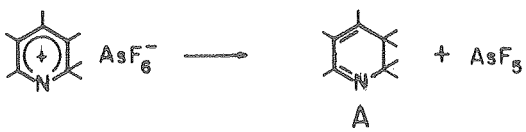

The reaction is remarkedly specific in products and, if our mechanism is correct, points to the carbon atom adjacent to the N atom as being the most positive carbon in $C_5F_5N^+$ and the carbon adjacent to the CF_2 group as the most positive in the $C_5F_6N^+$ cation.

A similar oxidation of perfluorotoluene by O_2^+ yields yellow-green $CF_3C_6F_5^+$ salts:

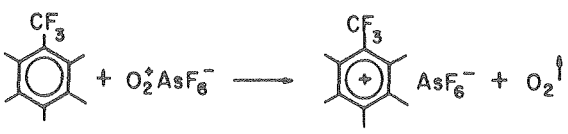

This salt also decomposes rapidly at room temperature:

$$2\ CF_3C_6F_5^+AsF_6^- \longrightarrow CF_3C_6F_5 + CF_3C_6F_7 + 2\,AsF_5.$$

The initial $CF_3C_6F_7$ isomer is the 1.3 diene (B). This slowly isomerizes (in C_6F_6 as solvent to yield a roughly equivalent amount of the 1,4 diene (C):

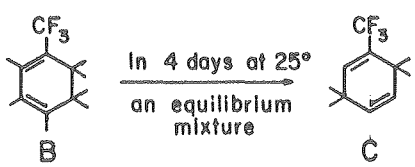

It seems probable that if the $C_5F_5N^+$ or the $CF_3C_6F_5^+$ salt were attacked by other anions the products would be analogous, but there is the possibility of stabilizing radicals such as $C_5F_5NX^{\cdot}$ and $CF_3C_6F_5X^{\cdot}$ if X^- is SO_3F^- or NO_2^- and if the reaction occurs in a flow system such that the radical has no opportunity to interact with unconsumed cation.

The magnetic susceptibility of solid $C_{10}F_8^+AsF_6^-$ shows a Curie-Weiss temperature dependence, but the Weiss constant is small (~ 4°) hence it is clear that there are no significant interactions between the cations in the solid. This is what was anticipated on the basis of the structural evidence.[1]

Attempts to prepare salts derived from large ring systems such as coronene, (where overlap of the cationic ring systems is anticipated to occur) has been hampered by the lack of solvents that are compatible with the strong oxidizers necessary to make the cations.

---

1. T. J. Richardson, (Ph.D. thesis), U. C. Berkeley, LBL-3183 (1974).

3. OXIDATION OF CHLORINE BY METAL HEXAFLUORIDES

Lionell Graham and Neil Bartlett

Tensimetry and gravimetry (Table 1) show that IrF_6 interacts, at ~20°, with chlorine to give a yellow solid of approximate composition Cl_2IrF_6.

The established oxidizing capability of iridium hexafluoride is such that one anticipates[1] that it could oxidize Cl_2 to form $Cl_2^+IrF_6^-$. We have, however, not been able to confirm this salt formulation. Raman and infrared spectra of the solid deposited, from reaction in the gas phase, on a silver chloride window held at ~12 K, show unmistakable evidence for the formation of $Cl_3^+IrF_6^-$. Raman spectra, at ~ -70°, of freshly precipated adduct, prepared at ~ 25°, also showed bands attributable to $Cl_3^+IrF_6^-$. The Cl_3^+ features correspond closely to those previously reported[2] for the salt $Cl_3^+AsF_6^-$ and the characteristic ν_1, ν_2 and ν_5 modes of IrF_6^- are also evident (Fig.1).

Since earlier work had established that the interaction of Cl_2 with IrF_6 was an excellent route to the then novel pentafluoride of iridium,[3] we were concerned to know what the intermediate steps were. We have found that the adduct slowly yields chlorine and another gaseous product, (X), which is characterized by an infrared absorption at 625 cm^{-1}. The product, X, is not Cl-F nor is it any other known chlorine fluoride.

The initial yellow product, which the vibrational data indicate is Cl_3IrF_6, falls in 48 hrs at ~ 25° to a new, deeper yellow, solid that gives a Raman spectrum indicative of $Cl_3^+Ir_2F_{11}^-$ (see Fig. 1). In approximately one week at ~ 25°, the material becomes a viscous liquid and in two or three weeks finally produces a crystalline solid that is iridium pentafluoride. The decomposition sequence is therefore:

$$2\ Cl_3IrF_6 \longrightarrow Cl_3Ir_2F_{11}^- + [Cl_3F]$$

$$2\ Cl_3Ir_2F_{11}^- \longrightarrow Ir_4F_{20} + 2\,[Cl_3F].$$

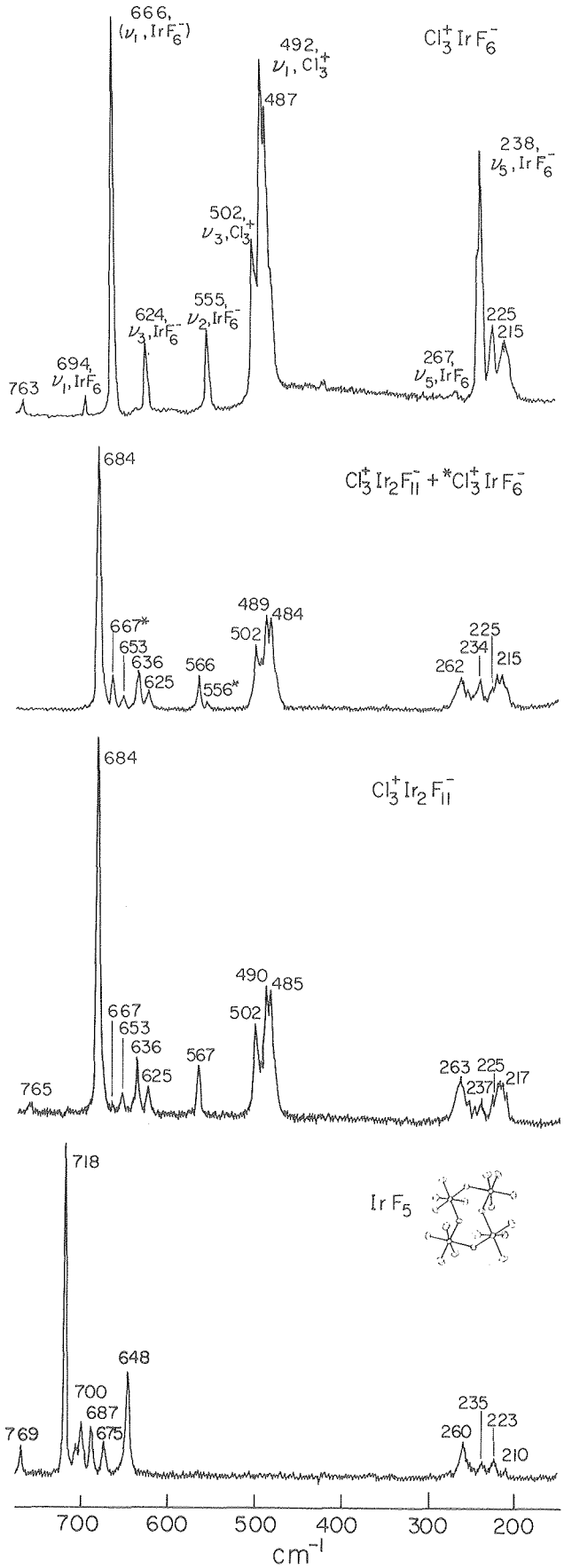

Fig. 1. Raman spectra of Cl_3IrF_6, $Cl_3Ir_2F_{11}$ and Ir_4F_{20}. (XBL 7711-6378)

Table 1. Tensimetric and gravimetric data for the Cl_2 + IrF_6 reaction.

Expt.	Pressure (mm Hg) measured in a fixed volume		
	Initial IrF_6	Initial Cl_2	Residual
1	77	186	131 (Cl_2)
2	33	99	67 (Cl_2)
3	73	66	11 (Cl_2)
4	123	125	∿ 0
5	165	320	120 (Cl_2)
6	114	517	380 (Cl_2)
	IrF_6	Cl_2/IrF_6 adduct	Combined Cl_2
	0.275 g	0.339 g	0.064 g
	0.898 mmoles	----	0.903 mmoles

It is possible that the gaseous species (X) referred to earlier is Cl_3F. This is not a known species and indeed one anticipates that it would be unstable with respect to Cl_2 and Cl-F. It is easy to visualize the formation of such a molecule by F^- abstraction from the anion by the strongly attracting Cl_3^+ ion:

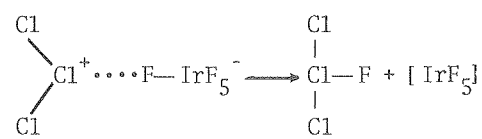

(the [IrF_5] monomer would F-bridge with an adjacent IrF_6^- to yield $Ir_2F_{11}^-$). The gas-phase species X has a half-life of minutes only, at room temperature, and only very small quantities have been available hitherto. It merits further physical and chemical investigation.

The Cl_3^+ salts are powerful oxidizers, e.g., they oxidize C_6F_6 to yield $C_6F_6^+$ salts:

$$Cl_3^+ + C_6F_6 \longrightarrow C_6F_6^+ + \frac{3}{2}\,Cl_2.$$

1. N. Bartlett, Angew. Chem. Int. Ed. 7, 433 (1968).
2. R. J. Gillespie and M. J. Morton, Inorg. Chem. 9, 811 (1970).
3. N. Bartlett and P. R. Rao, Chem. Commun., 252 (1965).

4. RESEARCH PLANS FOR CALENDAR YEAR 1978

Neil Bartlett

Synthesis of Highly Ordered Graphite Salts and Correlation of their Physical Behavior with Structural Features. The strong oxidizers such as O_2^+ salts, SO_3F radical, xeonon compounds such as $Xe(OTeF_5)_2$, and the transition metal hexafluorides, provide opportunities for the synthesis of graphic intercalates in which simple, highly symmetrical stable anions are incorporated in the galleries. Moreover by slow controlled intercalation of single crystals there is reason to believe that reliable (as distinct from the present "guesswork") structures for the important salts can be achieved.

A major aim is to solve the structure of a first stage compound such as C_8MF_6 (M either As or Ir). Low temperature (<< 3 K) heat capacity studies in collaboration with Professor N. Phillips' group and electrical conductivity studies in collaboration with Dr. T. Thompson at SRI will be undertaken simultaneously. These studies should provide the proper basis for an understanding of the electrical conductivity behavior. X-ray absorption fine structure studies will, hopefully, provide structural information to complement that from diffraction studies.

It also is our intention to study mixed intercalate systems. We will begin by preparing the second stage AsF_6^- salt (which we have already characterized in our single crystal studies) and will complete the intercalation by adding IrF_6:

$$C_{16}AsF_6 + IrF_6 \longrightarrow C_{16}AsF_6IrF_6.$$

These preparations will be carried out using single crystals and it should therefore be a straightforward matter to determine if the system is one of alternating AsF_6^- and IrF_6^- gallery occupancy or not. If all galleries are equivalently occupied, as is expected, there is still the possibiblity of there being order within the galleries. Because of the considerable difference in the x-ray scattering factors as As and Ir, any ordering should be readily detected. Again, the correlation of the physical behavior with the detailed structural features ought to provide great insight into these materials.

Electrochemical Evaluation of Graphic Salts. Mixed anion protonic acid salts will also be examined. A particularly interesting system is one first described by Ubbelohde:[1] $C_{24}^+ 2\ HSO_3F\ SO_3F^-$. This can be approximately described as C_8X where X is SO_3F^- or HSO_3F. The relationship to $C_{12}SO_3F$, prepared recently in these laboratories, is an exciting one since it suggests that the $C_{12}SO_3F$ stoichiometry is limited by the capability of the SO_3F oxidizer to withdraw electrons from the graphite. If so it will prove possible to incorporate neutral HSO_3F into the $C_{12}SO_3F$ material:

$$2\ C_{12}SO_3F + HSO_3F \longrightarrow C_{24}^{2+}(SO_3F^-)_2HSO_3F.$$

This material is then simply related to $C_{24}^+SO_3F^-$. 2 HSO_3F by an electron and proton transfer:

$$C_{24}^{2+}(SO_3F^-)_2HSO_3F + H^+ + e^- \longrightarrow C_{24}^+SO_3F^-,\ 2\ HSO_3F.$$

The similarity in size of HSO_3F and SO_3F^- will ensure that the gallery height will not change much with the oxidation and reduction cycle. Conceivably this cycle could operate in fluorosulfonic acid.

The excellent electrical conducting properties of the "salts" make them particularly attractive as electrodes.

---

1. A. R. Ubbelohde, Nature 210, 5034 (1966).

5. 1977 PUBLICATIONS AND REPORTS

Neil Bartlett and Associates

LBL Reports

1. N. Bartlett, Radon, LBL-6696, submitted to Encyclopedia della Chimica.

2. A. Zalkin, D. L. Ward, R. N. Biagioni, D. H. Templeton and N. Bartlett, The Crystal Structure of $(XeF^+)(AsF_6^-)$, LBL-6671, submitted to Inorganic Chemistry.

3. N. Bartlett, R. N. Biagioni, B. W. McQuillan, A. C. Thompson, Novel Salts of Graphite and a Boron Nitride Salt, LBL-6948, submitted to J.C.S. Chem. Communs.

4. C. J. Adams and N. Bartlett, Tautomerism in Xenon Haxafluoride: An Investigation of Xenon Hexafluoride and Its Complexes by Raman Spectroscopy, LBL-3136, invited paper for the issue of Israel Journal of Chemistry entitled "Perspective in Fluorine Chemistry."

Invited Lectures

1. A lecture entitled "From O_2^+ Salts to Synthetic Metals" was presented under the auspices of Gesellschaft Deutscher Chemiker at the following institutions:

Universities: Dortmund, May 2
Giessen, May 8
Frankfurt, May 10
Saarland, June 10

(Technical U.) Munich, June 12
Gottingen, June 16

Max Planck Institute, Stuttgart, May 16
Philips Gmbh Foschungslaboratorium, Aachen, May 4

2. A lecture entitled "Noble-Gas Chemistry" was delivered under the same auspices at the following universities:

Gottingen, May 12
Frankfurt, May 18

3. A lecture on "synthetic Metals" was given at IBM Research Laboratories, San Jose, Jan. 16

4. A talk entitled "Noble-Gas Chemistry - What if Anything Has It Taught Us" was presented as a dedication lecture to celebrate the new chemistry building at Loyola University, Chicago, March 18.

5. An invited lecture entitled "Salts of Novel Cations" at The Gordon Conference on Inorganic Chemistry Aug. 1-5.

6. The Henry Werner Lectures: "Noble-Gas Chemistry" and "From O_2^+ Salts to Synthetic Metals," University of Kansas, Oct. 24, 25.

III.

Nuclear Sciences

A. LOW ENERGY NUCLEAR SCIENCE

1. HEAVY ELEMENT RESEARCH

a. Actinide and Lanthanide Chemistry

Norman M. Edelstein, Richard A. Anderson, Neil Bartlett, John G. Conway, Kenneth Raymond, Glenn T. Seaborg, Andrew Streitwieser, Jr., David H. Templeton and Allan Zalkin, Principal Investigators

1. HIGHLY SELECTIVE SEQUESTERING AGENTS FOR PLUTONIUM AND OTHER ACTINIDES IN THE 4+ OXIDATION STATE

a. The Preparation of the Multichelate Catechols N,N',N'',N'''-Tetra(2,3-dihydroxybenzoyl)-tetraaza-cyclotetra- and hexadecanes.

Frederick L. Weitl and Kenneth N. Raymond

In response to the biological hazards associated with the nuclear fuel cycle and nuclear research sites, we have developed and are investigating a biomimetic design concept of sequestering agents for eight-coordinate actinide ions in general, and Pu (IV) in particular. Plutonium is a potent carcinogen[1] since once absorbed by body tissues, it exhibits long-term retention in mammals. This is known for humans[2] as well as test animals such as dogs.[3] Although plutonium commonly exists in aqueous solution in each of the oxidation states from III to VI, biological evidence indicates that most, if not all, exists in vivo as Pu(IV), where it is complexed by available bioorganic ligands.[4]

There are many similarities of Pu(IV) and Fe(III). These range from the similar charge/ionic-radius ratio for Fe(III), and Pu(IV) (4.6 and 4.2 e/Å, respectively) to their similar transport properties in mammals, where it is known that Pu(IV) is bound by the iron transport protein transferrin at the site that normally binds Fe(III).[4] Thus the design of Pu(IV) sequestering agents that are similar to naturally-occurring Fe(III) sequestering agents suggests itself as a biomimetic approach. Since the 2,3-dihydroxybenzoyl group (DHB) is a component of several siderophores and in particular is found in enterobactin [cyclotris(2,3-dihydroxybenzoyl)-N-ℓ-serine], a powerful iron transport and sequestering agent of enteric bacteria,[5] we anticipate that the macrocyclic tetra(DHB) conjugates of cyclam-14 (*6* in Fig. 1) and cyclam-16 (*7* in Fig. 1) are potentially selective Pu(IV) sequestering agents. Molecular models show that *6* and *7* readily form octadentate complexes of Pu(IV) in which the central metal ion is completely encapsulated by the ligand.

Our synthetic strategy has been to develop a generally applicable procedure for the preparation of DHB amides. To ensure tetra-substitution of *1* and *2*, we chose to react the 2,3-dioxomethylene benzoyl chloride (4 equivalents) with *1* and *2* at 95 to 105° C in N,N-dimethyacetamide in the presence of pyridine (4 equivalents). After 24 to 48 h reaction times, thin layer chromotography (TLC) showed only one product, the tetraamide (*3* or *5*). The 2,3-dimethoxybenzoyl chloride condensed equally well to give *4* (Fig. 1 and Table 1). Analytically pure products were obtained by column chromatography on silica gel. Previously it has been shown that the dioxomethylene acetal moiety can be removed selectively with BCl_3, and more readily than the corresponding demethylation. This is consistent with our results that show quantitative removal of the $-CH_2-$ group in *3* and *5* using BCl_3/CH_2Cl_2, but incomplete removal of the CH_3- groups in *4* with the same procedure. However, complete demethylation of *4* was accomplished with BBr_3/CH_2Cl_2. Model macrocyclic sequestering agent *6* (mp 287° dec.) was unchanged

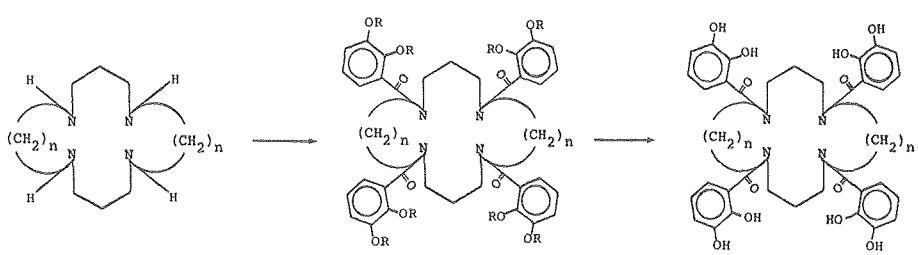

1 n = 2
2 n = 3

3 n = 2, R = $-CH_2-$
4 n = 2, R = CH_3
5 n = 3, R = $-CH_2-$

6 n = 2
7 n = 3

Fig. 1. Synthetic scheme and formulas of the title compounds.

(XBL 7712-10951)

Table 1. Title compounds and precursors.

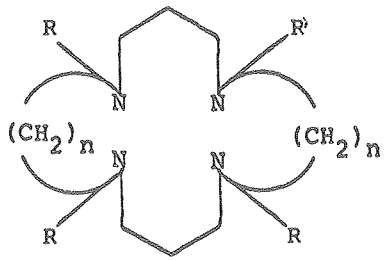

No.	n	R	mp, °C	Solvent of isolation	% Yield
1	2	H	182-3[a]	C_6H_5Cl	
3	2	2,3-dioxomethylenebenzoyl	236-8	$CHCl_3$	92
4	2	2,3-dimethoxybenzoyl	110-15	$MeOH/Et_2O$	87
6	2	2,3-dihydroxybenzoyl	287d.	$MeOH;H_2O$[b]	100
2	3	H	83-4[c]		
5	3	2,3-dioxomethylenebenzoyl	178-80	CH_2Cl_2	63
7	3	2,3-dihydroxybenzoyl	175-85	$MeOH;H_2O$[b]	100

[a]Lit. mp 184-5°; purified by sublimation.

[b]See Experimental; the reaction mixture is treated with both MeOH and H_2O resulting in hydrated products.

[c]Lit. mp 83-4°; purified by sublimation.

after base (pH 12) dissolution and acid (pH 1) precipitation at room temperature and was unaffected in pH 1 aqueous solutions (1 mg/ml) after 20h at room temperature. Neither *6* nor *7* exhibits its molecular ion in the low voltage mass spectrum: *6* does not sublime at 200°C at 10^{-7}mm Hg. After several weeks of room exposure *6* and *7* appear stable, indicating considerable resistance to air oxidation.

1. A. Catsch, Radioactive Metal Mobilization in Medicine, Thomas, Springfield, Illinois, 1964.
2. B. J. Stoves, D. R. Atherton and D. S. Buster, Health Phys. 20, 369 (1971).
3. H. Foreman, W. Moss and W. Langham, Health Phys. 2, 326 (1960).
4. P. W. Durbin, Health Phys. 29, 495 (1975), and references therein.
5. J. B. Neilands, Ed., Microbial Iron Metabolism, Academic Press, New York, N. Y., 1974.

b. A Status Report on the Biological Evaluation of New Plutonium Chelating Agents

Patricia W. Durbin, Frederick L. Weitl and Kenneth N. Raymond

Initially, biological evaluation of plutonium sequestering agents has been limted to two compounds: $(DHB)_4$-cyclam-16 (A – compound *7* in part a, above) and $(4\text{-}NO_2\text{-}DHB)_4$-cyclam-14 (B), on the basis of sufficient water solubility at or near pH 7. The data appearing in Table 2 were generated as follows: The control and test groups of 5 to 10,1.5-yr-old female Swiss-Webster mice (weight 25 g) were first injected with $^{238}Pu(IV)$ citrate (i.m.), then test groups were additionally injected (i.p.), 1 h or 48 h later, with 30-32 μM/kg of plutonium sequestering agent. (This dose is close to the optimal DTPA dose in animals.) The compound A test and control groups were sacrificed four days after compound administration, dissected, and organ distribution data were recorded as radioactivity levels. Compound A exhibited no acute toxicity (up to 15 days) and after six daily injections: grossly and microscopically both kidneys and livers appeared normal. The compound B test and control groups were sacrificed one day after ^{238}Pu and compound injections to obtain organ distribution data. Repeated compound B injections were fatal after three to four days and extensive liver damage was noted. In this manner, preliminary in vivo evaluation has revealed that even 1 h after intramuscular injection of $^{238}Pu(IV)$ citrate, intraperitoneal injection of compound A resulted in some $^{238}Pu(IV)$ being sequestered and deposited in the kidneys of the mice with some being eliminated in the urine (39% and 7% more than in the control group, respectively). A corresponding reduction

Table 2. Percent absorbed $^{238}Pu(IV)$ citrate.

Organ	$(DHB)_4$-Cyclam-16[a]			$(4\text{-}NO_2\text{-}DHB)_4$-Cyclam-14[a]		
	Control	Test	C-T	Control	Test	C-T
Liver	40	23	-17	38	37	-
Bone	44	20	-24	36	8	-28
Soft tissue	-	-	-	13	26	+13
Viscera	0.6	0.7	-	10	16	+ 6
G.I. tract	6.8	3.7	- 3	-	-	-
Kidneys	3.4	42	+39	1.3	6	+ 5
Urine	4.9	11.5	+ 7	0.9	1.8	+ 1
Feces	-	-	-	0.9	5.4	+ 4

[a]Compounds injected i.p. 1 hour after ^{238}Pu.

in the liver- and bone-bound ^{238}Pu (17% and 24% less than in the control group, respectively) is also notable. The total amount of ^{238}Pu deposited in the kidneys and urine of the group may be nearly equal to the total $^{238}Pu(IV)$ in the circulating blood of the animals at the time of i.p. injection of compound A. Since a larger fraction of intravenously (compared with intramuscularly) injected ^{239}Pu is present in the circulation during the first few hours, it is likely that injection of compound A one hour after ^{238}Pu (i.v.) would have resulted in even greater shunting of ^{238}Pu to the kidneys and urine with correspondingly lower amounts in liver and bone.

If the interval between injection of ^{238}Pu and compound A was extended to 48 h (when $\leqslant$ 2% of the ^{238}Pu is expected to be in the blood), the fraction of ^{238}Pu chelated (^{238}Pu in urine and kidneys in excess of controls) was only 10%, compared with 45% chelated at the one-hour interval. These data suggest that only ^{238}Pu in blood and extracellular fluid is available for chelation by this compound.

The insolubility of sequestering agent A at kidney pH < 7 may be responsible for the large amount of ^{238}Pu deposited in the kidneys. (It is pertinent that pK_{a1} 8.9 and pK_{a2} 13.1 correspond to the acidities of the ionizable constitutent catechoyl groups in A.)

It is currently anticipated that barring any increased toxicity, compound A bearing covalently bound $-SO_3Na$ groups will be a superior chelating agent due to its greatly increased water solubility at all pH's, and enhanced acidity of the constituent catechoyl groups. In fact, direct sulfonation of compound A has been accomplished resulting in water solubility on the order of 1 g/ml. The key question to be answered is whether the sulfonated compound will carry the ^{238}Pu through the kidneys into the urine and eliminate it entirely from the body.

Chelating agent B (pK_{a1} 5.6, pK_{a2} 11.8) is two to three times more soluble than A at pH near 7, but greatly increased toxicity and decreased lyophilicity due to the presence of the covalently bound $-NO_2$ groups rule it out as a potential drug. However direct chemical modification of the $-NO_2$ groups in B may hold some promise.

c. The High-Yield Syntheses and Crystal Structure of 1,5,9,13-Tetraazacyclohexadecane

William L. Smith, James D. Ekstrand and Kenneth N. Raymond

In the course of the design and synthesis of sequestering agents selective for the actinides, the tetraazacycloalkanes have been selected as "backbones" for the proposed ligands. The four nitrogens of these macrocyclic rings provide convenient sites for the attachment of bidentate groups that bind strongly to actinides. The size of the cavity thus formed is predicted to be the optimum size and geometry for the selective encapsulation of Pu(IV) and other tetravalent actinide ions. In order to gain insight into the conformation and geometry of the proposed sequestering agents the structure of 1,5,9,13-tetraazachclohexadecane, (designated as 2 in Table 1 of part (a) or by the trivial name 16-cyclam) has been determined, and a convenient high yield synthesis has been developed. The structure of 2 is also of interest in that it may be considered as a prototype for porphyrin, and other tetraazamacrocycles, about which there is much current interest and activity.

Compound 2 was synthesized as follows:

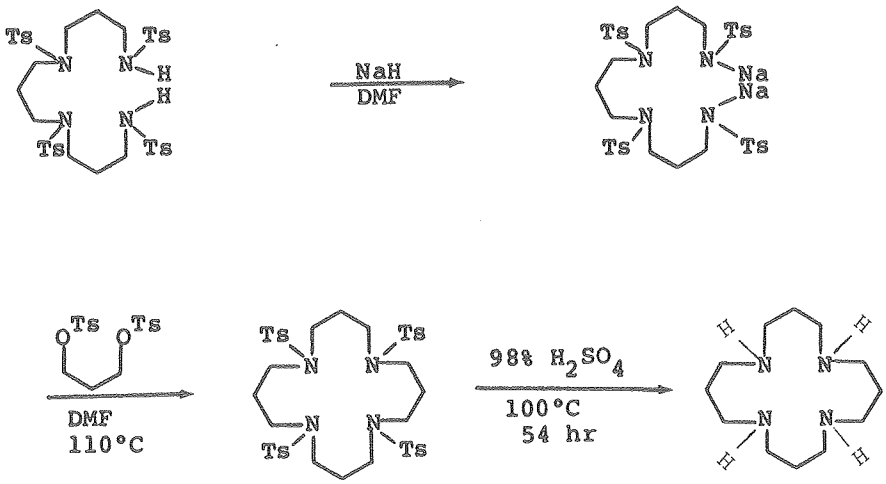

This method produced 16-cyclam in about 60% yield on both a 0.1 mole and a 0.2 mole scale.

The crystal structure of *2* was determined from x-ray diffraction data collected by counter methods. The overall symmetry of the molecule, excluding the nitrogen hydrogen atoms is D_{2d} (Figs. 2 and 3). That the amine hydrogens on adjacent nitrogens are *trans* lowers the molecular symmetry to S_4, which is obeyed within experimental error. The four nitrogens form a square with an average edge length of 2.925(4) Å. The trimethylene groups are in chair configurations with adjacent groups folding toward opposite sides of the nitrogen plane. Refinement of F^2 using all 1866 measured independent reflections by full-matrix least squares led to an R-factor of 6.6%. Unit cell dimensions in the space group $P2_1/n$ are: a= 21.764(6), b = 12.201(6), c = 9.579(4) Å, β = 108.13(3)°, and the calculated density is 1.07 g cm^{-3} for z = 4.

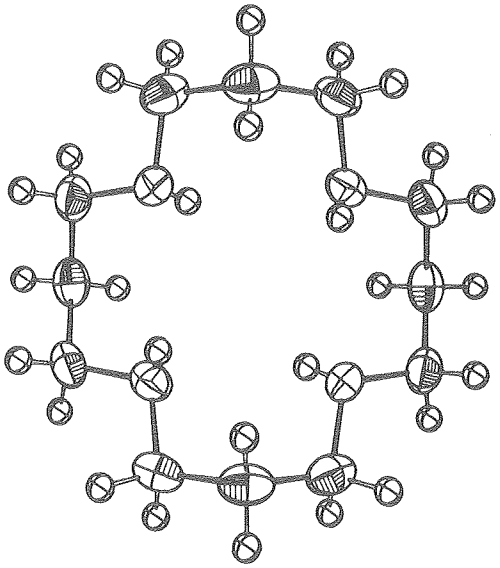

Fig. 2. View of 16-cyclam down the S_4 axis showing thermal ellipsoids for nonhydrogen atoms at the 40% probability level. The shaded ellipsoids are carbon atoms. (XBL 778-2669)

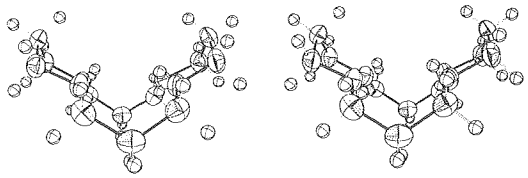

Fig. 3. Stereopair of 16-cyclam viewed perpendicular to the S_4 axis. The thermal ellipsoids are drawn at the 40% probability level for the nonhydrogen atoms. The shaded ellipsoids are carbon atoms. (XBL 778-2675)

There is no evidence for intermolecular hydrogen bonding in *2*. The symmetry of *2* divides the intramolecular nonbonded N-H interactions into two classes. The strongest interactions, with an average N•••H-N distance of 2.26(3) Å and an angle of 123.(2)° show the possibility of weak intramolecular hydrogen bonds. The other class is unimportant. Thus, the hydrogen bonds occur in pairs which, in addition to the stability of the chair configuration of the trimethylene chain, hold the nitrogens in the square planar arrangment.

d. Formation Constants of Specific Sequestering Agents for Plutonium

Alex Avdeef, Tom Bregante and Kenneth N. Raymond

Unless treatment follows immediately after an accidental incorporation of plutonium into the body, the radioactive metal becomes highly resistant to removal by chemical means.[1] Traditional chemotherapy has involved sequestering agents related to EDTA, such as DTPA. They don't work well, for several reasons: 1) Essential trace metals are

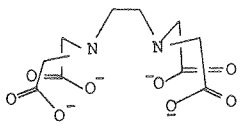

EDTA

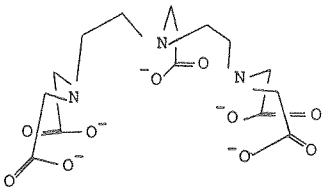

DTPA

removed. 2) The agents can't seem to penetrate cell walls to get better access to plutonium in its long term storage areas (ferritin and hemosiderin deposits in liver cells and the skeleton). 3) The ligands have been designed for metal ions much smaller than the actinides. Thus EDTA can't fully encapsulate Pu^{4+}.

The similarity between Fe^{3+} and Pu^{4+} in terms of biological transport and storage, as discussed in the previous sections, had led us to study catechol complexes with the actinides. Initial phases of the project have included the determination of the formation constants of Fe^{3+}, Th^{4+}, U^{4+}, and Pu^{4+} complexes with a wide variety of simple catechol

complexes. For iron, the equilibrium above has formation constants 10^{40}- 10^{45}. For a biological iron sequestering molecule, such as enterobactin, there is a chelate effect some ten orders of magnitude above the latter values! For Th^{4+} we found that with four catechols, the formation constants are as high

as 10^{42}, as discussed in last year's progress report.

Since then we have examined U^{4+} and Pu^{4+}. The formation constants for U^{4+} are higher than those of Th^{4+}, as expected. The observed titration curves for Pu^{4+} have not yet been interpreted. However, it may be noted that in solutions with pH as high as 12, no precipitates are observed and the solutions are orange in color, suggesting coordination by the simple catechol ligands and a formation constant of at least 10^{56}.

We have also examined the equilibria with Th^{4+} and Pu^{4+} and the synthetic "macro-chelate" DHB-cyclam-16. (See previous sections for details of the synthetic chelates.) One of the serious problems in the experiment has been that the synthetic chelate is very insoluble below pH 7, a region where important metal complexation occurs. A tentative result suggests that the above synthetic ligand does not fully encapsulate the metal. One of the simple catechol ligands, 4-nitrocatechol, has been studies with Th(IV) in some detail. Hydrolysis reactions in this system have been characterized. These hydrolysis reactions make the coordination chemistry of the actinides more complex than for the corresponding iron(III) compounds.

1. P. W. Durbin, Radiobiology of Plutonium, B. J. Stover and W. S. S. Jee, Eds., J. W. Press, Salt Lake City, (1972), pp. 469-530.

2. SYNTHETIC AND STRUCTURAL STUDIES OF ACTINIDE AND OTHER COMPOUNDS

a. Preparation and Properties of the Actinide Borohydrides: $Pa(BH_4)_4$, $Np(BH_4)_4$, and $Pu(BH_4)_4$

R. H. Banks, N. M. Edelstein, R. R. Rietz,* David H. Templeton and Allan Zalkin

Uranium(IV) borohydride, a volatile dark green solid, was first synthesized during the Manhattan Project.[1] Hoekstra and Katz[2] reported the preparation of the much less volatile, but isostructural, $Th(BH_4)_4$ in 1949. Recently uranium borohydride[3,4] and its etherate complexes[5] have again been the subject of structural and spectroscopic investigations. As part of our program on the properties of actinide borohydrides, we report in this communication the syntheses of $Pa(BH_4)_4$, $Np(BH_4)_4$, and $Pu(BH_4)_4$, the remaining borohydride complexes of the first five elements of the actinide series, and some of their physical properties.[6]

All five actinide compounds, $An(BH_4)_4$, are made by the solvent-free reaction of the anhydrous tetrafluoride with $Al(BH_4)_3$, viz.

$$AnF_4 + 2Al(BH_4)_3 \rightarrow An(BH_4)_4 + 2AlF_2BH_4.$$

One of the important properties characteristic of the metal borohydrides is their high volatilities, enabling them to be pumped out of the reaction mixture and purified by trap-to-trap sublimation. The vapor pressures increase with higher atomic number of the metal. $Th(BH_4)_4$, which sublimes at 120° in vacuum, exerts a pressure of 0.2 mm Hg at 150°[2] while Np and Pu borohydrides easily sublime at -10°. $Np(BH_4)_4$ has a vapor pressure of 10 mm Hg at 25° making it the most volatile compound of tetravalent Np known to date. $Pu(BH_4)_4$ appears to exhibit a vapor pressure similar to $Np(BH_4)_4$.

The synthesis of $Pa(BH_4)_4$ follows that of $Th(BH_4)_4$ by Hoekstra and Katz,[2] but the reaction tube was modified by the addition of a demountable cold finger from which the $Pa(BH_4)_4$ could be removed in an inert atmosphere dry box. $Pa(BH_4)_4$ is an orange, air sensitive solid sublimable at 55° in vacuum. X-ray powder diffraction photographs have shown that it is isomorphous with the uranium and thorium borohydrides. Its tetragonal unit cell with a = 7.54(3) Å and c = 13.23(5)Å contains four molecules, giving a calculated density of 2.63 g/cm^3.

The method used for making Np and Pu borohydrides differs from that above because their high volatilities require no cold finger and their thermal instabilities demand that the reaction be carried out at a lower temperature and for a shorter time. We have found that carrying out the reaction at 0° for 4 hours works well after which time the $An(BH_4)_4$ and unreacted $Al(BH_4)_3$ are collected in -78° and -196° traps, respectively. Yields were increased by returning the unused $Al(BH_4)_3$ to the reaction tube for another 4-hour period and repeating this procedure several times until no more $An(BH_4)_4$ was obtained. An earlier attempt to make $Np(BH_4)_4$ was reported[7] in which only a green, nonvolatile solid

was obtained in the reaction vessel. This was probably a mixture of NpF_4 and mixed Np fluoroborohydrides due to the presence of either metallic impurities (e.g., NiF_2) and/or improper reaction conditions. Hoekstra and Katz[7] noted a color change in their $PuF_4/Al(BH_4)_3$ reaction vessel from tan to blue-green, the same color change we observe in ours, however, their $Pu(BH_4)_4$, if it did form, must have decomposed before collection, as they obtained no volatile Pu compound.

$Np(BH_4)_4$ is a dark green, pyrophoric liquid that melts at 14.2°. It must be kept in a greaseless storage tube under liquid nitrogen since it decomposes fairly rapidly at 25° transforming into a yellow, nonvolatile solid with the evolution of H_2 and B_2H_6. This observation suggests that $Np(BH_4)_3$ is formed. At higher temperatures a shiny, metallic mirror is obtained that may be Np metal or NpB_4. $Pu(BH_4)_4$ is a bluish-black liquid with properties very similar to $Np(BH_4)_4$ but is even more unstable to thermal decomposition.

Diffraction patterns recorded with a low-temperature x-ray powder camera show that $Pu(BH_4)_4$ and $Np(BH_4)_4$ are isomorphous and have a new tetragonal crystal structure type, with a = 8.59(1)Å, c = 6.1(2) Å at -20° C for the Pu compound and a = 8.54(5)Å, c = 6.1(2)Å at -150° C for the Np compound. The low accuracy of the c dimensions is the result of strong preferred orientation of the crystals and absence from the films of reflections with ℓ values greater than 2. The unit cell contains two metal atoms at 0,0,0 and 1/2,1/2,1/2. No reflections were observed that indicate any deviation from body-centered symmetry. The diffraction data do not define the boron and hydrogen positions.

Each metal atom has two metal atom neighbors at 6.1Å and eight more at 6.8Å. These distances indicate that the solid is monomeric, like $Zr(BH_4)_4$ (Ref. 8) and $Hf(BH_4)_4$,[3b] rather than polymeric with borohydride bridges like those in $U(BH_4)_4$.[3a] The molecular volumes (225, 222, 186, 201, and 211Å,[3] respectively, for the Pu, Np, U, Zr, and Hf compounds) suggest the same conclusion. The metal atom positions in $Pu(BH_4)_4$ are closely related to those in solid $U(BH_4)_4$, but are more symmetrical. The structure can be converted into the $Zr(BH_4)_4$-type structure with little distortion if molecules at 1/2,1/2, 1/2 are moved to 1/2, 1/2,0.

The room temperature gas phase IR spectra of Hf, Np, and Pu borohydrides and of U borohydride at 50° (Fig. 1) were taken on a Perkin-Elmer 283 IR spectrophotometer with the sample contained in a 10 cm cell

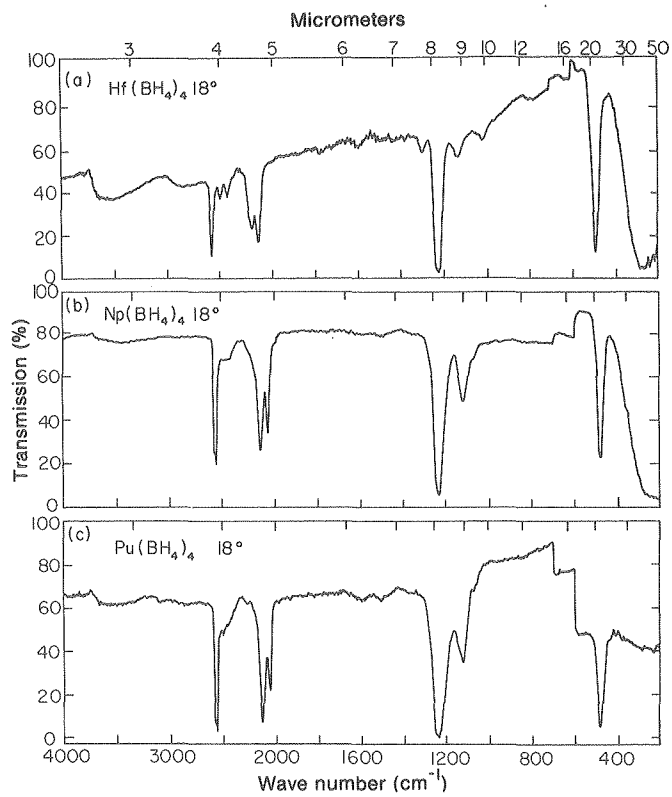

Fig. 1. Gas phase infrared spectra of metal borohydrides. The spectrum of $U(BH_4)_4$ was run at 50° in order to have sufficient vapor pressure. Peaks at 2511, 2345, 1604, and 1175 cm^{-1} were due to B_2H_6, a decomposition product. (XBL 772-397)

fitted with KBr windows. It can be seen that the Np and Pu compounds have similar spectra to $Hf(BH_4)_4$ in which four BH_4^- groups surround the metal in a tetrahedral array each coordinated via 3 hydrogen bridge bonds making the metal 12-coordinate.[9]

Our preliminary Raman spectrum on solid $Np(BH_4)_4$ at -85° is equivalent to that for single crystal $Hf(BH_4)_4$[9a] if one allows for effects due to the heavier Np atom. This reinforces our belief that $Np(BH_4)_4$ is a monomer in the solid state. Since polymeric linkages need not be broken upon vaporizing, $Np(BH_4)_4$ and $Hf(BH_4)_4$ therefore have much higher vapor pressures than $U(BH_4)_4$ which was shown to be a monomer and of the same structure as $HF(BH_4)_4$ in the gaseous state.[9b,10]

A summary of the physical properties of the actinide borohydrides is shown in Table 1.

Table 1. Physical properties of the actinide borohydrides.

COMPOUND	COLOR	STABILITY	M.P.	V.P.(MM)	RADIUS	SOLID	GAS	DENSITY
$Th(BH)_4$	WHITE	STABLE	203 D	.05/130°	.972	TETR	TD?	2.56
$Pa(BH_4)_4$	REDDISH ORANGE	STABLE	D	——	.935	TETR	TD?	2.63
$U(BH_4)_4$	DARK GREEN	V. SLOW DECOMP	D	.3/34°	.918	TETR	TD	2.71
$Np(BH_4)_4$	BLUISH GREEN	DECOMP	14	~10/25°	.903	TETR	TD	2.21
$Pu(BH_4)_4$	BLUISH BLACK	DECOMP	~14	~10/25°	.887	TETR	TD	2.20
$Hf(BH_4)_4$	WHITE	V. SLOW DECOMP	29	15/25°	.79	CUBIC	TD	1.86

Further studies are underway on the spectroscopic, structural, and magnetic properties of these new actinide borohydrides.

---

*Present address: Rockwell International, P. O. Box 250, Richland, WA 99352.

1. H. I. Schlesinger and H. C. Brown, J. Amer. Chem. Soc. 75, 219 (1953).
2. H. R. Hoekstra and J. J. Katz, J. Amer. Chem. Soc. 71, (1949).
3. a) E. R. Berstein, T. A. Keiderling, S. J. Lippand and J. J. Mayerle, J. Amer. Chem. Soc. 94, 2552 (1972). b) E. R. Bernstein, W. C. Hamilton, T. A. Keiderling, S. J. LaPlaca, S. J. Lippard and J. J. Mayerle, Inorg. Chem. 11, 3009 (1972).
4. E. R. Bernstein and T. A. Keiderling, J. Chem. Phys. 59, 2105 (1973).
5. R. R. Rietz, N. M. Edelstein, H. W. Ruben, D. H. Templeton and A. Zalkin, Inorg. Chem. (in press); R. R. Rietz, A. Zalkin, D. H. Templeton, N. M. Edelstein and L. K. Templeton, Inorg. Chem. (in press); A. Zalkin, R. R. Rietz, D. H. Templeton and N. M. Edelstein, Inorg. Chem. (in press).
6. For a recent review of actinide borohydride complexes see T. J. Marks and J. R. Kolb, Chem. Rev. 77, 263 (1977).
7. H. R. Hoekstra and J. J. Katz, Declassified Document, AECD 1894, Oak Ridge, Tennessee; B. D. James and M. G. H. Wallbridge, Prog. Inorg. Chem. 11, 99 (1970).
8. P. H. Bird and M. R. Churchill, Chem. Commun. 403 (1967).
9. a) T. A. Keiderling, W. T. Wozniak, R. S. Gay, D. Jurkowitz, E. R. Bernstein, S. J. Lippard and T. G. Spiro, Inorg. Chem. 14, 576 (1975). b) V. Plato and K. Hedberg, Inorg. Chem. 10, 590 (1971).
10. B. D. James, B. E. Smith and M. G. H. Wallbridge, J. Mol. Struct. 14, 327 (1972).

b. The Preparation and Crystal Structure of Uranium(IV) Borohydride N-Propyletherate

Allan Zalkin, Richard R. Rietz, David H. Templeton and Norman M. Edelstein

In our study of Lewis base adducts of uranium(IV) borohydride, we have discovered a number of volatile etherates. Structural characterization of two of these compounds,[1] $U(BH_4)_4 \cdot O(CH_3)_2$ and $U(BH_4)_4 \cdot O(C_2H_5)_2$, has shown them to be linear polymers in the crystalline state. The complex with tetrahydrofuran is a di-etherate and monomeric in the crystal.[2]

When $U(BH_4)_4$ and di-n-propyl ether were reacted a light green solid was formed that sublimed at room temperature (20°) some 20° lower than the sublimation temperature for the dimethyl or diethyl etherates. This unexpected increase in volatility with increased molecular weight prompted us to examine the crystal and molecular structure of this solid.

On standing in sealed capillaries for a few months the crystals changed to a red color. The structure was determined for this red material by the single crystal x-ray diffraction method. A powder diffraction pattern taken with the fresh green crystals corresponds to the single crystal results in its line positions and qualitative intensities. A similar color change from green to red, without a change of crystal structure, was observed for both the methyl and the ethyl adducts of uranium borohydride when they were exposed to x-rays.[1]

The crystals were shown to be triclinic, space group $P\bar{1}$, with $a = 12.043(10)$ Å, $b = 10.340(8)$ Å, $c = 14.752(13)$ Å, $\alpha = 82.81(5)°$, $\beta = 112.99(5)°$, and $\gamma = 110.76(5)°$, at 22°C. The calculated density is 1.68 g/cm^3.

The molecule structure, shown in Fig. 2, is an unsymmetrical dimer of two formula units in which two uranium atoms are bridged by a borohydride unit. One of the uranium atoms is at the center of an irregular octahedron consisting of two n-propyl ether ligands at the apices and four borohydride groups about the equator; the second uranium atom is associated with five borohydride groups alone. The first uranium atom environment is reminiscent of that found in the $U(BH_4) \cdot 2THF$ structure,[2] but lacks one hydrogen atom neighbor.

The nearest neighbors of uranium are the two oxygen atoms and the hydrogen atoms from the borohydride ions. The bridging borohydride contributes two hydrogen neighbors whereas the terminal ones each contribute three. The interatomic U-B distances of 2.9 Å and 2.5 Å are characteristic of the two types observed in $U(BH_4)_4$.[3] The first uranium atom has 13 nearest neighbors, including the oxygen atoms, and the second uranium atom has 14 neighbors, all hydrogen atoms. Fourteen coordination for uranium has been found in $U(BH_4)_4$,[3] $U(BH_4)_4 \cdot O(CH_3)_2$,[1] $U(BH)_4 \cdot O(C_2H_5)_2$,[1] and $U(BH_4)_4 \cdot 2(OC_4H_8)$,[2] but the thirteen coordination is unique.

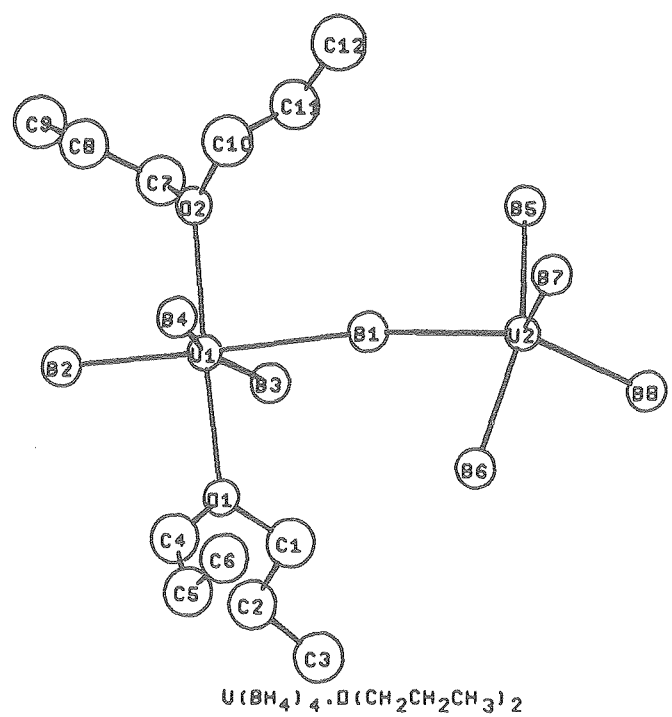

Fig. 2. An ORTEP view of $U(BH_4)_4 \cdot O(n\text{-}C_3H_7)_2$ dimer. (XBL 776-9352)

1. R. R. Rietz, A. Zalkin, D. H. Templeton, N. M. Edelstein and L. K. Templeton, N. M. Edelstein and L. K. Templeton, Inorg. Chem. (in press).
2. R. R. Rietz, N. M. Edelstein, H. Ruben, D. H. Templeton and A. Zalkin, Inorg. Chem. (in press).
3. E. R. Bernstein, W. C. Hamilton, T. A. Keiderling, S. J. Lippard and J. J. Mayerle, Inorg. Chem. 11, 3009 (1972).

c. Structure of Uranyl Nitrate Di-Tetrahydrofuran

John G. Reynolds, Allan Zalkin and David H. Templeton

Uranyl nitrate is soluble in a variety of organic solvents and forms various crystalline phases with them.[1,2] Extraction into ether was the classical method of purification of this salt, and today extraction with various nonaqueous solvents remains an important industrial technique. To extend our knowledge of the molecular basis for this solubility, we prepared the tetrahydrofuran complex, $UO_2(NO_3)_2 \cdot 2(C_4H_8O)$, and determined its crystal structure. Feder, Ross and Vogel[2] have reported a 1:1 addition compound of $UO_2(NO_3)_2$ with tetrahydrofuran.

Uranyl nitrate was extracted from an aqueous solusion with THF. The THF layer was dried and slowly evaporated to produce crystals of uranyl nitrate ditetrahydrofuran; these crystals were maintained under an atmosphere of THF to prevent crystal decomposition.

By x-ray diffraction the crystals were shown to be monoclinic, $P2_1/a$ with $a = 9.412(7)$ Å, $b = 12.649(9)$ Å, $c = 7.237(5)$ Å, $\beta = 117.12(6)°$. The calculated density is 2.33 g cm^{-3}. The molecular structure was determined by a single crystal x-ray diffraction analysis.

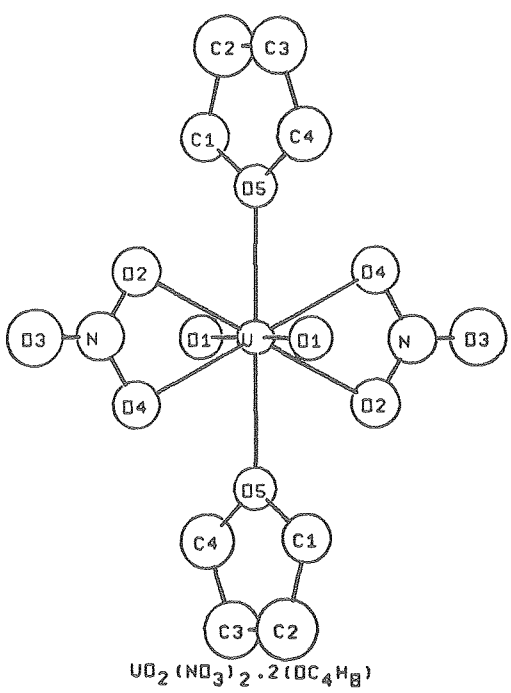

Fig. 3. An ORTEP view of $UO_2(NO_3)_2 \cdot 2(THF)$. Isotropic thermal parameters were used in preparing this figure. (XBL 773-8137)

The molecular structure (Fig. 3) consists of a uranium atom on a center of symmetry coordinated to eight oxygen atoms. The two uranyl oxygen atoms are perpendicular to the plane of the remaining coordinating oxygen atoms and with them form a hexagonal bipyramid about the uranium atom. This coordination geometry is typical of uranyl nitrate and is the same as that found in $UO_2(NO_3)_2 \cdot 6H_2O$,[3,4] $UO_2(NO_3)_2 \cdot 3H_2O$,[5] $UO_2(NO_3)_2 \cdot 2H_2O$,[6] $UO_2(NO_3)_2 \cdot 2[OP(OC_2H_5)_3]$,[7] and $UO_2(NO_3)_2 \cdot 4H_2O \cdot$(18- crown-6).[8] The agreement of corresponding distances and angles in these structures in most cases is within the quoted estimated errors.

The tetrahydrofuran molecule in this structure appears disordered as it does in most crystallographic determinations, presumably as a result of "pseudorotation."[9]

1. L. I. Katzin and J. C. Sullivan, J. Phys. and Colloid Chem. 55, 346 (1951).
2. H. M. Feder, L. E. Ross and R. C. Vogel, U. S. Atomic Energy Commission Report ANL-4868 (March 1952).
3. D. Hall, A. D. Rae and T. N. Waters, Acta. Cryst. 19, 389 (1965).
4. J. C. Taylor and M. H. Mueller, Acta. Cryst. 19, 536 (1965).
5. V. M. Vdovenko, E. V. Stroganov and A. P. Sokolov, Soviet Radiochem. 5, 83 (1963).
6. N. K. Dalley, M. H. Mueller, and S. H. Simonsen, Inorg. Chem. 10, 323 (1971).
7. J. E. Fleming and H. Lynton, Chem. and Ind. (London) 1960, 1415.
8. P. G. Eller and R. A. Penneman, Inorg. Chem. 15, 2439 (1976)
9. J. E. Kilpatrick, K. S. Pitzer, and R. Spitzer, J. Amer. Chem. Soc. 69, 2483 (1947).

d. Synthesis and Crystal Structure of a Neodymium Isopropoxide Chloride, $Nd_6[OCH(CH_3)_2]_{17}Cl$

Richard A. Andersen, David H. Templeton and Allan Zalkin

It has been reported that preparation of isopropoxide and metal chloride results in materials that are contaminated by chloride though nothing was known about their constitution.[1,2] We have carried out a single crystal x-ray analysis of the chloride-containing material and have shown it to be $Nd_6(O\text{-}i\text{-}Pr)_{17}Cl$.

Sodium isopropoxide was prepared from sodium and isopropyl alcohol in benzene; it was then added to a gently refluxing solution of neodymium trichloride in isopropyl alcohol. The resulting suspension was refluxed, centrifuged, and washed with benzene. The blue solid was recrystallized from toluene as light blue needles. The compound did not melt nor decompose when heated in a sealed capillary to 300°. The crystals are monoclinic, $P2_1/n$ with $a = 24.52(2)$ Å, $b = 22.60(2)$ Å, $c = 14.22(1)$ Å, $\beta = 101.05(5)°$ and

Dx = 1.64 g/cm^3 at 21°C. The molecular structure was determined by a single crystal x-ray diffraction analysis.

The neodymium atoms are at the corners of a very nearly regular trigonal prism in which the triangular edges average 3.808 ± 0.006 Å and the axial edges 4.230 ± 0.010 Å, in Fig. 4. All of the angles in the triangular faces are within 0.1° of 60°. Because of a slight twist of the triangular faces with respect to each other about the prism axis, the angles are about 1 degree from 90° for the three quadrilateral faces. The cause of this minor distortion is unknown; perhaps it is a result of some steric effects of the isopropoxide ligands. The chloride ion is equidistant from the six Nd atoms at a distance of 3.05 ± 0.01 Å, and is perhaps the stabilizing factor for this remarkable cluster of atoms.

There are three types of oxygen-Nd bonds. Each Nd atom is bonded singly to an isopropoxide ligand with an average Nd-O distance of 2.05 ± 0.02 Å. A bridging isopropoxide ligand bonds 2 Nd atoms at each edge of the prism to give 18 Nd-O bond lengths that average 2.36 ± 0.04 Å. The isopropoxide ligands that are centered on the triangular faces bond to three Nd atoms with an average bond length of 2.45 ± 0.05 Å.

The molecular packing resembles the hexagonal closest packing of spheres. The globular complexes with centers near y = 1/4 form a layers in which each cluster has six neighbors, and a similar layer occurs at y = 3/4. The stacking of these layers is according to the ABAB sequence of hexagonal closest packing. This description is imperfect because the molecules are not spherical, and Cl-Cl distances for the 12 nearest neighbors range from 12.94 to 16.34 Å.

The magnetic susceptibility of the complex followed the Curie-Weiss equation $\chi = C_M/T+\Theta$ in the temperature range 7.5 to 100 K. The magnetic moment, μ_{eff}, was 3.22 B.M. per neodymium atom with $\Theta = -2.8°$ and $C_M = 1.293$.

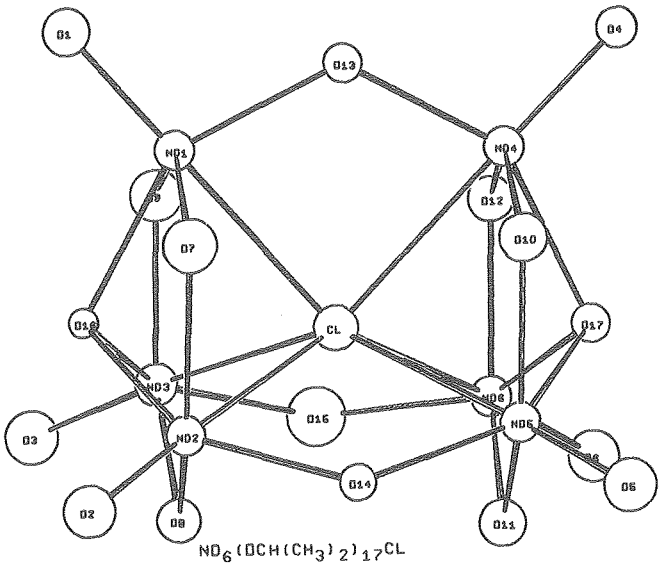

Fig. 4. ORTEP drawing of the Nd, Cl and O framework in $Nd_6[OCH(CH_3)_2]_{17}Cl$. (XBL 776-9355)

---

1. L. M. Brown and K. S. Mazdiyasni, Inorg. Chem. 9, 2783 (1970).
2. K. S. Mazdiyasni, C. T. Lynch and J. S. Smith, Inorg. Chem. 5, 342 (1966).

e. Crystal and Molecular Structure of bis-π-(cyclobutenocyclooctatetraene)uranium(IV), $U[C_8H_6(CH_2)_2]_2$

Stuart R. Berryhill, Wayne D. Luke, Andrew Streitwieser, Jr., David H. Templeton and Allan Zalkin

Following the initial characterization of bis (cyclooctatetraenyl) uranium(IV), "uranocene," by Streitwieser and Müller-Westerhoff,[1] its crystal and molecular structure was determined.[2] Subsequently the preparation[3] and structure[4] of bis(cyclooctatetraenyl)thorium (IV), "thoracene" was reported as well as the preparations and structures of octamethyl uranocene,[5,6] $U(C_8H_4(CH_3)_4)_2$, and octaphenyl uranocene,[7,8] $U(C_8H_4(C_6H_5)_4)_2$.

As part of a program to extend knowledge of the chemical and structural properties of compounds of actinide elements, we undertook a study of the structure of cyclobutenouranocene synthesized by Streitwieser, Berryhill and Luke.[9]

Crystals grown from a hexane solution were dark green. The material is extremely air sensitive.

Crystals of bis-π-(bicyclo[6.2.0]deca-1,3,5,7-tetraene)uranium(IV), $U(C_8H_6(CH_2)_2]_2$, are monoclinic, space group $P2_1/n$, a = 9.906(8) Å, b = 11.039(9) Å, c = 7.221(6) Å, β = 98.89(5)°, V = 780.15 Å^3, Z = 2, Dx = 2.122 g cm^{-3}, at 22° C.

The title compound exists as discreet molecules in the solid state. With the uranium at the origin of the unit cell, the molecule has a center of symmetry imposed on it by the space group and the C_8 rings are exactly eclipsed. The molecular symmetry is C_{2h}. The uranium atom is sandwiched by the two cyclobutenocyclooctatetraene moieties, and it is accurately centered on the cyclooctatetraene (C_8) rings; i.e., the U atom is very nearly equidistant to all of the atoms in the C_8 ring, see Fig. 5. The cyclobuteno (C_4) ring is planar and the plane of the ring is bent about 6.8° from the plane of the C_8 rings toward the center of the molecule; i.e., the two most distant carbon atoms are both 0.18 Å below the least squares plane through the C_8 ring; none of the atoms in the C_8 ring is more than 0.016 Å from its least-squares plane.

Bond angles and distances are comparable to those found in other uranocenes. The mean U-C value in this compound is 2.64 ± 0.02 Å; this compares to a value of 2.65 Å in uranocene,[5] 2.66 Å in $U(C_8H_4(CH_3)_4)_2$[7] and 2.65 ± 0.03 Å in octaphenyluranocene.[9] It is evident from the ORTEP drawing in Fig. 5 that there is considerable torsional motion in the plane of the ring. We estimate an increase to 1.41 Å for the average C-C bond length due to this motion.[9] This compares to 1.42 Å (after correction for torsional motion) in thoracene and uranocene.[5] The

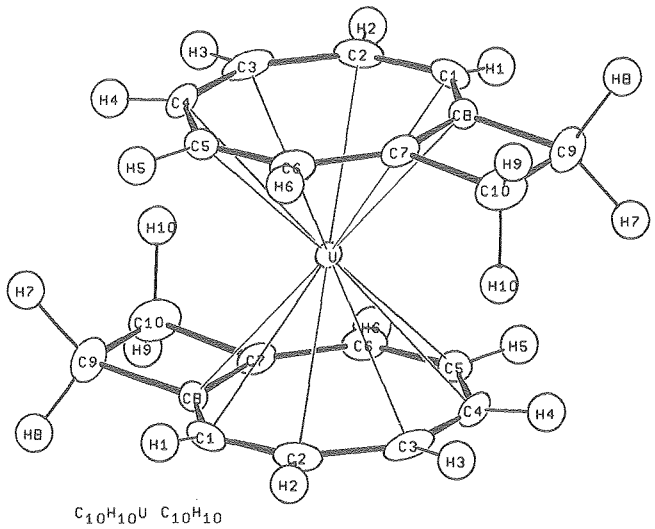

Fig. 5. An ORTEP view of the molecule. (XBL 7711-10665)

bond lengths of C(8)-C(9), C(7)-C(10) and C(9)-C(10) are aliphatic in nature with the first two being close to the accepted C-C bond length. The C(9)-C(10) bond length is 1.47(2) Å, which would increase to 1.49 Å with a correction for torsional motion, and is still somewhat short of the expected value of 1.54 Å.

---

1. A. Streitwieser, Jr. and U. Müller-Westerhoff, J. Amer. Chem. Soc. 90, 7364 (1968).
2. A. Zalkin and K. N. Raymond, J. Amer. Chem. Soc. 91, 5667 (1969).
3. A. Streitwieser, Jr. and N. Yoshida, J. Amer. Chem. Soc. 91, 7528 (1969).
4. A. Avdeef, K. N. Raymond, K. O. Hodgson and A. Zalkin, Inorg. Chem. 11, 1083 (1972).
5. A. Streitwieser, Jr., D. Dempf, G. N. La Mar, D. G. Karraker and N. Edelstein, J. Amer. Chem. Soc. 93, 7343 (1971).
6. K. O. Hodgson and K. N. Raymond, Inorg. Chem. 12, 458 (1973).
7. A. Streitwieser, Jr. and R. Walker, J. Organomet. Chem. 97, C41 (1975).
8. L. K. Templeton, D. H. Templeton and R. Walker, Inorg. Chem. 15, 3000 (1976).
9. A. Streitwieser and S. Berryhill, to be published.

f. The Crystal Structure of $[XeF^+][AsF_6^-]$

Allan Zalkin, Donald L. Ward, Richard N. Biagioni, David H. Templeton and Neil Bartlett

In an earlier paper Sladky et al. described[1] the preparation of the 1:1 XeF_2 - AsF_5 complex and showed that it lost AsF_5 readily under vacuum at ordinary temperatures to yield a 2:1 complex. The crystal structure of the 2:1 complex has already been described[2] and is consistent with formulation as the salt $Xe_2F_3^+AsF_6^-$. The structure of the 1:1 complex was of interest to us because of an earlier finding[3] that the structure of the 1:1 XeF_2 - RuF_5 complex was consistent with the $XeF^+RuF_6^-$ formulation and our expectation that the formulation of the 1:1 XeF_2 - AsF_5 complex would be similar.

Preparative conditions for 1:1 XeF_2 - AsF_5 complex have now been established, and we have determined the structure by single crystal x-ray diffraction. The crystals are monoclinic, $P2_1/n$, a = 6.308(3), b = 6.275(3), c = 16.023(5) Å, β = 99.97(5)°, V = 624.66 Å^3, Z = 4, D_x = 3.61 g cm^{-3}, at 24°C.

The crystal structure consists of an ordered arrangement of discrete $FXeFAsF_5$ units, the closest contact between units being 2.92 Å, a contact between F(1) and F(7). The structure of this molecule is compared with that of $FXeFRuF_5$ in Fig. 6. The amplitudes of thermal motion are considerable. In each case except Xe-F(6) the minimum amplitude of motion is nearly parallel to the bond, and in every case the largest amplitude is nearly perpendicular to the bond. These results lend credibility to the physical reality of the riding model as a description of the thermal motion.

In spite of the close similarity of molecular geometry and the fact that the arsenic and ruthenium compounds crystallize with the same space group symmetry, the unit cell shapes are dissimilar and,

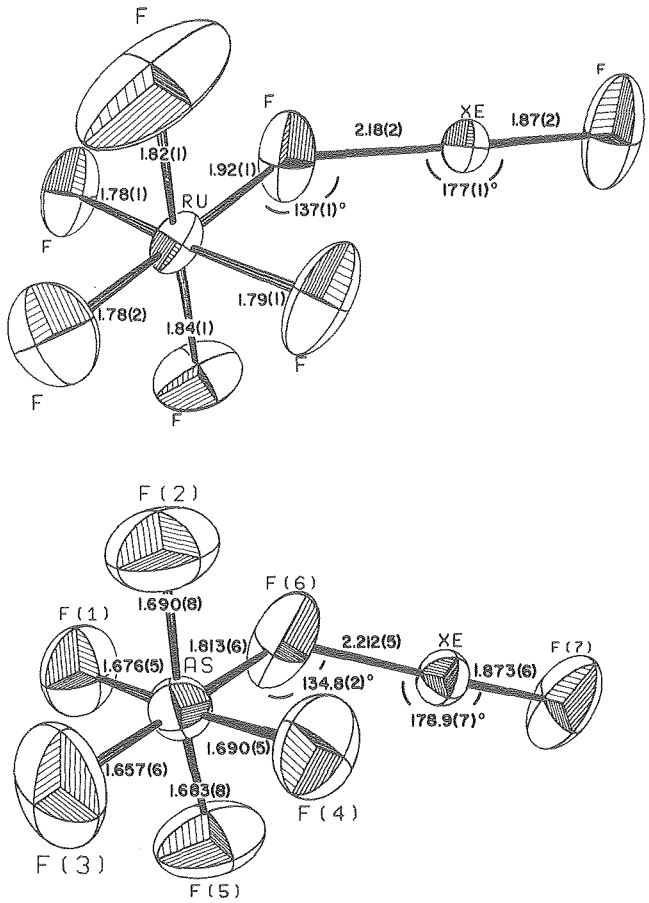

Fig. 6. The formula units of $XeFAsF_6$ and $XeFRuF_6$ (Ref. 3), the former with 50% probability ellipsoids, the latter with 30%. (XBL 7311-6807)

moreover, the molecular packing is quite different. In $FXeFAsF_5$ the long dimensions of the formula units are all nearly parallel to each other, while in $FXeFRuF_5$ there are two orientations nearly perpendicular to each other. To a first approximation we can represent the $FXeFRuF_5$ as developed from a CsCl (8:8 coordination) structure type whereas we can represent $FXeFAsF_5$ as derived from a NaCl type (6:6 coordination). We attribute this difference in coordinating capability of the anions with differences in polarizability of the F ligands in the MF_6^-.

1. F. O. Sladky, P. A. Bulliner and N. Bartlett, J. Chem. Soc. A, 2179 (1969).
2. N. Bartlett, B. G. Deboer, F. J. Hollander, F.O. Sladky, D. H. Templeton and A. Zalkin, Inorg. Chem. 13, 780 (1974).
3. N. Bartlett, M. Gennis, D. D. Gibler, B. K. Morrell and A. Zalkin, Inorg. Chem. 12, 1717 (1973).

g. Actinide Chemistry of Highly Substituted Cyclooctatetraenes*

Michael J. Miller and Andrew Streitwieser, Jr.

Although the highly hindered octaphenyluranocene (bis-π-1,3,5,7-tetraphenylcyclooctatetraene uranium) is remarkably air stable, its limited solubility precludes further solution experiments. A uranocene that is highly substituted with bulky alkyl groups should be both air stable and soluble. Such a uranocene should allow investigation of the solution chemistry of hindered uranocenes in order to gain further insight into the bonding in actinide organometallics.

The previously unkown compound, 1,3,5,7-tetra-t-butylcyclooctatetraene, 1, was prepared in several steps in 24% overall yield as a colorless, low-melting solid. Treatment of the cyclooctatetraene with potassium metal in THF slowly forms the dianion. Addition of a solution of UCl_4 in THF to a THF solution of the dianion resulted in immediate reaction to give a black insoluble precipitate with liberation of the neutral cyclooctatetraene, 1. The reduction potential of the cyclooctatetraene is apparently too high to allow formation of a stable uranocene and reduction of UCl_4 to uranium metal occurs instead. Similar results have been obtained with $ThCl_4$.

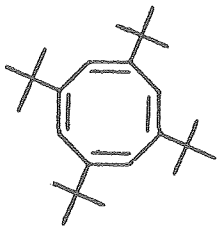

1

The dianion 2 has also been prepared. This dianion, upon treatment with UCl_4, forms the stable uranocene, 1,1',4,4'-tetra-t-butyluranocene. This uranocene is not air stable, though, presumably due to the ineffective shielding of the metal by only four t-butyl groups. The proton NMR spectrum of this uranocene is quite interesting. Although the t-butyl protons(-9.8δ) exhibit a resonance much the same as those in 1,1'-di-t-butyluranocene (-11.0δ), the ring protons show a very large variation. The value of -22.4δ for one set of ring protons is the lowest field shift yet observed for a uranocene ring proton. This is presumably due to the large electronic perturbation of the t-butyl groups on the ligand π-system, but may also be due to a distortion of the geometry of the system due to the presence of the large groups.

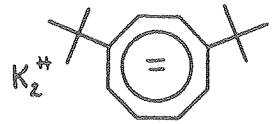

2

Table 2. Spectra of 1,1',4,4'-tetra-t-butyluranocene.

Proton NMR:	δ -9.8(s,18H),-24.4(s,4H),-38.0(s,4H),-40.4(s,4H).
Visible:	λ_{max} 631, 658, 725 nm.
Mass Spectrum(m/e):	670(M^+,$(C_{16}H_{24})_2U^+$), 454($C_{16}H_{24}U^+$), 216($C_{16}H_{24}^+$), 57($C_4H_9^+$)

*Partially supported by NSF.

h. Synthesis and Chemistry of Substituted Thorocenes*

Carole LeVanda and Andrew Streitwieser, Jr.

Disubstituted bis-cyclooctatetraene thorium(IV) (thorocene) complexes have been prepared in good yield by the reaction in Eq. (1), where RC_8H_7 includes n-butyl, phenyl, and 1,3,5,7-

$$2K_2RC_8H_7 + ThCl_4 \longrightarrow (RC_8H_7)_2Th + 4KCl \quad (1)$$

tetramethyl cyclooctatetraenes. Unlike thorocene itself, these substituted derivatives are soluble in common organic solvents that allows for exploration of their chemical and spectral properties. The substituted thorocenes provide the first group of diamagnetic bis-cyclooctatetraene actinide compounds for NMR analysis. Proton and ^{13}C NMR spectra of these air-sensitive complexes show a significant decrease in electron density in the rings relative to ionic cyclooctatetraene salts, which attests to their covalent nature. For example, in dibutylthorocene, the ring protons absorb at δ 6.5 ppm vs. 5.7 ppm for $K_2BuC_8H_7$. The ring carbon resonances in $(BuC_8H_7)_2Th$ are some 20 ppm downfield from the dipotassium salts.

Of particular importance is a comparison of thorocene chemistry with the known chemistry of uranocene, the U(IV) analog, to assess the effect of electronic structure on the relative reactivity of the cyclooctatetraene complexes of the lower actinides. The limited chemistry of uranocene has been rationalized on the basis that both the highest occupied and lowest vacant orbitals are predominantly metal in character. Reactions generally occur at the metal with consequent rupture of the metal-ligand bonds. With a closed shell configuration, the chemistry of thorocenes differs somewhat from that of uranocenes. For example, uranocene is remarkably stable to water when compared to ionic organometallic complexes of cyclooctatetraene. Dibutylthorocene was shown to react instantaneously with both water and acetic acid in THF to give butylcyclooctatetrienes. The rate of hydrolysis, however, is not a criterion for convalency. With two fewer f-electrons, thorocene is expected to be more susceptible to nucleophilic attack than uranocene.

Thorocenes were shown to react with nitro compounds to give azo compounds in a similar fashion to uranocenes. Previously, a mechanism had been proposed that involved an electron transfer to form a U(V) species. Since Th(V) oxidation state is unknown, this observation requires that an alternative mechanism be formulated.

It was shown that thorocenes undergo ligand exchange with cyclooctatetraene dianions (Eq. 2) in an analogous fashion to

$$(RC_8H_7)_2Th + R'C_8H_7^{=} \longrightarrow (RC_8H_7)(R'C_8H_7)Th + RC_8H_7^{=} \qquad (2)$$

uranocenes but that in some cases the reaction is slow. Dibutylthorocene also undergoes a slow reaction with UCl_4 to produce dibutyluranocene.

---

*Partially supported by NSF.

i. The Syntheses, Optical and Magnetic Properties of Tetrakis (Di N-Propylamido)Uranium(IV), Tetrakis (Di N-Butylamido)Uranium(IV), Tetrakis (Di N-Propylamido)Thorium(IV), and Tetrakis(Di N-Butylamido) Thorium(IV), Volatile Liquid Amides

John G. Reynolds* and Norman M. Edelstein

Transition metal amides have been utilized as reactive intermediates in the synthesis of transition metal alkoxides, thiols, and organometallic derivatives.[1] Recently, we have reported many new uranium amides, which are not only useful as extremely reactive intermediates,[2,3] but exhibit novel physical properties.[4-7] In the solid state, these new uranium compounds have exhibited monomeric,[6] dimeric,[4] trimeric,[5] and tetrametric[7] molecular units, with the U atoms being bridged by N atoms. The coordination about the U atom is four, five, or six in the crystals, while in solution the coordination about the U atom depends on the complexing ability of the solvent. In order to extend this work, we now report the preparation and isolation of the actinide amides, $U[N(CH_2CH_2CH_3)_2]_4$, $U[N(CH_2CH_2CH_2CH_3)_2]_4$, and their thorium analogs. These compounds are liquids at room temperature, and their physical and solution properties are markedly similar to those of $U(NEt_2)_4$ [4,8] and $Th(NEt_2)_4$,[9] respectively.

The reaction used for the syntheses of these new actinide amides is the same as employed previously for the large majority of transition metal amides:[10]

$$MCl_4 + 4LiNR_2 \xrightarrow{Et_2O} M(NR_2)_4 + LiCl \downarrow$$

$$M = U, Th$$

$$R = -CH_2CH_2CH_3, -CH_2CH_2CH_2CH_3.$$

Table 3 lists some of the physical properties of these actinide amides. Although the di-n-propyl and di-n-butyl actinide amides are the first reported actinide amides which are liquid at room temperature, this behavior is common in d-transition-metal amides.[1] The distillation temperatures of the corresponding thorium and uranium dialkyl amides are quite similar.

Table 3. Physical properties of some uranium amides.

Compound	Phase[a]	Distillation Temp.[b]
$U(N(CH_2CH_3)_2)_4$[4,8]	solid	40° - 50° C
$U(N(CH_2CH_2CH_3)_2)_4$	liquid	40° - 50° C
$U(N(CH_2CH_2CH_2CH_3)_2)_4$	liquid	90° - 100° C
$Th(N(CH_2CH_3)_2)_4$[9]	solid	40° - 50° C
$Th(N(CH_2CH_2CH_3)_2)_4$	liquid	50° - 60° C
$Th(N(CH_2CH_2CH_2CH_3)_2)_4$	liquid	90° - 100° C
$U(N(C_6H_5)_2)_4$[6]	solid	dec.[c]
$U_3(CH_3NCH_2CH_2NCH_3)_6$[5]	solid	dec.

[a]At room temperature.
[b]At less than 10^{-4} mm Hg pressure.
[c]Decomposition without sublimation.

The pmr spectra of the uranium and thorium amides in d_8 toluene and d_8 THF are given in Table 4. The proton spectra of the thorium amides are almost identical to those of the free ligands as expected for a diamagnetic Th^{4+} ion. The pmr spectra of the U amides can be classified into two groups depending on the solvent used. The proton spectra of the U amides in d_8 toluene have peaks asymmetrically placed about TMS, and significantly shifted from the corresponding diamagnetic positions. As the distance of the proton from the U atom is increased, the magnitude of the shift decreases. Also, resolution of the spin-spin coupling occurs at the γ carbon protons, suggesting that at this distance the effects

Table 4. Proton magnetic resonance spectra of some uranium amides[a] with respect to TMS (ppm).

Compound	Solvent	α	β	γ	δ	Temperature
$U(N(CH_2CH_3)_2)_4$ [4]	d_6 Benzene	-13.0[b]	+5.4[c]	—	—	24°C
$U(N(CH_2CH_2CH_3)_2)_4$	d_8 toluene	-8.4(s)	+1.9(s)	-.4(t)	—	25°C
$U(N(CH_2CH_2CH_2CH_3)_2)_4$	d_8 toluene	-9.4(s)	+3.1(s)	-.3(m)	+.5(t)	19°C
$U(N(CH_2CH_3)_2)_4$ [4]	d_8 THF	+18.2	+13.8	—	—	24°C
$U(N(CH_2CH_2CH_3)_2)_4$	d_8 THF	+19.8(s)	+12.9(s)	+8.04(t)	—	26°C
$U(N(CH_2CH_2CH_2CH_3)_2)_4$	d_8 THF	+17.9(s)	+11.6(s)	+6.5(s)	+2.6(t)	19°C
$U(N(CH_2CH_2CH_3)_2)_4$	neat	+1.1(s)	+11.4(s)	+9.3(t)	—	25°C
$U(N(CH_2CH_2CH_2CH_3)_2)_4$	neat	+3.5(s)	+16.5(s)	+13.3(m)	+14.1(t)	25°C
$Th(N(CH_2CH_2CH_3)_2)_4$	d_6 Benzene	-2.7(t)	-1.1(m)	-.5(m)	—	25°C
$Th(N(CH_2CH_2CH_2CH_3)_2)_4$	d_6 Benzene	-2.95(t)	-1.3(m)	-1.0(m)	-.7(t)	25°C

[a] α = α carbon proton, β = β carbon proton, γ = γ cargon proton, δ = δ carbon proton, t = triplet, s = singlet, m = multiplet.
[b] - = downfield relative to TMS.
[c] + = upfield relative to TMS.

of line width broadening due to the very fast electronic relaxation time of the paramagnetic U^{4+} ion, are much diminished. If we assume that the U species in toluene solution is monomeric as found for the $U(NEt_2)_4$ compound,[8] then the most likely structure for the U n-alkyl amides is tetrahedral. For this symmetry the pseudo-contact term vanishes, and only the Fermi contact hyperfine interaction contributes to the paramagnetic shift.[11] This interaction would be of a similar magnitude for each of the U n-alkyl amide compounds and would account for the similarity of the paramagnetic shifts in the series.

The same argument may be used for the pmr of the U n-alkyl amides in ether solvents. Table 4 shows the great similarity of the shifts for the three compounds. It appears that the ether solvents complex the U amides and the solution structures are very similar. Therefore, the g value anisotropy, the pseudo-contact shifts, and the Fermi contact term are similar for each of the compounds, which results in similar pmr spectra for each of α, β etc., protons in the alkyl chain for each compound.

The pmr spectra of the neat compounds are also given in Table 4. These relative splittings and the resolution of the multiplets are the same as found in toluene solution but there is an absolute shift of 10-13 ppm upfield in the line positions due to the effects of the bulk susceptibility of the solution. These observations support our assumptions that the U n-alkyl amides [and $U(N\phi_2)_4$] do not coordinate with hydrocarbon solvents and that they are monomeric at room temperature in these solvents.

The optical and near IR spectra of the uranium n-propyl amide in various solvents at room temperature are shown in Fig. 7 and tabulated for both uranium amides in Table 5. These spectra are almost identical to those of the previously published $U(NEt_2)_4$ and $U(N\phi_2)_4$ in the same solvents.[4,6] As in the pmr spectra we suggest the spectra in the ether solvent are due to a U molecule associated with the complexing ether solvent molecules, whereas in hydrocarbon solvents the spectra are due to the uncomplexed tetrahedral U molecule. The almost identical spectrum for each of the uranium n-alkyl amides in the same solvent shows that changing the alkyl chain has little effect on the f-f transitions. The major differences in the spectra come from changes in the first coordination sphere as shown by the effects of the ether solvent.

The inverse of the magnetic susceptibility of $U[N(CH_2CH_2CH_2CH_3)_3]_4$ in the temperature range 4.2 to 100 K is shown in Fig. 8. A similar curve is found for $U[N(CH_2CH_2CH_3)_2]$. The data for the three n-alkyl amides are collected in Table 6. In all cases there is Curie behavior down to ~30 K [20 K for $U(NEt_2)_4$] after which the inverse of the susceptibility tends

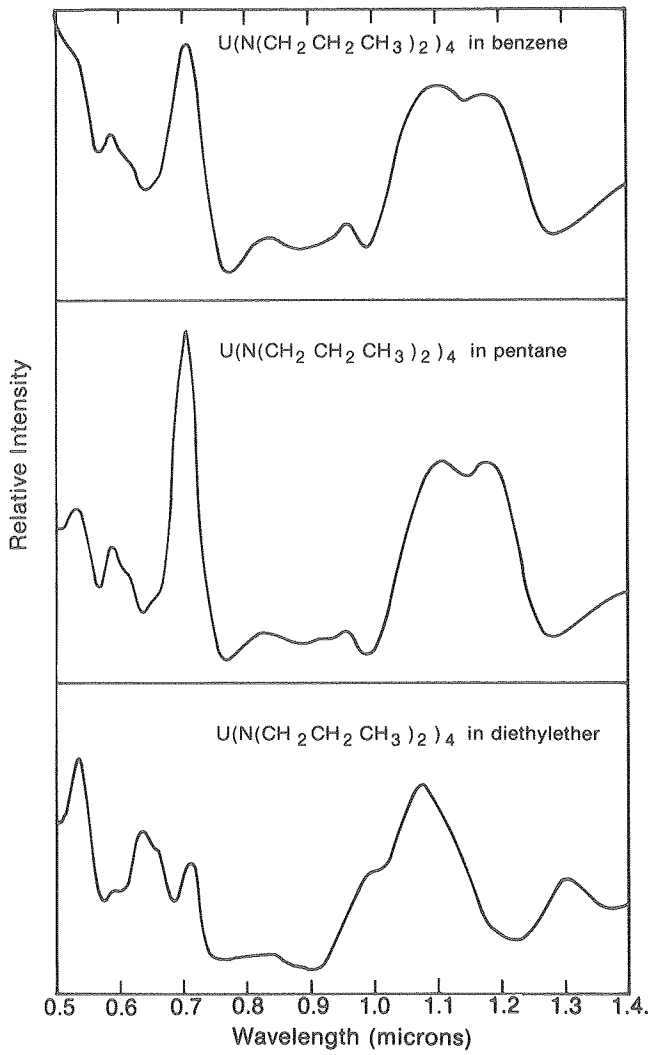

Fig. 7. Optical spectra of $U[N(CH_2CH_2CH_3)_2]_4$ in various solvents at room temperature. (XBL 7611-4390)

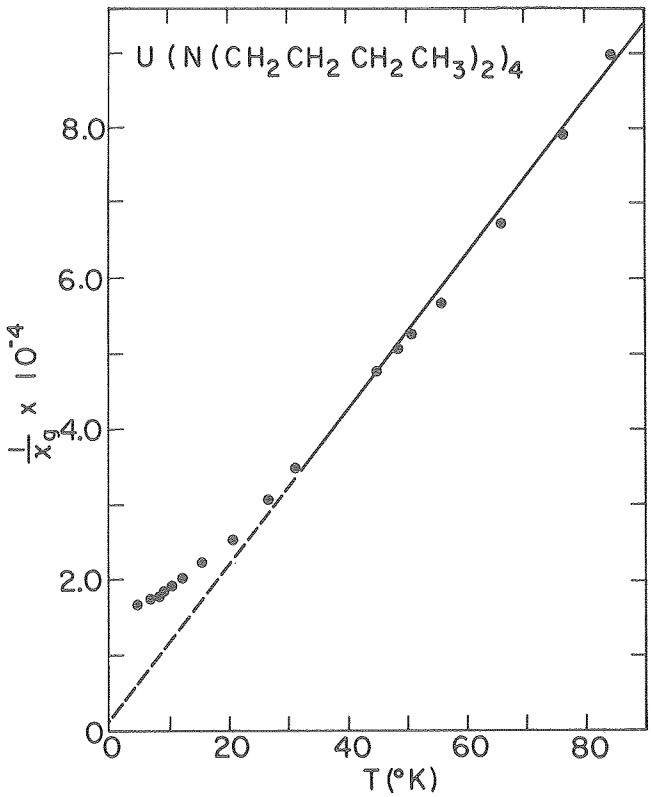

Fig. 8. Inverse susceptibility of $U[N(CH_2CH_2CH_3)_2]_4$ vs temperature. The straight line is the calculated inverse susceptibility in that temperature range with the parameters obtained from a least-squares fit as given in Table 6. (XBL 7611-4393)

Table 5. Peak positions and extinction coefficients of $U(N(CH_2CH_2CH_3)_2)_4$ and $U(N(CH_2CH_2CH_2CH_3)_2)_4$ in various solvents.

Compounds	Peak / Solvent	1 λ,μm	1 ε	2 λ,μm	2 ε	3 λ,μm	3 ε	4 λ,μm	4 ε	5 λ,μm	5 ε	6 λ,μm	6 ε
$U(N(CH_2CH_3)_2)_4$ [a]	Hexane	.704	50	b	—	c	—	1.104	25	1.188	25	c	—
$U(N(CH_2CH_2CH_3)_2)_4$	Pentane	.705	39	b	—	c	—	1.105	24	1.180	24	c	—
$U(N(CH_2CH_2CH_2CH_3)_2)_4$	Pentane	.702	45	b	—	c	—	1.100	25	1.170	24	c	—
$U(N(CH_2CH_3)_2)_4$ [a]	Benzene	.692	47	b	—	c	—	1.090	27	1.172	26	c	—
$U(N(CH_2CH_2CH_3)_2)_4$	Benzene	.705	44	b	—	c	—	1.105	32	1.180	30	c	—
$U(N(CH_2CH_2CH_2CH_3)_2)_4$	Benzene	.705	45	b	—	c	—	1.095	30	1.170	28	c	—
$U(N(CH_2CH_3)_2)_4$ [a]	Et_2O	.638	28	.660	24	.718	15	.990	20	1.070	32	1.302	19
$U(N(CH_2CH_2CH_3)_2)_4$	Et_2O	.638	22	.658	19	.710	17	1.000	16	1.078	28	1.310	12
$U(N(CH_2CH_2CH_2CH_3)_2)_4$	Et_2O	.640	24	.665	19	.710	17	1.005	17	1.070	30	1.305	18

[a] From Reference 4.
[b] Peaks were not split into two components.
[c] Peaks masked by solvent bands.

Table 6. Temperature dependent susceptibility values for some uranium amides.

Compound	C_M	μ_{eff}(BM)	θ(K)	Temp.(°K)
$U(N(CH_2CH_3)_2)_4$ [4]	1.052	2.74	-4.8	20-100
$U(N(CH_2CH_2CH_3)_2)_4$	1.00	2.69	7.2	30-102
$U(N(CH_2CH_2CH_2CH_3)_2)_4$	.74	2.44	2.2	27-84
$U(N(C_6H_5)_2)_4$ [6]	1.00	2.84	24.8	40-90

to become less temperature dependent. The symmetry in the solid state of the two new uranium amides is unknown but the susceptibility data could be due to a ground state singlet with a doublet state approximately ~35 cm^{-1} higher in energy. The effective moments of all the amides in the temperature range where they follow the Curie law are similar.

*Present Address: Department of Chemistry, Stanford University, Stanford CA 94305.

1. D. C. Bradley and K. J. Fisher, M. T. P. Int. Rev. Sci. Inorg. Ser. I, 5, 65 (1972).
2. J. D. Jamerson and J. Takats, J. Organomet. Chem. 78, C23 (1974).
3. K. W. Bagnall and E. Yanir, J. Inorg. Nucl. Chem. 36, 777 (1974).
4. J. G. Reynolds, A. Zalkin, D. H. Templeton, N.M. Edelstein and L. K. Templeton, Inorg. Chem. 15, 2498 (1976).
5. J. G. Reynolds, A. Zalkin, D. H. Templeton and N. M. Edelstein, Inorg. Chem. 16, 599 (1977).
6. J. G. Reynolds, A. Zalkin, D. H. Templeton and N. M. Edelstein, Inorg. Chem. 16, 1090 (1977)
7. J. G. Reynolds, A. Zalkin, D. H. Templeton and N. M. Edelstein, Inorg. Chem. 16, 1858 (1977).
8. R. G. Jones, G. Karmas, G. A. Martin, Jr., and H. Gilman, J. Am. Chem. Sco. 78, 4285 (1956).
9. G. W. Watt and K. F. Gadd, Inorg. Nucl. Chem. Lett. 9, 203 (1973).
10. D. C. Bradley, Adv. in Inorg. Chem. and Radiochem. 15, 259 (1972).
11. D. R. Eaton and W. D. Phillips, Advan. Magn. Resonance 1, 103 (1965).

j. Preparation and Structural Characterization of NpF_5

M. Baluka,* S. Yeh, R. Banks and N. Edelstein

Until recently, only the pentafluorides of uranium and protactinium had been prepared, although thermodynamic calculations suggested NpF_5 and possibly PuF_5 should be stable.[1] Russian workers[2] have recently reported the synthesis of NpF_5 by the oxidation of NpF_4 in anhydrous hydrogen fluoride with KrF_2 at room temperature. Analysis of this material by spectroscopic and analytical methods showed it to be NpF_5. We have recently developed a new and relatively simple synthesis for UF_5[3] by the reaction of UF_6 dissolved in anhydrous hydrogen fluoride with excess PF_3. A similar reaction has now been carried out with NpF_6 with the resultant product being NpF_5.

NpF_6 was dissolved in anhydrous hydrogen fluoride at room temperature in a Kel-F tube. This solution was frozen at 77K and an excess amount of PF_3 was condensed onto the frozen solution. The liquid N_2 bath was removed and the solution was allowed to warm to room temperature. A bluish-white ppt formed during the warming process. After warming to room temperature the anhydrous hydrogen fluoride, PF_3 and PF_5, were removed by distillation. X-ray powder diffraction samples of the ppt were prepared in an argon atmosphere box.

X-ray powder patterns were obtained with a 114 mm Debye-Scherrer camera using copper Kα radiation. All the lines in the powder pattern could be assigned on the basis of the α-UF_5 structure.[4] The observed lines were fitted to the calculated pattern using the least squares program LCR-2 with the Nelson-Riley correction. The measured d-spacings and lattice parameters are shown in Table 7.

Although the reaction utilized for the synthesis of NpF_5 was a low temperature one, the structure determined is the same as α-UF_5, the high temperature form. The α-NpF_5 structure is consistent with the infrared and Raman spectra reported by the Russian workers.[2]

The same reaction was run with PuF_6 but the product obtained was amorphous and had the same tan color as PuF_4.

Table 7. Powder diffraction data for α-NpF_5 at room temperature.

kkl	Observed d spacings Å	Observed 2 Θ^a (deg)	Calculated 2 $\Theta^{a,b}$ (deg)
110	4.611	19.25	19.26
101	3.678	24.20	24.23
200	3.258	27.37	27.35
211	2.440	36.83	36.84
220	2.308	39.03	39.04
002	2.222	40.60	40.54
310	2.062	43.90	43.87
112	2.004	45.24	45.24
301	1.955	46.45	46.46
202	1.840	49.55	49.58
321	1.676	54.77	54.74
400	1.633	56.35	56.38
222	1.604	57.47	57.53
330	1.537	60.19	60.14
312	1.514	61.22	61.24
411	1.492	62.22	62.23
420	1.459	63.77	63.77

[a]Cu radiation - λ = 1.5418 Å.

[b]Tetragonal lattice a = 6.53 ± 0.03 Å, b = 4.45 ± 0.03 Å.

---

*Present Address: Institute for Low-Temperature Research, Polish Academy of Sciences, Wroclaw, Poland.

1. D. Brown, Halides of the Lanthanides and Actinides, J. Wiley, London, 1968.
2. Y. V. Drobyshevskii, V. F. Serik, and V. B. Sokolov, Akad. Nauk. USSR Proc. Dokl. Chem. (English Trans.) 225, 675 (1975).
3. R. Rietz, T. O'Donnell and S. Yeh, unpublished work.
4. W. H. Zachariasen, Acta Cryst. 2, 296 (1949).

k. Fluorosulfates of Uranium

S. Yeh and Neil Bartlett

The preparation of $U(OTeF_5)_6$ in these laboratories several years ago[1] and the finding that this compound was readily volatile led us to suppose that $U(OSO_2F)_6$ would also be preparable and monomolecular. We were also interested in F_5UOSO_2F, as a possible monomeric pseudo-octahedral species of the type F_5UX. Our synthetic work was directed in the first instance towards F_5UOSO_2F.

Our approach was to oxidize UF_5 with $S_2O_6F_2$. Three solvents were tried: HSO_3F, SO_2ClF and HF.

In HSO_3F and in SO_2ClF, the UF_5 reacted rapidly with the $S_2O_6F_2$ to yield a blue-green solid and UF_6. Analysis of the blue-green solid indicated that it had the composition UF_4SO_3F (Found: U, 57.8; S, 7.49% Reqd. for UF_4SO_3F: U, 57.6, S, 7.75%). This material was neither soluble in the solvents used nor volatile. It is probable that it is polymeric by SO_3F or F bridging. Infrared spectra give some support for the former possibility. It appears that the reaction involves disproportionation of the reactant UF_5, with concurrent oxidation by the $S_2O_6F_2$:

$$2\ UF_5 \longrightarrow UF_6 + [UF_4];\quad [UF_4] + \frac{1}{2}\ S_2O_6F_2 \longrightarrow UF_4SO_3F.$$

The interaction in HF was different. The initial product was a yellow solid and the HF solution had a pale yellow tint. The yellow solid diminished with time, however. Rapid removal of HF following mixing of the UF_5 and $S_2O_6F_2$ gave a yield of yellow solid product and was indicative of the following reaction:

$$6\ UF_5 + 3\ S_2O_6F_2 \xrightarrow{HF} 5\ UF_6 + U(OSO_2F)6.$$

[Thus 3.148 g (9.45 mmoles) UF_5 yielded 1.42 g yellow solid (1.71 mmoles as $U(OSO_2F)_6$]. This is in accord with earlier findings[1] on the dismutation of F_5UOTeF_5.

The yellow solid was neither soluble in HSO_3F, SO_2ClF, $CFCl_3$, WF_6, nor volatile. At 165° it decomposed to yield SO_2F_2 and a blue-green solid. If, as the gravimetry, chemistry, and available spectroscopic evidence suggest, the yellow solid is $U(OSO_2F)_6$, its evident polymeric nature is puzzling. The compound will be examined further.

---

1. L. K. Templeton, D. H. Templeton, N. Bartlett and K. Seppelt. Inorg. Chem. 15, 2720 (1976).

3. PHYSICAL AND SPECTROSCOPIC STUDIES

a. Absorption and Emission Spectra of U^{4+} Diluted in $ThBr_4$ Single Crystals

M. Genet,* P. Delamoye,* N. Edelstein and J. Conway

High resolution optical studies of actinide ions have mainly dealt with the tripositive state in order to compare the $5f^n$ spectra directly with their lanthanide analogs. There have been some high resolution studies of tetrapositive actinide ions in O_h symmetry[1-3] and further studies of U^{4+} ($5f^2$) in D_{2d} symmetry. The first reported work in the lower symmetry sites was by McLaughlin[4] who grew a single crystal of UCl_4 and obtained and interpreted its optical spectrum. This work was later reexamined by Hecht and Gruber[5] who obtained more data and performed a more complete analysis. Richman, Kisliuk, and Wong[6] studied the absorption spectrum of U^{4+} diluted in $ZrSiO_4$ and their work was later extended and amplified by Mackey, Runciman, and Vance.[7] In both UCL_4 and $ZrSiO_4$ the local symmetry about the U^{4+} ion was D_{2d}. The spectra obtained consisted of many more lines than could be reasonably attributed to zero phonon electronic transitions.

The diamagnetic material, $ThBr_4$, is a new host material for tetravalent ions with an optical and near infrared window from 33000 cm^{-1} to 4000 cm^{-1}. The luminescent properties of pure $ThBr_4$ are well characterized and single crystals doped with various ions can easily be grown.[8-12] $ThBr_4$ has a tetragonal crystal structure isostructural with UCl_4[13,14] that allows the observation of polarized spectra, and its unique axis can easily be obtained by optical methods. The Th^{4+} ion is at a site of D_{2d} symmetry and presumably tetrapositive actinide ions will substitute in these sites. It has also been shown that impurity ions show greater fluorescence in bromide hosts than in oxide or chloride materials.[15] We report preliminary results on the absorption and emission spectrum of U^{4+} diluted in $ThBr_4$. This work represents the first report of the fluorescence spectrum of U^{4+}.

Spectra obtained on the Cary 17 are shown in Fig. 1. In high resolution spectra there were many more lines observed than could possibly be due to zero phonon lines of the $5f^2$ configuration. No constant differences could be found in the complete line list. We have arbitrarily chosen lines with an intensity

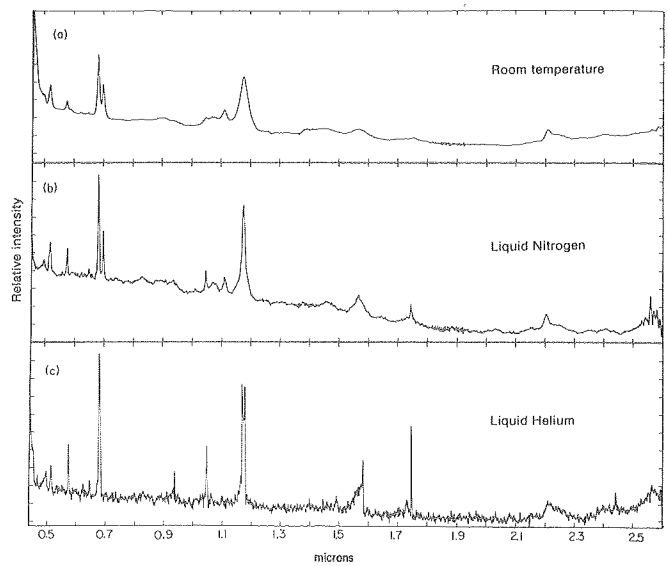

Fig. 1. Absorption spectra of U^{4+}:$ThBr_4$ at various temperatures. (XBL 772-332)

above 2 (on a scale of 1-10) and have used these lines for our fit. There was only one temperature dependent line observed. We assumed the ground state to be a Γ_4 state as found previously[5-7] and assigned a number of transitions that appeared fairly certain. We assigned 23 levels and obtained a mean energy deviation of 89 cm^{-1}. In Table 1 we list the values of the parameters obtained for U^{4+} in UCl_4, $ZrSiO_4$, and in $ThBr_4$.

The free ion parameters we obtained appear to be in line with Hartree-Fock calculations and empirical correlations done by Rajnak.[16] However, the crystal field parameters found are very tentative, and for B^6_0 even the sign of the parameter is in doubt. There does not appear to be any systematic trend for the values of the parameters for U^{4+} in D_{2d} symmetry for the three crystals studied.

The fluorescence spectrum of U^{4+} has been observed for the first time. These emission lines are strongly dependent on temperature and the energy of the exciting radiation. At room temperature there is no fluorescence while at 77 K only three broad features occur at 5190, 6000, and 6980 Å with excitation by the 3663 Å Hg line. At 4.2 K these bands are fully resolved into many lines. The 2537 Å Hg line did not produce fluorescence even though there is a strong absorption band of $ThBr_4$ at this frequency. When the crystal was slowly heated from 77 K to room temperature while being excited by the 3663 Å line, the fluorescence disappeared between 100 to 125 K.

Two emission lines correspond to transitions observed in the absorption spectrum. From our assignments the emission line at 6965 Å (u) corresponds to a transition from the $^3P_0$ to the $^3H_0$ ground state and the line at 5183 Å (a) corresponds to a transition from the $^1I_6$ to the $^3H_4$. Selective excitation of this band at 5100 Å causes transitions to two groups of levels, the ground term $^3H_4$ and another group approximately 4000 cm^{-1} higher in energy.

Table 1. Parameters for the U^{4+} ion in various crystals.

Crystal	UCl_4 [a]	$ZrSiO_4$ [b]	$ThBr_4$ [c]
F^2 [d]	38835	44257	43770 ± 797
F^4	42242	40293	31302 ± 4200
F^6	18883	31287	22248 ± 2425
ζ	1666	1740	1719 ± 44
α	--	22.8	36
β	--	--	-600
γ	--	--	1000
B_0^2	-582	-2000	-919 ± 85
B_0^4	-3027	2000	-305 ± 70
B_4^4 [e]	-5680	5125	-825 ± 137
B_0^6	-2262	-5792	636 ± 917
B_4^6 [e]	795	-428	-1937 ± 202

[a] Reference 5.
[b] Reference 7.
[c] This work, mean energy deviation for 23 levels is 89 cm^{-1}. The errors represent values for the parameters which increase the mean deviation by 5 cm^{-1}.
[d] All units are cm^{-1}.
[e] The signs of both B_4^4 and B_4^6 may be changed simultaneously without changing the calculated energies. See reference 6.

These emission data locate the first excited electronic term that we have assigned to the $^3F_2$. Again as in the absorption spectrum there are many more lines in the emission spectrum than can be reasonably assigned to zero phonon bands of the $5f^2$ configuration.

---

*Permanent Address: Institut de Physique Nucléaire, Université de Paris-Sud, BP No. 1 91406 Orsay, France.

1. W. W. Wagner, N. Edelstein, B. Whittaker and D. Brown, Inorg. Chem. 16, 1021 (1977).

2. D. R. Johnston, R. A. Satten, C. L. Schreiber and E. Y. Wong, J. Chem. Phys. 44, 3141 (1966).

3. R. A. Satten, C. L. Schreiber and E. Y. Wong, J. Chem. Phys. 42, 162 (1965).

4. R. McLaughlin, J. Chem. Phys. 36, 2699 (1962).

5. H. G. Hecht and J. B. Gruber, J. Chem. Phys. 60, 4872 (1974).

6. I. Richman, P. Kisliuk and E. Y. Wong, Phys. Rev. 155, 262 (1967).

7. D. J. Mackey, W. A. Runciman and E. R. Vance, Phys. Rev. B 11, 211 (1975).

8. R. Carlier and M. Genet, C. R. Acad. Sc. 281 C, 671 (1975).

9. M. Genet, M. Hussonnois, J. C. Krupa, R. Guillaumont and R. Carlier, J. of Lumin. 12, 953 (1976).

10. M. Genet, G. Goby, M. Hussonnois, J. C. Krupa and R. Guillaumont, Radiochem. Radioanal. Lett. 23, 19 (1975).

11. M. Genet, G. Goby, M. Hussonnois, J. C. Krupa and R. Guillaumont, Inorg. Nucl. Chem. Lett. 12, 179 (1976).

12. J. C. Krupa, M. Hussonnois and M. Genet, Inorg. Nucl. Chem. Lett. 12, 571 (1976).

13. D. Brown, T. L. Hall and P. T. Moseley, J. Chem. Soc. Dalton Trans. 6, 686 (1973).

14. J. T. Mason, M. C. Jha, D. M. Bailey and P. Chiotti, J. of Less-Common Metals 35, 331 (1974).

15. K. R. German, A. Kiel and H. Guggenheim, Phys. Rev. B 11, 2436 (1975).

16. K. Rajnak, Phys. Rev. A 14, 1979 (1976).

b. Parametric Energy Level Analysis of Np^{3+} in Single Crystals of $LaCl_3$ and $LaBr_3$

R. Sarup,* J. G. Conway, G. Shalimoff, N. Edelstein, W. T. Carnall,† H. M. Crosswhite,† and H. Crosswhite†

Recently it has been demonstrated for some lanthanide ions diluted in $LaCl_3$,[1-3] that when a detailed Hamiltonian is used and the complete matrices are diagonalized, a significant improvement in the fit between experimental and calculated levels can be obtained. The Hamiltonian included the following interactions: 1) two-body and three-body electrostatic operators for configuration mixing, 2) two-body pseudomagnetic (correlated spin-orbit and electrostatic configuration mixing) effective operators, 3) the conventional electrostatic, spin-orbit, and spin-other-orbit operators, and 4) four crystal-field operators for the D_{3h} point group symmetry of $LaCl_3$. The complete matrices for all these operators for the f^4 configuration have been generated and utilized for the analyses of Pm^{3+} and Ho^{3+} (4 holes) in $LaCl_3$.[2,3] Detailed experimental results have been reported for the $5f^4$ ion Np^{3+}, diluted in single crystals of $LaCl_3$[4] and $LaBr_3$,[5] and the analyses of these spectra are summarized in this report.

The original data of Cook[4] was collected on a $LaCl_3$ crystal that contained 5 wt% Np^{3+}. A 1 wt% Np^{3+}:$LaCl_3$ was grown and photographed in the wavelength region from 3365 to 10300 Å. The absorption spectra at 4.2 K were essentially the same in both the crystals. However the more dilute crystal allowed the observation of some new lines in the UV range. All the data utilized for the analysis of Np^{3+}:$LaBr_3$ was obtained from the paper of Krupke and Gruber.[5]

A nineteen parameter least squares fit to 177 observed levels was obtained for $Np^{3+}:LaCl_3$. For $Np^{3+}:LaBr_3$ 142 observed levels were used for the least squares fit. The parameters obtained are given in Table 2. The mean square deviation for $Np^{3+}:LaCl_3$ was 17.5 cm^{-1}; for $Np^{3+}:LaCl_3$ the mean square deviation was 13.0 cm^{-1}. These deviations are 2-3 times greater than that obtained for the fit of 128 levels for $Ho^{3+}:LaCl_3$. The larger deviations for the actinide ion probably reflects the inadequacy of the crystal field parametrization which, because of the greater magnitude of the crystal field in the actinide series, would result in more serious errors.

Table 2. Values of parameters obtained from the empirical fitting procedure.

Parameters	$Np^{3+}:LaCl_3$ (cm^{-1})	$Np^{3+}:LaBr_3$ (cm^{-1})
B_0^2	197(28)	133(27)
B_0^4	-512(46)	-594(46)
B_0^6	-1741(49)	-1317(50)
B_6^6	868(39)	927(32)
F_0	30018(21)	29384(21)
F^2	45132(176)	44437(168)
F^4	36945(244)	36684(237)
F^6	25136(190)	25027(172)
Zeta	1935(2)	1928(2)
α	32.2(3)	31.7(3)
β	-726(19)	-730(18)
γ	1022(63)	1083(56)
T^2	221(24)	259(24)
T^3	71(7)	48(6)
T^4	75(7)	39(6)
T^6	-393(20)	-406(20)
T^7	473(25)	470(25)
T^8	376(21)	382(21)
M^0	.80[a]	.80[a]
M^2	.44[a]	.44[a]
M^4	.31[a]	.31[a]
P^2	816(36)	963(36)
P^4	596[a]	824[a]
P^6	433[a]	568[a]
No. of levels	177	142
Mean error (cm^{-1})	17.5	13.0

[a]The values of these parameters were fixed.

---

*Present Address: Department of Physics, College of the Holy Cross, Worcester, MA 01610.

†Chemistry Division, Argonne National Laboratory, Argonne, IL 60439.

1. H. M. Crosswhite, H. Crosswhite, F. W. Kaseta and R. Sarup, J. Chem. Phys. 64, 1981 (1976).

2. W. T. Carnall, H. Crosswhite, H. M. Crosswhite and J. G. Conway, J. Chem. Phys. 64 3582 (1976).

3. H. M. Crosswhite, H. Crosswhite, N. Edelstein and K. Rajnak, J. Chem. Phys. 67, 3002 (1977).

4. S. P. Cook (Ph.D. thesis), The Johns Hopkins University, Baltimore, Maryland, 1959.

5. W. F. Krupke and J. B. Gruber, J. Chem. Phys. 46, 542 (1967).

c. Parametric Energy Level Analysis of $Ho^{3+}:LaCl_3$

H. M. Crosswhite,* H. Crosswhite,* N. Edelstein, and K. Rajnak†

In two recent papers it has been demonstrated for $Nd^{3+}:LaCl_3$ and $Pm^{3+}:LaCl_3$ that, when a sufficiently detailed Hamiltonian is used and when the complete matrix is diagonalized, significant reduction in the mean error between experimental and calculated energy levels can be realized.[1,2] The Hamiltonian includes (a) two-body[3] and three-body[4] electrostatic operators for configuration mixing and (b) two-body pseudomagnetic (correlated spin-orbit and electrostatic configuration mixing) effective operators,[5] in addition to conventional ones for electrostatic, spin-orbit and spin-other-orbit; plus the usual four which parametrize the crystal field.[6] The latter are single-particle effective operators, approximating the interactions with surrounding ligand ions, which produce a static interaction having D_{3h} point group symmetry. As in the Nd^{3+} and Pm^{3+} cases, there are indications that this assumption is not completely valid, but as before we find that this simplified model is capable (for the $LaCl_3$ host) of yielding mean errors of the order of 10 cm^{-1}. Although the actual symmetry is C_{3h} (permitting the B_6^0 parameter to be complex), we are at liberty to choose our phase such that it is real, making it equivalent to the D_{3h} case for the purpose of energy-level calculations.

D_{3h} selection rules for even-electron configurations provide unequivocable crystal quantum number assignments if the polarization of a line and the crystal quantum number of the initial state are known and if the Zeeman analysis can determine whether or not the final level is degenerate. This was

an important aid in the early analysis and does not depend on detailed accuracy in the Hamiltonian diagonalization.

Rajnak and Krupke[7] attempted to extend the interpretation of Dieke and Pandey's classical work[8] by taking advantage of the relative weakness of the crystal splitting compared to the atomic interactions. By a succession of diagonalizations of the "free-ion" Hamiltonian, then using computed centers of the Stark manifolds and diagonalizations of the crystal field Hamiltonian over the separate manifolds independently, they were able to extend the correct quantum number assignments for those groups of levels that did not interact too strongly. To proceed further it is necessary to perform all of these diagonalizations simultaneously and also to include specific crystal-induced interactions between groups. This requires dealing with matrices of rank up to 171, which is possible with modern computers. As discussed in the $Pm^{3+}(4f^4)$ case,[2] some saving in computer time can be gained by using a truncated intermediate-coupling Hamiltonian spanning a vector space of about half the rank. The final diagonalizations reported here, however, were done using the full Hamiltonian.

Dieke and Pandey were able to make SLJM quantum number assignments to most of the observed levels below 27000 cm^{-1}. None of their assignments below 23000 cm^{-1} have been changed by either the Rajnak-Krupke analysis or the present one, except 22079 (I_3), which in the present analysis has been changed from $\mu = 3^+$ to $\mu = \pm 1$.

In Dieke and Pandey's paper a number of lines are noted as being very sharp, showing no evidence of hyperfine structure. Any absorption from the lowest component z_1 of the ground state can be expected to show hyperfine structure unless the splitting of the upper state should happen to exactly correspond to that of the ground state. Dieke and Pandey have attributed some of these sharp lines to absorption from the first excited component z_2 that has $\mu = 0^+$ with no hyperfine splitting. There are 16 additional lines, 11 of which they ascribe to "unidentified impurities" (2 of which, however, are evidently neodymium). Of the remaining 5 only 2 can be identified with computed level positions and even these must be put down as dubious because of the above considerations.

A few of the groups proved very difficult to fit into the computations. The $^5K_8(H)$ group illustrates this particularly well. The group is experimentally complete and from the polarization and Zeeman data, quantum number assignments can readily be made. The discrepancies between observed and computed values are large and vary systematically between top and bottom of the group. The experimental width of the group is 121 cm^{-1} whereas the computed spread is only 70 cm^{-1}. The $^5K_7(L)$ group is less completely known but the behavior is similar.

This would seem to indicate an inadequacy in the theory. If we add ad hoc parameters that parametrize only the $^5K_2$ spectroscopic term, a much-improved fit can be found. The principal correction is for the sixth-order potentials, which are of the opposite sign and eight times larger than that assumed in the conventional theory. There seem to be similar problems with $^3L(O)$ and $^3M(R)$ groups but not enough detailed data are available for a quantitative determination. None of the levels associated with these three terms have been used in the final parametrization. Of the 168 levels for which correspondence could be made with the theoretical calculations, 40 were not included in the final parameter fit, for reasons given above. For the remaining 128, twenty atomic and crystal field variables were allowed to vary freely, with the results in Table 3.

These are indications that some sort of configuration interaction mechanism is needed beyond those absorbed by the current model. This might arise,

Table 3. Parameters for $Ho^{3+}:LaCl_3$.

Parameter	Run A
EAV	48189(15)
F^2	95409(133)
F^4	67232(111)
F^6	46789(114)
α	17.3(0.2)
β	-624(7)
γ	2084(32)
T^2	287(21)
T^3	37(1)
T^4	98(4)
T^6	-313(7)
T^7	421(13)
T^8	359(24)
ζ	2137(1)
B_0^2	216(9)
B_0^4	-282(14)
B_0^6	-444(13)
B_6^6	297(8)
	M^0 = 3.04(.08)
	M^2 = [1.70]
	M^4 = [1.15]
	P^2 = 528(14)
	P^4 = [396]
	P^6 = [264]
No. of levels	128
Mean error (cm^{-1})	5.2

for example, from second-order perturbation theory by correlated crystal field and Coulomb electronic interactions connecting the $4f^{10}$ configuration with other even ones;[9] or by covalent effects arising from overlap of 4f and ligand orbitals.[10,11] It is not possible from this to pinpoint the source of the trouble but it does give a clear indication that there are limitations to the model.

---

*Chemistry Division, Argonne National Laboratory, Argonne, IL 60439.
†Chemistry Division, Argonne National Laboratory, Argonne, IL 60439, and Kalamazoo College, Kalamazoo, MI 49007.

1. H. M. Crosswhite, Hannah Crosswhite, F. W. Kaseta and R. Sarup, J. Chem. Phys. 64, 1981 (1976).

2. W. T. Carnall, Hannah Crosswhite, H. M. Crosswhite and John G. Conway, J. Chem. Phys. 64, 3582 (1976).

3. B. G. Wybourne, Spectroscopic Properties of Rare Earths (Wiley, New York, 1965).

4. B. R. Judd, Phys. Rev. 141, 4 (1966).

5. B. R. Judd, H. M. Crosswhite and H. Crosswhite, Phys. Rev. 169, 130 (1968); H. Crosswhite and B. R. Judd, Atomic Data 1, 329 (1970).

6. For discussions of these operators, see B. R. Judd, Operator Techniques in Atomic Spectroscopy (McGraw-Hill, New York, 1963); Ref. 3 and Ref. 11.

7. Katheryn Rajnak and William F. Krupke, J. Chem. Phys. 46, 3532 (1967).

8. G. H. Dieke and B. Pandey, J. Chem. Phys. 41, 1952 (1964); G. H. Dieke, Physica 33, 212 (1967).

9. K. Rajnak and B. G. Wybourne, J. Chem. Phys. 41, 565 (1964).

10. D. J. Newman, Adv. Phys. 20, 197 (1971).

11. B. R. Judd, private communication.

d. Ionization Potentials of Rare Earths by Laser Spectroscopy*

J. G. Conway, E. F. Worden,† R. W. Solarz† and J. A. Paisner†

Photoionization and Rydberg spectra of ten lanthanide atoms have been studied using stepwise laser

Table 4. Summary of the ionization potentials by the photoionization and Rydberg methods. Included are the results for Eu, Tm, and Yb by absorption spectroscopy.

Element	Photoionization Threshold	Rydberg Convergence	Rydberg Convergence Others
Ce	5.537(5)	5.5387(4)	
Pr	$5.464(^{+12}_{-2})$	[5.473(10)]	
Nd	5.523(2)	5.5250(6)	
Pm	---	[5.582(10)]	
Sm	5.639(2)	5.6437(6)	
Eu	5.666(4)	5.6704(3)	5.67045(3)[a]
Gd	---	6.1502(6)	
Tb	---	5.8639(6)	
Dy	5.936(3)	5.9390(6)	
Ho	6.017(3)	6.0216(6)	
Er	6.104(2)	6.1077(10)	
Tm	---	---	6.18436(6)[b]
Yb	---	---	6.25394(25)[b]

( ) = error in last digit.
[ ] = extrapolated value.

[a]G. Smith and F. S. Tompkins, Proc. Roy. Soc. (London) A342, 149 (1975).

[b]P. Camus, Thesis, University of Paris, Orsay, 1971.

excitation and ionization methods. The equipment involves a crossed-beam spectrometer in which atoms in an atomic beam are irradiated and eventually ionized by the output of either two or three nitrogen-pumped tunable dye lasers. The detector is a channeltron in a quadrupole mass analyzer. The quadrupole mass analyzer is tuned to the mass of the atom under study and thus discriminates against detection of oxide or other impurities.

The first procedure is to identify the photoionization threshold for one or more excited levels of the atom under study using the two-step method. Laser one populates an excited state and laser two ionizes the atom. The photoionization threshold can usually be obtained to about 30 cm^{-1} by this method. Once this limit is known the search is made for Rydberg levels by tuning in the region of the first excited level of the ion and suitably time-delaying laser two (sometimes three lasers are used in a three-step method). Table 4 is a summary of the ionization potentials derived from both photoionization and Rydberg series.

---

†Lawrence Livermore Laboratory.
*Preprint UCRL-80034, accepted by J. Opt. Soc. Am.

e. Free Ion Studies of Actinides

J. G. Conway and E. F. Worden*

We are continuing work on the free ion spectra of the actinides. We now have a list of about 28,000 lines for Cf measured to an accuracy of ± 0.002 Å. About one-fifth of these lines have been assigned to either the neutral atom or the + 1 ion. Zeeman and isotope data have been obtained but not measured. When this information is needed we look up the line of interest on the plate and measure it. A revised version of the line list also has been prepared in which all lines of very low intensity have been removed. We are about to search this list for new levels after obtaining better values for our known assigned levels.

---

*Lawrence Livermore Laboratory.

f. Optical Beam Foil Studies at the SuperHILAC

J. G. Conway, H. A. Gould and R. Marrus

In a collaborative study[1] with the group at the University of Arizona and workers from University of Tennessee, Oak Ridge, and Brookhaven, we have studied the lifetime of transitions in FeXXIV, Fe^{23+} excited by the interaction of a 491 MeV iron beam. The $^2S_{1/2}$ - $^2P_{1/2}$ transition at 255 Å has a lifetime of 0.55 ± 0.02 ns and the $^2P_{3/2}$ transition at 192 Å has a lifetime of 0.235 ± 0.01 ns. These results are in good agreement with recent relativistic calculations. A Be-like transition in FeXXIII, Fe^{22+}, $2s^2\ ^1S_0$ - $2s2p\ ^3P_1^0$ at 264 Å was measured as 13 ± 4 ns mean life.[1]

A second phase of the program is to determine if there is sufficient light near the foil to record spectra on photographic plates. This technique would enable us to determine wavelengths accurately and also to identify unknown lines. We have obtained two features on a plate after a series of experiments with an argon beam. The lines were due to Li-like Argon XV. The lines are assigned to the $^2S_{1/2}$ - $^2P_{1/2,3/2}$ transitions at 387 and 351 Å. We plan to see if other lines can be observed to develop the method further.

---

1. D. Dietrich, J. A. Leavitt, S. Bashkin, J. G. Conway, H. Gould, D. MacDonald, R. Marrus, B. Johnson and D. J. Pegg, submitted to Phys. Rev. Lett.

g. Spectra of Highly Ionized Ions

J. G. Conway, G. V. Shalimoff, T. Hayhurst, B. Lulu and S. P. Davis

We have been studying the spectrum of Mn VI, $3d^2$. Previous work by W. H. King[1] at LBL had been limited to the 1000 to 2000 Å region. Since then plates have been taken and measured in the 200 Å region and we are now able to accurately relate the upper levels with the ground levels. In addition we have more accurate measurements in the 1000 to 2000 Å region and can improve on the accuracy of King's levels. We are also extending the analysis to new configurations that have transitions in the 200 Å region.

To obtain a better idea as to the location of these new configurations we have measured transitions of the 3d4f configuration of VIV directly to the ground state.[2] The levels have been previously assigned by a cascade from the 3d4f configuration through several intermediate configurations to the ground state. The direct observation of these transitions also supplies us with accurate wavelengths in a region where there are few standards. In fact these new lines supplement van Deurzen's V V line list and together these lists make a good set of wavelengths suitable for standards from 200 to 1000 Å.

---

1. W. H. King, J. of Physics B (accepted for publication).

2. G. V. Shalimoff and J. G. Conway, LBL-6915, J. Opt. Soc. Am. (in press).

4. RESEARCH PLANS FOR CALENDAR YEAR 1978

Norman M. Edelstein, Richard A. Andersen, Neil Bartlett, John G. Conway, Kenneth Raymond, Glenn T. Seaborg, Andrew Streitwieser, Jr., David H. Templeton, and Allan Zalkin

The basic purpose of this project is to study lanthanide and actinide materials in order to provide the basic knowledge necessary for their safe

and economic utilization in present and future technology. This work encompasses related problems of an applied nature in actinide chemistry.

This program includes the preparation of new gaseous, liquid and solid phases, and studies of their physical and chemical properties. Techniques utilized for characterization include x-ray diffraction, optical and vibrational spectroscopy, magnetic resonance, and magnetic susceptibility. Equilibrium and kinetic data for complex formation will be measured. From these complementary studies, new insights into the structural and chemical principles of actinide compounds will be obtained with which to design new synthetic schemes to produce new materials.

A major aspect of our program is the design of sequestering agents for actinide ions that can engulf the ion and generate neutral or negatively charged complexes. A number of new reagents already synthesized will be tested for their ability to complex Pu and other actinides and for their biological effects. Sulfonated derivates that increase the solubility of the sequestering agents will be synthesized and tested. Formation constant data of these ligands with actinide ions will be obtained.

The preparation of new organoactinide compounds and their characterization is of great chemical interest. We have obtained evidence for the existence of half-sandwich compounds of the type $C_8H_8ThCl_2$ and plan to isolate and characterize such structures. To follow up the structural and spectroscopic studies of the bis-cyclobutenouranocene I (Fig. 1) reported last year, we plan the synthesis and NMR spectroscopic study of uranocenes prepared from the cyclopentenocyclooctatetraenes II (Fig. 2) and III (Fig. 3). These compounds are significant because the protons are expected to be rigidly held in fixed locations to assist in the NMR analyses. The preparation in progress of the mesityluranocene IV (Fig. 4) should tell about barriers to rotation between rings and is part of the program to design stable sterically congested organouranium compounds. We plan to supplement these experimental studies with theoretical calculations to follow up our recent successful Xα-scattered wave SCF calculations of thorocene and uranocene. Finally, we plan to study the potential use of uranium metal as a reagent in organic chemistry.

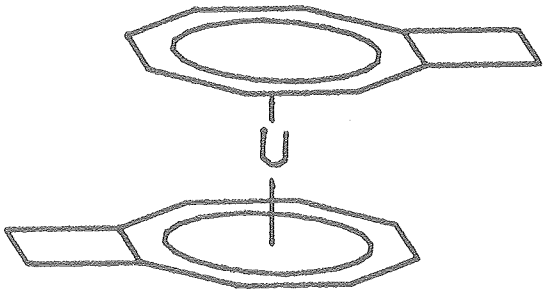

Fig. 1. Bis-cyclobutenouranocene I. (XBL 7712-10952)

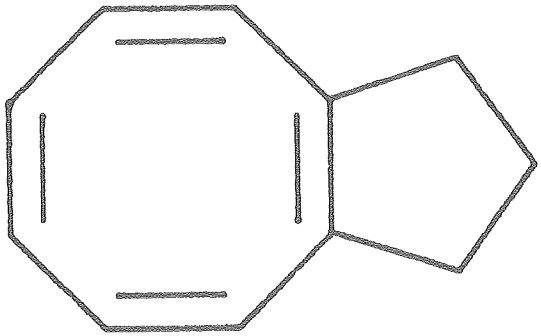

Fig. 2. Cyclopentenocyclooctatetraenes II. (XBL 7712-10953)

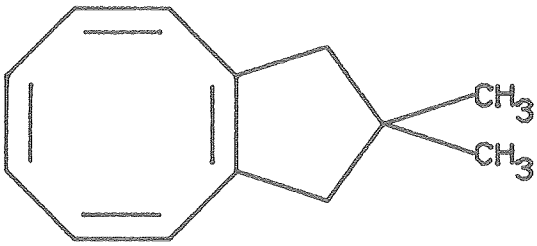

Fig. 3. Cyclopentenocyclooctatetraenes III. (XBL 7712-10954)

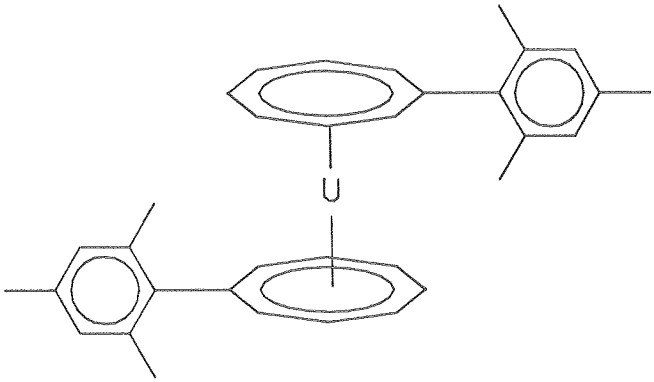

Fig. 4. Mesityluranocene IV. (XBL 7712-10955)

Studies on the preparation and physical studies of new actinide amides, alkoxides, alkyls, and borohydrides will continue. The properties of neptunium and plutonium borohydrides, liquids at room temperature, will be investigated in great detail, including x-ray diffraction experiments at low temperature. We will continue to attempt the preparation of discrete Np VII species such as $NpOF_5$, NpF_7^-, and NpF_6^+. The powerful oxidizers KrF_2 and XeF_6 in combination with fluorine will be exploited towards these ends.

The spectroscopic program will emphasize the crystal spectra of actinide and lanthanide ions in a

variety of host crystals. Special attention will be paid to the fluorescence of actinide ions in single crystal hosts excited by a laser. Studies of the spectra of highly ionized atoms will be made using the SuperHILAC and its injectors as sources. Work will continue on the classification of the emission spectra of Cf.

A new program just started is to explore the application of synchrotron radiation (at the Stanford Synchrotron Radiation Laboratory) as a source of x rays for diffraction experiments with heavy element compounds. The immediate objective is to measure both the real and imaginary components (f' and f'') of the dispersion correction (anomalous scattering) for cesium atoms at the L absorption edges, using diffractometer techniques and a crystal of cesium hydrogen tartrate.

5. 1977 PUBLICATIONS AND REPORTS

Norman M. Edelstein, Richard A. Anderson, Neil Bartlett, John G. Conway, Kenneth Raymond, Glenn T. Seaborg, Andrew Streitwieser, Jr., David H. Templeton, Allan Zalkin and Associates

Journals

1. F. R. Fronczek, G. W. Halstead and K. N. Raymond, The Synthesis, Crystal Structure, and Reactions of an Actinide Metallocarborane Complex, Bis(η^5-(3)-1, 2-dicarbollyl)dichlorouranium(IV) Dianion, $[U(C_2B_9H_{11})_2Cl_2]^{2-}$, J. Am. Chem. Soc. 99, 1769).*

2. E. C. Baker and K. N. Raymond, Synthetic, Structural, and Magnetic Properties of the Pyrazine-Bridged Lanthanide Organometallic Complex μ-Pyrazine-bis[tris-(cyclopentadienide)ytterbium(III)], $(C_5H_5)_3Yb(NC_4H_4N)$-$Yb(C_5H_5)_3$, Inorg. Chem. 16, 2710 (1977).*

3. C. A. Harmon, D. P. Bauer, S. R. Berryhill, K. Hagiwara and A. Streitwieser, Jr., Substituted Uranocenes with Alkoxy and Amino Groups, Inorg. Chem. 16, 2143 (1977).*

4. W. Wagner, N. Edelstein, B. Whittaker and D. Brown, Spectral Properties of $(Et_4N)_2UI_6$ and $(Et_4N)_2UF_6$, Inorg. Chem. 16, 1021 (1977).

5. M. Genet, P. Delamoye, N. Edelstein, and J. Conway, Absorption and Emission Spectra of U^{4+} Diluted in $ThBr_4$ Single Crystals, J. Chem. Phys. 67, 1620 (1977).

6. Norman M. Edelstein, Covalency in Octahedrally Coordinated $5f^1$ Complexes, Revue de Chimie Minerale 14, 149 (1977).

7. H. M. Crosswhite, H. Crosswhite, N. Edelstein and K. Rajnak, Parametric Energy Level Analysis of Ho^{3+}:$LaCl_3$, J. Chem. Phys. 67, 3002 (1977).

8. J. G. Reynolds and N. M. Edelstein, The Syntheses, Optical and Magnetic Properties of Tetrakis (Di N-Propylamido)uranium((V), Tetrakis(Di N-butylamido)uranium(IV), Tetrakis(Di N-propylamido) thorium(IV), and Tetrakis(Di N-butylamido)thorium(IV), Volatile Liquid Amides, Inorg. Chem. 16, 2822 (1977).

9. S. L. Edwards, G. Chapuis, D. H. Templeton and A. Zalkin, An Antitumor Agent, 2-(3,3-dimethyl-1-triazeno)phenyl-1-carboxamide, Acta Cryst. B 33, 276 (1977).

10. G. Chapuis, A. Zalkin and D. H. Templeton, Sodium 2-Methyl-6-endo-hydroxy-bicylo[2.2.1] heptane-2-endo-carboxylate trihydrate, Acta Cryst. B 33, 560 (1977).

11. N. J. Mammano, D. H. Templeton and A. Zalin, Lithium Bis(iminodiacetato) Nickelate (II) Tetrahydrate and Cesium Bis(iminodiacetato)Nickelate (II) Tetrahydrate, Acta Cryst. B 33, 1251 (1977).

12. G. Chapuis, A. Zalkin, and D. H. Templeton, 2-exo-hydroxy-7-methylbicyclo[2.2.1] heptane-7-syn-carboxylic Acid, Acta Cryst. B 33, 1290 (1977).

13. A. J. Olson, D. H. Templeton, and L. K. Templeton, 6-endo-Hydroxy-3-endo-aminomethylbicyclo[2.2.1] heptane-2-endo-carboxylic Acid Lactam, Acta Cryst. B 33, 2266 (1977).

14. A. G. Landers, M. W. Lynch, S. B. Raaberg, A. L. Rheingold, J. E. Lewis, N. J. Mammano and A. Zalkin, Preparation of Ferrocenium Phosphorus, Arsenic, Antimony and Bismuth Halides, The Structure of Ferrocenium Tetrachlorobismuthate, Chemical Communications, 931 (1976).

15. N. J. Mammano, A. Zalkin, A. Landers and R. L. Rheingold, The Crystal and Molecular Structure of Ferricenium Tetrachlorobismuthate, Inorg. Chem. 16, 297 (1977).

16. J. G. Reynolds, A. Zalkin, D. H. Templeton and N. M. Edelstein, Synthesis, Crustal Structure, and Optical and Magentic Properties of Tris[bis-N,N'-dimethylethylenediamido)uranium(IV)], a Trimeric Complex, Inorg. Chem. 16, 599 (1977).

17. J. G. Reynolds, A. Zalkin, D. H. Templeton and N. M. Edelstein, Synthesis and Crystal Structure of Tetrakis (diphenylamido)uranium(IV) and Bis(-oxo-tris(diphenylamido)uranium(IV) Lithium Dietherate, Inorg. Chem. 16, 1090 (1977).

18. J. G. Reynolds, A. Zalkin, D. H. Templeton and N. M. Edelstein, The Crystal Structure of Tetra (bis(N,N'-dimethylethylenediamido)uranium(IV), A Tetrameric Globular Complex, Inorg. Chem. 16, 1858 (1977).

19. E. F. Worden, E. K. Hulet, R. G. Gutmacher and J. G. Conway, The Emission Spectra of Curium, Atomic Data and Nuclear Data Tables 18, 459 (1976).

20. J. G. Conway, E. F. Worden, J. Blaise and J. Verges, The Infrared Spectrum of California-249, Spectrochim. Acta 32B, 97 (1977).

21. J. G. Conway, E. F. Worden, J. Blaise, P. Camus and J. Verges, The I.R. Spectrum of Berkelium-249, Spectrochim. Acta 32B, 101 (1977).

---

* Partially supported by NSF.

LBL and Other Reports

1. R. R. Rietz, N. M. Edelstein, H. W. Ruben, D. H. Templeton and A. Zalkin, Preparation and Crystal Structure of Uranium (IV) Borohydride Di-tetrahydrofuran, $U(BH_4)_4 \cdot 2(OC_4H_8)$, LBL-6626, Inorg. Chem. (in press).

2. R. R. Rietz, A. Zalkin, D. H. Templeton, N. M. Edelstein and L. K. Templeton, Preparation and Molecular and Crystal Structures of Uranium (IV) Borohydride Dimethyletherate and Uranium (IV) Borohydride Diethyletherate, LBL-6639, Inorg. Chem. (in press).

3. A. Zalkin, R. R. Rietz, D. H. Templeton and N. M. Edelstein, The Preparation and Crystal Structure of Uranium (IV) Borohydride n-Propyletherate, LBL-6641, Inorg. Chem. (in press).

4. J. G. Reynolds, A. Zalkin and D.H. Templeton, Structure of Uranyl Nitrate Di-Tetrahydrofuran, LBL-6642, Inorg. Chem. (in press).

4. J. G. Reynolds, A. Zalkin and D. H. Templeton, Structure of Uranyl Nitrate Di-Tetrahydrofuran, LBL-6642, Inorg. Chem. (in press).

5. L. K. Templeton and D. H. Templeton, Cesium Hydrogen Tartrate and Anomalous Dispersion of Cesium, LBL-6667, Acta Cryst. (in press).

6. A. Zalkin, D. . Ward, R. N. Biagioni, D. H. Templeton , and N. Bartlett, The Crystal Structure of $[XeF^+][AsF_6^-]$, LBL-6671, Inorg. Chem. (in press).

7. R. H. Banks, N. M. Edelstein, R. R. Rietz, D. H. Templeton and A. Zalkin, Preparation and Properties of the Actinide Borohydrides: $Pa(BH_4)_4$, $Np(BH_4)_4$, and $Pu(BH_4)_4$, LBL-6958, submitted to J. Am. Chem. Soc.

8. R. A. Anderson, D. H. Templeton and A. Zalkin, Synthesis and Crystal Structure of a Neodymium Isopropoxide Cloride, $Nd_6[OCH(CH_3)_2]_{17}Cl$, LBL-6988, submitted to Inorg. Chem.

9. F. L. Weitl, K. N. Raymond, W. L. Smith, and T. R. Howard, Specific Sequestering Agents for the Actinides. 1. N,N',N'',N'''-Tetra(2,3-dihydroxybenzoyl)tetraazacyclo-tetra- and hexadecanes, LBL-6231, J. Am. Chem. Soc., accepted for publication.

10. W. L. Smith, J. D. Ekstrand and K. N. Raymond, The High-Yield Synthesis and Crystal Structure of 1,5,9,13-Tetraazacyclohexadecane (16-Cyclam), submitted to J. Am. Chem. Soc.

11. E. F. Worden, R. W. Solarz, J. A. Paisner and J. G. Conway, First Ionization Potentials of Lanthanide by Laser Spectroscopy, UCRL-80034, J. Opt. Soc. Am. (in press).

12. G. V. Shalimoff and J. G. Conway, The $3d^2$-3d4f Transitions in V, IV, LBL-6915, J. Opt. Soc. Am. (in press).

13. W. H. King, The Sixth Spectrum of Manganese (MN VI), J. of Phys. (in press).

Theses

1. J. R. Hauser, I. The Indicatrix of Composite Crystals. II. Calculation of the Indicatrix of Silicate Minerals with the Classical Point-Dipole Model. III. The Structure of Two Sodium-Uranyl Fluorides, LBL-6233, April 1977 (Ph.D. thesis).

2. E. M. Price, Crystallographic Studies of Sodium Thorium Fluoride Precipitates and of a Thioniabicyclo Compound, LBL-5773, December 1976 (M.S. thesis).

Papers Presented

1. J. A. Paisner, R. W. Solarz, E. F. Worden and J. G. Conway, Identification of Rydberg States in Atomic Lanthanides and Actinides. Third International Conference on Laser Spectroscopy, Jackson Hole, Wyoming, July 4-8, 1977.

2. E. F. Worden, R. W. Solarz, J. A. Paisner, K. Rajnak, B. W. Shore and J. G. Conway, Rydberg Series in the Lanthanide and Actinide Observed by Stepwise Laser Excitation, International Conference on Atomic and Molecular States Coupled to a Continuum Highly Excited Atoms and Molecules, June 13-17, 1977, Aussois, France.

3. R. W. Solarz, J. A. Paisner, E. F. Worden, J.G. Conway, Rydberg Series in the Lanthanides, Fourth International Conference on Multiphoton Processes Sponsored by International Union of Pure and Applied Physics, June 6-9, 1977, Rochester, New York.

4. E. F. Worden, R. W. Solarz, J. A. Paisner, J. G. Conway, Accurate Ionization Potentials of Lanthanide Atoms by Laser Spectroscopy, Optical Society of America, Toronto, October 10-14, 1977.

5. R. R. Rietz, N. Edelstein, D. H. Templeton and A. Zalkin, Preparation and Structural Characterization of Volatile Ether Complexes of Uranium Borohydride, American Chemical Society Meeting, New Orleans, Louisiana, March 21-25, 1977.

6. A. Zalkin, R. R. Rietz, N. Edelstein, and D. H. Templeton, Structures of Two Etherates of Uranium Borohydride, $U(BH_4)_4 \cdot 2(C_4H_8O)$ and $U(BH_4)_4 \cdot O(CH_3)_2$, American Crystallographic Association Meeting, Pacific Grove, California, February 21-25, 1977.

7. Edgar C. Baker and Kenneth N. Raymond, Synthesis, Structure and Magnetic Properties of an Organometallic Pyrazine-Bridged Lanthanide Dimer, $Cp_3Yb(NC_4H_4N)YbCp_3$. American Crystallographic Association Meeting, Asilomar, California, February 21-25, 1977.

8. Alex Avdeef, Thomas L. Bregante, Jerome J. Bucher, Norman M. Edelstein and Kennth N. Raymond, The Enormous Stability Constants of Actinide(IV)-Catechol Complexes in Aqueous Solution. American Chemical Society Meeting, New Orleans, Louisiana, March 20-25, 1977.

9. Frederick L. Weitl and Kenneth N. Raymond, Design and Synthesis of Model Plutonium Ion Sequestering Agents. Pacific Conference on Chemistry, West Coast Regional Meeting of the American Chemical Society, Anaheim, California, October 14-19, 1977.

Invited Lectures

1. D. H. Templeton, Symmetry and Disorder in Crystal Structures, Symposium on Structure and Dynamics in Chemistry, Uppsala University 5th Centenary, Uppsala, Sweden, September 22-27, 1977.

2. Invited talks on uranocene chemistry were given by Andrew Streitwieser, Jr. at Columbia Univ,; Hunter College of the City University of N.Y., N.Y. City; The Ohio State Univ., Columbus, Ohio, San Francisco State University, San Francisco; Allied Chemical Co., Morristown, N.H.; and Ithaca College, Ithaca, N.Y.

3. An invited plenary address, "Aromatic Organometallic Chemistry", was given at the Third International Symposium on Novel Aromatic Compounds, San Francisco, by Andrew Streitwieser, Jr.

IV.

Advanced Isotope Separation Technology

1. LASER CONCEPTS

a. Selective Photochemistry

C. Bradley Moore, Principal Investigator

1. INFRARED MULTIPHOTON PROCESSES IN FORMALDEHYDE

Michael R. Berman

Infrared multiphoton processes have sparked considerable interest primarily due to their application to isotope separation and the possibility of promoting mode specific chemistry. During infrared multiphoton excitation and dissociation large amounts of vibrational energy are stored in a molecule. It is of considerable importance to know the dynamics of this excited molecule. In other words, how does this energy become distributed among the vibrational modes of the molecule. We are studying this problem in formaldehyde whose relatively small size permits distinct spectroscopic identification of its vibrational modes. In formaldehyde and deuterated formaldehydes we can also study the choice of dissociative pathway, H + HCO vs. H_2 + CO, which gives information on the rate of energy redistribution and the shape of the ground state potential surface.

Initially, multiphoton dissociation of HDCO and D_2CO was demonstrated at 944 cm^{-1}. We further characterized the dissociation behavior of D_2CO by a wavelength dependent quantum yield study. Samples were photolyzed with a grating tuned TEA CO_2 laser and the D_2 and CO photolysis products were quantitatively detected using gas chromatography. The most efficient laser wavelength for dissociation was found to be the P(14) 001 to 100 line at 949.5 cm^{-1}. Dissociation efficiency for 8 Torr D_2CO was 2×10^5 photons incident on the cell per molecule dissociated.

The two main photochemical routes available are:

$$D_2CO + nh\nu \rightarrow D_2 + CO \qquad (1)$$

$$D_2CO + nh\nu \rightarrow D + DCO. \qquad (2)$$

In pure D_2CO both routes ultimately yield equal quantities of D_2 and CO as the sole products. The molecular dissociation mechanism (1) is the lower energy pathway for ultraviolet photochemistry and would be favored by a statistical process.

In order to determine the operative mechanism small quantities (2 to 10 Torr) of a radical scavenger, nitric oxide, are added to the photolysis cell. If the radical pathway is favored, the NO will react with DCO radicals produced before two DCO's can recombine.

PURE D_2CO: $2DCO \rightarrow D_2CO + CO$

WITH NO: $2DCO + 2NO \rightarrow 2DNO + 2CO$.

A change in the relative production of D_2 and CO would result. In experiments with 8 Torr of D_2CO and low NO pressure we have found the molecular mechanism to be the only operative pathway. When higher NO pressures were used, the apparent onset of radical processes was seen. We believe this results from reactions such as

$$D_2CO^{\dagger} + NO \rightarrow DNO + DCO.$$

This possibility of IR multiphoton-induced reaction will be explored further.

Internal energy distribution and the rate of internal energy transfer during multiphoton excitation of D_2CO is being studied by observing the population of vibrational levels with time-resolved infrared fluorescence. Using a Ge:Hg detector and appropriate filters, fluorescence from the C - O stretch at 6 μ and the C - D stretches at 5 μ has been individually monitored. Under conditions of multiphoton excitation very fast rising emission has been observed and is now under investigation. By measuring the risetime of the emission from different modes we can study the internal energy transfer during multiphoton processes. Pressure dependent studies will give the effects of collisions. Through these studies we hope to obtain a better understanding of multiphoton excitation and dissociation.

2. ICl^* $(A^3\Pi_1, v')$ + H_2 PHOTOCHEMISTRY

Stephen J. Harris[†]

The subject of laser initiated photochemistry has received considerable attention in recent years. The hope is that if reaction rate constants and accessibility to various reactive trajectories are a strong function of internal excitation of reactants, then different chemical reaction paths can be accessed by selective laser excitation. Furthermore, if the reaction is a four-center, concerted, bimolecular reaction, then isotope scrambling and chain reaction processes involving radicals are avoided. A selective,

bimolecular reaction is an ideal type of reaction for isotope separation. The system

$$ICl^* + H_2 \xrightarrow{k_1} HI + HCl \qquad (1)$$

is such a reaction.

The rate of this laser-induced chemical reaction has been measured as a function of ICl* vibrational energy. Like the $I_2 + H_2$ and $Cl_2 + H_2$ systems, there is no dark reaction. The reaction appears similar to $I_2^*(I^1\Sigma_u^+) + H_2$.[1-3] Other examples are reported that involve electronic excitation of I_2.[4]

ICl (~ 5 or 9 Torr), prepared from I_2 and Cl_2,[5,6] and H_2 (10 to 600 Torr) are photolyzed for about 90 min in a 1 m quartz reaction cell by a Chromatix CMX-4 flashlamp-pumped dye laser ($\Delta\nu = 0.3$ cm^{-1}). A calibrated thermopile monitors the laser power. Approximately 60% absorption of the laser light is measured at $I^{35}Cl$ A-X bandheads. (Excitation of bandheads avoids hot bands.)

After photolysis HCl is distilled from the reactants. Care is taken to eliminate the Cl_2 that is necessarily present.[5] HCl pressure is measured with a Validyne capacitance manometer. Mass spectra confirm that the product is HCl. HI and ICl react to form HCl and I_2; thus, two molecules of HCl are formed in each reaction.

ICl* is removed by reaction (1) and by quenching:

$$ICl^* + ICl \rightarrow ICl + ICl \qquad (2)$$

$$ICl^* + H_2 \rightarrow ICl + H_2 \,. \qquad (3)$$

The quantum yield for reaction is

$$\Phi = \frac{(\text{HCl produced})/2}{\text{photons absorbed}} = \frac{k_1\,[H_2]}{k_2[ICl] + (k_1+k_3)[H_2]} \,. \qquad (4)$$

A Stern-Volmer plot of ICl* fluorescence lifetime vs. H_2 pressure gives $(k_1 + k_3) = 1.5 \times 10^{-11}$ cm^3 molecule^{-1} sec^{-1}. Similarly, Steinfeld[7] has measured $k_2 = 2.3 \times 10^{-10}$ cm^3 molecule^{-1} sec^{-1}; both are nearly independent of wavelength. k_1 is determined from the quantum yield, Fig. 1. The solid curve is a least square fit to the data using Eq. (4). Note that a two-parameter curve is fit with a single free parameter. The result, $k_1 = (9.0 \pm 0.8) \times 10^{-14}$ cm^3 molecule^{-1} sec^{-1} (90% confidence limits), corresponds to 9000 gas kinetic collisions. Assuming that the pre-exponential factor does not exceed the gas kinetic collision frequency, the activation energy is less than 5.5 kcal/mole. The reaction rate is quite large; the quantum yield is low because the quenching rate is even larger.

A single vibrational level of ICl* is excited initially, but vibrationally inelastic collisions spread the population distribution so that

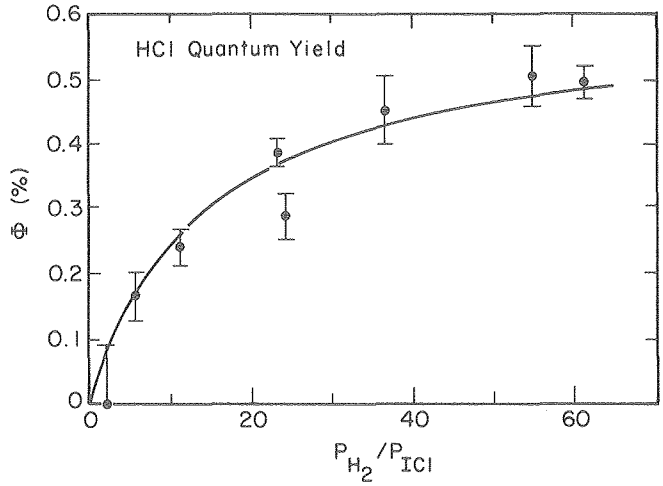

Fig. 1. Solid points are data without Ar, $P_{ICl} = 8.9$ Torr; the solid line is a fit to these points. Here, $P_{ICl} = 4.9$ Torr except for lowest pressure point, where $P_{ICl} = 8.9$ Torr. $\lambda = 616.8$ nm, exciting 1200 cm^{-1} below dissociation.
(XBL 782-7335)

reaction may occur from other levels. The extent of this spread, which is limited by quenching, can be estimated by comparison with the analogous H_2-$I_2^*(B^3\Pi_0, v' = 15)$ system.[8] Here, V-T events occur with a cross section of about 1/6 gas kinetic. This is expected to be an upper limit to the V-T rate in ICl*-H_2, since the energy level spacing in ICl* is greater than that in I_2^*. The result is that about 75% of the ICl* that reacts does so from within three-vibrational levels of the originally excited level. From the relative intensities of the resolved ICl* fluorescence spectrum and calculated Franck Condon factors, it was determined that for excitation to $v' = 18$, the time-averaged fractional populations are $v' = 16$, 5%; $v' = 17$, 14%; $v' = 18$, 42%; $v' = 19$, 24%; $v' = 20$, 15%. Thus approximately 80% of the fluorescence comes from $v' = 18 \pm 1$, in good agreement with the above estimate. Figure 2 shows the quantum yield (proportional to k_1) as a function of the excitation energy. About 600 cm^{-1}(3 kT) of vibrational energy increases the rate constant by a factor of e.[9]

Halogen atoms, formed from sufficiently energetic collisions of ICl*, could conceivably be contributing to the measured quantum yields. The dissociation probability, however, should decrease by about 1/e for each 200 cm^{-1} (kT) of vibrational energy,[10] dashed line in Fig. 2. I atoms formed simply recombine, and Cl atoms are mostly scavenged by the fast reaction $Cl + ICl \rightarrow Cl_2 + I$:[11] when ICl is excited 1400 cm^{-1} above dissociation there is a low quantum yield of HCl (Fig. 2), implying that for excitation well below dissociation, radical reactions are not important. Finally, a quenching gas may be added to the system. Experiments with ICl:H_2:Ar of 1:25:110, 1:19:95, 1:14:69, and 1:9:41 at $\lambda = 616.8$ nm ($v' = 15$) give quantum yields in very good agreement with those predicted from the

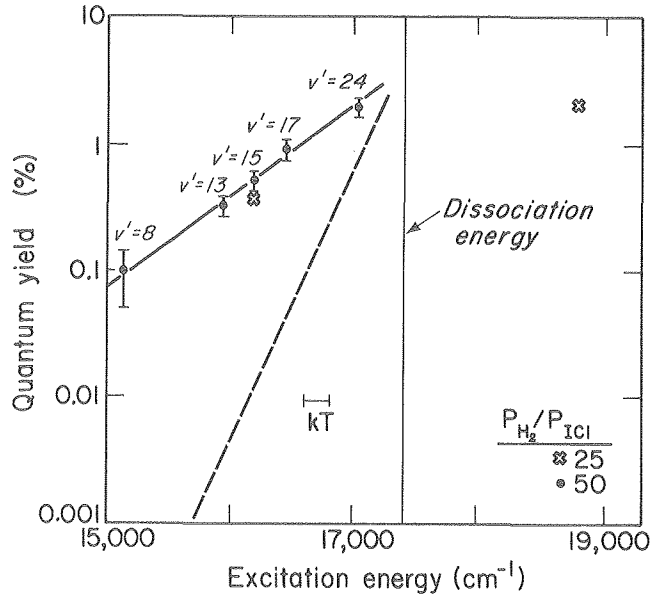

Fig. 2. Quantum yield vs excitation energy. P_{ICl} = 8.9 Torr. (XBL 774-722A)

measured quenching rate constant for ICl* by Ar, $(4.9 \pm .5) \times 10^{-12}$ cm^3 molecule^{-1} sec^{-1} (dashed line in Fig. 1). These results prove conclusively that radicals are not important, since Ar should not inhibit their reactions, and that ICl*($A^3\Pi_1$) is the reactive species.

The reactivity of ICl* may be due to the fact that the dipole moment changes sign upon excitation[12] to I^-Cl^+. The positive Cl atom, with its partially filled valence shell, might be expected to be very reactive. Experiments are in progress to learn more about the reactivity of this molecule.

---

†Fellow of the Miller Institute for Basic Research in Science.

1. G. M. Harris and J. E. Willard, J. Am. Chem. Soc. 76, 4678 (1954).
2. T. A. Grover and J. E. Willard, J. Am. Chem. Soc. 82, 3816 (1960).
3. L. C. Glasgow and J. E. Willard, J. Phys. Chem. 77, 1585 (1973).
4. V. I. Balykin, V. S. Letokhov, V. I. Mishin and V. A. Semchishen, Chem. Phys. 17, 111 (1976); F. Engelke, J. C. Whitehead and R. N. Zare, Faraday Discussions on Potential Energy Surfaces, Vol. 62, (1976), (in press).
5. G. V. Calder and W. F. Giauque, J. Phys. Chem. 69, 2443 (1965).
6. R. E. Buckles and J. M. Bader, Inorg. Synth. 9, 130 (1967) and references therein.
7. G. W. Holleman and J. I. Steinfeld, Chem. Phys. Lett. 12, 431 (1971).
8. R. Brown and W. Klemperer, J. Chem. Phys. 41, 3072 (1964).
9. M. H. Mok and J. C. Polanyi, J. Chem. Phys. 53, 4588 (1970).
10. A. Gelb, R. Kapral and G. Burns, J. Chem. Phys. 59, 2980 (1973).
11. M. A. A. Clyne and H. W. Cruse, J. Chem. Soc. Faraday Trans. II, 68, 1377 (1972).
12. F. E. Cummings and W. Klemperer, J. Chem. Phys. 60, 2035 (1974).

3. APPEARANCE RATES OF PHOTOCHEMICAL PRODUCTS IN FORMALDEHYDE PHOTODISSOCIATION*

Mohammad B. Zughul

Optical radiation in the near ultraviolet raises formaldehyde into the first excited singlet state from which it may predissociate into either molecular (H_2 + CO) or radical (H + HCO) products. Although much work has been done on the energy dependence of its radiative lifetimes and photochemical quantum yields, the mechanism by which formaldehyde predissociates is still unknown.

In a recent study of the energy distribution among molecular photoproducts, Houston measured the appearance rate of CO following 337 Nm excitation and found it to be much slower than the corresponding fluorescence decay rates from the first excited singlet state for both H_2CO and D_2CO.[1] This led to the conclusion that dissociation occurs through an intermediate state. The identity of this state (triplet, vibrationally excited ground, the valence isomer HCOH, or something else) is unknown. Also, it is not yet known whether radical dissociation occurs directly or through an intermediate state.

We have measured the appearance rate of molecular products at much lower energy of excitation by monitoring the intensity of CO IR fluorescence as a function of time. Using the third harmonic of a Nd:YAG laser at 355 nm (~ 28,200 cm^{-1}), H_2CO is excited to the origin of the first excited singlet (4_0^1); this subsequently predissociates giving off CO with a detectable population of the first vibrational level (v = 1). Figure 1 shows the pressure dependence of CO appearance rates; the straight line is a least square fit of data with a slope of 1.7 ± 0.3 μsec^{-1} Torr^{-1}. The rate is the same as that obtained earlier at 337 Nm, 1.65 ± 0.12 μsec^{-1} Torr^{-1}, thus indicating an energy barrier for molecular dissociation less than 28,200 cm^{-1}.

Appearance rates at higher energies of excitation (where radical production begins to compete) are needed. This will show whether the intermediate state remains important above the threshold for H + HCO and H + H + CO production. The magnitude of radical appearance rates will indicate whether radicals originate from the same electronic state as molecular products. The energy dependence of the molecular production rate will help establish the shape of the potential surface for dissociation. Attempts are now under way to measure rates at 299 and 266 nm for CO production. A search for the intermediate

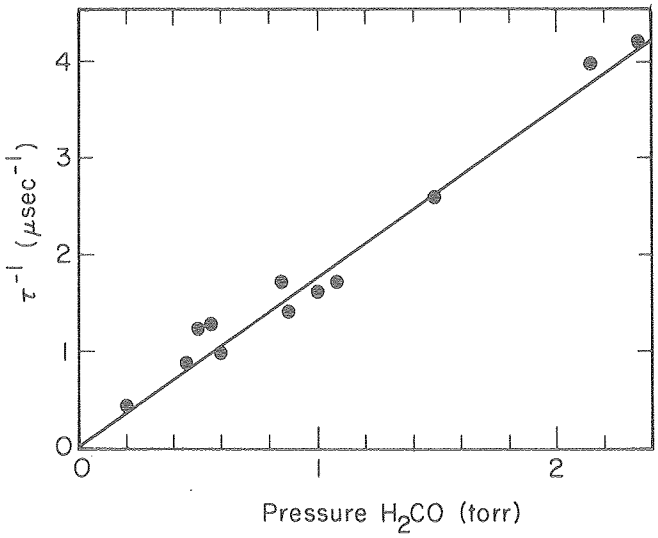

Fig. 1. Appearance rate of CO produced from H_2CO by photolysis at 355 nm. (XBL 781-70)

state(s) and HCO IR fluorescence will also be made. A study of the effect of some foreign gases on appearance rates is now in progress. These results will help to elucidate the non-radiative photophysical processes in formaldehyde, which will in turn serve as a key test for unproven theories of radiationless processes in intermediate size molecules.

---

*Partially supportes by the National Science Foundation and the Army Research Office, Triangle Park, NC.

1. P. L. Houston and C. B. Moore, J. Chem. Phys. 65, 757 (1976).

4. FLUORESCENCE DECAY TIMES AND ENERGY TRANSFER IN THE $\tilde{A}\ ^1A_2$ STATE OF FORMALDEHYDE*

J. Weisshaar, A. Baronavski and A. Cabello-Albala

Fluorescence lifetimes of H_2CO and D_2CO vapor have been measured as a function of pressure following selective laser excitation to either the 4^0 or 4^1 vibronic levels of the S_1 ($\tilde{A}\ ^1A_2$) electronic state. Selective excitation to particular rR sub-band heads was achieved with a N_2 laser pumped dye laser and two amplifier stages modeled after that of Hänsch et al.[1] The dye laser pulses were ~ 5 nsec long and ~ 0.2 Å FWHM spectral width. In addition, the 4^1_0 band of H_2CO was pumped with a frequency tripled Nd:YAG laser at 3547 Å. Fluorescence from either 4^0 or 4^1 was selectively viewed through various bandpass interference filters by a photomultiplier tube.

For D_2CO, it was possible to measure the rate constant for collisional energy transfer between the 4^0 and 4^1 levels, which are separated by only 69 cm^{-1}, by exciting the 4^0 level and observing the risetime of the 4^1 fluorescence as a function of pressure. The $4^0 \rightarrow 4^1$ rate constant is 21 ± 3 μsec^{-1} Torr^{-1}, or twice the gas kinetic rate of 10.6 μsec^{-1} Torr^{-1}.

The Stern-Volmer plot of $1/\tau$ vs pressure for D_2CO is linear from 0.1 to 5 Torr, with slope 0.96 ± 0.06 μsec^{-1} Torr^{-1}. Below 0.1 Torr there is significant negative curvature that is not adequately explained by 4^0 - 4^1 energy transfer alone. All decays are exponential except for the effects of energy transfer. The zero pressure lifetimes of the 4^0 and 4^1 vibronic levels are 7.8 ± 0.7 μsec and 6.0 ± 0.4 μsec, respectively. These values are comparable to the estimated radiative lifetime.

In contrast, the H_2CO fluorescence decays are biexponential below 0.1 Torr, at pressures for which energy transfer is negligible. The Stern-Volmer plots of $1/\tau_s$ (the slow decay component) vs pressure for excitation to 4^1 and to the K'' = 4 rR sub-band of 4^0 are shown in Fig. 1. The negative curvature below 1 Torr is quite dramatic. The plots linearize at very low pressures (< 20 mTorr) and exhibit low pressure slopes that are 7 to 15

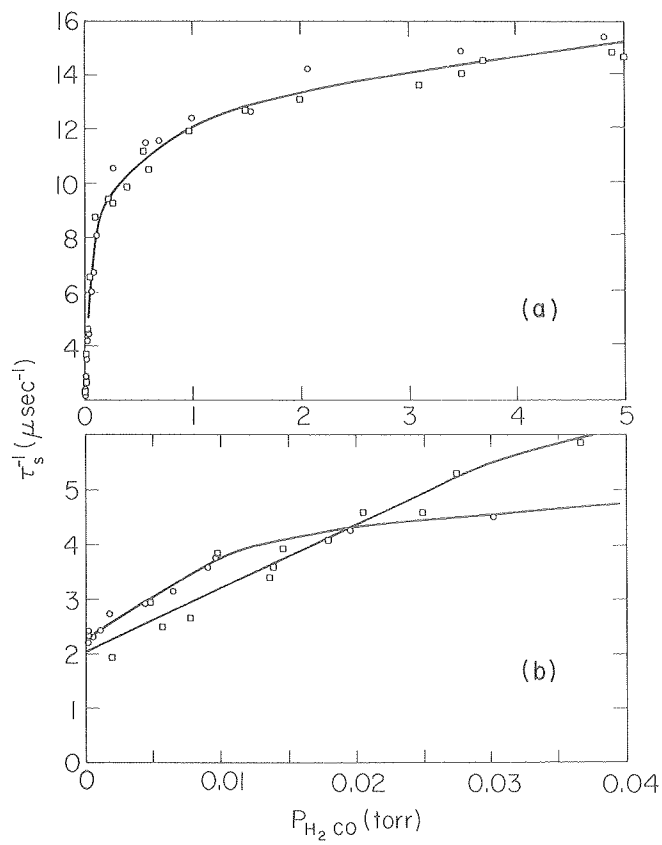

Fig. 1. Stern-Volmer plot for the slow decay component of H_2CO excited to 4^1 (circles) and to the K'' = 4 rR sub-band of 4^0 (squares). (XBL 7710-2038)

times the gas kinetic rate. The fast decay rate $1/\tau_f$, which is not due to energy transfer, also quenches very rapidly with pressure (Fig. 2) and vanishes at pressures $\gtrsim 0.1$ Torr. The zero pressure lifetimes and low pressure slopes of both the fast and slow components are summarized for various wavelengths in Table 1. The lifetimes and slopes depend significantly on the rR sub-band excited within 4^0_1, and hence on the K' rotational quantum number.

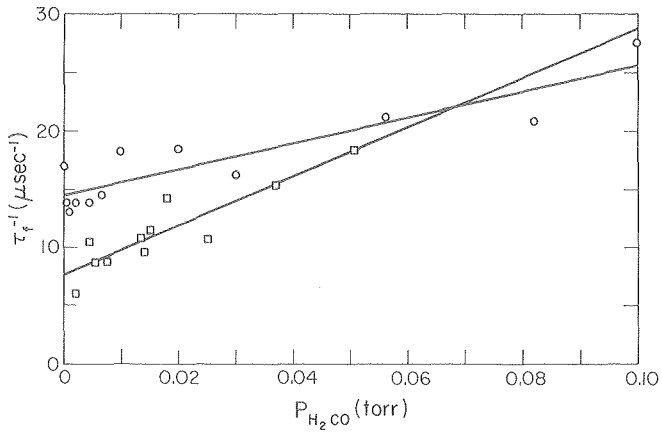

Fig. 2. Stern-Volmer plot for the fast decay component of H_2CO excited to 4^1 (circles) and to the K'' = 4 rR sub-band of 4^0 (squares).
(XBL 7710-2042)

The large quenching cross sections at very low pressure and the dramatic curvature of the Stern-Volmer plots for H_2CO can be understood in terms of a mixed state model of collisional internal conversion due to Freed.[2] At very low pressures, long range, low energy collisions can take the initial mixed S_1 - S_0 state (which is primarily S_1 in character) to essentially isoenergetic, primarily S_0 levels at rates comparable to rotational relaxation rates within S_0, or many times the gas kinetic rate. At higher pressures, the effect saturates as the isoenergetic S_0 levels are rapidly mixed by collisions to form a quasi-continuum. For D_2CO, such a process is of much smaller cross section due to weaker intramolecular S_1 - S_0 couplings and is only mildly apparent at pressures below 1 mTorr. Presumably the smaller slopes of the Stern-Volmer plots at high pressure are due to quenching to lower energy S_0 levels by hard collisions with ~ 0.1 gas kinetic cross section.

The zero pressure lifetimes of H_2CO are at least 10 times shorter than the estimated radiative lifetime, so that H_2CO decays non-radiatively in the absence of collisions. It is tempting to attribute this decay to dissociation due to mixing of continuum states with the bound S_0 levels, which are in turn coupled to S_1. However, Houston and Moore[3] have shown that at 3371 Å, the product CO appears on time scales much longer than the decay of S_1. An adequate explanation for the observed dynamics is not presently available.

The huge slope of the Stern-Volmer plots below 0.1 Torr renders the accuracy of previously

Table 1. H_2CO results.

λ_{air} (Å)	Vibronic band	rR sub-band	$1/\tau_s$ Results		$1/\tau_f$ Results	
			Low P Slope (μsec^{-1} torr^{-1})	Zero P Lifetime (nsec)	Low P Slope (μsec^{-1} torr^{-1})	Zero P Lifetime (nsec)
3547.0	4^1_0	None	145 ± 17	435 ± 15	110 ± 30	69 ± 7
3697.6	4^0_1	K'' = 0	71 ± 20	550 ± 90	60 ± 40	83 ± 10
3687.2	4^0_1	K'' = 4	115 ± 24	490 ± 90	210 ± 60	130 ± 24
3681.4	4^0_1	K'' = 6	70 ± 22	235 ± 22	No τ_f	-

obtained zero pressure lifetimes for other levels[4,5] uncertain. Future work will include very low pressure lifetime measurements for other vibronic levels and for selectively excited single rovibronic levels.

---

*Partially supported by the National Science Foundation and the Army Research Office, Triangle Park, NC.

1. T. W. Hänsch, Appl. Opt. 11, 895 (1972); R. Wallenstein and T. W. Hänsch, Opt. Comm. 14, 353 (1975).
2. K. F. Freed, J. Chem. Phys. 64, 1604 (1976); Chem. Phys. Lett. 37, 47 (1976).
3. P. L. Houston and C. B. Moore, J. Chem. Phys. 65, 757 (1976).
4. E. S. Yeung and C. B. Moore, J. Chem. Phys. 58, 3988 (1973).
5. R. G. Miller and E. K. C. Lee, Chem. Phys. Lett. 33, 104 (1975).

5. VIBRATIONAL RELAXATION OF MATRIX-ISOLATED HCl AND DCl*

Jay M. Wiesenfeld

Studies of vibrational relaxation and energy transfer in the gas phase have illuminated some important intermolecular interactions operating during molecular collisions, and hence have a direct bearing on processes like isotopic scrambling, chemical reactions, etc. Vibrational relaxation studies in the solid state are just beginning to yield interesting results. V → V processes have been observed to be rapid, and vibrational relaxation is observed to be slow in simple doped cryogenic solids (matrix-isolated samples). In matrix-isolated CO/Ar, V → V transfer within the CO system has concentrated excitation to levels as high as v = 8 on a single molecule and has preferentially excited heavier isotopes, while energy decay has been observed to be radiative.[1] Such high degrees of energy concentration and long lifetimes for vibrational excitation offer enticing possibilities for selective chemical reaction or energy storage applications. Recently, isotopically selective decomposition of SF_6 in an Ar matrix and $C_2N_4H_2$ in a benzene crystal and argon matrix has been reported.[2] Further studies of relaxation of matrix-isolated species are important in understanding the processes contributing to and competing with the above effects.

We have studied the vibrational relaxation of HCl and DCl in Ar, N_2, and O_2 matrices.[3] HCl/Ar is a particularly valuable system to study, since a great deal is known about its V → R, T relaxation behavior in the gas phase,[4] as well as about its bound complexes.[5] Vibrational lifetimes have been measured by a tunable infrared laser (optical parametric oscillator) induced, time-resolved, infrared fluorescence technique. Single rotation-vibration lines of the fundamental or overtone band of the guest species are excited. Single vibrational band fluorescence is observed. Fluorescence spectra and fluorescence excitation spectra have also been recorded.

Vibrational relaxation rates for isolated HCl and DCl species in an Ar matrix are shown in Table 1, for v = 2 → 1 and v = 1 → 0 relaxation. The relaxation rates are faster than radiative.[3] HCl relaxes more rapidly than DCl in spite of the fact that it has a larger vibrational frequency than DCl and so must ultimately transfer more energy to the host lattice. This result is explained if a V → R process, which creates a highly rotationally excited guest, is the rate-

Table 1. Vibrational relaxation rates of isolated guests ($msec^{-1}$).

System	K_{vib} (T) 9 K	15 K	20 K
HCl/Ar v = 2 → 1	3.8 ± .4	4.9 ± .6	5.7 ± .6
HCl/Ar v = 1 → 0	.81 ± .07	.89 ± .10	1.1 ± .1
DCl/Ar v = 2 → 1	.12 ± .01	.18 ± .01	.20 ± .01

limiting step in the relaxation process,[6] as shown in Fig. 1. Subsequent relaxation of rotation into lattice phonons is rapid, according to this model. The concentration (M/A) dependence of the relaxation rates for HCl/Ar are shown in Fig. 2. Relaxation from v = 2 is independent of concentration for the range shown. Relaxation from v = 1 is concentration independent from M/A > 2000; the rate increases rapidly for M/A < 1000. The increase is due to energy diffusion of v = 1 excitation from guest to guest by a resonant dipole-dipole coupling, which allows energy to be irreversibly transferred to the HCl dimer. Direct excitation experiments show that the dimer relaxation is fast and hence dimer, which is present in increasing concentration as M/A decreases, acts as an energy sink. The relaxation of v = 2 is insensitive to dimer (and all other guest species) since resonant transfer of two quanta is too weak to produce energy diffusion. Relaxation rates of v = 1 appearing in Table 1 correspond to dilute HCl samples (M/A > 2000). Rates increase slightly with temperature, as seen in Table 1. In N_2 and O_2 matrices, HCl relaxation is too rapid for observation, presumably due to rapid V → V transfer to the host matrix.

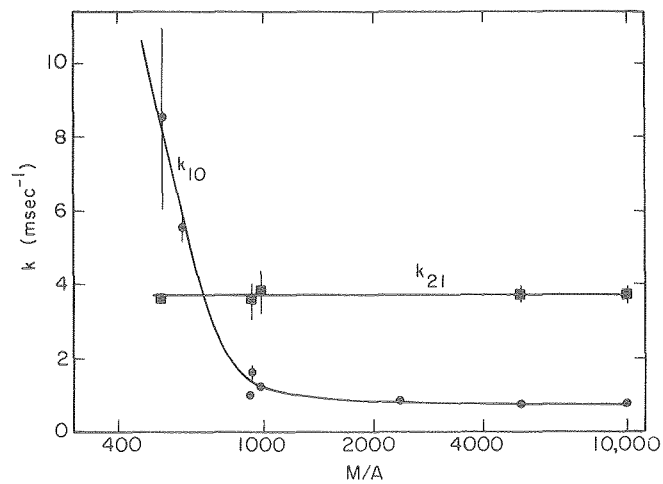

Fig. 2. Concentration dependence of relaxation of HCl/Ar. M/A is the host/guest mole ratio. All samples presented in this figure were prepared under identical conditions. (XBL 7710-10004)

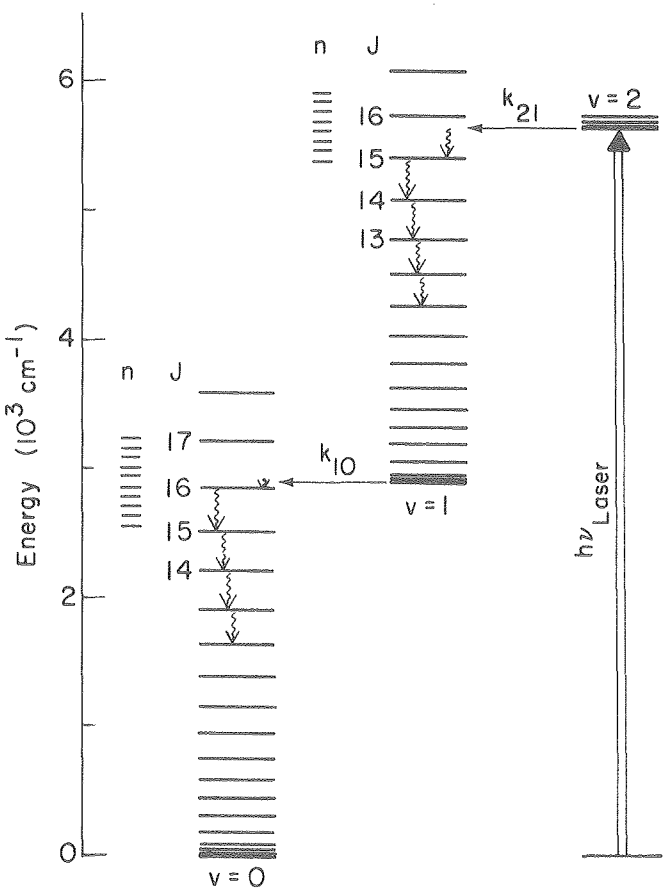

Fig. 1. V → R mechanism for relaxation of HCl in an Ar matrix. The rate-limiting steps, subsequent to excitation of v = 2, are k_{21} and k_{10}, in which guest rotation is the accepting mode. V → R rates decrease as the number of rotational quanta excited increases. (XBL 7710-10002)

The HCl and DCl kinetic results can be understood conceptually by a binary collision model, which proposes that V → R relaxation occurs in the solid during infrequent, close repulsive encounters between the guest and a host atom.[3] This model also correlates data of other workers.

The following points concerning vibrational relaxation in a simple doped solid can be concluded: 1) The non-radiative relaxation mechanism is V → R; 2) Energy diffusion by resonant dipole-dipole coupling of allowed transitions is rapid, allowing energy to be trapped or lost at an energy sink; 3) Molecular complexes such as polymer relax rapidly; and 4) The temperature dependences for these processes are weak.

---

*Partially supported by the National Science Foundation and the Army Research Office, Triangle Park, NC.

1. H. Dubost and R. Charneau, Chem. Phys. 12, 407 (1976).
2. R. V. Ambartzumian, Yu. A. Gorokhov, G. N. Makarov, A. A. Puretzky and N. P. Furzikov in Laser Spectroscopy III, J. L. Hall and J. L. Carlsten, Eds., Springer-Verlag, Berlin (1977); R. M. Hochstrasser and D. S. King, Laser Focus, November 1977, p. 32.
3. J. M. Wiesenfeld (Ph.D. thesis), University of California, Berkeley, 1977.
4. R. V. Steele and C. B. Moore, J. Chem. Phys. 60, 2794 (1974).
5. W. Klemperer, Faraday Disc. Chem. Soc. 62, 179 (1977) and references therein.
6. V. E. Bondybey and L. E. Brus, J. Chem. Phys. 63, 794 (1975).

6. OPTICAL PARAMETRIC OSCILLATOR DEVELOPMENT

A. H. Kung

Optical sources that have high average power, broad tunability, good spatial and temporal coherence and narrow bandwidth are particularly useful for the study of selective excitation of atoms and molecules and for making chemically analyzable amounts of photochemical reaction products. We have developed a tunable optical parametric oscillator (OPO) that meets most of these requirements. This OPO, using a 2.5 cm diam × 5.0 cm long lithium nitrate crystal as the nonlinear medium, converts the high energy pulses from a Nd:YAG laser at 1.06 μm to tunable infrared pulses from 1.5 μm to 4.0 μm with high efficiency. Running the system at ten pulses per second, we have obtained usable average powers of 0.3 to 0.5 watts between 1.5 μm and 2.1 μm and typically 60 mwatts from 3.0 μm to 3.6 μm. Comparable energies can be obtained from 2.1 μm to 3.0 μm. The overall photon conversion efficiency is better than 20%. Each infrared pulse is typically 10 nsec long and 3 cm^{-1} in bandwidth and is focusable to an area smaller than 10^{-3} cm^2. Thus a peak intensity of > 1 GW/cm^2 has been achieved for experimentation.

Two series of experiments using the OPO for excitation are under way. In one experiment, the OPO at 3.3 μm is used to study multiphoton excitation of molecules possessing one or more C-H stretching modes. The high intensity available from this OPO is essential for this study. Answers to questions about mode selectivity in the multiphoton process, the energy distribution in the products formed and the strength of coupling between the C-H stretching mode and the various lower frequency modes are being sought. In the other experiment, we make use of the high energy per pulse of the OPO to excite methyl fluoride molecules in Ar or Kr matrices. The aim is to study vibrational relaxation of isolated CH_3F in these matrices. In view of recent discoveries of isotopic selectivity in multiphoton excitation schemes and in matrix isolated molecular systems, understanding the fundamental kinetics involved in each of these systems is very important. Results of our studies will be reported in the near future.

Inprovements on the OPO that include reducing the linewidth of the output to less than 0.1 cm^{-1} and increasing the output power with a parametric amplifier are in progress. Also the tuning range could be extended by using other nonlinear methods or a different crystal for the parametric generation.

7. VIBRATIONALLY INDUCED PHOTOCHEMISTRY

R. Glen MacDonald

The effect of enhancing chemical reactions by the addition of internal energy to the reactant species is the subject of great current interest. The study of vibrationally induced photochemistry is not only important from a theoretical point of view since it enables valuable information to be obtained about potential energy hypersurfaces, but also has important practical applications such as isotope separation and possibly chemical systhesis.

The general reaction scheme is

$$HCl(v = 2) + H \xrightarrow{k_1} H_2 + Cl$$

$$\xrightarrow{k_2} HCl(v = 1) + H$$

$$HCl(v = 1) + H \xrightarrow{k_3} HCl(v = 0) + H$$

$$\xrightarrow{k_4} H_2 + Cl$$

$$HCl(v = 0) + H \xrightarrow{k_5} H_2 + Cl.$$

The HCl was excited directly to v = 2 by an optical parametric oscillator (OPO). Since the OPO is tunable with a bandwidth of ~ 0.005 cm^{-1} either species $H^{35}Cl$ or $H^{37}Cl$ may be excited to v = 2. The time dependence of HCl(v = 2) and (v = 1) was followed by monitoring the infrared fluorescence 2 → 1 and 1 → 0 of HCl. The 2 → 1 and 1 → 0 fluorescence may be separated using an HCl cold gas filter to absorb the 1 → 0 radiation. The population of HCl(v = 2) is directly proportional to the 2 → 1 fluorescence intensity. The reactions were carried out in a fast flow system. The atoms were produced in a microwave discharge of the parent diatomic molecule and the atom concentration determined by an appropriate gas phase titration.

By measuring the decay rates of HCl(v = 2) and HCl(v = 1) the rate constants $(k_1 + k_2)$ and $(k_3 + k_4)$ are determined. The fraction of HCl(v = 2) which goes into v = 1, $k_2/(k_1 + k_2)$, is determined from the relative intensities of v = 2 and v = 1 emission. The thermal rate constant k_5 is generally available from classical kinetic studies. For O and H k_4 is roughly known from laser excitation of (v = 1). For Br atoms k_4 and k_5 are zero since the reactions are endothermic.

For the system HCl + Cl only relaxation processes are observed

$$HCl(v = 2) + Cl \xrightarrow{k_2^{Cl}} HCl(v = 1) + Cl$$

$$\xrightarrow{k_6^{Cl}} HCl(v = 0) + Cl$$

$$HCl(v = 1) + Cl \xrightarrow{k_3^{Cl}} HCl(v = 0) + Cl.$$

Table 1. Observed rates (244 K).

Atom	$k_1 + k_2$	$k_3 + k_4$	% reaction of v = 2
	(cm^3 molecule^{-1} sec^{-1} x 10^{12})		
Br	1.7 ± .2	0.3 ± .1	17 ± 15[a]
H	26 ± 5	3.4 ± .8	65 ± 15
O	5.2 ± .40	0.89 ± 0.13	29 ± 23
Cl	33 ± 4	7.4 ± .5	---

[a]Increases to 34 ± 13 at 390 K.

Table 2. Δv = 1 vibrational relaxation rates.

System	$k_{v=1}/\bar{v}$ (Å^2)	$\frac{k_{v=2}}{k_{v=1}}$	$\frac{k_{v=3}}{k_{v=1}}$
HCl(v)+Cl	1.3	4.2±0.4	(8±2)[a]
HCl(v)+Br	0.056	5.0±1.4	
HCl(v)+O	0.11	5.0±1.3	
HCl(v)+H	0.31	1-5	
HCl(v) in[b] Ar matrix	0.8×10^3 sec^{-1}	4.8±0.6	

[a]Data of I.W.M. Smith.
[b]See article 5.

The two quantum transfer k_6^{Cl} is shown to have a rate of 0 ± 0.1 k_2^{Cl}. Therefore k_6^{Cl} is neglected for all systems in discussion below. The rate constants determined, Table 1, are temperature independent within the 10% error margins over the range 294 to 440 K.

Data for reactive collision partners are shown in Table 1. The reaction with Br is energetically possible only for v ≥ 2. It competes rather unfavorably with relaxation. Nontheless isotope enrichment has been reported for this reaction.[1] For H the reaction has an activation energy about equal to 1 quantum of vibrational excitation. Studies of v = 1 show that reaction is negligible compared to relaxation for that level. In v = 2, however, reaction dominates relaxation. The results for O have already been discussed in detail.[2]

The data in Table 2 show that the rate for v = 2 → v = 1 relaxation is 4 or 5 times faster than for v = 1 → v = 0 for HCl. By contrast first order perturbation of an harmonic oscillator would yield a factor of two (linear in v). The ratio of rates is independent of the absolute rate and of the rather large differences in intermolecular potentials among the collision partners shown. The ratio even holds for a solid Ar matrix at 9 K. The v = 3 data for HCl + Cl of Smith[3] indicate that probabilities may scale as v^2 rather than v.

1. D. Arnoldi, K. Kaufman and J. Wolfrum, Phys. Rev. Lett. 34, 1597 (1975).
2. R. Glen MacDonald and C. B. Moore, J. Chem. Phys. (to be published).
3. I. W. M. Smith, private communication.

8. RESEARCH PLANS FOR CALENDAR YEAR 1978

C. Bradley Moore

Multiphoton Excitation and Dissociation

The aim is to understand the kinetics of multiphoton excitation and dissociation and to demonstrate efficient schemes for isotope separation. Infrared multiphoton excitation work will be done using both CO_2 and OPO excitation. For excitation below the dissociation limit infrared fluorescence will be used to study the time evolution of different vibrational modes both with and without collisions. The first experiments employ the CO_2 laser to excite D_2CO,

a simple molecule with well documented infrared spectra. The tunable parametric oscillator will be used for excitation of hydrogen stretching vibrations. The formation of dislocation products will be monitored kinetically by infrared emission and visible absorption kinetic spectroscopy. Final products are measured by gas chromatography. A clear understanding of the dissociation mechanism may be obtained. The selectivity of two-frequency excitation will be explored by using the OPO at low power and a CO_2 laser at relatively high power. By exciting narrow three- and four-photon resonances near 3 μ and dissociating at 10 μ extremely high isotopic selectivity should be possible.

Detailed studies of level structure and dynamics require an ensemble of excited molecules of well-defined total excitation energy. This may best be accomplished in the 14,000 to 25,000 cm^{-1} range by single photon excitation using a cw dye laser. Optoacoustic spectroscopy is sufficiently sensitive to yield the spectral splittings and broadening that indicate transfer of energy among modes. Initial molecules for investigation include HCN, HCCH, etc.

Chemical Reactions of Selectively Excited Molecules

Extension of the work on reactions of ICl^* to more reactive systems is planned. Excitation of high vibrational overtones yields predissociation (HN_3), and highly reactive species (HCN, HCCH, etc). Experiments will be conducted with a flashlamp pumped dye laser and a cw ion laser for state resolved excitation. Product analysis will be done using gas chromatography and vacuum distillation.

Studies of vibrationally excited hydrogen halides and matrix isolated species (HCl, OCl, CH_3F ...) may also lead to reactions interesting for isotope separations.

Photochemistry of Air Pollution - Formaldehyde

The radical dissociation of formaldehyde, $H_2CO \rightarrow H + HCO$, is a major source of reactive species in photochemical smog. Techniques for quantum yield measurement and kinetic spectroscopy of HCO have recently been demonstrated in our group. They will allow (if funding becomes available) definitive measurement of the now unknown rate constants and quantum yields necessary for air pollution modeling calculations. Time is essential for this modeling with the evolution of alcohol-burning automobiles.

9. 1977 PUBLICATIONS AND REPORTS

C. Bradley Moore and Associates

Journals and Conference Proceedings

*1. J. H. Clark, J. P. Reilly and C. B. Moore, HCO Radical Kinetics: Conjunction of Laser Photolysis and Intracavity Dye Laser Spectroscopy, Int. J. Chem. Kin. (to be published).

†2. B. H. Johnston, M. A. Johnson, C. B. Moore, and J. E. Hearst, Psoralen-DNA Photoreaction: Controlled Production of Mono- and Di-Adducts Using Nanosecond UV Laser Pulses, Science 197, 906 (1977).

‡3. Chemical and Biochemical Applications of Lasers Vol. II, C. B. Moore, Ed., Academic Press, New York (1977).

‡4. V. S. Letokhov and C. B. Moore, Laser Isotope Separation, in Chemical and Biochemical Applications of Lasers Vol. III, C. B. Moore, Ed., Academic Press, New York (1977), p. 1-165.

‡§‖5. C. C. Mei and C. B. Moore, Temperature Dependence of the Total Reaction Rates for Cl + HI and Cl + HBr, J. Chem. Phys. 67, 3936 (1977).

*¶6. J. Finzi, F. E. Hovis, V. N. Panfilov, P. Hess and C. B. Moore, Vibrational Relaxation of Water Vapor, J. Chem. Phys. 67, 4053 (1977).

7. S. J. Harris, A Four-Center, Concerted, Bimolecular Reaction: $ICl^*(A^3\Pi_1) + H_2 \rightarrow HCl + HI$, J. Am. Chem. Soc. 99, 5798 (1977).

LBL Reports

‡§1. R. G. MacDonald and C. B. Moore, Reaction and Deactivation of HCl(v = 1,2) by O Atoms, J. Chem. Phys. (to be published), LBL-6965.

§‖2. Jay Martin Wiesenfeld (Ph.D. thesis), Vibrational Relaxation and Energy Transfer of Matrix Isolated HCl and DCl, December 1977.

Invited Lectures

1. Chemistry Colloquium, University of California, Santa Cruz, CA.

2. Chemistry Colloquium, University of North Carolina, Chapel Hill, NC.

3. Distinguished Speakers Series, Chemistry, University of Utah, Salt Lake City, UT.

4. Chemistry Colloquium, Johns Hopkins University, Baltimore, MD.

5. Physical Chemistry Seminar, Joint Ohio State University/Battelle Institute, Columbus, OH.

6. Laser Chemistry Winter Meeting, Park City, UT. (ERDA sponsored Conference).

7. National Meeting of the American Association for the Advancement of Science, Symposium on Lasers in Chemistry, Denver, CO.

8. Physical Chemistry Seminar, University of California, Los Angeles, CA.

9. General Chemistry Seminar, San Francisco State University, San Francisco, CA.

10. Gordon Research Conference on Molecular Energy Transfer, Brewster Academy, Wolfeboro, NH.

11. Seminar, Allied Chemical, Morristown, NJ.

12. Seminar, I.B.M. Yorktown Heights, NY.

13. Summer Course on Lasers, 6 hours, lecture, University of California, Los Angeles, CA.

---

*Sponsored jointly by the National Science Foundation and the U.S. Army Research Office, Triangle Park, NC and the U.S. Air Force Office of Scientific Research.

†Sponsored jointly by the National Science Foundation and the University of California.

‡Sponsored by the University of California.

§Partially sponsored by the U.S. Army Research Office, Triangle Park, NC.

‖Partially sponsored by the National Science Foundation.

¶Partially sponsored by the U.S. Air Force Office of Scientific Research.

b. Molecular Beam Laser Isotope Separation

Yuan T. Lee and Y. Ron Shen, Principal Investigators

1. MOLECULAR DIMER DISSOCIATION BY CO_2 LASER IRRADIATION*

P. A. Schulz and Aa. S. Sudbo

Molecular dimer formation in a supersonic expansion has been studied and used in various experiments. We have looked at the dissociation of molecular dimers by vibrationally exciting the molecular monomer with a relatively high power, pulsed CO_2 laser. The dimer fragments into two molecular monomers that can be detected by a rotatable electron bombardment mass spectrometer. Time-of-flight and angular distributions were measured for the monomers. The selective decomposition of van der Waals molecules shown in Fig. 1 is one of the schemes proposed for isotope separation.

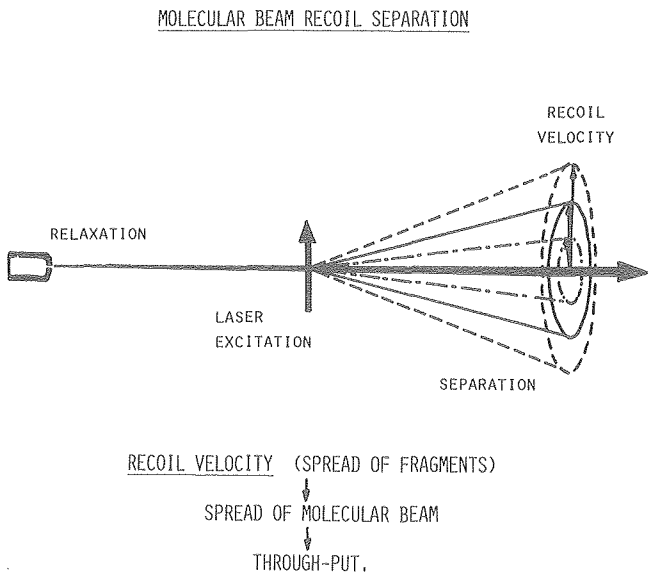

Fig. 1. Schematic diagram of selective decomposition of van der Waals molecules. (XBL 764-1085)

For $(CH_3NH_2)_2$ and $(NH_3)_2$ the average translational energy released in the dissociation was observed to be up to approximately 0.5 kcal/mole with no lower bound observed. The 0.5 kcal/mole translational energy released should be compared with the dissociation energy of the dimer, which in the case of $(NH_3)_2$ is between 4-5 kcal/mole and with the energy of the CO_2 laser photon which is 2.7-3.1 kcal/mole. $(CH_3NH_2)_2$ is expected to have a somewhat smaller dissociation energy than $(NH_3)_2$.

If in $(NH_3)_2$, the internal energy of the molecule is randomized among all the modes of the molecule other than hydrogen stretches, then approximately 1/12 of the energy should appear in translational energy of the molecule. If $(NH_3)_2$ absorbs only two photons, then a considerably larger fraction of the energy appears in translation than is expected using simple statistical arguments. That is, with two photons absorbed there is only 1-2 kcal of excess energy, of which, [in a significant fraction of $(NH_3)_2$] more than 1/4 appears to be released in the relative translational energy of the products.

Thus, if $(NH_3)_2$ is a statistical molecule, i.e., the energy is randomized, then it must be absorbing more than two infrared photons.

If the molecule is nonstatistical and the dissociation process is dominated by the time needed for energy transfer from the ν_3 excited mode of NH_3 to the NH_3 - NH_3 stretching, then one expects to see a strong peaking of the translational energy distribution at 0 energy, which is actually observed. Thus, in this experiment as in other previous experiments it is difficult to elucidate the mechanism for the dissociation of the dimers, or equivalently, the rate of energy transfer between vibrational modes in the $(NH_3)_2$ complex. However, further experiments have been done on the dimers to elucidate the dissociation mechanism.

The dissociation of $(NH_3)_2 \rightarrow 2NH_3$ as a function of power has revealed very little dependence of the yield on the power. The small dependence of the yield on the power is probably due to the increase in power broadening which means that more rotational states can be excited by the laser. Also, there is no evidence for a sharp power (or energy) threshold for the dissociation of the dimer (unlike the case of MPD of polyatomic molecules). If the molecule was statistical, an increase in the laser power density would cause an increase in the translational energy released, thus resulting in a change in the angular distribution that was not observed. Also, the angular distribution was observed at two different excitation frequencies for the dissociation of $(NH_3)_2$, at 944 cm^{-1} and 1080 cm^{-1}. The angular distributions were identical within the experimental uncertainty. Thus, a significant change in the energy available for translation makes no difference in the translational energy distribution, therefore strongly supporting the hypothesis of V-V energy transfer as the rate limiting process.

In the case of $(CH_3NH_2)_2$ dissociation, the same qualitative features were observed--a narrow angular distribution peaking at 0° and very little dependence of the dissociation yield or angular distribution on the laser intensity.

Thus, from the experiments on the dissociation of dimers one concludes that the dissociation mechanism is the V-V energy transfer from the vibrational mode excited by the laser into the dimer bond-stretching vibration. Of course, this vibrational mode will be broken and the energy will be released as translational and rotational motion of NH_3. In the dissociation of $(NH_3)_2$ the high-frequency vibrations of NH_3 cannot participate in the energy sharing and thus the molecule is

nonstatistical. Nor for $(CH_3NH_2)_2$ dissociation does energy randomization seem to occur, again probably because of the large number of high-frequency vibrations. However, for $(CH_3NH_2)_2$ dissociation there may be a partial energy randomization that may be elucidated by more experiments. It is hoped to extend the study of the dissociation of weak molecular bonds in van der Waals dimers and larger polymers.

---

*This work was carried out in collaboration with Professor Y. Ron Shen's group.

2. DYNAMICS OF INFRARED MULTIPHOTON DISSOCIATION OF POLYATOMIC MOLECULES*

P. A. Schulz, Aa. S. Sudbo and E. R. Grant

Using a Tachisto Model 215 line tunable CO_2 laser with 1 J of output in each pulse, observations of multiphoton dissociation of polyatomic molecules in a beam have been made. The translational energy distributions of the product fragments have been measured with an electron bombardment ionizer and mass spectrometer. In many cases, the dissociation has been observed also as a function of laser frequency and power to aid our understanding of the dynamics of the elimination of an atom.

A considerable amount of interest and excitement was generated with the suggestion that multiphoton dissociation is a very unusual method for energizing molecules, one that offered the potential for vibrational mode control of unimolecular reactions. For the present situation, this means deciding the dissociative outcome of a reaction by not only controlling how much energy is supplied to each molecule, but also, loosely speaking, by directing which vibrational modes the energy is to go into and producing dissociation products different from those of thermal activation. Initial evidence tended to support this hypothesis. The first reported primary product analysis for the multiphoton dissociation of SF_6 indicated that this molecule dissociated directly to SF_4 and F_2,[1] bypassing the lower energy SF_5 and F fragmentation channel. Results of gas cell experiments with $CFCl_3$ were interpreted to evidence direct dissociation to CFCl and Cl_2.[2] In addition, the observation of C_2 and CN from CH_3CN and CH_3NH_2 (Ref. 3) and prompt luminescence for a number of molecules[4] under conditions which were supposedly collision-free suggested explosive dissociation of very highly excited molecules.

The results of our experiments,[5] mainly derived from the dissociation pattern and the relation between the shape as well as the magnitude of translational energy distributions, are unambiguously consistent with a far more orderly picture of the excitation and dissociation process than that suggested by many earlier experiments and theoretical constructs. Work by Bloembergen, Yablonovitch, and their co-workers[6] on the measurements of multiphoton absorption by SF_6 and their theoretical interpretation of the experimental observations are in close agreement with our conclusion that although the initial excitation is selective, nearly complete energy randomization must take place in the molecular vibrational degrees of freedom before decomposition for molecules that dissociate by atomic elimination.

For polyatomic molecules with many vibrational degrees of freedom, (since the state density for the internal degrees of freedom is a steeply increasing function of energy, whereas that for translational is not), the statistical theory characteristically predicts a recoil energy distribution that is peaked near zero, i.e., most of the excess energy is stored as internal excitation of fragments, and correspondingly large amounts of translational energy release are improbable. The average recoil energy of the fragments is a function of laser energy, the number of vibrational degrees of freedom, and density of states associated with those vibrational degrees of freedom.

To date SF_6, CF_3Cl, CF_3Br, CF_3I, CF_2Cl_2 and CF_2Br_2 have revealed atomic elimination in the dissociation process, always eliminating the atom with the weakest bond. The RRKM statistical model predicts translational energy distributions that were then transformed to velocity space for comparison with the angular distribution and velocity distributions obtained in the experiment. The experimental translational energy distribution could be obtained from the RRKM model by slight variations in the translational energy distributions from the RRKM predictions. In each case, the RRKM model came close to fitting all the data. An example is given in Fig. 1 where the best fit to the SF_6 MPD experiment (data points only) is compared with the RRKM prediction for translational energy released for a molecule with 7, 9, and 11 excess photons absorbed (17.5, 22.9 and 28.3 kcal/mole beyond dissociation). It is evident that the fit between the experiment and the data is excellent.

If statistical theory is applied to CF_3Br and SF_6, observed translational energy distributions correspond respectively to an average absorption of 1-3, and 7-11 excess CO_2 laser photons beyond the dissociation energies of CF_3Br and SF_6. Although these numbers seem to suggest a vast difference in the ability of molecules to absorb excess photons beyond dissociation energy, they actually represent very similar degrees of excitation in terms of the lifetime of excited molecules. For both CF_3Br and SF_6 molecules, the range of excitations correspond to dissociation states with a lifetime ranging from 10^{-7} to 10^{-9} s, which is of the same order as the laser pulse width of $5 \cdot 10^{-8}$ s (see Fig. 2). Similar results are found when the calculations are done for the other molecules mentioned above.

Comparison of the theory with experiments is more difficult for SF_6 and $CFCl_3$ MPD because they can undergo a two-step dissociation to form SF_4 + 2F and CFCl + 2Cl, respectively. The two-step dissociation can be detected by a change in the fractionation ratio in the mass spectrometer when the laser energy fluence is changed (see

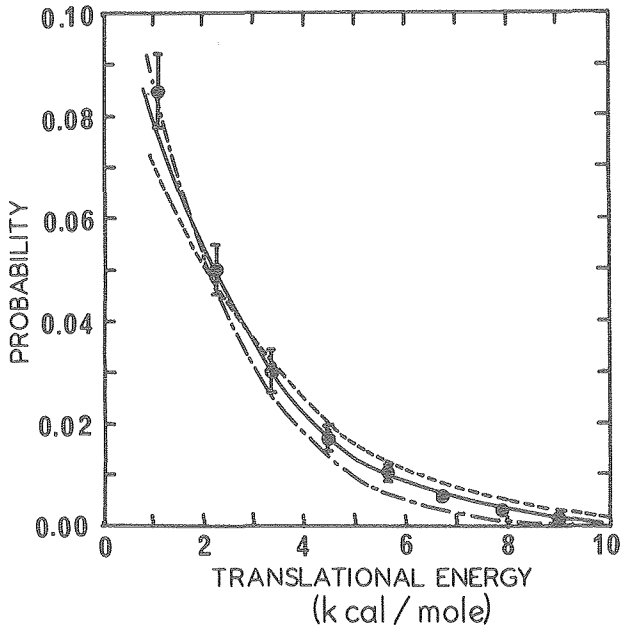

Fig. 1. Fragment recoil energy distributions for $SF_6 \rightarrow SF_5 + F$. Experimental data points obtained with ~6 J/cm^2 laser pulses are denoted by •. Curves are calculated from the RRKM theory assuming a molecular excitation of $E = E_0 + n\hbar\omega$ with $n = 7$(— • —), $n = 9$(—), and $n = 11$(----) where E_0 is the dissociation energy and $\hbar\omega$ is the CO_2 laser photon energy. (XBL 771-7431)

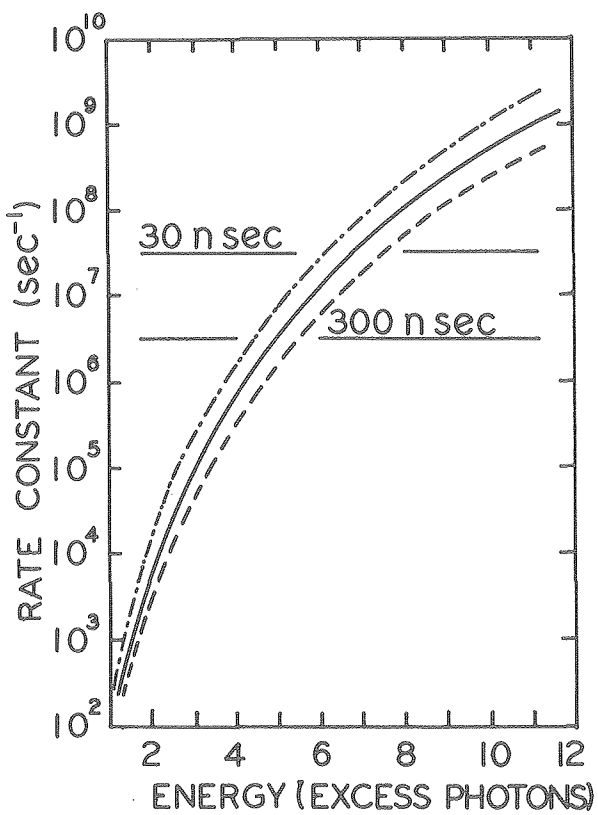

Fig. 2. Dissociation rate of SF_6 calculated from the RRKM theory as a function of level of excitation $n\hbar\omega = E - E_0$. (XBL 771-7437)

Fig. 3) because the ratio of $SF_3^+/SF_2^+ = 5$ for ionization of SF_5, but $SF_3^+/SF_2^+ = 2$ for the ionization of SF_4. Thus, for the purpose of looking at the dynamics of the dissociation of $SF_6 \rightarrow SF_5 + F$, the laser energy fluence must be lowered so that no SF_4 can be observed. In the future it is hoped to be able to compare RRKM predictions for the secondary dissociations ($SF_5 \rightarrow SF_4 + F$ and $CFCl_2 \rightarrow CFCl + Cl$) with the experimental results.

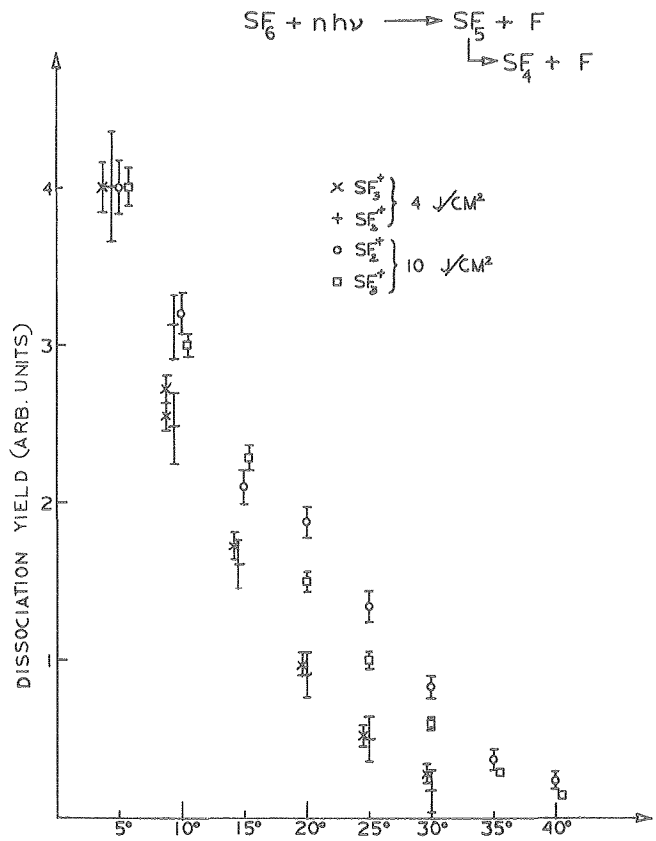

Fig. 3. Angular distributions of SF_3^+ and SF_2^+ at higher and lower laser intensity: lower intensity, X, SF_3^+; +, SF_2^+; higher intensity, □, SF_3^+; ○, SF_2^+. (XBL 776-8869)

MPD has been observed in one case where a single bond is broken and two molecular fragments are released ($N_2F_4 \rightarrow 2NF_2$). Tetrafluorohydrazine has a very low bond energy of only 22.3 kcal/mole (compared with 50-90 kcal/mole bond energies for the molecules just discussed). Such a small dissociation energy results in a very small prediction for the RRKM lifetime--only 3 ns for 1.0 kcal of excess energy beyond the dissociation limit. Thus, it is expected that the dissociation occurs after absorbing only 8 photons of energy 2.8 kcal/mole, (2.8 kcal/mole • 8 = 22.3 kcal/mole = dissociation energy). However, because the N_2F_4 population is initially Boltzmann distributed there will be a range of activated energies. The ambient temperature of the source,

300 K, corresponds to an energy in vibration of ~2 photons. Thus, an even distribution of molecules with activated energies between 0 and 2.8 kcal/mole (0-1 photon) beyond dissociation can be expected. Such a distribution is in excellent agreement with the data for the N_2F_4 MPD. On the other hand, an RRKM predicted translational energy distribution corresponding to any single activated energy does not give a good fit to the data. Thus, it can be concluded that the MPD of a polyatomic molecule is well described by an RRKM model, for the case in which a single bond of the molecule is broken.

---

*This work was carried out in collaboration with Professor Y. Ron Shen's group.

1. K. L. Komps, Tunable Lasers and Applications, Proceedings of the Nordfjord Conference, A. Mooradian, T. Jaeger, and P. Stokseth, Eds. (Springer-Velag, 1976), therein.
2. D. F. Dever and E. Grunwald, J. Am. Chem. Soc. 98, 5055 (1976).
3. K. Welge and co-workers, private communication.
4. R. V. Ambartzumian, N. V. Chekalin, V. S. Letokov and E. A. Ryabov, Chem. Phys. Lett. 36, 301 (1975); R. V. Ambartzumian, N. V. Chelkalin, V. S. Doljikov, V. S. Letokov and E. A. Ryabov, Chem. Phys. Lett. 25, 515 (1974).
5. E. R. Grant, P. A. Schulz, Aa. Sudbo, Y. T. Lee and Y. R. Shen, Multiphoton Processes, J. H. Eberly and P. Lambropoulos, Eds. (Wiley, New York, 1977).
6. J. G. Black, E. Yablonovitch, N. Bloembergen and S. Mukamel, Phys. Rev. Lett. 38, 1131 (1977); E. Yablonovitch, paper presented in Second Winter Colloquim on Laser Induced Chemistry, Park City, Utah, March 1977.

3. THREE-CENTER AND FOUR-CENTER ELIMINATION IN MULTIPHOTON DISSOCIATION OF MOLECULES*

Aa. S. Sudbo and P. A. Schulz

A number of halogenated hydrocarbons are known to dissociate by three-center and four-center elimination, as observed by chemical activation or in pyrolytic reactions. The same processes can be observed in the multiphoton dissociation of these compounds. Since it is possible to measure translational energy distributions of fragments in a molecular beam experiment, valuable information on the dynamics of three-center and four-center elimination, especially the nature of potential energy surfaces for decomposition has been obtained. Some preliminary results on this are summarized below.

Our experimental setup is described in Ref. 1. It is a molecular beam crossed with a focused CO_2-laser beam. A rotatable mass spectrometer detector is capable of giving us a translational energy distribution of the fragments from the interaction region. Table 1 lists the molecules we have investigated, grouped as three-center and four-center elimination. Very few general statements can be made about common features of these reactions on the basis of our experiments, so we will briefly comment on each of them.

The molecule CHF_2Cl is known to dissociate in pyrolytic reactions by a three-center HCl elimination, just as is observed in multiphoton dissociation. The barrier for the back reaction ($CF_2 + HCl \rightarrow CHF_2Cl$) is known to be between 5 and 6 kcal/mole. We have measured translational energy distribution of the HCl fragment from the dissociation, and performed an RRKM calculation of the translational energy released in the dissociation. Any RRKM distribution corresponding to dissociation lifetimes between 0.2 and 10 ns, and shifted 5-6 kcal/mole to allow for the barrier in the reaction channel to be released as translational energy, will peak very close to where the experimental distribution peaks. A better fit is obtained if the RRKM distribution is broadened and smoothed, as one would do to take into account interactions between the two fragments after the dissociating configuration is passed. The average energy of the distribution giving the best fit is 6 kcal/mole, with a FWHM of around 9 kcal/mole, indicating the presence of molecules excited with at least 4 photons above the dissociation threshold (corresponding to lifetimes around 1 ns). It thus looks as if quite an appreciable fraction of the excess energy (as referred to the fragment ground state) of the molecule is released as translational energy. As we shall see, this differs from the case of four-center elimination in CH_3CCl_3.

Although the data for $CHFCl_2$ is of much poorer quality, qualitatively similar results are obtained for this molecule.

Table 1.

Three-Center Elimination	Four-Center Elimination
$CHF_2Cl \longrightarrow CF_2 + HCl$	$CH_3CCl_3 \longrightarrow CH_2CCl_2 + HCl$
$CHFCl_2 \longrightarrow CFCl + HCl$	$CH_3CF_2Cl \longrightarrow CH_2CF_2 + HCl$
$CHClCF_2 \longrightarrow C_2F_2 + HCl$	

For the 1,1-difluorochloroethylene, however, the translational energy released seems to peak within 0.1 kcal/mole of zero energy. For this molecule the three-center elimination was found to compete with direct Cl atom elimination, with comparable probability in the energy range typically prepared by the laser excitation. This could be inferred from the observation of HCl^+ as well as $CHCF_2^+$ in the mass spectrometer. The absence of HF^+ indicated that HF was not produced. The two channels also have very similar distributions of translational energy in the fragments. The experimental results can be fit adequately with a distribution of the form $\exp(-\frac{E}{E_0})$ with E_0 between 1.0 and 1.5 kcal/mole. This is quite different from what is observed for the halogenated methanes, and implies that almost all the excess energy will remain as internal energy in the HCl and $:CCF_2$. The latter is expected to rearrange rapidly to vibrationally excited difluoroacetylene.

The molecule 1,1,1-trichloroethane is known to decompose in pyrolysis into CH_2CCl_2 + HCl, just as is observed by us in multiphoton dissociation. The difference in heat of formation between molecule and fragments is 12.3 kcal/mole, whereas the activation energy has been measured to be 54 kcal/mole at temperatures around 700 K. We performed an RRKM calculation which indicated that the excess energy in the molecule should be 20-30 kcal/mole above the dissociation threshold for lifetimes to be in the 10 ns range. Our experimental translational energy distribution, however, peaks at ca. 8 ± 1 kcal/mole and is considerably wider than the RRKM distribution (ca. 10 ± 1 kcal/mole FWHM experimental, as compared to about 2 kcal/mole for the pure vibrational-phases-space RRKM calculation). Thus, contrary to the conclusion that the barrier in CHF_2Cl appears as translational energy of the fragments, in the CH_3CCl_3 four-center eliminations the fragments must retain almost all of the excess energy (as referred to the fragment ground states) as vibrational energy. This can also explain the experimental observation that we were unable to detect the ion $CH_2CCl_2^+$ (CH_2CCl^+ was the major ion fragment observed in the mass spectrometer), whereas the tabulated mass spectral data for 1,1 dichloroethylene indicate that similar amounts of CH_2CCl^+ and $CH_2CCl_2^+$ will be formed from the ground state CH_2CCl_2 molecule. CH_3CF_2Cl is not qualitatively different--its dissociation products have a translational energy distribution peaked at a slightly higher energy (ca. 12 kcal/mole) than the CH_3CCl_3, but with approximately the same width.

So at least in our experiments, we have observed that in four-center elimination reactions in halogenated ethanes, very little (typically 10%) of the excess energy (referred to the fragment ground states) in the excited molecule is released in translational energy in the dissociation. Most of it will remain as vibrational energy in the two fragments.

---

*This work was carried out in collaboration with Professor Y. Ron Shen's group.

1. M. J. Coggiola, P. A. Schulz, Y. T. Lee and Y. R. Shen, Phys. Rev. Lett. 38, 17 (1977).

4. EFFECT OF HOT BAND EXCITATION IN MULTIPHOTON DISSOCIATION OF POLYATOMIC MOLECULES*

P. A. Schulz, Aa. S. Sudbo, and E. R. Grant

The absorption of light in multiphoton dissociation (MPD) of polyatomic molecules has been qualitatively explained by the Bloembergen model.[1] Multiphoton absorption through a vibrational manifold occurs at the start of a high power infrared laser pulse. The absorption may only involve 3 to 6 photons of excitation, after which the anharmonicity becomes too large for further absorption. In this region, the anharmonicity causes a coupling between the vibrational modes strong enough that the absorption spectrum becomes very broad. The molecule then is in the quasi-continuum.

The initial state of the system should have an effect on the multiphoton absorption; its effect on the quasi-continuum, however, should be minimal. In our molecular beam apparatus, although state selection cannot be performed, the vibrational and rotational temperatures can be adjusted independently. The rotational temperature in the molecular beam can be raised by lowering the stagnation pressure behind the nozzle that lowers the quality of the expansion. By changing the temperature of the gas behind the nozzle, the vibrational temperature in the beam can be adjusted. The nonequilibrium of the vibrations and rotations results from the fact that $R \rightarrow T$ energy transfer is faster than $V \rightarrow T$ transfer.

Neither the total dissociation yield nor the wavelength dependence of the dissociation was affected by changes in the rotational temperature. The molecular beam was operated with stagnation pressures behind the nozzle of between 20 and 200 Torr with no change in the dissociation yield nor the wavelength dependence for SF_6 and CF_3I dissociations. The rotational temperatures of these beams are expected to vary from approximately 150 K to 50 K.

On the other hand, for SF_6, a change in the vibrational temperature of the beam results in a radical shift in the wavelength dependence of the dissociation yield (see Fig. 1). When the beam is created from an expansion at room temperature the FWHM of the dissociation yield as a function of frequency is 13 cm^{-1} at 105°C the FWHM is ~20 cm^{-1}, and at 180°C the FWHM is larger than 20 cm^{-1}. Because the CO_2 laser is line tunable only over a limited range of frequencies, the wavelength dependence shows only the points to which the laser could be tuned. At frequencies below 929 cm^{-1} the CO_2 laser decreased in power so that the constant laser energy density/pulse could not be maintained. The laser energy density used to obtain Fig. 1 is about 5 J/cm^2.

To explain the wavelength dependence of the dissociation yield as a function of vibrational

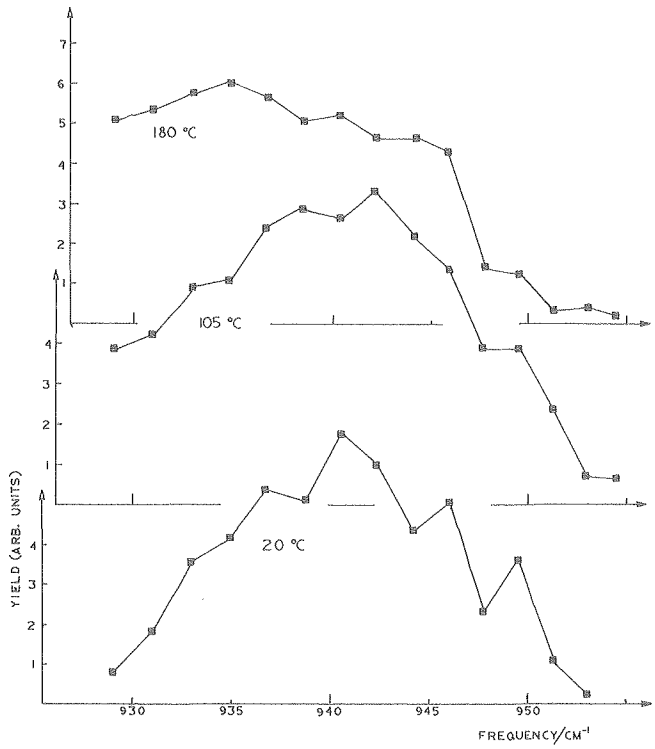

Fig. 1. Frequency dependence of the multiphoton dissociation of SF_6. The SF_6 beam source was operated at three different temperatures. (XBL 776-8870)

temperature requires consideration of the hot band absorption in SF_6. Anharmonicity causes excited SF_6 to absorb at a lower frequency than the fundamental.[2] The shift to lower frequency is even larger due to the fact that the MPD involves a multiphoton and not a single photon absorption. Because vibrationally heating the beam did not affect the translational energy distribution (as measured by an angular distribution), the absorption in the quasi-continuum is believed to be independent of the initial vibrational state.

Heating of the nozzle beam has been used to shift the vibrational frequency of many different molecules into resonance with the CO_2 laser. Using this effect, MPD has been performed on a wide variety of molecules for which the dissociation could not otherwise be observed.

*This work was carried out in collaboration with Professor Y. Ron Shen's group.

1. N. Bloembergen, Optics Commun. 15, 250 (1976).
2. D. M. Larsen, Optics Commun. 19, 404 (1976).

5. INTERNAL ENERGY DEPENDENCE OF THE CCl_4 CONDENSATION COEFFICIENT DETERMINED FROM MOLECULAR BEAM SURFACE SCATTERING EXPERIMENTS

Steven J. Sibener

In this report an experiment will be described that directly confirms the existence of an internal mode dependence of molecular sticking probabilities for collisions of molecules with a cold surface. Recent articles, both theoretical[1] and experimental[2,3] have suggested that condensation coefficients should have this dependence. However, the previous bulk kinetic experiments performed by the Russian groups could not probe the dynamics of the condensation process. Moecular beam surface scattering techniques are uniquely suited in their ability to study the dynamics of gas/solid-surface collision events.

Utilizing our universal molecular beam machine modified to include a liquid nitrogen cooled target surface, we have studied the scattering of CCl_4 from a CCl_4 ice surface. The underlying target substrate was polycrystalline copper. At a surface temperature of T_S = 280 K the copper surface was undoubtedly contaminated with diffusion pump oil and other molecules (background pressure $\sim 10^{-7}$ Torr); but at the experimental target temperature of 90 K, where the sticking probability of CCl_4 was found to be greater than 99%, a relatively "clean" surface of solid CCl_4 was presented to the incident molecular beam due to constant CCl_4 deposition. Figure 1 is an assembly diagram showing the important experimental components. The effusive, heated, and velocity selected beam source constructed for this experiment permits the independent variation of T_B and v_B, the beam temperature and beam velocity, respectively. This permits the study of gas/surface collisions with CCl_4 molecules having

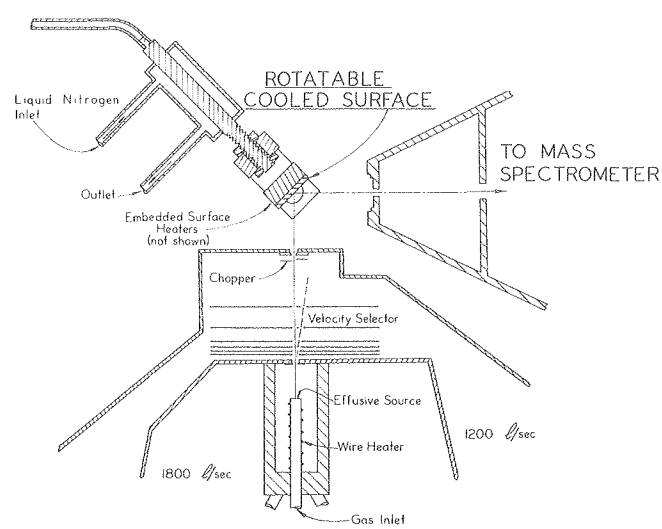

Fig. 1. Assembly diagram of the experimental scattering configuration. (XBL 7712-10907)

different internal energies (i.e., beam temperatures) but the same translational energies. The beam temperatures used were 298 K and 560 K, while five translational velocities in the range 2.5×10^4 cm/sec to 5.1×10^4 cm/sec were used. The target surface was cooled with liquid nitrogen and had an ultimate temperature T_S = 90 K. Nichrome wire heaters embedded in the surface support block permitted operation above 90 K. The surface temperature was monitored with two calibrated iron-constant thermocouples. The incident beam-surface angle θ_i is variable and was set at 50° measured from the surface normal. Alignment was accomplished by reflecting a He-Ne laser from the surface and noting the angle of reflected light. The reflected particles were then detected by a mass spectrometer that rotates about the surface allowing angular scattering distributions to be obtained for reflected angles $\theta_r = 30° \rightarrow 90°$. The entire surface assembly could also be rotated to permit direct viewing of the beam by the detector. Only in-plane scattering was detected in these experiments with the plane determined by the surface normal and the incident beam.

The experiment was performed at 90 K in order to minimize reevaporation background and to lengthen residence times of trapped molecules to significantly greater than 1 ms. This allows us to detect the reflected CCl_4 molecules that have short (relative to 1 ms) residence periods on the surface. In short, we have operated in the realm of 99+% sticking probability in order to help distinguish inelastic collisions from absorptions followed by subsequent reevaporation.

The angular distributions obtained for CCl_4 scattered from a warm, T_S = 280 K "dirty" surface for various v_i and T_B conditions are shown in Fig. 2. Note the cosine behavior of the experimental data. This indicates virtually complete energy accommodation with the surface, which subsequent time-of-flight analysis verified. Hence the scattered molecules come off at a velocity corresponding to T_S = 280 K regardless of their incident internal or translational energies.

Figure 3 shows the angular distributions for collision with T_S = 90 K and T_B = 560 K. The distributions are fairly broad and peak superspecularly 15° from the specular angle. The angular distributions appear identical over the velocity range explored. Within the hardcube approximation[4] this implies that a constant relative momentum loss is taking place. Figure 4 shows the T_S = 90 K and T_B = 298 K angular distributions. These also peak 15° from the specular angle and appear somewhat narrower than

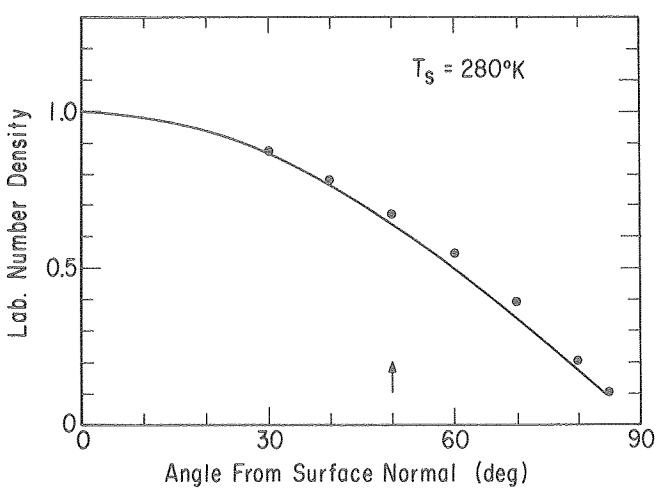

Fig. 2. T_S = 280 K experimental scattering distributions for translational energies of 2.5×10^4 cm/s and 5×10^4 cm/s at beam temperatures of 298 K and 560 K are all described by the solid dots (•). The solid line is a plot of the cosine (θ) function. (XBL 7711-10900)

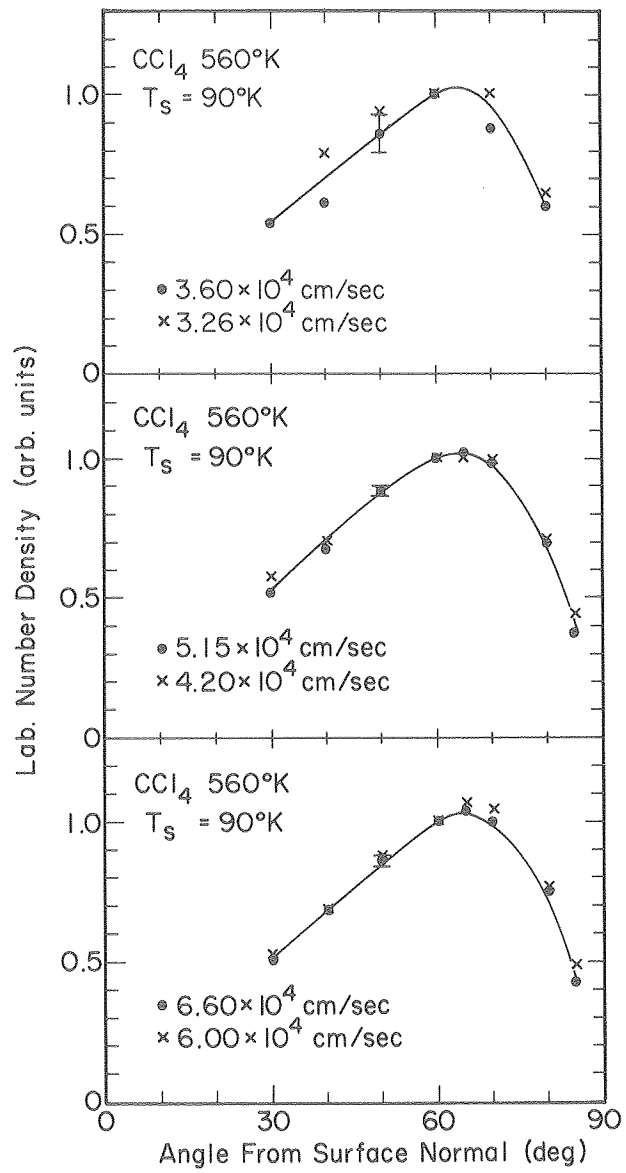

Fig. 3. Scattering distributions obtained with T_S = 90 K for six translational velocities with T_B = 560 K. The peaks all fall at approximately 15° from the specular angle, denoted by the arrow at 50°. (XBL 7711-10905)

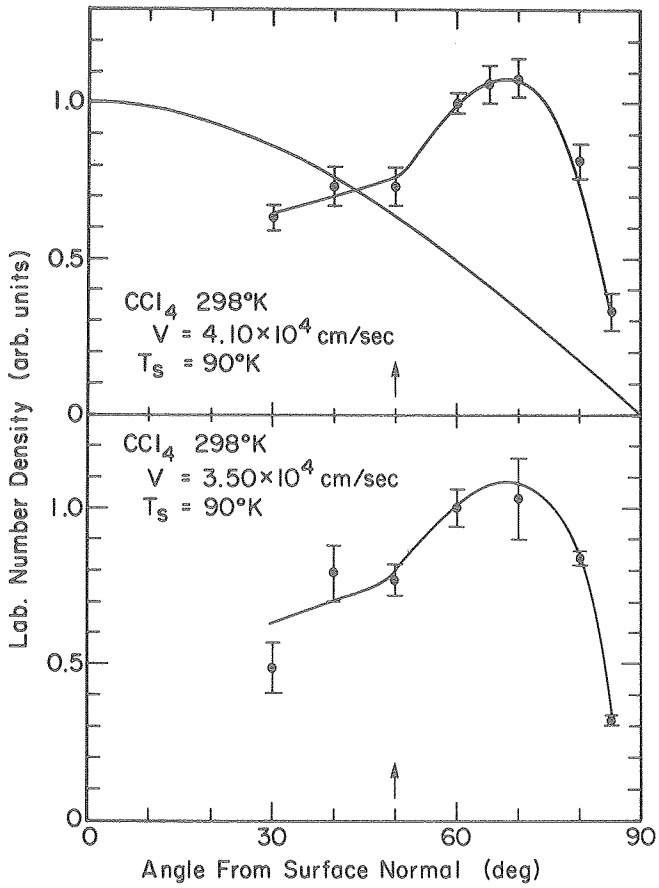

Fig. 4. Scattering distributions obtained with T_S = 90 K for two translational velocities with T_B = 298 K. Cosine (θ) is also plotted in the upper graph. (XBL 7711-10903)

do the hot beam distributions. From these angular distributions we can infer approximate values for energy accommodation coefficients, α_E, within the hardcube approximation:

$$\alpha_E = \frac{E_i - E_r}{E_i - E_s}$$

where E_i is the incident beam translational energy, E_r is the reflected beam translational energy, E_s is the translational energy of a molecule at T_S. For $v_i = 2.5 \times 10^4$ cm/s, α_E is found to be 0.37 while for $v_i = 5.0 \times 10^4$ cm/s α_E is 0.30. These values correspond to a 15% relative momentum loss for all velocities studied (45% loss in the velocity component perpendicular to the surface). Figure 5 shows the angular distribution obtained for a slightly heated surface with T_S = 117 K. The relatively flat behavior for θ_r = 30 to 65° indicates the presence of accommodated as well as inelastic scattering in the detected signal. This may be due to significantly shorter residence times at 117 K.

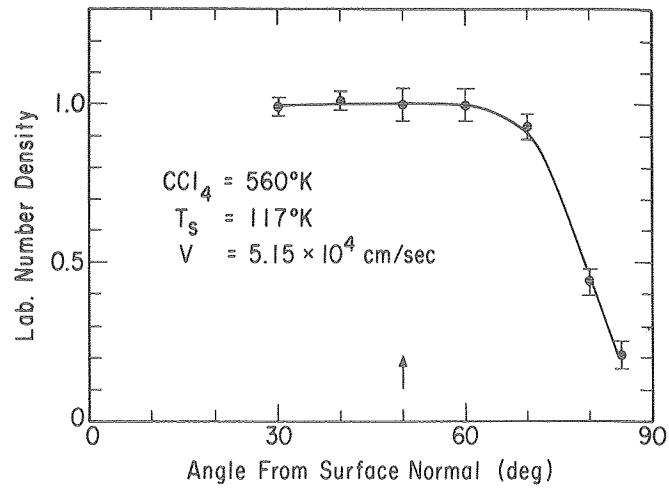

Fig. 5. Scattering distribution obtained for T_S = 117 K. The plateau behavior before the far angle fall-off indicates a significant amount of accommodated CCl_4 is contributing to the scattered intensity. (XBL 7711-10901)

The relative sticking probabilities for each T_B as a function of incident translational velocity were computed in the following way:

$$\text{Relative Sticking Probability (RSP)}_j \equiv \frac{\left.\left(\dfrac{n_r^{90}\ v_r^{90}}{n_r^{280}\ v_r^{280}}\right)\right|_{\text{beam condition } j}}{\left.\left(\dfrac{n_r^{90}\ v_r^{90}}{n_r^{280}\ v_r^{280}}\right)\right|_{\text{reference beam, velocity} \approx 5 \times 10^4 \text{ cm/s}}}$$

where the n_r^{90} and n_r^{280} are the reflected number densities measured at θ_r = 65°. The experiments were conducted by first measuring the amount of reflected CCl_4 flux, $n_r^{280}\ v_r^{280}$, for T_S = 280°. Note that this is proportional to the overall incident beam flux. Next, using the same beam conditions, T_S was changed to T_S = 90 K and reflected number densities were measured. Since the angular distributions are identical for each T_B value, this determination based upon only one angle is warranted. Figure 6 shows the RSP values obtained as a function of translational energy for T_B = 298 K and T_B = 560 K. A very strong dependence of RSP on incident beam translational energy is observed. The two curves shown in Fig. 6 merge at high velocities but the T_B = 298 K curve clearly shows less reflected signal at low velocities.

Finally, we have determined the internal energy dependence of sticking probability and have expressed this in the form of an enhancement

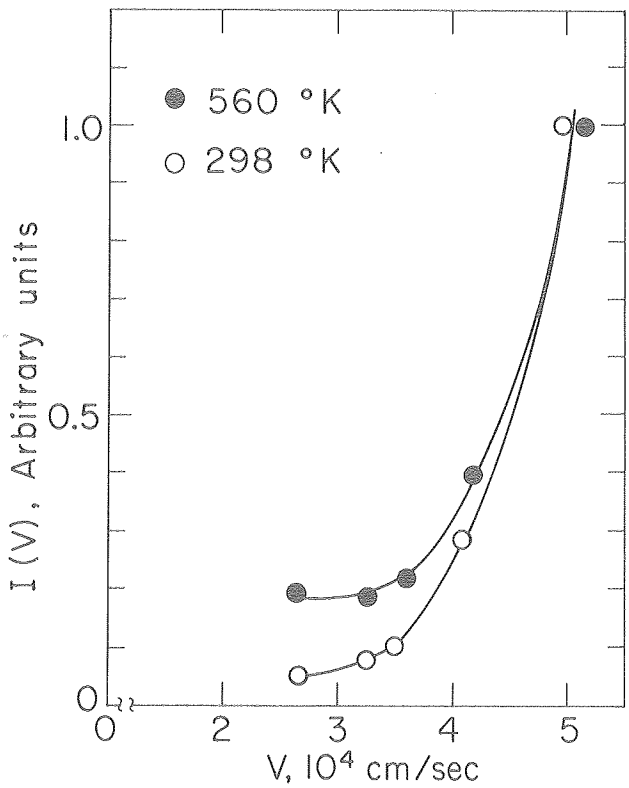

Fig. 6. Translational energy dependence of relative sticking probability for T_B = 298 K and T_B = 560 K. (XBL 7712-11075)

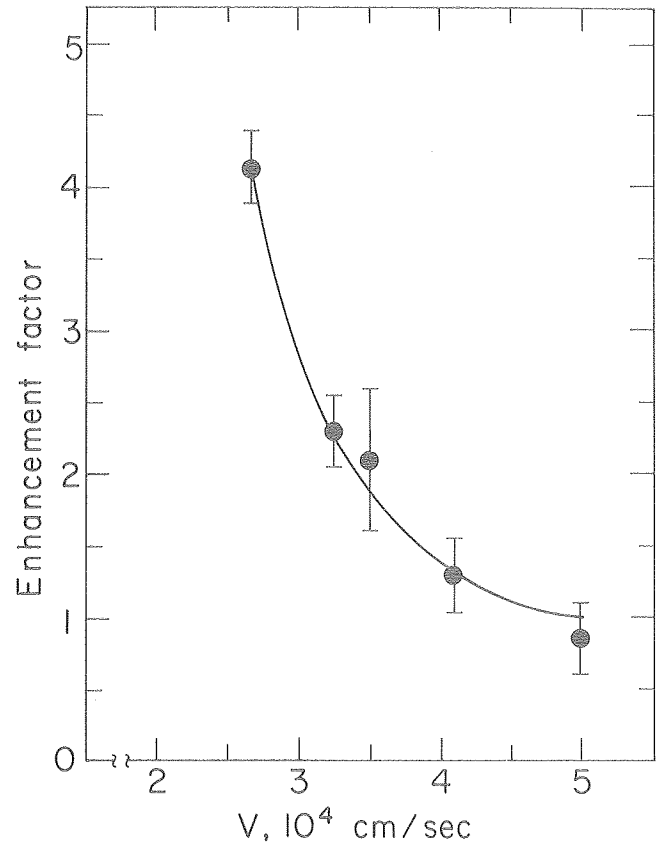

Fig. 7. Internal energy desorption enhancement factors as a function of translational energy. At low velocities EF begins to increase dramatically. EF = 4 implies that the hot CCl_4 molecules have a four times higher probability of scattering relative to the cold molecules. (XBL 7712-11076)

factor, EF, which is the ratio of relative reflected fluxes for molecules having the same translational velocity v_i, but different internal energies due to different beam temperatures:

$$EF = \frac{\left(\dfrac{\text{flux reflected, } T_s = 90\text{ K}}{\text{flux reflected, } T_s = 280\text{ K}}\right)\Bigg|_{T_B = 560\text{ K};\ v_i}}{\left(\dfrac{\text{flux reflected, } T_s = 90\text{ K}}{\text{flux reflected, } T_s = 280\text{ K}}\right)\Bigg|_{T_B = 298\text{ K};\ v_i}}.$$

Figure 7 shows the EF values determined for five velocities between 2.5×10^4 cm/s and 5×10^4 cm/s. EF ~ 4 was observed for the slowest velocities studied. This implies that the internally excited CCl_4 molecules are four times more likely to scatter from the surface than the vibrationally cold molecules.

The velocity selector used in these studies transmits a 17% FWHM velocity distribution. The actual distributions transmitted have been studied using time-of-flight analysis and are shown in Fig. 8. At 125 Hz and 165 Hz the transmitted distributions essentially overlap for T_B = 298 K and T_B = 560 K transmitted. For higher frequencies the hot beam distributions are seen to shift to slightly higher velocities due to the steep slope of the T_B = 298 K Maxwell-Boltzmann distribution in that velocity region. The EF factors in Fig. 7 have been corrected for these shifts.

Note that is translational energy decreases the internal energy of a molecule becomes important in determining sticking probabilities. Using the vibrational quantum partition function for an ideal polyatomic, the internal energy difference between CCl_4 at 298 K and 560 K is found to be about 3.7 kcal/mole. The translational energies studied here range from about 1.1 kcal/mole to 4.6 kcal/mole. Clearly this indicates that internal excitation of a molecule, by either thermal heating or laser irradiation (SF_6, for example), can significantly affect sticking probabilities. The enhancement factor, EF, will be large when translational energies are decreased to the point where the escaping (inelastically scattered) molecules have only a small excess (or deficit) of translational energy above the outer attractive potential wall of the surface.

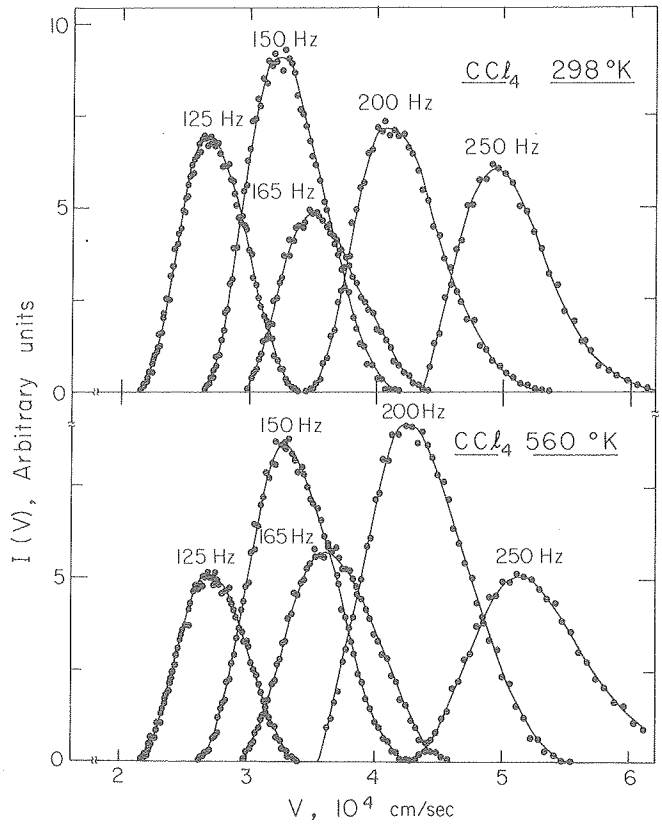

Fig. 8. Flux distributions transmitted by the velocity selector at the five settings used in the determination of EF. These were determined by placing a time-of-flight wheel in front of the detector and looking directly at the beam with the rotatable detector. (XBL 7712-11073)

Future studies will be conducted using a target surface that can operate at still lower T_S values. This will allow us to probe the sticking behavior of other molecules that do not condense at 90 K. Mode selective excitation of appropriate molecules using a continuous wave CO_2, CO, or HF laser will also be explored to further our understanding of internal mode influence on sticking probabilities.

1. J. D. Doll, J. Chem. Phys. 66, 5709 (1977).
2. N. F. Basov, et al., JETP Lett. 22, 102 (1975).
3. K. S. Gochelashvili, et al., Zh. Eksp. Teor. Fiz. 70, 531 (1976).
4. R. M. Logan and R. E. Stickney, J. Chem. Phys. 44, 195 (1966).

6. RESEARCH PLANS FOR CALENDAR YEAR 1978

Yuan T. Lee and Y. Ron Shen

The completion of the construction of the neodymium yag laser optical parametric oscillator in early 1978 will give some significant impact to the program of molecular beam laser isotope separation.

With this tunable IR laser, the scheme of selective decomposition of van der Waals molecules will be evaluated thoroughly. The first series of molecule that will be tested are the complexes of hydrogen halides. For example,

$$Ar \cdot HCl^{35} \rightarrow ArHCl^{35\ddagger} \rightarrow Ar + HCl \ .$$

The practicality of the concept of the separation through recoil velocity will be assessed from the careful measurements of angular and velocity distributions of dissociated molecules.

The program on the dynamics of multiphoton decomposition will mainly be concerned with decomposition using two frequencies. The understanding of this process will give a great impact to the success of the separation of uranium isotopes by the multiphoton dissociation process. Some investigations will also be carried out on the chemical behavior of highly vibrationally excited molecules by multiphoton excitation.

The process of selective condensation of vibrationally excited molecule that was carried out with thermal excitation during the last year will be carried out by laser excitation in the coming year.

7. 1977 PUBLICATIONS AND REPORTS

Y. T. LEE and Y. R. Shen and Associates

1. See Y. T. Lee in Molecular Sciences Section, p. 379.

2. See Y. R. Shen in Materials Sciences Section, p. 180.

V.

Energy Technology

ENERGY TECHNOLOGY

a. Development of Electrochemical Synthesis and Energy Conversion

J. W. Evans, R. H. Muller, J. Newman, and C. W. Tobias, Principal Investigators

Introduction. The aim of this program is to improve the energy efficiency, lower the capital cost, and increase the materials yield of electrochemical cell processes employed in the reversible conversion of chemical to electrical energy in galvanic cells and in the production of materials by electrolysis.

1. PROCESS EVALUATION FOR THE ELECTROWINNING AND REFINING OF POTASSIUM

Henry Law and Charles W. Tobias

Overpotentials associated with potassium deposition in propylene carbonate (P.C.) containing 0.5m $KAlCl_4$ solute have been performed by 1) galvanostatic pulse method on a stationary electrode, 2) current interruption following steady-state electrolysis on a rotating disk electrode. The substantially lower overpotentials observed on the rotating disk (Fig. 1) indicates that in steady-state cathodic reduction the passivation of the surface by solvent impurities is subdued by containuing reduction of potassium.

Reliable evaluation of current efficiency of potassium deposition is critically dependent on our ability to collect and remove all the metal deposited and separate it from the electrolyte. Significant difficulties are experienced in obtaining potassium in a coherent form, allowing easy collection and removal from cells. The deposit morphology is strongly temperature dependent: at 30°C deposits are generally powdery and nonadherent; at 50° they tend to be loosely spongy (Fig. 2); and at 70° (above the m.p.) they are present in small liquid globules, which do not coalesce into larger droplets (Fig. 3). Development of a practical method for the collection and removal of potassium from cathode compartments represents the highest priority task in this project.

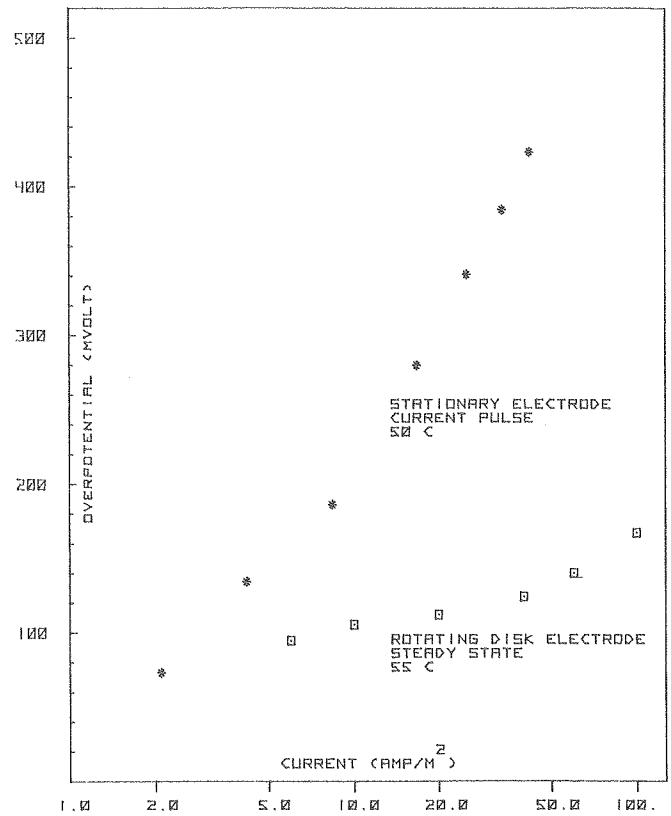

Fig. 1. Comparison of different overpotential measuring techniques in potassium deposition from 0.5 m $KAlCl_4$/propylene carbonate solution. The galvanostatic pulse duration is 72 msec; the rotational speed of the disk electrode is 1400 rpm. (XBL 782-7011)

Fig. 2. Spongy potassium deposit obtained from 0.5 m $KAlCl_4$/propylene carbonate electrolyte at 50°C. Cathode potential was maintained constant at -200 mV relative to potassium reference electrode. (XBB 781-791)

2. ANODIC SURFACE LAYERS ON BATTERY MATERIALS

Newly developed techniques for in situ observation of electrode surfaces are being used to provide direct experimental evidence about properties and modes of formation of anodic surface layers with desirable electrochemical properties on materials of interest for use in batteries.

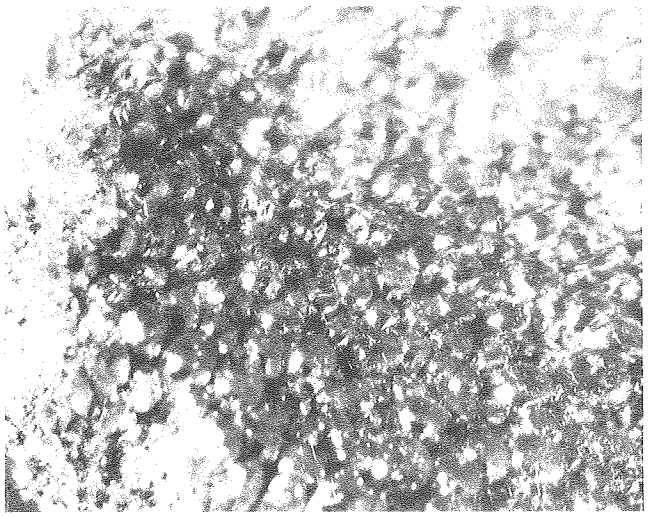

Fig. 3. Spherical globules of molten potassium deposited from 0.5 m $KAlCl_4$/propylene carbonate electrolyte at 70°C at 1.5 mA/cm^2. Magnification: 20x. (XBB 781-792)

a. Alkaline Battery Reactions

Craig G. Smith and Rolf H. Muller

Anodic film formation in stagnant electrolyte on Zn, Ag, Cd, and Cu single crystals has been studied by ellipsometry. The concentration of KOH has been varied from 0.5 to 6.0 M, and current densities suitable for each metal have been used. These have ranged from 5 μA/cm^2 for Cd to 0.5 μA/cm^2 for Zn. Resultant film properties have been found to depend on current density, electrolyte concentration, and crystal orientation. Figure 1 illustrates a

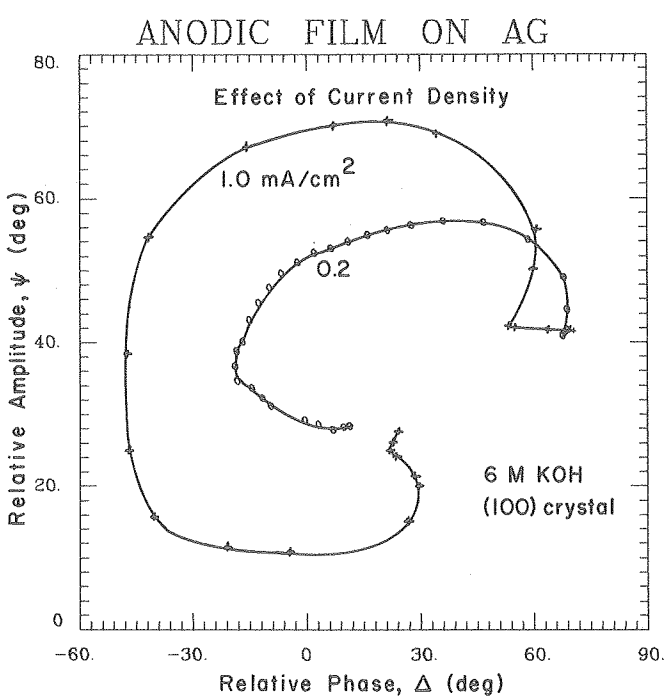

Fig. 1. Anodic film formation on Ag. Effect of current density on ellipsometer parameters ψ and Δ. Single crystal (100), stagnant 6 M KOH. (XBL 773-7988)

dependence on current density, which according to preliminary computations, is caused either by a greater porosity of the film or a smaller roughness of the substrate at the lower current density.

A flow cell is presently being used to study film formation under forced convection. Figure 2 shows the response of our automatic ellipsometer to anodic current pulses on zinc. These measurements are consistent with the formation of a colloid layer in the electrolyte adjacent to the electrode surface. Ellipsometer observations also indicate that the rapid increase in electrode potential, characteristic of electrode passivation, occurs simultaneously with the formation of a very thin (10 Å) surface layer.

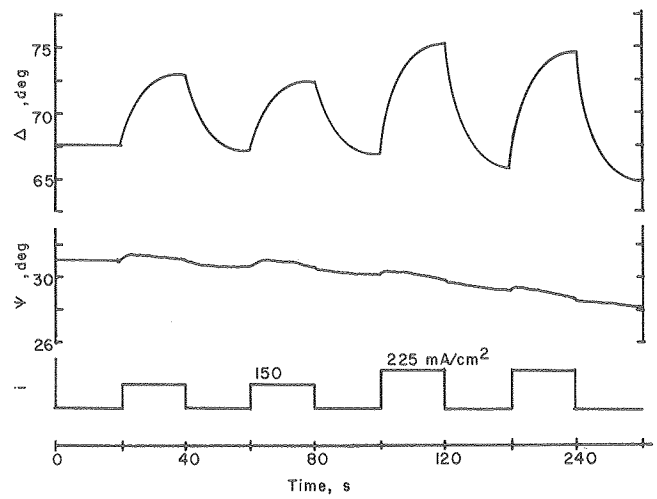

Fig. 2. Anodic film formation on Zn. Response of the relative phase Δ and the relative amplitude ψ to anodic current pulses. Single crystal (1000), Re = 850, 6 M KOH + 0.25 M ZnO. (XBL 7712-10956)

b. Acidic Battery Reactions

Richard D. Peters and Rolf H. Muller

The nature of anodic film growth on lead in sulfuric acid is being investigated. Lead sulfate is the first anodic reaction product; it is formed upon discharge on the negative plate of a lead acid battery and is also a corrosion product that appears during open-circuit wet stand. The purpose of this work is to determine factors that control nucleation, growth and structure of $PbSO_4$ layers on Pb.

Dissolution-precipitation mechanisms with homogeneous or surface nucleation[1,2] have been proposed for $PbSO_4$ formation. Ellipsometry is being used to determine the optical properties of surface layers and adjacent electrolyte regions. Thickness and porosity of the solid film are derived from the measurements. Of interest are the conditions under which passivation of the metal occurs.[3] In addition, the existence of a layer of colloidally-dispersed[4] $PbSO_4$ in the liquid phase is being investigated. Such a layer could be formed by a

homogeneous precipitation mechanism and may account for some poorly understood phenomena in lead-acid batteries.

Experiments have been conducted with pure (99.96%) lead in 3M H_2SO_4 under controlled mass-transport conditions. Optically smooth lead surfaces have been prepared by compression with a polished steel die at 30,000 psi. The observed initial film growth is illustrated in Fig. 3. Up to 900 Å thickness, the measurements are consistent with calculations for dense $PbSO_4$ (n = 1.88). Upon interruption of the anodic current, the $PbSO_4$ film is found to dissolve in the flowing electrolyte.

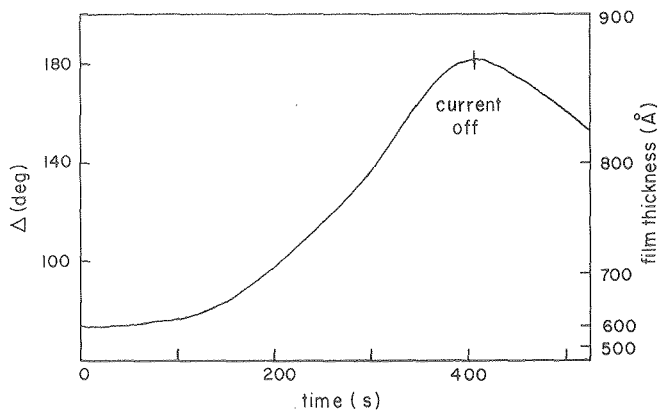

Fig. 3. Formation and dissolution of anodic $PbSO_4$ film on Pb in 3M H_2SO_4. Measured ellipsometer parameter Δ and derived film thickness. (1.3 mA/cm^2, Re = 780). (XBL 7712-10957)

The observation of the removal of any colloidal layer upon current interruption will require the elimination or precise prediction of film dissolution.

1. G. Archdale and J. A. Harrison, J. Electroanal. Chem. 34, 21 (1972).
2. T. Chiku and K. Nakajima, J. Electrochem. Soc. 118, 1395 (1971).
3. O. Pavlov and R. Popova, Electrochim. Acta 15, 1487 (1970).
4. H. Bode, Lead Acid Batteries, Wiley, New York, (1977), p. 147.

c. Lithium in Aqueous Electrolytes

Richard D. Peters and Rolf H. Muller

The behavior of the Li-H_2O battery is largely controlled by film formation on the Li metal anode. The feasibility of using ellipsometry for in situ observation of lithium anodes in aqueous electrolyte has been investigated for the determination of thickness and optical constants of protective surface layers. The properties of these films depend on mass transport conditions at the anode.

Experiments were conducted galvanostatically with current densities ranging from 10 to 250 mA/cm^2 and electrolyte flow rates ranging from zero to 30 cm/s (Re = 4500). Lithium samples were polished and transferred from a glove box to the flow channel in an inert atmosphere. Observations began when flowing electrolyte contacted the Li anode and electrolysis with a preset current density was initiated.

Saturated 4.8 M LiOH and 14 M KOH saturated with 0.6 M LiOH were used to keep the activity of water low. In the upper range of current densities and the lower range of flow rates, mass-transport theory predicts that the interfacial concentration of LiOH exceeds its solubility. The principal difficulty in this study was found to be the initial spontaneous reaction of lithium metal with aqueous electrolytes. This process causes light scattering of the incident beam by hydrogen bubbles and results in a reflected light beam of extremely low intensity during the first second after immersion. Reaction between lithium and water subsides after several seconds, however, by that time the metal surface has been significantly roughened. Combined with a poorly reflecting precipitate layer of LiOH, the reflected light intensity is again too low for analysis of the state of polarization.

A further decrease in water activity has been achieved by use of water vapor diluted with argon. Light reflection from Li surfaces reacting with this mixture is strong enough for ellipsometer measurements. Figure 4 shows experimentally measured ψ and Δ values for the growth of a layer on lithium resulting from the reaction with water vapor at a partial pressure of 1.5 Torr.

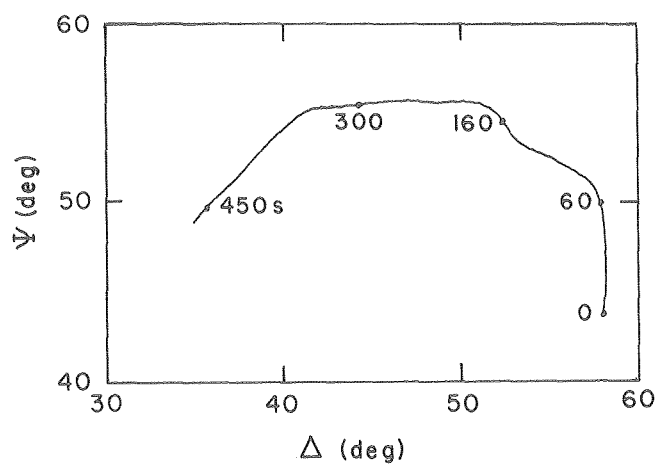

Fig. 4. Ellipsometer measurement of lithium surface reacting with water vapor of 1.5 Torr partial pressure. Time in seconds given along the curve. (XBL 7712-10959)

Homogeneous film calculations assuming a porous transparent film and a mixture of Li and LiOH are not able to reproduce the experimental data. Better agreement can be obtained with computations for a porous transparent film on a rough substrate.

d. Modeling of Anodic Film Formation

Craig G. Smith and Rolf H. Muller

Results of conventional computations[1] for the interpretation of ellipsometer measurements of the electrochemical oxidation of silver in alkaline solution indicate that in addition to a porous solid film a colloidal layer[2,3] is formed in the electrolyte adjacent to the electrode surface. These interpretations are, however, not unique. In order to search for all possible values of the parameters that describe the electrode processes, models for the automated interpretation of ellipsometer measurements of anodic film formation are being developed. These models are designed to make full use of the time-dependence of the ellipsometer data and the current and potential measurements. By the consideration of mass-transport processes, continuous mass and charge balances are established. Thus, the interdependence of the observed quantities, which has not been previously considered, is brought to bear on the multidimensional interpretation problem.

The first model that has been investigated[1] is illustrated in Fig. 5. It assumes the formation of a homogeneous solid film covered by two inhomogeneous layers in the liquid phase. The porosity of the solid film may vary with time; the inhomogeneous layers represent colloidal and mass-transport boundary layers in the electrolyte adjacent to the electrode surface. Flux densities across the interfaces between these layers, in conjunction with the conservation of mass and charge, are used to compute changes in the thicknesses of the films with time. Seven parameters are evaluated by a least squares fit of the experimental data. Figure 6 shows the accuracy with which the model describes the electrode processes. The accuracy of the curve fit is found to decrease if later portions of the experiment were also considered. Changes in the film formation processes at the later stages, which are not part of the model, are indicated by this disagreement.

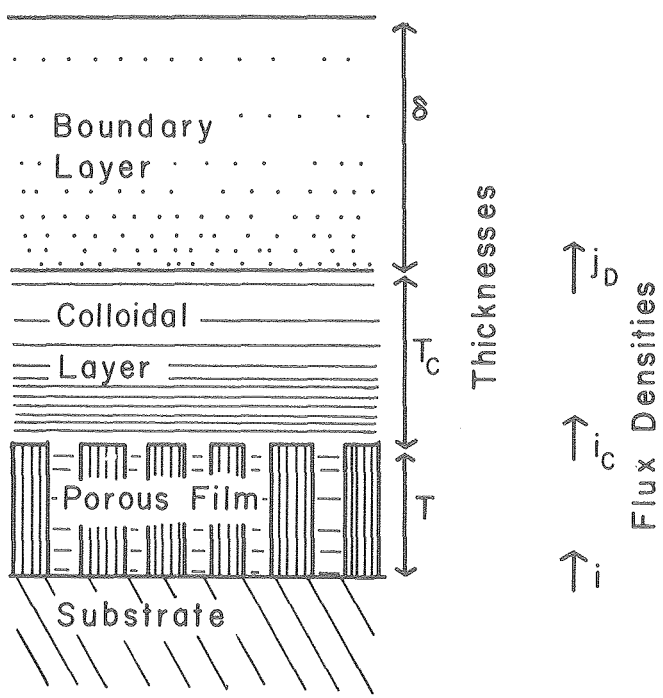

Fig. 5. Optical model for the automated interpretation of ellipsometer measurements. Definitions of layer thicknesses and flux densities between layers. (XBL 772-7782A)

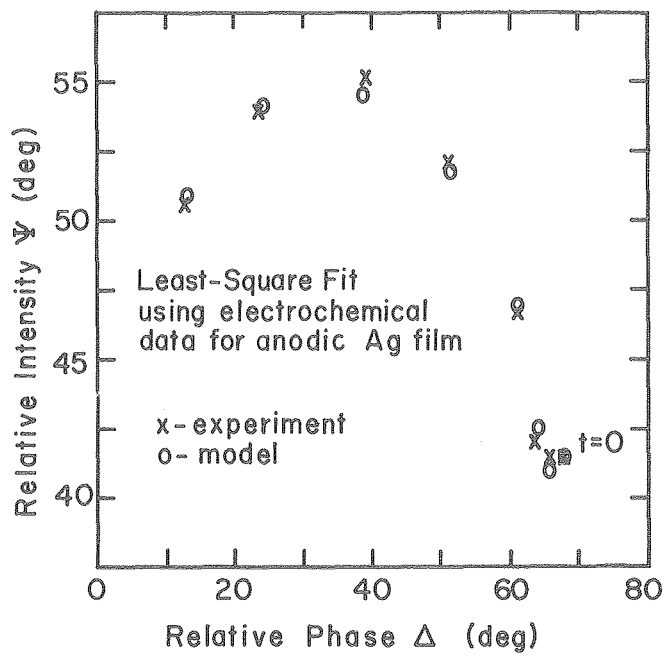

Fig. 6. Automated interpretation of ellipsometer measurements of Ag single crystal (100) in 6 M stagnant KOH. Experiment (x), model (o), 0.6 mA/cm^2. (XBL 777-9501)

A more sophisticated model is in preparation. It includes roughening of the metal substrate, dual solid film structure, and variable film porosities. Constant current and constant potential experiments with either stagnant or forced convection transport conditions may be analyzed. The experimentally measured electrode potential and current density are coupled through homogeneous and heterogeneous nucleation mechanisms to the rates of formation of solid films, the colloidal layer, and the mass-transport boundary layer.

1. C. G. Smith and R. H. Muller, in Optical Polarimetry, Instrumentation and Applications, Soc. Photo-Opt. Instr. Engrs., Bellingham, Wash., Proc. Vol. 112, (1977), LBL-6640 (1977).
2. D. A. Vermilyea, Anodic Films, in Advances in Electrochemistry and Electrochemical Engineering, P. Delahay, Ed. Vol. 3, (Interscience, New York, 1963), p. 227.
3. C. Wagner, J. Electrochem. Soc. 101, 60 (1954).

e. Operation of Ultrahigh Vacuum System

Craig G. Smith and Rolf H. Muller

We have previously reported[1] on the construction of an ultrahigh vacuum system in which surface films may be analyzed by ion-etching, Auger spectroscopy, and ellipsometry. Film profiles of porosity and chemical composition may thus be investigated.

Calibration of the Auger spectroscopy capability has been performed by the use of silver and stainless steel samples. After modification of the electronics to improve the resolution, agreement with literature values was obtained. Modification of the vacuum system was required to optimize the position of the ion-etch gun.

---

1. C. G. Smith and R. H. Muller, MMRD Annual Report for 1976, LBL-6016, p. 427.

3. SURFACE MORPHOLOGY OF METALS IN ELECTRODEPOSITION

a. The Effect of Hydrodynamic Flow on Surface Morphology in the Deposition of Cu and Zn

Andrew Kindler, Milan Jaksic and Charles W. Tobias

Our channel flow system, developed in this laboratory earlier for the measurement of mass transfer coefficients along planar electrodes,[1,2] has been substantially modified to facilitate surface morphological studies in copper deposition. Because dissolved oxygen in the electrolyte attacks the copper deposit before it can be removed from the cell for examination, a nitrogen sparging system and oxygen monitor has been installed. A new digital data acquisition system has been added that is capable of recording current and overpotential from nine electrically isolated mass transfer sections in the 15×40 cm segmented electrode. The new system has a suitable time base that allows determination of the number of coulombs that have passed through each segment. The flow apparatus is capable of providing fully developed turbulent flow conditions in the 1 cm deep channel up to Re = 150,000.

A rotating disk electrode system is being used for the study of the effect of hydrodynamic flow on the morphology of zinc deposited from $ZnCl_2$ solutions in the Ph range of 1-5. Solution composition, current density and rotational speed is varied over broad ranges. Platinum, polycrystalline zinc and zinc single crystals were used to evaluate the effect of the nature of substrate.

Over a wide range of current densities (1 to 100 mA/cm^2), and always well below the limiting current density, upon prolonged deposition (up to 180 min), distinct Archimedes spiral patterns appear in the deposit. The profile (depth) and angular frequency of these spirals depend on current density but not on rotational speed (Fig. 1).

(a)

(b)

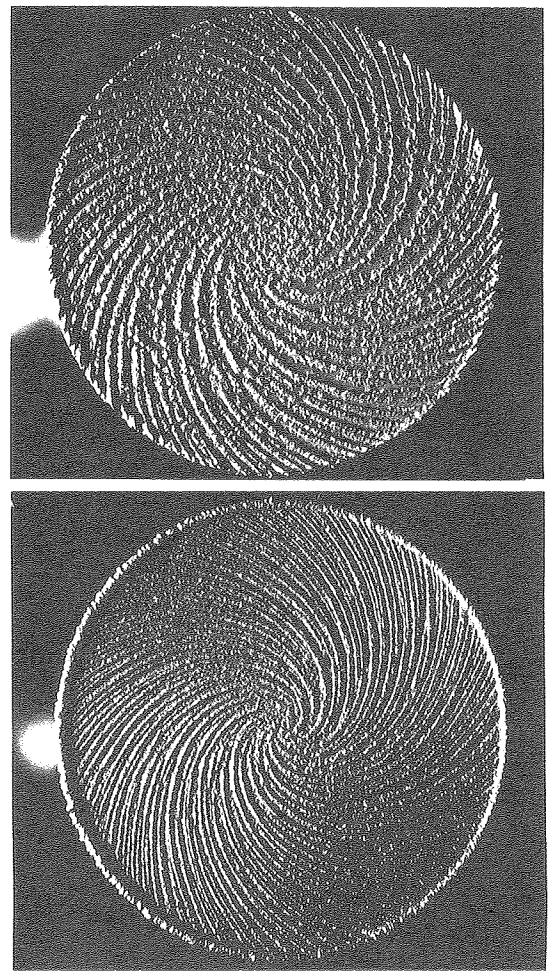

Fig. 1. Effect of current density on angular frequency of spiral patterns in zinc deposited from 1 m $ZnCl_2$ • t = 25°C, time: one hour, rpm: 360, pH = 2.5. (a) 10 mA/cm^2; (b) 30 mA/cm^2. (XBB 781-793)

These spiral helix patterns have been observed to occur over the entire concentration range of $ZnCl_2$ investigated (0.1 - 0.4 m).

Addition of low concentrations of a surfactant (fluorosubstituted betaine, "Zonyl" by the DuPont Co.) drastically changes the appearance of the zinc deposits; while the presence of spirals is still evident (Fig. 2), these are much more closely spaced and less deep than in the absence of the additive. The deposit also demonstrates a much lower surface roughness and a better uniformity of structure. The growth of zinc beyond the edges of the rotated disk is lateral, in the plane of the disk. Presence of 10 ppm Fe^{++}, Ni^{++} or Cu^{++} drastically changes the surface morphology; spongy, plack regions appear, and eventually entirely cover the surface.

The effect of flow on macromorphology well below the limiting current level may be caused by instability phenomena in the velocity boundary layer, initiated by developing roughness as the deposition progresses. A detailed explanation of this phenomenon may lead to an improved understanding of the rather baffling morphological changes

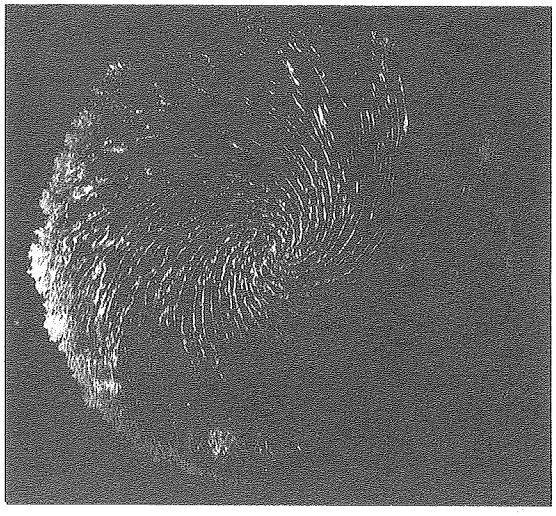

Fig. 2. Fiber-like structure and lateral growth of spiral patterns in zinc deposit extending beyond original disk diameter. 4.0 m $ZnCl_2$ + HCl, 0.1% "Zonyl" surfactant. t = 25°C, time: four hours, 3 pm: 710, current density: 30 mA/cm^2. (XBB 781-794)

that have been observed both in batteries, and in metal winning and refining process.

1. J. R. Selman and C. W. Tobias, IMRD Annual Report for 1970, UCRL-20500, pp. 31-38.
2. U. Landau, A. Kindler and C. W. Tobias, MMRD Annual Report for 1975, LBL-4550, p. 165.

b. Dynamic Modeling of Surface Profiles in Electrodeposition/dissolution

Geoffrey Prentice and Charles W. Tobias

A computer implemented model to determine the profile of an electrodeposit as a function of time is being developed. A finite-difference technique is employed, and successive-overrelaxation is used to hasten convergence of the potential distribution in the region where Laplace's equation applies. Accurate and efficient computation of the normal to the surface is facilitated by approximating the profile by a cubic spline. The components of the current density, calculated by numerically differentiating the potential distribution at the surface, are projected on the normal to the profile to determine the local thickness of the deposit.

As a test of the precision of the technique, the primary current distribution on a low amplitude sinusoidal profile has been determined; it is in good agreement with the analytical results derived by Wagner.[1] The developing profiles that result from continuing deposition were calculated at suitably small time intervals by advancing the local deposit thickness according to the specific charge (coulombs/cm^2) passed (Fig. 3).

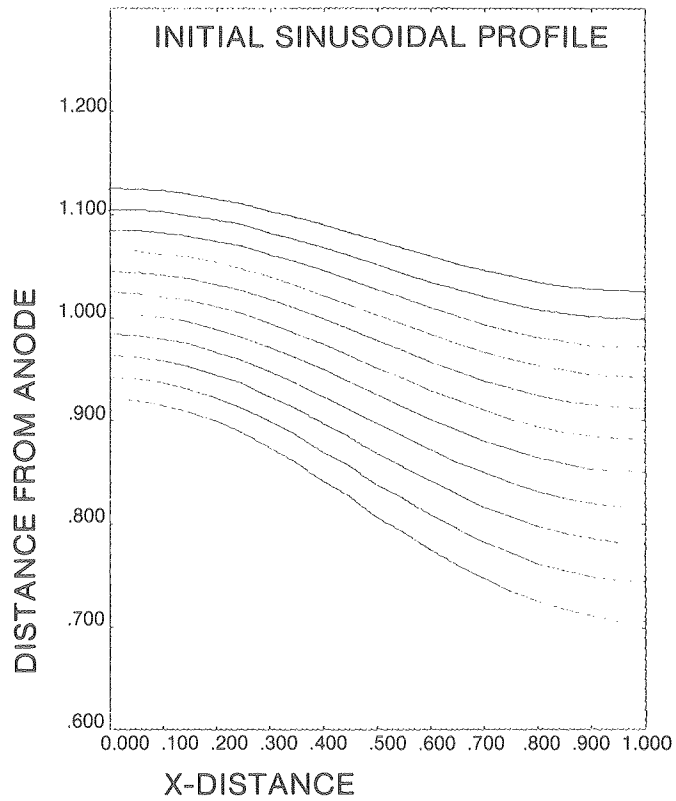

Fig. 3. Surface contours at ten time steps. Upper curve is the initial profile. At each time step metal is above, electrolyte below. Right and left sides are insulated. Distances are in arbitrary units. (XBL 782-7113)

The method previously reported[2] was not sufficiently accurate to overcome difficulties resulting from the development of inherently unstable geometries, and the costs associated with evaluating a single moving boundary problem were quite excessive. The new technique is accurate and cost efficient: the complete solution of the problem illustrated in Fig. 3 required an execution time of 0.68 sec. on a CDC 7600 system.

1. C. Wagner, J. Electrochem. Soc. 101, 225 (1954).
2. J. B. Riggs, Modeling of the Electrochemical Machining Process, (Ph.D. thesis), LBL-6019, January 1977.

4. ANALYSIS AND SIMULATION OF ELECTROCHEMICAL SYSTEMS

a. High Temperature Batteries

Richard Pollard and John Newman

The Li,Al/LiCl,KCl/FeS_x battery is a candidate for storage of off-peak electrical energy and for electric vehicle propulsion. A mathematical

model is needed to be able to predict the operational characteristics of the battery and to be able to obtain pertinent information for its design and optimization.

With this goal, concentrated electrolytic solution theory has been generalized to provide a framework for the description of transport processes in a mixture of two molten salts with a common anion. Non-steady state material balances for the solid and liquid phases have been developed together with equations for the ohmic potential drop and for the overall conservation of volume. These equations, combined with a description of the kinetic behavior of the system, may be used to predict the time-dependent and position-dependent behavior of electrolyte concentration, porosity, current, and reaction rate in the porous electrodes.

b. Design of Flow-Through Porous Electrodes for Redox Energy Storage

James A. Trainham and John Newman

To store off-peak electrical energy for later use during peak demand periods, various rechargeable batteries are under consideration. One of these systems is the flow-redox battery. The major advantage of this system over other batteries is that it has theoretically an unlimited cycle life. This is due to the fact that redox reactions do not affect the morphology of the electrode materials.

In the cell configuration considered here, the current and fluid flow are in parallel. This configuration is advantageous because a membrane separator is not required.

A one-dimensional model for flow-through porous electrodes has been developed. This will be used to predict the optimum current density and flow-rate both on charge and discharge. The chemical system considered is the Ti(III)|Ti(IV)||Fe(III)|Fe(II) redox complex in a HCl solution.

c. The Effect of Electrode Placement and Finite Matrix Conductivity on the Performance of Flow-Through Porous Electrodes

James A. Trainham and John Newman

A one-dimensional model for flow-through porous electrodes is used to predict the effluent concentration as a function of matrix conductivity and electrode length for upstream and downstream placement of the counterelectrode and current collector relative to the fluid inlet to the working electrode.[1] Two chemical systems are considered: 1) the removal of copper from sulfate solutions and 2) the removal of silver from thiosulfate solutions.

For an infinite matrix conductivity, the lowest effluent concentration is achieved when the counterelectrode is placed upstream to the fluid inlet of the working electrode. When the matrix conductivity is small, the lowest effluent concentration is still achieved for upstream placement of the counterelectrode; however, the optimum placement of the current collector depends on the chemical system and the value of the matrix conductivity that can be achieved in practice.

Calculations show that for downstream placement of the counterelectrode a limiting current distribution cannot be achieved (for electrode lengths of interest here). The most undesirable configuration for achieving a low effluent concentration when the matrix conductivity is low is when both the counterelectrode and current collector are placed downstream of the fluid inlet.

Distribution of potential, reaction rate, and electric driving force are presented for four different configurations: 1) upstream counter-electrode, downstream current collector, 2) downstream counterelectrode, upstream current collector, 3) upstream counterelectrode, upstream current collector and 4) downstream counterelectrode, downstream current collector.

---

1. James A. Trainham and John Newman, The Effect of Electrode Placement and Finite Matrix Conductivity on the Performance of Flow-Through Porous Electrodes, LBL-6260, May 1977.

d. Low Péclet Number Behavior of the Transfer Rate in Packed Beds

Peter Fedkiw and John Newman

The asymptotic behavior of the mass-transfer coefficient in a packed bed reactor at low Péclet numbers is dependent upon how the coefficient is defined. A singular perturbation approach coupled with heuristic arguments[1] is used to demonstrate that the film mass-transfer coefficient in deep beds approaches a constant value as the Péclet number decreases. The film coefficient is utilized in the one-dimensional model of a bed as a sink term in the governing equation. The volumetric, or effective, mass-transfer coefficient that relates the overall reactant conversion to a logarithmic mean concentration driving force, decreases linearly with the Péclet number as the Péclet number approaches zero. The distinction between the two coefficients is important in the low Péclet number region. Analogous results apply to heat transfer. Reported experimental data support these predicted trends.

---

1. Peter Fedkiw and John Newman, Low Péclet Number Behavior of the Transfer Rate in Packed Beds, LBL-6074, March 1977.

e. Numerical Calculations for the Asymptotic, Diffusion Dominated Mass-Transfer Coefficient in Packed Bed Reactors

Peter Fedkiw and John Newman

For deep beds, the effective Sherwood number approaches a proportional relationship to the Péclet number as the Péclet number tends to zero. Using a sinusoidal periodically constricted tube model for the voids in the bed, the constant of proportionality has been calculated. This constant

depends upon the dimensionless ratios of three lengths: tube radius, oscillation amplitude, and wavelength.

f. High Pressure Flow-Through Porous Electrodes: Application to Metal Ion Removal from Dilute Streams

Gary Trost and John Newman

Flow-through porous electrodes offer a high ratio of surface area to bed volume and as such find potential application in industrial electrochemistry. Increased interest has been generated in the use of porous electrodes for removal of heavy metal ions from dilute waste streams. In this area it has been shown that the porous electrode reactor can out perform other electrochemical methods. If comparison to other more established processes is to be made, a firm mathematical description of electrode behavior is needed.

Recently a sophisticated model[1] has been developed that incorporates one primary reactant and allows for a single competing side reaction. It has been determined that the model agrees well with published data on copper deposition. The model will be further tested against data on other metal systems, most notably lead deposition.

The removal of lead ions from aqueous solutions is particularly troublesome due to the undesirable hydrogen side reaction. It is necessary to run the porous electrode reactor under pressure to increase the current efficiency for the lead deposition reaction and inhibit nucleation of any dissolved hydrogen. Data will be taken on a lead system to determine reactor performance as a function of electrode pressure. Results will be compared to model predictions.

1. James A. Trainham and John Newman, A Flow-Through Porous Electrode Model: Application to Metal-Ion Removal from Dilute Streams, LBL-6041.

5. CURRENT INEFFICIENCIES IN ALUMINUM REDUCTION CELLS

J. W. Evans and Y. Zundelevich

This investigation, which started in the Fall of 1977, is being carried out within a group concerned with rate phenomena (fluid flow, heat transfer, mass transfer, chemical and electrochemical reaction kinetics) that govern the productivity and performance of processes for producing metals. Other recent investigations of this group have been concerned with the kinetics of iron ore reduction, the electrodeposition of copper and cobalt by fluidized bed electrodes and melt flow in electric induction furnaces.

Of particular interest in this investigation is the circulation of molten aluminum and cryolite (electrolyte) in the Hall-Heroult cells that are used for the electrolytic production of aluminum. This production of aluminum entails an energy consumption of the order of 100 billion kWh per/yr in the United States, representing approximately 7% of the total energy consumption of the metals and mineral industries. The production rate of aluminum per unit of electricity passed through the cell is well below the theoretically expected value in commercial Hall-Heroult cells. There is evidence in the literature[1] that the failure to achieve the expected production rate arises from a small solubility of aluminum in the molten cryolite. This dissolved aluminum is then carried by the convection of the cryolite to the cell anodes where it re-oxidizes. The convection of the cryolite arises partly from gas bubbles generated at the anode and partly from natural convection but in the main it is a consequence of electromagnetic stirring forces acting on the cryolite and molten aluminum. It is therefore expected that if these electromagnetic stirring forces can be controlled, so as to minimize cryolite circulation, there will be an increase in cell productivity and a corresponding decrease in the electrical energy needed to produce unit mass of metal. This is the objective of the investigation.

The research group working on this project has been concerning itself for a few years with the computation of electromagnetically driven flows including a study of metal circulation in induction furnaces[2,3] and electroslag remelting units.[4] The computational algorithms developed in these prior studies are being extended to the Hall-Heroult cell.

The group has been able to reach a tentative agreement with Kaiser Aluminum's Reduction Research Center in Permanente, California. This Research Center has two full scale reduction cells that are used for experimental purposes. For some time the Center has been performing velocity measurements on the aluminum within the cells and electromagnetic field measurements in and around the cells. Velocity measurements were made by determining the rate of dissolution of an iron rod immersed in the molten aluminum. This dissolution rate is dependent on the local aluminum velocity in a reproducible manner. Kaiser Aluminum is willing to allow the use of some of their data in order to test mathematical models for computing metal velocities.

It is believed that a similar technique can be developed to measure cryolite velocities by measuring the rate of dissolution of ceramic rods in the cryolite. An apparatus has been built at Berkeley with the intention of testing this conjecture. The apparatus consists of an inductively heated carbon lined steel crucible that contains molten cryolite. A low speed regulated motor drives a ceramic rod through the melt at known velocity and the dissolution rate is determined by measurement of the diameter change following immersion for a given time. If the device proves successful this technique will be used by Kaiser to generate cryolite velocity measurements that will be invaluable in testing the velocity computations.

1. A. M. Arthur, Metallurgical Trans. 5, 1225 (1974).
2. E. D. Tarapore and J. W. Evans, Metall. Trans. 7B, 343 (1976).

3. Ibid 8B, 179 (1977).
4. E. D. Tarapore, Fluid Flow in ESR Units, unpublished report.

6. RESEARCH PLANS FOR CALENDAR YEAR 1978

J. W. Evans, R. H. Muller, J. Newman and C. W. Tobias

a. Process Evaluation for the Recovery of Potassium Metal

New methods will be systematically explored for the collection and removal of potassium deposits from cells equipped with Nafion membranes. Steady-state mass and voltage balances will be established in a 1 A cell, to enable evaluation of the economic feasibility of large scale electrowinning and refining of potassium at ambient temperatures. Alternatives for practical solvent preparation techniques will be compared using gas chromatography and electrochemical methods of analysis.

b. Anodic Surface Layers on Battery Materials

The automated computer interpretation of ellipsometer data will be refined in order to derive the dependence of anodic film properties on transport conditions, electrolyte composition and growth rate. Of particular interest are determinations of the interfacial concentration of dissolution products at the onset of film formation on Zn, Ag, Cd and Pb. Ion etching, Auger spectroscopy and ellipsometry will be used in combination to determine structural and chemical characteristics of anodic films.

c. Surface Morphology of Metals in Electrodeposition

The initiation and propagation of surface roughness and of macroscopic irregularities in copper deposition from acid $CuSo_4$ electrolyte will be evaluated over a broad range of Re and Sc numbers in our semiwork scale channel flow apparatus. Attempts will be made for the quantitative interpretation of the mechanism responsible for the development of regularly periodic surface profiles in zinc deposition. Secondary and tertiary current distributions will be computed for an initially sinusoidal surface contour, using our moving boundary theoretical model. Experiments will be initiated to compare actual profiles with those obtained from the model. The development of flexible, economical, user-oriented computer simulation of the metal deposition/dissolution process is the primary objective.

d. Analysis and Simulation of Electrochemical Systems

A mathematical model that describes the behavior of high temperature batteries will be applied to the $Li,Al/LiCl,KCl/FeS_x$ system. Digital simulations for individual electrodes and the separator will be combined to predict the characteristics of the battery as a whole. A high pressure, porous flow-through electrode will be used to study the effect of pressure on the current efficiency of the removal of lead from a dilute waste stream.

Fundamental study of mass-transfer limited reactions in packed beds will be continued. The periodically constricted tube model of a bed will be used to predict high Péclet number mass transfer coefficients. An experimental correlation will be developed.

e. Current Inefficiences in Aluminum Reduction Cells

The method for measuring cryolyte velocities by dissolution of ceramic rods will be developed on a laboratory scale and the test of the method on a large scale will be carried out at Kaiser Aluminum Reduction Research Center. A first mathematical model for computing the cryolyte and metal flow will be completed and tested against data from Kaiser.

7. 1977 PUBLICATIONS AND REPORTS*

J. W. Evans, R. H. Muller, J. Newman, C. W. Tobias and Associates

Journals and Books

1. R. H. Muller, Ellipsometry of Electrochemical Surface Layers, in Optical Polarimetry, Instrumentation and Applications, Soc. Photo-Opt. Instr. Engrs., Bellingham, Wash., Proc. Vol. 112 (1977), p. 68-73.

2. C. G. Smith and R. H. Muller, Interpretation of Ellipsometer Observations of Anodic Films, in Optical Polarimetry, Instrumentation and Applications, Soc. Photo-Opt. Instr. Engrs., Bellingham, Wash., Proc. Vol. 112 (1977), p. 104-109.

3. J. Newman, R. White, J. A. Trainham and T. W. Chapman, Potential-Selective Deposition of Copper from Chloride Solutions Containing Iron, J. Electrochem. Soc. 124, 669 (1977).

4. J. Newman and P. Fedkiw, Mass Transfer at High Péclet Numbers for Creeping Flow in a Packed-Bed Reactor, AIChE J. 23, 255 (1977).

5. J. Newman and J. A. Trainham, A. Thermodynamic Estimation of the Minimum Concentration Attainable in a Flow-Through Porous Electrode Reactor, J. Appl. Electrochem. 7, 287 (1977).

6. J. Newman and J. A. Trainham A Flow-Through Porous Electrode Model: Application to Metal-Ion Removal from Dilute Streams, J. Electrochem. Soc. 124, 1528 (1977).

7. J. Newman, Simultaneous Reactions at Disk and Porous Electrodes, Electrochim. Acta 22, 829 (1977).

Papers presented

1. R. H. Muller, Ellipsometry of Electrochemical Surface Layers, Soc. Photo-Opt. Instr. Engrs., San Diego, Aug. 23-24, 1977, (Paper No. 112-09).

2. C. G. Smith and R. H. Muller, Interpretation of Ellipsometer Observations of Anodic Films, Soc. Photo-Opt. Instr. Engrs., San Diego, Aug. 23-24, 1977 (Paper No. 112-17).

3. C. W. Tobias, The Role of Electrochemical Engineering in Energy Conservation, Keynote Address, Fifth Yugoslav Symposium on Electrochemistry, Dubrovnik, June 1-4, 1977.

4. C. W. Tobias, Modern Problems in Current Distribution, Invited Address, Yugoslav Academy of Sciences, Zagreb, June 6, 1977; University of Banja Luka, June 8, 1977.

5. J. Newman, Summary of Lawrence Berkeley Laboratory Programs on Battery Support Research and Development, ERDA Battery Contractor's Coordination Meeting, Germantown, Maryland, January 27, 1977.

LBL Reports

1. R. R. White, (Ph.D. thesis) Simultaneous Reactions on a Rotating-Disk Electrode, LBL-6094, March 1977.

2. Peter Fedkiw and John Newman, Mass Transfer at High Péclet Numbers for Creeping Flow in a Packed-Bed Reactor, LBL-5406 Rev., December 1976.

3. James Trainham and John Newman, A Flow-Through Porous Electrode Model: Application to Metal-Ion Removal from Dilute Streams, LBL-6041, January 1977.

4. Peter Fedkiw and John Newman, Low Péclet Number Behavior of the Transfer Rate in Packed Beds, LBL-6074, March 1977.

5. James Trainham and John Newman, The Effect of Electrode Placement and Finite Matrix Conductivity on the Performance of Flow-Through Porous Electrodes, LBL-6260, May 1977.

---

* A full list of publications, presentations and reports includes listings given in other sections as follows: Electrochemical Processes, Charles W. Tobias, Principal Investigator, p. 228; Electrochemical Phase Boundaries, Rolf H. Muller, Principal Investigator, p. 247; Electrochemical Systems, John Newman, Principal Investigator, p. 439.

VI.

Fossil Energy

FOSSIL ENERGY

a. Interfacial Properties of Coal in Relation to Its Direct Utilization

*Douglas W. Fuerstenau, Principal Investigator**

1. THE INTERFACIAL PROPERTIES OF COAL

Douglas W. Fuerstenau

The objective of this research program is to carry out investigations that will lead to a better understanding of the role played by surface phenomena in the processing and direct utilization of coal. Coal is an extremely complicated and variable material, and only through careful physical and chemical studies of the surface and bulk nature of coal can optimal utilization of coal as an energy resource be achieved. The research program "Interfacial Properties of Coal in Relation to its Direct Utilization" was initiated in January 1977. Since the program is a new one, most of the projects are in progress and none has reached the state of completion. However, significant progress has been made in understanding the porous nature of coal and in evaluating certain interfacial properties of coal particulates in aqueous medium.

Nearly all processes involved with the direct utilization of coal are, in some measure, based on the nature of the surface of coal. For example, coal that is utilized directly should be separated from contaminating shale and pyrite, and such separation methods as flotation and selective flocculation which appear promising or have already proven successful in some instances, depend to a large extent on the surface properties of coal and associated mineral matter in aqueous and nonaqueous media. Direct-fired boilers utilize comminuted coal, and the efficiency of producing finely-divided coal particulates is directly related to the surface characteristics of these particulates. Hence, to improve coal utilization processes currently in use or to bring many coal deposits, which are currently unusable due to high ash and sulfur content, into vogue, a systematic study of the surface chemical properties of coal and associated mineral matter is necessary.

In the past, research on coal characterization has involved mainly petrographic studies with but limited research on surface characterization, including gas adsorption and electrokinetic behavior. Coal, being a complex material, has a wide range of composition and characteristics, depending upon its rank and type. Extensive studies are necessary to eventually be able to understand and predict the behavior of any coal, let alone different coals, during processing and utilization. Hence, for a comprehensive investigation it is necessary to work with various types of coal. The coals under investigation are anthracite, eastern bituminous coal, western bituminous coal, subbituminous coal, lignite, and cannel coal. These coals vary in rank as well as in sulfur content, thus giving a broad spectrum of properties for study. Both proximate and ultimate analyses of these coals have been made and the results are given in Table 1.

Table 1. Proximate and ultimate analyses of coal samples used in this research.

ID #	Rank	% daf C	Fixed C[a]	BTU[a]	Ash	Vol. Matter	Total S[b]	% Pyrite	% Sulfate[b]	% Org. Sulfur[b]
A-1	Anthracite	89.74	94.31	13701	1.67	4.02	0.76	0.10	0.04	0.62
V-1	Bituminous	79.31	49.73	12540	14.39	35.88	9.13	6.76	0.49	1.88
E-1	Subbituminous	76.01	43.33	10543	21.09	35.58	1.22	0.42	0.05	0.75
R-1	Bituminous	77.18	53.12	12757	5.53	41.35	0.68	0.06	0.00	0.62
L-1	Cannel	83.27	31.31	15093	7.73	61.36	2.31	1.07	0.03	1.11
1-1	Lignite	70.05	35.69	8798	25.10	39.21	1.15	0.07	0.01	1.07

[a]Dry basis.
[b]Dry ash-free basis.

The porous nature of coals of various rank has been investigated through nitrogen gas and water vapor adsorption techniques using a Micromeritics model 2100D Orr surface area/pore volume analyzer. The nitrogen adsorption/desorption isotherms on a sample of Navajo coal are given in Fig. 1. The marked hysteresis between the adsorption and desorption branches of the isotherm (that is a result of capillary condensation in the pores) indicates the presence of macropores in this particular material. Other coals exhibit much finer pores, namely micropores, of a few Angstroms diameter. The results of the nitrogen gas adsorption experiments show that the total surface areas of coals could be as low as 0.5 m^2/g or as high as 100 m^2/g, depending on the rank and type (Table 2). These numbers are in line with published values and scanning electron micrographs show that the gross topography is also in accord with these values. The calculation of porosity and pore size distribution from adsorption/desorption data show that pore size and distribution in coal is a function of its rank.

The results of the water-vapor adsorption experiments have revealed some very interesting things regarding the nature of the interaction of water molecules with various coals. Coal is an amphipathic material with the polar groups

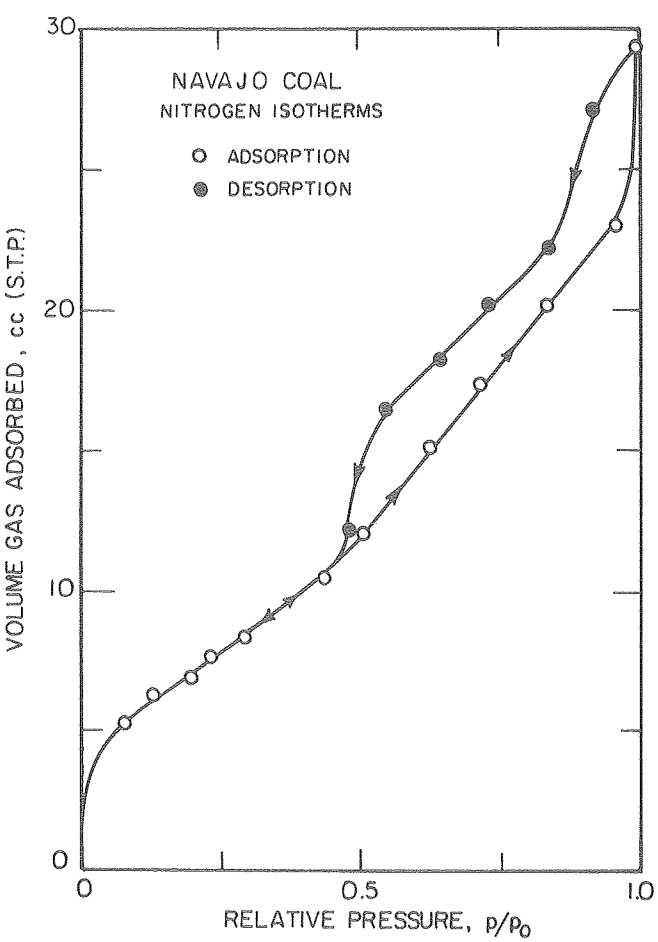

Fig. 1. Nitrogen adsorption/desorption isotherms at 77 K on Navajo coal. (XBL 781-71)

Table 2. Measured specific surface area of coal samples (nitrogen adsorbate).

Coal I.D. #	Surface Area m^2/g
A-1	0.43
V-1	14.04
E-1	29.89
R-1	83.01
L-1	0.87
I-1	19.00

rendering surface sites of a hydrophilic nature and with carbon-carbon bonds resulting in a hydrophobic nature. Since the relative proportion of polar and nonpolar groups varies with the rank of coal, one can expect the interaction of water with coals of varying rank to differ considerably. Our experiments indicate that the adsorbed water can be desorbed completely only from anthracite. With coals of other ranks, only partial desorption could be achieved, which reflects some type of chemical interaction between the coal surface and water vapor (Fig. 2). However, since water molecules may interact strongly with the mineral matter in coal (shale and pyrite), great effort must be made to separate the mineral matter to be certain of the meaning and significance of the results. Steps are being taken to use high-gradient magnetic separation for the purpose of making coal/mineral matter separations.

Although the surface structure of coal is far from completely established, evidence for the presence of various organic functional groups such as alcohols, aldehydes, carboxylic acids, nitrogeneous bases and acids is abundant. These functional groups together with the numerous carbon-carbon double bonds in the coal structure render it susceptible to oxidation when exposed to humid atmosphere. The surface oxidation of coal particulates can be expected to have a pronounced effect on the surface charge, wettability and acid-base properties of coals. Several different approaches are being taken to study these effects. For example, we are currently investigating the change in the surface charge of coal particulates with the degree of oxidation, using acid-base titration techniques. Contact angle measurements are being made to assess the deleterious effect of the degree of oxidation on the natural hydrophobicity of coal. Since polar groups on the surface of coal particles are known to be responsible for the establishment of surface charge when they come into contact with an aqueous medium, the surface charge characteristics of coals of different ranks and surface treatment are being investigated by means of electrokinetic (streaming potential) measurements. Since solution pH should control the ionization of surface ionogenic groups, electrokinetic potentials of different coals have been measured as a function of pH. The

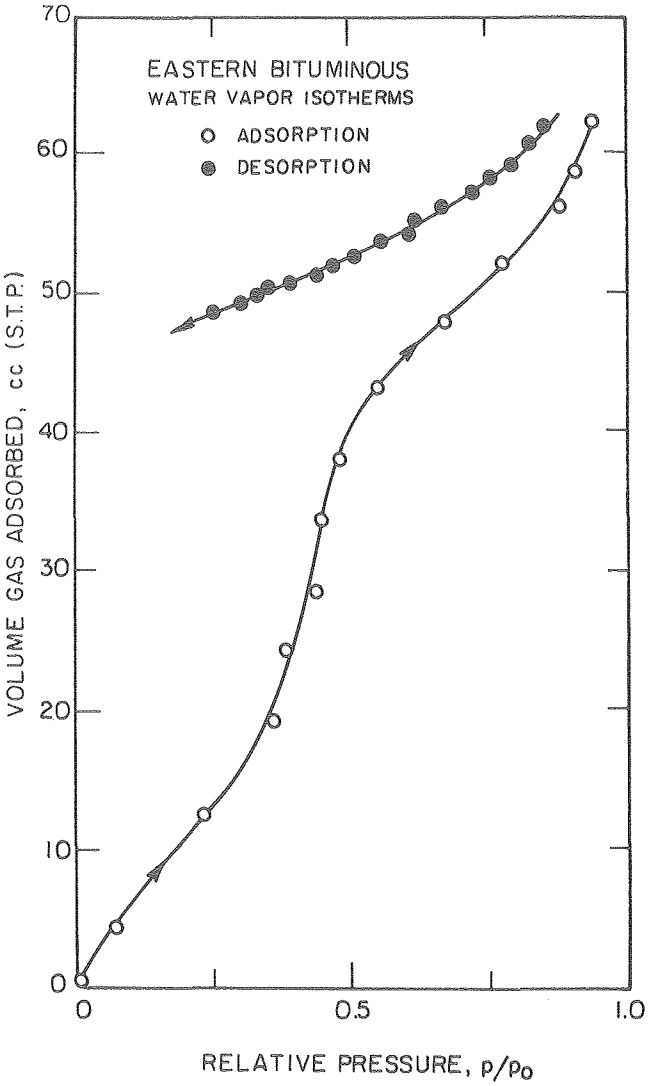

Fig. 2. Adsorption/desorption isotherms of water vapor at 0 C on eastern bituminous coal. (XBL 781-72)

pH at which the surface charge is reversed, called the point of zero charge (pzc), is one of the most important parameters for characterizing the nature of the surface in liquid environment. The observed pzc's of coals appear to occur at pH values between 4 and 7. Figure 3 summarizes how the zeta potential (i.e., the potential at a plane located a few molecular diameters from the solid surface) varies with pH. The pzc of the different coals is the pH at which the zeta potential changes from positive to negative. Since the sign of the surface charge controls the adsorption of ions from solution, eventually the nature and magnitude of charge might be exploited in effecting a selective separation of coal particles from associated mineral matter. As can be seen from the data given in Fig. 3, no correlation seems to exist between the measured pzc values and the ash content of the various coals investigated.

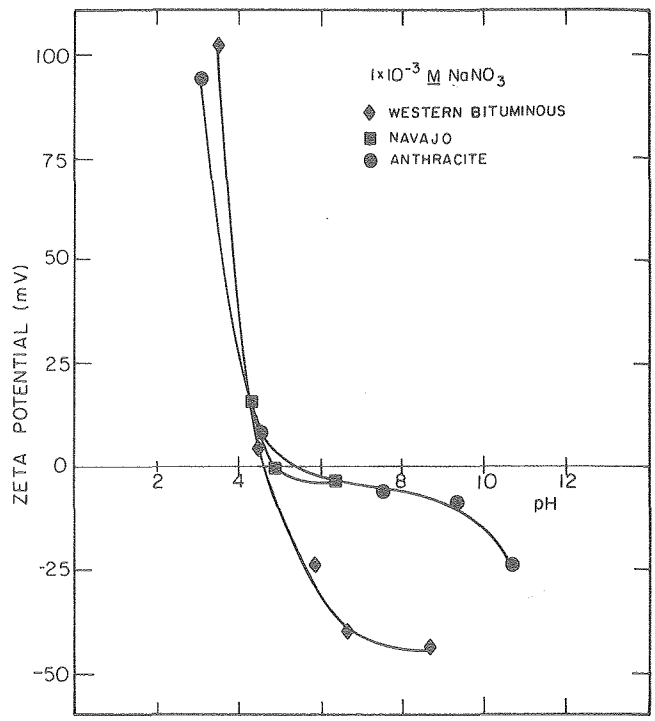

Fig. 3. Streaming potential measurements on western bituminous, Navajo and anthracite coal. (XBL 781-73)

---

*Assistant Research Engineer: S. Raghavan.

2. RESEARCH PLANS FOR CALENDAR YEAR 1978

Douglas W. Fuerstenau

During 1978, the investigations on the surface chemical characteristics of fine coal particles will be continued with special emphasis on the determination of surface charge using titration and electrokinetic techniques in aqueous systems and water vapor adsorption in gaseous systems. Particular attention will be paid to preparing coals from which the mineral matter has been separated by high-gradient magnetic separation so that surface chemical results are not biased by the contained mineral matter.

3. 1977 PUBLICATIONS AND REPORTS

Douglas W. Fuerstenau and Associates

Paper Presented

1. S. Raghavan, Surface Properties of Coal, Engineering Foundation Conference on Particle Science and Engineering in the Coal Processing Industry, Rindge, New Hampshire, 1977.

b. Applied Alloy Design

Victor F. Zackay and Earl R. Parker, Principal Investigators

Introduction. In the past year, the group has made some major changes in the direction and content of its research effort. These changes have been directed toward: one, the attainment of a more balanced spectrum of research activities, and two, toward a better identification of the real material needs of the Department of Energy.

In the first instance, several large projects have been initiated that are now the mainstay of the group's research effort. These are projects funded by the Fossil Energy Research Group of Energy Technology. These projects encompass both an oriented basic and a long-range applied type of research. Another project on campus, sponsored by the Nuclear Energy Research Group of Energy Technology involves the cooperative effort between several departments in the College of Engineering. The project is addressed to the development and study of metallic energy absorbing systems.

In the second instance, the group has consolidated its ties with the functional elements of the Department of Energy, working on mid-to-long range material problems and needs, as enunciated by experts in government and industry. It has truly been a satisfying experience to the group this past year to be in the enviable position of translating the understanding, achieved in the past 15 years, of basic research into the synthesis of useful structural alloys required by the advanced energy conversion systems of the future.

The group leadership will, in coming years, continue to balance its research content, emphasizing the interface between materials science and the advanced technology of materials.

1. WEAR RESISTANT ALLOYS FOR COAL HANDLING EQUIPMENT

M. S. Bhat

A program to develop wear resistant alloys for coal transport and fragmentation equipment was initiated at the Materials and Molecular Research Division of the Lawrence Berkeley Laboratory. The program was divided into the three tasks below.

Task I. Establish alloy design criteria through studies of the relationships between mechanisms and alloy microstructure for the principal wear components of coal transport and fragmentation equipment. Develop evaluation tests that will simulate, in the laboratory, the service operation of the components.

Task II. Develop steels with increased hardness and sufficient toughness that will have acceptable costs in mill/foundry production, and characterize their microstructure, mechanical properties and wear resistance.

Task III. Produce and evaluate experimental quantities of components from the developed alloys through laboratory and in-service tests.

The progress made to date is described below.

Task I. Alloy Performance Criteria. Discussions with coal equipment producers, designers and contractors were helpful in defining the expected operating conditions in coal transportation and fragmentation equipment. An extensive literature survey was conducted in the general area of abrasion mechanisms, wear testing, and relevant metallurgical factors and details of the survey have been reported elsewhere.[1] An alloy screening device which would test for abrasion resistance under high stress two body conditions was designed, constructed and calibrated with standard materials. An overall view of the tester is shown in Fig. 1.

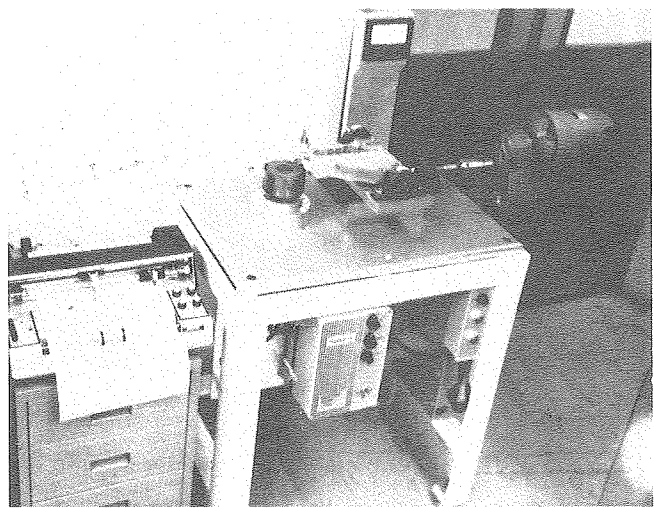

Fig. 1. Overall view of high stress abrasion tester. (XBB 777-6580)

Abrasive wear ratios under high stress conditions were determined for an experimental low alloy ultra high strength steel in various heat treated conditions, using a jaw crusher. The wear ratios compared favorably with data available in the literature as shown in Table 1.

Task II. Alloy Design. A review of the alloy steel literature, and experience gained in past research on high strength steels at LBL was used in the design of alloy steels used for this program. In general, two types of steels were investigated viz. low alloy ultrahigh strength steels and secondary hardening steels. It was believed that the low alloy steels would meet the requirements of the ambient temperature applications that are within the scope of the current program. The higher alloyed steels would be useful for abrasive wear situations where a) the application involved the use of elevated temperatures and b) where surface temperatures in certain wear situations are increased drastically by

Table 1. Hardness and wear ratios of modified 4340 steels and some commercial steels.

Steel	Austenite Temp. (°F)	Tempering Temp. (°F)	Hardness BHN	Wear Ratio[a]
4340+1.5Al+1.5Si (#X-3574)	1832	572 (1h)	578	0.232
4340+1.5Al+1.5Si (#X-3584)	1832	572 (2h)	555	0.220
4340+1.5Al+1.5Si (#X-3585)	1832	572 (1h)	514	0.248
12S	-	-	514	0.266
HiC/12S	-	-	555	0.242
AISI4340 #22A	1750	Normalized	320	0.67
AISI4340 #22B	1600	1200 (1h)	340	0.72
AISI4340 #22C	1600	400 (1h)	529	0.23

[a] Wear ratio = $\frac{\text{Wt. loss of test speciment}}{\text{Wt. loss of standard}}$

The standard used was Steel T1, heat treated to 269BHN. The data on steels 12S and HiC/12S were provided by ESCO Corporation. The data on the AISI14340 steels were obtained from D. E. Diesburg and F. Borik, Materials for the Mining Industry, Climas Molybdenum Company, U.S.A., 1974, p. 15.

friction and plastic deformation. Substantial progress was made in developing the high alloyed secondary hardening type steels and the results of the studies are presented below by the individual investigators.

1. M. S. Bhat, V. F. Zackay and E. R. Parker, Wear Resistant Alloys for Coal Handling Equipment, Progress Report for period Jan. 1 - Sept 30, 1977, submitted to Fossil Energy Div. of Dept. of Energy, Lawrence Berkeley Laboratory, Univ. of California, Berkeley.

a. The Effect of Al and Si Additions on the Mechanical Properties of Secondary Hardening Steels

W. Garrison

Most steels become progressively softer as the tempering temperature is increased. However, a certain class of steels regain hardness at higher tempering temperatures (450 to 600°C) by the precipitation of very fine secondary carbides. Some elements that form carbides are Mo, Cr, W and V. However, most secondary hardening steels exhibit a drop in hardness in the tempering range from 200 to 400°C. It is known that steels with Si and Si + Al additions can maintain hardness on tempering to 400°C.[1] Therefore it appeared that a steel with the appropriate amounts of Al and Si and secondary carbide formers would result in a steel exhibiting a "flat" tempering response and a range of temperatures from 200 to 600°C.

Two base compositions containing secondary carbide formers were designed and the effects of Si and Si + Al additions on the tempering response of these alloys were investigated. The alloy contents used were dictated by a desire to have the minimum amount of carbon and of secondary carbide forming elements, consistent with a desired hardness of RC 53 to 55. The basis for choosing these alloying elements have been discussed in detail elsewhere.[2]

An austenitization temperature was chosen at which no undissolved carbides were observed metallographically. The steels were austenitized at 1100°C and oil quenched following which they were tempered at various temperatures up to 650°C. Some of the results are shown in Figs. 2 through 6. It was observed that the alloys with 2Si (Alloy A16) and 1Al + 1Si (Alloy A19) exhibited a "flat" tempering response up to 550°C. The addition of V

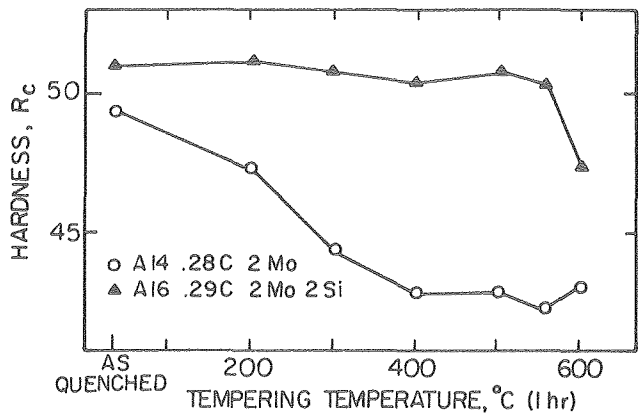

Fig. 2. Plot of hardness vs tempering temperature of steels Fe - 0.28C - 2Mo - 3Ni and Fe - 0.29C - 2Mo - 3Ni - 2Si. (XBL 776-5662A)

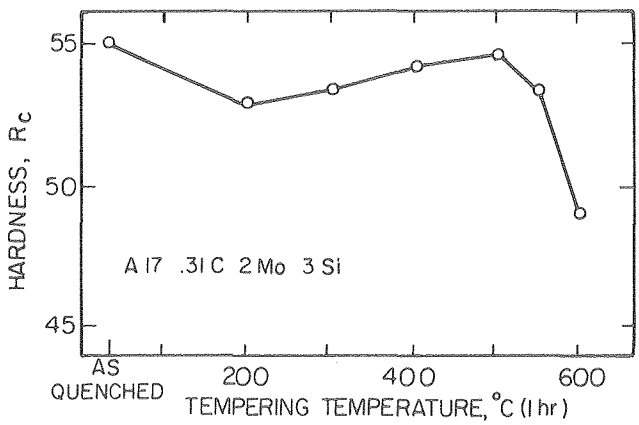

Fig. 3. Plot of hardness vs tempering temperature of steel Fe - 0.31C - 2Mo - 3Ni - 3Si. (XBL 776-5663C)

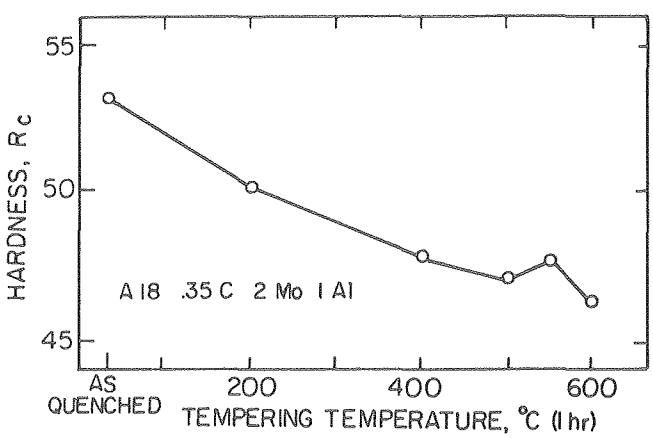

Fig. 4. Plot of hardness vs tempering temperature of steel Fe - 0.35C - 2Mo - 3Ni - 1Al. (XBL 776-5664C)

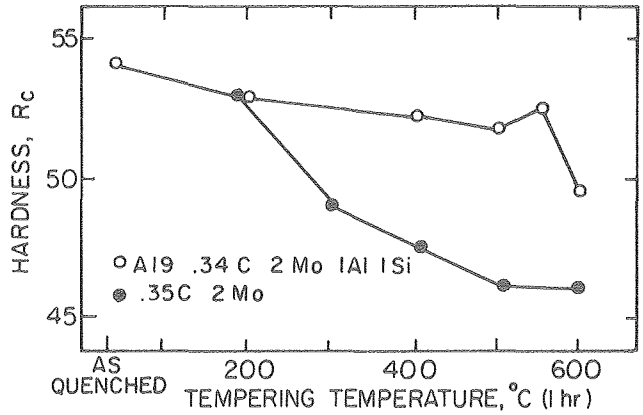

Fig. 5. Plot of hardness vs tempering temperature of steel Fe - 0.34C - 2Mo - 3Ni - 1Al - 1Si and Fe - 0.35C - 2Mo - 3Ni. (XBL 776-5664B)

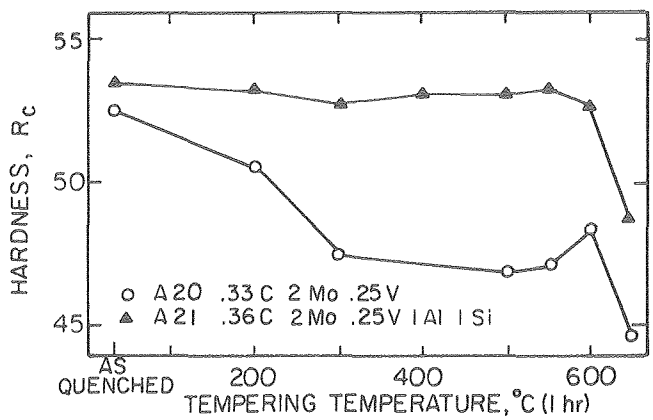

Fig. 6. Plot of hardness vs tempering temperature of steel Fe - 0.33C - 2Mo - 3Ni - 0.25V and Fe - 0.26C - 2Mo - 3Ni - 0.2V - 1Al - 1Si. (XBL 776-5665B)

to the 1Al + 1Si steel (Alloy A21) extended the hardness to 600°C. From these results it was concluded that:

a) The addition of Si resulted in an increase in the secondary hardening response and also a shift of peak to lower temperatures. The magnitude of the effect was dependent on the amount of Si added; the greater the amount of Si, the larger was the effect.

b) The effect of Al additions was similar to Si except that the magnitude of the changes were lower.

c) The effect of adding Al + Si combinations was more potent than the effect of Al and Si additions individually.

d) The addition of V extended the temperature beyond which there was a sharp drop off in hardness.

A preliminary investigation of the impact toughness of these steels indicated that the addition of Si could lead to an improvement in toughness if the tempering was done at temperatures below which the drop off in hardness was observed. However at higher temperatures some form of embrittlement occurred. This behavior is shown in Fig. 7 that shows scanning electron fractographs taken from broken Charpy specimens of the steels with 1, 2 and 3 Si tempered at 550°C. The causes of this embrittlement are presently under study.

---

1. M. S. Bhat, Microstructure and Mechanical Properties of AISI4340 Steel Modified with Aluminum and Silicon (Ph.D. thesis), LBL-6046, February 1977.
2. M. S. Bhat, V. F. Zackay and E. R. Parker, Wear Resistant Alloys for Coal Handling Equipment, Progress Report for period Jan. 1 through Sept. 30, 1977, submitted to Fossil Energy Division of Dept. of Energy (UCID-3921), Lawrence Berkeley Laboratory, University of California, Berkeley.

b. Investigation of Isothermal Transformations in Secondary Hardening Steels

N. Kar

It has been suggested in the literature[1] that the microstructural constituents, lower bainite and retained austenite, are likely to have a positive effect in abrasive wear studies. In the present investigation, isothermal transformations were carried out on a series of Fe - Mo - V secondary hardening steels modified with additions of Si, Al and Ni. One of the reasons for these modifications was to promote the presence of austenite in isothermally transformed steels. All the three alloying elements are known to have this effect on steels.[2-4] The Ni was also added for the purpose of balancing the ferrite stabilizers Si, Al, Mo and V. The effect of the microstructural variables on the mechanical properties was investigated.

The isothermal decomposition kinetics of one of the alloys (Fe-0.4C-4Mo-1V-1.5Si-1.5Al-3Ni) investigated are shown in Fig. 8 as determined by dilatometry. Using this diagram, temperature-time paths were chosen to obtain microstructures containing lower bainite, retained austenite, and martensite. The isothermally transformed steel was tempered at temperatures up to 650°C, and the hardness, room temperature charpy impact energy and amounts of untransformed austenite were measured. The results are shown in Fig. 9. It was observed beyond a tempering temperature of 400°C that an interesting combination of events occurred. The steel hardened rapidly to fairly high hardness levels; the charpy impact energy decreased rapidly and the amount of retained austenite decreased dramatically. This behavior suggested that the

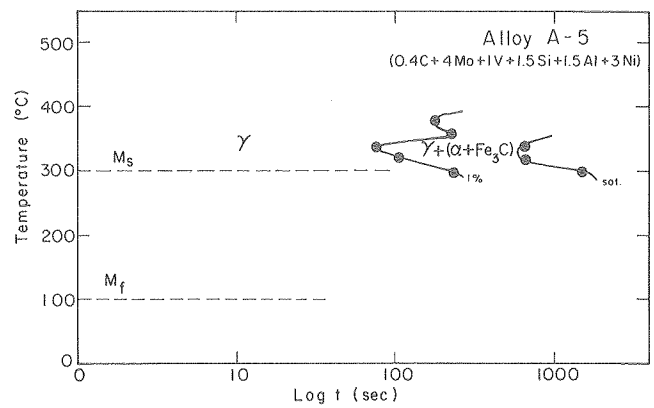

Fig. 8. TTT diagram of steel Fe - 0.4C - 4Mo - 1V - 3Ni - 1.5Al - 1.5Si showing the bainite and martensite transformation ranges. (XBL 776-1238A)

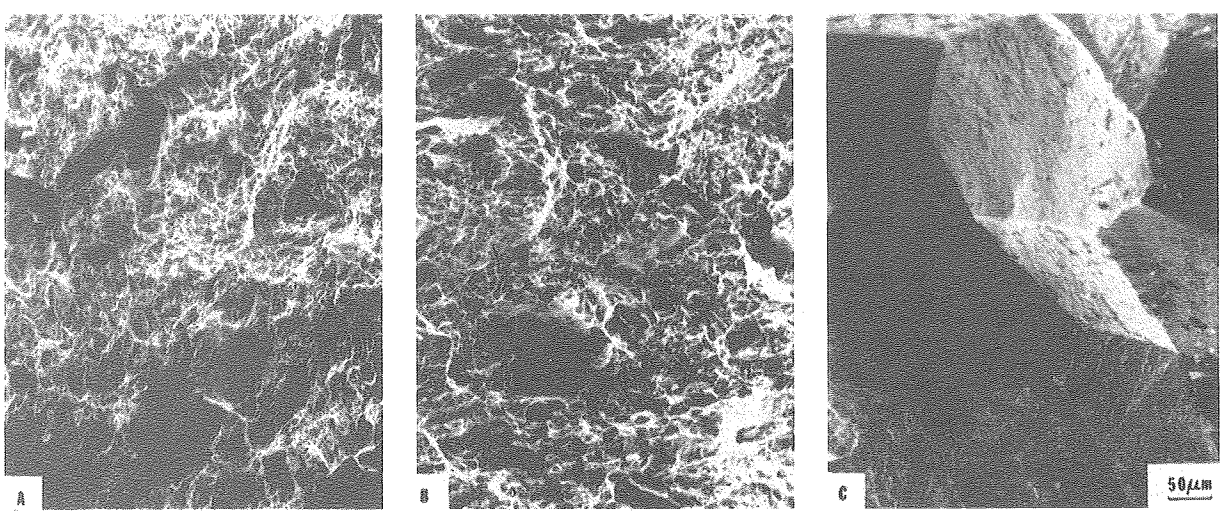

Fig. 7. Scanning electron fractographs taken from broken Charpy impact specimens. A, B and C correspond to the steels containing 1, 2 and 3 Si, respectively; all tempered at 550°C. (XBB 770-12420)

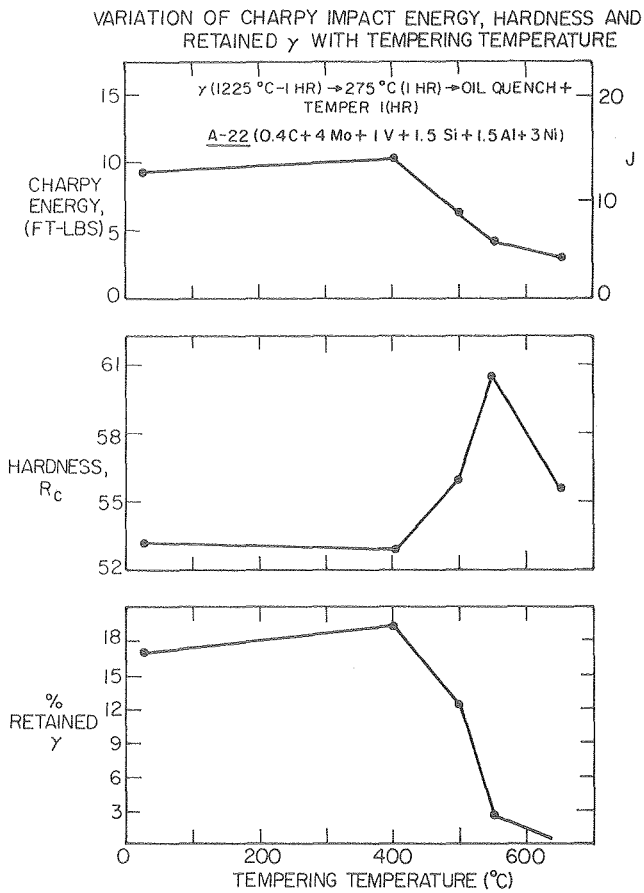

Fig. 9. Variation of Charpy impact energy, hardness and retained austenite with tempering temperature of steel Fe - 0.4C - 4Mo - 1V - 3Ni - 1.5Al - 1.5Si. (XBL 779-6128)

transformation of the austenite could have caused the steep drop in charpy energy. This behavior is being investigated further. A steel containing no Al or Si, the elements that are strong promoters of austenite retention in isothermally transformed steels, has been cast. The hardening behavior of this steel and the variation in impact toughness is being determined.

---

1. P. L. Hurricks, Wear 26, 285 (1973).
2. B. N. P. Babu, An Investigation of Bainite Transformation in Medium Carbon Low Alloy Steels (D. Eng. thesis), LBL-2772, August 1974.
2. G. Kohn, Effects of the Trip Phenomenon on the Toughness of Heat Treatable Alloy Steels (Ph.D. thesis), LBL-5466, November 1976.
4. M. S. Bhat, Microstructure and Mechanical Properties of AISI4340 Steel Modified with Aluminum and Silicon (Ph.D. thesis), LBL-6046, February 1977.

c. Design of Wear-Resistant Matrix Steels

T. Lechtenberg

Matrix steels are secondary hardening steels that are single phase after austenitization. This means all the primary alloy carbides have been dissolved in the austenite. A commercial steel, Vasco MA, was one that was studied in this laboratory.[1] It was found that primary carbides were present even after austenitization at 1350°C. Initial work on this alloy showed that the as-quenched hardness did not increase significantly until 1200°C from which it was inferred that carbon remained out of solution until that temperature. It was also found by EDAX analysis that these carbides were rich in W and V. This led to the design of two alloys with lower W and V contents.

A study of the austenitization temperature and hardness of these new alloys demonstrated that most of the carbon dissolved at 1000°C. This is shown in Fig. 10 that is the microstructure of

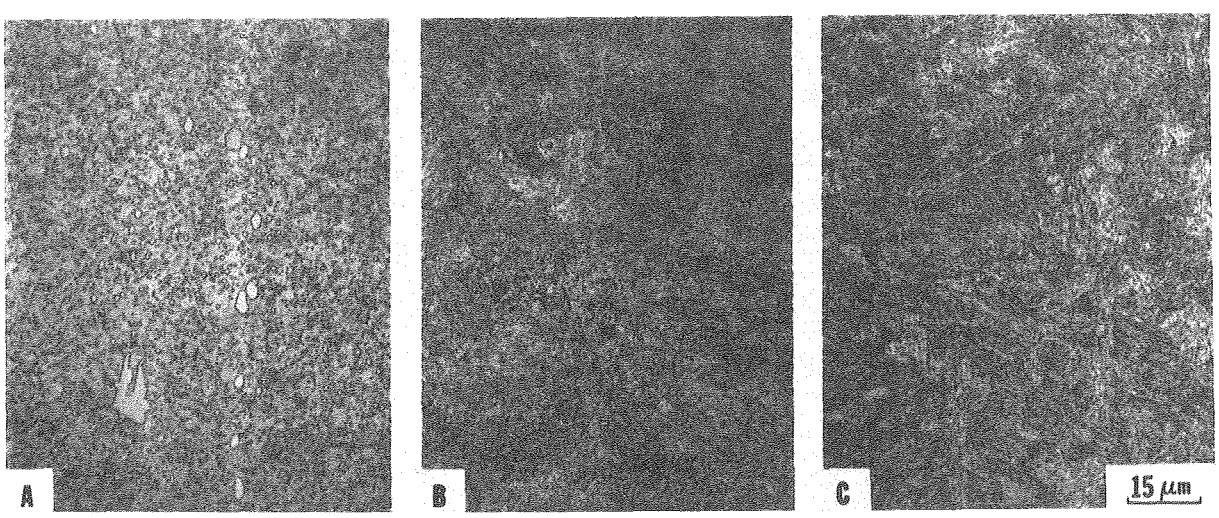

Fig. 10. Optical micrographs of as-quenched steels austenitized at 1000°C: a) base VASCO MA steel b) steel with lower W, and c) steel with lower V. (XBB 777-6458)

a) Vasco MA, b) the new alloy with lower W, and c) lower V, after 1 hour at 1000°C and ice-brine quenched. All the primary carbides were either dissolved or in a very fine dispersion in the two new alloys. Large undissolved carbides were present in the base Vasco MA steel.

Figure 11 displays the tempering response for the two new alloys and the base steel tempered through the secondary hardening range. It was observed that steel B5 (alloy with lower V content) maintained the highest level of hardness over the secondary hardening range. The peak in hardness appeared to occur at a lower temperature (500°C) as compared to that of steel B1 that was located at 550°C. Steel B4, with lower W, also exhibited higher hardness than Steel B1. The increased hardness levels in steels B4 and B5 was attributed to the greater amount of C and secondary carbide forming elements in solution following austenitization, which allowed more secondary carbides to precipitate. Charpy impact tests were performed at room temperature on alloy B1, B4 and B5 austenitized at 1000°C. The results are shown in Fig. 12. It is seen from the figure that the base alloy B1 had the poorest impact energies and alloy B4 had the highest energy values. The poor impact values of Steel B1 could be attributed to the presence of undissolved carbides.

Thus it was shown that modification of existing alloys resulted in an improvement in hardness and toughness even though the amount of alloying elements was reduced.

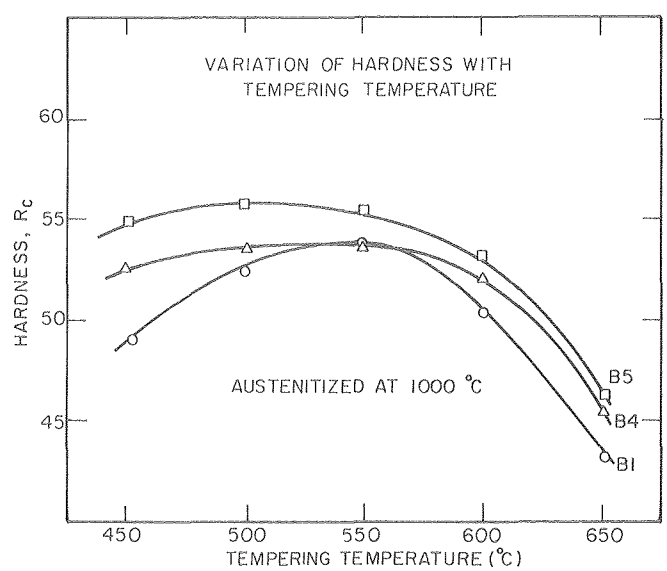

Fig. 11. Plot of hardness vs tempering temperature of steels B1 (base VASCO MA steel), B4 (steel with lower W), and B5 (steel with lower V). (XBL 776-5673)

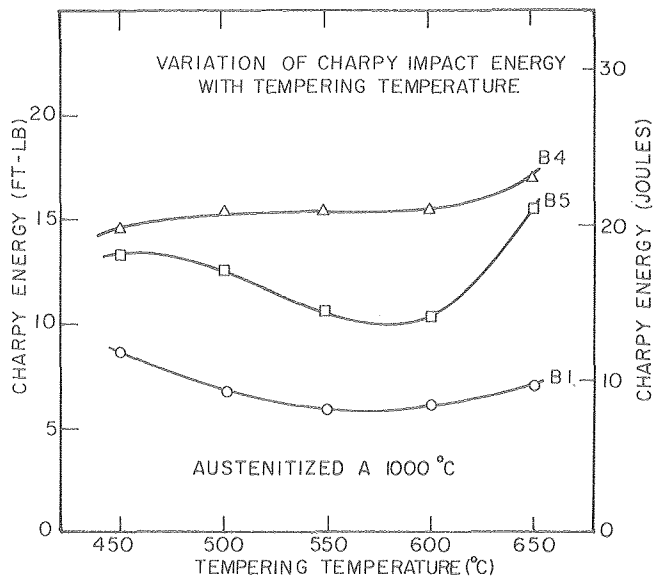

Fig. 12. Plot of room temperature Charpy impact energy vs tempering temperature of steels B1, B4 and B5. (XBL 776-5674A)

---

1. N. Kar, Interrelationships Between Thermal History and Mechanical Properties of a Secondary Hardening Steel (M.S. thesis), LBL-5449, December 1976.

2. ALLOY DEVELOPMENT FOR SULFIDATION RESISTANCE AND MECHANICAL PROPERTIES AT ELEVATED TEMPERATURES

M. S. Bhat, K. Wang, and R. B. Mundhe

The objective of this program was to develop an alloy for applications in coal gasifier internals (viz. cyclones, diplegs, etc.) with acceptable corrosion resistance and mechanical properties. The typical conditions encountered in a coal gasifier are a) temperatures of 1500 to 1800°F, b) pressure up to 1500 psig, and c) a gaseous environment containing a mixture of $CO - CO_2 - H_2O - H_2 - CH_4 - NH_3 - N_2S$. Under these conditions the most severe metallurgical problem is sulfidation attack. Work done by others[1] has shown that existing, commercial, highly alloyed, corrosion resistance steels such as the 310 stainless steel do not possess the necessary corrosion resistance. These steels contain about 20 wt% Ni, which can form a low melting eutectic with NiS that can form from reaction with Si. Since this eutectic has a melting point of about 1200°F, it would be in the liquid phase in the temperature range of interest, and hence would lead to catastrophic failure of the alloy. Chromium additions need to be minimized since it

is considered to be a strategic element. Recent work at the Lockheed Palo Alto Research Laboratories and the University of California, Berkeley[2] has shown that acceptable corrosion resistance can be obtained in Fe - Cr - Al type alloys where the amount of Cr is kept to as low a level as possible with Al being a partial substitute for Cr. The mechanical properties of these alloys were investigated and have been reported elsewhere.[2] It was found that the developmental alloys possessed good ductility at all temperatures and good mechanical properties at temperatures up to about 1200°F. Based on these findings, and a knowledge of strengthening mechanisms, a program was initiated to design iron based sulfidation resistant alloys that would possess better mechanical properties at elevated temperatures. The details of the program are discussed below.

It was found that alloys with 16Cr and 5Al offered the best sulfidation resistance. These Fe - Cr - Al alloys, however, were single phased and their strengths were not very high at elevated temperatures, even with the presence of solid solution strengtheners. By introducing a dispersion of second phase particles, it was felt that mechanical properties could be improved.

Commercial, high temperature ferritic steels presently in use utilize carbide dispersions. These carbides are thermally unstable, and not all are capable of altering mechanical properties to a great extent. Laves phases, on the other hand, are stable and have been shown to be effective strengtheners, in Fe when dispersed as fine particles within the matrix.[3]

Alloys in this study were of the type Fe - 16Cr - 5Al - 1Mo - 1X (or 2X), where X was either Ta, W or Hf. Ta, W and Hf are known to form Laves phases of the type XFe_3 with the $MgZn_2$ type crystal structure and W can form another intermetallic compound, Fe_7W_6.

Initial heat treatments and Vicker's hardness data established the existence of a quench-age type hardening phenomenon in these alloys. Aging curves for the 1Ta and 1W alloys are plotted in Fig. 1. The alloys were solution treated at 1350°C, hot water quenched and then aged at 650°C, followed by air cooling. It is seen that the 1Ta alloy required a longer time to reach the peak hardness. The behavior was probably due to the higher activation energy for diffusion of Ta as compared to that of W.

The laves phase tends to precipitate at grain boundaries upon quenching from the solid solution δ phase. Aging at 650°C facilitated precipitation within the matrix. Bend test results indicated that the Ta alloy was embrittled following these heat treatments, whereas the W alloy was comparatively ductile. To enhance ductility, the grain boundary network will be broken through mechanical working, which is accomplished by either plastically deforming the matrix prior to or during aging, or warm working after aging.

TEM studies are planned to identify and reveal the size and morphology of each of these Laves phases, as well as the precipitation sequence.

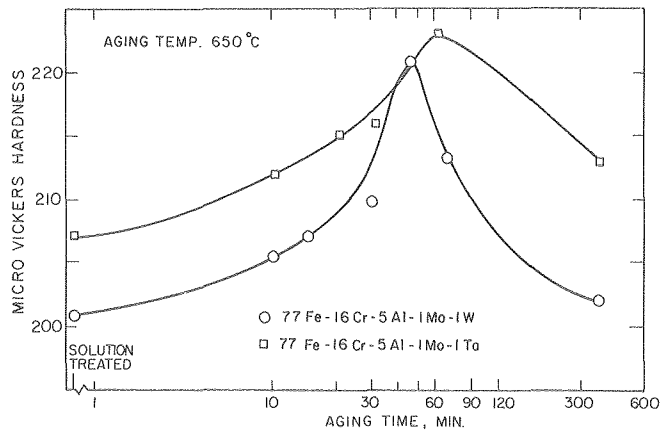

Fig. 1. Plot of hardness vs aging time for alloys Fe - 16Cr - 5Al - 1W and Fe - 5Al - 1Mo - 1Ta. (XBL 7712-6578)

Mechanical properties will be characterized from high temperature and room temperature tensile and creep-rupture tests.

---

1. M. S. Howes, Selection of Materials Used in Coal Gasification Plants, AGA-ERDA-MPC Program on Materials for the Gasification of Coal, presented to the AGA 7th Pipeline Symposium, 1975.
2. R. A. Perkins and M. S. Bhat, Sulfidation Resistant Alloy for Coal Gasification Service, Annual Report for period 24 May 1976 through 21 May 1977, Fossil Energy Division, Department of Energy, Washington, D.C. FE-2299-12.
3. M. D. Bhandarkar, M. S. Bhat, E. R. Parker, and V. F. Zackay, Met. Trans. 7A, 753 (1976).

3. LOW ALLOY STEELS FOR THICK WALL PRESSURE VESSELS

R. M. Horn

The objective of this research program is to adopt or develop low alloy steels that can be fabricated into large diameter, thick wall pressure vessels for coal gasifiers. The pressure vessels proposed for advanced gasification systems, capable of producing 250 M cu.ft of synthetic natural gas per day, will be greater than 20 ft in diameter, more than 100 ft high and must be capable of operating at 650°F at pressures up to 1500 psig. Such a vessel would necessarily be 8 to 12 in. thick and contain over 1500 tons of steel. These vessels must be assembled on site and must maintain structural integrity in contact with a potentially reactive environment. Therefore the steels must have 1) improved environmental resistance, 2) improved strength and toughness to insure reliability, and 3) sufficient fabrication "forgiveness" requiring a limited post-weld heat treatment.

In order to perform research aimed at thick section steels, methods were developed for simulating thermal histories experienced by thick slabs during cooling from the austenization treatment. Commercial data combined with numerical heat transfer analysis were used to determine appropriate cooling paths. An induction furnace was instrumented for programmable control, to perform the necessary heat treatments.

During the first year, two primary research investigations were undertaken. These investigations were based on modification of existing commercial steels for use in thick wall pressure vessels. The alloy modifications were chosen to satisfy the first two requirements. It is expected that improved toughness will have a beneficial affect on weldability.

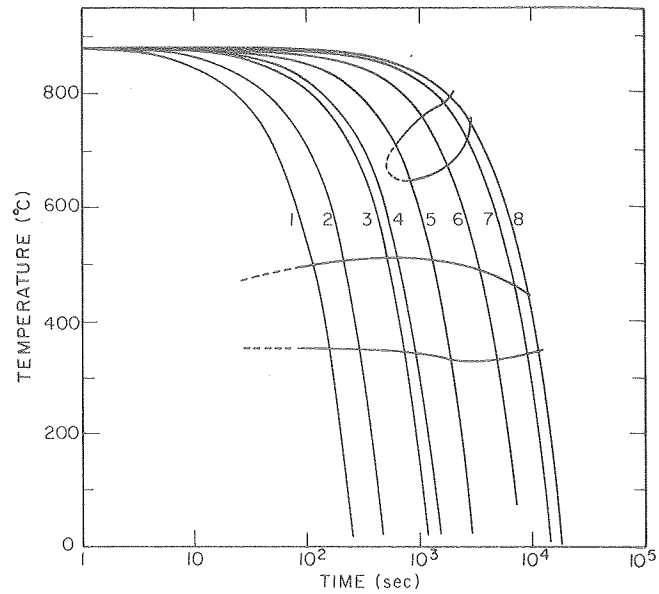

Fig. 1. Continuous cooling transformation diagram of A542 steel showing different cooling rates. (XBL 771-4983)

a. Modified Low Alloy Cr-Mo Pressure Vessel Steels

Rameshchandra J. Kar

ASTM grade A 542 (quenched and tempered version of 2.25 Cr-1 Mo) pressure vessel steel has found vast usage in the petro-chemical industry because of its excellent high temperature properties and low susceptibility to attack by hydrogen. However, its use in the quenched and tempered condition has been restricted to sections up to 6 in. thick. The problem of inadequate hardenability can be analyzed if one refers to the CCT diagram of A 542, (Fig. 1). Cooling rates slower than 0.25 C/s (rates 5 to 8 in Fig. 1) subsequent to austenitization, as is characteristic within the bulk of 8 to 12 in. thick spray quenched specimens, result in the formation of large amounts of polygonal or "free" ferrite that lead to a degradiation of mechanical properties in thick sections.

Based on classical hardenability calculations, a matrix of ingots was designed using alloy additions of Ni, Mn and Cr to a base 2.25 Cr-1Mo steel. Heat treatments to simulate thick sections, either spray quenched or air cooled after austenitization, were carried out using a programmable induction furnace in conjunction with actual cooling curves for thick sections. Using high speed dilatometry, the CCT diagrams for the different alloys were plotted. Mechanical properties and optical microstructures of the test systems were also evaluated.

It was found that addition of Ni or Mn, either alone or in combination, completely eliminated free ferrite in very thick sections, resulting in a more uniform microstructure and improved mechanical properties. At comparable or slightly higher yield and ultimate tensile strength levels, the test alloys showed a sharp improvement in impact toughness, when compared with base 2.25 Cr-1Mo (Fig. 2). Addition of Ni or Mn caused a decrease in the impact transition temperature. The increase in upper shelf energy was attributed to the low S content of the test alloys as well as to the absence of polygonal ferrite.

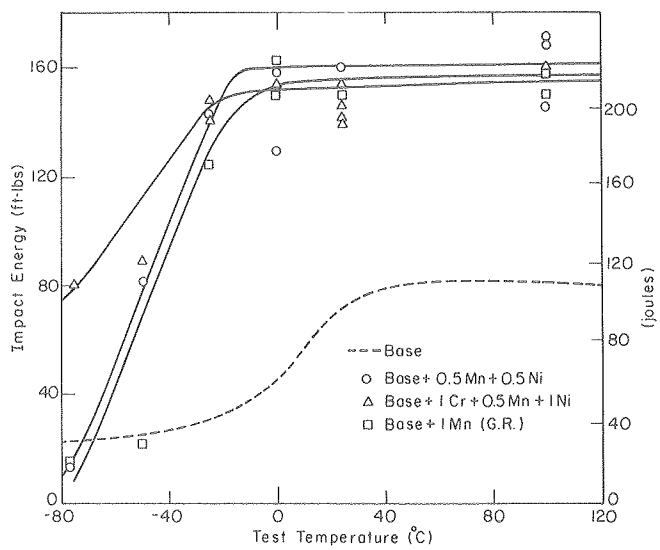

Fig. 2. Charpy impact energies as a function of test temperatures of A542 and modified alloys. (XBL 7710-6186)

Figure 3 displays an optical photomicrograph and scanning electron fractograph of a 0.5%Mn+0.5%Ni modified alloy. The specimen was heat treated to represent an 8 in. thick specimen austenitized and spray quenched, and tested at 1/4T location. The lower bainitic microstructure showed total absence of free ferrite, normally found in A 542. The fine dimples in the fractograph are characteristic of a ductile fracture at room temperature.

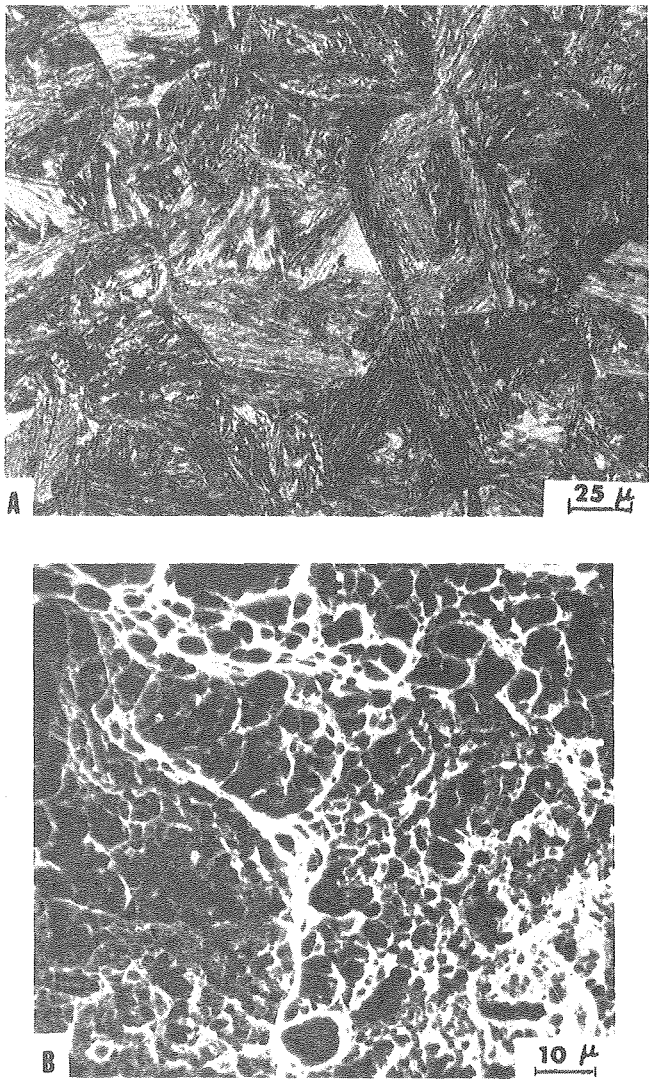

Fig. 3. Optical micrograph (A) and scanning electron fractograph (B) of a 0.5Mn + 0.5Ni modified steel at the 1/4T location (8 in. thick specimen, spray quenched from austenitization temperature). (XBB 779-9095)

Future research plans include complete characterization of commercial developmental melts of the test systems. Mechanical tests planned include room and high temperature tensile tests, and evaluation of fracture toughness using J integral testing to supplement Charpy V-notch tests. Transmission electron microscopy is being done to fully characterize the microstructures. In order to evaluate property degradation of the test alloys in reactive environments, some hydrogen attack tests at high temperatures are also being done. A limited amount of temper embrittlement studies and Gleeble tests to simulate weld microstructures are also being planned.

b. Influence of Alloy Modification on the Thick Section Mechanical Properties of Mn-Mo-Ni Steels

W. Kurtz

Low alloy steels based on Mn-Mo additions have been used successfully for pressure vessel application. A particular grade, ASTM designation A533B steel (a quenched and tempered steel of nominally 0.2 C, 1.4 Mn, 0.6 Mo, 0.6 Ni) has been used in thick section application in nuclear pressure vessels. This steel has sufficient hardenability to prevent free ferrite from forming in spray quenched thick slabs, but lacks adequate environmental resistance. Degradation by hydrogen during gasification could lead to loss of strength and toughness. Any improvement in the steel that leads to increased strength with an associated toughness increase would also be beneficial.

The major alloy additions considered were Cr and Si for improved environmental resistance, and Mn for increased strength and toughness. Microalloying additions of V and Al were also used for grain refinement. The reasons for these alloy modifications are as follows: Environmental resistance to hydrogen attack is dependent on the stability of the strengthening carbide to hydrogen at elevated temperature. The addition of Cr to the base composition is expected to change the chemistry of the carbides formed on tempering; and Si additions would influence the kinetics of carbide formation and thereby have an indirect influence on the carbide chemistry. The Mn additions should result in higher hardenability that would lead to more desirable as-quenched microstructures.

Initial studies were aimed at determining the influence of these elemental additions, singly or in combination on mechanical properties. Chromium and manganese additions improved toughness, with the chromium addition promoting marked increases in strength in material heat treated to represent 8 in. thick slab at the 1/4 thickness location. Silicon additions, however, had a detrimental effect on the toughness. The kinetics of tempering were changed, resulting in higher strength levels for equivalent tempering treatments.

The largest effect was observed for combined alloy additions. Figure 4 shows the continuous cooling transformation behavior for the base steel alloyed with chromium, silicon and manganese. Rate 6, which corresponds to the cooling path experienced by an 8 in. slab at the 1/4 thickness location, led to a very desirable lower bainitic structure. The alloy conventionally heat treated developed a yield strength of 100 ksi. The associated impact properties were also very good. Figure 5 shows this steel in comparison to the base material. The transition temperature was shifted to below -40°C.

Future research will be aimed at thorough characterizations of modified steels in thick section. Characterizations will focus on determining the carbide structure and explaining the response of the steels in hydrogen environments in terms of this structure.

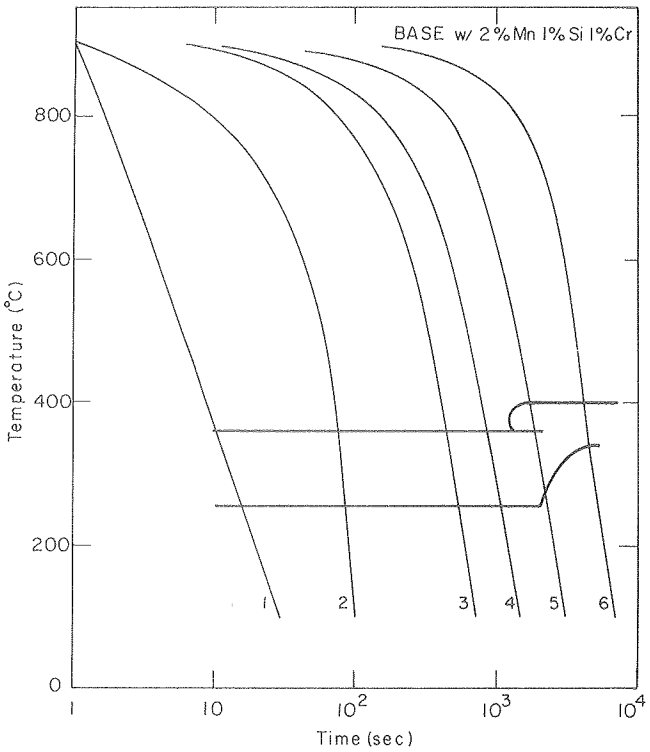

Fig. 4. Continuous cooling transformation diagram of steel A533B + 2Mn + 1Si and 1Cr. Also shown on the diagram are different cooling curves. (XBL 7710-6327)

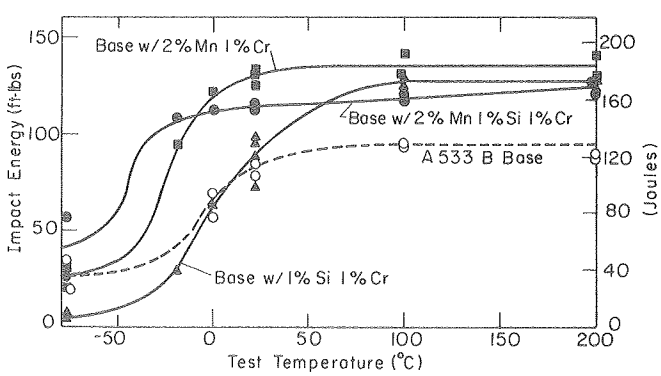

Fig. 5. Impact properties of base A533B steel and modified alloys. (XBL 7710-6322)

4. 1977 PUBLICATIONS AND REPORTS

Earl R. Parker, Victor F. Zackay and Associates

Journals

1. E. R. Parker, Interrelations of Compositions, Transformation Kinetics, Morphology, and Mechanical Properties of Alloy Steels, Met. Trans. 8A, 1025 (1977).

2. R. O. Ritchie, M. Castro-Cedeno, E. R. Parker and V. F. Zackay, Effects of Silicon Additions and Retained Austenite on Stress Corrosion Cracking Behavior of Commercial Ultra-High Strength Steels in Aqueous Solution, Met. Trans. 9A, (January 1977).

3. R. O. Ritchie, Influence of Impurity Segregation on Temper Embrittlement and on Slow Fatigue Crack Growth and Threshold Behavior in 300-M Ultra-High Strength Steel, Met. Trans 8A, No. 7, 1131 (July 1977).

4. R. O. Ritchie, B. Francis and W. L. Server, Author's reply to: Discussion of "Evaluation of Toughness on AISI 4340 Steel Austenitized at Low and Higher Temperature", Met. Trans. 8A, No. 7, 1197 (July 1977).

5. R. O. Ritchie, Effects of Strength and Grain Size on Near-Threshold Fatigue Crack Propagation in Ultra-High Strength Steel, D. M. R. Taplin, Ed., in Proceedings of the 4th International Conference on Fracture, Waterloo, June 1977, Vol. 2, p. 1325-1331.

6. R. O. Ritchie, Near-Threshold Fatigue Crack Propagation in Ultra-High Strength Steel: Influence of Load Ratio in Cyclic Strength, Journal of Eng. Mat'l and Technology, Trans. of ASME, Series H 99, No. 3, 195 (July 1977).

7. R. O. Ritchie, Influence of Microstructure on Near-Threshold Fatigue Crack Propagation in Ultra-High Strength Steels, Met. Sciences, 11, No. 8/9, 368 (Aug./Sept. 1977).

8. M. F. Carlson and R. O. Ritchie, On the Effect of Prior Austenite Grain Size on Near-Threshold Fatigue Crack Growth, Scripta Met. 11, No. 12, (December 1977).

9. R. O. Ritchie and R. M. Horn, Further Consideration on the Inconsistency in Toughness Evaluation of AISI 4340 Steel Austenitized at Increasing Temperatures, Met. Trans. 9A, No. 3 (March 1977).

LBL Reports

1. G. Kohn, Effects of the TRIP phenomenon on the Toughness of Heat Treatable Alloy Steels, (Ph.D. thesis), LBL-5466, November 1976.

2. R. J. Kar, Optimization of Strength and Toughness in a High-Carbon Steel, (M.S. thesis), LBL-5448, December 1976.

3. N. J. Kar, Interrelationships Between Thermal History and Mechanical Properties of a Secondary Hardening Steel, (M.S. thesis), LBL-5449, December 1976.

4. R. M. Horn, The Influence of Retained Austenite on the Thick-Section Mechanical Properties of a Commercial Low Alloy Ultra-High Strength Steel, (Ph.D. thesis), LBL-5787, December 1976.

5. Ana-Maria Llopis, Isothermal Transformation Studies on the Effect of Alloying Elements (Mo, Ni, Cr, Mn, Al, Si, Co) on the Kinetics of the Austenite to Bainite Transformation, (Ph.D. thesis), LBL-6068, December 1976.

6. L. D. Thompson, The Mechanical Properties and Microstructural Relationships in Iron-Manganese-Chromium Alloys, (M.S. thesis), LBL-6234, January 1977.

7. M. S. Bhat, The Influence of Al and Al Plus Si Additions on the Mechanical Properties of AISI 4340 Steel, LBL-4920, February 1977.

8. M. S. Bhat, Microstructure and Mechanical Properties of AISI 4340 Steel Modified with Aluminum Plus Silicon, (Ph.D. thesis), LBL-6046, February 1977.

9. Earl R. Parker, Interrelationships of Composition, Transformation Kinetics, Morphology, and Mechanical Properties of Alloy Steels, LBL-6092, March 1977.

10. Mario Castro-Cedeno, The Effect of Silicon on the Environmental Cracking Behavior of a High Strength Steel, (M.S. thesis), LBL-6012, May 1977.

11. Robert O. Ritchie, Victor F. Zackay, Earl R. Parker, and Mario Castro-Cedeno, Effects of Silicon Additions and Retained Austenite on Stress Corrosion Cracking Behavior of Commercial Ultra-High Strength Steels in Aqueous Solution, LBL-5499, June 1977.

12. Lorin Brass, The Effect of Microstructure of Ductile Alloys in Solid Particle Erosions, (M.S. thesis), LBL-6277, June 1977.

13. Robert O. Ritchie, R. M. Horn, Further Evaluations of the Inconsistency in Toughness Evaluation of Ultra-High Strength Steel Austenitized at Increasing Temperatures, LBL-6606, July 1977.

14. R. M. Horn, R. O. Ritchie, Mechanisms of Tempered Martensite Embrittlement in Ultra-High Strength Steels, LBL-6607, November 1977.

15. T. Lechtenberg, A Comparison of the Microstructure and Mechanical Properties of 300-M Steel Manufactured by the Vacuum Arc Remelt and the Electroslag Remelt Processes, (M.S. thesis), LBL-6686, December 1977.

UCID Reports

1. R. M. Horn, E. R. Parker, V. F. Zackay and A. V. Levy, Low Alloy Steels for Thick Wall Pressure Vessels, Quarterly Report, UCID-3898, February 1977.

2. M. Dilip Bhandarkar, M. S. Bhat, Victor F. Zackay and Earl R. Parker, Wear Resistant Alloys for Coal Handling Equipment, Quarterly Report, UCID-3921, Jan.-Mar. 1977.

3. R. M. Horn, E. R. Parker, and V. F. Zackay, Low Alloy Steels for Thick Wall Pressure Vessels, Quarterly Report, UCID-3921, May 1977.

4. R. M. Horn, E. R. Parker, and V. F. Zackay, Low Alloy Steels for Thick Wall Pressure Vessels, Quarterly Report, UCID-3943, August 1977.

5. M. S. Bhat, Victor F. Zackay, and Earl R. Parker, Wear Resistant Alloys for Coal Handling Equipment, Quarterly Report, UCID-3945, August 1977.

6. R. M. Horn, Design Criteria for Pressure Vessel Steels, Topical Report, UCID-3992, December 1977.

7. R. M. Horn, E. R. Parker, and V. F. Zackay, Low Alloy Steels for Thick Wall Pressure Vessels, Yearly Report, UCID-3993, Oct. 1976 - Sept. 1977.

8. M. S. Bhat, Victor F. Zackay and Earl R. Parker, Wear Resistant Alloys for Coal Handling Equipment, Yearly Report, UCID-3994, Oct. 1976-Sept. 1977.

Presentations

1. E. R. Parker, Interrelations of Composition, Transformation Kinetics, Morphology, and Mechanical Properties of Alloy Steels, The 1977 Institute of Metals Lecture, Annual Meeting of the Metallurgical Society of AIME, Atlanta, Georgia, March 6-10, 1977.

2. R. O. Ritchie, M. Castro-Cedeno, V. F. Zackay, and E. R. Parker, Stress-Corrosion Cracking in Ultra-High Strength Steels: Effects of Retained Austenite and Silicon Modifications to AISI4340 Steels, Annual Meeting of the Metallurgical Society of AIME, Atlanta, Georgia, March 6-10, 1977.

3. R. M. Horn and R. O. Ritchie, Effects of Microstructure on Tempered Martensite Embrittlement in AISI4340 and 300-M Alloy Steels, Annual Meeting of the Metallurgical Society of AIME, Atlanta, Georgia, March 6-10, 1977.

4. R. O. Ritchie, Influence of Microstructure and Mean Stress on Near-Threshold Fatigue Crack Propagation in Steels, Annual Meeting of the Metallurgical Society of AIME, Atlanta, Georgia, March 6-10, 1977.

5. R. O. Ritchie, Influence of Impurity Segregation and Temper Embrittlement on Near-Threshold Fatigue Crack Propagation in 300-M Steel, Annual Meeting of the Metallurgical Society of AIME, Atlanta, Georgia, March 6-10, 1977.

6. V. F. Zackay, E. R. Parker and G. Thomas, The Control of Retained Austenite in Alloy Steels, nnual Meeting of the Metallurgical Society of AIME, Atlanta, Georgia, March 6-10, 1977.

7. L. D. Thompson, E. R. Parker and V. F. Zackay, The Development of Nickel-Free Austenitic Stainless Steels, WESTEC Conference, Los Angeles, CA., March 14-17, 1977.

8. G. Haddick, L. D. Thompson, E. R. Parker and V. F. Zackay, The Development of Nickel-Free Austentic Stainless Steels for Ambient and Cryogenic Applications, ASM/OTA/FMS Conference on Materials Substitution, Chicago, Ill., Sept. 27-28, 1977.

9. R. M. Horn, Developments in Low Alloy Steels for Thick Walled Pressure Vessels, First International Conference on Materials for Coal Conversion and Utilization, Gaithersburg, Md., October 11-13, 1977.

10. T. Lechtenberg, M. S. Bhat and V. F. Zackay, Design of Wear Resistant Matri Steels, Fall AIME Meeting, Chicago, Ill., October 24-27, 1977.

11. N. Kar, M. S. Bhat and V. F. Zackay, Investigations of Isothermal Transformations in Secondary Hardening Steels, Fall AIME Meeting, Chicago, Ill., October 24-27, 1977.

12. W. M. Garrison, M. S. Bhat and E. R. Parker, The Effect of Si and Al Additions on the Mechanical Properties of Secondary Hardening Steels, Fall AIME Meeting, Chicago, Ill., October 24-27, 1977.

13. R. J. Kar, E. R. Parker, R. M. Horn and V. F. Zackay, Modified Low Alloy Pressure Vessel Steels, Fall AIME Meeting, Chicago, Ill., October 24-27, 1977.

14. J. S. Kallend, Prediction of Yield Loci for Textured Sheets of Cubic Metals, Fall AIME Meeting, Chicago, Ill., October 24-27, 1977.

15. J. A. Wert, E. R. Parker and V. F. Zackay, Elimination of Precipitate Free Zones in Precipitation Hardening Fe-NB Alloys, Fall AIME Meeting, Chicago, Ill., October 24-27, 1977.

c. Solid State NMR Analysis of Coal

Alexander Pines, Principal Investigator

1. NMR ANALYSIS OF WHOLE AND PROCESSED COALS*

D. Wemmer, T. Tufano and A. Pines

Together with The Central Research Division of Mobil Oil Company and with EPRI and DOE support, we are characterizing materials used in fuel technology, in particular coal and oil shale. Using solid state NMR techniques we can distinguish four types of carbon functional groups--condensed aromatic, simple aromatic, oxygen bonded aliphatic, and simple aliphatic. These have been used to characterize coals by rank and to understand the changes that occur during processing of the coals. No large scale aromatic condensation is found in coals other than anthracite. The aromatic aliphatic ratio is found to be sensitive to contact time in liquification and an extensive table of characteristic data has been produced. Previously, spectroscopic analysis of whole coal samples in the solid state has been essentially impossible.

Figure 1 shows an example of the analysis of a processed coal by ^{13}C double resonance NMR into the four major constituents. The lineshapes for these constituents are stored in computer and are obtained by analysis of hundreds of model samples with known magnetic shielding and structure. The agreement between the experimental line and the simulated one (noise added artificially for comparison) gives us some confidence in this method of analysis. Techniques are now being worked out to analyze deuterium so that the evolution of the chemistry during coal processing can be followed.

*Supported in part by DOE Materials Research Program

2. HIGH RESOLUTION DEUTERIUM NMR IN SOLIDS

J. Ackerman, D. Eckmann and A. Pines

We have constructed a probe capable of producing high intensity fields upon samples rotating at 0.25 million revolutions per minute, about an axis inclined at an arbitrary angle with respect to a high magnetic field. The probe is equipped with fiber optics which allow the rotation to be monitored and synchronized with the radiofrequency and digital logic circuitry of the spectrometer. A photograph of the probe and optics is shown in Fig. 1. Using this setup we have produced the first resolved NMR spectra of deuterium in the solid state, providing the basis for a potentially useful analytical technique. Even though deuterium has long been considered a good candidate for NMR labeling studies, the quadrupolar broadening causes linewidths of ~ 100 kHz in polycrystalline samples making it essentially useless. As shown in Fig. 2 the solid state NMR with synchronized sampling of the rotating sample produces lines of ~ 50 Hz width and different species are resolved. The limitation on resolution comes from two courses: (a) magnetic field strength and inhomogeneity (b) instability of the spinner that is critical due to the large quadrupolar broadening. This spinning is now being combined with our technique Fourier Transform Double Quantum NMR that eliminates quadrupolar broadening (see next section) to provide high resolution.

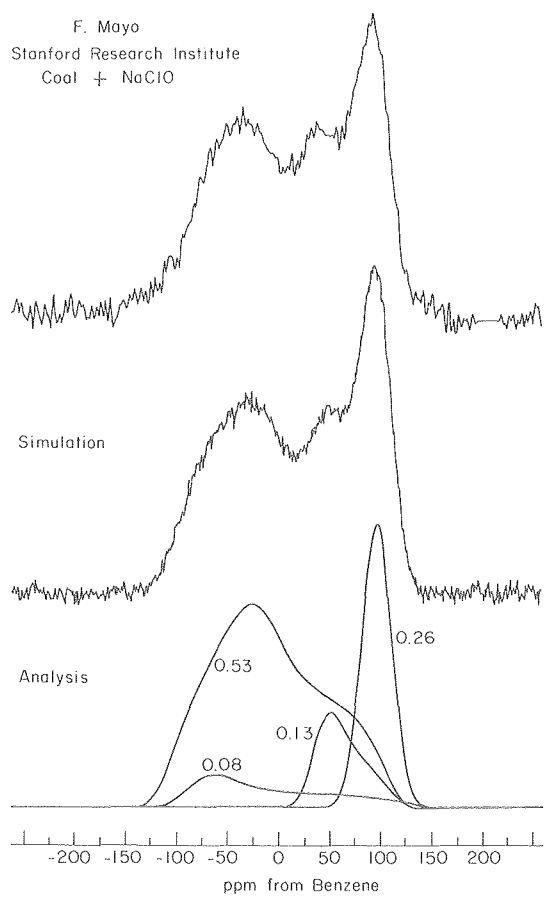

Fig. 1. Analysis of coal and coal processing intermediates by ^{13}C NMR. The top experimental spectrum is decomposed into four functional carbon types (simple aliphatic, oxygen-bonded aliphatic, simple aromatic, condensed aromatic) in the lower trace producing (with some artifically added noise) the computer simulated center spectrum. (XBL 773-8219)

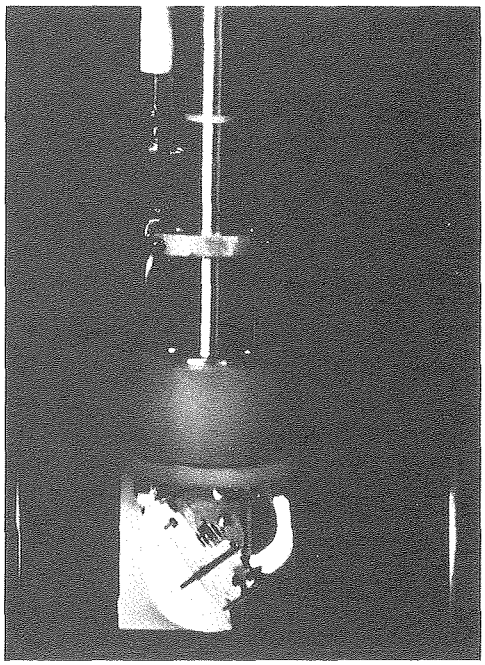

Fig. 1. Photograph of Andrew-type NMR probe for high power rf, magic angle sample-spinning (0.25 million rpm) and optics for synchronization of rotation to spectrometer logic. (CBB 770-9649A)

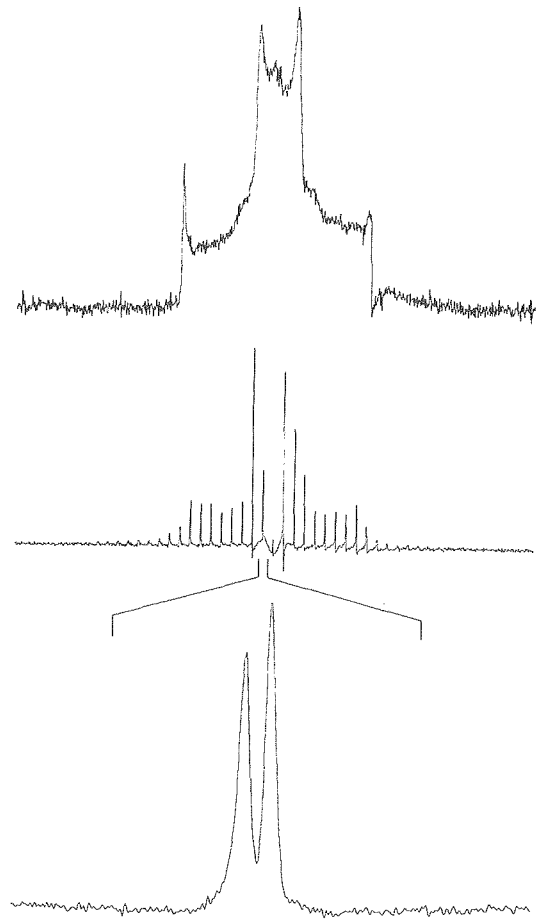

Fig. 2. Illustration of first high resolution solid state deuterium NMR spectrum. Top is normal wideline deuterium spectrum of mixture of perdeuterohexamethylbenzene and perdeuteroferrocene showing extremely broad resonance due to quadrupole effect. Center shows effect of rapid sample spinning at magic angle and lower trace shows rapid sample spinning with synchronous detection using optical system. The two peaks from the inequivalent deuterium positions are now resolved. (XBL 7710-6843)

3. DOUBLE QUANTUM DEUTERIUM NMR

D. Wemmer and A. Pines

The magic angle spinning technique with synchronized detection produces isotropic resolved deuterium NMR spectra. We have also continued the development of two other aspects of solid state deuterium NMR which should be useful for the analysis of whole samples.

1. In Fourier transform double quantum NMR, the double quantum-transition is excited and its evolution monitored with detection pulses. Fourier transformation then yields a spectrum devoid of quadrupolar broadening. This contains the chemical shift anisotropy lineshape that is analogous to the ^{13}C case. We have made the first measurements of deuterium chemical shift tensors in this way, including aromatic and other deuterium functional groups.

2. In a perdeuterated material, the deuterium spin can be decoupled and the residual proton NMR measured. This yields good proton NMR resolution since the deuterium spins are decoupled by double quantum transitions, and not much power is required. We have investigated the quantitative aspects of this double quantum decoupling process to provide criteria for producing high resolution solid state proton NMR. Figure 1 shows an example of the excess proton NMR linewidth as the deuterium spins are irradiated with an rf field of increasing intensity ν_1. Although the deuterium linewidth is ~ 100 kHz, a ν_1 of only 10 kHz already induces efficient decoupling. The solid line is calculated from our double quantum operator theory.

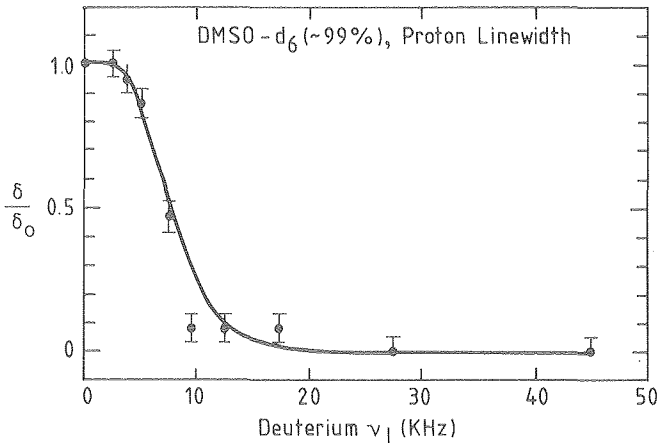

Fig. 1. Dependence of proton NMR linewidth in ~99% deuterated DMSO as the deuterium of decoupling intensity is changed. The decoupling threshold occurs at ~10 kHz which satisfies the double quantum criterium. (XBL 7710-10314)

These double quantum processes when coupled with magic angle spinning should provide high resolution solid state spectra.

4. RESEARCH PLANS FOR CALENDAR YEAR 1978

Alexander Pines

1. Measure deuterium chemical shift tensors using double quantum NMR.

2. Combine double quantum NMR and double quantum decoupling with magic angle spinning to produce high resolution deuterium and proton NMR spectra.

3. Begin development of techniques for solid state NMR of other isotopes (^{14}N, ^{33}S, ...)

4. Develop and construct high field NMR spectrometer for high sensitivity high resolution solid state NMR.

5. Begin application of our techniques to isotopic labeling studies in coal processing research.

5. 1977 PUBLICATIONS AND REPORTS

Alexander Pines and Associates

Books

1. S. Vega and A. Pines, Theory of Double-Quantum Coherence and High Resolution Deuterium NMR in Solids, in Magnetic Resonance and Related Phenomena, K. Hausser Ed., Heidelberg (1977), p. 305.*

2. A. Pines, S. Vega, D. J. Ruben, T. W. Shattuck and D. Wemmer, Double Quantum NMR in Solids, in Magnetic Resonance in Condensed Matter, R. Blinc Ed. University of Ljubljana Press, (1977), p. 127-179.*

Presentations and Invited Lectures*

1. A. Pines, Coherent Multiple Quantum NMR, Annual Meeting of the Western Spectroscopy Association, Asilomar, California, January, 1977, invited talk.

2. A. Pines, Solid State Physics Seminar, University of California, Berkeley, February 1977.

3. D. Wemmer, S. Vega, S. Hsi and H. Zimmerman, Dipole-Dipole Coupling in Fourier Transform Double Quantum NMR, 18th Experimental NMR Conference, April 1977, invited talk.

4. A. Pines, Nuclear Magnetic Resonance with Lots of Photons, Plenary Lecture for the Award Symposium of the American Chemical Society, St. Louis, Missouri, April 1977, invited talk.

5. A. Pines, Chemistry Department, Iowa State University, April 1977, Seminar.

6. J. L. Ackerman and A. Pines, High Resolution Deuterium NMR in Solids, VI International Symposium on Magnetic Resonance, Banff, May 1977, LBL-6081 Abstract.

7. L. Sterna, S. Bustamente, S. Vega and A. Pines, Nuclear Magnetic Isotope Effect, VI International Symposium on Magnetic Resonance, Banff, May 1977, LBL-6082 Abstract.

8. D. Wemmer, S. Vega and A. Pines, Fourier Transform Double-Quantum NMR in Powders, VI International Symposium on Magnetic Resonance, Banff, May 1977, LBL-5783 Abstract.

9. A. Pines, Double Quantum NMR in Solids: Theory and Experiment, University of Waterloo NMR Summer School, Waterloo, Canada, June 1977, invited lectures.

10. S. Vega, Double Quantum Spectroscopy and Deuterium NMR in Solids, Gordon Research Conference, New Hampshire, June 1977, invited talk.

11. A. Pines, Isotope Division, Weizmann Institute of Science, Rehovot, Israel, July 1977, three lectures on "Photon Dressing Picture of Multiple Quantum Processes."

12. A. Pines, Physics Department, University of Dortmund, West Germany, August 1977, three lectures on "Photon Dressing Picture of Multiple Quantum Processes."

13. A. Pines, Physics Department, Free University of Berlin, Germany, September 1977, Seminar.

14. D. Wemmer and A. Pines, Developments in Fourier Transform Multiple Quantum NMR, 3rd Conference on Molecular Structural Methods in Biological Research, Stanford University, November 1977, invited talk.

LBL Reports

1. D. Suwelack, M. Mehring and A. Pines, Quantitative Aspects of Deuteron (Spin 1) Spin-Decoupling in Solids, submitted to Chem. Phys., LBL-7373.*

2. D. Wemmer and A. Pines, Developments in Solid State NMR and Potential Applications to Fuel Research, American Chemical Society Symposium, Anaheim, March 1978, invited talk, LBL-6971.

3. A. Pines, Fourier Transform Multiple Quantum NMR, NMR Symposium of the Faraday Division, Queen Elizabeth College, London, December 1978, LBL-6597 Abstract.*

*Also supported in part by Basic Energy 4081.

VII.

Solar Energy Development

1. PHOTOVOLTAIC ENERGY CONVERSION

a. Research on CdS-Cu_xS and (CdZn)S-Cu_xS Solar Cell Materials

Jack Washburn, Principal Investigator

1. GROWTH OF (Cd,Zn)S and CdS Thin Films

Barry Chin

The addition of ZnS to the n-type side of the conventional CdS/Cu_xS photovoltaic cell has been shown to have important advantages. The mixed sulfide (Cd,Zn)S cells, however, have resulted in anomalously low short circuit currents in devices made to date. In order to better understand this problem and also to obtain cell structures similar to the thin film, polycrystalline cells without the complications of grain boundaries, the epitaxial growth of (Cd,Zn)S films by a hot-wall vacuum deposition technique was undertaken.

(Cd,Zn)S films of different compositions have been grown on single crystal GaAs substrates of various orientations. Different surface preparations have been tried along with a sputter-etch of the GaAs substrate prior to deposition to improve the epitaxy. The grown films were found to be mostly single crystal from x-ray diffraction analysis.

To evaluate the compositional uniformity of these films the energy-dispersive analysis of x-rays system (EDAX) of the scanning electron microscope (SEM) was utilized. Figure 1 shows an x-ray line scan at the cleaved surface indicating the weight percentages of Cd,Zn and S to be nearly uniform through the thickness of the mixed sulfide film. The line-scan images are superimposed on the SEM micrograph of the surface being analyzed. It has been found that both the growth rate and composition are extremely sensitive to the relative rates of evaporation of the ZnS and CdS charges. Figure 2 shows the variation of x, the ZnS mole fraction in the film, with θ, the ZnS mole fraction of spent charge. This hyperlinear relationship indicates a preferential incorporation of ZnS in the single crystal films.

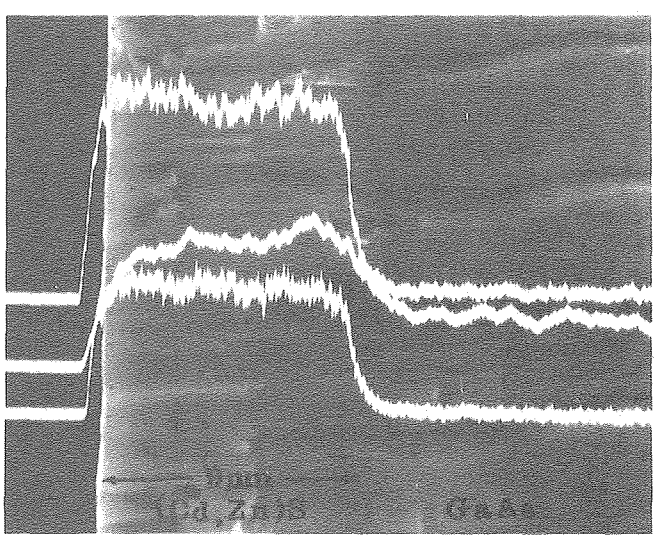

Fig. 1. SEM micrograph of cleaved edge of (Cd,Zn)S film on GaAs substrate. Superposed are EDAX line scans showing spatial distribution of Cd, Zn and S. (XBB 777-6727)

Heterojunctions of these grown films with Cu_xS have been formed by solid state reaction and by sputtering.

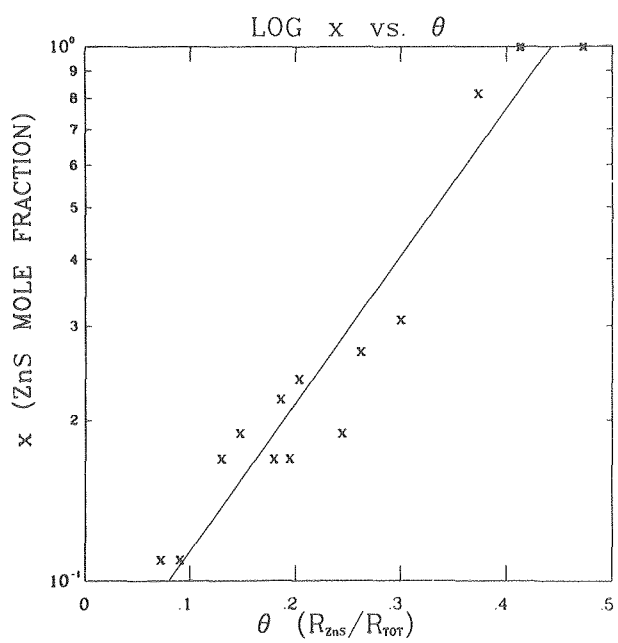

Fig. 2. Plot of mole fraction ZnS incorporated in single crystal film vs mole fraction ZnS evaporated. (XBL 776-9280)

2. DEFECTS IN EPITAXIAL CdS and (Cd,Zn)S LAYERS

Terry Peterson and Krishna Seshan

The epitaxial films grown as described in the preceding article are being examined in the transmission electron microscope. To date we have

found that the structural perfection of CdS films and (Cd,Zn)S films grown under similar conditions are comparable; however, perfection of the films has been found to be markedly affected by the orientation of the substrate crystal.

On the (111) Ga- or A-face substrates, we have obtained relatively perfect film growth as is shown in Fig. 1. Only isolated dislocations are seen in such a film. The films grown on the As or B-face substrates, however, exhibit high defect densities. Figure 2 shows a typical microstructure of these films, containing a network of dislocations, dislocation loops, and stacking faults. The lack of inversion symmetry in these crystal affects the growth rate at a given supersaturation of the vapor. Apparently, nucleation of defects is also much more frequent when the crystal grows on the B face.

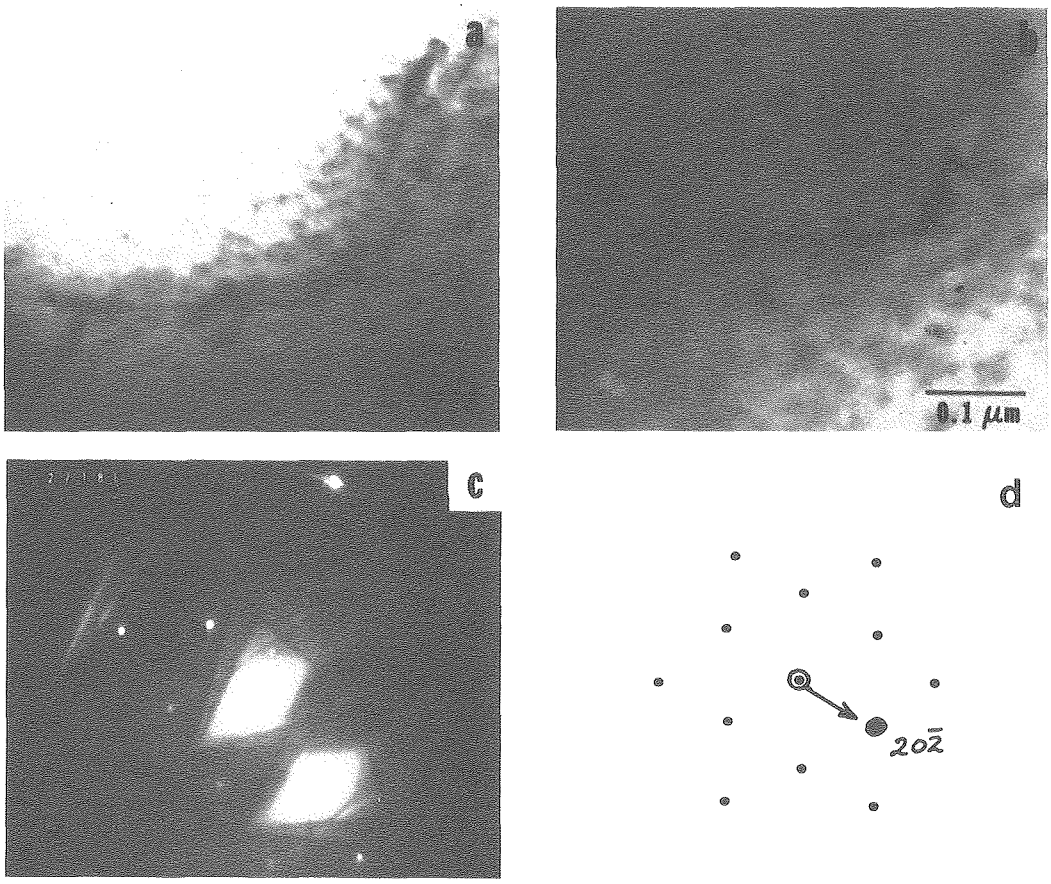

Fig. 1. (a) and (b) Isolated dislocations in Ga-face substrate CdS film and (d) diffraction pattern and diagram showing diffraction conditions in (a) and (b). (XBB 779-9237)

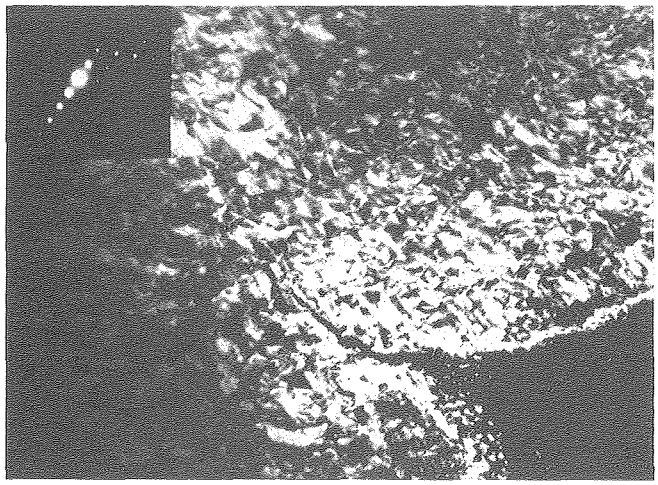

Fig. 2. Highly defected structure of As-face substrate CdS film. (XBB 781-232)

Both the hexagonal (wurtzite) and cubic (sphalerite) phases of (Cd, Zn)S have been observed--sometimes in different regions of the same microscope specimen. Figure 3 shows a pair of diffraction patterns: (a) one hexagonal and (b) one cubic obtained on a single sample. Since the hexagonal phase is the thermodynamically stable one, it is believed the cubic growth is stabilized by the symmetry of the GaAs substrate. It seems plausible that the epitaxial growth always begins as the cubic phase. Then at some point removed from the substrate, faulting occurs to allow hexagonal growth.

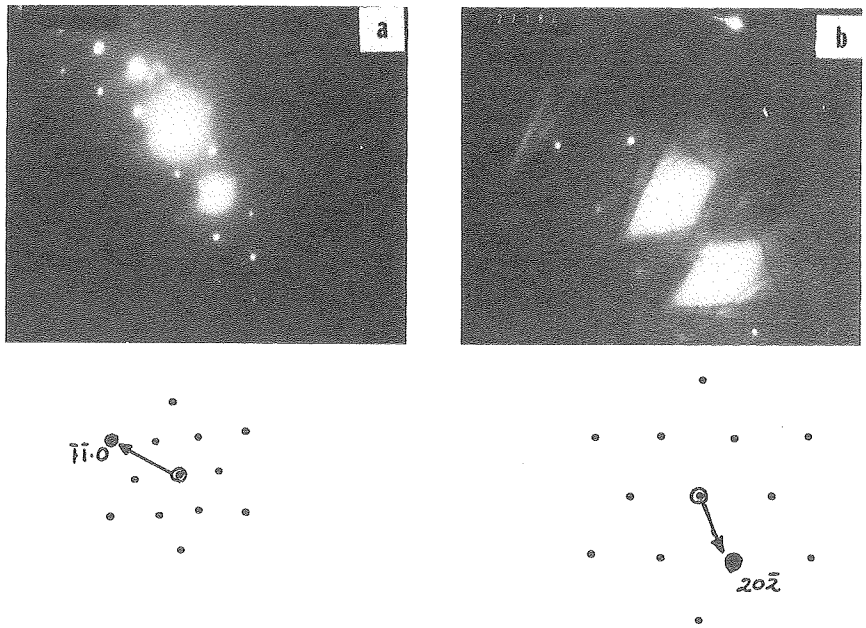

Fig. 3. CdS film electron diffraction patterns: a) hexagonal phase; b) cubic phase. (XBL 779-9243).

3. THEORETICAL AND EXPERIMENTAL HETEROJUNCTION CHARACTERIZATION

Terry Peterson

The method used in our elastic tunneling model calculations has been fully described in LBL-3985 and UCID-3940. Briefly it consists of approximating the one-dimensional, effective mass or "nearly-free" electron potential in a solid by a large number of very small steps. The solution to the Schröedinger equation describing the electron trajectory in the approximation can be found via N 2 × 2 complex matrix multiplications, where N is the number of steps in the approximating potential. By suitable integration of the electron probability flux as a function of electron energy one is then able to arrive at the current density through the given potential.

We have applied this method to the problem of calculating the forward bias currents at the (Cd,Zn)S-Cu_xS junction. Our results support the view that these currents are dominated by the tunneling component of the electron flux and that the rate limiting part of the conduction process is the transfer of an electron from the conduction band of the (Cd,Zn)S to an interface state at the junction. Further testing of this modeling procedure awaits more detailed experimental data.

In order to obtain the data on electrical and electro-optical characteristics of (Cd,Zn)S-Cu_2S heterojunctions required for correlation with the electron microscope studies and with the model calculation results, we have undertaken the design and construction of an apparatus to measure the current-voltage and spectral response characteristics as a function of temperature. The block diagram of the spectral response portion of this apparatus is shown in Fig. 1. The heart of this apparatus is a microprocessor based computer that is programmable in BASIC. An experiment is conducted on this apparatus by simply informing the computer/ controller of the desired experimental conditions and executing the stored program. Since the main program is in BASIC, it is very easy for the experimenter to modify the program--and hence the experiment. A further advantage of the computer is the ability to perform "on-line" processing of the incoming data that allows one, for example, to insure that steady-state conditions are observed.

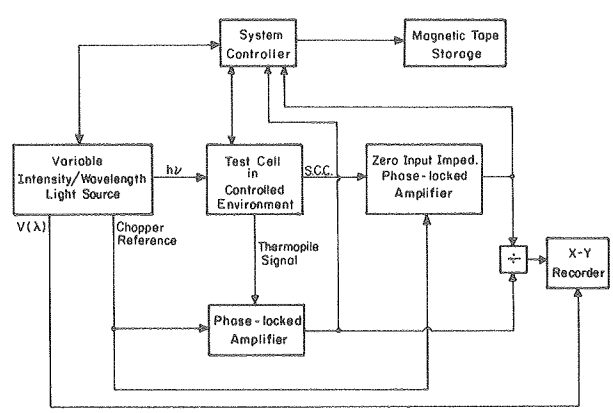

Fig. 1. Photovoltaic cell measurement system spectral response configuration. (XBL 779-6123)

4. RESEARCH PLANS FOR CALENDAR YEAR 1978

Jack Washburn

This continuing study of the Cu_xS-(CdZn)S heterojunction is for the purpose of furthering the understanding of its operation and providing insight for its further development as a solar energy converter. Work will be concentrated in the following three areas:

1) Growth of single crystal mixed-crystal layers of (Cd,Zn)S using the hot wall vapor deposition (HWVD) technique on (111)-GaAs substrates; the effects of substrate preparation and orientation on the growth kinetics and crystalline perfection of the mixed crystal layers; effects of deposition parameters, such as source and substrate temperature, and amount of incorporated zinc sulfide on the mixed crystal layers.

2) Characterization using transmission and scanning electron microscopy, (TEM, SEM-EDAX), and x-ray diffraction (XRD) of the growth defects present in the single crystal layers as well as comparison of these layers with the polycrystalline layers of CdS deposited by other DOE contractors, e.g., University of Delaware Institute of Energy Conversion (IEC), Westinghouse Research Labs and others.

3) Automated spectral response and electrical measurement on both single crystal cells from our program and polycrystalline cells of other labs using either monochromatic or two-beam illumination to give information on dark and illuminated current-voltage characteristics, as a function of temperature (liquid nitrogen-room temperature) yielding I-V-T information on the fundamental processes which affect the efficiency of these cells.

5. 1977 PUBLICATIONS AND REPORTS

Jack Washburn and Associates

LBL Reports

1. T. Peterson, B. Chin and J. Washburn, Recent Results on Mixed Crystal (Cd,Zn)S-Cu_xS Heterojunctions, LBL-5780.

2. T. M. Peterson, B. L. Chin and J. Washburn, Recent Progress in Single Crystal (Cd,Zn)S Thin Film Growth and (Cd,Zn)S-Cu_xS Heterojunction Research: Quarterly Report for March-June 1977, UCID-3940.

3. T. M. Peterson, B. L. Chin, K. Seshan and J. Washburn, Second Quarterly Report of Research of Cu_xS(Cd-Zn)S Photovoltaic Solar Energy Converters.

Papers Presented

1. T. M. Peterson, Description of (CdZn)S-Cu_xS Research Program at Lawrence Berkeley Laboratory, ERDA Semi-Annual Photovoltaic Program Review Meeting, Washington D.C., March 1977.

2. T. M. Peterson, Recent Progress in Research on Single Crystal (CdZn)S-Cu_xS Photovoltaic Cells, AIME 19th Electronic Materials Conference, Ithaca, N.Y., July 1977.

3. T. M. Peterson, Status of (CdZn)S-Cu_xS Single Crystal Cell Research at Lawrence Berkeley Laboratory, DOE Semi-Annual Photovoltaic Program Review Meeting, Golden, CO, October 1977.

VIII.

Appendices

APPENDIX A

MATERIALS AND MOLECULAR RESEARCH DIVISION STAFF - 1977

Principal Investigators	Postdoctoral and Other Scientists	Graduate Students
Neil Bartlett	T. Richardson	R. Biagioni L. Graham E. McCarron B. McQuillan F. Tanzella S. Yeh
Robert Bragg	S. Justi	D. Baker S. Bose S. Ho L. Valero
Leo Brewer	R. Lamoreaux *M. Raymont	G. Bullard *D. Davis D. Goodman B. Lin
John Clarke	C. Chi *W. Goubau M. Ketchen	T. Gamble T. Hsiang M. Ketchen T. Kommers R. Lee S. Lee C. Tesche N. Yeh
Marvin Cohen	*P. Allen *G. Kerker *W. Pickett *A. Zunger	*K. Ho *J. Ihm *S. Louie *M. Yin
Robert Connick	*C. B. Meyer *G. Rosenblatt T. Tam E. Von Deuster	K. Klotter E. Livingston
Lee Donaghey	*A. Lin	T. Anderson
Norman Edelstein J. Conway K. Raymond G. Seaborg A. Streitwieser D. Templeton	*R. Anderson A. Avdeef *J. Baluka *D. Bauer *D. Brown J. Bucher *H. Burghard *C. Carrano *S. Davis *P. Delamoye *W. Harris *E. Juaristi *J. Krupa *C. LeVanda *R. McLaughlin T. O'Donnell *K. Palmer *D. Perry H. Ruben *R. Sarup G. Shalimoff *J. Smart *L. Templeton F. Weitl A. Zalkin	*K. Abu-Dari E. Baker R. Banks *C. Berke *S. Berryhill C. Eigenbrot *G. Girolami G. Halstead J. Hauser T. Hayhurst J. Hildebrand E. (Sibley) Hillard W. Luke B. Lulu *V. Mainz *J. Miller E. Price W. Smith *R. Sofen *E. Strauss *T. Tilley

Principal Investigators	Postdoctoral and Other Scientists	Graduate Students
James Evans	Y. Zundelevich	*C. Natalie *B. Tracy
Douglas Fuerstenau	S. Raghavan	*B. Bilimoria M. Drozd Y. You
Richard Fulrath	D. Biswas *A. Lugassy *Y. Nakamura *M. Nishioka *H. Riegger D. Wang	S. Chandratreya S. Chiang P. Flaitz S. Hewett D. Miller V. Nagesh B. Powell P. Sharps J. Wallace D. Wang
Warren Garrison	M. Jayko H. Sokol	
Charles B. Harris	*A. Campion *E. Liu	A. Burns J. Chao P. Cornelius A. Gallo *S. George M. Lewellyn *S. Marks H. Robota R. Shelby M. Tarrasch *M. Vernon *P. Whitmore D. Wroge D. Zwemer
Carson Jeffries	*A. Hansen R. Markiewicz R. Westervelt	B. Black J. Culbertson J. Furneaux S. Kelso R. Westervelt
Harold Johnston		B. Bicknell P. Connell J. Girman *R. Hampton M. Kowalczyk D. Littlejohn *K. Lubic F. Magnotta *W. Marinelli H. Nelson J. Podolske G. Selwyn *S. Solomon *C. Truesdale
William Jolly	*H. Chen *T. Lee	*S. Avanzino A. Bakke T. Briggs J. Reed D. Yang
George Jura	K. Kim	

Principal Investigators	Postdoctoral and Other Scientists	Graduate Students
Yuan T. Lee	*P. Casavecchia	*S. Anderson
	M. Coggiola	C. Becker
	*M. Faubel	R. Buss
	E. Grant	*S. Bustamente
	*T. Hirooka	*L. Carlson
	K. Shobatake	*S. Ceyer
	*P. Tiedemann	*C. Hayden
	J. Valentini	C. Kahler
		*D. Krajnovich
		*P. Kronebush
		*C. Ng
		P. Schulz
		*S. Sibener
		R. Sparks
		D. Trevor
		*M. Vernon
		A. Wang
Alan Levy	*W. Coons	L. Brass
	*I. Cornet	P. Doyle
	I. Finnie	T. Foerster
	*M. Holt	B. Gordon
	V. Nagarajan	H. Hirano
	E. Ossio	J. Keller
	D. Rao	J. Laitone
	*F. Ravitz	P. Liang
	*G. Sheldon	R. Mayville
	*J. Stringer	R. Miner
	W. Toutolmin	W. Piercy
	*W. Worrell	F. Pourahmadi
	G. Zambelli	M. Yeung
		W. Yeung
Bruce Mahan		R. A. Davis
		F. Grieman
		S. Hansen
		J. Kleckner
Richard Marrus	H. Gould	
	P. Mohr	
William Miller	*C. W. McCurdy	J. Adams
	*H. Morgner	B. Garrett
	*M. Quack	A. Isaacson
		B. Skuse
		R. Stratt
C. Bradley Moore	*A. Albala	M. Berman
	*D. Douglas	H. Dai
	*S. Harris	*C. Dasch
	*R. Hedges	*P. Ho
	A. Kung	*F. Hovis
	*N. Nogar	C. Mei
		J. Weisshaar
		J. Wiesenfeld
		*J. Wong
		L. Young
		M. Zughul

Principal Investigators	Postdoctoral and Other Scientists	Graduate Students
J. W. Morris, Jr.	K. Hanson	S. Altintas
	*S. Hooker	K. Chang
	S. Hwang	S. Chen
	*A. Khachaturyan	B. Fultz
	*D. Klahn	D. Grivas
	F. Nabarro	*D. Gutzler
	*M. Niikura	M. Hong
	*C. Syn	*S. Hwang
		J. Kim
		A. Ma
		K. Mahin
		E. Pundarika
		J. Sanchez
		D. Wedge
		D. Williams
Earl Muetterties		*C. Friend
Rolf Muller	*J. Winnick	*B. Dissaux
		K. Hanson
		R. Peters
		J. Riggs
		C. Smith
Rollie Myers		*B. Bobsein
		W. Glad
		D. Lindner
John Newman		P. Fedkiw
		C. Law
		P. Pierini
		R. Pollard
		J. Trainham
		G. Trost
		D. Ullman
		R. White
Donald Olander	*M. Balooch	D. Dooley
	R. Behrens	*M. Farnaam
	*A. Srivastava	K. Kim
		S. Shann
		D. Sherman
		C. Tsai
		R. Yang
Earl Parker Victor Zackay	*D. Bhandarkar	L. Brass
	*M. Bhat	M. Carlson
	*A. Gorum	M. Castro-Cedeno
	*M. Holt	J. Conn
	R. Horn	P. Doyle
	R. Imbsen	W. Garrison
	S. Jahanmir	J. Giovanola
	J. Kallend	B. Gordon
	A. Levy	G. Haddick
	V. Nagarajan	H. Hirano
	*W. Owen	N. Kar
	V. Pujari	R. Kar
	D. Rao	J. Keller
	*F. Ravitz	W. Kurtz
	*R. Ritchie	J. Laitone
	*G. Sheldon	T. Lechtenberg
	*J. Stringer	R. Mayville
	E. Tarapore	R. Miner
	W. Toutolmin	Y. Mishima
	*W. Worrell	A. Misra
		R. Mundhe
		*C. Nealley
		W. Piercy
		D. Swain

Principal Investigators	Postdoctoral and Other Scientists	Graduate Students
Earl Parker Victor Zackay (Cont'd)		L. Thompson L. Tran R. Turner K. Wang J. Wert K. White M. Yeung
Joseph Pask	*P. Dokko *V. Draper W. Kriven *R. Langston *Y. Nurishi *P. Spencer	*N. Cassens G. Holmquist S. Johnson A. Rana *M. Sacks *P. Spencer S. Tso
Norman Phillips	G. Brodale J. Ho E. Hornung	J. Boyer W. Fogle B. Krusor
Milton Pickus	J. Wang	K. Douglas E. Kannatey-Asibu, Jr. T. Lam G. MacLeod M. Malekzadeh J. McCormick A. Noman D. Nordin G. Pech B. Phung G. Quinn C. Rutan C. Steinmetz
Alexander Pines	J. Ackerman H. Edzes S. Emid *E. Hahn S. Hsi *B. Lamotte Z. Luz *D. Ruben *K. Utsunomiya *S. Wolfe H. Zimmerman	B. Bicknell L. Brodsky G. Drobny R. Eckman J. Murdoch *S. Sinton L. Sterna *J. Tang *W. Warren C. Weitekamp D. Wemmer
Kenneth Pitzer	W. Ermler Y. Lee	Y. Lee P. Rogers
John Prausnitz		W. Whiting
†Otto Redlich		
Paul Richards	*C. Andriesse *J. Claassen *T. Iri *A. Kazanskii N. Nishioka *D. Woody	*R. Bailey J. Bonomo S. Chiang *M. Hueschen D. Lambert S. McBride T. Shen
Henry Schaefer		B. Brooks *C. Dykstra J. Meadows W. Swope S. Ungemach

Principal Investigators	Postdoctoral and Other Scientists	Graduate Students
Alan Searcy	*R. Berger *D. Beruto *A. Buchler D. Meschi E. (Knauf) Powell J. Roberts	T. Dai J. Ewing M. Huang N. Jacobson G. Knutsen E. (Knauf) Powell T. Reis *S. Roche R. Shukla
Y. Ron Shen	D. Bethune T. Bischofberger *K. Chu *J. Davies *F. DeMartini *P. Salvi	C. Chen T. Chiang *P. Hislop R. Hsu A. Jacobson R. Smith A. Sudbo
David A. Shirley	H. Basch *O. Dabbousi *C. DeLange *B. Garrison W. Heppler B. Lu *P. Perfetti *V. Rehn S. Rice *T. Sasaki J. Stohr G. Thornton *N. Winograd	G. Apai R. F. Davis D. Denley S. Kevan K. Mills *E. Pellach F. Poliakoff *J. Pollard R. Rosenberg *D. Rosenblatt *S. Southworth P. Wehner *J. White M. White R. Williams
Howard Shugart E. Commins	S. Chu T. Hadeishi M. Prior	P. Bucksbaum R. Conti R. Knight D. Neuffer *L. Schipper
Gabor Somorjai A. Bell J. Smart P. Vollhardt	*L. Atanasoska R. Bastasz *J. Biberian *J. Blakely *D. Dwyer J. Hemminger *A. Jablonski L. Kesmodel D. Mitchell *Y. Nihei *S. Palfi *M. Salmeron *B. Sexton *W. Siekhaus *I. Toyoshima K. Urabe H. Wise *K. Yoshida	W. Aalbersberg S. Abensohn D. Castner Y. Chung R. Colborn C. Curtis *S. Davis L. Dubois J. Ekerdt L. Firment J. Fritch R. Funk R. Gale W. Gillespie W. Guthrie R. Hillard *A. Huston S. Kellner *R. Koestner W. Lo G. Low B. Pinsky J. Robbins A. Sievert C. Smith *J. Sokol P. Stair *F. Wagner

Principal Investigators	Postdoctoral and Other Scientists	Graduate Students
Gareth Thomas	*D. Clarke	J. Ahn
	*B. Francis	*Y. Belli
	R. Gronsky	M. Carlson
	*P. Karnthaler	P. Costello
	J. Koo	*U. Dahmen
	*O. Krivanek	J. Koo
	*V. Kurdjumov	K. Kubarych
	R. Mishra	B. Narasimha Rao
	*P. Rez	M. Okada
	*R. Sinclair	T. O'Neill
	*P. Swann	T. Rabe
	K. Westmacott	T. Roth
		T. Shaw
		B. Steinberg
		D. Swain
		*P. Williams
		C. Wu
		*M. Young
Charles W. Tobias	R. Atanasoski	A. Kindler
	M. Jaksic	H. Law
		G. Prentice
		D. Roha
		P. Sides
		S. Yu
Jack Washburn	T. Peterson	*P. Angelides
	J. Punglia	B. Chin
	K. Seshan	R. Drosd
	*A. Srivastava	T. Huo
		C. Lampert
		H. Ling
		T. Mowles
Kenneth Westmacott	*J. Laval	*A. Forouhi
		M. Sung

MMRD SUPPORT STAFF

C. Peterson - Division Administrator

Administrative Staff

M. Janzen - Staff Assistant - Administration
E. Skrydlinski - Staff Assistant - Personnel
S. Stewart - Staff Assistant - Purchasing

Clerical and Secretarial Staff

K. Altes
J. Amoroso
L. Betters
J. Boehlert
G. Brazil
M. Chin
§ A. Czerwinski
C. Davis
J. Denney
C. Eaton
L. Fernander
C. Hacker
J. Ingraham
L. Irvin
K. Janes
D. Jeffery
S. Jennings
R. Jones
Y. Kim
K. Krushwitz
V. Lam
§ M. Larsen
M. Leullier
R. McCollough
V. Narasimhan
C. Payne
M. Penton
§ A. Ramirez
B. Rancatore
M. Schonborn
M. Stefonetti
P. Swain
E. Walker
A. Weightman
C. Yoder

Technical Staff

§ E. Edwards - Mechanical Coordinator
W. Toutolmin - Technical Coordinator

P. Adler
D. Ambrose
S. Bandel
§ G. Baum
R. Bellman
G. Boyd
M. Brass
T. Bregante
§ M. Brown
R. Carr
K. Chin
D. Dietderich
J. Dillon
E. Dittmar
E. Elliott
K. Evans
J. Fattaruso
B. Fisher
J. Frease
R. Freitag
J. Frischkorn
L. Galovich
R. Garriga
W. Giba
L. Gooden
C. Gosnell
J. Hanson
H. Harrell
G. Hirsch
P. Hislop
J. Holthuis
L. Holton
T. Howard
J. Jachetta
J. Jacobsen
N. Jacobson
§ L. Johnson
M. Johnson
D. Johnston
D. Jurica
W. Koide
E. Kostlan
E. Kozak
§ D Krieger
S. Lee
D. Leong
K. Leong
G. Lesh
V. Lewis
§ R. Lindberg
M. Lindley
R. Lucchese
J. Maasberg
J. Maccoun
D. MacDonald
G. Martin
R. Mayer
J. Mori
§ D. Newhart
H. Okamoto
K. Pedrotti
C. Phillips
§ B. Pope
J. Randall
J. Remer
J. Reynolds
§ H. Riebe
K. Sakai
H. Sawhill
A. Schwartzman
J. Sender
§ J. Severns
A. Sferrazza
D. Shirley, Jr.
L. Sindelar
B. Synder
§ P. Stagnaro
A. Tarafder
C. Thom
E. Tobias
M. Trenary
P. Trevor
D. Wedge
H. Weeks
J. Wong
§ W. Wong
J. Wu
G. Wang
P. Yarnold
Y. Yen

---

* Participant Status
† Emeritus
§ LBL Support Staff

APPENDIX B

SURFACE SCIENCE AND CATALYSIS SCIENCE SEMINARS

Date	Speaker and Affiliation	Seminar Title
1-19-77	Dr. C. B. Duke Xerox Webster Research Center Rochester, NY	The Structure of Solid Surfaces
1-21-77	Prof. T. Rhodin Dept. of Applied Physics Cornell University	Chemisorption and Reaction of Molecular Gases and Olefins on Iridium Surfaces
1-26-77	Prof. E. Muetterties Miller visiting Professor Dept. of Chemistry University of California, Berkeley	Metal Clusters in Catalysis
2-2-77	Prof. J. McTague Dept. of Chemistry University of California Los Angeles	Structure, Dynamics, and Phase Transitions in Physisorbed Monolayers
2-3-77	Prof. G. J. Lapeyre Dept. of Physics Montana State University	Angle-Resolved Photoemission of Adsorbates on Ni(100) and W(100) Surfaces
2-4-77	Dr. J. Rabo Union Carbide Research Tarrytown, NY	The Role of Zeolites as Solid Electrolytes in Hydrocarbon Catalysis
2-9-77	Prof. J. Halpern Dept. of Chemistry University of Chicago	Aspects of the Catalytic Chemistry of Metal-Oxygen Complexes
2-16-77	Prof. J. R. Katzer Dept. of Chemical Engineering University of Delaware	Kinetics of Quinoline Hydrodenitrogenation
2-23-77	Dr. G. E. Langlois Chevron Research Company	Synthetic Fuels--Prospects and Problems
2-25-77	Prof. L. Brockway Dept. of Chemistry University of Michigan	Surface Oxidation of Copper Single Crystals
3-2-77	Prof. J. R. Katzer Dept. of Chemical Engineering University of Delaware	Infrared Spectroscopy Investigation of the Absorption and Reactions of SO_2 on CuO
3-9-77	Prof. W. E. Spicer Stanford Electronics Laboratories	Recent Studies of Electronics and Structural Aspects of Adsorption and Surface Reactions
4-6-77	Prof. A. T. Hubbard Dept. of Chemistry University of California Santa Barbara	Electrochemistry of Chemisorbed Molecules
4-8-77	Prof. E. Muetterties Miller visiting Professor Dept. of Chemistry University of California Berkeley	Mechanistic Features of Homogeneous Catalytic Reactions

Date	Speaker and Affiliation	Seminar Title
4-13-77	Dr. J. D. E. McIntyre Bell Laboratories	Optical Spectroscopy of Electrocatalyst Surfaces
4-15-77	Prof. E. Muetterties Miller visiting Professor Dept. of Chemistry University of California Berkeley	Introduction to Metal Cluster Chemistry
4-20-77	Prof. W. A. Goddard, III Dept. of Chemistry California Institute of Technology	Theoretical Studies of Chemisorption
5-4-77	Prof. M. Boudart Dept. of Chemical Engineering Stanford University	Single and Multiple Sites in Catalysis by Metals and Alloys
5-11-77	Prof. R. J. Madix Dept. of Chemical Engineering Stanford University	Reaction Kinetics and Mechanisms on Single-Crystal Surfaces
6-3-77	Prof. A. A. Maradudin University of California Irvine	Dynamical Properties of Solid Surfaces
7-29-77	Prof. M. Bienfait Dept. of Physics University of Marseilles Marseilles, France	Zero Order Adsorption or Desorption Kinetics: Xenon Covered (0001) Graphite
8-9-77	Prof. H. Ibach Institut fur Grenzflachenforschung und Vakuumphysik Julich, W. Germany	Vibrational Spectroscopy from Atoms and Molecules on Surfaces
10-5-77	Prof. Alex Bell Dept. of Chemical Engineering University of California Berkeley, and MMRD-LBL	The Search for Novel Coal Liquefaction Catalysts
10-12-77	Dr. R. C. Brundle IBM Research San Jose, California	XPS, UPS, and LEED Studies of Adsorption (CO,O_2) and Oxidation of Single Crystal and Polycrystalline Metal Surfaces (Cu,Co,Fe)
10-19-77	Dr. L. L. Kesmodel MMRD-LBL	Quantitative Studies of Surface Structure with Low-Energy Electron Diffraction
10-26-77	Dr. D. W. Blakely Chevron Research Company Richmond, California	Atomic Structure Study of Ni-Mo/γAl_2O_3 Catalysts by Extended X-ray Absorption Fine Structure (EXAFS) Analysis
11-1-77	Prof. A. C. Zettlemoyer Sinclair Laboratory Lehigh University Bethlehem, Pennsylvania	Four-Phase Systems
11-2-77	Prof. L. M. Falicov Dept. of Physics University of California Berkeley	Surface Physics: A Personal Overview
11-9-77	Dr. S. Hagstrom Xerox Laboratories Palo Alto, California	Oxidation Studies on Single Crystal Faces of Aluminum
11-16-77	Prof. D. R. Frankl Pennsylvania State University	Diffraction and Selective Adsorption of Atomic Beams

Date	Speaker and Affiliation	Seminar Title
11-23-77	Dr. A. West Sandia Laboratories Livermore, California	Engineering Applications of Surface Analysis Techniques
11-28-77	Dr. H. H. Madden, Jr. Sandia Laboratories Albuquerque, New Mexico	Search for Valence Band Information in the Auger Spectra from Lithium and Copper
11-30-77	Dr. J. Yates, Jr. National Bureau of Standards	Surface Chemistry: A Molecular View
12-6-77	Dr. A. Novrotski Dept. of Chemistry Arizona State University Tempe, Arizona	Thermodynamic Studies of High Pressure Silicates
12-7-77	Dr. R. Bastasz Sandia Laboratories Livermore, California	Ion Impact Desorption of Adsorbates on Metal Surfaces
12-8-77	Dr. H. Wise Stanford Research Institute Menlo Park, California	Solid State Defects and Catalytic Activity
12-14-77	Dr. F. Lytle Boeing Company Seattle, Washington	Investigation of the Structure of Heterogeneous Catalysis by the Extended X-Ray Absorption Fine Structure (EXAFS) Technique

GPO 794-570/257

This report was done with support from the Department of Energy. Any conclusions or opinions expressed in this report represent solely those of the author(s) and not necessarily those of The Regents of the University of California, the Lawrence Berkeley Laboratory or the Department of Energy.